University of Belgrade
Technical Faculty in Bor
Mining and Metallurgy
Institute Bor

56th International October Conference on Mining and Metallurgy

PROCEEDINGS

Editors:
Ljubiša Balanović
Dejan Tanikić

IOC 2025
International October Conference

22-25 October 2025,
Bor Lake, Serbia

University of Belgrade
Technical Faculty in Bor
Mining and Metallurgy
Institute Bor

56th International October Conference on Mining and Metallurgy

PROCEEDINGS

Editors:
Ljubiša Balanović
Dejan Tanikić

IOC 2025
International October Conference

22-25 October 2025,
Bor Lake, Serbia

PROCEEDINGS,

56th INTERNATIONAL OCTOBER CONFEERNCE

on Mining and Metallurgy

Editors:

Prof. dr Ljubiša Balanović

Prof. dr Dejan Tanikić

University of Belgrade - Technical Faculty in Bor

Technical Editors:

MSc Miljan Marković

MSc Kristina Božinović

University of Belgrade - Technical Faculty in Bor

Proceedings cover design:

MSc Aleksandar Cvetković,

University of Belgrade - Technical Faculty in Bor

Publisher: University of Belgrade - Technical Faculty in Bor

For the publisher: Dean Prof. dr Dejan Tanikić

Circulation: 200 copies

Publication Place, Year: Bor, 2025

Printed by "*GRAFIKA GALEB DOO" NIŠ, 2025*

CIP - Каталогизација у публикацији Народна библиотека Србије, Београд

622(082)(0.034.2)
669(082)(0.034.2)

INTERNATIONAL October Conference on Mining and Metallurgy (56 ; 2025 ; Bor Lake)

Proceedings [Elektronski izvor] / 56th International October Conference on Mining and Metallurgy - IOC 2025, 22-25 October, 2025, Bor Lake, Serbia ; [organized by] University of Belgrade, Technical Faculty in Bor and Mining and Metallurgy Institute Bor ; editors Ljubiša Balanović, Dejan Tanikić. - Bor : University of Belgrade, Technical Faculty, 2025 (Niš : Grafika Galeb). - 1 USB fleš memorija ; 1 x 1 x 5 cm

Sistemski zahtevi: Nisu navedeni. - Nasl. sa naslovne strane dokumenta. - Tiraž 200. - Preface / Ljubiša Balanović. - Bibliografija uz svaki rad.

ISBN 978-86-6305-164-5

a) Рударство -- Зборници b) Металургија -- Зборници

COBISS.SR-ID 177493257

Bor Lake, Serbia, October 22-25, 2025

The conference is financially supported by
The Ministry of Science, Technological
Development and Innovation
of the Republic of Serbia

Platinum Donors

HBIS SERBIA

ZIJIN
SERBIA ZIJIN MINING

Gold Sponsor

DPM METALS

Gold Donors

ZIJIN
SERBIA ZIJIN COPPER DOO BOR

Sevojno
VALJAONICA BAKRA
COPPER MILL

Silver Donor

MC LABOR

Exhibitions

Donor of official opening

Epiroc

Friends of the Conference

MESSER
Gases for Life

CHINA-SERBIA
JOINT LABORATORY
ON GREEN STEEL
MANUFACTURING
HBIS and University of Belgrade

THE FOUNDATION
'B.SC. ENG. BOŠKO INJAC'

SCIENTIFIC COMMITTEE

Prof. Dr Dejan Tanikić, University of Belgrade, Technical Faculty in Bor (Serbia) - president
Prof. Dr Nada Štrbac, University of Belgrade, Technical Faculty in Bor (Serbia) - vice-president
Prof. Dr Radoje Pantović, University of Belgrade, Technical Faculty in Bor (Serbia) - vice-president
Dr Ana Kostov, Mining and Metallurgy Institute Bor (Serbia) - vice-president

Prof. Dr Milan Antonijevic, University of Belgrade, Technical Faculty in Bor (Serbia)
Prof. Dr Hasan Avdušinović, University of Zenica, Faculty of Engineering and Natural Sciences (Bosnia and Herzegovina)
Dr Ana Alil, University of Belgrade, Institute of Chemistry, Technology and Metallurgy (Serbia)
Prof. Dr Ljubiša Balanović, University of Belgrade, Technical Faculty in Bor (Serbia)
Prof. Dr Farzet Bikić, University of Zenica, Faculty of Engineering and Natural Sciences (Bosnia and Herzegovina)
Prof. Dr Grozdanka Bogdanović, University of Belgrade, Technical Faculty in Bor (Serbia)
Prof. Dr Pavel Broz, Masaryk University, Faculty of Science, Department of Chemistry (Czech Republic)
Dr Mile Bugarin, Mining and Metallurgy Institute Bor (Serbia)
Prof. Dr Ilhan Bušatlić, University of Zenica, Faculty of Engineering and Natural Sciences (Bosnia and Herzegovina)
Prof. Dr Nicanor Cimpoesu, Gheorghe Asachi Technical University from Iasi (Romania)
Prof. Dr Mira Cocić, University of Belgrade, Technical Faculty in Bor (Serbia)
Dr Vladan Ćosović, University of Belgrade, Institute of Chemistry, Technology and Metallurgy (Serbia)
Prof. Dr Pasquale D. Cavaliere, University of Salento, Department of Innovation Engineering (Italy)
Prof. Dr Kemal Delijić, University of Montenegro, Faculty of Metallurgy and Technology (Montenegro)
Prof. Dr Nikhil Dhawan, Indian Institute of Technology, Department of Metallurgical and Materials Engineering (India)
Prof. Dr Savas Dilibal, Istanbul Gedik University, Department of Mechatronics Engineering (Turkey)
Prof. Dr Aleksandar Dimitrov, Ss. Cyril and Methodius University in Skopje, Faculty of Technology and Metallurgy (Republic of North Macedonia)
Prof. Dr Natalija Dolić, University of Zagreb, Faculty of Metallurgy (Croatia)
Prof. Dr Yong Du, Central South University Changsha (China)
Prof. Dr Luis Filipe Malheiros, University of Porto, Faculty of Engineering (Portugal)
Prof. Dr Almaida Gigović-Gekić, University of Zenica, Faculty of Engineering and Natural Sciences (Bosnia and Herzegovina)
Prof. Dr Mirko Gojić, University of Zagreb, Faculty of Metallurgy (Croatia)
Prof. Dr Adam Grajcar, Silesian University of Technology, Department of Engineering Materials and Biomaterials (Poland)
Prof. Dr Vesna Grekulović, University of Belgrade, Technical Faculty in Bor (Serbia)
Prof. Dr Daniela Grigorova, University of Chemical Technology and Metallurgy, Faculty of Metallurgy and Material Science (Bulgaria)
Prof. Dr Stojan Groudev, University of Mining and Geology "Saint Ivan Rilski" (Bulgaria)
Prof. Dr Dragoslav Gusković, University of Belgrade, Technical Faculty in Bor (Serbia)
Prof. Dr Tomaš Havlik, Institute of Recycling Technologies, Faculty of Materials, Metallurgy and Recycling, Technical University of Kosice (Slovakia)
Prof. Dr Karl Heinz Spitzer, Technical University of Clausthal, Institute for Metallurgy (Germany)
Dr Slavomír Hredzák, Institute of Geotechnics of the Slovak Academy of Sciences (Slovakia)
Prof. Dr Svetlana Ivanov, University of Belgrade, Technical Faculty in Bor (Serbia)
Prof. Dr Dejan Ivezić, University of Belgrade, Faculty of Mining and Geology (Serbia)
Mirjam Jan-Blažić, Slovenian Foundryen Society (Slovenia)
Prof. Dr Dominika Jendrzejczyk-Handzlik, AGH University of Science and Technology in Kraków, Faculty of Non-Ferrous Metals (Poland)
Prof. Dr Željko Kamberović, University of Belgrade, Faculty of Technology and Metallurgy (Serbia)
Prof. Dr György Kaptay, University of Miskolc, Faculty of Materials and Metallurgical Engineering (Hungary)
Dr Vladan Kašić, Institute for Technology of Nuclear and other Mineral Raw Materials (Serbia)

Prof. Dr Vladislav Kecojević, West Virginia University (USA)
Dr Dragan Komljenović, Research Institute, Hydro-Québec (Canada)
Prof. Dr Komnitsas Konstantinos, Technical University of Crete, School of Mineral Resources Engineering (Greece)
Prof. Dr Borut Kosec, University of Ljubljana, Faculty of Natural Science and Engineering (Slovenia)
Prof. Dr Maria Krasteva, University of Chemical Technology and Metallurgy, Faculty of Metallurgy and Material Science (Bulgaria)
Prof. Dr Vladimir Krstić, Functional Materials Manufacturing, Inc. (Canada)
Prof. Dr Stefan Kuvendžiev, Ss. Cyril and Methodius University in Skopje, Faculty of Technology and Metallurgy (Republic of North Macedonia)
Prof. Dr Silvia Lavrova-Popova, University of Chemical Technology and Metallurgy, Faculty of Chemical and Systems Engineering (Bulgaria)
Dr Milenko Ljubojev, Engineering Academy of Serbia (Serbia)
Prof. Dr Xuewei Lv, Chongqing University, School of Materials Science and Engineering (China)
Prof. Dr Nedeljko Magdalinović, Engineering Academy of Serbia (Serbia)
Prof. Dr Dragan Manasijević, University of Belgrade, Technical Faculty in Bor (Serbia)
Prof. Dr Vaso Manojlović, University of Belgrade, Faculty of Technology and Metallurgy (Serbia)
Prof. Dr Boštjan Markoli, University of Ljubljana, Faculty of Natural Science and Engineering (Slovenia)
Dr Branislav Marković, Institute for Technology of Nuclear and other Mineral Raw Materials (Serbia)
Prof. Dr Desimir Marković, University of Belgrade, Technical Faculty in Bor (Serbia)
Prof. Dr Ivana Marković, University of Belgrade, Technical Faculty in Bor (Serbia)
Prof. Dr Nobuyuki Masuda, Tokyo University of Science, Faculty of Advanced Engineering (Japan)
Prof. Dr Jožef Medved, University of Ljubljana, Faculty of Natural Science and Engineering (Slovenia)
Vladan Mihailović, Executive Director for Production at HBIS Serbia (Serbia)
Prof. Dr Ivan Mihajlović, Faculty of Mechanical Engineering, University of Belgrade (Serbia)
Dr Dragan Milanović, Mining and Metallurgy Institute Bor (Serbia)
Prof. Dr Snežana Milić, University of Belgrade, Technical Faculty in Bor (Serbia)
Prof. Dr Dragan Milovanović, University of Belgrade, Faculty of Mining and Geology (Serbia)
Prof. Dr Duško Minić, University of Priština, Faculty of Technical Sciences (Serbia)
Prof. Dr Srba Mladenović, University of Belgrade, Technical Faculty in Bor (Serbia)
Prof. Dr Adnan Mujkanović, University of Zenica, Faculty of Engineering and Natural Sciences (Bosnia and Herzegovina)
Prof. Dr Cornelia Muntean, Politehnica University of Timisoara (Romania)
Prof. Dr Tatiana N. Aleksandrova, Saint Petersburg Mining University, Department of Mineral Processing (Russia)
Prof. Dr Goran Načevski, Ss. Cyril and Methodius University in Skopje, Faculty of Technology and Metallurgy (Republic of North Macedonia)
Prof. Dr Adina Negrea, Politehnica University of Timisoara (Romania)
Prof. Dr Irena Nikolić, University of Montenegro, Faculty of Metallurgy and Technology (Montenegro)
Prof. Dr Đorđe Nikolić, University of Belgrade, Technical Faculty in Bor (Serbia)
Prof. Dr Daniel Ogochukwu Okanigbe, Tshwane University of Technology, Department of Extractive Metallurgy and Mineral Processing (South Africa)
Prof. Dr Dušan Oráč, Institute of Recycling and Environmental Technologies, Faculty of Materials, Metallurgy and Recycling, Technical University of Kosice (Slovakia)
Prof. Emeritus Dr. Sc. Mirsada Oruč, University of Zenica, Faculty of Engineering and Natural Sciences (Bosnia and Herzegovina)
Prof. Dr Dimitris Panias, National Technical University of Athens, School of Mining Engineering and Metallurgy (Greece)
Prof. Dr Perica Paunović, Ss. Cyril and Methodius University in Skopje, Faculty of Technology and Metallurgy (Republic of North Macedonia)
Prof. Dr Mitar Perušić, University of East Sarajevo, Faculty of Technology Zvornik (Bosnia and Herzegovina)
Prof. Dr Batrić Pešić, University of Idaho, College of Engineering (USA)
Prof. Dr Marija Petrović Mihajlović, University of Belgrade, Technical Faculty in Bor (Serbia)
Prof. Dr Miljana Popović, University of Belgrade, Faculty of Technology and Metallurgy (Serbia)
Prof. Dr Milena Premović, University of Priština, Faculty of Technical Sciences (Serbia)
Prof. Dr Charikleia Prochaska, Aristotle University of Thessaloniki, Faculty of Sciences, School of Chemistry, Division of Chemical Technology and Industrial Chemistry (Greece)

Prof. Dr Miljana Radivojević, Institute of Archaeology, University College London (UK)
Prof. Dr Velimir Radmilović, Serbian Academy of Sciences and Arts (Serbia)
Prof. Dr Milan Radovanović, University of Belgrade, Technical Faculty in Bor (Serbia)
Prof. Dr Nenad Radović, University of Belgrade, Faculty of Technology and Metallurgy (Serbia)
Prof. Dr Žarko Radović, University of Montenegro, Faculty of Metallurgy and Technology (Montenegro)
Prof. Emeritus Karlo Raić, University of Belgrade, Faculty of Technology and Metallurgy (Serbia)
Prof. Dr Mirjana Rajčić Vujasinović, University of Belgrade, Technical Faculty in Bor (Serbia)
Dr Andrei Rotaru, University of Craiova, Department of Chemical Thermodynamics (Romania)
Prof. dr. eng. Elena Scutelnicu, "Dunarea de Jos" University of Galati, Faculty of Engineering (Romania)
Prof. Dr Snežana Šerbula, University of Belgrade, Technical Faculty in Bor (Serbia)
Dr Rustam Sharipov, JSC "Kazakh-British Technical University (Kazakhstan)
Dr Miroslav Sokić, Institute for Technology of Nuclear and other Mineral Raw Materials (Serbia)
Prof. Dr Jovica Sokolović, University of Belgrade, Technical Faculty in Bor (Serbia)
Prof. Dr Petr Solozhenkin, Russian Academy of Sciences (Russia)
Prof. Dr Dimitriu Sorin, Polytechnic University of Bucharest (Romania)
Dr Jasna Stajić Trošić, University of Belgrade, Institute of Chemistry, Technology and Metallurgy (Serbia)
Prof. Dr Velizar Stanković, University of Belgrade, Technical Faculty in Bor (Serbia)
Prof. Dr Rodoljub Stanojlović, University of Belgrade, Technical Faculty in Bor (Serbia)
Dr Jasmina Stevanović, University of Belgrade, Institute of Chemistry, Technology and Metallurgy (Serbia)
Dr Zoran Stevanović, Mining and Metallurgy Institute Bor (Serbia)
Prof. Dr Saša Stojadinović, University of Belgrade, Technical Faculty in Bor (Serbia)
Dr Srećko Stopić, RWTH Aachen University, Faculty of Georesouces and Materials Engineering (Germany)
Prof. Dr Jasmin Suljagić, University of Tuzla, Faculty of Technology (Bosnia and Herzegovina)
Dr Zhongmei Sun, Zijin Mining and Metallurgy Research Institute (China)
Dr Nadežda Talijan, Academy of Engineering Science of Serbia (Serbia)
Prof. Dr Jarmila Trpčevská, Faculty of Materials, Metallurgy and Recycling, Technical University of Kosice (Slovakia)
Dr Biserka Trumić, Mining and Metallurgy Institute Bor (Serbia)
Prof. Dr Milan Trumić, University of Belgrade, Technical Faculty in Bor (Serbia)
Dr Walter Valery, University of Queensland (Australia)
Prof. Dr Dmitry Vasilyev, A.A.Baikov Institute of Metallurgy and Materials Science, Russian Academy of Sciences (Russia)
Prof. Dr Iveta Vaskova, Faculty of Materials, Metallurgy and Recycling, Technical University of Kosice (Slovakia)
Prof. Dr Petrica Vizureanu, Gheorghe Asachi Technical University from Iasi (Romania)
Prof. Dr Tatjana Volkov-Husović, University of Belgrade, Faculty of Technology and Metallurgy (Serbia)
Prof. Dr Maja Vončina, University of Ljubljana, Faculty of Natural Science and Engineering (Slovenia)
Prof. Dr Milovan Vuković, University of Belgrade, Technical Faculty in Bor (Serbia)
Prof. Dr Nenad Vušović, University of Belgrade, Technical Faculty in Bor (Serbia)
Prof. Dr Kaikun Wang, School of Materials Science and Engineering, University of Science and Technology Beijing (China)
Prof. Dr Ridvan Yamanoglu, Kocaeli University, Engineering Faculty, Metallurgical and Materials Engineering Department (Turkey)
Prof. Dr Onuralp Yucel, Istanbul Technical University, Faculty of Chemical and Metallurgical Engineering (Turkey)
Prof. Dr Zdenka Zovko Brodarac, University of Zagreb, Faculty of Metallurgy (Croatia)

ORGANIZING COMMITTEE

Prof. Dr Ljubiša Balanović, Full Professor (UB TF Bor) – president
Prof. Dr Radoje Pantović, Full Professor (UB TF Bor) – vice-president
Dr Ana Kostov, Principal Research Fellow (MMI Bor) – vice-president
Dr Ivana Marković, Full Professor (UB TF Bor)
Prof. Dr Jovica Sokolović, Full Professor (UB TF Bor)
Dr Maja Nujkić, Associate Professor (UB TF Bor)
Dr Žaklina Tasić, Associate Professor (UB TF Bor)
Dr Milan Gorgievski, Full Professor (UB TF Bor)
Dr Ana Radojević, Associate Professor (UB TF Bor)
Dr Тања Калиновић, Associate Professor (UB TF Bor)
Dr Dejan Petrović, Associate Professor (UB TF Bor)
Dr Jelena Ivaz, Associate Professor (UB TF Bor)
Dr Anđelka Stojanović, Associate Professor (UB TF Bor)
Dr Uroš Stamenković, Assistant Professor (UB TF Bor)
Dr Jasmina Petrović, Assistant Professor (UB TF Bor)
Dr Vladimir Nikolić, Assistant Professor (UB TF Bor)
Milan Nedeljković, Assistant (UB TF Bor)
Milijana Mitrović, Assistant (UB TF Bor)
Marina Marković, Assistant (UB TF Bor)
Kristina Božinović, Assistant (UB TF Bor)
Milica Zdravković, Assistant (UB TF Bor)
Miljan Marković, Assistant (UB TF Bor)
Pavle Stojković, Assistant (UB TF Bor)
Avram Kovačević, Assistant (UB TF Bor)
Sandra Vasković, English Lecturer (UB TF Bor)
Oliver Marković, IT service (UB TF Bor)
Bojana Janković, Accountant (UB TF Bor)

LIST OF REVIEWERS

Prof. Dr Ridvan Yamanoglu, Kocaeli University (Turkey)
Prof. Dr Peizhong Feng, School Materials Science and Physics, China University of Mining and Technology (China)
Prof. Dr Srećko Stopić, IME Process Metallurgy and Metal Recycling, RWTH Aachen University (Germany)
Prof. Dr Nebojiša Tadić, University of Montenegro - Faculty of Metallurgy and Technology (Montenegro)
Dr Aleksandra Mitovski, Engineering Dobersek GmbH (Germany)
Prof. Dr Žarko Radović, University of Montenegro - Faculty of Metallurgy and Technology (Montenegro)
Prof. Dr Ljubiša Balanović, University of Belgrade - Technical Faculty in Bor (Serbia)
Prof. Dr Milan Gorgievski, University of Belgrade - Technical Faculty in Bor (Serbia)
Prof. Dr Jan Vreštal, Masaryk University, Centre for Nanotechnology and Microtechnology (Czech Republic)
Prof. Dr Claire Utton, University of Sheffield, Department of Materials Science and Engineering (UK)
Prof. Dr Marija Petrović Mihajlović, University of Belgrade - Technical Faculty in Bor (Serbia)
Doc. Dr Jelena Ivaz, University of Belgrade - Technical Faculty in Bor (Serbia)
Prof. Dr Radoje Pantović, University of Belgrade - Technical Faculty in Bor (Serbia)
Prof. Dr Miodrag Banješević, University of Belgrade - Technical Faculty in Bor (Serbia)
Dr Danijel Kržanović, Mining and Metallurgy Institute Bor (Serbia)
Dr Predrag Stolić, University of Belgrade - Technical Faculty in Bor (Serbia)
Dr Vladan Marinković, Mining and Metallurgy Institute Bor (Serbia)
Prof. Dr Saša Stojadinović, University of Belgrade - Technical Faculty in Bor (Serbia)
Doc. Dr Ana Simonović, University of Belgrade - Technical Faculty in Bor (Serbia)
Doc. Dr Dejan Petrović, University of Belgrade - Technical Faculty in Bor (Serbia)
Dr Dragana Medić, University of Belgrade - Technical Faculty in Bor (Serbia)
Prof. Dr Milan Trumić, University of Belgrade - Technical Faculty in Bor (Serbia)
Prof. Dr Jovica Sokolović, University of Belgrade - Technical Faculty in Bor (Serbia)
Prof. Dr Ivana Marković, University of Belgrade - Technical Faculty in Bor (Serbia)
Prof. Dr Maja Trumić, University of Belgrade - Technical Faculty in Bor (Serbia)
Dr Dejan Todorović, Institute for Technology of Nuclear and Other Minerel Raw Materials (Serbia)
Prof. Dr Zoran Štirbanović, University of Belgrade - Technical Faculty in Bor (Serbia)
Prof. Dr Vesna Grekulović, University of Belgrade - Technical Faculty in Bor (Serbia)
Prof. Dr Dejan Tanikić, University of Belgrade - Technical Faculty in Bor (Serbia)
Prof. Dr Dominika Jendrzejczyk-Handzlik, AGH University of Science and Technology in Kraków, Faculty of Non-Ferrous Metals (Poland)
Prof. Dr Grozdanka Bogdanović, University of Belgrade - Technical Faculty in Bor (Serbia)
Prof. Dr Dragan Manasijević, University of Belgrade - Technical Faculty in Bor (Serbia)
Prof. Dr Milan Radovanović, University of Belgrade - Technical Faculty in Bor (Serbia)

Dr Vesna Conić, Mining and Metallurgy Institute Bor (Serbia)
Dr Marija Korać, University of Belgrade - Faculty of Technology and Metallurgy (Serbia)
Dr Sanja Martinović, University of Belgrade - Institute of Chemistry, Technology and Metallurgy (Serbia)
Doc. Dr Uroš Stamenković, University of Belgrade - Technical Faculty in Bor (Serbia)
Dr Jasmina Petrović, University of Belgrade - Technical Faculty in Bor (Serbia)
Prof. Dr Srba Mladenović, University of Belgrade - Technical Faculty in Bor (Serbia)
Prof. Dr Saša Marjanović, University of Belgrade - Technical Faculty in Bor (Serbia)
Dr Viša Tasić, Mining and Metallurgy Institute Bor (Serbia)
Prof. Dr Junxue Zhao, School of Metallurgical Engineering, Xian University of Architecture and Technology (China)
Prof. Dr Miljana Radivojević, Institute of Archaeology, University College London (UK)
Prof. Dr Milena Premović Zečević, University of Priština, Faculty of Technical Science (Serbia)
Dr Ana Alil, University of Belgrade - Institute of Chemistry, Technology and Metallurgy (Serbia)
Prof. Dr Đorđe Nikolić, University of Belgrade - Technical Faculty in Bor (Serbia)
Prof. Dr Velimir Radmilović, University of Belgrade - Faculty of Technology and Metallurgy (Serbia)
Prof. Dr Tatjana Volkov-Husović, University of Belgrade - Faculty of Technology and Metallurgy (Serbia)
Prof. Dr Žaklina Tasić, University of Belgrade - Technical Faculty in Bor (Serbia)
Prof. Dr Tanja Kalinović, University of Belgrade - Technical Faculty in Bor (Serbia)
Dr Jelena Jordanovć, University of Belgrade - Technical Faculty in Bor (Serbia)
Prof. Dr Maja Nujkić, University of Belgrade - Technical Faculty in Bor (Serbia)
Prof. Dr Milica Veličković, University of Belgrade - Technical Faculty in Bor (Serbia)
Prof. Dr Snežana Milić, University of Belgrade - Technical Faculty in Bor (Serbia)
Dr Jelena Kalinović, University of Belgrade - Technical Faculty in Bor (Serbia)
Doc. Dr Ana Radojević, University of Belgrade - Technical Faculty in Bor (Serbia)
Dr Dragana Božić, Mining and Metallurgy Institute Bor (Serbia)
Prof. Dr Dejan Riznić, University of Belgrade - Technical Faculty in Bor (Serbia)
Dr Vaso Manojlović, University of Belgrade - Faculty of Technology and Metallurgy (Serbia)
Prof. Dr Predrag Đorđević, University of Belgrade - Technical Faculty in Bor (Serbia)
Dr Emina Požega, Mining and Metallurgy Institute Bor (Serbia)
Dr Vladan Ćosović, University of Belgrade, Institute of Chemistry, Technology and Metallurgy (Serbia)
Prof. Dr Duško Minić, University of Priština, Faculty of Technical Science (Serbia)

PREFACE

On behalf of the Organizing Committee, it is a great honor and pleasure to welcome all esteemed participants of the **56th International October Conference on Mining and Metallurgy (IOC 2025)**, scheduled to take place at **Bor Lake, Serbia**, from **October 22nd to 25th, 2025**.

The collaborative efforts of the University of Belgrade – Technical Faculty in Bor and the Mining and Metallurgy Institute Bor have once again brought together academia, industry, and research institutions to organize this year's IOC. Our focus remains firmly set on presenting the latest research achievements and technological advancements in geology, mining, metallurgy, materials science, technology, environmental protection, and other engineering disciplines.

This year's conference program is rich and diverse, featuring **4 plenary lectures, 4 invited lectures, 158 full papers, and 6 abstracts**. The proceedings reflect the contributions of authors from **19 countries**: Austria, Bosnia and Herzegovina, Bulgaria, Canada, China, Croatia, Germany, Hungary, India, Mexico, Montenegro, Poland, Romania, Russia, Serbia, Slovakia, Slovenia, Turkey, and the United Kingdom. Among the submitted papers, eight young researchers under the age of 35 have qualified to participate in the "**MDPI Young Researcher Award**" competition, further emphasizing the conference's commitment to supporting and recognizing excellence among the new generation of scientists and engineers.

We are also delighted to host the **9th International Student Conference on Technical Sciences (ISC 2025)**, running in parallel with IOC 2025. The student conference brings together young researchers from Serbia and the wider region, with **one plenary** and **50 student papers** presented, offering an invaluable opportunity for the next generation of scientists and engineers to share their ideas and discuss the future of their disciplines with experts. The "**Professor Dragana Živković Best Student Paper Award**" will be presented to the most outstanding student contribution based on originality, research quality, and presentation.

The Organizing Committee expresses its deepest gratitude to all who have supported this event. Our General Sponsor is the Ministry of Science, Technological Development, and Innovation of the Republic of Serbia. We are especially grateful to our Platinum Donors, HBIS Serbia and Serbia Zijin Mining, as well as our Gold Sponsor, DPM Metals Inc., and our Gold Donors, Copper Mill Sevojno and Serbia Zijin Copper Bor. This year, the conference is also supported by the Silver Donor, "MC LABOR" d.o.o. Beograd.

We proudly host a diverse exhibition, featuring Indemak, Labtim SE d.o.o., MERIS d.o.o., Krug International LTD, Altium International d.o.o., Metalurg Foundry Ltd., Fugro Germany Land GmbH, Analysis d.o.o., Lola institut, Tescan and Mikrolux d.o.o., Trokuttest Serbia, Novos d.o.o., Changsha Rui Rui Technology Co., Ltd., MDPI and the Winery of Bukovo Monastery. The official opening of the conference has been supported by Epiroc Srbija a.d.. Finally, we warmly acknowledge our Friends of the Conference: Messer Tehnogas AD Belgrade, the China-Serbia Joint Laboratory on Green Steel Manufacturing, and the Foundation B.Sc. Boško Injac.

We sincerely thank all authors, committees, reviewers, speakers, and chairpersons for their invaluable contributions to shaping IOC 2025. We are confident that the conference will once again serve as a alive platform for scientific exchange, professional networking, and the promotion of sustainable development in mining, metallurgy, and related fields.

On behalf of the 56th IOC Organizing Committee,
Prof. dr Ljubiša Balanović

TABLE OF CONTENTS

Plenary Lectures

Markus A. Reuter *(GERMANY)*
Fundamental limits of green metal and mineral processing supply chains within the circular economy 3-5

Miljana Radivojević *(UNITED KINGDOM)*
Metals and the making of the ancient world: environmental and economic legacies of Eurasian bronze age metallurgy 6-6

Peizhong Feng, Baojing Zhang, Zhi Liu, Shiheng Li, Xiaohong Wang *(CHINA)*
Recycling and utilization of spent molybdenum disilicide: preparation of coating and metal recovery via synergistic smelting 7-9

Srećko Stopić, Alexander Birich, Bernd Friedrich *(GERMANY)*
Advances in understanding of reduction processes in extractive metallurgy 10-10

Invited Lectures

Buxin Chen, Mao Chen, Meilong Hu, Kaihui Ma, Hongqing Liu, Chenguang Bai *(CHINA)*
Development of hydrogen metallurgy in China 13-16

Alejandro Cruz-Ramírez, José Enrique Sanchez-Vite, Teresita del Refugio Jiménez-Romero, Margarita García-Hernández, Heriberto Mendoza-Cárdenas *(MEXICO)*
Characterization of industrial jarosites from the Mexican zinc extraction process 17-20

Nicanor Cimpoeșu, Ionuț Adomniței, Corneliu Munteanu, Mihai Axinte, Marian Luțcanu, Mihai Alin Pop, Marius Telișcă, Ana Maria Roman *(ROMANIA)*
Characterization of ceramic coatings with thermal barrier role obtained by atmospheric plasma jet spraying 21-24

Cemalettin Okay Aksoy, Güzin Gülsev Uyar Aksoy, Hasan Berker Sarisan *(TURKEY)*
Computational fluid dynamics analysis of ventilation strategies for mitigating geothermal gas leakage in subsurface infrastructure projects 25-28

Conference Papers

Geology and Mining

Zoran Marković, Milić Erić, Aleksandar Milićević, Rastko Jovanović, Nikola Živković, Ivan Lazović, Milica Jovčevski *(SERBIA)*
Optimization of the electrostatic precipitators in unit A1 of the Kostolac a thermal power plant *33-36*

Stefano Utili, Dainius Jenkus, Akanksha Mishra, Filippo Bianchi, Riccardo Castellanza *(UNITED KINGDOM)*
Optimal pitwall design for open pit mines in the presence of faults *37-44*

Katarina M. Mihajlović, Jovica Stojanovic, Slavica Mihajlović, Ivana Jelić, Ana S. Radosavljević-Mihajlović, Suzana Erić *(SERBIA)*
Comparative mineralogical analysis of two zeolitic tuff Slanci and Zlatokop *45-47*

Edita Lazarová, Mária Bali Hudáková, Víťazoslav Krúpa, Alexander Kiovský, Pavol Vavrek, Lucia Ivaničová *(SLOVAKIA)*
Results from experimental research of rock breaking by small diameter diamond core drill bits *48-51*

Edita Lazarová, Víťazoslav Krúpa, Pavol Vavrek, Mária Bali Hudáková, Lucia Ivaničová, Alexander Kiovský *(SLOVAKIA)*
Failure criterion of limestone and granodiorite determined by laboratory tests and theoretical processing of drilling process results *52-55*

Mária Bali Hudáková, Edita Lazarová, Víťazoslav Krúpa, Pavol Vavrek, Lucia Ivaničová, Alexander Kiovský *(SLOVAKIA)*
Optimisation of the rock drilling process conducted with small diameter drilling tools *56-59*

Vladan Kašić, Ana Radosavljević-Mihajlović, Jovica Stojanović, Slavica Mihajlović, Nataša Đorđević, Ivana Jelić *(SERBIA)*
Geological and technological characteristics of the Igroš-Vidojevići zeolite tuff deposits *60-64*

Marija Jonović, Dejan Bugarin, Tanja Stanković *(SERBIA)*
Sensitivity analysis of a copper ore exploitation investment project using COMFAR III software *65-68*

Branimir Farkaš, Ana Hrastov, Iva Štefičar *(CROATIA)*
Factors influencing the occurrence of flyrock phenomena on surface mines-case study *69-72*

Petar Radichev *(BULGARIA)*
Strategic planning, design and mine management under the conditions of the Asarel open pit mine *73-76*

Gergana Meracheva, Efrosima Zaneva-Dobranova, Nikolay Hristov *(BULGARIA)*
Geological conditions of natural H2 exploration on the Balkan peninsula for prosperity mapping *77-80*

Güzin Gülsev Uyar Aksoy, Cemalettin Okay Aksoy, Ozan Savaş *(TURKEY)*
Seismic intelligence in surface blasting: seisblast-promax as a next-generation design and optimization tool *81-84*

Milenko Jovanović, Daniel Kržanović, Miroslava Maksimović, Vladan Marinković, Stefan Trujić, Miomir Mikić *(SERBIA)*
The importance of geogrids for landfill security and environmental protection *85-89*

Daniel Kržanović, Milenko Jovanović, Radmilo Rajković, Miljan Gomilanović, Miloš Stojanović *(SERBIA)*
NPV based optimization of final pit contours in the cementacija mining complex *90-93*

Ivica Vojinović, Dragan Šabaz, Miloš Stojanović *(SERBIA)*
Implementation of the sublevel caving mining method in the T4 ore body at the Jama Bor underground mine *94-97*

Miloš Stojanović, Ivica Vojinović, Dragan Šabaz *(SERBIA)*
Application of neural networks for optimizing rock bolt system in underground mining *98-101*

Ivica Vojinović, Miloš Stojanović, Dragan Šabaz *(SERBIA)*
Technological innovations transforming the mining industry: a short review *102-105*

Danka Kostadinović, Dušan Ranđelović, Zoran Marković *(SERBIA)*
Implementation of ground-mounted and floating solar panels in mines *106-109*

Milan Protić, Ana Bijelić, Miomir Raos, Marjan Popović *(SERBIA)*
Kinetic modeling of oak wood thermal degradation using the distributed activation energy model (DAEM) *110-114*

Dragan Šabaz, Ivica Vojinović, Miloš Stojanović *(SERBIA)*
Monitoring techniques for subsidence induced by mining operations: a review *115-118*

Vladan Marinković, Miroslava Maksimović, Milenko Jovanović, Željana Novaković, Anđela Maričić *(SERBIA)*
Geological structure and genesis of Zn, Pb deposit Ribnik-Šuplja Stijena *119-122*

Radmilo Rajković, Vladan Marinković, Daniel Kržanović, Miomir Mikić, Milenko Jovanović *(SERBIA)*
The possibility of long-term exploitation of copper ore in ore bodies of the Majdanpek copper mine *123-126*

Miomir Mikić, Ivana Mikić, Milica Međedović, Radmilo Rajković *(SERBIA)*
The global impact of climate change on the mining sector *127-131*

Miomir Mikić, Daniel Kržanović, Milenko Jovanović, Sandra Milutinović, Ivana Mikić *(SERBIA)*
The impact of climate change on mining in serbia, an overview *132-135*

Milan Grozdanović, Živana Jovanović Pešić, Jelena Đoković, Dejan Tanikić *(SERBIA)*
Analysis of the energy potential of briquettes made from ground plum, date, and avocado pits *136-139*

Milivoje Zlatić, Dejan Petrović, Jelena Ivaz, Mladen Radovanović, Milan Stajić *(SERBIA)*
Selection of primary support system for the river Mali Pek tunnel *140-143*

Snežana Ignjatović, Branislav Petrović *(SERBIA)*
Applying electrical survey to detect the thickness of the Epikartst *144-147*

Nikola Jovanović, Jelena Stefanović, Miloš Živanović, Zlatko Pavlović, Nikola Miljković, Jelena Đorđević, Nikola Lekić *(SERBIA)*
Building information modeling (BIM) as a tool for enhancing technical solutions in mining design: A case study of the main process building in Brskovo, Montenegro *148-152*

Samil Hoskan, Bayram Kahraman *(TURKEY)*
Comparing the accuracy of Kriging and IDW interpolation for estimating a Cu-Zn deposit in Turkey *153-156*

Nenad Vušović, Milica Vlahović *(SERBIA)*
Challenges in mining subsidence engineering *157-160*

Mineral Processing and Recycling

Igor Zh. Bunin, Alexey N. Kochanov *(RUSSIA)*
On the mechanism of selective disintegration of rocks under explosive and pulse-discharge impacts *163-166*

Renguo Li, Lanjie Li, Heng Ji, Minglei Gao, Shiwei Wang *(CHINA)*
Experimental study on pelletization of blended sea sand ores *167-170*

Milić Erić, Zoran Marković, Aleksandar Milićević, Rastko Jovanović, Danka Kostadinović, Ivan Lazović, Milica Jovčevski *(SERBIA)*
Experimental research of the lignite drying process in packed bed *171-174*

Slavko Todić, Predrag Lazić *(SERBIA)*
Investigation of the flotation potential of sulfideoxide ore from the Veliki Majdan deposit *175-178*

Vladimir Nikolić, Milan Trumić *(SERBIA)*
Refinement of the bond work index calculation method for finer samples *179-182*

Jose Enrique Sanchez-Vite, Alberto Hernandez-Casimiro, Teresita del Refugio Jiménez-Romero, Alejandro Cruz-Ramírez, Margarita García-Hernández *(MEXICO)*
Mineralogical evolution in industrial jarosite through flux-assisted roasting *183-186*

Albin Dobersek, Aleksandra Mitovski, Olga Mishina, Andrej Avrachov, Pavel Saltykov, Viktoriia Zhmurova, Alexandra Friesen, Theresa Schulz *(GERMANY)*
Gold recovery from flotation tailings in copper metallurgy: A sustainable approach to resource valorization *187-190*

Ivana Jovanović, Dragan Milanović, Vesna Conić, Miloš Janošević, Daniela Urošević, Mile Bugarin *(SERBIA)*
Chemical-mineralogical characterization of carbonate-clay type lithium ore *191-194*

Jelena Đorđević, Jelena Stefanović, Sandra Guševac, Nevena Marković, Zoran Avramović, Nikola Jovanović, Nikola Lekić *(SERBIA)*
Effect of recycled asphalt (RAP) and copper slag (CS) as partial substitution of natural aggregate in asphalt mixtures *195-198*

Artur Hubert, Felix Heinicke *(GERMANY)*
Transferring common HPGR application from copper to lithium ore *199-202*

Venkateswara Rao, Jayapal Reddy *(INDIA)*
Mathematical modeling and statistical analysis of sub grade iron ore beneficiation using wet high intensity magnetic separator (WHIMS) *203-210*

Dušica Mirović, Yuankun Yang, Shengli Yu *(SERBIA)*
Safety challenges in transport of copper concentrate: TML as a boundary parameter of maritime cargo stability *211-214*

Klaudia Kundráková, Jana Pirošková, Jakub Klimko, Jarmila Trpčevská, Petra Růžičková, Dušan Oráč *(SLOVAKIA)*
Electrospinning of ZnO nanofibers from zinc galvanizing flue dust *215-220*

Dragana Marilović, Grozdanka Bogdanović *(SERBIA)*
Leaching of covellite in ionic liquid solution *221-224*

Nadezhda Kazakova, Vladislava Stefanova, Petar Iliev, Biserka Lucheva *(BULGARIA)*
Analytical study of zinc recovery from spent solutions resulting after galvanization process *225-228*

Katarina Balanović, Maja Trumić, Tamara Gavrilović *(SERBIA)*
Influence of hidden neuron number on the performance of ANN models applied to deinking flotation data *229-232*

Extractive Metallurgy and Process Innovations

Teresita del Refugio Jiménez-Romero, José Enrique Sanchez-Vite, Alejandro Cruz-Ramírez, Margarita García-Hernández, Ángel de Jesús Morales-Ramírez *(MEXICO)*
Recovery of copper from a chalcopyrite ore using natural deep eutectic solvents (NADES) of choline chloride-urea as a leaching agent *235-238*

Alexey M. Amdur, Sergei A. Fedorov *(RUSSIA)*
Droplet flotation in metallurgical melts *239-242*

Yuchao Shi, Taibai Fu, Xinyi Zhang, Liang Zhang, Shiyi Wen, Yuling Liu, Yingbiao Peng, Jiangxing Wang, Ziqing Xie, Yong Du *(CHINA)*
Development of ICALPHAD software for phase diagram calculation and intelligent thermodynamic optimization *243-246*

Vesna Grekulović, Milica Zdravković, Milan Gorgievski, Nada Štrbac, Miljan Marković, Marina Marković, Kristina Božinović *(SERBIA)*
Electrochemical behavior of copper in chloride medium in the presence of pine cone macerate *247-250*

Ana Kostov, Aleksnadra Milosavljević, Ivan Jovanović *(SERBIA)*
DTA thermodynamic behaviour of the ternary system Ga-Ge-Sb *251-254*

Dimitrije Anđić, Aleksandar Jovanović, Nikola Vuković, Ivana Jelić, Mladen Bugarčić, Vaso Manojlović, Miroslav Sokić *(SERBIA)*
Innovative oxidative system for leaching of Fe^{2+} from sphalerite concentrate *255-259*

Vanja Trifunović, Snežana Milić, Ljiljana Avramović, Dragana Božić, Zoran Avramović *(SERBIA)*
Behavior of zinc, calcium and iron in the two-stage leaching process of the EAF dust *260-263*

Petar Petrov *(BULGARIA)*
Creation of sintering cup for laboratory sintering installation *264-268*

Angel Iliev, Daniela Grigorova *(BULGARIA)*
Thermodynamic investigation of carbothermic reduction of electric arc furnace dust *269-272*

Xiaohua Liu, Renhao Tian, Yang You, Zhixiong You, Xuewei Lv *(CHINA)*
Numerical simulation of temperature field in a rotary hearth furnace under infrared-assisted heating conditions *273-276*

Sara Lukovac, Nebojša Tadić, Dijana Đurović, Irena Nikolić *(MONTENEGRO)*
S/S treatment for aluminium slag waste using fly ash-based geopolymers *277-280*

Xing Han, Hongqiang Liu, Lanjie Li, Pengyang Li, Xiaolong Guo *(CHINA)*
The role of hydrogen based shaft furnaces in steel industry decarbonization *281-286*

Gvozden Jovanović, Dimitrije Anđić, Danijela Smiljanjić, Dragana Ranđelović, Branislav Marković *(SERBIA)*
Behavior of plant micronutrients (Fe, Cu) during combustion of contaminated Sorghum spp. *287-290*

Igor Zlatković, Živko Đorović *(SERBIA)*
Analysis of the new sinter line in HBIS Group Serbia and creating conditions for production improvement *291-295*

Nebojša Tadić, Irena Nikolić, Nina Jović, Dejana Dizdar, Vanja Asanović, Milena Tadić *(MONTENEGRO)*
Valorization of fly ash and plastic waste using geopolymerization technology *296-299*

Miloš Vuleta, Milodarka Žugić, Vladan Andrejić, Tamara Ristić *(SERBIA)*
Industrial optimization of BOF steelmaking: increasing scrap ratio through hot metal parameter control *300-303*

Milivoje Zlatić, Dejan Petrović, Jelena Ivaz, Mladen Radovanović, Milan Stajić *(SERBIA)*
Artificial intelligence challenges in modern alloy design *304-307*

Vesna Conić, Miloš Janosević, Dragan Milanović, Ivana Jovanović, Daniela Urošević, Mile Bugarin *(SERBIA)*
Overview of methods for bor separation *308-311*

Sandra Guševac, Nevena Marković, Jelena Đorđević, Jelena Stefanović *(SERBIA)*
The possibility of using copper slag aggregate in concrete *312-315*

Emine Sayılgan, Patrick Zhang *(TURKEY)*
Leaching behaviour of phosphogypsium with different acids *316-318*

Duško Minić, Milena Zečević, Aleksandar Đorđević, Veljko Minić *(SERBIA)*
Electrical resistivity of the Al-Bi-Ge ternary alloys *319-322*

Velizar Stanković, Miljan Marković, Milan Gorgievski, Stefan Đorđievski *(SERBIA)*
On the leachability of copper from coper-iron minerals mixture *323-326*

Ferenc Kristaly, László Farkas, Andrea Mihalkó, Bence Tamás, Balázs Szeleczki *(HUNGARY)*
Recoverable Pd and Pt accumulation in a $Ca(OH)_2$ based CO_2 filter of a hydrogenation organic byproduct plant *327-330*

Oliver Dimitrijević, Ivana Jovanović, Vesna Conić, Dragan Milanović, Tanja Stanković *(SERBIA)*
Example of dense media cyclone selection *331-334*

Petra Růžičková, Klaudia Kundráková, Kristína Talianová, Jakub Klimko, Dušan Oráč *(SLOVAKIA)*
Selective recovery of copper from hydrometallurgical processing of e-waste *335-340*

Alloys, Composites, and Advanced Materials

Anca Cazac, Diana-Petronela Burduhos-Nergis, Andrei Victor Sandu, Mihai Popa, Costica Bejinariu *(ROMANIA)*
Strontium phosphate conversion coatings: A short review *343-346*

Maja Vončina, Jožef Medved, Tinkara Smolar, Matej Steinacher *(SLOVENIA)*
Influence of heat treatments on mechanical properties of aluminium alloy EN AW-2011 *347-350*

Alexandra Tamara Sutic, Gheorghe Bădărău, Romeu Chelariu, Ramona Cimpoeșu, Ana-Maria Roman, Mihai-Adrian Bernevig, Nicanor Cimpoeșu *(ROMANIA)*
An assessment of corrosive and mechanical performance of biodegradable ZnMgTi alloys *351-354*

Jožef Medved, Tilen Balaško, Stanislav Kores, Maja Vončina *(SLOVENIA)*
In-situ synthesis of Mg_2Si-reinforced amc *355-359*

Karlo T. Raić, Mile B. Đurđević, Srećko Manasijević, Aleksandra Patarić, Marija Mihailović *(SERBIA)*
Statistical evolution of non-metallic inclusions in continuous cast Al-killed steel *360-363*

Kristina Božinović, Dragan Manasijević, Ljubiša Balanović, Milan Gorgievski, Uroš Stamenković, Miljan Marković *(SERBIA)*
Microstructural analysis and thermal properties of Ag-Sn alloys *364-370*

Srđan Matijašević, Mirko Grubišić, Nataša Đorđević, Ana Radosavljević-Mihajlović, Slavica Mihajlović *(SERBIA)*
The effect of the free energy change on crystallization in lithium-germanate glass *371-374*

Jovana Ružić, Jelena Stašić, Marko Simić, Andrijana Žekić, Branislava Vučetić, Dušan Božić *(SERBIA)*
Influence of the heat treatment on the structural parameters of the CuCrZr-TiB_2 alloy *375-377*

Ionuț Adomniței, Daniela Lucia Chicet, Bogdan Istrate, Marcelin Benchea, Gheorghe Bădărău, Nicanor Cimpoeșu *(ROMANIA)*
Obtaining and characterization of high yttria content in zirconia coatings *378-381*

Florin Sorin Todirică, Daniela Lucia Chicet, Dragoș-Cristian Achiței, Vasile Manole, Mihai-Adrian Bernevig, Ioan Stirbu, Nicanor Cimpoeșu *(ROMANIA)*
Using energy dispersive spectroscopy for a stainless steel-brass welding interface characterization *382-385*

Shehret Tilvaldyev, América Yamile Amaya Diaz, Adrian Alberto Castro De La Cruz *(CANADA)*
Analysis of the variations of the wing lift coefficient of unmanned aerial vehicles with increasing Reynolds number of airflow *386-389*

Nebojša Tadić, Žarko Radović *(MONTENEGRO)*
Investigation of the influence of residual stresses on the mechanical properties of aluminum alloy strips *390-393*

Aida Imamović, Mirsada Oruč, Milenko Rimac, Gorazd Kosec, Safet Hamedović *(BOSNIA AND HERZEGOVINA)*
Influence of dimensional size of rolled product made of S690QL steel on impact toughness and grain size *394-400*

Krzysztof Pancikiewicz, Mariusz Maslak, Paulina Zajdel, Marcin Klimek *(POLAND)*
Phase transformations in a welded joint of unalloyed steel after long-term subcritical annealing *401-404*

Franjo Kozina, Zdenka Zovko Brodarac, Ivica Buljeta, Natalija Dolić *(CROATIA)*
Analysis of crack formation in AlSi11 alloy automotive rim *405-408*

Žaklina Tasić, Marija Petrović Mihajlović, Ana Simonović, Milan Radovanović, Milan Antonijević *(SERBIA)*
Carbon-based electrochemical sensor modified with metal oxide nanoparticles *409-412*

Almaida Gigović-Gekić, Elvis Agović, Hasan Avdušinović, Branka Muminović *(BOSNIA AND HERZEGOVINA)*
Testing the impact of toughness of the welded joint of steel S21800 *413-416*

Lovro Liverić, Tamara Holjevac Grgurić, Marko Kršulja, Matej Fonović *(CROATIA)*
TEM Investigation of Cu-10Al-7Ag Shape Memory Alloy in As-Cast State *417-420*

Marko Kršulja, Damir Karabaić, Lovro Liverić, Samir Grudić *(CROATIA)*
Comparison of non-destructive and destructive welding assessment tests on MAG-welded AISI316L and DH36 steels using K-309LT filler *421-425*

Dana Bolibruchová, Martina Sýkorová, Marek Matejka *(SLOVAKIA)*
Influence of Be addition on mechanical and physical properties of alloys with low Si content *426-429*

Milan Nedeljković, Srba Mladenović, Vladan Ćosović, Ivana Marković, Jasmina Petrović, Uroš Stamenković, Milijana Mitrović, Avram Kovačević *(SERBIA)*
Microstructures and wettability behavior of Sn-0.7Cu solder doped with graphene nanosheets *430-433*

Srba Mladenović, Nikola Marinković, Dragica Milojković, Jasmina Petrović, Milan Nedeljković *(SERBIA)*
Structural characterization of welded joints of AlSiMg alloys *434-437*

Martina Sýkorová, Dana Bolibruchová, Marek Matejka *(SLOVAKIA)*
Development of the Al-Si alloy with niobium addition for gigacastings *438-441*

Veljko Savić, Vladimir Topalović, Jelena Nikolić, Marija Đošić, Milena Obradović, Danijela Smiljanić, Snežana Grujić *(SERBIA)*
Insights into the glass network structure of coal fly ash-based glass *442-445*

Uroš Stamenković, Ivana Marković, Dragan Manasijević, Milan Nedeljković *(SERBIA)*
Termomechanical treatment of S275JR steel: impact on microstructure, hardness, and impact toughness *446-449*

Milan Protić, Momir Praščević, Nikola Mišić, Miomir Raos, Viša Tasić *(SERBIA)*
Flammability assessment of acoustic insulation materials using mass loss calorimetry *450-453*

Marek Matejka, Dana Bolibruchová, Martina Sýkorová *(SLOVAKIA)*
Analysis of selected properties of Al-Si-Cu based alloy with tungsten addition *454-457*

Žarko Mišković, Radivoje Mitrović, Danilo Pejčić, Jovana Antić *(SERBIA)*
Overview of installations and methodologies for conveyor idlers testing-developed at the Faculty of Mechanical Engineering at the University of Belgrade *458-461*

Mile B. Đurđević, Srećko Manasijević, Aleksandra Patarić, Marija Mihailović, Karlo Raić *(SERBIA)*
Role of magnesium in solidification feeding of hypoeutectic Al-Si5-Mg alloys *462-465*

Jelena Gligorijević Sokolović, Jasmina Petrović, Emina Požega *(SERBIA)*
Casting of bronze castings with thin walls using wax-paraffin models and CO_2 hardened sand molds *466-469*

Shi Wenli, Tanja Marinković Stojanović, Aleksandar Djuga, Marko Radosavljević, Stefan Nešić *(SERBIA)*
Metallurgical and process challenges in flash butt welding of different dimensions of micro-alloyed steel on continuous pickle line *470-473*

Emina Međedović, Vanja Asanović, Milena Tadić, Jasmina Grbović Novaković, Irena Nikolić, Anđela Mitrović Rajić *(MONTENEGRO)*
Structural changes in pyrophyllite induced by mechanochemical modification and zinc oxide doping *474-477*

Biljana Zlatičanin, Branislav Radonjić *(MONTENEGRO)*
Effect of copper content on phase formation and mechanical response of Al-Cu alloys *478-481*

Biljana Zlatičanin, Branislav Radonjić *(MONTENEGRO)*
Combined effect of cooling conditions and Mg content on the microstructure and properties of Al-15Cu alloys *482-485*

Vladimir Glushchenkov *(RUSSIA)*
Improvement in the technology of pouring copper plates for their further use in electrolysis production *486-489*

Marko Pavlović, Marina Dojčinović, Mirjana Stojanović *(SERBIA)*
Cavitation resistance of talc-reinforced pyrophyllite ceramics *490-493*

Salko Ćosić, Almir Osmanović, Jasmin Halilović *(BOSNIA AND HERZEGOVINA)*
Probabilistic analysis of press fit joint load carrying capacity *494-497*

Saša Marjanović, Milijana Mitrović, Emina Požega, Dragana Božić *(SERBIA)*
Influence of cold rolling and annealing on the hardness of Cu-Al bimetallic strip *498-501*

Emina Požega, Slavko Bernik, Dragana Božić, Srđana Magdalinović, Miloš Đukić, Jelena Gligorijević Sokolović, Radmilo Rajković *(SERBIA)*
Properties of Se doped Bi_2Te_3 based material: Part I *502-505*

Nandita Gupta, Kamlesh Kumar Singh, Manoj Kumar, Himanshu Khandelwal *(INDIA)*
A study of single piece ceramic shell core for geometrically complex investment casting *506-510*

Veljko Minić, Jelena Miladinović, Miljana Popović, Milena Zečević, Aleksandar Đorđević *(SERBIA)*
Experimental characterization of the Bi-Ge-Pb ternary alloys *511-514*

Ondrej Kožej, Iveta Vasková, Ladislav Jankovčin *(SLOVAKIA)*
Investigation of gas and shrinkage porosity in AlSi10Mg alloy gearbox castings manufactured by HPDC *515-521*

Jasmina Petrović, Srba Mladenović, Uroš Stamenković, Milan Nedeljković, Milijana Mitrović *(SERBIA)*
Effect of oxy-cutting on the microstructure and hardness of high-carbon steel *522-525*

Ivana Marković, Uroš Stamenković, Dragan Manasijević, Ljubiša Balanović *(SERBIA)*
Changes in hardness and microstructure during isothermal aging of nickel-aluminum bronze *526-529*

Ferenc Kristaly, László Farkas, Andrea Mihalkó, Bence Tamás, Balázs Szeleczki *(HUNGARY)*
Microscale features of Pd-Pt aggregates resulted from aniline hydrogenation tar incinerating process *530-533*

Sandra Milutinović, Ljubiša Obradović, Sanja Petrović, Srđana Magdalinović, Ivana Mikić *(SERBIA)*
Reinforcements in composite materials *534-537*

Milijana Mitrović, Saša Marjanović, Biserka Trumić, Milan Nedeljković, Jasmina Petrović, Uroš Stamenković *(SERBIA)*
Influence of temperature and annealing time on changes of the mechanical properties of the CuFe1 alloy *538-541*

Zoran Karastojković, Radiša Perić, Srba Mladenović *(SERBIA)*
Limitations for wider usage of gold-aluminium alloys based on intermetallic compound Au-Al_2 *542-545*

Dragan Jeremić, Željko Šutović, Milić Ječmenica, Dragomir Glišić, Stefan Dikić, Nenad Radović *(SERBIA)*
Development of 12.0mm thick hot rolled strip of S640MC grade steel in HBIS Serbia *546-549*

Technology and Energy

Margarita García-Hernández, Alejandro Cruz-Ramírez, Ángel de Jesús Morales-Ramírez, José Enrique Sanchez-Vite, Teresita del Refugio Jiménez-Romero *(MEXICO)*
Decay time determination from luminescence emissions of Eu^{3+} doped Y_2O_3 powder *552-555*

Valery Pierre Vassiliev, Cristopher Stanley *(RUSSIA)*
Optimization of heat capacities of sphalerite and wurtzite phases as a single system *556-559*

Rastko Jovanović, Ivan Lazović, Milić Erić, Zoran Marković, Marija Živković *(SERBIA)*
Predicting CO emissions using novel numerical model for particle ignition/combustion *560-563*

Marija Jeremić, Andreas Krammer, Markus Lehner (AUSTRIA)
Biomass to BioSNG-Methanation of syngas from biomass gasification *564-567*

Duško Kostić, Mitar Perušić, Srećko Stopić, Dragan Kostic, Jelena Vuković, Nebojša Vasiljević, Radislav Filipović, Vladimir Damjanović *(BOSNIA AND HERZEGOVINA)*
High-pressure oxygen leaching of tionite residue for titanium recovery *568-574*

Zoran Avramović, Dragana Božić, Vanja Trifunović, Jelena Stanković *(SERBIA)*
Cathodic protection of metals *575-578*

Milica Zdravković, Slađana Savić, Vesna Grekulović, Dalibor Stanković, Iva Dimitrievska *(SERBIA)*
ATR-FTIR characterization of the white willow bark extract used as a copper corrosion inhibitor *579-582*

Milica Zdravković, Edina Huseinović, Jasmina Dedić, Emir Horozić, Vesna Grekulović *(SERBIA)*
Extraction of bioactive compounds from nettle seeds as a potential inhibitor of metal corrosion *583-587*

Milica Zdravković, Slađana Savić, Vesna Grekulović, Dalibor Stanković *(SERBIA)*
HPLC-DAD identification of compounds in corrosion inhibitor Salix Alba bark extract and the hydrolate *588-592*

Milos Đukić, Stefan Đorđievski, Sanela Vasiljević, Dragana Adamović-Marković, Emina Požega, Jelena Nikolić, Vesna Stankov-Jovanović *(SERBIA)*
Internal quality control of ICP-MS method for water analysis *593-596*

Environmental Protection, Remediation and Risk Assessment

Aleksandar Grigorov, Silviya Lavrova, Daniela Grigorova *(BULGARIA)*
Application of nanomaterials in water treatment from manganese *599-602*

Ana Marinković, Jovana Buha Marković, Jasmina Savić, Milica Mladenović, Milić Erić, Zoran Marković, Biljana Vučićević *(SERBIA)*
Assessment of mercury content in different fuel types *603-606*

Marija Koprivica, Marija Simić, Jelena Petrović, Jelena Dimitrijević, Marija Ercegović, Marija Marković *(SERBIA)*
Tree leaf biochar as a potential adsorbent for lead ion removal from aqueous solution *607-610*

Vesna Krstić, Danijela Simonović, Renata Kovačević, Daniel Kržanović, Mirjana Šteharnik, Daniela Urošević, Sunčica Stanković *(SERBIA)*
Multivariate statistical evaluation of agricultural soil contamination near the city of Bor *611-615*

Ana Petrović, Stefan Đorđievski, Miloš Đukić, Emina Požega, Jelena Gligorijević Sokolović, Dragana Adamović-Marković *(SERBIA)*
Application of metal foams for the water purification process *616-619*

Viša Tasić, Tatjana Apostolovski-Trujić, Renata Kovačević, Bojan Radović, Nevena Ristić *(SERBIA)*
State of air quality in the city of Bor in 2024 *620-623*

Aleksandra Papludis, Slađana Alagić, Snežana Milić, Dragana Medić, Jelena Nikolić, Snežana Jevtović, Ivana Zlatanović Đaić *(SERBIA)*
Distribution of PAHs in soils from Bor region, taken from the rooting zone of poison ivy *624-627*

Žarko Radović, Nebojša Tadić *(MONTENEGRO)*
Effect of air oxygen enrichment on gaseous fuels combustion and GHG emission *628-631*

Maja Nujkić, Žaklina Tasić, Sonja Stanković, Dragana Medić *(SERBIA)*
Optimizing cadmium ion adsorption: predictive modeling based on literature data *632-635*

Miljan Marković, Milan Gorgievski, Marina Marković, Vesna Grekulović, Nada Štrbac, Kristina Božinović, Milica Zdravković *(SERBIA)*
Statistical modeling of copper ions biosorption onto sunflower hulls *636-640*

Miloš Stojanović, Nicoleta Sorina Nemes, Adina Negrea, Mihaela Ciopec, Ivan Svrkota, Daniel Kržanović, Igor Svrkota *(SERBIA)*
Environmental sampling strategy for the Romania–Serbia border mining region *641-644*

Danka Kostadinović, Milić Erić, Ivan lazović *(SERBIA)*
Application of waste materials in green roofs *645-648*

Branislava Matić, Snežana Živković Perišić, Srđan Mančević *(SERBIA)*
Use of AIRQ+ software in assessing the impact on health from exposure to particles in Bor, Serbia *649-654*

Jelena Kalinović, Tanja Kalinović, Ana Radojević, Snežana Šerbula, Jelena Jordanović *(SERBIA)*
Assessment of element accumulation efficiency in plant parts using biological factor analysis *655-658*

Milan Gorgievski, Marina Marković, Miljan Marković, Vesna Grekulović, Nada Štrbac, Kristina Božinović, Milica Zdravković *(SERBIA)*
Equilibrium and thermodynamic analysis of the adsorption of copper ions on sunflower hulls *659-663*

Marina Marković, Milan Gorgievski, Miljan Marković, Vesna Grekulović, Nada Štrbac, Kristina Božinović, Milica Zdravković *(SERBIA)*
Kinetic analysis of copper ions adsorption on sunflower hulls *664-668*

Danijela Simonović, Daniel Kržanović, Renata Kovačević, Daniela Urošević, Mirjana Šteharnik, Sunčica Stanković, Vesna Krstić *(SERBIA)*
Assessment of heavy metal contamination of soil and the ecological risk based on national limit values and quantitative indices *669-673*

Aleksandra Petrović, Stefan Đorđievski, Bojan Radović, Renata Kovačević *(SERBIA)*
Assesment of PAH and PCB concentrations in Bor River bed sediments affected by mining and metallurgy *674-677*

Stefan Đorđievski, Ana Radojević, Tanja Kalinović, Maja Nujkić, Jelena Kalinović, Jelena Jordanović, Renata Kovačević, Yasumasa Ogawa *(SERBIA)*
Assessment of the copper availability by extraction of riverbed sediments from Eastern Serbia with 0.5 M HCl *678-681*

Miloš Đukić, Stefan Đorđievski, Sanela Vasiljević, Dragana Adamović-Marković, Ana Petrović, Jelena Nikolić, Vesna Stankov-Jovanović *(SERBIA)*
Cerovo river-Annual monitoring of impact of the Cerovo open-pit mine *682-685*

Emine Sayilgan, Patrick Zhang *(TURKEY)*
A review on recovery of REEs and radioactive materials from phosphogypsium *686-688*

Industrial Management, Digitalization and Quality Control

Yufei Wang, Xiaoyu Zheng, Xiangyang Ying, Qi Huang, Xiong Shuai, Changfa Du, Ya Li, Yingbiao Peng, Yuling Liu, Yong Du *(CHINA)*
Integrated computational material engineering practice paths by Changsha Ruirui Technology: From CALPHAD to phase field and crystal plastic finite element *691-694*

Aleksandra Fedajev, Sanela Arsić *(SERBIA)*
Is mining and quarrying most efficient and profitable export sector in Serbia? Insights from a multi-criteria performance analysis *695-699*

Predrag Stolić, Zoran Jovanović, Željko Mravik, Marko Jelić, Sonja Jovanović, Aleksandra Milosavljević *(SERBIA)*
The path to better education of engineers using open data-A practical example in the Republic of Serbia *700-703*

Tatjana Volkov Husović, Ana Alil, Sanja Martinović *(SERBIA)*
NDT methods for monitoring degradation of refractory lining for blast furnace and converter *704-711*

Maria Krasteva, Petar Raykov *(BULGARIA)*
Quality control in the production of vacuum pumps for the automotive industry *712-715*

Anđelka Stojanović, Isidora Milošević, Dragan Manasijević *(SERBIA)*
Intra- and extra-EU trade in recyclable metals: opportunities for industrial symbiosis *716-720*

Marijana Pavlov-Kagadejev, Aleksandra Milosavljević *(SERBIA)*
Application of metaheuristic algorithms in metallurgical industry: A review of methods and applications *721-724*

Abstracts

Eugeniu Martac, Christine Laskov, Katarzyna Staniewska *(GERMANY)*
Mining after mining: Real-time XRF-CPT for strategic resource estimation in tailings reprocessing *727-727*

Tilen Balaško, Aleš Nagode, Jiehua Li, Jožef Medved, Maja Vončina *(SLOVENIA)*
The role of lanthanium addition in the microstructural evolution of an EN AW-7175 alloy during solution annealing *728-728*

Wei Su, Yi Xing, Yang Zheng, Rongrong Lei *(CHINA)*
Construction and technological progress of a comprehensive carbon reduction system for CCUS in the steel industry *729-729*

Stefan Trujić, Miroslav Popović, Milenko Jovanović, Katarina Milivojević, Boško Vuković *(SERBIA)*
Geological investigations of the 'Povlatna zona' and 'Istočno polje' of the Gacko Coal Basin (BiH) for coal quality assessment and design of a beneficiation plant (2023–2025) *730-730*

Roxana Hobjâlă, Nicolae Răzvan Mititelu, Ştefana Agop, Laurenţiu Slătineanu, Diana Diaconu *(ROMANIA)*
The contribution and application of polymeric materials in the metallurgical industry *731-731*

Stefana Agop, Bogdan-Ionut Dochita, Roxana Hobjâlă, Nicanor Cimpoeșu, Tiberiu Sutic *(ROMANIA)*
The behavior description of CuZnAl shape memory alloys through the dynamics of multifractal complex systems *732-732*

Publishing partners *733-738*

Donors *739-772*

Author Index *773-780*

PLENARY LECTURES

The 56th International October Conference on Mining and Metallurgy
22-25 October 2025, Bor Lake, Bor, Serbia
www.ioc.tfbor.bg.ac.rs

DOI: 10.5937/IOC25003R | Plenary lecture | Extended Abstract

FUNDAMENTAL LIMITS OF GREEN METAL AND MINERAL PROCESSING SUPPLY CHAINS WITHIN THE CIRCULAR ECONOMY

Markus A. Reuter

SMS Group GmbH, Am SMS Campus 1, 41069 Mönchengladbach, Germany
markusandreas.reuter@sms-group.com, 0000-0003-0500-4863

Abstract

There is a lot of talk about greening society, greening the supply chain, circular economy etc. The question that needs to be answered, how green is all of this and what is the shade of green (or grey) is achievable. The circular economy integrates many stakeholders to possibly achieve this objective. To fully understand the performance of the systems an exergetic basis is required as shown in Figure 1 [1]. This implies all processes, streams, stakeholder activities etc., in the circular economy must be quantifiable in terms of the unit kW to fully understand the losses from the system. This means both the flow of mass and the exergy (both chemical and physical Ex=(H-H°)-T°(S-S°)) dissipation must be included. This should be the basis of any rigorous analysis. Life-Cycle Assessment (LCA) is too simplistic to fully understand the complex systems in these terms. Therefore, methods must be inclusive of thermochemistry, mass and heat transfer, technology etc., which all affect the economics of the circularity economy.

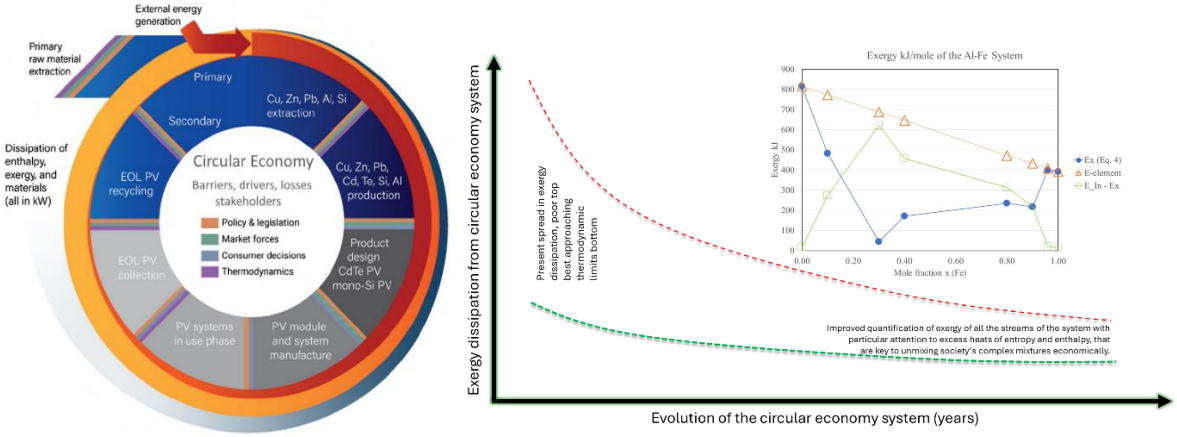

Figure 1. Various stakeholders in the circular economy, barriers as well as the exergetic downward spiral of the system [1,2].

This lecture will discuss the key role of metallurgy by applying its simulation methods and theory to understand the greenness of systems and in fact what the limits are of the system and thence of the circular economy, as reflected by Figure 2. To analyse the systems from, among others, an industry perspective, artificial intelligence (AI) techniques will be implemented, as well as simulation tools linked to LCA and similar types of methodologies [1,3].

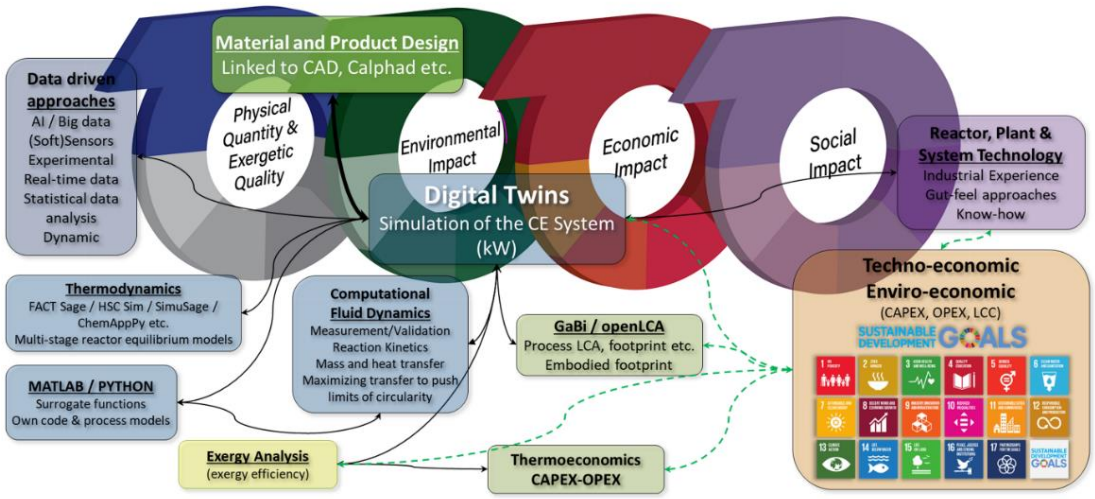

Figure 2. An overview of tools that need to be integrated to evaluate green systems on a fundamental basis [1].

As illustrations, various cases will be shown how methods and techniques have been applied to understand the fundamental limits of supply chains as a part of the circular economy. A large body of published information will be highlighted rooted in industrial practice to illustrate how far the industry has also progressed to address green issues fundamentally, while bringing a simulation basis to footprint analysis. For example, the presentation will discuss:

- *Various examples showing the simulation of metallurgical and recycling systems to understand their exergetic limits in an industrial and applied context as shown by Figure 2 [1,2].*
- *Show the analysis of supply chains including their critical metals on system performance using simulation tools. Integration of AI methods into simulation and process control in industry to push processes and systems to their physics as well as mass and heat transfer limits and thence obviously also economic limits [3].*
- *Use of Finite Element Method (FEM) to understand the liberation of particles from products [4], thus showing true design for recycling using physics to understand liberation linked to material properties.*
- *EU projects that are applying these techniques for design for recycling and show the link to product design with example from automotive and consumer electronics [5, 6]. A typical result of design for recycling of modules from the automotive industry is given by Figure 3, showing different recyclabilities of car parts as well as a recyclability label.*

In conclusion, the methods can be used to fundamentally describe the supply chains of the circular economy and quantify the exergetic limits of the circular economy. For this we advanced the theory of exergy [2] to include the thermodynamic approaches such as represented by FactSage [9] and discuss how this must be used in the analysis of supply chains within the circular economy.

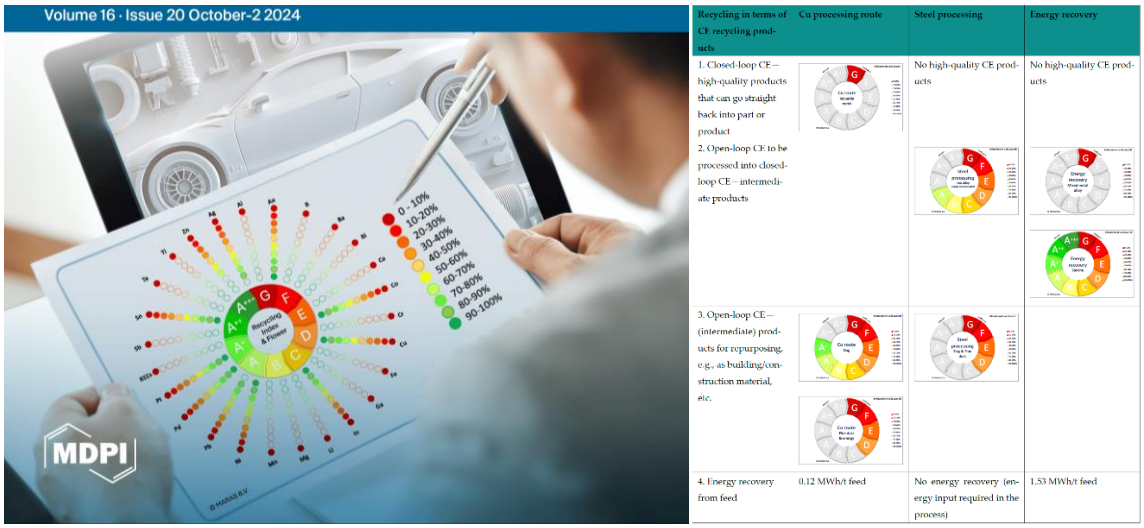

Figure 3. Recyclability of different car parts using different recycling options and flowsheets with the definition of a recycling label for products [5-8].

***Keywords**: Circular economy; green metal and mineral processing; AI simulation*

References

[1] C. Meskers, E. Worrell, M.A. Reuter. 2024. Handbook of Recycling 2nd Edition, Elsevier, 729p.
[2] K. Hack, M.A. Reuter. J. Sustain. Metall. (2025).
[3] M.A. Reuter. Metall. Mater. Trans. B. 47 (2016) 3194–3220.
[4] M. Heibeck, J. Richter, A. Hornig, T. Mütze, M. Rudolph, M. Reuter, N. Modler. Mater. Des. 232 (2023) 112167.
[5] TREASURE: https://www.treasureproject.eu/
[6] CIRCUITS: https://circuitsproject.eu/
[7] G. Sonneman, S.V. Digges La Touche, M.A. Reuter, R. Hamberg, Life Cycle Assessment and Product Environmental Footprint studies for critical and strategic raw materials. Report for Directorate General Environment European Commission (in press), (2025).
[8] A. Van Schaik, M.A. Reuter. Sustainability. 16 (20) (2024) 9048.
[9] C.W. Bale, E. Bélisle, P. Chartrand, S.A. Decterov, G. Eriksson, A.E. Gheribi, K. Hack, I.H. Jung, Y.B. Kang, J. Melançon, A.D. Pelton, S. Petersen, C. Robelin, J. Sangster, P. Spencer, M.A. Van Ende. FactSage thermochemical software and databases, 2010-2016. Calphad 54, 35 (2016).

DOI: 10.5937/IOC25006R Plenary lecture Abstract

METALS AND THE MAKING OF THE ANCIENT WORLD: ENVIRONMENTAL AND ECONOMIC LEGACIES OF EURASIAN BRONZE AGE METALLURGY

Miljana Radivojević

UCL Institute of Archaeology, University College London, 31-34 Gordon Square, London, UK
m.radivojevic@ucl.ac.uk, 0000-0001-7329-305X

Abstract

The Bronze Age (c. 3500–1000 BCE) witnessed the emergence of large-scale metallurgy as a transformative force across Eurasia. This period saw the development of extensive mining and smelting networks that powered the production of vast quantities of copper and bronze artefacts—an industrial-scale endeavour often referred to as the 'Metal Road.' These networks connected remote ore-rich regions to far-flung consumer communities, laying the foundations for long-distance exchange that foreshadowed the later Silk Roads. Yet, behind this technological achievement lies a lesser-known environmental story.

This paper explores the environmental and economic impact of Bronze Age metallurgy by integrating archaeological, archaeometallurgical, and paleoenvironmental evidence. Through key case studies such as Kargaly in the Urals and Dzhezkazgan in Kazakhstan—where Late Bronze Age production alone may have exceeded 100,000 tonnes of copper—we reconstruct the scale of extraction and its ecological footprint. The production of just one kilogram of copper could require up to 94 kilograms of wood, highlighting the immense pressure on ancient forests and landscapes. Over generations, this resource demand likely led to deforestation, soil degradation, and early anthropogenic carbon emissions—impacts that are only beginning to be fully appreciated in archaeological discourse.

Simultaneously, metallurgy reshaped the economic and political terrain of Eurasian societies. With over half a million artefacts in circulation, metal became both a medium of value and a marker of power, innovation, and interconnection. This paper argues that metallurgy was not merely a technological achievement but a force of historical consequence—altering landscapes, economies, and human relationships to the environment in ways that resonate with today's challenges around sustainability, resource management, and ecological resilience.

***Keywords**: Bronze Age, archaeometallurgy, environment, carbon emission, First Industrial Age*

The 56th International October Conference on Mining and Metallurgy
22-25 October 2025, Bor Lake, Bor, Serbia
www.ioc.tfbor.bg.ac.rs

DOI: 10.5937/IOC25007F | Plenary lecture | Original scientific paper

RECYCLING AND UTILIZATION OF SPENT MOLYBDENUM DISILICIDE: PREPARATION OF COATING AND METAL RECOVERY VIA SYNERGISTIC SMELTING

Peizhong Feng [1a], Baojing Zhang [1b], Zhi Liu [1c], Shiheng Li [1d], Xiaohong Wang [1e]

[1] School of Materials Science and Physics, China University of Mining and Technology, Xuzhou, 221116, P. R. China

[1a] pzfeng@cumt.edu.cn, 0000-0002-9853-6457
[1b] zhangbj@cumt.edu.cn, 0000-0001-9499-0137
[1c] ts23180038a31@cumt.edu.cn, 0009-0001-6436-604X
[1d] lishiheng@cumt.edu.cn, 0000-0001-7373-066X
[1e] wxhcumt@cumt.edu.cn, 0000-0001-7391-3263

Abstract

Molybdenum disilicide ($MoSi_2$) heating elements are widely used in the industrial and laboratory high-temperature heating field. Based on the excellent oxidation resistance of $MoSi_2$, solid waste from spent heating elements was used as raw material to fabricate silicide-based anti-oxidation coatings on refractory metals (Mo, Nb, etc.). After oxidation at 1500 °C for 40 hours, the coating exhibited a minimal weight gain of 2.78 mg/cm^2, and the surface formed a crack-free, continuous SiO_2 oxide film. The coating demonstrated dense morphology, controllable thickness, uniform composition, and strong interfacial bonding.

Given the high molybdenum content in spent molybdenum disilicide and the elevated iron content in metallurgical iron-containing slags, the two solid wastes were subjected to synergistic reduction smelting. Through high-temperature pyrolysis of $MoSi^2$, silicon and iron reduction, in situ generation of molybdenum and iron, the key metal molybdenum in retired silicon molybdenum was selectively recovered, and molybdenum alloy was synchronously prepared in situ. The recovery efficiencies reached 99.97 % for molybdenum and 85.49 % for iron, achieving synergistic high-value utilization of high-grade metals from multi-component solid wastes.

Keywords: *Spent molybdenum disilicide; Coating; Molybdenum iron recovery; Comprehensive recovery*

1. INTRODUCTION

$MoSi_2$ is a widely applied Dalton-type intermetallic compound with excellent high-temperature oxidation resistance [1], commonly used as a raw material for high-temperature electric furnace heating elements [2]. However, with the increasing demand for $MoSi_2$ heating elements, large quantities of spent $MoSi_2$ components are discarded, posing significant environmental and resource challenges [3]. Due to its oxidation-resistant properties, spent $MoSi_2$ can serve as a precursor for high-temperature oxidation-resistant coatings [4]. Additionally, its high molybdenum content and the reducibility potential of silicon enable $MoSi_2$ to act as a reductant for recovering valuable metals from iron-rich slags with high oxygen potential. Copper slag, a major byproduct of pyrometallurgical copper production (generating 2.2–3 tons per ton of copper produced) [5], contains 35–45 wt.% Fe and holds significant recycling value. Currently, most copper slag is directly disposed of in slag disposal pits without treatment, causing severe resource waste and environmental hazards. Its efficient processing and recycling have become urgent priorities.

This study employs spark plasma sintering (SPS) to fabricate dense, thickness-controlled $MoSi_2$ coatings on Nb substrates, addressing high-temperature oxidative demands. SiC/$ZrSi_2$ additives modulate thermal expansion mismatch, enhancing high-temperature durability. A synergistic smelting process recovers spent $MoSi_2$ and copper slag: Si acts as a reductant, generating SiO2 slag to optimize dynamics, while in situ MoFe formation improves metal capture. Copper slag

serves as a low-melting flux and Fe source, accelerating $MoSi_2$ decomposition and enabling efficient slag-metal separation. This strategy achieves selective MoFe recovery.

2. EXPERIMENTAL

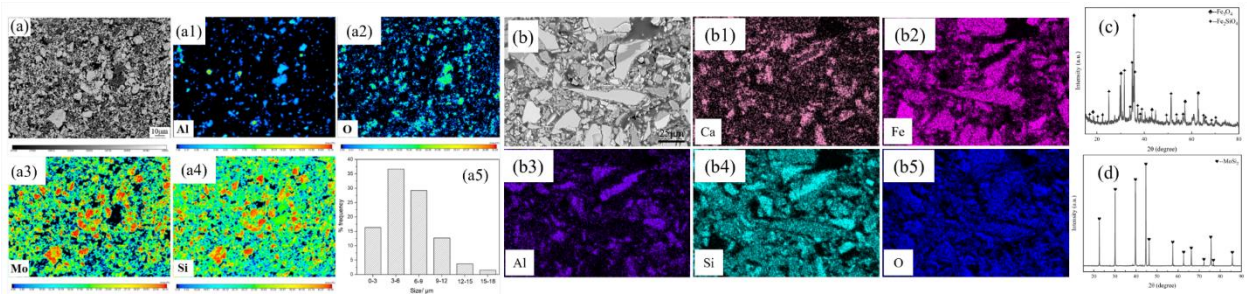

Figure 1. (a) EPMA image of spent $MoSi_2$ powder; (b) SEM image of copper slag powder; (c) XRD results of copper slag; (d) XRD results of spent $MoSi_2$ powder.

The spent $MoSi_2$ powder used in the experiments was derived from Grade 1800 molybdenum disilicide rods, prepared via crushing and ball-milling. It was primarily composed of the $MoSi_2$ phase (confirmed by XRD, Fig. 1d). EPMA mapping (Fig. 1a) revealed Mo, Si, Al, and O elements, minor Mo_5Si_3 phase. The copper slag (from a Chinese enterprise) was depleted slag dominated by fayalite and magnetite phases (Fig. 1c). SEM-EDS mapping (Fig. 1b) showed fayalite as regular gray blocks, magnetite as bright white regions, and interspersed dark-phase gangue. Coating sintering was performed at 1500 ℃ using an SPS system (Labox-125, Sinter Land Inc., Japan). Synergistic smelting of copper slag and spent $MoSi_2$ was conducted in a tube furnace.

3. RESULTS AND DISCUSSION

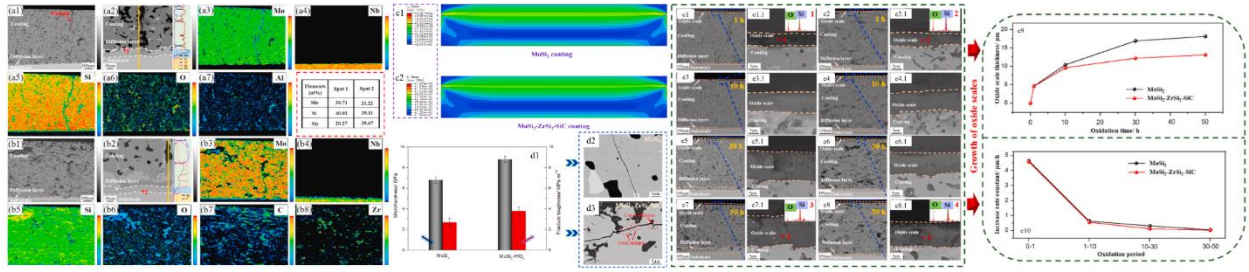

Figure 2. (a) Cross-section BSE micromorphology and WDS analysis of SPSed $MoSi_2$ and (b)$MoSi_2$-$ZrSi_2$-SiC coatings; Stress distribution diagrams of $MoSi_2$ (c1) and $MoSi_2$-$ZrSi_2$-SiC (c2) coatings on Nb substrate after SPS; Microhardness and fracture toughness of SPSed $MoSi_2$ and $MoSi_2$-$ZrSi_2$-SiC coatings (d1); indentation morphologies of the crack propagation path of $MoSi_2$ (d2)and $MoSi_2$-$ZrSi_2$-SiC (d3) coatings; (e) Cross-section BSE micromorphology and EDS analysis of XRD patterns of $MoSi_2$ and $MoSi_2$-$ZrSi_2$-SiC coatings after oxidation of 1-50 h at 1500 ℃; Corresponding oxide scale thickness and increase rate constant of $MoSi_2$ and $MoSi_2$-$ZrSi_2$-SiC coatings during oxidation

After high-temperature sintering, the $MoSi_2$ coating exhibited strong adhesion to the substrate (Fig. 2a), with an 11.2 μm $(Nb, Mo)_5Si_3$ diffusion layer formed beneath the coating, enhancing interfacial bonding. However, CTE mismatch induced through-thickness cracks in the MoSi2 coating post-sintering. SiC incorporation mitigated CTE mismatch, improving coating integrity (Fig. 2b). Residual thermal stresses were primarily localized in the $MoSi_2$ coating, but the $MoSi_2$-$ZrSi_2$-SiC composite coating showed a more uniform stress distribution due to optimized CTE compatibility (Fig. 2c). Calculated residual stresses in monolithic $MoSi_2$ (0.5 GPa) exceeded those in the composite coating (0.2 GPa), indicating reduced interfacial thermal stress. This ensured robust bonding, suppressed crack propagation after SPS, and enhanced fracture toughness via

crack deflection, complex propagation paths, and energy absorption (Fig. 2d). SiC particles further increased coating hardness.$ZrSi_2$ addition promoted the formation of high-melting-point $ZrO_2/ZrSiO_4$ skeletons during oxidation, improving oxide scale stability and density (Fig. 2e).

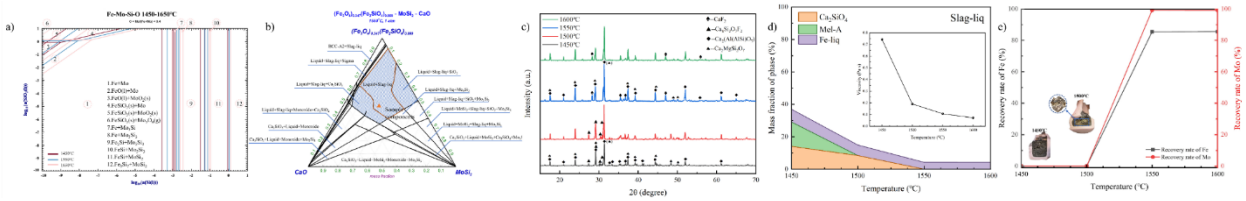

Figure 3. (a) Phase diagram of the Fe-Mo-Si-O system at different temperatures; (b) The ternary phase diagram of the main components of copper slag - $MoSi_2$ - CaO system; (c) XRD results of secondary slag; (d) Phase composition at different temperatures; (e) The influence of temperature on the extraction yields of Mo and Fe

The Fe–Mo–Si–O equilibrium predominance area diagram (Fig. 3a) shows that Fe and Mo can co exist as metallic phases with enrichment. However, Si's reducing capability weakens at elevated t emperatures, causing Mo oxidation loss. Calculations of the $MoSi_2$–copper slag major componen ts–CaO ternary phase diagram (Fig. 3b) indicate that moderate CaO addition expands the coexist ence region of slag and alloy liquids, reduces high-melting-point phases, and optimizes reaction t hermodynamics and processing environments. High-temperature melting experiments (Fig. 3c) re veal dominant slag phases as CaO–SiO_2 glass melt and gehlenite. CaF_2 addition lowers melt visc osity and melting point by acting as a diluent for [SiO_4] networks. Increasing temperature signific antly enhances refractory phase dissolution (Fig. 3d), reduces melt viscosity, and improves reacti on conditions and settling efficiency, achieving Mo and Fe recovery rates of 99.97 % and 85.49 %. However, excessive temperatures induce Mo oxidation loss (Fig. 3e).

4. CONCLUSION

This study employed SPS to fabricate composite coatings on Nb substrates using spent MoSi2 as the primary raw material, with minor additions of SiC and ZrSi2. The coatings exhibited excellent mechanical properties and high-temperature oxidation resistance, demonstrating robust anti-oxidation and oxygen-barrier capabilities during a 50-hour oxidation test at 1500 °C. Leveraging the reducing potential of silicon in spent MoSi2, synergistic smelting of copper slag and spent MoSi2 was conducted to in-situ fabricate ferromolybdenum alloys. Under optimal process conditions, Mo and Fe recovery efficiencies reached 99.97% and 85.49%, respectively. This approach achieved waste-to-waste treatment and cradle-to-cradle life cycle recycling of wastes.

REFERENCES

[1] Z. Ye, S. Wang, Y. Zou, G. Chen, S. Yu, L. Wen, L. Zhao, G. Zhang, Y. Wang, D. Jia, Y. Zhou, Compos. B: Eng., (2024).
[2] C. Mao, X. Ren, X. Ji, L. Xu, X. Wang, N. Zhu, P. Zhang, P. Feng, Ceram. Int., (2023).
[3] L. Zhu, S. Zhang, F. Ye, X. Ren, P. Feng, Compos. B: Eng., (2024).
[4] P. Chen, L. Zhu, X. Ren, X. Kang, X. Wang, P. Feng, Ceram. Int., (2019).
[5] Y. Zhou, H. Wang, H. Wang, K. Dong, R. Zhu, Z. Jiang, G. Wei, J. Clean. Prod., (2023).

DOI: 10.5937/IOC25010S *Plenary lecture* *Abstract*

ADVANCES IN UNDERSTANDING OF REDUCTION PROCESSES IN EXTRACTIVE METALLURGY

Srećko Stopić [1a], Alexander Birich[1b], Bernd Friedrich [1c]

[1] IME Process Metallurgy and Metal Recycling, RWTH Aachen University, Germany
[1a] SStopic@ime-aachen.de, 0000-0002-1752-5378
[1b] abirich@ime-aachen.de, 0000-0002-5424-6124
[1c] bfriedrich@ime-aachen.de, 0000-0002-2934-2034

Abstract

Reduction processes at higher temperatures with carbon and hydrogen are widely used in industrial production of metal powders. Chemical reduction at lower temperatures usually involves the reduction of metal ions such as gold, silver and copper in some type of solvent and a separate reducing agent. This method is typically used for the preparation of magnetic metal nanoparticles, such as iron, cobalt, nickel and its alloys. In this process, metal nanoparticles are formed in aqueous solution by various reduction processes such as electrowinning, microwave reduction, and using various types of reducing agents and metal precursors such as metallic chloride and metallic nitrate. It allows controlling the particle size, morphology, and crystallinity, but requires costly precursors, toxic or hazardous solvents, chemical reductants like sodium borohydride or hydrazine, and stabilizers to prevent the aggregation of particles or to make them physiologically compatible. The ultrasonic spray pyrolysis (USP) is droplet generation phenomenon induced by ultrasonic field including its simplicity, cost-effectivity, continuous operation, and high deposition rate using an electrostatic filter. Synthesis of metallic, oxidic and composite powders is enabled using USP with hydrogen reduction. Reduction processes were also used in recycling of titanium from aluminium residues aiming iron removal in the first step of the research strategy. Reduction of iron oxides in solid state, at atmospheric pressure, is an already implemented industrial process that yields iron feedstock suitable for steel production in electric arc furnaces. Thermochemical modeling of reduction for bauxite residues containing iron oxides has been done by FactSage for hydrogen and carbon as reducing agents at 1700°C what is very important for the analysis of iron formation and mass losses.

Keywords: *reduction, hydrogen, carbon, ultrasonic spray pyrolysis, bauxite residues*

INVITED LECTURES

The 56th International October Conference on Mining and Metallurgy
22-25 October 2025, Bor Lake, Bor, Serbia
www.ioc.tfbor.bg.ac.rs

DOI: 10.5937/IOC25013C *Invited lecture* *Original scientific paper*

DEVELOPMENT OF HYDROGEN METALLURGY IN CHINA

Buxin Chen[1a], Mao Chen[2a], Meilong Hu[1b], Kaihui Ma[2b], Hongqiang Liu[3a], Chenguang Bai[1c*]

[1] College of Materials Science and Engineering, Chongqing University, Chongqing, 400044, China
[2] State Key Laboratory of Vanadium and Titanium Resources Comprehensive Utilization, Pangang Group Research Institute Co., Ltd., Panzhihua, Sichuan, 617000, China
[3] HBIS Materials Technology Research Institute Co., Ltd., Shijiazhuang, Hebei, 050000, China
[1a] 202009131240@cqu.edu.cn, 0000-0002-5461-6949
[1b] hml@cqu.edu.cn, 0000-0002-5071-0700
[1c] bguang@cqu.edu.cn, 0000-0003-1795-6503
[2a] Mao.chen@uqconnect.edu.au, 0000-0002-8642-1062
[2b] makaihuiii@163.com, 0009-0005-5186-1243
[3c] liuhongqiang@hbisco.com, 0000-0003-2897-8134

Abstract

China is actively promoting its carbon peaking and carbon neutrality goals. Hydrogen metallurgy characterized by the replacement of carbon with hydrogen has attracted widespread attention as a vital component of low-carbon metallurgy. This study provides a statistical analysis of publications and patents related to hydrogen metallurgy in Chinese databases over the past five years, and summarizes the current industrial practices in hydrogen metallurgy in China. The results reveal a rapidly growing trend in theoretical research and technological development related to hydrogen metallurgy in China over recent years. Several major steel enterprises have carried out industrial practices of hydrogen-based shaft furnace and hydrogen-rich blast furnace smelting, offering initial confirmation of the feasibility of hydrogen metallurgy. Currently, the industrialization of hydrogen metallurgy in China faces a challenge of high hydrogen production costs. Therefore, this study reviews and analyzes the economics of the main hydrogen sources, including coke oven gas, natural gas, coal gasification, hydrogen from by-product during chemical processes, and hydrogen produced by water electrolysis. Although the current hydrogen sources mainly rely on gray hydrogen produced from fossil fuels, the large-scale and cost-effective production of green hydrogen from renewable energy sources in the future is expected to substantially accelerate the industrial application of hydrogen metallurgy. In summary, hydrogen metallurgy technology in China has established a solid foundation in research and accumulated certain industrial application experience. However, further research is required to improve hydrogen utilization efficiency and decrease hydrogen production costs, thereby enabling the widespread industrial application of hydrogen metallurgy.

Keywords*: hydrogen metallurgy, low-carbon metallurgy, hydrogen sources, hydrogen production costs.*

1. INTRODUCTION

Controlling CO_2 emissions has become a global consensus and an urgent necessity in the fight against climate change and the pursuit of sustainable development. In response, China has announced its “dual carbon” goals-aiming to reach peak carbon emissions by 2030 and attain carbon neutrality by 2060. The steel industry is one of the largest sources of CO_2 emissions in China, contributes approximately 15% of the country’s total industrial emissions [1]. With the ongoing implementation of the “dual carbon” goals, the decarbonization of the steel industry has become essential. Hydrogen metallurgy, which replaces traditional carbon-based reductants with hydrogen(H_2), offers significant decarbonization potential, as its reduction byproduct is water (H_2O) rather than CO_2. Therefore, it is regarded as a promising pathway for the Chinese steel industry to achieve deep emission reductions and long-term carbon neutrality. This study provides an overview of the development of hydrogen metallurgy in China, focusing on trends in academic

publications and patent authorizations over the past five years, industrial implementation of hydrogen metallurgy by Chinese steel enterprises, and the techno-economic analysis of viable hydrogen sources.

2. RESEARCH PROGRESS AND INDUSTRIAL PRACTICE OF HYDROGEN METALLURGY IN CHINA

Using the China National Knowledge Infrastructure (CNKI), a major Chinese-language academic database, paper and patent data from 2020 to 2024 were collected based on keywords including "hydrogen metallurgy," "hydrogen-rich blast furnace (BF)," "hydrogen-based shaft furnace," and "hydrogen reduction," as shown in Figure 1. Statistical data show that the number of relevant papers increased significantly from 55 (2020) to 198 (2024), accompanied by a growth in patent filings from 90 to 313. This trend clearly reflects the rapid development of fundamental research and technological innovation in hydrogen metallurgy in China since the announcement of the "dual carbon" goals in September 2020.

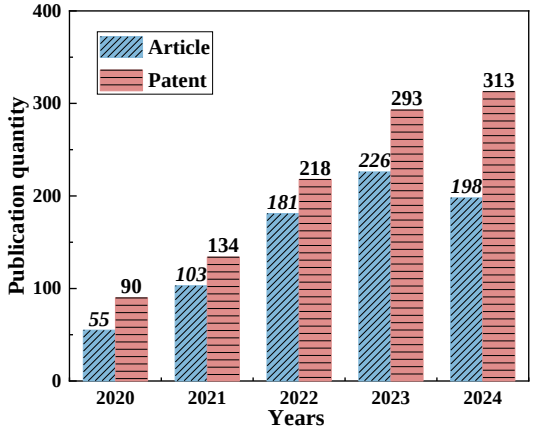

Figure 1. Number of hydrogen metallurgy-related papers and patent in the CNKI (2020-2024)

At present, industrial applications of hydrogen metallurgy in China primarily follow two technological pathways: H_2-rich BF and hydrogen-based shaft furnaces. Given that the BF-BOF (basic oxygen furnace) route accounts for approximately 90% of China's steel production, H_2-rich BF is expected to remain the dominant decarbonization strategy for the industry over the next 10 to 20 years. This technology involves injecting H_2-rich gas either at the tuyeres or furnace shaft, reducing coke consumption while simultaneously lowering CO_2 emissions. In recent years, several major Chinese steel producers have actively implemented H_2-rich BF in industrial practice (see upper part of Figure 2). In 2010, Jinan steel injected coke oven gas (COG) into a 350 m^3 BF, reducing the fuel ratio by 45.91 kg/THM and CO_2 emissions by 75 kg/THM at an injection rate of 62.51 m^3 per ton of hot metal (m^3/THM) [2]. In 2021, Jinnan Steel injected COG into an 1860 m^3 BF, achieving a 32 kg/THM reduction in fuel ratio and about 80 kg/THM decrease in CO_2 emissions at 65 m^3/THM injection [3]. In 2022, Bayi Steel completed an industrial trial of a 400 m^3 H_2-rich carbon recycling oxygen blast furnace, integrating H_2-rich gas injection, 1200 °C top-gas recycling, and full oxygen smelting, resulting in a 21% reduction in CO_2 emissions [4]. In 2021, Xingguo Foundry successfully performed pure H_2 injection in a 40 m^3 pilot BF. Industrial practice indicates that tuyere injection of COG is currently the mainstream H_2-rich BF technology in China, with a relatively high level of process. However, due to the irreplaceable the coke as the structural support in the BF and the relatively low utilization efficiency of hydrogen, the carbon emission reduction of H_2-rich BF is generally limited to the range of 10% to 20%.

In contrast, hydrogen-based shaft furnaces use an H_2-CO mixed gas as the reductant, offering substantial carbon reduction potential (50%-95%). Although this technology started later in China, its industrialization is accelerating. Recent landmark projects include Zhongjin Taihang, Baosteel,

and Hebei Iron & Steel Group (HBIS), China Iron & Steel Research Institute Group (CISRI) (see lower part of Figure 2) [5]. In June 2021, Zhongjin Taihang built the world's first COG-based hydrogen shaft furnace direct reduced iron (DRI) production line with an annual capacity of 300,000 tons, supported by a 1 million ton coke plant, proving the feasibility of hydrogen-based direct reduction in China. In December 2022, HBIS completed a 1.2 million ton-scale COG zero-reforming hydrogen shaft furnace and began continuous production in 2023, decreasing CO_2 emissions by about 70%. In December 2023, Baosteel commissioned a million-ton hydrogen shaft furnace, achieving a CO_2 emission reduction of 58%-89%. In 2024, CISRI started the world's first pure hydrogen shaft furnace in Linyi, using 100% green hydrogen and achieving an 87% reduction in CO_2 emissions. In summary, large-scale industrial practices in China have preliminarily demonstrated the engineering feasibility and CO_2 emission reduction potential of hydrogen metallurgy.

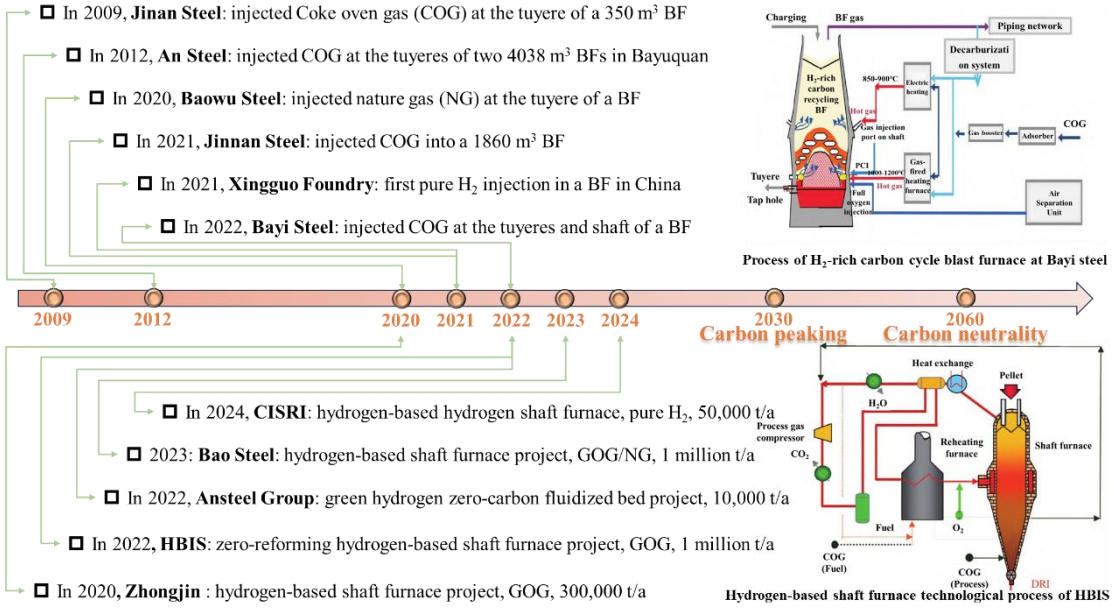

Figure 2. Schematic Diagram of Hydrogen Metallurgy Industrial Practices in China

3. ANALYSIS OF HYDROGEN SOURCES FOR HYDROGEN METALLURGY IN CHINA

The large-scale development of hydrogen metallurgy requires a hydrogen supply that is both low-cost and low-carbon. Currently, hydrogen sources mainly include fossil fuels (coal and natural gas), industrial by-product hydrogen, water electrolysis, and biomass-based hydrogen production. At present, China's hydrogen production is predominantly based on fossil fuels, with 62% derived from coal, 19% from natural gas, and approximately 18% from industrial by-product hydrogen. Hydrogen produced via water electrolysis accounts for only 1% [6]. To systematically compare the economic performance and CO_2 emission reduction potential of different hydrogen sources, this study normalizes hydrogen share, unit cost, and CO_2 emissions, and presents a ternary comparison diagram (figure 3). Coal-based hydrogen benefits from China's abundant coal resources and mature industrial system, offering a significant cost advantage (0.45-0.78 CNY/Nm^3) [7]. However, its high CO_2 emission (25-30 kg CO_2/kg H_2) [8] makes its share expected to decrease to 20% by 2025 [1]. Industrial by-product hydrogen and natural gas-based hydrogen also face challenges related to high CO_2 emission.

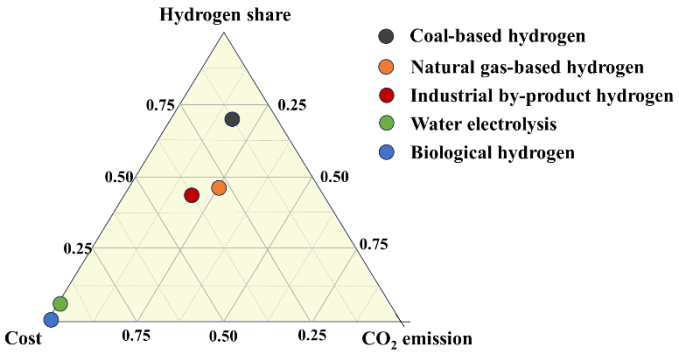

Figure 3. Ternary diagram of share-cost-carbon emissions for different hydrogen sources

In the future, water electrolysis is expected to become the major hydrogen source for hydrogen metallurgy in China. Its share is projected to increase to approximately 15% by 2030 and reach 70% by 2050 [1]. However, the current cost of hydrogen produced by electrolysis is relatively high at 2.69 CNY/Nm^3, which is two to three times that of fossil fuel-based hydrogen [8]. Moreover, over 50% of China's power generation still relies on coal, resulting in a carbon emission of 9-12 kg CO_2/kg H_2 for coal-based hydrogen production. In contrast, electrolysis powered by renewable energy (solar and wind) can achieve near-zero emissions, making it the most promising pathway for green hydrogen. Therefore, the Chinese steel industry should strengthen the integration of renewable energy-powered electrolysis with hydrogen metallurgy technologies. This integration should rely on renewable hydrogen production processes to support the development of hydrogen metallurgy, improve energy efficiency of electrolysis, and expand hydrogen production capacity to significantly reduce green hydrogen costs. Besides electrolysis, emerging technologies such as nuclear-based and biomass-based hydrogen production also hold potential. Nuclear-based hydrogen production boasts thermochemical efficiencies above 50% but faces challenges related to equipment costs, safety, and high-temperature materials. Biomass hydrogen production remains at the research stage with costs as high as 25-33 CNY/kg, making industrial application difficult.

4. CONCLUSION

Under the "dual carbon" goals, China has made notable progress in both hydrogen metallurgy research and industrial application. Over the past five years, the number of hydrogen metallurgy related papers and patents in Chinese databases has steadily increased. Chinese steel enterprises have successively implemented industrial practices including H_2-rich blast furnace and hydrogen-based shaft furnace, promoting the industrialization of hydrogen metallurgy technologies. However, current hydrogen sources are dominated by grey hydrogen with high CO_2 emissions and green hydrogen production remains costly. Achieving low-cost, large-scale green hydrogen production is urgently needed to underpin the rapid development of hydrogen metallurgy in China.

REFERENCES

[1] S. Tong, L. Ai, L. Hong, et al., Mater. Rep., 37 (23) (2023) 22050271.
[2] X. Liu, X. Mao, T. Bo, et al., Ironmaking, 38 (2) (2019) 39-42.
[3] J. Gao, L. Zhu, J. Ke, et al., AISI, 57 (9) (2022) 42-48.
[4] S. Ji., Xin Jiang, AISI, (1) (2022) 5-11.
[5] F. Li, M. Chu, J. Tang, et al., STF, 3 (4) (2024) 44-57.
[6] Z. Zhang, B. Xu, B. Liang, et al., Nat. Gas Ind., 45 (4) (2025) 179-192.
[7] J. Chen, M. Su, X. Zhang, et al., Chin. Metall., 33 (1) (2023) 24-33.
[8] X. Zhang, Q. Wang, Y. Wei, et al., Henan Huagong., 42 (5) (2025) 1-6.

The 56th International October Conference on Mining and Metallurgy
22-25 October 2025, Bor Lake, Bor, Serbia
www.ioc.tfbor.bg.ac.rs

DOI: 10.5937/IOC25017C | Invited lecture | Original scientific paper

CHARACTERIZATION OF INDUSTRIAL JAROSITES FROM THE MEXICAN ZINC EXTRACTION PROCESS

Alejandro Cruz Ramírez[1a], José Enrique Sanchez Vite[2a], Teresita del Refugio Jiménez Romero[2b], Margarita García Hernández[1b], Heriberto Mendoza Cárdenas[3a]

[1]UPIIH, Instituto Politécnico Nacional, DESCTI, San Agustín Tlaxiaca, 42162, Hidalgo, México
[2]ESIQIE, Instituto Politécnico Nacional, UPALM, 07738, Ciudad de México, México
[3] CECyT 16, Instituto Politécnico Nacional, DESCTI, San Agustín Tlaxiaca, 42162, Hidalgo, México
[1a] alcruzr@ipn.mx, 0000-0002-0972-596X
[2a] jsanchezv2105@alumno.ipn.mx, 0009-0006-5001-0495
[2b] tjimenezr@ipn.mx, 0009-0003-8012-6817
[1b] margarciah@ipn.mx, 0000-0002-3850-3901
[3a] hmendozacar@ipn.mx, 0009-0005-5687-4238

Abstract

A novel pyrometallurgical route was developed to obtain a Pb-Ag alloy by recycling two metallurgical wastes: lead paste obtained from spent lead-acid batteries and a jarosite residue obtained from the Mexican hydrometallurgical production of zinc. Both metallurgical wastes were characterized by atomic absorption spectrometry (AAS), X-ray diffraction (XRD), and scanning electron microscopy with energy-dispersive spectra (SEM-EDS). Mixtures of both wastes were pyrometallurgically treated with sodium carbonate in a silicon carbide crucible at 1200 °C. A mixture ratio of 30% Na_2CO_3 – 40 % Lead paste – 30 % Jarosite produced the highest amount of Pb-Ag alloy, while the slags produced contained compounds such as $Na_2(SO_4)$ and $Na_2Fe(SO_4)_2$, which have a high sulfur-fixing, contributing to the minimization of atmospheric pollution.

***Keywords**: Jarosite, lead paste, Pb-Ag alloy, pyrometallurgy, waste minimization*

1. INTRODUCTION

The metallurgical industry generates significant quantities of hazardous waste, such as jarosite from zinc hydrometallurgy and lead paste from spent lead-acid batteries. These residues pose severe environmental risks due to their potential to release toxic elements (e.g., Pb, Cd, As) into soil and water, while also representing a loss of valuable metals like silver and lead [1,2]. Jarosite, an iron sulfate precipitate, contains trace amounts of Ag, whereas lead paste consists primarily of Pb and sulfur compounds. Traditional disposal methods, such as landfilling, are increasingly unsustainable due to stricter environmental regulations and the need for resource recovery [3,4]. Current recycling approaches face limitations. Hydrometallurgical methods for jarosite, though effective in metal extraction, often involve complex leaching steps and generate secondary wastes [5,6]. Standalone pyrometallurgical treatments for jarosite require extreme temperatures (1400–1700 °C) to recover metals, resulting in high energy costs and volatile emissions [2,6]. Similarly, lead paste recycling typically focuses on lead recovery but overlooks the potential to co-extract silver from other waste streams [7,8]. This study introduces an innovative low-temperature pyrometallurgical co-processing route for the simultaneous treatment of jarosite and lead paste, to recover a Pb-Ag alloy and a slag with high fixing sulfur. The pyrometallurgical treatment is carried out using Na_2CO_3 as a fluxing and SiC crucibles, which allow the obtaining liquid phases at 1200 °C.

2. EXPERIMENTAL

The lead paste used in this study was obtained from spent lead-acid batteries through a recycling process. The black powder residue was dried at 120°C for 8 hours, then ground using an agate

mortar and sieved to obtain 90 μm particles. The jarosite residue, sourced from a Mexican zinc hydrometallurgical plant, is presented as a yellow-brown fine powder with clay-like characteristics. After drying at 100°C for 12 hours, the material was classified to obtain particles ≤75 μm. The chemical composition of both residues was determined by AAS while the mineralogical characterization was performed using a Bruker D8 Advance X-ray diffractometer with Cu Kα radiation (λ = 1.5406 Å) operating at 40 kV and 30 mA. Qualitative chemical analysis, morphology, and resulting slag size were analyzed by scanning electron microscopy with energy dispersive spectra.

Three mixture compositions were designed to evaluate the effect of lead paste to jarosite ratio on metal recovery and slag formation (Table 1). All mixtures maintained 30 wt.% sodium carbonate (Na_2CO_3, Fermont, 99.5% purity, ≤198 μm) as fluxing agent:

Table 1. Mixing ratios of raw materials (wt.%)

Trial Identification	Na_2CO_3	Lead Paste	Jarosite
30Na:55P:15J	30	55	15
30Na50P:20J	30	50	20
30Na:40P:30J	30	40	30

Each 100 g batch was homogenized in a polypropylene flask that rotated at 25 rpm for 30 minutes. The mixtures were then charged into silicon carbide crucibles (SiC, 0.5 kg capacity) and processed in an electric resistance furnace. The temperature was controlled using a Eurotherm 2408 controller with a K-type thermocouple positioned 5 mm from the crucible wall, maintaining ±10°C of the setpoint (1200°C). After the holding period, the molten material was poured into a preheated (200°C) cast iron mold to promote phase separation.

3. RESULTS AND DISCUSSION

Table 2 shows the chemical composition of the industrial jarosite and lead paste determined by Atomic Absorption Spectrometry.

Table 2. Chemical composition of metallurgical wastes (wt.%)

	Chemical Composition (wt.%)									
Jarosite	**Pb**	**S_{Total}**	**Cu**	**Fe**	**Ag**	**Ca**	**Na**	**Si**	**Zn**	**NH_4**
	0.45	17.47	0.17	8.36	0.0143	16.31	0.46	1.10	4.88	1.2
Lead Paste	90.65	5.34	0.03	0.07	0.001	-	-	-	-	-

The lead paste is predominantly composed of Pb and S. On the other hand, the jarosite residue contains significant amounts of Fe, S, and Ca, along with trace amounts of Ag. The presence of ammonium indicates that during the removal of iron in the leaching of zinc, ammonium-jarosite was precipitated.

Figure 1 shows the mineralogical composition of the jarosite and lead paste determined by XRD.

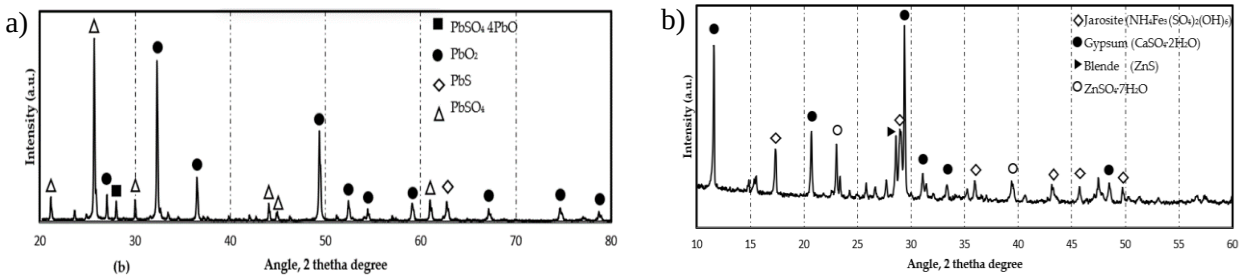

Figure 1. X-ray pattern diffractions for (a) lead paste and (b) jarosite residue

The lead paste primarily consists of galena (PbS) and lead oxide (PbO), with minor amounts of lead sulfate ($PbSO_4$) and lead oxide sulfate ($PbSO_4 \cdot 4PbO$). In contrast, the jarosite residue is composed mainly of ammonium jarosite ($(NH_4)_2Fe_3(SO_4)_2(OH)_6$). Tables 3 and 4 show the

amounts and the chemical composition of the metallic and slag phases obtained by the reduction trials by mixing the metallurgical wastes with a fixed amount of sodium carbonate based on Table 1.

Table 3. Chemical composition of the metallic phase

Table Designation	Metallic Ingot (g)	Chemical Composition (wt.%)						
		$Pb_{balance}$	Ag	Na	Si	Fe	Ca	Cu
30Na:55P:15J	34.51	99.21	0.0073	0.17	0.36	0.14	0.11	0.01
30Na:50P:20J	41.24	99.17	0.0080	0.16	0.37	0.14	0.14	0.01
30Na:40P:30J	35.27	99.33	0.0126	0.17	0.21	0.12	0.14	0.02

Table 4. Chemical composition of the slag phase

Table Designation	Slag (g)	Chemical Composition (wt.%)						
		Pb	Ag	Na	Si	Fe	Ca	S
30Na:55P:15J	36.28	2.73	0.0002	8.93	3.45	3.1	5.87	3.04
30Na:50P:20J	42.02	3.22	0.0002	18.53	1.97	3.82	4.34	6.94
30Na:40P:30J	53.22	3.71	0.0003	18.89	3.49	4.19	7.29	9.47

All trials maintained exceptional Pb purity (99.17-99.33 wt.%) minimal variation (±0.08%) across compositions indicates process stability; silver recovery progressive increase from 73 ppm (30Na:55P:15J) to 126 ppm (30Na:40P:30J) the strong correlation with jarosite content confirms efficient Ag capture; impurity profile consists in sodium (0.16-0.17 wt.%) consistent flux contribution, silicon (0.21-0.37 wt.%) higher in low-jarosite mixes (crucible interaction) and iron (0.12-0.14 wt.%), minimal variation despite jarosite Fe content. Sulfur fixation efficiency improved from 78% to 93% with higher jarosite $Na_2Fe(SO_4)_2$ formation (42 vol% in 30Na:40P:30J), enhanced environmental stability.

The metallic phase (Figure 2a) consisted primarily of lead with silver in a solid solution. The increasing Ag content with higher jarosite proportion demonstrates effective silver capture by the lead matrix, following the Pb-Ag binary phase diagram which shows complete miscibility in the liquid state at 1200°C. The slag phases (Figure 2b) showed progressive transformation with increasing jarosite content: Low-jarosite (15-20%): Dominated by Na_2SO_4 (60-65 vol%) and $CaSiO_3$ (25-30 vol%), high-jarosite (30%): Developed $Na_2Fe(SO_4)_2$ (42 vol%) alongside persistent Na_2SO_4 (38 vol%).

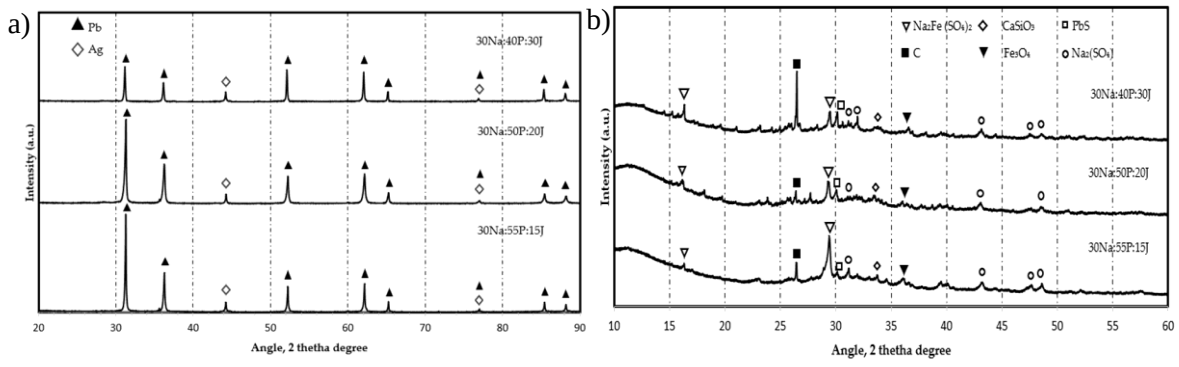

Figure 2. X-ray diffraction patterns of (a) lead paste and (b) jarosite residue

Figure 3 shows SEM-EDS micrograph samples of the metallic and slag phases for the 30Na:55P:15J trial.

Microstructural analysis of the metallic phase (Figure 3a) reveals a lead-silver primary matrix that dominates over 95% of the analyzed area. Beyond the metallic matrix, three distinct non-metallic

inclusions were identified. These non-metallic inclusions with angular morphologies ranging from 5 to 15 μm originate from flux interactions and are chemically inert, posing no interference with silver recovery. MEB-EDS characterization of the slag phase (Figure 3b) reveals a heterogeneous distribution of three distinct regions: a sulfate-rich matrix, iron-silicate zones, and calcium-silicate inclusions.

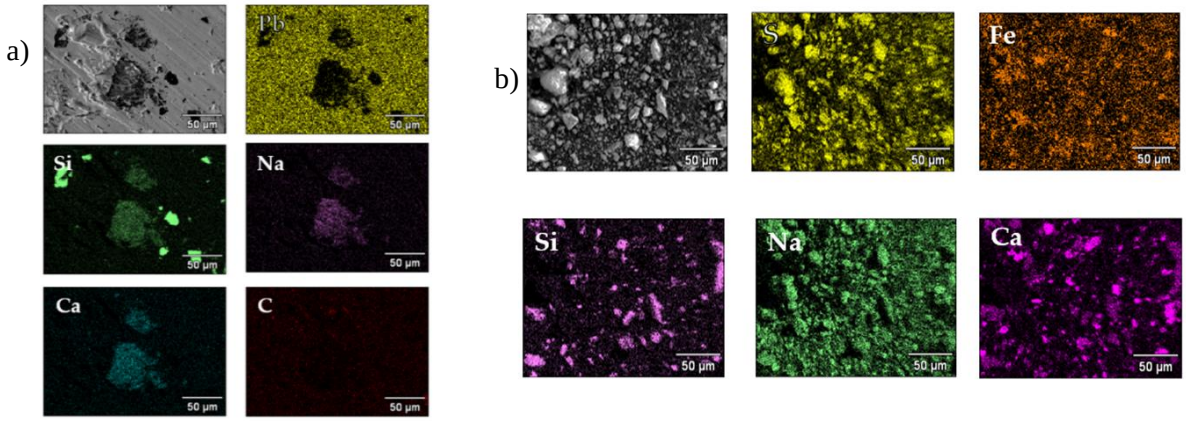

Figure 3. Micrograph of the a) metallic sample and b) slag sample of trial 30Na:55P:15J

4. CONCLUSIONS

This study successfully demonstrates an innovative pyrometallurgical approach for co-processing jarosite and lead paste wastes, with three key advancements: resource recovery, achieved 126 ppm Ag in Pb-Ag alloy (30Na:40P:30J); recovered >99% pure lead suitable for battery recycling and valorized 100% of input waste with <12% mass loss. Besides, environmental benefits such as 93% sulfur fixation as stable $Na_2Fe(SO_4)_2$ compounds, reduced SO_2 emissions by 83% compared to conventional methods and produced an inert slag. The process advantages consist of operation at 1200°C (vs 1400-1700°C conventional), and a 30% lower energy requirement than standalone jarosite processing. The 30Na:50P:20J mixture emerged as the optimal formulation, balancing high metal recovery (82.5% Pb, 78% Ag), efficient slag formation, and minimal environmental impact.

ACKNOWLEDGEMENTS

A. Cruz wishes to thank the fund of the government of the state of Hidalgo through the Council of Science, Technology, and Innovation of the State of Hidalgo (CITNOVA)

REFERENCES

[1] M.K. Jha, V. Kumar, R.J. Singh, Resour. Conserv. Recycl., 33 (2001) 1–22.
[2] M. Kerolli, L. Curkovic, H. Fajkovic, Croat. Chem. Acta, 88 (2015) 189 -196.
[3] J. Dutrizac, J. Jambor, Rev. Miner. Gechem., 40 (2000) 405–462.
[4] J. Salminen, J. Nyberg, M. Imris, B. Magnus, Springer, (2020) 391–403.
[5] K. Yanamandra, D. Pinisetty, A. Daoud, N. J. Gupta, Indian Inst. Sci., 102 (2022) 281–295.
[6] A. Sánchez, V. Gutiérrez, A. Cruz, R. Sánchez, Russ. J. Non-Ferrous Met., 57 (2016) 316–324.
[7] Y. Li, Y. Chen, C. Tang, L. Klemettinen, M. Rämä, X. Wan, A. Josikilaakso, Springer, (2018) 1109–1120.
[8] C. Jiménez, M. Favela, A. Romero, A. Hernández, J. Rodríguez, A. Cruz, E.J. Colin, Min. Metall., 60 (2024) 205–214.

The 56th International October Conference on Mining and Metallurgy
22-25 October 2025, Bor Lake, Bor, Serbia
www.ioc.tfbor.bg.ac.rs

DOI: 10.5937/IOC25021C *Invited lecture* *Original scientific paper*

CHARACTERIZATION OF CERAMIC COATINGS WITH THERMAL BARRIER ROLE OBTAINED BY ATMOSPHERIC PLASMA JET SPRAYING

Nicanor Cimpoeşu [1a], Ionuț Adomniței [1b], Corneliu Munteanu[2a], Mihai Axinte [1c], Marian Luțcanu[3a], Mihai Alin Pop[4a], Marius Telișcă[5a], Ana Maria Roman[1d]

[1] Mat. Sci. and Eng. Faculty, Tech. Univ. Gheorghe Asachi from Iasi, 700050, Iasi, Romania
[2] Mechanics Faculty, Tech. Univ. Gheorghe Asachi from Iasi, 700050, Iasi, Romania
[3] Dep. of Phys., Mach. Build. and Ind. Man. Fac. Tech. Univ. ″Gh. Asachi″ from Iasi, 700050, Iasi, Ro
[4]Department of Materials Science, Faculty of Mat. Sci. and Eng., Transilvania University of Brasov, Ro
[5]Fac. of Hydraulics, Geodesy and Env. Eng., Tech. Univ. ″Gheorghe Asachi″ from Iasi, Romania
[1a] nicanor.cimpoesu@academic.tuiasi.ro , 0000-0003-4373-017X
[1b] ionut.adomnitei@student.tuiasi.ro , 0009-0000-7135-7494
[1c] mihai.axinte@academic.tuiasi.ro, 0000-0003-2547-618X
[1d] ana-maria.roman@academic.tuiasi.ro, 0000-0001-8798-1849
[2a] corneliu.munteanu@academic.tuiasi.ro, 0000-0002-3878-9129
[3a] marian.lutcanu@staff.tuiasi.ro, 0000-0002-4177-3881
[4a] alinpma@gmail.com, 0000-0003-2753-2907
[5a] marius.telisca@academic.tuiasi.ro, 0000-0001-7350-1584

Abstract
This paper presents the characterization of ceramic thermal barrier coatings (TBCs) obtained by atmospheric plasma spraying (APS), focusing on their functional, structural, and chemical performance under extreme thermal conditions. The study highlights the critical requirements of TBC systems, including low thermal conductivity, high phase stability above 1200 °C, resistance to thermal shock, and strong adhesion between the ceramic top coat, bond coat, and metallic substrate. Special attention is given to YSZ (zirconia stabilized with yttria) coatings with a high yttria content (38 wt% Y_2O_3), which ensure cubic phase stabilization and enhanced durability at elevated temperatures. Recent advances in TBC design are discussed, such as optimized ceramic compositions, controlled microstructures, and multifunctional architectures that integrate chemical protection and sensing capabilities. The advantages of ceramic TBCs compared to massive or non-ceramic barriers are also outlined, emphasizing their reduced weight, improved thermal insulation, chemical stability, and thermomechanical compatibility. These results confirm the potential of advanced YSZ-based coatings to provide reliable thermal protection in aerospace and energy applications, contributing to increased efficiency and reduced environmental impact.

***Keywords**: ceramic coatings, TBC, YSZ, microstructure*

1. INTRODUCTION

In order to ensure effective and durable protection of components exposed to extreme temperatures, a Thermal Barrier Coating (TBC) system must simultaneously meet a rigorous set of functional and structural requirements, Figure 1. Firstly, the low thermal conductivity of the ceramic layer is fundamental in limiting the heat flow to the substrate, thus helping to keep the temperature below the thermal critical of the structural alloy and prolonging the lifetime of the whole assembly [1]. At the same time, it is essential that the ceramic material exhibits outstanding phasic stability at high temperatures (≥1200 °C) without spontaneous structural transformations (such as tetragonal-monoclinic transition in conventional YSZ), which can lead to internal stresses, cracking or exfoliation [2].

Another essential criterion is thermal shock resistance, which refers to the coating's ability to withstand sudden temperature variations without cracking or loss of adhesion. This implies a suitable microstructure (e.g. controlled porosity, vertical cracks), but also good thermomechanical

compatibility between the ceramic layer, the bond coat and the substrate - in particular in terms of the coefficient of thermal expansion (CTE), which must be as close as possible to prevent the build-up of interfacial stresses during thermal cycling [3].

Also, interlayer adhesion is crucial: without good adhesion between the ceramic layer and the bonding layer (e.g. NiCrAlY), the coating is prone to delamination and spalling under operating conditions. Finally, the TBC system must resist oxidation and corrosion, especially in aggressive firing environments that may contain reactive gases such as SO_2 or H_2O, or contaminants such as Cl^- and Na^+, which may favor infiltration processes, phasic reactions or accelerated degradation [4].
Therefore, a high-performance TBC system must not only be an effective thermal insulator, but also a stable chemical barrier, a strong mechanical structure and a well-balanced interfacial layer - all of which are prerequisites for its operation in extreme environments, such as aircraft turbines or the combustion chambers of high-power engines.

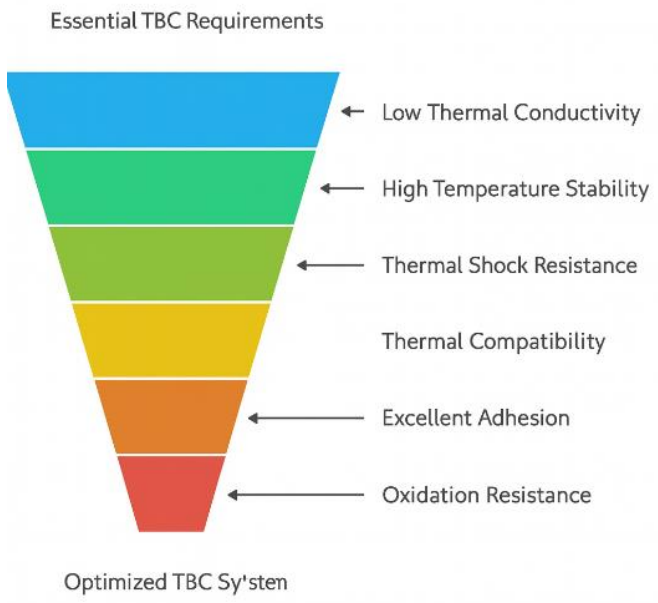

Figure 1. Main characteristics of a ceramic thermal barrier coating

Evaluation of these characteristics is done by standardized methods, such as cyclic thermal shock tests, adhesion tests, post-test morphological analysis (SEM, XRD), and conductivity and hardness measurements.

2. CURRENT TRENDS IN THE DEVELOPMENT OF TBC

Modern research in the field of Thermal Barrier Coatings aims to overcome the limitations of conventional systems by developing innovative solutions that combine thermal stability at extreme temperatures, microstructural adaptability and extended functionalities, Figure 2. A first condition for success is the optimization of the ceramic composition, where attention is focused on YSZ with high Y_2O_3 content (>20 mol%), able to stabilize the cubic phase (c-YSZ) even at temperatures above 1400 °C, thus preventing destructive phase transformations. In parallel, alternative oxides, such as $Gd_2Zr_2O_7$, $La_2Zr_2O_7$, CeO_2 or HfO_2, are being explored, which offer even lower thermal conductivity and improved resistance to chemical attack or accelerated sintering [1].

A second direction is advanced microstructure control, where columnar (EB-PVD) or layered porous microstructures (SPS) are being developed, offering high thermal flexibility, cyclic stress accommodation and superior durability in thermal shock. These architectures allow efficient stress

dissipation through vertical intergranular openings and maintenance of low thermal conductivity even after prolonged exposure [5].

At the same time, the direction of multifunctional coatings is taking shape, where TBC coatings no longer only have a passive thermal insulation role, but also integrate chemical protection (oxidation, molten silicate deposits corrosion) or even smart functions such as embedded sensors (e.g. piezoelectric structures, optical or fluorescent markers) for real-time degradation monitoring [6]. These solutions bring added reliability and enable predictive maintenance in critical applications.

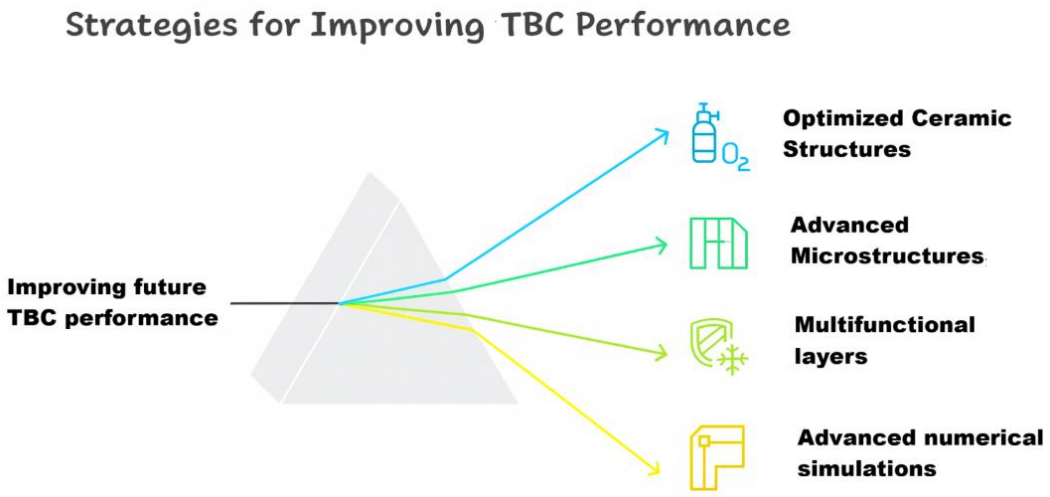

Figure 2. Main methods to improve the performance of ceramic thermal barrier coatings

Last but not least, an increasingly important role is played by advanced numerical modeling, through the integration of CFD (Computational Fluid Dynamics), FEM (Finite Element Method) and thermomechanical failure models, which allow the optimization of the design of TBC systems from the concept phase, thus reducing the time and costs associated with experimental testing. Through these synergistic directions - compositional, microstructural, functional and digital - new perspectives are opening up for the realization of resilient, intelligent and extreme conditions-adapted TBCs for future energy and aerospace technologies. In conclusion, modern TBC systems represent a complex and evolving interdisciplinary field with a direct impact on the efficiency and reliability of energy and aeronautical equipment. The investigation of alternative ceramic compositions, such as YSZ with 38% Y_2O_3, is a promising direction to overcome the limitations of current commercial systems.

3. MAIN ADVANTAGES OF CERAMIC THERMAL BARRIERS OVER OTHER TYPES OF SOLID OR NON-CERAMIC THERMAL BARRIERS

Ceramic thermal barriers in the form of thin coatings have a number of significant advantages over traditional methods of thermal protection, which involve either massive layers of refractory materials or metallic or composite solutions without a ceramic component. These advantages concern both functional properties and technological and economic efficiency.

Light weight and geometric adaptability: ceramic coatings have typical thicknesses in the order of 100-500 μm, compared to a few millimeters for solid refractory insulations. This makes them ideal for aero and automotive applications where weight is a critical parameter. They can be applied on components with complex geometries, including turbine blades, injectors, valves, etc., where solid materials are impossible to fit or would affect functionality.

Low thermal conductivity: YSZ-based ceramics have a thermal conductivity of 1-2 W/m-K, compared to metals (>20-100 W/m-K) or even some metal composites. This allows a high thermal gradient to be achieved at low thicknesses, providing superior thermal protection without requiring large volumes of material [6]. Chemical stability and corrosion resistance: YSZ ceramics are inherently stable at high temperatures and have high oxidation resistance, unlike metal alloys which oxidize rapidly at >1000 °C. It is resistant to aggressive environments (combustion gases, erosive particles), making it durable in severe industrial conditions.

Thermomechanical compatibility and thermal shock resistance: Modern ceramic coatings, due to their porous and layered microstructure, exhibit good thermal conformability, capable of absorbing cyclic expansion/contraction without generating critical cracks. In combination with a flexible bonding layer, they provide superior durability in cyclic conditions, where solid materials can crack or peel [2]. Easy technology integration: TBC coatings can be deposited directly onto finished metal components without requiring additional assemblies or major part design changes. They are compatible with automated industrial processes and have a lower overall cost than alternative volumetric thermal protection methods.

Increased overall thermal efficiency: thanks to their ability to increase the working temperature of components by up to 150-200 °C without degradation, TBCs contribute directly to the thermodynamic efficiency of engines or turbines. This translates into lower fuel consumption and reduced CO_2 emissions - major goals in aviation, energy and transportation . All in all, ceramic thermal barriers offer a performance-to-weight-to-cost ratio incomparably superior to other thermal protection solutions. Combining advanced insulation, stability and resistance properties, they are the reference solution for modern applications in extreme environments.

4. CONCLUSIONS

Plasma sprayed ceramic coatings exhibit low thermal conductivity (1-2 W/m-K), which allows effective protection of the metal substrate even at low thicknesses (100-500 μm). The structural stability of YSZ with high Y_2O_3 content (≈ 38 wt%) ensures cubic phase maintenance and temperature resistance > 1200 °C, reducing the risk of destructive phase transformations. The porous and layered microstructure favors thermal shock resistance and thermomechanical compatibility between the ceramic layer, the bonding layer and the substrate. TBC coatings demonstrate good resistance to oxidation and corrosion, including in aggressive combustion environments, extending the service life of protected components. The major advantages of these coatings (low weight, applicability on complex geometries, high thermal efficiency) recommend them as the reference solution for aero, energy and automotive applications.

REFERENCES

[1] A. Sezavar, S.A. Sajjadi, J. Eur. Ceram. Soc., 45 (8) (2025) 117274.
[2] M. Luțcanu, M. Coteață, M.A. Bernevig, C.D. Nechifor, M.M. Cazacu, P. Paraschiv, B. Istrate, G. Bădărău, N. Cimpoeșu, Arch. Metall. Mater., 67 (2022) 479–485.
[3] G. Barbero, L.R. Evangelista, R.S. Zola, E.K. Lenzi, A.M. Scarfone, Fractal Fract., 8 (7) (2024) 369.
[4] X. Teng, H. Peng, L. Li, H. Guo, J. Eur. Ceram. Soc., 43 (12) (2023) 5373–5380.
[5] M. Luţcanu, C. Munteanu, A.M. Kicsi, C.G. Roman, B.A. Croitoru, M.M. Prisecariu, I. Cazacu, D.L. Ştirbu, N. Chicet, N. Cimpoeşu, Mater. Today, 72 (2023) 550–553.
[6] M. Ramesh, K. Marimuthu, P. Karuppuswamy, L.N. Rajeshkumar, Bol. Soc. Esp. Ceram. Vidr., 61 (2022) 641–652.

The 56th International October Conference on Mining and Metallurgy
22-25 October 2025, Bor Lake, Bor, Serbia
www.ioc.tfbor.bg.ac.rs

DOI: 10.5937/IOC25025O | Invited lecture | Original scientific paper

COMPUTATIONAL FLUID DYNAMICS ANALYSIS OF VENTILATION STRATEGIES FOR MITIGATING TOXIC GAS LEAKAGE IN SUBSURFACE INFRASTRUCTURE PROJECTS

Cemalettin Okay Aksoy [1*], Güzin Gülsev Uyar Aksoy[2], Hasan Berker Sarisan[3]

[1*]Dokuz Eylül University Department of Mining Engineering, İzmir, Türkiye
[2]Hacettepe University Department of Mining Engineering, Ankara, Türkiye
[3]GOA Mining, Ankara, Türkiye
[1*] okay.aksoy@deu.edu.tr, 0000-0002-4328-4862
[2] gulsev.aksoy@hacettepe.edu.tr, 0000-0002-9328-9899
[3] berkersarisan@goamining.com, 0009-0005-8082-8186

Abstract

The removal of toxic gases leaking during excavation in infrastructure projects is crucial for both human health and environmental protection. In this process, Computational Fluid Dynamics (CFD) simulations are highly valuable for modeling and analyzing complex physical processes associated with the transport and dispersion of gases. During infrastructure projects in geothermal regions, various gases may leak from underground sources. These gases may include toxic and/or flammable substances such as hydrogen sulfide (H_2S), carbon dioxide (CO_2), and methane (CH_4). Designing an effective ventilation system is essential for the removal of toxic gases through ventilation. CFD simulations can be utilized to evaluate the design and performance of ventilation systems. Modeling gas leaks from sources encountered during excavation using CFD simulations can help understand how gases move throughout infrastructure projects and their environmental impacts. CFD simulations can assist in optimizing factors such as the placement of ventilation systems, duct design, air flow rates, and filtration efficiency. This optimization ensures the effective removal of toxic gases and minimizes environmental impacts. CFD simulations can also be used to assess the efficiency and safety of ventilation systems designed for the mitigation of toxic gases. Additionally, simulating the operation of ventilation systems during potential emergency situations can help in evaluating associated risks.

***Keywords**: Computational Fluid Dynamics, gas leakage, ventilation strategies, gas dispersion, subsurface infrastructure*

1. INTRODUCTION

The removal of toxic gases during excavation in infrastructure projects is critical for both human health and environmental safety. Computational Fluid Dynamics (CFD) simulations are valuable tools for modeling the transport and dispersion of hazardous gases such as H_2S, CO_2, and CH_4, which may leak from underground sources, especially in geothermal regions. Designing an effective ventilation system is essential, and CFD can be used to assess and optimize system performance, including fan placement, duct layout, airflow rates, and filtration. This helps ensure efficient gas removal and reduced environmental impact. CFD simulations also support safety evaluations by modeling system behavior in potential emergency scenarios. The study was conducted by modeling the T2 tunnel located on the İzmir–Ankara High-Speed Rail line. During the excavation works of the T2 tunnel, gas leakage consisting of 8000 ppm CO_2 and 40 ppm H_2S was detected along a 400-meter stretch starting from the tunnel face. The gas leakages were modeled in the analyses based on field measurements. Although the T2 tunnel is located within a geothermal basin, the leakages encountered during excavation are not of geothermal origin. Furthermore, it is assumed that the ventilation ducts used are airtight and that there are no other factors (such as machinery, personnel, or vehicles) influencing the airflow inside the tunnel. All surfaces of the tunnel are supported and covered with Ground Sheet lining. Based on field investigations, a surface roughness of 3 cm was applied to all tunnel surfaces in the simulations.

The temperature of the gases leaking from the ground is 28°C, while the nominal temperature of the tunnel is 26°C. Therefore, the thermal effect of the leaking gases is considered negligible. ANSYS Fluent software was used to perform the CFD analyses.

2. COMPUTATIONAL FLUID DYNAMICS

To conduct CFD analyses, the three-dimensional geometry of the structure must be created using a computer-aided design (CAD) program. In this project, the SpaceClaim module of the ANSYS software was used as the design tool. The tunnel geometry created has a length of 815 meters and a surface area of 130 m². Within the tunnel geometry, a fan duct with a diameter of 2200 millimeters and a length of 765 meters was modeled (ANSYS Education Tutorials, 2016).

Figure 1. 3D Tunnel geometry

2.1 Analysis No 1

The airflow rate supplied to the tunnel by the fan is 39 m³/s. The surface area of the fan is 3.8013 m². The cross-sectional area of the tunnel is 130 m², and the average airflow velocity inside the tunnel toward the outlet (–Y direction) is 0.3 m/s.

The following analyses were carried out using a fan and duct system with a length of 765 meters and a diameter of 2200 mm, providing an airflow rate of 39 m³/s. This setup represents the existing ventilation system of the T2 Tunnel. To ensure an airflow rate of 39 m³/s, the fan's air discharge velocity was calculated (Goodfellow, 2020):

$$39\ m^3 = (3{,}8013\ m^2) * (V1) \quad (1)$$

As a result of these calculations, the fan's air discharge velocity V1 was determined to be 10.2596 m/s.

Table 1. CO_2 and H_2S Mass Contours on Tunnel Geometry (Analysis No 1)

	First 400 meters	Last 400 meters
CO_2 Mass Countours	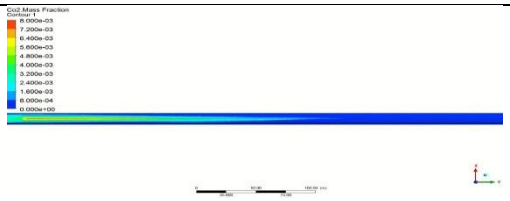	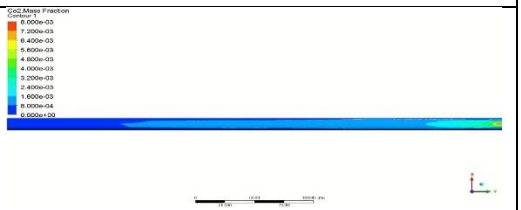
H_2S Mass Contours	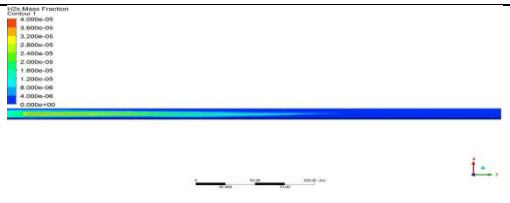	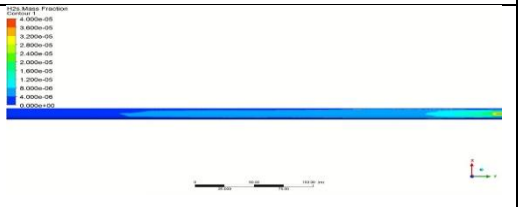

2.2 Analysis No 2

In addition to the ventilation configuration used in the first analysis, a fan was installed at the 100th meter of the tunnel, and a fan duct was defined from this fan to the tunnel outlet. This fan duct has a diameter of 2200 mm, like the initial fan duct. The second fan extracts air from within the tunnel at a flow rate of 39 m³/s.

Table 2. CO_2 and H_2S Mass Contours on Tunnel Geometry (Analysis No 2)

	First 400 meters	Last 400 meters
CO_2 Mass Countours	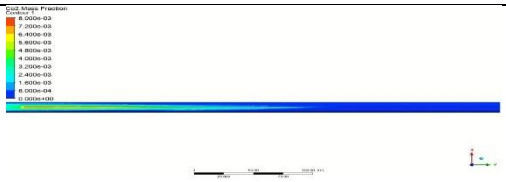	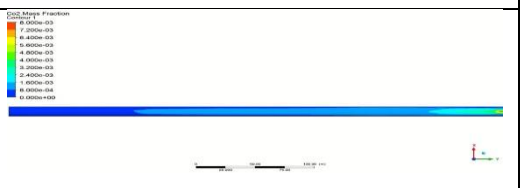
H_2S Mass Contours	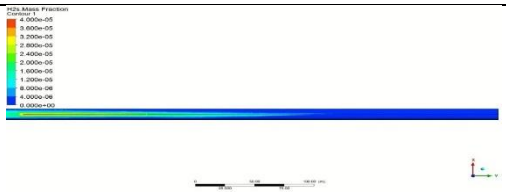	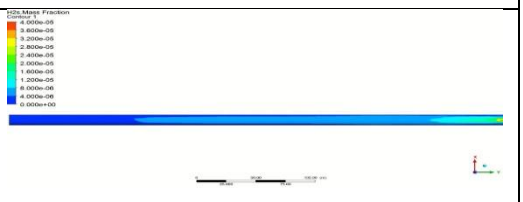

2.3 Analysis No 3

In this scenario, the length of the fan duct was increased from 765 meters to 790 meters. The second fan was not used. The diameter of the fan used is 2200 mm, and the airflow rate supplied from the fan duct into the tunnel is 39 m³/s.

Table 3. CO_2 and H_2S Mass Contours on Tunnel Geometry (Analysis No 3)

	First 400 meters	Last 400 meters
CO_2 Mass Countours	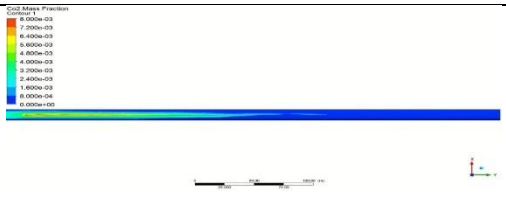	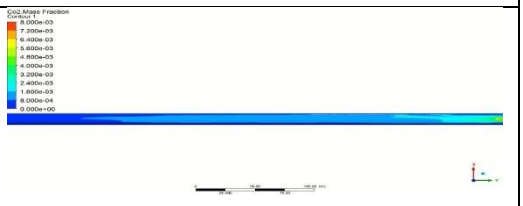
H_2S Mass Contours	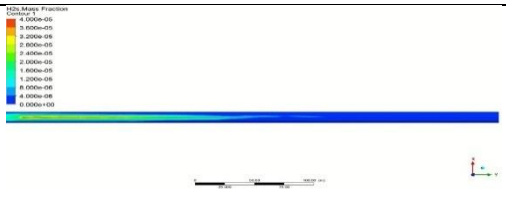	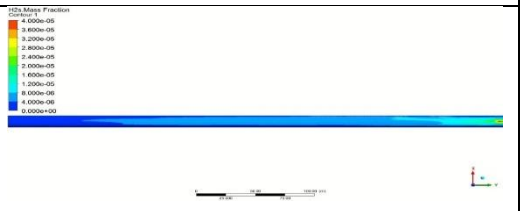

2.4 Analysis No 4

In the fourth analysis, a second 2200 mm diameter fan was added 375 meters from the tunnel outlet, with a duct of the same diameter extending to the exit. Both the first (790 m) and second (375 m) fan ducts operate with an airflow rate of 39 m³/s.

Table 4. CO_2 and H_2S Mass Contours on Tunnel Geometry (Analysis No 4)

CO_2 800 meters mass contours	H_2S 800 meters mass contours
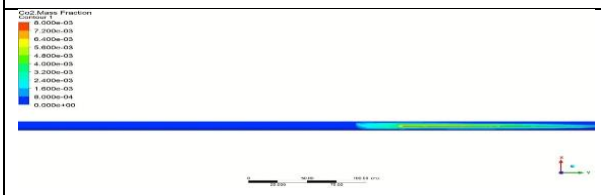	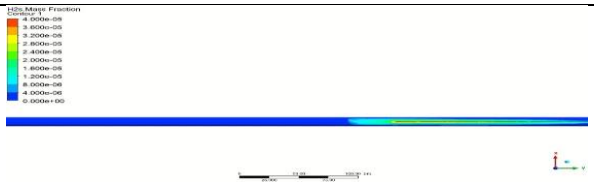

3. RESULTS AND DISCUSSION

Flow analyses show that airflow near the tunnel face reaches approximately 3 m/s, reducing CO_2 and H_2S concentrations to 0 ppm in this region. Toward the tunnel outlet, airflow velocity decreases to nearly 0 m/s, causing gas accumulation around the 400th meter—up to 8000 ppm CO_2 and 40 ppm H_2S in the first analysis. In the second analysis, a fan added 100 meters from the outlet had no effect, as it was positioned in a gas-free zone. In contrast, the fourth analysis—where the second fan was placed closer to the source (375 m from the outlet) and connected via a duct—significantly improved gas evacuation, reducing CO_2 and H_2S concentrations to 0 ppm downstream. Extending the first fan duct from 765 m to 790 m, however, did not yield notable improvement. These results highlight that the position of the second fan is the most influential parameter for effective ventilation. CFD simulations proved valuable in optimizing fan placement, duct configuration, and airflow rates, helping minimize toxic gas accumulation. Moreover, CFD serves as a powerful tool for evaluating ventilation strategies under varying structural conditions, supporting safer and more efficient infrastructure development.

REFERENCES

[1] J.F. Brune, Mine Ventilation Systems. In: Hartman, H. L., Mutmansky, J. M., Ramani, R. V., Wang, Y. J. (Eds.), Mine Ventilation and Air Conditioning, Wiley-Interscience, 1996.
[2] J. Bear, Dynamics of Fluids in Porous Media, Dover Publications, 1972.
[3] M.J. O'Sullivan, K. Pruess, M.J. Lippmann, Geothermics, 30 (4) (2001) 395–429.
[4] ANSYS Training Courses, SpaceClaim Introduction, Meshing Introduction, Fluent Introduction, 2016.
[5] Y.A. Çengel, J.M. Cimbalak, Fluid Mechanics: Fundamentals and Applications, 2004.
[6] H.D. Goodfellow, R. Kosonen, Industrial Ventilation Design Guide: Volume 1: Fundamentals, 2020.
[7] C. Liu, G.H. Yeoh, J. Tu, , Computational Fluid Dynamics: A Practical Approach, 2007.
[8] J.H. Ferziger, M. Perić, Computational Methods for Fluid Dynamics, 2002.

PAPERS

Geology and Mining

The 56th International October Conference on Mining and Metallurgy
22-25 October 2025, Bor Lake, Bor, Serbia
www.ioc.tfbor.bg.ac.rs

DOI: 10.5937/IOC25033M *Original scientific paper*

OPTIMIZATION OF THE ELECTROSTATIC PRECIPITATORS IN UNIT A1 OF THE KOSTOLAC A THERMAL POWER PLANT

Zoran Marković[1a] , Milić Erić[1b], Aleksandar Milićević[1c], Rastko Jovanović[1d], Nikola Živković[1e], Ivan Lazović[1g], Milica Jovčevski[2a]

[1]Vinca Institute of nuclear sciences - National Institute of the Republic of Serbia - University of Belgrade, Mike Petrovića Alasa 12-14, 11351 Vinča – Belgrade, Serbia
[2]Faculty of Mechanical Engineering, University of Niš, Niš, Serbia
[1a] zoda_mark@vinca.rs, 0000-0003-0553-3263
[1b] milic@vinca.rs, 0000-0001-6850-3112
[1c]amilicevic@vinca.rs, 0000-0003-4615-8789
[1d]virrast@vinca.rs, 0000-0003-0265-2304
[1e]nikolaz@vinca.rs, 0000-0003-3399-1229
[1g]ivan.lazovic@vinca.rs, 0000-0002-3877-5157
[2a] milica.jovic@masfak.ni.ac.rs, 0000-0002-5699-5831

Abstract
The plate-wire electrostatic precipitator (ESP) achieves maximum efficiency by simultaneously generating the maximum spark voltage via a homogeneous velocity field of the flue gas between the plates. The consortium, consisting of the Vinča Institute of nuclear sciences and the Nikola Tesla Electrotechnical Institute, has successfully developed and applied new measuring equipment and the original methodology for diagnosing the actual working conditions and optimization of the ESP. This paper presents the results of testing and optimization of the ESP of the Kostolac A thermal power plant unit A1. Based on the results of measurements of particulate emissions, flue gas velocity distribution in the flue ducts and chambers of the ESP, the reconstruction of the mechanical turning and damping elements of the ESP and the installation of new power control elements have been proposed. The effectiveness of the proposed measures can be seen in the improvement of the homogeneity parameters of the velocity distribution in the vertical cross-sections in the front of the first and behind the last electric field of the electrostatic precipitator.

***Keywords**: electrostatic precipitator, particulate emission, on site measurements, CFD*

1. INTRODUCTION

Between 2004 and 2022, all 15 units of the Joint stock company ‘’Elektroprivreda Srbije’’ (EPS) system underwent ESP refurbishment and modernization, with an investment of €97 million, reducing particulate emissions from 66,626 t in 2003 to 6,344 t in 2022. Unit 1 of TPP Kostolac A later exceeded the emission limit values (ELV) due to equipment aging, failures of the electrical fields of the high-voltage supply systems, etc. If we take the coefficient of variation $CV = S_{tdev} / v_{ave}$ as the measure of homogeneity of the flue gas flow in the vertical cross-section of the ESP, where S_{tdev} is standard deviation and v_{ave} average velocity, than the Matts-Öhnfeldt generalized form of the ordinary Deutsch-Anderson equation indicate that maximum theoretical ESP collection efficiency results from perfectly uniform gas velocity distribution over the ESP’s chamber cross section [1].

Also, the dust removal efficiency depends on the intensity of the electric field in the ESP chamber. If present the dust removal efficiency by using the power density of the corona, $P/Q\,[W/1000\cdot m^3/h]$, then high efficiency could be obtained only for high values of P/Q [2].

Therefore, a high dust removal efficiency of ESP is achieved by simultaneously establishing a homogeneous flue gas velocity field through the optimally regulated electric field inside ESP.

Vinča Institute of nuclear sciences has been successfully developed and applied new measurement equipment [3] for determination of the velocity distribution in large vertical cross section of the ESP chamber (15 m x 15 m). In consortium with Nikola Tesla Institute of Electrical Engineering an original methodology for diagnosing the working conditions of the ESP have been developed and applied. The methodology consists of: ***inspection*** of the electrical and mechanical equipment of the ESP; ***on-site measurements*** of the flue gas velocity distribution, temperature and composition in the flue gas ducts, particulate matter emissions, homogeinity of air velocity in vertical cross-sections of the ESP chamber, and laboratory analyses of coal, fly ash and bottom ash; ***CFD simulations*** of numerical models with various geometric solutions of the structural elements of the ESP and ***numerical simulation of the electrical parameters*** of various ESP power supply solutions. The results of application of this methodology on optimization of the ESP of unit TEKO A1 are presented in this paper.

For assesing flow homogeinity we have used the dimensionless momentum M_k and energy correction coefficient N_k [4]:

$$M_k = \frac{\int v^2 dA}{v_{avg}^2 A_{tot}} = \frac{1}{A_{tot}} \sum_{i=1}^{n} \left(\frac{v_i}{v_{avg}} \right)^2 \Delta A_i, \qquad N_k = \frac{\int v^3 dA}{v_{avg}^3 A_{tot}} = \frac{1}{A_{tot}} \sum_{i=1}^{n} \left(\frac{v_i}{v_{avg}} \right)^2 \Delta A_i$$

where v_i [m/s] is a mean velocity through the elementary surface *i* of the cross-section of the ESP chamber, v_{avg} [m/s] – mean velocity in the cross-section, ΔA_i [m^2] – elementary surface and *n* – number of elementary surfaces in the cross-section of the ESP chamber. The values of M_k and N_k are equal to unity only under the uniform flow conditions. The additional two criteria used to assess the flow homogeneity is that the area of all fields where the measured velocity is greater than $1.15 \cdot v_{avg}$ must be $\leq 25\%$ of the measuring cross-section area, e.g. $v_{avg\ >115\%} \leq 25\%$ and where the measured velocity is lower than $0.85 \cdot v_{avg}$ must be $\leq 25\%$ of the measuring cross-section area, e.g. $v_{avg\ <85\%} \leq 25\%$ [5].

The ESP of the TEKO A1 unit is the only ESP within EPS in which all gas passages are 500 mm wide. The maximum design value of the effective migration velocity is $\omega = 0.2456$ m/s. This ESP has relatively small specific surface area of the deposition electrodes $SCA = 29.2$ m^2/(m^3/s), with maximum design values of the specific corona current of 0.593 mA/m^2. The corona current values of ESP of unit TEKO A1 in all electrical fields were below the design value of 1250 mA, especially in zones 1 and 2, the temperature and oxygen content in the flue gas were above the design values, while the flue gas flow and the concentration of PM at the entrance to the ESP was around the design value. The flue gas channels and the elbow with set of turning vanes in the front of the ESP diffuser are correctly designed so the conditions for the occurrence of erosion are completely eliminated. In the confusor at the ESP chamber exit, no distribution plate was originally designed or installed.

2. EXPERIMENTAL

The velocity measurements in the vertical cross-section of the ESP chamber in the front of the first electrical field indicate that there are two zones with increased velocities in both chambers [6]. One zone is near the centre of the section, closer to the left wall, and the other occupies almost the entire centre of the right half of the section. The velocities at the top and bottom of the cross-sections are at the level of the mean of that cross-section. There are zones of very low velocities near the walls and along the height of the left and right half of the cross-section.

The velocity measurements in the vertical cross-section of the ESP chamber behind the last electrical field indicated that there is a large zone of increased velocities in the centre of the cross-section towards the ceiling of the chamber, while in the lower third of the cross-section and in the upper corners the velocities are well below the average value of the cross-sectional velocity. This distribution of velocities is a direct consequence of the suction effect of the exit from the confusor

and extends through the third and partly through the second electrical zone. It has a very unfavourable effect on dedusting efficiency in these zones. The most of the particles are carried away by the high velocity flow because it does not give the ash particles enough time to charge and separate on the collecting electrodes. On the other hand, there is almost no gas flow and therefore no particle separation in a large part of these electrical zones (Figure 1).

Table 1 presents results of homogeneity evaluation of velocities measured in the vertical cross sections in the front of the first and behind the last electrical field of left / right ESP of unit A1.

Table 1. Parameters for evaluating the homogeneity of the velocity distribution in the ESP chambers

Parameter	S_{tdev} [%]	M_K [-]	N_K [-]	$v_{avg>115\%}$ [%]	$v_{avg<85\%}$ [%]
Recommended value	**≤ 25**	**≤ 1,2**	**≤ 1,8**	**≤ 25**	**≤ 25**
Inlet left ESP	34.2	1.10	1.32	32.7	36.3
Inlet right ESP	42.4	1.10	1.44	32.0	41.2
Outlet left ESP	41.5	1.13	1.42	37.4	34.1
Outlet right ESP	44.5	1.15	1.51	33.3	43.5

The measurement also revealed irregularities in the flows through the flue gas ducts at the entrance to the diffuser, where higher flow rate was measured in the right flue gas duct of the left ESP than in the left flue gas duct. In the case of the right-hand ESP, the flow rate through the left-hand flue gas duct was greater than that through the right-hand duct. This non-uniformity is also reflected in the homogeneity of the flow rate through the ESP chamber.

3. RESULTS AND DISCUSSION

From Table 1 we can see that the condition for the parameter S_{tdev} is not fulfilled in any of the observed sections for both chambers. The values of the parameters M_k and N_k calculated for each of the observed sections are in agreement with the recommendations of the literature [4].
Homogeneity criteria $v_{avg>115\%}$ and $v_{avg<85\%}$ are not fulfilled in any of the observed sections. The series of the CFD numerical simulations for the ESP model with different design of new turning and distribution elements were conducted. To further reduce the increased velocities in the upper zones of the chamber, it is proposed to install a distribution grid in the confusor with 16 horizontal panels, 300 mm wide, 9 m span and a vertical distance of 300 mm.

Results of CFD numerical simulation of the velocity distribution behind the last electrical field in the numerical model of the left ESP chamber whit new design of distribution grid with 16 horizontal panels in the ESP confusor are presented in Figure 2. Comparing to measured velocity distribution presented on Figure 1, one can notice much better homogeneity in the cross-section behind the last electrical field, influenced by the new distribution grate design. Numerical results also confirmed propagation of this positive influence through the ESP chamber up to the first electrical field.

4. CONCLUSION

The CFD analysis of the flow in the ducts and ESP chamber for the existing/original geometry of the turning and damping elements confirms the presence of pronounced velocity unevenness in the entire chamber of ESP of unit TEKO A1 which was also established by detailed measurements. CFD analysis of the flow in the channels and ESP chamber for the newly proposed geometry of the distribution grid in the confusor indicates that it is possible to significantly improve the homogeneity of the velocity field in the chambers (especially in fields 2 and 3) and thus increase the dedusting efficiency of ESP. It is suggested to choose suitable locations in front of the diffuser and to install suitable pressure transducers and thermometers to measure the necessary parameters to equalize the flue gas flow through the ducts.

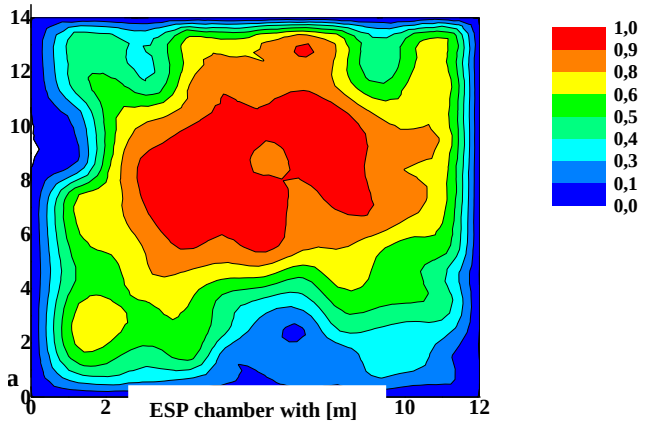

Figure 1. Measured velocity distribution [m/s] in a vertical cross section behind the last electrical field of the left ESP chamber of unit A1

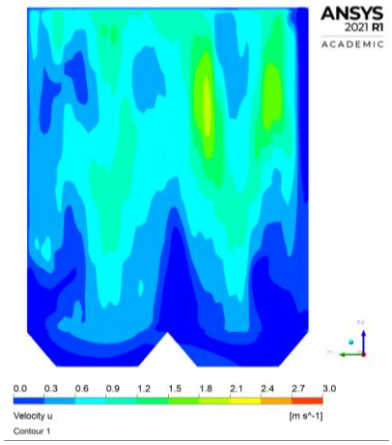

Figure 2. CFD numerical simulation of velocity distribution [m/s] behind the last electrical field of left ESP chamber whit new proposed design of distribution grid

ACKNOWLEDGEMENTS

The research was funded by the Ministry of Science, Technological Development and Innovation of the Republic of Serbia (Contract Annex: 451-03-136/2025-03/200017). The authors are very grateful for the support of this work by the Joint Stock Company ''Elektroprivreda Srbije''.

REFERENCES

[1] A. Bäck, Int. J. Plasma Environ. Sci. Technol., 11 (1) (2017) 104-111.
[2] Ken Parker, Electrical Operation of Electrostatic Precipitators (IEE power & energy series; no. 41), Institution of Engineering and Technology, London, UK, printed by MPG Books Ltd, Bodmin, Conwall, UK (2007), p. 74, ISBN 978-0-85296-137-7.
[3] I. Lazović, Z. Marković, M. Erić, R. Jovanović, V. Tasić, ''Transport trolleys for anemometers for testing the air velocity profile in the chambers of electrostatic precipitators of large emitters'', Petty Patents, Intellectual Property Gazette 2022/11 (12/12), published 30.11.2022., Republic of Serbia, ISSN 2217-9143 (Online) Intellectual property office .
[4] Zhou, J., et al., Water Sci Eng., 14(4) (2021) 337-344.
[5] Publication ICAC-EP-7, Electrostatic Precipitator Gas Flow Model Studies, Institute of Clean Air Companies, Washington, DC, USA (2004) 5-6.
[6] P. Stefanović, Z. Marković, I. Stevanović and M. Erić, Conceptual solution and conceptual project for the reconstruction of the electrostatic precipitator TEKO A1 and the creation of a CFD analysis of the electrostatic precipitator of unit A1, Report NIV – LTE – 701 ver. 1.0, Vinča-Belgrade (2023).

The 56th International October Conference on Mining and Metallurgy
22-25 October 2025, Bor Lake, Bor, Serbia
www.ioc.tfbor.bg.ac.rs

DOI: 10.5937/IOC25037U *Original scientific paper*

OPTIMAL PITWALL DESIGN FOR OPEN PIT MINES IN THE PRESENCE OF FAULTS

Stefano Utili[1a,2], Dainius Jenkus[1b], Akanksha Mishra[1c], Filippo Bianchi[3a], Riccardo Castellanza[3b],

[1] OptimalSlope, Harwell, United Kingdom
[2] Newcastle University, School of Engineering, Newcastle upon Tyne, United Kingdom
[3] Universita Milano Bicocca, Milano, Italy
[1a] stefano_utili@optimalslope.com, 0000-0003-3156-8013
[1b] dainius_jenkus@optimalslope.com, 0009-0005-8065-8527
[1c] akanksha_mishra@optimalslope.com, 0009-0005-3589-0685
[3a] f.bianchi86@campus.unimib.it, 0009-0000-9539-6471
[3b] riccardo.castellanza@unimib.it, 0000-0001-8591-1978

Abstract

Slope Optimiser is a novel software tool that determines non-planar optimally shaped slope profiles which are featured by a depth varying inclination. These profiles are obtained as result of topological optimisation carried out in order to determine the slope profile featuring the maximum Overall Slope Angle (i.e. the overall slope inclination from crest to toe) for prescribed input ground strength parameters - Mohr-Coulomb (M-C) or Generalised Hoek-Brown (G-H-B) and a target Factor of Safety. Bench geometries (bench height, face inclination, minimum berm width) are prescribed in the optimisation as constraints constraining the maximum local inclination of the sought optimal profile, together with any other constraints stemming from any geological discontinuity that may influence slope failure.

In this paper a novel formulation to account for the effect of discrete faults on slope stability is introduced. The failure mechanism considered are mixed accounting for failure along intact rock and along the fault. To provide a rigorous quantification of the benefits brought by Slope Optimiser, we consider case studies of metalliferous open pit mines and performed two designs: one employing planar pit walls and another one adopting the optimal pitwall profiles determined by Slope Optimiser. Here, a new mine case study is presented where pitwalls have to be designed in a mine featured by several faults. The Factor of Safety of the optimal pitwalls determined by Slope Optimiser were independently verified by Finite Element analyses with shear strength reduction technique performed using Rocscience RS2 and Midas FEA NX.

Keywords*: slope topological optimisation; discontinuities; optimal pitwalls; waste-rock reduction; carbon footprint reduction*

1. INTRODUCTION

Pitwall inclinations bear a very significant effect on mine environmental impact and profitability since they control to a large extent the amount of rockwaste to be excavated [1]. Consequently, ensuring pitwalls are as steep as possible is essential.

[2], [3] and [4] employed a novel geotechnical software, Slope Optimiser [5], that computes the slope optimal profile for any specified lithological sequence without unduly restricting the search to any predefined family of shapes to design the pitwalls of three open pit mines achieving important increases of NPV and carbon footprint reductions in comparison with the traditional design based on planar pitwalls. To be able to quantify the gains of NPV and carbon footprint reduction in a consistent way in [2-4] the open pit mines considered were designed twice employing the same pit optimiser software, economic parameters and optimisation strategy, with the only difference between the two designs being the pitwall profiles adopted. Financial and environmental gains were calculated as the difference between the NPV, carbon footprint and

energy consumptions resulting from the two designs. Net Present Value increases and carbon footprint and energy consumption reductions obtained by the adoption of optimal pitwall shapes are rigorously quantified with gains up to 52.7% of Net Present Value and carbon footprint reductions averaging at 600,000 tonnes CO_2 equivalent.

A fundamental limitation of the current topological optimisation is the non-consideration of discontinuities like faults. As the LOP guidelines [6-7] state faults are often encountered in the excavation of pitwalls and depending on their inclination they may severely reduce slope stability so their correct consideration in slope stability assessment is paramount. In this paper, we first describe and then showcase the extension of the current algorithm that seeks the Factor of Safety in 2D for a given slope profile to include faults.

The paper is structured as follows: in Section 2, the methodology adopted to include the discontinuity in the calculation of the FoS of a 2D cross-section are introduced; in Section 3 case studies of pitwalls of existing open pit mines employed to test the methodology are introduced; in Section 4 the results of the simulations performed using Slope Optimiser on the case studies are illustrated; in Section 5 conclusions are provided.

2. METHODOLOGY

2.1 Optimal pitwall design by slope optimisation

A detailed explanation of how slope profile optimisation works can be found in [2], therefore it will not be repeated here. The input data required are the rock mass strength (expressed as either Mohr-Coulomb or Generalised Hoek- Brown criterion), unit weight, and the geometries of benches, namely bench height, bench face inclination and the minimum berm width. Moreover, any ramps (roads) can be prescribed as a constraint for the slope to be designed together with any surcharge load as well. In Figure 1, typical input and output data for Slope Optimiser are reported.

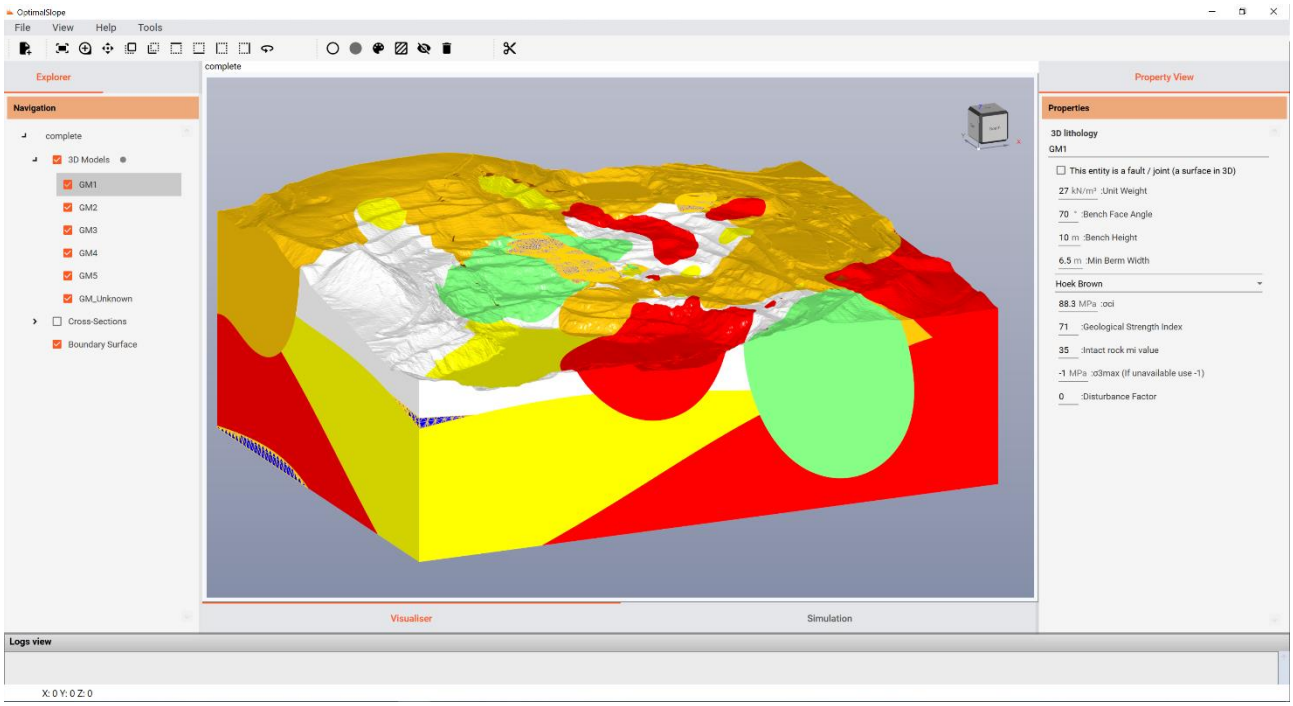

a)

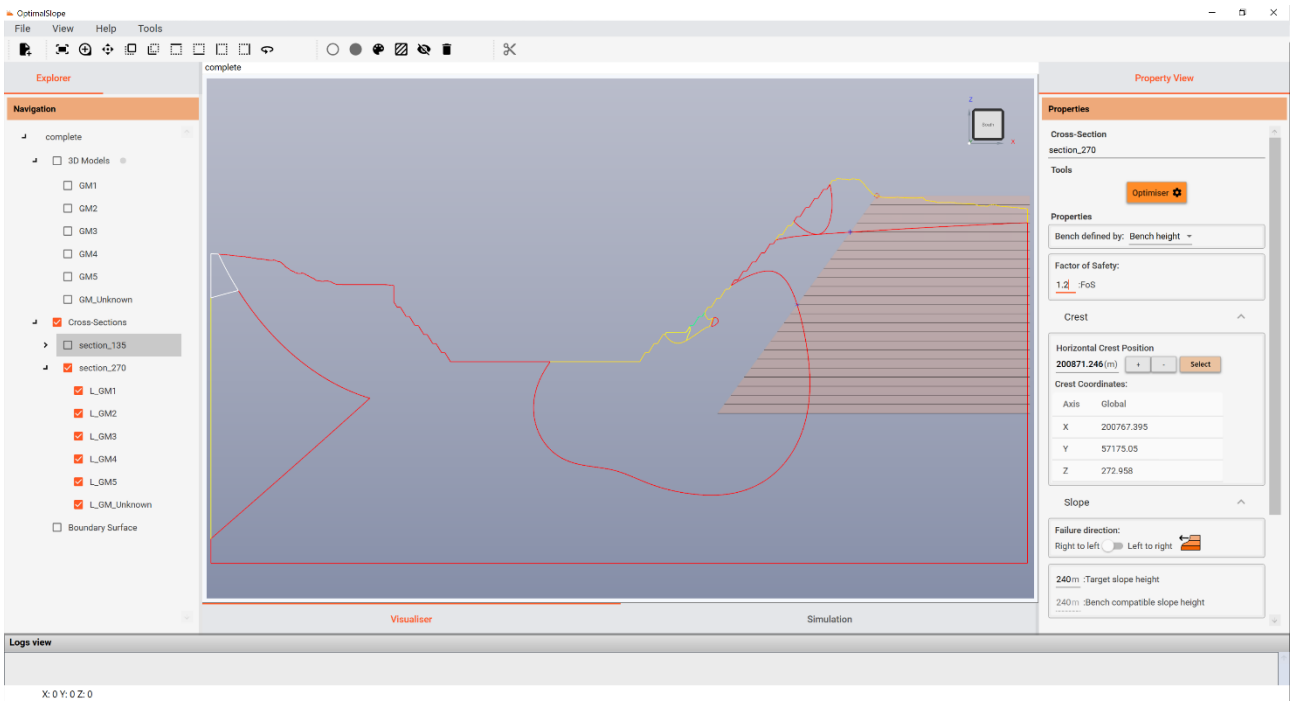

b)

Figure 1. Slope Optimiser graphical user interface: a) example of a 3D input stratigraphy. For each lithological unit, rock strength parameters - c and φ for the Mohr-Coulomb criterion or GSI, UCS and m_i for the Generalised-Hoek-Brown criterion - are specified together with unit weight. Bench and ramp geometries are specified also for each lithological unit. b) Example of a vertical cross section, obtained by slicing the 3D stratigraphy (it is also possible to import 2D section directly).

Slope Optimiser typically considers several thousands of candidate slope profiles, each defined by a discrete set of points in the vertical plane: see the (x_i, z_i) coordinates in Figure 2a, with z_i being values specified according to the bench height (Δz = bench height) input by the user, and x_i unknown variables to be determined. The search for the optimal profile is constrained to feasible profiles (which lie within the blue bounds of Figure 2a). A profile is feasible if $\frac{z_i - z_{i-1}}{x_i - x_{i-1}} \leq tan\alpha_{i_max}$ for every i (i.e. the inclination of each segment of the profile is capped to α_{i_max}). The α_{i_max} values are determined by the software before the optimisation algorithm is called on the basis of bench height, bench face inclination, and minimum berm width provided by the user (see Figure 2b). If a ramp needs to be included as part of the pitwall profile, a lower α_{i_max} value is imposed for the profile segment corresponding to the vertical position of the ramp.

The optimal pitwall profile is defined as the overall steepest safe profile that meets the FoS design criterion (*i.e.*, $OSA=OSA_{max}$), with OSA being the inclination over the horizontal of the line joining the pitwall toe to the crest (see Figure 2a). The logical steps used to calculate the optimal pitwall profile are summarised in Figure 2c. Firstly, an initial OSA is heuristically determined. The main algorithm then calculates the optimal pitwall shape for the assigned OSA and geometric constraints (bench height, bench face inclination, minimum berm width, and road width). The FoS_i associated with the optimal profile found at the i-th iteration is then compared to the FoS_{target}. If it is higher, a steeper OSA is prescribed at the next iteration; if it is lower, a flatter OSA is prescribed. The termination criterion is specified in terms of the percentage difference between FoS_{target} and FoS_i.

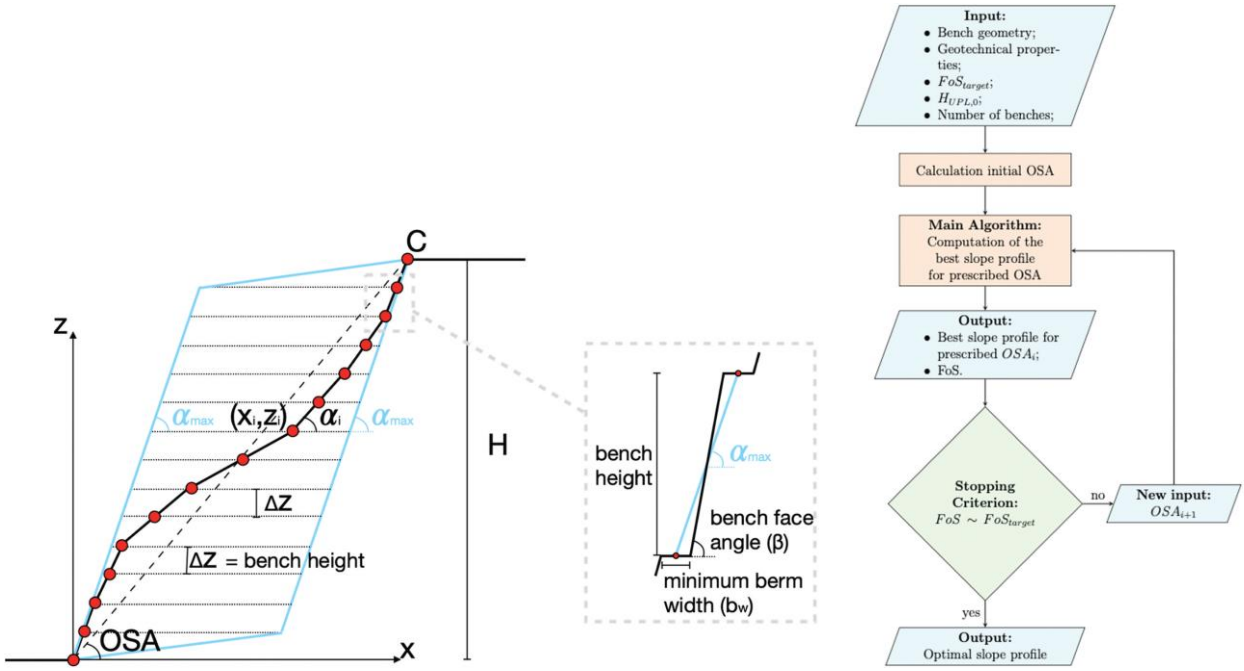

a) *b)* *c)*

Figure 2. After (Agosti et al., 2025): a) generic candidate slope profile. A uniform discretization along the z direction is adopted. The blue lines enclose the region where the profiles are sought. The profile is discretised in n Δz intervals so there are n-1 unknowns to be determined: x_1, x_2, . . . x_{n-1}. b) determination of α_{i_max} based on bench geometry. c) Flow chart summarizing the iterative procedure used to determine the optimal profile for a given pitwall.

2.2 Algorithm to include faults into calculation of the FoS

Discontinuities, eg. faults, are represented in a data structure (each fault as a vector of points) of their own since they are open polylines with their own strength properties: friction angle and cohesion. Every time intersection of the rotational mechanism under consideration with a fault is detected, a new failure mechanism is generated on top of the failure mechanism under consideration. This mechanism is made by a logspiral, which is the most efficient rotational failure mechanism in a homogenous rock layer, until the point A of intersection (see Figure 3) and then by the fault geometry which needs to be followed. There are two directions that can be taken along the fault, we want to follow the direction compatible with a feasible failure mechanism, hence from A upwards towards B. The algorithm can be described by the following steps:

1. Detect intersection of the rotational mechanism under consideration (logspiral) with any fault
2. Follow the fault until either of the two options occurs:
   a) The fault daylights on the slope face or exits at the topography
   b) The fault terminates inside a lithological unit (dangling fault)
   c) The fault re-intersects the composite logspiral

The external work (or the driving moment M_d) performed by the self-weight and surcharges are calculated as shown in [2] according to the limit analysis upper bound theorem or equivalently the limit equilibrium method for the case of a single rotating wedge [8]. In equations (1) and (2) below, both formulations are provided.

The calculation of the resisting moment involves two components: one along the rotational part of the rotational mechanism and one along the fault. $M_{res\ fault}$ is to be calculated as the sum of each piecewise linear segment multiplied by the lever arm to the Centre of Rotation (CoR).

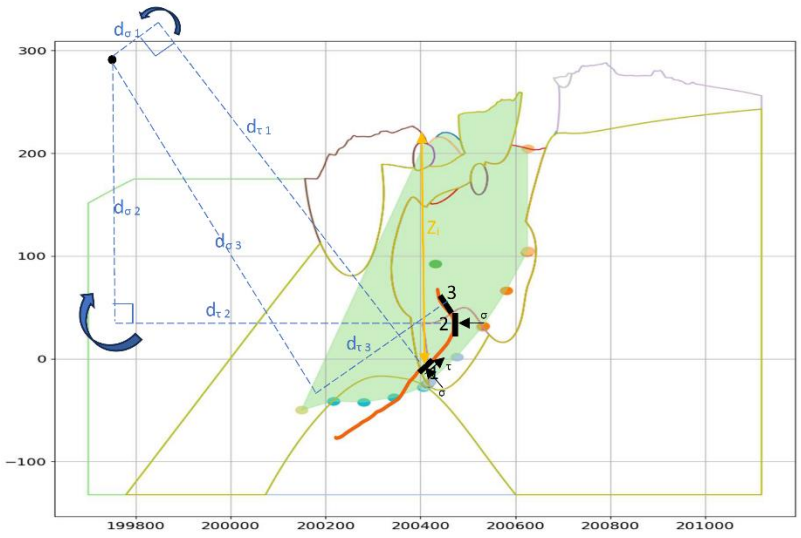

Figure 3. Calculations of resisting moment (or dissipated energy for the limit analysis upper bound method) along the fault (in red): the vector σ and τ indicate the normal and tangential stresses respectively along a fault segment.

$M_{res\,fault}$ is due to both tangential stresses, τ_{fault}, and normal stresses, σ_{fault} (see Figure 3). The fault is discretised into i segments, with the discretisation (length of the fault segment) being a function of the precision of the geotechnical model available. The moment is calculated from the summation of the stresses along each fault segment, so the following formula is derived:

$$M_{res\,fault} = \frac{W_d}{\Omega} = \sum_{i=1}^{N} \tau_i * l_i * d_{\tau\,i} + \sigma_i * l_i * d_{\sigma\,i} \quad (1)$$

with W_d the dissipated energy and Ω the rotational speed of the sliding mass, l_i being the fault segment length, $d_{\tau\,i}$ being the distance to the CoR of the segment i and $d_{\sigma\,i}$ being the distance to the CoR of the perpendicular to the segment i.

Then we substitute $\tau_i = \sigma_i tan\varphi_{fault} + c_{fault}$

$$M_{res\,fault} = \frac{W_d}{\Omega} = \sum_{i=1}^{N} \left(\sigma_i tan\varphi_{fault} + c_{fault}\right) * l_i * d_{\tau\,i} + \sigma_i * l_i * d_{\sigma\,i} \quad (2)$$

with c_{fault} being the cohesion and φ_{fault} being the friction angle along the fault (ideally measured by direct shear test).

3. RESULTS AND DISCUSSION

To test the new algorithm we considered an open pit mine located in Asia. For reasons of confidentiality we are unable to name it. The data were taken from the geotechnical reports of the mine. In Figure 4a the plan view of the lithological units is provided. The mine presents several faults which are also reported in red in Figure 4b each of them features by different strength values.

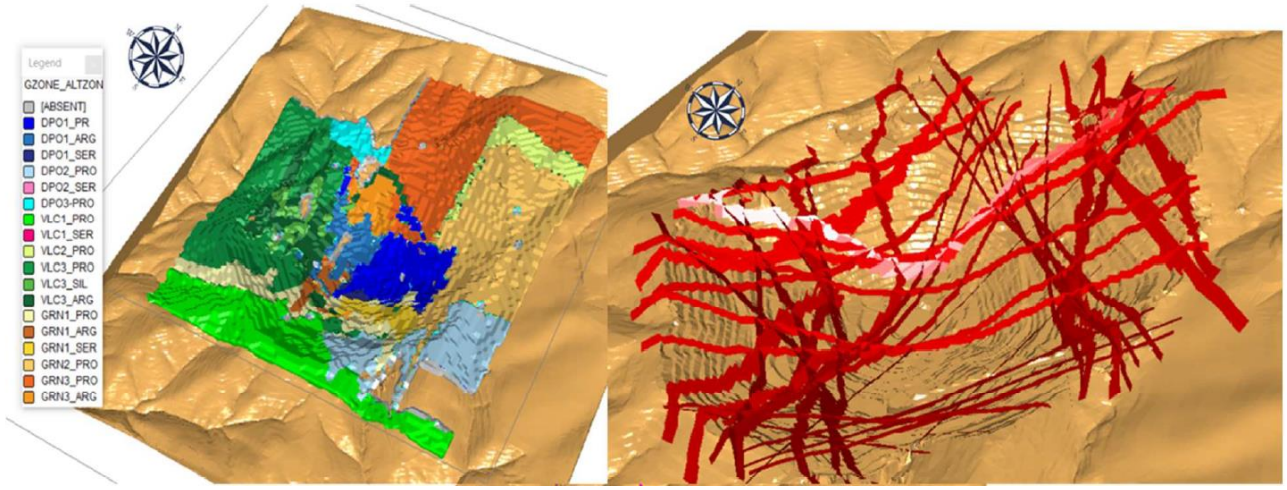

a) b)

Figure 4 lithological units and faults (in red); b) plan view with cross-sections.

3.1 Calculation of optimal pitfall profiles by Slope Optimiser

In the design of pit walls, we followed the standard practice of starting with the design of benches and then moving to the overall pitwall profiles [6]. The height of the benches to be adopted is a mine specific input parameter which often within the same mine, eg. higher benches in stronger rock layer. In Slope Optimiser, bench heights are to be specified for every lithological unit (rock layer) in the 3D stratigraphy. The properties are then inherited after slicing into any 2D cross-section made. The bench face inclination is another user specified input. In the 2 case studies here considered, bench face inclinations were calculated following a kinematic analysis at the bench scale.

The minimum bench width is the third geometric input required by Slope Optimiser which together with bench height and bench face inclination is used to calculate the angles α_{i_max} to be prescribed as geometric constraints in the search for the optimal slope (see Figure 2b). This geometric parameter depends on the type of mining equipment employed (eg. size of excavation machinery and type of blasting techniques) and the requirement to keep rockfalls under control.

Then, we computed the geotechnically optimal slope profiles for the representative cross-section of the mine using Slope Optimiser.

3.2 Verification of optimal profiles by Strength Reduction Finite Element Analyses

In Figure 5, the optimal cross section determined for the mine is shown. The excavation goes through 4 different layers of rock (identified by different colours) and several faults in orange. The optimal cross section obtained from Slope Optimiser was exported as .dxf file and then imported into into Rocscience RS2 (Figure 5a). Then a Finite Element Analysis with Shear Strength Reduction (FEASSR) technique was run resulting in a Strength Reduction Factor of 1.23; a similar analysis was run in Midas NX resulting in a Strength Reduction Factor of 1.23. Note that the FEASSR is performed in RS2 and in Midas are performed according to two different methods: in RS2 bracketing and bisection is employed [9], ie several analyses are performed for different values of SRF each resulting in either convergence or non convergence of the analysis with the next value of SRF selected on the basis of bisection, whereas in Midas NX a single FEA is performed with SRF increasing monotonically [10] until displacements exceed a prescribed threshold, when failure is declared. In both techniques, the steps of SRF decrease can be prescribed

as small as desired. The fact that the two methods give rise to very similar results is reassurance of the validity of the analyses performed.

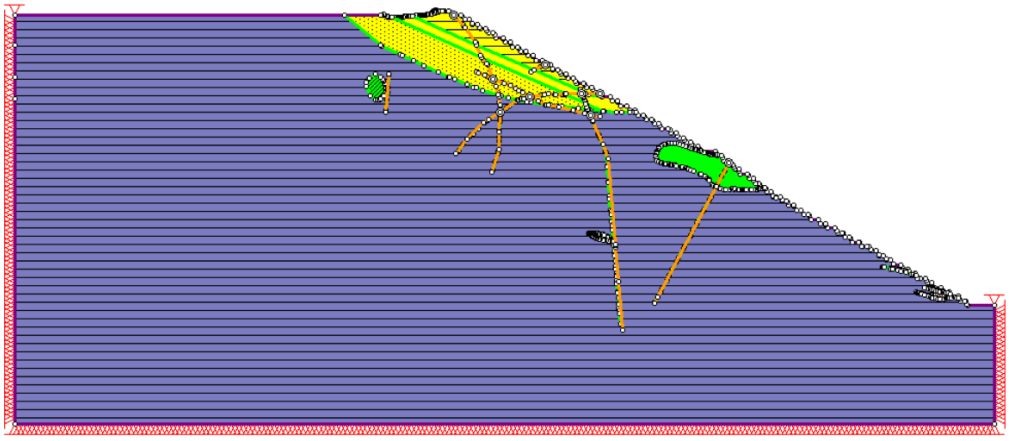

a)

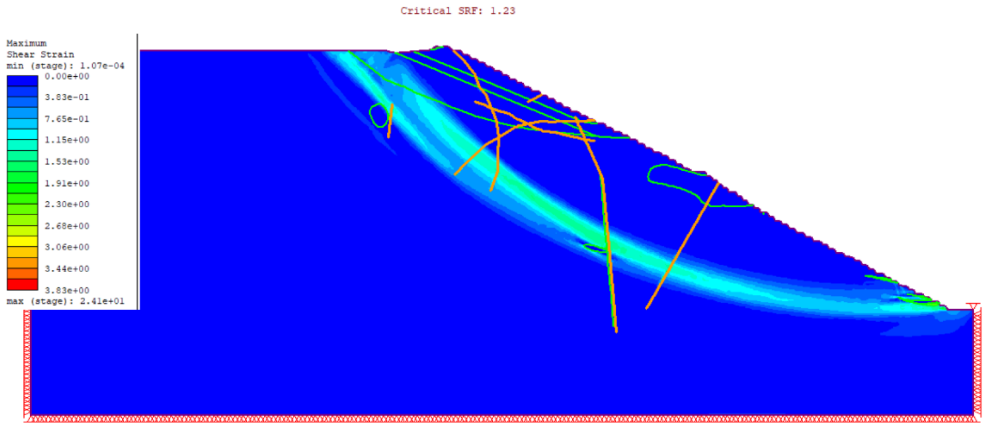

b)

Figure 5. Finite Element Analysis with Strength Reduction of the optimal slope profile determined by Slope Optimiser. a) geotechnical model (faults are visible in orange, each lithological unit is in a different colour); b) shear strain field from Rocscience RS2 with slope instability detected for SRF=1.23.

It is well known that Finite Element Analyses may be subject to mesh dependency and in case of non-normality of geomaterials to spurious results [11]. Therefore in order to ensure results are not unduly dependent on mesh size, 1) the normality rule, ie dilation angle chosen as equal to the internal friction angle φ, was adopted in all analyses, 2) simulations were performed for different mesh sizes until the mesh size was small enough not to affect the results in terms of both FoS values and geometry of the failure mechanism. Asymptotic convergence to the Strength Reduction Factor for decreasing size of the mesh adopted was observed in all cases.

An extra difficulty of these FEASSR analyses was about the selection of elastic stiffnesses for the faults in both normal and tangential directions for Midas FEA NX since the code requires these input parameters. In order to select these values, we ran several parametric analyses for an idealised case of a slope with a single oblique fault dominating its behaviour and selected the stiffnesses such that the displacements obtained were equal to those achieved from the same simulation run in Rocscience RS2.

4. CONCLUSIONS

A new methodology to extend topological optimisation of slopes to account for the presence of any number of discontinuities, eg. faults, is presented to determine geotechnically optimal profiles

– profiles that maximise the overall slope angle for a prescribed FoS, considering the geometry of benches and any ramps – for rock masses featuring several discrete discontinuities.

In current design practices, mines tend to be designed on the basis of planar pitwalls, i.e. with a constant inter-ramp angle (IRA) in each sector of the mine. However, looking at the final geometry of any pit cross-section, this is anything but planar due to the need to accommodate for benches, step-outs and roads, therefore the assumption of constant IRA adopted at the design stage is a simplification which can and should be removed if a better design can be achieved as result. It seems only natural to wonder whether pitwalls of non-linear shape could be used instead of planar ones. OptimalSlope' Slope Optimiser has been developed to find geotechnically optimal shapes for non-uniform slopes accepting any number of layers as input and geomaterials whose strength is described by either the Mohr–Coulomb criterion or the Generalised Hoek–Brown criterion.

In the presence of faults failure mechanisms end up being much more complex since they are determined by a combination of failure along the geometry of the discontinuity and rotational failure along a logspiral segment across the rock intact material. For each candidate slope profile considered, the critical failure mechanism, the one associated to the lowest FoS value, is found, then the best slope profile is found as the results of constrained optimisation and an iterative process where different OSA inclinations are trialled. The new formulation was demonstrated on an open pit mine case studies in the presence of several distinct faults. The Factor of Safety values and the failure mechanisms identified were verified by running Finite Element simulations with Shear Strength Reduction using two state-of-the-art commercial software packages for slope stability analyses: Rocscience RS and Midas NX.

REFERENCES

[1] W. Hustrulid, M Kuchta, and R Martin, Open Pit Mine Planning & Design, CRC Press, London, 2013.
[2] S. Utili, A Agosti, N. Morales, C. Valderrama, R. Pell, G. Albornoz, MME, (2022).
[3] A. Agosti, S. Utili, D. Gregory, A. Lapworth, J. Samardzic, A Prawasono, CIM Journal, (2021) 1–20.
[4] A. Agosti, S. Utili, C. Valderrama, G. Albornoz, Proceeding of SSIM 2021: Second Int Slope Stability in Mining, Australian Centre for Geomechanics (P. Dight), Australian Centre for Geomechanics Publisher, 2021, pp. 69–82.
[5] OptimalSlope, Slope Optimiser computer software user manual, 2025, https://optimalslope.github.io/manual/.
[6] J. Read, P. Stacey, Guidelines for Open Pit Slope Design, CSIRO Publishing, Collingwood, 2009.
[7] D Martin and P Stacey, Guidelines for Open Pit Slope Design in Weak Rocks, CSIRO Publishing, Clayton, 2018.
[8] WF Chen, Limit Analysis and Soil Plasticity, Elsevier, Amsterdam, 1975.
[9] EM Dawson, WH Roth, AA Drescher, Geotechnique, 49 (6) (1999) 835–840.
[10] DV Griffiths, PA Lane, Geotechnique, 49 (3) (1999) 387–403.
[11] SW Sloan, Geotechnique, 63 (7) (2013) 531-572.

The 56th International October Conference on Mining and Metallurgy
22-25 October 2025, Bor Lake, Bor, Serbia
www.ioc.tfbor.bg.ac.rs

DOI: 10.5937/IOC25045M *Review paper*

COMPARATIVE MINERALOGICAL ANALYSIS OF TWO ZEOLITIC TUFF SLANCI AND ZLATOKOP

Katarina M. Mihajlović[1a], Jovica Stojanović[2a], Slavica Mihajlović[2b], Ivana Jelić[2c], Ana S. Radosavljević-Mihajlović[2d], Suzana Erić[2b]

[1] Mining and Geology faculty, University of Belgrade, Đušina 7, Serbia
[2] Institute for technology of nuclear and other raw materials, Franche d Eperea 86, 11000 Belgrade, Serbia
[1a] miha.katarina9@gmail.com, 0009-0007-2001-5794
[2a] j.stojanovic@itnms.ac.rs, 0000-0002-2752-6374
[2b] s.mihajlovic@itnms.ac.rs, 0000-0003-0904-3878
2[c]i.jelic@itnms.ac.rs, 0009-0000-9901-9323
[2d] a.radosavljevic@itnms.ac.rs, 0000-0003-1228-4058
[1b] suzana.eric@rgf.bg.ac.rs, 0000-0003-2303-2497

Abstract
The paper presents the comparative results of quantitative X-ray powder analysis and cation exchange capacity for zeolitic tuffs Slanci and Zlatokop. The basic mineral composition is represented by Ca-clinoptilolite (Zlatokop) and Ca-heulandite (Slanci), feldspars, quartz and clay appear as accompanying components. The X-ray powder diffraction method on a polycrystalline sample and the Sirquant software program were used to determine the quantitative composition.

***Keywords**: zeolitic tuff, quantitative analysis, Siroquant software*

1. INTRODUCTION

The heulandite series of zeolites is represented by isostructural minerals clinoptilolite and heulandite, with a general crystalochemical formula $(Na,K,Ca,Mg)_6(Al_6Si_{30}O_{72})\cdot nH_2O$. Depending on the dominant extra-framework cation present in the zeolite structure, there are Ca-heulandite, Ba-heulandite, Ca-clinoptilolite, or K-clinoptilolite [1]. The minerals of heulandite series were formed as a product of devitrification of volcanic glass, and are related to lacustrine and marine sedimentary deposits [2]. In these sedimentary rocks, zeolites occur in the form of small crystals ranging in size from 0.1 to 100 μm, associated with other mineral components, such as clay minerals and other aluminosilicate and silicate forms of similar densities. The subject of this study was a comparative analysis of the quantitative mineral composition, and an analysis of the content of exchangeable cations in zeolitic tuffs.

2. EXPERIMENTAL

The samples used in this study are zeolitic tuffs from the Zlatokop and Slanci deposits, in a raw state with a grain size of +100% - 63 μm. Quantitative chemical analysis was performed by gravimetric method. To monitor the concentration of exchangeable inorganic cations Na^+, K^+, Ca^{2+}, and Mg^{2+}, the total cation exchange capacity (CEC) was determined by a standard method [3]. The XRD technique was used for identification of the crystalline phases in the powdered samples. The XRD patterns were obtained using a Philips PW-1710 automated diffractometer with a Cu tube operated at 40kV and 30mA. The instrument was equipped with a diffracted beam curved graphite monochromator and an Xe-filled proportional counter. The diffraction data were collected in the 2θ Bragg angles from 4 to 65 ° with a step size of 0.02° counting for 1s. For quantitative analysis, the Siroquant V4.0 software was used [4].

3. RESULTS AND DISCUSSION

The chemical analyses of zeolitic tuffs show a high content of silicon, as well as the presence of oxides of alkali and alkaline earth metals. The SEM photomicrographs shown in Figure 1 provides the results of the chemical analyses and the morphological appearance of the zeolitic tuff from Slanci and Zlatokop.

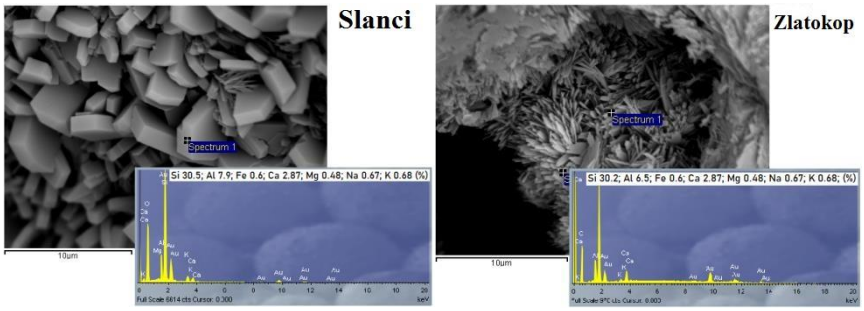

Figure 1. SEM photomicrographs of zeolitic tuff from Slanci and Zlatokop (magnification × 2.000).

Based on crystalochemical analysis, it was determined that the dominant cation for both tuffs is Ca, and the Si/Al ratio amounts to 3.86 (Slanci) and 4.64 (Zlatokop). It can be concluded that the zeolitic tuff from Slanci is rich in Ca-heulandite, while Zlatokop is rich in Ca-clinoptilolite, which is in accordance with previous studies [5-7]. The mineral composition of both zeolitic tuffs is uniform: heulandite, quartz, clay minerals (montmorillonite), and feldspar minerals (mainly plagioclase). The most dominant mineral in the samples is a zeolite mineral from the heulandite series, while contents of other accompanying minerals are lower. The zeolitic tuff from the Slanci locality (lacustrine Miocene formations located east of Belgrade in the Danube Ključ area, within the territories of Veliko Selo and Slanci) [2], rich in HEU minerals, is presented in the SEM photomicrographs in Figure 1. SEM photomicrograph of zeolitized dacitic tuffs from Zlatokop, which are interbedded in marlstone rocks of Middle Miocene to Pliocene age, is also shown in Figure 1. The zeolite minerals occur in the matrix as well developed crystals of monoclinic forms (pinacoids and monoclinic prisms), with sizes up to 10 μm. Comparative refined X-ray powder diffraction diffractograms of the zeolitic tuffs are given in Figure 2.

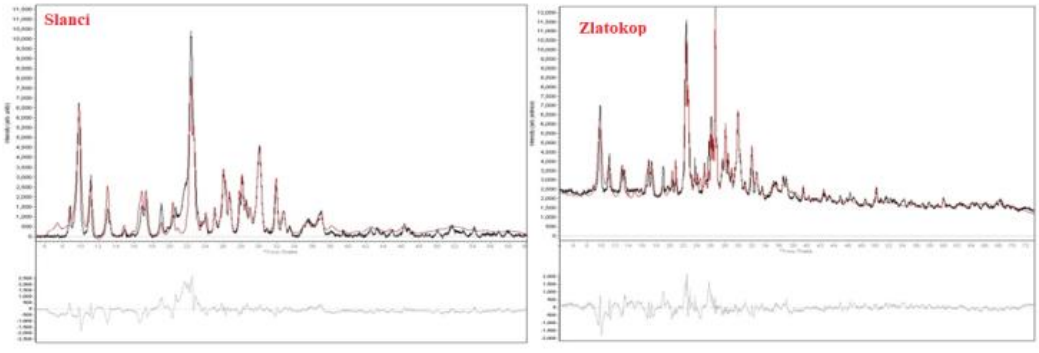

Figure 2. Comparative refined X-ray powder diffraction diffractograms of the zeolitic tuffs from Slanci i Zlatokop.

The main difference between these two tuffs lies in the quartz content. It is significantly more abundant in the zeolitic tuff from Zlatokop, indicating higher crystallinity, compared to the zeolitic tuff from Slanci which is characterized by the presence of amorphous matter of biogenic origin. Based on the X-ray powder diffraction diffractogram shown in Figure 2, the unit cell parameter

are as follows: SLANCI (a = 17.55 Å (4), b = 17.94 Å (3), c = 7.38 Å (4), α = 90°, β = 116.48° (3), γ= 90°, V = 2078 (4) Å^3) and ZLATOKOP (a = 17.673 Å (4), b = 17.926 Å (3), c = 7.413 Å (4), α = 90°, β = 116.46° (3), γ= 90°, V = 2102 Å^3). It can be observed that the unit-cell of the zeolitic tuff from Slanci is smaller compared to that of the Zlatokop tuff. From quantitative X-ray diffraction analysis (Figure 2), the following phases were identified in Slanci: heulandite 85.1 %, quartz 1.9 %, muscovite 5.9%, albite 6.6 %, orthoclase 0.6% and calcite 0.21%. Quantitative X-ray analysis (Figure 2) of Zlatokop yielded following mineral composition: heulandite 77.2 %, quartz 8.8 %, pyrite 0.12%, muscovite 3.8 %, albite 6.3 %, orthoclase 3.2% and calcite 0.7%. The content of the zeolitic phase in Slanci is 10% higher, than in Zlatokop. All zeolites contain various monovalent, divalent, or trivalent cations in extra-framework positions. The types and contents of exchangeable cations in the starting clinoptilolitic tuffs are presented in Table 1. The total cation exchange capacity was determined as the sum of the exchangeable cation contents.

Table 1. Content of exchangeable cations in zeolitic tuff from Slanci and Zlatokop deposit.

	Exchangeable cations [MmolM$^+$/100g]				
Tuff	Ca^{2+}	Mg^{2+}	Na^+	K^+	CEC
Slanci	145	3.0	4.1	8.0	160
Zlatokop	95	11.2	18.2	15.7	140.1

4. CONCLUSION

Based on the presented results, it can be concluded that there is a correlation between the cation exchange capacity and the content of the heulandite component in the zeolitic tuff. The heulandite phase is most abundant in the zeolitic tuff from the Slanci deposit, with 85% HEU minerals, while in the Zlatokop deposit it is at 77%. The total cation exchange capacity values for the examined zeolitic tuffs are in correlation with the content of the zeolitic phase.

ACKNOWLEDGEMENTS

The authors would like to thank the Ministry of Science, Technological Development and Innovations of the Republic of Serbia for supporting the research (Grant No: 451-03-136/2025-03/200023).

REFERENCES

[1] A. Radosavljević-Mihajlović, B. Matović., Tehnika., 13 (2) (2008) 107-119.
[2] J .Obradović, Geol anali Balkanskog poluostrva., XLI, (1977) 293-302.
[3] M. Pansu, J. Gautheyrou., Handbook of Soil Analysis. Mineralogical, Organic and Inorganic Methods, Springer-Verlag. Berlin, 2006, p. 709-754.
[4] J.C. Taylor, Powder Diffraction., 6 (1991) 2-9.
[5] J. Stojanović, A. Radosavljević-Mihajlović, V. Kašić. Zbornik radova VIII Simpozijuma JAM, Mineralogija Godišnjak JAM, Beograd, Srbija, 2003.
[6] A. Radosavljević-Mihajlović, J. Stojanović, V, Kašić, J. Lemić., Bull. Geoinstitute., 38 (2003) 149-155.
[7] A. Radosavljević-Mihajlović, J. Stojanović, V. Kašić., Radovi Geoinstituta., 40 (2005) 191-200.

The 56th International October Conference on Mining and Metallurgy
22-25 October 2025, Bor Lake, Bor, Serbia
www.ioc.tfbor.bg.ac.rs

DOI: 10.5937/IOC25048L *Original scientific paper*

RESULTS FROM EXPERIMENTAL RESEARCH OF ROCK BREAKING BY SMALL DIAMETER DIAMOND CORE DRILL BITS

Edita Lazarová[1a], Mária Bali Hudáková[1b], Víťazoslav Krúpa[1c], Alexander Kiovský[1d], Pavol Vavrek[1e] Lucia Ivaničová[1f]

[1] Institute of Geotechnics of the Slovak Academy of Sciences, Watsonova 45, 04001 Košice, Slovakia
[1a] lazarova@saske.sk, 0000-0003-4682-6433
[1b] krulakova@saske.sk, 0000-0002-3897-4762
[1c] krupa@saske.sk, 0009-0004-5030-0914
[1d] kiovsky@saske.sk, 0009-0002-7278-0360
[1e] vavrek@saske.sk, 0000-0002-1125-1361
[1f] ivanic@saske.sk, 0000-0003-3844-9703

Abstract
The rock drilling process involves a wide range of factors that affect it to varying degrees, and this influence is then reflected in the output parameters. It is complicated to predict them and to determine the degree of their impact on the rock breaking efficiency. In order to simulate the real drilling process without the impact of the drill string, a horizontal laboratory drill rig was designed and constructed at the Institute of Geotechnics of the Slovak Academy of Sciences. The goal of experimental research on a test facility is to provide accurate and immediate information in real time and, based on their evaluation and analysis, to identify parameters that significantly affect this process. The article presents our findings from experimental research on diamond core drill bits.

Keywords*: rotary drilling, experimental drill rig, drill bit, wear, rock, specific energy, optimization,*

1. INTRODUCTION

The rock drilling performance is affected by the constructional and performance parameters of the drilling equipment and the drill bit, the parameters related to the drilling process and the parameters related to the properties of the drilled rock [1]. For the purpose of evaluating the impact of changes in various combinations of the operational parameters on the potential financial and operational benefits of the drilling operations, multiple studies have been conducted [2]. In order to accurately determine the factors that enter the drilling process and identify their impact on the rock breaking efficiency, the process must be subjected to experimental research. The studies on rock breaking by drilling, conducted in laboratory conditions, improve our understanding of the interactions between the rocks and the drill bits and provide the information required for the purpose of evaluating and optimally controlling the drilling process in terms of the drilling performance and energy consumption, which may significantly reduce the costs.

2. EXPERIMENTAL RESEARCH

In order to accurately determine the key factors that enter the drilling process and to identify their impact on the rock breaking efficiency, the drilling process was subjected to experimental research. At the Institute of Geotechnics of the Slovak Republic, an experimental laboratory drilling rig was designed and constructed for the simulation of a real drilling process without the influence of the drill string. The test device is intended for horizontal drilling with small-diameter bits up to a diameter of 70 mm, commonly used in industry. Diamond or carbide core drill bits were used for research purposes. The rock for experiments was treated using a circular saw for rock cutting. The tested samples were approximately cuboid-shaped with dimensions of approximately 150x150x300 mm. Water without any additives was used as the flushing fluid. It was supplied by

a pump from a water tank with a quasi-constant flow rate $10^{-3}.m^3.s^{-1.}$ Position measurement switch allowed rock specimen drilling up to 260 mm length.

The experiments carried out on this device were intended to improve our understanding of the interactions between the drilled rock and the drill bits, to examine of the effect of a drilling mode on the course of the rock drilling process, to investigate the rock drillability, to study the energy consumption in drilling, to assess the tested drill bits in terms of their usability in real operating conditions, to determine the effect of rock changes, rock drilling mode and drill bit on vibrations generated during rock drilling, to determine the relationship between the drill bit wear and energy requirement for the rock drilling, to investigate the relationship between the drilling tool, the applied drilling mode, energy demands in breaking and the characteristics of drilled rock debris.

The device is equipped with an on-line measurement system, that enables continuous data acquisition and archiving, controls and monitors the experiment, provides measured values of process parameters in the form of time changes – electric current, thrust force, rotation speed, torque, enables online visualization of the torque and three orthogonal components of cutting forces, provides values of vibration acceleration in three orthogonal directions and their visualization, records the drilled length and calculates the drilling speed and specific energy using the pre-defined equations from the monitored data. It is equipped with a system that captures crushing products – drilled rock debris, which are then used for further analysis.
The measured data was used to calculate the advance rate and specific energy in real time during drilling. These values enabled the quantification of the rock drilling efficiency.

3. RESULTS FROM EXPERIMENTAL RESEARCH

3.1 Determining the zone of efficient drilling

Based on the experiments performed and the processing of the obtained data, a mathematical model of penetration depth as a function of the thrust force was derived [3]:

$$p(F) = p_{max}[1 - e^{-\omega.F}(1 + \omega.F)] \quad (mm), \tag{1}$$

where F (N) is the applied thrust force; p_{max} (mm) is the maximum penetration depth to which the equation solution converges; and ω (N^{-1}) is the substitution coefficient.
Mathematical model of p(F) exhibited a very high correlation tightness between the experimental and theoretical values in all 116 evaluated experiments, with a correlation coefficient value higher than 0.97.

Through gradual mathematical adjustments, equations were derived for calculating the limit values of thrust forces and penetration depths defining the zone of efficient drilling. The optimal thrust force was identified at which the specific energy curve reaches the minimum at a relative high rock breaking efficiency.

The highest probability of efficient drilling (chipping) occurs near of inflection point F_{inf} of the penetration-thrust curve. The most intensive deceleration of an increase in the penetration depth was observed at the F_{up} thrust force value (the upper boundary of the zone of efficient drilling) which was twice the F_{inf} value (the lower boundary). The relationships were derived for calculating penetration depths corresponding thrust F_{inf}, F_{up} and F_{opt}.

The analysis of the used mathematical apparatus revealed the simplicity of the optimization of the drilling process in terms of the minimization of energy consumption. This requirement was met when the drill bit operated at a low value of specific energy by controlling the penetration depth in the zone of efficient drilling. Figure 1 shows the limit values of thrust force and penetration depth defining the zone of efficient drilling in terms of minimum specific energy values.

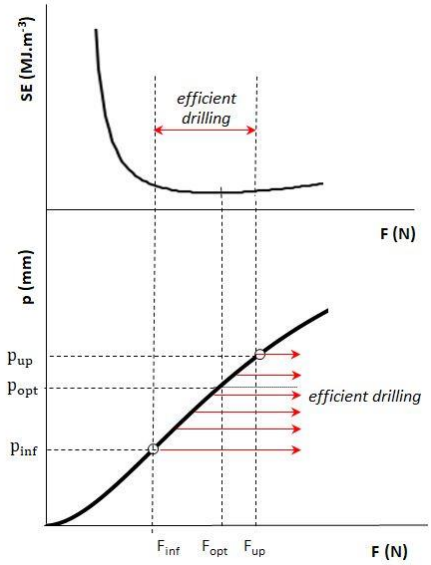

Figure 1. Limited values of thrust force and penetration depth determining the zone of efficient drilling with regard to the minimum values of specific energy.

3.2 Determination of drill bit wear using 3D optical technologies

In the segment of research into rock drilling, there is a growing need for state-of-the-art monitoring, documentation and efficient evaluation of wear of drill bits by applying contactless measurement methods [4]. One of them is the use of 3D technologies – 3D scanning, photogrammetry and the use of software to process the created 3D models. Figure 2 illustrates the results of the wear evaluation of the small-diameter surface-set diamond drill bit of the outer diameter of 46 mm. The 3D model was created by scanning with a Discovery microscope. Microscope facilitated the acquisition of sufficiently detailed data for the purpose of processing them in CloudCompare software. Fig. 2a) shows the surface of the drill bit before evaluation. Fig. 2b) shows the worn surface after evaluation by the software, scaled in colour. Fig. 2c) presents the scanned surface after the experiments. The drill bit exhibits asymmetrical wear as a result of the mechanism used for fixing the drill bit on the thread. Threads of the fixing mechanism and the contact surface of the drill bit were moderately worn caused by drilling. The bit drilled three samples of granodiorite with a total length of 480 mm and two samples of limestone with a total length of 400 mm. When drilling the limestone, the following settings were used: thrust force 17 kN; rotation speed 1000 rpm. For granodiorite, the rotation speed was 1000 rpm and the thrust force was increased from 10 kN to 14 kN due to faster wear of the drill bit.

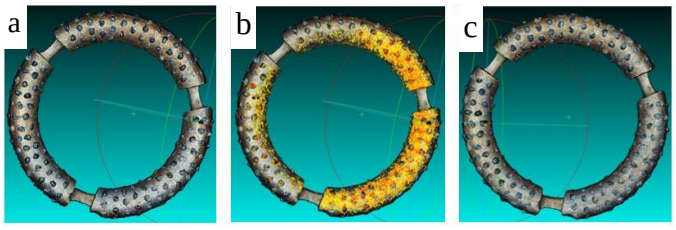

Figure 2. Colour-scaled wear of the surface of the surface-set diamond drill bit; drilled length 480 mm granodiorite and 400 mm limestone

The 3D method for identifying the bit wear, compared to conventional methods, such as weighing and measurement, is more accurate and provides a much wider range of outputs, such as wear distribution, more accurate calculation of material volume removed between the individual measurements, and colour scaling based on the wear quantification. The method may also be applied to impregnated and hard-metal small-diameter drill bits, provided that some of the procedures are adjusted.

3.3 Vibration signal for assessing the drilling process

Our research is also focused on alternatives for the use of vibrations for the control of the drilling process. We used experimental laboratory measurements to determine the effect of applied regime changes on vibrations. It has been shown that vibration acceleration values responded quite sensitively to changes in thrust force and increase linearly with rotation speed. The found correlation of the specific energy with the inverse of the average effective vibration acceleration values in the direction of the drilling axis as a function of the rotation speed, provided a prerequisite for the use of the vibration signal for the optimization of the control of the drilling process in terms of the maximum tool life and therefore the minimum wear intensity. From the processing of the recorded vibration signal in the frequency domain, it can be concluded that the rock grain size is probably the decisive characteristic affecting the intensity of the vibration signal.

Based on the recorded and subsequently processed vibration signal from experimental drilling, it was confirmed that the induced vibrations carry the information about the current state and conditions of drilling and that each applied drilling mode, as well as the drilled rock, has a specific vibration response.

3.4 Use of drill debris for drilling process assessment

Laboratory drilling rig was adjusted for collection of drill debris from flushing fluid aiming to involve the drill debris characteristics into the drilling process assessment. Roughness index CI was used for changes in grain size, determined by sieve analysis of the drill debris. Complex analysis of drilling process effect on shape, size and distribution of drill debris was performed using the dynamic image analysis instrument Camsizer X2.

Analysis of rock debris will provide new useful information to monitor the cutting capability of the drill bit. The size and shape of drill cuttings fragments are related to the rock breaking mechanism and the energy consumption of the drilling process.

4. CONCLUSION

The long-term experimental research of rock drilling running at the Institute of Geotechnics SAS has been focused on the study of rock-tool interactions. Most of the knowledge gained from research of small-diameter diamond drill bits, carbide drill bits and chisel drill bits has been processed into comprehensive mathematical models that allow generalization of rock breaking processes for a wide range of different types of drilling tools. This created the basis for exact optimization procedures for these processes.

ACKNOWLEDGEMENTS

This research was supported by projects VEGA 2/0090/23 and APVV-23-0364.

REFERENCES

[1] M. Babaei Khorzoughi, R. Hall, Int. J. Min. Sci. Technol., 26 (6) (2016) 989–994.
[2] U. Sakız, H.Aydın, O.Yaralı, Bulletin of Engineering Geology and the Environment, 81(1) (2022) 24.
[3] V. Krupa, M. Krul'akova, E. Lazarova, M. Labas, K. Feriancikova, L. Ivanicova, MEASUREMENT, 117 (2018) 65–175.
[4] Z. Wang, W. Sun, J. Kang, Y. Tao, S. Tan, L.Duan, Int. J. Refract. Met. Hard Mater., 123 (2024) 106793.

The 56th International October Conference on Mining and Metallurgy
22-25 October 2025, Bor Lake, Bor, Serbia
www.ioc.tfbor.bg.ac.rs

DOI: 10.5937/IOC25052L *Original scientific paper*

FAILURE CRITERION OF LIMESTONE AND GRANODIORITE DETERMINED BY LABORATORY TESTING AND THEORETICAL PROCESSING OF THE DRILLING PROCESS

Edita Lazarová[1a], Víťazoslav Krúpa[1b], Pavol Vavrek[1c], Mária Bali Hudáková[1d], Lucia Ivaničová[1e], Alexander Kiovský[1f]

[1] Institute of Geotechnics of the Slovak Academy of Sciences, Watsonova 45, 04001 Košice, Slovakia
[1a] lazarova@saske.sk, 0000-0003-4682-6433
[1b] krupa@saske.sk, 0009-0004-5030-0914
[1c] vavrek@saske.sk, 0000-0002-1125-1361
[1d] krulakova@saske.sk, 0000-0002-3897-4762
[1e] ivanic@saske.sk, 0000-0003-3844-9703
[1f] kiovsky@saske.sk, 0009-0002-7278-0360

Abstract
The results of experimental laboratory research on rock drilling, conducted with the use of diamond core bits, were processed mathematically. The developed theoretical models of rock resistance to disintegration facilitated the identification of three compatible views on calculating the ultimate stress state of rock drilled in the dynamic drilling mode with the use of diamond-embedded core drill bits. The contact surface strength of the rock σ_p [kN/mm], the dynamic cutting strength of the rock σ_μ [kN/mm], and the contact bulk strength of the rock σ_c [MPa] were defined. The strength values obtained from drilling into limestone and granodiorite were compared with the results of laboratory tests with the aim of identifying their uniaxial compressive strength, Brazilian tensile strength, punch shear, and Brinell hardness.

Keywords: *rock drilling, contact surface strength, cutting strength, laboratory testing*

1. INTRODUCTION

The ultimate stress state of rocks is determined by the conditions in which an external force, exerted on rocks, causes disturbance or disintegration of the rocks [1]. The existing experimental knowledge and empirical experience were used as the basis for the development of rock strength theories, micro-disturbance theories, crack propagation theories, and energetic and technological disturbance theories [2]. Relevant literature [3,4,5,6] presents models for the estimation of rock strength by investigating the interactions between the drill bits and the rocks; they are categorised into two groups: models based on the balance of forces; and models based on the balance of energies. This article presents the results of laboratory testing of limestone and granodiorite, as well as the results of the identification of rock resistance to disintegration, which was based on the theoretical processing of experimental drilling into limestone and granodiorite with the use of two diamond core drill bits with a diameter of 46 mm and the following diamond sizes: Drill Bit A (16/25 pcs.ct^{-1}); and Drill Bit B (25/40 pcs.ct^{-1}). The obtained values of strength of the drilled limestone and granodiorite samples were compared with the results of laboratory testing conducted with the aim of identifying uniaxial compressive strength, Brazilian tensile strength, punch shear, and Brinell hardness.

2. LABORATORY TESTING OF LIMESTONE AND GRANODIORITE

The testing of rocks, performed in the laboratory, is an important part of the engineering discipline of rock mechanics. The data needed for designing structures in rock-based materials (geotechnical engineering) is primarily gathered through testing, either in the laboratory or in the field. Much information can be obtained from laboratory tests of rock samples with a known orientation.

Laboratory tests usually consist of simple experiments that are appropriate to the nature of the rock, in which important quantities, often stress and strain, are determined. By drilling and cutting, the test samples of a regular shape were prepared from the individual rock types for the purpose of testing procedures compliant with the ISRM (International Society of Rock Mechanics) methodology, aimed at identifying the properties of the rocks. Their mechanical properties were determined using the INSTRON 1000RD testing machine, while the static Brinell Hardness (BH) was identified using the HDT-BRV 130 device. Bulk density ρ ($kg.m^{-3}$) at a natural moisture content was identified for cylindrical test samples with a diameter d = 54.4 mm. The aim of the uniaxial compression strength testing was to identify compressive strength of intact rock samples. Following the ISRM recommendations [7], the tests were carried out with cylindrical samples of regular dimensions with a height-to-diameter ratio of 2.0–3.0 and with a diameter of 54.4 mm.

Uniaxial compressive strength UCS (MPa) was identified by dividing the peak load P attained during the test to failure by the initial cross sectional area A. Tensile strength of rocks is usually defined as the maximum tensile stress that a particular rock mass can withstand. The Brazilian Test is a laboratory test conducted in rock mechanics in order to indirectly determine the tensile strength of rocks in MPa [8]. Hardness of a mineral and rock is its resistance to abrasion. Static hardness testing is based on rock indentation with the use of a hard tool. Hard metal balls or diamond cones or pyramids can act as indenters. The test load is applied with a defined initial application time and duration, and it has to be applied perpendicularly to the sample [9]. The Brinell hardness (kg/mm^2) test for limestones and granodiorites consisted of applying a constant load of 125 kg for a specified period of time (30 s) using a hardened steel ball with a diameter of 5 mm. For a punch shear τ_{ps} (MPa) test, flat rock discs are fitted into the testing jig [10]. The test is commenced by placing a rock sample at the bottom of the casing of a piston-shaped cylindrical jig having a puncher head which fits into a circular shear hole of another hollow cylinder. Then the puncher is placed in position and the entire device is placed in the compression-testing machine and loaded.

The results of laboratory testing of limestone are given in Table 1 and of granodiorite in Table 2.

Table 1. Properties of limestone

Statistical values	Bulk density	UCS	Brazilian test	HB	Punch shear
Number of samples evaluated	14	15	10	10	10
Mean	2 691	85.1	9.3	466.4	9.5
Median	2 691	77.8	9.5	457.1	10.0
Minimum	2 682	55.1	6.5	416.3	5.2
Maximum	2 702	119.2	10.8	521.8	14.2

Table 2. Properties of granodiorite

Statistical values	Bulk density	UCS	Brazilian test	HB	Punch shear
Number of samples evaluated	14	15	10	10	10
Mean	2,705	85.8	13.2	831.1	16.5
Median	2,706	85.4	13.1	873.9	17.7
Minimum	2,693	53.7	9.5	638.4	8.6
Maximum	2,717	122.3	16.9	927.6	24.3

The limestone specimens were taken from a quarry in Včeláre, located approximately 40 km southwest of the city of Košice – the centre of the Eastern Slovakia. The granodiorite piece specimens were taken from a quarry at Podhradová, located on the northern edge of the city of Košice.

2.1 Identification of rock resistance to disintegration

During the small-diameter drilling, the values of penetration depth p(F) and torque T(F) as a function of external force F were monitored. Equation (1), derived for calculating contact bulk strength of the rock σ_C, was as follows:

$$\sigma_C = \frac{F}{p(F)N\pi\overline{r_d}} \quad \text{(MPa)} \tag{1}$$

wherein the surface area of the contact surface between the drill bit and the rock is determined by the size (the diameter of spherical diamonds $\overline{r_d}$) and number N of diamonds and the penetration depth p(F). As the magnitude of the external force F changed, the penetration depth p(F) also changed. For the purpose of identifying σ_C, the drilling mode applied was the mode in which drilling is carried out at a minimum value of specific energy SE_{min}.

Contact surface strength σ_p (N/mm) was calculated using Equation (2):

$$\sigma_p = \frac{F_{inf}}{p_{max}} \quad \text{(N/mm)} \tag{2}$$

wherein F_{inf} is the external force in the inflexion point of the p(F) curve, and p_{max} is the maximum penetration depth. The cutting resistance of rock, which is a modification of the contact surface strength, is defined by Equation (3):

$$\sigma_\mu = Z.\mu.\sigma_p \qquad \text{(N/mm)} \tag{3}$$

wherein μ = cutting coefficient, calculated with the use of the torque value, and Z=3.351 is a derived constant applicable to drilling at the minimum value of specific energy. Table 3 and Table 4 present the calculated values obtained and processed with the use of data measured in the rotary small-diameter drilling into rock samples with the use of Drill Bit A and Drill Bit B. Each drill bit was used in drilling into limestone (L) and subsequently into granodiorite (G). After drilling into granodiorite, the drilling process was repeated alternately with limestone and granodiorite.

Table 3. Contact bulk strength and minimum specific energy

Drill Bit A	L_1	G_1	L_2	G_2	L_3	G_3	L_4
σ_C (MPa)	98.41	62.12	353.8	346.22	503.97	1059.2	717.73
SE_{min} (MPa)	1,072	734	3,561	3,366	5,046	6,540	6,128
Drill Bit B	L_1	G_1	L_2	G_2	L_3	G_3	L_4
σ_C (MPa)	89.44	79.32	376.4	252.31	487.68	236.92	393.96
SE_{min} (MPa)	1,056	984	4,102	2,714	4,855	2,737	4,033

Table 4. Contact surface strength and cutting strength

Drill Bit A	L_1	G_1	L_2	G_2	L_3	G_3	L_4
σ_p (N/mm)	7,343	4,635	26,400	25,830	37,600	79,030	53,550
σ_μ (N/mm)	6,356	4,478	19,260	20,000	27,210	40,000	34,390
Drill Bit B	L_1	G_1	L_2	G_2	L_3	G_3	L_4
σ_p (N/mm)	6,518	5,780	27,430	18,390	35,530	17,260	28,710
σ_μ (N/mm)	6,273	5,830	21,440	15,150	28,840	13,800	23,960

3. RESULTS AND DISCUSSION

As indicated by data in Table 1 and Table 2, limestone and granodiorite exhibited approximately the same uniaxial compressive strength (UCS). A more significant difference was observed for HB and τ_{ps} values. The calculated values of contact bulk strength σ_C (Table 3) for unworn diamonds are comparable to the UCS values. The greatest difference between limestone and granodiorite was observed in a comparison of their abrasiveness values. As for limestone, its abrasiveness value was identified as 0.0186 mg/m, while for granodiorite it was 1.4092 mg/m. Since granodiorite exhibited higher abrasiveness, as the drill bit wear increased, after the application with abrasive granodiorite, the values of rock resistance to disintegration also increased, while the same rising trend was observed for the values of specific energy. It means that the values of rock resistance to disintegration (as well as contact surface strength σ_p and cutting strength σ_μ, shown in Table 4) significantly increased due to increasing wear of diamonds. *(Note: The calculated values of σ_p and σ_μ for unworn diamonds were of the same order of magnitude as the values of Brinell hardness converted to MPa.)*

4. CONCLUSION

The defined values of rock resistance to disintegration significantly increased with changes in the condition of the rock-tool contact zone as the wear increased. Those changes were reflected in the values of specific energy. The presented laboratory tests with limestone and granodiorite were not affected by changes in the contact surfaces.

ACKNOWLEDGEMENTS

This research was supported by projects VEGA 2/0090/23 and APVV-23-0364.

REFERENCES

[1] E. Hoek, C. Carranza-Torres, B. Corkum, Hoek-Brown failure criterion – 2002 Edition. Proc. NARMS-TAC Conference, Toronto, 2002.
[2] Krúpa, V., Pinka, J.: Rozpojovanie hornín. TU Košice, 1997.
[3] S. Kalantari, H. Hashemolhosseini, A. Baghbanan, Int. J. Rock Mech., 104 (2018) 45–52.
[4] P. Kolapo, Geotech. Geol. Eng. 39 (2021) 1715–1726.
[5] C. R. Lakshminarayana, A. K. Tripathi, S. K. Pal, Int. J. Geo-Eng. 12, 23 (2021).
[6] Sh. Wang, Y. Wu, X. Cai, Z. Zhou, J. Cent. South University 30 (2023), 4036-4051.
[7] ISRM Commission on Standardization of Laboratory and Field Tests. Suggested methods for determining the uniaxial compressive strength and deformability of rock materials. September 1977.
[8] ISRM Commission on Standardization of Laboratory and Field Tests. Suggested methods for determining tensile strength of rock materials. March 1977.
[9] H. Konietzky, T. Fruhwirt, Overview about rock mechanical lab testing – part I: mechanical test. TU Bergakademie Freiberg, 2023.
[10] A.R. Jumikis, Rock Mechanics. Trans Tech Publications. First Edition, 1979.

The 56th International October Conference on Mining and Metallurgy
22-25 October 2025, Bor Lake, Bor, Serbia
www.ioc.tfbor.bg.ac.rs

DOI: 10.5937/IOC25056H *Original scientific paper*

OPTIMISATION OF THE ROCK DRILLING PROCESS CONDUCTED WITH SMALL-DIAMETER DRILLING TOOLS

Mária Bali Hudáková[1a], Edita Lazarová[1b], Víťazoslav Krúpa[1c], Pavol Vavrek[1d], Lucia Ivaničová[1e], Alexander Kiovský[1f]

[1] Institute of Geotechnics of the Slovak Academy of Sciences, Watsonova 45, 04001 Košice, Slovakia
[1a] krulakova@saske.sk, 0000-0002-3897-4762
[1b] lazarova@saske.sk, 0000-0003-4682-6433
[1c] krupa@saske.sk, 0009-0004-5030-0914
[1d] vavrek@saske.sk, 0000-0002-1125-1361
[1e] ivanic@saske.sk, 0000-0003-3844-9703
[1f] kiovsky@saske.sk, 0009-0002-7278-0360

Abstract
This paper deals with rotary drilling into andesite in laboratory conditions, conducted on an experimental horizontal drilling rig. The processing of experimental data after the experiments contributed to the application and verification of mathematical models of penetration depth and torque as a function of the thrust force. The output is the identification of intervals of the applied thrust force levels for the efficient drilling zone. Designing of an optimisation algorithm for controlling the rock drilling process and monitoring the tool condition was based on changes in the thrust forces level at which specific energy reached minimum values. The criterion applied was the monitoring of the penetration depth, which together with the theoretical value of the torque defined the calculation of the specific energy values.

***Keywords**: penetration depth, specific energy, optimisation algorithm*

1. INTRODUCTION

A description of the process of rotary drilling into rocks consists of the creation of mathematical equations describing mathematical correlations between the output variables and the controllable as well as uncontrollable input variables. The monitoring of input drilling parameters (thrust, rotational speed, flushing) and output drilling parameters is crucial for the purpose of identifying optimal operating parameters [1] and tool wear [2]. Due to significant variability of the properties of disintegrated rock, it is currently impossible to produce a mathematically accurate description of rocks and in in-situ conditions the drilling modes and performance of drilling tools vary. Many researchers have investigated the Measurement While Drilling (MWD) techniques and their possible application in the prediction of rock mass properties [3]. The importance of analysing and interpreting data obtained from drilling is equal to the importance of recording data for the purpose of creating mathematical models and algorithms for the development of artificial intelligence (AI) and big data technology [4], which optimise changes in the output parameters of the drilling process. Those parameters change since rocks are inhomogeneous and anisotropic materials. Higher efficiency of the process is based on reducing mechanical specific energy [5, 6]. Penetration rate is an essential indicator in a drillability analysis and estimation. This parameter is of great importance in mining projects. There are almost no models that can estimate the penetration rate for core drilling operations [7]. A focus of the research presented in this paper is the optimisation of core drilling by applying a mathematical model of penetration depth [8] and torque as a function of the magnitude of the thrust force applied, with the use of data obtained after drilling into andesite in laboratory conditions.

2. EXPERIMENTAL

A series of experiments, conducted during the drilling into andesite, confirmed a trend similar to that shown in Figure 1. Experimental samples were rectangular blocks sized 150 x 150 x 300 mm. The testing was carried out with three diamond core drill bits: a 16/25 drill bit; a 12/18 drill bit; and a 25/35 drill bit. They only differed in sizes of the diamonds embedded. In total, 116 experiments were carried out and the drilled length was 35.95 m. Drilling modes applied were those with a constant rotational speed (500 rpm; 1,000 rpm; 1,500 rpm; and 2,000 rpm) and a gradually increasing thrust force value (0–20 kN). Although the application of drilling modes with a constantly increased thrust force at a constant rotational speed was not particularly appropriate in terms of the drill bit service life, it facilitated the creation of models describing the changes that occurred in the rock-tool interaction zone. Figure 1 shows a correlation typically applied in studies dealing with drillability.

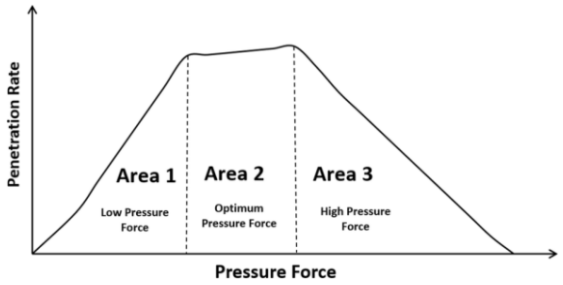

Figure 1. Corelation between the penetration rate and the pressure force

As the pressure force increased, the penetration rate also increased. An optimal penetration rate was achieved at a certain pressure force, while after that point was exceeded, the penetration rate decreased as the pressure force increased.

2.1 Theoretical background

The energy consumption of the drilling process is identified using the values of specific energy SE ($MJ.m^{-3}$), which was introduced into the drilling research by Teale [9]. It expresses the amount of energy necessary to break a unit volume of rock. Equation 1, a mathematical expression of specific energy,

$$SE(F) = \frac{2\pi\, T(F)}{A.\ p(F)} \qquad (MJ.m^{-3}) \tag{1}$$

clearly shows that the variable parameter in that equation is $\frac{T(F)}{p(F)}$, wherein T (Nmm) is the torque and p (mm) is the penetration depth as a function of the thrust force F (N). In the equation, A (mm^2) is a constant expressing the surface area of the contact surface between the tool and the rock. The mathematical model of torque T (Nmm) is described in Equation 2, which represents, for an astatic system, the solution of a second-order differential equation with constant coefficients:

$$T(F) = \kappa\left[F + \Theta\left(e^{-\frac{F}{\Theta}} - 1\right)\right] \qquad (N.mm) \tag{2}$$

wherein F (N) is the applied thrust force. The substitution coefficient κ (mm) expresses a linear response of the torque to the growing thrust force; and θ (N) represents a delay in the response of the drilling set at low thrust force values. The mathematical model of penetration depth p (mm) as a function of the thrust force F (N) is the solution of the second-order differential equation with constant coefficients [8]:

$$p(F) = p_{max}[1 - e^{-\omega.F}(1 + \omega.F)] \qquad (mm) \tag{3}$$

wherein F (N) is the applied thrust force, p_{max} (mm) is the maximum penetration depth to which the equation solution converges, and ω (N^{-1}) is the substitution coefficient. After the substitution

of Equation 2 and Equation 3 to Equation 1, the resulting mathematical model of specific energy was as follows: $$SE(F) = \frac{2\pi}{A} \frac{\kappa\left[F+\Theta\left(e^{-\frac{F}{\Theta}}-1\right)\right]}{p_{max}\,[1-e^{-\omega F}\,(1+\omega F)]} \quad (MJ.m^{-3}) \ . \tag{4}$$

The second derivative of penetration depth Equation 3 with respect to thrust force determines the inflection point F_{inf} of the p-F curve: $$F_{inf} = \frac{1}{\omega} \quad (N) \tag{5}$$

The inflection point values were calculated for all of the executed andesite borehole drillings. Since the inflection point F_{inf} determines the area of the efficient rock disintegration by chipping, this efficient area continuously moves towards higher thrust force values with an increasing total drilled length due to continuous wear of the drill bit. Mathematical models *p(F)* and *T(F)* were used for calculating the lower limit F_{inf} and the upper limit $F_2 = 2.F_{inf}$ of the trust force values that delimitate the efficient drilling area, in which, in theory, specific energy is minimal. Also, the optimal thrust force area F_w was identified for each drilling into andesite, as calculated using Equation 6, wherein $|\varepsilon| = \frac{|\theta|}{F_{inf}}$.

$$F_w = \frac{1}{2}\left[|\theta|(1-|\varepsilon|)+F_{inf}\right] + \sqrt{|\varepsilon|.\theta^2\left(\frac{1}{4}.|\varepsilon|-\frac{1}{2}\right) - F_{inf}\left(\frac{3}{4}.F_{inf}+\frac{1}{2}.|\theta|\right)-\frac{1}{4}.\theta^2} \tag{6}$$

The thrust force values, calculated using Equation 6, were used to calculate the optimal thrust force values, which ranged in the interval $F_w \in$ <1.37;1.66>, while the average value, calculated with the use of all drillings and tested drill bits, was $F_w \cong 1.45\ F_{inf}$.

3. RESULTS AND DISCUSSION

For all of the drill bits tested, the results showed that the difference between the values of specific energy at thrust force values F_w and F_2 was negligible. However, the penetration rate at thrust force F_2 was higher while the energy-intensity of the process was practically unchanged. Those axioms were used as the basis in the process of designing an optimisation algorithm presented in Figure 2.

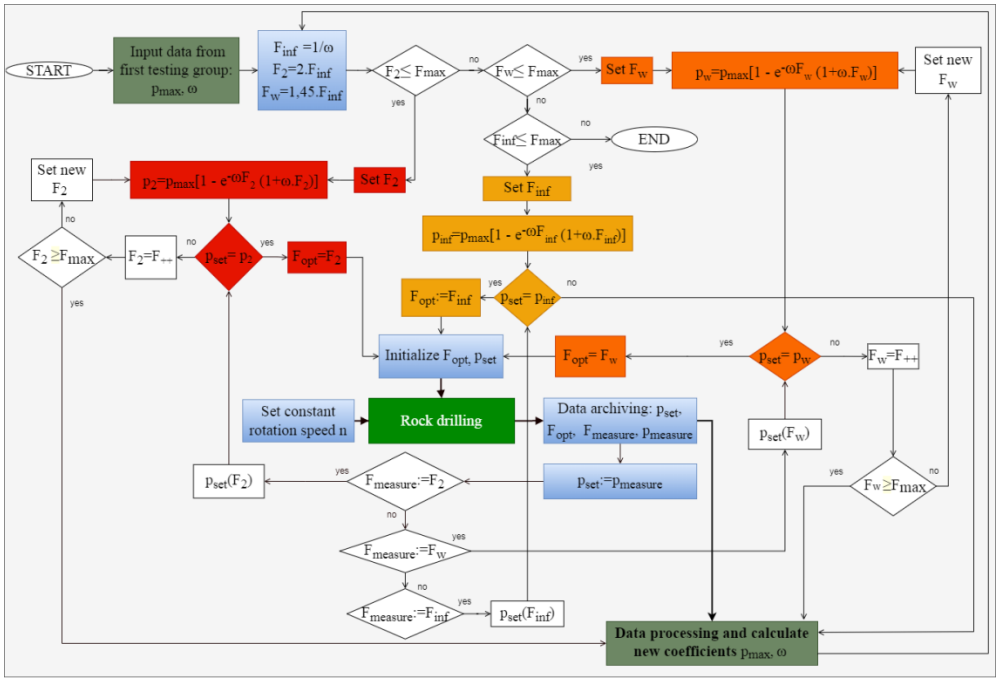

Figure 2. Optimisation algorithm

The newly-designed algorithm, shown in Figure 2, monitors dynamic properties of the process of experimental drilling with the use of the identified solution of the differential equation for a mathematical model of the p-F curve – Equation 3, in particular by identifying substitution coefficients ω and p_{max}, as well as its higher derivations, based on the thrust force value – Equation

5. That facilitates efficient control of the drilling process by simply changing the magnitude of the applied thrust force to the optimal value F_{opt}. In the case that the identification criterion (penetration depth) is not met, as verified by the online control in experimental drilling, it is necessary to identify a new optimal thrust force level using the mathematical model of the p-F curve for calculating new substitution coefficients as a response to the dynamic property of the process of a changing condition of the tool with an increasing drilled length. In such a case, the calculation of a new optimal thrust force level is based on the archived data obtained in experiments conducted with a gradually increasing thrust force and a constant rotational speed. Similarly, the first adjustment of the optimal thrust force level is preceded by the creation of trial experimental drillings and data processing.

4. CONCLUSION

The analysis of the used mathematical apparatus revealed simplicity of the solution aimed at optimising the drilling process in terms of minimising energy intensity of drilling into rocks. Yet, numerous publications indicate that there is a linear correlation between specific energy and wear intensity (wear degree per drilled length), which is primarily affected, as to the resulting values, by the abrasiveness of the rock drilled. As a result, the minimisation of energy intensity of a rock drilling process leads to a significant increase in the lengths drilled, and hence to the extension of the service life of the drilling tool.

ACKNOWLEDGEMENTS

This research was supported by projects VEGA 2/0090/23 and APVV-23-0364.

REFERENCES

[1] F.E. Dupriest, W.L. Koederitz, Maximizing Drill Rates with Real-Time Surveillance of Mechanical Specific Energy, in: All Days, SPE, Amsterdam, Netherlands, 2005.
[2] M. Klaic, Z. Murat, T. Staroveski, D. Brezak, Wear. 408–409 (2018) 222–227.
[3] H. Basarir, J. Wesseloo, A. Karrech, E. Pasternak, A. Dyskin, The use of soft computing methods for the prediction of rock properties based on measurement while drilling data, in J Wesseloo (ed.), Deep Mining 2017: Proceedings of the Eighth International Conference on Deep and High Stress Mining, Australian Centre for Geomechanics, Perth, 2017.
[4] G. Li, X. Song, S. Tian, Z. Zhu, Engineering, 18 (2022) 33–48.
[5] F. Shangxin, W. Yujie, Z. Guolai, Z. Yufei, W. Shanyong, C. Ruilang, X. Enshang, J. Pet. Sci. Eng., 193 (2020) 107376.
[6] P. Kolapo, Geotech. Geol. Eng. 39 (2021).
[7] N. Bilim, E. Karakaya, MME, 38 (2021) 359-366
[8] V. Krúpa, M. Kruľáková, E. Lazarová, M. Labaš, K. Feriančiková, L. Ivaničová, MEASUREMENT 117 (2018), 165–175.
[9] R. Teale, Geom. Abstr., 2 (1) (1965) 57–73.

The 56th International October Conference on Mining and Metallurgy
22-25 October 2025, Bor Lake, Bor, Serbia
www.ioc.tfbor.bg.ac.rs

DOI: 10.5937/IOC25060K *Original scientific paper*

GEOLOGICAL AND TECHNOLOGICAL CHARACTERISTICS OF THE IGROŠ-VIDOJEVIĆI ZEOLITE TUFF DEPOSITS

Vladan Kašić[1a], Ana Radosavljević-Mihajlović[1b], Jovica Stojanović[1c], Slavica Mihajlović[1d], Nataša Djordjević[1e], Ivana Jelić[1f]

[1] Institute for Technology of Nuclear and Other Raw Mineral Materials, Applied Mineralogy Unit, P.O. Box 390, Franschet d'Esperey 86, 11000 Belgrade, Serbia.

[1a] v.kasic@itnms.ac.rs, 0000-0002-4430-567X
[1b] a.radosavljevic@itnms.ac.rs, 0000-0002-9194-161X
[1c] j.stojanovic@itnms.ac.rs, 0000-0002-2752-6374
[1d] s. mihajlovic@itnms.ac.rs, 0000-0003-0904-3878
[1e] n.djordjevic@itnms.ac.rs, 0000-0002-2353-6751
[1f] i.jelic@itnms.ac.rs, 0009-0000-9901-9323

Abstract

In this work presents investigations of zeolitic tuff samples from the "Igroš-Vidojevići" deposit. The aim of the research was to determine the quality of samples taken from all deposit parts. Thus, samples were taken from the footwall ("Zeolit 1"), and four samples from the central deposit part ("Zeolit 2", "Zeolit 3", "Zeolit 4" and "Zeolit 5"). Characterization of the samples included chemical analysis, determination cation-exchange capacity (CEC), X-ray powder diffraction analysis (XRPD) and differ- ential thermal and thermogravimetric analysis (DTA and TGA). Results have shown that the footwall consists mostly of clays, whereas zeolite minerals dominate in the rest of the deposit.

***Key words**: Zeolite, Igroš-Vidojevići deposit, cation- exchange capacity, thermal analysis, X-Ray powder diffraction analysis*

1. INTRODUCTION

A large number of occurrences and deposits of natural zeolites of pyroclastic origin, widely distributed in Miocene sediments of Serbia, such as Zlatokop (Vranj basin), Igroš, Jablanica 1 (Kruševački basin), Beočin (Fruška Gora), Toponica (Kosovska Kamenica), and Slanci (Danube key near Belgrade), are spatially and genetically related to volcanic and volcaniclastic rocks of marine environments of Senonian and Neogene age and lake sediments of Neogene age [1,5]. The zeolitic tuff deposits were created as a product of the devitrification of volcanic glass. The lake environment had a great influence on the diagenesis of the sediments and the formation of clinoptilolites at the expense of volcanic glass. The zeolitic tuffs themselves are mostly composed of zeolitic minerals of the HEU-type clinoptilolite-hoylandite series, which are present in the form of small acicular to plate-like crystals with dimensions from 0.1 to 100 μm.

2. GEOLOGY OF THE ZEOLITIC TUFF DEPOSIT IN IGROS

The Igroš zeolitic tuff deposit covers the southernmost edge of the Miocene Kruševac basin. In the deposit area, two ore fields [2] have been identified: Šovići-Đorđevići and Igroš-Vidojevići.

Igroš-Vidojevići ore field: The zeolitic layer of tuff stretches from the northwest to the southeast and can be followed intermittently for a length of 1.1 km. Geological investigations [2] at the "Igroš-Vidojevići" ore field identified two ore bodies: "ore body 1" and "ore body 2".

The mapping of the terrain, as well as the exploitation works on "ore body 1" revealed that the layer of zeolitized tuff extends in a north-south direction and can be followed for about 170 m along its length and about 50 m on average. The layer of zeolitized tuff is interstratified within the

Miocene-Pliocene series of marly green clays that comprise the basement, as well as the brown clays and green sandstones that form the bedrock. The zeolitic tuff layer is light gray to white with an average thickness of 1.64 m, with a general north-south strike and a mean statistical dip to the north at an angle of about 4 °. The samples of zeolitic tuff that were used for the tests presented in the paper were taken from the exploitation field "Igroš-Vidojevići" - atar of the village of Igroš. 5 samples were selected for analysis: the sample marked "Zeolite 1" is a representative sample of the bottom of the deposit, while the samples marked "Zeolite 2, 3, 4, and 5" belong to the central part of the deposit. "Zeolite 2" and "Zeolite 5" are representative samples created by crushing excavated tuff, sample "Zeolite 3" is formed from crushed tuff of class 100+30 mm, and "Zeolite 4" is a sample of size -100 μm obtained by grinding.

3. RESULTS AND DISCUSSION

X-ray analysis

The mineral composition of the samples was determined by the X-ray powder diffraction (XRD) method using a "Philips" powder diffractometer, model PW-1710. Since all samples of zeolite tuffs (Zeolite 2, 3, 4, and 5) have a very similar mineralogical composition, two characteristic X-ray diffractograms of zeolite samples 2 and 4 are shown in Figure 1. Namely, the presence of zeolite minerals of the clinoptilolitic type, quartz, feldspar, and mica was determined in all analyzed samples. Feldspars and quartz are far less present, while micas are present in traces.

Chemical composition

The results of the chemical analysis of the examined samples using the AAS method (classical chemical analysis for aluminosilicates [3]) are shown in Table 1 [4]. The results show that in addition to the structural elements (silicon and aluminum), the tested samples also contain Ca, Mg, Na, and K. Also, a significant presence of iron is noted, especially in the sample "Zeolite 1", which is expected considering the volcanic origin of this rock mass. The content of other heavy metals in all examined samples (Pb, Mn, Cu, Zn, Cd, Sb, Cr, and Sn) is relatively low.

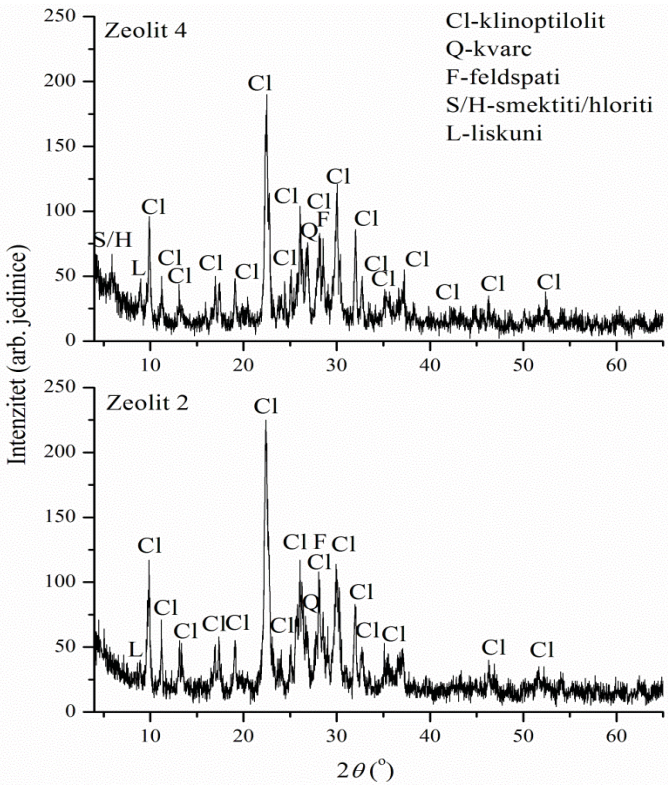

Figure 1. X-ray diffractograms of "Zeolite 2 and 4" samples of zeolite tuff from the "Igroš-Vidojevići".

Table 1. Chemical composition of samples from the "Igroš-Vidojevići" zeolite tuff deposits

Component, mas. %	Zeolite 1	Zeolite 2	Zeolite 3	Zeolite 4	Zeolite 5
SiO_2	49,76	63,52	62,88	65,58	60,41
Al_2O_3	21,04	15,32	15,26	10,68	16,46
CaO	2,27	4,71	4,90	4,90	4,19
MgO	4,78	1,55	1,90	2,06	1,91
Fe_2O_3	7,58	1,00	1,82	3,00	2,44
K_2O	4,20	0,93	0,87	1,21	1,41
Na_2O	2,15	1,13	1,13	1,23	1,56
TiO_2	1,17	0,337	0,337	0,839	1,52
PbO	0,0059	0,0038	0,0051	0,0037	0,0096
MnO	0,046	0,017	0,022	0,042	0,034
Cu	0,008	0,011	0,066	0,033	0,064
Zn	0,016	0,0053	0,011	0,0054	0,012
Cd	0,0002	0,0003	0,0002	0,0001	0,00014
Sb	0,005	0,004	0,004	0,0037	0,007
Cr	0,009	0,0003	0,0005	0,0012	0,0013
Sn	<0,0005	<0,0005	<0,0005	<0,0005	<0,0005
Loss on Ignition (T_{max}=900 ^{0C})	6,95	11,42	10,79	10,41	9,97

Cation exchange capacity (CEC)

Cation exchange capacity (KKI-CEC) was determined by the standard method with 1 mol/dm3 NH4Cl [6]. In the case of zeolite, the ions that participate in the exchange are Ca2+, Mg2+, Na+ and K+, while their sum determines the total capacity, which is expressed in mmol/100 g. The total KKI is 141.99 mmol/100 g, followed by the sample "Zeolite 3" which is 121.01 mmol/100 g. The CEC of the "Zeolite 4" sample is slightly lower, 89.48 mmol/100 g, and is close to the CEC of the "Zeolite 5" sample (83.75 mmol/100 g). The smallest CEC was obtained for the bottom sample - "Zeolite 1" and is 46.98 mmol/100 g, which indicates that clay mass dominates in this part of the deposit (Table 2).

Table 2. Results of the cation exchange coefficient (CEC / mmol (100 g)–1) of zeolitic tuff samples

Zeolite	Na	K	Ca	Mg	Σcation
1	6,18	1,75	31,56	7,49	46,98
2	29,71	12,66	90,57	9,05	141,99
3	19,05	8,18	87,82	5,96	121,01
4	11,31	6,34	65,87	5,96	89,48
5	23,38	9,85	43,36	7,16	83,75

Thermal analysis (TG and DTA)

Thermal analysis provides information on the dehydration processes, dehydroxylation, and thermal stability of aluminosilicate minerals. Figure 4 shows the comparative characteristic TG/DTG/DTA diagrams of zeolitic tuff samples 1, 2, and 3. Continuous mass loss is observed in the temperature range from 25 to 1000 ºC. The loss of mass on the TG diagram in the temperature range up to 300 ºC comes from the release of water bound to various cation centers in the zeolite channels or on the surface (dehydration). On the DTA diagrams of the "Zeolite 2 and 3" samples, in the temperature interval from 25 to 300 ºC, one endothermic peak with a minimum at ≈130 ºC, originating from dehydration, and a bend at ≈220 ºC, which are characteristic of calcium zeolite [7], can be observed. "Zeolite 1" is significantly different from the diagrams of the other examined

samples. This type of TG and DTA diagram indicates the presence of clay minerals in the sample "Zeolite 1".

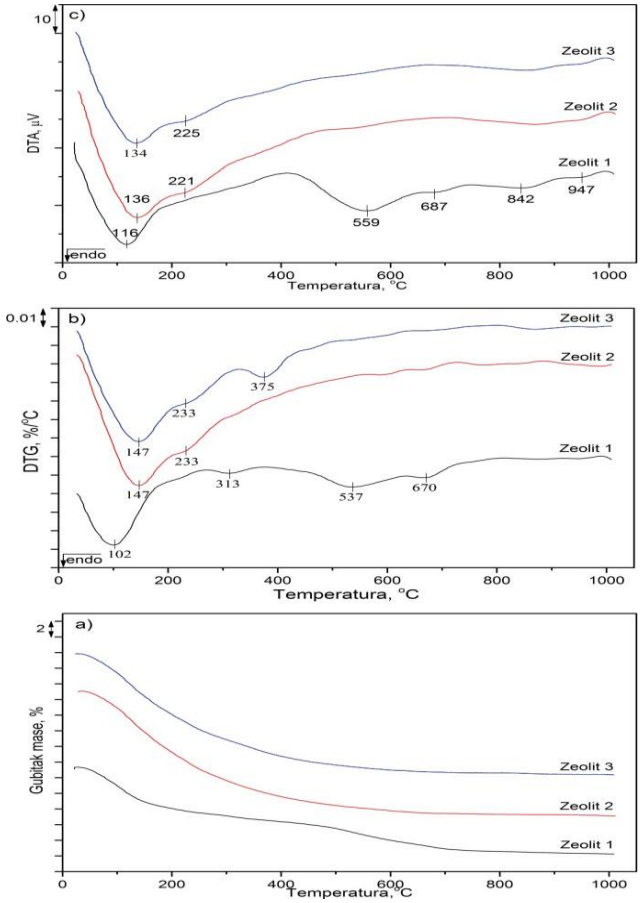

Figure 2. Thermal analysis of „Zeolite 1“, „Zeolite 2“ and„Zeolite 3“. a) TGA; b) DTG; c) DTA.

Results of infrared spectroscopy analysis

FTIR analysis confirmed the presence of hydrated aluminosilicates in the tested samples. The results showed the absence of any significant differences in the infrared spectra of the tested samples. For this reason, only one representative spectrum is shown and explained in Figure 3. In the infrared spectrum, the bands in the frequency range from 1150 to 400 cm^{-1} are the result of structural vibrations. Thus, the band at 1005 cm^{-1} originates from the asymmetric stretching vibrations of the Al–O–Si group, which in clinoptilolite-type zeolites usually occur at frequencies from 1150 to 930 cm^{-1}.

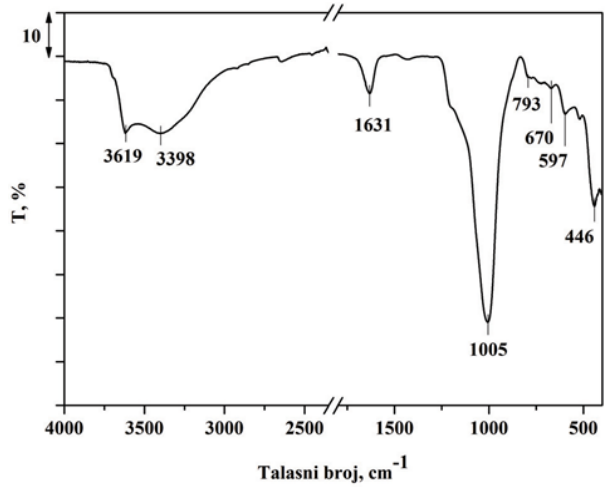

Figure 3. FTIR diagram of the sample from the “Igroš-Vidojevići” zeolite tuff deposit.

4. CONCLUSION

The largest part of the floor of the zeolite tuff deposit "Igroš-Vidojevići" is made up of clay, while in other parts, zeolite dominates. The X-ray analysis of the "Zeolite 1" sample revealed the presence of the clay minerals smectite and kaolinite. In the samples that belong to the central part of the "Zeolite 2-5" deposit, XRD and SEM/EDS analyses revealed the presence of zeolite-clinoptilolite, and the clay mineral content is less than 10%. The results of the infrared spectroscopic analysis indicated a slightly lower presence of quartz in the samples "Zeolite 2-5" compared to the sample "Zeolite 1". The results of thermal analysis (DTA and TG diagrams) of the "Zeolite 1" sample indicate the presence of clay minerals at the bottom of the deposit. For "Zeolite 2–5" samples, peaks characteristic of clinoptilolite appear in the DTA diagram.The results of determining the cation exchange capacity showed that the CEC of the sample "Zeolite 1" was the lowest, and was 46.98 mmol/100 g, which confirms the conclusion that the clay mass is located at the bottom. The highest CEC was obtained for the samples "Zeolite 2" and "Zeolite 3", 141.99 and 121.01 mmol//100 g, respectively, which corresponds to clinoptilolite. The results of determining the chemical composition and heavy metal content showed that Fe2O3 in the sample "Zeolite 1" increased to 7.58%. Therefore, further research will be based on finding a way to remove the magnetic impurities to exploit this clay part of the deposit.

Based on the results obtained, it can be concluded that zeolite taken from any part of this deposit, except from the bottom, can be valorized and applied for certain purposes. Due to the high cation exchange capacity and content of zeolite minerals, samples with a CEC greater than 120 mmol/100 g ("Zeolite 2" and "Zeolite 3") may have potential application in wastewater treatment or decontamination of animal feed. Zeolite with a CEC of up to 90 mmol/100 g ("Zeolite 4" and "Zeolite 5") can be used for improving soil quality and the like.

ACKNOWLEDGMENT

The authors would like to thank the Ministry of Science, Technological Development and Innovations of the Republic of Serbia for supporting the research (Grant No: 451-03-136/2025-03/200023).

REFERENCES

[1] V. Kašić, Doctoral dissertation, RGF, Belgrade, (2017), 168.
[2] S. Mojić, (2010): Elaborate on the reserves of zeolitized tuff with zeolite in the "Igroš" deposit near Brus in the "Igroš-Vidojevići" ore field, Fund of professional documentation of the Geological Institute of Serbia, 225 pages.
[3] I. Voinovitch, J. Debrad-Guedon, J. Louvrier, The Analysis of Silicates. Israel Program for Scientific Translations. Jerusalem. 1966.
[4] V. Kašić, S. Mihajlović, D. Životić, V. Simić, J. Stojanović, Ž. Sekulić, M. Kragović, Chem. Ind., 72 (1) (2018) 29-37,
[5] V. Kašić, V. Simić, D. Životić, A. Radosavljević-Mihajlović, J. Stojanović, Chem. Ind. 2017; 71: 49-60. (In Serbian)
[6] F.A. Mumpton, P.H. Fishman, J. Anim. Sci. 45 (1977) 1188-1203.
[7] A.D. Vujaković, M.A. Đurić, M.R. Tomašević-Čanović, Therm. Anal. Cal. 63 (2001) 161-172.

The 56th International October Conference on Mining and Metallurgy
22-25 October 2025, Bor Lake, Bor, Serbia
www.ioc.tfbor.bg.ac.rs

DOI: 10.5937/IOC25065J

Original scientific paper

SENSITIVITY ANALYSIS OF A COPPER ORE EXPLOITATION INVESTMENT PROJECT USING COMFAR III SOFTWARE

Marija Jonović[1a], Dejan Bugarin[1b], Tanja Stanković[1c]

[1] Mining and Metallurgy Institute Bor, Alberta Ajnštajna 1, 19210 Bor, Serbia
[1a] marija.jonovic@irmbor.co.rs, 0009-0000-8418-2523
[1b] dejan.bugarin@irmbor.co.rs, 0000-0002-9103-4614
[1c] tanja.stankovic@irmbor.co.rs, 0000-0002-2714-7016

Abstract

Investing comes with inherent risks, especially in complex economic environments. Using the COMFAR III software package enables detailed analysis of economic parameters, including investment risk assessment and sensitivity analysis, which are used in investments to better understand the impact of changes in key variables on the outcome of an investment project. This study presents the application of the COMFAR III software package on a specific example of a mining project for the exploitation of copper ore from the Bor river mine (B. R.) deposit above the XIX horizon. Identification of the variables with the greatest impact on the final results was performed using the COMFAR III software package. The internal rate of return (IRR) is 48.75%. The sensitivity analysis findings indicate that the project is most sensitive to changes in revenue, where each successive change in revenue by ±6% alters the IRR by ±10.94 – 14.8%. The project also shows significant sensitivity to changes in expenses, with each successive change in expenses by ± 6% altering the IRR by ±7.56 – 10.14%. The least sensitivity of the project is to changes in investments, where each continuous change in investments by ± 6% changes the IRR by only ± 2.88 – 6.93%. Sensitivity analysis using the COMFAR III software package clearly shows that the priority is effective management of revenues and expenses to ensure stable and positive project profitability, which is crucial for making investment decisions.

***Keywords*:** *COMFAR III Expert, Internal rate of return, Investment risk, Sensitivity analysis.*

1. INTRODUCTION

In today's climate of high-risk capital investments, particularly within the mining sector, the increasing demands for precise economic modeling necessitate the application of advanced analytical tools. Feasibility studies, as fundamental instruments for investment decision-making, must encompass technical, market, and financial dimensions, with particular attention given to risk assessment. In this context, sensitivity analysis plays a central role, as it enables the identification of variables with the greatest impact on profitability indicators, such as the Internal Rate of Return (IRR) and the Payback Period (PP). This paper presents the application of sensitivity analysis within a feasibility study aimed at rapidly defining the optimal production capacity in both mining and ore processing operations. The evaluation incorporates selected technologies, capital investments, projected costs, and revenues that ensure an adequate return, i.e., investment efficiency. Sensitivity analysis helps project teams anticipate future variability, set clear operational alerts and performance thresholds, embed risk management into decision-making, and launch forward-looking strategies. These strategies include expanding exploration of existing deposits (brownfield sites), applying cost-reduction initiatives, and improving efficiency across mining and processing operations [1].

The economic assessment and sensitivity analysis of key parameters were conducted using the COMFAR III Expert business Planner for Windows, **(***Computer Model for Feasibility Analysis and Reporting, Version III Expert, United Nations Industrial Development Organization,Vienna, 2003. available at* https://www.unido.org/comfar***)*** which facilitates comprehensive modeling of

the project's financial performance. The accuracy of feasibility studies, particularly those focused on investment and cost estimation, is typically within a margin of ±10% [2]. COMFAR III, developed by the United Nations Industrial Development Organization (UNIDO), enables modeling of financial and economic projects, feasibility analysis, and report generation. Sensitivity analysis is a powerful technique used in investment contexts to assess how changes in key variables may affect project outcomes. It serves as a vital tool for making informed and resilient investment decisions. By evaluating the potential impact of critical project parameters on economic indicators, sensitivity analysis helps identify the most significant risk factors. This approach facilitates modeling of boundary, optimistic, and pessimistic scenarios, defining the variability range for selected variables such as revenues, expenses, and investments. The aim of this research is to assess the influence of key financial variables on the Internal Rate of Return (IRR). Through sensitivity analysis, investors gain deeper insight into the potential risks and rewards of an investment and can formulate strategies to mitigate those risks. The subject of the study is to demonstrate that sensitivity analysis, supported by COMFAR III software, combined with adequate economic expertise, is essential for identifying risks and assessing the influence of variable factors on the profitability of mining projects. The COMFAR III Expert software, also developed by UNIDO, enables users to simulate financial and economic performance of investment projects, including feasibility analysis and comprehensive reporting. It supports the evaluation of variability in key factors and their impact on indicators such as Net Present Value (NPV), IRR, and Payback Period (PP), thereby facilitating more informed investment decisions. [3]. Especially in the context of financial risks, it is necessary to develop sensitivity and uncertainty analyses in order to first model the variables to which the outcome (NPV, IRR, or PP) is most sensitive, with a precise indication of the extent to which financial results will change in accordance with variations in those variables, assuming all other conditions remain constant [4].

2. EXPERIMENTAL

This research presents a sensitivity analysis of a copper ore exploitation investment project, conducted using COMFAR III software. Having in mind data protection the authors will not mention the name of a mining project for the exploitation of copper ore from the from the Bor river mine (B. R.) deposit above the XIX horizon.

General parameters of the mining project:

Project lifespan: 4.5 years; Production period: 4 years; Investment period: 6 months; Currency of calculation: $ USD; Discount rate: 10%; Mineral resource usage fee: 5% of net revenue (included in ore processing cost;

Ore Tonnage: 3,253,130 t (Ore Tonnage by Year: Year 1: 808,130 t; Year 2: 815,000 t; Year 3: 815,000 t; Year 4: 815,000 t;)

Copper cathode: 16,453.28 t.

The accepted price of copper cathode for revenue calculation is: $8,799 per ton.

Production Value (USD by year: Year 1: $ 35,963,803; Year 2: $ 36,269,535; Year 3: $ 36,269,535; Year 4: $ 36,269,535;) Total: $ 144,772,408

Total investment in fixed assets amounts to $ 23,697,254, and in initial working capital $ 4,000,000, totaling $ 27,697,254.

Cost Structure Overview:

Overlapping Operational Activities (Preparation of facilities, Ore excavation, Transport, export, and primary crushing of ore, Ventilation, drainage, and servicing) and Normative Costs for all 4 years: $ 29,683,187.

Depreciation costs are calculated at a rate of 2.5% of building value and 10% of equipment value; Maintenance costs are calculated at a rate of 3% of total fixed assets value; Insurance costs are calculated at a rate of 0.5% of total fixed assets value.

It is assumed that the investor will finance the project entirely from own funds. Therefore, the economic analysis does not include loan financing, and no financing costs are incurred.
According to available data, the mine currently employs 533 workers. The estimated average gross monthly salary is $ 1,500, resulting in an average net monthly salary of approximately $ 900.
Ore processing in flotation is calculated at $ 4.94 per ton of dry ore; Metallurgical processing is calculated at $ 644.35 per ton of copper cathode (as provided by the investor), with no additional cost for gold and silver refining; General and administrative costs are calculated at $ 3.5 per ton of copper cathode; Contingency costs are calculated at 3.5% of annual normative costs; Mineral resource usage fee is calculated at the legally prescribed rate of 5% of net revenue (total revenue minus metallurgical costs); Corporate income tax is calculated at the statutory rate of 15% of gross profit.
Based on the given parameters, economic and financial projections were carried out using the COMFAR III software. The resulting Internal Rate of Return (IRR) is 48.75%. Having in mind data protection, the authors will not mention the name of a mining project for the exploitation of copper ore from the B. R. deposit above the XIX horizon. The sensitivity analysis of a project will be presented with illustrations in Chapter 3.

3. RESULTS AND DISCUSSION

Table 1. Project Sensitivity to Changes in Revenues, Expenditures, and Investments

Change (%)	Revenues (%)	Investments (%)	Expenditures (%)
-30	-7.52	76.39	96.90
-24	3.42	69.46	86.76
-18	13.83	63.37	76.86
-12	24.85	57.96	67.21
-6	36.49	53.12	57.84
0	48.75	48.75	48.75
6	61.59	44.77	39.95
12	75.00	41.12	31.46
18	88.92	37.77	23.28
24	103.31	34.67	15.40
30	118.11	31.79	7.84

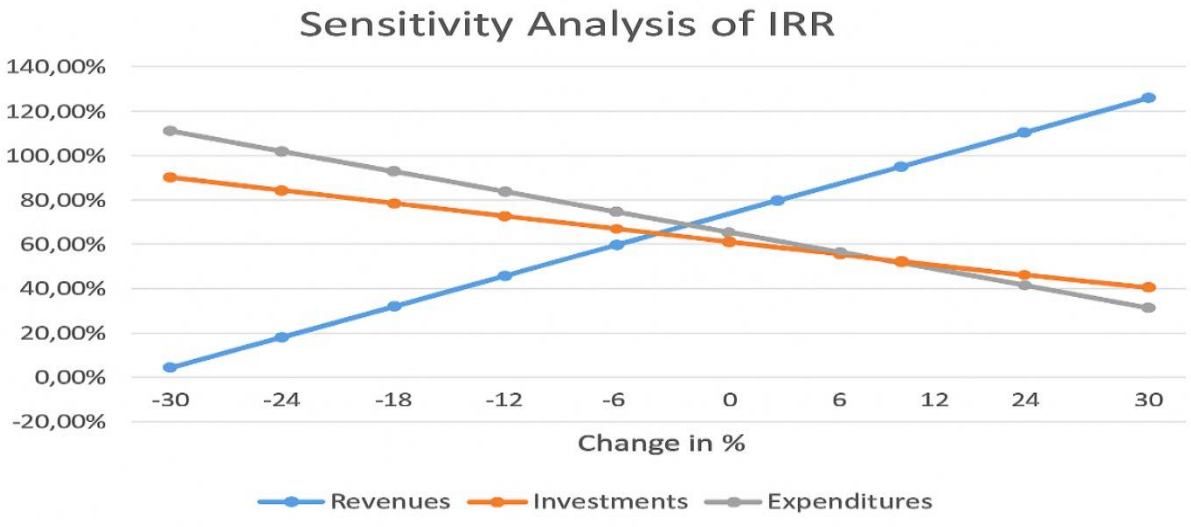

Figure 1. Movement of Economic Cash Flow and Its Cumulative Trend

Sensitivity Assessment by Risk Category:

Highest Risk: Revenues The project is most sensitive to changes in revenues. With each successive ±6% change in revenues, the Internal Rate of Return (IRR) shifts by approximately ±10.94–14.8 percentage points (pp). This indicates that even small fluctuations in revenues can significantly impact the project's profitability. Revenues represent the highest risk factor, as future income streams are difficult to forecast with a high degree of accuracy.

Lowest Risk: Investments The project demonstrates the least sensitivity to changes in investment levels. Each ±6% change in investment results in only a ±2.88–6.93 pp shift in IRR. This means that variations in capital expenditures have a relatively minor influence on overall project profitability, making this factor the least risky.

Moderate Risk: Expenditures The project shows a relatively high sensitivity to changes in operating expenditures. Every ±6% change in costs alters the IRR by ±7.56–10.14 pp. Although expenditures have a notable impact, their influence is smaller compared to that of revenues. While expenditures are generally more controllable than revenues, they still represent a significant source of risk.

4. CONCLUSION

The project carries the highest risk in the revenue segment due to the high sensitivity of the internal rate of return to changes in revenues. Investors should pay special attention to strategies for increasing and stabilizing revenues in order to mitigate risks. The project is least sensitive to changes in investments, while changes in expenditures represent a medium level of risk. Given this information, managing revenues and expenditures should be a priority to ensure stable and positive project profitability. Sensitivity analysis supported by COMFAR III software, along with a proper interpretation of economic indicators, is essential for a reliable assessment of the profitability of mining projects. This contributes to a more transparent and professional investment decision-making process, in accordance with international standards and best practices in capital investment evaluation.

ACKNOWLEDGEMENTS

This work was financially supported by the Ministry of Science, Technological Development and Innovation of the Republic of Serbia, Contract on realization and financing of the scientific research work of the Mining and Metallurgy Institute Bor in 2025, contract number: 451-03-136/2025-03/ 200052.

REFERENCES

[1] L. de la Torre Palacios, J.A. Espi, Bol. Geol. Min., 130 (1) (2019).
[2] M. Bugarin, G. Slavković, Z. Stevanović, Geološko-ekonomska ocena rudnih ležišta., ISBN978-86-7827-039-0; Bor, (2012) p.16.
[3] COMFAR III Expert: Computer Model for Feasibility Analysis and Reporting, Version III Expert, United Nations Industrial Development organization.Vienna, (2003). p.371. Available at https://www.unido.org/comfar).
[4] L. Suárez Nieto, G. Fidalgo Valverde, A. Krzemień, P. Riesgo Fernández, F. J. Iglesias Rodríguez, Resour. Policy, (2024) 105427.

The 56th International October Conference on Mining and Metallurgy
22-25 October 2025, Bor Lake, Bor, Serbia
www.ioc.tfbor.bg.ac.rs

DOI: 10.5937/IOC25069F *Original scientific paper*

FACTORS INFLUENCING THE OCCURRENCE OF FLYROCK PHENOMENA ON SURFACE MINES – CASE STUDY

Branimir Farkaš[1a], Ana Hrastov[2a], Iva Štefičar[2b]

[1] Faculty of Mining, Geology and Petroleum Engineering, Pierottijeva 6, 10000 Zagreb, Croatia
[2] RUDAR PROJEKT d.o.o., Ante Pandakovića 11, 10000 Zagreb, Croatia
[1a] branimir.farkas@rgn.unizg.hr, 0000-0002-2377-9446
[2a] ana.hrastov@rudar-projekt.hr, 0009-0003-9087-4413
[2b] iva.steficar@rudar-projekt.hr, 0009-0003-9735-5675

Abstract
Drilling and blasting, which involve the application of explosive energy to fragment the rock mass, represent one of the most employed methods of extracting mineral raw materials in surface mines. However, blasting activities can generate potential hazards, the occurrence of which is influenced by various factors. These factors can be categorised into three primary groups: natural factors (mining-geological conditions in the deposit), technical-technological factors (depending on the rock mass extraction technology) and the human factor (related to operator expertise and procedural adherence). The consequences of such events may lead to significant material damage, including harm to mining machinery, surrounding infrastructure, and even pose risks to human health and safety. On the example of the "O2" quarry, the factors that influenced material being propelled outside the safety zone defined by verified mining documentation were observed. A comprehensive risk assessment was subsequently performed to identify the underlying causes of these deviations, highlight procedural deficiencies, and prevent further incident events, i.e., for risk mitigation.

***Keywords**: flyrock phenomena, blasting, safety, risk assessment, risk mitigation*

1. INTRODUCTION

Explosive energy is one of the most employed methods for extracting mineral resources in quarries. Blasting activities, however, can pose potential hazards, most notably flyrock phenomena, air shock waves, and seismic effects, i.e., ground vibrations like earthquakes. Several factors, including natural conditions, technical-technological parameters, and human factors, can impact the results of a blast and increase the likelihood of associated hazards. The consequences of these events can have a significant impact, potentially causing damage not only to mining equipment and nearby structures but also posing a serious risk to human health.

Various authors have studied accidents related to the causes of hazardous incidents during blasting operations [1,2]. Furthermore, before conducting a blast, it is possible to analyse all relevant factors that may influence flyrock phenomena, thereby reducing the potential for damage [3,4,5].

In this study, through the analysis of the “O2” quarry, the previously mentioned factors influencing flyrock phenomena beyond the designated safety zone were analysed to determine which had the greatest impact. The goal was to identify the primary contributors to flyrock phenomena to prevent future incidents and reduce overall risk.

The “O2” quarry is in the northwestern part of Croatia (Figure 1a) is covering a total area of 30 ha. The analysed blast site is situated in the south-west part of the quarry, at an elevation of +440 meters above sea level (Figure 1b).

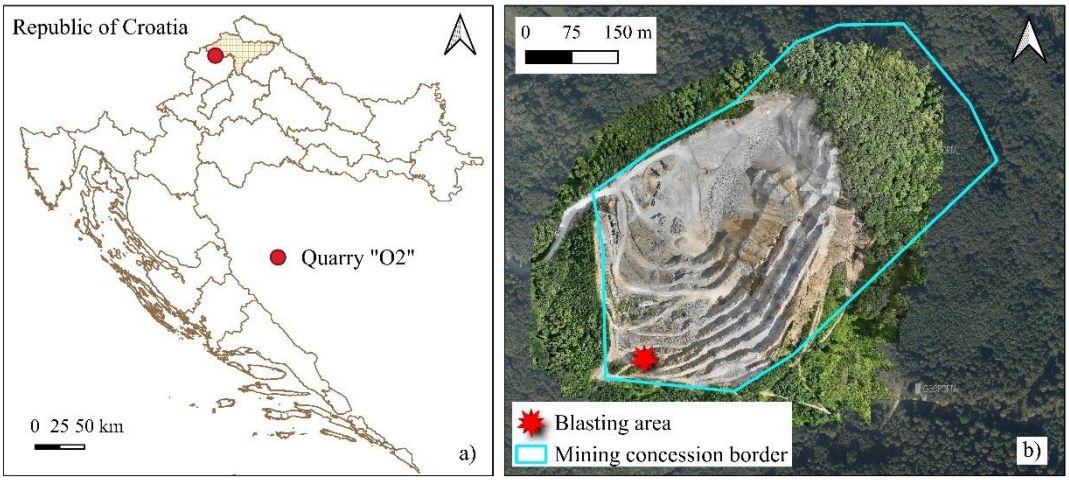

Figure 1. Site location of "O2" quarry and blasting area

2. METHODOLOGY

To minimise the occurrence of incidents related to blasting activities, the factors contributing to flyrock phenomena in the quarry were analysed. The negative effects of blasting operations are influenced by several key factors [6,7]: natural factors, such as the mining and geological conditions of the deposit; technical-technological factors, which involve the blasting technologies and operational procedures; and individual (personal) factors. The presence of any one of these factors can increase the likelihood of hazardous outcomes during blasting operations.

2.1 Potential Hazard Occurrences – Defining Safety Zones

Clearly defined safety zones for all potential blasting-related hazards are essential to protect people, buildings and machinery in and around the quarry. Safety zones are established based on mining design [8]. Accordingly, the safety zone for air shock waves is defined as 85 meters, while the safety zone for flyrock extends to 353 meters. Seismic effects of blasting were assessed through ground vibration velocity measurements, which confirmed that the recorded particle velocities at observation points did not exceed 5 mm/s [8].

2.2 Influential Factors

Mining and Geological Factors

The rock mass extracted from "O2" quarry consists of late diagenetic dolomites from Anisian (Middle Triassic), light grey in colour, massive, and of homogeneous texture. The "O2" quarry also contains clastic rock deposits from the Lower Triassic, Ladinian (Middle Triassic), and the Lower Miocene.

The primary discontinuity is defined by bedding with a general strike direction from E-W to SE-NW and a dip towards the S to SW at angles ranging from 30° to 40°. The bedding is often not well-defined due to numerous secondary discontinuities, which have caused the rock mass in the surface weathering zone to fragment into pieces approximately 5 cm in size. The engineering-geological characteristics of the rock mass in the quarry, along with experience from the nearby closed quarry, indicate that unstable slopes and block detachment can be expected. The stability of the slopes is further influenced by increased infiltration of rainfall due to the intersection of gullies, along which surface water, before the development of quarry benches, drained into a stream located north of the mine [9].

Technical-technological factors

Technical-technological factors and factors related to the working environment influence the execution of a specific task, in this case, the drilling of blast holes, their outfitting, and the activation of the blasting field. Technical and technological factors include the location of the worksite, the equipment layout, and the accessibility and visibility of the equipment used, while working environment factors encompass the physical and chemical parameters of the surroundings [7]. Since the work is carried out outdoors, the prevailing conditions are often very unfavourable, affecting human labour and behaviour, specifically regarding safety and the potential for accidents.

Individual Factors

Personal (individual) factors are human factors in the strictest sense, as they stem from the basic characteristics of each person (e.g., age, gender, health status, expertise). Individual factors contribute to accidents, as they often represent a lack of certain abilities, insufficient knowledge to perform a task, fatigue, stress while working, etc. [7]. Given the demanding working conditions during drilling and blasting operations, it is assumed that the likelihood of an accidental situation arising during blasting is the same regardless of who is performing the task.

3. RESULTS AND DISCUSSION

As a result of blasting in the southern part of the "O2" quarry, rock material was projected beyond the defined safety zone at over 500 meters. This caused damage to a residential building and a parked vehicle (Figure 2).

a) b)

Figure 2. Damage caused by flyrock: a) damaged vehicle in an employee parking lot (525 m), b) damaged roof of residential building 10

Figure 3 shows the location of the analysed blast site, the geology of the immediate area of the surface mine, the defined safety zones and surrounding structures.

The occurrence of flyrock (shown by yellow arrows in Figure 3) was largely influenced by the drilling parameters of the blast holes. Due to the drilling operator's limited experience, the holes were connected at the bottom of the bench. The first row of holes was drilled at a 70° angle, and the second row at a 60° angle. Additional influence came from the geological setting, as the blast site is located at the boundary between massive grey dolomites and the weathered zone (Figure 3), resulting in lithological heterogeneity within the blasting area and variable explosive performance. Furthermore, the terrain configuration favoured the extended range of the flyrock. The blast site is positioned at +440 m above sea level, whereas the damaged structures are located at +250 m above sea level. The analysis indicates that all contributing factors, to varying degrees, played a role in the occurrence of flyrock.

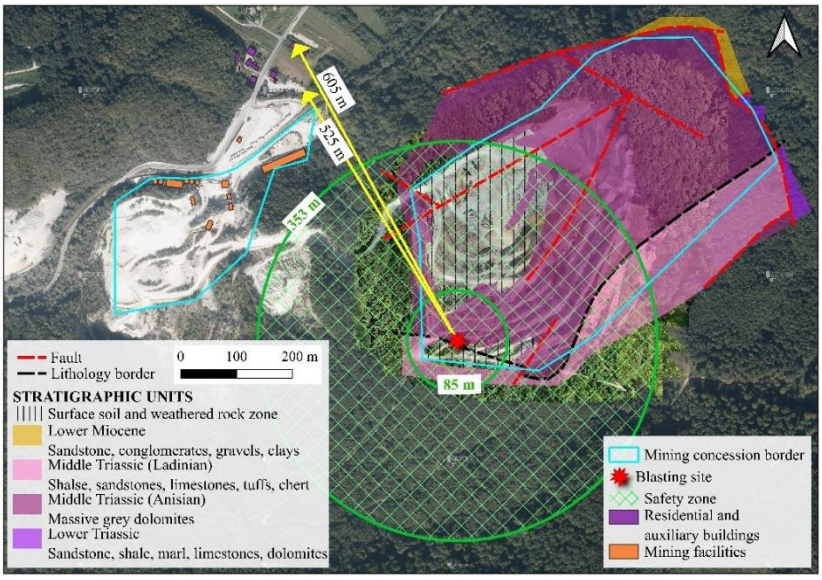

Figure 3. Safety zones, in conjunction with the geological map [9] and the presence of flyrock

4. CONCLUSION

In the case of the "O2" quarry, mining-geological, technical-technological, and individual factors were analysed, all of which influenced the occurrence of flyrock during blasting. Each of these factors contributed to the potential hazards and damage to varying extents; specifically, in the analysed case, this resulted in damage to a residential building and a vehicle. Analysing each factor individually and its mutual effects is essential to prevent similar incidents in the future blasting operations.

REFERENCES

[1] V. Kecojevic and M. Radomsky, Saf. Sci., 43 (2005) 739–750.
[2] E.T. Mohamad, B.R. Murlidhar, D.J. Armaghani, R. Saad, and C. Shiang Yi, J. Teknol. 78 (8–6) (2016) 15–21.
[3] M. Rout Mishra, World Environment, 1 (2012) 1–5.
[4] A. Aghajani-Bazzazi, Y. Azimi, Flyrock prediction by multiple regression analysis in Esfordi phosphate mine of Iran, in Rock Fragmentation by Blasting Proceedings of the 9th Int. Symp. on Rock Fragmentation by Blasting - Fragblast 9, J. A. Sanchidrian, Ed., London: Taylor & Francis Group, 2010, pp. 649–657.
[5] J. Zhou et al., Nat. Resour. Res., 29 (2) (2020) 625–639.
[6] J. Visković, Analiza ozljeda na radu u rudarstvu u RH, Final paper, Karlovac University of Applied Science, Karlovac, 2020.
[7] D. Vukušić, Novi pogled na ulogu ljuskih čimbenika u uzroku akcidenta, Zbornik Veleučilišta u Rijeci, 4 (2016) 193–212.
[8] J. Pranjić, I. Zorić, M. Hatlak, F. Pranjić, and N. Gizdavec, Dopunski rudarski projekt eksploatacije tehničko-građevnog kamena na eksploatacijskom polju "O2" – prva dopuna. SPP d.o.o., 2018.
[9] I. Matjašić, Elaborat o rezervama na EP "O2" – 5. obnova, Calx d.o.o., 2017
[10] Google, "Google maps." Accessed: Jun. 02, 2025. [Online]. Available: https://www.google.com/maps

The 56th International October Conference on Mining and Metallurgy
22-25 October 2025, Bor Lake, Bor, Serbia
www.ioc.tfbor.bg.ac.rs

DOI: 10.5937/IOC25073R *Original scientific paper*

STRATEGIC PLANNING, DESIGN AND MINE MANAGEMENT UNDER THE CONDITIONS OF ASAREL OPEN PIT MINE

Petar Radichev

Asarel-Medet JSC, 4500 Panagyurishte, Bulgaria
pradichev@asarel.com, 0009-0003-6745-2773

Abstract
Asarel-Medet JSC Mining and Processing Complex is the first, largest and leading Bulgarian mining company for copper ores open pit mining and processing.
Ore mining at the Asarel mine was initiated in 1976. The company has been implementing unique mining machines for the country, state-of-the-art flotation equipment and automated systems for management and control of technological processes ensuring top production indices ever since.
Open pit mining specialists at the Asarel mine have been using the software solutions of the company Datamine for mine planning, design and geological modeling since 2004.
The main planning and control activities according to the mining periods and purpose are:
- Long-term development, Medium-term mining plans, Short-term mining plans, Ten-day and daily mining plans.
Control over the design implementation and mining organization is conducted using data and records from the dispatch system modules and pit surveys and references.
***Keywords**: Asarel-Medet, open pit copper mine, mine planning, Datamine, mining periods*

1. INTRODUCTION

Asarel-Medet JSC Mining and Processing Complex is the first, largest and leading Bulgarian mining company for copper ore open-pit mining and processing.

The open-pit mining specialists at the Asarel mine have been using the software solutions developed by Datamine, including Studio OP, Studio RM and NPV Scheduler, for mine planning, design and geological modelling since 2004.

2. PRESENTATION

2.1. Geologocal Block Models

The major data set required for pit design using the software referred to above is the Geological Block Model. Two Geological Block Models are used at Asarel: Resource Geological Block Model and Updated Geological Block Model, the latter being used primarily for short-term planning.

The resource model is built only with data from the exploration core drilling. The block sizes within the geological model have been determined at 25/25/15m, respectively along the X, Y and Z axes through various geostatistical methods for analyzing the useful components variability. The 100/100 m exploration drilling pattern for the Asarel deposit has a significant impact on the block sizes within the model for most of the ore body. The block size in the vertical direction (15m) is determined by the height of the operational benches (mining levels) during the deposit mining. The model may also have smaller cells in places where there is contact between different ore bodies or in the contact zone at the surface.

The updated Geological Block Model is actually the Resource Model, but it is further adjusted with data from the detailed exploration taken from the chemical assays from the blast holes during

its updating on a regular basis. All analyses that are used have different weights in the model updating process. The results from the detailed exploration analyses have an impact on the uppermost part of the model which is closest to them and that will be subject to mining as soon as possible.

The Geological Block Models (obtaining values for useful and deleterious components for all blocks) are built at Asarel-Medet using the Ordinary Kriging method and Inverse Power of Distances method.

Comparative analysis is performed on the reconciliation between the Resource Model and the data from the continuous detailed exploration. It is the main database, a key factor for the accurate pit design and its subsequent operation.

2.2. Core Activities on Planning and Controlling the Ore Mining According to its Deadlines and Purpose

2.2.1. Long-Term Development

The long-term development designs are prepared using Studio NPVS (NPV Scheduler) which is one of the modules of the Datamine software at Asarel Medet JSC.

The main principle on which the NPV Scheduler software application for pit designing (optimizing) is based and developed is the Lerchs-Grossman method (LG-method). This is a mathematical algorithm belonging to the Network Flows method family and in this case it aims at determining the ultimate pit, the implementation of which will lead to a maximum profit over time (maximum Net Present Value). The Ultimate Pit designed using the software is the final boundary of the pit for a particular deposit. Some colleagues also call them LG Ultimate Pit.

The LG method is used to determine the "optimal ultimate pit" at certain expected commodity sales prices at known financial parameters for mining, processing and selling the commodity. Preliminarily calculated maximum theoretical values for the overall slope angles of the targeted optimal ultimate pit are also used to design the pit shell. The ultimate pit is a theoretically determined phase (shape) that will lead to the highest profit at the specified costs of extraction, processing and sale of the production. There are many factors that can influence the ultimate pit definition, the most important of which is the mineral distribution in the deposit: often "more valuable" blocks with higher mineral grade are located at depth, far below other smaller blocks of the ore body.

The price factor is used most often for optimal design and construction of the so-called "most profitable pit" where the study step is set to 1% and the optimal pit is searched for at 100% of the set sales price. This practice has been proven all around the world and has also been recommended the software authors. This study ensures a pit construction with maximum NPV and at the same time conducts a sensitivity analysis of the results when the price changes. The other factors are recommended in most analysis cases. The software generates an optimal sequence of geological block extraction (OES - Optimal Extraction Sequence) for each ultimate phase which is actually the foundation of the entire design process optimization. The optimal sequence of block extraction will be changing in all subsequent processes until the design is finalized.

The phases themselves are open pit mines embedded in each other with each phase being optimal when selling the commodity at a price corresponding to the percentage at which the given phase is built. This means the smallest phase (the smallest ultimate pit of a mine) will be optimal (will give the highest NPV) at a price equal to 1% of the set sales price. The next phase will be optimal at 2% of the set price, and so on until it reaches 100%. The analysis can be continued above 100%. Each subsequent phase is larger than the previous one and includes all the previous ones.

The following stages of the design development are quite long, but in general they aim to find a solution for the following:

- Ore mining at uniform rates and constant average grades of useful and deleterious components (as far as possible).
- Uniform mining of waste.
- Temporary mining limitations from the existing infrastructure perspective (if any).
- Compliance throughout the life-of-mine with engineering conditions during mining and processing – overall slope angles and parameters of the faces during the pit mining, parameters of the mineral ore dilution (losses and dilution during mining) and dilution parameters during ore processing.

Achieving all these goals (and not only) by the designers and mine planning specialists necessarily leads to a change in the block optimal extraction sequence (OES) in the already selected optimal pit and therefore to a change in cash flows and respectively in NPV.
For this reason, when working with this type of design software, it is incorrect to compare the NPV of designs for which only an optimal ultimate pit has been generated (ideal cash flows) with designs for which a practical calendar schedule has been developed (completely genuine and feasible cash flows).

2.2.2. Medium Term Mine Plans

Most often they are for a period of one to five calendar years. These plans are more detailed than the long-term ones and their monitoring and implementation ensures the accomplishment of the set ore mining and processing parameters: an optimal amount of waste and a precisely defined amount of ores with appropriate quality parameters are provided.

The actual development of the annual designs goes through several stages:

- Updating the current annual design for the last months of the year, if necessary. The update provides the baseline for the annual design or the expected pit state at the beginning of the next calendar year.

- Designing the mining operations for the next year – a plan with berms and roads is presented in the way the pit should look at the end of the design year.

- The distribution of the mined material throughout the year is presented by pit levels and ore type.

- The pit development is forecasted for two more subsequent years. This is done in order to prove the provision of the required ore for the periods after the year for which the main design is prepared. Most often, these plans are developed with both modules *Studio OP* and *Studio NPVS*. They show the mining sites in the respective year and again a tabular distribution of the mined material by levels and type.

- Finally, the average haulage distances by type of mined material to the various unloading locations are determined. The required number of dump trucks and other finishing works necessary for proper planning of the cost and provision of all main and auxiliary activities related to the pit development is determined.

2.2.3. Short-Term Mine Plans

These are quarterly and monthly plans which are also developed in detail. A large part of the material intended for mining is also assessed with current chemical assays from the detailed exploration, but not only according to the data from the block models. This makes these designs much more reliable than the long-term and medium-term ones considering the ore quality indicators. The block extraction sequence is indicated in this case in order to comply with the main parameters for optimal ore blending. The mined ore to be fed to the Concentrator Plant is ensured with its appropriate parameters: average copper, sulfur and copper dioxide grades and an optimal ratio at which the host rocks are blended. The latter is of a crucial significance for maximum efficient grinding of the ore at the Concentrator Plant at optimal throughput (processing of a certain

ore amount for a certain time). Grinding the ore to certain particle sizes, in turn, will ensure maximum extraction of the useful component from the entire process. The average grade of the deleterious components in the ore for the flotation process - sulfur and copper dioxide - also has a significant impact on the ore processing.

2.2.4. Ten Day and Daily Mine Plans

- A ten-day plan is prepared as a table. It reflects the available quantities and quality indicators of the already blasted or only drilled blocks. The outstanding drilling designs are also indicated and their quality indicators are calculated with the Geological Block Model. In these ten-day plans, a very large part (and sometimes 100%) of the ore to be mined is qualified with direct analyses and a very small part is qualified with assumed data from the Geological Block Model. This makes these plans very reliable in terms of the ore quality to be mined in the shortest possible period.

- The daily mining schedule is prepared for 24 hours and is even more detailed, foreseeing mining only from blocks with current chemical assays from the detailed exploration. It specifies the shovel that will be used and the exact block number and bench level from the mine fleet management dispatch system.

2.2.5. Provision of the Wenco Mining Dispatch System

The dispatch of the ore mining and all auxiliary activities carried out at the Asarel mine is performed by a software application developed by the WENCO company. The system hardware is installed on the available shovels, drill rigs, dump trucks, bulldozers, graders and all other auxiliary units for refueling, lubrication, water tank trucks, etc. All have high-end GPS receivers installed for positioning the units in real time. The shovels and drill rigs have two receivers each for accurate and precise positioning.

The main system administration in terms of mining, shovel relocation and ore blending is conducted by the specialists at the Mine Planning unit. The files of all work blasting fields are processed and imported according to the requirements of the dispatch software. Loading and unloading locations are created and updated on a daily basis, routes for mined material haulage are prepared, data on the blasted blocks with their quality parameters is imported, etc.

2.2.6. Control on the Design Implementation at the Asarel Mine

The Mine Planning Unit exercises daily control on the ore mining, implementation of blast patterns and the operation of loading equipment in the planned blocks. The control relies on numerous reports from the WENCO dispatch system software packages and survey measurements of the face lines. Control is also exercised on the implementation of long-term, medium-term mining plans and the mining technology in order to ensure an optimal ore blending. Control is performed over the implementation of all specific designs in the Asarel mine.

3. CONCLUSION

The design and updating of various options and development strategies is a dynamic and almost continuous process in the open pit mining of mineral deposits.

The optimal engineering conditions for ore mining and processing such as specified overall slope angles and face parameters during the pit mining, the mineral resources dilution parameters (losses and dilution), among others, have to be continuously monitored throughout the life-of-mine.

The 56th International October Conference on Mining and Metallurgy
22-25 October 2025, Bor Lake, Bor, Serbia
www.ioc.tfbor.bg.ac.rs

DOI: 10.5937/IOC25077M *Original scientific paper*

GEOLOGICAL CONDITIONS OF NATURAL H_2 EXPLORATION ON THE BALKAN PENINSULA FOR PROSPECTIVITY MAPPING

Gergana Meracheva[1a], Efrosima Zaneva-Dobranova[1b], Nikolay Hristov[1c]

[1] University of Mining and Geology "St. Ivan Rilski", 1700 Sofia, Bulgaria
[1a] g.meracheva@gmail.com, 0000-0003-3124-7578
[1b] e.zaneva@gmail.com, 0000-0001-9096-3764
[1c] nk.hristov@gmail.com, 0000-0001-8242-6758

Abstract
Natural hydrogen (H_2), generated by geological processes in the subsurface, is considered a sustainable, low-carbon energy source. In the past few years, exploration activities for H_2 in different countries have increased, and some of the results received have been shared and published. A few published papers are concerning field observation and geochemical studies in the Balkan Peninsula area. The analysis of exploration efforts indicates that most potential sites for H_2 exploration appear to be those with ophiolite associations. The primary purpose of the research is to clarify the possibilities for general prediction and mapping of the H_2 potential in the Balkan Peninsula area. The goal will be achieved based on analyses of previous research experience and its application in the territory of Bulgaria by evaluating existing and obtained geological data, mapping methodologies and approaches, and potential benefits and limitations. The expected results of the current review study will enable the way for regional mapping of H_2 exploration potential areas on the Balkan Peninsula.

***Keywords**: Natural Hydrogen, ophiolite, Balkan Peninsula*

1. INTRODUCTION

Natural hydrogen (H_2), generated by geological processes, holds significant promise as a sustainable and low-carbon energy source. The expectations, that this resource would actively answer the purpose in the transition to clean energy are based on the results of active exploration in North America, Asia, Africa, and Australia [1], with significant quantities found in Mali's Baurakebougou field, Albania's Bulqize chromite mine, France's Lorraine mining basin, and Turkey's Chimaera. The discoveries often occur by chance. Effective exploration methods are required to comprehend subsurface processes that control H_2 generation, migration, and trapping. Generally, H_2 observations are linked to water reacting with ultramafic rocks (serpentinisation); water radiolysis; radioactive decay of U, Th, K; deep H_2 sources; thermal maturation of organic matter [2]. Exploration should concentrate on areas associated with serpentinised ophiolite series, mid-oceanic spreading ridges, transform faults, passive and convergent margins, intracontinental rifts, and fault zones. Considering significant quantities of H_2 have been discovered in the Bulqize chromite mine in Albania, it is important to examine the distribution of similar rock associations on a regional scale within the Balkan Peninsula and explore possibilities for their preliminary mapping to assess their prospects. As a foundational approach, it is suggested to trace the "hydrogen window" areas, where some or all mechanisms are present and suitable for modelling.

2. EXPERIMENTAL

As suggested by previous studies [2], preliminary work was undertaken in this research. This work involved a thorough review and analysis of all available data on the occurrence of H_2 and the presence of hydrogen source rocks. This regional-scale evaluation was instrumental in identifying and defining a prospective area for exploration. The Balkan Peninsula's geological environments and geotectonic settings play a key role in understanding the behaviour and evolution of the region.

Previous studies [3, 4, 5] highlight notable similarities in emplacement mechanism and characteristics typical of the Tethyan ophiolites (obduction) type of geotectonic settings [6], which occur when oceanic crust lithosphere, formed in a fore-arc or back-arc, known as a supra-subduction zone (SSZ) setting, is obducted over a continental passive margin that has failed or is failing to subduct (Fig. 1A). The analysis indicates that most potential sites for H_2 exploration appear to be those with ophiolite associations. The Tethyan obduction type highlights promising ophiolite associations for H_2 exploration on the Balkan Peninsula, shaped by the subduction-collision dynamics of the Eurasia and Apulia plates and the extensive Vardar-Izmir-Ankara suture [3]. Extending from west to east, several ophiolite complexes have been identified that share similar features (Fig. 1 B) and geographically cover the territories of Albania, Kosovo, Bosnia and Herzegovina, Serbia, Greece, Turkey, and Bulgaria.

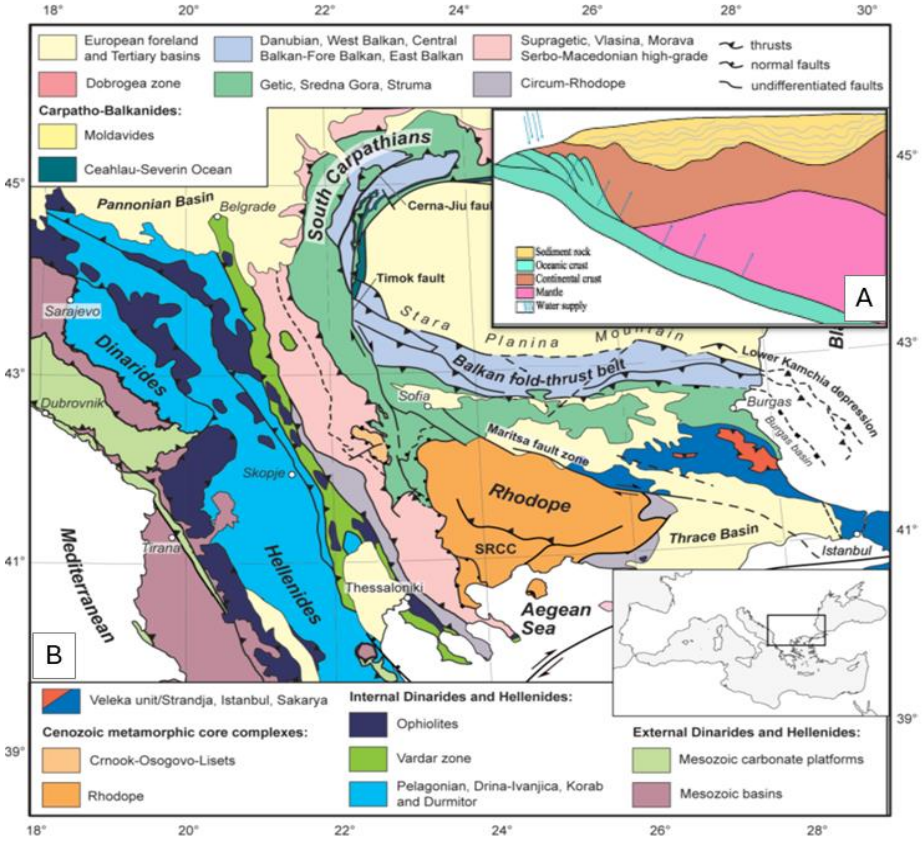

Figure 1. Natural hydrogen potential ophiolite complexes in the Balkan Peninsula: A) Tethyan ophiolite obduction zone type geotectonic setting, modified after [6], B) Tectonic map, modified after [7]

3. RESULTS AND DISCUSSION

Ophiolites are found in the Dinarides, the Vardar zone, the Circum-Rhodope belt, around the periphery of the Rhodope massif, as well as to the south of the Rhodopes - specifically on the island of Samothrace, along the lower reaches of the Maritsa River, on the island of Lesbos, and south of the Dardanelles on the Biga Peninsula in NW Turkey. To the east, they continue into the Tavshanli zone, located south of the Vardar-Izmir-Ankara suture.

3.1 Dinaride ophiolite belt

This ophiolite belt [4] was partly generated above a subduction zone and represents a subduction complex controlled by tectonic accretion and sedimentary reworking in fore-arc basin settings. The metamorphic soles of the Dinaride ophiolites formed during the Middle–Late Jurassic Age. A possible cause for the formation of the Dinaride ophiolites is the collision of a subduction trench with a continental margin. Generally, subduction in a northward direction caused ophiolite

formation in the SSZ during the Late Cretaceous. During the Upper Jurassic, ophiolites were obducted, which are observed on underlying Triassic and Upper Jurassic carbonates and are transgressively overlain by Tithonian and Lower Cretaceous terrigenous rocks.

3.2 Ophiolites of the Western Vardar zone

Studies [8] in Albania and Kosovo show that the main structures in which H_2 leakage from natural springs has been detected are related to the Western Vardar ophiolites. In the region of Albania, the Western Vardar ophiolite is represented by the Mirdita ophiolite, located in the Albanides mountain belt, which is in the Dinaride-Albanides-Hellenides segment of the Alpine orogenic system, and interpreted as derived from an SSZ. The ophiolites are of Middle Jurassic age and were formed during the beginning of the closure of the Neo-Tethys, as a result of the subduction of the Adria plate under the Eurasian plate. Some rocks from the ophiolite mélange trace the beginning of the obduction to the Late Jurassic. These are mainly lenticular serpentinite bodies ranging in size from 10 to 100 m. They are mostly deformed and folded. Peridotites and dunites, metagabbro bodies and diabase dikes are rare. The Upper Jurassic (155–150 Ma) ophiolite complex was covered by Tithonian and Lower Cretaceous sediments. The complete closure of the basin occurred between the Late Cretaceous and the Paleogene, leading to the formation of the Sava suture zone. The Bulqize mine is situated within the Jurassic ultramafic Bulqize massif, where H_2 is produced from depths of up to 1000 m. This occurs in a highly fractured zone through which water seeps from the upper levels of the mine. This water, along with meteoric water, contributes to the serpentinisation process.

3.3 Ophiolites of the Eastern Vardar zone

The Eastern Vardar Ophiolite Zone (EVZ) in the Pannonian Basin has two branches: one bends west from Fruška Gora, while the other extends northeast to Transylvania [7]. EVZ overlies the Tisza-Dacia mega-unit further north [5]. In the Belgrade surroundings, EVZ's oldest layers include Upper Jurassic deepwater claystones and radiolarites associated with syndepositional basalts, serpentinized peridotites and ophiolitic melange with fragments of serpentinites, diabases, limestones, claystones, and cherts. The eastern boundary features complex tectonic structures, with Serbomacedonian metamorphics to the east and EVZ formations to the west. During the Upper Tithonian, EVZ ophiolites were obducted eastward over the Serbomacedonian unit, later moving west-southwest as part of a forearc basin [7]. Both zones of ophiolites in the Dinarides (i.e. Dinaride Ophiolite Zone and Ophiolites of Western Vardar Zone), along with the ophiolites of the Eastern Vardar Zone, all contain ophiolitic melanges with similar ages of fragments beneath the obducted ophiolites.

3.4 Balkan-Carpathian ophiolite segment

The Balkan-Carpathian segment [9, 10] consists of a complex assembly of lower-grade ophiolite massifs across Romania, Serbia, and Bulgaria, with an origin corresponding to a mid-ocean ridge setting, with the protolith estimated to date back to 563 million years ago. Key ophiolite massifs within this segment include Tcherni Vrach, Zaglavac, Deli Jovan, and South Banat, featuring structures like pillow lavas, pyroxenites, and gabbro-porphyrite dikes. These ophiolites, shaped by ocean floor metamorphism and obduction alongside an island-arc association in the subduction zone, highlight intricate geological processes. Stratigraphically, the ophiolite formations in NW Turkey exhibit similarities to those found within the Balkan-Carpathian region [9]. The South Banat ophiolite massif, located at the northwestern edge of the Carpathian-Balkan segment, is thought to predate the Early Caledonian period and comprises two main rock types: ultramafic tectonites and cumulative gabbros mingled with ultramafic rocks throughout the ophiolite profile.

3.5 Circum-Rhodope belt

In the Circum-Rhodope belt, also known as the innermost Hellenic ophiolite belt, various rock materials are observed as an incomplete ophiolite sequence [3]. The same age (Jurassic-Cretaceous) is also found in the ophiolites of the Circum-Rhodope zone from the outcrops in Northern Greece and those in Western Thrace, which are exposed beneath the Tertiary sediments or tectonically cover the Rhodopean high-grade metamorphites. They are in Makri, Maronia, Drymos–Melia, Mikron–Derion, Mandritsa–Metaxades, Agriani and Didymotychon, and are united in the Evros ophiolite complex. These rocks, along with associated low-grade volcanic and sedimentary materials, are considered part of the Circum-Rhodope belt. The Circum-Rhodope Belt of northern Greece is metamorphosed and is tectonically emplaced eastward on the Serbo-Macedonian Massif during the Late Jurassic, probably by obduction [7].

3.6 Rhodope ophiolite association

The metamafic rocks exposed in the metamorphic basement of the Rhodope Massif are supposed [11] to form a Rhodope ophiolite association, developed concurrently with primary rock formation and subsequent metamorphism. The association consists of three main complexes: a) metavolcanites, b) metaintrusives, and c) metaserpentinites. Geochemical analysis suggests an SSZ origin for metabasites, which aligns with the characteristics of the exposed metasediments. The broader geological setting of this ophiolite suite, along with its associated sedimentary sequences, represents obducted ophiolites deposited onto the ancient terrain of the Rhodope Massif, closely connected to the Vardar Ocean.

4. CONCLUSION

The examination of the geological conditions for exploring natural hydrogen within the confines of the Balkan Peninsula reveals that ophiolite zones and segments are prevalent. They belong to a single type of obduction – Tethyan, which can serve as a basis for mapping and tracing the areas of “hydrogen windows”.

REFERENCES

[1] Q. Tian, S. Yao, M. Shao, W. Zhang, H. Wang., China Geology, 5 (2022) 722-733.
[2] D. Lévy, V. Roche, G. Pasquet, V. Combaudon, U. Geymond, K. Loiseau, I. Moretti., STET, 78, 27 (2023) 1-34.
[3] H. Spiridonov., BAS, Problems of geography, 3-4 (2013) 1-35 (In Bulgarian).
[4] A. Robertson, S. Karamata, K. Šarić., Lithos, 108, (1-4) (2009) 1-36.
[5] M. Toljić, U. Stojadinović, N. Krstekanić., II Kongres Bosne I Herzegovine, 2-4 October 2019, Laktasi, 2019.
[6] O. Jackson, S. Lawrenece, I. Hutschinson, A. Stocks, A. Barnicoat, M. Powney., Geoenergy, 2 (2024) 1-21.
[7] S. Schmid, D. Bernoulli, B. Fugenschuh, L. Matenco, S. Schefer, R. Schuster, M. Tischler, K. Ustaszewski., Swiss J. Geosci., 101 (2008) 139-183.
[8] D. Lévy, M. Boka-Mene, A. Meshi, I. Fejza, T. Guermont, B. Hauville, N. Pelissier., Front. Earth Sci., 11:1167634 (2023) 1-14.
[9] I. Haydoutov, Origin and evolution of the Precambrian Balkan-Carpathian ophiolite segment, Publishing house of BAS, Sofia, 1991, p. 179.
[10] I. Haydoutov, S. Pristavova, L. Daieva. Late Neoproterozoic-Early Palaeozoic evolution of the Balkan terrane (SE Europe) - a probable fragment of Iapetus Ocean, UMG, Sofia, 2012, p. 132.
[11] E. Kozhoukharova, Rev. Bulg. Geol. Soc., 82 (1) (2021) 63-73.

The 56th International October Conference on Mining and Metallurgy
22-25 October 2025, Bor Lake, Bor, Serbia
www.ioc.tfbor.bg.ac.rs

DOI: 10.5937/IOC25081G *Original scientific paper*

SEISMIC INTELLIGENCE IN SURFACE BLASTING: SEISBLAST-PROMAX AS A NEXT-GENERATION DESIGN AND OPTIMIZATION TOOL

Güzin Gülsev Uyar Aksoy[1a], Cemalettin Okay Aksoy[2b], Ozan Savaş[3c]

[1]Hacettepe University, Mining Engineering Department, Ankara; GOA Mining Company Ankara
[2]Dokuz Eylul University, Mining Engineering Department, Izmir; GOA Mining Company Ankara
[3]GOA Mining Company, Ankara
[1a] gulsev.aksoy@goamining.com, gulsevaksoy@hacettepe.edu.tr 0000-0002-9328-9899
[2b] okay.aksoy@goamining.com, okay.aksoy@deu.edu.tr 0000-0002-4328-4862
[3c] ozan.savas@goamining.com, 0009-0009-0751-8033

Abstract

Seisblast-Promax is a new-generation software that enhances surface blasting through seismic wave analysis. Developed with academic collaboration, it integrates classical blast design with real-time sismograph data and seismic modeling tools. Its most distinctive feature is the Q-Factor-based vibration modeling, enabling high-resolution vibration control, slope stability monitoring, and regulatory compliance. Unique delay optimization algorithms, such as seismic energy damping, ensure minimal environmental impact while maintaining fragmentation quality. The software outperforms traditional burden-relief methods, as confirmed by field tests involving over 300 blast holes. Seisblast-Promax also supports proprietary electronic delay schemes and integrates advanced mapping and reporting features, establishing a new benchmark in controlled blasting.

Keywords: *surface blasting, seismic design, vibration control, delay optimization, Seisblast-Promax*

1. INTRODUCTION

Blasting remains the primary method for rock fragmentation in mining and construction, yet it poses challenges, especially near sensitive areas such as residential zones or geothermal sites. Blast-induced vibrations can threaten infrastructure, slope stability, and regulatory compliance [1]. Traditional approaches typically attempt to minimize explosive quantities or rely on empirical delay rules, which often prove insufficient in close-proximity blasting environments. Seisblast-Promax was developed in response to these limitations [2]. It is the first software to integrate classical blast design modules with seismic wave analysis, providing an intelligent and adaptable system. Its core innovation lies in the application of a Seismic Quality Factor (Q-Factor) model that allows precise vibration predictions by accounting for geological variations. Moreover, the software incorporates a computational delay optimization algorithm based on seismic energy damping. This technique uses destructive interference of seismic signals to minimize overall vibration intensity at target locations. In this study, we present the application of Seisblast-Promax in a real-world blasting scenario, emphasizing the system's unique capabilities compared to conventional burden-relief and non-electric delay methods. Key performance metrics include peak vibration velocity (PVS), dominant frequency, and waveform duration across multiple distances from the blast source. The study highlights the software's effectiveness in reducing vibration impacts without compromising fragmentation performance.

2. EXPERIMENTAL

The experimental blasting study was conducted in a quarry located in the Çanakkale-Lapseki region of Türkiye, where sensitive structures lie within 50 meters of operational zones. A pilot hole and three group blasts were conducted under controlled conditions. All holes were 102 mm in diameter and 5.5 m deep, using 23 kg of explosive. While Groups 1 and 2 utilized electronic

detonators, Group 3 employed non-electric delay systems. Group 1 utilized Seisblast-Promax's energy damping algorithm to calculate inter-hole delays that would minimize the cumulative vibration energy via destructive interference. Group 2 used standard burden-relief delays provided by commercial blast design software. Group 3 followed fixed delays of 25 ms between holes and 42 ms between rows. Each blast group included 100 holes. Seismographs were placed at four distances (9 m, 26 m, 45 m, 67 m) along a fixed line to measure peak vibration velocities (PVS) and dominant frequencies. The pilot hole's seismic waveform, recorded at 67 meters, was used as the input signal for Group 1 delay optimization. The Seisblast-Promax software computed ideal delays iteratively by superimposing time-shifted waveforms and selecting the configuration yielding the lowest combined energy output. Figure 1 illustrates the principle behind the damping algorithm, where sequential signals cancel each other out due to phase differences. This strategy was applied progressively, integrating each hole's delay to dampen the overall signal. Figure 2 shows three-component seismic data at 60 meters for all three blasting methods, with Group 1 clearly exhibiting lower amplitudes. Table 1 summarizes the vibration and frequency values recorded at each sensor point.

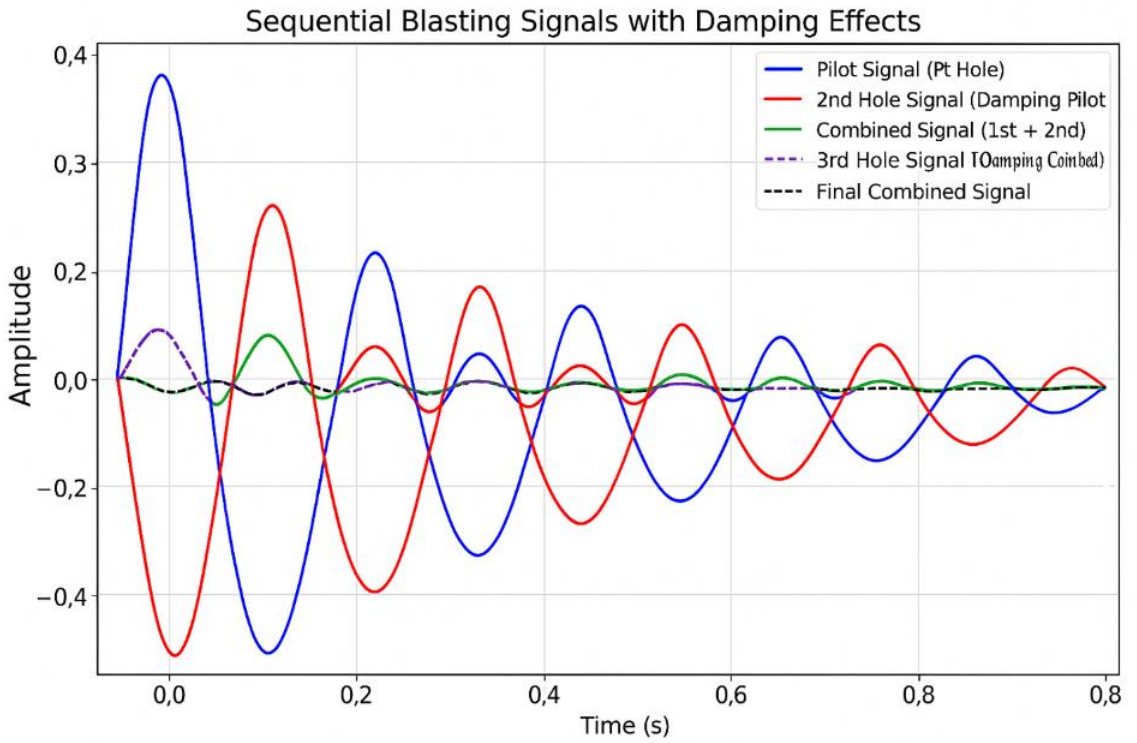

Figure 1. Representative sequential blasting signals with damping effects. The pilot signal (blue) is sequentially dampened by the signals from the second hole (red) and third hole (green), resulting in the final combined signal (black dashed line)

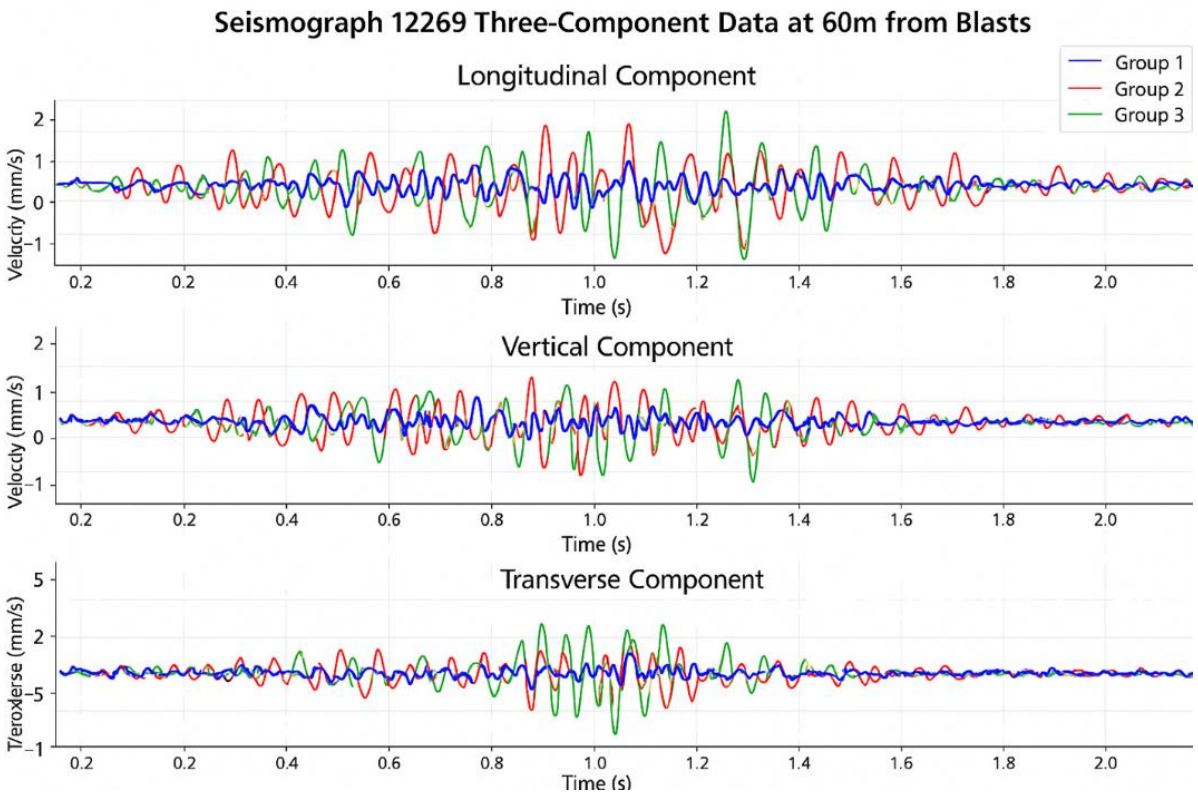

Figure 2. Seismograph 12269 three-component data at 60m from blasts

Table 1. Vibration and frequency values recorded at varying distances for three different blasting groups

Seismograph	Group	Scale Distance (m)	PVS (mm/s)	Dominant Frequency (Hz)
12270	1st Group	9	216.9	11
	2nd Group	12	290.2	23
	3rd Group	12	292.5	34
micro	1st Group	26	76.1	30
	2nd Group	27	63.1	37
	3rd Group	27	85.6	36
14465	1st Group	45	23.1	24
	2nd Group	45	22.1	26
	3rd Group	42	40.5	22
12269	1st Group	67	4.7	12
	2nd Group	62	11.5	39
	3rd Group	60	14.6	18

3. RESULTS AND DISCUSSION

The effectiveness of the Seisblast-Promax energy damping algorithm was validated through comparative analysis of the recorded seismic data. Group 1, optimized via Seisblast-Promax, consistently yielded lower PVS values at all measured distances compared to both the burden-relief method (Group 2) and conventional delays (Group 3). At 67 meters, Group 1 recorded a PVS of 4.7 mm/s with a dominant frequency of 12 Hz. This was markedly lower than Group 2 (11.5 mm/s, 39 Hz) and Group 3 (14.6 mm/s, 18 Hz), as presented in Table 1. This result underscores the efficiency of Seisblast-Promax in minimizing structural vibration risk without sacrificing fragmentation effectiveness. Figure 2 shows that although Group 1's signals lasted longer, their amplitude was significantly reduced in all three axes. The use of the pilot signal recorded at the critical distance (67 m) as a baseline for delay calculation was instrumental in this success. It confirms that site-specific signal modeling is essential for accurate delay optimization. Furthermore, Seisblast-Promax provides a user-friendly platform for integrating geological data, sismograph inputs, and blasting geometry, enabling engineers to iteratively test delay sequences before actual field application. Unlike traditional software that relies solely on geometrical assumptions, Seisblast-Promax integrates real-time vibration prediction with customizable delay schemes. Figure 1 demonstrates the principle of cumulative damping via destructive interference, a concept rarely implemented in commercial blast design tools. This feature sets Seisblast-Promax apart as a comprehensive, scientifically grounded tool in modern blasting operations.

4. CONCLUSION

This study demonstrated the superior performance of Seisblast-Promax in reducing blast-induced vibrations through advanced seismic modeling and delay optimization. The results confirm that the energy damping method used in Group 1 significantly lowered peak vibration values compared to conventional and burden-relief-based blasting strategies. At 67 meters, the vibration levels achieved with Seisblast-Promax were less than half of those observed in other methods, showcasing its potential for use in sensitive environments. The integration of site-specific seismic signals, vibration mapping, and dynamic delay sequencing marks a transformative step in modern blast design. Seisblast-Promax offers a scalable and field-validated solution for operations that demand both efficiency and environmental responsibility.

ACKNOWLEDGEMENTS

The authors would like to thank TUMAD Mining Industry and Trade Inc. for their support during field experiments, and GOA Mining R&D for technical infrastructure and Seisblast-Promax development contributions.

REFERENCES

[1] M. Akbari, G. Lashkaripour, A.Y. Bafghi, M. Ghafoori, Int. J. Min. Sci. Technol., 25 (2015) 59–66.
[2] G.G.U. Aksoy, C.O. Aksoy, Teydep, (2023) 1507-7210032.

The 56th International October Conference on Mining and Metallurgy
22-25 October 2025, Bor Lake, Bor, Serbia
www.ioc.tfbor.bg.ac.rs

DOI: 10.5937/IOC25085J *Review paper*

THE IMPORTANCE OF GEOGRIDS FOR LANDFILL SECURITY AND ENVIROMENTAL PROTECTION

Milenko Jovanović[1a], Daniel Kržanović[1b], Miroslava Maksimović[1c], Vladan Marinković[1d], Stefan Trujić[1e], Miomir Mikić[1f]

[1] Mining and Metallurgy Institute Bor, Alberta Ajnštajna 1, 19210 Bor, Serbia
[1a] milenko.jovanovic@irmbor.co.rs; 0000-0002-6757-4143
[1b] daniel.krzanovic@irmbor.co.rs; 0000-0003-3841-8667
[1c] miroslava.maksimovic@irmbor.co.rs; 0000-0002-5001-238X
[1d] vladan.marinkovic@irmbor.co.rs; 0000-0002-2974-9563
[1e] stefan.trujic@irmbor.co.rs; 0009-0003-5297-4309
[1f] miomir.mikic@irmbor.co.rs; 0000-0001-7659-769X

Abstract

The area intended for the disposal of (mining...) waste is represented by earthen surfaces. Soil is a natural universal water purifier in which rainwater is filtered and thus protects the quality and correctness of underground drinking water. The soil has a great absorption capacity, both physical and chemical. The cleanliness of the earth's surface is greatly impaired (worsened) by the disposal of (mining) waste on the surface of the soil, which is (eventually) permitted (by the project) for that purpose. In order to protect the soil (the wider surroundings of the site) from the harmful effects of waste (erosion, pollution, etc.), we must first protect it, whereby we widely use, as one of the solutions, different types of geosynthetics and accompanying geomaterials.

The waste disposal site is a complex geotechnical building, the main purpose of which is the safe (without active risks to the living environment) and environmentally friendly disposal of waste, which cannot or is not cost-effectively recycled, or otherwise usefully used.

At landfills of various types of waste (materials), geogrids are used as reinforcement as an independent element or as an integral part of a geocomposite. Of course, this refers to geomembranes, geotextiles and other types of geosynthetics as part of one of the covered - protected or drainage layers of the landfill. The geogrid must meet the requirements (resistance) of mechanical strength, as well as resistance to chemical agents and elevated temperature.

Keywords: *(mining) waste disposal sites, geosynthetics, geogrids, mining waste, pollution*

1. INTRODUCTION

Geogrids are relatively easy to manage, large quantities of this material can be installed quickly with minimal labor and lower installation costs. The geogrid can be installed in all weather conditions without demanding equipment or special construction techniques. Geogrids provide tensioning for: various types of landfills, foundations, foundations of railway lines and roads, earthen reinforcement of earthen embankments, transfer of loads on terrain of extreme mass, etc. With their tensile strength, geogrids are suitable for various types of demanding projects.

Engineering solutions that include the use of geogrids can preserve natural mineral resources by reducing the thickness of the roadbed and the need for large amounts of soil to stabilize steep slopes. Geogrids are relatively easy to manage, large quantities of this material can be installed quickly with minimal labor and lower installation costs. The geogrid can be installed in all weather

conditions without demanding equipment or special construction techniques. Geogrids provide tensioning for: various types of landfills, foundations, foundations of railway lines and roads,

By crossing (combining) types (materials) of geogrids (geotextiles) in the form of a certain hybrid technology of manufacturing these products, we obtain usable parameters suitable in the field of environmental protection and the necessary mechanical and temporal usability (longevity).

The basic division according to the type of material from which geogrids are made is synthetic and natural (organic). Organic geogrids have unique characteristics consisting of biologically and chemically degradable natural fibers. They are designed to hold the soil in place until natural vegetation is established. On the other hand, geogrids and geotextiles made of synthetic materials have much greater strength, elasticity and durability. [1,2,3,4]

Geogrids are most often used in the cover protective structure of the landfill so that the cover structure can take over the tension that may occur due to differential settlement of the deposited waste. And since landfills are sometimes located in abandoned quarries, it is often necessary to arrange steep rock slopes in order to make the best use of the space for waste disposal.

At waste disposal sites, geogrids are most often used to strengthen the sides - the edges under the waste, as well as to strengthen the cover in the zones above the geomembrane (if necessary) (Fig. 1). In geotechnical engineering, they are most often used to strengthen and stabilize weakly load-bearing soil. In this case, the material whose fraction size is larger than the opening of the mesh is piled on the geogrid and the material is trapped in the openings of the geogrid and a system resistant to external forces is created (1,2,3,10).

Figure 1. Presentation of covering (covering) the slope of the landfill with a geogrid

2. EXPERIMENTAL

2.1 Geogrids for the purpose of slope stabilization

The greatest role of vegetation in protecting the slope from erosion and its stabilization is ensured when its surface enables the establishment of a given vegetation and allows water to flow at a certain speed and intensity on the surface, thereby preventing the degradation of the vegetative cover.

In difficult conditions (such as slopes with a critical angle, channels with high flow, etc.) the vegetative cover, even when well established, will not be able to survive under the erosive force of the water.

Figure 2. Reinforcement of supporting slopes with a geogrid, with the additional help of natural vegetation

Synthetic geogrids are made of UV-stabilized polyethylene that ensures long-term soil retention. The flexibility of the product allows it to follow the contours of the ground and prevents the formation of voids. If the soil is not anchored, it will become subject to the influence of underground water flows and erosion. The use of these nets works by lining the working surface when creating steeper slopes.

Organic geogrids have unique characteristics, they consist of biologically and chemically photo-degradable natural fibers. They are designed to hold the soil in place until vegetation is established.

Organic geogrids are more flexible than most types of synthetic geogrids. This allows them to easily follow the contour of the soil surface. The ability to make direct contact between the fibers and the soil and allow the bond between them to develop allows soil loss to be reduced by 90% or more.

In addition to the above, organic geogrids act as "mulch" and thereby improve the establishment of vegetation. After degradation, they do not leave any toxic material.

Hydroseeding enables easier greening immediately after the installation of the geogrid (Fig. 2). (8,9,12)

3. CONCLUSION

Geosynthetics are mainly polymer products that are used to stabilize and isolate terrain (materials) and have a wide range of applications.

Geotextiles, geomembranes and geodrains are most commonly used in the rehabilitation of geosynthetic landslides. The primary function of geomembranes and geodrains on landslides is

drainage, while geotextile performs multiple functions: filtering, draining, reinforcement and separation.

Geogrids have a reinforcing function, while with geocomposites it is variable, depending on the combination of constituent materials.

The characteristics of geotextile materials can be determined using mechanical models. Thus, every type of deformation of real materials is imitated by a simple model or this imitation is represented by complex models that are formed by a combination of simple models. Simple models used to describe elastic, viscoelastic and plastic deformation are models that define the properties of materials that do not exist in nature, but whose properties, under certain load conditions and other external influences, approximately reflect the behavior of real materials (5,9).

A special type, geogrids (and geotextiles) made of natural (organic) material (coconut, jute...) represent a 100% biodegradable solution for erosion control (geoggrids or geotextile mats made of coconut or jute fibers). Organic geogrids have unique characteristics, they consist of biologically and chemically photo-degradable natural fibers. They are designed to hold the soil in place until vegetation is established. A geogrid or permeable geotextile provides a natural support system (improvement of characteristics) to soil and vegetation. In addition to the above, organic geogrids act as "mulch" and thereby improve the establishment of vegetation. After degradation, they do not leave any toxic material.

As a possible solution in many cases, where an effective result is sought both in terms of ecology and construction, safety, and terrain security, there is a hybrid approach to the use of building materials. Namely, by using (hybrid) different types of materials when making geogrids or geotextiles, we can solve seemingly contradictory requirements in their application.

Such hybrid (combined) materials, which would contain crossed bundles of organic and synthetic origin, can, depending on the need (purpose) and their mutual relationship, be an "ideal compromise", that is, a saving solution. Material of organic origin would have a positive effect on the development and preservation of vegetation and the entire eco system, while geosynthetic materials would have a primary application of a mechanically stabilizing nature, as many times stronger and more weather-stable materials. In addition to the above, organic geogrids act as "mulch" and thereby improve the establishment of vegetation. After degradation, they do not leave any toxic (harmful) material.

Because geogrids are relatively easy to manage, large quantities of this material can be installed quickly with minimal labor and lower installation costs. The geogrid can be installed in all weather conditions without demanding equipment or special (in)construction techniques.

Special attention in further development should be paid to the use of new (natural) materials and hybrid technology for the production of geomaterials, as products of the future (4,10,11,12).

ACKNOWLEDGEMENTS

This work is financially supported by the Ministry of Science, Technological Development and Innovation of the Republic of Serbia, for financial support according to the contract with the registration number 451-03-136/2025-03/ 200052.

REFERENCES

[1] E. Nonweiler, Sliding and stabilization of slopes, School book, Zagreb, 1987.
[2] Ž. Veinović, P. Kvasnička, Surface landfills, Internal script, Faculty of Mining, Geology and Petroleum, University of Zagreb, Zagreb, 2007.

[3] M. Zidar, Methods of rehabilitation of landslides, Faculty of Geotechnical Engineering, University of Zagreb, Varaždin, 2009.
[4] M. Bogićević - Gradjevinarstvo.rs (December 3, 2008)
[5] D.M. Đorđić, Investigation of the deformation characteristics of non-woven geotextile materials made of polyester and polypropylene fibers - Doctoral Dissertation, 2016.
[6] SRPS EN ISO 10318:2015 - Geosynthetics - Terms and definitions: ISO 10318 (2015).
[7] Final thesis (2010/2011): On geosynthetics and their applications in landfill rehabilitation; Lukavečki Iva (1821)
[8] N. Gojković, R. Obradović, V. Čebašek, Stability of the slope of open pit disposal sites; University of Belgrade, Faculty of Mining and Geology in Belgrade, Belgrade, 2008.
[9] M. Juras, Application of geosynthetics in a landfill, Final thesis; Faculty of Geotechnical Engineering, University of Zagreb, Varaždin, 2017.
[10] Milenko Jovanović (June, 2019'), Study research II (Doctoral dissertation): "Geosynthetics - purpose and application (in mining)", University of Belgrade, Technical Faculty in Bor.
[11] Milenko Jovanović (July, 2019'), Study Research III (Doctoral Dissertation): "Organic Geonetworks", University of Belgrade, Technical Faculty in Bor.
[12] M. Jovanović, D. Kržanović, R. Rajković, M. Mikić, M. Maksimović, Application of geogrids in recultivation measures against land degradation. XV International Mineral Processing and Recycling Conference, 17-19 May 2023, Belgrade, Serbia, pp. 435-440. ISBN 978-86-6305-133-1.

The 56th International October Conference on Mining and Metallurgy
22-25 October 2025, Bor Lake, Bor, Serbia
www.ioc.tfbor.bg.ac.rs

DOI: 10.5937/IOC25090K Original scientific paper

NPV BASED OPTIMIZATION OF FINAL PIT CONTOURS IN THE CEMENTACIJA MINING COMPLEX

Daniel Kržanović[1a], Milenko Jovanović[1b], Radmilo Rajković[1c], Miljan Gomilanović[1d], Miloš Stojanović[1e]

[1] Mining and Metallurgy Institute Bor, Alberta Ajnštajna 1, 19210 Bor, Serbia
[1a] daniel.krzanovic@irmbor.co.rs, 0000-0003-3841-8667
[1b] milenko.jovanovic@irmbor.co.rs, 0000-0002-6757-4143
[1c] radmilo.rajkovic@irmbor.co.rs, 0000-0001-5905-6613
[1d] miljan.gomilanovic@irmbor.co.rs, 0000-0002-1209-7423
[1e] milos.stojanovic@irmbor.co.rs, 0000-0003-0044-5491

Abstract
The final pit contour optimization for the Cementacija 2 and Cementacija 3 open pit was carried out using Whittle™ Four-X (LG 3D) algorithms. A series of pit shells was generated based on varying Revenue Factors (RF) to reflect changes in metal prices. The objective was to maximize the Net Present Value (NPV), using input parameters, such as mining capacity, slope angles, dilution, recovery rates, processing costs, and metal prices. A total of 77 pit shells were evaluated across three scenarios: Best Case, Worst Case, and Specified Case. Shell whose RF is 1 was identified as the most suitable final contour, achieving the highest NPV in the Best Case scenario (USD 117.15 million) and demonstrating strong economic performance across alternative cases. This shell also satisfies spatial constraints, making it suitable for detailed design and long-term planning.

***Keywords**: open pit optimization, NPV, Whittle, Revenue Factor, pit shell*

1. INTRODUCTION

Open pit mine design and planning are critical components of surface mining operations. Determining the final pit limit ensures that ore extraction is technically feasible, economically optimized, and environmentally compliant. Optimization of the pit boundary involves the geological and operational modeling, which is realized through the application of optimization software that uses some of the mathematical algorithms. The process involves identifying the combination of controlled variables that maximize the project value in the context of a given set or range of assumptions [1].

Advances in computational algorithms have enabled the use of optimization software such as Whittle™ Four-X, which applies the Lerchs-Grossmann algorithm to determine the most profitable pit shell [2,3]. In this study, final pit contours for the Cementacija 2 and 3 deposits were optimized to maximize project value while considering site-specific constraints and economic assumptions.

2. METHODOLOGY

2.1 Input parameters

Input parameters were established based on technical studies and economic forecasts:

- Annual mining capacity: 3.5 million tons of ore.
- Final pit slope angle: 38°, reflecting geotechnical assessments.
- Dilution and recovery: 3% dilution; 96% recovery.
- Cut-off grade: 0.15% Cu.

- Processing and recovery data: Based on flotation and metallurgical recovery historical figures.
- Metal prices: Copper, gold, and silver prices defined in accordance with internal pricing models.

2.2 Block model of the Cerovo ore body

Block model of the Cementacija 2 and Cementacija 3 open pit is represented by mini-blocks with dimensions of 5.0 × 5.0 × 5.0 meters.

A block model was formed with: 600 rows, 420 columns, 180 levels.

By creating a block model, the following values were defined for each block: type of rock, volumetric mass, content of useful and harmful components Cu (%), Au (g/t), Ag (g/t), S (%), Cuox (%), Cus (%) and the economic value of the block, i.e. the amount of copper in the block or profit, which is realized by mining that block.

2.3 Optimization process

Using Whittle™ Four-X (LG 3D), 77 pit shells were generated across a Revenue Factor range of 0.3 to 2.0 in steps of 0.02 [2]. For each shell, technical (ore, waste, grades) and economic (NPV) indicators were calculated [4]. The analysis involved three scenarios:

- Best Case: Assumes ideal operational angles and sequential shell mining.
- Worst Case: Reflects conservative bench-by-bench mining with minimal slope angles.
- Specified Case: Combines selected shells (7, 12, 14, 18, 36) chosen via the automated NPV pushback tool.

NPV calculations used an 8% discount rate and considered direct operational costs. Capital costs, land acquisitions, and legal compensations were excluded at this stage.

3. RESULTS AND DISCUSSION

The analysis of discounted cash flows was performed with the aim of determining the final contour of the Open Pit Cementacija 2 and Cementacija 3. During the optimization, the base price of metal was varied in the Revenue Factor range from 0.30 to 2.00 with a step of 0.02, and in this way the 77 potential surface open pit contours were generated. The amounts of waste, ore and metal are determined for each open pit contour individually with the operational NPV discounted by 10%.

Figure 1 shows the Pit by pit graph with the economic optimization parameters.

Each generated pit shell provided insight into reserve tonnage, waste volume, metal grades, and financial return. Notable findings include:

- **Shell 36 (RF 1.00)**: Highest Best Case NPV (USD 117.15 million), and favorable results in the Specified (USD 110.33 million) and Worst Case (USD 79.37 million).
- **Shell 30 (RF 0.88)**: Top Specified Case NPV (USD 111.62 million), but lower Best/Worst Case values.

Shell 36 was chosen as optimal due to a combination of maximum reserve utilization and spatial compatibility with field constraints:

- **West**: Bor-Majdanpek railway.
- **South**: Water reservoir and administrative facilities.
- **East**: Cerova River.
- **North**: License boundary.

Although full operational and capital cost data were not included, results provide a preliminary framework for pit design. Future optimization will refine phase development (pushbacks), year-by-year production schedules, and full economic models [2,5].

The parameters of the optimal open pit contour are listed in Table 1.

Table 1. Techno-economic parameters of the optimal open pit

Parameter	Unit	Value
Ore	ton	23,641,304
Waste	ton	53,684,070
Stripping ratio	t/t	2.27
Average copper grade	%	0.250
Average gold grade	g/t	0.100
Average silver grade	g/t	1.300

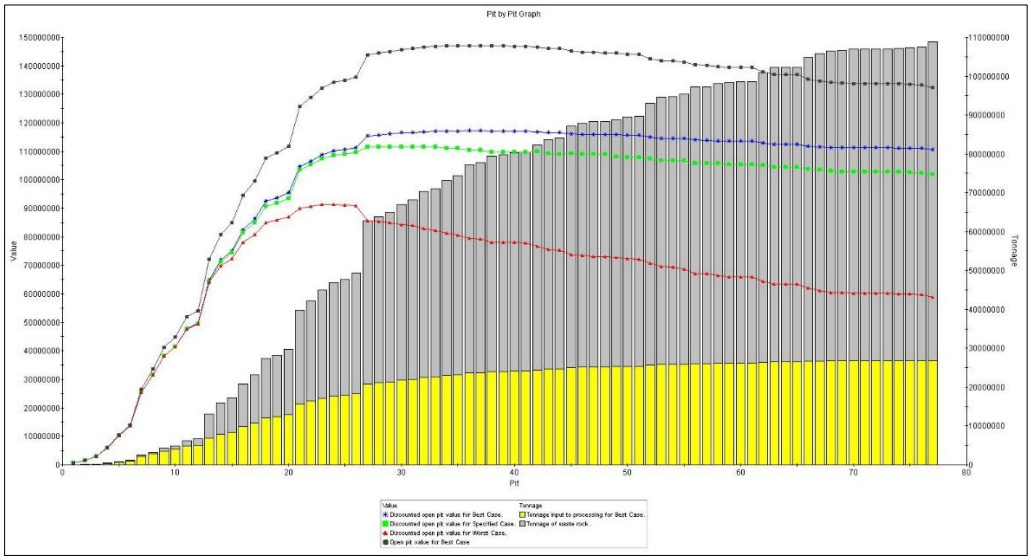

Figure 1. Pit by pit graph

A graphic representation of the Whittle shell of the final contour of pit number 36 is given in Figure 2.

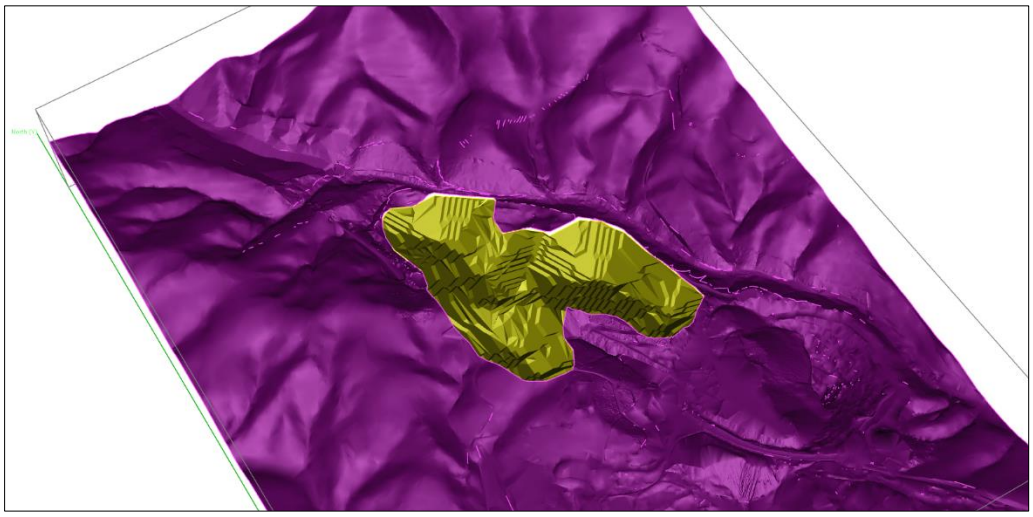

Figure 2. Whittle 3D view of the optimal pit number 36

4. CONCLUSION

The optimization of the final pit contour for the Cementacija 2 and 3 open pits, conducted using the Whittle™ Four-X (LG 3D) algorithm, successfully identified the most economically viable pit shell based on Net Present Value (NPV) analysis. By evaluating 77 pit shells under varying revenue factors and three development scenarios (Best, Worst, and Specified Case), shell 36 (RF 1.00) was determined to offer the highest economic potential while also respecting the spatial and environmental constraints of the site. Although the input parameters used are preliminary and exclude certain capital and operating costs, the results provide a reliable foundation for further detailed design, phase planning, and economic assessment of the project. The chosen contour ensures the exploitation of maximum ore reserves with a favorable project lifespan, supporting strategic decision-making for future mine development and investment planning.

ACKNOWLEDGEMENTS

This work was financially supported by the Ministry of Science, Technological Development and Innovation of the Republic of Serbia, Contract on realization and financing of the scientific research work of the Mining and Metallurgy Institute Bor in 2025, contract number: 451-03-136/2025-03/ 200052.

REFERENCES

[1] Daniel Kržanović, Radmilo Rajković, Ivana Jovanović, Milenko Jovanović, Miomir Mikić, Determination the final contour of the open pit Veliki Krivelj for the mining capacity 23.1 million tons of ore, The 54th International October Conference on Mining and Metallurgy, 18-21 October 2023, Bor Lake, Serbia, Proceedings, pp. 132-135.
[2] Whittle Consulting. Whittle Four-X User Manual (2021).
[3] Lerchs, H., & Grossmann, I. F.. Canadian Mining and Metallurgical Bulletin (1965).
[4] D. Kržanović, M. Ljubojev, I. Jovanović, N. Vušović, An Analysis the Effects of Changes in Price of Metal and Operating Costs to the Profit in Exploitation the Copper Ore Deposits, A Case Study: Copper Mine Majdanpek, Serbia, Mining & Metallurgy Engineering Bor, No. 3-4 2017, pp. 51-58.
[5] Hustrulid, W., Kuchta, M., & Martin, R. K. CRC Press (2013).

The 56th International October Conference on Mining and Metallurgy
22-25 October 2025, Bor Lake, Bor, Serbia
www.ioc.tfbor.bg.ac.rs

DOI: 10.5937/IOC25094V Original scientific paper

IMPLEMENTATION OF THE SUBLEVEL CAVING MINING METHOD IN THE T4 ORE BODY AT THE JAMA BOR UNDERGROUND MINE

Ivica Vojinović[1a], Dragan Šabaz[1b], Miloš Stojanović[1c]

[1] Mining and Metallurgy Institute Bor, Alberta Ajnštajna 1, 19210 Bor, Serbia
[1a] ivica.vojinovic@irmbor.co.rs, 0009-0006-3658-6922
[1b] dragan.sabaz@irmbor.co.rs, 0000-0002-1373-413X
[1c] milos.stojanovic@irmbor.co.rs, 0000-0003-0044-5491

Abstract

Within the Bor copper ore field, a total of 33 ore bodies have been exploited since the beginning of the last century, with only two remaining available for future extraction—ore bodies T3 and T4—while the Borska Reka ore body is currently under active exploitation. The T4 ore body represents a massive pyrite-type mineralization, for which the sublevel caving mining method has been selected as the most suitable extraction approach. In order to maximize ore recovery, reduce mining costs, and improve occupational health and safety conditions, modern software tools such as Datamine Aegis have been employed for the design of development and preparation workings, as well as for planning drilling and blasting operations.

***Keywords**: Bor, ore body T4, sublevel caving, Datamine Aegis*

1. INTRODUCTION

The Bor copper ore field is located within the central part of the Timok Magmatic Complex (TMC). Since the beginning of the 20th century, mining activities both underground and open-pit have encompassed a total of 33 ore bodies within this field. Of these, only the T3 and T4 ore bodies remain available for future exploitation, while the Borska Reka copper deposit is currently being mined. As part of the "Geological Exploration Project at the Bor Mine," the exploration drillhole -150ZK350-1 intersected massive pyrite ore located south of the previously identified T ore body, subsequently designated as the T4 ore body. The T4 ore body is situated in the central portion of the Bor deposit, within a fault zone. The surrounding rocks exhibit intense alteration in the immediate vicinity of the ore body, which rapidly diminishes into weakly altered and eventually fresh andesites. The most prominent hydrothermal alterations observed include pyritization, silicification, kaolinization, chloritization, and sulphatization [1].

In the zone of the T4 ore body, the rock mass is characterized by kaolinization and disintegration, with kaolinization occurring as the dominant type of alteration in the footwall and, to a lesser extent, in the hanging wall. Sulphatization is manifested by the presence of anhydrite (gypsum) both within the host rock and along fracture surfaces. This type of alteration has an adverse effect on the physical and mechanical properties of the rock mass and, similarly to kaolinization, negatively impacts overall rock mass stability. Sulphatization within the host rock appears as localized accumulations (nests), while in fractures it forms infillings ranging from a few millimeters to several centimeters in thickness. These gypsum-filled fractures are generally continuous, gently undulating to planar, with smooth surfaces that often exhibit slickensides indicating movement. Such fractures represent weakened zones within the rock mass and are a highly unfavorable factor for the stability of underground openings and the rock mass as a whole. On the other hand, pyritization and associated mineralization (typically accompanied by silicification) generally lead to an improvement in the physical-mechanical characteristics and engineering-geological parameters. A notable increase in all parameter values is observed within mineralized zones. This improvement applies both to the intact rock matrix and, not infrequently, to fractures filled with this type of mineral assemblage [1].

In the selection of a mining method, the most influential factors include the type and value of the ore determined by its metal content, the surrounding rock mass, as well as the specific requirements set by the Investor and outlined in the project design brief. In this case, the geometry and dip of the ore body are considered favorable; however, the substantial size of the ore body, combined with its economic value, strongly suggests the need for a mining method that ensures high ore recovery. In addition to these factors, the engineering-geological characteristics of the rock mass play a critical role in method selection. According to the ore reserves report for the T4 ore body, the intact rock matrix is predominantly affected by pyritization and propylitization, while the fractures exhibit pyritization, mineralization, and sulphatization. Within all fault zones, the rock mass is kaolinized and disintegrated, with kaolinization occurring as the dominant alteration in the footwall and, to a lesser extent, in the hanging wall [1].

2. EXPERIMENTAL

Considering all influencing factors and the requirements set by the Investor, the sublevel caving method was adopted for ore extraction. Sublevel caving is applied under a variety of geological and structural conditions; however, it is most effective in steeply dipping ore bodies, where blasted ore can descend by gravity to the sublevel drift, from which it is subsequently loaded and hauled. Depending on the thickness and dip angle of the ore body, the project provides appropriate design solutions for the development and preparation of the mining blocks. The ore may possess relatively low mechanical strength, as the extraction process does not involve the creation of large open voids; instead, mining is conducted directly from sublevel drifts. In sublevel caving methods, favorable conditions exist when the hanging wall rocks are more prone to caving. This facilitates the natural backfilling of the mined-out voids with caved waste rock, which is one of the most important prerequisites for the efficient and safe application of caving-based mining methods. Additionally, the likelihood of forming large caving arches with wide spans is reduced, which consequently results in lower stress concentrations on the extraction and development drifts Sublevel caving methods are characterized by the ability to integrate the most modern equipment for drilling, blasting, loading, and haulage operations within the stoping blocks. This enables high production rates and increased productivity in the extraction process, ultimately resulting in ore recovery at lower mining costs [2, 3].

The development and preparation of the T4 ore body involves its division into three mining levels, with a vertical spacing of 15 meters, specifically: level k-60 m, level k-45 m, and level k-30 m. Each of these mining levels is accessed through development workings originating from the existing exploration raise of the T4 ore body, Figure 1 and Figure 2 [2].

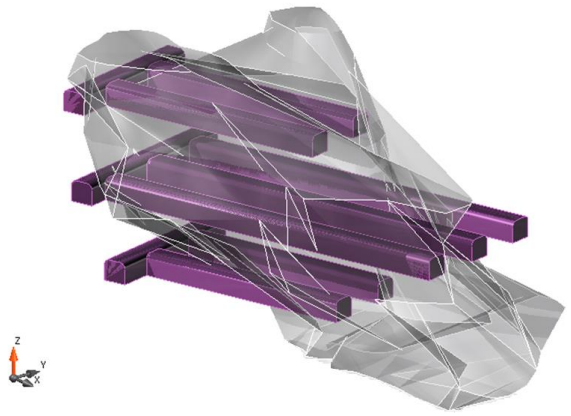

Figure 1 Development of T4 ore body

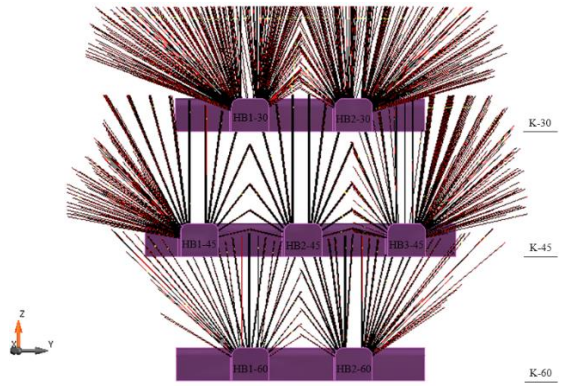

Figure 2 Vertical crosscut of drifts and ring design

At each level, the slot drifts (HZ) and drilling drifts (HB) are developed in a "chessboard" layout, resulting in a rhomboidal shape of the ore block to be extracted. In each slot drift, a slot raise with dimensions of 2×2 meters is constructed at both ends by drilling and blasting operations. Along

the entire length of each slot drift, fan-shaped boreholes (rings) are drilled at intervals of 1 meter. [2].

From the drilling drifts, rings are also drilled, spaced 2 meters apart. The height of the drilling is determined by the upper sublevel, while the drilling width is defined by the contour of the ore body, Figure 3 and Figure 4 [2].

The extraction process is preceded by slot development, which involves blasting of slot raises as well as ring drilling and blasting within the slot drifts. Blasting of the rings in the production drifts is carried out only after all rings in the slot drifts have been completed, and is performed uniformly across the level to ensure proper flow control of the blasted material. The blasting proceeds one ring at a time, followed by the draw and loading of the excess broken ore before initiating the next round. Upon completion of ring blasting and removal of excess material at level K-30, the same procedure is repeated at level K-45, and finally at level K-60, following the same sequence of slot raise development and staged ring blasting, leading to the final drawdown and loading of the ore. Ore dilution control is carried out operationally through geological sampling and using loader bucket weight monitoring systems, due to the sharp contact between the ore body and waste rock, as well as their significant differences in bulk density. The extraction sequence proceeds from the upper levels to the lower levels [2].

In the application of the sublevel caving method, the use of long blast holes arranged in a fan pattern is characteristic. When designing drilling and blasting operations, it is essential to consider all relevant characteristics of the explosives and the rock mass. In cases of deviation, changes in drilling geometry, or variations in explosive types, appropriate optimization must be conducted. Poorly designed blasting operations can significantly impact the safety of personnel, equipment, as well as underground structures and production processes, which can also lead to negative economic consequences [4, 5].

The design of drilling and blasting operations for the application of the sublevel caving method in ore body T4 was carried out using the Datamine Aegis software, Figure 3 and Figure 4. Aegis includes an integrated database containing accumulated experience and parameters from various ore deposits related to drilling and blasting activities. This database enables the user to efficiently and effectively perform modeling in geologically similar environments. Furthermore, the user has the ability to create a custom database, which allows for more precise future modeling and optimization [6].

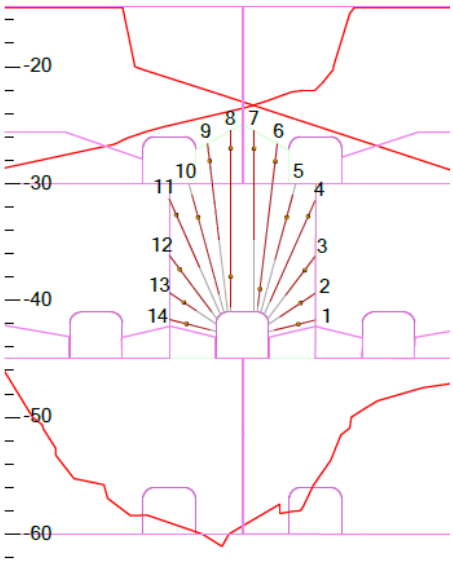

Figure 3 Crosscut of ring design on the level K-45

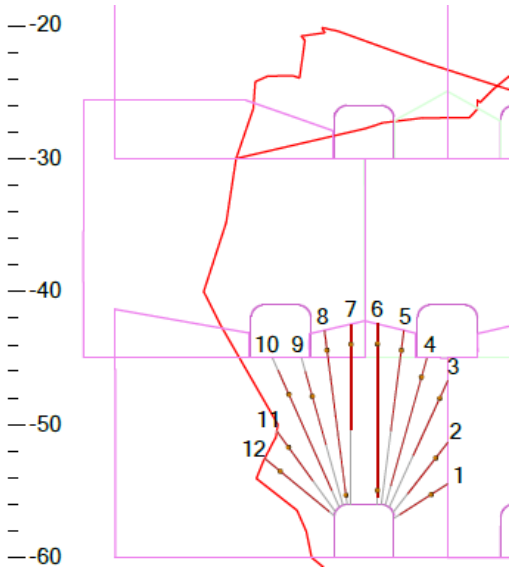

Figure 4 Crosscut of ring design on the level K-60

3. RESULTS AND DISCUSSION

The application of Aegis software enabled a comprehensive spatial visualization of ore body T4. This facilitated the design of an optimal development and preparation layout, as well as the planning of drilling and blasting operations. Through the optimal design of these activities, the resulting benefits include higher ore recovery and reduced dilution.

4. CONCLUSION

Ore body T4, located in the central part of the Bor deposit, is characterized by massive pyritic mineralization, pronounced hydrothermal alterations, and complex engineering-geological conditions. Considering the dimensions of the ore body, its thickness, dip, and the investor's requirements regarding high ore recovery and operational safety, sublevel caving was selected as the most suitable mining method. The analysis of geological, geomechanical, and production-related factors confirmed the justification of this choice. The application of the sublevel caving method enables efficient draw control, gradual extraction by levels, and safe backfilling due to caving of mined-out voids, thereby minimizing the risk of ground instability.

A particular value of this approach lies in the use of the specialized Aegis software, which enabled three-dimensional visualization of the ore body, precise design of development drifts, and drilling and blasting operations. This ensured high ore recovery, reduced dilution, increased productivity, and lower extraction costs.

The results of this study confirm that the application of modern mining methods, combined with advanced software solutions, represents a key factor for the successful exploitation of complex ore bodies in contemporary underground mining operations.

ACKNOWLEDGEMENTS

This work was financially supported by the Ministry of Science, Technological Development and Innovation of the Republic of Serbia, Contract No. 451-03-136/2025-03/ 200052.

REFERENCES

[1] Elaborat o rezervama ležišta bakra rudnog tela „T4“ u Jami Bor, Serbia Zijin Copper doo Bor, 2023
[2] Dopunski rudarski projekat eksploatacije rudnog tela T4 u Jami Bor, Institut za rudarstvo i metalurgiju Bor, Centar za projektovanje metaličnih mineralnih sirovina, 2024
[3] Ž. Milićević: Metode podetažnog i blokovskog zarušavanja; Univerzitet u Beogradu, Tehnički fakultet u Boru, 2008, p.15.
[4] I. Vojinović, I. Svrkota, M. Stojanović, D. Šabaz, R. Rajković., Slot development using the controlled blasting in the ore body „Borska reka“., Mining and Metallurgy Engineering Bor, 2/2024 11-20
[5] I. Vojinović, M. Stojanović, D. Šabaz., The influence of explosive properties on the optimisation of drill and blast ring design., Mining and Metallurgy Engineering Bor, 2/2023 1-8
[6] https://iring.ca/knowledge-base/

The 56th International October Conference on Mining and Metallurgy
22-25 October 2025, Bor Lake, Bor, Serbia
www.ioc.tfbor.bg.ac.rs

DOI: 10.5937/IOC25098S *Original scientific paper*

APPLICATION OF NEURAL NETWORKS FOR OPTIMIZING ROCK BOLT SYSTEM IN UNDERGROUND MINING

Miloš Stojanović[1a], Ivica Vojinović[1b], Dragan Šabaz[1c]

[1] Mining and Metallurgy Institute Bor, Alberta Ajnštajna 1, 19210 Bor, Serbia
[1a] milos.stojanovic@irmbor.co.rs, 0000-0003-0044-5491
[1b] ivica.vojinovic@irmbor.co.rs, 0009-0006-3658-6922
[1c] dragan.sabaz@irmbor.co.rs, 0000-0002-1373-413X

Abstract
This paper explores the application of artificial neural networks (ANN) in optimizing drift support systems in underground mining. Using input parameters such as rock bolt length, diameter, and quantity, a multilayer ANN model was developed to predict key stability indicators: total displacement and safety factors. The model was trained and validated using numerical simulation results based on finite element analysis. The ANN demonstrated high accuracy and generalization capability, providing a reliable tool for decision-making in geotechnical design.

Keywords*: neural networks, rock bolt system, underground mining*

1. INTRODUCTION

Rock bolting is a widely used method for stabilizing underground excavations due to its adaptability, cost-effectiveness, and ability to support staged excavation. Optimal design of rock bolts considering length, diameter, density, and tension is crucial for site-specific stability but remains challenging due to varying geological and stress conditions [1]. Artificial neural networks (ANNs) have recently emerged as powerful tools in geomechanical engineering, capable of modeling complex, nonlinear relationships. They have shown high accuracy in predicting deformation and stability outcomes in tunnels, slopes, and retaining walls. In several studies, ANNs trained on finite element method (FEM) data have acted as efficient surrogate models, providing predictions that closely match numerical results while drastically reducing computation time. These speed and accuracy benefits make ANNs suitable for iterative optimization tasks in geotechnical design. In underground mining, the use of ANNs for support system design is still developing. However, initial studies show they can outperform traditional empirical models in predicting optimal bolt parameters [2, 3, 4].

This paper presents an ANN-based predictive model for optimizing rock bolt support systems in underground drifts. FEM simulations are used to generate training data for various bolt configurations, and the ANN learns to predict drift displacement and safety factor outcomes. The methodology, model architecture, and validation results are presented and compared to FEM benchmarks to evaluate the potential of this approach for practical mining applications.

2. EXPERIMENTAL

The study considered a section of an underground drift (mining room) excavated in the T3 ore body at the Jama Bor mine, which requires a rock bolt support system. A numerical model of the drift was created using finite element method (FEM) software to simulate the rock mass behavior and support interaction. The drift was approximately 4.5 m in width and 4.3 m in height, situated in andesite host rock (hydrothermally altered) with geomechanical properties characterized by prior site investigations. The Hoek–Brown failure criterion was used to represent rock mass

strength, as it provides a reliable approximation for heavily jointed rock masses and was found to yield accurate safety factor estimates in this context.

A series of numerical experiments was conducted, varying three key rock bolt parameters within practical ranges:

- Bolt length (embedded length in rock), in the range 1.6 – 2.2 m.
- Bolt diameter, in the range 22 – 24 mm.
- Number of bolts in the drift crown, from 8 to 10 (per 4.5 m width of drift).

Using a full factorial combination of these parameters, 16 different support configurations (models) were analyzed (each corresponding to a unique combination of length, diameter, and number within the given ranges). For each model, the FEM simulation provided two primary outputs of interest: (1) the maximum wall displacement in the surrounding rock (i.e. the convergence of the drift walls in meters), and (2) the factor of safety (FS) of the rock mass around the opening, as computed by the shear strength reduction technique. The maximum displacement values obtained from the numerical models ranged from about 7.2 mm up to 13.9 mm, while the safety factor ranged from about 1.02 (in the weakest support case) up to 1.55 (in the strongest support case). All displacement values fell within a generally acceptable convergence limit (on the order of 1 cm or less) for a drift of this size, indicating that even the minimal support case was just at the threshold of acceptability. The trends observed were intuitive: increasing bolt length, diameter, or quantity tended to reduce the maximum displacement and increase the safety factor of the drift. For example, the worst-case support (shortest, thinnest, fewest bolts: 1.6 m × 22 mm, 8 bolts) yielded 13.9 mm convergence and FS ≈ 1.02, whereas the best-case support (longest, thickest, most bolts: 2.2 m × 24 mm, 10 bolts) reduced convergence to 7.2 mm and raised FS to 1.55 (a comfortably stable condition). These FEM-generated results formed the supervised learning dataset for the neural network model.

A feed-forward artificial neural network was designed to map the rock bolt parameters to the resulting displacement and safety factor. The network input layer has three neurons corresponding to the three input variables: bolt length, bolt diameter, and number of bolts. The output layer has two neurons, producing the predicted maximum displacement (continuous value) and predicted safety factor for a given set of inputs. After experimenting with a few configurations, a single hidden layer with five neurons was selected, as it provided sufficient model capacity to fit the data without overfitting (given the relatively small dataset).

The network was implemented in MATLAB using the Neural Network Toolbox. Prior to training, all input and output values were normalized to a similar scale (0 to 1) to aid convergence. A Levenberg–Marquardt backpropagation algorithm was employed for training, as it is known for fast convergence in small- to medium-sized networks. The transfer functions in the hidden and output neurons were differentiable sigmoid and linear functions, respectively, to meet the requirements of the training algorithm. The 16 available data samples were used to train and validate the network. To make the most of the limited data, we used a leave-one-out cross-validation strategy: at each iteration, 15 samples were used for training and 1 held-out sample for validation/testing, cycling through all samples. The network weights were initialized with small random values, and the training proceeded until the performance goal was met (mean squared error, MSE, below 10^{-4}) or no further improvement was seen on the validation sample. Regularization (Bayesian regularization in MATLAB) was applied to prevent overfitting given the small dataset. Training was successfully completed with rapid error reduction – the final model achieved a mean squared error on the order of 10^{-5} and an excellent fit to the data. Figure 1 shows the correlation between the ANN's predicted outputs and the target values from FEM for all data points. The points lie almost on the 45° line, and the correlation coefficient R for both outputs is over 0.99, indicating that the network has learned the relationship extremely well. In essence, the

ANN can reproduce the FEM results of maximum displacement and safety factors with very high fidelity for the cases it was trained on.

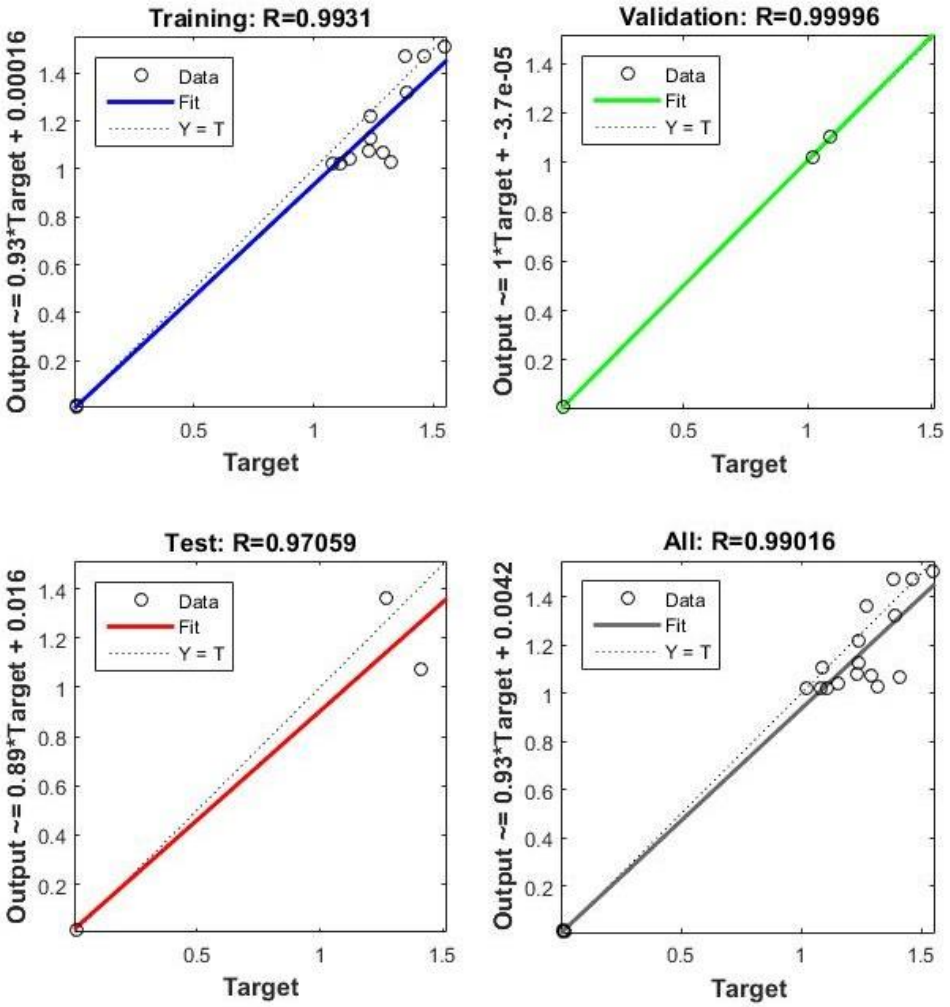

Figure 1. ANN prediction performance: correlation of network-predicted vs. FEM-calculated values. The plots show that the predicted maximum displacement and safety factor closely match the target values (all points near the diagonal), with correlation coefficient R ≈ 1.0 for both outputs, demonstrating excellent learning of the input-output mapping.

3. RESULTS

After training, the ANN model was used to predict the outcomes for new support parameter inputs. As an initial test, the ANN was tested on a new scenario (Model A) with support parameters outside the training set: bolt length 1.4 m, diameter 27 mm, and 9 bolts. The ANN predicted 12.2 mm displacement and a safety factor of 1.1518. FEM analysis of the same case yielded similar results: 11.8 mm and 1.147, confirming high prediction accuracy (Table 1). This strong match shows that the ANN can reliably estimate ground response, offering a fast alternative to time-consuming FEM simulations. Once trained, the network instantly predicts drift stability for different support setups, enabling rapid optimization. The ANN captures realistic behavior, such as reduced displacement with longer/thicker bolts and diminishing returns. It serves as a model useful for parametric studies and design decisions. However, its accuracy depends on the quality and scope of the FEM training data. For new geological settings, retraining may be required. Despite being trained on only 16 samples, the ANN generalized well thanks to its simple structure and regularization. In conclusion, ANN models can significantly accelerate and enhance support design in underground mining by replacing repetitive simulations with intelligent prediction, improving both safety and cost-efficiency. This scenario, called Model A, used intermediate or

slightly extrapolated values: bolt length 1.4 m (shorter than any training sample), bolt diameter 27 mm (thicker than any training sample), and number of bolts 9.

The network, when given Model A inputs, predicted a maximum displacement of 0.0122 m (12.2 mm) and a safety factor of 1.1518 for the drift. To verify these predictions, a full FEM analysis was then conducted for the same support scenario. The FEM results for Model A indicated a maximum displacement of 0.0118 m (11.8 mm) and a safety factor of 1.147.

Table 1. Comparison of ANN prediction and FEM result for a new bolt configuration (Model A: bolt length 1.4 m, diameter 27 mm, number of bolts 9).

	ANN		Finite Element Method (Phase)	
Model	Total displacement	Safety factor	Total displacement	Safety factor
	(m)	/	(m)	/
A	0.0122	1.1518	0.0118	1.147

4. CONCLUSION

This paper presented an ANN-based method for optimizing rock bolt support in an underground drift, using data from FEM simulations at the Jama Bor mine. The trained neural network accurately predicted maximum displacement and safety factors across various support configurations, achieving high level of correlation with FEM results and generalizing well to unseen scenarios. The ANN proved to be an effective surrogate model, enabling rapid support system optimization without the need for repeated numerical simulations. It offers immediate predictions, helping engineers identify optimal bolt setups with minimal effort and high reliability.

The method is adaptable to other mining projects by generating a small set of FEM data specific to local conditions. This fusion of numerical modeling and AI improves design efficiency, supports safer excavations, and aligns with the broader trend of smart mining technologies.

Future work may expand the input space (e.g., bolt spacing, stiffness, rock quality) or integrate hybrid models and optimization algorithms to further enhance predictive power and design automation.

ACKNOWLEDGEMENTS

This work was financially supported by the Ministry of Science, Technological Development and Innovation of the Republic of Serbia, Contract No. 451-03-136/2025-03/ 200052.

REFERENCES

[1] X.T. Dang, L.N. Vo, P.T. Nguyen, H.V.V. Tran, T.A. Nguyen, Eng. Technol. Appl. Sci. Res. 15 (2) (2025) 21526-21531.
[2] S. Keawsawasvong, S. Seehavong, C. Ngamkhanong, Front. Built Environ., 8 (2022) 837745.
[3] S. Shi, Y. Miao, C. Di, Q. Zhao, Y. Zheng, C. Liu, Sci. Rep. 15 (2025) 11018.
[4] D. Tanikić, Veštačke neuronske mreže, fazi logika i genetski algoritmi, TF Bor, Bor, 2016, 184-186

The 56th International October Conference on Mining and Metallurgy
22-25 October 2025, Bor Lake, Bor, Serbia
www.ioc.tfbor.bg.ac.rs

DOI*: 10.5937/IOC25102V* *Review paper*

TECHNOLOGICAL INNOVATIONS TRANSFORMING THE MINING INDUSTRY: A SHORT REVIEW

Ivica Vojinović[1a], Miloš Stojanović[1b], Dragan Šabaz[1c]

[1] Mining and Metallurgy Institute Bor, Alberta Ajnštajna 1, 19210 Bor, Serbia
[1a] ivica.vojinovic@irmbor.co.rs, 0009-0006-3658-6922
[1b] milos.stojanovic@irmbor.co.rs, 0000-0003-0044-5491
[1c] dragan.sabaz@irmbor.co.rs, 0000-0002-1373-413X

Abstract
The mining industry is undergoing a profound technological transformation driven by the imperative to increase efficiency, enhance operational safety, and meet stringent environmental standards. In response to the growing complexity of ore bodies and rising productivity demands, the sector is rapidly adopting advanced solutions such as wireless initiation systems, NOx-free explosives, autonomous mining fleets, AI-driven analytics, IoT-based condition monitoring, and muon tomography for subsurface imaging. These technologies enable greater precision in drilling and blasting, real-time data integration for decision-making, reduced human exposure to hazardous conditions, and minimized environmental impact. As the industry transitions toward automation and data-centric operations, continuous technological innovation has become essential to ensure the efficiency, sustainability, and competitiveness of modern mining operations.

Keywords*: AI, IoT and automation, NOx-free explosives, muon tomography, sustainable mining*

1. INTRODUCTION

Historically, the mining sector has relied on conventional methods that often compromised safety and environmental standards. However, rising regulatory pressure, deeper ore bodies, and operational cost challenges have fueled a wave of innovation. From wireless blast initiation systems to green explosives and AI-based monitoring, the sector is embracing transformative tools. This paper explores key innovations with a focus on practical applications in surface and underground mining environments.

2. EXPERIMENTAL: Review of Innovations

2.1 NOx-Free Explosives

Traditional AN-based explosives (e.g., ANFO, emulsions) are effective but can emit toxic nitrogen oxides (NOx) during detonation. A study by Araos and Onederra (2017) developed a NOx-free explosive using hydrogen peroxide (HP) and fuel, with void sensitization enabling detonation at low HP concentrations and without confinement [1]. These explosives demonstrated detonation velocities (VOD) between 1,700–6,000 m/s and critical diameters as low as 8 mm. Unlike AN-based products, these HP/fuel explosives maintained detonation even at high water content (up to 56.6 wt.%), offering both safety and environmental benefits [1, 2]. In practice, companies such as Hypex Bio have begun commercial deployment of hydrogen peroxide-based explosives as environmentally responsible alternatives to ANFO, promoting NOx-free blasting in sensitive environments. Their formulations, developed for both surface and underground operations, are designed to meet stringent environmental standards while maintaining competitive detonation performance [3].

2.2 Wireless Initiation Systems

Conventional detonator systems limit blast flexibility and pose risks related to surface wiring. Wireless initiation system eliminates these limitations by using fully programmable, untethered primers. In Teck's Carmen de Andacollo mine in Chile, WebGen™ enabled the detonation of 384 charged holes in a single blast window, quadrupling productivity (400,823 tonnes) compared to conventional methods [4]. It also allowed decoupling of blast timing from weather constraints, thus preserving community relationships and reducing unplanned downtimes. At the Kittilä underground gold mine in Finland, WebGen™ enabled longitudinal uphole stopes to be charged in a double-layer configuration, allowing for larger blast heights and eliminating re-entry in geomechanically unstable zones [5]. In the Sierrita open pit mine in Arizona, the system reduced delays caused by weather and eliminated tie-in time by removing surface wiring, significantly improving blast cycle efficiency and on-bench safety [6]. Meanwhile, at the New Afton block caving mine in British Columbia, WebGen™ allowed adjacent slot blasts to be preloaded and fired separately without exposing personnel to hazardous brow conditions, leading to over CAD 1 million in development cost savings across 18 drives [7]. These cases exemplify the flexibility and reliability of wireless initiation technology in both surface and underground applications, enabling optimized blast designs, increased production rates, and improved safety performance.

2.3 Subsurface Imaging

Accurate visualization of subsurface structures is critical in mass mining methods such as block caving, where ore recovery, dilution control, and geotechnical stability are highly dependent on understanding cave propagation and material flow. Traditional monitoring techniques such as seismic arrays and microgravity surveys are limited by resolution, latency, and coverage. In contrast, novel subsurface imaging technologies, particularly muon tomography, provide high-resolution, real-time insights into cave back evolution, undercut advance, and muck pile morphology [8, 9]. Muon tomography, as presented at MassMin 2024, uses cosmic rays muons and by analyzing their attenuation patterns, 3D density maps of underground voids and materials can be constructed with remarkable precision generating 3D visuals of cave backs and muck piles. Muon tomography was successfully used to detect early cave breakthrough, validate numerical models, and guide production sequences. These results indicate that the technology not only enhances operational safety but also improves ore recovery and reduces overbreak and dilution through timely feedback to engineering and production teams. When integrated with other digital systems, muon imaging becomes a critical tool in building real-time, geotechnically-informed digital twins of active ore bodies [9].

2.4 Integration of IoT, AI, and Automation

The integration of Internet of Things (IoT), Artificial Intelligence (AI), Machine Learning (ML), and automation technologies is increasingly shaping the digital transformation of the mining industry. IoT platforms allow for real-time monitoring of equipment conditions, environmental variables, and geotechnical parameters, supporting predictive maintenance and safety management across all stages of production [10, 11]. When enhanced with AI and ML algorithms, these systems facilitate data-driven decision-making, anomaly detection, and operational optimization, particularly in drilling, hauling, and ventilation control [11, 12]. Autonomous technologies, initially introduced through driverless haul trucks, are now applied in drilling, loading, and even orebody modeling, enabling continuous operation with minimal human intervention [12]. Moreover, the use of low-cost IIoT components such as Arduino-based sensor networks has shown potential for wider adoption in small and mid-scale mining operations, providing affordable solutions for monitoring and automation [13]. Despite infrastructure and cybersecurity challenges, the gradual implementation of these technologies is essential for improving productivity, reducing environmental impact, and enhancing worker safety. The integration of these systems into digital

twins enables real-time simulation and optimization of entire mine operations. A digital twin is a real-time, virtual replica of a physical mining operation that continuously receives data from IoT sensors embedded throughout the site. These systems allow operators to simulate scenarios, predict equipment failures, and optimize resource allocation with high precision. For instance, digital twins can model the impact of changes in drilling parameters or ventilation flows before implementing them on-site, thereby reducing risk and downtime. Coupled with remote monitoring, they enable centralized control centers to oversee multiple operations simultaneously, enhancing both responsiveness and safety in hazardous environments. According to the World Economic Forum (2024), companies adopting digital twins have reported up to 30% improvements in predictive maintenance accuracy and significant reductions in unscheduled stoppages [14].

2.5 Sustainable Extraction Technologies

Sustainable extraction technologies are redefining the environmental and economic framework of modern mining by minimizing chemical usage, water consumption, and ecological disturbance. A prominent example is bioleaching, which uses microorganisms to extract metals such as copper, gold, and uranium from low-grade ores. Unlike traditional smelting or cyanidation, bioleaching operates at ambient conditions and generates significantly less waste. Watling emphasizes that biohydrometallurgy has proven particularly effective in processing polymetallic ores where conventional methods are less selective and environmentally taxing [15]. Another emerging technique is electrokinetic in-situ recovery (EK-ISR), which applies low-voltage electric currents to mobilize and extract metals directly from the orebody without physical excavation, thereby preserving surface integrity and drastically reducing energy input. The U.S. Department of Energy's Critical Materials Institute identifies EK-ISR as a key innovation for extracting rare earth elements and other critical materials in a low-impact manner [16]. These technologies are increasingly supported by regulatory frameworks and industry commitments to reduce the carbon footprint and environmental legacy of mining operations.

3. RESULTS AND DISCUSSION

The reviewed technologies show a strong shift toward automation, efficiency, and sustainability in mining. NOx-free explosives offer safe and effective blasting without harmful emissions, addressing both operational and environmental concerns. Wireless initiation systems improve blast flexibility and significantly increase productivity by removing the constraints of wired detonators. Subsurface imaging with muon tomography provides real-time, high-resolution data critical for cave mining, improving ore recovery and geotechnical safety. When combined with digital twins, these systems allow predictive modeling and real-time decision support. IoT and AI enhance equipment monitoring and operational efficiency, while sustainable extraction methods reduce chemical use, energy consumption, and surface disturbance.

4. CONCLUSION

Technological innovation is transforming mining into a safer, smarter, and more sustainable industry. Key advancements in blasting, automation, monitoring, and extraction support higher productivity and reduced environmental impact. As ore bodies become deeper and more complex, continuous adoption of advanced, data-driven, and low-impact technologies will be essential to ensure the long-term viability and competitiveness of modern mining operations.

ACKNOWLEDGEMENTS

This work was financially supported by the Ministry of Science, Technological Development and Innovation of the Republic of Serbia, Contract No. 451-03-136/2025-03/ 200052.

REFERENCES

[1] M. Araos, I. Onederra., Cent. Eur. J. Energ. Mater., 14 (4) (2017) 759-774.
[2] G. Rarata, J. Smętek., High-Energetic Materials., 8 (2016) 56 – 62.
[3] Hypex Bio., Sustainable Blasting Solutions: Hydrogen Peroxide Based Explosives, https://www.hypexbio.com, accessed May 24, 2025.
[4] N. Ortega S.M., Case study: Productivity and operational continuity through wireless initiation technology Tech, Carmen de Anadacollo (Coquimbo, Chile)., Orica Blast Engineering., Chile 2024.
[5] J. Näsi., Case study: Double layer blind blast (DLBB) - Webgen™, Agnico Eagle Kittilä mine, Finland., Orica Blast Engineering 2024.
[6] B. Marriott., Case study: Increasing efficiency and safety through wireless blasting technology, Sierita mine, Arizona, United States of America., Orica Blast Engineering 2024.
[7] K. Deneka., Case study: Webgen™ enables safer undercutting in block caving operations, New Afton mine, British Columbia, Canada., Orica Blast Engineering 2023.
[8] Z.-X. Zhang, T. Enqvist, M. Holma, P. Kuusiniemi., Rock Mech. Rock Eng., 53 (2020) 4893–4907,.
[9] D. Schouten, N. Phillips, R. Merrill., Cosmic-ray Muon Tomography: Application in Block Cave Mapping and Modelling., Proceedings of 9th International Conference and Exhibition on Mass Mining, Kiruna, Sweden, 17–19 September 2024.
[10] N. Kyrylenko, V. Korobiichuk, V. Mamrai., IoT for Sustainable Mining: EU-UA Insights on Research, Education, and Business., Zhytomyr Polytechnic State University, Ukraine, 2023.
[11] F. Molaei, E. Rahimi, H. Siavoshi, S. G. Afrouz, V. Tenorio., A Comprehensive Review on Internet of Things (IoT) and its Implications in the Mining Industry., University of Arizona, USA, 2020.
[12] Z. Hyder, K. Siau, F. Nah., Use of Artificial Intelligence, Machine Learning, and Autonomous Technologies in the Mining Industry., Missouri University of Science and Technology, USA, 2023.
[13] I. Vojinović, M. Stojanović, D. Šabaz., IIoT in Mining – Potential Application of "Low-Cost" Sensors and the Arduino Platform., Proceedings - 55th International October Conference on Mining and Metallurgy, 15 – 17 October, Kladovo, Serbia, 2023., DOI: 10.5937/IOC24145V
[14] World Economic Forum., 13 Innovations Making the Mining and Metals Industry More Sustainable, 2024. https://www.weforum.org/stories/2024/11/13-innovations-making-the-mining-and-metals-industry-more-sustainable .
[15] H. R. Watling., Miner. Eng., 75 (2015) 1–17.
[16] U.S. Department of Energy., 2023 Critical Materials Assessment., Critical Materials Institute, Washington, DC, 2023. https://www.energy.gov/eere/amo/critical-materials-institute, accessed May 24, 2025.

The 56th International October Conference on Mining and Metallurgy
22-25 October 2025, Bor Lake, Bor, Serbia
www.ioc.tfbor.bg.ac.rs

DOI: 10.5937/IOC25106K Review paper

IMPLEMENTATION OF GROUND-MOUNTED AND FLOATING SOLAR PANELS IN MINES

Danka Kostadinović[1a], Dušan Ranđelović[2b], Zoran Marković[1c]

[1] Vinča Institute of Nuclear Sciences-National Institute of the Republic of Serbia, University of Belgrade, Mike Petrovića Alasa 12-14, 11000 Belgrade, Serbia
[2] Faculty of Civil Engineering and Architecture, University of Niš, Aleksandra Medvedeva 14, 18000 Niš, Serbia
[1a] dankak@vin.bg.ac.rs, 0000-0003-2890-4979
[2b] dusan.randjelovic@gaf.ni.ac.rs, 0000-0002-8542-224X
[1c]zoda.mark@vin.bg.ac.rs, 0000-0003-0553-3263

Abstract
The mining industry is one of the most difficult sectors to turn greener due to its significant environmental impact. Mines have high energy and water consumption due to the equipment, lighting, and ventilation required. The application of renewable energy in mines can contribute to clean energy production and a sustainable mining industry. This paper provides insights into solar projects in several active and abandoned mines worldwide and discusses potential benefits and challenges associated with this topic. Integrating renewable energy into the mining industry can reduce costs by 25% in mining operations and up to 50% for new mines. A great opportunity exists for the use of mine sites for hosting solar panels to recover the land, produce green energy, reduce greenhouse gas emissions, ensure energy independence, and create new jobs.

Keywords: *solar energy, mine, renewable*

1. INTRODUCTION

Solar energy helps achieve several Sustainable Development Goals (7-Affordable and Clean Energy, 13-Climate Action, and 9-Industry, Innovation and Infrastructure). Solar energy is one of the fastest-growing renewable energy in Europe and the world. Moreover, floating solar projects have attracted increased interest worldwide. Floating solar panels have higher efficiency than ground-mounted due to the water-cooling effect, light reflection from the water, and less dust deposition [1], [2]. Floating solar panels reduce water evaporation and excessive algae growth [3]. Attention should be paid to mitigating the environmental and ecological impact on the local communities after the closure of the mine. The mine reclamation implies land restoration and reuse of flooded areas or electrical facilities. Planning and development of solar power plants in mine areas can be a good way for the redevelopment of such areas. Surface coal mining usually causes the apparition of flooded areas (mining pit lakes) and coal waste heaps, while underground coal mining usually causes the apparition of flooded underground galleries with needs of dewatering pumps, abandoned buildings, infrastructure, and facilities to restore and also coal waste heaps [4]. Mine sites appear as suitable locations to deploy solar panels due to land use limitations and exiting power grid which reduces costs. The power grid in coal areas has usually high capacity, due to the existence of thermal power plants. The existing power network in such locations can accept new power generation from solar panels. The terrain in post-mining areas is slope, loose, and challenging for installation of traditional solar ground-mounted systems. Therefore, the geotechnical study of the terrain is necessary to obtain soil type, moisture content, and rock quality, which can affect the stability and performance of the mounting system panels [4]. Floating solar panels can be a viable solution in postmining areas where ponds can appear. Some best practice case examples of solar project installation in post-mining areas are shown below. The mining

industry has faced many challenges, such as rising demand, fluctuating energy prices, increasing energy consumption, and environmental concerns [5]. Power consumption in the mining industry generates 0.4 gigatons of CO_2 equivalent to greenhouse gas emissions each year [6]. Reducing greenhouse gases and carbon dioxide levels in mining areas due to renewable energy use improves the health of local communities [7]. Solar energy provides the mining industry with the opportunity to become more sustainable.

2. POTENTIAL IN SERBIA

Serbia added around 80 MW of solar in 2024, bringing total capacity above 200 MW, according to the Association of Renewable Energy Sources of Serbia. By 2028, the country plans to develop solar power plants of a total 1 GW across six locations. In the regions of "Kolubara" and the "Kostolac" coal basins the specific photovoltaic power output is 3.5 kWh/kWp while the global tilted irradiation is 4.3 kWh/m^2 [8]. The first solar power plant "Petka" will be built at the 15 ha of disposal side of the open pit mine "Ćirikovac" within the thermal power plant and coal basin "Kostolac". The installed power will be 9.75 MW, while the planned electricity production is 15.6 GWh annually. The 18,720 solar panels with individual power of 580 W and efficiency of 21% will be fixed under a 25° angle. The solar project includes 98 inverters and 10 transformers. This solar project will cost 8.5 million euros financed by Serbian state-owned energy producer "Elektroprivreda Srbije". In Serbia, the "Kostolac" wind farm with a power capacity of 66 MW is situated in coal mined-out areas and landfills. "Elektroprivreda Srbije" also plans to build two solar power plants (up to 9.9 MW each) on the coal ash dump sites of thermal power plants "Morava" and "Kolubara A". In 2029, it is planned to build a 150 MW solar power plant within the "Kostolac" mining basin at the ash and slag dump "Srednje kostolačko ostrvo" (270 ha) which will be closed in the future. Moreover, the construction of two solar power plants "Stiško Polje 1" and "Stiško Polje 2" (350 W and 500 MW) is planned. The Klenovnik location within "Kostolac" should host a 250 MW solar project.

3. CASE STUDIES

Solar energy is deployed in several abandoned mines in the USA, China, Finland, Poland, North Macedonia, and Germany as well as in several active mines in Australia, South Africa, Madagascar, Saudi Arabia, and Chile [5]. A 3 MW "Prapretno" solar power plant (Figure 1) was built in Slovenia in rehabilitated landfill that belonged to the shutdown coal-fired "Trbovlje" thermal power plant. The facility can be expanded to 13 MW. The 8.7 million tons of fly ash and slag from the thermal power plant were deposited on this site. The solar power plant has 6,748 solar panels. The power plant produces more than 3 GWh per year and can supply 800 households.

a) b)

Figure 1. a) Solar plant in rehabilitated landfill of defunct coal-fired power plant (Slovenia) [9]

b) "RWE Neuland" solar power plant (German) [10]

In the North Rhine-Westphalia region in Germany, two solar power plants, one of which has an integrated battery storage system, were built at the shoreline of "Hambach" opencast mining lake (Figure 1). The power plant provides 12 MW of electricity while the battery storage is configured

for a two-hour charging and supply cycle of 4.1 MW. The 14,500 households can be supplied with green electricity. A 5.3MW solar power project was completed in the "Northern Star's Carosue Dam" gold mine in Australia (Figure 2). This power plant produces green energy for the mine reducing carbon emissions by displacing diesel and natural gas use. In this location were installed solar panels with an innovative "Maverick" mounting system from the Australian company "5B" pattern that creates alternating east and west-facing panels. Power plant produce 10,480 MWh per year and avoid emission of 6,686 tonnes of CO_2 per year.

a) b)

Figure 2. a) The Carosue Dam solar plant in mine (Australia) [11]

b) Floating solar plant (Grafenwörth, Austria) [12]

Floating solar plants can be installed on abandoned coal pits and mining ponds. In 2023, the fourth largest floating solar plant (Figure 2) in Europe is launched in Austria. A 24.5 MW floating solar plant is located on the 14 ha water surface created by former sand and gravel pits of two lakes. The 45,304 solar modules were installed. They produce 26.7 GWh of electricity per year and supply around 7,500 households. In Chile, in 2019 solar plant was built over a "Tórtolas" tailing pond of the "Los Bronces" copper mine. The project (Figure 3) consists of 256 solar panels with the capacity to generate 86 kW. This solar plant will produce 150,000 kWh of electricity per year, reduce CO_2 emissions by 58 tonnes, and reduce water evaporation by 80%. This water savings will be available for recirculation in the mining process.

a) b)

Figure 3. a) Floated solar panels in a pond of "Los Bronces" mining plant (Chile) [13]

b) Floating solar plant in flooded abandoned coal mine (China) [14]

A 70 MW floating solar power plant (Figure 3) was built on the lake of an abandoned coal mine in the Chinese province of Anhui in 2018. This region is recognized by its coal industry. The explosion caused the mine to collapse and a lake was formed. The 148.4 ha of flooded area hosts 13 floating islands with total a of 52,000 float elements and 194,731 solar panels. Solar power plants can generate 40 MW of power to supply 21,000 homes and decrease CO_2 emissions by 150,000 tonnes per year. The Fraunhofer Institute of Solar Energy Systems has estimated that the potential of floating solar panels on pit lakes in abandoned lignite mines in Germany is 56 GW [15]. The biggest diamond mine "Diavik" in Canada is the first of its kind that hosts 6,620 solar panels that generate 4.2 GWh of electricity. In Madagascar in 2023, a 20 MW solar power plant with an 8.25 MWh battery storage system was constructed to power the titanium and zircon mine.

This plant reduces mine CO_2 emissions by 26,000 tonnes yearly. Deployment of renewable energy can reduce operating costs by 25% in mining operations and up to 50% for new mines [16].

4. CONCLUSION

The mining industry is one of the most difficult sectors to turn greener. Due to their remote locations, mine sites worldwide are heavily dependent on power generated from fossil fuels which becoming more expensive. Deployment of renewable energy in mining areas can be an effective solution to reduce this problem. A large number of mines worldwide are abandoned or closed. Promotion policies and projects have been launched to achieve environmental restoration of abandoned mines. Solar energy provides the mining industry with the opportunity to become greener and more sustainable. A multicriteria analysis should be conducted to determine the best solar technology due to the different types and features of mine sites.

ACKNOWLEDGEMENTS

The research was funded by the Ministry of Science, Technological Development and Innovation of the Republic of Serbia (Grant No. 451-03-136/2025-03/200017).

REFERENCES

[1] A. Amer, S. As'ad, S. Alsaqoor, H. Attar, J. Ecol. Eng., 24 (10) (2023) 324-339.
[2] A. Ghosh, Ocean Eng., 281 (2023), 115044.
[3] S. Wu et al., Discussion on the development of offshore floating photovoltaic plants, emphasizing marine environmental protection. Front. Mar. Sci., 11 (2024).
[4] Solar Photovoltaic deployment, Leveraging the competitive advantages of end of-life underground coal mines to maximise the creation of green and quality jobs (Project Acronym: GreenJOBS, Grant Agreement No 101057789)
[5] E. M. Valikandi, Y. Choi, J. Sustain. Min., 23 (4) (2024) 388-396.
[6] https://vivopower.com/news-and-insights/why-solar-power-in-mining-makes-perfect-sense
[7] M. Pouresmaieli, M. Ataei, A. Nouri, A. Barabadi, RESULTS ENG, 20 (2023) 101412.
[8] N. Pavlovic, D. Ignjatovic, T. Subaranovic, Mater. Proc., 5 (1) (2021) 50.
[9] https://balkangreenenergynews.com/slovenia-inaugurates-prapretno-its-biggest-solar-power-plant/
[10] https://www.rwe.com/en/the-group/countries-and-locations/hybrid-pv-storage-hambach/
[11] https://www.nomadic-energy.com/projects
[12] https://www.offshore-energy.biz/baywa-r-e-inaugurates-largest-floating-solar-plant-in-central-europe
[13] https://komonews.com/news/tech/chile-tests-floating-solar-panels-to-power-mine-save-water
[14] https://www.facebook.com/ChineseEmbassyInNigeria/posts/floating-solar-farm-a-fish-solar-farm-in-nanping-town-of-huaibei-city-east-china/982092317298955
[15] https://eurec.be/fraunhofer-ise-analyzes-potential-of-solar-power-plants-located-on-pit-lakes-in-former-lignite-mines/
[16] https://pt.atlasrenewableenergy.com/what-can-renewable-energy-do-for-the-mining-sector/

The 56th International October Conference on Mining and Metallurgy
22-25 October 2025, Bor Lake, Bor, Serbia
www.ioc.tfbor.bg.ac.rs

DOI: 10.5937/IOC25110P *Original scientific paper*

KINETIC MODELING OF OAK WOOD THERMAL DEGRADATION USING THE DISTRIBUTED ACTIVATION ENERGY MODEL (DAEM)

Milan Protić[1a], Ana Bijelić[1b], Miomir Raos[1c], Marjan Popović[2a]

[1] Faculty of Occupational Safety, University of Nis, Carnojevica 10A, 18000 Nis, Serbia
[2] Miphem, Matice Srpske 57e, 11000 Belgrade, Serbia
[1a] milanprotic@gmail.com, 0000-0003-4957-7882
[1b] ana.bijelic@znrfak.ni.ac.rs, 0000-0002-8073-1641
[1c] miomir.raos@znrfak.ni.ac.rs, 0000-0001-5586-0276
[2a] marjan@miphem.rs, 0009-0001-7621-9346

Abstract
This study investigates the thermal degradation behavior of oak wood using non-isothermal thermogravimetric analysis (TGA) under inert conditions. The Distributed Activation Energy Model (DAEM) was applied to model the pyrolysis kinetics, capturing the complex decomposition of lignocellulosic components. The pre-exponential factor, mean activation energy, and standard deviation were determined by fitting the DAEM to experimental data. The model showed excellent agreement with the observed TGA curve, achieving a high coefficient of determination ($R^2 = 0.9834$). The results highlight the dominance of hemicellulose degradation in early pyrolysis stages and demonstrate the suitability of DAEM for representing the thermal behavior of hardwood biomass. The derived kinetic parameters offer valuable input for reactor design and simulation in bioenergy applications.

***Keywords**: oak wood, pyrolysis, thermal degradation, DAEM, kinetic modeling, TGA*

1. INTRODUCTION

The increasing demand for renewable energy sources has positioned biomass, such as oak wood, as a critical component in the transition towards a sustainable energy future. Thermochemical conversion processes, including pyrolysis, gasification, and combustion, are the primary pathways for transforming this solid feedstock into valuable energy and chemical products. The design, optimization, and scaling of reactors for these processes depend fundamentally on a precise understanding of the material's thermal degradation behavior. In this context, kinetic studies are indispensable, as they provide the essential parameters (activation energy and pre-exponential factor) that quantify the reaction rates governing the decomposition process. These parameters serve as vital inputs for robust process modeling and simulation. However, modeling the kinetics of biomass is challenging. Oak wood is a heterogeneous composite of hemicellulose, cellulose, and lignin, each degrading through complex and overlapping reactions over a wide temperature range. Consequently, simpler kinetic approaches are often not adequate. Model-fitting methods, for example, which assume a single reaction mechanism for the entire process, are a significant oversimplification that can yield parameters with limited physical meaning. Model-free (isoconversional) methods, such as the Ozawa-Flynn-Wall (OFW) [1,2] and Kissinger-Akahira-Sunose (KAS) [3,4] models, represent an improvement as they do not assume a reaction model and can show how the effective activation energy varies with the extent of conversion. Despite this advantage, they typically do not provide a complete kinetic model capable of accurately reconstructing the original experimental data from the derived parameters. The Distributed Activation Energy Model (DAEM) provides a more physically realistic and powerful framework. DAEM presumes that the complex overall reaction is a superposition of countless independent, parallel, first-order reactions, where the activation energies are not a single value but follow a statistical distribution, typically Gaussian [5]. This approach elegantly captures the energetic

heterogeneity of the biomass components. The primary merit of DAEM is that it yields a complete and compact “kinetic triplet" (the pre-exponential factor (A), the mean activation energy (E_0), and the standard deviation of the distribution (σ)). This triplet constitutes a full kinetic model that can be used to accurately predict the material’s degradation behavior, offering a robust method for model validation [6]

Therefore, the aim of this study is to apply the DAEM to non-isothermal thermogravimetric analysis (TGA) data to determine the complete kinetic triplet for the pyrolysis of oak wood and to validate the model’s accuracy in describing its complex thermal degradation process.

2. EXPERIMENTAL

2.1 Material and Thermogravimetric Analysis (TGA)

The feedstock material used in this study was oak wood (Quercus sp.). The sample was prepared by drying at 105°C for 24 hours to remove moisture, then milling and sieving to obtain a particle size fraction of < 100 μm.

The thermal degradation behavior of the oak wood sample was investigated using a Perkin Elmer TGA 4000 (Norwalk, CT, USA). A sample mass of approximately 10 mg was placed in a ceramic crucible. The analysis was conducted under a nitrogen atmosphere with a constant flow rate of 20 mL/min to ensure an inert environment and prevent thermo-oxidative degradation. The sample was heated from 30°C to 900°C at a constant heating rate (β) of 5°C/min. The instrument recorded the sample mass as a function of time and temperature. The resulting data provides the basis for the kinetic analysis.

2.2 Kinetic Modeling: The Distributed Activation Energy Model (DAEM)

To describe the complex kinetics of oak wood pyrolysis, the Distributed Activation Energy Model (DAEM) was employed. The thermal degradation of lignocellulosic biomass, such as oak wood, is not a single-step reaction. It is a complex process involving the simultaneous and overlapping decomposition of its primary components: hemicellulose, cellulose, and lignin. Each of these components degrades through a multitude of chemical reactions. Simpler kinetic models, like single-step model-fitting methods, fail to capture this inherent complexity and can lead to kinetic parameters that lack true physical meaning. The DAEM provides a more physically realistic framework by assuming that the overall pyrolysis process consists of an infinite number of independent, parallel, first-order reactions. Each of these reactions is characterized by its own activation energy, *E*. The central concept of DAEM is that these activation energies are not discrete values but are continuously distributed around a mean value, following a statistical probability distribution function, $f(E)$. The overall conversion rate at any given time or temperature is the sum of the rates of all these individual reactions. The rate of a single first-order reaction can be described by the Arrhenius equation:

$$\frac{d\alpha}{dt} = A \cdot \exp\left(-\frac{E}{RT}\right) \cdot (1-\alpha)$$

where: α is the conversion fraction; t is time (s); A is the pre-exponential factor (s^{-1}); E is the activation energy (J/mol); R is the universal gas constant (8.314 J/mol·K) and T is the absolute temperature (K).

The conversion, α, is defined based on the mass loss measured during TGA:

$$\alpha = \frac{m_0 - m_t}{m_0 - m_f}$$

where m_0, m_t, and m_f are the initial, instantaneous, and final mass of the sample, respectively.

Derivation expressed here follow exposition provided in [5]. For a non-isothermal process with a constant heating rate, $\beta = dT/dt$, the rate equation can be integrated to find the conversion for a single reaction with activation energy E:

$$1 - \alpha(T, E) = \exp\left(-\frac{A}{\beta}\int_{T_0}^{T} \exp\left(-\frac{E}{RT'}\right) dT'\right)$$

To obtain the total conversion for the entire material, this expression is integrated over the distribution of activation energies, $f(E)$:

$$1 - \alpha(T) = \int_0^{\infty} \exp\left(-\frac{A}{\beta}\int_{T_0}^{T} \exp\left(-\frac{E}{RT'}\right) dT'\right) \cdot f(E) dE$$

It is commonly assumed, and has been shown to be effective for biomass, that the activation energies follow a Gaussian distribution:

$$f(E) = \frac{1}{\sigma\sqrt{2\pi}} \exp\left(-\frac{(E - E_0)^2}{2\sigma^2}\right)$$

This distribution is defined by two key parameters: the mean activation energy (E_0) and the standard deviation (σ). The standard deviation, σ, represents the width of the distribution and is an indicator of the energetic heterogeneity of the reacting components. A larger σ value implies a more complex material with a wider range of simultaneous reactions. The goal of the DAEM analysis is to determine the three kinetic parameters (A, E_0, and σ) that best describe the experimental TGA data. This "kinetic triplet" provides a complete and physically meaningful description of the thermal degradation process. In this work, the kinetic triplet was determined by fitting the DAEM equation to the experimental TGA data using a non-linear least-squares optimization algorithm implemented in Python. The algorithm minimizes the sum of the squared differences between the experimental conversion values (α_{exp}) and the model-predicted values (α_{pred}).

3. RESULTS AND DISCUSSION

The thermal decomposition of the oak wood sample under an inert nitrogen atmosphere was investigated using thermogravimetric analysis (TGA) and its derivative (DTG) curve. Figure 1 shows the TG and DTG curves, which represent the percentage of mass loss and the corresponding mass loss rate as functions of temperature. An initial mass loss of approximately 3% below 100 °C corresponds to moisture evaporation and the release of light volatiles. This is followed by a major decomposition stage between 235 and 360 °C, attributed to the breakdown of structural polymers. Above 360 °C, mass loss continues at a slower rate due to the pyrolysis of more stable compounds, resulting in approximately 11% char residue at 900 °C. The DTG curve exhibits a sharp peak around 355 °C (cellulose degradation), a shoulder near 285 °C (hemicellulose), and a broad tail above 400 °C (lignin), reflecting the complex nature of lignocellulosic pyrolysis. Hemicellulose decomposes first, overlapping with cellulose, while lignin degrades gradually starting around 200 °C. Cellulose and hemicellulose primarily contribute to volatile product formation, whereas lignin is mainly responsible for char production [7].

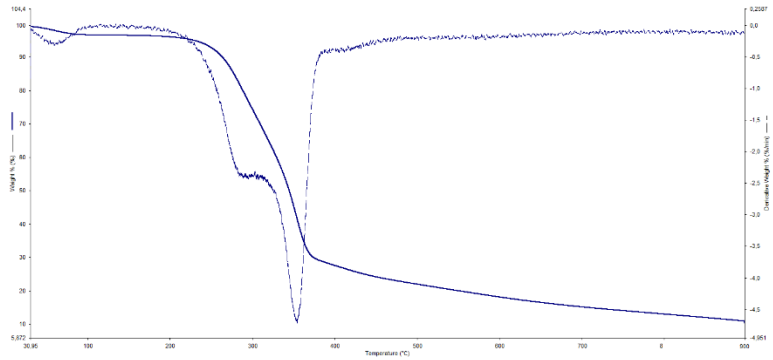

Figure 1. Thermogravimetric (TG, solid line) and derivative thermogravimetric (DTG, dashed line) curves of oak tree biomass obtained during thermal analysis in an inert nitrogen atmosphere at a heating rate of 5 °C/min.

The experimental data was fitted to the Distributed Activation Energy Model (DAEM) to obtain a comprehensive kinetic description of the pyrolysis process. The obtained kinetic parameters are: Pre-exponential Factor (A): 1.00×10^{8} s^{-1}; Mean Activation Energy (E_0): 131.23 kJ/mol and Standard Deviation (σ): 15.64 kJ/mol. The model yielded a coefficient of determination (R^2) of 0.9834, indicating a strong correlation between the experimental data and the DAEM-predicted curve, confirming the model's suitability for describing the overall process. The mean activation energy (E_0) of 131.23 kJ/mol is a particularly interesting result. This value is lower than the overall activation energy typically reported for the bulk pyrolysis of hardwoods, which often falls in the 170-200 kJ/mol range [6,8]. However, it is highly characteristic of the thermal degradation of hemicellulose. This suggests that the DAEM fit, while modeling the entire conversion curve, has identified the initial, lower-temperature decomposition of hemicellulose as the dominant energetic barrier controlling the onset and early stages of pyrolysis for this oak wood sample. The pre-exponential factor (A) is correspondingly lower than many values reported for bulk biomass pyrolysis. This is consistent with the kinetic compensation effect, a phenomenon where a lower activation energy is mathematically compensated by a lower pre-exponential factor to describe a given reaction rate. The combination of a lower E_0 and A accurately models the observed reaction, particularly in the crucial low-temperature regime. The standard deviation (σ) of 15.64 kJ/mol quantifies the width of the energy distribution. This value reflects the inherent heterogeneity of the material, accounting for the overlapping reactions of not just hemicellulose, but also the initial stages of cellulose and lignin degradation that occur within this energetic spectrum. The robustness of the derived kinetic triplet was validated by comparing the TGA curve predicted by the model against the experimental data across the entire temperature range. As shown in Figure 2, the DAEM curve closely follows the experimental data in the main pyrolysis region but slightly deviates above 400 C, where the model predicts a faster decline than observed experimentally.

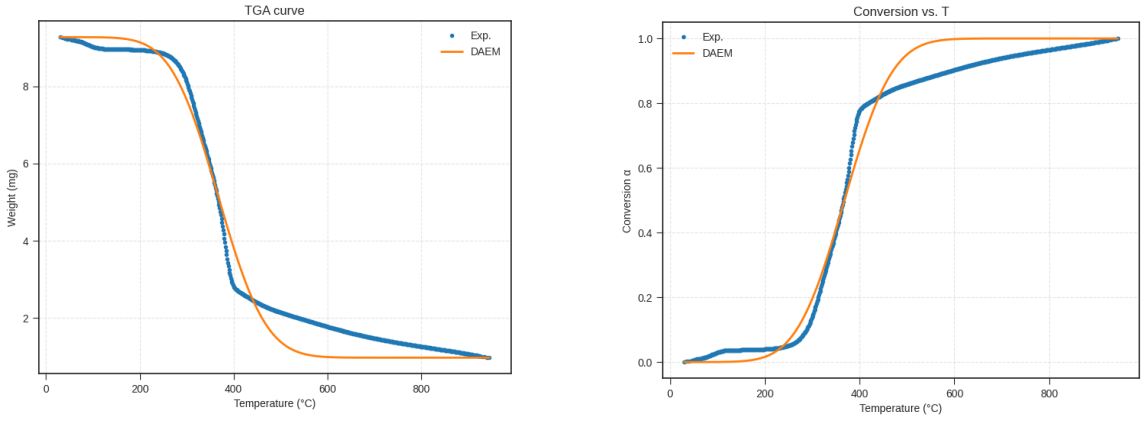

Figure 2. Weight lost curve (left) and conversion profile (right) for oak wood pyrolysis, illustrating model accuracy (experimental TGA curve (blue) and DAEM fit (orange))

The successful application of the DAEM provides a reliable kinetic model for oak wood pyrolysis. The obtained kinetic triplet serves as a compact and physically meaningful tool for predicting the material's thermal behavior.

Obtained DAEM parameters reveal that the oak sample was energetically easy to decompose, as its transformation during the early pyrolysis phase was largely influenced by less energetic routes. The main devolatilization window (ca. 235–360 °C) with a DTG peak near 355 °C and a lower-temperature shoulder around 285 °C aligns with hemicellulose–cellulose overlap. Residual char of ≈11% at 900 °C also falls in the expected hardwood range. To compare our results with those from the literature, we referred to an international round-robin study on beech wood [6]. That study, which fitted three parallel reactions (cellulose, hemicellulose, lignin), reported component activation energies of approximately 150 kJ mol^{-1} for hemicellulose and ca. 180 kJ mol^{-1} for cellulose. The standard deviations were moderate (ca. 8–15 kJ mol^{-1}), while lignin showed markedly higher and less stable values at high conversion. Cai et al. used a three-parallel DAEM and found peaks centered near 178 kJ mol^{-1} (xylan) and 210 kJ mol^{-1} (cellulose), with narrow σ for cellulose and broader distributions for lignin, reflecting component heterogeneity [8]. Taken together, our single-Gaussian E_0 = 131 kJ mol^{-1} is lower than the component-wise DAEM means commonly reported for hardwoods. This can be attributed to the model fit being most constrained by the initial, dominant mass loss from low-energy hemicellulose pathways, which are averaged with less-emphasized, high-temperature reactions in the single-distribution DAEM.

4. CONCLUSION

This study applied the Distributed Activation Energy Model (DAEM) to non-isothermal TGA of oak wood (Quercus sp.) and produced a compact kinetic triplet (A, E_0, σ) that accurately reconstructed the experimental TG curve. The parameters ($A = 1.00 \times 10^8$ s^{-1}, E_0 = 131.23 kJ mol^{-1}, σ = 15.64 kJ mol^{-1}) indicate that early, lower-barrier pathways dominate conversion under the present conditions. This is consistent with a prominent hemicellulose contribution in the main devolatilization regime. When contrasted with DAEM studies on hardwoods, our E_0 lies below typical literature means for component-resolved fits. This difference can be attributed to (i) the single-distribution representation and (ii) the emphasis on the major mass-loss window.

ACKNOWLEDGEMENTS

This work is supported by the Ministry of Science, Technological Development and Innovation of the Republic of Serbia pursuant to agreement № 451-03-137/2025- 03/200148 with the University of Niš, Faculty of Occupational Safety and ERASMUS+ Jean Monnet Module "Workplace and Process Safety in Next Generation Europe - Teaching for Learning".

REFERENCES

[1] J.H. Flynn, L.A. Wall, J. Polym. Sci. B., 4 (5) (1966) 323-328.
[2] T. Ozawa, Bull. Chem. Soc. Jap., 38(11) (1965) 1881-1886.
[3] H.E. Kissinger, Anal. Chem., 29(11) (1957) 1702-1706.
[4] S. Vyazovkin, Thermochim. Acta, 355(1-2) (2000) 155-163.
[5] K. Miura, ENFL, 9(2) (1995) 302-307.
[6] A. Anca-Couce, C. Tsekos, S. Retschitzegger, F. Zimbardi, A. Funke, S. Banks, N. Kienzl, Fuel, 276 (2020) 118002.
[7] M. Protic, A. Miltojevic, M. Raos, P. Đekić, Facta Univ., Work. Living Environ. Prot., (2020) 135-145.
[8] J. Cai, W. Wu, R. Liu, G.W. Huber, Green Chem., 15(5) (2013) 1331-1340.

The 56th International October Conference on Mining and Metallurgy
22-25 October 2025, Bor Lake, Bor, Serbia
www.ioc.tfbor.bg.ac.rs

DOI: 10.5937/IOC25115S *Review paper*

MONITORING TECHNIQUES FOR SUBSIDENCE INDUCED BY MINING OPERATIONS: A REVIEW

Dragan Šabaz[1a], Ivica Vojinović[1b], Miloš Stojanović[1c]

[1] Mining and Metallurgy Institute Bor, Alberta Ajnštajna 1, 19210 Bor, Serbia
[1a] dragan.sabaz@irmbor.co.rs, 0000-0002-1373-413X
[1b] ivica.vojinovic@irmbor.co.rs, 0009-0006-3658-6922
[1c] milos.stojanovic@irmbor.co.rs, 0000-0003-0044-5491

Abstract
Mining-induced ground deformation, particularly subsidence, poses a major challenge to the safety, efficiency, and environmental sustainability of underground mining operations. This paper presents a comprehensive review of modern monitoring techniques used to detect and analyze rock mass movements and surface deformations. The review highlights that no single method is universally sufficient; however, the combined application of multiple techniques significantly improves the reliability and accuracy of subsidence detection. Effective monitoring is crucial for early risk identification, informed decision-making, and ensuring the long-term stability of mining environments.

Keywords*: monitoring, subsidence, mine safety*

1. INTRODUCTION

Underground mining activities often cause complex geomechanical changes in the surrounding rock mass, with ground subsidence being one of the most critical consequences. This gradual or sudden downward movement of the surface, driven by stress redistribution and underground void formation, poses serious risks to infrastructure, safety, and the environment.

As global demand for mineral resources increases, mining operations are expanding in depth and scale, intensifying deformations in both underground and surface zones. Effective monitoring of subsidence has therefore become essential for mine planning, risk management, and environmental protection.

A variety of geodetic, geotechnical, and remote sensing techniques are now used to track ground movements in real time. These methods support early warning, validate numerical models, and inform operational decisions. Ultimately, subsidence monitoring plays a key role in ensuring safety, optimizing mining efficiency, and protecting both infrastructure and the environment.

2. EXPERIMENTAL

Monitoring ground subsidence during mining activities is a critical component of modern risk management and safety strategies in the mining industry. Various methods and types of instrumentation are employed based on proven technologies and best practices established across the sector. Given the dynamic nature of ground deformation, the selection and application of monitoring tools may evolve over time in response to changing conditions and new insights. The recommended measurement frequencies for different phases of mining are based on initial estimates of how subsidence is expected to develop. However, as data becomes available during operations, it is essential to adjust the monitoring frequency to accurately reflect actual subsidence behavior and ensure that the collected data represents the true ground conditions.

2.1.Interferometric synthetic aperture radar (InSAR)

InSAR (Interferometric Synthetic Aperture Radar) is a highly effective remote sensing technique for detecting and measuring ground subsidence caused by mining activities. This method involves analyzing multiple radar image pairs captured over time to generate interferograms, which depict phase differences between the images. Each pixel in the interferogram reflects the phase shift, and by comparing these shifts across different acquisition dates, ground displacement can be accurately calculated. The resulting deformation data is then overlaid on satellite imagery, allowing for precise identification of movement patterns and affected areas. InSAR is particularly valuable for continuous, large-scale monitoring of surface deformation, providing critical information for risk assessment and decision-making in active mining regions [1].

2.2.3D Laser scaning

3D laser scanning technology offers a fast and accurate method for monitoring ground deformation by capturing high-density, three-dimensional coordinate data of the terrain. Unlike traditional point-based measurements, this method collects comprehensive surface point cloud data, enabling detailed spatial deformation analysis without the need to place instruments in hazardous collapse areas. The system typically includes a laser scanner, power supply, PC, and tripod, and allows for high-speed data collection while minimizing equipment exposure to harsh field conditions. However, its effectiveness can be limited by terrain complexity and line-of-sight requirements, as accuracy decreases with distance and obstructions such as forests and buildings may hinder scanning in large or uneven mining areas [2].

2.3.Global positioning system (GPS)

The Global Positioning System (GPS) is a satellite-based technology that provides precise positioning, displacement, and timing data worldwide. Known for its high accuracy, reliability in all weather conditions, and global coverage, GPS is widely used in monitoring various geological hazards such as landslides, dam deformation, and ground fissures. In subsidence monitoring related to mining activities, GPS detects changes in the three-dimensional coordinates of surface points, including both vertical and horizontal displacements. However, GPS is limited to surface-level monitoring and cannot fully capture the spatial extent of subsidence. Additionally, the vertical accuracy and geodetic height obtained through GPS measurements may not always be directly applicable for detailed subsidence analysis [3].

2.4.Global navigation satellite system (GNSS)

The Global Navigation Satellite System (GNSS) encompasses all satellite navigation systems, including GPS (USA), GLONASS (Russia), Galileo (EU), BeiDou (China), and various augmentation systems like WAAS, EGNOS, and MSAS. GNSS-based deformation monitoring is an efficient and precise method for detecting ground or structural movement. High-precision GNSS positioning, through static or real-time kinematic (RTK) observations, enables the detection of displacement by comparing coordinates over time. The system calculates position using signal travel time from satellites, though atmospheric interference introduces pseudo-range errors. GNSS monitoring stations are composed of multi-frequency receivers, antennas, batteries, solar power modules, and communication units, offering flexible installation and real-time or periodic data acquisition. The technology is widely adopted due to its high accuracy, reliability, and ease of use in diverse monitoring applications [4].

2.5.Unmanned aerial vehicle (UAV)

Unmanned Aerial Vehicle (UAV) photogrammetry involves using aerial cameras mounted on drones to capture continuous images of a target area. These images are combined with ground control points to produce 3D models and topographic maps. The UAV system includes hardware

(flight platform, sensors, monitoring and support systems) and software (flight planning and data processing tools). Predefined flight parameters ensure efficient aerial surveys, while post-processing software corrects image distortions and generates accurate geospatial data. UAV photogrammetry is widely used for fast and detailed terrain mapping [5].

2.6. Borehole camera monitoring

Borehole camera monitoring technology is used to detect and assess the condition of mined-out areas by drilling boreholes from the surface or underground. A camera probe is inserted into the borehole to capture real-time images of rock fractures, voids, and caving boundaries. The technology provides visual and quantitative data on rock mass stability, roof thickness, and the geometry of mined-out spaces. It allows for early detection of roof collapse and helps monitor the progression of caving over time [6].

2.7. Time domain reflectometry (TDR)

Time Domain Reflectometry (TDR) is an electronic measurement technology originally developed for military applications and later widely used in the electronic and communication industries. It works by transmitting a step voltage pulse along a coaxial cable and detecting the reflections caused by impedance changes, which indicate faults such as breaks or deformations in the cable. When the cable is embedded in a cement mortar body, sudden tension and breakage reflect the location and timing of roof collapse. Although minor deviations may exist between the cable break point and the actual collapse location, the scale of the monitored rock mass ensures that TDR remains an effective method for assessing overall roof stability [7].

2.8. Microseismic monitoring

Induced mining activities can impact rock mass stability. Certain areas of a mine may become hazardous due to the progression of excavations and headings. As stress is redistributed, the rock mass responds with movement, which generates acoustic P and S waves either due to blasting or natural adjustments. To ensure production safety, microseismic monitoring systems are used in active mining zones to detect and analyze these movements [8].

2.9. Acoustic emission (AE)

Acoustic emission (AE) monitoring is a technique used to assess the stability of rock masses by detecting high-frequency elastic waves generated during rock deformation and failure. Unlike microseismic monitoring, which targets larger-scale rock movements, AE focuses on detecting signals from micro-fractures such as crystal breakage and intergranular cracking. These signals are converted into voltage and analyzed to determine fracture location, time, and energy. AE monitoring is applied to assess ground pressure in horizontal roadways and ore tunnel entrances, providing early warning for ground instability [9].

2.10. Electromagnetic radiation (EMR)

Electromagnetic radiation (EMR) monitoring is a method developed from the observation that electromagnetic anomalies often precede earthquakes. During the rock fracture process, significant EMR is emitted. By applying damage mechanics, statistical analysis, fractal theory, and supported by numerical simulations, laboratory tests, and field monitoring, researchers have identified the characteristics and mechanisms of EMR during rock failure. This method is used to predict dynamic events like pressure bumping. EMR monitoring assesses the extent and rate of coal and rock damage by analyzing signal amplitude and pulse count. It offers non-contact, easy-to-use monitoring, but its limitations include a small detection range and susceptibility to environmental and operational interference, as well as limited ability to accurately locate ground pressure events [10].

3. RESULTS AND DISCUSSION

This study presents a comprehensive review of current monitoring methods used in mining to assess ground stability and deformation. Each of the reviewed monitoring methods presents specific advantages and limitations, depending on the monitoring objectives, environmental conditions, and required spatial or temporal resolution. Remote sensing techniques like InSAR and UAV photogrammetry are effective for large-scale surface deformation detection but are limited in subsurface monitoring. In contrast, contact-based methods such as TDR, microseismic, and acoustic emission provide detailed information on internal rock mass behavior but require sensor installation. Electromagnetic monitoring shows promise for early warning of rock failure but is highly sensitive to external noise and has a limited detection range. GNSS/GPS and 3D scanning offer high precision for localized surface movement but are less suitable for detecting underground changes.

4. CONCLUSION

This study reviewed a range of modern monitoring technologies applied in geotechnical and mining environments. The analysis demonstrates that while each method offers valuable insights into rock mass behavior and ground stability, none is universally applicable under all conditions. Each technique carries inherent strengths and limitations related to spatial coverage, sensitivity, resolution, cost, and susceptibility to external disturbances. Effective monitoring in complex subsurface environments often requires a multi-method approach, where complementary technologies are integrated to provide more comprehensive and reliable data. Future developments should focus on enhancing data interpretation algorithms, improving sensor durability, and enabling real-time decision-making to increase safety and efficiency in underground operations.

ACKNOWLEDGEMENTS

This work was financially supported by the Ministry of Science, Technological Development and Innovation of the Republic of Serbia, Contract on realization and financing of the scientific research work of the Mining and Metallurgy Institute Bor in 2025, contract number: 451-03-136/2025-03/ 200052.

REFERENCES

[1] Y. Chen, G. Zhang, X. Ding, Z. Li., Journal of Geospatial Engineering, 2 (1) (2000) 3-21.
[2] L. Wang, Z. Shangjun, J. Chuang, L. Jingyua, J. Kegui, T. Chaoqun, W. Tao, G. Qing-biao, KSCE J. Civ. Eng., 25 (4) (2021) 1-14.
[3] L. Ge, C. Rizos, S. Han, H. Zebker. Proceedings of 10th FIG International Symposium on Deformation Measurements, 19–22 March 2001, Orange, California, USA.
[4] Y. Cai, Y. Jin, Z. Wang, T. Chen, Y. Wang, W. Kong, W. Xiao, X. Li, X. Lian, H. Hu., Int J. Coal. Sci. Technol., 10 (2023) 32.
[5] S. An, L. Yuan, Y. Xu, X. Wang, D. Zhou., Geomech. geophys. geo-energy geo-resour., 10 (2024) 57.
[6] M. Pak, R.P. Preston, C. Groccia, J. Taylor., Proceedings of Underground Mining Technology, 2017, Sudbury, Canada.
[7] K.M. O'Connor, E.W. Murphy., Int. J. Rock Mech. Min. Sci., 34 (3–4) (1997) 230.e1-230.e15.
[8] S. Prahastudhi, A. Muttaqi, E. Sitorus, E. Riyanto, J. Geosaintek, 4 (1) (2018) 23.
[9] M. Khoshouei, R. Bagherpour, MGPB., 2019, pp. 19-32.
[10] E. Wang, X. He, X. Liu, W. Xu, Saf. Sci., 50 (4) (2012) 885-893.

The 56th International October Conference on Mining and Metallurgy
22-25 October 2025, Bor Lake, Bor, Serbia
www.ioc.tfbor.bg.ac.rs

DOI: 10.5937/IOC25119M
Original scientific paper

GEOLOGICAL STRUCTURE AND GENESIS OF Zn, Pb DEPOSIT RIBNIK-ŠUPLJA STIJENA

Vladan Marinković [1a], Miroslava Maksimović [1b], Milenko Jovanović [1c], Željana Novaković[1d], Anđela Maričić[1e]

[1]Mining and Metallurgy Institute Bor, Alberta Ajnštajna 1, 19210 Bor, Serbia,
[1a] vladan.marinkovic@irmbor.co.rs, 0000-0002-2974-9563
[1b] miroslava.maksimovic@irmbor.co.rs, 0000-0002-5001-238X
[1c] milenko.jovanovic@irmbor.co.rs, 0000-0002-6757-4143
[1d] zeljana.novakovic@irmbor.co.rs, 0000-0001-5905-2874
[1e] andjela.maricic@irmbor.co.rs, 0009-0001-0142-4775

Abstract

The Zn Pb Ribnik deposit is the last in a series of Šuplja Stijena-Đudjeve vode-Paljevine-Ribnik deposits going from the northwest to the southeast, and it is connected to all of them by an adit, which connects all four deposits of the "Šuplje Stijene" ore field. The Šuplja Stijena ore field is located on the Ljubišnja mountain.

Geological investigations of lead and zinc mineralization in the Šuplja Stijena ore field were carried out over a long period of time, and resulted in the discovery of economically significant deposits: Šuplja Stijena (within which the East area, West area and Stara jama were opened), Đurđeve vode, Ribnik and Paljevine.

The geological structure of the Ribnik deposit consists of andesites that are in direct contact with the Ladinian limestones.

***Keywords**: Zn Pb deposit, andesites, hydrothermal polymetallic sulphide lead-zinc deposit of vein impregnation type.*

1. INTRODUCTION

The Zn Pb Ribnik deposit is the last in a series of Šuplja Stijena-Đudjeve vode-Paljevine-Ribnik deposits going from the northwest to the southeast, and it is connected to all of them by an adit, which connects all four deposits of the "Šuplja Stijena" ore field. The Šuplja Stijena ore field is located on the Ljubišnja mountain.

The lead and zinc mine Šuplja Stijena, and therefore the Ribnik deposit, are located in the area of the former mining settlement of Šula, which is connected to Pljevlja via Gradac.

The ore-bearing area of the Ljubišnja mountain, which includes the zinc and lead deposit Ribnik, is located in the northern part of Montenegro and the eastern part of Bosnia and Herzegovina.

Geological investigations of lead and zinc mineralization in the Šuplja Stijena ore field were carried out over a long period of time, and resulted in the discovery of economically significant deposits: Šuplja Stijena (within which the East area, West area and Stara jama were opened), Đurđeve vode, Ribnik and Paljevine [1 i 2].

Geological investigation in the Ribnik deposit began in 1955 with mining exploration works and lasted until 1960. In 1967, research was continued in the deeper parts of the deposit by drilling from the surface. Continuation of the geological investigation moved to the southeast using geophysical methods during 1970. In 1972, geophysical anomalies were verified by the drilling. In the period from 1987 to 2012, no geological investigation was carried out in the area of the Šuplja Stijena mine. New geological investigations in the Ribnik deposit were carried out in 2021

and 2022, and they were carried out by drilling as the basic method, namely inclined exploratory drillholes [1].

2. GEOLOGICAL STRUCTURE AND GENESIS OF THE DEPOSIT

The geological structure of the Ribnik deposit consists of andesites that are in direct contact with the Ladinian limestones [1] (Figures 1 and 2).

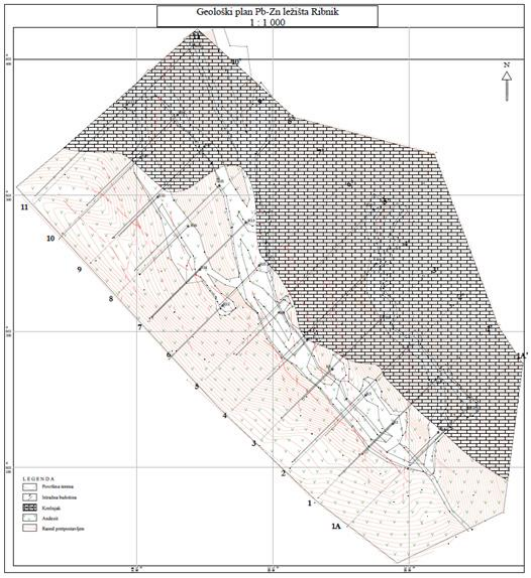

Figure 1. Geological plan of the Ribnik deposit

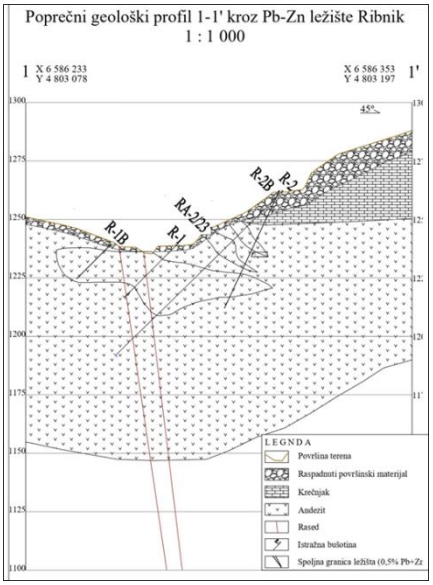

Figure 2. Transverse vertical cross section 1-1'

Geological loging of the core of exploration drillholes shows that the andesites are compact or crushed, partially silty to silty, oxidized.

Macroscopic examination of the samples showed that the andesites are light gray to greenish in color, predominantly green (on a fresh fracture). There are frequent deviations in color, and the appearance of thin crust in dark gray, light to dark brown color, which indicates that the andesites have been intensively hydrothermally altered [1 i 2] (Figure 3).

Some of the samples taken for ore microscopy were found to be kaolinite alteration, which was also defined by earlier research. Sulfide mineralization occurs in the form of bursts and accumulations that form nests and veins, and impregnations of pyritic +Pb-Zn mineralization that form vein forms and smaller lenses are visible on the andesites.

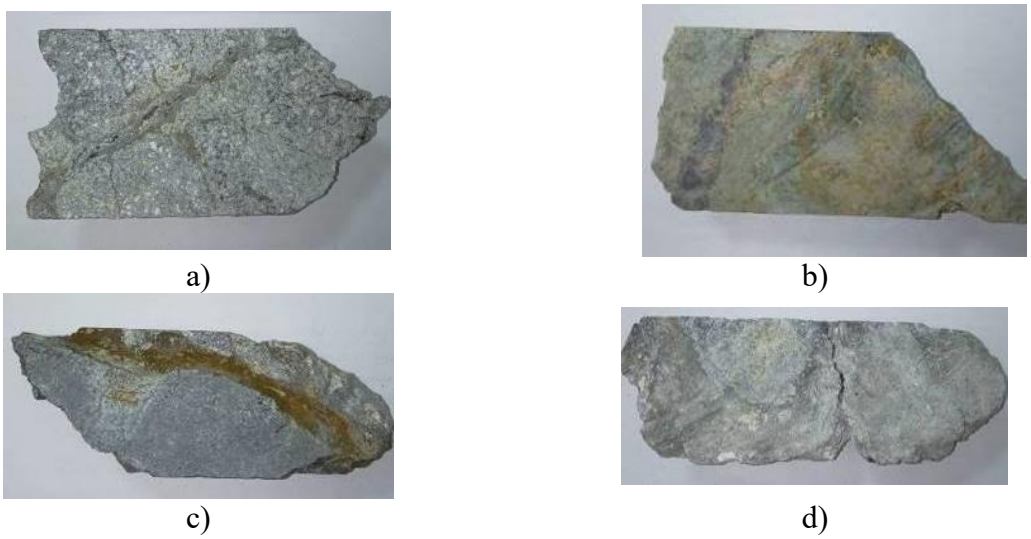

a) b)

c) d)

Figure 3. Characteristic appearance of andesite from the Ribnik deposit

a) hydrothermally altered andesite (drillhole R-18, interval 5.10-5.20 m, sample dimensions ~10×8×4 cm); b) hydrothermally altered andesite (drillhole R-14, interval 36.60-36.70, sample dimensions ~10×8×4 cm), c) hydrothermally altered andesite (drillhole R-4, 58.60-58.70, sample dimensions ~15×6×3 cm); d) intensive kaolinized andesite (drillhole R-8, 88.25-88.40, sample dimensions ~15×6×3 cm).

The limestone is crushed, cracked, broken, partly compact, silty, breccia. The color is dark to light gray (Figure 4).

Figure 4. Appearance of limestone from the Ribnik deposit

- On which ore mineralization (Pb-Zn +pyrite –chalcopyrite) is visible in the form of veins and wires (well R-16, interval 39.50-39.60, sample dimensions ~10×8×4 cm)

The ore body is represented by two ore vein with 5-6 apophyses that separate from the main veins. The direction of extension is northwest-southeast, with a dip of 50-60°. By loging of the exploratory drillholes, smaller lenses were also identified. The ore veins are interrupted in their southeastern part, probably cut by a fault [1 i 2].

The Ribnik deposit, which belongs to the "Šuplja Stijena" ore field, is a hydrothermal polymetallic sulphide lead-zinc deposit of the vein impregnation type.

Based on existing data, it is considered that the Ribnik deposit was created at shallower depths and at slightly lower temperatures than the other deposits in the "Suplja Stijena" ore field, as indicated by the frequent gel structures [1 i 2].

The parent rocks are built mainly of andesite-lava, in which the deposition of ore minerals was carried out in several phases (at least three) in the Triassic, but after the hardening of the volcanics, in which the largest amounts of mineral deposits known so far occur.

The deposits of the "Suplja Stijena" ore field were created in a very wide temperature interval of the hydrothermal area - from high temperature representatives to minerals that are the product of low temperatures [1 i 2].

3. CONCLUSION

On the basis of the results obtained by testing the physical and chemical processes that took place during the formation of "Šuplja Stijena" ore field, it can be concluded:

1. That regional pyritization, involving eruptive masses, was carried out at the time of propylitization;
2. That the oldest generation of pyrite is not directly related to the formation of the mine, but precedes this process;
3. That the main ore minerals of the "Šuplja Stijena" ore field were created in the temperature interval from 225 to 300°;
4. That the presence of sphalerite stars in chalcopyrite, in the deeper parts of the deposit, allows the interpretation of raising the limit of the formation temperature to the highest level of hydrothermal processes.

On the basis of the tests carried out, it is considered that the ore-bearing solutions were acidic in nature.

ACKNOWLEDGEMENTS

This work was financially supported by the Ministry of Science, Technological Development and Innovation of the Republic of Serbia, Contract on realization and financing of the scientific research work of the Mining and Metallurgy Institute Bor in 2025, contract number: 451-03-136/2025-03/ 200052.

REFERENCES

[1] M. Strahinjić, B. Vuković, R. Krsmanović, The project of detailed geological research of zinc and lead deposit "Ribnik".
[2] B. Vuković, R. Krsmanović, M. Strahinjić, Elaborate on the classification, categorization and calculation of zinc and lead reserves of the "Đurđeve vode" deposit, 31, 2019.

The 56th International October Conference on Mining and Metallurgy
22-25 October 2025, Bor Lake, Bor, Serbia
www.ioc.tfbor.bg.ac.rs

DOI: 10.5937/IOC25123R *Original scientific paper*

THE POSSIBILITY OF LONG-TERM EXPLOITATION OF COPPER ORE ON ORE BODIES OF THE MAJDANPEK COPPER MINE

Radmilo Rajković[1a], Vladan Marinković[1b], Daniel Kržanović[1c], Miomir Mikić[1d], Milenko Jovanović[1e]

[1] Mining and Metallurgy Institute Bor, Alberta Ajnštajna 1, 19210 Bor, Serbia
[1a] radmilo.rajkovic@irmbor.co.rs, 0000-0001-5905-6613
[1b] vladan.marinkovic@irmbor.co.rs, 0000-0002-2974-9563
[1c] daniel.krzanovic@irmbor.co.rs, 0000-0003-3841-8667
[1d] miomir.mikic@irmbor.co.rs, 0000-0001-7659-769X
[1e] milenko.jovanovic@irmbor.co.rs, 0000-0002-6757-4143

Abstract
The additional mining projects for the exploitation of deposits in the Northern area and the Southern area of the Majdanpek copper mine defined the optimal pits and the dynamics of exploitation. It is planned that the exploitation of ore at the North area open pit will take place until 2042 and at the South area open pit until 2037. This paper presents an overview of the remaining ore reserves with a proposal for further exploration, as well as preparatory activities for the period after the end of exploitation according to the existing project documentation.

***Keywords**: Majdanpek copper mine, ore reserves, long-term exploitation*

1. INTRODUCTION

The basic driving goal of any mining activity is the realization of profit, but in addition to this, the exploitation of mineral raw materials can be motivated by other more specific factors such as the maximum (or as large as possible) utilization of resources and the economic development of the local community where the project is located, etc. Profitable exploitation of mineral deposits requires a certain economic assessment and exploitation planning. Strategic long-term planning generally determines the production value of a mining company, by defining the basic elements of mining production: the limit content that defines the material as ore or waste, the exploitation limit of the surface mine, i.e. the total reserves of ore and tailings, the general development of mining works with the aim of meeting the qualitative and quantitative conditions of production, methods and technologies of exploitation and processing, production capacity, i.e. the life of the mine [1].

1.1 North area and South area open pits

In the Majdanpek copper mine, two open pit mines are in exploitation. The long-term planning of the development of open pit mines in the North area and South area is based on the valid Elaborations on reserves for these deposits. Copper ore resources and reserves in the studies were estimated based on the developed geological block models of deposits. Optimization and selection of the final contour of surface mines and planning and design of the phased development of works was carried out using Gemcom Gems and Whittle software, which in modern mining represent a standard for strategic planning and design of surface mines.

1.2 Optimization of open pit mines

The optimization was done using Whittle Four-XTM algorithms (LG 3D), whereby a series of open pit mine shells was determined based on different revenue factors with an iterative step of changing the price of the metal in relation to the base price. The optimization criterion is based on the determination of the maximum net present value of income (NPV), that is, the discounted

difference between income from metal sales and total operating costs [1-3]. The block models of the deposit were taken from the study on reserves. The limit copper content in the ore is 0.10%. Techno-economic parameters for optimization: annual ore mining capacity, utilization during exploitation and processing, costs and sales prices, are defined by the investor. The general end slopes of surface mines are defined on the basis of previous geotechnical tests.

Based on the optimization results, the exploitation life of the South area open pit mine is until 2042, and of the South area open pit mine until 2037 [4,5].

2. ORE RESERVES

2.1 Ore reserves of the North area deposit

Based on an overview of all available data on geological research carried out until the end of 2011, given that there is no data available on research of a later date, it can be concluded that the Nort area deposit has not been explored to a sufficient extent, primarily in terms of depth, and it is necessary to conduct additional geological research in order to increase the mineral raw material base of this deposit [6].

The remaining ore reserves of the Nort area deposit after 2042 in the 0.10% Cu contour are shown in Table 1.

Table 1 - Ore reserves that remain unmined after the end of exploitation in 2042

Ore	Volume, m^3	Volumetric mass, t/m^3	Reserves, t	Cu, %	Cu, t	Ag, g/t	Ag, kg
Cu	40.196.992	2,708	108.839.913	0,279	303.492	1,614	175.678
Pb+Zn+Cu	4.166	3,150	13.124	0,043	6	3,496	46

Ore	Au, g/t	Au, kg	S, %	S, t	Zn, %	Zn, t	Pb, %	Pb, t
Cu	0,202	21.976	2,640	2.873.226	0	0	0	0
Pb+Zn+Cu	0,331	4	4,841	635	1,207	158	0,173	23

The eastern rim of the Tenka 3 ore body remained "open", and in order to more precisely outline this orebody, further exploration of the eastern rim should be carried out. Further exploration also needs to be carried out in depth in the north direction, since the ore body remains undefined in that direction as well, as indicated by the results of the underground exploration works.

The central ore body is the largest ore body of the North area copper deposit. This ore body is very well contoured laterally, however its depth limit remains open.

The number of boreholes with which the deeper levels of this ore body were drilled is very small, amounting to 12 boreholes. It is suggested to explore the deeper levels of this ore body.

The Dolovi 1 ore body, like the Central ore body, is very well contoured laterally in the east-west direction, in the south direction its contour remains "open", so further exploration east and west of these boreholes is recommended.

2.2 Ore reserves of the South area deposit

Based on an overview of all available data on geological research carried out until the end of 2011, given that there are no available data on research from a later date, it can be concluded that the South area deposit has not been explored to a sufficient extent, primarily in terms of depth [7].

The remaining ore reserves of the South area deposit after 2037 in the 0.10% Cu contour are shown in Table 2.

Table 2 - Ore reserves that remain unmined after the end of exploitation in 2037

Ore	Volume, m^3	Volumetric mass, t/m^3	Reserves, t	Cu, %	Cu, t	Ag, g/t	Ag, kg
Cu	105.444.585	2,650	279.428.159	0,283	790.943	1,262	352.522

Ore	Au, g/t	Au, kg	S, %	S, t	Zn, %	Zn, t	Pb, %	Pb, t
Cu	0,157	43.919	1,170	3.269.098	0	0	0	0

A certain quantity of reserves is located below the -100 m level, which is why it is necessary to conduct additional geological research in order to outline the deposit below this level as well. Further explorations are also needed in the north, east, south and west.

2.3 Dynamics of geological research

The proposed geological research should be started as soon as possible. The geological research itself is preceded by the preparation of the Project of detailed geological research in the subject area. The project should not work for a period of time that is shorter than three research years. After the expiration of three research years, and the submission of the Final Report on the completed geological research, it is possible to extend the research two more times for two years, which would make the total time for geological research equal to seven research years. After the completion of the geological research, it is necessary to prepare the Elaboration on Resources and Reserves.

3. PREPARATORY ACTIVITIES FOR THE PERIOD AFTER 2037 AND 2045

After the investigations, it will be necessary to contour in the 0.1% Cu contour, since the parameters for the economic assessment have changed drastically since 2011. It is possible to have a positive economy even in this context of marginal content. It is necessary to perform a new calculation of reserves within the contour of the limit content of 0.1% Cu. It is also necessary to recategorize the reserves and create a new economic evaluation of the deposits with the evaluation parameters valid at that moment.

After additional geological research, depending on the results, three scenarios are possible for the period after 2037, i.e. 2045:

The first scenario is the continuation of surface exploitation with the expansion of the open pit mines according to plan and depth.

The second scenario is the underground exploitation of the Nort area deposit using one of the mass excavation methods, such as the Block caving method - self-destruction. Extraction of ore from the Nort area ore body would be carried out from the excavated area of the South area open pit mine. Underground exploitation of the South area deposit using the block crushing method, due to the low content of copper in the ore.

The third scenario is the closure of surface mines. For this scenario, it is necessary that every year, starting from the eighth year until the end of the exploitation period for the Nort area, that is, starting from the fourth year until the end of the exploitation period for the South area, the investor allocates funds for the process of closing surface mines. The project documentation would define the technology of closing surface mines, as well as the operation of the water treatment plant as long as it is necessary. For this scenario, it is necessary to prepare the North area and South Area open pits mine closure programs.

4. CONCLUSION

It is necessary to carry out geological investigations on the deposits of the Nort area and South area of the Majdanpek copper mine in order to determine the remaining ore reserves quantitatively, qualitatively and spatially.

Depending on the results of the geological investigations, three scenarios for the further development of the mine are possible, which would be decided after the feasibility study:

1. Continuation of surface mining exploitation;
2. Continuation of exploitation by underground excavation;
3. Closure of open pit mines.

For all three scenarios, the preparation of technical documentation is required in accordance with the legislation of the Republic of Serbia.

All the mentioned documentation, depending on the scenario, must be done and approved before the end of the exploitation according to the valid project documentation.

ACKNOWLEDGEMENTS

This work is financially supported by the Ministry of Science, Technological Development and Innovation of the Republic of Serbia, Agreement on the realization and financing of scientific research work of the Institute of Mining and Metallurgy Bor in 2025, registration number 451-03-136/2025-03/ 200052.

REFERENCES

[1] D. Kržanović, R. Rajković, M. Jovanović, M. Mikić, S. Milutinović, Strategic long-term planning of ore exploitation in the Majdanpek copper mine, Republic of Serbia, "Mining 2024" – 15. symposium with international participation – Sustainable development in energy and mining. May 21 - 24, 2024, Vrnjačka banja, Serbia. pages 53-61. ISBN 978-86-80420-12-7.

[2] D. Kržanović, R. Rajković, M. Jovanović, I. Jovanović, M. Mikić, The impact of an error in selection the pushbacks in the long-term planning of the open pit production on project quality, case study: open pit Veliki Krivelj, Bor, Serbia, Mining & Metallurgy Engineering Bor 1/2023; pages: 1-6; UDK: 622.271:681.325(045)=111; DOI: 10.5937/mmeb2301001K; ISSN: 2406-1395.

[3] D. Kržanović, R. Rajković, M. Jovanović, M. Mikić, S. Milutinović, Medium-term planning of copper ore exploitation at the open pit Veliki Krivelj near Bor, Serbia, The 53rd International October Conference on Mining and Metallurgy, ISBN 978-86-7827-052-9, pages 29-32, 2022.

[4] Additional mining project of the excavation of the Nort area open pit mine in the Majdanpek Copper Mine, Bor Institute of Mining and Metallurgy, 2024.

[5] Additional mining project for the excavation of the South area open pit mine in the Majdanpek Copper Mine for the annual ore mining capacity of 9.9 Mt/year, Bor Institute of Mining and Metallurgy, 2025.

[6] Elaborate on the reserves of the copper deposit "South area" and the deposit of polymetallic mineral raw materials (Zn-Pb-Cu) "Tenka" – South area near Majdanpek, June 30, 2011, Institute of Mining and Metallurgy Bor, 2011.

[7] Elaborate on the reserves of the copper deposit "South revir" - Majdanpek, as of January 1, 2011, Institute of Mining and Metallurgy Bor, 2011.

The 56th International October Conference on Mining and Metallurgy
22-25 October 2025, Bor Lake, Bor, Serbia
www.ioc.tfbor.bg.ac.rs

DOI: 10.5937/IOC25127M *Review paper*

THE GLOBAL IMPACT OF CLIMATE CHANGE ON THE MINING SECTORINSTRUCTIONS

Miomir Mikić[1a], Ivana Mikić[1b], Milica Međedović[2a], Radmilo Rajković[1c]

[1] Mining and Metallurgy Institute Bor, Alberta Ajnštajna 1, 19210 Bor, Serbia
[2] University of Kragujevac, Faculty of Natural Sciences and Mathematics, Radoja Domanovića 12, 34000 Kragujevac, Serbia
[1a] miomir.mikic@irmbor.co.rs, 0000-0001-7659-769X
[1b] ivana.mostarac@irmbor.co.rs, 0009-0006-2592-1916
[1c] radmilo.rajkovic@irmbor.co.rs, 0000-0001-5905-6613
[2a] milica.medjedovic@pmf.kg.ac.rs, 0000-0002-2024-2344

Abstract
Climate change poses a profound and multifaceted challenge to industries worldwide, and the mining sector is no exception. As a foundational industry for global development, providing essential raw materials for everything from infrastructure to renewable energy technologies, mining is simultaneously a significant contributor to greenhouse gas emissions and highly vulnerable to the physical impacts of a changing climate. Extreme weather events, shifting precipitation patterns, and rising temperatures directly affect mining operations, supply chains, and the communities in which mines operate. This paper explores the complex interplay between climate change and the global mining industry, examining its climate footprint, vulnerabilities, and the critical role it plays in both contributing to and adapting to a changing world. It will also highlight the need for proactive strategies and international cooperation to foster a more resilient and sustainable mining sector globally.
***Keywords**: climate change, mining, globally*

1. THE CLIMATE FOOTPRINT OF MINING

The mining sector is inherently energy-intensive, making it a significant contributor to global greenhouse gas (GHG) emissions. The total carbon dioxide (CO2) emissions from mining operations vary considerably depending on the type of resource being extracted and the specific mining processes employed, such as open-pit versus underground mining. For instance, coal mining, while providing a substantial portion of the world's primary energy demand, contributes to global warming not only through the combustion of coal but also through fugitive emissions released during the extraction process.

Historically, mining has relied heavily on fossil fuels for power generation, transportation, and heavy machinery. As readily accessible, high-grade ore deposits become scarcer, mining operations are forced to extract from deeper and lower-grade reserves. This trend necessitates increased energy consumption, greater water usage, and the generation of larger volumes of mine waste, thereby expanding the industry's overall climate footprint [1].

Recent data indicates that the mining sector continues to face pressure to reduce its emissions. While the provided 2016 report highlights efforts by some companies to trap fugitive emissions and explore renewable energy options, particularly in regions like Chile, the overall progress in decarbonization remains a critical area of focus. The push for electrification of mining equipment, adoption of renewable energy sources (solar, wind, and geothermal), and improvements in energy efficiency are key strategies being pursued to mitigate the sector's climate impact. However, the scale of these efforts needs to accelerate to align with global climate targets.

2. VULNERABILITY OF THE MINING INDUSTRY TO CLIMATE CHANGE

The mining industry is particularly vulnerable to the direct and indirect impacts of climate change due to its inherent dependence on natural environmental conditions and its fixed geographical locations. Unlike some other industries, mining operations cannot simply relocate if environmental conditions become unfavorable. The long-term viability of mining operations is directly tied to factors such as a habitable climate, access to water resources, and supporting infrastructure.

Climate change manifests its impacts on mining through various pathways:

- Water-related impacts: This includes increased frequency and intensity of droughts, floods, cyclones, and storms. Droughts can lead to water scarcity, impacting ore processing, dust suppression, and even causing temporary shutdowns. Conversely, extreme rainfall and floods can inundate open-pit mines, damage infrastructure, and lead to the overflow of tailings dams, releasing contaminated materials into the environment. The 2010-2011 floods in Queensland, Australia, for instance, caused significant losses to the coal mining sector, highlighting the economic vulnerability to such events [2,3].
- Heat-related impacts: Rising temperatures can lead to heat stress for workers, increasing health and safety risks and potentially reducing productivity. Bushfires, often exacerbated by hotter and drier conditions, can also threaten mining sites and infrastructure.
- Sea-level rise: For coastal mining operations, rising sea levels pose a direct threat of inundation and increased saltwater intrusion, affecting freshwater sources and infrastructure.

Many of the world's largest mining operations are located in remote, climate-sensitive regions, such as the Gobi Desert in Mongolia or the Atacama Desert in Chile. These regions are already experiencing significant climatic shifts, making mining operations there increasingly precarious. The complex interplay of these impacts can create second-order effects, making it challenging for the industry to ascertain and address the full scope of risks in the short term [4].

Beyond operational risks, climate change also poses significant reputational risks to mining companies. Mismanagement of climate-related impacts, such as tailings dam failures due to extreme flooding or competition over scarce water resources with local communities during droughts, can severely damage a company's social license to operate and investor confidence. This growing awareness of climate vulnerability is pushing the industry to seek adaptive measures to maintain functionality and longevity.

3. MINING AND DEVELOPMENT IN A CHANGING CLIMATE

The extractives sector plays an indispensable role in the economic development models of many regions and countries, particularly in developing and emerging economies. It often serves as a primary pathway for poverty alleviation and economic growth, offering significant potential for quick returns on investment. However, for these positive effects to materialize, mining operations must adhere to international performance standards and operate within robust regulatory environments.

In the absence of such preconditions, mining can bring a suite of enduring costs and impacts throughout its lifecycle. These challenges extend beyond disciplinary boundaries, encompassing social, cultural, environmental, economic, and institutional concerns that fundamentally influence sustainable development pathways. Key impacts often include changes to labor patterns, influx of transient workforces, income inequality, conflicts, human rights issues, inequitable redistribution of profits, loss of ancestral lands, and gendered effects [5,6,7].

Crucially, there is a recognized knowledge gap regarding the specific connection between climate change and natural resource development in developing countries, which are projected to experience greater vulnerability to climatic shifts. While mining offers a significant development

pathway, it also carries the potential to exacerbate changes in natural environmental conditions, for example, by restricting access to land and water. This can disrupt traditional, resource-dependent livelihoods such as herding, agriculture, and fisheries.

Furthermore, many developing nations already face challenges with limited technical and financial resources for climate adaptation. This makes it even more critical to understand and integrate the complex interlinkages between the extractives sector and climate change into policy and strategic decision-making. The case study of Mongolia, for instance, highlights how a rapidly expanding, water-intensive mining industry in a climate hotspot experiencing reduced rainfall can intensify competition over already compromised water sources, potentially leading to long-term conflicts between various actors [8,9]. This underscores the need for responsible mining practices that consider both economic development and environmental sustainability in the face of climate change.

4. SUPPLY CHAIN RISKS AND SECURITY OF SUPPLY

Global supply chains for minerals and metals are increasingly exposed to climate-related risks, impacting both developed and developing nations. Countries heavily reliant on the mining sector for their development, as well as industrialized nations dependent on a secure and stable supply of resources, share these vulnerabilities. Climate change acts as a multiplier effect on existing supply chain risks, adding complexity and intensifying or altering existing threats.

These risks include disruptions caused by extreme weather events, such as floods, droughts, and storms, which can halt production, damage infrastructure, and impede transportation. Beyond physical disruptions, political and policy reactions to climate risks, such as export bans or tariffs aimed at promoting domestic supply, can also destabilize global supply chains. The volatility in commodity prices, while influenced by various factors, can be exacerbated by climate-induced supply shocks.

Resource extraction is becoming more challenging and expensive due to declining ore grades and the increasing necessity to operate in more fragile regions, which in turn elevates political risks. These factors contribute to supply inelasticity, making it harder to quickly increase supplies in response to demand, thereby driving price volatility [10].

Factors such as regulations and policies, prices, tariff and non-tariff trade barriers, development levels and changing life styles are usually not considered (European Commission 2014b), figure 1.

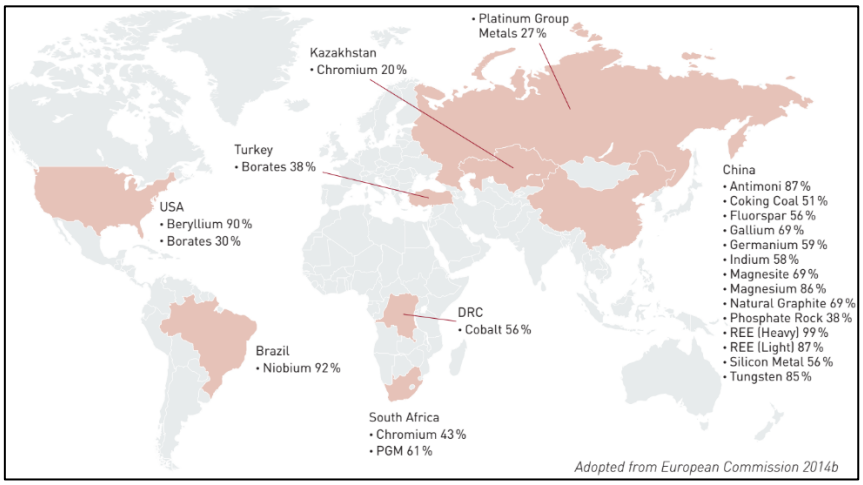

Figure 1. EU critical minerals: World primary supply of the 20 critical raw materials

In addition, these methodologies often do not take into account whether a mining operation is located in regions with increased seismic risks, water stress or ecologically sensitive regions [11].

The same is true for climate change and how it will impact individual mining areas, which in most cases is not included in criticality assessments [12].

Efforts are underway internationally to improve governance around mineral supply chains, particularly concerning high-risk and conflict areas. However, there has been limited systematic integration of a 'climate' focus into these discussions. Given that a significant and growing proportion of extractive resources originate from developing nations—which often lack adequate resources for climate adaptation—there is an urgent need for robust measures to ensure climate-resilient supply chains. This includes improved due diligence mechanisms that assess potential impacts from climatic changes across all stages of the supply chain, from mineral extraction to product manufacturing and distribution.

5. CONCLUSION

The global mining sector stands at a critical juncture, facing unprecedented challenges and opportunities presented by climate change. While mining is essential for providing the raw materials necessary for modern society and the transition to a low-carbon economy, its operations are simultaneously a significant source of greenhouse gas emissions and highly susceptible to the physical impacts of a changing climate. Extreme weather events, water scarcity, and rising temperatures pose direct threats to operational continuity, supply chain stability, and the social license to operate.

Addressing these complex interdependencies requires a multi-faceted approach. Decarbonization of mining operations through the adoption of renewable energy, improved energy efficiency, and technological advancements is crucial to mitigate the sector's climate footprint. Simultaneously, robust adaptation strategies are necessary to enhance the resilience of mining infrastructure and operations to the inevitable impacts of climate change. This includes advanced water management systems, climate-proof infrastructure design, and effective disaster preparedness.

Furthermore, the role of foreign policy and international cooperation is paramount in fostering responsible mining practices globally. Integrating climate risks into critical minerals policies, improving social and environmental standards across the extractive sector, and supporting national and regional dialogues on sustainable mining are vital steps. By proactively addressing climate change, the mining industry can not only safeguard its future but also contribute significantly to global efforts in building a more sustainable and resilient world.

ACKNOWLEDGEMENTS

The authors are grateful to the Ministry of Science, Technological development and Innovation of the Republic of Serbia for financial support according to the contract with the registration number 451-03-136/2025-03/ 200052.

REFERENCES

[1] G.M. Mudd, Z. Weng, R. Memary, S.A. Northey, D. Giurco, S. Mohr, L. Mason, 2012: Future greenhouse gas emissions from copper mining: assessing clean energy scenarios. Study prepared for CSIRO Minerals Down Under Flagship by Monash University and Institute for Sustainable Futures, UTS.
[2] QFCI [Queensland Floods Commission of Inquiry] 2012: Final report, Volume 2. Brisbane, Australia.
[3] ABARES [Australian Bureau of Agricultural and Resource Economics and Sciences] 2011: The impact of recent flood events on commodities: Special report. Canberra: Australian Bureau of Agricultural and Resource Economics and Sciences.
[4] R. Gledhill, D. Hamza-Goodacre, L.P. Low, 2013: Resilience: A journal of strategy and risk. Retrieved 11 December 2015 from http://www.pwc.com/gx/en/governance-risk-compliance-consulting-services/resilience/publications/pdfs/issue3/business_not_as_usual.pdf.
[5] F. Solomon, E. Katz, R. Lovel, Res. Policy 33 (2008) 142-149.

[6] C. Hill, K. Newell, 2009: Women, communities and mining:the gender impacts of mining and the role of gender impact assessment. Carlton: Oxfam Australia
[7] D. Kemp, C.J. Bond, D.M. Franks, C. Cote, J. Clean. Prod. 18:15 (2011) 1553-1562.
[8] C. Upton, 2012: Mining, resistance and pastoral livelihoods in contemporary Mongolia. In: Dierkes, J. (ed.): Change in Democratic Mongolia: social relations, health, mobile pastoralism, and mining. Leiden: Brill, pp. 223-248.
[9] J. Wang, D.G. Brown, A. Agrawal,: Glob. Environ. Change, 23 (6) (2013) 1673-1683
[10] World Bank 2014: Commodities Market Outlook October 2014.Retrieved 11 December 2015 from http://www.worldbank.org/content/dam/Worldbank/GEP/GEPcommodities/commodity_markets_outlook_2014_october.pdf.
[11] R. Vogt, 2015: Ökologische Effekte bei der Gewinnung abiotischer Rohstoffe in Deutschland und weltweit.Conference: Ressourcen schonen – biologische Vielfalt erleben, Frankfurt/Main, 25.03.2015.
[12] L. Mason, D. Giurco, 2013: Climate change adaptation for Australian minerals industry professionals. Final Report. National Climate Change Adaptation Research Facility. Retrieved 7 June 2015 from http://www.nccarf.edu.au/sites/default/files/attached_files_publications/Mason_2013_Climate_change_adaptation_minerals_industry_professionals.pdf.

The 56th International October Conference on Mining and Metallurgy
22-25 October 2025, Bor Lake, Bor, Serbia
www.ioc.tfbor.bg.ac.rs

DOI: 10.5937/IOC25132M Review paper

THE IMPACT OF CLIMATE CHANGE ON MINING IN SERBIA, AN OVERVIEW

Miomir Mikić[1a], Daniel Kržanović[1b], Milenko Jovanović[1c], Sandra Milutinović[1d], Ivana Mikić[1e]

[1] Mining and Metallurgy Institute Bor, Alberta Ajnštajna 1, 19210 Bor, Serbia
[1a] miomir.mikic@irmbor.co.rs, 0000-0001-7659-769X
[1b] daniel.krzanovic@irmbor.co.rs, 0000-0003-3841-8667
[1c] milenko.jovanovic@irmbor.co.rs, 0000-0002-6757-4143
[1d] sandra.milutinovic@irmbor.co.rs, 0000-0003-0146-8636
[1e] ivana.mostarac@irmbor.co.rs, 0009-0006-2592-1916

Abstract
This paper aims to analyze the impact of climate change on the mining sector in Serbia, with a particular focus on the consequences of droughts and floods, as well as broader ecological implications. Through a review of existing data and research, the key challenges facing mining will be presented, as well as potential adaptation and mitigation measures that can contribute to reducing the sector's vulnerability to climate change.

***Keywords**: climate change, mining, ecology.*

1. INTRODUCTION

Climate change represents one of the greatest global challenges of the 21st century, with far-reaching consequences for all sectors of the economy and society. The Republic of Serbia, as a country located in a region particularly vulnerable to climate change, is facing increasingly pronounced extreme weather events. In recent decades, a significant increase in average temperatures, an increased frequency of heatwaves, and changes in precipitation patterns resulting in more frequent droughts and more intense floods have been recorded. These changes directly affect natural resources and ecosystems, as well as key economic sectors, including mining.

Mining in Serbia has a long tradition and represents an important segment of the national economy, contributing to the gross domestic product and employment. However, mining activities are inherently associated with significant environmental impacts, including air, water, and soil pollution, as well as landscape degradation. In the context of climate change, these impacts become even more complex, as climate extremes can exacerbate existing risks and create new challenges for the sustainability of the mining sector. Understanding and adapting to these changes are crucial for minimizing negative consequences and ensuring the long-term sustainability of mining in Serbia.

2. CLIMATE CHANGE IN SERBIA: AN OVERVIEW

The Republic of Serbia is facing significant climate changes that are manifested through multiple aspects. Analyses of climate data for the period 2001–2020, compared to the reference period 1961–1990, show a clear warming trend. The average surface air temperature in Serbia has increased by 1.4 °C, while in the more recent period (2011–2020), this increase is even more pronounced, reaching 1.8 °C. Particularly concerning is the increase in the average maximum temperature during the summer months (June-July-August), which in the period 2011–2020 reached as much as 2.6 °C compared to the reference period. Projections indicate a continuation

of this trend, with an expected temperature increase of about 2.2 °C by 2040, 3.1 °C by 2060, and according to the RCP8.5 scenario, even 5.8 °C by the end of the century (2100).

Parallel to the temperature increase, Serbia is also experiencing an increased frequency and intensity of heatwaves. In the period 2011–2020, the average number of heatwaves per year increased by three compared to the reference period. It is predicted that by 2040, there will be 4-5 more heatwaves annually, while by the end of the century, according to the RCP8.5 scenario, the average number of heatwaves could reach 8-10 annually, which would mean about two months of extremely hot weather. These changes have a direct impact on human health, agriculture, water resources, and energy.

Regarding precipitation, changes in its regime have been observed, although annual precipitation sums do not show significant changes. However, a decrease in precipitation during the summer months (JJA season) was recorded, with an 8% drop in the period 2011–2020 compared to the reference period. At the same time, the frequency and intensity of extreme precipitation have increased, leading to more frequent and devastating floods. Droughts, as a consequence of reduced summer precipitation and rising temperatures, are becoming increasingly pronounced, threatening water resources, river flows, and groundwater. These climate changes create complex challenges for all sectors, including mining, which is particularly sensitive to changes in water availability and extreme weather events.

3. THE IMPACT OF CLIMATE CHANGE ON THE MINING SECTOR IN SERBIA

The mining sector in Serbia, although vital to the economy, faces significant challenges due to climate change. These challenges are manifested through direct and indirect impacts of extreme weather events, such as droughts and floods, as well as through the exacerbation of existing environmental problems associated with mining activities[1].

Droughts and Water Scarcity

Mining is an industry that requires significant amounts of water for various processes, including ore processing, equipment cooling, and dust suppression. Increasingly frequent and intense droughts in Serbia directly threaten the availability of water resources necessary for mining operations. Water scarcity can lead to reduced production capacities, increased operating costs, and even temporary mine closures. In addition, droughts affect groundwater levels and river flows, further complicating water supply for mines and surrounding communities. Studies show that prolonged droughts also affect hydropower capacities, which can indirectly impact mining, an energy-intensive industry that relies on a stable electricity supply.

Floods and Their Consequences

On the other hand, the increased frequency of extreme precipitation and floods poses a serious threat to mining facilities. Open-pit mines are particularly vulnerable to floods, which can lead to the inundation of the entire pit, production interruptions, and significant material damage [2]. Examples from 2014, when floods hit Serbia, showed that mine tailings were affected, with thousands of tons of mining waste spilling into the environment. This not only represents an ecological catastrophe but also causes long-term pollution of soil and watercourses. Floods can also damage mine infrastructure, including roads, bridges, and energy systems, further hindering recovery and resumption of operations [3].

Broader Environmental Impacts and Climate Change

The mining sector in Serbia is recognized as one of the largest polluters of air, water, and soil. Mineral extraction generates huge amounts of waste, pollutes natural habitats, and releases toxic substances into the environment [4,5]. Climate change exacerbates these negative impacts. For example, in conditions without wind or with reduced precipitation, pollutants from mines remain

in the atmosphere longer, worsening air quality. Increased soil erosion due to extreme precipitation can lead to the spread of pollution from tailings. Even so-called 'green mining,' such as lithium extraction, carries significant environmental risks, including high water consumption and the use of toxic chemicals, which is particularly problematic in the context of increasingly severe droughts. The increase in extreme weather events due to climate change makes mining operations inherently riskier, requiring comprehensive adaptation and mitigation measures.

Adaptation and Mitigation Measures in the Serbian Mining Sector

Addressing the challenges posed by climate change in the Serbian mining sector requires a comprehensive approach that includes adaptation and mitigation measures. Adaptation refers to adjusting existing mining operations and infrastructure to unavoidable climate changes, while mitigation involves reducing greenhouse gas emissions and minimizing the environmental footprint of mining.

Water Resource Management

Given the increasing frequency of droughts and floods, efficient water resource management becomes imperative. This includes implementing advanced monitoring and forecasting systems for water levels, optimizing water consumption in mining processes through recycling and reuse, and rainwater harvesting. The construction and maintenance of adequate drainage systems and dams around mines and tailings facilities are crucial for preventing flooding and the spread of pollution during extreme precipitation. Also, considering alternative water sources and wastewater treatment technologies can significantly reduce the vulnerability of mines to water scarcity.

Reclamation and Remediation

Reclamation of degraded mining areas is an important adaptation and mitigation measure. Biological reclamation, which includes afforestation and greening of tailings, contributes to soil stabilization, erosion reduction, and soil quality improvement. The selection of plant species resistant to drought and high temperatures is crucial for the success of these projects in changing climate conditions. Remediation of old and abandoned mines and landfills is also necessary to prevent further pollution and reduce the risks of landslides and spills of toxic substances, especially during intense precipitation [6]. Examples of tailings reclamation in Bor show the potential for reducing pollution and contributing to the fight against climate change through carbon dioxide absorption.

Emission Reduction and Energy Efficiency

Mitigation measures in mining include reducing greenhouse gas emissions. This can be achieved through transitioning to cleaner energy sources, such as renewable energy (solar, wind), to power mining equipment and facilities. Increasing energy efficiency in all phases of the mining process, from extraction to processing, also contributes to reducing fossil fuel consumption and emissions. The implementation of new technologies that reduce dust and harmful gas emissions, as well as improving air ventilation and filtration systems, directly impact air quality and reduce health risks for workers and local communities.

Integrated Planning and Cooperation

Successful adaptation and mitigation require integrated planning at national and local levels. This involves incorporating climate risks into mining development strategies, spatial plans, and environmental impact assessments. Cooperation among mining companies, scientific institutions, government bodies, and local communities is crucial for knowledge exchange, developing innovative solutions, and effective implementation of measures. Raising awareness about the importance of climate change and its impact on mining, as well as educating workers and the public, contributes to creating a more resilient and sustainable mining sector in Serbia.

4. CONCLUSION

Climate change poses an increasing challenge for the mining sector in Serbia, bringing with it risks from extreme weather events such as droughts and floods, which directly threaten mining operations and infrastructure. In addition, climate extremes exacerbate existing environmental problems related to mining, such as water, air, and soil pollution. Rising temperatures and changes in precipitation patterns require an urgent and comprehensive response to ensure the sustainability of this vital economic sector.

Successful adaptation and mitigation in the Serbian mining sector involve implementing a range of measures, including efficient water resource management, reclamation and remediation of degraded areas, reduction of greenhouse gas emissions, and increased energy efficiency. Integrated planning, cooperation among all relevant stakeholders, and raising awareness about the importance of climate change are also crucial. Only through a proactive approach and the application of sustainable practices can the Serbian mining sector become more resilient to future climate challenges and contribute to broader efforts for environmental protection and achieving climate neutrality.

ACKNOWLEDGEMENTS

The authors are grateful to the Ministry of Science, Technological development and Innovation of the Republic of Serbia for financial support according to the contract with the registration number 451-03-136/2025-03/ 200052.

REFERENCES

[1] V. Martin, Economic themes, 62 (3) (2024) SCIENDO, 413-428.
[2] Dr S. Sakan, Jalovišta kao potencijalni izvor toksičnih elemenata, Rudarstvo – opasnosti i izazovi u zaštiti životne sredine, CEKOR, 2022, p.95-98.
[3] https://bif.rs/2014/06/fren-uticaj-poplava-i-sanacije-steta-na-imovinu-bdp-i-fiskalni-deficit/
[4] V. Pecina, D. Juřička, J. Hedbávný, M. Klimánek, J. Kynický, M. Brtnický, R. Komendová, Sci. Rep. 13:2763 (2023) p.1-12.
[5] M.M. Dehkordi, Z.P. Nodeh, K.S. Dehkordi, H. Salmanvandi, R.R. Khorjestan, M. Ghaffarzadeh, Results Eng. 23 (2024) 102729, p.1-21.
[6] https://forbes.n1info.rs/biznis/kako-sektor-rudarstva-u-srbiji-utice-na-zivotnu-sredinu-ministarstvo-objavilo-nacrt-izvestaja/
[7] United Nations Environment Programme Finance Initiative, Climate Risks in the Metals and Mining Sector, 2024.

The 56th International October Conference on Mining and Metallurgy
22-25 October 2025, Bor Lake, Bor, Serbia
www.ioc.tfbor.bg.ac.rs

DOI: 10.5937/IOC25136G Original scientific paper

ANALYSIS OF THE ENERGY POTENTIAL OF BRIQUETTES MADE FROM GROUND PLUM, DATE, AND AVOCADO PITS

Milan Grozdanović[1a], Živana Jovanović Pešić[2a], Jelena Đoković[1b], Dejan Tanikić[1c]

[1] University of Belgrade – Technical Faculty in Bor, V.J. 12, 19210 Bor, Serbia
[2] Faculty of Engineering, University of Kragujevac, Sestre Janjić 6, 34000 Kragujevac, Serbia
[1a] mgrozdanovic@tfbor.bg.ac.rs, 0000-0002-5618-9274
[1b] jdjokovic@tfbor.bg.ac.rs, 0000-0001-5542-8088
[1c] dtanikic@tfbor.bg.ac.rs, 0000-0003-0702-5721
[2a] zixi90@gmail.com, 0000-0002-1373-0040

Abstract
This paper presents an analysis of the energy potential of briquettes made from ground plum pits. The higher and lower calorific values of briquettes produced from ground plum pits were determined experimentally. To assess the energy potential more comprehensively, the calorific values of briquettes made from date and avocado pits were also determined. Based on the results presented, briquettes made from date pits have an average calorific value of around 19 MJ/kg, placing them in the same range as certain types of wood. Plum pit briquettes exhibit even higher energy potential, exceeding 21 MJ/kg, while avocado pit briquettes show a slightly lower value, around 16 MJ/kg. The results indicate that briquettes made from plum, date, and avocado pits possess notable energy potential, though sample preparation is essential to achieve maximum efficiency.

***Keywords**: briquettes, plum pits, calorific value of solid fuel*

1. INTRODUCTION

The issue of ensuring an adequate energy supply ranks immediately after food supply in terms of importance. Biomass as a fuel can be used effectively to generate thermal energy, especially by small and medium-sized consumers located at or near the site of biomass production. Numerous organic materials can be used to produce environmentally friendly fuels, including straw from various cereals, soya and rapeseed residues, maize stalks, sunflower stalks, pruning residues from orchards and vineyards, and fruit stones and peel [1]. Waste biomass in the form of plum pits represents a high-quality fuel class. Although this fuel can be used in bulk form, combustion problems can occur due to particles falling through the grate. To overcome these problems, plum pits are subjected to briquetting.

The aim of this study is to determine the energy potential of residues from plum processing used as a fuel source. For this purpose, the high and low calorific values of briquettes made from ground plum pits are determined. In order to evaluate the energy potential of briquettes made from ground plum pits, their calorific value is compared with that of briquettes made from date and avocado pits, whose calorific values were also determined experimentally. In addition, literature data is available for peach and apricot kernels [2].

2. DETERMINATION OF THE CALORIFIC VALUE OF SOLID FUELS

The calorific value of a fuel is defined as the ratio between the amount of heat released during complete combustion and the amount of fuel from which the heat is generated [3]:

$$H = Q / m_g , \tag{1}$$

where: H - calorific value of the fuel in kJ/kg, Q - amount of heat released in kJ and m_g - mass of the fuel in kg.

The higher calorific value or gross calorific value (H_g) of a fuel is the amount of heat released during the complete combustion of a unit mass of the fuel, assuming that the water produced during combustion remains in the liquid state. The lower calorific value (H_d) is the amount of heat released during the complete combustion of a unit mass of a fuel, assuming that the water produced during combustion remains in the gaseous state.

The calorific value of solid fuels is determined using a bomb calorimeter. The procedure is as follows: A certain amount of water is poured into the calorimetric bomb. A crucible with a measured mass of fuel is placed on a base and an ignition wire is embedded in the fuel, the ends of which are connected to the ignition terminals. The bomb is sealed, filled with oxygen to a certain pressure and placed in the calorimetric vessel with a measured quantity of water so that the bomb is completely submerged. After connecting the electric ignition cables to the lid of the bomb, the calorimeter is sealed and the stirrer is activated. A thermometer is immersed in the water. As soon as the water temperature has stabilized, the fuel is ignited. The heat released during combustion is transferred to the surrounding water and the rise in temperature is recorded. Combustion is considered complete when no soot is visible on the walls of the bomb and no unburnt carbon remains in the crucible.

The determination of the higher calorific value of solid fuels with a bomb calorimeter is based on the complete combustion of a measured amount of fuel in an oxygen-rich atmosphere, under increased pressure and constant volume. The heat generated by the combustion is transferred to the surrounding medium, i.e. the water. By measuring the mass of the water and the rise in temperature, the amount of heat released can be calculated:

$$Q = m_v \cdot c_v \cdot \Delta t_v \,, \tag{2}$$

where: Q - amount of heat released in kJ, m_v - mass of water in kg, c_v - specific heat capacity of water, whose value is 4.2 kJ/(kg°C) and Δt_v - increase in water temperature in °C.

Based on the determined amount of heat released and the mass of the fuel, the calorific value of the fuel is calculated using the following equation (1):

$$H_g = \frac{C \cdot \Delta t_v - Q_z}{m_g} \,, \tag{3}$$

where: H_g - higher calorific value of the fuel in kJ/kg, C - calorimeter constant in J/°C, Δt_v - increase in water temperature in °C, Q_z - the amount of heat generated by the combustion of the wire in J and m_g – mass of the fuel in g.

The hygroscopic moisture content of the fuel is calculated using the following formula

$$W_H = \frac{m_1 - m_2}{m_1} \cdot 100 \,, \tag{4}$$

where: W_H - hygroscopic moisture content in %, m_1 - initial mass of the fuel sample in g i m_2 - measured mass of the fuel sample after drying in g.

The lower calorific value of the fuel is calculated using the following equation:

$$H_d = H_g - 25 \cdot (9 \cdot H + W_G + W_H) \,, \tag{5}$$

where: H_d - lower calorific value of the fuel in kJ/kg, H_g - higher calorific value of the fuel in kJ/kg, W_G - gross moisture content, expressed in %, is not normally taken into account as it is assumed that the gross moisture has already been removed from the fuel, W_H - hygroscopic moisture content in % and H - hydrogen content of the fuel sample in %.

3. RESULTS AND DISCUSSION

The briquettes shown in Figure 1 were produced by drying plum pits at 100°C for 12 hours and then grinding them into powder using a ceramic mill. This was followed by the briquetting process, i.e. filling the mould and applying compression. The resulting briquettes diameter is 10.5 mm.

Figure 1. Briquetting of plum pits

The calorific value of the plum briquettes was measured with a Berthold-Mahler type bomb calorimeter (manufacturer: LABOUR) in the Laboratory of Propulsion Materials at the Faculty of Engineering, University of Kragujevac. The measurement results are shown in Table 1.

Table 1: Determination of the calorific value of solids according to SRPS ISO 1928:2022

Information on the test substance			
Type of substance: pits	plum	date	avocado
Moisture content: W [%]	5.5	5	5
Hydrogen content: H [%]	5.9*	5.9*	5.9*
Details of the measuring device			
Water equivalent of the device: m_e [g]	450.9	450.9	450.9
Mass of water in the calorimeter: m_w [g]	2800	2800	2800
The amount of heat generated by the combustion of the wire: q_z [J/g]	6698.5	6698.5	6698.5
Specific heat capacity of water: c_w [J/(gK)]	4.186	4.186	4.186
Results of the measurement			
Mass of the sample of the test substance: m_g [g]	2.323	1.588	1.791
Mass of the wire: m_{z1} [g]	0.056	0.063	0.05
Mass of the unburnt wire: m_{z2} [g]	0.016	0.014	0.011
Mass of the water in bomb: m_b [g]	10	10	10
Calculations			
Corrected temperature change during the main measurement period: Δt [°C]	3.66	2.236	2,123
The amount of heat generated by the combustion of the wire: $Q_z = (m_{z1} - m_{z2}) \cdot q_z$, [J/g]	267.94	328.227	261,241
Higher calorific value of the test substance: $H_g = \frac{c_w \cdot \Delta t \cdot (m_e + m_w + m_b) - Q_z}{m_g}$, [J/g]	21391	19014	16035
Lower calorific value of the test substance: $H_d = H_g - 25 \cdot (9 \cdot H + W)$, [J/g]	19926	17562	14583

*(literature reference)

Figure 2 shows a graphical representation of the results obtained in Table 1.

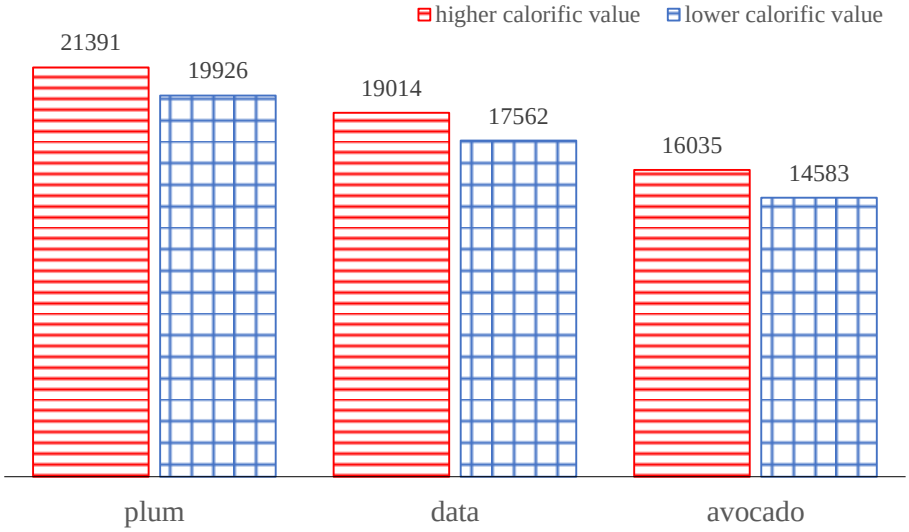

Figure 2: Higher and lower calorific values of briquettes made from plum, date and avocado pits

Based on the results shown in Figure 2, briquettes made from plum pits have the highest calorific value, followed by briquettes made from date kernels, while briquettes made from avocado kernels have the lowest calorific value. The results indicate that briquettes made from plum, date and avocado pits have some energy potential; however, proper sample preparation is required to maximize efficiency.

4. CONCLUSION

Plum, date and avocado pits are produced in large quantities as waste during the processing of these fruits in the food industry. Instead of ending up in landfill sites, these pits can be utilized as valuable raw materials for briquette production.

The analysis presented in this study shows that briquettes made from date pits have an average calorific value of around 19 MJ/kg, which is on a par with certain types of wood. Plum pit briquettes are even more energy-rich with a potential of up to 21 MJ/kg, while avocado pit briquettes have a slightly lower value of around 16 MJ/kg.

Briquettes made from ground plum, date and avocado pits are a promising and sustainable source of energy. Their production and use can contribute significantly to reducing dependence on fossil fuels and improving energy efficiency, while having a positive impact on the environment.

ACKNOWLEDGEMENTS

This research was partially supported by the Ministry of Education, Science and Technological Development of the Republic of Serbia, within the funding of the scientific research work at the University of Belgrade, Technical Faculty in Bor, according to the contract with registration number 451-03-137/2025-03/ 200131.

REFERENCES

[1] M. Đević, A. Dimitrijević, D. Blažin, and S. Blažin, Mogućnosti korišćenja ostataka iz prerade voća kao gorivnog materijala, Časopis za procesnu tehniku i energetiku u poljoprivredi / PTEP, 12 (3) (2008) 111-114.
[2] V. Janić, T. Janić, S. Igić, V. Višacki, State and perspectives of biomass potential for combustion, Cont. Agr. Engng., 44 (2) (2018) 45-92,
[3] SRPS ISO 1928:2022, Coal and coke — Determination of gross calorific value, 2022

The 56th International October Conference on Mining and Metallurgy
22-25 October 2025, Bor Lake, Bor, Serbia
www.ioc.tfbor.bg.ac.rs

DOI: 10.5937/IOC25140Z *Original scientific paper*

SELECTION OF PRIMARY SUPPORT SYSTEM FOR THE RIVER "MALI PEK" TUNNEL

Milivoje Zlatic[1a], Dejan Petrovic[1b], Jelena Ivaz[1c], Mladen Radovanovic[1d], Milan Stajic[1e]

[1] Technical Faculty Bor, University of Belgrade, V.J. 12, 19210 Bor, Serbia
[1a] mzlatic@tfbor.bg.ac.rs, 0009-0000-9101-2063
[1b] dpetrovic@tfbor.bg.ac.rs, 0000-0001-8588-2046
[1c] jivaz@tfbor.bg.ac.rs, 0000-0001-9263-6804
[1d] mlradovanovic@tfbor.bg.ac.rs, 0000-0002-0703-2780
[1e] mstajic@tfbor.bg.ac.rs, 0000-0002-3030-1934

Abstract
The open-pit "Juzni revir" in Majdanpek is threatened by an active landslide on the north and northwest sides. The landslide threatens production at the open-pit and the "Mali Pek" riverbed. By building a tunnel, we would shift the riverbed and thus eliminate the danger posed by an active landslide. Before starting tunnel construction, it is necessary to define the condition of the rock mass and determine the support system for each working environment.

***Keywords**: landslide, tunnel, support system*

1. INTRODUCTION

Numerous authors have attempted to define the quality of the field under consideration using basic data on the properties of the rock mass (compressive strength, modulus of elasticity, angle of internal friction, etc.) and to propose a support system based on the rock characteristics. This is a complex task because each work environment has its own specific characteristics. Various classification systems have been developed such as GSI, RMR, Q, etc. For this paper, the required primary support was determined based on the known GSI value and known correlations between GSI and RMR system. The secondary support will be made of monolithic concrete. The thickness of the concrete support will vary depending on the lithological area and will range from 25 - 45 cm. Determining the secondary support will not be the topic in this paper. The selected primary support was tested by the Convergent-Confinement Method.

2. ROCK MASS CLASSIFICATION

2.1 Geological Strength Index (GSI)

The Geological Strength Index (GSI) is a system of rock-mass characterization that has been developed in engineering rock mechanics to meet the need for reliable input data, particularly those related to rock-mass properties required as inputs into numerical analysis or closed form solutions for designing tunnels, slopes, or foundations in rocks [1].

2.2 The Rock Mass Rating (RMR)

The Rock Mass Rating (RMR) system, otherwise known as the Geomechanics Classification, was developed by the Bieniawski during 1972-1973. It was modified over the years as more case histories became available and to conform with international standards and procedures [2]. The following relationship has been established between the GSI and RMR classifications [3]:

$$\mathrm{GSI} = \mathrm{RMR}_{89} - 5 \quad (1)$$

Table 1. Guidelines for Excavation and Support of Rock Tunnels in Accordance with the Rock Mass Rating System [2]

Rock Mass Class	Excavation	Rock Bolts (20 mm Dia, Fully Grouted)	Shotcrete	Steel Sets
Very good rock, I, RMR: 81-100	Full face 3 m advance	Generally, no support required except for occasional spot bolting		
Good rock, II, RMR: 61-80	Full face 1-1.5 m advance. Complete support 20 m from face	Locally, bolts in crown 3 m long, spaced 2.5 m, with occasional wire mesh	50 mm in crown where required	None
Fair rock, III, RMR: 41-60	Top heading and bench 1.5-3 m advance in top heading. Commence support after each blast. Complete support 10 m from face	Systematic bolts 4 m long, spaced 1.5-2 m in crown and walls with wire mesh in crown	50-100 mm in crown and 30 mm in sides	None
Poor rock, IV, RMR: 20-40	Top heading and bench 1.0-1.5 m advance in top heading. Install support concurrently with excavation 10 m from face	Systematic bolts 4-5 m long, spaced 1-1.5 m in crown and wall with wire mesh	100-150 mm in crown and 100 mm in sides	Light to medium ribs spaced 1.5 m where required
Very poor rock, V, RMR: <20	Multiple drifts, 0.5-1.5 m advance in top heading. Install support concurrently with excavation. Shotcrete as soon as possible after blasting	Systematic bolts 5-6 m long, spaced 1-1.5 m in crown and walls with wire mesh. Bolt invert	150-200 mm in crown, 150 mm in sides, and 50 mm on face	Medium to heavy ribs spaced 0.75 m with steel lagging and forepoling if required. Close invert

The route of the designed tunnel passes through the following lithological units: 1. Granitoid gneisses, 2. Amphibole-biotite gneisses and mica schists, 3. Limestones and 4. Andesites and tectonic breccias. According to relation (1) values of RMR was determined and shown in Table 2.

Table 2. Correlation values between different classification of rock mass

Lithological area	GSI	RMR
Amphibole-biotite gneisses and mica schist	34	39
Limestones	49	54
Andesites and tectonic breccias	20.76	25.76
Granitoid gneisses	41	46

3. SELECTED PRIMARY SUPPORT SYSTEM

According to the recommendations from Table 1, the following primary support system was selected and shown in Table 3.

Table 3. Selected primary support system

Lithological area	Primary support system
Amphibole-biotite gneisses and mica schist	Mesh reinforced concrete, thickness 15 cm in crown and sides, Tensioned bolts 4 m long, spaced 1.5x1 m in crown and wall, Steel sets at a distance of 1 m (as needed).
Limestones	Mesh reinforced concrete, thickness 10 cm in crown and sides, Bolts 4 m long, spaced 2x2m in crown and wall.
Andesites and tectonic breccias	Mesh reinforced concrete, thickness 15 cm in crown and sides, Tensioned bolts 5 m long, spaced 1x1 m in crown and wall, Steel sets at a distance of 1 m (as needed).
Granitoid gneisses	Mesh reinforced concrete, thickness 10 cm in crown and sides, Bolts 4 m long, spaced 2x2m in crown and wall.

3.1 Determination of the required pressure of the primary support system

Considering the original Unal equation, substituting the GSI for RMR, and considering the reduction factor for rock mass quality through disturbance and strength factors, the new equation to estimate the support pressure was proposed [4]:

$$P = \frac{100 - ((1 - \frac{D}{2})\sqrt{\frac{\sigma_{cr}}{100}}\ GSI)}{100} C_s S_q D_e \gamma \quad (2)$$

where is:
D – disturbance factor
D_e – equivalent diameter of the excavation
$\sigma_{cr} = s_r \cdot \sigma_{ci}$, s_r = post-peak strength reduction factor. s_r = 1 for poor rock masses (GSI<27).
S_q – correction factor for squeezing ground condition, S_q = 1
C_s – stress correction factor, C_s = 1.4.
Required pressure of the primary support system according to different lithological area are shown in Table 4.

3.2 Convergence-Confinement Method

The Convergent-Confinement Method is based on an elastoplastic model that allows for closed mathematical solutions. Stresses and the displacement in the rock mass around the tunnel and in the support depend on the properties of the rock mass, the primary state of stress, the stiffness of the support, as well as the time of its installation. The Convergent-Confinement Method consists of two characteristic lines: the characteristic line of the Ground reaction Curve and Support Characteristic Curve (Figure 1). These lines represent the relationship between radial stress and radial deformation in the rock mass around the underground opening and in the surrounding area [5]. The support stiffness, maximum pressure support system and safety factor of support system are shown in Table 4.

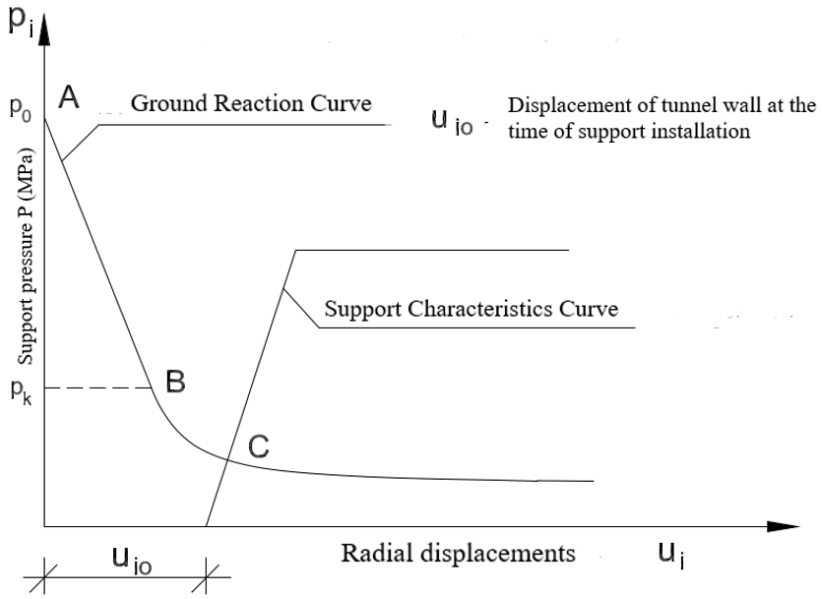

Figure 1. Convergence-confinement curves [5]

Table 4. Characteristics of selected primary support system

Lithological area	P – Required pressure of the primary support system [MPa]	K – Support stiffness [MPa]	Pmax – Maximum pressure support system [MPa]	SF = Pmax/P – Safety factor of support system
Amphibole-biotite gneisses and mica schist	0.225	673.87	1.75	7.78
Limestones	0.211	397.3	1.41	6.7
Andesites and tectonic breccias	0.196	638.93	1.64	8.37
Granitoid gneisses	0.22	426.26	1.46	6.64

4. CONCLUSION

The mentioned recommendation for support can serve as a good guide for supporting when we are still unsure about what rock mass we will work with. During the construction of any underground space, it is necessary to conduct exploratory work to obtain information about the rock, and in this way, we will adapt our support system.

ACKNOWLEDGEMENTS

This work was financially supported by the Ministry of Education, Science and Technological Development of the Republic of Serbia, Grant No. 451-03-137/2025-03/200131.

REFERENCES

[1] V. Marinos, P. Marinos, E. Hoek, Bull. Eng. Geol. Enviro.n 64 (2005) 55-65.
[2] Z.T. Bieniawski, Engineering Rock Mass Classifications, Wiley, New York, 1989, p.51,62.
[3] E. Hoek, P.K. Kaiser, W.F. Bawden, Support of underground excavations in hard rock, AA Balkema, Rotterdam, 1995, p.104.
[4] R.R. Osgoui, E. Unal, Eng. Geol. 107 (2009) 154-166.
[5] L. Gizdić, Conceptual design of underground structures for wastewater treatment device "Bilosevac" in Makarska, Master's thesis, Split, 2017, p.29-31.

The 56th International October Conference on Mining and Metallurgy
22-25 October 2025, Bor Lake, Bor, Serbia
www.ioc.tfbor.bg.ac.rs

DOI: 10.5937/IOC25144I *Original scientific paper*

APPLYING ELECTRICAL SURVEY TO DETECT THE THICKNESS OF THE EPIKARST

Snežana Ignjatović[1a], Branislav Petrović[1b]

[1]Faculty of Mining and Geology, University of Belgrade, Đušina 7, 11000 Beograd, Serbia,
[a]snezana.ignjatovic@rgf.bg.ac.rs, 0000-0003-0629-9982
[b]branislav.petrovic@rgf.bg.ac.rs, 0000-0002-7861-3291

Abstract
Defining the thickness of the epikarst plays an important role in hydrogeological surveys. The epikarst has an impact on the regime, balance, and groundwater quality. Electrical surveys, especially the technique of vertical electrical sounding (VES), can help to define the thickness of the epikarst. The paper presents the results obtained using the VES technique on the survey area located in the eastern part of Suva planina Mt. for detecting the thickness of the epikarst. The results obtained for the survey area bring new information about the thickness of the epikarst in the survey area.

Keywords*: the epikarst, vertical electrical sounding, Suva planina Mt.*

1. INTRODUCTION

Epikarst is the highest part of the rock mass that is exposed to karstification, and, in a karst area, this layer plays an important role in protecting the karst formation. The main characteristics of epikarst are the accumulation of underground water and the creation of conditions for the formation of concentrated flows in the bedrock [1]. The thickness of the epikarst zone varies in the range from 10 cm to 30 m and is generally estimated from a few meters to 10-15 meters [2].

In this paper we present the results of electrical surveys that we applied to detect the thickness of the epikarst. Electrical surveys were done by the technique of vertical electrical sounding (VES).

As a practical example, we used the VES measurements which were done in the eastern part of Suva planina Mt., on location Rakoš and Bukovica.

2. METODOLOGY

Electrical surveys were done using the technique of vertical electrical sounding (VES). The VSE technique is often used in karst investigation [3]. The VSE technique is applied to detect the change of electrical resistivity with depth using the Schlumberger array.

The Schlumberger array consists of four electrodes, which are sited in a line around a common midpoint. Two electrodes A and B are current electrodes – outer electrodes, and two electrodes M and N are potential electrodes – inner electrodes. To get the maximum depth penetration in the VES procedure, the current electrodes are moved away, and the distance between the potential electrodes does not change, hence increasing the depth penetration. The electrical sounding diagrams were obtained by application of this technique, and the electrical resistivity is given as a function of the half-distance of the current electrodes (AB/2) [4].

During the investigation in the survey area, the distance between the current electrodes (AB/2) ranges from 30 m to 110 m.

3. STUDY AREA

Suva planina Mt. is in SE part of Serbia, approximately 230 km from Belgrade (Fig. 1). In Suva planina Mt. the karst aquifer system is formed in the limestones of Middle and Upper Jurassic and Lover Cretaceous age [1].

The study area is situated in the eastern part of Suva planina Mt. in location Rakoš and Bukovica (Fig. 1).

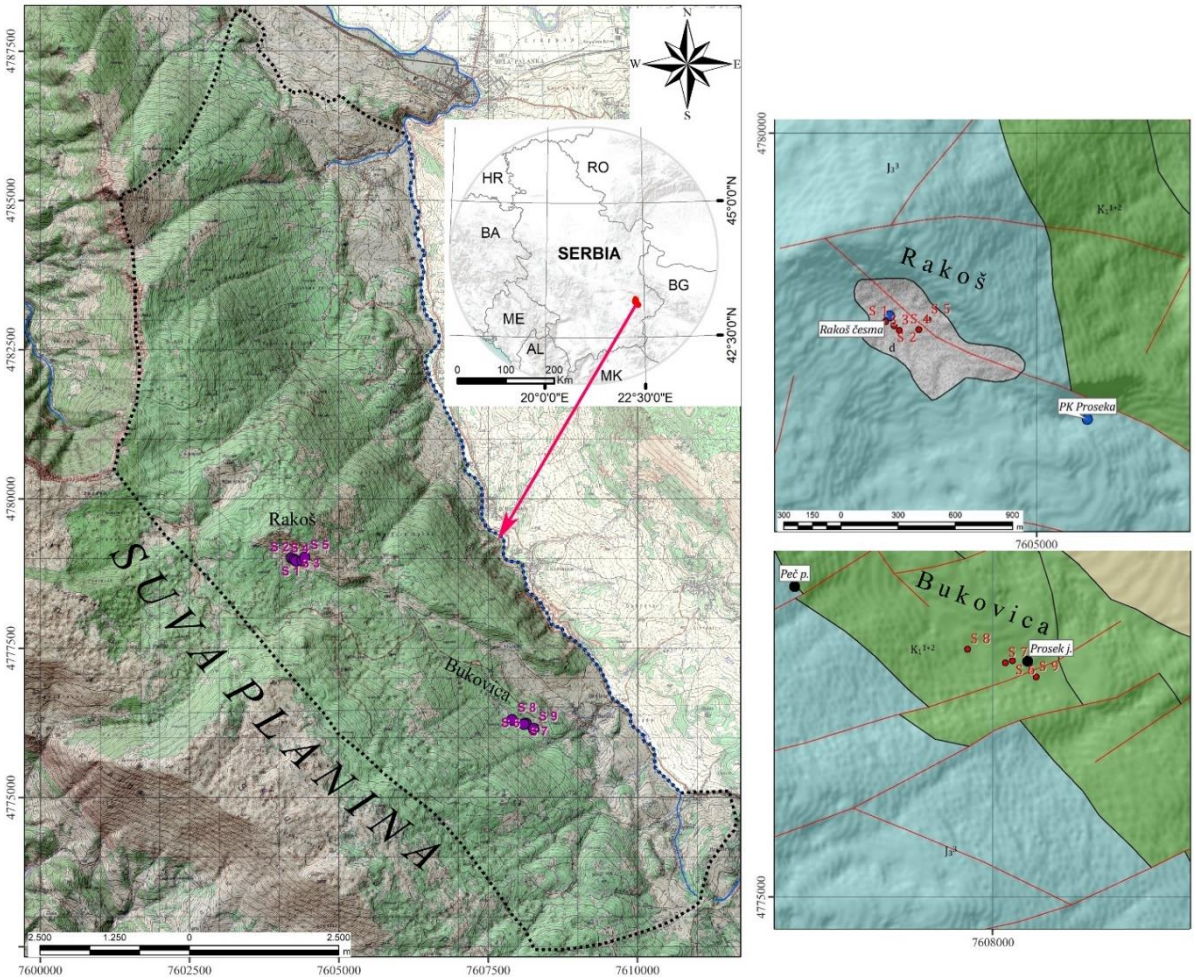

Figure 1. Map of survey area (easter part of Suva planina Mt.) with position of VES points - location Rakoš S1-S5 and location Bukovica S6-S9

4. RESULTS AND DISCUSSION

In the survey area, the thickness of the epikarst was defined by the VES technique. Measurements applying the VSE technique were done on locations Rakoš and Bukovica. The distance between the current electrodes (AB/2) was 30 m in the Rakoš area, while the distance between the current electrodes in the Bukovica area was 30 m and 110 m.

At the Rakoš location, the VES measurements were done along profiles S1-S5 (Fig. 1). The results in points S1, S2 and S3 show that the measurements were done in the fault zone (Fig. 2). This zone is without a diluvial overlayer with high values of specific electrical resistivity from the surface to a depth of over 2 m. Measuring points S1 and S2 are placed over the fault zone on a relatively raised block with a diluvial layer and debris material in it. Measuring points S4 and S5 are located on the raised flank of the fault, and S5 is positioned the farthest from the fault zone. The data from S5 shows that diluvium and clay are found in this part, which are washed closer to the fault and

eroded onto the flank that descends (Fig. 2). There are zones of lower and higher resistivity that are the results of VES measurements at the Rakoš. The resistivity in the shallowest part of the terrain is high and indicates that this part of the terrain contains limestone rubble in a dried clay matrix. The change by depth of high and low resistivity (S1-S4) is related to the change of dry, larger limestone blocks and degraded limestone belts with water or clay as filling. At point S5 (Fig. 2), the VES measurements show that such heterogeneity of the limestone is not visible, but under the clay layer lies weakly cracked limestone, to a depth of almost 20 m.

The results of VES on location Rakoš (Fig. 2) indicate the layer consisting of decomposed and altered limestone rock material (breccia and debris) and soil, which in this case represents epikarst. The thickness of the epikarst at the Rakoš ranges from 3 to 15 meters.

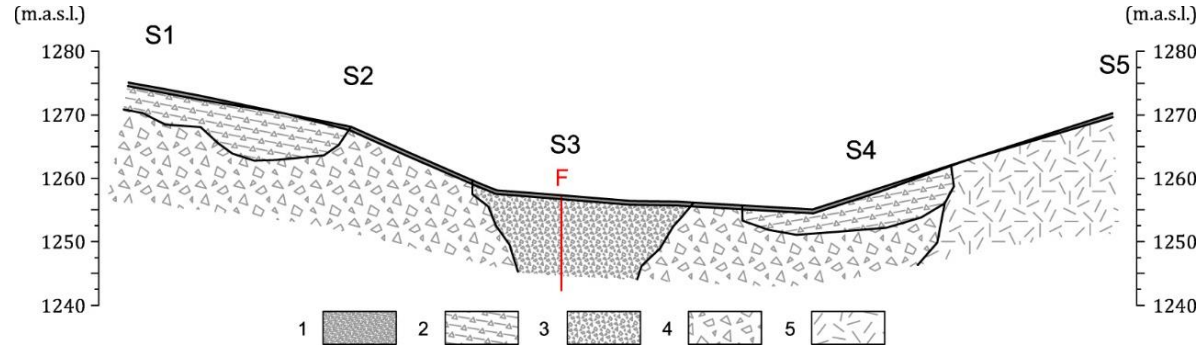

Figure 2. The interpretation of the VES measurements (S1-S5) at location Rakoš: 1- soil, 2 - colluvium with clay infill (epikarst), 3 – resedimented breccias (epikarst), 4 – limestone (epikarst), 5 – highly karstified limestone, F – fault (according [1])

On location Bukovica, the measurements of VSE were completed along profiles S6-S9 (Fig. 1). In points S6, S7, S8 and S9 the results of measurements show that it is done in the fault zone (Fig. 3). Along the S6-S9 profile, the results indicate that resistivity increases with depth and that there is a dry system of cracks, pits and caverns below the surface.

The results of VES on location Bukovica indicate the layer consisting of decomposed and altered limestone rock material (breccia) and soil, which represents epikarst in this case (Fig. 3). The thickness of the epikarst at Bukovica ranges from 1.5 to 9 meters. The epikarst lies over a well karstified limestone in which there is a system of caverns, dry cracks, and larger channels in this area.

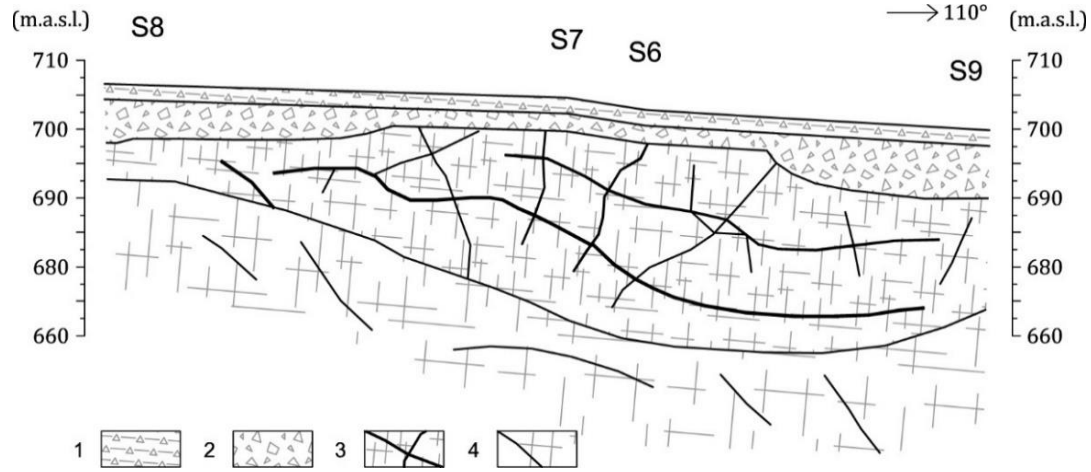

Figure 3. The interpretation of the VES measurements (S6-S9) at location Bukovica: 1- soil and colluvium with clay infill (epikarst), 2 – limestone breccias (epikarst), 3 – well karstified limestone, 4 – weak karstified limestone (according [1])

5. CONCLUSION

The results obtained using the VES technique on the survey area located in the eastern part of Suva planina Mt., on location Rakoš and Bukovica, helped to define the thickness of the epikarst in the survey area. At the Rakoš, the thickness of the epikarst ranges from 3 to 15 meters. The thickness of the epikarst at Bukovica ranges from 1.5 to 9 meters. The results of VES measurements bring new information about the thickness and distribution of fractured and karstified zones in the survey area. The thickness of the epikarst decreases with declining quality (cleanliness) of carbonate rocks, enhancement of slope, and distance from fault zones. The new information about the thickness of the epikarst in survey areas can help in future hydrogeological surveys.

ACKNOWLEDGEMENTS

The authors would like to thank the Ministry of Science, Technological Development and Innovation for providing resources under Contract no. 451-03-136/2025-03/200126.

REFERENCES

[1] B. Petrović, Funkcionisanje i uticaj epikarsta na režim, bilans i kvalitet podzemnih voda istočnog dela karstnog sistema Suve planine, Doktorska disertacija, Univerzitete u Beogradu Rudarsko– geološki fakultet, Beograd, 2020, p.291.

[2] A.B. Klimchouk, Towards defining, delimiting and classifying epikarst: Its origin, processes and variants of geomorphic evolution, speleogenesis and evolution of karst aquifers. – Speleogenesis and Evolution of Karst Aquifers, 2/1, (2004) 1-13.

[3] T.D. Bechtel, F.P. Bosch, M. Gurk, Geophysical methods, in: Methods in Karst Hydrogeology, (eds. Goldscheider N. & Drew D.), IAH, vol 26. Taylor & Francis/Balkema, London, (2010) 171-200.

[4] J.M. Reynolds, An Introduction to Applied and Environmental Geophysics, 2nd Edition. – Wiley-Blackwell, (2011) p.712

The 56th International October Conference on Mining and Metallurgy
22-25 October 2025, Bor Lake, Bor, Serbia
www.ioc.tfbor.bg.ac.rs

DOI: 10.5937/IOC25148J
Original scientific paper

BUILDING INFORMATION MODELING (BIM) AS A TOOL FOR ENHANCING TECHNICAL SOLUTIONS IN MINING DESIGN: A CASE STUDY OF THE MAIN PROCESS BUILDING IN BRSKOVO, MONTENEGRO

Nikola Jovanović[1a], Jelena Stefanović[1b], Miloš Živanović[1c], Zlatko Pavlović[1d], Nikola Miljković[1e], Jelena Đorđević[1f], Nikola Lekić[1g]

[1]Mining and Metallurgy Institute Bor, Alberta Ajnštajna 1, 19210 Bor
nikola.jovanovic@irmbor.co.rs, 0009-0008-0982-2576
jelena.stankovic@irmbor.co.rs, 0000-0001-6418-1814
milos.zivanovic@irmbor.co.rs, 0009-0006-3331-4294
zlatko.pavlovic@irmbor.co.rs, 0000-0001-8102-1820
nikola.miljkovic@irmbor.co.rs, 0009-0008-0982-2576
jelena.djordjevic@irmbor.co.rs, 0000-0001-5406-0074
nikola.lekic@irmbor.co.rs, 0009-0005-9399-9849

Abstract

Modern mining systems require advanced architectural and construction solutions to ensure functionality, safety, and efficiency. Traditional two-dimensional design methods are increasingly insufficient for managing complex facilities. Building Information Modeling (BIM) offers a modern, integrated approach to digital project modeling.

This paper examines the use of BIM tools in mining facility design, focusing on architectural and structural aspects. It highlights key benefits such as improved technical coordination, visualization, and documentation quality, while addressing implementation challenges. Through practical examples, the study demonstrates the potential of BIM to enhance the efficiency and quality of mining design processes.

***Keywords**: BIM, mining facilities, architectural and structural design, digital modeling, technical coordination*

1. INTRODUCTION

Modern mining infrastructure demands high standards of technical precision, safety, energy efficiency, and functional integration within complex engineering and technological systems. The architectural and civil engineering phase plays a key role in shaping processing plants, auxiliary facilities, underground spaces, communication corridors, and service areas, as well as resolving structural and spatial relationships within the complex [4]. To improve project documentation, reduce errors, and enhance interdisciplinary coordination, the use of digital tools has increased significantly in recent years. Among these, Building Information Modeling (BIM) has emerged as one of the most transformative methodologies in the Architecture, Engineering, and Construction (AEC) industry. BIM enables the creation of intelligent 3D models enriched with technical and operational data, supporting integrated planning, design, construction, and lifecycle management of complex facilities [8].

Although BIM is widely applied in conventional construction, its use in mining infrastructure — especially within architectural and civil engineering — remains at an early stage. The unique nature of mining facilities, combining complex functionality, limited space, strict safety standards, and multidisciplinary coordination, makes BIM particularly suitable for this field [1]; [5]. Moreover, integrating BIM with digital twins, GIS platforms, and simulation tools is increasingly relevant for optimizing performance and sustainability in large-scale mining projects [10], [11]. The aim of this paper is to examine the potential of BIM solutions in architectural and civil

engineering design for mining structures, focusing on principles, benefits, implementation challenges, and practical applications, with emphasis on improving technical documentation, coordination, and spatial visualization.

1.1 Theoretical Background

Building Information Modeling (BIM) is a digital methodology for designing, documenting, and managing construction projects through intelligent 3D models that combine geometric, technical, and functional data [4]. Unlike traditional CAD-based drafting with separate 2D drawings, BIM provides a unified environment where all disciplines work within a single, coordinated digital model [8].BIM can also include additional dimensions such as time (4D), cost (5D), and facility management data (6D/7D), offering advanced tools for planning, visualization, and lifecycle management. These features are particularly valuable in mining, where spatial constraints and multidisciplinary coordination are essential [1]. Standardized formats like IFC ensure interoperability between different BIM tools, while international standards such as ISO 19650 provide a framework for consistent information management throughout the project lifecycle [6]. Although BIM is well established in general construction, its use in mining design is still developing, especially in architectural and civil engineering.

1.2 Specifics of Architectural and Civil Engineering in Mining Design

Mining design presents unique challenges for architectural and civil engineering due to complex functionality, harsh environmental conditions, and strict safety requirements. Unlike standard construction projects, mining facilities often include underground structures, processing plants, ventilation shafts, haul roads, and other specialized infrastructure, each with specific design criteria [2], [3]. Architectural and civil components must address spatial constraints caused by geological conditions and mining operations, requiring precise integration with mechanical, electrical, and process engineering. Effective coordination is essential to prevent design conflicts and ensure structural safety [4].

Mining environments also demand durable materials and resilient structural solutions capable of withstanding vibrations, dynamic loads, and corrosive conditions. These factors make visualization, clash detection, and iterative design critical — areas where **BIM** provides significant advantages [8]; [9]. Applying BIM enables optimized layouts, better multidisciplinary coordination, improved regulatory compliance, and clearer stakeholder communication, resulting in safer and more efficient project delivery [1].

2. DISCUSSION – CASE STUDY OF THE MAIN PROCESS BUILDING IN BRSKOVO

The case study of the main process building in Brskovo, as shown in Figure 1 and Figure 2, clearly demonstrates the practical value of BIM methodology in the architectural and structural design of large-scale, technically complex mining facilities. The design of this structure — which includes flotation, milling, and dewatering zones, with foundations and equipment platforms — required the precise coordination of architectural, structural, technological, and electrical systems within a constrained spatial envelope.

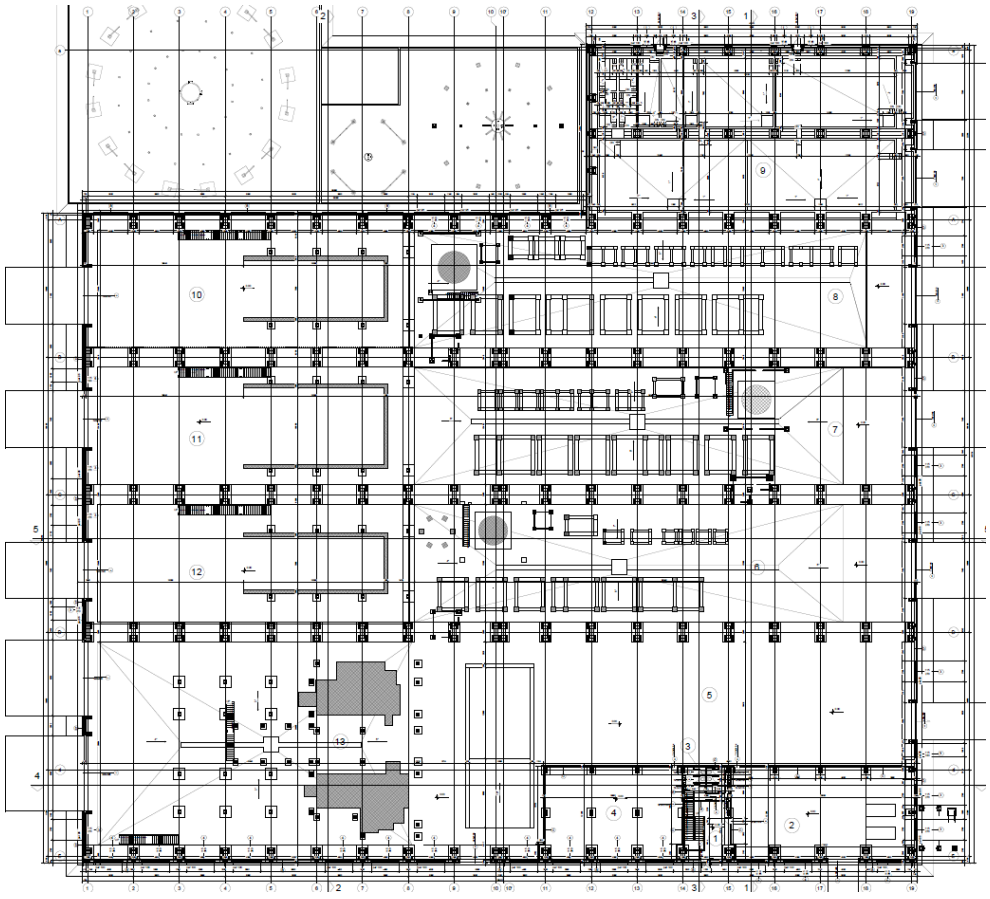

Figure 1. Flotation plant ground floor plan.

One of the most significant advantages observed during the design process was the ability of BIM tools to manage geometric complexity. The hall spans over 108 meters in length and features multiple structural zones with spans up to 29.35 meters, multiple floor elevations, and a series of bridge cranes on different operational levels. BIM enabled the integration of structural elements such as lattice columns composed of HEA600 profiles and HOP bracing systems with the positioning of flotation equipment, stair towers, service platforms, and crane tracks [1]. The hall is divided by a 1-meter expansion joint into two technological areas (milling/filtration and flotation/control), which was fully represented in the BIM model, enabling precise functional zoning and clear construction phases. The model also included elevation changes from +0.60 m to +22.10 m, integrating steel and reinforced concrete elements, equipment platforms, and maintenance walkways essential for operations like reagent preparation and equipment maintenance. Stair towers and vertical ladders were accurately modeled and verified within BIM [4], [8].

Advanced clash detection using Navisworks and Revit resolved over a dozen spatial conflicts early in planning, including misalignments between equipment supports, crane clearance zones, and vertical ducts. While the HOP façade frames and sandwich panels did not contribute to seismic load transfer, their inclusion in the BIM model improved visual planning, daylight simulation, and façade coordination. BIM also optimized the sequencing of steel elements, such as trapezoidal sheet-metal platforms and composite decks, aligning construction with crane installation and process workflows [9].

Figure 2. 3D rendering of the Main process building.

However, several challenges were noted. The absence of mining-specific BIM object libraries (e.g., flotation cells, filter presses, reagent tanks) required custom modeling, increasing design time. Additionally, integration with external software like Tower 8 for structural analysis was limited, as these tools remain partially disconnected from the BIM environment.

Despite these issues, BIM enabled the integration of 3D geometry, technical data, and operational requirements into a single model, improving documentation quality and coordination between disciplines. Given the scale and complexity of the flotation plant, the BIM-based approach proved essential for delivering a safe, efficient, and reliable facility.

3. CONCLUSION

This study has explored the application of BIM in the architectural and structural design of mining facilities, focusing on the case of the flotation plant hall in Brskovo. The findings confirm that BIM represents a powerful tool for managing complexity, improving technical coordination, and enhancing the overall quality of design documentation in the mining sector.By integrating spatial data, equipment geometry, structural systems, and construction sequencing into a unified 3D environment, BIM allowed the design team to address the challenges posed by large spans, multiple elevation levels, heavy equipment loads, and dense process zones. Clash detection, visual simulations, and digital collaboration platforms significantly reduced design risks and increased efficiency in both planning and communication. Despite the evident benefits, the application of BIM in mining projects remains limited by the lack of standardized tools and domain-specific object libraries. Additionally, the need for interoperability between BIM platforms and specialized structural or geotechnical software is still an open issue. Overcoming these limitations will require coordinated efforts by industry stakeholders, software developers, and regulatory bodies.Nonetheless, the Brskovo flotation hall project demonstrates that even within the current constraints, BIM can provide substantial value in the design of mining infrastructure. As digital transformation accelerates across the construction and resource sectors, broader BIM adoption is expected to become a key enabler for more sustainable, efficient, and safe development of mining operations.

ACKNOWLEDGEMENTS

This work was financially supported by the Ministry of Science, Technological Development and Innovation of the Republic of Serbia, as well as the Contract on realization and financing of the scientific research work of the Mining and Metallurgy Institute Bor in 2024, contract number: 451-03-66/2024-03/200052.

REFERENCES

[1] Autodesk. (2023). BIM for infrastructure: Transforming construction and design. Autodesk Inc. Retrieved from https://www.autodesk.com/solutions/bim
[2] S. Azhar, Leadership and Management in Engineering, 11 (3) (2011) 241–252.
[3] F. Bosché, (2016). Towards automated construction progress monitoring using 3D data and BIM. Automation in Construction, 72 (2016) 145–164.
[4] C. Eastman, P.Teicholz, R. Sacks, K. Liston, (2018). BIM handbook: A guide to building information modeling for owners, designers, engineers, contractors, and facility managers (3rd ed.). Hoboken, NJ: Wiley.
[5] International Organization for Standardization. (2018). Building information modelling – Information delivery manual (ISO 29481-1:2016). ISO.
[6] International Organization for Standardization. (2018). ISO 19650-1:2018 – Organization and digitization of information about buildings and civil engineering works, including building information modelling (BIM) — Information management using building information modelling — Part 1: Concepts and principles. Retrieved from https://www.iso.org/standard/68078.html
[7] MMI Bor. (2024). Main Mining Design for the Processing of Mineral Raw Materials from the Žuta Prla, Višnjica and Brskovo Deposits near Mojkovac – Grinding, Flotation and Dewatering Facility (Book VI, Vol. VI.3.1, Certificate 6208/R). Unpublished internal technical documentation.
[8] R. Sacks, C. M. Eastman, G. Lee, P. Teicholz, (2018). BIM handbook: A guide to building information modeling for owners, designers, engineers, contractors, and facility managers (3rd ed.). Wiley.
[9] B. Succar, Autom. Constr., 18 (3) (2009) 357–375.
[10] X. Wang, Y. Song, Autom. Constr., 138 (2022) 104289.
[11] D. Zhao, A.P. McCoy, T. Bulbul, C. Fiori, J.M. Vance,. Tunn Undergr Space Technol., 92 (2019) 103028.

The 56th International October Conference on Mining and Metallurgy
22-25 October 2025, Bor Lake, Bor, Serbia
www.ioc.tfbor.bg.ac.rs

DOI: 10.5937/IOC25153H *Original scientific paper*

COMPARING THE ACCURACY OF KRIGING AND IDW INTERPOLATION FOR ESTIMATING A CU-ZN DEPOSIT IN TURKEY

Samil Hoskan[1a], Bayram Kahraman[1b]
[1] Dokuz Eylül University, Mining Enginering Department, İzmir, Turkey
[1a] hoskan.samil@ogr.deu.edu.tr; 0009-0007-8313-6139
[1b] bayram.kahraman@deu.edu.tr; 0000-0001-9429-6591

Abstract

In mining, resource and reserve estimation is used to determine both the quantity and quality of ore. Mineral resources can be defined as the concentration of economically important material within the Earth's crust, while mineral reserves are the portions of a mineral resource that can currently be economically mined. Different portions of a deposit may contain different concentrations of minerals and structural components, and therefore a geological model of the deposit allows for the selection of the most appropriate exploration technique. Accurate reserve estimates for mining sites require accurate calculations of ore quantity and grade. For metal ores in particular, IDW and kriging are well-known interpolation methods that have been used for many years. Inverse distance weighting (IDW) is a deterministic interpolator that produces estimates without associated error measures, while geostatistical kriging is a probabilistic technique that allows both the estimates and the assessment of their uncertainty through the estimated variances. This study aims to calculate and compare interpolation methods such as IDW and kriging for a Cu-Zn mineral deposit in Turkey.

Keywords: *Resource estimation, interpolation, geostatistics*

1. INTRODUCTION

When choosing an investment project, it's natural for an investor to choose between a low-risk and a higher-risk option. However, in the mining industry, this situation unfolds somewhat differently. Mining projects carry higher risks and the time it takes to pay off the investment, and the exploration process, in particular, requires significant time and money [1]. The first and often most critical phase of a mining operation is the exploration phase. It is also one of the most difficult assessments to make when accurate data is lacking. The primary goal of mineral exploration is to identify locations with sufficient, economical mineral deposits, including metals such as gold, silver, copper, and iron, or industrial minerals such as gypsum, limestone, and potassium. The value-added component of a significant exploration success can be many times the company's initial value. While crucial for the company, it is difficult to predict the likely outcome of an exploration program, especially for external investors. However, it is important to be aware of some basic exploration principles and terminology when dealing with resource companies. It is important to note that exploration results are critical for establishing confidence by providing a clear picture of three key characteristics of the orebody: ore grade, volume, and ore continuity. Confidence regarding the ore's grade, volume, and ore continuity will increase as the number of data points increases. That is why ore characteristics must be verified using different interpolation techniques.[2]

2. GEOLOGICAL MODEL

The project area is predominantly underlain by the Upper Cretaceous (Maastrichtian) volcanics unit, composed of mafic to intermediate lavas and volcanoclastics like spilite, spilitic basalt, and andesite. Mineralization is associated with rock types including basalt, trachyandesite, sosuritic basalt, and dolerite. The geological interpretation suggests the basalts and andesites formed the

original volcanic structure, which was subsequently intruded by dolerite. Additionally, granite of presumed Tertiary age is present within the project boundaries.

- Andesit (AND)
- Basalt (BAS)
- Dolomit (DOL)
- Silisified zone (SZ)
- Silisified basalt (SB)

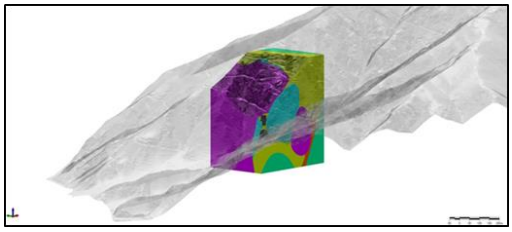

Figure 1- Lithological model

3. WIREFRAMING

As it is known explicit modeling is the traditional method, where the geologist manually draws and edits each polygon and surface, relying largely on artistry and expert interpretation. It is time-consuming, and different geologists may produce different results (subjective interpretation). Therefore, implicit modeling method is preffered in this study. Impicit modelling uses mathematical algorithms to create a "scalar field" (grade values or geological affiliation) in 3D space using geological boundaries and grade thresholds. A specific threshold value in this field (0.3% Cu grade and 0.5% Zn grade) automatically defines the 3D surface (solid model) of the ore body. It is more objective, faster, and repeatable.

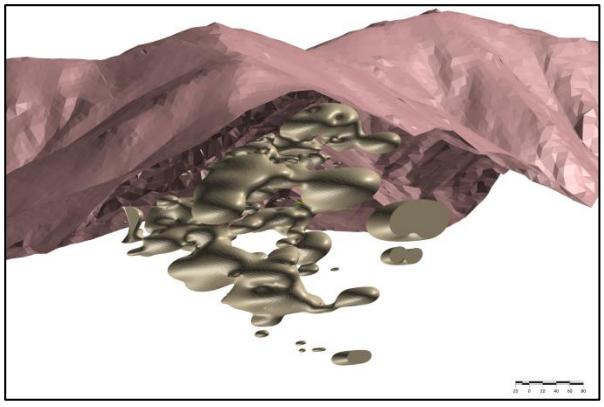

Figure 2- İmplicit solid model

4. INVERSE DISTANCE WEIGTHINING (IDW)

IDW, the inverse distance weighting method, is an interpolation method that uses spatial distance in correlation calculations. For an unknown point D with a location (A0, B0, C0), there are known points in its vicinity. Considering the spatial coordinates of each known point as (Ai, Bi, Ci) and the grade value to be assigned to the unknown points as G, the distance between each known point and the unknown point is (A, B, C) [6]. The inverse distance weighting force is set to three separate estimations were performed with continuously increasing search parameters to maximize the number of blocks within the specified model. After this stage, we examined whether grade assignments were made to the majority of the blocks, observed the blocks by comparing them with the borehole data, and examined whether the borehole spacings were consistent with the generated block model.

• Measured block calculation: Calc 1, minimum sample size (point) ≥25

• Indicated block calculation: Calc 1, Calc 2, minimum sample size (point) ≥15

• Inferred block calculation: Calc 1, Calc 2, Calc 3, minimum sample size (point) <15

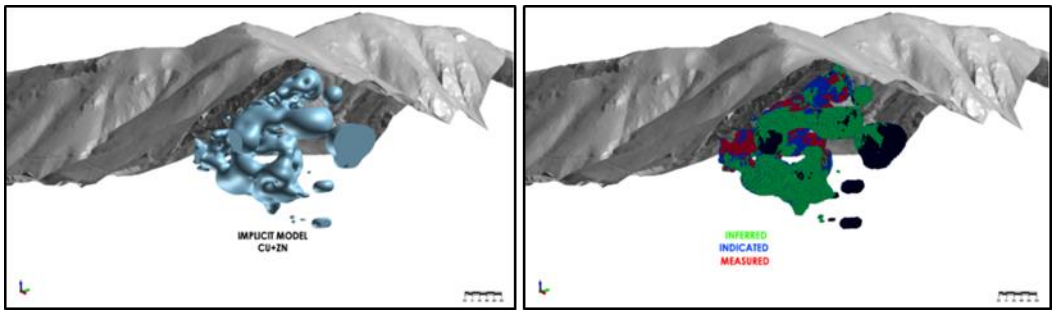

Figure 3- Block model in terms of resource clasiffication

Table 1- Grade and tonnage by IDW calculation

Category	Cu	Zn	Cu	Zn	Cu	Zn
	Ore Tonnage		Grade (%)		Metal (Ton)	
Mea	1,356,976	1,447,877	0.97	1.27	13,163	18,388
Ind	3,540,080	3,882,626	0.98	1.84	34,693	71,440
Inf	506,468	639,522	0.85	2.04	4,305	13,046
Mea+Ind+Inf	5,403,524	5,970,025	0.97	1.72	52,160	102,684

5. KRIGGING

The first requirement for using the Kriging spatial interpolation technique is the calculation of a variogram and covariance functions. Subsequently, an unsampled location must be evaluated [3]. Variograms are one of the most successful methods for demonstrating spatial consistency in geostatistical estimations. Geostatistical estimations are based on the spatial structure of the data. [4]. An empirical variogram is ideal for examining local data and is constructed based on a basic measure of heterogeneity. Variograms are measures of spatial correlation and can determine anisotropy if the extent of such spatial correlation varies with direction. To determine the anisotropy of a spatial variation, an empirical variogram must be generated in several directions. Consequently, the anisotropic direction is determined using variogram modeling in two or three orientations. Anisotropy can be divided into geometric anisotropy, which responds to differences in the range or area of the variograms, and regional anisotropy. Anisotropy can be used to predict and simulate subsurface conditions based on their orientation and dimensions [5]. Z(x0) represents the block with an unknown grade and is calculated using a linear combination of known values. wi represents the weight value of sample number w, and Z(xi) represents the grade value of sample xi.The important point here is that the amount of error must be accounted for when assigning values. Calculating a variogram is a prerequisite for reserve calculation using kriging, a geostatistical method. A variogram is a measure of the change in the target variable depending on direction and distance.

Table 2- Grade and tonnage by kriging calculation

Category	Cu	Zn	Cu	Zn	Cu	Zn
	Ore Tonnage		Grade (%)		Metal (Ton)	
Mea	1,455,522	1,550,808	0.98	1.29	14,264	20,005
Ind	3,650,877	3,901,742	1.02	1.88	37,238	73,352
Inf	511,900	640,090	0.83	2.01	4,248	12,865
Mea+Ind+Inf	5,618,299	6.092,640	0.99	1.74	55,750	106,222

6. CONCLUSION

This study, the reserve modeling of a real Copper-Zinc mine site was conducted using two fundamental interpolation methods in geostatistics: Inverse Distance Weighted (IDW) and Ordinary Kriging (OK), and the results were comprehensively compared. The analyses demonstrated that both methods reasonably captured the overall grade distribution and geometry of the site. However, the radical differences in the fundamental philosophies of the methods resulted in significant and significant deviations in the final estimates, reflected in the evaluation of estimation errors, and the block model to be selected. According to the findings, the Inverse Distance Weighted Method highlighted local anomalies and high-grade samples more clearly because it is based only on the distance to the sample points, without relying on a precise mathematical model. In contrast, the Ordinary Kriging Method produced more reliable and objective results because it works by building a variogram model that represents the statistical and spatial behavior of the data. Kriging provides a critical measure of the reliability of the estimates by providing the variance of the estimates for each block (kriging variance) along with the estimates.

REFERENCES

[1] V. Rudenno, The mining valuation handbook, John wiley, 1998 p. 121
[2] J. Charles Moon, K.G Michael, Introduction to Mineral Exploration, Blackwell, 2006 p.43
[3] C.A. Calder, N.Cressie, International Encyclopedia of Human Geography. 1 (2009) 49-55.
[4] F. C. Curriero, M. E. Hohn, A. M. Liebhold, S. R. Lele, Subhash. Environ. Ecol. Stat.. 9 (2002).
[5] E. Hosseini, R. Gholami, F. Hajivand, J. Petrol. Explor. Prod. Technol. 9 (2009) 1051–1073.
[6] Z. Liu, Z. Zhang, C. Zhou, M. Weihua, Z. Du, Geosciences. 11 (2021) 51.

The 56th International October Conference on Mining and Metallurgy
22-25 October 2025, Bor Lake, Bor, Serbia
www.ioc.tfbor.bg.ac.rs

DOI: 10.5937/IOC25157V *Original scientific paper*

CHALLENGES IN MINING SUBSIDENCE ENGINEERING

Nenad Vušović[1a], Milica Vlahović[2a*]

[1] University of Belgrade, Technical Faculty in Bor, Vojske Jugoslavije 12, 19210 Bor, Serbia;
[2] University of Belgrade, Institute of Chemistry, Technology and Metallurgy-
National Institute of the Republic of Serbia, Njegoševa 12, 11000 Belgrade, Serbia
[1a] nvusovic@tfbor.bg.ac.rs, 0000-0001-5246-4243
[2a,*] m.vlahovic@ihtm.bg.ac.rs, mvlahovic@tmf.bg.ac.rs, 0000-0002-7893-9101

Abstract
Subsidence represents one of the most complex and debated issues in rock mechanics and geotechnical engineering. It can significantly impact the environment and endanger the stability of surface and subsurface structures and infrastructure. Reliable prediction methods are therefore essential to mitigate the adverse effects of mining-induced subsidence. This paper examines the mechanisms of mining subsidence and outlines different excavation-induced forms, with emphasis on trough and sinkhole subsidence. The key factors influencing subsidence above underground workings are briefly reviewed. Finally, several case studies of sinkhole subsidence worldwide are presented to highlight the scale and significance of the problem.
Keywords*: underground mining, mine subsidence, sinkhole subsidence, residual subsidence*

1. INTRODUCTION

Underground excavations disturb the natural equilibrium of the rock mass, causing load redistribution that leads to deformation and displacement of surrounding strata. As these displacements propagate towards the surface, they result in ground subsidence, which typically manifests in two main forms:

- ***Displacement*** refers to changes in the position of specific points within the undermined rock mass and on the ground surface, as primary or secondary consequences of underground mining. Geometrically, it is defined as a vector connecting the initial position of a point in the undisturbed rock mass with its new position after equilibrium has been re-established. If the displacement process is ongoing, the vector represents its instantaneous value. The vertical projection of this vector corresponds to settlement, while the horizontal projection represents horizontal displacement [1].
- ***Subsidence*** is a general term describing the downward vertical movement of the Earth's surface, which may result from both natural processes and human activities [2].

Mining subsidence, a universal phenomenon associated with voids formed by the extraction of solid or liquid resources under the surface, is influenced by multiple factors including mining method, extraction depth, deposit thickness, topography, and the geomechanical properties of the overlying strata.

Certain underground mining methods, particularly those designed to induce caving (e.g., pillar extraction, longwall mining, block caving, sublevel caving) commonly result in surface subsidence. While mining-induced subsidence is often relatively predictable in magnitude, extent, and pattern, unexpected collapses of pillars or shallow workings (typically in old mines) can lead to sudden, severe ground failures [2].Associated surface effects such as horizontal tensile and compressive strains, curvature, tilting, and horizontal displacements are among the most frequent causes of damage to buildings and infrastructure [3].

2. SUBSIDENCE AND THE DIFFERENT SUBSIDENCE TYPES

The development of mining subsidence is primarily governed by geological and mining-related factors such as the mechanical behavior of the rock mass, mining depth, excavation geometry, surface topography, and the applied mining method. For example, partial extraction methods (e.g., shallow room-and-pillar mining in weak rock) show distinct subsidence mechanisms compared to total extraction methods (e.g., deep longwall mining or top-coal caving). In longwall mining, caving progresses rapidly, and surface subsidence occurs almost immediately after extraction, typically stabilizing within a short period. However, a portion of ground movement continues later, caused by the re-compaction of caved material. The rate and duration of these movements depend on the depth, extraction speed, and geotechnical properties of overburden strata. This form of ground depression, common in longwall mining, is known as ***trough subsidence***, a broad, shallow sag of the surface [3,4]. Another form, more typical of shallow excavations with partial extraction, is ***sinkhole subsidence*** (also referred to as pit, crown-hole, or chimney subsidence). It occurs due to localized mine roof failure that propagates upward to the surface, resulting in sudden sinkhole formation.

Research shows that a large share of surface structure damage and casualties is caused by sinkhole subsidence. The reason lies in the fact that trough subsidence can be recognized early in its development, allowing for preventive measures to reduce its impact [1,3,4]. By contrast, sinkhole subsidence is often catastrophic, appearing without warning and without reliable prediction of timing or location. Moreover, while longwall mining affects vast areas and thus causes relatively uniform deformations, sinkhole subsidence is localized, leading to more severe structural damage on the surface [5].

2.1 Sinkhole Subsidence

Sinkhole subsidence represents one of the most hazardous post-mining problems, with highly complex mechanisms. Before investigating subsidence processes, it is essential to understand the modes of failure and conditions that trigger sinkhole formation. This type of subsidence is usually caused by the sudden collapse of roof strata into underground voids, progressing upward through the overburden in the form of a chimney until it reaches unconsolidated surface materials. Alternatively, sinkholes may develop when loose sediments and rock debris migrate downward into mine voids through fractured or weathered overlying strata.

Such failures are especially common in shallow, abandoned room-and-pillar workings where the roof lacks long-term stability. Over time, progressive collapse of roof layers and flow of broken material into the void ultimately leads to sinkhole formation at the surface [5].

Figure 1. Sinkholes above Berezniki potash mine, Russia: a) June 2007 and b) November 2008 (source: Itar-Tass news agency and ru.wikipedia.org).

Most sinkholes appear circular or elliptical, with typical diameters of less than 10 m and depths under 15 m. However, in extreme cases, their dimensions may exceed several hundred meters [5,6]. Typical examples are shown in Figure 1, illustrating sinkholes above the Berezniki potash mine in Russia (June 2007 and November 2008).

2.2 Trough Subsidence

The mechanisms of trough subsidence caused by longwall mining have been widely investigated and documented in the literature. Although this phenomenon is generally well understood, a number of questions still remain concerning the role of certain influencing factors. Subsidence development in such excavations is controlled by a range of geological and mining conditions, and therefore requires detailed study to fully capture the contribution of each parameter [1].

The most significant factors include, but are not limited to: the mechanical behavior of rock masses, the geometry and properties of discontinuities and their mechanical responses, groundwater levels and their adverse influence on rock mass strength, the magnitude and orientation of in-situ stresses, the extraction method applied, and the rate of resource exploitation.

Accurate determination of rock mass parameters is a fundamental prerequisite for analyzing the mechanisms of mining subsidence, since they serve as input data for analytical and numerical deformation simulations [3,4]. However, estimating these parameters is often extremely delicate. Without reliable values for the mechanical properties of rock strata, the outcomes of subsidence modeling cannot be considered trustworthy.

Surface topography is another key factor controlling the development of trough subsidence. When mining takes place beneath sloping terrains, the mechanisms of ground movement differ substantially from those observed in flat terrains, where the overburden behaves more symmetrically [3].

2.3 Active and Residual Subsidence

Subsidence may accompany both active and abandoned mining operations. ***Active subsidence*** encompasses all ground movements that occur simultaneously with the mining process, while ***residual subsidence*** refers to deformations that develop after mining activities have ceased [7].

Understanding the forms of deformation and their timing is essential for predicting the impacts on surface structures and planning mitigation measures.

Although predicting the duration of subsidence is a critical aspect of mine design and land-use planning, only limited research has addressed the influence of geological and mining factors on the length of deformation processes [3,4].

At present, there is no universally accepted and practical method for estimating subsidence duration. Experimental approaches are often costly and technically demanding. For longwall operations, considerable effort has been devoted to analyzing the time frame of subsidence development, but in the case of sinkhole subsidence, especially above room-and-pillar mines, reliable predictive models are still lacking.

One of the main reasons is that the duration of such deformations is largely governed by the long-term mechanical response of roof and floor strata, as well as the stability of the supporting pillars.

The interactions between pillars and surrounding strata play a crucial role in this mechanism [5].

Residual subsidence is a particularly severe issue in urban areas built over abandoned mine workings. Assessing long-term stability in such settings is a highly complex task, because time-dependent processes such as creep, progressive weakening, and deterioration of rock mass properties must be considered. These effects may extend subsidence over several decades. Reliable

prediction of residual subsidence is therefore of great importance for evaluating the long-term safety of surface structures and infrastructure [3,6].

3. CONCLUSION

Mining-induced subsidence has long been recognized as a serious geotechnical challenge. Consequently, extensive efforts have been devoted to the development of theories, empirical models, and analytical methods for estimating the magnitude and geometry of subsidence profiles. Nevertheless, accurate prediction, particularly of sinkhole subsidence, remains a difficult task. The complexity of the problem arises from numerous interrelated factors, including uncertainties in the mechanical behavior of the rock mass and caved materials, the in-situ stress regime, groundwater conditions, and the geometry and properties of discontinuities such as joints, bedding planes, and faults. The progressive deterioration of rock mass properties further complicates prediction and analysis.

Although a variety of approaches, such as graphical methods, profile function models, and influence function techniques, have been successfully applied to estimate the shape and extent of trough subsidence above longwall panels, these methods are generally unsuitable for shallow excavations where sinkhole subsidence dominates. In such cases, both the magnitude and duration of ground movements are far more difficult to forecast. Sinkhole subsidence above room-and-pillar workings may be delayed for decades, and its sudden occurrence poses severe risks to infrastructure and human safety.

Developing reliable methods to approximate the timing and scale of these deformations remains a priority in geotechnical engineering, particularly for stability assessments of structures in undermined areas.

ACKNOWLEDGEMENTS

This study was funded by the Ministry of Science, Technological Development and Innovation of the Republic of Serbia (grant numbers 451-03-137/2025-03/200131 and 451-03-136/2025-03/200026).

REFERENCES

[1] D. Đorđević, N. Vušović., Prognosis of the Displacement and Deformation of the Underground Terrain, University of Belgrade, Faculty of Mining and Geology, Belgrade, 2014, p. 19-28.
[2] M. Allaby., A dictionary of Geology and Earth Sciences, Oxford: Oxford University Press, Oxford, 2013.
[3] N. Vušović, R. Hejmanowski, M. Vlahović., Appl. Sci. 15 (2025) 1-30.
[4] N. Vušović, M. Vlahović, D. Krzanović., Environ. Earth Sci. 80 (2021) 67.
[5] T. Waltham, F.G. Bell , G. Martin, M.G. Culshaw., Sinkholes and Subsidence, Karst and Cavernous Rocks in Engineering and Construction, Springer with Praxis Publishing, Chichester, 2005.
[6] E.F. Salmi, M. Karakus, M. Nazem., Tunn. Undergr. Sp. Tech. 88 (2019) 169-185.
[7] E.F. Salmi., A numerical investigation of the mechanisms of post-mining subsidence, Doctoral thesis, The University of Newcastle, Australia, 2016.

Mineral Processing and Recycling

The 56th International October Conference on Mining and Metallurgy
22-25 October 2025, Bor Lake, Bor, Serbia
www.ioc.tfbor.bg.ac.rs

DOI: 10.5937/IOC25163B *Original scientific paper*

ON THE MECHANISMS OF DISINTEGRATION OF ROCKS UNDER THE EXPLOSIVE AND PULSE-DISCHARGE IMPACTS

Igor Zh. Bunin[1a], Alexey N. Kochanov[1b]

[1]N.V.Melnikov's Institute of Comprehensive Exploitation of Mineral Resources Russian Academy of Science, 4, Kryukovsky Tupik, Moscow, 111020, Russia
[1a] bunin_i@mail.ru, 0000-0002-8618-5119
[1b] kochanov@mail.ru, 0000-0001-7896-8546

Abstract
This paper presents new experimental results derived from studies that involved the explosive impact and nonthermal effect of high-power nanosecond electromagnetic pulses have on the formation of microdefects in rock samples in the "pre-fracture" stage. Using atomic force and scanning electron microscopy, nanoindentation and microhardness testing, we studied the change in surface morphology (microdefects) and mechanical properties of rock samples and natural minerals under these dynamic types of impacts. The minimum values of the microcrack opening width in rocks after explosive and electromagnetic pulse impacts were ~0.2–0.5 μm, and the most typical opening width was 2–3 μm.

***Keywords**: Rocks, disintegration, microcracks, explosive impact, high-power nanosecond pulses*

1. INTRODUCTION

Pre-fracture state of rocks, minerals and ores (pre-destruction of geomaterials [1]) is considered as the initial stage of the evolution of the internal microstructure of geomaterials, on which the deformation and reorientation of individual grains of rocks, disruption of bonds, development of microdefects, change in the properties and state of a certain volume of the mineral environment occur [1,2]. It is at the stage of pre-fracture of solids that the sequential generation and development of the defects at various scale, mainly nano- and microstructural levels develops [2]. The prospects for the practical application of the explosion energy to improve the efficiency of the complex processing of hard-beneficiation mineral raw materials [3], and at the same time the introduction into industry of electric pulse technologies for crushing (comminution) and selective disintegration of rocks and ores [4], predetermine the need to conduct the research into the mechanisms of dynamic (explosive, electric explosive) destruction of rocks using modern methods of microstructural analysis. Analysis of the mechanical, electrical and physicochemical properties of the surface of natural mineral substances provides important information about the distribution of structural-material associations in geomaterials and their local properties. The research to determine the mechanical properties of individual mineral grains, micromechanisms of deformation and destruction of minerals that make up the rock, taking into account the influence of interphase boundaries, is relevant. This paper presents experimental data on the influence of shock-wave loading from an explosion, as well as the influence of high-voltage pulse discharges of nanosecond duration on the morphology, structure of surface defects and mechanical properties of rock samples and natural minerals with different mechanical and electrical (dielectric) strength.

2. EXPERIMENTAL

Experimental studies were carried out on the samples of ferruginous quartzites, quartz, granite, dolomite and coal in the form of the specially prepared polished sections of minerals and rock plates, as well as fragments of irregularly shaped specimens 4–5 mm in size (wide). When conducting experiments on explosive impact, we used the samples (blocks) of granite with a characteristic size of one of the sides from 15 to 25 cm. A cylindrical hole was created in the center of the samples using a diamond drill, into which a charge of a small explosive substance of ~0.1 g

was placed [5]. After the explosive impact, individual plates were cut from the samples for surface analysis by the methods of optical and electron microscopy. The conditions of exposing the mineral samples to the effect of high-power nanosecond electromagnetic pulses (HPEMP [6]) in air under standard conditions were described in detail in [7,8], along with the electro-physical parameters of the high-voltage pulse generators. The duration of sample treatment varied in the range t_{treat}= 10–100 s. Let us specify, that with the HPEMP effect, the duration of high-voltage nanosecond pulses was 4–10 ns, the leading edge of a pulse was 2–5 ns. Pulse amplitude was U_A = 25 kV, strength of the electric field in the 5 mm interelectrode gap, E~10^7 V×m^{-1}, and the rate of nanosecond pulse repetition was f = 100 Hz. The parameters of energy impacts established for conducting our experiments (both in the case of explosion and HPEMP) did not lead to fragmentation of samples into separate parts; however, the numerous traces of local violations of the continuity of the mineral substance in the form of macro- and microcracks, electrical breakdown channels and exposed microinclusions of secondary phases were formed on the surface of the samples.

The morphological features of the mineral surface and the trajectories and characteristic sizes of cracks on the samples surface were studied by atomic force microscopy (AFM) and analytical scanning electron microscopy (SEM–EDX), and the elemental composition was determined by X-ray spectral microanalysis. Scanning probe microscope SMM-2000 (JSC "PROTON Plant", Zelenograd) and electron microscopes LEO-1420VP with an Oxford INCA Energy 350 EDX System, and JSM-6610LV microscope were used. AFM images of surface fragments (scans of 8x8 μm in size) were obtained in contact scanning mode using silicon cantilevers of the CSG01 series (the tip curvature radius was 10 nm, the force constant was 0.05 N/m, the resonance frequency was 12 kHz). The nanotriboindentometer TI-950 (Scientific Center of Tambov State University named by G.R. Derzhavin, Tambov, Russia) was used to measure the minerals hardness at the nanostructural level (nanoindentation testing). The microhardness of quarz samples was determined by the Vickers method (HV, kgf/mm^2) on a PMT-3M microhardness tester (LOMO, Russia), with an indenter load of 150-200 g and a loading time of 10–15 s.

3. RESULTS AND DISCUSSION

Analysis of AFM images of fragments of the surface of rock samples (Figure 1) in the initial state (after preparatory mechanical processing) showed that the spread of heights across the frame for quartzite, granite and dolomite was 1.2; 1.35; 2.33 μm, respectively; the average arithmetic roughness (S_a, nm; average roughness, ISO 4287/1) of the surface of the samples was 116, 141, 250 nm, respectively.

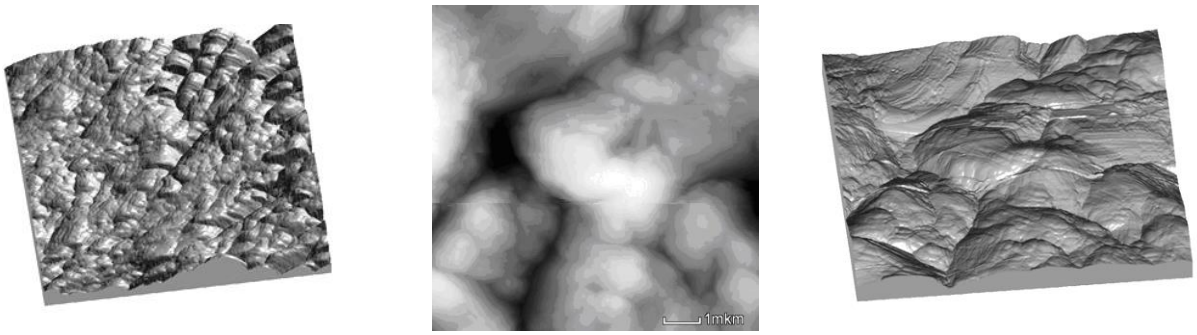

a *b* *c*

Figure 1. AFM images of 8×8 μm quartzite (a) and granite (b), (c) surfaces: 2D brightness image (b) and 3D relief visualization (a), (c) of rock surfaces

The average grain size of quartzite was S_{gr} = 1.59 μm, and the average subgrain size (or the nanograin from which the grains are composed) was S = 277 nm; for the granite sample – S_{gr} = 2.73

μm, S = 234 nm; for dolomite – S_{gr} = 3.26 μm, S = 351 nm. It's obviously that at the microlevel, the geometric characteristics of the morphological features of the samples surface are related to the parameters of the rocks grain structure. The microrelief of the granite surface (Figure 1*c*) was noticeably more pronounced compared to the quartzite sample (Figure 1*a*).

The structure of rocks is heterogeneous, the rocks consist of individual mineral grains and they have structural features, including defects of different scale levels (cracking properties or fracturing). For the most rocks, the fracture toughness does not exceed 0.5 – 2.0 MPa×m$^{1/2}$ (for example, the fracture toughness of the marble, sandstone and serpentine is 0.75, 1.1, 1.4 MPa×m$^{1/2}$, respectively), while the crack resistance (K_{1c}) of brittle ceramics reaches ~5 MPa×m$^{1/2}$. For the ferruginous quartzite samples a comparatively low fracture toughness of the non-metallic phase (quartz) was established using the nanoindentation method. The fracture toughness of quartz was 0.5 MPa×m$^{1/2}$; the K_C of quartz was ~1.5 – 2.0 times lower than the fracture toughness of the iron ore mineral grains (hematite and magnetite). At the boundaries of the intergrowth of quartz-magnetite and quartz-hematite grains, the value of K_C was 0.68 and 0.38 MPa×m$^{1/2}$, respectively; this value is ~2–3 times smaller than at the boundary of the intergrowth of magnetite–hematite ore mineral grains.

SEM data show that most of the microcracks which developed in rocks due to the action of the blast wave (zone of the wave prefracturing of rocks under blasting [2]) are of the plane-mode type (mode I of the cracking). No shear-type (mode II) formation of defects was observed. Under explosive action, the newly formed cracks propagated inside the grain boundaries in the rocks; i.e., the character of disintegration was primarily transcrystalline. However, some number of microcracks were also observed along grain interfaces that were connected or coincided fully. The characteristic features of the crack propagation trajectories (discontinuity, discreteness, unevenness of crack edges (Figure 2*a*)) testify about dynamic, jump-like growth of cracks, which stop at the obstacles and overcome the areas of localization of microdamage at the crack tips.

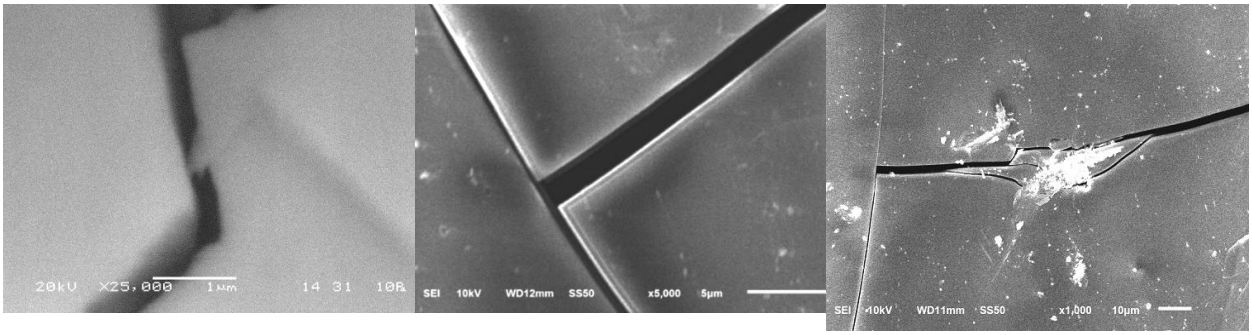

a *b* *c*

Figure 2. Morphology of microcracks on the surface of rock samples after the various energy impacts: explosion (quartzite) (a), and HPEMP (coal) (b), (c). SEM, scale bars: 1 (a), 5 (b) and 10 (c) μm

As a result of HPEMP with t_{treat} = 300 s, the systems of microcracks formed on the surfaces of the coal samples and usually propagated along strictly linear trajectories (Figure 2*b*). The minimum values of the microcrack opening width in rocks were ~0.2–0.5 μm, and the most typical opening width was 2–3 μm. The formation and propagation of microcracks was affected by microinclusions in the coal (Figure 2*c*). Newly formed cracks exposed particles of secondary phases (sulfides), they spread along the boundaries of sulfide particles (selective disintegration of mineral complexes). Structural modifications after electropulse treatment were more typical of samples taken from seams of outburstprone coal that are brittle.

As a result of ultrasonic measurements of the propagation parameters of longitudinal and transverse waves in the rock samples, we found that the development of microcracks leads to a

decrease in the velocity of longitudinal waves (possibly due to the development of fracture porosity), and, consequently, to the degradation of the strength properties of geomaterials. In this report we discuss the results of a study of the influence of explosion and high voltage nanosecond pulses on the mechanical properties of rock samples. For example, under non-thermal action of HPEMP for t_{treat} = 150 s, the softening of milky-white quartz surface (Mohs hardness 7) occurred, and a decrease in microhardness (HV) from 1430 to 1010 kgf/mm2 (ΔHV ~30%) was observed. Apparently, the mechanism of the quartz softening consisted of microwave decrepitation of gas-liquid inclusions in the host mineral. This effect can be used in the technologies of deep beneficiation of natural quartz at the stages of mechanical crushing (grinding) and electrical fragmentation to clean the mineral from microimpurities.

The formation of crystallographically oriented discharge channels in silicon dioxide suggests the realization of an specific (certain) electrical breakdown mechanism. The authors of paper [9] considered the formation of breakdown channels in silicon dioxide in terms of the model of impact ionization of the valence band by fast nonequilibrium electrons, and also, in terms of the model of primary electron generation by cascade Auger transitions in the valence band of the dielectric. The disintegration of mineral media, due to the formation of microchannels of electric breakdown, lie in planes of silicon ions, as a result of charge carriers (primary electrons) being generated by cascade Auger transitions in the valence zone of the dielectric mineral with regard to the crystallochemical stricture of quartz [9] is a possible mechanism of the quartz surface softening under the influence of high-voltage nanosecond pulses.

4. CONCLUSION

Under explosive type action, the newly formed cracks propagated inside the grain boundaries in the studied rocks; i.e., the character of disintegration was primarily transcrystalline. In contrast, under the impact of high-voltage nanosecond pulses, the formation and propagation of microcracks in the rock samples was recorded primarily along grain boundaries (intercrystalline fracture, which determines the selective disintegration of ores exposed to HPEMP). The effectiveness of the nonthermal effect high-power electromagnetic pulses has on the formation of microcracks in the considered rocks was most apparent in our coal samples. The minimum values of the microcrack opening width in rocks after explosive and electromagnetic pulse impacts were ~0.2–0.5 μm, and the most typical opening width was 2–3 μm.

ACKNOWLEDGEMENTS

The authors are grateful to the engineer A.S. Loginova of JSC PROTON Plant and head of the laboratory of atomic modification and analysis of semiconductor surfaces of the National Research University of Electronic Technology (MIET) B.A. Loginov for their help in the AFM-experimental studies.

REFERENCES

[1] S.D. Viktorov, A.N. Kochanov, V.N. Odintsev, J. Min. Institute, 171 (1) (2007) 153-157.
[2] A.N. Kochanov, V.N. Odintsev, J. Min. Sci., 52 (6) (2016) 1080-1089.
[3] A.V. Rasskazova, A.G. Sekisov, A.A. Galim'yanov, J. Min. Sci., 59 (6) (2023) 1036-1044.
[4] A.V. Kharlov, Instruments and Experimental Techniques, 65 (1) (2022) 1-28.
[5] S.D. Victorov, A.N. Kochanov, Bull. Russ. Acad. Sci.: Phys., 81 (5) (2017) 616-618.
[6] V.A. Cherepenin, Physics – Uspekhi, 49 (10) (2006) 1097-1102.
[7] I.Zh. Bunin, V.A. Chanturiya, N.E. Anashkina, et al., J Min Sci., 51 (4) (2015) 799-810.
[8] I.Zh. Bunin, V.A. Chanturiya, M. V. Ryazantseva, et al., Bull. Russ. Acad. Sci.: Phys., 83 (6) (2019) 668-672.
[9] R. Emlin, S. Barakhvostov, V. Kulikov, Tech. Phys. 54 (7) (2009) 1076-1079.

The 56th International October Conference on Mining and Metallurgy
22-25 October 2025, Bor Lake, Bor, Serbia
www.ioc.tfbor.bg.ac.rs

DOI: 10.5937/IOC25167L *Original scientific paper*

EXPERIMENTAL STUDY ON PELLETIZATION OF BLENDED SEA SAND ORES

Renguo Li [1a], Lanjie Li [1b], Heng Ji [1c], Minglei Gao[1d], Shiwei Wang[1e]

[1] Hebei HBIS Materials Technology Research Institute Co., Ltd, Shijiazhuang 050023, Hebei, China
[1a] lirenguo@hbisco.com, 0009-0009-2920-6428
[1b] lilanjie@hbisco.com, 0009-0006-3261-3225
[1c] jiheng@hbisco.com, 0009-0009-0192-2641
[1d] gaominglei31135@hbisco.com, 0009-0007-0487-7204
[1e] wangshiwei01@hbisco.com, 0009-0004-3957-2900

Abstract

Sea sand ore (SSO), an abundant secondary vanadium-titanium magnetite resource formed through fluvial, wave, and current erosional processes, is readily minable yet remains underutilized due to challenges in metallurgical processing caused by its complex mineral composition. This study utilizes SSO as raw material to produce oxidized pellets, thus enabling its application in blast furnace (BF) ironmaking processes and promoting comprehensive utilization of sea SSO resources. This study systematically investigated the effects of SSO blending ratios on the metallurgical properties of vanadium-titanium magnetite oxidized pellets. Results demonstrate that compared with Heishan vanadium-titanium ores, SSO exhibits superior pelletization performance despite slightly higher V-Ti content. As the SSO ratio increased, the strength of green pellets progressively declined, with the 100% SSO pellets showing zero drop strength – failing to meet production requirements. Furthermore, the compressive strength(CP) and low-temperature reduction degradation index ($RDI_{+3.15}$) of oxidized pellets initially decreased then increased with rising SSO ratios. Industrial basket trials using 80% SSO confirmed pellet strength reaching 2,578 N, satisfying BF operational criteria.

***Keywords**: sea sand ore; vanadium-titanium magnetite; oxidized pellets; blast furnace ironmaking*

1. INTRODUCTION

Sea sand ore (SSO), a unique coastal iron ore resource formed by geological processes like fluvial sedimentation and marine erosion, is widely distributed in coastal areas of Japan, the Philippines, Indonesia, Australia, New Zealand, and China's Hainan Island. It boasts abundant reserves, easy mining, and low cost, ranking as the world's second-largest marine mining operation after offshore oil[1].

As a type of vanadium-titanium magnetite, SSO contains about 60% TFe and 6-9% TiO_2, with high refractory components (V_2O_5, Al_2O_3, K_2O, Na_2O) that hinder sintering[2]. Its particles are coarse (0.5-2.0 mm), regularly spherical/ellipsoidal with smooth surfaces, and feature a compact, complex mineral texture[3].

While current research on utilizing SSO as ironmaking feedstock predominantly focuses on sinter production, its blending ratio remains limited due to inherent material constraints[4]. This study pioneers an alternative approach by investigating the metallurgical properties of green pellets and oxidized pellets produced from SSO blends through laboratory-scale pelletizing. Building on experimental findings, industrial strand tests were conducted to validate the technical feasibility of incorporating SSO in pelletization processes.

2. EXPERIMENTAL

2.1 Material

The pelletizing raw materials employed in this study comprised SSO, Heishan vanadium-titanium ore(HVO), conventional vanadium-titanium ore (CVO), and bentonite. Specifically, SSO was processed into concentrate through grinding and beneficiation prior to use. The properties ore powders are listed in Table 1. Based on the data in Table 1, SSO exhibits higher vanadium and titanium content as well as a better balling index compared to HVO.

Table 1. The properties ore powders (mass/%)

Sample	Chemical composition, %									Balling index
	TFe, %	TiO_2	V_2O_5	SiO_2	Al_2O_3	P	S	MgO	CaO	
SSO	61.81	6.09	0.59	2.79	1.84	0.03	0.02	0.95	0.68	1.7
HVO	61.65	6.31	0.67	1.78	2.52	0.02	0.21	0.97	0.34	1.4
CVO	60.62	2.58	0.36	5.10	1.36	0.01	0.01	2.65	1.66	2.1

2.2 Method

The pelletizing experiment with sea sand ore blending was conducted according to the optimized ore blending principle. The proportion of sea sand ore was gradually increased from 0% to 100%, with 1.5% bentonite externally added. The specific blending scheme is presented in Table 2. The roasting regime employed during pellet firing was as follows: the preheating temperature was 950°C for 30 minutes, followed by roasting at 1300°C for 25 minutes. Based on laboratory findings, we conducted two industrial basket trials at the pelletizing line of X Iron and Steel Plant in China, validating the performance of maximum-SSO-loaded pellets under actual production conditions.

Table 2. The blending scheme

Number	Ore, %		
	HVO	CVO	SSO
A	50	50	0
B	50	30	20
C	50	10	40
D	40	0	60
E	20	0	80
F	0	0	100

3. RESULTS AND DISCUSSION

3.1 Analysis of cold-state performance of green pellets

Green ball strength is a crucial indicator for evaluating the quality of pellets during the transportation process from the completion of balling to the start of roasting. Sufficient green ball strength ensures that the pellets do not break during transportation, maintaining a high yield rate. Typically, green balls used for blast furnace smelting require a drop strength >4 drops/0.5m and a CP >10N.

Table 3 presents the experimental strength results of green balls produced by adding SSO. The experiment demonstrates that as the proportion of SSO increases, the green ball strength continuously decreases. When the proportion of SSO reaches 100%, the drop strength of the green balls falls to 0 drops/0.5m, and the CP decreases to 5N. This strength level is too low and fails to meet the actual production requirements for pellets.

Table 3 The experimental strength results of green balls produced by adding SSO

Number	SSO, %	drop strength, drops/0.5m	CP, N
A	0	6	15
B	20	5.5	14.2
C	40	5.2	13
D	60	4	11
E	80	5	12
F	100	0	3

3.2 Analysis of metallurgical properties of oxidized pellets

Following oxidation roasting, the CP of pellets significantly increases due to solid-phase bonding between ore particles. The metallurgical properties of the oxidized pellets after roasting are shown in Figure 2. As shown in Figure 1, pellets blended with SSO exhibit strengths ranging from 2100N to 3000N. The CP initially decreases then increases with higher SSO proportions, reaching its minimum (2195N) at 60% SSO loading. This occurs because CVO (critical bonding component) is fully replaced at this ratio, leaving only HVO and SSO – both inferior in consolidation properties. All other blends exceed 2500N, meeting blast furnace specifications. All oxidized pellets exhibit a Low-Temperature Reduction Disintegration Index ($RDI_{+3.15}$) exceeding 90%, effectively preventing excessive pulverization during blast furnace smelting that could degrade burden permeability.

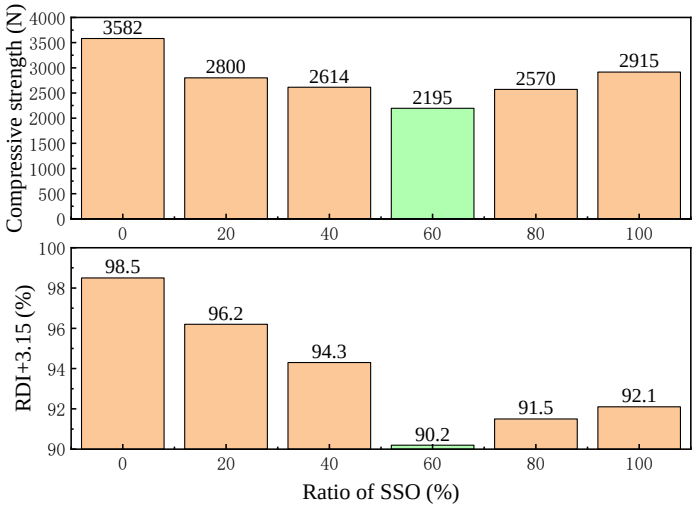

Figure 1. The metallurgical properties of oxidized pellets

3.3 Analysis of industrial basket trial results

Building on prior laboratory research confirming a maximum 80% sea sand ore (SSO) ratio, we initiated industrial basket trials to facilitate scaled-up application. Pellets were produced via a six-stage grate-kiln process: downdraft drying → updraft drying → preheating → roasting → primary cooling → secondary cooling. Two trials employed raw material Blend E (consistent with lab Study E). Process parameters for each stage in both trials are detailed in Table 4, with key schemes: Scheme 1 (standard production parameters) and Scheme 2 (laboratory-optimized parameters with adjusted thermal profiles). This experimental design enabled systematic evaluation of pellet quality evolution under industrial conditions with controlled parameter variations.

Table 4. The Process parameters for each stage in both trials

Stage	Scheme 1		Scheme 2	
	Temperature, ℃	Time, min	Temperature, ℃	Time, min
Downdraft dry	90	4	95	5
Updraft drying	308	4	310	5
Preheat	1044	7	1070	9
Roast	1270	11	1300	14
Primary cool	--	11	--	14
Secondary cool	--	7	--	9

The metallurgical properties of oxidized pellets after two industrial basket trials are presented in Table 5. Results reveal that increasing both preheating-roasting temperature and holding time significantly improves the CP and RDI of oxidized pellets. Under the operational conditions of Scheme 1, the produced oxidized pellets exhibited relatively low strength, primarily attributed to the high contents of Al, V, and Ti in the raw materials. These components, as high-melting-point compounds, necessitate elevated roasting temperatures and extended holding times for complete sintering. Consequently, adjusting the preheating-roasting temperature and prolonging the holding duration led to substantial enhancements in the metallurgical performance of the pellets.

Industrial basket trial results confirm that blending 80% SSO in the pelletizing process can yield oxidized pellets meeting the technical requirements for blast furnace operation, thereby establishing a novel approach for the resource utilization of SSO.

Table 5. The metallurgical properties of oxidized pellets after two industrial basket trials

Sample	CP，N	RDI，%		
		$RDI_{+6.3}$	$RDI_{+3.15}$	$RDI_{-0.5}$
Scheme 1	1437	93.4	93.5	6.4
Scheme 2	2578	95.1	95.3	4.7

4. CONCLUSION

This study investigates the influence of iron sand ore blending ratios on the metallurgical properties of pellets. Industrial basket trials were conducted to validate pellet performance at the highest iron sand ore ratio. The main conclusions are as follows:

(1) As the SSO ratio increases, the strength of green pellets decreases. Pellets made entirely from SSO exhibit zero drop strength, failing to meet production requirements.

(2) The CP and RDI of fired pellets first decrease and then increase with rising SSO ratios.

(3) Industrial basket trials using pellets with an 80% SSO ratio demonstrated that their compressive strength reached 2578 N, satisfying blast furnace production requirements.

(4) Comparison of industrial basket trial results under different thermal parameters revealed that producing SSO pellets requires higher preheating/roasting temperatures and longer durations compared to conventional pellets.

ACKNOWLEDGEMENTS

This study was supported by the National key research and development program (No.2024YFE0215000).

REFERENCES

[1] G. Yu, X. Hu, J. Fang, et al. J. Mar. Sci. Eng. 12 (9) (2024) 1561.
[2] Z. Xing, J. Ma, G. Cheng, et al. J. Sustain. Metall., 8 (3) (2022) 1358-69.
[3] G. Cheng, Z. Xin, Y. He, et al. Minerals. 11 (1) (2021) 87.
[4] Y. Qin, Q. Ling, K. Zhang, et al. Minerals, 11 (8) (2021) 793.

The 56th International October Conference on Mining and Metallurgy
22-25 October 2025, Bor Lake, Bor, Serbia
www.ioc.tfbor.bg.ac.rs

DOI: 10.5937/IOC25171E *Original scientific paper*

EXPERIMENTAL RESEARCH OF THE LIGNITE DRYING PROCESS IN PACKED BED

Milić Erić[1a], Zoran Marković[1b], Aleksandar Milićević[1c], Rastko Jovanović[1d], Danka Kostadinović[1e], Ivan Lazović[1f] and Milica Jovčevski[2a]

[1]Vinca Institute of Nuclear Sciences - National Institute of the Republic of Serbia - University of Belgrade, Mike Petrovića Alasa 12-14, 11351 Vinča – Belgrade, Serbia
[2]Faculty of Mechanical Engineering, University of Niš, Niš, Serbia
[1a]milic@vinca.rs, 0000-0001-6850-3112
[1b]zoda_mark@vinca.rs, 0000-0003-0553-3263
[1c]amilicevic@vinca.rs, 0000-0003-4615-8789
[1d]virrast@vinca.rs, 0000-0003-0265-2304
[1e]dankak@vinca.rs, 0000-0003-2890-4979
[1f]ivan.lazovic@vinca.rs, 0000-0002-3877-5157
[2a] milica.jovic@masfak.ni.ac.rs, 0000-0002-5699-5831

Abstract
One of the biggest challenges is the development of low-carbon technologies for coal utilization. Clean coal technologies are a group of measures aimed at reducing carbon dioxide emissions by increasing the energy efficiency of coal-fired power plants. Experimental studies were carried out on the convective drying of lignite. The drying process was investigated under the packed bed conditions. The effects of sample size, temperature and coal grain size on the drying rate were investigated. Temperature was recognized as the most influential parameter.

***Keywords**: convective drying, lignite, moisture, packed bed*

1. INTRODUCTION

The methods for reducing the moisture content of low-rank coals may be divided into two main groups: conventional evaporative drying (direct or indirect dryers, packed bed or fluidised bed dryers, rotary kilns, etc.) and non-evaporative dewatering methods (mechanical-thermal expression, hydrothermal dewatering, etc.).

In the combustion of coals with high moisture content the thermal efficiency is reduced and increased CO_2 emissions that contribute to the greenhouse effect. This is because in conventional coal-fired power plants a part of the fuel's heat is consumed in the boiler during combustion and mill drying to evaporate coal moisture. The coal moisture leaves the power plant as steam together with the flue gas, so that this heat cannot be used in the plant process and is lost.

Kolubara lignite is the mostly used coal in the Republic of Serbia. It belongs to low quality coals with moisture content in the range of 45% to 52% [1] . As a first step in researching the process of convective drying in the Vinca Institute of Nuclear Sciences, Laboratory for Thermal Engineering and Energy, a number of experiments were performed in the in the packed bed drying process.

Conventional convective evaporative drying involves complex transport phenomena consisting of three successive processes. The first is the movement of moisture in solids, which occurs from the moist interior to the gas-solid interface (internal pores, particle surface, etc.). This process is slower for larger solids and/or materials with low moisture content. The second process is evaporation, which is favoured by heat (energy) that is either supplied from the outside or extracted from the solid and used to convert liquid into vapour. The last process is the movement of the vapour into the surrounding gas by diffusion and convection. The slowest of these processes determines the

overall drying rate, etc.). Predicting the kinetics of falling desiccation by theory alone is very difficult. Therefore, precise experiments on a small scale are required instead. Concepts such as the "characteristic drying curve" ([2-3] or the "drying coefficient" ([4-5]) can be used to predict the drying rates under different conditions.

2. EXPERIMENTAL RESEARCH

Convective drying experimental research in packed bed of Kolubara lignite had the following objectives: determination of the Kolubara lignite drying kinetics curve, analysis of the drying agent influence, determination of the influence of temperature of the drying agent and material particle size and validation of the mathematical model. The Sherwood Tornado M501 fluidised bed dryer with a 5 litre sample tube, Figure 1 was used to carry out experiments to dry Kolubara lignite samples in a packed bed [1].

The decrease in moisture content of the Kolubara lignite samples was determined by measuring the air mass flow balance at the dryer inlet and the dryer outlet. The following measured parameters were used for the calculations described above: volume flow rate at the inlet, temperature and relative humidity of the air at the inlet and outlet of the dryer. The minimum fluidisation velocities upstream of the sample were determined for all grain sizes and air temperatures. The magnitude of the air velocity upstream of the sample was approximately 0.6 m/s to 0.7 m/s.

The air is fed into the dryer by means of a centrifugal blower and then passed through an electric heater (electric power 2 kW). The blower is operated and controlled by a thyristor circuit which allows the motor speed to be regulated over a wide range of operating conditions. The dryer is fitted with feedback to ensure that the blower motor is kept at the same programmed speed regardless of the effects of the power supply and heating. The projected operating flow rate is in the range of 0 to 2 m^3/min, while the maximum blower load can be achieved at 2.5 m^3/min.

The air temperature downstream of the heating element is measured by a thermocouple connected to a control unit that activates and deactivates the heating element based on a specific air temperature at the inlet upstream of the sample. The air temperature upstream of the sample can be set within a range of 20 to 200 °C. It should be noted that at higher air flows with air temperatures upstream of the sample above the value of 150 °C, there were difficulties in keeping the air temperature upstream of the sample constant. This could affect the measured values and influence the accuracy of the results obtained.

Figure 1. Sherwood Tornado M501 dryer and other instruments for experimental research

The experimental apparatus was upgraded with the orifice plate with suction tube is installed at the device inlet and complies with the standards SRPS EN ISO 5167-1 and SRPS EN ISO 5167-2 "Measurement of fluid flow by means of pressure differential devices inserted in circular cross-

section conduits running full", Part 1: "General Principles and Requirements" and and Part 2: "Orifice plates" and additional equipment for measuring the air flow.

The measurements of the differential pressure and the static air pressure at the orifice plate were carried out with two AlnorAXD 560 digital micromanometers. The air temperature was measured using a type K thermocouple and a Testo 925 digital thermometer, while the relative humidity was measured in front of the measurement opening using a Testo175-H2 hygrometer. A DB3 PCE Instruments digital barometer was used to measure the barometric pressure.

The most widely used domestic lignite from Kolubara, which has a relatively low calorific value (6200 – 9300 kJ/kg) and an extremely high moisture content (47.2 – 51.4%), was selected to carry out experiments on drying coal in a packed bed [6].

3. RESULTS

The average diameter of the lignite particles is determined using the openings of the sieves used to sieve the coal. The initial mass of the sample was 200 g, and each additional increase in mass was 50 % of the initial mass. The initial temperature of the dried air was 30 ºC, and each additional increase in temperature was 30 ºC. Figures 2-4 show the comparative results of drying in the packed bed for two different sample masses, two particle sizes and two temperatures[1].

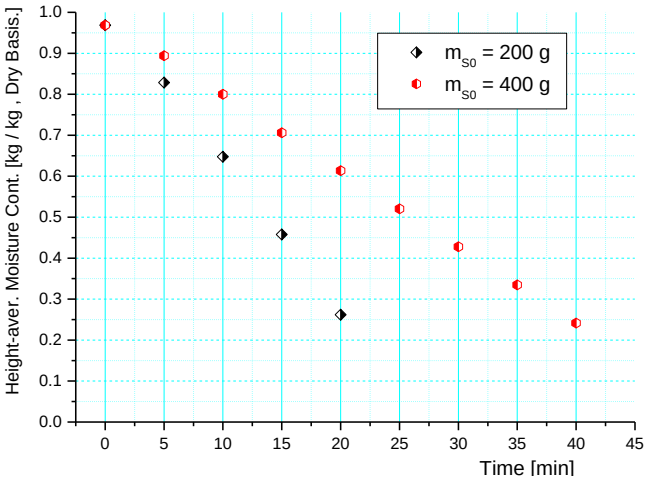

Figure 2: Results of the drying kinetics of lignite in the packed bed for two different sample masses with the same particle size and an air temperature of 90 ºC in the front of the dryer heater

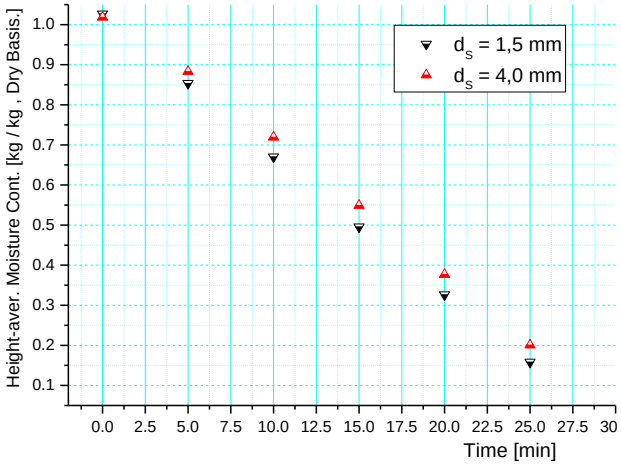

Figure 3: Results of the drying kinetics of lignite in the packed bed for two different particle sizes with the same sample mass of 200 g and an air temperature of 90 ºC in front of the dryer heater

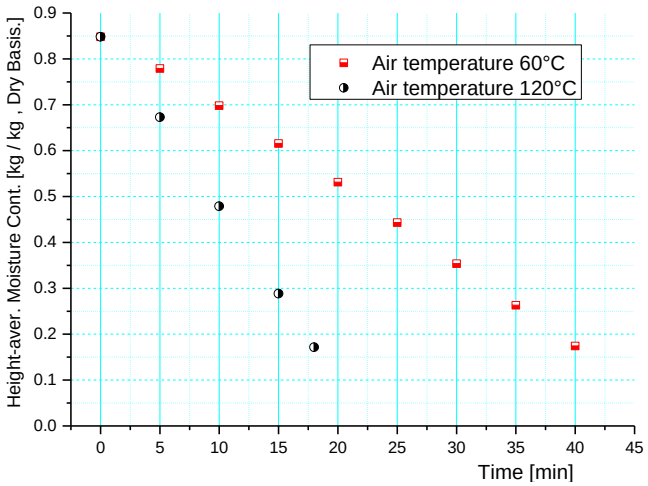

Figure 4: Results of the drying kinetics of lignite in the packed bed for two different air temperatures in front of the dryer heater with the same sample mass of 200 g and 4 mm particles

4. CONCLUSIONS

A series of experiments were conducted on convective drying in the packed bed of the Kolubara lignite samples. The experimental investigations of the drying process in the packed bed were carried out for several different coal sample masses and different coal particle sizes at different air temperatures from 30 to 120 ºC, which were measured in front of the sample and the dryer heater. The test results obtained show that the drying time increases proportionally with the increasing mass of the sample. The size of the lignite particles has no significant influence on the drying rate of the sample. Figure 3 shows that the differences in the amount of moisture removed are very small for two particle sizes where the ratio of the mean diameter of the particles is 2.7 times. As the temperature increased, the drying rate of the sample increased, while the drying time decreased. Temperature is the most influential of the three parameters analysed.

ACKNOWLEDGEMENTS

The research was funded by the Ministry of Science, Technological Development and Innovation of the Republic of Serbia (Contract Annex: 451-03-136/2025-03/200017). The authors are very grateful for the support of this work by the Joint Stock Company Elektroprivreda Srbije.

REFERENCES

[1] M. Erić, Drying processes of lignites with highmoisture content in packed andfluidized bed, Doctoral Dissertation, University of Belgrade, Mechanical Faculty, Belgrade, 2016.
[2] D.A. van Meel, Chem. Eng. Sci., 9 (1958) 36-44.
[3] E. Tsotsas, Measurement and modeling of intraparticle drying kinetics: A review, Proceedings of the 8th International drying symposium (IDS ’92), Montreal, 1992, pp. 17-41
[4] A.V. Luikov, Drying theory, 1st ed., Energiya, Moscow, 1968 (in Russian)
[5] D. Milojević, M. Stefanović, Chem. Eng. Commun., 13 (1982) 261-269.
[6] Erić M., Marković Z, Kostadinović D., Jovanović R., Lazović I. and Gigov M., Results of the Temperature Variation in Experimental Research of the Kolubara Lignite Drying Process in Fluidized Bed, Proceedings of the 21st International Conference on Thermal Science and Engineering of Serbia, Faculty of Mechanical Engineering Niš, Serbia, October 22-25, 2024, pp. 309-316.

The 56th International October Conference on Mining and Metallurgy
22-25 October 2025, Bor Lake, Bor, Serbia
www.ioc.tfbor.bg.ac.rs

DOI: 10.5937/IOC25175T *Original scientific paper*

INVESTIGATION OF THE FLOTATION POTENTIAL OF SULFIDE-OXIDE ORE FROM THE VELIKI MAJDAN DEPOSIT

Slavko Todic[1a], Predrag Lazic[1b]

[1] Faculty of Mining and Geology, University of Belgrade, Djusina 7, 11000 Belgrade, Serbia
[1a] slavko.todic@rgf.bg.ac.rs, 0009-0001-7941-9255
[1b] predrag.lazic@rgf.bg.ac.rs, 0000-0002-3953-2202

Abstract

This paper presents the results of an investigation into the applicability of single-stage flotation for processing complex lead sulfide–oxide ore from ore body RT255-37 at the Veliki Majdan deposit. The study aimed to optimize key technological parameters of the process, including grinding, pulp conditioning, flotation reagent dosage, and flotation regime. Granulometric analysis (particle size distribution) indicated that the ore is relatively hard. The optimal grinding conditions were defined as a grinding time of 9 minutes under a typical solid content in the pulp, which provided a suitable particle size distribution for flotation.

Special attention was given to the application of sulfidization, which creates favorable conditions for the flotation of lead oxide minerals. This step is essential for achieving high recovery. The required sodium sulfide dosage was relatively high, amounting to 3700 g/t. The reagent regime was further enhanced by increasing the dosage of the collector KEX and introducing a more efficient frother, Florrea Frother 520. Flotation kinetics were evaluated under conditions comparable to those in industrial operations.

Under laboratory conditions, recoveries of 93.37 % for lead sulfide minerals and 86.56% for oxide minerals were achieved, with a final concentrate grade of 68.67 % Pb. Locked cycle flotation test confirmed the stability and reliability of the optimized flotation regime, resulting in a concentrate with 69.55 % Pb and an overall lead recovery of 88.41 %. The results demonstrate the technical and technological feasibility of applying the optimized flotation process to the treatment of such complex lead ores.

Keywords: *flotation concentration, sulfidization, sulfide–oxide ore*

1. INTRODUCTION

Flotation concentration is one of the most efficient and widely used methods for the selective separation of mineral components based on their surface properties. The key property exploited in flotation is the wettability, or lack thereof, of specific minerals [1]. In addition to these differences in physical properties, flotation reagents play a crucial role in enhancing the separation process.

It is well known that the floatability of lead oxide minerals and oxidized sulfide minerals can be improved by surface sulfidization. [3] In ores that contain oxidized lead minerals, such as cerussite ($PbCO_3$), prior chemical activation is required, most commonly through sulfidization using sodium sulfide (Na_2S), to enable effective attachment to collectors such as xanthates.

The aim of this study is to investigate, through laboratory-scale testing, the efficiency of single-stage flotation applied to a complex sulfide–oxide ore from ore body RT255-37. The study focuses on determining the optimal parameters for grinding, pulp conditioning, reagent dosage, and flotation conditions. In addition, the quality of the resulting concentrate and the overall metal recovery under locked cycle flotation test conditions were evaluated.

2. EXPERIMENTAL

2.1. General Information about the Deposit and Mine

The Veliki Majdan lead–zinc deposit is classified as a hydrothermal–metasomatic type of mineralization, developed within a carbonate host environment during the Tertiary magmatic–volcanic activity of the Boranja Complex. The ore bodies are morphologically complex and spatially associated with the contacts between marbled limestones, quartz latite dikes, and terrigenous sediments. Among the oxidized lead minerals, cerussite ($PbCO_3$) and, to a lesser extent, hydrocerussite have been identified, while hemimorphite and likely smithsonite ($ZnCO_3$) are dominant among the zinc oxide minerals. [2]

2.2. Materials and Methods

For the purpose of laboratory testing, a composite sample with a total mass of 20 kg was provided by the geological service of the mine, originating from ore body RT255-37. The sample preparation included the following procedures: crushing and homogenization, density determination using the pycnometer method (3.11 g/cm³), wet sieving to determine particle size distribution, chemical analysis of Pb and Zn content, and phase-specific distribution of these elements.

Chemical analysis indicated an elevated content of non-sulfide Pb and Zn minerals. Given the known technological challenges associated with the flotation of non-sulfide Zn minerals, they were excluded from experimental flotation testing.

Due to the pronounced presence of oxidized Pb phases, sulfidization using sodium sulfide (Na_2S) was applied in the flotation process to enhance mineral hydrophobicity and improve collector adsorption.

Following sample preparation, the subsequent procedures were conducted: determination of optimal grinding time, optimization of reagent dosages, flotation kinetics analysis, and a final locked-cycle flotation test. All flotation products were processed using standardized laboratory protocols and subjected to chemical analysis to determine metal content and recovery.

3. RESULTS AND DISCUSSION

This section presents the obtained results along with the corresponding comments and interpretations.

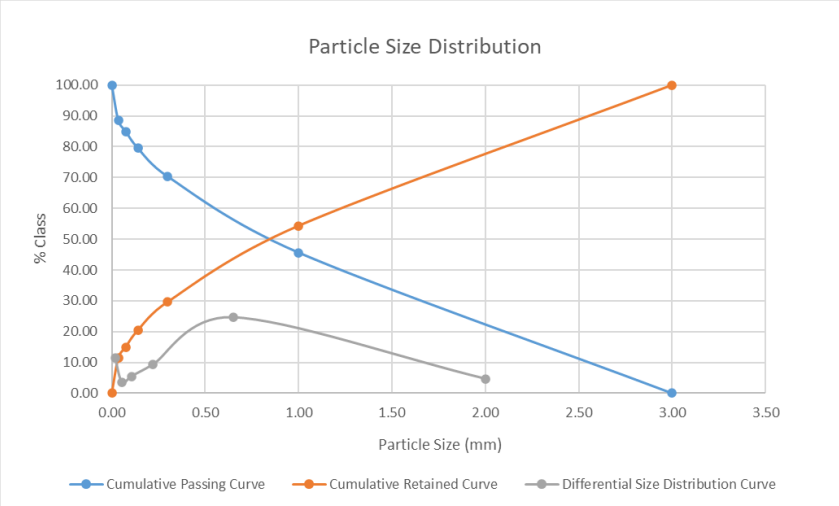

Figure 2. Particle size distribution of the final crushed sample

From the particle size distribution diagram, the upper grain size limit (d_{95}) was determined to be 2.55 mm. The most represented size fraction is -1 +0.3 mm, with a mass fraction of 45.66 %, while the least represented fraction is -0.074 +0.035 mm, with a mass fraction of 3.49 %. Based on these results, the ore can be considered relatively hard to grind. The results of the granulometric analysis are presented in Figure 1.

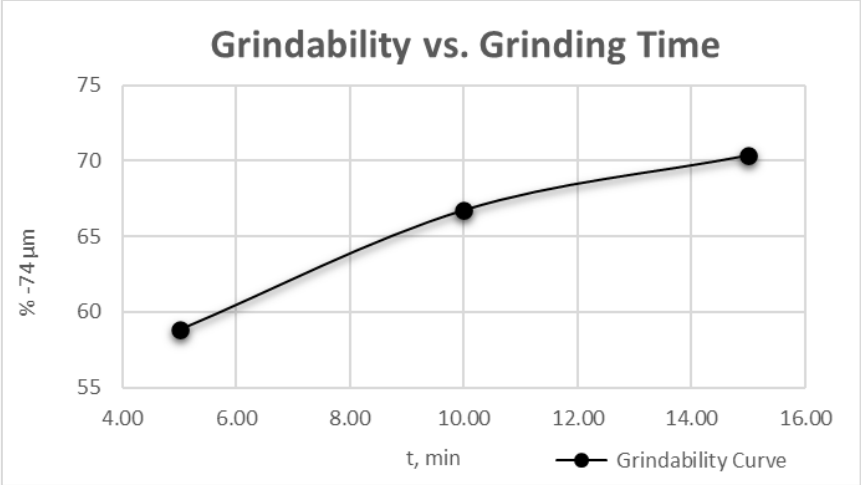

Figure 3. Diagram of grindability as a function of grinding time

Based on the analysis of Figure 2, the optimal grinding time of 9 minutes was selected to achieve approximately 65% of the -74 µm particle size fraction.

The reagent regime adopted for flotation included a sodium sulfide dosage of 3700 g/t to ensure complete sulfidization. The dosage of the potassium ethyl xanthate (KEX) collector was increased to 230 g/t. The consumption of depressants, specifically sodium cyanide and zinc sulfate, remained unchanged compared to the existing plant regime. The frother Florrea Frother 520 was used at a dosage of 120 g/t.

The durations of the individual flotation stages were as follows: rougher flotation – 20 minutes, scavenger flotation – 23 minutes, first cleaning – 10 minutes, and the second and third cleaning stages – 5 minutes each.

Table 5. Metal Balance for the Final Experiment

	M, g	M, %	Pb-tot, %	R Pb-tot, %		Pb-sul ,%	R Pb-sul, %		Pb-ox, %	R Pb-ox, %	
FEED	906.73	100.00	5.36	100.00	100.00	2.11	100.00	100.00	3.25	100.00	100.00
Final Conc	21.23	2.34	**68.67**	30.01		24.50	27.17		44.17	31.85	
C1 MID	16.37	1.81	29.02	9.78		9.87	8.44		19.15	10.65	
C2 MID	6.11	0.67	40.94	5.15	**89.25**	12.68	4.05	**93.37**	28.26	5.86	**86.56**
C3 MID	4.74	0.52	55.55	5.42		17.85	4.42		37.70	6.07	
Scav Conc	111.81	12.33	16.90	38.89		8.44	49.29		8.46	32.13	
Tailings	746.47	82.33	0.70	10.75	10.75	0.17	6.63	6.63	0.53	13.44	13.44

The analysis of the results indicates that a high lead recovery of 89.25 % was achieved in the primary concentrate, which is highly favorable considering the complexity of the sulfide-oxide ore. Recovery of galena was also successful despite sodium sulfide typically acting as a depressant for this mineral. Additionally, the recovery of oxidized lead minerals reached 86.56 %. The quality of the final concentrate is satisfactory, with a lead grade of 68.67 % Pb after the third cleaning stage. Throughout the process, a high pH range of 10.9–11.3 was maintained, which did not hinder the efficient flotation of galena. The summarized flotation test results are presented in Table 1. Following the laboratory tests, locked cycle flotation test was performed to better simulate industrial conditions, with the results discussed in the subsequent section of this paper.

Table 6. Metal Balance of the Locked Cycle Flotation Test

	M, g	M, %	Pb-tot, %	R Pb-tot, %		Pb-sul, %	R Pb-sul, %		Pb-ox, %	R Pb-ox, %	
FEED	2706.08	100.00%	5.52	100.00%	100.00%	2.82	100.00%	100.00%	2.70	100.00%	100.00%
Final Conc	107.02	3.95%	**69.55**	49.82%		42.56	59.64%		26.99	39.55%	
C1 MID	205.57	7.60%	19.97	27.48%		10.66	28.69%		9.31	26.20%	
C2 MID	28.09	1.04%	13.2	2.48%	**88.41%**	4.65	1.71%	**94.69%**	8.55	3.29%	**81.85%**
C3 MID	31.43	1.16%	28.08	5.91%		7.19	2.96%		20.89	8.99%	
Scav Conc	8.47	0.31%	48.17	2.73%		15.24	1.69%		32.93	3.82%	
Tailings	2325.50	85.94%	0.74	11.59%	11.59%	0.17	5.31%	5.31%	0.57	18.15%	18.15%

The results of the locked cycle flotation test confirmed the previous findings and demonstrated excellent process performance. The concentrate quality was further improved, reaching a lead grade of 69.55 % Pb, while lead recovery in the primary concentrate slightly decreased to 88.41 %. A high recovery of the sulfide lead mineral galena was also confirmed, amounting to 94.69 %, despite the presence of sodium sulfide acting as a depressant. The recovery of non-sulfide lead minerals remained relatively high at 81.58 %, further confirming the effectiveness of the applied sulfidization process. A detailed overview of the locked-cycle flotation results is presented in Table 2**.**

4. CONCLUISON

Based on the conducted research, it was determined that for efficient grinding of ores containing hard particles, a grinding time of 9 minutes under typical pulp density conditions enables achieving approximately 65% of the -74 μm size fraction in the ground material. For complete sulfidization of the oxide minerals, a sodium sulfide (Na_2S) dosage of 3700 g/t is required, while the collector potassium ethyl xanthate (KEX) was optimized to 230 g/t. The quantities of depressants (sodium cyanide and zinc sulfate) remained unchanged compared to the existing operational regime. Replacing the D-250 frother with Florrea Frother 520 at a dosage of 120 g/t contributed to an improvement in concentrate quality. The flotation kinetics were established with the following stage durations: rougher flotation for 20 minutes, scavenger flotation for 23 minutes, first cleaning flotation for 10 minutes, and second and third cleaning flotations for 5 minutes each.

Under laboratory conditions, a galena recovery of 93.37 % and lead oxide mineral recovery of 86.56 % were achieved, with a lead content in the concentrate of 68.67 % Pb after the third cleaning stage. It is important to emphasize that the use of sodium sulfide (Na_2S), although known as a depressant for galena, did not negatively affect the recovery of this mineral. The locked cycle flotation test confirmed these results, achieving an even higher lead content in the concentrate of 69.55 % Pb and a lead recovery of 88.41 %, including 94.69 % recovery of sulfide minerals and 81.58 % recovery of nonsulfide minerals. These results confirm the efficiency of the optimized technological regime and its applicability under industrial conditions.

ACKNOWLEDGEMENTS

This work was supported by the Ministry of Science, Technological Development and Innovation of the Republic of Serbia, Contract No. 451-03-136/2025-03/200126, and the authors express their appreciation for the financial support.

REFERENCES

[1] N. D. Knežević, Pirpema mineralnih sirovina, RGF, Beograd, 2012, 169 str.
[2] Technical documentation of the Veliki Majdan lead and zinc mine. Internal report, Veliki Majdan Mine, Ljubovija, 2025.
[3] D. Chuan-Shan, S. Qi, Sep. and Purif. Technol., 226 (2019), 190–197. [Online]. Available: https://www.sciencedirect.com/science/article/abs/pii/S0892687519300597 [Accessed: July 11, 2025].

The 56th International October Conference on Mining and Metallurgy
22-25 October 2025, Bor Lake, Bor, Serbia
www.ioc.tfbor.bg.ac.rs

DOI: 10.5937/IOC25179N *Original scientific paper*

REFINEMENT OF THE BOND WORK INDEX CALCULATION METHOD FOR FINER SAMPLES

Vladimir Nikolić[a], Milan Trumić[b]

Technical Faculty Bor, University of Belgrade, V.J. 12, 19210 Bor, Serbia
[a] vnikolic@tfbor.bg.ac.rs, 0000-0003-1885-1156
[b] mtrumic@tfbor.bg.ac.rs, 0000-0002-4321-5218

Abstract
The Bond work index (BWI) is a widely recognized method used for selecting comminution equipment, evaluating grinding efficiency, and calculating the required grinding power. Although it is considered an industry standard, Bond did not fully define all steps in his original procedure, which can lead to significant variability in test results. One such undefined aspect is the initial particle size of the test material-specifically, the commonly used 3.35 mm feed size. This raises the question of whether the BWI can be reliably determined using finer samples. In practice, materials with particle sizes smaller than 3.35 mm are often encountered. This study continues previous research by examining whether the proposed model for calculating the BWI on fine samples is applicable to medium-hard ores. The validation of the model on medium-hard samples resulted in an error of less than 1%, confirming its high accuracy.

***Keywords**: Bond Work Index, Finer Samples, Grindability.*

1. INTRODUCTION

The BWI is a fundamental parameter used to assess the grindability of materials and to estimate the energy requirements in comminution processes. It has long been considered a standard tool in the mining and mineral processing industries for the selection, sizing, and evaluation of grinding equipment. The BWI is determined through a laboratory procedure that simulates closed-circuit grinding under standardized conditions, typically using material with a starting particle size of 3.35 mm.

However, in real industrial and laboratory conditions, raw materials are often available in finer samples, which introduces practical limitations to the standard Bond procedure. Since the original method was not fully defined in terms of input sample characteristics, particularly particle size distribution, there is a growing interest in adapting the procedure for finer samples. The ability to accurately determine the BWI from such materials would provide greater flexibility in testing and expand the method's applicability to a wider range of industrial scenarios. [1]

Several recent studies have proposed modifications to the traditional Bond method to accommodate finer samples, often involving recalibrated test conditions, energy calculations, or mathematical models. These alternative approaches aim to maintain the reliability and reproducibility of results while enabling the analysis of materials that fall outside the standard testing range.

This study builds upon a previously developed method for calculating the BWI using fine samples. The main objective is to evaluate the extended applicability of this approach, with a focus on maintaining accuracy and consistency in grindability assessment, regardless of initial particle size.

Levin (1989) [2] developed a method for assessing the grindability of fine samples based on the evaluation of the energy required for their comminution, primarily applied in ball milling. Later, Magdalinović et al. (2012) [3] adapted the determination of the BWI for samples of non-standard particle sizes, achieving a method accuracy with an error of less than 5%. Nikolić and Trumić

(2021) [4] investigated the possibility of determining the BWI for fine samples. They proposed a model for calculating the BWI of fine samples based on the known value for a standard particle size sample. Their study was conducted exclusively on a zeolite sample, yielding an error of less than 2.5%. The present study continues this line of research to examine whether the proposed model can also be applied to medium-hard samples.

2. EXPERIMENTAL

In mineral raw material comminution practice, samples with particle sizes smaller than -3.35 mm are frequently encountered, raising the question of whether the standard Bond method can be applied to such fine samples for the determination of the BWI. Bond (1961) [5] did not explicitly address this situation; instead, his standard grindability test requires that all samples must have an initial particle size below -3.35 mm, but provides no guidelines for cases where samples are already finer than this threshold at the outset. In such instances, the assessment of grindability may rely solely on data obtained from existing industrial plants, which can be used to estimate the BWI. However, this approach is limited, as it requires access to operational data and is often not feasible under laboratory conditions. Therefore, there is a growing need to develop methodologies that enable reliable determination of the BWI for fine samples. To date, only a limited number of researchers have addressed this issue, and the literature lacks systematic studies on the subject. The present study focuses precisely on this open problem, aiming to explore the possibilities for determining the BWI on finer samples.

The testing was conducted on a dacite sample, using different particle size classes: -3.35 + 0 mm; -2.36 + 0 mm; -1.70 + 0 mm; -1.18 + 0 mm; and -0.850 + 0 mm (particle size distribution (PSD) presented in Table 1 and Figure 1). A 75 μm closing screen size (P100) was used. The BWI is calculated using Equation (1).

$$W_i = 1.1 \cdot \frac{44.5}{{P_{100}}^{0.23} \cdot G^{0.82} \cdot \left(\frac{10}{\sqrt{P_{80}}} - \frac{10}{\sqrt{F_{80}}} \right)} \quad (1)$$

where in:

P_{100} - closing screen size (μm),
G - net mass of undersize product per unit revolution of the mill, in g/rev,
P_{80} - the 80% passing product particle size (μm),
F_{80} - the 80% passing feed particle size (μm).

Table 1. Dacite sample PSDs

Particle Size	Class size in mm (%)				
(mm)	- 3.35 + 0	- 2.36 + 0	- 1.70 + 0	- 1.18 + 0	- 0.850 + 0
- 3.35 + 2.36	27.77				
- 2.36 + 1.70	15.60	21.08			
- 1.70 + 1.18	12.59	18.24	23.42		
- 1.18 + 0.850	7.99	11.28	14.83	17.54	
- 0.850 + 0.600	7.52	10.18	12.98	16.40	20.91
- 0.600 + 0.425	6.10	8.28	10.36	13.47	16.02
- 0.425 + 0.300	5.45	7.39	8.76	11.94	14.62
- 0.300 + 0.212	4.05	5.46	6.73	9.21	10.95

- 0.212 + 0.150	3.39	4.57	5.55	7.76	9.25
- 0.150 + 0.106	2.08	3.00	3.78	5.46	5.93
- 0.106 + 0.075	1.77	2.39	2.92	3.68	5.02
- 0.075 + 0.00	5.69	8.13	10.67	14.54	17.30
∑	100.00	100.00	100.00	100.00	100.00

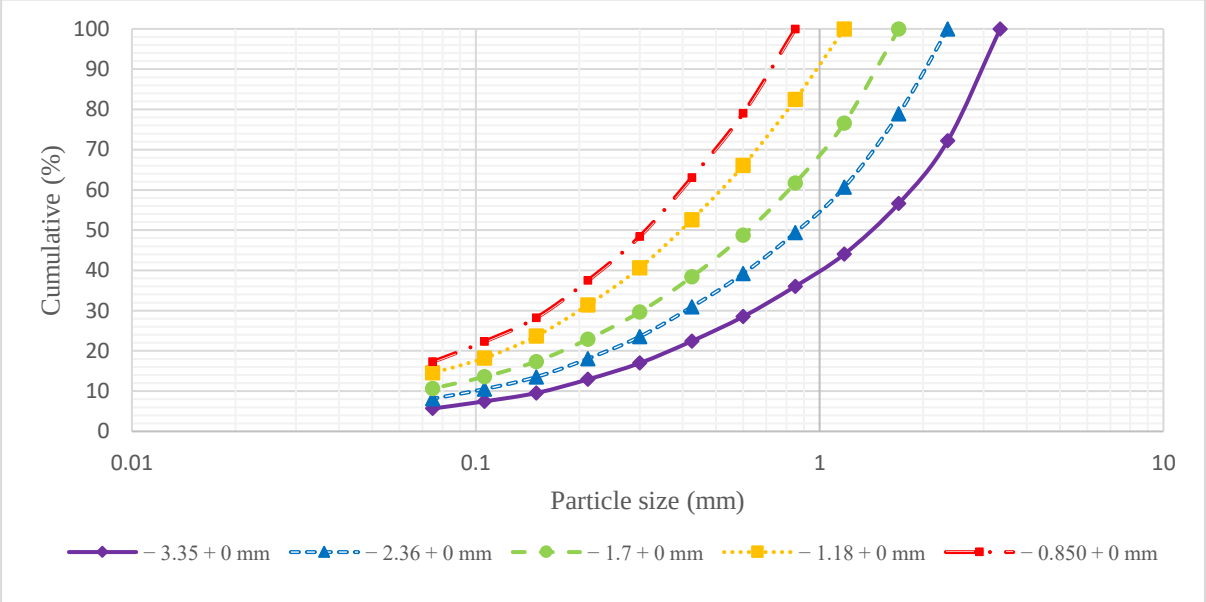

Figure 1. Dacite sample PSDs

3. RESULTS AND DISCUSSION

The results of determining the grindability on a samples of dacite on fine size classes are shown in Table 2.

Table 2. Parameters F_{80}, P_{80}, G and value of Wi for finer size classes

Sample	Size (mm)	F_{80} (μm)	P_c=75 μm		
			P_{80} (μm)	G (g)	Wi (kWh/t)
Dacite	- 3.35 + 0	2646	64.70	0.96	17.800
	- 2.36 + 0	1729	64.76	1.00	18.130
	- 1.70 + 0	1253	65.76	1.05	18.333
	- 1.18 + 0	807	65.20	1.10	18.827
	- 0.850 + 0	609	65.64	1.12	19.196

Nikolić and Trumić (2021) [4] proposed a model for calculating the BWI for finer samples (Equation 2), based on the grindability test results of a zeolite sample. The authors emphasized that Equation (2) was tested exclusively on a zeolite sample, which is classified as a soft ore. In the present study, Equation (2) was also tested on a dacite sample in order to determine whether the proposed model can be applied to medium-hard ores as well.

$$W_{Fm} = k \cdot \frac{W_i}{F_{Fm}^{0.05}} \quad (2)$$

where in:

W_{Fm} - BWI for fine materials, (kWh/t);
W_i - BWI for a standard size sample (- 3.35 + 0) mm, (kWh/t);

F_{Fm} - the 80 % passing fine material particle size, (μm),
k - coefficient whose value is $(k = 1.47)$.

When Nikolić and Trumić (2021) [4] presented their model for calculating the BWI for finer samples, based on a zeolite sample, the coefficient *k* was determined to be 1.47. However, when the model was tested on a dacite sample, it was observed that this coefficient *k* is not constant, but varies with the hardness of the sample. For medium-hard ores, the value of the coefficient *k* was found to be $(k = 1.48)$. The results of testing Equation (2) on the dacite sample are presented in Table 3.

Table 3. Comparative results obtained experimentally and using the Eq. (2).

Sample	Size (mm)	F_{80} (μm)	$P_c = 75$ μm			
			W_i (kWh/t)	k	W_{Fm} (kWh/t)	Error Δ (%)
Dacite	- 3.35 + 0	2646	17.800	1.48	-	-
	- 2.36 + 0	1729	18.130		18.146	- 0.88
	- 1.70 + 0	1253	18.333		18.441	- 0.60
	- 1.18 + 0	807	18.827		18.851	- 0.13
	- 0.850 + 0	609	19.196		19.118	+ 0.41

The results of testing the defined model indicate that the difference between the Bond Work Index values obtained by computational and experimental methods is very small-less than 1%. Such a result confirms the high reliability of the model. It was also established that when the model is applied to moderately hard samples, the coefficient value $(k = 1.48)$ should be used.

4. CONCLUSION

The research presented in this paper demonstrates that the proposed model for calculating the (BWI) using finer samples can be successfully applied not only to soft ores, as previously verified, but also to medium-hard materials. The comparison between experimentally obtained BWI values and those calculated by the model revealed very small deviations, generally below 1%, which confirms the high accuracy and reliability of the method. Furthermore, it was established that the coefficient k, is not constant but varies depending on the hardness of the tested material. For medium-hard ore, the appropriate coefficient value was determined, ensuring that the model provides consistent and precise results. Further research will include the verification of the model on very hard samples.

ACKNOWLEDGEMENTS

"The research presented in this paper was done with the financial support of the Ministry of Science, Technological Development and Innovation of the Republic of Serbia, within the funding of the scientific research work at the University of Belgrade, Technical Faculty in Bor, according to the contract with registration number 451-03-137/2025-03/200131".

REFERENCES

[1] V. Nikolić, J. M. Pierres, M. S. Calvo, J. M. Menéndez-Aguado, M. Trumić, M. S. Trumić, V. Milošević, Minerals, 15 (2025) 35.
[2] J. Levin, J. South. Afr. Inst. Min. Metall., 89 (1) (1989) 13-21.
[3] N. Magdalinovic, M. Trumic, G. Trumic, S. Magdalinovic, M. Trumic, Int. J. Miner. Process., 114-117 (2012) 48-50.
[4] V. Nikolić, M. Trumić, Min. Eng., 165 (2021) 106858.
[5] F. C. Bond, British Chemical Engineering 6 (6 and 8) (1961) 378-385 & 543-548.

The 56th International October Conference on Mining and Metallurgy
22-25 October 2025, Bor Lake, Bor, Serbia
www.ioc.tfbor.bg.ac.rs

DOI: 10.5937/IOC25183E

Original scientific paper

MINERALOGICAL EVOLUTION IN INDUSTRIAL JAROSITE THROUGH FLUX-ASSISTED ROASTING

Jose Enrique Sanchez-Vite[1a], Alberto Hernandez-Casimiro[1b] , Teresita del Refugio Jiménez Romero[1c], Alejandro Cruz-Ramírez[2a], Margarita García-Hernández[2b]

[1] ESIQIE, Instituto Politécnico Nacional, UPALM, 07738, Ciudad de México, México
[2] UPIIH, Instituto Politécnico Nacional, DESCTI, San Agustín Tlaxiaca, 42162, Hidalgo, México
[1a] jsanchezv2105@alumno.ipn.mx, 0009-0006-5001-0495
[1b] ahernandezc2200@alumno.ipn.mx, 0009-0004-2097-9305
[1c] tjimenezr@ipn.mx, 0009-0003-8012-6817
[2a] alcruzr@ipn.mx, 0000-0002-0972-596X
[2b] margarciah@ipn.mx, 0000-0002-3850-3901

Abstract
Industrial jarosite residues from zinc hydrometallurgy are both an environmental liability and a secondary resource for valuable metal recovery (Zn, Pb, Ag). The mineralogical evolution of an ammonium-jarosite residue during oxidizing roasting was evaluated, comparing (i) pure residue and (ii) a flux-assisted/reducing formulation (45 wt% jarosite + 40 wt% Na_2CO_3 + 15 wt% SiC). Thermogravimetric analysis shows decomposition events related to dehydration, dehydroxylation, and sulfate breakdown with an overall mass loss of ~49%. X-ray diffraction measurements to temperature in the range from 600 to 1400 °C evidence the pathway of spinel formation: jarosite → hematite + ZnO → $ZnFe_2O_4$ (spinel) for pure jarosite roasting, which immobilizes Zn. In contrast, the addition of Na_2CO_3 and SiC to jarosite suppresses $ZnFe_2O_4$, fixes sulfur predominantly as Na_2SO_4 and $CaSO_4$, while iron is contained in oxide and sulfate compounds. SEM/EDS reveals a locally Pb-rich droplet domain at elevated temperatures, indicating partial metal liberation under optimized redox conditions.

Keywords: *(Jarosite; Thermal decomposition; Flux-assisted roasting; Sulfur fixation; Zinc ferrite)*

1. INTRODUCTION

Jarosite-type residues produced during iron removal in zinc hydrometallurgy are widely produced and incorporate valuable and hazardous elements (e.g., Zn, Pb, Ag), thus posing both an environmental liability and a secondary resource opportunity [1,2]. Thermogravimetric studies typically reveal a multistage pathway dehydration, dehydroxylation and (for ammonium jarosite) NH_4^+ release, followed by sulfate breakdown between ~100–700 °C [3]. At higher temperatures, hematite and zincite emerge and may couple to form $ZnFe_2O_4$ spinel, a refractory phase that immobilizes zinc and hinders hydrometallurgical recovery [3,4]. To circumvent this, strategies such as leaching, sulfidization–flotation, stabilization, and reducing/flux-assisted roasting have been explored [2,5,6]. Building on this body of work, an industrial jarosite was treated with Na_2CO_3 (flux) and SiC (reducing agent) to promote sulfur fixation in sulfates and to suppress $ZnFe_2O_4$ formation [4–8].

2. EXPERIMENTAL

An industrial ammonium jarosite residue (−75 µm) was thermally treated in static air at 600, 800, 1000, 1200, and 1400 °C (10 °C min^{-1}; 2 h hold) using high-purity alumina crucibles. Two compositions were studied: Case 1: 100 wt% jarosite and Case 2: 45 wt% jarosite + 40 wt% Na_2CO_3 + 15 wt% SiC (10 g per trial). Characterization included TGA/DTG (RT–1000 °C), XRD (10–70° 2θ), and SEM/EDS. The industrial jarosite contained Fe (~8 wt%), total S (~17 wt%), Zn

(~5 wt%), Pb (~0.45 wt%) and Ag (~143 ppm). XRD of the as-received residue showed ammonium jarosite with minor gypsum, ZnS and $ZnSO_4 \cdot 7H_2O$ compounds (Figure 1).

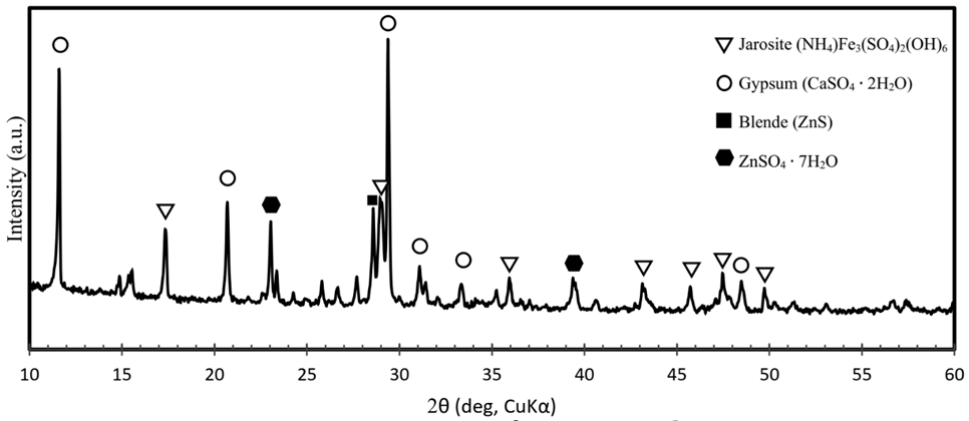

Figure 1. XRD pattern of jarosite residue.

3. RESULTS AND DISCUSSION

3.1 Thermal decomposition (TGA/DTG)

The residue exhibits a multistage mass-loss sequence (total ≈49%): initial dehydration (<100 °C), dehydroxylation and deammoniation (≈140–230 °C), lattice collapse with onset of sulfate breakdown (≈380 °C), and a minor event above ≈750–780 °C associated with conversion of residual sulfates to oxide/slag species fully consistent with literature on ammonium jarosite [3]. Multistage behavior is clearly illustrated in the TGA profile (Figure 2). These landmarks define roasting windows for phase steering and for avoiding extensive $ZnFe_2O_4$ growth [3,4].

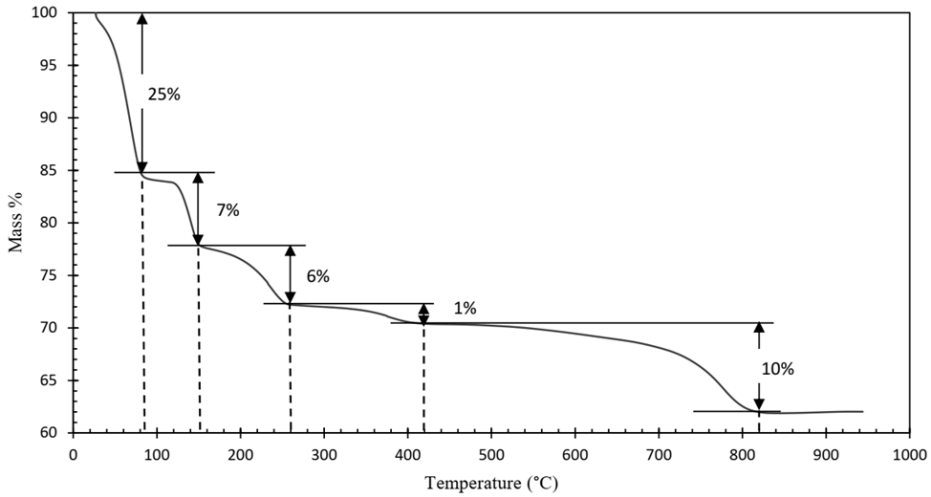

Figure 2. Thermogravimetric analysis (TGA) of the industrial ammonium jarosite sample.

3.2 Unfluxed roasting (100% jarosite)

XRD evolution follows jarosite → α-Fe_2O_3 + ZnO → $ZnFe_2O_4$ as temperature rises in air. The tendency of ZnO to react with hematite to form zinc ferrite is pronounced at ≥800–1000 °C and is a well-known barrier to zinc recovery due to the spinel's chemical robustness [3,4]. The corresponding phase evolution identified by XRD is shown in Figure 3.

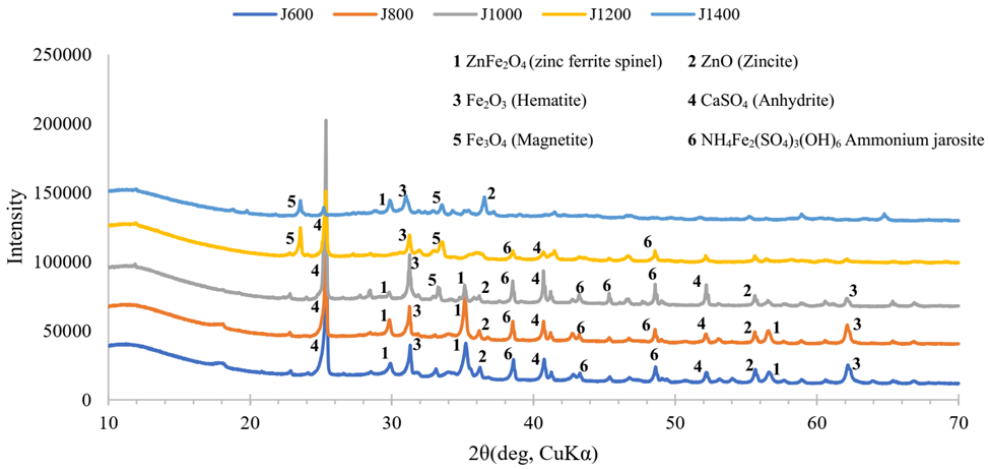

Figure 3. XRD pattern of phase evolution of pure jarosite roasted in air at different temperatures.

3.3 Flux-assisted roasting (jarosite + Na_2CO_3 + SiC)

The Na_2CO_3 and SiC additions modify the compounds formation: by 600–800 °C, jarosite has decomposed, and thenardite (Na_2SO_4) dominates, indicating efficient sulfur fixation in condensed phases. Fe partitions mainly into magnetite (Fe_3O_4) and hematite (Fe_2O_3). $ZnFe_2O_4$ is suppressed or delayed relative to the pure jarosite within 600–1200 °C. Fe–Si–O frameworks may appear via reaction of FeO-bearing domains with SiO_2 formed from SiC oxidation. At 1400 °C, sintering/incipient liquid is evident, with Na_2SO_4 still detectable and Fe_3O_4/α-Fe_2O_3 prevailing [4–8]. These transformations are confirmed by the XRD patterns displayed in Figure 4.

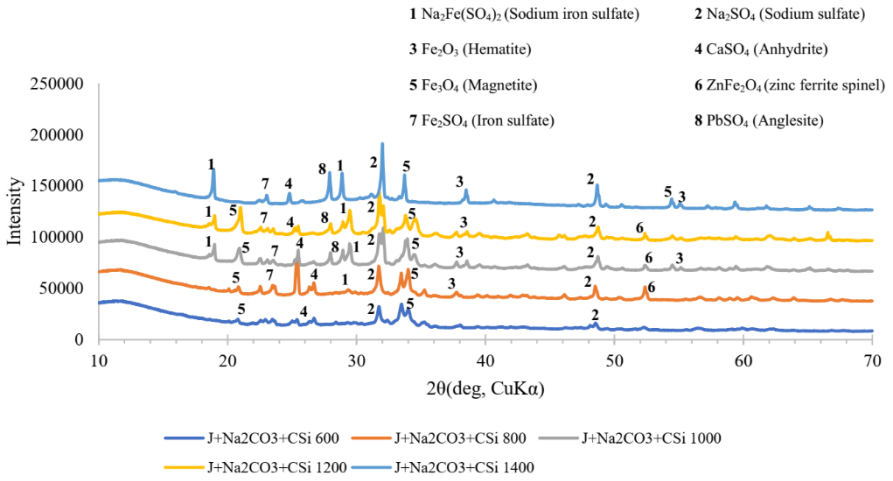

Figure 4. Phase evolution of roasted jarosite with fluxing and reducing agent at different temperatures.

Na_2CO_3 ties sulfur into stable alkali/alkaline-earth sulfates ($Na_2SO_4 \pm CaSO_4$), diverting Fe away from Zn–ferrite coupling; SiC fosters $Fe^{3+} \rightarrow Fe^{2+}$ and magnetite stabilization under globally oxidizing but locally reducing conditions. The combined effect yields magnetite-rich, spinel-lean assemblages advantageous for downstream processing or immobilization, consistent with prior thermogravimetric/thermodynamic demonstrations for jarosite residues [4–8].

3.4 Microstructure and elemental speciation (SEM/EDS)

Figure 5 shows a SEM-EDS analysis of the jarosite roasted with the addition of Na_2CO_3 and SiC reagents at 1200 °C. The image obtained using backscattered electrons of the fluxed products reveals alkali–silicate domains (Si–Al–Na), sulfate-rich grains (Na_2SO_4/$CaSO_4$), and oxide/silicate

matrices that host Fe. EDS confirms strong S and Na signals in sulfate grains (sulfur fixed in condensed phases). At the same time, Zn and Pb show low counts in the matrix consistent with (i) dispersion into submicrometric phases below SEM resolution, (ii) partial incorporation into amorphous silicate/sulfate matrices, or (iii) redistribution among minor sulfide/silicate hosts. Ag remained below EDS detection in the surveyed fields. These observations corroborate the XRD-inferred sulfur fixation and spinel suppression along the flux-assisted route [4–7] and are consistent with thermodynamic and experimental evidence that, at ~1200 °C under Na_2CO_3–SiC conditions, liquid-assisted segregation can promote Pb–Ag alloy droplet formation and matrix differentiation in jarosite-bearing systems [8,9].

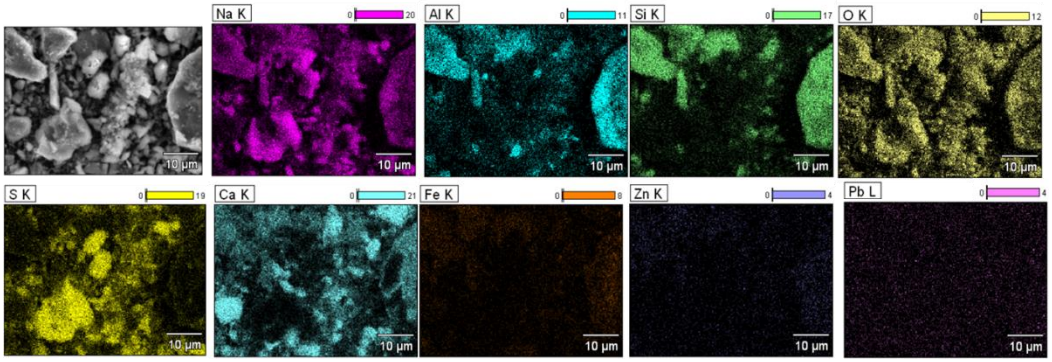

Figure 5. SEM / EDS analysis for jarosite with fluxing and reducing agent at 1200°C.

3.5 Process implications

Pure roasting efficiently removes structural water/NH_4^+ but traps Zn in $ZnFe_2O_4$, limiting leachability. In contrast, Na_2CO_3 + SiC simultaneously fixes sulfur, suppresses $ZnFe_2O_4$, and steers Fe into magnetite/oxide–silicate matrices. This phase tailoring is a promising platform for selective recovery (e.g., Zn via targeted leaching; Pb–Ag coalescence under optimized, more reducing co-roast conditions) or for environmental immobilization [4–8].

4. CONCLUSIONS

Flux-assisted roasting of industrial ammonium jarosite with Na_2CO_3 + SiC (600–1400 °C, air) delivers sulfur fixation (Na_2SO_4/$CaSO_4$), suppresses $ZnFe_2O_4$, and favors magnetite/oxide–silicate matrices, in agreement with recent reports on jarosite valorization. These outcomes define processing windows to minimize gaseous S, reduce refractory spinel formation, and condition residues for metallurgical recovery or stabilization.

REFERENCES

[1] J.E. Dutrizac, J.L. Jambor., Rev. Miner. Geochem., 40 (2000) 405–452.
[2] Y. Wang, H. Yang, G. Zhang, J. Kang, C. Wang., Chem. Eng. J. Adv., 3 (2020) 100023.
[3] D. Lu, Y. Bai, W. Wang, Y. Fu, F. Xie, Y. Chang, Y. Han., Metals, 13 (2023) 261.
[4] B. Zhang, S.H. Ju, L.B. Zhang, J.H. Peng, Z. Shi, S.H. Guo, B.G. Liu, Y.J. Wang., Metall. Mater. Trans. B, 50 (2019) 761–773.
[5] C. Liu, S.H. Ju, L.B. Zhang, C. Srinivasakannan, J.H. Peng, T.Q.X. Le, Z.Y. Guo., Can. Metall. Q., 56 (2016) 1–9.
[6] H. Han, W. Sun, Y. Hu, B. Jia, H. Tang., J. Hazard. Mater., 278 (2014) 49–54.
[7] C. Jiménez-Lugos, M. Flores-Favela, A. Romero-Serrano, A. Hernández-Ramírez, J. López-Rodríguez, L. Cuéllar-Herrera, E. Colin-García., Metals, 14 (2024) 954.
[8] J.E. Sanchez Vite, A. Cruz Ramírez, M.E. Flores Favela, J.A. Romero Serrano, M. Pérez Labra, V.H. Gutiérrez Pérez, R.G. Sánchez Alvarado, J.C. Jiménez Lugos., Recycling, 9 (2024) 119.
[9] J.E. Sanchez Vite, A. Cruz Ramírez, M.E. Flores Favela, R.G. Sánchez Alvarado, J.A. Romero Serrano, M. García Hernández, T.d.R. Jiménez Romero, J.C. Jiménez Lugos., Recycling, 10 (2025) 136.

The 56th International October Conference on Mining and Metallurgy
22-25 October 2025, Bor Lake, Bor, Serbia
www.ioc.tfbor.bg.ac.rs

DOI: 10.5937/IOC25187D *Review paper*

GOLD RECOVERY FROM FLOTATION TAILINGS IN COPPER METALLURGY: A SUSTAINABLE APPROACH TO RESOURCE VALORIZATION

Albin Dobersek[1a], Aleksandra Mitovski[1b], Olga Mishina[1c], Andrej Avrachov[1d], Pavel Saltykov[1e], Alexandra Friesen[1f], Viktoriia Zhmurova[1g], Theresa Schulz[1h]

[1]Engineering Dobersek GmbH, Vorster Straße 493, 41169 Moenchengladbach, Germany
[1a] albin.dobersek@ed-mg.de 0009-0008-7386-0796
[1b] aleksandra.mitovski@ed-mg.de 0009-0000-6840-1095
[1c] olga.mishina@ed-mg.de 0009-0004-5156-2641
[1d] andrej.avrachov@ed-mg.de 0009-0006-5345-1528
[1e] pavel.saltykov@ed-mg.de 0009-0002-8406-8688
[1f] alexandra.friesen@ed-mg.de 0009-0003-7920-5278
[1g] viktoriia.zhmurova@ed-mg.de 0009-0000-7835-9898
[1h] theresa.schulz@ed-mg.de 0009-0003-4857-9963

Abstract

Flotation tailings generated during copper ores beneficiation processes are often regarded as waste byproducts, although they may contain valuable trace amounts of gold, particularly in ores with gold-bearing copper and iron sulphides. Traditionally, the recovery of gold from this type of tailings has been overlooked due to low concentrations and high costs associated with conventional recovery methods. However, the increase of gold price and the growing emphasis on resource optimization and sustainability in the mining and metallurgical industry have prompted renewed interest in the recovery of gold from flotation tailings.

Actual methods used for gold extraction from flotation tailings in copper metallurgy are reviewed in this paper, including cyanide leaching, gravity separation, bioleaching, and flotation reprocessing. It explores the technical challenges involved, such as the fine particle size of gold and the complex mineralogical composition of flotation tailings, which can hinder efficient recovery. Additionally, the environmental and economic benefits of integrating more sustainable methods, such as bioleaching and non-toxic leaching agents, like thiourea, are highlighted.

Industrial case studies from a few global operators demonstrate the practical application of these techniques and their potential for improving resource recovery and minimizing waste. Future directions in the field were also reviewed, emphasizing the importance of technological innovations for enhancing the recovery of gold from flotation tailings, thus contributing to a more sustainable and circular industrial economy.

***Keywords**: Gold Recovery, Flotation Tailings, Copper Metallurgy, Resource Valorization*

1. INTRODUCTION

Copper mineral processing is a cornerstone of global industry, but it also produces large volumes of flotation tailings as a byproduct. These tailings, primarily composed of fine particles from the beneficiation process, are often regarded as waste and consequently overlooked by many producers. On the other hand, these tailings can still hold significant value, especially in the form of residual gold. Although copper is the primary target, flotation tailings from copper processing often contain trace amounts of gold. Over the years, there has been growing interest in recovering this precious metal from tailings, both as a resource recovery strategy and a mean for reduction the environmental impact of tailing ponds.

Historically, gold extraction from flotation tailings didn't have priority because the gold concentrations were too low to justify the cost of extraction. But with the rising demand for gold

and a push for more sustainable mining practices, extracting gold from flotation tailings has become an increasingly viable option.

This paper reviews the potentials for gold recovery from flotation tailings in copper metallurgy, exploring the applied methods and technological challenges, adding some examples from actual industrial practice. The topic discussed here is well-explored in the available literature. Numerous studies and case reports relate to the recovery of gold from flotation tailings in copper metallurgy, employing various methods such as cyanide leaching, gravity separation, bioleaching, and flotation reprocessing. Research by Hoang et al. [1] investigated recovery of fine gold in tailings using advanced pneumatic flotation reactor Imhoflot^{TM}. Studies on cyanide leaching of copper-bearing flotation tailings are documented in the paper of Medina and Anderson [2]. Additionally, bioleaching techniques for gold recovery from mine tailings was explored in paper of Falagan et al. [3]. Bioleaching of gold in mine tailings by *Alcaligenes faecalis* is reported by Pineda et al. [4]. Thiosulphate leaching emerges as an alternative to cyanide leaching, offering a non-toxic method for gold recovery from flotation tailings [5]. Innovative methods, such as microwave-assisted comminution and mechanochemical activation, as two advanced material processing techniques that aim to alter the physicochemical properties of ores or minerals to improve efficiency in downstream processes, show promise for enhancing the liberation of gold from flotation tailings.

1.1 Gold in Copper Flotation Tailings: A Hidden Resource

Flotation tailings in copper metallurgy are produced after separation of copper minerals from gangue material in the flotation process. They are typically considered as low-grade material and are stored in tailing ponds. Gold, although present in small quantities, is often found in flotation tailings, especially in ores that contain gold-bearing copper- and iron sulphide. In many cases, gold exists in these tailings as free particle-liberated gold or as gold associated with sulphides or silicates (encapsulated gold). Gold concentration in flotation tailings can range from as low as 0,1 g/t to higher values, depending on the ore body. Tailings from some copper operations have been reported to contain gold concentrations between 0,2 to 0,5 g/t. Although it seems low, the cumulative amount of gold locked in these tailings can be significant, making its recovery profitable. Due to the fine nature of the gold particles in tailings, ranging from submicron- to 5 μm size for gold locked in very fine inclusions, up to 5-50 μm for liberated gold [5], along with their association with other minerals, recovery is often challenging and demands a complicated extraction process. As a result of high processing costs and low recovery rates, the recovery of gold from flotation tailings was not in the producers' focus of interest in the past. Nevertheless, advances in processing technologies and the continuous growth of gold price have spurred new approaches to gold extraction, for this type of secondary resource.

2. METHODS FOR GOLD RECOVERY FROM FLOTATION TAILINGS

Several methods are employed to recover gold from flotation tailings, ranging from traditional cyanide leaching to more modern and innovative techniques. Each method has its advantages and disadvantages, and the choice of technique depends on the mineralogy of the tailings, the occurrence and concentration of gold, and the overall cost-effectiveness.

2.1 Cyanide Leaching

Cyanide leaching is the most widely used method for extracting gold from ores and tailings. The process involves dissolving gold from the ore using a cyanide solution, followed by gold recovery through processes like activated carbon adsorption (CIP/CIL) or zinc precipitation. For flotation tailings, cyanide leaching can be an effective way to recover gold, especially if the gold is free or only weakly associated with sulphide minerals [6]. On the other hand, cyanide leaching poses significant environmental and safety concerns due to the toxic nature of cyanide, which can contaminate surrounding ecosystems if not managed properly. To mitigate these risks, many

operators have turned to more sustainable alternatives, such as cyanide recycling or using less toxic leaching agents like ammonium thiosulphate [7]. Practical insights show that thiourea alone can leach gold [8] and moderately leach copper, but efficiency improves when paired with other reagents (e.g., glycine, thiocyanate), controlled pH (~1.5–2), temperature (~30 °C), and adequate agitation [9].

2.2 Gravity Separation

Gravity separation is another widely used method to recover gold from flotation tailings, especially in cases where the gold is in a free or coarse form. Techniques like centrifugal concentrators or shaking tables are used to separate gold particles based on density differences. This method is environmentally friendly as it does not require chemicals, making it an attractive option for some operators [10]. In some copper flotation tailings, gravity separation can recover a significant portion of the gold content. For example, at the Zijin Mining Group's operation in China, tailings from copper flotation were treated using a combination of gravity separation and flotation, resulting in a recovery rate of over 60% of the gold content [11].

2.3 Bioleaching

Bioleaching, or usage of microorganisms for breaking down sulphide ores and releasing gold, has emerged as a promising alternative to traditional methods. This process involves the use of bacteria that naturally oxidize sulphide minerals and release metals like gold into solution. Bioleaching has been used to recover gold from complex ores and flotation tailings, with the added benefit of being more environmentally friendly [8,12]. Bioleaching for gold recovery from flotation tailings is still in the pilot and experimental stages, but the potential for scaling up this method is significant. A study conducted on samples from several flotation tailings in Romania demonstrated the feasibility of bioleaching in recovering both copper and gold from tailings. Still, challenges like longer processing times and variable recovery rates still need to be addressed [13].

2.4 Flotation

Tailings reprocessing through flotation and size classification can be applied as a way to avoid 'whole stream' processing. Tailings are reintroduced into the flotation circuit to separate the gold from the remaining gangue minerals. Process can be enhanced by regrinding, thus increasing mineral liberation and adjusting flotation reagents to optimize gold recovery, such as using collectors that selectively bind to gold-bearing particles or remove hydrophilic surface layers from fine, free, gold particles [14].

3. EXAMPLES FROM THE INDUSTRIAL PRACTICE

Thanks to advancements in technology, such as sensor-based sorting, data analysis and chemical advancement, tailings reprocessing became more efficient and cost-effective. Several mining and metallurgical companies have demonstrated the viability of gold recovery from mine and flotation tailings in copper metallurgy.

Las Cruces mine (Spain) has successfully reprocessed copper flotation tailings using a flotation circuit to recover gold [15]. At the Olympias mine (Greece), previously mined tailings were reprocessed in the existing concentrator plant, refurbished for tailings processing, with production of 20.000 oz/year of gold during 2012-2016 [16]. This method has the advantage of utilizing existing flotation infrastructure, making it a cost-effective way to boost gold recovery.

At El Indio mine (Chile), after processing the high-grade copper, gold, and silver ores, flotation tailings are treated using a cyanide leach, followed by carbon-in-pulp (CIP). The cyanide leach/CIP circuit was implemented primarily as a scavenging step, improving overall recovery [17].

BIOX® Process is used in Fairview mine (South Africa) for pretreatment of refractory gold ores and flotation concentrates. It is also recently applied for treatment of their flotation tailings containing pyrite and arsenopyrite with gold. BTRP (Barberton Tailings Retreatment Plant) was designed to treat 100.000 t/month of tailings. Basic principle of the BIOX® process is the use of bioleaching organisms like *Acidithiobacillus ferrooxidans* and *Leptospirillum ferrooxidans* to oxidize sulphides, thus liberating encapsulated gold for further cyanidation. The results showed more than 90% of gold was recovered after biooxidation and cyanidation [18]. BIOX® is also implemented as state-of-the art process in the plant for gold extraction from complex copper ores in Navoi Mining and Metallurgical Company in Uzbekistan, as one of many successful projects realized by Engineering Dobersek GmbH (project planning, delivery and commissioning) [19].

4. CONCLUSION

Gold production from flotation tailings in copper metallurgy is an increasingly viable and sustainable approach to resource recovery. With advancements in processing technologies such as gravity separation, flotation reprocessing and bioleaching, gold recovery from tailings has become more efficient and environmentally friendly. Mining operations around the world, including Olympias, El Indio and Fairview mines, have demonstrated the potential of this practice, turning waste into a valuable resource. As the demand for gold continues to rise and environmental concerns intensify, the recovery of gold from flotation tailings will likely play an essential role in the future of copper and precious metal production. One of the primary obstacles is the fine nature of gold particles in tailings, which often makes it difficult to achieve high recovery rates. Environmental concerns, particularly with cyanide use, also continue to be a major issue in gold recovery. As such, there is a strong push for alternative, less toxic methods such as bioleaching or thiosulphate leaching. Research into these greener technologies is ongoing, and their future implementation could dramatically improve the sustainability of gold recovery from flotation tailings.

REFERENCES

[1] D. H. Hoang et al., Min. Eng., 184 (2022) 107649.
[2] D. Medina, C.G. Anderson, SME Annual Meeting, 2020.
[3] C. Falagán et al., Min. Eng., 106 (2017) 71-78.
[4] Y.S. Pineda et al., Minerals, 13 (3)(2023) 410.
[5] R.R. Large, V.V. Maslennikov, Minerals 10 (2020), 339.
[6] M.G. Jiang et al., AMR, 616–618 (2012) 628–32.
[7] K. Income et al., Curr. Appl. Sci. Technol., 21 (4)(2021).
[8] M. Kanuchova et al., Acta Montan. Slovaca, 26 (1)(2021) 98-105.
[9] E.J.M. Hernandez et al., TMS 2024, (2024) 1858-1866.
[10] C. Guang et al., Multipurp. Util. Miner. Resour, 186 (2)(2022) 131-134.
[11] Internet page: https://www.zijinmining.com/global/ (accessed on 18.06.2025).
[12] X. Gao et al., Adsorpt. Sci. Technol., (2021), 1-13.
[13] S. Ubaldini et al., Metals, 9 (3)(2019) 274.
[14] E. Ozdemir et al., AMMS, 12 (2)(2024) 1366-1377.
[15] Carrasco, Mine Water Environ., 40 (2021) 16-22.
[16] Eldorado Gold Corporation, Technical Report Olympias mine Greece, Vancouver, 2023.
[17] E.H. Smith et al., Mining Latin America, Springer, Dordrecht, (1986) 361–371.
[18] M. Mokgojwa, Pan African Resources PLC, Integrated Annual Report, (2024) 98-99.
[19] Internet page: https://www.dobersek.com/en/reference/ (accessed on 23.06.2025).

The 56th International October Conference on Mining and Metallurgy
22-25 October 2025, Bor Lake, Bor, Serbia
www.ioc.tfbor.bg.ac.rs

DOI: 10.5937/IOC25191J *Original scientific paper*

CHEMICAL-MINERALOGICAL CHARACTERIZATION OF CARBONATE-CLAY TYPE LITHIUM ORE

Ivana Jovanović[1a], Dragan Milanović[1b], Vesna Conić[1c], Miloš Janošević[1d], Daniela Urošević[1e], Mile Bugarin[1f]

Mining and Metallurgy Institute Bor, Alberta Ajnštajna 1, 19210 Bor, Serbia
[1a] ivana.jovanovic@irmbor.co.rs, 0000-0002-7450-6632
[1b] dragan.milanovic@irmbor.co.rs, 0000-0002-5589-9127
[1ac] vesna.conic@irmbor.co.rs, 0000-0002-4268-3626
[1d] milos.janosevic@irmbor.co.rs, 0000-0002-0818-1235
[1e]daniela.urosevic@irmbor.co.rs, 0000-0003-3490-7834
[1f] mile.bugarin@irmbor.co.rs, 0000-0002-6992-5154

Abstract
The need for lithium minerals has surged significantly in recent years due to their use in lithium compounds for lithium-ion batteries, portable electronic devices, and energy storage systems. Spodumene is the primary lithium-containing mineral being explored and processed today because of its high lithium concentration and the widespread availability of deposits. However, other types of ores containing minerals such as lepidolite, petalite, zinnwaldite and hectorite are becoming increasingly important. This paper presents the characterization of carbonate-clay ore type, in which an increased lithium and boron content was determined – 1010 ppm and 4351 ppm respectively. Based on the findings, lithium is mainly associated with clay minerals such as smectite and illite, while boron commonly exists in the minerals probertite and sirlesite. The ore originates from a previously unexamined deposit from the European territory. Petrological analyses have determined that the ore sample lies at the border of fine-grained carbonate clastite and low carbonate marl.

***Keywords**: Clay-carbonate lithium ore, Chemical composition, Mineralogical composition*

1. INTRODUCTION

Due to its role in the production of electric cars, lithium has become a valuable resource worldwide. The need for highly efficient lithium compounds is expected to grow exponentially in response to the growing demand for electric vehicles and other strategic lithium-based technologies [1]. This is in line with the goals of the climate-neutral European Union until 2050, which is why there is an increasing demand for new sources of domestic lithium raw materials. It is believed that by 2040, up to 90% of the need for lithium will exist precisely because of its key role in the production of batteries, which is a crucial factor for environmentally friendly technologies [2]. As there is currently no viable alternative to lithium-ion batteries, the use of lithium in the market is growing faster than other essential materials used in batteries: for example, some electric vehicle batteries can function without one or two common components, such as Ni, Co, Mn or graphite, but not without Li [3]. In accordance with the above, and taking into account the criticality of lithium as a raw material, it is necessary to adjust the national production base of the countries of the European Union, in order to meet the growing demand for certain forms of lithium, such as lithium carbonate. Therefore, the expansion of lithium ore production in the EU is necessary in order to increase domestic supplies in the lithium market [4]. However, lithium deposits in the EU are associated with different mineralizations in solid host rocks, which require a special approach during processing and refining to achieve lithium carbonate of suitable battery quality. Spodumene from pegmatite deposits is expected to be the main source of lithium from ores at present, although future sources would most probably include other minerals such as

lepidolite, petalite, zinnwaldite, jadarite and hectorite [1]. Physico-chemical and mineralogical characterization of lithium ore of the clay-carbonate type is given in the paper.

2. EXPERIMENTAL

2.1 Sample preparation

Lithium-bearing ore sample was homogenized by multiple application of the cone-ring methodology, and after homogenization, shortening of the sample was performed by quartering and reduction on the Jones riffle splitter (Figure 1). A chessboard method was used for taking the representative samples for physico-chemical and mineralogical analyzes (see Figure 2).

Figure 1. Shortening of the sample on the Jones riffle splitter

Figure 2. Taking the representative samples by chessboard method for

2.2 Physical characteristics

Density of the tested sample is 2,494 t/m^3, while the bulk mass in the loose and compacted state is 1333.30 kg/m^3 and 1566.90 kg/m^3, respectively. The Bond work index in the rod and ball mills is 16.06 kWh/t and 10.38 kWh/t, respectively, and the natural pH is 9. The sample is very fine-grained, and was later found to be very suitable for lithium extraction by the bioleaching process.

2.3 Chemical composition of sample

Chemical analysis of the sample was performed at the Mining and Metallurgy Institute Bor. The results of chemical analysis are presented in Table 1 i Table 2.

Table 1. Chemical composition of lithium-bearing ore sample (macro components)

Content, %							
SiO_2	Al_2O_3	CaO	K_2O	Fe_2O_3	Na_2O	MgO	P_2O_5
29.78	7.44	18.32	4.07	3.73	2.21	9.82	0.055
MnO	TiO_2	LOI	Org. C	O.M.	V_2O_5	Cr_2O_3	/
0.085	0.23	23.02	<0.05	<0.10	0.011	0.017	/

Table 2. Chemical composition of lithium-bearing ore sample (micro components)

Content, mg/kg								
Li	B	Sr	Cd	As	Hg	Ba	Be	Bi
1010.5	4351	2482.2	0.19	16.5	0.1	464.2	1.7	<1.0
Co	Ga	Ge	Hf	Nb	Ta	W	Ni	Sc
11.1	11.9	<5.0	1.2	6.3	<1.0	1.3	81.2	8.9
Y	La	Ce	Pr	Nd	Sm	Eu	Gd	Tb
10.2	15.5	35.7	4.1	15.1	3	0.64	2.4	0.37
Dy	Ho	Er	Tm	Yb	Lu	Th	U	/
2	0.39	1.1	0.15	1.1	0.15	6.6	2.6	/

Based on the results of the chemical analysis, it was determined that the average lithium content in the sample is 1010.5 ppm, while the boron content is 4351 ppm. The samples show a relatively high content of SiO_2, Al_2O_3, CaO and MgO (29.78%, 7.44%, 18.32% and 9.82%, respectively), as well as a significant value of loss on ignition (23.02%), which indicates the significant presence of aluminosilicates and silicates, as well as typical carbonate minerals (calcite, magnesite/dolomite) in the samples.

2.4 Mineralogical composition of sample - X-ray method

Phase composition of the sample. The X-ray powder diagram (diffractogram) of the investigated sample is given in Figure 3. The database search revealed that the following minerals are present in the sample: **probertite**, $NaCaB_5O_7(OH)_4 \cdot 3H_2O$, **calcite**, $CaCO_3$, **dolomite**, $CaMg(CO_3)_2$, a mineral from the **potassium feldspar** group, $KAlSi_3O_8$, a mineral from the **plagioclase group**, $(Na,Ca)(Si,Al)_4O_8$, **analcime**, $NaAlSi_2O_6 \cdot H_2O$ and **searlesite,** $NaBSi_2O_5(OH)$. A significant presence of minerals from the group of layered silicates was also observed, which were indirectly identified using X-ray diffractograms of oriented preparations. The diffraction peak at 26.70° 2θ (d ~ 3.34 Å) indicates the possible presence of quartz.

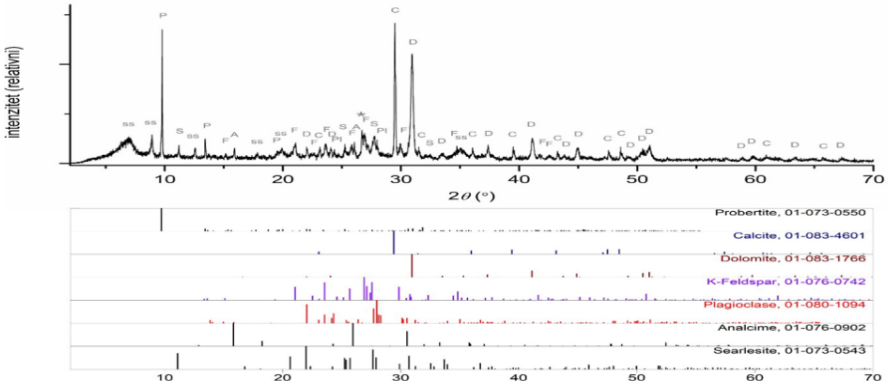

Figure 3. X-ray diffractogram of sample with reflections of identified phases. Peak legend: P – probertite, C – calcite, D – dolomite, F – K-feldspar, Pl – plagioclase, A – analcime, S – searlesite, ss – minerals from the layered silicate group.

Figure 4 shows X-ray diffractograms of oriented preparations made from the sample. Using them, the following clay minerals were identified: minerals from the **smectite** group, minerals from the **illite** group and minerals from the **chlorite** group.

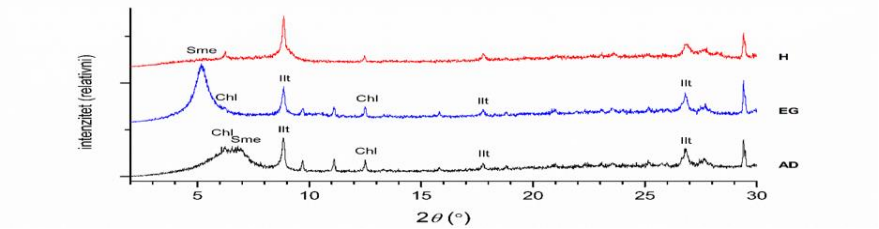

Figure 4. X-ray diffractograms of oriented "composite" sample preparations with identified minerals from the layered silicate group. Legend: Sme – smectite, Ilt – illite, Chl – chlorite; AD – oriented untreated, EG – saturated with ethylene glycol, H – annealed for 1h at 550 °C.

The proportion of individual crystalline phases in the samples identified by the WPPF method ("whole-powder-pattern fitting") using PDXL 2.8.4.0 software. (Rigaku, 2007) given in Table 2.

Table 2. Phase composition of the tested samples.

Phase	dolomite	calcite	K-feldspar	plagioclase	probertite	searlesite	analcime	smectite	illite	chlorite
Mass share	23	15	16	3	14	5	1	9	11	3

In addition to the identification of the minerals present, emphasis was placed on the determination of the minerals carrying the chemical element lithium. The results of the X-ray diffraction method on polycrystalline material (PXRD method) did not identify minerals that contain lithium in their chemical composition. However, based on the chemical analysis (Table 1), an increased content of lithium is observed. The presence of lithium is probably related to clay minerals (minerals from the layered silicate group). Lithium mineralizations in smectite clays are known (primarily the mineral hectorite $Na_{0.3}(Mg,Li)_3Si_4O_{10}(OH)_2$ – the so-called hectorite deposits), while mineralization in illite-type clays has also been mentioned recently.

2.5 Petrological analysis

Macroscopic appearance of the rock.The rock is light gray with brown tones. According to the reaction to HCl, the rock is at the border of carbonate fine-grained clastite and low carbonate marl. If the brown color is more pronounced, then the laminae in those sets have more carbonate components. According to the sample, the rock is thinly layered where each layer over 1 cm thick represents a set or coset. The sets of laminae are slightly deformed. Rare white, slightly wavy laminae were also observed, which may be tuffaceous. Flaky forms are present in the rock (Fig. 5) and small individual irregular grains of sulphide.

Microscopic appearance of rock. The rock is laminated, the sets are built from laminae that differ from each other in terms of carbonate content, i.e. clay minerals. Therefore, the rock is a mixture of dolomicrite and fine-grained clastites (Fig. 6). Certain deformed laminae have a high content of sulfide flakes and may be primarily tuffaceous, which was observed macroscopically. Definition of the rock: ***dolomitic marl.***

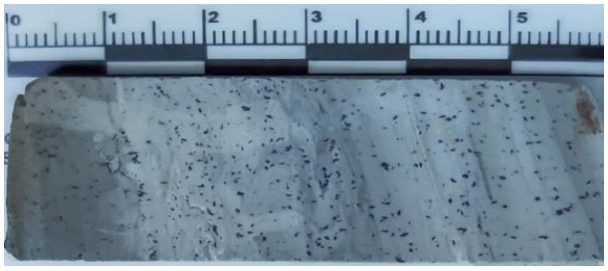

Figure 5. Macroscopic appearance of sample

Figure 6. Laminated dolomite marl. XPL.

3. CONCLUSION

Characterization of lithium-bearing ore is performed regarding chemical and mineralogical-petrological composition. This type of ore contain increased amount of lithium (1010 ppm), as well as boron (4351 ppm). According to the mineralogical X-ray analysis, lithium is primarily bound to clay minerals of the smectite and illite type, while boron is predominantly present in the form of the minerals probertite and sirlesite. Petrological tests have shown that this type of ore belongs to dolomitic marls.

ACKNOWLEDGEMENTS

This paper has been developed under the framework of Li4Life project (Grant Agreement n° 101137932), and all results can be found on its official website [5] and social channels [6]. Views and opinions expressed are however those of the author(s) only and do not necessarily reflect those of the European Union or the European Climate, Infrastructure and Environment Executive Agency (CINEA). Neither the European Union nor CINEA can be held responsible for them.

REFERENCES

[1] B. Tadesse, F. Makuei, B. Albijanic, L. Dyer, Miner. Eng., 131 (15) (2019) 170-184.
[2] www.iea.org/reports/the-role-of-critical-minerals-in-clean-energy-transitions/mineral-requirements-for-clean-energy-transitions.
[3] P.M. Tembo, C. Dyer, V. Subramanian, NPG Asia Materials, 16 (2024) Art. no 43.
[4] E. Rietveld, T. Bastein, T. Van Leeuwen, S. Wieclawska, N. Bonenkamp, D. Peck, M. Klebba, M. Le Mouel, N. Poitiers, 2022. Strengthening the security of supply of products containing Critical Raw Materials for the green transition and decarbonisation. Publication for the Committee on Industry, Research and Energy (ITRE), Policy Department for Economic, Scientific and Quality of Life Policies, European Parliament, Luxembourg.
[5] https://li4life.eu/
[6] https://www.linkedin.com/company/li4life-eu-project https://x.com/li4LIFEProject

The 56th International October Conference on Mining and Metallurgy
22-25 October 2025, Bor Lake, Bor, Serbia
www.ioc.tfbor.bg.ac.rs

DOI: 10.5937/IOC25195D *Original scientific paper*

EFFECT OF RECYCLED ASPHALT (RAP) AND COPPER SLAG (CS) AS PARTIAL SUBSTITUTION OF NATURAL AGGREGATE IN ASPHALT MIXTURES

Jelena Đorđević[1a], Jelena Stefanović[1b], Sandra Guševac[1c], Nevena Marković[1d], Zoran Avramović[1e], Nikola Jovanović[1f], Nikola Lekić[1g]

[1] Mining and Metallurgy Institute Bor, Alberta Ajnštajna 1, 19210 Bor, Serbia
[1a] jelena.djordjevic@irmbor.co.rs, 0000-0001-5406-0074
[1b] jelena.stankovic@irmbor.co.rs, 0000-0001-6418-1814
[1c] filipovic@irmbor.co.rs, 0000-0002-6776-9899
[1d] nevena.markovic@irmbor.co.rs, 0009-0005-1278-8805
[1e] zoran.avramovic@irmbor.co.rs, 0009-0006-7585-976X
[1f] nikola.jovanovic@irmbor.co.rs, 0009-0008-0982-2576
[1g] nikola.lekic@irmbor.co.rs, 0009-0005-9399-9849

Abstract
The expansion of the road network requires the use of a large amount of natural resources. On the other hand, industrial development leads to the creation and deposition of a large amount of industrial waste. Large amounts of this waste accumulate in landfills close to the production process and represent a major environmental and economic problem, which can be solved by reusing industrial waste in the construction sector. Many researchers dealt with the topic of using copper slag as a partial replacement of natural aggregate in asphalt mixtures and as a result obtained favorable physical and mechanical characteristics of asphalt mixtures. One of the negative impacts of this alternative material is the high porosity of the slag, which required a higher amount of bitumen in the asphalt mixtures. However, this problem is solved by adding recycled asphalt (RAP-Recycled asphalt pavement) in the mixes.

***Keywords**: copper slag, recycled asphalt, asphalt mixture, environmental protection*

1. INTRODUCTION

Every year, more than 1.6 billion tons of asphalt are produced in the world [1], and there is information that between 260 and 300 million tons are produced in Europe [2]. According to the data of the Republic Institute of Statistics [3], in recent years, production in Serbia was about 2.4 million tons of asphalt, with the exception of 2020, when production was slightly lower due to the COVID-19 pandemic.

For the construction and maintenance of roads, solutions aimed at reducing the negative impact on the environment in terms of greenhouse gas emissions and energy consumption, as well as the preservation of natural resources through the maximum use of recycled and alternative materials with the condition of maintaining the durability and satisfactory characteristics of the facilities during exploitation, are increasingly being applied. In this sense, copper slag, as well as scraped asphalt in asphalt mixes, is particularly important.

Copper slag is a by-product of copper smelting. This material has a high content of copper and precious metals, but is traditionally classified as waste that is disposed of in landfills near the production process.

The annual average of copper production in the world in the last 10 years is close to 19 million tons of copper, where from each ton of copper between 2 and 2.5 tons of copper slag is generated, which represents a significant amount of material in landfills. [4] The International Copper Study Group [5] has published statistical data on copper production in the period between 1900 and 2023, where one can see the successive growth of production both on a global level and on individual continents. Since 1960, when world production was less than 500,000 tons of copper, world

production in copper mines has grown by 3.14% peryear and will reach 22.4 million tons in 2023. [5]

Copper production capacity is estimated to reach 32.4 million tons by 2028. [5], which indicates the need to dispose of copper slag as waste generated in the copper production process and the possibility of using this alternative material for industrial purposes as a partial or complete replacement of natural raw materials. This would solve the problem of depositing copper slag, and on the other hand, it would save natural resources.

An alternative material successfully used in many countries for road construction is scraped asphalt (RAP). The use of this material affects the lower consumption of natural resources, the reduction of asphalt mixture production costs, as well as the reduction of negative impacts on the environment.

2. USE OF RECYCLED ASPHALT (RAP) AND COPPER SLAG (CS) AS PARTIAL REPLACEMENT OF NATURAL AGGREGATE IN ASPHALT MIXTURES

RAP is very successfully used in asphalt mixtures, and the amount of use is affected by the binder, which is an integral part of this material and which has lost its initial rheological characteristics. Studies of asphalt mixtures with high RAP content have shown changes in the physical behavior of the mixture, which affects durability. The percentage content of RAP in the mixtures between 40-60% affects the increase of stiffness and strength in indirect tension from 60% to 70%, while the Marshall flow decreases from 20% to 50%. Changes in these characteristics of asphalt mixtures affect the improvement of pavement resistance to rutting, but also the greater susceptibility to the formation of cracks due to fatigue and thermal effects. [4] The use of RAP in asphalt mixtures with copper slag can have a beneficial effect and reduce the negative impact of slag in terms of the need for a larger amount of bitumen, which is a consequence of the higher porosity of the slag. Adding RAP can replace bitumen, which additionally requires slag.

In order to solve the negative effects of RAP in asphalt mixtures, it is necessary to use a softer binder and/or add bitumen rejuvenation additives to the mixtures, in order to reactivate the aged binder in the RAP. In this way, the increase in stiffness and strength during indirect tensioning would be limited.

A.C. Raposeiras and other authors [4] investigated the physico-chemical and mechanical characteristics of asphalt mixtures with RAP and replacement of natural aggregate with copper slag.

The research work of this group of authors [4] was related to the examination of Marshall stiffness, indirect tensile strength and stiffness modulus of asphalt mixtures with different contents of copper slag, RAP and natural aggregate (table 1), in order to determine the mechanical characteristics of the mixtures.

Marshall stability results for all mix combinations showed that for mixes containing only natural aggregate and RAP, Marshall stability values increased from 40% to 80% with increasing RAP content in the mixes. However, when adding CS, variable results were obtained for Marshall stability. In mixtures without RAP, CS affects the increase of the resistance of the mixture, which is a consequence of the greater stiffness of the mixture, the shape of the grains of CS and good adhesion with the binder. In mixes containing both alternative materials, RAP and CS, there is a compensating increase in stability. If the asphalt mixture contains 20% RAP, the highest values of Marshall stability were obtained with the addition of 15% CS in the mixture, and if the content of copper slag increases to 35%, the stability of the mentioned mixture is close to the stability of the conventional mixture. For a RAP percentage of 30% in asphalt mixtures, 25% copper slag is required to achieve stability similar to conventional mixtures. Based on the mentioned test results, it can be concluded that in asphalt mixtures CS controls the Marshall stability, and with the

addition of RAP the growth of stability can be controlled and lead to similar values that occur in conventional mixtures. As an explanation of these results, the fact that CS is affected by the aged binder from RAP, which is not adequately activated, and thus the workability of that binder is poor and the coating of CS grains is irregular, which affects the reduction of the resistance of the mixture. [4]

Table 1. Percentage participation of alternative materials in asphalt mixtures for mechanical analysis

Percentage content of material			
Asphalt mixture	**RAP (%)**	**Copper slag (%)**	**Natural aggregate (%)**
M1	-	-	100
M2	20	25	55
M3	30	15	55
M4	40	35	25
M5	20	15	65
M6	30	35	35
M7	40	25	35
M8	-	15	85
M9	-	25	75
M10	-	35	65
M11	40	15	45
M12	30	25	45
M13	20	35	45
M14	40	-	60
M15	30	-	70
M16	20	-	80

Flow results also vary depending on the ratio of participation of alternative materials in asphalt mixtures. Mixtures containing RAP without the participation of copper slag record an increase in deformations proportional to the increase in the participation of RAP in the mixtures. Also, mixtures containing only CS from alternative materials have an increase in Marshall flow, which the authors explain by the fact that copper slag has hydrophobic properties and as such does not absorb the binder as a natural aggregate, but the binder only sticks to the surface of the slag grains, which causes deformation of the binder before the mixture cracks. Combining RAP and CS stabilizes deformations, i.e. flow in the mixture. A content of 20% of RAP requires the participation of 35% of CS to obtain yield values similar to those of the conventional mixture, while a content of 40% of RAP in the mixture requires 15% of CS to stabilize deformations. The increase in deformation occurs due to the decrease in the amount of binder needed to bind the aggregates in the mixture, which leads to greater freedom of movement of the aggregate grains. CS affects the reduction of deformations due to the shape of the grains, which enables a good packing of the aggregates.

The results of indirect tensile strength and stiffness modulus in asphalt mixtures with RAP and CS change according to the same principle as stability and Marshall flow parameters. The presence of RAP in the mixtures increases the indirect tensile strength, while the addition of CS controls the large growth of this parameter.

Mohi ud din, Ishfaq and Mir, Mohammad studied the behavior of hot process asphalt mixtures with recycled asphalt and copper slag as partial replacement of natural materials. [6]

The authors had interesting observations related to surface permanent deformation - ruts. The most common causes of rutting are: low content of air-filled voids, high amount of binder in asphalt mixtures, excess sand or mineral filler and rounded aggregate grains. Analyzing mixtures with RAP and CS, the authors stated that asphalt mixtures containing RAP in percentages between 40% and 60% have increased stiffness and reduced Marshall flow. These mixes have shown favorable

results in terms of resistance to permanent deformation, but are prone to fatigue and thermal cracking. This problem was solved by adding rejuvenators to the mixtures, which improved the rheological properties of the bitumen to some extent. Mixes with 50% RAP and 20% CS showed a 25% increase in stiffness and reached Marshall yield values close to those of the conventional mix. These results can be explained by the angular shape of the CS grains, which leads to an increase in internal friction, which further results in a higher resistance to rutting. [6]

The resistance of asphalt mixtures to the action of water is an important characteristic for the durability of pavements. The sensitivity of asphalt mixtures to the action of water is a complex phenomenon and serious experimental work is necessary to understand the behavior of CS under the action of water. However, the test results of many researchers show that asphalt mixtures containing CS have a higher resistance to the harmful effects of water, which is a consequence of the good adhesion of CS grains with bitumen. Although CS is more hydrophilic than limestone aggregates, the strong bond formed between CS and bitumen prevents water from reaching its surface. On the other hand, limestone aggregate containing a higher ratio of CaO/SiO_2 has a strong bond with the asphalt binder, but this same ratio of chemical compounds contributes to the leaching of the binder from the aggregate grains, which again leads to the conclusion that CS as an aggregate has a better resistance to the action of water. [6]

Good adhesion of CS grains and bitumen was achieved due to the rough surface texture of the slag grains, a large number of pores, cavities and unevenness. On the other hand, good adhesion requires a larger amount of bitumen, which the RAP content can replace if the rheological properties of the aged binder are activated with additives.

3. CONCLUSION

Tests of asphalt mixtures containing RAP and CS as a partial replacement of natural aggregates showed better results than conventional mixtures, if the appropriate measure of the content of these alternative materials was determined.

The general conclusion is that based on the available data from various research works in the world, RAP and CS can be used in road construction, as a partial replacement of natural aggregates. As there are landfills with a large amount of CS in our country, it should be investigated whether this alternative material in combination with RAP can be used in the construction industry in our country, which has already been investigated to a certain extent.

ACKNOWLEDGEMENTS

The paper presents a part of research that was supported by the Ministry of Science, Technological Development and Innovation of the Republic of Serbia, registration number of the Contract 451-03-136/2025-03/ 200052.

REFERENCES

[1] EAPA. The Asphalt Paving Industry, A Global Perspective; EAPA: Brussels, Belgium, 2011.
[2] Asphalt in Figures 2023, European Asphalt Pavement Association (EAPA), Brussels, Belgium, 2024.
[3] Statistički godišnjak Republike Srbije 2023, Republički zavod za statistiku, Beograd, 2023.
[4] A.C. Raposeiras, D. Movilla-Quesada, R. Bilbao-Novoa, C. Cifuentes, G. Ferrer-Norambuena, D. Castro-Fresno, Constr. Build. Mater., 190 (2018) 427-438.
[5] https://icsg.org (18.03.2025.)
[6] Mohi ud din, M. Mir, Can. J. Civ. Eng. 47 (4) 2019.

The 56th International October Conference on Mining and Metallurgy
22-25 October 2025, Bor Lake, Bor, Serbia
www.ioc.tfbor.bg.ac.rs

DOI: 10.5937/IOC25199H

Technical paper

TRANSFERRING COMMON HPGR APPLICATION FROM COPPER TO LITHIUM ORE

Artur Hubert[1a], Felix Heinicke[1b]

[1] Köppern Aufbereitungstechnik GmbH & Co.KG, Agricolastr. 24, 09599 Freiberg, Germany
[1a] a.hubert@koeppern.com, 0009-0008-5209-1174
[1b] f.heinicke@koeppern.com, 0009-0007-3377-8571

Abstract

During the past 45 years, HPGR technology has made continuous progress, while simultaneously drawing on more than 125 years of experience with high-pressure processing of materials between counter rotating rolls for briquetting and compaction.

Following the success stories in the cement industry, HPGR technology became known and caught on in the mining industry as well. Especially the continuous development of wear resistant grinding tools made the economical use of HPGR possible. Typical benefits are energy savings, metallurgical advantages, reduced specific wear costs, production increases and investment savings.

Whereas the physical activation through micro cracking has been in use in the Copper industry from the beginning, the application for Lithium ore has become public only within the last years. As both materials heavily supply for growing industries such as electrical cars and battery productions this contribution will strive to explain experiences in detail along with new developments in the field of HPGR grinding circuits.

***Keywords**: HPGR, copper, lithium*

1. INTRODUCTION

Processing of powders in between two rollers is a unique technology applicable for various industries. Figure 1 shows some typical classes of use, with Briquetting and Compaction forming small to coarse particles and comminution forming coarse to fines ones. The HPGR comminution practice is based on the research work of the German Professor Klaus Schönert [for example 2, 3, 4, 11]. Köppern, as one supplier of HPGR's, has worked more than 125 years on roller presses, starting with the formation of coal briquettes between two synchronized rollers. The first HPGR grinding solutions were implemented in the cement industry, where the downstream energy savings provided an advantage for this medium-cost product [5]. Since this success, state of the art mining projects evaluate the application of HPGR technology versus SAG milling [1].

Figure1. Overview of roller pressing applications; left Briquetting, middle Compaction, right Comminution

Transitioning the grinding principles of HPGR to mineral applications however was not straightforward, due to the much higher wear rates caused by the significantly more abrasive materials. However due improvements of the roller surfaces, especially through the use of studded

tires, mineral grinding applications ranging from copper and iron ore to hard rock applications are now commonplace [6][8].

Through such innovations, the benefits of HPGRs in mineral processing applications have been successfully proven not only through test work, but also in many industrial applications (for example [9] [10]). The increase of throughput, overall energy savings and reductions of the workload on downstream equipment, such as ball mills, are all well-known advantages of the implementation of HPGRs. The total benefit, however, depends on the minerals being processed and the material activation within the working gap [7]. Fugere 2 shows an open HPGR during assembly for general todays sizes references.

Figure 2. Modern size HPGR in production workshop

2. KNOWN COPPER EFFECT

Various publications are available which prove the results of mechanical activation towards the downstream of HPGR [summery overview in 12].

The activation and grinding between the HPGR gap is enhanced by four main effects [8]:

a) The retention time in the grinding zone is short, about 10 ms,
b) The stress is multiaxial as particles are activated in a bulk,
c) The stress level in the activation zone is very high (≥ 250 MPa).
d) All material has to pass the gap and the volumetric usage of machine is up to 100%.

For materials with a small proportion of elastic components in the feed, the activation results in [8]:

a) A high share of fines in the product and effective grinding,
b) A preferred breakage along the grain boundaries,
c) A low amount of ultrafine particles (< 0.010 mm), small particles can hide in bulk gaps and the amount of attrition is low,
d) A pre-weakening of grain structures due to formation of micro-cracks (example see Figure 3)

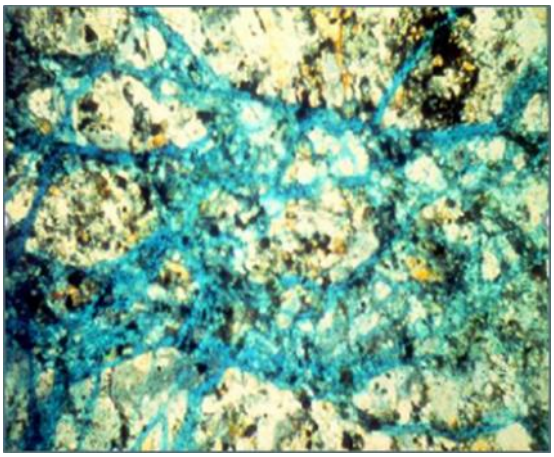

Figure 3.Micro-cracks coloured in a HPGR product [13]

Figure 4 gives an example of the downstream effects of copper leaching results after HPGR according to Baum with typical high speed up potentials [13].

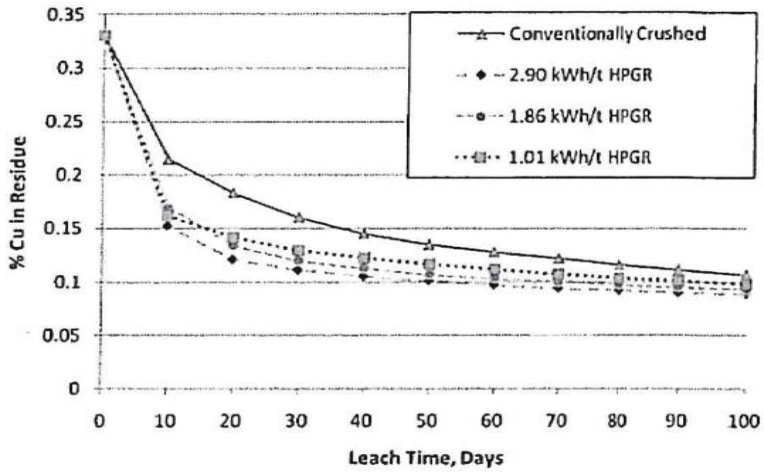

Figure 4. Comparison to leach kinetics between conventional cone crush and HPGR comminution [13]

3. TRANSFER TO LITHIUM

Independent of the above mentioned micro-fractures, HPGR stress paths through the material in the gap show significant effect on various minerals phases. Figure 5 shows one example for iron ores [14].

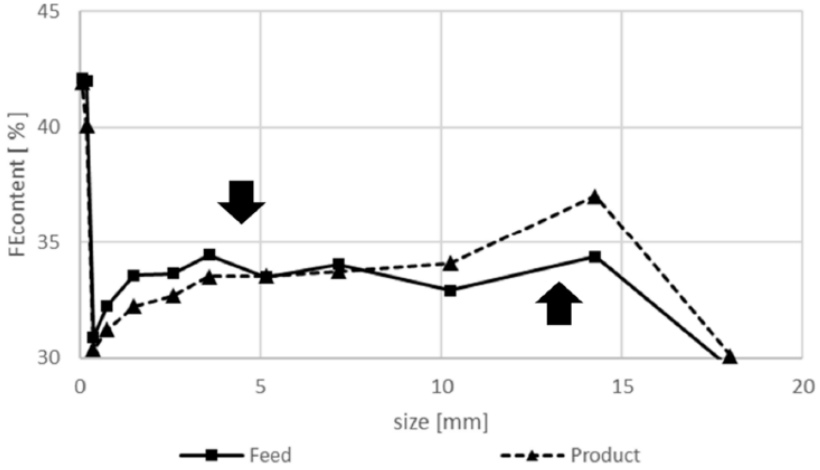

Figure 5. Preferential breakage inside the HPGR [14]

Following the battery boom of the last years and the high demand for Lithium based ores, HPGR machines have also been implemented in Pegmatite process lines. Because of their coarse grained rock structure certain lithium ore deposits are especially suitable for selective comminution of HPGR. Due to the physical principles acting in particle bed comminution and the fundamental laws of fractures mechanics HPGR have shown to increase liberation size and shift valuable Lithium away from ultra fine particle sizes. A secondary result is the increase of silica in the middle size ranges where dense media separation set ups can be used for early sorting.

4. SUMMARY

Selective grinding is a key effect within HPGR processes. The extended abstract refers to various studies assessing this topic and possible solutions in view to optimizing down stream recoveries. Upcoming possibilities for finer cut sizes by using dry air classification systems may be a key driver to boost both the Copper and Lithium industries as well as Battery CAPEX prices.

ACKNOWLEDGEMENTS

The authors thank Köppern for the right to publish the paper and the Technical University Freiberg for the excellent research cooperation to boost past and future HPGR developments.

REFERENCES

[1] B. Costello, J. Brown, A tabletop cost estimate review of several large HPGR projects. Proceedings of the SAG conference (2015), p. 1-24
[2] K. Schönert, Einzelkorn-Druckzerkleinerung und Zerkleinerungskinetik. Untersuchungen an Kalkstein-, Quarz-, und Zementklinkerkörnern des Größenbereiches 0,1-0,3mm. Dissertation. TH Karlsruhe, 1966
[3] K. Schönert, Zur Auslegung von Gutbett-Walzenmühlen. Zement Kalk Gips Jg. 38 (1985) Nr.12, p. 728-730
[4] K. Schönert, Energetische Aspekte des Zerkleinerns spröder Stoffe. Zement Kalk Gips Jg.32 (1979) Heft1, p. 1-9
[5] K. Schönert, O. Knobloch, Mahlen von Zement in der Gutbett-Walzenmühle. Zement Kalk Gips 37 (1984) 563-568
[6] R. Klymowsky, Selection and sizing of High Pressure Grinding Rolls. SME Handbook 2002, S. 1-40
[7] F. Heinicke, A. Hubert, Improvement of CIS standard iron ore circuit by HPGR. Proceedings of SAG 2019 in Vancouver, p. 1-10
[8] F. Heinicke, Beitrag zur Modellierung der Zerkleinerung in Gutbettwalzenmühlen. Dissertation. Rheinisch-Westfälische Technische Hochschule Aachen, 2012
[9] A. Gardula, First year operation of HPGR at Tropicana Gold Mine. Case study. SAG conference in Vancouver, 2015
[10] J.L. Vanderbeek, A.J. Gunson, Cerro Verde 240.000 t/d concentrator expansion. Proceedings of the SAG conference, 2015
[11] A.M. Abouzeid, D.W. Fuerstenau, Int. J. Miner. Process., 93 (2009) 59-65
[12] F. Heinicke, M. Pfeifer, HPGR Downstream Effects for leaching of gold ores. Proceedings of Comminution in Cape Town, 2025, p. 1-7
[13] W. Baum, K. Ausburn, M&MP, 28 (2) (2011) 77-81
[14] F. Heinicke, M. Pfeifer, H. Lieberwirth, R. Kühnel, The benefit of selective grinding by HPGR in air separation process. . Proceedings of Comminution in Cape Town, 2020, p. 1-8

The 56th International October Conference on Mining and Metallurgy
22-25 October 2025, Bor Lake, Bor, Serbia
www.ioc.tfbor.bg.ac.rs

DOI: 10.5937/IOC25203R *Original scientific research*

MATHEMATICAL MODELLING AND STATISTICAL ANALYSIS OF SUB GRADE IRON ORE BENEFICIATION USING WET HIGH INTENSITY MAGNETIC SEPARATOR (WHIMS)

Venkateswara Rao[1a], Jayapal Reddy[2a]

[1]Project Manager, Pellet Plant, NMDC Limited, Donimalai, Karnataka, India
[2]Executive Director (RP, RED, PC & Environment), NMDC Limited, Hyderabad, India
[1a] gvrao@nmdc.co.in; 0000-0001-7466-2494
[2a] jayapal@nmdc.co.in; 0009-0003-0047-3940

Abstract
Beneficiation of sub-grade iron ore from Bailadila, India (40.80% Fe, 40.90% SiO2, 0.24% Al2O3) was studied using Vertical Pulsating Wet High Intensity Magnetic Separation (VP-WHIMS). Fine grinding to 80% passing 150 microns enabled sufficient liberation of hematite and goethite from quartz. Thirty experiments were designed using a Central Composite approach and Response Surface Methodology, optimizing magnetic field intensity, pulp density, ring speed, and pulsating frequency. A quadratic model ($R^2 = 0.95$) was established using Minitab 17, and ANOVA confirmed that both individual parameters and their interactions significantly affected iron recovery and concentrate grade. Response surface plots visualized optimal operating conditions, offering practical insights for industrial application and effective process control.

Keywords: *Sub Grade Iron Ore, Beneficiation, VP-WHIMS, Bailadila, Anova and Surface plot*

1. INTRODUCTION

The world's iron feedstock is transitioning to low- and sub-grade resources such as ultrafine slimes, lean hematite, and complex ores, making robust recovery strategies essential. Conventional gravity and flotation are sub-optimal for such fines due to particle size, surface associations, and weak magnetic susceptibility. Extensive research exists for beneficiation of slimes and low-grade ores for pelletisation. Wet High-Intensity Magnetic Separation (WHIMS) selectively recovers weakly magnetic iron oxides engineered by key variables [4–6], and has re-emerged for slime treatment, tailings reprocessing, and low-grade fines upgrading [7–11]. However, most WHIMS studies are empirical and offer limited predictive ability for variable feed conditions . The mechanisms — magnetophoretic attraction, hydrodynamic transport, particle detachment, and liberation — act in complex ways. While modeling sub-systems with CFD or DEM is common, integrated mathematical frameworks that couple population balance models, magneto-hydrodynamic capture, and uncertainty quantification are rare, limiting predictive control and robust process design. Magnetization roasting and advanced magnetic separation approaches also add to the evolving beneficiation toolkit [13–19].

2. MATERIAL AND METHODS

2.1 The Sample

'As received' sub-grade iron ore from Bailadila, Chhattisgarh (ROM, -150 mm where–1 mm is 36%) was homogenized, sampled, and characterized (physical, chemical, mineralogical). The chemical composition (Table 1) and Minerological indicates Hematite is the main ore with Quartz as major gangue and the liberation particle size is ~150 microns.

Table 1. Size analysis of 'as received' ROM

Table 1. Chemical analysis of 'as received' ROM sample.

Constituent	Fe	FeO	SiO_2	Al_2O_3	LOI	P	S	TiO2	CaO	MgO	MnO
Assay %	40.80	0.30	40.90	0.24	0.22	0.05	<0.01	0.091	0.119	0.110	0.045

2.2 Experimental

2.2.1 Vertical Pulsating Wet High Intensity Magnetic Separator (VP-WHIMS)

A Longi LGS 500 VP-WHIMS (rotor Ø 500 mm, matrix gap 2 mm, semi-continuous) processed ore ground to 100 mesh (152 microns). Parameters varied: pulp density (15–35%), field intensity (2000–10000 G), ring speed (0.6–3 rpm), and pulsation (50–250 cpm). Batches of 10 kg ore were tested; concentrate, middlings, and tailings dried and analyzed.

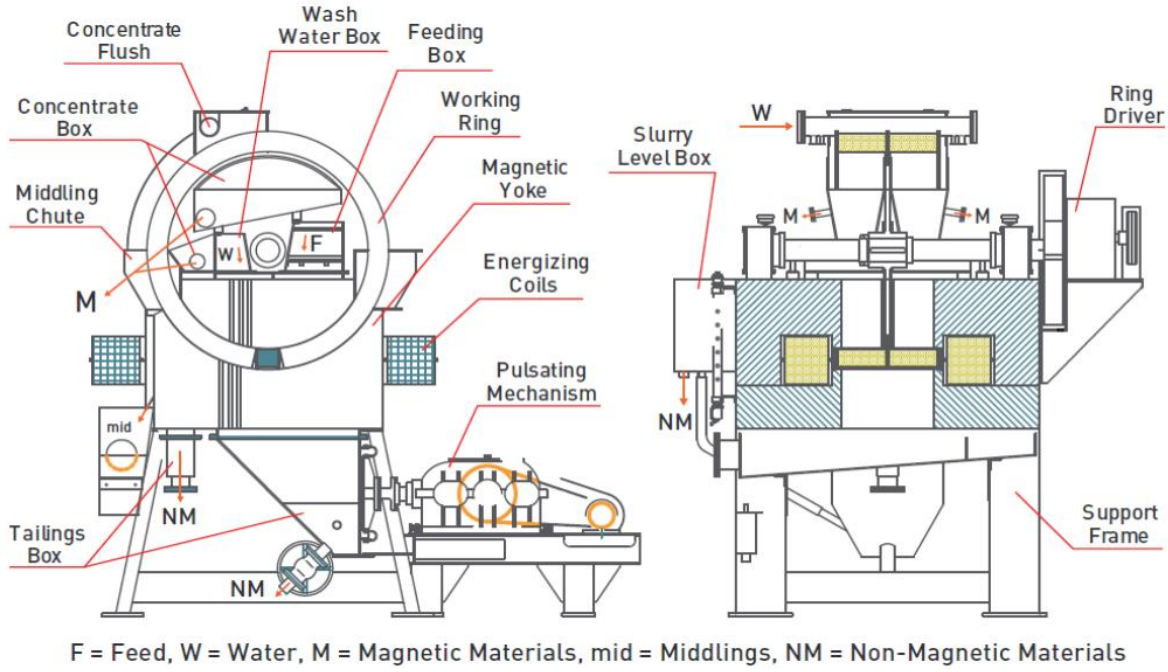

Figure 1. Schematic diagram of Vertical pulsating Wet High Intensity Magnetic Separator

2.2.2 Response Surface Methodology

RSM (Central Composite design, 4 variables, 5 levels, 30 runs) modeled the relationship between independent variables and process responses (Table 2), with equations and ANOVA generated by Minitab 17 [20–22].

Table 2. Experimental range and levels of independent process variables

Variable	Unit	Variable	(-2) Very Low	(-1) Low	0 Mid level	(+1) High	(+2) Very High
Magnetic Field Intensity	GAUSS	A	2000	4000	6000	8000	10000
Pulsating Frequency	Cycles/min	B	50	100	150	200	250
Ring Rotational Speed	RPM	C	0.6	1.2	1.8	2.4	3
Slurry concentration	%	D	15	20	25	30	35

3. RESULTS AND DISCUSSION

3.1 Results

Thirty experimental runs examined effects of the four main variables on concentrate grade, yield, and iron recovery (Tables 3). Mathematical models predicted performance; surface and contour plots were generated.

Table 3. Test results of Central Composite Design (CCD).

Test No.	Magnetic Field Intensity	Pulsating Frequency	Rotational Speed	Slurry concentration	% Yield	%Fe	% Iron Values recovery
	A	B	C	D	Yield	Grade	Recovery
1	0	-2	0	0	46.00	52.00	58.63
2	0	0	-2	0	32.00	55.50	43.53
3	0	2	0	0	50.00	55.00	57.40
4	0	0	0	2	40.00	55.50	54.41
5	0	0	0	-2	44.00	56.00	60.39
6	0	0	0	0	44.79	55.90	61.37
7	-2	0	0	0	40.50	58.00	57.57
8	0	0	0	0	44.79	55.90	61.37
9	2	0	0	0	54.00	55.00	72.79
10	0	0	2	0	39.00	56.00	53.53
11	0	0	0	0	44.79	55.90	61.37
12	1	1	1	1	53.70	55.00	72.39
13	-1	-1	1	1	42.50	55.00	57.29
14	0	0	0	0	44.79	55.90	61.37
15	1	-1	-1	1	39.40	53.50	51.66
16	-1	-1	-1	-1	44.00	55.00	59.31
17	-1	1	-1	1	35.64	56.80	49.62
18	-1	1	1	-1	40.00	56.20	55.10
19	1	-1	1	-1	43.50	55.00	58.64
20	1	1	-1	-1	50.00	54.70	67.03
21	1	-1	-1	-1	42.10	54.50	56.24
22	1	1	1	-1	56.00	54.50	74.80
23	-1	-1	-1	1	41.80	54.50	55.84
24	-1	1	1	1	38.20	56.20	52.62
25	-1	-1	1	-1	41.00	56.90	57.18
26	0	0	0	0	44.79	55.90	61.37
27	-1	1	-1	-1	33.00	56.80	45.94
28	1	1	-1	1	43.50	56.20	59.92
29	1	-1	1	1	44.00	53.60	57.70
30	0	0	0	0	44.79	55.90	61.37

Concentrate Grade = 55.900-0.5750*A + 0.4917*B + 0.1667*C - 0.0500*D
+ 0.1604*A*A - 0.5896*B*B - 0.0271*C*C - 0.0271*D*D- 0.212*A*B
+ 0.037*A*C + 0.288*A*D - 0.513*B*C + 0.262*B*D-0.012*C*D

Concentrate Yield = 44.790 + 3.440*A + 0.843*B+ 1.790*C - 0.807*D
+ 0.582 A*A + 0.770 B*B- 2.355 C*C - 0.730 D*D+ 3.572*A*B
+ 0.902*A*C - 0.728*A*D+ 1.410*B*C - 0.285*B*D + 0.385*C*D

Iron Values recovery in Concentrate = 61.370 + 4.089*A +0.787*B+2.599*C -1.123*D
+ 1.130*A*A - 0.662*B*B - 3.033*C*C
- 0.815*D*D + 4.626*A*B+ 1.214*A*C
- 0.666*A*D+ 1.401*B*C - 0.104*B*D +0.499*C*D

3.2 Discussion

Contour plots are two-dimensional visualizations showing how two factors simultaneously affect a response (such as yield, grade, or recovery), with response values indicated by lines or color bands of equal value—much like a topographic map. Surface plots offer a three-dimensional view, where the response surface is visualized as a "landscape" shaped by the two variables on the axes. These plots help identify response peaks, valleys, and ridges as the variables are varied. Contour and surface plots, built from the mathematical model, are powerful tools to visualize and optimize the complex relationships between operational variables in VP-WHIMS. Proper interpretation guides not only to the optimal settings but also highlights process sensitivity, robustness, and crucial interactions—ensuring the best possible balance between concentrate grade, yield, and iron recovery in continuous plant operation.

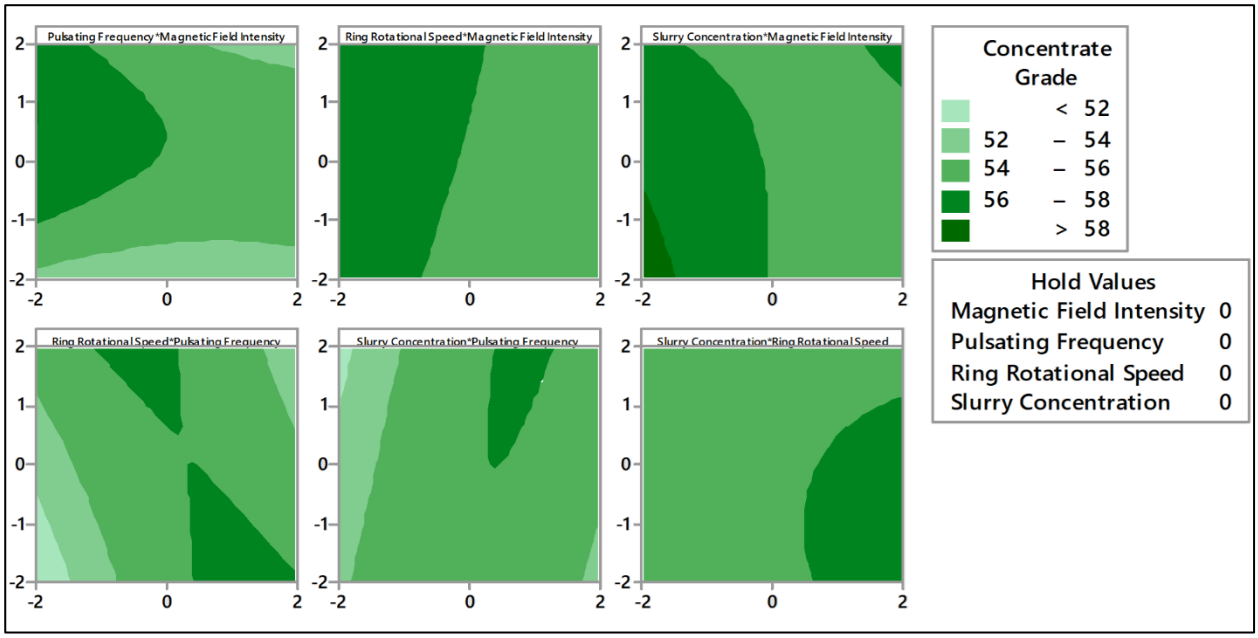

Figure 2. Contour plots of concentrate grade

3.2.1. Effects of magnetic field strength:

Increased field intensity raised yield and recovery but slightly reduced product quality at higher intensities, likely due to entrapment of non-magnetics.

3.2.2. Effects of Slurry concentration

Higher pulp density (>25%) reduced Fe recovery due to matrix overcrowding; lower densities (<30%) optimized recovery and grade.

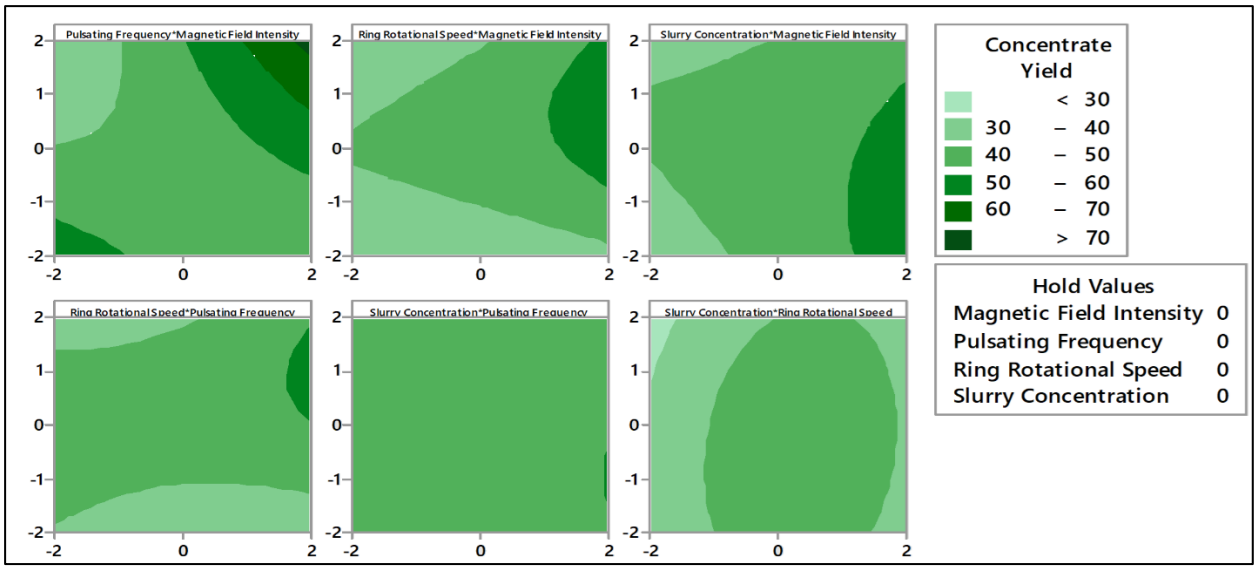

Figure 3. Contour plots of concentrate yield (weight percentage)

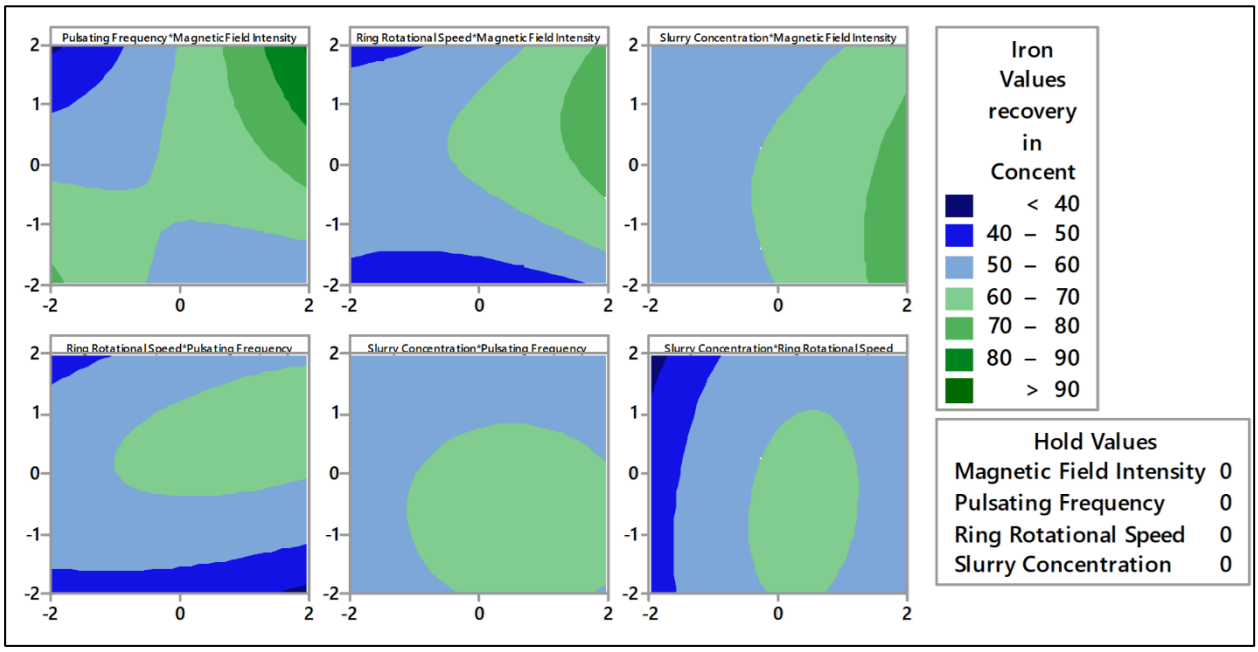

Figure 4. Contour plots of percent iron values recovery in concentrate

3.2.3. Effects of pulsation frequency

Higher frequency improved selectivity and minimized entrapment, increasing both yield and Fe grade.

3.2.4 Ring Rotational Speed (RPM)

Increased RPM elevated yield and recovery but marginally reduced grade unless compensated by pulsation/fine-tuned field intensity.

3.2.5 Statistical analysis:

ANOVA showed major effects from magnetic field intensity and pulsation frequency, and significant variable interactions. Optimal conditions (8,000 G, 200% pulsation, 2.4 rpm, 20% solids) maximized yield, grade, and Fe recovery, confirmed by response surface plots.

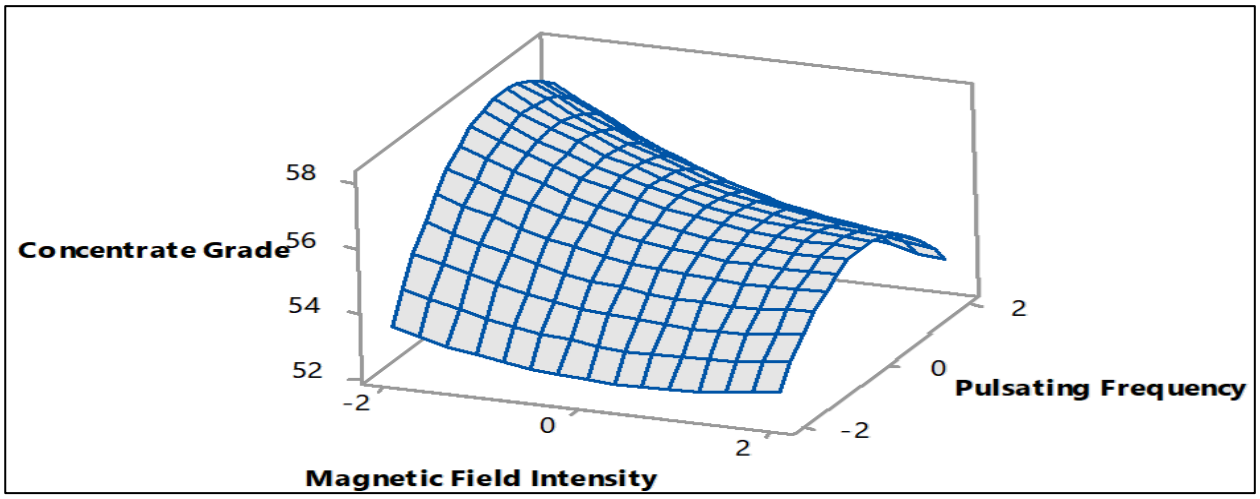

Figure 5. Concentrate Grade Plot (Ring rotational speed and Slurry concentration are at Mid level)

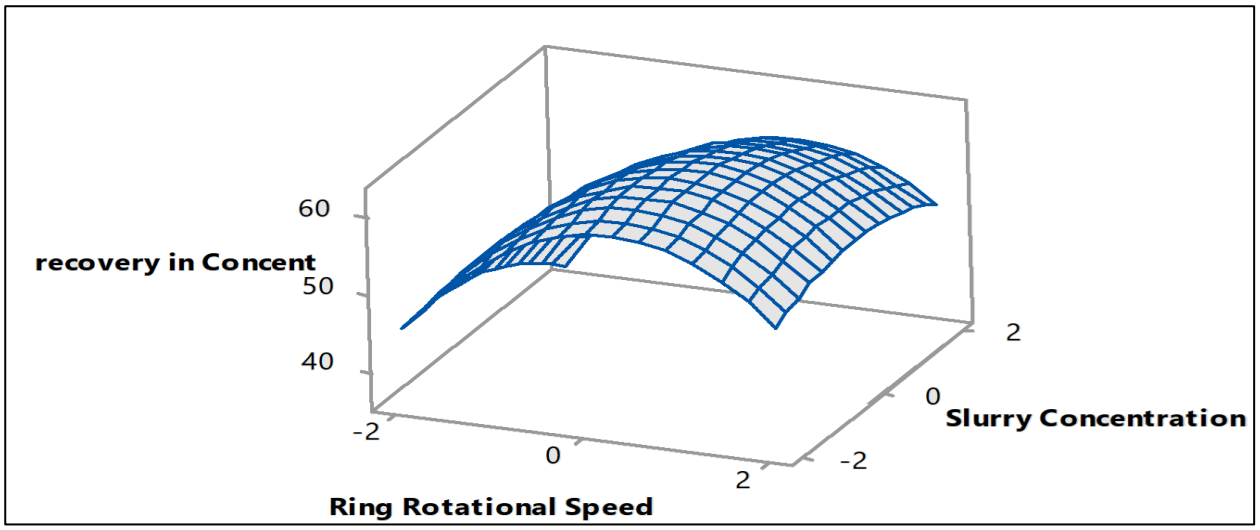

Figure 6. Percent recovery of Iron values in Concentrate plot (Magnetic Field Intensity and Pulsating frequency are at mid-levels)

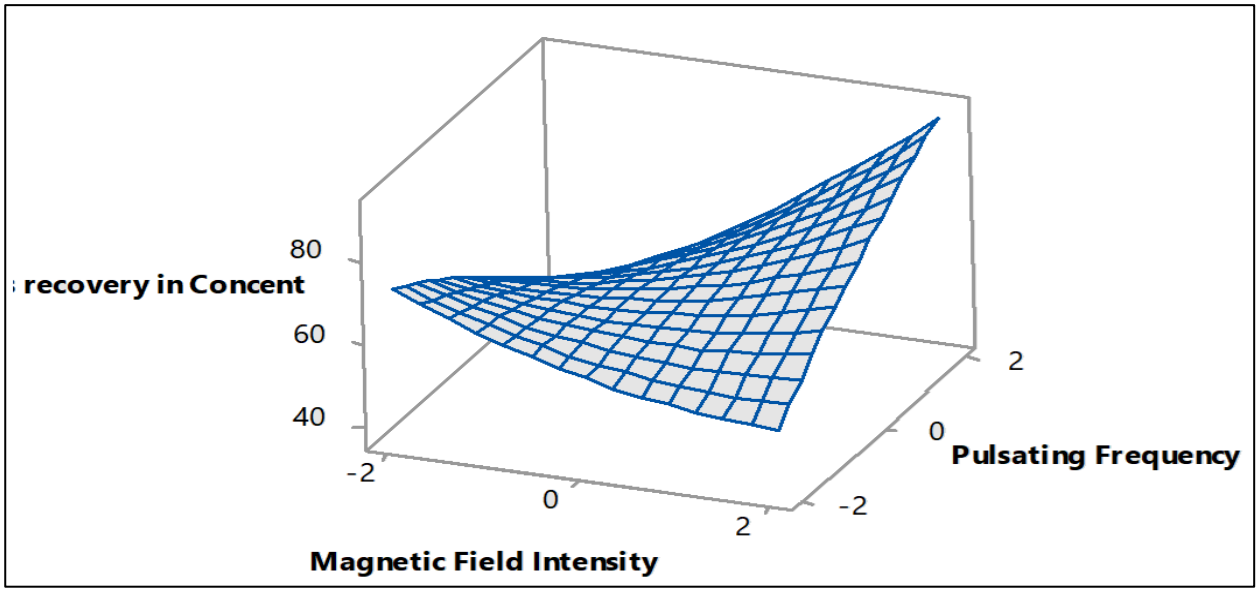

Figure 7. Percent recovery of Iron values in Concentrate plot (Slurry concentration and Ring rotational Speed are at mid-levels)

Table 4. Model Summary

Product	S	R-Sq	R-Sq (adj)	R-Sq (pred)
Concentrate grade	0.414667	93.86%	86.30%	53.68%
Concentrate yield	0.966838	98.63%	96.94%	89.51%
Percent recovery of Iron Values	1.86850	96.77%	92.79%	74.41%

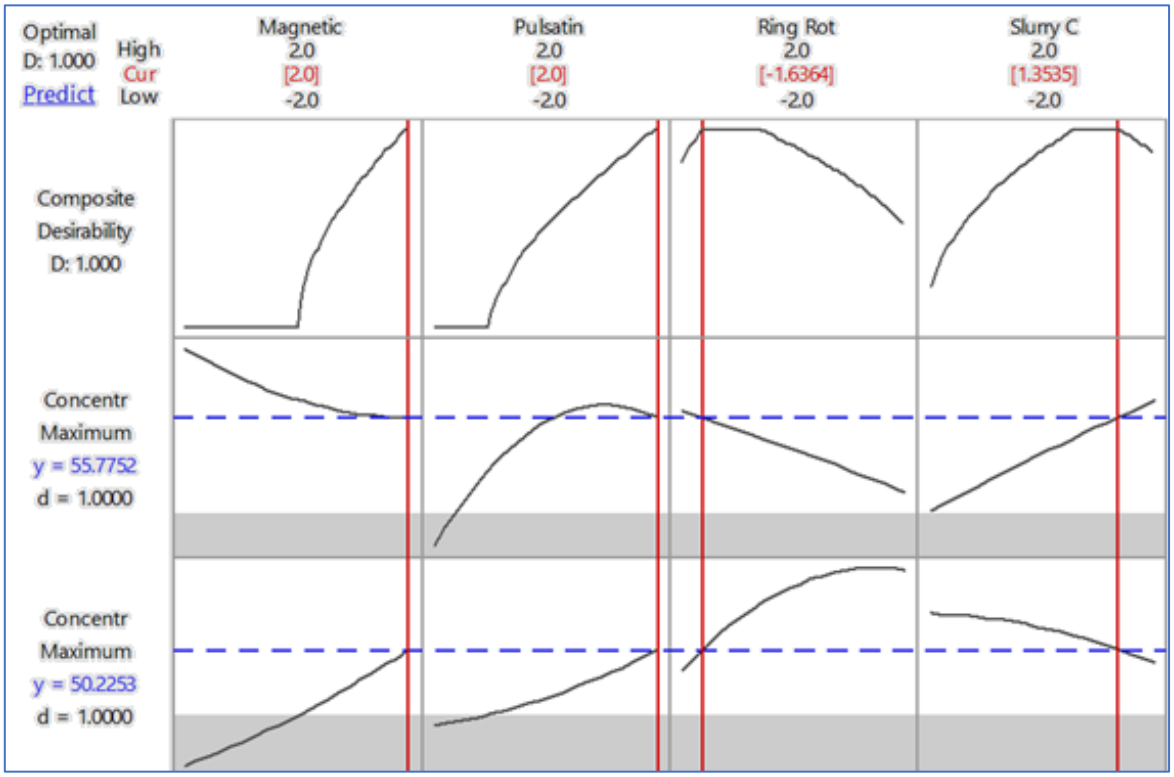

Figure 8. Optimisation plot (prediction of concentrate grade)

4. CONCLUSION

The effects of varying the magnetic field intensity, pulsating frequency, ring rotational speed and slurry concentration provide detailed beneficiation capabilities of the newly developed Longi LGS 500 WHIMS on a low grade iron ore stage crushed and ground to 100mesh material. From the research investigations, the following conclusions were drawn: (1) It was observed that the Longi LGS 500 is potentially good for beneficiating low grade iron ore fines, and the back scattered electron (BSE) images showed that the ore is predominantly Fe oxide in a form of hematite with silicates as main gangue minerals. (2) It was noted that the increase in pulp density from 15% to 25% and 35% had a negative effect on the mass yield of concentrate. At pulp solids >20%, the matrix was overloaded resulting in the concentrate mass yields concentrate and Fe recoveries decreasing with no significant effects on the Fe grade. (3) The changes in magnetic intensity from 2,000 to 10,000 Gauss increased the mass yield of the concentrates, while the pulsation mechanism, on the other hand, positively affected the overall quality of the product. An increase from 50% to 250% showed an increase in both the mass yield concentrates and Fe grade. (4) The interactions between parameters were shown to be essential, and most notable was between magnetic field intensity and pulsation frequency having the most effect.

These results supported the fact that of the two variables investigated, the A and the B had a major individual effect on this particular sample. (5) The optimum conditions for this particular sample are 8000 gauss magnetic field intensity, 200% pulsating frequency, 2.4 rpm and 20% solids feed concentration, where highest recovery of iron values were obtained with good yield and grade.

ACKNOWLEDGEMENTS

The Authors express their profound gratitude to Shri Amitava Mukherjee Chairman cum Managing Director, NMDC Limited for providing the necessary approval and encouragement to pursue this research, his visionary leadership and unwavering support were instrumental in enabling this work to be carried out and presented at this prestigious international forum. we are deeply grateful to our colleagues at the R&D Centre for their collaborative spirit, and diligent efforts were crucial at every stage of the experimental work.

REFERENCES

[1] G. Venkateswara Rao, R. Markandeya, Rajan Kumar, J. Inst. Eng. India Ser. D 99 (2018) 63–70.
[2] G.V. Rao, R. Markandeya, S.K. Sharma, Transactions of Indian Institute of Metals, Series D, 69 (2016) 143- 150.
[3] G. Venkateswara Rao, R. Markandeya, Rajan Kumar, IJERT, 5 (01) (2016) 900-909.
[4] R.P. Sahoo, H. Sahoo, M.K. Mohanta, Int. J. Miner. Process., 130 (2014) 24-31.
[5] A.R. Roy, B. Pradhan, P. Patra, Miner. Eng., 124 (2018) 1-8.
[6] H.V. Vardhan, S.K. Tripathy, B. Subhadra, Sep. Sci. Technol., 55 (1) (2020) 164-171
[7] S.K. Basu, V.N. Misra, Magnetic Separation of Minerals. CRC Press. (2007), 45.
[8] V.K. Gupta, D. Yan, Mineral Processing Design and Operations: An Introduction. Elsevier. (2006) 891.
[9] B.A. Wills, J.A. Finch, Wills' Mineral Processing Technology: An Introduction to the Practical Aspects of Ore Treatment and Mineral Recovery. Butterworth-Heinemann, 8th edition, (2015), 407.
[10] A.F. Taggart, Handbook of Mineral Dressing. John Wiley & Sons, (1945) 452.
[11] E.G. Kelly, D.J. Spottiswood, Introduction to Mineral Processing. John Wiley & Sons, (1982) 457.
[12] M. Tahami, M.R. Mohammadi, M. Schaffie, *et al,* Sci. Rep. 14 (2024) 22578.
[13] C. K. Prabhu, K. Shravan, et al., 9 (7) (2024) 7634–7642.
[14] M. Dobbins, P. Dunn, I. Sherrell, The 7th International Heavy Minerals Conference 'What next', The Southern African Institute of Mining and Metallurgy, (2009), 63 -70.
[15] M.M. Bulayani, P. Raghupatruni, T. Mamvura, Gwiranai Danha, Minerals, 14 (8) (2024) 796.
[16] V. Shukla, C. Raghu Kumar, D.P. Chakraborty, U. Shivangi, J. Du, IJERT, 10 (09) (2021).
[17] K. Quast, W. Skinner, Miner. Eng., 152 (15) (2020) 106346.
[18] C. Bazin, R. Sista, B. Légaré, J. Caron, F. Lavoie, Miner. Eng., (218) (2024) 109003.
[19] M. Amini, S. Papi, JME, 6 (2) (2015) 173-182.
[20] D.C. Montgomery, Design and Analysis of Experiments. John Wiley & Sons. (2017)
[21] G.E.P. Box, J.S. Hunter, W.G. Hunter, Statistics for Experimenters: Design, Innovation, and Discovery. John Wiley & Sons. (2005).
[22] G .Venkateswara Rao, R. Markandeya, R. Kumar, IJMPEM, 2 (4) (2017) 46-56.

The 56th International October Conference on Mining and Metallurgy
22-25 October 2025, Bor Lake, Bor, Serbia
www.ioc.tfbor.bg.ac.rs

DOI: 10.5937/IOC25211M *Original scientific paper*

SAFETY CHALLENGES IN TRANSPORT OF COPPER CONCENTRATE: TML AS A BOUNDARY PARAMETER OF MARITIME CARGO STABILITY

Dušica Mirović[1a], Yuankun Yang[1b], Shengli Yu[1c]
[1] Serbia Zijin Mining doo Bor, Cvetna šuma, 19210 Bor, Serbia
[1a] dusica.mirovic@zijinmining.rs, 0009-0006-5149-7071
[1b] yang.yuankun@zijinmining.rs, 0009-0006-7701-7275
[1c] yu.shengli@zijinmining.rs, 0009-0001-8044-2022

Abstract
Transportable Moisture Limit (TML) is a boundary safety parameter in maritime transport of bulk cargoes. This paper integrates the IMSBC Code framework, laboratory methodologies, and experimental results for Serbia Zijin copper concentrates. Results show that TML is influenced primarily by sulfide content and mineral composition, while granulometry and flotation reagents have limited effects. A novel microstructural hypothesis is introduced, suggesting that inter-particle correlations, capillary forces, and surface energy significantly affect TML values. Preliminary indications also suggest potential for industrial application through surface modification approaches. Integrating standard IMSBC methods with micro-scale analysis may improve predictive accuracy and enhance maritime safety.

***Keywords**: TML, IMSBC Code, copper concentrate, sulfides, liquefaction, maritime safety*

1. INTRODUCTION

Copper concentrate export from Serbia Zijin exceeds 95% of production, mainly by sea. Ensuring safe transport requires strict control of cargo moisture. If the moisture exceeds TML, the concentrate may behave like a liquid under ship motions, producing free-surface effects and loss of stability [1].

Since 2021, winter shipments have repeatedly exceeded TML values due to rainfall during handling. Corrective actions such as re-blending, lime addition, or overturning of cargo in ports generate delays, economic losses, and safety risks.

2. WHAT IS TML AND WHY IT IS IMPORTANT

TML is defined as 90% of the Flow Moisture Point (FMP). Exceeding this limit can cause liquefaction, leading to catastrophic ship accidents. Historical incidents with nickel ore illustrate the consequences of improper TML determination [5].

In addition to defining the critical moisture threshold, TML also serves as a practical tool for risk management, since it provides ship operators and shippers with a measurable boundary parameter that must be respected during loading.

2.1 Fundamental mechanism of liquefaction (ISO N1166)

According to ISO N1166, a wet granular material consists of solid particles and voids filled with water and air. Under cyclic loading, particle rearrangement tends to reduce pore volume. If the voids are water-filled and drainage is restricted, pore pressure rises, leading to a potential loss of shear strength. This mechanism provides the physical foundation of liquefaction, directly linking moisture content, pore water pressure, and cargo instability. This mechanism is of particular importance in maritime transport, since cyclic ship motions continuously generate such pore pressure build-up.

3. IMSBC CODE: RULES AND SAFETY REQUIREMENTS

The International Maritime Solid Bulk Cargoes (IMSBC) Code governs safe transport. Copper concentrates fall into Group A cargoes (prone to liquefaction). Testing must be performed by accredited laboratories. Misjudgment of TML can determine the difference between safe voyage and disaster [1].

The Code also emphasizes the responsibility of shippers to provide accurate laboratory certificates, and of carriers to verify that the cargo complies with declared moisture limits.

3.1 Implications for Maritime Transport

Lower TML values directly increase liquefaction risks. Even a shipment loaded with 1% moisture above the TML threshold could destabilize a vessel in heavy seas. While ship design features (double hulls, drainage systems) provide mitigation, precise laboratory determination remains the most reliable safeguard.

Seasonal variations and precipitation during transport highlight the importance of continuous moisture monitoring and application of corrective measures.

4. LABORATORY METHODS FOR DETERMINING TML

Several laboratory methods are prescribed under the IMSBC Code to establish TML values:

- Flow Table Test: simulates cargo vibration to determine the Flow Moisture Point.
- Penetration Test: measures the depth at which moisture triggers collapse or flow.
- Proctor/Fagerberg Test: evaluates compaction, porosity, and density changes under applied load.
- Gravimetric Method: determines the actual water content of samples.

In this study, the Proctor/Fagerberg method was selected due to its higher accuracy for sulfide-rich concentrates [2]. The test involves controlled compaction of prepared samples while progressively increasing their moisture content. Measurements of bulk density and pore volume allow precise identification of the saturation threshold at which liquefaction becomes possible. This method is especially suitable for fine-grained concentrates, where micro-pores and sulfide minerals strongly affect water retention. In practice, the selection of method depends on cargo mineralogy, particle size distribution, and available laboratory capacity.

5. EXPERIMENTAL ANALYSIS

Three types of concentrates were analyzed: VK (coarser particles), direct-milled (medium particles), and flotation (finest particles). Multi-element and granulometric analyses were combined with TML measurements.

Table 1. Copper concentrates analysis results

Concentrate type	Granulometry	Main minerals	TML (%)
VK concentrate	Coarser	Chalcopyrite, pyrite, quartz, aluminosilicates	14.2
Direct-milled conc.	Medium	Covellite, tetra-chalcopyrite, pyrite, alunite	9.2
Flotation concentrate	Finest	Covellite, tetra-chalcopyrite, pyrite, alunite	7.7

The results revealed pronounced differences among the three concentrate types. The VK concentrate exhibited the highest TML value (14.2%), despite its relatively coarse texture. Direct-

milled samples showed intermediate stability (9.2%), whereas flotation concentrate—although expected to yield higher TML values due to its finer granulometry—displayed the lowest value (7.7%).

Contrary to the expected trend, finer particle size did not result in higher TML values. Instead, mineralogical composition, particularly sulfide content, exerts a stronger influence. Higher sulfide content correlates with lower TML values, as observed in flotation and direct-milled concentrates. Granulometry showed only a limited effect, while flotation reagents had no significant impact on TML values. This suggests that surface chemistry and particle interactions play the dominant role [2,4].

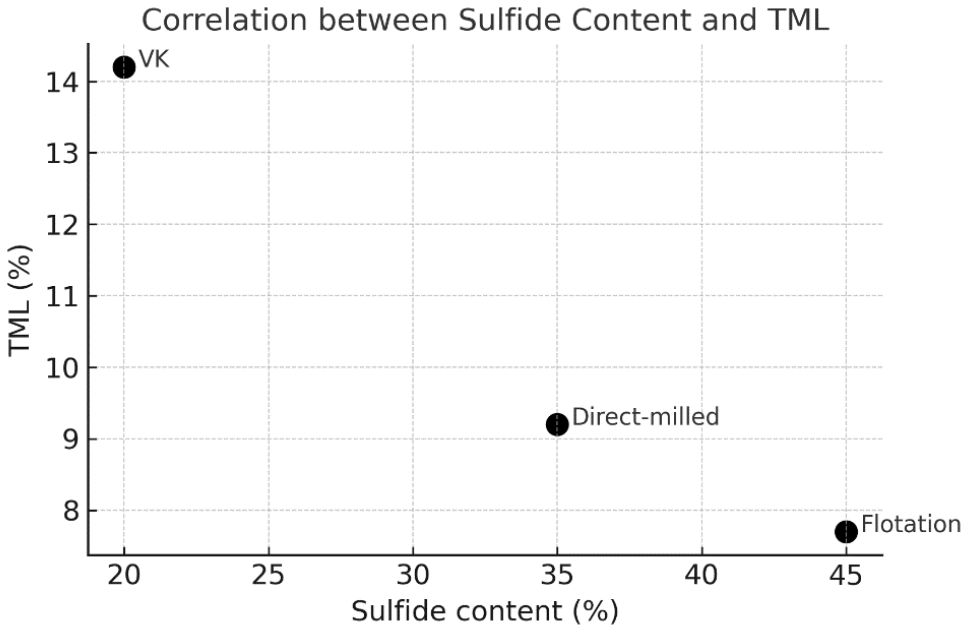

Figure 1. Correlation between sulfide content and TML values for VK, direct-milled, and flotation concentrates.

These findings provided the basis for developing a microstructural hypothesis: that inter-particle correlations, capillary forces, and surface energy effects—rather than granulometry alone—govern the moisture behavior of sulfide concentrates.

6. NEW THEORY: MICROSTRUCTURAL INTERACTIONS

Laboratory results indicate that TML is not simply a function of particle size or water content. Microstructural interactions between fine particles strongly influence the behavior of concentrates.

Aggregates of chalcopyrite and pyrite modify pore structures and capillary effects, reducing TML even for finer fractions.

Surface energy and capillary bridges between particles contribute to water retention in ways not detected by classical methods.

This explains why flotation concentrates, although finer, often display unexpectedly low TML values. Further work should apply SEM imaging, surface energy measurements, and computational modeling to validate these assumptions and improve predictive models [4].

7. CONCLUSION

This study showed that TML determination is shaped by particle size, mineral composition, and especially sulfide content. Experimental results confirmed that VK concentrate has the highest

TML (14.2%), direct-milled intermediate (9.2%), and flotation the lowest (7.7%). Sulfide minerals exert the strongest influence, while granulometry and flotation reagents have only limited effects.

Microstructural interactions—particle correlations, surface energy, and capillary effects—emerged as critical hidden factors. The most promising industrial approach is the addition of surface-active agents into concentrate mixing tanks, as this modifies particle interactions without disrupting current operations [3].

Integrating micro-scale analysis with IMSBC Code testing can improve predictive accuracy, reduce liquefaction risks, and enhance maritime safety.

Collaboration with research institutions is planned to further validate this method, with the goal of enabling industrial application.

ACKNOWLEDGEMENTS

The authors acknowledge Serbia Zijin Mining and partner institutions for support in experimental and analytical work.

REFERENCES

[1] IMO, International Maritime Solid Bulk Cargoes (IMSBC) Code, latest edition.
[2] J. Li, P. Zhang., Miner. Eng., 135 (2019) 25–34.
[3] A.S. Patra., Miner. Eng., 81 (2016) 62–69.
[4] M. Garshasb, R. Saulters., Physical and Mineralogical Impact of Copper Concentrate on Transportable Moisture Limit (TML), Canadian Institute of Mining, Metallurgy and Petroleum, 2019.
[5] IMO, Case studies of maritime accidents caused by cargo liquefaction, IMO Safety Reports.

The 56th International October Conference on Mining and Metallurgy
22-25 October 2025, Bor Lake, Bor, Serbia
www.ioc.tfbor.bg.ac.rs

DOI: 10.5937/IOC25215K *Original scientific paper*

ELECTROSPINNING OF ZNO NANOFIBERS FROM ZINC GALVANIZING FLUE DUST

Klaudia Kundráková[1a], Jana Pirošková[1b], Jakub Klimko[1c], Jarmila Trpčevská [1d], Petra Růžičková [1e], Dušan Oráč [1f]

[1] Institute of Recycling and Environmental Technologies, Faculty of Materials, Metallurgy and Recycling, Technical University of Kosice, Letná 9, 04200 Kosice, Slovakia Republic
[1a] klaudia.kundrakova@tuke.sk, 0009-0009-5393-744X
[1b] jana.piroskova@tuke.sk, 0000-0002-9290-1521
[1c] jakub.klimko@tuke.sk, 0000-0002-5369-4283
[1d] jarmila.trpcevska@tuke.sk, 0000-0002-6413-9066
[1e] petra.ruzickova@tuke.sk, 0009-0008-9542-6042
[1f] dusan.orac@tuke.sk, 0000-0003-0392-8544

Abstract

The research investigates the utilization of zinc galvanizing flue dust as a secondary resource for the preparation of ZnO ceramic nanofibers. The applied methodology combined acidic leaching with electrospinning of the obtained zinc solutions, with emphasis on the effect of leaching agents and waste-derived impurities on fiber morphology. Results revealed that 0.5 M HCl produced coarse oval fibers, whereas 0.5 M H_2SO_4 generated hollow ribbon-like nanostructures with increased surface area. Importantly, the presence of impurities in real waste solutions did not adversely affect fiber formation. The study confirms that electrospinning is a viable and low-waste approach for converting industrial zinc residues into advanced ceramic nanomaterials, providing a sustainable pathway for nanotechnology development.

Keywords*: zinc galvanizing flue dust; electrostatic spinning; ZnO; ceramic nanofibers*

1. INTRODUCTION

Approximately 60 % of global zinc production is used for steel corrosion protection, with hot-dip galvanizing being one of the most important processes [1]. While widely applied, this technology generates significant zinc-rich by-products. Besides bottom and top dross, a fine particulate waste known as zinc galvanizing flue dust is formed [1]. This dust, typically 1–2 μm in size and containing over 20% Zn, originates from the interaction of steel with molten zinc, producing the so-called white smoke [2]. Due to the presence of chlorides and organic residues, it is classified as hazardous waste (KO61) [3]. Industrial-scale treatment of flue dust remains undeveloped. Research has mainly focused on hydrometallurgical methods, investigating leaching in water, HCl, and H_2SO_4 under different conditions [4-8]. Some attempts with pyrometallurgical processing, similar to zinc ash treatment, have also been reported [9].At the same time, electrospinning is emerging as a powerful technique for producing nanofibers with high surface area, porosity, and excellent mechanical–chemical properties. Based on strong electrostatic fields, this process enables fiber formation from liquid precursors and provides a promising route for converting zinc-containing waste into functional ZnO nanomaterials.

1.1 Electrospinning

Electrospinning can be performed by several approaches, including needle-based, needle-free, and rod-assisted techniques, each differing in the way fibers are generated from the polymer solution [10-11]. Needle spinning provides high control and is widely used, while needle-free and rod-based methods enable higher productivity by producing multiple fibers simultaneously. In the

synthesis of ZnO nanofibers, electrospinning is particularly advantageous, as polymer–zinc precursor solutions can be spun into composite fibers and subsequently calcined to remove organic components [12]. This process yields pure ceramic nanofibers with tailored morphology and structural properties [13].

2. MATERIAL AND METHODOLOGY

2.1 Input material

The zinc flue dust sample used in this study was obtained from a Slovak hot-dip galvanizing plant. Prior to analysis, the material was homogenized by particle size adjustment to ensure a representative sample. Elemental composition (Zn, Fe, Al, Cu, Pb) was determined using HRCS AAS, while chloride content was measured by titration. Additional elemental data were obtained by XRF, and the crystalline structure was characterized by XRD. A thermodynamic study was also performed with HSC Chemistry 6.0 to calculate Gibbs free energy changes and construct Eh–pH diagrams [14].

2.2 Leaching and preparation of solutions

For comparison, two feedstocks were used in the leaching experiments – real zinc flue dust and high-purity zinc oxide. Synthetic solutions were prepared by dissolving ZnO (99.6%, Centralchem) in HCl and H_2SO_4 at concentrations of 0.01 M, 0.5 M, and 1 M, targeting a Zn concentration of about 40 g/L. Leaching was carried out at 60 °C for 30 minutes under constant stirring. The same conditions were applied to fine fractions of zinc flue dust, with two liquid-to-solid ratios tested (30:1 and 5:1). After the process, solutions were filtered and subsequently analyzed.

2.3 Electrostatic spinning

Leachates from both synthetic and real sources were used to prepare solutions for electrospinning, containing PVP, ethanol, citric acid, and acetic acid in a weight ratio of 48:6:6:2.6:1. The mixtures were stirred for 48 hours at 25 °C to achieve a homogeneous solution. Electrospinning was performed on a Nanospider™ device using needle-free electrostatic technology at 75–80 kV and an electrode distance of 130–140 mm. The resulting composite fibers were calcined in air at 550–600 °C to remove the polymer matrix. This process yielded ceramic ZnO nanofibers with the desired morphology and chemical properties. Do not put numbers on the pages.

3. RESULTS AND DISCUSSION

AAS analysis revealed that the sample contained 25.33 % Zn and 24.87 % chlorides, while other elements (Al, Fe, Pb, Cu) were present at concentrations below 1 % (see table 1). XRF confirmed the dominant presence of zinc and chlorides, with minor contributions from other elements. X-ray diffraction identified the main zinc-containing phases as complex salts, specifically $(NH_4)_2[ZnCl_4]$ and $[ZnCl_2](NH_3)_2$. Iron was also detected in the form of an ammonium chloride complex, $(NH_4)_3[FeCl_5]$.

Thermodynamic analysis of the Zn–Al–Cl–Fe–H_2O and Zn–Al–Fe–S–H_2O systems at 60 °C confirmed that zinc occurs predominantly as $ZnCl^+$ within the water stability region, up to pH ~ 5 in HCl and up to pH ~ 4.3 in H_2SO_4. Experimental results further indicated that 0.5 M HCl and 0.5 M H_2SO_4 solutions are the most suitable for ZnO nanofiber fabrication.

Table 1. *Chemical composition of zinc galvanizing flue dust*

Sample	**Zn [%]**	**Fe [%]**	**Al [%]**	**Cu [%]**	**Pb [%]**	**Cl^- [%]**	**Residual [%]**
Average	25.33	0.38	0.91	0.006	0.09	24.87	48.41
S	0.46	0.01	0.14	0.0008	0.06	2.07	-
RSD	1.81	2.63	650	750	150	8.32	-

S- Standard deviation
RSD- Relative standard deviation

Figure 1a shows precursor fibers obtained from the real solution (0.5 M HCl), characterized by oval morphology with diameters between 100 and 400 nm. After calcination at 550 °C (Figure 1b), the fibers preserved their fibrous shape but exhibited slight shrinkage. A detailed view in Figure 1c highlights their morphology, displaying a textured and mildly porous surface. At 600 °C (Figure 1d), the fibers retained their structure after complete carbon removal, confirming their thermal stability.

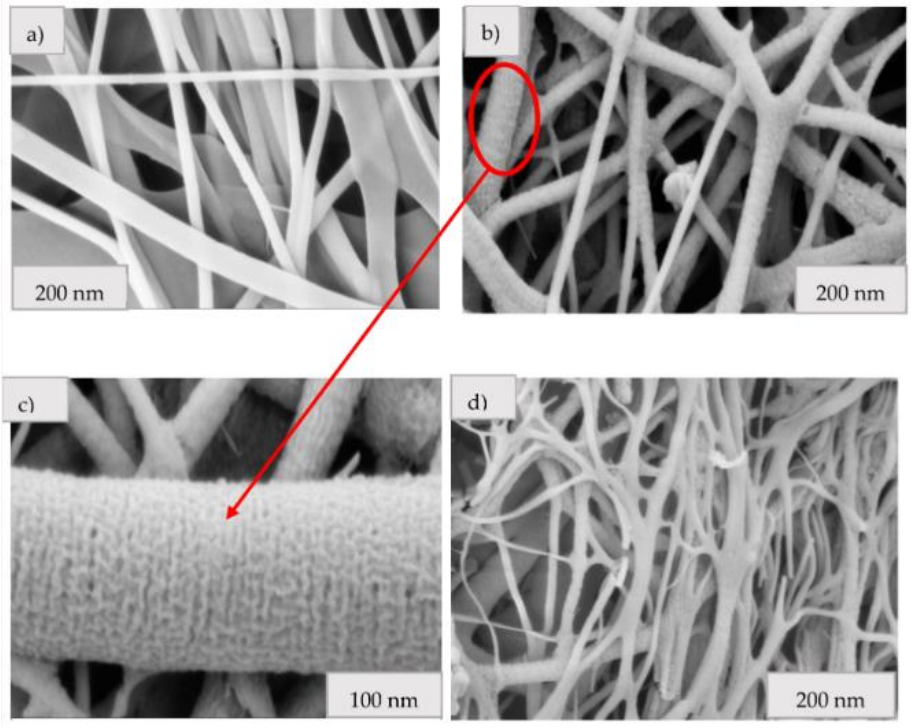

Figure 1. SEM images of (a) precursor fibers 0.5 M HCl, (b) ceramic fiber 0.5 M HCl at the temperature of 550 °C, (c) fiber morphology, (d) ceramic fibers 0.5 M HCl at 600 °C

In Figure 2a, precursor fibers from the real solution of 0.5 M H_2SO_4 are shown. The precursor fibers are very fine, with a thickness of less than 100 nm. Figure 2b shows ceramic nanofibers after calcination at 550 °C, which are highly structured and porous. Figure 2c shows ceramic fibers after calcination at 600 °C, which have a structured surface composed of fine ZnO layers. The detail in Figure 2d highlights the hollow structure of the fibers.

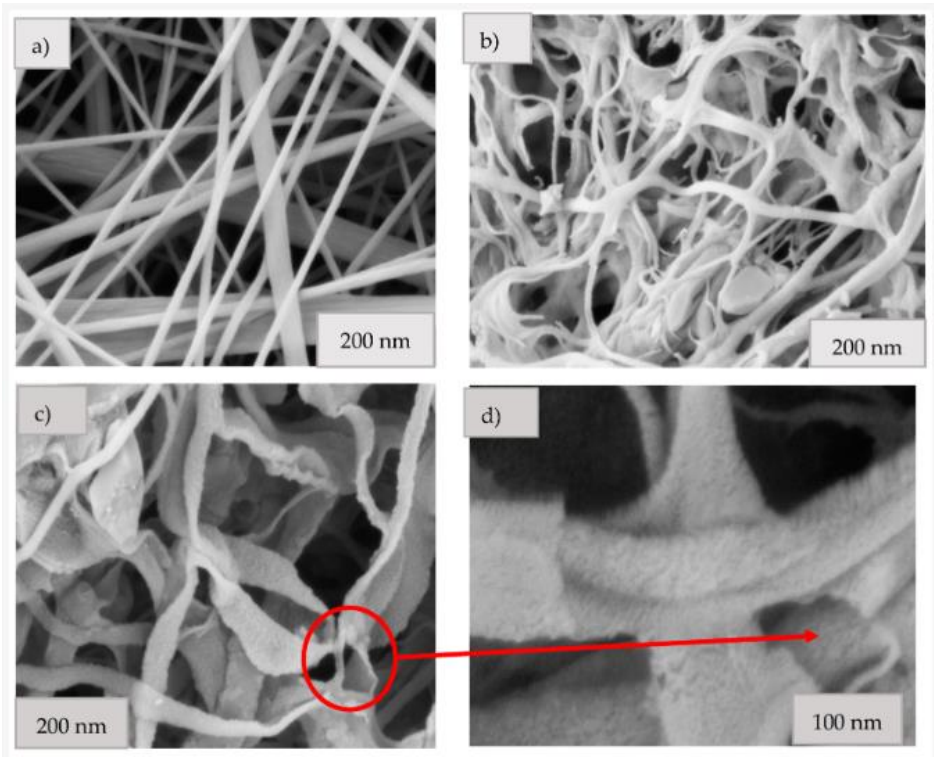

Figure 2. SEM images of (a) precursor fibers 0.5 M H_2SO_4, (b) ceramic fibers 0.5 M H_2SO_4 at the temperature of 550 °C, (c) ceramic fibers 0.5 M H_2SO_4 at the temperature of 600 °C, (d) fiber morphology

3.1 Structural and Morphological Comparison of ZnO Fibers from Synthetic vs. Real Solutions

For the purpose of comparison, ceramic nanofibers obtained from both synthetic and real solutions prepared with 0.5 M HCl and 0.5 M H_2SO_4 were investigated. The results demonstrate that ZnO ceramic nanofibers derived from these conditions exhibit comparable structural characteristics (Figures 3-4), confirming the suitability of the selected acid concentrations for their fabrication. Specifically, nanofibers synthesized using 0.5 M HCl predominantly display oval morphologies with irregular and rough surfaces, whereas the application of 0.5 M H_2SO_4 leads to the formation of hollow ribbon-like fibers, which are expected to provide an increased specific surface area. Complementary XRD analysis verified the presence of the principal crystalline zinc phases (Figure 5), thereby substantiating the successful formation of ZnO nanostructures.

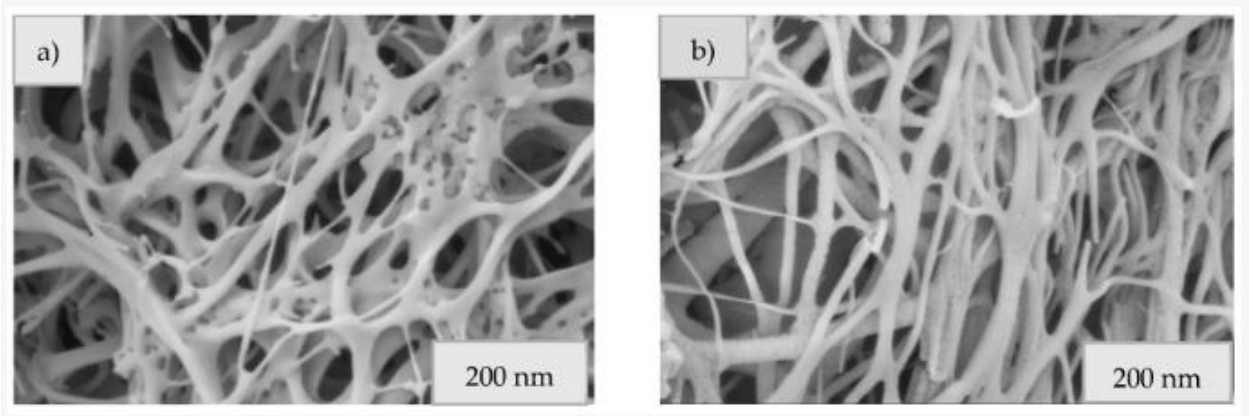

Figure 3. Images of (a) ceramic fibers from synthetic solution of 0.5 M HCl at 600 °C and (b) ceramic fibers from real solution of 0.5 M HCl at 600 °C.

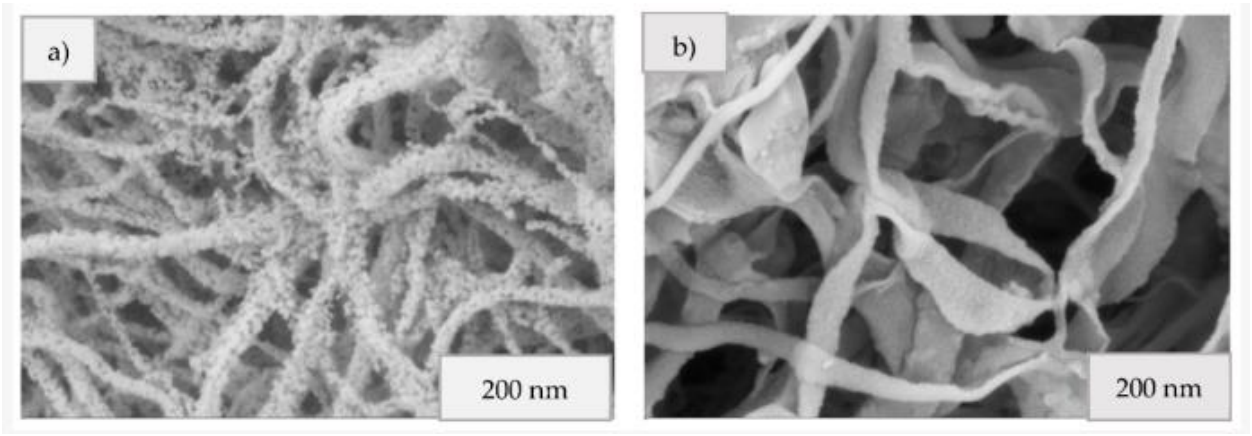

Figure 4. Images of (a) ceramic fibers from synthetic solution of 0.5 M H_2SO_4 at 600 °C and (b) ceramic fibers from real solution of 0.5 M H_2SO_4 at 600 °C.

Complementary XRD analysis verified the presence of the principal crystalline zinc phases (Figure 5), thereby substantiating the successful formation of ZnO nanostructures.

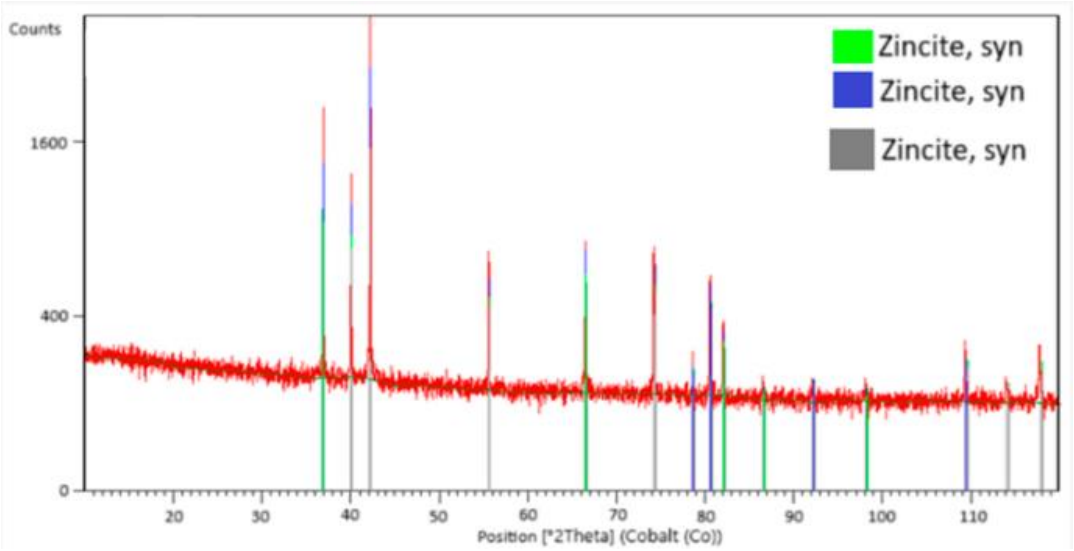

Figure 5. XRD analysis of ceramic nanofibers from the real 0.5 M H_2SO_4 solution.

4. CONCLUSION

This study explores the hydrometallurgical processing of zinc galvanizing flue dust for the fabrication of ceramic ZnO nanofibers. The experiments demonstrated that electrospinning is a reliable method, and the use of flue dust did not compromise nanofiber quality compared to synthetic precursors. The resulting fibers showed comparable morphology and properties, confirming the feasibility of this approach. In addition to reducing waste disposal and associated costs, the method provides an environmentally sustainable route for resource recovery. These findings highlight the potential for industrial application of the process. Overall, the work contributes to innovation in nanotechnology and sustainable waste management.

ACKNOWLEDGEMENTS

This work was supported by the Slovak Research and Development Agency under contract no. APVV-23-0055.

REFERENCES

[1] J. Trpčevská, Odpady zinku a ich spracovanie, Košice: TU, lectures.
[2] P.Maaß, P. Peißker, Handbook of Hot-Dip Galvanization; 2000,p.123
[3] Odpady-portal.sk, Katalóg odpadov 365/2015,[online], Dostupné na internete: <https://www.odpady-portal.sk/Dokument/100124/katalog-odpadov.aspx>.
[4] L. Rahman et al., IOSR-JAC, 2017, p. 21–26.
[5] F. Bisol., Process for Treating Metallic Dust, Mostly Oxididised Waste, in Particular Galvanising Dust and/or Steel works Smoke, EP0935005 A1, 24 April 2002.
[6] G. Thorsen. Et al., JOM, 1981, p. 24–29.
[7] Pirošková., Metals, (2022) 1-11.
[8] Pirošková et al., Metals, (2024) 1-14.
[9] M.A. Barakat., JOM (2003) 26–29.
[10] D. Lukáš, A. Sarkar, L. Martinová, K. Vodsed'álková, D. Lubasová, J. Chaloupek, P. Pokorný, P. Mikeš, J. Chvojka, M. Komárek, Text. Prog. 41 (2009) 59–140.
[11] M. Ahmadi Bonakdar, D. Rodrigue, Macromol. 4 (2024) 58–103.
[12] R. CeCe, L. Jining, M. Islam, J.G. Korvink, B. Sharma, Adv. Eng. Mater. 26 (2024) 2301297.
[13] M. Zhang, W. Song, Y. Tang, X. Xu, Y. Huang, D. Yu, Polymers 14 (2024) 351.
[14] A. Roine, HSC Chemistry® [Software] 2021.

The 56th International October Conference on Mining and Metallurgy
22-25 October 2025, Bor Lake, Bor, Serbia
www.ioc.tfbor.bg.ac.rs

DOI: 10.5937/IOC25221M *Original scientific paper*

LEACHING OF COVELLITE IN IONIC LIQUID SOLUTION

Dragana Marilović[1a], Grozdanka Bogdanović[1b]

[1] Technical Faculty Bor, University of Belgrade, V.J. 12, 19210 Bor, Serbia
[1a] dmarilovic@tfbor.bg.ac.rs, 0000-0001-8301-750X
[1b] gbogdanovic@tfbor.bg.ac.rs, 0000-0002-1013-4075

Abstract
Covellite is refractory to conventional hydrometallurgical processes, therefore alternative methods are required to improve copper extraction. The aim of this work was to investigate the leaching of covellite concentrate in an ionic liquid solution ([bmim]HSO_4) with hydrogen peroxide as a strong oxidizing agent. The results indicate that the presence of hydrogen peroxide significantly improves copper extraction due to its strong oxidizing ability, which facilitates the dissolution of sulfide species. Although only preliminary data are presented, the results confirm the potential of ionic liquids in combination with oxidizing agents for the treatment of copper sulfide concentrates. When covellite concentrate was leached in an ionic liquid solution without oxidants, the leaching degree of copper was 1.03 %. The results showed that the maximum dissolution of copper in the presence of 3.0 mol/dm^3 hydrogen peroxide was 28.97 %. This approach provides a basis for the development of more environmentally friendly and efficient leaching processes for complex copper ores and concentrates.

***Keywords**: Covellite, Ionic liquid, Hydrogen peroxide, Leaching.*

1. INTRODUCTION

Copper is obtained by pyrometallurgical processing of high-grade sulfide ores, whereby the metal is extracted by smelting and refining. Conventional pyrometallurgical copper extraction processes require high temperatures and emit significant amounts of harmful gasses, making them environmentally and economically unfavorable. Hydrometallurgical processes represent an alternative that enables lower energy costs and less environmental impact. This has led to increased interest in the extraction of copper from low-grade sulfide ores in aqueous solution, where secondary copper sulfides being recognized as an important resource. [1-3]

The most common secondary copper mineral in nature is Covellite (CuS). It is classified as an intermediate product made during the oxidation process of chalcocite (Cu_2S) and other complex copper sulfide minerals. Covellite is more stable during oxidation in the presence of sulfur then other copper sulfide minerals. In addition, during the leaching in strongly acidic medium, elementary sulfur may formed passivation layer and block the surface from contact with solution. [4]

Research shows that covellite is leached in different media such as ammonia [5], nitrates [6], chlorides [7-8] and bioleaching [9-10]. Most of the previous studies focused on the dissolution of pure mineral phases or synthetic samples [11-12]. However, in industrial conditions, copper is not obtained from individual minerals, but from ores containing various mineral components, including oxides, sulfides and gangues. Ionic liquids represent a new class of solvents characterized by low vapor pressure, chemical and thermal stability and reusability [13]. Their use in hydrometallurgy has increased significantly in recent years. Numerous studies have shown that ionic liquids can increase the effectiveness of sulfide dissolution, especially in combination with oxidizing agents [14,15]. Dong et al. [14] have shown that Brønsted acid ionic liquids can effectively dissolve chalcopyrite, while Aguirre et al. [15] finds that imidazolium ionic liquids achieve significantly higher extraction in the presence of chloride ions.

In this work, as-received covellite concentrate, obtained from an industrial plant, was used without additional treatment. The results of copper concentrate leaching with the ionic liquid 1-butyl-3-

methyl imidazolium hydrogen sulfate ([bmim]HSO_4) in the absence and presence of hydrogen peroxide (H_2O_2) are presented.

2. EXPERIMENTAL

For the purposes of this research, a sample obtained from the flotation process plant of Serbia Zijin Mining d.o.o. Bor was used. After collection, the sample was dried at room temperature, homogenized, and prepared for further analysis and experiments. The main elements present in the concentrate are copper and iron. Table 1 shows the chemical composition of the sample:

Table 1. Chemical composition of the copper concentrate

Element	Cu	Fe	Zn	Pb	S	SiO_2	CaO	MgO
%	15.17	25.34	0.07	0.02	36.72	8.87	0.52	0.03

X-ray diffraction analysis was used to determine the phase composition of the samples. The samples were analyzed with a PHILIPS X-ray diffractometer PV-1820/1710 (Cu Kα radiation 0.154178 nm; 40 kV; 30 mA).

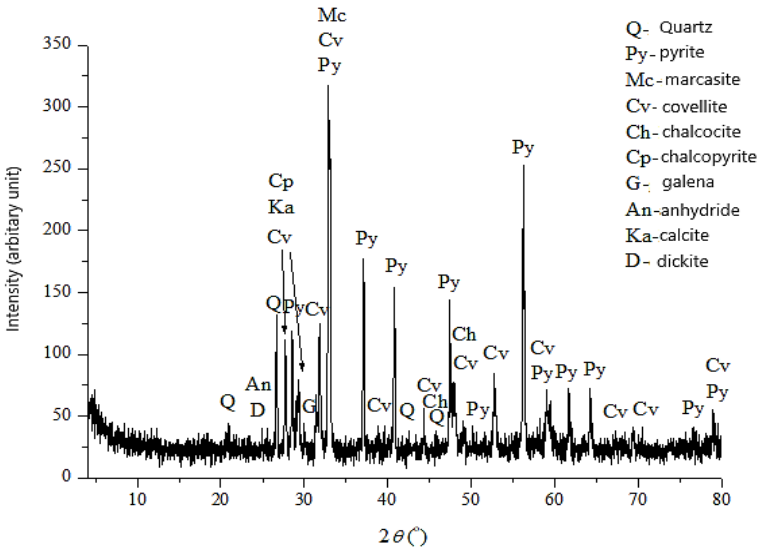

Figure 1. X-ray diffraction pattern of initial covellite concentrate

Figure 1 shows that the predominant sulfide minerals are pyrite and covellite. Marcasite, chalcocite, chalcopyrite and galena were also identified in the analyzed sample, but they are present in significantly smaller amounts. The presence of gangue minerals such as quartz, anhydrite, calcite and dickite was also observed.

2.1 Experimental procedure

The leaching experiments were carried out in 600 cm^3 glass reactor with 100 cm^3 leaching solution and 1 g of solid sample. The magnetic stirrer was used and stirring speed was set up to 600 rpm for all experiments. Ionic liquid solution ([bmim]HSO_4 concentration of 0.5 mol/dm^3 was prepared and used as a leaching reagent. In the experiments where the oxidizing agent was used, hydrogen peroxide was added to the solution at a certain concentration (0.5-3.0 mol/dm^3).
After the leaching time of 120 min, 1 cm^3 of the solution was taken and diluted to 50 cm^3 in a volumetric flask. The concentration of copper in the diluted samples was determined using optical

emission spectrometer with inductively coupled plasma (ICP-OES Optima 8300; Perkin Elmer) and a multiparameter photometer Hanna (HI 83200).

3. RESULTS AND DISCUSSION

Table 2 and Figure 2 show the results of the copper concentrate leaching at a concentration of 0.5 mol/ dm^3 ionic liquid solution ([bmim]HSO_4) without oxidizing agent and in the presence of hydrogen peroxide (H_2O_2)concentration 0.5-3.0 mol/dm^3.

Table 2. Effect of different leaching solutions on copper leaching degree from covellite concentrate after 120 minutes of leaching

Leaching conditions	[bmim]HSO_4 concentration (mol/dm^3)	H_2O_2 concentration (mol/dm^3)	Copper leaching degree (%)
[bmim]HSO_4	0.5	/	1.03
[bmim]HSO_4 + H_2O_2	0.5	0.5	11.70
		1.0	12.72
		2.0	20.67
		3.0	28.97

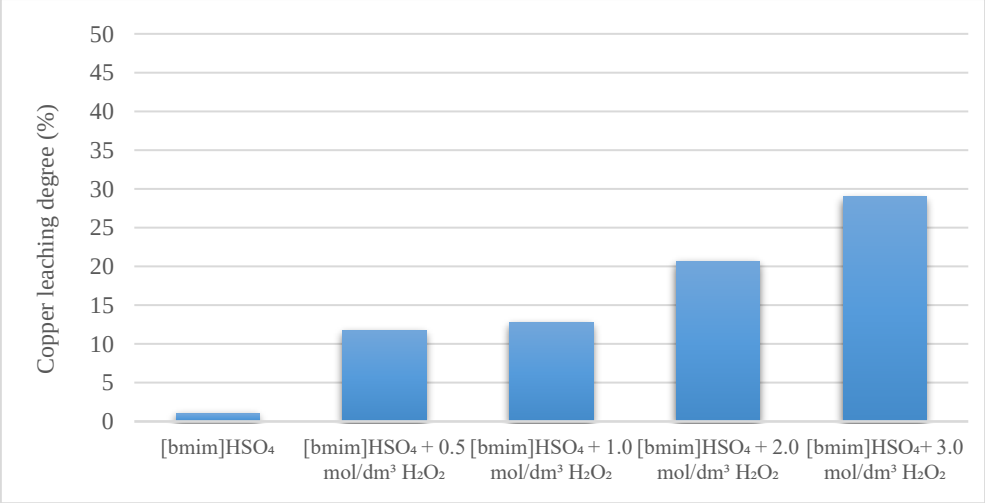

Figure 2. Influence of H_2O_2 concentration on copper extraction from covellite concentrate in ionic liquid solution

Leaching of the copper concentrate with an ionic liquid solution without hydrogen peroxide was less efficient than leaching in the presence of the oxidising agent. The results indicate that the ionic liquid [bmim]HSO_4 solution without oxidising agent is not sufficient for the effective dissolution of covellite, according to the very low copper extraction efficiency (1.03 %) after 120 minutes of reaction time. Previous studies [4] have shown that covellite is difficult to dissolve in acidic media without an oxidising agent, mainly due to the formation of a passive layer of elemental sulfur on the surface of the mineral, which prevents further leaching. The addition of H_2O_2 significantly increases the leaching efficiency.

The addition of 0.5 mol/dm^3 H_2O_2 resulted in an increased copper leaching degree (up to 11.70 %) after 120 minutes of processing time, while only a slight increased occurred at a 1.0 mol/dm^3 H_2O_2 (12.72 %). With a higher concentration of oxidising agent up to 2.0 mol/dm^3 the copper leaching degree significantly enhanced to 20.67%. The copper leaching degree increased to 28.97 % with increasing concentration of the oxidising agent up to 3.0 mol/dm^3. These results show that the presence of an oxidising agent plays a crucial role in the extraction of copper ions in solution. The previous studies [3, 7] shows that the dissolution of covellite and other secondary sulfides is limited in the absence of oxidising agents, while the addition of oxidising agents (H_2O_2, Fe^{3+}, NaClO or O_2) significantly accelerates the process.

The results confirm that the ionic liquid solution in combination with hydrogen peroxide can be a promising approach for hydrometallurgical processing of covellite. However, these data were obtained for a single time point (120 min). For a complete kinetic analysis of the process, the dissolution dynamics as a function of time should be investigated.

4. CONCLUSION

Leaching experiments were done to dissolve the copper from the covellite concentrate. The results show that the application of the ionic liquid solution ([bmim]HSO_4) in the presence of hydrogen peroxide (H_2O_2) has a potential for efficient leaching of copper from covellite. The addition of hydrogen peroxide improves the leaching efficiency, with the highest copper leaching degree (28.97%) achieved at 0.5 mol/dm^3 [bmim]HSO_4 and 3.0 mol/dm^3 H_2O_2. The copper leaching efficiency in the presence of 0.5 mol/dm^3 [bmim]HSO_4 without oxidizing agent was 1.03 %. These data indicate the role and importance of the oxidising agent in the oxidation of sulfide minerals.

ACKNOWLEDGEMENTS

The authors are grateful to the Ministry of Education, Technological development, and Innovations of the Republic of Serbia for financial support, within the funding of the scientific research at the University of Belgrade – Technical Faculty in Bor (No. 451-03-137/2025-03/ 200131).

REFERENCES

[1] Q. Yin, D.J. Vaughan, K.E.R. England, G.H. Kelsall., J. Coll. Int. Sci., 166 (1994)133–142.
[2] O. Salmani Nuri, E. Allahkarami, M. Irannajad, A. Abdollahzadeh., Geosyst. Eng., 20 (2017) 41–50.
[3] W.D. Xing, M.S. Lee., Geosyst. Eng., 20 (2017) 216–223.
[4] L. Jaeryeong, K. Suyun, K. Byoungjin, L. Jae-chun., Metall., 8 (2018) 150.
[5] A.A. Baba, A.F. Balogun, D.T. Olaoluwa, R.B. Bale, F.A. Adekola, A.G.F. Alabi., Korean J. Chem. Eng., 34 (2017) 1133–1140.
[6] R.Ž. Vračar, N. Vučković, Ž. Kamberović., Hydrometall., 70 (2003) 143–151.
[7] M. Nicol, P. Basson., Hydrometall., 172 (2017) 60–68.
[8] H. Miki, M. Nicol, L. Velásquez-Yévenes, Hydrometall., 105 (2011) 321–327.
[9] L. Falco, Pogliani C., Curutchet G., Donati E., Hydrometall., 71 (2003) 31–36.
[10] J. Lee, S. Acar, D.L. Doerr, J.A. Brierley, Hydrometall., 105 (2011) 213–221.
[11] J. Lee, S. Kim, B. Kim, J-C. Lee, Metall., 8 (3) (2018) 150.
[12] K. Pérez, N. Toro, M. Saldaña, E. Salinas-Rodríguez, P. Robles, D. Torres, R.I. Jeldres, Metall., 10(4) (2020) 477.
[13] M.A. Alreshidi et al., Mater. Tod. Sus. 31 (2025) 101160.
[14] T. Dong, Y. Hua, Q. Zhang, D. Zhou, Hydrometallurgy 99 (2009) 33–38.
[15] C.L. Aguirre, N. Toro, N. Carvajal, H. Watling, C. Aguirre, Min. Eng. 99 (2016) 60–66.

The 56th International October Conference on Mining and Metallurgy
22-25 October 2025, Bor Lake, Bor, Serbia
www.ioc.tfbor.bg.ac.rs

DOI: 10.5937/IOC25225K *Original scientific paper*

ANALYTICAL STUDY OF ZINC RECOVERY FROM SPENT SOLUTIONS RESULTING AFTER GALVANIZATION PROCESS

Nadezhda Kazakova[1a], Vladislava Stefanova[1b], Petar Iliev[1c], Biserka Lucheva[1d]

[1]Metalurgy and Materials Science Faculty, University of Chemical Technology and Metallurgy, Sofia, 1756, Bulgaria

[1a] n_kazakova@uctm.edu, 0009-0001-4096-1776
[1b] vps@uctm.edu, 0009-0008-3304-0638
[1c] pkiliev@uctm.edu, 0009-0000-2311-0972
[1d] plasma@uctm.edu, 0000-0002-7502-5646

Abstract

Galvanization is a widely employed process in metallurgical practice for the protection of steel products against corrosion. The spent, hydrochloric acid solutions generated from this process contain considerable amounts of valuable metals, such as zinc (40–60 g/L) and manganese (1–2 g/L). The recovery of these metals is not only economically advantageous but also environmentally sustainable. The fundamental difficulty in the treatment of such solutions lies in their high acidity and the high concentration of iron (160–190 g/L).

Based on a comprehensive literature review, the following scheme can be proposed for the recovery of zinc in the form of zinc sulfate. The processes include removal of iron through precipitation as iron hydroxide; the precipitation of zinc and manganese hydroxides; dissolution of these precipitates in sulfuric acid to generate a sulfate solution.

The objective of the present study is to carry out a detailed thermodynamic evaluation of the possible chemical interactions at each stage using the HSC Chemistry software, version 10.5, specifically the modules: Reaction Equations and Eh–pH Diagrams.

***Keywords**: Thermodynamic; Galvanic waste solutions; Iron removal, Zinc and manganese recovery.*

1. INTRODUCTION

Worldwide, more than 50 % of zinc is used for galvanizing each year. Due to the high consumption of zinc, ore reserves of this metal are decreasing [1]. This necessitates the recovery of zinc from secondary products, including the recycling of waste solutions from hot-dip galvanizing facilities. They represent hazardous waste due to the high concentration of heavy non-ferrous metals (mainly zinc and manganese) and the high concentration of hydrochloric acid. The concentration of zinc in the spent solutions may reach up to 130 g/L, that of iron up to 190 g/L, and of hydrochloric acid up to 10% [2,3].

Typical methods for the treatment of these solutions include precipitation with alkaline reagents, most often with $Ca(OH)_2$. As a result, large amounts of precipitates containing iron, calcium, and relatively low zinc content (<20 %) are formed. Alternative methods for separating iron from zinc include ion exchange, solvent extraction and chemical precipitation [4,5].

The present work proposes an analytical study of the processes of separation of iron from zinc and manganese based on chemical interactions in the multi-component systems: Fe-Zn-Mn-Ca-Cl-H_2O; Zn-Cl-Mn-Na-H_2O and Zn-Mn-S-H_2O. Combined Eh-pH diagrams for each system gives visual information about the existence of ionic and non-ionic forms of the substances as a function of redox potential (Eh) and pH at given temperature.

2. THERMODYNAMICAL ANALYSIS

The analytical study was focused on the three multicomponent water systems: **Fe-Zn-Mn-Ca-Cl-H_2O**, **Zn-Cl-Mn-Na-H_2O** и **Zn-Mn-S-H_2**O. The thermodynamic estimation of possible chemical interactions in the three studied systems was made based on the calculated values of the free Gibbs energy and the equilibrium constant. The calculations were made using the professional software program HSC Chemistry, ver. 10.5, module Equation Reaction.

Combined Eh-pH diagrams were calculated for the following waste solution, in g/L: 165 Fe, 43 Zn, 1.5 Mn and 75 HCl. The quantities of: $Ca(OH)_2$, NaOH and H_2SO_4 were determined based on chemical reactions. For the calculation of the Eh-pH diagrams relevant elements in mol/kg_{H2O} (Table 1) and types of ionic and non-ionic species are given in Table 1 and 2 respectively.

Table 1. Concentrations of elements used in calculation of diagrams in mol/kg_{H2O}

	Fe	Zn	Mn	Ca	Cl	Na	S
Stage I	2.95	0.66	0.03	4.67	7.97	-	-
Stage II	-	0.66	0.03	-	-	0.68	-
Stage III	-	0.66	0.03	-	-	-	0.68

Table 2. Type of ionic and nonionic forms in the investigated systems and theirs free Gibbs energy of formation at T = 25 ºC and T = 60 ºC

Species	ΔG, kJ/mol		Species	ΔG, kJ/mol		Species	ΔG, kJ/mol	
	T = 25 ºC	T = 60 ºC		T = 25 ºC	T = 60 ºC		T = 25 ºC	T = 60 ºC
Fe			**Zn**			**Ca**		
Fe(+2a)	-91.52	-91.36	**Zn(+2a)**	-147.25	-146.50	**Ca(+2a)**	-552.80	-553.89
Fe(+3a)	-17.18	-13.28	**$Zn(OH)_2$**	-555.92	-545.39	**$CaCl_2$**	-748.78	-743.34
Fe_3O_4	-1012.3	-1000.28	**ZnCl(+a)**	-279.65	-280.05	**CaCl(+a)**	-684.89	-682.56
$Fe(OH)_2$	-486.97	-477.36	**ZnCl3(-a)**	-531.56	-519.91	**$Ca(OH)_2$**	-898.24	-887.96
$Fe(OH)_3$	-703.28	-688.38	**ZnCl4(-2a)**	-669.94	-655.59			
FeCl(+2a)	-156.89	-150.35	**Cl**					
Mn			**Cl(-a)**	-131.26	-126.76	**S**		
Mn(+2a)	-229.97	-231.06	**ClO_4(-a)**	-7.89	-6.41	**H_2S(a)**	-115.66	-111.25
Mn2O3	-880.97	-871.84	**Na**			**HS(-a)**	52.07	67.20
Mn3O4	-1281.2	-1269.2	**Na(+a)**	-261.90	-264.49	**HSO_4(-a)**	-3161.74	3096.36
MnCl(+a)	-360.95	-360.10	**NaOH(a)**	-379.65	-374.24	**SO_4(-2a)**	-3115.90	3031.85
Mn(OH)2	-617.68	-608.18	**NaCl(a)**	-384.07	-380.91			

3. RESULTS AND DISCUSSION

Table 3 shows the calculated values of the Gibbs energy and equilibrium constants for the three systems at two temperatures: 25ºC и 60 ºC.

It can be shown that in stage-I, the most thermodynamically possible reaction is precipitation of iron as $Fe(OH)_3$ in the presence of oxygen. The second reaction is of hydrochloric acid with $Ca(OH)_2$. From the other reactions only the reaction of $MnCl_2$ with $Ca(OH)_2$ is almost thermodynamically impossible. At the neutralization with NaOH (stage-II), the most thermodynamically possible reaction is precipitation of zinc as $Zn(OH)_2$. In the third stage (stage III), gypsum will be formed followed by the reactions of the formation of zinc and manganese sulfate.

Combined Eh-pH diagrams of the system **Fe-Zn-Mn-Ca-Cl-H_2O are shown on the Figure 1 and 2**

Table 3. Computed values of the free Gibbs energy and equilibrium constant of the possible chemical interactions during each stage of separation of the metals

Reactions	T = 25ºC		T = 60ºC	
	ΔG, kJ/mol	LogKp	ΔG, kJ/mol	LogKp
I-stage Neutralization with calcium hydroxide				
$2HCl(a) + Ca(OH)_2 = CaCl_2(a) + 2H_2O$	-133.27	23.35	-135.10	21.18
$FeCl_2(a)+Ca(OH)_2=Fe(OH)_2+CaCl_2(a)$	-92.98	16.29	-87.75	13.76
$4FeCl_2(a)+4Ca(OH)_2+O_2(g)+2H_2O=4Fe(OH)_3+4CaCl_2(a)$	-190.72	33.42	-183.03	28.67
$ZnCl_2(a) + Ca(OH)_2 = Zn(OH)_2 + CaCl_2(a)$	-58.14	10.19	-54.79	8.59
$MnCl_2 + Ca(OH)_2 = Mn(OH)_2 + CaCl_2$	-27.81	4.87	-27.92	4.38
II-stage Neutralization with sodium hydroxide				
$ZnCl_2 + 2NaOH = Zn(OH)_2+2NaCI$	-81.85	14.27	-82.54	12.94
$MnCl_2 + 2NaOH = Mn(OH)_2 +2NaCl$	-59.49	10.42	-61.74	9.68
$CaCl_2 + 2NaOH = Ca(OH)_2 + 2NaCl$	-14.15	2.48	-17.76	2.78
III-stage Resulting of $ZnSO_4.7H_2O$ and MnO_2				
$Zn(OH)_2 + H_2SO_4 + 5\ H_2O = ZnSO_4.7H_2O$	-131.77	23.09	-124.53	19.53
$Mn(OH)_2 + H_2SO_4 = MnSO_4 + 2H_2O$	-123.85	21.70	-123.86	19.42
$Ca(OH)_2 + H_2SO_4 = CaSO_4.2H_2O$	-208.96	36.61	-207.27	32.50

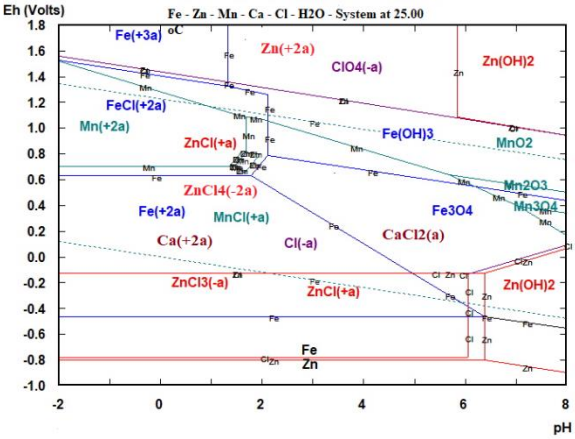

Figure 1 - Combined Eh-PH diagram of the system Fe-Zn-Mn-Cl-H_2O

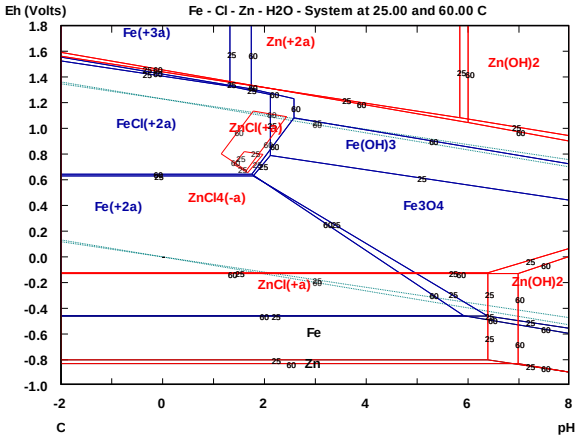

Figure 2 - Impact of the temperature on the stability regions of ionic and non-ionic species in the system Fe-Cl-Zn-H_2O.

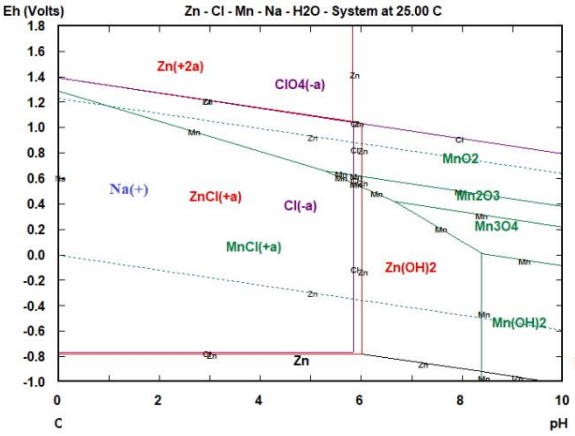

Figure 3 - Combined Eh-PH diagram of the system Zn-Cl-Mn-Na-H_2O

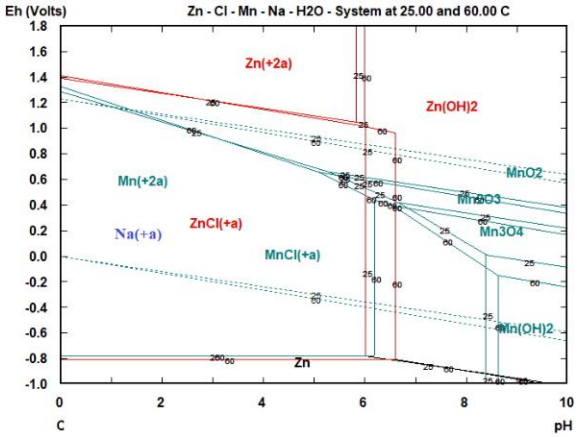

Figure 4 - Impact of the temperature on the stability regions of ionic and non-ionic species in the system Zn-Cl-Mn-Na-H_2O

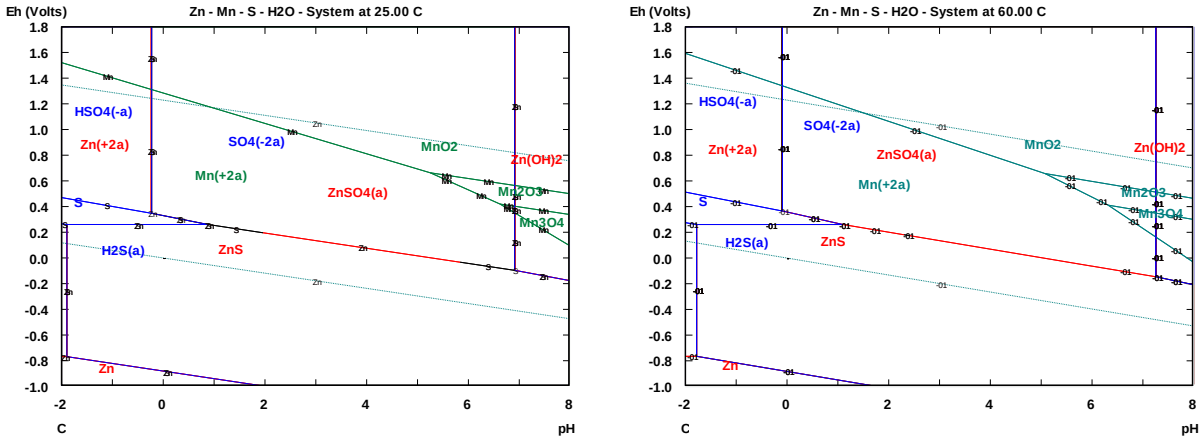

Figure 5 - Combined Eh-pH diagram of the system Zn-Mn-S-H_2O at temperature 25°C and 60°C

In the first system (Figure 1) Fe^{2+} ions present in solution are oxidized to Fe^{3+} under controlled conditions (Eh > 1.3V), leading to hydrolysis and subsequent precipitation as amorphous $Fe(OH)_3$ (pH > 1.8). Effect of the temperature on the stability of ionic and non-ionic forms is insignificant. In the system, **Zn-Cl-Mn-Na-H_2O,** the focus shifts to the **selective precipitation of zinc and manganese hydroxides (Figures 3 and 4). It can be shown that $Zn(OH)_2$ and $Mn(OH)_2$ are precipitated at pH > 6 and > 8.5 respectively and relatively low potential of the systems.** An increase of temperature reduces the area of stability of the formed hydroxides. The third system, **Zn-Mn-S-H_2O (Figure 5),** describes the final stage, involving the **formation of $ZnSO_4$ and $MnSO_4$** sulfates. Manganese can be removed from solution by oxidation with peroxide to insoluble MnO_2.

4. CONCLUSIONS

Based on the thermodynamic analysis and computed of combined Eh-pH diagrams it has been established that iron removal in the form $Fe(OH)_3$ is thermodynamically possible at high oxidation potential and pH > 2 with using of $Ca(OH)_2$. From the resulting filtrate zinc and manganese are precipitated with NaOH, selectively in the form of hydroxides at pH above 6 and 8 respectively. Further, resulting precipitations are dissolved in sulfuric acid. The processes are thermodynamically possible and with an increase of the temperature, an expansion of the stability of zinc sulfate is observed. Manganese can be removed in the form of MnO_2 at a higher oxidation potential.

ACKNOWLEDGEMENTS

This study was supported by the research project № 403-32 Research of the zinc extraction process from used hydrochloride solutions obtained after the galvanization process.

REFERENCES

[1] European Commission, CRM List 2020. https://rmis.jrc.ec.europa.eu/?page=crm-list-2020-e294f6
[2] J. Pirošková , J. Klimko, J. Trpčevská , M. Laubertová, P. Liptai, T. Vindt, D. Oráč, Metals, 12 (2022) 744.
[3] S.B. Zueva, F. Ferella, V. Innocenzi, I. De Michelis, V. Corradini, N. M. Ippolito, F. Veglio, MDPI, Sustainability, 13 (2021) 407.
[4] P.L. Ferro, S. Vocciante, Chem. Eng. J., 341 (2018) 539–546.
[5] M. Regel-Rosocka, A. Cieszyñska, M. Wiœniewski, Pol. J. Chem. Technol., 9 (2) (2007) 42-45.

The 56th International October Conference on Mining and Metallurgy
22-25 October 2025, Bor Lake, Bor, Serbia
www.ioc.tfbor.bg.ac.rs

DOI: 10.5937/IOC25229B *Original scientific paper*

INFLUENCE OF HIDDEN NEURON NUMBER ON THE PERFORMANCE OF ANN MODELS APPLIED TO DEINKING FLOTATION DATA

Katarina Balanović[1a], Maja Trumić[1b], Tamara Gavrilović[2a]

[1] Technical Faculty in Bor, University of Belgrade, V.J. 12, 19210 Bor, Serbia
[2] Faculty of Technical Sciences, University of Pristina, Knjaza Miloša 7, 38220 Kosovska Mitrovica, Serbia
[1a] kbalanovic@tfbor.bg.ac.rs, 0000-0002-2197-5718
[1b] majatrumic@tfbor.bg.ac.rs, 0000-0001-9361-4412
[2a] tamara.gavrilovic@pr.ac.rs, 0000-0003-3448-7753

Abstract
In this paper, the influence of the optimal number of neurons in an artificial neural network model, applied to data obtained from deinking flotation is presented and analyzed. The results indicate that when a well-performing model is selected, it is not necessary to search for the optimal number of hidden neurons. However, when the applied model does not yield satisfactory results, determining the optimal number of neurons becomes essential.

***Keywords**: Artificial neural networks, Hidden neurons, Flotation, Deinking.*

1. INTRODUCTION

Artificial intelligence is one of the fastest-developing fields in computer science in recent decades [1]. It represents a discipline within computer science dedicated to creating programs that allow machines to act and make decisions in ways that resemble intelligent behavior. In this context, intelligent thinking refers to the capacity to reason and respond appropriately to new, previously unknown situations [2]. Machine learning is a subfield of artificial intelligence concerned with developing programs that can learn from previously collected data. Once a solution to a problem is identified, the program is able to store this knowledge and apply it to similar situations. Machine learning is generally categorized into three main types: supervised learning, unsupervised learning, and reinforcement learning [3]. In supervised learning, the program is provided with a set of input data (x_1, x_2, …, x_n) along with the corresponding desired output values, where each input x_i is associated with the correct output y_i. The goal of the program is to learn how to correctly predict the output value for new, unseen input data. Algorithms that use supervised learning include artificial neural networks, decision trees, support vector machines, Gaussian processes, among others [3].

An Artificial Neural Network (ANN) is a system of interconnected simple processing elements (neurons) inspired by the functioning of biological neurons. A typical ANN architecture is organized into three types of layers: input, hidden, and output layers [2,3]. The optimal number of hidden neurons depends on multiple factors, including the number of inputs and outputs, number of training pairs, level of noise in the training pairs, complexity of the error function, network architecture, and training algorithm. It can be said that the choice of architecture depends on the type and complexity of the problem being studied [3].

A precise and reliable method for determining the minimum required number of neurons has not yet been established. What can be estimated, to some extent, is the upper limit, that is, the maximum number of neurons in the hidden layer that can be used for modeling a system represented by a given dataset. The most common approach to determining the number of neurons in hidden layers is to train multiple networks with varying neuron counts, gradually increasing the

number of neurons until the desired result is achieved [3,4]. The determination of the optimal number of hidden layer neurons is still most commonly carried out experimentally, using the trial-and-error approach [5]. In this case, it is recommended to start with the minimal structure, i.e., a network with a single neuron in the hidden layer, and then gradually increase the number of neurons while evaluating the obtained results. The main drawback of this method lies primarily in the large number of networks that need to be trained and tested [3].

The optimal number of neurons in the hidden layer is very important for the correct functioning of the model. A network with too many neurons will have an excessive number of parameters, making it prone to overfitting. Conversely, a network with too few neurons will not be able to properly approximate the given nonlinear relationships, leading to a problem of underfitting [3].

The flotation process has been used in mineral processing plants to separate valuable minerals from the gangue. This process takes place in a specific environment – flotation pulp – which consists of three phases: solid (mineral particles), liquid (water) and gaseous (air). Separation of mineral particles is made possible due to the differences in their surface hydrophobicity (feature of material characterizing its ability to be wetted with a liquid in the presence of a gas phase) [6]. Compared to mineral flotation, deinking flotation (ink removal from cellulose fibers) is a relatively young process. The basis of deinking flotation is pulp that contains the following components: water, as the carrier medium (approximately 98-99%); fibers, material obtained as a clean fraction (1-2%); fillers (<0.6%), printing ink and other impurities (<0.15%) that need to be removed; and reagents required for the fiber purification process (<0.1%) [7].

The efficiency of the flotation process can be shown through the toner recovery in foam product and cellulose fiber recovery in sink product, effective residual ink concentration in the final product (ERIC), the whiteness and brightness of the fibers. The main parameters that influence flotation are temperature, pH, toner particle size, air flow, water hardness (concentration of calcium ions in the water), and others. All parameters are interdependent, so the flotation process is defined exclusively by their interaction-i.e., by the mechanism of their combined effect [8,9]. Our understanding of the fundamental physical and chemical processes underlying the deinking processes is growing. But, due to the great variability of the raw material as well as the complexity of the physical processes which occur at the microscopic level, processing problems and process instability remain as challenges [10].

In the following study, an algorithm with supervised learning was analyzed, specifically, a model based on artificial neural networks for data obtained by deinking flotation.

2. EXPERIMENTAL

The Neural Fitting tool from the Matlab software package was used to create and train the network, as well as to evaluate its performance accuracy using mean squared error (MSE) and regression analysis. The time of deinking flotation (in the range 1-20 min), pH value (in the range 3-12), reagents such as oleic acid, oleic acid with $CaCl_2$, oleic acid with $AlCl_2$ as well as concentration of reagents (0.1 kg/t, 0.4 kg/t, 1 kg/t) were used as input model variables. The recovery of toner particles in froth was used as the output model parameters. From the total dataset of 225 parameters, 200 (88.89%) were randomly allocated for network training, validation, and testing, while the remaining 25 (11.11%) were reserved for evaluating the trained network's accuracy.

3. RESULTS AND DISCUSSION

The neural network was created, trained, and tested with 10, 15, and 20 hidden neurons. From the available dataset of 200 parameters, 140 (70%) were used for training, while 30 parameters each (15%) were allocated for validation and testing (Table 1, Figure 1). The training was performed using the Levenberg–Marquardt and Scaled Conjugate Gradient algorithms.

Table 1. Network performance accuracy obtained with the Levenberg–Marquardt and Scaled Conjugate Gradient algorithms

Training algorithm	Number of neurons in hidden layer	Mean squared error (MSE)	Coefficient of correlation (R)
Levenberg-Marquardt	10	136.83548	0.942087
	15	275.72803	0.932717
	20	269.38345	0.967081
Scaled Conjugate Gradient	10	208.42001	0.713716
	15	253.86608	0.630678
	20	251.27352	0.629073

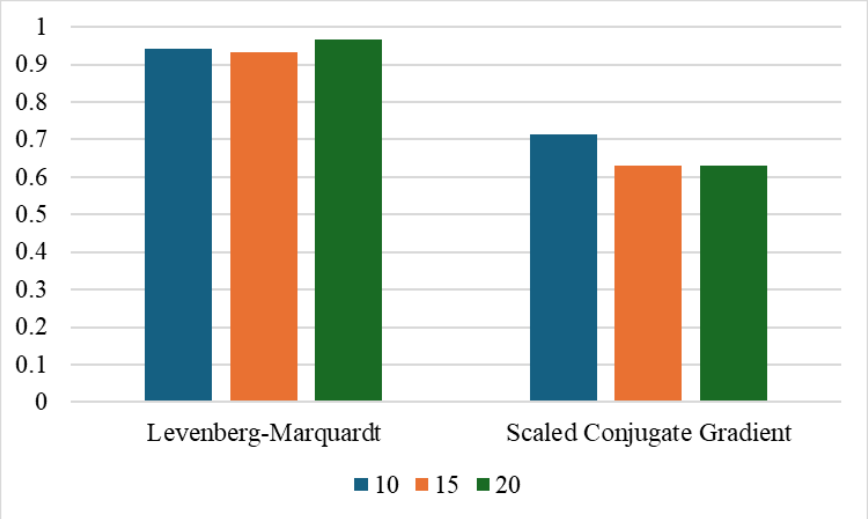

Figure 1. Comparison of correlation coefficients for neural networks trained with the Levenberg–Marquardt and Scaled Conjugate Gradient algorithms

Testing of the neural network trained with the Levenberg–Marquardt algorithm achieves good results, as shown by a correlation coefficient above 0.9 [11]. In contrast, the neural network trained with the Scaled Conjugate Gradient algorithm did not provide satisfactory results, as reflected in a lower correlation coefficient. Moreover, for the network trained with the Scaled Conjugate Gradient algorithm, the correlation coefficient decreased with an increasing number of hidden neurons, which may indicate overfitting. This issue was not observed in the network trained with the Levenberg–Marquardt algorithm.

From the above, it can be concluded that achieving good results depends more on selecting the optimal training algorithm, while in cases where the optimal model cannot be used, it is necessary to determine the optimal number of neurons in the hidden layer for the given dataset. The required number of neurons should be determined iteratively, starting with a network containing a single neuron in the hidden layer, and then gradually increasing the number of neurons until satisfactory results are obtained.

The greater the number of neurons, the more complex the function that can be approximated. On the other hand, a higher number of neurons requires more data, which may also lead to overfitting. The obtained neural networks can be reset or initialized with new initial weights and retrained; the number of neurons can be reduced; the training dataset can be expanded; the number of input values can be adjusted; the ratio of data used for training, validation, and testing can be modified; alternative learning and training algorithms can be applied; and preprocessing of inputs and outputs can be performed [10].

4. CONCLUSION

In this study, supervised learning algorithms were analyzed, with a focus on artificial neural network models applied to data obtained from deinking flotation. The neural network architecture consisted of a single hidden layer with 10, 15, and 20 neurons. The networks were created, trained, and tested using the Levenberg–Marquardt and Scaled Conjugate Gradient algorithms.

The inputs of the models were time of deinking flotation, pH, reagents such as oleic acid, oleic acid with $CaCl_2$, oleic acid with $AlCl_2$ as well as concentration of reagents, while the output values were recovery of toner particles in froth.

Testing of the neural network trained with the Levenberg–Marquardt algorithm achieved better results compared to the Scaled Conjugate Gradient algorithm. Based on the obtained results, it can be concluded that achieving good performance depends more on the choice of an optimal training algorithm, while in cases where the optimal model cannot be applied, it is necessary to determine the optimal number of hidden neurons for the given dataset. Since this study used 10, 15, and 20 hidden neurons in the neural network architecture, determining and applying the optimal number of neurons for this specific dataset could potentially yield even better results.

ACKNOWLEDGEMENTS

The research presented in this paper was done with the financial support of the Ministry of Science, Technological Development and Innovation of the Republic of Serbia, within the funding of the scientific research work at the University of Belgrade, Technical Faculty in Bor, according to the contract with registration number 451-03-137/2025-03/ 200131.

REFERENCES

[1] J.Đ. Novaković., Rešavanje klasifikacionih problema mašinskog učenja, Fakultet tehničkih nauka u Čačku, 2013.
[2] D. Tanikić., Veštačke neuronske mreže, fazi logika i genetski algoritam, Univerzitet u Beogradu, Tehnički fakultet u Boru, 2016.
[3] M.M. Kovačević., Model za prognozu i procenu troškova izgradnje armirano-betonskih drumskih mostova, Doctoral dissertation, University of Belgrade, Serbia, 2018.
[4] M. Kovačević, N. Ivanišević, T. Dašić, Lj. Marković., Gradjevinar, 1 (2018) 1-10.
[5] H.R. Maier, G.C. Dandy., Envir. Model. Softw., 15 (2000) 101-124.
[6] N. Ćalić., Teorijski osnovi pripreme mineralnih sirovina, Faculty of Mining and Geology, University of Belgrade, 1990, 496, (in Serbian).
[7] M. Kemper., Int. J. Miner. Process., 56 (1-4) (1999) 317-333.
[8] J.K. Borchardt., Colloids Surf. A Physicochem. Eng. Asp., 88 (1) (1994) 13-25.
[9] R. Svensson., The influence of surfactant chemistry on flotation deinking, 2011.
[10] W. J. Pauck., Neural network modelling and prediction of the flotation deinking behaviour of complex recycled paper mixes, Doctoral dissertation, Faculty of Engineering, University of KwaZulu Natal, Durban, 2011.
[11] M. Trumić, K. Balanović, T. Gavrilović., Prediction of results of floatation process using artificial neural networks, in Proceedings of XVI International Mineral Processing and Recycling Conference, Belgrade, Serbia, 2025, 659-664.

Extractive Metallurgy and Process Innovations

The 56th International October Conference on Mining and Metallurgy
22-25 October 2025, Bor Lake, Bor, Serbia
www.ioc.tfbor.bg.ac.rs

DOI: 10.5937/IOC25235R *Original scientific paper*

RECOVERY OF COPPER FROM A CHALCOPYRITE ORE USING NATURAL DEEP EUTECTIC SOLVENTS (NADES) OF CHOLINE CHLORIDE-UREA AS A LEACHING AGENT

Teresita del Refugio Jiménez Romero[1a], José Enrique Sánchez Vite[1b], Alejandro Cruz Ramírez[2a] Margarita García Hernández[2b], Ángel de Jesús Morales Ramírez[3a]

[1] ESIQIE, Instituto Politécnico Nacional, UPALM, 07738, Ciudad de México, México
[2] UPIIH, Instituto Politécnico Nacional, DESCTI, San Agustín Tlaxiaca, 42162, Hidalgo, México
[3] CIITEC, Instituto Politécnico Nacional, Azcapotzalco, 02250 Ciudad de México
[1a] tjimenezr@ipn.mx, 0009-0003-8012-6817
[1b] jsanchezv2105@alumno.ipn.mx, 0009-0006-5001-0495
[2a] alcruzr@ipn.mx, 0000-0002-0972-596X
[2b] margarciah@ipn.mx, 0000-0002-3850-3901
[3a] amoralesra@ipn.mx, 0000-0002-5143-2626

Abstract

Due to the environmental impact caused by using strong acids as leaching agents, research on more environmentally friendly leaching agents has increased over the past decade. In this study, a natural deep eutectic solvent (NADES) called Reline (ChCl;2Urea) was used as a leaching agent to recover copper from sulfide ore. Variables such as NADES/water weight ratio, pH, and temperature were analyzed to determine the optimal recovery conditions over 4 hours and to allow extrapolation to longer durations. The ores used were characterized by X-ray diffraction (XRD), scanning electron microscopy (SEM), and X-ray fluorescence (XRF), while the NADES was analyzed using infrared spectroscopy (FTIR). The results showed that at 25°C, pH = 7, and stirring at 300 rpm, significant copper recovery begins with a 20% NADES-to-water ratio, demonstrating high selectivity for copper over iron. The efficiency of the organic leaching process improves as the values of the three analyzed variables increase, with temperature having the most significant effect. The best recovery conditions were pH = 12, T = 100°C, w = 300 rpm, and 30% NADES, achieving an 11.68% recovery rate. The kinetic data of the leaching process fit the Kröger-Ziegler model, with an activation energy value of 5.8 kcal/mol, demonstrating that the process is controlled by the transport stage. It was observed that at 100°C, from t = 160 min onwards, the process rate increases. This copper recovery process proposal could pave the way for further research into mineral extraction processes using environmentally friendly systems, particularly biodegradable green solvents.

***Keywords**: leaching, NADES, waste minimization, copper recovery*

1. INTRODUCTION

The increasing demand for copper (Cu) in the industry to meet human needs has placed greatly emphasized on its recovery through hydrometallurgical, pyrometallurgical, and recycling processes. However, these processes require large amounts of energy and involve significant quantities of harmful substances that negatively impact the ecosystem, making them costly and leading to severe environmental issues. Therefore, it is necessary to propose new methods for obtaining copper. Recycling and recovering copper from various sources using novel recovery methods aims to reduce greenhouse gas emissions and contribute to environmental preservation. Currently, different studies have shown that deep eutectic solvents (DES) are promising for recovering various metallic species by dissolving them due to their components (hydrogen bond donors and hydrogen bond acceptors, HBD-HBA) [1]. Recently, among the wide variety of DES, natural deep eutectic solvents (NADES) have emerged as the most attractive alternative to conventional solvents due to their environmentally friendly qualities, such as biodegradability, ease of synthesis, and low cost [2]. Thus, their apparent dissolving power and ecological characteristics make NADES one of the best options for metal recovery while avoiding soil and

water contamination caused by current methods. NADES exhibit biodegradability, biocompatibility, and high selectivity in metal extraction [1]. For this reason, the main objective of this research is to recover copper using a NADES solution and determine the optimal operating conditions, including temperature, agitation, NADES/water ratio, and recovery time. The present study hypothesizes that using deep eutectic solvents (NADES) will promote the selective recovery of copper through the dissolution of oxide and sulfide compounds found in the analyzed minerals. Therefore, the goal is to recover copper from a mineral containing copper, iron, zinc, and manganese through an organic leaching process using choline chloride-urea as the leaching agent. The study evaluates the effect of temperature, pH, and water/solvent ratio to determine the optimal parameters in the leaching process to achieve the highest copper recovery. A kinetic study was carried out to evaluate the leaching reaction.

2. EXPERIMENTAL

For the development of the experiments, two variables were considered: temperature and the amount of NADES in the organic leaching process. Experiments were conducted by varying these two parameters. The first parameter is the amount of NADES in the solution, which was tested within a range of 5 to 30 g in the solution. The temperature variation was carried out to determine the optimal temperature at which the mineral is leached with the highest efficiency. Similarly, the variation in the NADES/water ratio was performed to identify the best extraction/time relationship. The temperature varied within a range of 25 to 100 °C to determine the optimal NADES/water ratio. The total contact time was kept constant at 4 hours of leaching. Finally, the optimal pH for copper recovery was determined by varying this parameter at values of 3, 7, and 12

3. RESULTS AND DISCUSSION

Ore characterization was carried out by X-ray Diffraction Figure 1, and the quantitative results obtained through X-ray Diffraction are shown in Table 1.

Table 7. DRX ore composition results

Species	Formula	Content [%]
Calcite	$CaCO_3$	1.6
Quartz	SiO_2	19.1
Chalcopyrite	$CuFeS_2$	1
Muscovite	$H_2Al_{2.43}K_{0.77}O_{12}Si_{3.5}$	70.3
Periclase	MgO	0.9
Covellite	CuS	7.1

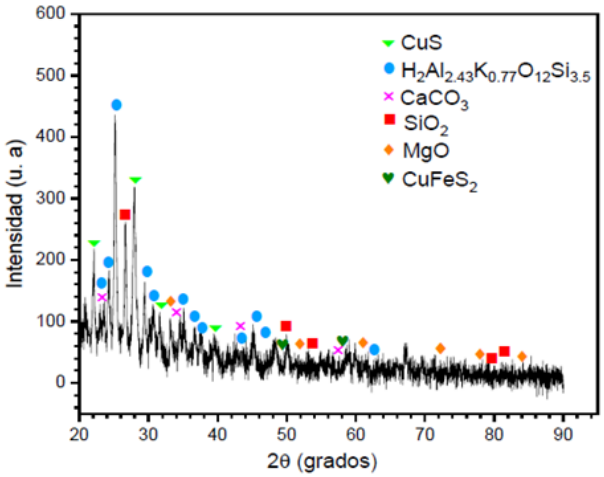

Figure 4. XDR ore analysis.

Table 2 shows the chemical analysis of the copper ore developed by X-ray fluorescence analysis.

Table 8. X-ray fluorescence copper ore analysis.

Sample	Wt. %							
	Cu	Fe	Si	Ca	Zn	Mn	Al	Mg
1	0.239	9.305	21.979	7.779	0.0171	0.154	10.682	4.28
2	0.237	9.156	21.942	7.217	0.0148	0.147	10.783	4.47
3	0.222	8.491	20.418	6.748	0.0137	0.135	9.895	4.182
4	0.239	9.765	21.874	7.324	0.0185	0.155	11.011	4.465
Average	0.234	9.179	21.553	7.267	0.0160	0.148	10.593	4.352

The average copper content in the ore is 0.23%, while the average iron content is 9.17%. A high content of silicon, aluminum, and calcium is observed, which is consistent with the results obtained through X-ray diffraction regarding the presence of aluminosilicates.

The leaching process was carried out at different pH and the results are shown in Figure 2.

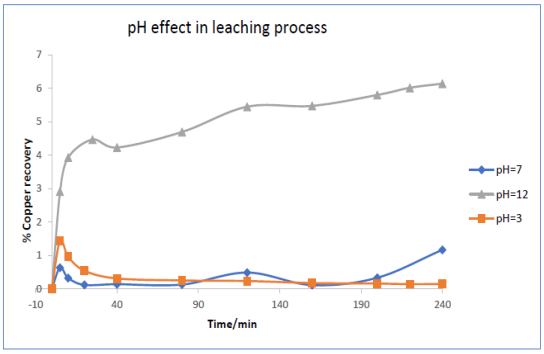

Figure 5. pH effect in the leaching process.

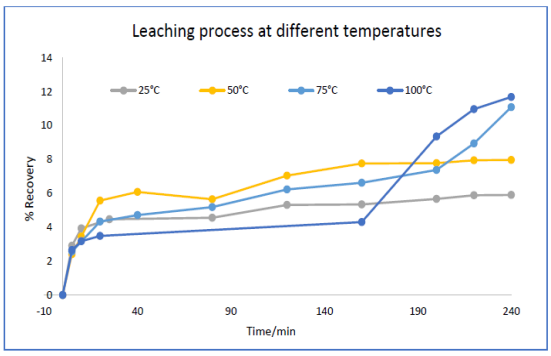

Figure 6. Leaching process at different temperatures.

It can be observed that at a pH of 3, the maximum copper recovery reaches 1.4% at minute 5; however, the recovery decreases to 0.14% at minute 240. On the other hand, at a pH of 7, the recovery increases to 1.16% at minute 240. Finally, at a pH of 12, a recovery of 3.79% is achieved at minute 25, and although the recovery decreases by minute 40, it continues to increase, reaching a final recovery of 6.13% at minute 240. Under basic conditions, the system exhibits the best recoveries. The reason for this effect is likely related to the species formed by the dissolution of NADES in water. Experiments were conducted under the best pH conditions and NADES content, varying the temperature. The results are shown in Figure 3. It is worth highlighting that at higher temperatures, a greater amount of copper is recovered, starting with a 5.9% recovery at 25°C and reaching an 11.68% recovery at 100°C. This represents an almost twofold increase in recovery compared to that obtained at 25°C over 240 minutes. However, the kinetics indicate that longer reaction times will lead to higher recoveries, given that the current recoveries are still low.
With the results shown in Figure 3, kinetic analysis was carried out by evaluating the 29 models compiled by C.F. Dickson and G.R. Heal [3]. Once the modeling was performed for all the mentioned equations, it was found that the best fit corresponds to the Zhuravlev, Leksohin, and Templeman (ZLT) model:

$$kt = \left(\frac{1}{(1-\alpha)^{1/3}} - 1\right)^2 \quad (1)$$

And for the Krogler and Zieger (KZ) equation:

$$klnt = [1 - (1-\alpha)^{\frac{1}{3}}]^2 \quad (2)$$

These two models assume that diffusion is the rate-controlling step in the kinetics [4]. Based on the correlation coefficient results, the D7 model of Kröger-Ziegler was selected. This model assumes that the diffusion coefficient is not constant but instead is inversely proportional to the reaction time. Unlike the ZLT model, the Kröger-Ziegler model suggests that the diffusion coefficient decreases over time [4]. The Kröger-Ziegler model assumes that, during the initial stage of the reaction, rapid surface diffusion covers the particles with a continuous product layer [5]. This means that the applicability of this model implies that, during the leaching process with NADES, a layer of by-products forms on the mineral surface, leading to a decrease in the diffusion coefficient over time. This explains why recovery is low for many systems. In other words, as the reaction progresses, this by-product layer makes it increasingly difficult for fresh NADES to reach the particle. The exact nature of these by-products must be determined in future studies to enhance process efficiency. Moreover, this kinetic behavior also explains the trend observed in Figure 3. As the temperature increases, it is expected that these by-products will become less stable, allowing better diffusion of NADES to the particle, which accounts for the increased recovery. Additionally, at higher temperatures (75°C and 100°C), there is a moment in time when the dissolution rate increases sharply (at minute 160 and minute 200 for 75°C and 100°C, respectively). It is therefore plausible that, at this point, the combined effect of agitation and temperature enhances NADES diffusion in the system, accelerating the reaction rate.

4. CONCLUSION

Given the fit to the Kröger-Ziegler model, it can be concluded that during the leaching process with NADES, a layer of by-products likely forms on the mineral surface, causing a decrease in the diffusion coefficient over time. This explains why recoveries are low in many systems, as the by-product layer progressively hinders the access of fresh NADES to the particle. The activation energy (Ea) is 5.8 kcal/mol, indicating that the process is transport-controlled, further confirming the observations that the system depends on diffusion.

REFERENCES

[1] E. Smith, A. Abbot, K. Ryder, P.E.L. Smith, Chem. Rev., 114 (21) (2014) 11060-11082.
[2] H. Vanda, Y. Dai, E. Wilson, R. Verpoorte, Y. Hae. Henni, C. R. Chim., 21 (6) (2018) 628-638.
[3] C. Dickinson, G. Heal, Thermochim. Acta, 340-341 (1999) 89-103.
[4] P. Prihutami, A. Prasetya, W. Sediawan, H. Petrus, F. Anggara, J. Sustain. Metall., 7 (2021) 1241-1253.
[5] I. Sharma, I. Bhushan, B. Saroj, B. Sulekha, IJC, 24A (8) (1985) 674-676.

The 56th International October Conference on Mining and Metallurgy
22-25 October 2025, Bor Lake, Bor, Serbia
www.ioc.tfbor.bg.ac.rs

DOI: 10.5937/IOC25239A *Original scientific paper*

DROPLET FLOTATION IN METALLURGICAL MELTS

Alexey M. Amdur[1a], Sergei A. Fedorov[1,2b]

[1] Ural State Mining University, Kuibysheva str. 30, 620144 Yekaterinburg, Russian Federation
[2] Vatolin Institute of Metallurgy of Ural Branch of the Russian Academy of Sciences, Amundsena str. 101, 620016 Yekaterinburg, Russian Federation
[1a] engineer-ektb@rambler.ru, 0000-0001-7825-2505
[1b] saf13d@mail.ru, 0000-0002-4201-5177

Abstract
The paper considers one of the main mechanisms of transition of precious and non-ferrous metals into slag. This happens during the melting of sulfide materials. Sulfide droplets together with their associated precious metal particles are carried into the slag by gas bubbles. The size of metal particles reaches up to 25 microns. The high values of the calculated adhesion values for gold – matte and platinum – matte systems indicate the strength of metal adhesion to sulfide droplets. Analytical expressions describing flotation are obtained.

Keywords*: sulfide droplet, particle, matte, slag, bubble, flotation, gold, platinum, silver*

1. INTRODUCTION

Liquid droplet flotation is often used to purify industrial and wastewater from oil [1-3], mercury [4]. Geologists consider flotation as a method of transporting metal and sulfide droplets to the upper layers of magma [5].

Most of the world's production of copper, nickel, and platinum group metals is carried out by melting sulfide ores and concentrates into matte [6-7]. In the settling chambers of the furnaces, the melt is separated into slag and matte. Sulfide droplets are deposited in the slag into the matte layer. Losses of non-ferrous and precious metals are largely since some of the sulfide droplets do not reach the matte boundary and are removed together with the slag into landfills. It was previously shown that these droplets are retained in the slag due to flotation by gas bubbles [8]. However, if conditions are created that increase the flotation rate, this will lead to the accumulation of sulfide droplets due to coagulation. Further, the rate of droplet deposition will increase, and the "mechanical" losses of valuable components will decrease [9-11].

Thus, the study of the droplet flotation process in metallurgical melts is an actual problem.

The purpose of the study is to consider the conditions of flotation of liquid sulfide droplets in oxide melts.

2. EXPERIMENTAL

The samples are represented by platinum-containing copper-nickel sulfide ore, gold-containing copper-pyrite ore and silver-containing sulfide material from landfills of host rocks. In order to determine the forms of existence of precious metals in sulfide melts using microscopes, their content was increased by adding dispersed metals (platinum to 1000 ppm, gold to 1300 ppm and silver to 100 ppm). The concentrations of chemical elements in the starting material and in the melting products were determined on Spectroflame Modula S atomic emission spectrometer with inductively coupled plasma. The melting products were analyzed on a Vega LMS scanning electron microscope equipped with an Xplore30 energy dispersive attachment. The materials were heated and melted in corundum crucibles in a resistance furnace at temperatures of 1300-1350 °C.

3. RESULTS AND DISCUSSION

Metallic gold, alloy (Au, Cu), aurostibite $AuSb_2$, alloy (Pt, Fe), and silver-containing particles were found during the study of matte samples after melting sulfide materials. The matte consists mainly of troilite (FeS), with small amounts of copper sulfides, Fe-Ni alloys, and iron oxides. Slags are represented by a porous brownish glassy mass. They contain many sulfide droplets (up to 15 vol.%). Droplet size reach 4 mm. The composition of the droplets is like that of the matte. The droplets contain teardrop-shaped gold particles (up to 17 μm, Fig. 1a), crystals (Pt, Fe) of predominantly needle shape and their aggregates (up to 25 μm, Fig. 1b), particles containing silver of irregular shape (up to 10 μm, Fig. 1c).

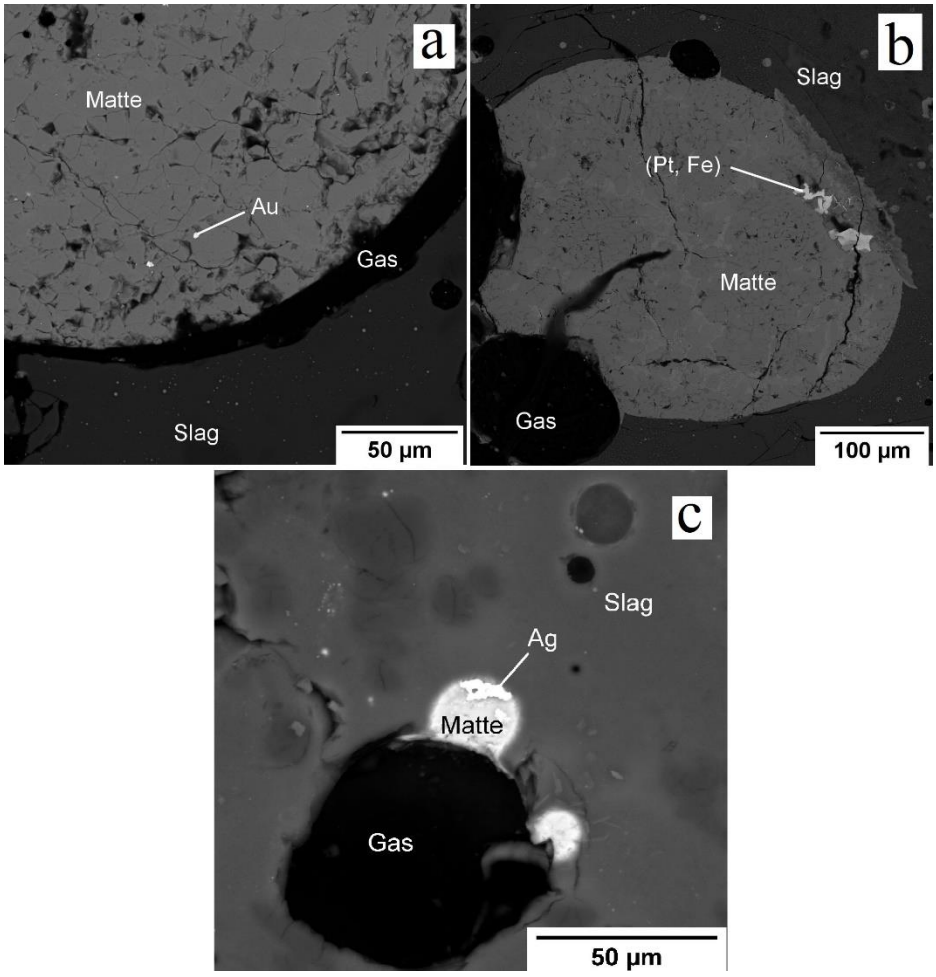

Figure 1 Sulfide droplets (Matte) attached to gas bubbles in slags after melting sulfide materials. The shooting was done in BSE mode. Sulfide droplets contain a – gold (Au), b – alloy (Pt, Fe), c – silver (Ag)

Chemical analysis of copper-nickel sulfide ore smelting products (Table 1) shows that the slag contains from 0.4 to 15% of precious metals. In industrial conditions, after smelting sulfide materials in ore-thermal and depleted electric furnaces, up to 1-2% of these metals pass into slag [12-13].

Table 1 The content of precious metals in matte and slag after smelting of copper-nickel sulfide ore, ppm

Materials	**Metal content**						
	Ru	**Rh**	**Pd**	**Ir**	**Pt**	**Au**	**Ag**
Matte	0.21	2.08	5.36	0.02	1.26	1.77	5.9
Slag	0.004	0.07	1.66	0.013	0.13	0.42	0.67

The most likely reason for the transition of dispersed sulfide droplets from matte to slag is their flotation by gas bubbles. Bubbles appear due to the decomposition of sulfides [8-11]. During the passage of the boundary of two immiscible liquids (matte and slag), the bubble can capture and float a drop of heavier liquid (matte). The conditions of flotation [10, 14] are as follows. The force of the drop's adhesion to the bubble must be greater than its gravity. The buoyant force applied to the bubble must be greater than the gravity of the drop:

$$\begin{cases} 2\pi r\sigma_{m-s}\sin\theta > c\frac{4}{3}\pi r^3\rho_m g, \\ \frac{4}{3}\pi R^3(\rho_s-\rho_g)g \geq c\frac{4}{3}\pi r^3(\rho_m-\rho_s)g \end{cases}, \quad (1)$$

where r is the radius of the sulfide droplet;

R is the radius of the gas bubble;

$\sigma_{m\text{-}s}$ is the interfacial tension at the matte – slag boundary;

θ is the angle between the tensions at the matte – slag and matte – gas boundary;

c is the volume fraction of the whole droplet;

p_m, p_s, p_g are the densities of the matte, slag and gas accordingly;

g is the acceleration of gravity.

For experimentally studied slag and matte, the maximum possible radius of floated sulfide droplet is about 4.2 mm. Sulfide droplets with a radius of up to 2 mm were found in the slags. The size of the bubble may be smaller than the size of the sulfide droplet that this bubble floats. This is confirmed experimentally [14].

For ultrafine particles and sulfide droplets, flotation is possible not only due to the formation of a three-phase wetting perimeter, but also due to the action of wedging pressure [15].

Since gold droplets and platinum solid particles are deposited in the slag together with sulfide droplets, their adhesion W_A to matte was evaluated. These metals interact with the components of the matte. Therefore, we are talking about dynamic wetting angles and dynamic (non-equilibrium) adhesion. As for the gold droplets, it does not matter whether the dynamic or equilibrium tension values act on it. Only the magnitude of these tensions is important. The adhesion for the gold – matte – slag and platinum – matte –slag systems was calculated using the Dupree equation:

$$W_A = \sigma_{Me-m}(1+\cos\theta), \quad (2)$$

where $\sigma_{Me\text{-}m}$ is the interfacial tension of the metal–matte;

θ is the wetting angle.

The wetting angles included in equation (2) were determined from images of the gold – matte – slag and platinum – matte – slag boundaries. The images were taken with an electron microscope. The adhesion work for the gold – matte system is ~ 1600 mJ/m^2, for platinum – matte system is ~ 3000 mJ/m^2 [14]. The values obtained are very significant and comparable to the work of cohesion for gold and platinum. Consequently, these metals are firmly bonded to the matte droplets and move with them in the slag. The adhesion values are also consistent in order of magnitude with those calculated based on the theory of dielectric formalism in the absence of a gap between metal surfaces: Cu/Al – 3100, Fe/Cu – 4200 mJ/m^2.

4. CONCLUSION

The paper considers one of the main mechanisms of transition of precious and non-ferrous metals into slag. This happens during the melting of sulfide materials. Sulfide droplets together with their associated precious metal particles are carried into the slag by gas bubbles. The size of metal

particles reaches up to 25 microns. The high values of the calculated adhesion values for gold–matte and platinum–matte systems indicate the strength of metal adhesion to sulfide droplets. Analytical expressions describing flotation are obtained.

ACKNOWLEDGEMENTS

The study was carried out in accordance with the state assignment for the Ural State Mining University No. 075-03-2025-325 dated January 16, 2025 and the state assignment of the IMET UrB RAS using the equipment of the Ural-M Central Research.

REFERENCES

[1] M. Piccioli, S.V. Aanesen, H. Zhao, M. Dudek, G. Øye., Energy and Fuels, 34 (12) (2020) 15579-15592.
[2] M. Dudek, G. Øye. Energy and Fuels, 32 (10) (2018) 10513-10521.
[3] S. Yan, X. Yang, Z. Bai, X. Xu, H. Wang., Chem. Eng. Sci., 223 (2020) 115740.
[4] A.A. Zubkov, Z.M. Shulenina, Ecol. Indust. Prod., (4) (2012) 75-78.
[5] J.E. Mungall, J.M. Brenan, B. Godel, S.J. Barnes, F. Gaillard., Nature Geosci., 8 (3) (2015) 216-219.
[6] T.S. Gabasiane, G. Danha, T.A. Mamvura, T. Mashifana, G. Dzinomwa., Crystals, 11 (12) (2021) 1504.
[7] J. Kulczycka, Ł. Lelek, A. Lewandowska, H. Wirth, J.D. Bergesen., J. Indust. Ecol., 20 (2) (2016) 304-316.
[8] T. Utigard, J.M. Toguri, T. Nakamura., Metall. Trans. B, 17 (1986) 339-346.
[9] X. Cheng, Z. Cui, L. Contreras, M. Chen, A. Nguyen, B. Zhao., JOM, 71 (2019) 1897-1903.
[10] A. Amdur, E. Selivanov, S. Fedorov, V. Pavlov, S. Krasikov., J. Min. Metall. Sect. B., 57 (2) (2021) 209-215.
[11] A.V. Vanyukov, V.Ya. Zaitsev., Slags and Matte of Non-ferrous Metallurgy, Metallurgy, Moscow, 1969, p. 408.
[12] L.Sh. Tsemekhman, L.B. Tsymbulov, R.A. Pakhomov, et al. Tsvetnye Metally., 11 (2016) 50-56.
[13] L.Sh. Tsemekhman, et al., Atlas of mineral raw materials, technological industrial products and marketable products of JSC MMC Norilsk Nickel, Ore and Metals, Moscow, 2010, p. 336.
[14] A.M. Amdur, S.A. Fedorov, V.V. Yurak., Metals, 11 (10) (2021) 1-14.
[15] B.V. Deryagin, S.S. Dukhin, N.N. Rulev, Uspekhi khimii, 1 (1982) 92-118.

The 56th International October Conference on Mining and Metallurgy
22-25 October 2025, Bor Lake, Bor, Serbia
www.ioc.tfbor.bg.ac.rs

DOI: 10.5937/IOC25243S *Original scientific paper*

DEVELOPMENT OF ICALPHAD SOFTWARE FOR PHASE DIAGRAM CALCULATION AND INTELLIGENT THERMODYNAMIC OPTIMIZATION

Yuchao Shi[1a], Taibai Fu[2a], Xinyi Zhang[2b], Liang Zhang[1b], Shiyi Wen[1c], Yuling Liu[1d], Yingbiao Peng[3a], Jiangxing Wang[2c], Ziqing Xie[2d], Yong Du[1e]

[1] State Key Laboratory of Powder Metallurgy, Central South University, Changsha, Hunan, 410083, PR China
[2] Key Laboratory of Computing and Stochastic Mathematics (Ministry of Education), Changsha, Hunan, 410081, PR China
[3] Changsha Ruirui Technology Co., Ltd., Changsha, Hunan, 410000, PR China
[1a] s1373735472@163.com, 0000-0003-2035-6349
[2a] ftbvenus@163.com, 0000-0002-5758-0785
[2b] zhangxinyi26@hunnu.edu.cn, 0009-0002-9207-4877
[1b] zhangliang8595@163.com, 0000-0002-5973-7491
[1c] shiyi_wen@csu.edu.cn, 0000-0002-0262-7697
[1d] liu.yuling@csu.edu.cn, 0000-0002-5898-567X
[3a] pengyingbiao1987@163.com, 0000-0002-0590-6878
[2c] jxwang@hunnu.edu.cn, 0000-0002-5413-3939
[2d] ziqingxie@hunnu.edu.cn, 0000-0001-9372-7011
[1e] yong-du@csu.edu.cn, 0000-0002-4187-3989

Abstract
This paper presents the ICALPHAD software, which enables the calculation of phase diagrams and thermodynamic properties for various material systems. The software integrates a new optimization algorithm based on multi-objective optimization to efficiently handle incomplete or missing experimental data. Key features include modules for binary and ternary phase diagrams, thermodynamic property calculations (e.g., Gibbs energy, enthalpy, heat capacity), and the ability to model external conditions such as magnetic fields. These developments demonstrate the potential of the software as an intelligent platform for phase diagram calculation and thermodynamic optimization in computational materials science.

***Keywords**: ICALPHAD, optimization, phase diagrams, thermodynamics, multi-objective optimization.*

1. INTRODUCTION

Accurate calculation of phase diagrams and thermodynamic properties is essential for materials design and process optimization. The CALPHAD method provides a well-established framework for such calculations, but existing tools often require complete datasets and involve complex manual optimization steps [1]. To address these limitations, the ICALPHAD software has been developed as a modular and extensible platform. It integrates binary and ternary phase diagram modules, thermodynamic property calculations, and external field modeling. A key feature is an intelligent optimization framework based on multi-objective methods, which improves efficiency and reliability when experimental data are incomplete [2]. The software is designed with an engineering-oriented graphical interface, supporting streamlined data input, automated parameter handling, and real-time visualization. This makes ICALPHAD suitable for both research and industrial applications where accuracy, robustness, and usability are critical.

2. SOFTWARE DEVELOPMENT

ICALPHAD has been developed as a modular and extensible software platform for the calculation of phase diagrams and thermodynamic properties. Its design philosophy emphasizes flexibility,

reusability, and scalability, making it suitable for both academic research and industrial applications. The software consists of several functional modules that can operate independently or in combination, ensuring that users can tailor calculations according to their needs.

2.1 Binary Phase Diagrams

The binary phase diagram module enables the calculation of multiple binary alloy systems, such as Ag-Pb, Al-Ta, Cu-Mg, and Fe-Ni. Each binary system can be independently loaded through database files, and the software supports visualization of equilibrium phase boundaries, liquidus and solidus curves, as well as metastable extensions. Special attention has been given to accuracy and flexibility, allowing researchers to dynamically adjust composition and temperature ranges.

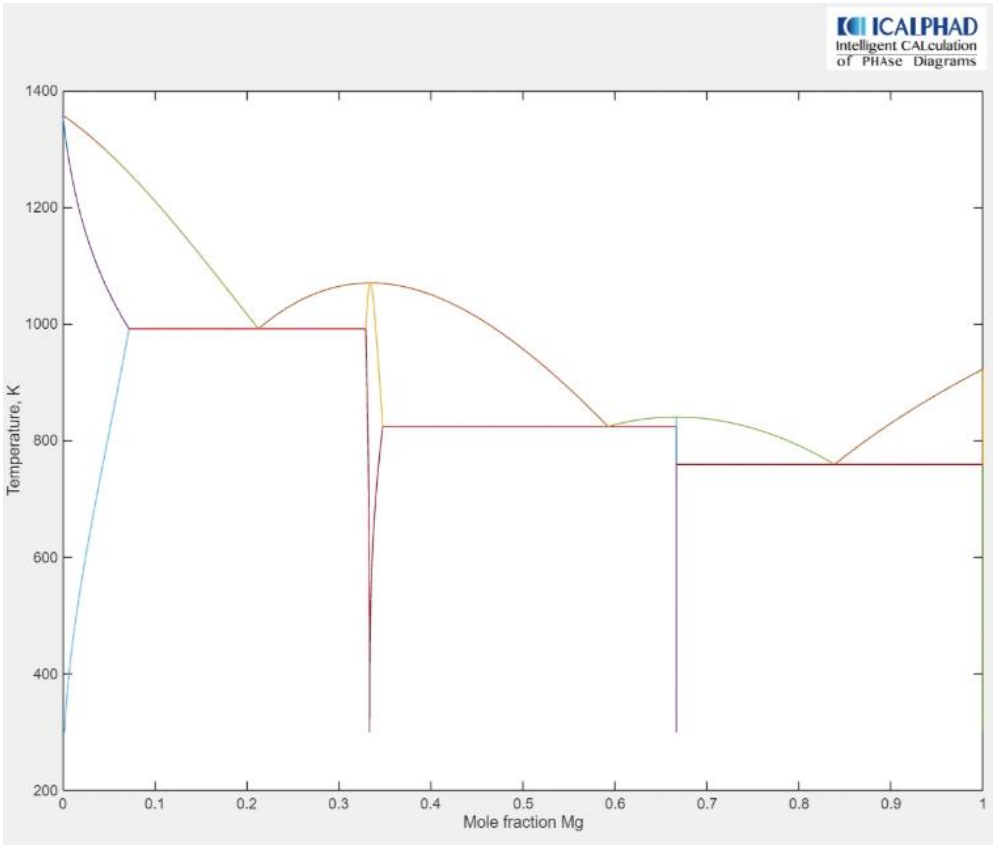

Figure 1. Cu-Mg binary phase diagram calculated by using ICALPHAD software

2.2 Ternary Phase Diagrams

For ternary systems, ICALPHAD provides dedicated modules for both isothermal sections and vertical sections. For example, in the Fe-Mo-Zr system, users can generate phase diagrams across a range of fixed temperatures (isothermal sections) or along specific compositional paths (vertical sections). The software also supports liquidus surface projections, providing a comprehensive view of phase equilibria in complex multi-component systems. These features make it possible to analyze solidification paths and phase stability in greater detail.

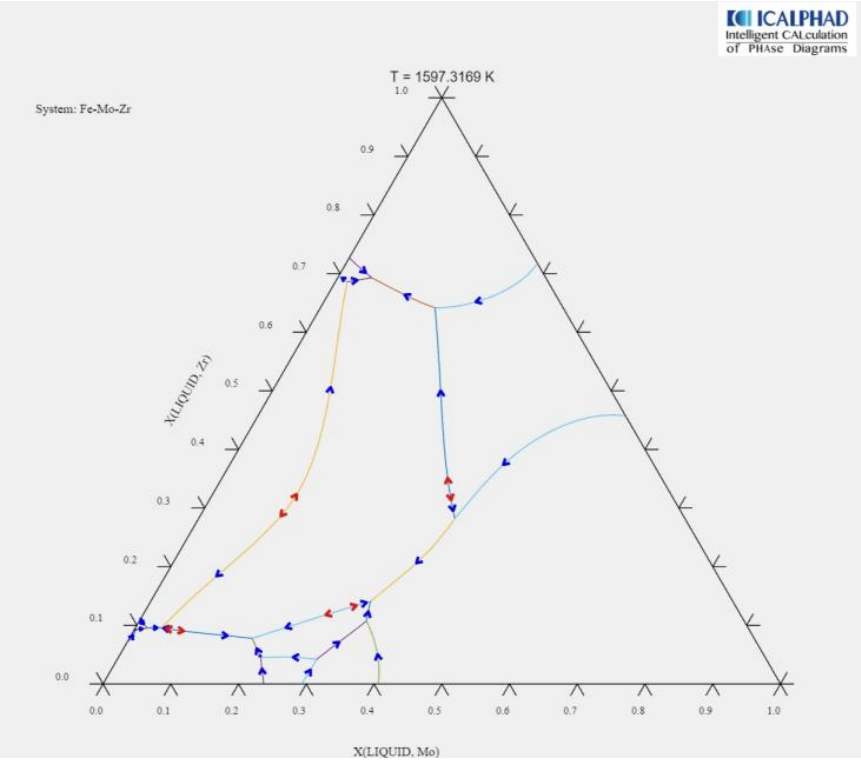

Figure 2. Fe–Mo–Zr liquidus projection calculated by using ICALPHAD software

2.3 Thermodynamic Property Calculations

Beyond phase diagram generation, ICALPHAD includes a thermodynamic property module. This allows calculation and plotting of fundamental properties such as Gibbs free energy, enthalpy, heat capacity, entropy, chemical potentials, and activities. The properties can be evaluated at both the system level and for individual phases, enabling detailed analysis of thermodynamic stability and reaction driving forces. High-resolution curves are automatically generated for visualization and export.

2.4 External Field Calculations

An advanced feature of ICALPHAD is its ability to model external field effects. For instance, modules have been implemented to calculate phase diagrams under applied magnetic fields, covering systems such as Fe-Co, Fe-Ni, and Co-Cr. These modules extend the software's applicability to emerging fields of functional materials design, where magnetic, electric, or stress fields strongly influence phase equilibria.

2.5 Optimization Framework

A distinguishing feature of ICALPHAD is its intelligent optimization framework. The framework employs a multi-objective approach, combining thermodynamic property data, two-phase equilibrium information, and invariant reaction data into a single optimization problem. A weighted sum method aggregates the different objectives, and the optimization is performed using the Barzilai–Borwein method, which provides rapid convergence while avoiding dependence on arbitrary initial parameter guesses[3]. This enables robust parameter optimization even when experimental datasets are incomplete, which is often the case in high-order systems.

2.6 User Interface and Workflow

The software is equipped with an intuitive graphical user interface (GUI) designed for usability in both research and engineering contexts. Users can:

Import database files (.TDB, .m, or other supported formats).
Select elements, phases, and parameter ranges via interactive panels.
Dynamically compute phase diagrams by adjusting temperature, composition, or pressure.
Visualize results in real time, including diagrams and thermodynamic property curves.
Export diagrams and datasets into multiple formats (e.g., PNG, PDF, CSV).

The GUI also integrates calculation logs and error reporting, which facilitate reproducibility and debugging. By automating routine steps such as parameter initialization and data parsing, ICALPHAD reduces the manual workload and minimizes user errors, ensuring a smooth workflow for both novice and expert users.

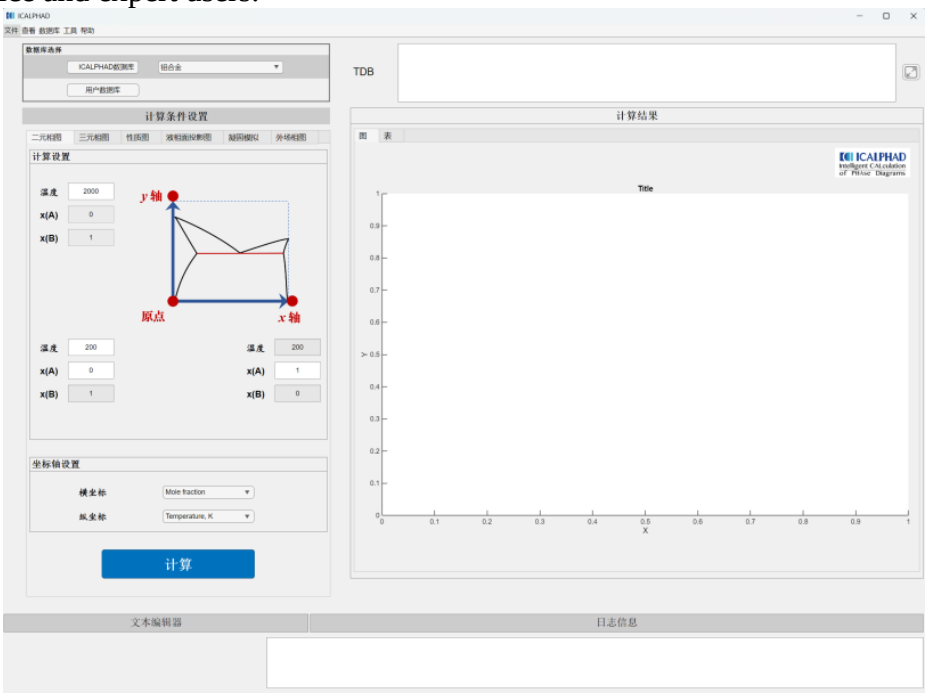

Figure 3. Graphical user interface of the ICALPHAD software

3. CONCLUSION

The ICALPHAD software provides an integrated platform for phase diagram calculation and thermodynamic property evaluation. By incorporating an intelligent multi-objective optimization framework, it achieves robust performance even with incomplete experimental data. With its modular design and user-friendly interface, ICALPHAD offers a reliable tool for computational thermodynamics, with potential for further extension to more complex systems.

ACKNOWLEDGEMENTS

The financial supports from the National Natural Science Foundation of China (No. 52401003 and No. 52331002), Hunan Provincial Natural Science Foundation (No. 2024JJ6041) are greatly acknowledged.

REFERENCES

[1] Z.-K. Liu., Acta Mater., 200 (2020) 745–792.
[2] L. Kaufman, H. Bernstein., Computer Calculation of Phase Diagrams, Academic Press, New York, 1970.
[3] H. Lukas, S.G. Fries, B. Sundman., Computational Thermodynamics: The CALPHAD Method, Cambridge University Press, Cambridge, 2007.

The 56th International October Conference on Mining and Metallurgy
22-25 October 2025, Bor Lake, Bor, Serbia
www.ioc.tfbor.bg.ac.rs

DOI: 10.5937/IOC25247G *Original scientific paper*

ELECTROCHEMICAL BEHAVIOR OF COPPER IN CHLORIDE MEDIUM IN THE PRESENCE OF PINE CONE MACERATE

Vesna Grekulović[1a], Milica Zdravković[1b], Milan Gorgievski[1c], Nada Štrbac[1d], Miljan Marković[1e], Marina Marković[1f], Kristina Božinović[1g]

[1] Technical Faculty Bor, University of Belgrade, V.J. 12, 19210 Bor, Serbia
[1a] vgrekulovic@tfbor.bg.ac.rs, 0000-0001-6871-4016
[1b] mboskovic@tfbor.bg.ac.rs, 0000-0001-9488-9151
[1c] mgorgievski@tfbor.bg.ac.rs, 0000-0002-9899-719X
[1d] nstrbac@tfbor.bg.ac.rs, 0000-0003-4836-1350
[1e] mmarkovic@tfbor.bg.ac.rs, 0000-0002-4734-1481
[1f] marina.markovic@tfbor.bg.ac.rs, 0009-0007-7553-6423
[1g] kbozinovic@tfbor.bg.ac.rs, 0000-0002-9834-448X

Abstract
The article presents the results of the study of the electrochemical behavior of copper during oxidation in a 0.5 mol/dm^3 NaCl solution in the absence and presence of pine cone macerate of different concentrations. The electrochemical behavior of copper was investigated using the cyclic voltammetry method and the potentiostatic method. The results of cyclic voltammetry show that three current peaks appear on the anodic polarization curves, which correspond to the formation of copper chloride and copper oxide. Potentiostatic polarization was performed at 0.5 mV vs. SCE for 100 s and at 25°C. Potentiostatic curves show that the steady-state currents decrease with increasing concentration of macerate in the electrolyte. Microscopic images confirm that a protective layer has formed on the copper surface in the presence of the pine cone macerate, which prevents the corrosion process.

***Keywords**: electrochemical behavior, copper, chloride medium, pine cone macerate*

1. INTRODUCTION

Corrosion of copper and its alloys is a major problem because it causes considerable material and financial losses. To protect against corrosion, it is important to investigate the effect of various potential inhibitors in different environments. So far, a large number of potential inhibitors have been investigated. Research should be focussed on the application of ecological - "green" inhibitors, with the main criterion for application being their ecological compatibility. Research into plant extracts has recently been of great interest when it comes to corrosion inhibitors [1,2]. They are also natural antioxidants that are cheap and have no negative impact on the environment. The inhibitory effect of some plant extracts is achieved by the presence of tannins in their composition. In perennial herbaceous plants, the underground organs (rhizomes and roots) are richest in tannins, while in woody plants the bark of roots, stems and thicker branches, leaves, fruits, etc. are richest in tannins [3].

This paper presents the results of the investigation of the influence of pine cone macerate on the corrosion behaviour of copper in 0.5 mol/dm^3 NaCl.

2. EXPERIMENTAL

To prepare a solution of 0.5 mol/dm^3 NaCl, NaCl produced by d.d.."Zorka Pharma" Šabac was used. The solution was prepared with chemicals of p.a purity and distilled water. The working solutions were prepared by pouring 10, 20, 30 and 40 mL of pine cone macerate (Pinophyta) into volumetric flasks of 100 mL each and then adding a solution of 0.5 mol/dm^3 NaCl, always

maintaining the concentration of sodium chloride in the solution. The macerate of pine cones was prepared as follows: first, 1000 mL of distilled water was heated up to 60 °C and then 100 g of crushed sporophylls of pine cones were added. The process to obtain the macerate takes 4 hours, mixing with a magnetic stirrer at 400 min^{-1}. After 4 hours, the resulting macerate is filtered in a Bichner apparatus and stored in a refrigerator.

The experiments were carried out using a system consisting of an electrochemical cell with three electrodes (working, reference and auxiliary electrode), hardware (PC, Burr-Brown PCI-20428W, AD/DA converter and an analogue interface developed at the Faculty of Engineering in Bor) [4]. The study of the electrochemical behaviour of copper in 0.5 mol/dm^3 NaCl solution in the absence and presence of pinecone macerate was carried out by recording the anodic polarization curves. The curves were recorded in the potential range from -0.4 V vs. SCE to 1 V vs. SCE with a scan rate of 20 mV/s. The potentiostatic curves were recorded at 0.5 V vs. SCE for 100 s. Optical microscopy was used to characterize the electrode surface after potentiostatic oxidation.

3. RESULTS AND DISCUSSION

Figure 1 shows the anodic polarization curves for pure copper in 0.5 mol/dm^3 NaCl solution with and without pine cone macerate.

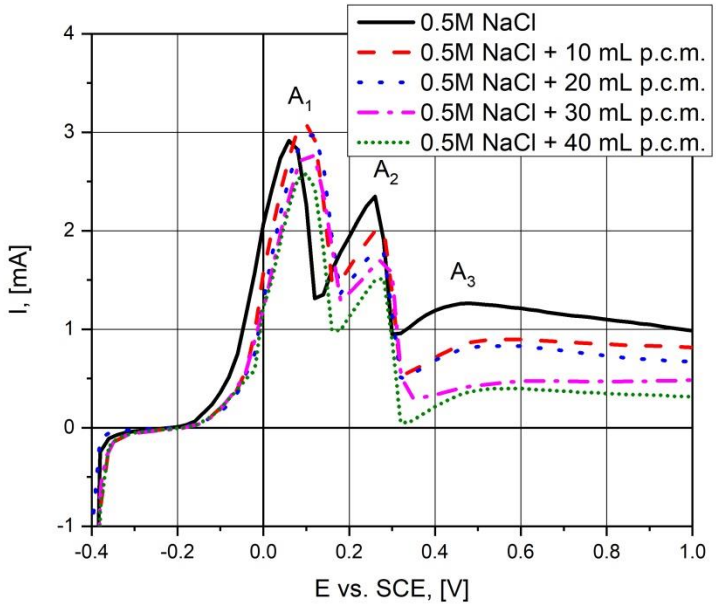

Figure 1. Anodic polarization curves for copper with a scan rate of 20 mV/s in 0.5 mol/dm^3 NaCl with and without the addition of pine cone macerate (p.c.m.- pine cone macerate)

Three current peaks corresponding to the formation of chloride (current peaks A_1 and A_2) and copper oxide (current peak A_3) appear on the anodic polarization curve obtained in 0.5 mol/dm^3 NaCl [5,6]. With the addition of 10 mL and 20 mL of pine cone macerate, the current strength values for current peak A_1 are higher compared to the current strength value without the addition of pine cone macerate, while the current strength values with the addition of 30 mL and 40 mL of pine cone macerate are lower compared to the current strength value without the addition of macerate. In the area of the potential where the current peaks A_2 and A_3 occur, the values of the current strength of the current peaks in the presence of pine cone macerate are lower than the value of the current strength without the addition of pine cone macerate at all macerate concentrations. From the polarization curves obtained, it can be concluded that pine cone macerate slows down

the process of copper chloride and oxide formation on the copper surface and that pine cone macerate acts as an anodic inhibitor of copper corrosion in 0.5 mol/dm^3 NaCl.

Figure 2 shows the potentiostatic curves after potentiostatic treatment of copper for 100 s in 0.5 mol/dm^3 NaCl solution without and with pine cone macerate.

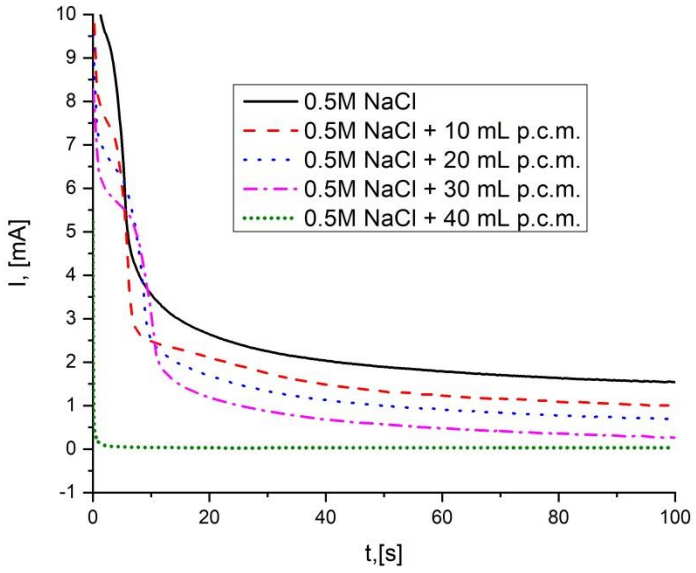

Figure 2. Potentiostatic curves for copper in 0.5 mol/dm^3 NaCl without and with the addition of pine cone macerate (p.c.m.- pine cone macerate) at 0.5 V vs. SCE

The potentiostatic curve obtained for copper with the addition of 10 mL of pine cone macerate drops sharply in the first 7 seconds, then the curve decreases monotonically until about 90 seconds when it stabilizes and the value of the steady-state current is 1 mA. The potentiostatic curve obtained for copper with the addition of 20 mL of pine cone macerate drops sharply in the first 10 seconds and then continues to decrease slowly until it stabilizes after about 80 seconds and the value of the steady-state current is 1.6 mA. The potentiostatic curve obtained for copper with the addition of 30 mL of macerate drops sharply in the first 10 seconds, then continues to decrease slightly and stabilizes at around 90 seconds, with the value of the steady-state current being 0.3 mA. When 40 mL of pine cone macerate is added, stabilization occurs in the first few seconds and the value of the steady-state current is 0 mA. This means that the pine cone macerate protects the copper surface well against corrosion. Figure 3a shows a photomicrograph of untreated copper. Figures 3b, 3c, 3d, 3e and 3f show microphotographs of the copper surface after potentiostatic treatment in 0.5 mol/dm^3 NaCl without and with the addition of pine cone macerate.

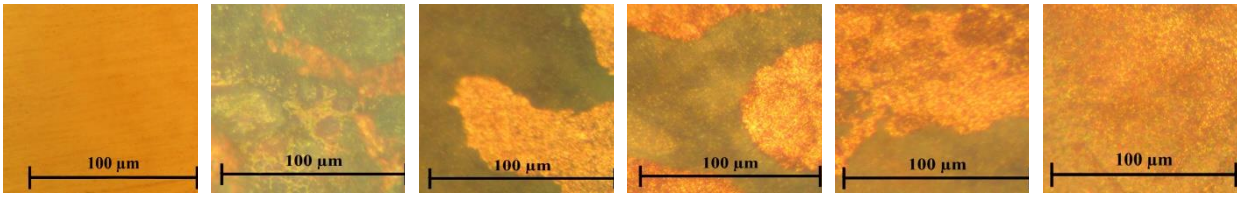

a) b) c) d) e) f)

Figure 3. Microphotographs of the copper surface after potentiostatic treatment on the potential of 0 V vs. SCE during 100 s: a) untreated surface; b) in 0,5mol/dm^3 NaCl; c) in 0,5mol/dm^3 NaCl + 10 mL pine cone macerate; d) in 0,5mol/dm^3 NaCl + 20 mL pine cone macerate; e) in 0,5mol/dm^3 NaCl + 30 mL pine cone macerate; f) in 0,5mol/dm^3 NaCl + 40 mL pine cone macerate

4. CONCLUSION

Increasing concern for the protection of the environment has led to stricter regulations on the use of chemicals that can have a harmful effect on the environment. This has resulted in the use of a number of very effective inhibitors being reduced or discontinued.

Based on the experiments carried out, the following conclusions can be drawn:

- When investigating the electrochemical behavior of copper using the cyclic voltammetry method in 0.5 mol/dm^3 NaCl, it was found that three current peaks appear on the anodic polarization curve. The current peaks A_1 and A_2 correspond to the formation of copper chloride, while the current peak A_3 corresponds to the formation of copper oxide on the surface. In the presence of pine cone macerate, the inhibitory effect of the macerate is achieved in the area of potential A_1 with the addition of more than 20 mL, while in the area of potential A_2 and A_3 the pine cone macerate has an inhibitory effect at all investigated concentrations of pine cone macerate.

- The results of the potentiostatic measurement show that stabilization is achieved more quickly in the presence of pine cone macerate. The values of the steady-state current in the 0.5 mol/dm^3 NaCl solution in the presence of macerate are lower than the value of the steady-state current without the presence of macerate. This indicates that a protective film forms on the copper surface in the presence of the macerate, which slows down the copper oxidation process.

- Photomicrographs after potentiostatic treatment of copper in a 0.5 mol/dm^3 NaCl solution clearly show the presence of a green phase, representing copper chloride, and a black phase, representing copper oxide. When pine cone macerate is added, the photomicrographs show green and black phases on a smaller scale. This indicates that pine cone macerate acts as a copper corrosion inhibitor.

ACKNOWLEDGEMENTS

The research presented in this paper was done with the financial support of the Ministry of Education, Science and Technological Development of the Republic of Serbia, within the funding of the scientific research work at the University of Belgrade, Technical Faculty in Bor, according to the contract with registration no. 451-03-137/2025-03/200131.

REFERENCES

[1] M. Emad, M. AL-Rasheedi, J. Mater. Environ. Sci., 6 (1) (2015) 201-206.
[2] P. B. Raja, M. G. Sethuraman, Matt. Lett., 62, (2008)113–116.
[3] R.M. Palou, O.O. Homelt, N.V. Likhanova, Chapter 19, InechOpen, (2014) 431-463.
[4] Z. Stević, M. Rajčić Vujasinović, Hem. Ind., 61 (2007) 1-6.
[5] T. Kosec, I. Milosev, B. Pihlar, Appl. Surf. Sci., 253 (2007) 8863-8873.
[6] M. Rajčić Vujasinović, V. Grekulović, Z. Stević, D. Dragulović, S. Dimitrijević, Bakar, 41 (2) (2016) 35-40.

The 56th International October Conference on Mining and Metallurgy
22-25 October 2025, Bor Lake, Bor, Serbia
www.ioc.tfbor.bg.ac.rs

DOI: 10.5937/IOC25251K *Original scientific paper*

DTA THERMODYNAMIC BEHAVIOUR OF THE TERNARY SYSTEM Ga-Ge-Sb

Ana Kostov[1a], Aleksandra Milosavljević[1b], Ivan Jovanović[1c]

[1] Mining and Metallurgy Institute Bor, Alberta Ajnštajna 1, 19210 Bor, Serbia
[1a] ana.kostov@irmbor.co.rs, 0000-0001-6436-9091
[1b] aleksandra.milosavljevic@irmbor.co.rs, 0000-0003-3841-7357
[1c] ivan.jovanovic@irmbor.co.rs, 0009-0000-5174-3734

Abstract

Finding new types of materials, usually by modernizing classic materials by introducing and combining some of the new components within the already existing standard ones, based on improved and innovated classical materials, leads to the production of materials that are characterized by a complex of new features that enable a wide range of their practical applications.

It is widely known that rare metals such as gallium and germanium possess special features that are necessary for further progress in electronics. These materials are used in electrical engineering, radio engineering and electronics, in optical and electronic devices and instruments as functional materials for transistors, diodes, integral circuits, optical cables, conductors, rectifiers, etc. in atomic and astrophysical testing, aerospace industry, laser technology, sensors of neural networks, atomic reactors and the semiconductor industry.

Given the wide range of applications and use of these materials in almost all-important areas and techniques, there is a need for a more complete knowledge of the properties of not only these elements, but also the systems of which they are integral parts, from the aspect of their fuller description and thermodynamic determination.

Therefore, in this paper, research in the ternary system Ga-Ge-Sb will be presented in order to complete the thermodynamic description of the system. Its practical significance and application are mostly in the semiconductor industry, from the point of view of defining the thermodynamic quantities of the components constituting this system, as well as the results characterization of the thermodynamic behavior of the investigated alloys by DTA analysis of this system.

***Keywords**: ternary system Ga-Ge-Sb, DTA, thermodynamic*

1. INTRODUCTION

Gallium is element of the III group of the periodic table and represents elemental semiconductor element. It is often mixing with elements that belong to the V group of the periodic table especially with arsenic and form a lot number of compounds based on gallium arsenide, which is the materials used a lot in the laser technology, making CD and DVD devices, etc. [1] Also, a lot of compounds can be formed by combining III (Al, Ga, In) and V (Si, Ge, Sn) groups or II (Zn, Cd, Hg) and VI (S, Se, Te) groups of the periodic table and make combinations of elements that exhibit semiconductor properties. Some of those combinations and compounds possess special semiconductor properties and behavior's which enable their application and numerous branches of the electrical industry [2].

The knowledge of their special characteristics is necessary for the further progress in electronics and optoelectronics, because of their large use in optical and electronical devices as materials for semiconductors, transistors, optical cables, integrated circuits, power plants and space technologies [1,3]. Therefore, these materials and compounds are the subject of numerous investigations.

The phase equilibria in the systems Ga,Ge-Sb-Gd–Fe were investigated from Ivan Franko National University of Lviv in Ukraine [4] for the different content of elements at 500 ºC and the corresponding isothermal section of the phase diagram was constructed. The crystal structures of the few semiconductor compounds were refined.

Electrical and optical properties of Sb-rich nanoparticles for phase-change memory applications have been examined in Reference [5]. The results show that phase-change properties of Ge15Sb85 material still exist for nanoparticles of 8.0 nm size and Ge15Sb85 nanoparticles are a good candidate for phase-change memory applications in terms of long data retention time. The observed phase transition in Ge15Sb85 nanoparticles is promising for down scaling the size of phase change solid-state memory devices.

Chalcogenide glasses of $(GeSe4)_{1-x}Ga_x$ and $(GeSe5)_{1-x}Ga_x$ systems, with 5, 10, 15, 20 at % Ga were investigated as well as basic properties such as density, molar volume and compactness of the samples were calculated in Reference [6]. According to obtained properties and due to some unique optical and electrical phenomena, these materials are expected to be promising material in the IR optics, microelectronics.

Structural analysis of RF sputtered Ge-Sb-Se thin films by Raman and X-ray photoelectron spectroscopies are given in [7].

A phase diagram of the Ga–Ge–Sb ternary system was calculated by the CALPHAD approach, using only optimized thermodynamic parameters for the constitutive binary systems [8-13]. The CALPHAD method is based on constrained minimization of Gibbs energy for a given temperature, pressure and overall composition [14,15].

Considering the fact that the thermodynamic data for the Ga-Ge-Sb ternary system do not exist, the existing literature data mainly relate to the thermodynamic analysis of the binary systems as the constituents of the ternary system, which can also be concluded on the basis of the aforementioned literature review, there is a need for a complete thermodynamic determination of this ternary system as well as DTA analysis of the investigated ternary alloys in the aim to obtained thermodynamic values which after that will be used for calculation the phase diagram of the investigated ternary system.

2. EXPERIMENTAL

All experimental research whose results are presented in this paper, were carried out with pure metal gallium, germanium and antimony p.a. cleanliness. Weighed pieces of gallium, germanium and antimony were melted in the low-frequency induction furnace under argon inert gas atmosphere and cast in charcoal molds. First it was prepared pre-alloys: Ga-Ge and Ge-Sb, and after that from pre-alloys, the Ga-Ge-Sb alloys were made.

DTA experiments were performed on the Labsys EVO TG-DTA/DSC instrument (SETERAM). Experiments were carried out in an atmosphere of argon inert gas with pressure of 1,5 bar and in water cooling system. A constant heating rate was 5 ^{0}C/min.

3. RESULTS AND DISCUSSION

Six alloys of a certain composition and a constant volume of 1 cm^3 were selected from the concentration region of the Ga-Ge-Sb ternary system. The data of the selected alloys are given in Table 1.

DTA investigations of the selected alloys were performed at three different temperatures: 1073K, 1173K and 1273K. The activity, Gibbs energy of mixing and Gibbs excess energy for gallium were obtained. The diagram of dependence of the gallium activity from the composition at temperatures of 1073K, 1173K and 1273K is presented in Figure 1.

Table 1. Data of the selected alloys in Ga-Ge-Sb ternary system

Composition	%Ga	%Ge	%Sb
1	0	9.2	90.8
2	13.24	8.48	78.28
3	28.84	7.19	63.97
4	47.79	5.06	47.15
5	70.96	2.86	26.18
6	100	0	0

A negative deviation from Raoult's law was observed from the diagram. This indicates a good miscibility of the constituent components of the examined Ga-Ge-Sb ternary system and formation of alloys with good homogenous liquid alloys. The dependences of Gibbs energy of mixing and Gibbs excess energy from the compositions at temperatures 1073K, 1173K and 1273K are shown in Figures 2 and 3, respectively. The dependence of the integral Gibbs energy of mixing and the integral Gibbs excess energy in the Ga-Ge-Sb ternary system is shown in Figure 4.

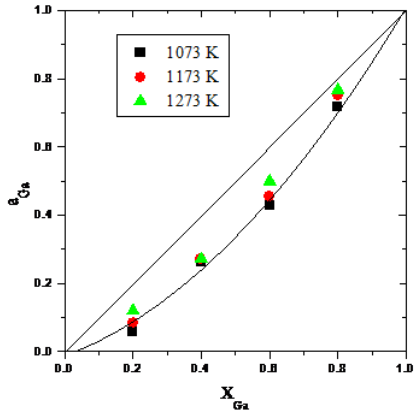

Figure 1. The dependence of gallium activity on the composition in the Ga-Ge-Sb ternary system at temperatures of 1073K, 1173K and 1273K

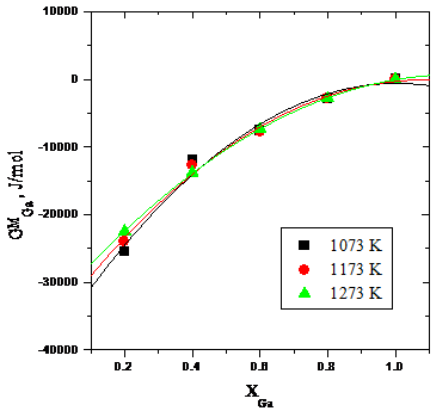

Figure 2. Dependence of Gibbs energy of mixing of gallium from the composition in the Ga-Ge-Sb ternary system at temperatures of 1073K, 1173K and 1273K

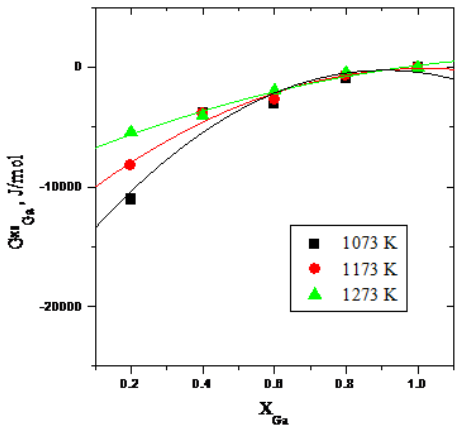

Figure 3. Dependence of Gibbs excess energy of gallium from the composition in the Ga-Ge-Sb ternary system at temperatures of 1073K, 1173K and 1273K

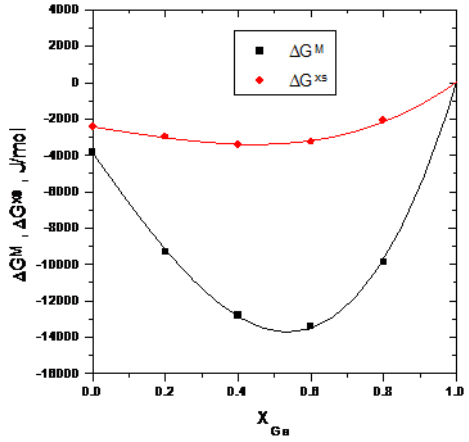

Figure 4. Dependence of integral molar Gibbs energy of mixing and excess energy in the Ga-Ge-Sb ternary system

A negative deviation from Raoult's law was observed, indicating good mixing of the component components in the Ga-Ge-Sb ternary system. Activity of gallium in the entire concentration range

are less than 1. With increasing gallium content, its activity is uniformly increasing at all investigated temperatures, which points to the fact that deviation from Raoult's law is less. Also, with increasing temperature for all investigated compositions, activity of gallium is increasing equally. The dependence of the partial Gibbs energy of mixing for gallium from the composition and temperature indicates that as the gallium content grows in the solution, the negativity of the given function increases with the temperature decreases. The obtained values of partial excess Gibbs energy for gallium, derived from known values for activity of gallium and confirm the conclusions about the behavior of this solution in relation to Raoult's law.

4. CONCLUSION

Obtained values for gallium activities show a negative deviation from Raoult's law throughout the concentration range. With the rise of mole content of gallium, activity of gallium increases uniformly. Dependence and compositions show a minimum in the composition $x_{Ga} \sim 0.4$, which corresponds to the eutecticum in the phase diagram of the Ga-Ge-Sb ternary system. Integral molar Gibbs excess energy along the whole area of the ternary system Ga-Ge-Sb has a negative value. The negativity of this function grows with gallium content. With the increase in the content of the components, the negativity of the function increases to $x_{Ga} = 0.2$, $x_{Ge} = 0.4$ and $x_{Sb} = 0.4$, and then decreases. It is noted that the minimum value is characteristic of the central part of the concentration triangle, and it can be expected that the mixing of the constituents in this part of the system is greatest.

ACKNOWLEDGEMENTS

This work was financially supported by the Ministry of Science, Technological Development and Innovations of the Republic of Serbia, Contract on Realization and Financing the Scientific and Research Work of the Mining and Metallurgy Institute Bor in 2025, Registration No. 451-03-136/2025-03/ 200052.

REFERENCES

[1] S.J. Pearton, F. Ren, Devices for High-Frequency Applications, Encyclopedia of Materials: Science and Technology, 2001, pp. 2101-2108.
[2] D.K. Schroder, Semiconductor Material and Device Characterization, Third Edition, John Wiley and Sons, Inc., Hoboken, New Jersey, 2006.
[3] M. Levinstein, S. Rumyantsev, M. Shur, Handbook Series on Semiconductor Parameters, Vol. 1, 2, World Scientific, London, 1996, 1999.
[4] V. Gvozdetskyi, N. German, R. Gladyshevskii, Visnyk of the Lviv University, Series Chemistry, 53 (2011) 12-19.
[5] S.T. Mahmoud, A.I. Ayesh, N.N. Qamhieh, S.J. Ahmad, J. Appl. Phys., 112 (3) (2012) 034308-034308-5.1.
[6] T. Petkova, Y. Nedevaa, P. Petkova, J. Optoelectron. Adv. M., 3 (4) (2001) 855-860.
[7] E. Baudet, C. Cardinaud, A. Girard, E. Rinnert, K. Michel, B. Bureau, V. Nazabal, J. Non-Cryst. Solids., 444 (2016) 64-72.
[8] I. Ansara, J.P. Bros, M. Gambino, Calphad, 3 (1979) 225-233.
[9] I. Ansara, C. Chalillon, H.L. Lukas, T. Nishizawa, H. Ohtani, K. Ishida, M. Hillert, T.G. Chart, T. Anderson, Calphad, 18 (2) (1994) 177-222.
[10] P.Y. Chevalier, Thermochim. Acta, 155 (1989) 227-240.
[11] J. Wang, C. Leinenbach, M. Roth, J. Alloys Compd., 485 (2009) 577–582.
[12] N. Nasir, A. Grytsiv, P. Rogl, A. Saccone, G. Giester, J. Solid State Chem., 182 (2009) 645–656.
[13] J. Liu, C. Guo, C. Li, Z. Du, Thermochim. Acta, 520 (2011) 38–47.
[14] N. Saunders, A.P. Miodownik, Calphad (A Comprehensive Guide), Elsevier, London, 1998.
[15] H.L. Lukas, S.G. Fries, B. Sundman, Computational Thermodynamics: The Calphad Method, Cambridge University Press, Cambridge, UK 2007.

The 56th International October Conference on Mining and Metallurgy
22-25 October 2025, Bor Lake, Bor, Serbia
www.ioc.tfbor.bg.ac.rs

DOI: 10.5937/IOC25255A *Original scientific paper*

INNOVATIVE OXIDATIVE SYSTEM FOR LEACHING OF Fe^{2+} FROM SPHALERITE CONCENTRATE

Dimitrije Anđić[1a], Aleksandar Jovanović[1b], Nikola Vuković[1c], Ivana Jelić[1d], Mladen Bugarčić[1e], Vaso Manojlović[2a], Miroslav Sokić[1f]

[1] Institute for Technology of Nuclear and Other Mineral Raw Materials, Belgrade, Serbia
[2] University of Belgrade, Faculty of Technology and Metallurgy, Belgrade, Serbia
[1a] d.andjic@itnms.ac.rs, 0009-0001-6824-5202
[1b] a.jovanovic@itnms.ac.rs, 0000-0001-9867-9282
[1c] n.vukovic@itnms.ac.rs, 0000-0002-3607-5907
[1d] i.jelic@itnms.ac.rs, 0009-0000-9901-9323
[1e] m.bugarcic@itnms.ac.rs, 0000-0002-6119-4414
[2a] v.manojlovic@tmf.ac.bg.rs, 0000-0002-3009-2909
[1f] m.sokic@itnms.ac.rs, 0000-0002-4468-9503

Abstract
Sphalerite is a sulfide zinc mineral, which also contains supporting metals such as iron, copper and lead. In this work, we dealt with the extraction of iron from sphalerite in a new oxidation system. Manganese dioxide was used as the primary oxidant, and KI was used as a secondary oxidizing agent with the aim of creating an I_2/I^- oxidation cycle in a sulfuric acid medium. The thoughtful characterization (XRD, SEM, EDS) of the initial sample, as well as the precipitate formed after leaching was done. During the leaching tests, process parameters were varied.

***Keywords**: hydrometallurgy, chemical oxidation, leaching efficiency*

1. INTRODUCTION

Sphalerite is often found in a dispersed form alongside other sulfide minerals and tailings, characterized by a complex mineralogical composition and fine-grained texture. It can appear as impregnations, inclusions, and both simple and complex intergrowths within the ore matrix. Conventional hydrometallurgical techniques typically involve leaching sphalerite concentrates in an acidic medium, most commonly sulfuric acid combined with various oxidants. These processes enhance metal recovery while also minimizing air pollution risks. The main byproducts of these reactions include sulfuric acid and/or elemental sulfur, along with the formation of soluble sulfate salts. However, due to the inherent resistance of sphalerite in acidic solutions, oxidizing agents are required to promote its oxidative dissolution [1]. In addition to sphalerite, the concentrate may contain trace amounts of other metals, such as iron, which is most commonly present in the form of pyrite. The chemical composition of pyrite is iron (II)-sulfide (FeS_2), which contains 46.6 % Fe and 53.4 % S [2]. When leaching sulfides with sulfuric acid, oxygen or some other compound with very strong oxidizing abilities (H_2O_2, MnO_2, $KMnO_4$...) can be used as an oxidant [3, 4]. A. Chandra et al. [5] found that pyrite leaching occurs more slowly when sulfuric acid is used as leaching agent. Therefore, the goal of this work is to introduce a new oxidation system (MnO_2-KI) during the leaching of sphalerite with sulfuric acid, in order to increase the extraction yield of iron.

2. EXPERIMENTAL

Zinc concentrate was taken from the ore deposit "Rudnik" (Rudnik), Serbia. Prior leaching tests, the concentrate was ground with a vibro mill (KHD Humboldt Wedag AG, Germany). Chemicals used for experiments are manganese dioxide (Alkaloid, purity > 95%, North Macedonia) and

potassium iodide (Merck, purity > 95%, Germany) and 1.5 M analytically prepared sulfuric acid solution (Zorka, PA, Serbia).

2.1. Structural characterization

Surface morphology was determined by scanning electron microscopy (SEM) using a JEOL JSM-7001F (Japan) instrument coupled with an energy-dispersive spectrometer (EDS) (Oxford Xplore 15, UK). Additional structural insights were gained through qualitative ore microscopic analyses conducted with a polarizing microscope (Carl Zeiss-Jena Axioscope 5 Pol, Germany). The microscope featured a color camera (Axiocam 105 color, USA), and photomicrographs were captured using the Carl Zeiss AxioVision SE64 Rel. 4.9.1 software with the "Multiphase" module. The mineral compositions of the concentrate and leaching residues were analyzed using X-ray diffraction (XRD) to determine the phase composition (Philips PW 1710/1820, Netherlands).

2.2. Leaching experiments

For leaching experiments, a 1.2 dm^3 glass reactor (Zhengzhou Great Wall, China) was employed. Detail experimental procedure of all leaching tests was presented in work of Bugarčić et al. [5]. At specified intervals, aliquots were taken and analyzed using atomic absorption spectrophotometry (AAS, PERKIN ELMER 703, USA). The AAS results were used to calculate the iron extraction rate (%).

3. RESULTS AND DISCUSSION

3.1. Materials characterization

Under the optical microscope (Figure 1), it was noted that around 80 % of the sphalerite exists as free grains, while the rest is found in simple to complex intergrowths with other minerals. Chalcopyrite is the mineral most commonly associated with sphalerite in this concentrate, followed by pyrite, galena, gangue minerals, and chalcopyrite impregnations. The size of the sphalerite grains ranges from approximately 10 μm to more than 350 μm.

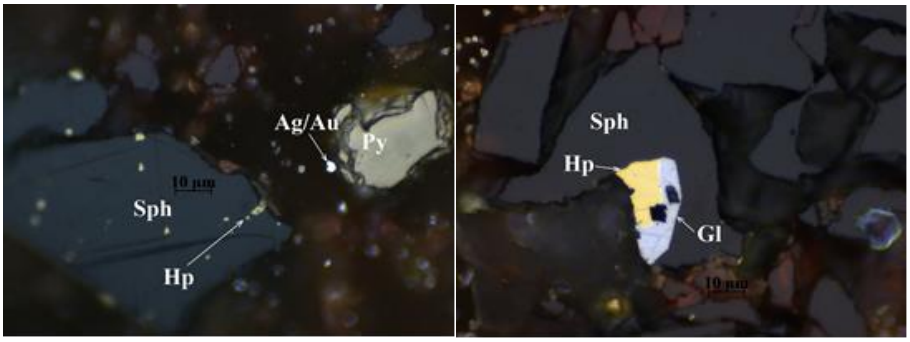

Figure 1. Native silver/gold (Ag/Au) next to pyrite (Py) in the Zn concentrate sample (left subfigure) and complex assemblage of sphalerite (Sph), chalcopyrite (Hp) and galena (Gl) in the Zn concentrate sample (right subfigure)

The minerals identified in the examined sample by XRD included sphalerite, chalcopyrite, pyrite and quartz (Figure 2). Sphalerite was by far the most dominant mineral, while chalcopyrite, pyrite, and quartz were present in much smaller quantities.

The SEM image (Figure 3) reveals that the concentrate particles have distinct, smooth edges. Constituents are in the diameter range 50 – 100 μm.

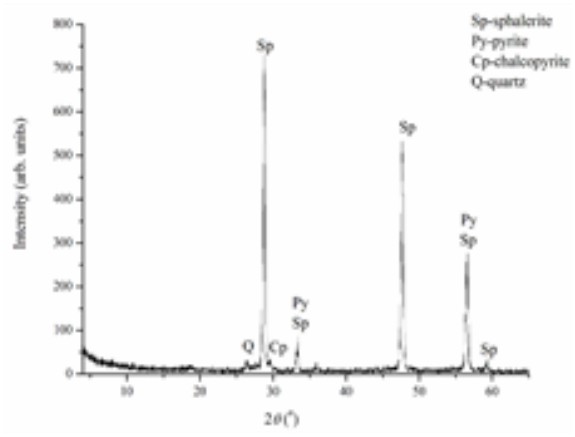

Figure 2. Powder diffractogram of the ZnS sample [6]

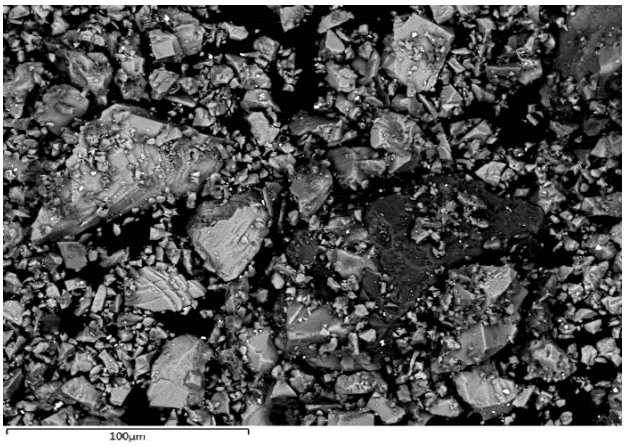

Figure 3. SEM micrograph of ZnS sample

3.2. Leaching experiments

The leaching efficiency of iron (Fe) from zinc concentrate rises with temperature, ranging from 40 °C to 80 °C. Increased temperatures provide extra thermal energy, promoting particle movement and increasing the frequency of effective collisions between sulfide minerals and the intermediary oxidant (I_2). This leads to more efficient leaching of iron from zinc concentrate.

Figure 4. shows the XRD analysis of the precipitate after leaching the zinc concentrate at lower temperatures.

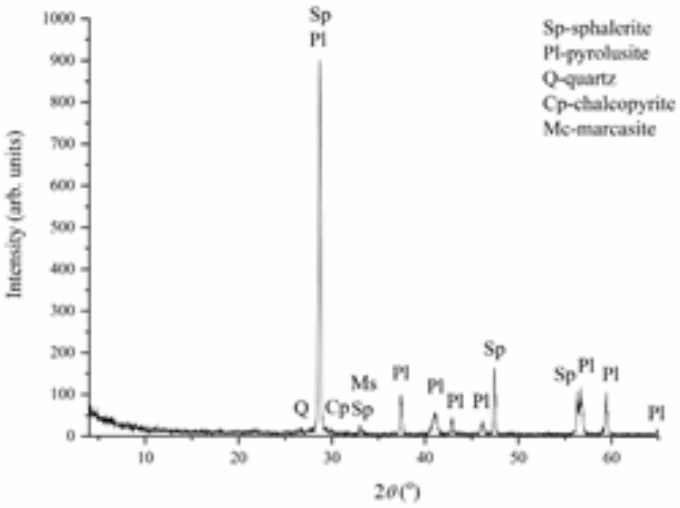

Figure 4: XRD pattern with legend for leaching residue; experiment parameters (3 wt. % KI + stoichiometric amount of MnO_2 at 40 °C) [6]

Based on the qualitative mineralogical composition, it can be concluded that the most abundant phase in the precipitate after leaching is pyrolusite. After pyrolusite - 54.3 wt.%, the most abundant is sphalerite - 41.2 wt.%, followed by quartz - 0.8 wt.%, chalcopyrite - 1.1 wt.%, and marcasite - 1.0 wt.%.

The microscopic image (Figure 5) clearly shows that, in addition to the phases that make up the initial concentrate, pyrolusite is also present in the precipitate largely.

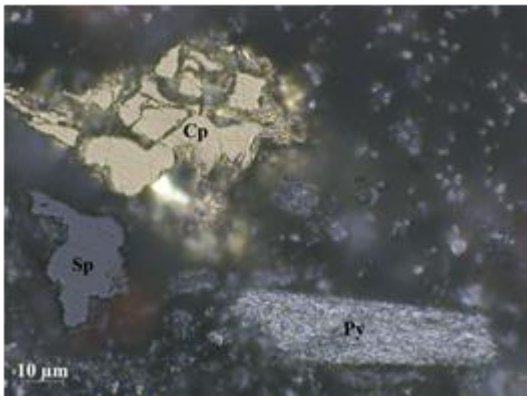

Figure 5. Liberated grains of sphalerite (Sp), chalcopyrite (Cp) and pyrolusite (Pl)

Using the XRD method (Figure 6), was established that elemental sulfur is released during leaching at a high temperature (80 ^{o}C). The explanation for this phenomenon is that the crystallization and formation of elemental sulfur is temperature dependent. At elevated temperatures, oxidation reactions lead to rapid migration of sulfur atoms from the sphalerite surface, where they are grouped into crystal structures.

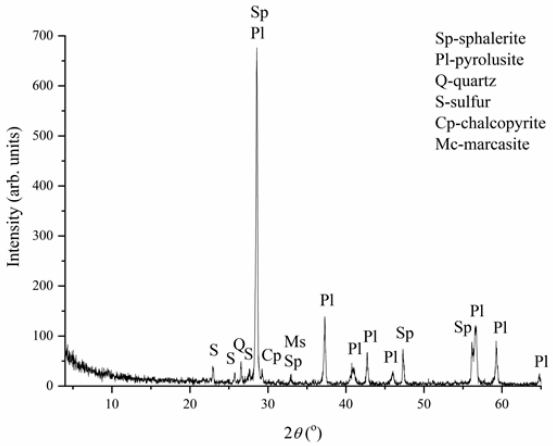

Figure 6: XRD pattern with legend for leaching residue; experiment parameters (3 wt. % KI + stoichiometric amount of MnO_2 at 80 °C) [6]

Based on Figure 6, it can be seen that the most abundant phase in the analyzed sample is pyrolusite, and below it is sphalerite, quartz, sulfur, chalcopyrite and marcasite. In Figure 7, we can see that elemental sulfur is separated in the form of irregular grains.

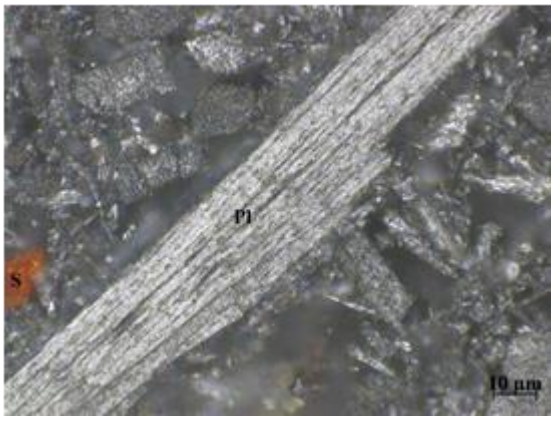

Figure 7. Irregular grain of sulfur [6]

Figure 8 shows the influence of temperature and time on the degree of leaching of Fe and sphalerite concentrate. Based on the obtained results, we can conclude that the degree of iron leaching

increases with the increase in temperature. The reason for this is that with an increase in temperature, the particles move faster, and therefore the leaching agent comes into contact with a larger number of particles of the initial concentrate, and thus the degree of valorization of iron increases. According to the identical principle, time has an influence on the degree of iron leaching.

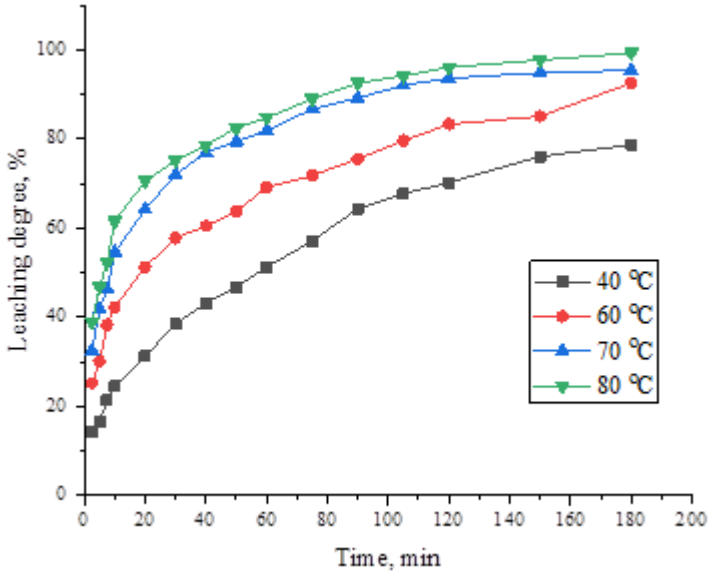

Figure 8. Influence of temperature and reaction time on leaching degree of Fe (3 wt. % KI + stoichiometric amount of MnO_2)

4. CONCLUSION

This research examined the dissolution characteristics of iron (Fe) from sphalerite concentrates in a sulfuric acid solution, utilizing manganese dioxide (MnO_2) as the main oxidizing agent. The process was conducted at temperatures ranging from 40 °C to 80 °C under atmospheric pressure, with the presence of potassium iodide (KI). Increasing the temperature enhanced Fe leaching efficiency due to faster reaction kinetics. However, XRD analysis identified crystalline sulfur phases at 80 °C, whereas no such phases were observed at 40 °C. This suggests that higher temperatures facilitate the crystallization of elemental sulfur, leading to the formation of detectable crystalline structures. In contrast, at lower temperatures, sulfur remains in an amorphous or finely dispersed form, which is not detectable by XRD but can be observed using reflected light microscopy. This research leaves the possibility of finding a new system that would enable the maximum degree of valorization of iron from sphalerite concentrate.

ACKNOWLEDGEMENTS

This work was supported by the Ministry of Science and Technological Development and Innovation of the Republic of Serbia (Contract No. 451-03-136/2025-03/200023).

REFERENCES

[1] M. Sokić, M. Bugarčić, A. Jovanović, MMD, 1 (2023) 33–43.
[2] S. Janjić, P. Ristić, Mineralogija, Naučna knjiga, Beograd, 1995, 217.
[3] M. Sokić, The mechanism of leaching of polymetallic Pb-Zn-Cu concentrates with sulfuric acid in the presence of selected oxidants. TMF UB 2008.
[4] S. Aydogan, J. Chem. Eng., 123 (2006) 65–70.
[5] A.P. Chandra, A.R. Gerson, GCA 75 (22) (2011) 6893-6911.
[6] M. Bugarčić, A. Jovanović, D. Anđić, I. Jelić, M. Miletić, B. Marković, M. Sokić, Metals, 15 (1) (2025) 50.

The 56th International October Conference on Mining and Metallurgy
22-25 October 2025, Bor Lake, Bor, Serbia
www.ioc.tfbor.bg.ac.rs

DOI: 10.5937/IOC25260T *Original scientific paper*

BEHAVIOR OF ZINC, CALCIUM AND IRON IN THE TWO-STAGE LEACHING PROCESS OF THE EAF DUST

Vanja Trifunović[1a], Snežana Milić[2a], Ljiljana Avramović[1b], Dragana Božić[1c], Zoran Avramović[1d]

[1] Mining and Metallurgy Institute Bor, Alberta Ajnštajna 1, 19210 Bor, Serbia
[2] Technical Faculty Bor, University of Belgrade, V.J. 12, 19210 Bor, Serbia
[1a] vanja.trifunovic@irmbor.co.rs, 0000-0003-4839-8751
[2a] smilic@tfbor.bg.ac.rs, 0000-0002-5000-9156
[1b] ljiljana.avramovic@irmbor.co.rs, 0000-0002-3747-1530
[1c] dragana.bozic@irmbor.co.rs, 0000-0003-1055-8449
[1d] zoran.avramovic@irmbor.co.rs, 0009-0006-7585-976X

Abstract

The treatment of the EAF dust was carried out by applying the leaching process in two technological stages in order to selectively separate certain components from the EAF dust. In the first stage, a pre-treatment was performed to selectively remove water-soluble components from the original EAF dust sample, while in the second stage, zinc was selectively separated from the resulting solid residue by acid leaching. In the second stage of the leaching process, the influence of the acid leaching process time on the zinc, calcium and iron leaching rates were investigated. Selective zinc recovery from the EAF dust was achieved with the following optimal parameters of the acid leaching process: leaching reagent 1.0 M solution of H_2SO_4, ambient temperature, S:L ratio =1:4, time 10 min and stirring speed 500 rpm. The zinc leaching rate in the second leaching stage was 60.74%, while the Ca and Fe leaching rates were significantly lower and amounted to 12.18% and <0.01%, respectively.

***Keywords**: EAF dust, two-stage leaching, selectivity*

1. INTRODUCTION

In steel production, as in other branches of industry, waste is generated. The production of steel in electric arc furnaces, for which scrap iron is used as a batch, generates electric arc furnace dust (EAF dust) as an intermediate product of the process. During the production of 1 t of crude steel, 10-20 kg of EAF dust containing Zn, Fe, Pb, Cl, Ca, Na, K, Cr, Mg, Mn, Ni, Si, Cd and others is obtain [1-4]. If the EAF dust is disposed of in an inadequate way, due to the action of atmospheres, the heavy metals contained in it may self-leach and have a negative impact on the environment. For this reason, EAF dust has been characterized worldwide as a hazardous industrial solid waste [5-7]. Despite the harmful characteristics of the EAF dust, there are several benefits of its further treatment. The first is environmental protection, with the aim of reducing hazardous waste or its transformation into non-hazardous waste, as well as its safe disposal at a landfill. Another benefit is the valorization of valuable metals present in the EAF dust, primarily zinc, and the achievement of [1,2,5]. Treatment of the EAF dust can be carried out in three ways, namely by: hydrometallurgical, pyrometallurgical or combined process which represents a combination of elements of both previous processes [2-5,7].

The application of the pyrometallurgical process for the EAF dust treatment leads to the consumption of a large amount of energy, because the processes take place at high temperatures and it is not possible to apply it to raw materials with a zinc content lower than 15%. The product obtained by applying this process - ZnO, has little commercial value [3,8]. On the other hand, the hydrometallurgical process takes place at temperatures lower than 100°C, and is applied to raw materials with a low zinc content, using low-cost and easily available chemicals, and the obtained product is of high quality. The hydrometallurgical process includes three technological stages:

leaching, purification of the pregnant leaching solution and recovery of metals or compounds from the purified pregnant leaching solution [2-4,7].

In this paper, the chemical and mineralogical characterization of the original EAF dust sample was carried out, and then the two-stage leaching process of the EAF dust was investigated, which aimed to selectively separate zinc into the pregnant leaching solution, with minimal extraction of other components, in the paper, iron and calcium.

2. EXPERIMENTAL

2.1 Chemical and mineralogical characterization of the original EAF dust sample

The chemical composition of the original EAF dust sample was performed using an Atomic Absorption Spectrophotometer, brand Perkin Elmer PinAAcle 900F (USA), and an Inductively Coupled Plasma Atomic Emission Spectroscopy (ICP-AES), brand Spectro Ciros CCD/Vision (Germany). X-Ray diffractometer (XRD), model RigakuMiniFlex 600 (Japan) was used for mineralogical characterization of the original EAF dust sample.

2.2 Two-stage leaching of the EAF dust

The aim of the two-stage leaching process of the EAF dust is to leach zinc, with minimal leaching of other components that will contaminate the zinc solution and further make difficult its recovery as a final product. The leaching process investigated in this paper was carried out in a glass reactor with a volume of 2L, in two stages. The first stage was pretreatment of the EAF dust - water leaching, and the second stage - acid leaching of the solid residue obtained after the pretreatment. In the pretreatment stage of the EAF dust, the original EAF dust sample was leached with distilled water, in order to selectively separate water-soluble components from the EAF dust. The pretreatment was carried out at ambient temperature, with a ratio of solid to liquid phase of 1:10, in time of 30 minutes, at a stirring speed of 500 rpm, as defined in the investigation of the authors Trifunović et al. [1]. The second stage of the EAF dust leaching process was the acid leaching of the solid residue obtained after the applied pretreatment. In this stage, the influence of the leaching time (5, 10, 15, 20, 30 and 60 minutes) on the zinc, calcium and iron leaching rates were investigated. The experimental investigations were carried out at ambient temperature, with a ratio of solid to liquid phase 1:4, stirring speed 500 rpm, and sulfuric acid with an initial concentration of 1.0 M was used as the leaching reagent. The applied acid leaching process parameters are similar to the process parameters in the investigations of other authors [4,5]. The goal of this leaching stage was the selective separation of zinc, with a significant leaching rate, and with as little leaching rate of iron and calcium, present in the EAF dust.

3. RESULTS AND DISCUSSION

The chemical composition of the original EAF dust sample indicated the content of the following elements: Zn - 36.40%; Fe - 21.58%; Ca - 3.02%; Pb - 1.86%; Na - 1.18% and others, with a significantly smaller share. The mineralogical phases of the original EAF dust sample, determined by XRD analysis, are presented in Figure 1. Four phases were identified, namely: franklinite ($ZnFe_2O_4$), magnetite (Fe_3O_4), zincite (ZnO) and simonkolleite ($Zn_5(OH)_8Cl_2 \cdot H_2O$). Franklinite, magnetite and zincite occur as the main phases, while simonkolleite was the least abundant phase of the EAF dust. The obtained results of the XRD analysis for the identified mineralogical phases of the analyzed EAF dust are in agreement with the literature [1-3,5].

With the first stage of the two-stage leaching process the selective separation of water-soluble components from the EAF dust, that is, Cl, Na and K. Zinc and iron after the pretreatment remain in the solid residue completely, while Ca in it was about 90% of the initial amount in the original EAF dust sample. The amount of Ca in the solid residue, in the investigated EAF dust, is most likely in the form of compounds that are not soluble in water, such as $Ca(OH)_2$ and $CaSO_4$. The

same conclusion is reached by Montenegro et al. [4] and Al-Harahshes et al. [8] in their investigations, in which they applied a pretreatment, leaching the EAF dust with water.

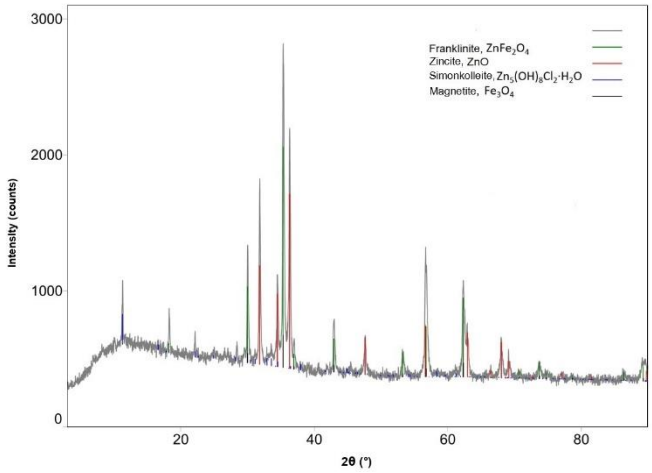

Figure 1. Diffractogram of the original EAF dust sample

Chemical analysis of the solid residue obtained from the pretreatment of the EAF dust determined the following contents: Zn - 39.4%; Fe - 23.37%; Ca - 2.70%; Pb - 2.02%; Na - 0.27% and very low concentrations of other elements.

The application of the pretreatment leads to a number of advantages for the next stage of the leaching process. Contamination of the pregnant leaching solution with water-soluble components is avoided, there is a mass reduction of about 6% compared to the mass of the initial sample, and the consumption of sulfuric acid in the next stage of acid leaching is also reduced. Figure 2 presents the zinc, calcium and iron leaching rates depending on the time of the sulfuric acid leaching process.

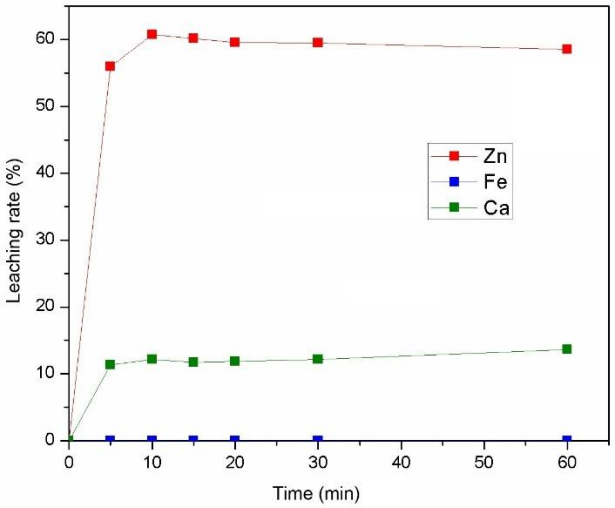

Figure 2. Zinc, calcium and iron leaching rates depending on the time of the acid leaching process

Based on the obtained results, it can be concluded that the highest level of zinc leaching was achieved after 10 minutes of the acid leaching process and is 60.74%. Further, with time, the zinc leaching rate decreases slightly. A calcium leaching rate of 12.18% is also achieved after 10 minutes of the leaching process, it decreases to 11.70% at 15 minutes, and with further time, at 60 minutes it is 13.60%. The iron leaching rate, at all investigated times of the acid leaching process, was negligible, amounting to less than 0.01%. The chemical and mineralogical composition of the EAF dust affects the leaching rates of elements, as do the leaching process conditions. With the application of elevated temperatures and higher acid concentrations, it is likely that the Fe leaching rate would increase. Given that in this paper there are no significant changes in the leaching rates

of zinc, calcium and iron after 10 min, this time can be considered the optimal parameter of the acid leaching process, which achieves the selective separation of zinc from the EAF dust, with minimal leaching of other components.

The reactions of zinc, iron and calcium compounds from the EAF dust with sulfuric acid can be described by the following equations [5]:

$$ZnO + H_2SO_4 = ZnSO_4 + H_2O \quad (1)$$
$$ZnFe_2O_4 + 4H_2SO_4 = ZnSO_4 + Fe_2(SO_4)_3 + 4H_2O \quad (2)$$
$$Fe_3O_4 + 3H_2SO_4 = Fe_2(SO_4)_3 + 3H_2O \quad (3)$$
$$Ca(OH)_2 + H_2SO_4 = CaSO_4 + H_2O \quad (4)$$
$$CaCO_3 + H_2SO_4 = CaSO_4 + H_2O + CO_2 \quad (5)$$

In a study by Montenegro et al. [4] after the pretreatment (water leaching), the solid residue was leached with a 1.0 M solution of H_2SO_4, at a ratio of S:L=20%, for 20 min, at a stirring speed of 500 rpm. The zinc leaching rate was 74%, while the iron leaching rate in the investigation of these authors was 8%. Kukurugya et al. [5] in their investigation of the acid leaching process monitored the leaching rates of Zn, Fe and Ca at concentrations of H_2SO_4 from 0.05 to 1.0 M, at the ratio S:L=50, at temperatures from 20 to 95°C, for times: 1, 5, 10, 15, 30, 60 and 90 min. The maximum zinc leaching rate of 87% was achieved with a concentration of H_2SO_4 of 1.0 M, at a temperature of 80°C and for a time of 60 min.

4. CONCLUSION

The results of the experimental investigations in this paper showed that the selective separation of Zn from the investigated EAF dust can be achieved by applying the two-stage leaching process. In the first stage, the pretreatment stage, the removal of water-soluble components from the original EAF dust sample is achieved, while in the second stage, by acid leaching of the solid residue obtained after the pretreatment, with appropriate process parameters, Zn is selectively separated, in the amount of 60.74%, with low levels of Ca and Fe leaching. The Fe leaching rate is determined by the chemical and mineralogical composition of the EAF dust, as well as the process parameters. It is likely that a higher leaching rates would be achieved by applying more rigorous leaching conditions, i.e. higher temperatures and acid concentrations. In the second stage of acid leaching, the optimal process parameters in this paper were: 1.0 M solution of H_2SO_4 as leaching agent, ambient temperature, S:L ratio =1:4, time 10 min and stirring speed 500 rpm.

ACKNOWLEDGEMENTS

The authors are grateful to the Ministry of Education, Science and Technological development of the Republic of Serbia for financial support according to the contract with the registration number 451-03-136/2025-03/200052 and number 451-03-137/2025-03/200131.

REFERENCES

[1] V. Trifunović, S. Milić, Lj. Avramović, M. Bugarin, S. Đorđievski, M.M. Antonijević, M.B. Radovanović., Metals, 14 (2024) 426.
[2] V. Trifunović, S. Milić, Lj. Avramović, R. Jonović, V. Gardić, S. Đorđievski, S. Dimitrijević., Hem. Ind., 76 (4) (2022) 237-249.
[3] J. Gamutan, S. Koide, Y. Sasaki, T. Nagasaka., J. Environ. Chem. Eng., 12 (2024) 111789.
[4] V. Montenegro, S. Agatzini-Leonardou, P. Oustadakis, P. Tsakiridis., Waste Biomass Valorization., 7 (6) (2016) 1531–1548.
[5] F. Kukurugya, T. Vindt, T. Havlík., Hydrometallurgy, 154 (2015) 20–32.
[6] P.K. Hazaveh, S. Karimi, F. Rashchi, S. Sheibani., Ecotoxicol. Environ. Saf., 202 (2020) 110893.
[7] J. Wang, Y. Zhang, K. Cui, T. Fu, J. Gao, S. Hussain, T.S. AlGarni., J. Cleaner Prod., 298 (2021) 126788.
[8] M. Al-Harahsheh, Y. Orabi, S. Al-Asheh., J. Environ. Chem. Eng., 9 (2021) 105410.

The 56th International October Conference on Mining and Metallurgy
22-25 October 2025, Bor Lake, Bor, Serbia
www.ioc.tfbor.bg.ac.rs

DOI: 10.5937/IOC25264P *Original scientific paper*

CREATION OF SINTERING CUP FOR LABORATORY SINTERING INSTALLATION

Petar Petrov

Faculty of metallurgy and material science, University of chemical technology and metallurgy,
8 "St. Kliment Ohridski" blvd., 1756, Sofia, Bulgaria
pbpetrov@uctm.edu, 0009-0006-6957-0097

Abstract
Globally, not all ores and concentrates in the field of ferrous metallurgy meet the requirements for direct processing into a final product. The concentrates obtained as a result of various enrichment operations, the fines from ore extraction, throat dust and others must be agglomerated before their next use. The importance of the sintering method has grown especially much due to the use of ever-increasing quantities of iron concentrates. On the other hand, the agglomerated products, which have sufficiently high strength, uniform granulometric and chemical composition, allow for the intensification of the blast furnace process. In the Republic of Bulgaria, there is currently no capacity for the production of agglomerated product for ferrous metallurgy. This limits the possibility of modern research on the sintering process of waste materials, such as throat dust from steelmaking, fine scale from rolling production, fine fractions of promising raw materials for our country, etc. In this regard, at the University of Chemical Technology and Metallurgy, Sofia, Department of Metallurgical Technologies, Electrical Engineering and Electronics, there is potential for experimentation in laboratory conditions on the agglomeration of fine raw materials of importance in metallurgy. However, it is necessary to create agglomeration equipment suitable for laboratory conditions. The aim of the development is to design and create a compact sintering cup as the first stage of the creation of a laboratory sintering installation.

Keywords*: design and creation of a laboratory sintering cup*

1. INTRODUCTION

To design the elements of the sintering assembly unit (consisting of a cup, a collector and a stand), specialized literature was used, as well as an available semi-industrial sintering installation located in a laboratory hall at the Department of Metallurgical Technologies, Electrical Engineering and Electronics [1 - 4]. When determining the dimensions of the individual elements, the available technological space in the room where the sintering cup will be used was taken into account - a laboratory at the same department. The volume of the cup must meet the needs of the furnace units in the laboratory, in terms of the volumetric amount of charge that they can process. The elements of the cup and the collector must be made of a steel billet with a thickness of at least 3 mm, suitable for welding [5, 6].

2. EXPERIMENTAL

After careful analysis, it was found that it was necessary for the upper square section of the sintering cup to be 100 x 100 mm in size, and the lower one to be 80 x 80 mm. The height of the cup was determined to be 170 mm. This would form an effective working volume of 1000 cm^3. With regard to the collector, a constant square section of 100 x 100 mm in size was determined. Its height should be 140 mm [7 - 9]. The stand for the assembled unit should ensure relatively quick disassembly and relocation of the equipment for cleaning, repair, etc. It should be calculated so that the distance from the bottom of the collector to the base, where the assembled sintering unit will stand, is at least 50 mm [10]. Another key point in the design is to provide space for a sealing element between the cup and the collector. Therefore, it is necessary to have a rim of a certain width, both at the lower edge of the cup and at the upper edge of the collector. It is also planned

that the cup will be removable after the end of the temperature process, but during the process it will be firmly assembled to the collector. This leads to the creation of holes in the mentioned sides and their adhesion to each other by means of washers with metric bolts and nuts. The temperature reading and the vacuum reached will be controlled by thermocouples and a manometric system, for which holes will also be provided [10, 11]. Last but not least, it is necessary to create a hole in one of the walls of the agglomeration collector, through which air will seep through the agglomerating layer. The diameter of the hole is set to be up to 50 % of the height of the collector wall, and a pipe of the appropriate size with a flange to it will be attached to it for the purpose of further connecting the agglomeration unit with the rest of the agglomeration installation. It is necessary to create a grid between the cup and the collector to prevent the entrainment of larger particles from the batch as a result of the vacuum created under the grid during sintering [11].
As a result of the research study conducted, the individual elements of the agglomeration aggregate were schematically created, shown in points 2.1, 2.2 and 2.3.

2.1 Schematic representation of the elements of the sintering cup

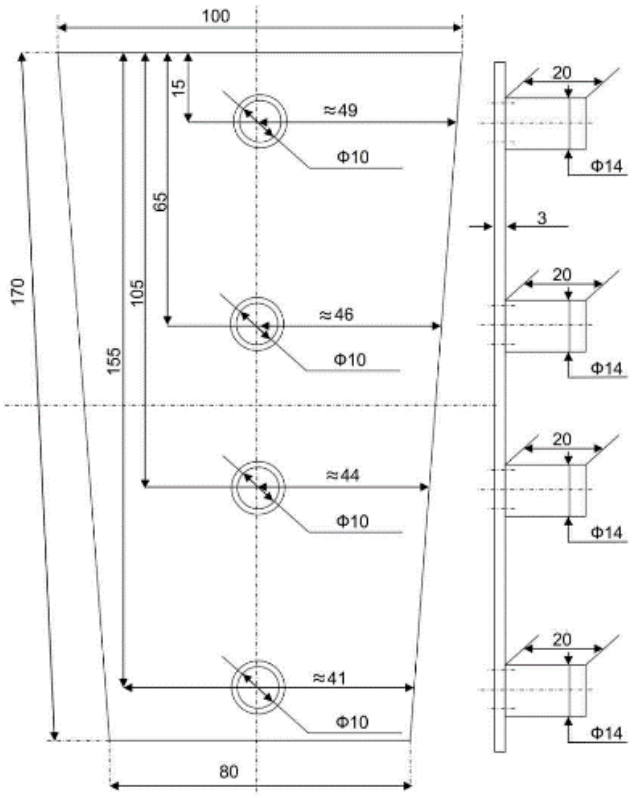

Figure 1. Wall (front) with thermocouple connections

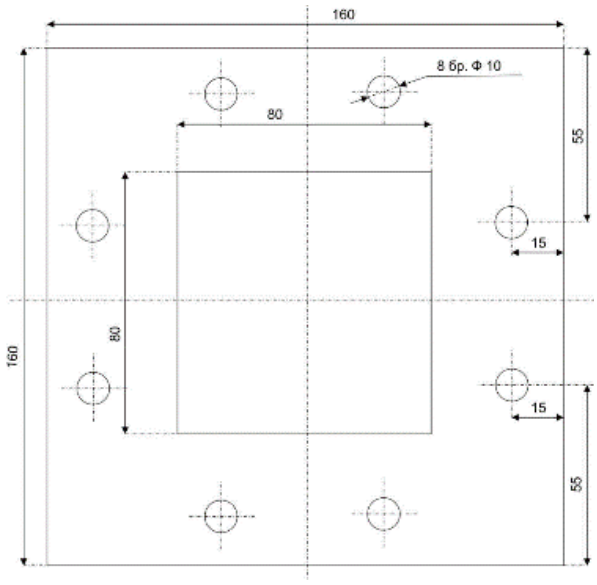

Figure 2. Wall (side) with handle, 2 pcs.

The back wall is designed like the front wall, but without the thermocouple connections.

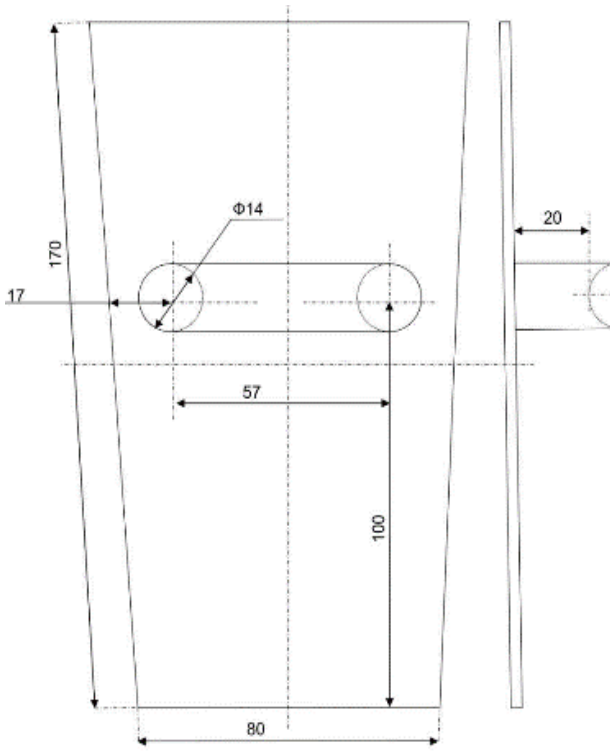

Figure 3. Bottom rim

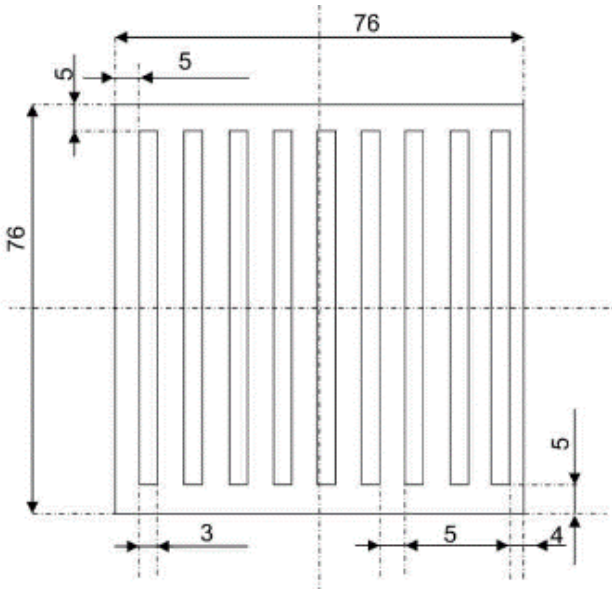

Figure 4. Grid

The upper rim is like the bottom rim, except for the eight holes, which are not needed, and the internal dimensions are 100 x 100 mm.

2.2 Schematic representation of the elements of the sintering collector

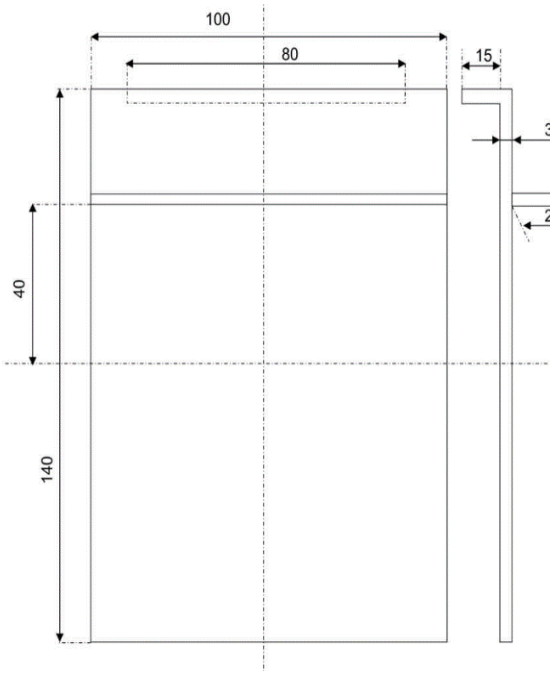

Figure 5. Wall (front and rear) with bases for grid and stand, 2 pcs.

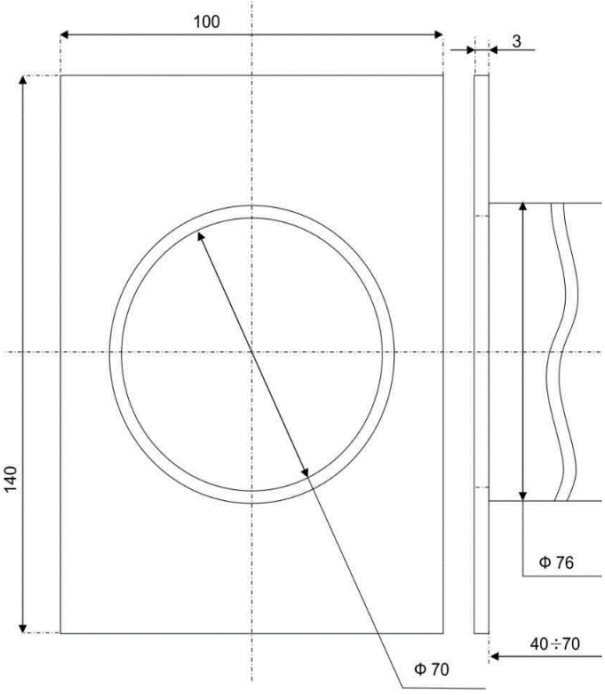

Figure 6. Wall (side) with outlet to filter

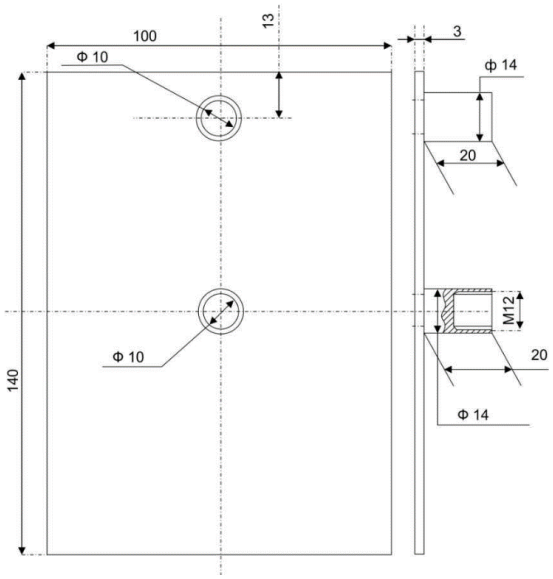

Figure 7. Wall (side) with connections for pressure gauge and thermocouple

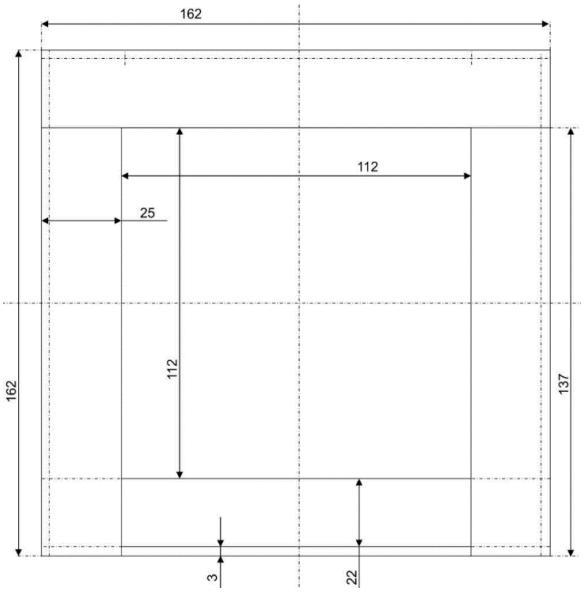

Figure 8. Stand – top view

The bottom of the sintering collector is designed as a flat square plate with dimensions of 110 x 110 mm.
The collector has one rim with the same dimensions as in Fig. 3, with the inner square opening measuring 100 x 100 mm.

2.3 Schematic representation of a stand

The total height of the stand is set to be 190 mm, and the distance from the base to the top is 165 mm.

3. RESULTS AND DISCUSSION

In accordance with the designdocumentation and with the help of a cutting machine, a series of cut-out boards were made, representing blanks for assembling the cup, collector and stand, Fig. 9.

Figure 9. Cutting of steel plates

Figure 10. Forming the necessary holes for thermocouples, pressure gauge and exhaust gases

The fabrication of the holes for thermocouples, pressure gauge and exhaust gases is presented in Fig. 10.
Using a welding machine, the individual cut-out panels were joined to form a sintering cup, collector, and stand for them, shown in Fig. 11.

Figure 11. Welding of elements according to the design

Figure 12. Assembled sintering facility

The final stage of the fabrication is the assembly of the sintering unit, using bolts and nuts through the rimes of the cup and the collector. The assembly is shown in Fig. 12.

4. CONCLUSION

A small sintering cup with the possibility of application in laboratory conditions has been designed and created. The compact size of the facility is expected to intensify research activities related to sintering of fine fractions of materials, which are raw materials for metallurgy. Using the cup in a laboratory will allow students to become practically acquainted with the operation of such a sinter unit and to gain a more detailed understanding of the sintering process.

ACKNOWLEDGEMENTS

The author thanks graduate engineer Anislav Dimitrov, majoring in Metallurgy, for his assistance.

REFERENCES

[1] B. Drakaliyski, Ts. Tsanev, Cast Iron Metallurgy, Technics, Sofia, 1998. (in Bulgarian)
[2] A. Avramov, I. Ivanchev, T. Tsanev, Iron Metallurgy, Technics, Sofia, 1994. (in Bulgarian)
[3] E. Wegman, Influence of the height of the charge layer on the process of sintering of agglomerate under pressure, Bulletin of the Ministry of Ferrous Metallurgy, Moscow, 1975. (in Russian)
[4] E. Wegman, Production of iron ore sinter and pellets, ITN, v. 17, 1977. (in Russian)
[5] A. Kamenov, Complex modeling of agglomeration and pelletizing of ores, Metallurgy, M., 1978. (in Russian)
[6] Yu. Yusfin et al., Production of sinter and pellets, Directory, Metallurgy, Moscow, 1984. (in Russian)
[7] A. Sigov, V. Shurkhal, Sinter process, Technique, Kyiv, 1969. (in Russian)
[8] A. Zhunev et al., Improvement of the sinter processing unit – one of the ways to improve the quality of sinter, Works of Uralmekhanobr, Sverdlovsk, 1984. (in Russian)
[9] V. Korotich, Fundamentals of Theory and Technology of Preparation of Raw Materials for Blast Furnace Melting. Metallurgy, Moscow, 1978. (in Russian)
[10] L. Heng, J. Whiteman, ISIJ International, 29 (1989) 24-32.
[11] I. Valchev, Ts. Tsanev, Manual for exercises in cast iron metallurgy, Tehnics, Sofia, 1979. (in Bulgrian)

The 56th International October Conference on Mining and Metallurgy
22-25 October 2025, Bor Lake, Bor, Serbia
www.ioc.tfbor.bg.ac.rs

DOI: 10.5937/IOC25269I *Original scientific paper*

THERMODYNAMIC INVESTIGATION OF CARBOTHERMIC REDUCTION OF ELECTRIC ARC FURNACE DUST

Angel Iliev[1a], Daniela Grigorova[1b]

[1] University of Chemical Technology and Metallurgy, 8 Kl. Ohridsky blvd., 1756 Sofia, Bulgaria
[1a] angel.iliev@kcm.bg, 0009-0002-1768-1300
[1b] d.dimitrova@uctm.edu, 0000-0001-8440-4368

Abstract
Electric arc furnace dust (EAFD) is a by-product generated after the gas cleaning systems in the steelmaking industry. This material is among the fastest-growing types of industrial waste and is classified as hazardous due to its high content of metal oxides. The management and utilization of EAFD represent a key aspect of sustainable industrial practices and circular economy principles. In the present study, waste dust samples from three different steel production sources were characterized. The chemical composition and properties of the dusts were determined. The thermodynamics of reduction processes for both synthetic and real mixtures were investigated using a galvanic cell method. The equilibrium oxygen pressure was determined by EMF measurements. The emphasis is on the thermodynamic features of zinc extraction. Based on experimental data, the dependencies of ΔG = f(T) were derived. The initial reduction temperature and the optimal amount of carbon were determined.

Keywords*: electric arc furnace dust (EAFD), steel, zinc, thermodynamics, EMF measurement*

1. INTRODUCTION

The electric arc furnace (EAF) production is one of the most well-known processes for steel production [1-3], due to its flexibility in operations, lower capital investments, and the ability to use up to 100% scrap. About 20 kg of dust is generated for every ton of steel produced [4-6]. The waste dust has different sizes and shapes [7], depending on the process, the type and composition of the scrap used, and the type of steel grade. The formation of the dust is complex and involves the evaporation and subsequent condensation of volatile elements and process-generated particles [1, 6, 8]. The resulting dust in the gas phase is captured by gas cleaning equipment, mainly by bag filters or electrostatic precipitators. The captured dust from the electric arc furnace (EAF) contains on average about 19 mass % zinc and 3 mass % lead [1, 4, 6]. Worldwide, the dust from electric arc furnaces is not fully utilized. Due to its high zinc content, the main focus is on its extraction. Several studies have been conducted using pyrometallurgical [6, 7, 9] and hydrometallurgical routes [5] for the recovery of zinc from electric arc furnace dust (EAFD). Most pyrometallurgical methods, such as the Waelz process, sintering, FASTMET and FASTMELT, OXYCUP, ZincOX, Primus, and ArcFume, are based on high-temperature reduction of EAFD using a suitable reducing agent such as carbon, carbon monoxide, or hydrogen gas [10, 11]. Carbothermal reduction uses carbon, most often in the form of coke breeze, as the reducing agent. The process occurs at temperatures above 1000°C, with a high consumption of fluxes and coke. Processes using coke (coke breeze) are energy-intensive pyrometallurgical technologies and lead to significant emissions of greenhouse gases, especially CO_2 [13]. The purpose of this investigation is to optimize the processes for recovering the zinc contained in electric arc furnace dust, based on a thermodynamic assessment of its reduction.

2. EXPERIMENTAL

In this work, waste dusts from electric steelmaking processes at iron and steel plants in the Republic of Bulgaria (BG), the Republic of Greece (GR), and the Republic of Serbia (RS) were

investigated. The chemical composition is determined by ICP analysis and is represented in Table 1. The sieve analysis was carried out according to ISO 13796:2012 standard. The sieving was carried out on a shaking machine. The structure and phase composition were determined by X-ray diffractometer (PANalytical Empyrean) and computed X-ray microtomograph.

The thermodynamic properties of phase reactions in ZnO-Zn, Fe_2O_3-ZnO-C, and the multicomponent real system of EAFD have been studied by electromotive force (EMF) measurements in a concentration galvanic cell - a galvanic cell with a solid electrolyte ZrO_2 and a reference electrode Ni/NiO:

$$\underset{P'_{O_2}}{\text{Pt}|\ \textit{studied mixture}\ |}\ |\text{ZrO}_2(\text{CaO})\ |\ |\ \underset{P''_{O_2}}{\textit{NiO, Ni}|\ \text{Pt}} \qquad (1)$$

3. RESULTS AND DISCUSSION

According to the chemical composition (Table 1), the iron content is in the range from 22.97% to 24.05%, and zinc is in the range of 25.66%-29.79%. The X-ray diffraction patterns of the three materials are presented in Figures 1 to 3. The main predominant phase in the three samples is magnetite (Fe_3O_4) with a spinel-type structure and zinc oxide. In sample 1BG, the main phases are zinc oxide (ZnO) - 30.8%, Magnetite (Fe3O4) 53.2%, Diopside (CaMgO6Si2)- 15.1%, and Litharge (PbO) – 0.7%. The main phase in sample 2GR is Fe_3O_4 - 43.2%, and zinc oxide is 17.5%. In this powder, a higher content of $CaMgO_6Si_2$ - 38.9% was determined. This indicates that this dust was generated from a process using steel scrap having less galvanized materials in a higher oxidizing environment. Sample 3RS contains the highest percentage of zinc oxide – 39.9% and 51.8% Magnetite. The Diopside content is the lowest compared to the other two samples, 7.6%. The result of the performed magnetic separation shows a magnetic fraction of over 96-99%.

Table 1. Main chemical compositions of EAFD (wt.%)

Source	Moisture	Zn	Fe	Pb	Cu	Al	SiO_2	CaO	MgO
1BG	6.56	24.75	38.48	2.06	0.27	0.64	3.71	6.52	3.42
2GR	11.37	17.60	31.25	3.36	0.23	0.55	4.06	5.55	1.76
3RS	16.70	31.79	37.50	2.14	0.23	0.60	3.60	4.38	0.94

Table 2 presents the theoretically derived thermodynamic equations for the change in Gibbs free energy as a function of temperature. The samples were dried and quartered. Depending on their availability and considering their mutual recycling, a mixture was made with a percentage ratio of 1BG:2GR:3RS - 30:40:30.

Table 2. Thermodynamic parameters (A and B) for $\Delta G^0 = A + B \cdot T$

Reaction	**A (J/mol)**	**B (J/mol·K)**	**No.**
ZnO (s) + C (s) → Zn (g) + CO (g)	247891	−209.18	(2)
ZnO (s) + C (s) → Zn (g) + CO_2 (g)	314114	−225.83	(3)
ZnO (s) + CO (g) → Zn (g) + CO_2 (g)	66223	−16.654	(4)
ZnO (s) + Fe (s) → Zn (g) + FeO (s)	87017	+210.02	(5)
ZnO (s) + C (s) + CO (g) → Zn (g) + CO_2 (g)	380501	−242.65	(6)
Fe_3O_4 (s) + CO (g) → 3FeO + CO_2 (g)	35386	−40.166	(7)
Fe_3O_4 (s) + C (s) → 3FeO (s) + CO (g)	236403	−231.9	(8)

A sieve analysis was carried out. The distribution by fractions is presented in Figure 4. The density of the powders was determined pycnometrically using a wetting component of ethyl alcohol. The determined density was 0.4136 g/cm^3. The fractional distribution after sieve analysis showed that the largest portion of the material (31.16%) falls within the 0.20–0.32 mm size range, indicating a predominantly fine-grained composition.

Zinc oxide does not decompose on heating at ordinary temperatures, but remains stable up to very high temperatures (~1975°C). Figure 5 shows the dependence of mass loss in percent on temperature during carbothermic reduction. It can be seen that by increasing temperature, the reduction becomes more intense, and at 1400°C, the mass loss reaches about 85%. The dependence of the percentage recovery of zinc on the carbon content in the carbothermic reduction of zinc oxide is presented in Figure 6.

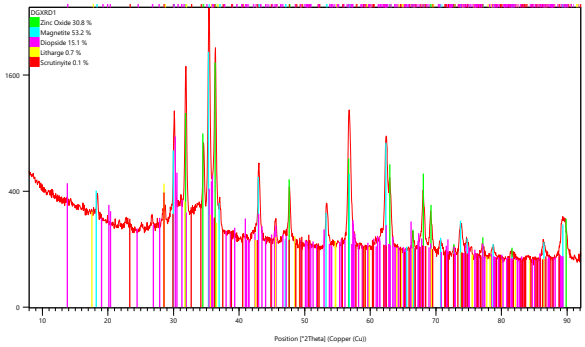

Figure 7. XRD pattern of 1BG EAFD sample

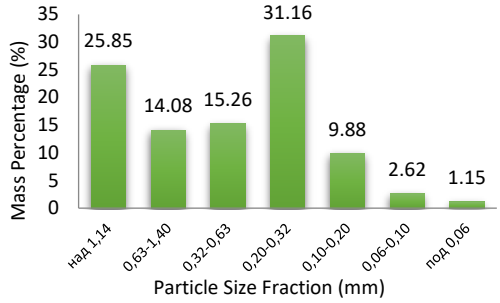

Figure 4. Particle size distribution of EAFD

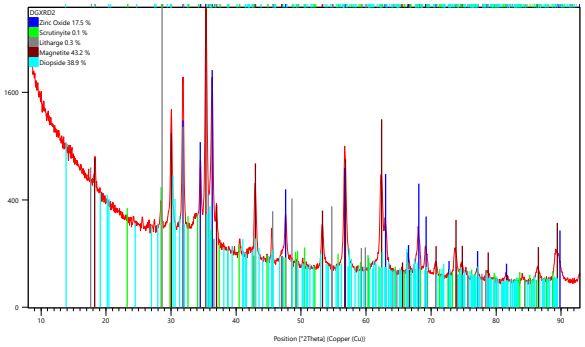

Figure 8. XRD pattern of 2GR EAFD sample

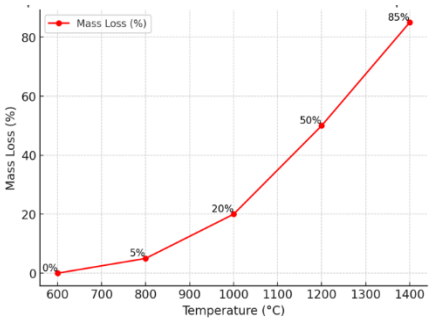

Figure 5. Dependence of zinc oxide mass loss on reduction temperature

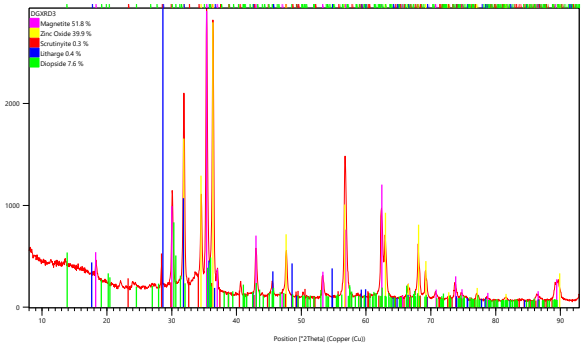

Figure 9. XRD pattern of 3RS EAFD sample

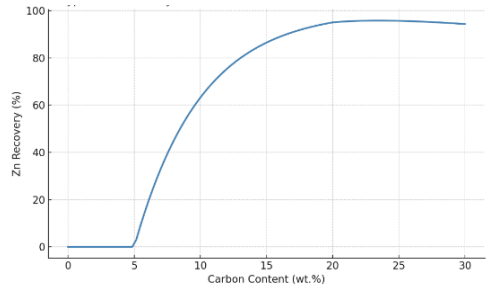

Figure 6. Zinc recovery vs carbon content in carbothermic reduction of zinc oxide

Zinc oxide is challenging to reduce. Its reduction temperature is 1100 °C. The presence of Franklinite, common in EAFD, indicates the occurrence of complex spinel phases. The reduction process of $ZnFe_2O_4$ involves three steps: $ZnFe_2O_4 \rightarrow FeO + ZnO \rightarrow Fe + ZnO \rightarrow Fe + Zn$ (g).

The thermodynamics of the reduction of synthetically prepared mixtures were studied. Mix 1 contains zinc oxide and carbon, Mix 2 contains Fe2O3-ZnO-C in an amount of carbon relative to the stoichiometrically calculated amount, and Mix 3 contains twice the amount of reducing agent. Mix 4 contains the EAFD presented in Table 1. From the experiments carried out by measuring EMF in a galvanic cell, equations of the dependences of the change in ΔGexp.= f(T) have been derived. The theoretical (Table 2) and experimental models are compared graphically in Figure 7.

ΔG° (J/mol)	R^2
Mix 1 ΔG° = 279802− 214·T	0.9671
Mix 2 ΔG° = 204654 - 164,79 T	0.9029
Mix 3 ΔG° = 119742-89,267·T	0.8786
Mix 4 ΔG° = 82636-81,78·T	0. 8482

The reaction ZnO+Fe=Zn+FeO is thermodynamically impossible in the studied temperature range.

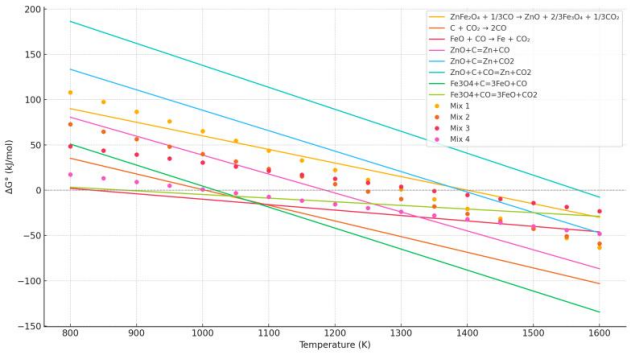

Figure 7. Gibbs Free Energy vs Temperature

Carbon usage below 5 wt.% is low and insufficient for reduction. A sharp increase in zinc recovery is observed with carbon contents of 5–20 wt.%. However, at higher carbon levels (>20 wt.%), zinc recovery either plateaus or declines, likely due to the onset of side reactions, reoxidation phenomena, or reduced process efficiency. Within the temperature range of 600–1000 °C and under carbon-rich conditions, zinc volatilizes into the gas phase, while iron oxides are reduced potentially to metallic iron accompanied by significant evolution of CO and CO_2. At elevated temperatures (>1200 °C) with an excess of carbon, iron may absorb carbon and form Fe–C alloys. Under such conditions, zinc losses may occur due to volatilization or carbide formation. In particular, reactions with excess carbon can lead to the formation of zinc carbide (ZnC_2) or promote the reverse oxidation of metallic zinc via the reaction: $Zn + CO \rightleftharpoons ZnO + C$. This reversible reaction may result in partial reoxidation of the reduced zinc back to ZnO.

4. CONCLUSION

The investigated samples, collected from three distinct regions, reflect variations in production technologies, raw material composition, and oxidation conditions. The identified predominant structural phases include magnetite, zinc oxide, and franklinite, as well as a crystallized calcium–magnesium silicate phase. The behavior of synthetic experimental mixtures aligns closely with theoretical predictions and provides insight into the underlying reduction mechanisms. Effective reduction is achieved when the carbon content in the charge is maintained between 15–20 wt.%. Excess carbon does not enhance reduction efficiency and may instead promote undesirable side reactions, zinc losses, increased fuel consumption, and elevated greenhouse gas emissions.

REFERENCES

[1] I. Ivanchev, Modern Steelmaking Processes. Theory and Practice, Sofia, 1994, p. 358.
[2] D. Llewellyn, R. C. Hudd, Steels metallurgy and applications, Elsevier Science, 1998.
[3] O. Ruiz, C. Clemente, M. Alonso, F.J. Alguacil, J. Hazard Mater., 141 (2007), 33-36.
[4] Tsv. Dimitrova, I. Zhabinski, et al., Industry and Environment, Sofia, 1993, p. 140.
[5] F. Kukurugya, T. Vindt, T. Havlík, Hydrometallurgy, 154 (2015), 20-32.
[6] E. Aries, G. Benavides et al., BAT for the ferrous metals processing industry, Office of the European Union, Luxembourg, 2022.
[7] J.M.A. Geldenhuis, Recovery of valuables from flue dust fines, Minerals Engineering, 2002.
[8] A.G. Guézennec et al., Powder Technol. 157(1-3), (2005), 2-11.
[9] D. Grigorova, R. Paunova, Metalurgija. 61(1) (2022), 189-92.
[10] J.M. McClelland, G.E. Metius, JOM, 55, (2003) 30–34.
[11] M.H. Morcali, O. Yucel et al., J. Min. Metall. Sec. B Metall., 48(2), (2012) 173-184.
[12] V.A. Shumskiy, et al. Russ. J. Non-Ferrous Met 60(3), (2019) 259–267.

The 56th International October Conference on Mining and Metallurgy
22–25 October 2025, Bor Lake, Bor, Serbia
www.ioc.tfbor.bg.ac.rs

DOI: 10.5937/IOC25273L *Original scientific paper*

NUMERICAL SIMULATION OF TEMPERATURE FIELD IN A ROTARY HEARTH FURNACE UNDER INFRARED−ASSISTED HEATING CONDITIONS

Xiaohua Liu[1a], Renhao Tian[1b], Yang You[1c], Zhixiong You[1d]*, Xuewei Lv[1e]

College of Materials Science and Engineering, Chongqing University, Chongqing 400044, China.
[1a] liuxiaohua@stu.cqu.edu.cn, 0009-0001-7491-7722
[1b] trh17843610794@163.com, 0009-0000-5443-0733
[1c] youyang@cqu.edu.cn, 0000-0002-5403-0673
[1d] youzx@cqu.edu.cn, 0000-0002-4405-7004
[1e] lvxuewei@cqu.edu.cn, 0000-0003-1690-4373

Abstract

In steel production, significant quantities of steel dust and sludge are generated, among which iron- and zinc-bearing residues hold high recycling potential. Currently, the rotary hearth furnace (RHF) process is one of the most widely used technologies for treating such byproducts in the steel industry. This study employs Fluent-based numerical simulations to analyze the temperature distribution in an RHF under infrared-assisted heating, assessing the feasibility of infrared integration and its potential to reduce carbon emissions. The results indicate that infrared-assisted heating significantly enhances the RHF system's thermal efficiency.

Keywords : *RHF, infrared−assisted heating, Numerical simulations, Reducing carbon emissions*

1. INTRODUCTION

Steel Steelmaking dust sludge, a solid waste byproduct derived from dry and wet flue gas purification processes in iron and steel manufacturing, constitutes 8%–12% of China's annual steel production by mass [1]. Notably, 20%–30% of this residue is classified as iron-zinc-bearing dust sludge due to its elevated concentrations of iron, zinc, potassium, sodium, and other metallic elements [2,3]. Current disposal practices such as open-air stockpiling or landfilling not only impose environmental hazards and land-use inefficiencies but also squander the resource recovery potential of these metal-rich wastes [4,5,6]. The rotary hearth furnace (RHF) process, recognized for its operational efficiency and feedstock versatility, has emerged as the predominant treatment method for iron-zinc-bearing sludge [7,8]. However, conventional RHF systems suffer from excessive carbon emissions and suboptimal chamber space utilization, limitations stemming from their reliance on gas-fired combustion—a heating method with inherent inefficiencies and a substantial carbon footprint.

To mitigate these challenges, improving thermal efficiency while minimizing gas consumption is critical. Infrared-assisted heating, an external energy field technology, presents a promising solution owing to its high thermal efficiency, material penetration capacity, and carbon-neutral operation, all of which are well-documented in industrial applications [9,10]. This study utilizes computational fluid dynamics (CFD) via ANSYS Fluent to simulate temperature field distributions within RHF systems under both gas combustion and infrared-assisted heating conditions. The objective is to assess the feasibility of infrared integration for enhancing RHF thermal performance and reducing carbon emissions.

2. EXPERIMENTAL

2.1 Geometry model of RHF

This study developed a full−scale computational model of RHF from an integrated steel enterprise, as depicted in Figure 1. Specifically, Figure 1(a) illustrates the geometric configuration of the RHF model, while Figure1(b) details its internal structural characteristics. The Rotary Hearth Furnace (RHF) model has a diameter of 30 m and incorporates an annular furnace chamber with a width of 5 m and a height of 1.5 m. Infrared radiation tubes, each with a diameter of 50 mm, are symmetrically installed on both lateral inner walls of the chamber. The central axes of these tubes are positioned 500 mm above the furnace hearth. To reflect operational configurations, the furnace is divided circumferentially into six functional zones: one preheating section and five reduction sections (I–V). Each zone contains a distinct number of burners aligned along the mid-height plane of the lateral walls. These burners are designed to inject gas-air mixtures, enabling controlled combustion heating.

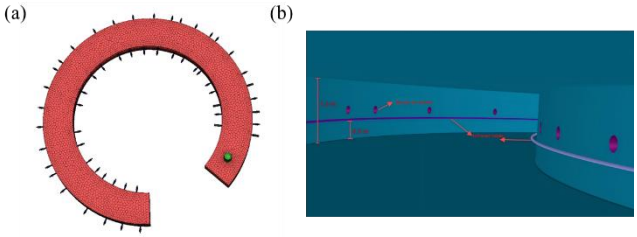

Figure 1. Geometry model of RHF: (a) External structure, (b) Internal structure

2.2 Numerical simulation conditions

2.2.1 Radiative heat transfer

In this paper, after the use of infrared assisted heating, the furnace chamber is mainly through the radiation heat transfer to heat the object, in the case of scattering is not taken into account, in the position $\vec{r}$, the radiative propagation equation (RTE) along the propagation direction $\vec{s}$ is:

$$\frac{dI\left(\vec{r},\vec{s}\right)}{ds} = -aI\left(\vec{r},\vec{s}\right) + aI_b(\vec{r}) \qquad (1)$$

Where: $\vec{r}$ is the position vector, $\vec{s}$ is the vector of radiation propagation direction, a is the absorption coefficient, I is the radiation intensity, $W \cdot m^{-2} \cdot s \cdot r^{-1}$.

The Discrete Ordinates (DO) radiation model is widely employed in numerical simulations of radiative heat transfer to calculate gas-phase radiation across varying optical thicknesses. This method is particularly effective for solving thermal engineering problems involving localized heat sources. Within the model framework, gas absorption coefficients are derived using the Weighted Sum of Gray Gases Model (WSGGM), which enables spectrally resolved estimation of radiation properties for participating media.

2.2.2 Boundary Conditions

The numerical framework incorporated infrared radiation tubes with thermal parameters set to a surface temperature of 1800 K, an emissivity of 0.9, and a radiative flux density of 464,800 W/m². The pellet layer thickness was fixed at 20 mm. Turbulent gas flow was modeled using the k-epsilon turbulence model, selected for its proven efficacy in simulating complex engineering flows. Boundary conditions defined distinct velocity profiles across process zones: thermal air inlets (723 K) were maintained at 21.69 m/s in Reduction Zone V and 30.69 m/s in other sections, while gas

injections (300 K) were regulated to 9.59 m/s in Zone V compared to 12.95 m/s elsewhere. The gas composition, rigorously validated against operational data from the referenced steel plant, is systematically presented in Table 1.

Table 1. Volume fraction of gas composition (vol%)

Species	H_2	CO	CH_4	CO_2	N_2
Fraction	13.8	36.4	6.0	17.0	26.6

3. RESULTS AND DISCUSSION

3.1 Temperature field under gas combustion condition

This study conducted numerical simulations to analyze temperature distributions in a rotary hearth furnace under gas combustion heating conditions incorporating infrared radiation modules. Figure 2 illustrates the simulated temperature field profiles. Figure 2 (a) indicates that combustion reactions within the burners produce high-temperature gases with a cross-sectional average temperature of 1510 K. As depicted in Figure 2 (b) and (c), the pellet bed exhibits uniform temperature distribution across the reduction zones, achieving a mean temperature of 1497 K, which meets metallurgical process requirements. Lower temperatures were observed only in the preheating section.

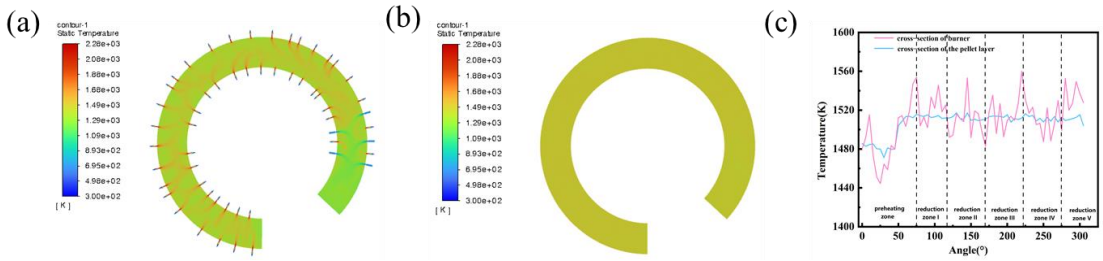

Figure 2. Temperature field: (a) cross−section of burner, (b) and (c) cross−section of the pellet layer.

3.2 Temperature field under infrared heating condition

Numerical simulations of temperature distribution under infrared-only heating conditions were conducted for the rotary hearth furnace model equipped with infrared radiation modules. As shown in Figure 3, the thermal profile within the pellet layer exhibits significantly greater temperature uniformity compared to gas-fired heating configurations. The infrared-assisted system achieved homogeneous thermal distribution with minimal spatial variation, reaching a mean temperature of 1227 K. This improvement stems from the superior heating efficiency of infrared radiation, which facilitates simultaneous surface and core heating of pellets, thereby reducing interfacial temperature gradients.

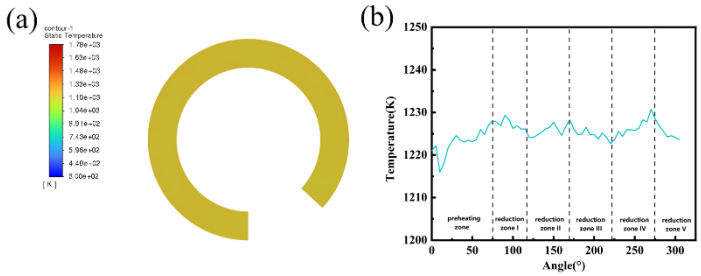

Figure 3. Temperature field ：(a) and (b) cross−section of the pellet layer

3.3 Temperature field under infrared and gas synergistic heating conditions

Numerical simulations of hybrid infrared-gas heating conditions were performed on the rotary hearth furnace, with the resulting thermal and velocity distributions illustrated in Figure 4. Figure 4(a) indicates a cross-sectional mean burner temperature of 1495 K. Figures 4(b) and 4(c) reveal an average pellet bed temperature of 1640 K, representing a 140 K increase over gas-only heating configurations. This improvement significantly enhances heating efficiency and thermal uniformity, attributed to the synergistic coupling of radiative and convective heat transfer mechanisms.

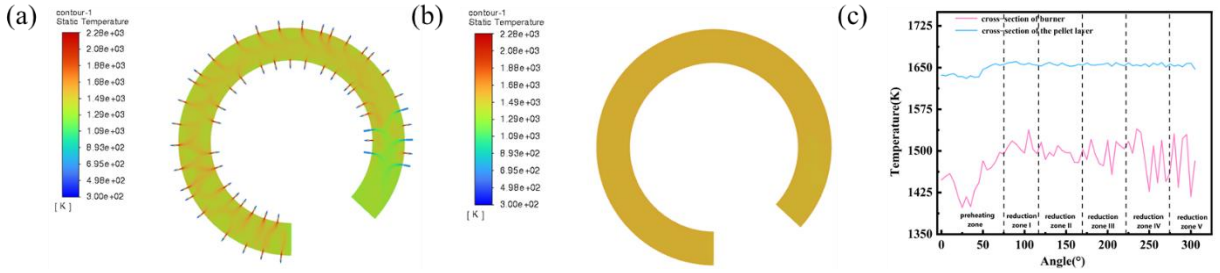

Figure 4. Temperature field: (a) cross−section of burner, (b) and (c) cross−section of the pellet layer

4. CONCLUSIONS

(1) A three-dimensional RHF model was developed in ANSYS Fluent for radiative heat transfer analysis, integrating the k-epsilon turbulence model and the DO radiation framework. Under gas-fired heating conditions, numerical simulations produced a pellet bed mean temperature of 1497 K, aligning with metallurgical process specifications.

(2) Simulations of hybrid infrared-gas heating conditions demonstrated a synergistic thermal enhancement effect, achieving an average pellet layer temperature of 1640 K. This represents a 143 K increase compared to conventional gas heating, significantly improving thermal efficiency and uniformity.

ACKNOWLEDGMENTs

The authors are grateful to the National Key Research and Development Program (2022YFC3901404) for the financial support of this research.

REFERENCES:

[1] J. Kim, M.S. Son, J.K. Park, et al., Fuel Process. Technol., 237 (2022) 107450.
[2] X. He, S.F. Xie, X.F. Li, et al., JOM, 74 (8) (2022) 3039−3048.
[3] P.J. Liu, Z.G. Liu, M.S. Chu, et al., J. Hazard. Mater., 413 (2021) 125403.
[4] D.C. Zhang, R. L. Liu, H. Wang, et al., J. Cent. South Univ., 28 (9) (2021) 2701-2710.
[5] R. Bayoumi, N.M. Abdelmonem, M.A. Soliman, et al., Proceedings of 11th International Conference on Chemical and Environmental Engineering, Cairo, Egypt, 2022.
[6] X.L. Lin, Z.W. Peng, J.X. Yan, et al., J. Clean. Prod., 149 (2017) 1079-1100.
[7] X.F. She, J.S. Wang, G. Wang, et al., J. Iron Steel Res. Int., 21 (5) (2014) 488-495.
[8] H. Tsutsumi, S. Yoshida, M. Tetsumoto, R&D Kobe Steel Eng. Rep., 60 (1) (2010) 36-42.
[9] K. Myroniuk, V. Shepitchak, Y. Furdas, et al., Constr. Optim. Energy Potential, 13 (1) (2024) 129-142.
[10] D. Mauduit, M. Le Fournier, K. Grondin, et al., Proceedings of International Conference on Technology of Plasticity, Cambridge, UK, 2017, p.1904-1909.

The 56th International October Conference on Mining and Metallurgy
22-25 October 2025, Bor Lake, Bor, Serbia
www.ioc.tfbor.bg.ac.rs

DOI: 10.5937/IOC25277L *Original scientific paper*

S/S TREATMENT FOR ALUMINUM SLAG WASTE USING FLY ASH-BASED GEOPOLYMERS

Sara Lukovac[1a], Nebojša Tadić[2a], Dijana Đurović[3a], Irena Nikolić[2b]

[1]Institute for interdisciplinary and multidisciplinary studies, University of Montenegro, Cetinjska br. 2, Podgorica, Montenegro
[2] Faculty of Metallurgy and Technology, University of Montenegro, Džordža Vašingtona bb, Podgorica, Montenegro
[3]Institute for Public Health of Montenegro, Džona Džeksona bb, Podgorica, Montenegro
[1*]sara.lukovac@edu.ucg.ac.me, 0009-0007-0141-2786
[2a] nebojsa@ucg.ac.me, 0009-0007-5458-8232
[2b] irena@ucg.ac.me, 0000-0001-6781-3485
[3a] dijana.djurovic@ijzcg.me, 0000-0003-3327-6647

Abstract
Fly ash(FA) is one of the four by-products of coal combustion in thermal power plant boilers, accounting for 40–90% of the total amount of by-products. Due to its physico-chemical properties and applied treatments, FA utilization offers environmental, economic, and sustainable benefits for waste management. The aim of this paper is to investigate the influence of aluminum slag waste (ASW) addition on the mechanical properties of FA-based geopolymers primarly prepared to evaluate the potential for ASW stabilisation/solidification. The experimental part was conducted under define parameters required for geopolymerisation: S/L ratio (1), NaOH concentation (10 M), mass ratio Na_2SiO_3/NaOH (1.5) with varying ASW contents from 1% to 10%. EN 12457-2 leachability test was performed with and without ASW loaded geopolymers. Experimental results indicate that the addition of ASW reduces the compressive strength of FA-based geopolymers while the leachablity test confirmed that ASW-loaded geopolymers meet the leaching limits defined for stable non-reactive hazardous waste.

***Keywords**: Fly ash, geopolymers, aluminum slag, stabilization/solidification*

1. INTRODUCTION

Montenegro as an EU candidate has the obligation to establish an integrated waste management system which is according to the European Commission considered one of the priority goals on the path to EU accession. If the best economic and environmental waste management solution is to be achieved in Montenegro in the future it is important to implement environmentally friendly techniques for processing waste materials of various origins. The Thermal power plant "Pljevlja" annually consumes an average of 1.6 million tons of lignite coal to produce electricity and thermal energy of which 20–30% is generated as by-products 480.000 tons of fly ash and 320.000 tons of slag [1]. As a geopolymer binder in the solidification/stabilization process causes physical and chemical changes in the structure of the waste material leading to the immobilization of pollutants and reducing their migration potential in different environmental compartments [2,3]. The utilization of fly ash through geopolymerization results in a reduction of CO_2 emissions by enabling the process to be carried out under milder conditions compared to the production of Portland cement (OPC) while also decreasing the amount of ash that would otherwise be disposed of in landfills without pretreatment [4].

The aim of this work is to utilize fly ash as an eco-friendly binder for geopolymer synthesis and to evaluate the application of fly ash-based geopolymers in S/S treatment with varying dosages of ASW. Leachability test, EN 12457-2, was used to asses the S/S potential of fly ash-based geopolymers.

2. EXPERIMENTAL

Fly ash was collected from the coal fired power station in Pljevlja and ASW from the Aluminum plant in Podgorica. Synthesis of fly ash-based geopolymer (FO) was performed by mixing of fly ash with an alkaline activator in a solid to liquid ration 1. Alkali activator was prepared by mixing of 10 M NaOH and Na_2SiO_3 solution (commercial water glass) in a mass ratio of 1.5. Fly ash based geopolymers contaminated with slag (ASW) were prepared by adding ASW to the starting mixture by fly ash replacement with a 1- 10% to the total solid content. First aluminum slag was mixed with alkali activator and then, fly ash was added. Then, the both, FO and ASW, geopolymer mixtures were poured into cylindrical plastic molds (28× 60 mm) sealed with a lid to minimize water evaporation. The prepared samples were oven-dried at 65 °C for 48 hours. The solid specimens were allowed to cool to room temperature, removed from mould and left to rest for a period of 15 days before any testing was performed. After 15 days, in order to evaluate the compressive strength, the surfaces of three specimens per mixture were polished flat and tested using a compression testing machine. The fragment of geopolymers remained after the strength testing were used to assess the immobilization potential of metals and chloride from aluminum slag in accordance with the EN 12457-2 leaching procedure. Metal content in filtrate remained after the leaching test was analyzed using an Ametek Spectro Arcos FHE12 Spectrometer Analyzer while the content of chloride was analyzed by argentometry titration.

3. RESULTS AND DISCUSSION

3.1 Influence of ASW dosage on compressive strenght

The figures of obtained FO and ASW geopolymer samples with a different dosage of aluminum slag are given in Fig. 1.

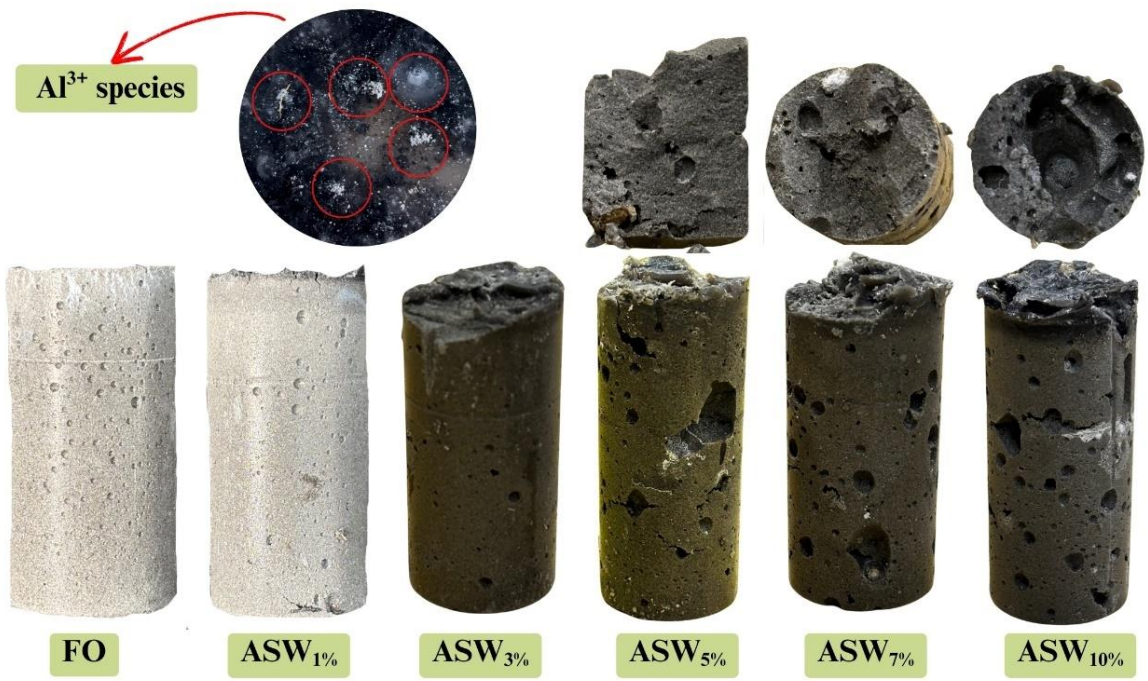

Figure 1. FA-based geopolymers with ASW (1-10%)

The results have shown that optimal dosage of aluminium slag was up to 3 %. Further increase of slag addition caused the highly porous and britle structure with a weak mechanical properties. Geopolymer samples containing more than 3% of aluminum slag had a tendency to crack during

the drying process and these samples did not meet the criteria for further mechanical property testing. Thus, only geopolymers containing the 1 and 3 % of aluminum slag were used for further investigation. Influence on different ASW dosages (1 and 3%) on compressive strenght of fly ash based geopolymers are presented in Figure 2.

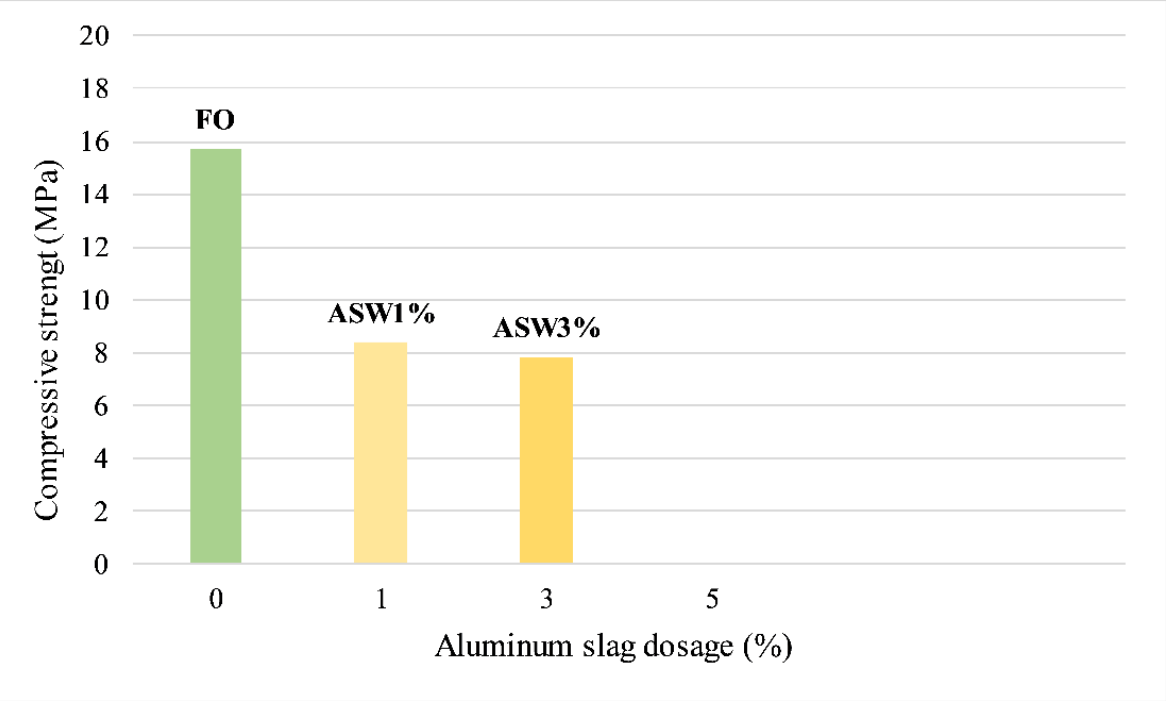

Figure 2. Influence of ASW dosage on compressive strenght

As shown in Figure 2. the highest compressive strength (15.71 MPa) displayed the FA-based geopolymer (FO). The replacement of fly ash with slag led to a decrease in compressive strength of geopolymers. The geopolymers with a 1% and 3 % of slag (denoted as ASW1% and ASW3% respectively) displayed the strength of 8.39 MPa and 7.85MPa, respectively. The introduction of slag into fly ash based geopolymer lead to the weakening of geopolymer structure due to the increase of porosity caused by to the release of hydrogen during the dissolution of aluminum from AS in the alkali activator as presented by equations (1) and (2), where Me_{1A} represents sodium or potassium [5]:

$$2Al + 2Me_{1A}OH + 6H_2O \rightarrow 2Me_{1A}Al(OH)_4 + 3H_2\uparrow \quad (1)$$

$$2Al + 2NaOH + 6H_2O \rightarrow 2Na[Al(OH)_4] + 3H_2\uparrow \quad (2)$$

3.2 Leaching behavior of FA/ASW geopolymers

The efficiency of S/S of aluminum slag through geopolymerization process was evaluated using EN 12457-2 compliance tests, comparing the metals and chloride concentration in EN 12457 leachates with limits established by EULFD (European Landfill Directive) [6].

The metal and chloride release, from ASW1% and ASW 3% geopolymers structure according the EN 12457-2 leaching test is shown in Table 1. As shown in Table 1, the concentrations of metal and Cl released from FO and ASW1% and ASW3% geopolymers meet the criteria for waste acceptance in non-hazardous landfills.

Table 1-Results of EN 12457-2 leaching test with limit values for landfill waste acceptance criteria

Element (mg/kg)	Inert waste	Stable Non-Reactive Waste (in NH class)	Hazardous waste	FO	$ASW_{1\%}$	$ASW_{3\%}$
As	0.5	2	25	7.68	8.51	9.08
Ba	20	100	300	0.239	0.165	0.547
Cd	0.04	1	5	<0.0006	0.001	0.016
Cr	0.5	10	70	0.337	0.342	0.581
Cu	2	50	100	0.138	0.047	0.200
Hg	0.01	0.2	2	0.03	0.032	0.002
Mo	0.5	10	30	0.839	0.90	1.26
Ni	0.4	10	40	0.107	0.116	0.219
Pb	0.5	10	50	0.227	0.343	0.613
Sb	0.06	0.7	5	0.193	0.401	0.852
Se	0.1	0.5	7	0.894	1.52	2.29
Zn	4	50	200	0.144	0.071	0.314
Cl	800	15000	25000	2500	3750	2500

4. CONCLUSION

Fly ash based geopolymers were used for S/S treatment of aluminum slag waste. Fly ash replacement with an aluminum slag led to the weaking of geopolymer structure. The structure of geopolymers with a content of slag more than 3 % did not match criteria for mechanical testing. Pure fly ash based geopolymers reach the compressive strength of 15.71 MPa and fly ash replacement with a slag in a quantity of 1% to 3% lead to the decreased compressive strength to 8.39 MPa to 7.85 MPa, respectively. The results of EN 12457-2 leaching test have shown that FO, $ASW_{1\%}$ and $ASW_{3\%}$ geopolymers meet the EULFD criteria for non- hazardous waste.

ACKNOWLEDGEMENTS

This work was supported by the Ministry of Education, Science and Innovation of Montenegro through the program Scholarships for Excellence in Doctoral Research *in Montenegro No. 0403-082/24-1552/6***.**

REFERENCES

[1] Ministarstvo održivog razvoja i turizma, Nacrt integrisane dozvole za rad postrojenja TE Pljevlja. Podgorica: Agencija za zaštitu prirode i životne sredine, 2018. Available at:https://www.epa.org.me/images/integrisanadozvolaTEPljevlja-nacrt.pdf

[2] Environmental Protection Agency (EPA), Community Guide to Solidification and Stabilization, 2021. Available at:https://semspub.epa.gov/work/HQ/401621.pdf

[3] R. Singh, S. Budarayavalasa., J. Mater. Cycles Waste Manag., 23 (5) (2021) 1699–1725.

[4] I. Luhar, S. Luhar., J. Compos. Sci., 6 (8) (2022) 219.

[5] M. Sitarz, T. Zdeb, K. Mróz, I. Hager, K. Setlak., Mater., 17 (6) (2024) 1449.

[6] EULFD, 2002. EN 12457. Characterisation of waste–Leaching–Compliance test for leaching of granular waste materials and sludges–Part 2: one stage batch test at a liquid to solid ratio of 10 L/kg for materials with particle size below 4 mm. European Landfill Directive, European Committee for Standardisation

The 56th International October Conference on Mining and Metallurgy
22-25 October 2025, Bor Lake, Bor, Serbia
www.ioc.tfbor.bg.ac.rs

DOI: 10.5937/IOC25281H *Review paper*

THE ROLE OF HYDROGEN BASED SHAFT FURNACES IN STEEL INDUSTRY DECARBONIZATION

Xing Han[1a], Hongqiang Liu[1b], Lanjie Li[1c], Pengyang Li[1d], Xiaolong Guo[1e]

HBIS Group Co., Ltd., Shijiazhuang 050023, Hebei, China
[1a] hanxing@hbisco.com, 0009-0002-9051-0946
[1b] liuhongqiang@hbisco.com, 0000-0003-2897-8134
[1c] lilanjie@hbisco.com, 0009-0006-3261-3225
[1d] lipengyang@hbisco.com, 0009-0006-6936-2394
[1e] guoxiaolong@hbisco.com, 0009-0001-3917-2227

Abstract

This study provides a systematic review of current hydrogen-based metallurgical processes, analyzing their technical pathways across multiple dimensions including raw material preparation, reaction mechanisms, critical equipment design, and system integration. A comparative evaluation reveals the distinct advantages and limitations of each technological route. The paper highlights HBIS Group's pioneering HyMEX demonstration project - the world's first industrial-scale application of coke oven gas direct reduction without reforming. This breakthrough technology eliminates the conventional dependence on natural gas for reducing gas production and achieves the highest hydrogen utilization rate among operational shaft furnace processes. The successful implementation establishes a new benchmark for hydrogen metallurgy industrialization. Furthermore, this analysis examines China's unique position for hydrogen metallurgy development, considering both policy frameworks and resource characteristics. With abundant coke oven gas resources and dominant steel production capacity, China possesses distinctive advantages for scaling hydrogen-based ironmaking. The study concludes that as hydrogen infrastructure matures and production costs decline, shaft furnace hydrogen metallurgy will likely become a cornerstone technology for the industry's low-carbon transformation, providing critical technical support for national climate commitments.

Keywords*: low-carbon transition; hydrogen direct reduction; alternative ironmaking; coke oven gas zero-reforming; industrial demonstration*

1. INTRODUCTION

Amid global energy restructuring and climate challenges, hydrogen energy has emerged as a clean, high-efficiency solution for sustainable development [1-3]. The steel industry, a major CO_2 emitter (1.7B+ tons annually in China, 70% from blast furnaces [4, 5]), faces urgent decarbonization needs. While blast furnaces dominate (90% of China's production), their carbon reduction potential is limited even with hydrogen substitution [6-7]. Non-blast furnace processes (direct reduction, molten reduction) offer greater decarbonization potential by maximizing hydrogen use and eliminating coke. Hydrogen-based shaft furnaces are mature, while fluidized bed reduction - enabling fast, pellet-free processing - gains traction. Smelting reduction remains developmental. This paper reviews global non-blast furnace technologies and highlights China's pioneering coke-oven-gas-to-hydrogen demonstration project. It proposes tailored hydrogen metallurgy pathways to guide the industry's low-carbon transition.

2. DEVELOPMENT STATUS OF NON-BLAST FURNACE TECHNOLOGY

2.1 Development status of smelting reduction iron making

The original intention of developing molten reduction was to use non-coking coal as the energy source or reducing agent to reduce iron oxides in a high-temperature molten state. After the separation of slag and iron, molten iron was obtained. Coal could be used instead of coke and fine

ore could be directly smelted to simplify the ironmaking process and reduce pollutant emissions. However, from the actual operation results, both the COREX and FINEX processes that have achieved commercial operation require a small amount of coke, and the fuel consumption is as high as over 850 kg/t. The HISMELT process was jointly developed by CRA of Australia (now Rio Tinto) and MIDREX of the United States and was sold to Shandong Molong of China in 2012. During the introduction process, Shandong Molong combined the production practice of the original Australia and optimized and improved the mineral powder pretreatment, high-temperature flue gas treatment system, etc. The process was renamed ML-HISMELT. The transformation and upgrading relocation and renovation project of Xingsteel introduced the ML-HISMELT technology of Shandong Molong. It is planned to build three new ML-HISMELT melting reduction furnaces with a total pig iron production capacity of 1.65 million tons per year. Currently, the engineering construction is underway. HBIS Group has also developed a new full-oxygen hydrogen-rich carbon cycle ironmaking process with independent intellectual property rights. A 30 m^3 pilot demonstration line has been built, and the feasibility verification of the process is awaiting. Comparison of different smelting reduction iron-making processes are shown in Table 1.

Table 1. Comparison of different smelting reduction iron-making processes [8-10]

Technology	COREX	FINEX	HISMELT	New technology of HBIS
Developer	Voestalpine	Voestalpine and POSCO	Rio Tinto	HBIS and Northeastern University
Application unit	Baosteel Group Xinjiang Bayi Iron & Steel Co., Ltd., etc	POSCO	Shandong Molong Group introduced technology re-innovation	HBIS
Monomer maximum (10000 t/a)	150	200	80	Pilot test (about 2)
Ingredients	pellet and lump ore (6.0-16.0 mm)	Sinter powder under sieve (0.5-1.0 mm)	Ore powder (＜6.0 mm)	Pellet, sinter and lump ore
Fuel	Coke and coal	Coke, pulverized coal and briquette	Non-coking coal (＜3 mm)	Coke and hydrogen
Prereductor	Shaft furnace (Metallization rate 50%)	Fluidized bed (Metallization rate 65-80%)	Rotary kiln (Metallization rate 15%)	Upper part of reactor (Metallization rate 85%-90%)
Final reductor	Molten gasifier	Molten gasifier	SRV furnace	Lower part of reactor
Fuel consumption	about 1 000 kg/t Fe	about 850 kg/t Fe	about 850 kg/t Fe	Coke: about 307 kg/t Fe hydrogen: about 369 Nm^3/t Fe
Oxygen consumption /(Nm^3/t-Fe)	550 (Pure oxygen)	530 (Pure oxygen)	Air consumption 2600, oxygen volume fraction 39%	180 (Pure oxygen)
Main component of hot metal /%	C: 3.5-4.0 Si: 0.8-1.5 S: about 0.025 P: about 0.120	C: 3.5-4.0 Si: 0.6-1.2 S: about 0.030 P: about 0.120	C: 3.5-4.0 Si: trace S: about 0.156 P: about 0.035	C: about 4.5 Si: 0.4-0.5 S: about 0.020 P: about 0.100
Advantage	The adaptability of raw materials is broad	Reduction temperature is low; There are no strict restrictions on the composition and variety of iron ore	Wide range of raw materials, can smelt high phosphate rock, vanadium titanium magnetite and so on	Hydrogen-rich carbon cycle smelting, large carbon reduction range
Drawback	Fusion gasifier high temperature flue gas dust bonding plugging	Low reduction efficiency	The FeO content in slag is high, the yield of molten iron is low, and the life of furnace cylinder is short	Pending confirmation of validity

2.2 Development status of fluidized bed reduction

Fluidized direct reduction ironmaking method refers to the method of reducing iron ore powder in a fluidized bed using gas, reformed natural gas or hydrogen. The basic process flow is as follows: the reducing gas is heated to 400-900 ℃ and passes through 2 to 4 stages of fluidized beds step by step. Under the interaction of gravity and reducing gas flow, the iron ore powder enters the preheating, pre-reduction and reduction stages of fluidized beds in sequence. The reduced sponge iron powder is pressed into blocks and used in the subsequent smelting process. FIOR/FINMET and CIRCORED are typical fluidized bed reduction processes. The reduction part of the FINEX process adopts a fluidized bed device, but essentially falls within the category of molten reduction ironmaking. The HyREX process is an improvement based on the FINEX technology. The reducing agent uses natural gas instead of coal combustion to produce gas for reduction, and the fluidized bed reduction process is retained. Replace the original melting gasifier with an electric furnace. Overall, the fluidization direct reduction ironmaking technology has been industrialized and commercialized. However, issues such as the loss of flow due to the reduction and bonding of mineral powder during the production process, the stable operation of fluidization equipment, and the availability of reduction gas resources have hindered the rapid development of fluidization reduction technology. In terms of production scale and stability, it still cannot be compared with the gas-based shaft furnace reduction process, and it is difficult to surpass the scale of the gas-based shaft furnace in the short term. Comparison of different types of fluidized direct reduction iron making processes are shown in Table 2.

Table 2. Comparison of different types of fluidized direct reduction iron making processes [11, 12]

Technology	FINMET	CIRCORED	FINEX	HyREX	Fluidized bed of Ansteel
Developer	Voestalpine	Lurgi Metallurgical Company	Voestalpine and POSCO	POSCO and Primetals Technologies	Institute of Process Engineering, Chinese Academy of Sciences
Application unit	BHP	Cleveland-Cliffs Inc. and partners	POSCO	POSCO	Ansteel Bayuquan
Monomer maximum (10 000 t/a)	100	50 (Idle state)	200	30 (Production is scheduled in 2026)	about 1 (Not in service)
Number of fluidized beds	4	3	4	4	2
Melting furnace	None	None	Molten gasifier: Pulverized coal is burned with oxygen to generate heat to melt DRI	ESF furnace with electric melting	None
Ingredients	Ore powder (0.1-8.0 mm)	Ore powder (0.2-8.0 mm)	Sinter powder under sieve (0.5-1.0 mm)	Sinter powder under sieve (0.5-1.0 mm)	Pellet (0.5-1.6 mm)
Reduction gas consumption/(m^3/t DRI)	(Natural gas: about 450	Hydrogen: about 1 000	Melt gasifier gas: 1 350-1 480	Natural gas: about 404	Hydrogen: about 890
Parameter	1) Reactor temperature: R4 (550-570 ℃); R1 (780-800 ℃) 2) Reactor pressure (1.1-1.4 MPa)	1) Reactor temperature: Primary preheated circulating fluidized bed (850-950 ℃); Two stage pre-reduction fluidized bed (630-650 ℃); Three stage horizontal bubbling fluidized bed (630-650 ℃) 2) Reactor pressure:	Reactor temperature: R3 (about 450 ℃); R2 (600-700 ℃); R1 (about 750 ℃)	Reactor temperature: R4 (441 ℃); R3 (636 ℃); R2 (706 ℃); R1 (758 ℃) 2) Reactor pressure (0.5 MPa)	Reactor temperature: First stage (about 700 ℃); Second stage (about 700 ℃)

		about 0.4 MPa			
DRI metallization rate/%	93	93	65-80	about 85	≥92 (predict)
Advantage	High metallization rate of DRI	The choice of ore and reducing agent is flexible	The reduction temperature is low, and there is no strict restriction on the composition and variety of iron ore	Strong adaptability to raw materials, low quality ore can be used	It is claimed that it can solve the problems of bonded loss of flow and slow loss of flow of powdered iron ore
Drawback	It is easy to cause adhesive plugging in the fluidized bed. The process is more complicated	The reduction time of bubbling fluidized bed is long and the efficiency is low	High investment cost and operating cost, low metallization rate, easy to bond plugging	Pending confirmation of validity	Pending confirmation of validity

2.3 Development status of hydrogen-based shaft furnace

Since the WIBERG process was developed in Sweden at the beginning of the 20th century, more than ten gas-based reduction processes have emerged successively. However, the MIDREX process and HYL process are currently widely adopted. These two processes are recognized as relatively mature and stable large-scale production processes with output comparable to that of the blast furnace process. In 2024, the two processes will produce nearly 100 million tons of DRI. It accounts for more than 70% of the total output. Compared with the MIDREX process, the HYL/ENERGIRON process, due to the high H_2 content in the reducing gas, has a large space for carbon reduction and its future capacity share may show an increasing trend. In China, due to the large amount of coke oven gas produced by integrated steel enterprises, the HyMEX shaft furnace hydrogen metallurgy process with zero reforming of coke oven gas has development potential. Comparison of reduction processes of different types of hydrogen-based shaft furnaces are shown in Table 3.

Table 3. Comparison of reduction processes of different types of hydrogen-based shaft furnaces [13-15]

Technology	MIDREX	HYL/ENERGIRON	HyMEX
Developer	Midrex Technologies, Inc., America	HYLSA, Mexico	HBIS Group Zhangxuan technology
Classification	STANDARD: Conventional natural gas reforming and reduction AREX: Natural gas zero-reforming without reforming furnace MXCOL: Non-catalytic partial oxidative reforming of coke oven gas MIDREX H_2: Pure hydrogen shaft furnace reduction technology	HYL-III: Natural gas reforming HYL-ZR: Zero reforming of natural gas or coke oven gas	Zero reforming of coke oven gas
Monomer maximum (10000 t/a)	250 Algerian Qatari Steel Company; Tosyari Company; Thyssenkrupp Steel Duisburg steel plant (Production is scheduled in 2026)	250 Nucor Steel; Jindal Steel Group Volcan Green Steel; Suez Steel Company (Production is scheduled in 2025)	—
Ingredients	The main stream uses 9-16 mm pellet, and a small proportion of 10-35 mm lump ore can be added	The main stream uses 9-16 mm pellet, and a small proportion of 10-35 mm lump ore can be added	9-16 mm pellet
Reduction gas consumption	Natural gas: 280-290 m^3/t DRI	Natural gas: 275-290 m^3/t DRI	Coke oven gas: 550 m^3/t DRI
Parameter	750-900 ℃ 0.2-0.3 MPa	960-1080 ℃ 0.4-0.8 MPa	1000-1050 ℃ 0.7-0.8 MPa

	$\varphi_{H_2}/\varphi_{CO} < 2$	$\varphi_{H_2}/\varphi_{CO}$ = 4-8	$\varphi_{H_2}/\varphi_{CO} \approx 8$
Advantage	Low working pressure and temperature; The process is simple and easy to operate	High production efficiency; High H_2 ratio with large carbon emission reduction range	
Drawback	Low production efficiency	Harsh conditions with high temperature and high pressure operation	

3. HBIS's Zero-Reforming Hydrogen Metallurgy Breakthrough

Leveraging regional advantages, HBIS launched the world's first zero-reforming coke oven gas hydrogen metallurgy project at Zhangxuan Tech. (process flow shown in Figure 1), achieving stable operation in May 2023. The 600,000-ton/year DRI facility sets industry benchmarks:Metallization rate ≥94%, carbon content 2.5-3.0%; 29.3% lower gas use (from 750 to 530 m^3/t); 30.3% power reduction (from 330 to 240 kWh/t).

Through the digestion and absorption of the "zero Reforming Direct reduction Technology for coke oven Gas", HBIS Group has successfully developed the following key technologies: (1) The hydrogen shaft furnace process utilizes high-quality pellets featuring a pelletizing rate exceeding 95%, along with superior reduction characteristics including ≤15% expansion rate and $I_{RD,<3.2mm}$ less than 10% for optimal smelting performance; (2) The advanced purification process achieves exceptional gas quality with H_2/CO ratio exceeding 8, while delivering industry-leading impurity removal rates of 98% for H_2S and 85% for hydroxyl sulfur. Notably, naphthalene content is reduced to just 5mg/m^3 while maintaining a competitive purification cost of 0.1¥/m^3; (3) The DRI-EAF breakthrough enables stable production of premium steel grades (including auto slabs and bearing steel) at 20-45% DRI ratios, achieving >80% yield while reducing nitrogen content by 20ppm compared to traditional processes; (4) The near-zero CO_2 utilization system achieves annual capture of 60,000 tons at 230¥/ton, producing 99.999% pure food-grade CO_2 while enabling innovative microbial protein synthesis from flue gas at 10kg/m^3/day productivity.

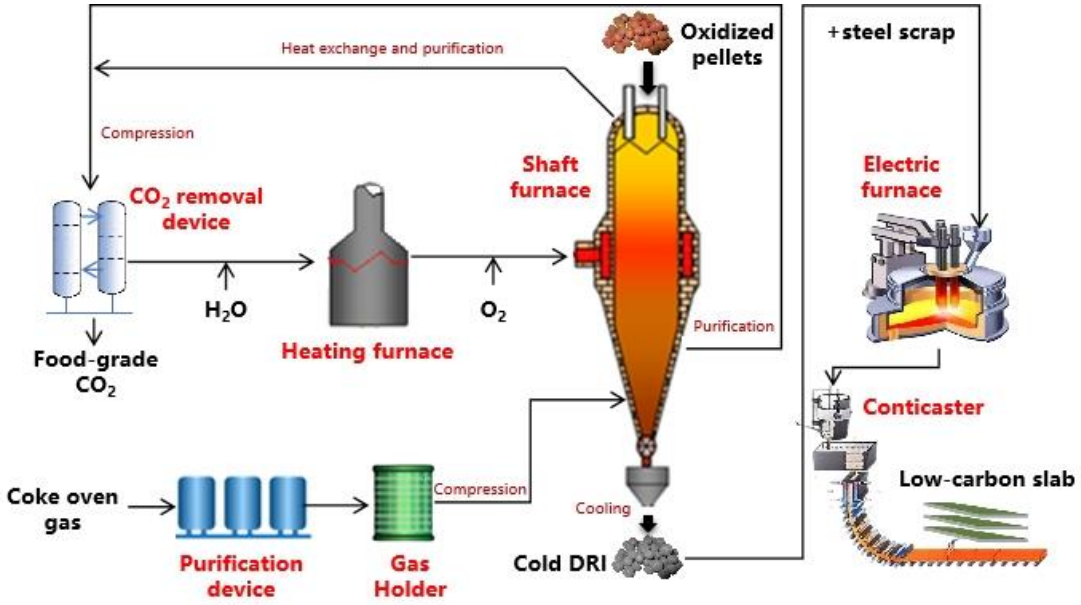

Figure 1. The process flow chart of hydrogen metallurgy based on coke oven gas in HBIS

4. CONCLUSION

Hydrogen metallurgy is internationally recognized as a revolutionary pathway for low-carbon steel production, offering a fundamental solution to energy and emission challenges while enabling the development of low/zero-carbon steel products. Among various technologies, gas-based shaft furnace direct reduction stands out for its high hydrogen utilization, environmental friendliness and compact process flow, having established a mature global technical system. Given China's

limited natural gas resources, coke oven gas-based hydrogen metallurgy with zero-reforming technology currently represents the most viable and scientifically sound approach aligned with domestic resource endowments. Looking forward, as hydrogen metallurgy and supporting EAF technologies mature alongside renewable hydrogen production advances, green hydrogen is poised to become the primary hydrogen source for shaft furnaces, accelerating the steel industry's transition toward zero-carbon emissions.

ACKNOWLEDGEMENTS

The research is funded by China's key R&D program project China-Serbia "Belt and Road" joint laboratory construction and joint research project for green steel manufacturing (NO·2024YFE0215000).

REFERENCES

[1] Q. Fi, G. Yang, H. Jin, et al. Pet. New Energy, 36(4) (2024)19-30.
[2] X. Meng, X. Wu, A. Gu, et al. S&T Foresight., 3(4) (2024) 121-133.
[3] Z. Mao, X. Meng., S&T Foresight., 2024, 3(4) (2024) 4-8.
[4] J. Zhang, Y. Zong, K. Li, et al. Iron Steel., 59(9) (2024) 45-55.
[5] B. Zhang, C. Li. Hebei Metall., 10 (2024) 1-7.
[6] H. Li, C. Guo, X. Wang, et al. Iron Steel., 59(9) (2024) 56-70.
[7] S. Zhang, S. Wu, Y. Qie, et al. China Metall., 35(1) (2025) 32-39.
[8] C. Lan, Y. Gao, Q. Lv, et al. Util. Miner. Resour., 45(3) (2024) 96-101.
[9] M. Wang, R. Ren, H. Dong, et al. Iron Steel., 55(8) (2020) 145-150.
[10] Z. Ying, M. Chu, J. Tang, et al. Hebei Metall., 6 (2019) 1-7+31.
[11] K. Pang, M. Sun, F. Liu, et al. Shanghai Metals, 47(2) (2025) 1-8.
[12] C. Fan, Z. Du, F. Pan, et al. Chin. J. Process Eng, 22(10) (2022) 1325-1332.
[13] J. Tang, F. Li, H. Tian, et al. Beijing: Metall. Ind. Press, 2025.
[14] X. Wang, Y. Qie, N. Li, et al. China Metall., 34(11) (2024) 1-9.
[15] X. Han, C. Zhang, L. Li, et al. Hebei Metall., 4 (2024) 1-5.

The 56th International October Conference on Mining and Metallurgy
22-25 October 2025, Bor Lake, Bor, Serbia
www.ioc.tfbor.bg.ac.rs

DOI: 10.5937/IOC25287J *Original scientific paper*

BEHAVIOR OF PLANT MICRONUTRIENTS (Fe, Cu) DURING COMBUSTION OF CONTAMINATED *Sorghum* spp.

Gvozden Jovanović[1a], Dimitrije Anđić [1b], Danijela Smiljanjić[1c], Dragana Ranđelović[1d], Branislav Marković[1e]

[1] Institute for Technology of Nuclear and Other Mineral Raw Materials, Boulevard Franchet d`Esperey 86, Belgrade, Serbia
[1a] g.jovanovic@itnms.ac.rs, 0000-0002-9754-2230
[1b] d.andjic@itnms.ac.rs, 0009-0001-6824-5202
[1c] d.smiljanic@itnms.ac.rs, 0000-0003-3560-1415
[1d] d.randjelovic@itnms.ac.rs, 0000-0003-4976-7766
[1e] b.markovic@itnms.ac.rs, 0000-0001-9477-8267

Abstract
Forage sorghum (Sorghum spp.) is a fast-growing annual plant that contains certain micronutrients, the most abundant of which is iron, and the least abundant is copper. This paper presents the behavior of these two micronutrients in sorghum species during combustion at different times and temperature conditions. Combustion of the homogenized sample was performed at temperatures of 400 °C, 450 °C, 500 °C and 600 °C in times of 120, 240 and 360 minutes. Differential thermal analysis (DTA) is carried out at a heating rate of 3 K/min from 25 to 500 °C. It was found that the combustion of forage sorghum increased the concentration of these two micronutrients in it. The highest concentration of Fe (7777 mg/kg) was achieved after 360 minutes of combustion at 600ºC, while the highest concentration of Cu (105 mg/kg) was achieved after 240 minutes of combustion at 450ºC.

***Keywords**: Forage sorghum, combustion, differential thermal analysis, iron, copper*

1. INTRODUCTION

Forage sorghum (*Sorghum* spp.) is a fast-growing annual plant known for its tolerance to heat and drought and production of large quantity of biomass. It may be able to withstand soil toxicities without significantly lowering the biomass yield and can be cultivated on variety types of soil. Certain researches revealed that sorghum exhibits phytoremediation potential on multi-metal contaminated sites by using exclusion strategy, where elements remain predominantly stored in plant roots [1,2]. Lima et al. tested the phytoremediation potential of sorghum for Cu in a greenhouse experiment [3]. In treatments with Cu gradient *S. bicolor* showed slight decrease of photosynthetic rates with increase of Cu concentration in soil, however, plant metabolism was not abruptly challenged and transfer of element from root to shot remained low (with ration 0.1-0.6). Use of *S. bicolor* for phytoremediation of iron showed active absorption by root system and limited translocation to shoots [4]. Although concentration of metals in sorghum aboveground biomass after the phytoremediation experiment can remain under the toxicity levels, it can still represent a potential environmental or disposal hazard.

Plant micronutrients, including iron and copper, are necessary components for plant growth and development. In majority of plant species they are found in less than 1% of dry weight mass. Iron and copper uptake in plants is influenced by different environmental factors, including soil type, element solubility, plant species, management practices, and presence of other elements in soil. Crosstalk between Fe and Cu is noticed in plant tissues, where Fe and Cu were found modifying adsorption of each other [5]. Average content of Fe in fodder plants greatly varies from 20-1000 mg/kg, [6]. Average concentration of Cu in sorghum biomass from unpolluted sites is 5.3 mg/kg [7].

Investigation of micronutrient accumulation in sorghum biomass performed by Calvavante et al. showed that Cu was the least adsorbed among investigated macronutrients with ~270 g per ha, while Fe was the most adsorbed element with ~2030 g per ha [8]. Similarly, Aide and Mueller confirmed this phenomenon by testing varieties of sweet sorghum where micronutrient adsorption rates were found to be the highest for Fe (up to 1030 g/ha) and the lowest for Cu (120 g/ha) [9].

The aim of this paper is to show how the most and least abundant plant micronutrient (Fe, Cu) in the sorghum species behave during combustion at different times and temperature conditions. It is important to see how these elements behave in order to properly determine following steps for their use in the valorization of the ash or their removal beforehand.

2. EXPERIMENTAL

Forage sorghum's (*Sorghum* spp.) potential for phytoextractions of multi-element contaminated dredged sediment landfill located along the Begej canal, north-eastern Serbia. This sediment is characterized by multi-metal contamination [10]. Two- month's old *Sorghum spp.* biomass was harvested in July 2024, air-dried and homogenized prior to analysis. The combustion of the samples was carried out in a furnace equipped with thermocouple and temperature control unit. Combustion was performed on homogenized samples at four different temperatures (400 ºC, 450 ºC, 500 ºC, 600 ºC) and three different times (120 min, 240 min, 360 min). The concentration of micronutrients in the plant mass and ash after combustion was determined using atomic absorption spectrometry (AAS) (PinAAcle 900T PerkinElmer, Inc, Norwalk, CT, USA). Differential termal analysis was carried out by Netzsch STA 449 F5 Jupiter, using an synthetic air atmosphere flow (50 ml/min), with a heating rate of 3 K/min from 25 ºC to 500 ºC and an isothermal segment of 4 hours.

3. RESULTS AND DISCUSSION

As seen in Figure 1, the reduction in mass varied from time and temperature between 88,7 % to 92,9 % while the average loss was 90,8%. These values are expected when it comes to plant matter combustion at such elevated temperatures.

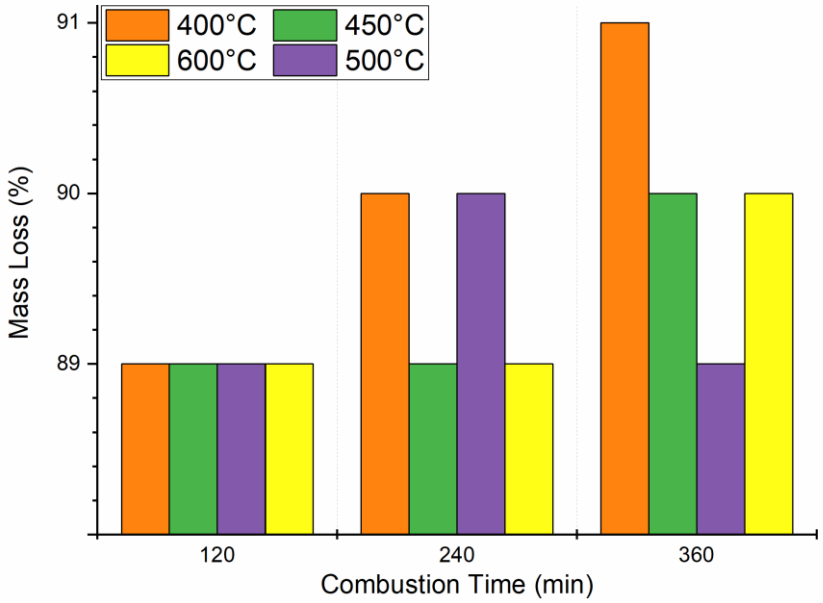

Figure 1. Loss of sample mass after combustion.

Before combustion the homogenized powdered biomass was analyzed for its chemical composition, given in table 1. As expected for the *Sorghum spp.* the highest adsorption rates were for Fe (201,5 mg/kg) and the lowest were for Cu (8,37 mg/kg).

Table 1. Elemental content of plant micronutrients in dry homogenized Sorghum biomass.

Element Concentration (mg/kg)				
Cu	Zn	Fe	Cr	Ni
8,37	55,61	201,5	11,12	11,24

The changes in concentration for Fe and Cu in the combust ashes follow very different patterns, as can be seen in Figure 2. The concentration of Fe is much higher in range of 2600 to 7800 mg/kg, while the Cu concentration is rather low and ranges from 65 to 105 mg/kg. The highest Fe concentration is found after 360 min at 600 ºC, and the highest concentration of Cu is found after 240 min at 450 ºC. A similar spike in concentration of both elements can be seen at 450 ºC after 240 min of combustion. However, what is more interesting is the drop in concentration at 500 ºC, more pronounced for Fe but still present for Cu as well.

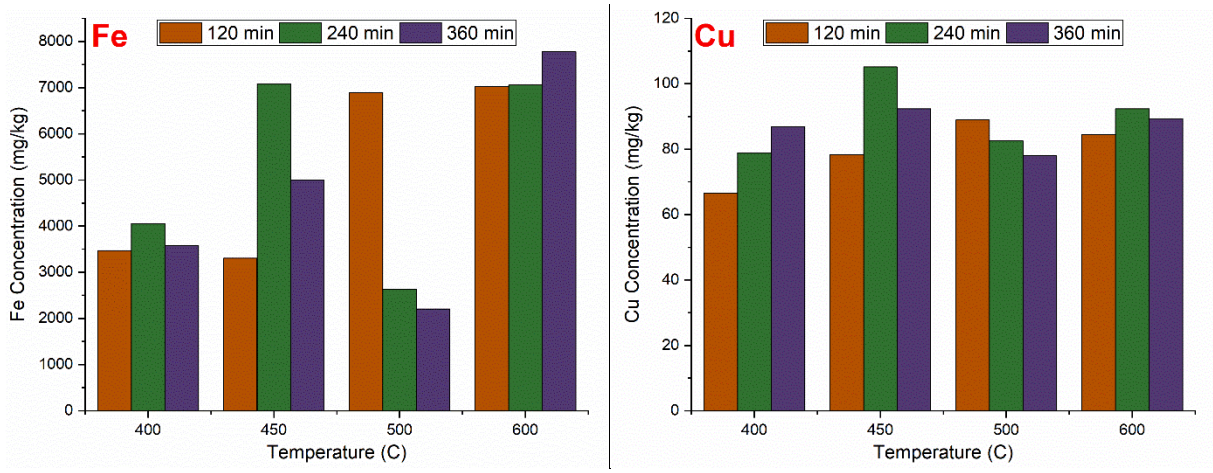

Figure 2. Changes in Fe and Cu concentration in combustion ash according to combustion time and temperature.

As shown in Figure 3, differential thermogravimetric analysis showed a mass loss of 8,05 % between 25 and 150 ºC, about 58,03 % from 150 to 400 ºC and finally 18,09 % from 400 to 500 ºC, and isothermally at 500 ºC around 7,05%. This makes up a total loss of mass 91,22 %, which is in agreement with the measured loss after combustion given in Figure 1.

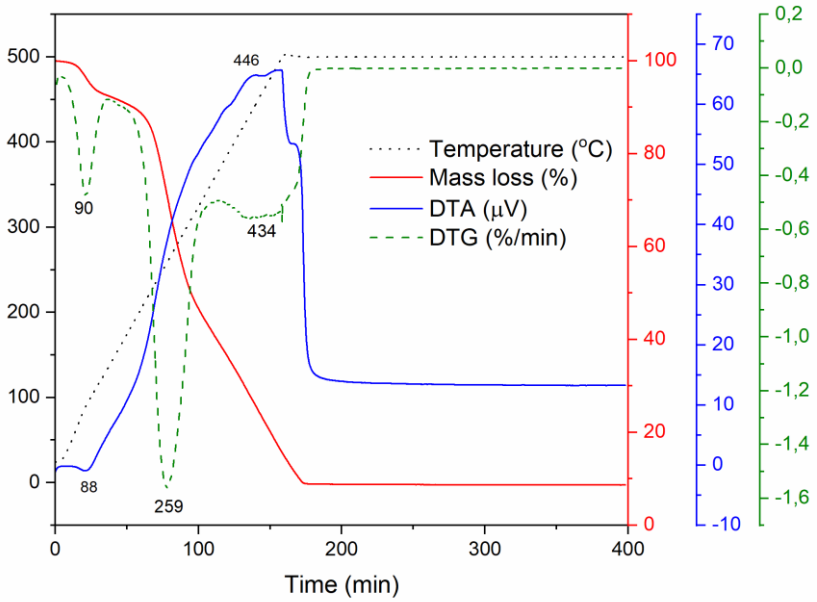

Figure 3. DTA/DTG results for sample combusted at 500 ºC for 240 min.

If we look at the values of Fe and Cu given in Table 1 and Figure 2, the increase of the concentration of these elements is notable, due to the huge reduction of mass from plant to ash. The minimal increase in concentration of Fe is 378% (500 ºC/ 360 min) and for Cu it is 254% (400 ºC/ 120 min). However, the highest increase in concentration of Fe is 1585% (600 ºC/ 360 min) and for Cu it is 459% (450 ºC/ 240 min).

4. CONCLUSION

This study has shown how Fe and Cu, the most and among least absorbed plant micronutrient for the *Sorghum* species, behave during combustion at different times and temperatures. The loss of mass around 90% during combustion, confirmed both by DTA and scale, contributed to their high increase in concentration. The highest concentration for Fe (7777 mg/kg) was achieved after 360 min of combustion at 600ºC while the highest concentration for Cu (105 mg/kg) was achieved after 240 min of combustion at 450ºC. Further studies need to be conducted on the behavior of all the plant micronutrient and their influence on potential valorization of the combusted ash. Depending on the chosen micronutrient for valorization the presence of other elements can decrease the purity of the valorized product thus it is important to have a clear idea on how their concentration behaves during combustion to ease future purification steps.

ACKNOWLEDGEMENTS

This work was supported by the Ministry of Science and Technological Development and Innovation of the Republic of Serbia (Contract No. 451-03-136/2025-03/200023)

REFERENCES

[1] K. Oh, T. Cao, H. Cheng, X. Liang, X. Hu, L. Yan, S. Yonemochi, S. Takahi, JBM, 3 (2015) 9-14.
[2] A. May, E. da Silva, M. dos Santos, R. Viana, F. dos Santos, M. Filho, Res., Soc. Dev., 9 (9) (2020) e95996770.
[3] L.R. Lima, H.F. Silva, A.S. Brignoni et al., Physiol. Mol. Biol. Plants, 25 (2019) 433–441.
[4] S.V. Gorelova, A.P. Kolbas, A.Y. Muratova, M.V. Frontasyeva, I. Zinicovscaia, O.I. Okina, in Phytoremediation (L. Newman, A.A. Ansari, S.S. Gill, M. Naeem, R. Gill, eds.), Springer, Cham, 2023.
[5] S. Rai, P.K. Singh, S. Mankotia, J. Swain, S.B. Satbhai, Plant Stress, 1 (2021) 100008.
[6] A. Kabata-Pendias, Trace Elements in Soils and Plants, Taylor and Francis Group, LLC, London, 2011.
[7] G. Hacisalihoglu, P.R. Armstrong, Plants, 11 (3) (2022) 451.
[8] T.J. Cavalcante, G. Castoldi, C.R. Rodrigues, M.M. Nogueira, A.M. Albert, Pesquisa Agropecuária Tropical, 48 (4) (2018) 364-373.
[9] M. Aide, W. Mueller, Int. J. Appl. Agric. Res., 11 (2) (2016) 159-171.
[10] B. Dalmacija, M. Prica, I. Ivancev-Tumbas, A. Van der Kooij, S. Roncevic, D. Krcmar, I. Bikit, I. Teodorovic, Environ. Int., 32 (5) (2006) 606-615.

The 56th International October Conference on Mining and Metallurgy
22-25 October 2025, Bor Lake, Bor, Serbia
www.ioc.tfbor.bg.ac.rs

DOI: 10.5937/IOC25291Z *Original scientific paper*

ANALYSIS OF THE NEW SINTER LINE IN HBIS GROUP SERBIA AND CREATING CONDITIONS FOR PRODUCTION IMPROVEMENT

Igor Zlatković[1a], Živko Đorović[1b]

[1] HBIS GROUP Serbia Iron & Steel d.o.o. Beograd, Serbia
[1a] izlatkovic@hbisserbia.rs, 0009-0006-9125-3063
[1b] zdjorovic@hbisserbia.rs, 0009-0000-4993-3440

Abstract
In order to create adequate conditions for increasing of production and improving the productivity of sinter, the multidisciplinary sinter production team of HBIS GROUP SERBIA IRON & STEEL analyse all technical and technological production parameters of the New Sinter Line. Trying to create conditions for increasing productivity through the analysis of production parameters and through an innovative approach, thus enabling the realization of a predetermined production plan, meeting the legal requirements for limiting the emission of polluting exhaust gases. With the new sinter line, three segments, which are the subject of this paper, has been improved:

1. *production - technological goal, which includes increasing sinter production, increasing productivity, improving the quality of produced sinter, rationalizing production, as well as reducing costs per unit of product,*
2. *rationalization of energy consumption and energy efficiency of the newly built Sinter plant*
3. *improvement of environmental protection through the technological process as well as the application of adequate technological systems for environmental protection within the New Sinter plant.*

1. INTRODUCTION

Sinter production is a pivotal step in iron-making, converting fine iron-bearing materials into a porous agglomerate (sinter) suitable for blast furnace feed. Efficient sinter strand operation affects raw material utilization, energy consumption and emissions. HBIS GROUP Serbia commissioned a modern sinter strand in Smederevo in 2022. This installation was designed for a theoretical capacity of 1.6 million tonnes per year and incorporates state-of-the-art combustion, air handling, dedusting and desulphurization systems [1-5].

Objectives of this paper are to:

1. Present the technical description of the sinter strand and its control/operation concept.
2. Summarize operational experience and discuss the best production year (2023).
3. Analyze energy usage and outline sustainability measures and opportunities for further improvement.

2. EXPERIMENTAL (PLANT DESCRIPTION AND OPERATIONAL METHODOLOGY)

2.1 Plant technical data and layout

Theoretical capacity: 1.6 million t/year (continuous operation). This corresponds to approximately 4,384 t/day or ~183 t/h (24/7 operation).
Layer height: 700 mm.
Ignition temperature: 1100 °C (set point for ignition furnace operation and start of sinter bed combustion).

Suction chambers: 22 chambers with average burn-through temperature of 350–360 °C; designed suction in the range 10–12 kPa.

Ignition furnace: 3 rows × 12 burners per row (36 burners total); fuel used exclusively: blast furnace gas.

Dedusting and gas cleaning: Electrostatic precipitator (ESP) for particulate capture and a desulphurization tower for SOx reduction.

Staffing and control: Machine crew of 6 operators (on-site maintenance/operation) and 3 SCADA operators who oversee material dosing, sinter strand parameters and sinter distribution to the blast furnace.

2.2 Operational methodology and data collection

Operational data discussed here were collected from the plant control system (SCADA), maintenance records and production logs. Key performance indicators (KPIs) include: throughput (t/day), fuel consumption (Nm^3 BF gas per tonne sinter), sinter quality indices (e.g. tumbler index, reducibility), emissions (particulate matter, SOx) and availability/downtime statistics. The best production year (2023) is used as a reference for performance analysis and benchmarking.

3. RESULTS AND DISCUSSION

3.1 Throughput and production performance

Theoretical capacity of 1.6 million t/year translates to an average continuous throughput of about 4,384 t/day (1,600,000 / 365) or roughly 183 t/h (24 h operation). During the plant's best production year (2023) the strand achieved its highest availability and production rates; operational practices that likely contributed to the success included tight process control via SCADA, optimized burner management in the ignition furnace (using only blast furnace gas), and effective dedusting and off-gas handling which minimized unplanned stoppages.

3.2 Thermal design and combustion control

Ignition at 1100 °C and a layer height of 700 mm define the thermal regime of the sinter bed. The ignition furnace (3 rows × 12 burners) operating on blast furnace gas provides a homogeneous ignition front and reduces reliance on liquid or purchased fuels. Burn-through temperatures in the suction chambers (350–360 °C) are within typical industry ranges for stable burn-through and gas permeability. Suction levels (10–12 kPa) are moderate and indicate robust air management; consistent suction control is crucial for uniform burnt-hrough and sinter quality.

Proper burner staging, frequent calibration of nozzle flows and regular monitoring of BF gas composition ensure consistent heat input and avoid local overheating or under-ignition that would degrade sinter quality or increase energy consumption.

3.3 Dedusting and desulphurization performance

The modern ESP provides high-efficiency particulate removal from off-gases and protects downstream equipment (including the desulphurization tower) while reducing fugitive emissions. The desulphurization tower targets sulphur oxides—especially important given the use of blast furnace gas and the large throughput—reducing SOx releases and contributing to compliance with environmental regulations.

Key operational considerations:

ESP performance is dependent on gas temperature, humidity and dust load; maintaining optimal gas temperature is necessary for consistent capture efficiency.

The desulphurization tower efficiency depends on reagent quality, gas-liquid contact and residence time. Online monitoring of inlet and outlet SOx concentrations helps to maintain target removal efficiencies.

3.4 Energy usage and sustainability

Energy use in sintering stems primarily from the ignition furnace (fuel), off-gas handling (fans, dedusting), and auxiliary systems (dosing, conveyors, cooling). Using blast furnace gas as the exclusive fuel for the ignition furnace is a strong sustainability measure because it utilizes a by-product gas from iron-making that would otherwise require flaring or external treatment; this improves overall plant energy integration and reduces external fossil fuel consumption.

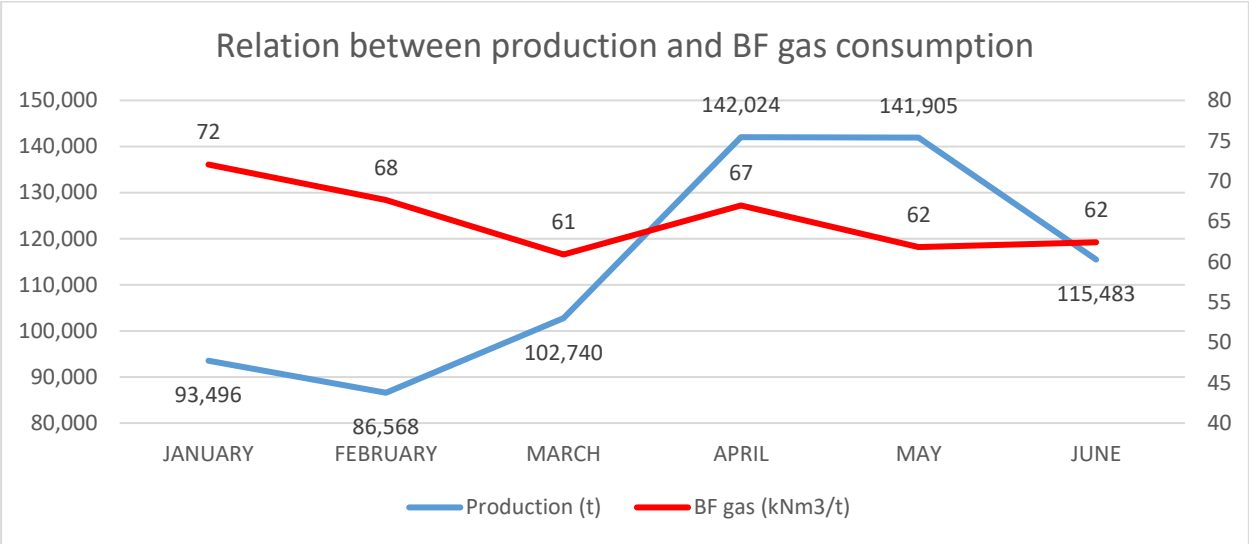

Figure 1. Production/BF gas consumption graph

Specific energy considerations and opportunities:

Fuel recycling and heat recovery: High-temperature off-gases (from ignition and burn-through) can be routed through waste-heat recovery systems to preheat combustion air, dry feed materials or generate low-pressure steam. Heat recovery reduces net primary fuel demand per tonne of sinter.

Optimization of BF gas use: Continuous monitoring of BF gas calorific value and adaptive burner control can optimize energy input. Using only BF gas eliminates natural gas use, lowering the carbon footprint of sinter ignition.

Electrical energy: Efficient energy management is one of the key factors in modern sinter plant operation. While the sinter strand represents the dominant consumer of electricity during production, significant savings can be achieved by focusing on consumption patterns when the strand is not in operation. In many cases, auxiliary equipment such as blowers, pumps, conveyors, cooling fans, or dust extraction units continue to run even when the strand is idle. This practice leads to unnecessary energy losses and increased operational costs.

At HBIS GROUP Serbia, particular attention is placed on eliminating non-essential electricity consumption during downtime. A systematic approach has been introduced, where equipment is categorized into critical and non-critical groups. Critical equipment required for maintaining safe conditions, such as cooling water circulation or essential instrumentation, remains active. All other equipment is subject to controlled shutdown through predefined operating procedures and automated interlocks tied to the strand's operational status.

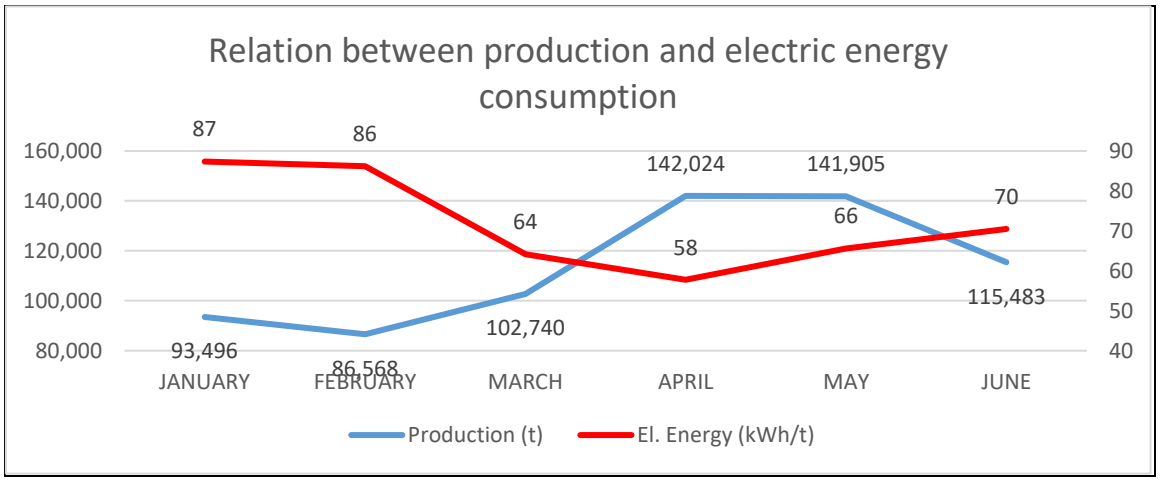

Figure 2. El. Energy consumption/Production graph

This strategy ensures that only the devices directly needed for strand operation are consuming power, while auxiliary units are automatically disconnected during idle periods. In addition to lowering electricity consumption, this approach reduces mechanical wear, prolongs equipment life, and lowers maintenance requirements. By managing electricity in this way, the plant minimizes its environmental footprint and strengthens overall production efficiency, without compromising safety or process stability.

Process control and SCADA: The plant SCADA system that controls material dosing and distribution to the blast furnace contributes to energy savings by stabilizing the sintering process, reducing overuse of fuel due to poor bed permeability or insufficient ignition.

The circular cooler's off-gas represents the largest single source of recoverable sensible heat on the new sinter strand. In the next phase, this heat will be captured from the early cooling zones and routed to a waste-heat boiler to generate low-pressure steam and hot water. The recovered energy will be used to preheat ignition hood/combustion air, condition boiler-feedwater. This integration cuts natural-gas consumption on the strand, lowers specific CO_2 emissions, and stabilizes strand thermal balance—supporting higher productivity and more consistent burn-through.

Sustainability impacts:
Utilization of BF gas reduces external fuel consumption and CO_2 emissions associated with purchased fuels.

Effective ESP and desulphurization control particulate and SOx emissions, improving local air quality and regulatory compliance.

Opportunities for further CO_2 reduction include waste-heat recovery, electrification of auxiliary systems using low-carbon grid electricity, and process optimization to reduce specific energy consumption (GJ/t).

3.5 Economical advantage

One of the key advantages of modern sinter strand technology is the direct correlation between productivity and production cost. With higher strand utilization and improved process stability, the fixed operational expenses—such as labor, maintenance, and energy consumption of auxiliary equipment—are distributed over a larger output. This results in a lower cost per ton of sinter produced. The increase of productivity on the new sinter strand not only ensures higher annual output, but also creates a sustainable reduction in production costs, strengthening the competitiveness of the steel plant in a highly demanding market.

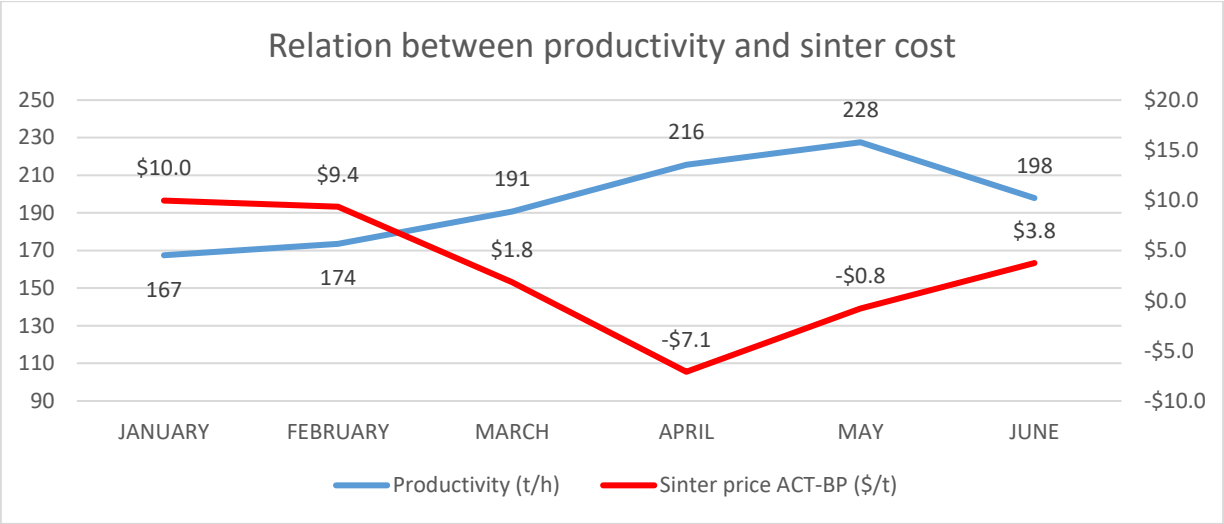

Figure 3. Productivity/cost difference

3.6 Operational staffing and automation

A compact machine crew (6) supported by 3 SCADA operators reflects a high degree of automation. Centralized SCADA control of dosing, strand speed, distributor control and off-gas handling enables consistent product quality and energy-efficient operation. Key human factors considerations include operator training, alarm management and clear procedures for manual interventions.

4. CONCLUSION

The new sinter strand at HBIS GROUP Serbia, commissioned in 2022 and achieving its best production year in 2023, demonstrates modern sinter technology integrated with energy-conscious practices. Principal conclusions:

1. The strand's theoretical capacity of 1.6 million t/year (~4,384 t/day, ~183 t/h) positions it as a high-throughput unit; robust suction management (10–12 kPa) and burnthrough temperatures (350–360 °C) indicate stable combustion and gas permeability.
2. The ignition furnace design) that uses only blast furnace gas is an important sustainability feature, enabling internal fuel recycling and reduced external fuel dependence.
3. Modern dedusting (ESP) and desulphurization minimize particulate and SOx emissions, aligning with environmental standards and supporting sustainable development goals.
4. Energy efficiency can be further improved through waste-heat recovery, fine-tuning of BF gas utilization and continued process automation and operator training.

Overall, the plant represents a strong step toward integrated, energy-aware sinter production for HBIS GROUP Serbia.

ACKNOWLEDGEMENTS

The authors thank the HBIS GROUP Serbia operations, maintenance and manager teams for providing technical data and operational insights. Special thanks to the commissioning team and operations staff whose efforts made the best production year possible.

REFERENCES

[1] W.R.A. INSTITUTE, Sintering of Iron Ores and Agglomeration, 3rd ed.,.
[2] J. Smith, A. Kumar, "Energy optimization in sinter plants," Ironmaking Journal, 100–112.
[3] International Energy Agency (IEA), "Industrial energy efficiency pathways," Repor.
[4] K. Zhang et al., "ESP performance in sinter plant gas cleaning," Environmental Progress.
[5] M. Rossi, "Desulphurisation technologies for sinter off-gases," Metallurgical Transactions,

The 56th International October Conference on Mining and Metallurgy
22-25 October 2025, Bor Lake, Bor, Serbia
www.ioc.tfbor.bg.ac.rs

DOI: 10.5937/IOC25296T Original scientific paper

VALORIZATION OF FLY ASH AND PLASTIC WASTE USING GEOPOLYMERIZATION TECHNOLOGY

Nebojša Tadić[1a], Irena Nikolić[1b], Nina Jovović [1c], Dejana Dizdar[2a, 3a], Vanja Asanović[1d], Milena Tadić[1e]

[1] Faculty of Metallurgy and Technology, University of Montenegro, Džordža Vašingtona bb, Podgorica, Montenegro
[2]MONTWAYLCC, Cetinjski put -NEST Coworking bb, Podgorica, Montenegro
[3]Faculty for Food Technology, Food Safety and Ecology, University of Donja Gorica, Podgorica, Oktoih 1, Podgorica, Montenegro
[1a] nebojsa@ucg.ac.me, 0009-0007-5458-8232
[1b] irena@ucg.ac.me, 0000-0001-6781-3485
[1c] jovovicnina12@gmail.com, 0009-0000-5154-2465
[1d] vanjaa@ucg.ac.me, 0000-0001-8592-3266
[1e] milenak@ucg.ac.me, 0000-0001-7321-8842
[2a] dejana.dizdar30@gmail.com, 0009-0002-6590-3895

Abstract

This paper aimed to investigate the possibility of synthesis of geopolymers based on the fly ash with the addition of plastic waste (high-density polyethylene (HDPE) and polypropylene PP). Influence of plastic waste dosage and time of curing and solid to liquid (S/L) ratio on the compressive strength of fly ash-based geopolymes were investigated.

The results have shown that fly ash-based geopolymers synthesized with plastic waste can be successfully prepared under the S/L ratio of 0.9 and 1, mass ratio of alkali activator (Na_2SiO_3/NaOH) of 1, and plastic dosage up to 30%. The highest strength displayed the geopolymers synthesized by the fly ash replacement with plastic waste of 10 %, cured for 48 h at S/L ratio of 0.9. Generally, flay ash-based geopolymer with the addition of HDPE reaches a higher strength in comparison to those prepared with PP under the same conditions of synthesis.

Keywords: *Fly ash, geopolymers, plastic waste, high-density polyethylene (HDPE), polypropylene (PP), compressive strength*

1. INTRODUCTION

In line with the Paris Agreement from 2016. year, global warming must be limited to 1.5 ºC to minimise the greenhouse effect [1]. So, it is necessary to minimise anthropogenic inputs of carbon dioxide into the atmosphere from major sources, including the cement production industry. Approximately 0.9 tonnes of carbon dioxide are released in the production of one tonne of cement [2]. It is estimated that global cement production contributes a significant 8% to total carbon dioxide emissions [3], and its replacement with secondary raw materials could reduce the annual global carbon dioxide emissions by up to 1.3 gigatons [4]. From this point of view, fly ash, the waste material from coalfired power stations, has been extensively researched in the past two decades as a partial or full replacement for cement binder in construction.

The innovative technology known as geopolymerization enables the utilization of fly ash to produce new eco-friendly building materials known as geopolymers, which are currently considered an alternative to cement binders. Geopolymers are produced under alkali activator action of natural minerals, or solid industrial waste rich in silicon and aluminium. These materials are environmentally friendly binders due to their lower carbon dioxide emissions from the

manufacturing process and elimination of natural resources consumption, while the compressive strength and durability are comparatively high.

On the other hand, current levels of plastic usage and disposal at the global level generate serious environmental problems since it is a persistent organic pollutant. Every year, millions of tons of plastic end up in the environment, posing environmental, economic, health and aesthetic problems. Since plastic waste can also be utilized in building materials [5], this research aimed to investigate the possibility of co-valorisation of fly ash and plastic waste (high-density polyethylene (HDPE) and polypropylene (PP)) through the geopolymerization process.

2. EXPERIMENTAL

Fly ash was supplied from a coal fired power station in Pljevlja and plastic waste (PP and HDPE) from the MONTWAY Podgorica. Figures of source materials are given in Figure 1 (a-c). Fly ash-based geopolymers containing plastic waste PP (denoted as FPP) and HDPE (denoted as FHDPE) were prepared by adding PP and HDPE to the starting mixture by fly ash replacement with a 10-30% to the total solid content. First, fly ash was mixed with alkali activator at solid to liquid (S/L) ratios of 0.9 and 1, and then, plastic waste was added. Alkali activator was prepared by mixing 7M NaOH solution and Na_2SiO_3 solution (commercial water glass) at a mass ratio of 1:1. Prepared geopolymers were casted in a plastic mould, sealed with a lead and cured in the oven at a temperature of 65 °C for a period of 24 h and 48 h. After 7 days, the samples were removed from mould and tested for compressive strength.

3. RESULTS AND DISCUSSION

The initial components (fly ash, PP, HDPE) and resulting geopolymers are shown in Figure 1 (a–e), and the influence of plastic waste dosage on compressive strength of fly ash-based geopolymers is given in Figure 2.

The results have shown that fly ash-based geopolymers can be synthesized with both PP and HDPE plastic waste addition (Figure 1). The results presented in Figure 2 generally show that prolongation of curing time from 24 h to 48 h leads to the strengthening of the geopolymeric structure, regardless of the type of plastic added to the geopolymeric mixture. Geopolymers prepared with a mixture of fly ash and HDPE reach a higher compressive strength in comparison to geopolymers prepared with the addition of PP plastic. The highest strength (13.5 MPa) exhibited the fly ash-based geopolymers prepared with the addition of 10% HDPE. The increase of fly ash replacement with HDPE to 30% led to the weakening geopolymeric structure and strength decrease to 6.2 MPa. The geopolymer prepared with a PP follows the same pathway of strength change upon the PP addition. The highest strength of geopolymer prepared with PP was obtained for geopolymers containing 10% PP (11.5 MPa), and the lowest strength (4 MPa) was obtained for geopolymers containing 30% of PP.

The influence of S/L ratio on the strength of fly ash-based geopolymers containing plastic waste (PP and HDPE) is given in Figure 3. The influence of S/L ratio on the strength of geopolymers is only evident at the plastic waste dosage of 10%. Geopolymers containing 10% plastic waste prepared at the S/L ratio of 0.9 reach higher strength in comparison to those synthesized at S/L=1. When a higher plastic waste dosage was applied, practicaly there was no influence of S/L ratio on the strength of geopolymers.

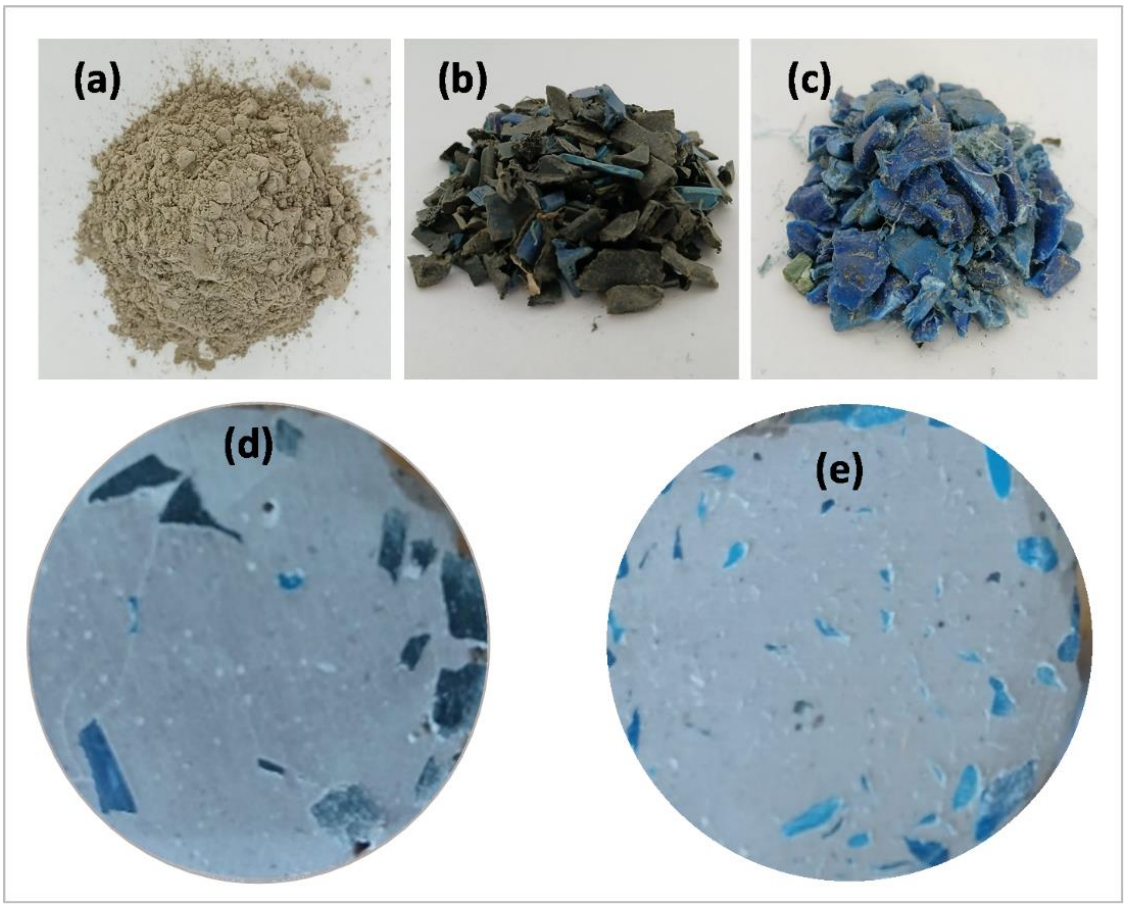

Figure 1. Figures of source materials (a) - fly ash, (b) - PP, (c) - HDPE, and fly ash-based geopolymers with (c) - PP and (d) - HDPE

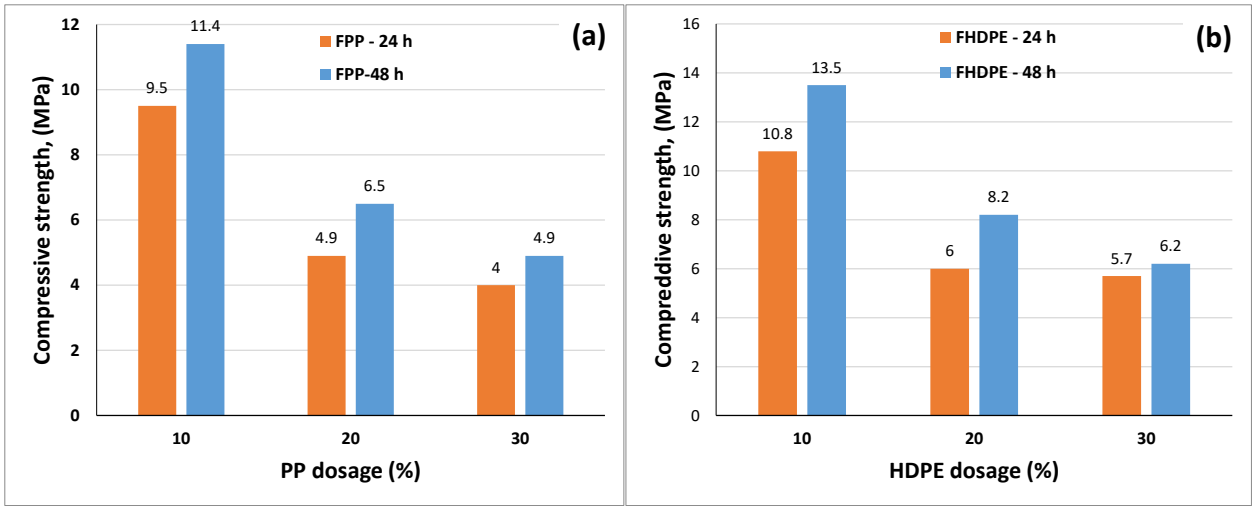

Figure 2. Influence of plastic waste dosage FPP (a) and FHDPE (b) on compressive strength of fly ash-based geopolymers at S/L=0.9

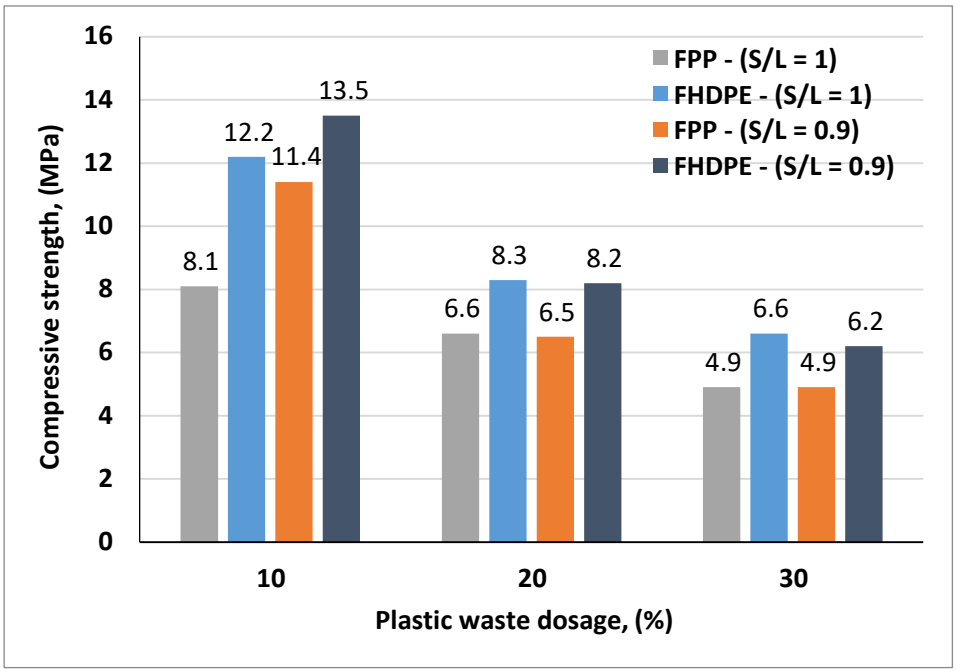

Figure 3 - Change of compressive strength of fly ash-based geopolymers prepared at different S/L ratios and plastic waste dosage

4. CONCLUSION

Fly ash-based geopolymers were synthesized with the addition of plastic waste (PP and HDPE) up to 30 %. The highest strength was exhibited by the geopolymers synthesized with a 10% replacement of fly ash with plastic waste. Geopolymers synthesized with HDPE were generally stronger than those prepared with PP. The highest strength of fly ash-based geopolymers with plastic waste was achieved at the S/L ratio of 0.9. Prolongation of the time of curing from 24 h to 48 h slightly strengthens the geopolymers' structure.

ACKNOWLEDGEMENTS

This work is funded by the Innovation Fund of Montenegro, Grant Contract No. CGI-004-24.

REFERENCES

[1] UN, The Paris Agreement, https://unfccc.int/process-and-meetings/the-paris-agreement (accessed: June 15, 2025.)
[2] F.N. Stafford, F. Raupp-Pereira, J.A. Labrincha, D. Hotza, J. Cleaner Prod., 137 (2016) 1293-1299.
[3] F. Belaïd, Resour. Conserv. Recyl. Adv., 15 (2022) 200084.
[4] I.H. Shah, S.A. Miller, D. Jiang, R. Myers, J. Nat. Commun, 13 (1) (2022) 5758.
[5] K.H.D. Tang, CSUE, 2 (2) (2022) 96-109.

The 56th International October Conference on Mining and Metallurgy
22-25 October 2025, Bor Lake, Bor, Serbia
www.ioc.tfbor.bg.ac.rs

DOI: 10.5937/IOC25300V Original scientific paper

INDUSTRIAL OPTIMIZATION OF BOF STEELMAKING: INCREASING SCRAP RATIO THROUGH HOT METAL PARAMETAR CONTROL

Miloš Vuleta[1a], Milodarka Žugić[1b], Vladan Andrejić[1c], Tamara Ristić[1d]

[1] HBIS Serbia, Smederevo, Carigradska 55, 11300 Smederevo, Serbia
[1a] mvuleta@hbisserbia.rs, 0009-0004-4729-6707
[1b] mzugic@hbisserbia.rs, 0009-0004-1403-1323
[1c] vandrejic@hbisserbia.rs, 0009-0004-3831-1565
[1d] tamararistic@hbisserbia.rs, 0009-0000-7048-1469

Abstract

This paper presents the results of an industrial process improvement in BOF converters aimed at increasing the consumption of steel scrap by stabilizing the input parameters of hot metal, primarily its temperature and silicon content. By implementing control points and making technical and technological adjustments to the blast furnace operating regime and hot metal transport, consistency of the input raw material was achieved. This directly enabled a higher and more secure scrap charge in the converter process.

Through systematic process monitoring and statistical analysis of results from October 2023 to December 2024, an increase in average steel scrap consumption of 2.36% was recorded, representing a significant improvement compared to the previous reference period. At the same time, energy savings were achieved, oxygen consumption was reduced, and converter yield was improved. The planned targets were exceeded, with the achieved result being 1.62% above the initially defined goals.

The obtained results confirm that stabilizing the quality of hot metal in terms of temperature and chemical composition represents a key factor for the successful and sustainable integration of increased amounts of steel scrap in the BOF process. This study provides a foundation for further digital optimization of the converter charging process and greater flexibility in raw material management under modern steel plant operating conditions.

Keywords: *BOF converter, steel scrap, hot metal, input stability, process optimization*

1. INTRODUCTION

In modern basic oxygen furnace (BOF) steelmaking, increasing the share of steel scrap in the charge is one of the main process optimization objectives, as it directly contributes to cost reduction, lower energy consumption and CO_2 emissions, and greater flexibility in the use of available raw materials. However, achieving this goal under industrial conditions requires high stability and predictability of the hot metal input parameters, primarily its temperature and chemical composition.

One of the key challenges in this process is controlling the energy balance in the converter, since excessive temperature losses during hot metal transport from the blast furnace to the steel shop limit the potential for increasing scrap rates. At the same time, the chemical composition—particularly silicon content—has a direct impact on the thermal balance of the reaction and the efficiency of decarburization. By increasing the silicon content and reducing temperature fluctuations, it is possible to provide more stable conditions for scrap melting, enabling a safe and consistent increase in its share in the charge.

This paper presents the results of an industrial process improvement implemented from October 2023 to December 2024, during which targeted technical and technological measures were applied

to the blast furnace operation and hot metal transport. The collected data show that the average scrap consumption increased by 2.36% compared to the reference period, exceeding the planned target by 1.62%. In addition, oxygen consumption was reduced, steel yield was improved, and the process energy balance was optimized.

2. EXPERIMENTAL

The chart 1 shows the monthly share of steel scrap in the total BOF converter charge mass for the period October 2023 – December 2024. The target value is 20.5%. In 2023, the share was 19.76%, while from October 2023 onwards, the values remained consistently above the target, ranging from 20.56% (November 2023) to 23.17% (August 2024). The data represent weighted monthly averages from production records, calculated based on all heats produced during the observed month.

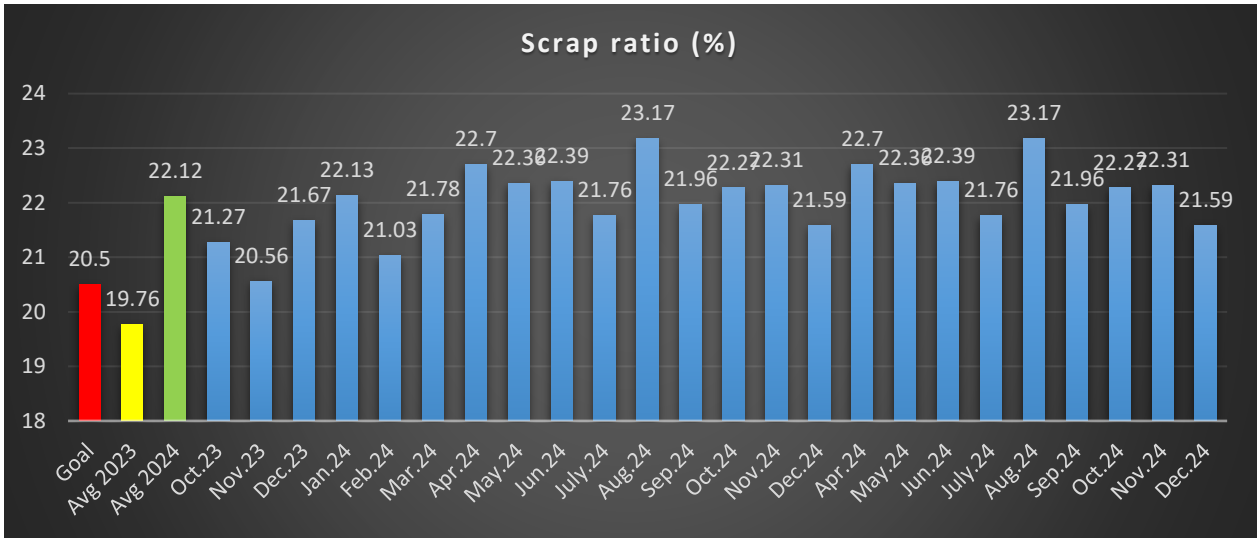

Chart 1. Scrap ratio

The chart 2 depicts the monthly average temperature of hot metal (HM) charged into the BOF converters, measured using disposable thermocouple probes during each delivery from the blast furnace and before charged in convertors from mixer or transport ladles. In 2023, the average temperature was 1294°C, while from October 2023 to December 2024, values ranged between 1304°C and 1333°C and average temperature was 1321°C in 2024.

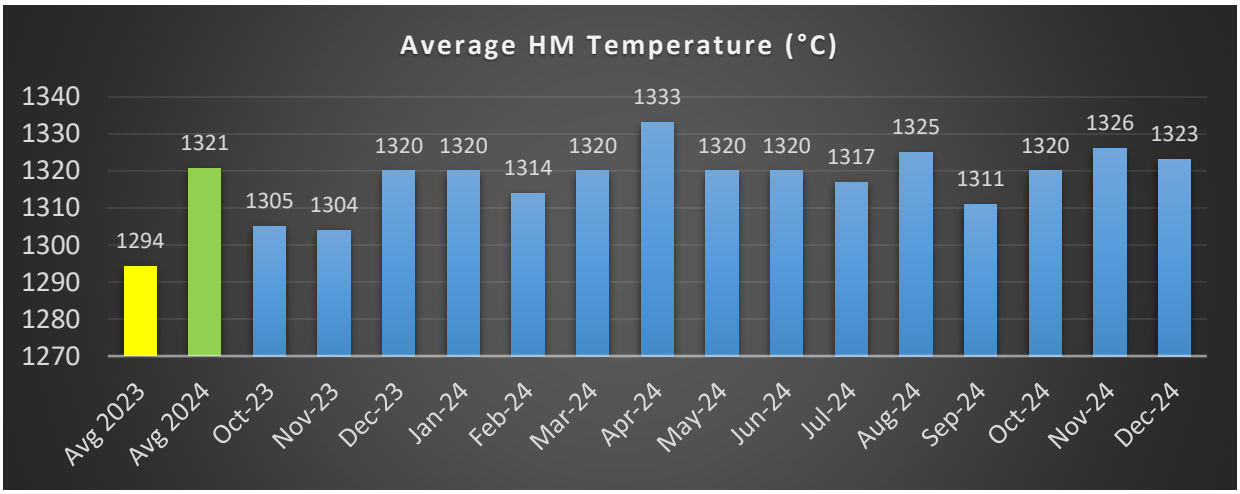

Chart 2. Average HM temperature charged in convertors

The chart 3 depicts the monthly average silica content in HM charged into the BOF converters, determined by chemical analysis of samples taken from the transport ladles using a spectrometer.

In 2023, the average content was 0.749%, and from October 2023 onwards, values ranged between 0.693% and 0.811%. The average value for the observed 2023 period was 0.761%, while in 2024 it was 0.720%. To improve control of hot metal Si contains in blast furnace (BF) process the following was undertaken. Screens of ore materials were reconstructed, new equipment for sampling raw material and sample preparation was purchased and installed.

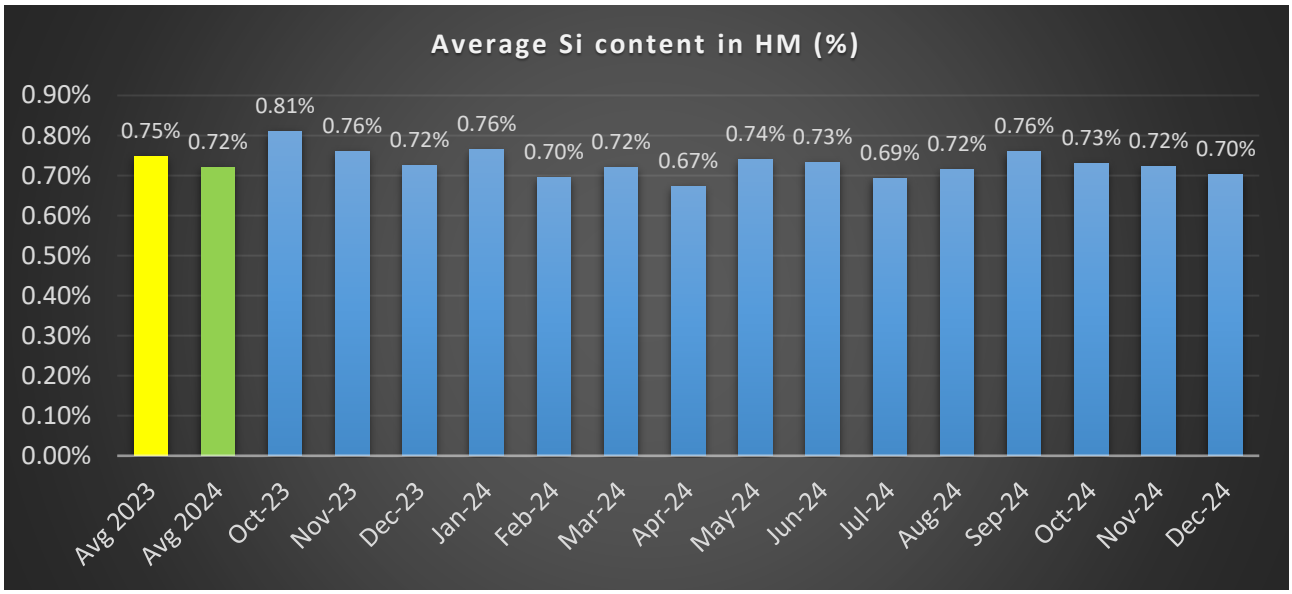

Chart 3. Average silica content in hot metal

Transport of hot metal from BF to the desulphurization station (DS) is carried out by ladles with a capacity of 80 tons of liquid metal. In order to reduce the heat loss of the hot metal, the following measures were taken. After filling the ladle with liquid metal, rice ash was sprinkled over the surface to reduce heat loss by radiation. An analysis was performed and the optimal number of ladles in circulation was determined in order to reduce the cooling of the refractory lining of the ladle before filling.

Graph 4 shows the average temperature drop of HM during transport from BF to the desulfurization station, where in 2024 the result was better by 7 °C compared to 2023.

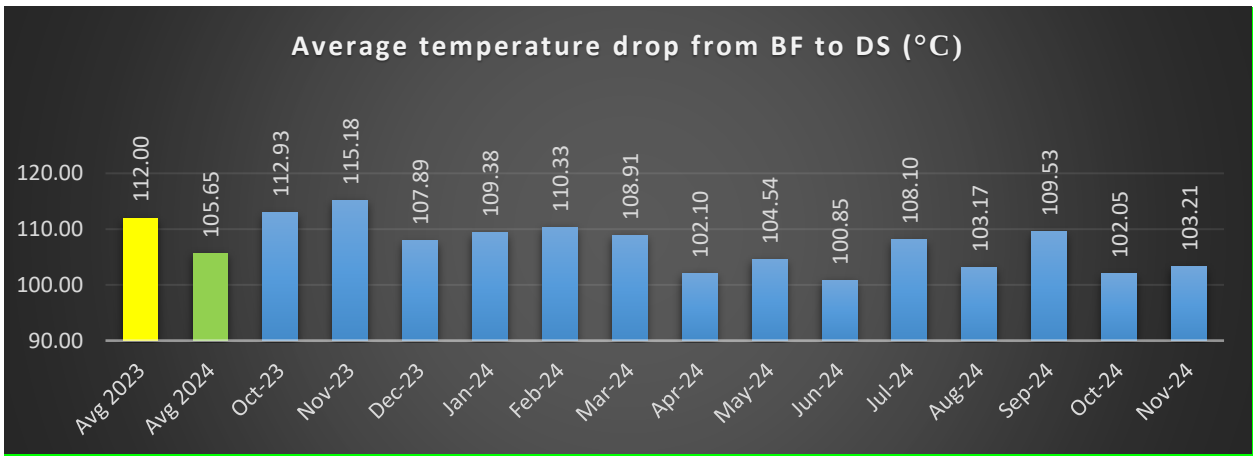

Chart 4. Average temperature drop

Also, there are prescribed instructions for handling the transport ladles during filling and for maintaining of the ladles. On graphic 5, you can see a reduction in the number of ladles that waited more than 8 hours to be filled. A key role in reducing HM temperature drops from the BF to the

BOF converters, particularly after the desulfurization process, is played by the mixer, which—through proper temperature maintenance and controlled HM charging, significantly minimizes temperature losses.

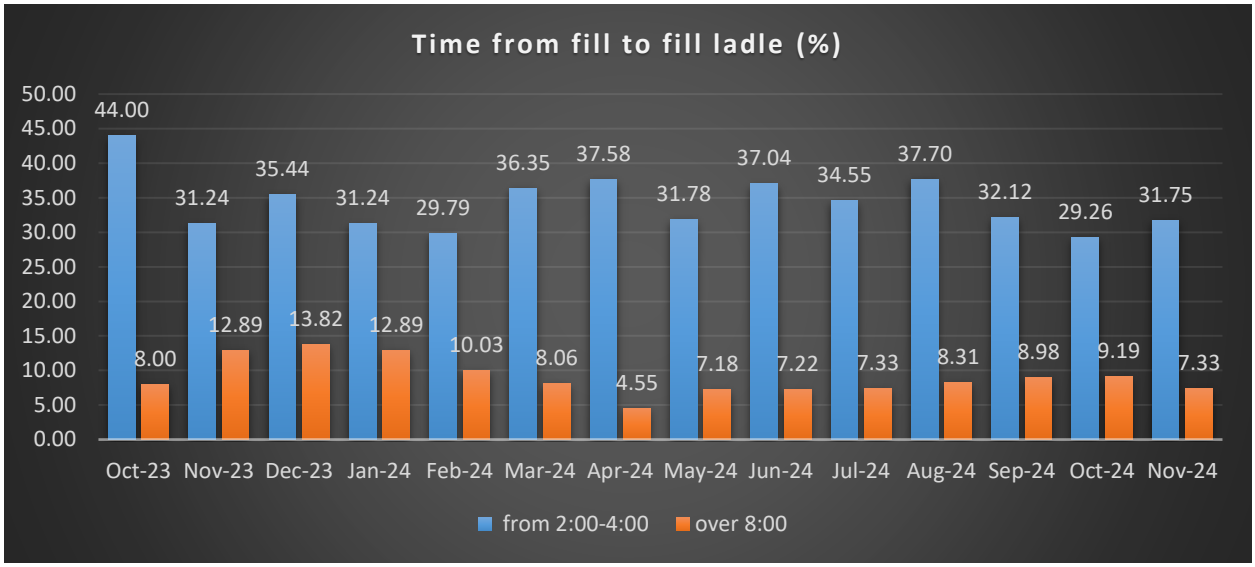

Chart 5. Ladles waiting for filing

3. CONCLUSION

The stabilization of hot metal temperature and silicon content had a significant and measurable impact on increasing steel scrap consumption in BOF converters. During 2023, both temperature and silicon levels exhibited noticeable fluctuations, which contributed to process variability and required frequent corrective interventions. From October 2023 onward, hot metal temperatures stabilized in the range of 1304–1333°C, while the silicon content narrowed to 0.69–0.81%. This consistent control of input parameters improved the predictability of converter reactions, reduced unexpected deviations, and allowed for a more precise adjustment of process conditions.

As a result, the steel scrap ratio consistently exceeded the target of 20.5%, with most months of 2024 reaching values above 22%. The observed improvements in temperature and chemical composition not only facilitated higher scrap utilization but also contributed to enhanced thermal efficiency and energy balance of the process. These findings highlight the critical role of monitoring and controlling key hot metal parameters to optimize converter operation, minimize process variability, and support sustainable steel production practices. The combination of higher and more stable temperatures with a uniform and slightly lower silicon content created optimal conditions for reliable and efficient steelmaking, demonstrating a clear link between input material stabilization and improved process outcomes.

The 56th International October Conference on Mining and Metallurgy
22-25 October 2025, Bor Lake, Bor, Serbia
www.ioc.tfbor.bg.ac.rs

DOI: 10.5937/IOC25304M

Review paper

ARTIFICIAL INTELLIGENCE CHALLENGES IN MODERN ALLOYS DESIGN

Aleksandra Milosavljević[1a], Ana Kostov[1b], Marijana Pavlov-Kagadejev[1c]

[1] Mining and Metallurgy Institute Bor, Alberta Ajnštajna 1, 19210 Bor, Serbia
[1a] aleksandra.milosavljevic@irmbor.co.rs, 0000-0003-3841-7357
[1b] ana.kostov@irmbor.co.rs, 0000-0001-6436-9091
[1c] marijana.pavlov@irmbor.co.rs, 0000-0003-1090-6351

Abstract
Artificial intelligence (AI) is used in everyday research and in all fields, including materials science. Various AI models can predict the optimal chemical compositions, mechanical properties, microstructure and phase transformations of materials instead of long-term experiments or expensive simulations, especially for multicomponent alloys. However, its application, in addition to multiple advantages, also brings numerous challenges. This paper presents a brief overview of these challenges in modern alloy design.

***Keywords**: alloys, artificial intelligence, challenges, design*

1. INTRODUCTION

Materials science is very complex and demanding because of its essence - finding and developing new materials with certain properties, at the lowest possible cost and respecting environmental requirements. It is not at all an easy task, bearing in mind that it is necessary to conduct a lot of experiments under certain conditions. As the conditions for conducting experiments become more complex, the cost of experiments increases, as well as the duration. In order to save money and time, various forecasting methods, as well as simulations, have been developed. All these predictions and simulations were still limited, so over time the need for even more universal solutions grew.

With the progress of artificial intelligence, new possibilities have opened up. AI models use large data sets to be able to predict the properties of materials with high accuracy, and are therefore applied in all stages of the creation of a new material - from design to characterization, even in spectroscopy and electronic microscopy [1]. There are numerous examples of AI applications in alloys, and some of them have been experimentally confirmed [2,3,4,5].

As one of the few examples where machine learning (ML) models proposed the composition of a new alloy with improvements, it can be mentioned Ni-based superalloy [4]. In order to optimize physical properties (up to 11 parameters), the researchers used a artificial neural network (ANN). The network trained on existing experimental data. New Ni-base superalloy was designed and has the optimal properties (some of them better than previous) and cost [4]. Experimental tests confirmed that oxidation resistance and yield strength for this new alloy are superior to existing commercial superalloys [4].

This example clearly shows how AI can predict the optimal chemical composition and thus save us from expensive and time-consuming experiments. However, it is necessary to look at the other side, that is, the challenges that may arise when it comes to the alloys design.

2. CHALLENGES

One of the key problems is the lack of sufficiently large, high-quality and consistent dataset. Most of the existing data on alloys comes from different sources (literature, experiments, simulations). These data are often not standardized, and depending on the type of alloy, the available data may be limited, which makes it difficult for training AI models.

In multicomponent systems, there are a large number of combinations of elements that need to be processed and a large number of data that need to be collected. It represents an obstacle to finding the regularities based on which AI models will propose optimal solutions.

As an example, a machine learning approach for developing heat-resistant aluminum alloys with 15 alloying elements and 6 different heat treatment conditions was given in work [6]. The data set consists of aluminium alloys composition, heat treatment conditions and tensile test temperatures, while the ultimate tensile strength (UTS) values are output. In Figure 1a comparison of results with and without descriptors is shown. The presence of descriptors is better because the information about elements (physical, crystal, and chemical information) is more reliable then. Various models were compared based on the cross-validation (CV) results using the mean absolute error (MAE) as the scoring metric within the training set [6] and the values of R^2 for training and testing sets are given in Figure 1b.

It should be noted that this data set was for Al alloys obtained by conventional casting [6] which refers to another challenge – generalization of model and the lack of universality. Models trained on certain classes of alloys often cannot be easily applied to other systems.

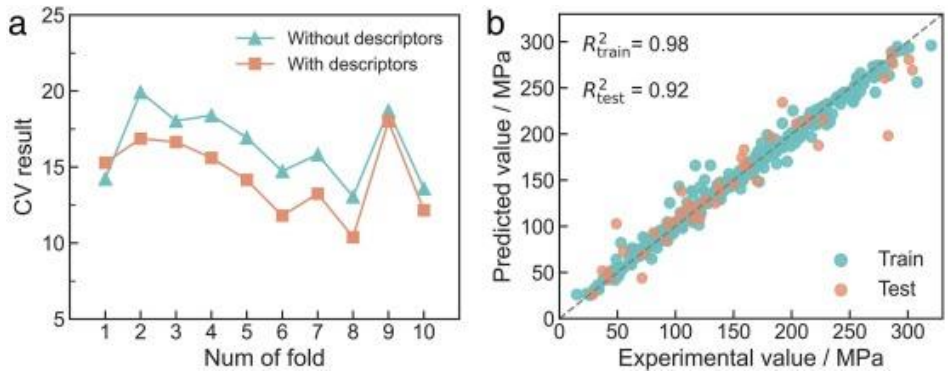

Figure 1. a Comparison of CV results with and without additional descriptors; b fitness based on the training set and testing set. [6] used under the terms of CC-BY-NC-ND

Considering that the microstructure of alloys depends on many factors (composition, cooling rate, heat treatment, deformation), it is very difficult to generate AI models that would predict the microstructure of a specific alloy. Therefore, the integration of artificial intelligence with thermodynamic models and simulations (CALPHAD) is desirable [7].

As an example, integration of various AI techniques along with thermodynamic calculations was used in design of refractory high entropy alloys (RHEA), which are very suitable for applications in extreme conditions [7]. In this study, metaheuristic methods, thermodynamic calculations and artificial neural networks (ANNs) were combined in order to specify and identify certain RHEA alloys [7]. The results were proved by experiments on $Ti_{17.5}Nb_{17.5}Zr_{13.5}Ta_{15.5}Mo_{17.5}V_{18.5}$ alloy [7]. Despite extensive testing, it can be said that even after this combination of models, certain limitations remained, but progress was made for the future directions.

So, the big problem in design of new alloys is the lack of data. In this scientific area, it is very important to know why certain composition or microstructure leads to certain properties, not just to get a prediction. Consequently, experimental confirmation is still necessary. An additional challenge related to the need of experiments is that there is a difference between experiments in laboratory conditions and the real environment in industry.

Considering the complexity of alloys, a multi-functional approach is needed with large dataset, both theoretical and experimental means, it is necessary to combine various types of knowledge. An integration of external knowledge, tools, logic, reasoning, etc. can be effectively implemented through the deployment of a multimodal multiagent AI system driven by large language models (LLMs) [8]. Multiagent systems produce new knowledge from various external resources from literature through databases to simulations. In Figure 2, the multimodal multiagent approach is shown as a multi-functional approach to materials design, which can ensure improvements in solving some of the challenges mentioned above.

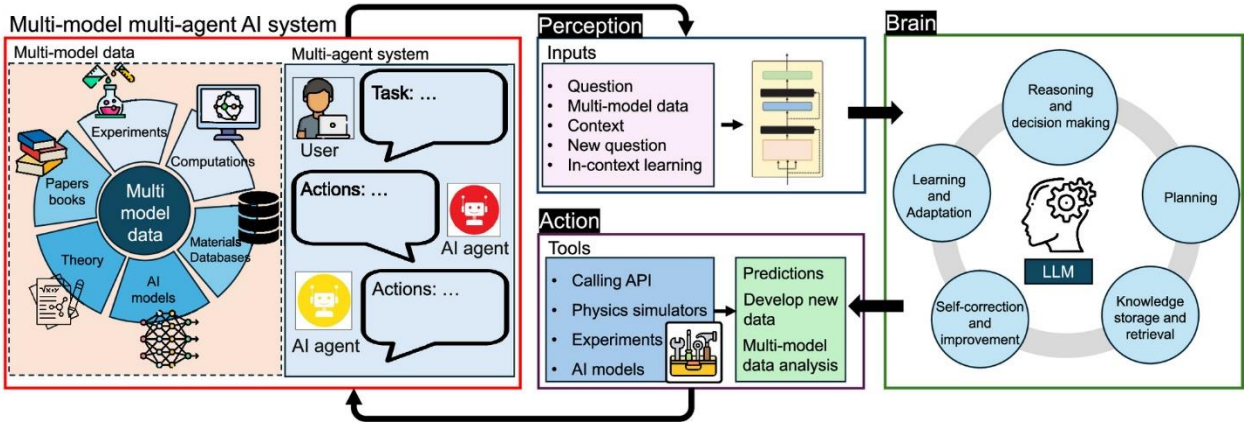

Figure 2. Multimodal multiagent approach as a flexible modeling strategy for materials discovery, modeling, and prediction. Multiagent modeling can extend the power of large-language models by enabling the integration of multimodal data from diverse sources, including simulations, experiments, materials databases,and theoretical models. [8] used under the terms of CC-BY-NC-ND

Apart from the integration of external knowledge from diverse sources, the advantages of the multiagent AI approach are in the reduction of the need for human intervention, accessibility for nonexperts as well as interpretability [8]. Proposed "AtomAgents," a physics-aware multiagent framework given in work [8] comprises a team of agents constructing the core who collaborate to solve complex alloy design tasks with the help of a set of tools for different purposes. Besides that, certain tools that are implemented in AtomAgents, cover computations by atomistic simulations, knowledge retrieval from external sources, coding, plotting, and image analysis, making together LLM based framework for materials design and analysis [8].

3. CONCLUSION

Artificial intelligence is used in material science as well as in all spheres of life. As such, it opens up great possibilities in the alloys design, cost reduction and reduction of numerous experiments as well.

In order to fully use its potential, it is necessary to try to solve the challenges it brings in alloys design:

- development of standardized, open databases,
- combine AI with physically based models (CALPHAD, DFT, etc.),
- improve the interpretability of the model,
- establish a strong link between experiment and prediction.

In this way, artificial intelligence will not only serve as model for prediction itself, yet for understanding and optimizing complex phase transformations, structure and properties of modern alloys. It will be very helpful in education, for nonexperts as for industry, and for everyone who need knowledge and work in the area of alloys design and analysis.

ACKNOWLEDGEMENTS

This work was financially supported by the Ministry of Science, Technological Development and Innovations of the Republic of Serbia, Contract on Realization and Financing the Scientific and Research Work of the Mining and Metallurgy Institute Bor in 2025, Registration No. 451-03-136/2025-03/200052.

REFERENCES

[1] E. Chavez-Angel, M.B. Eriksen, A. Castro-Alvarez, J.H. Garcia, M. Botifoll, O. Avalos-Ovando, J. Arbiol, A. Mugarza., Adv. Intell. Syst., 7 (8) (2025) 2400986.
[2] J. Peng, Y. Yamamoto, J.A. Hawk, E. Lara-Curzio, D. Shin., npj Comput. Mater., 6 (2020) 141.
[3] A.S. Kotykhov, K. Gubaev, M. Hodapp, C. Tantardini, A.V. Shapeev, I.S. Novikov., Sci. Rep., 13 (2023) 19728.
[4] B.D. Conduit, N.G. Jones, H.J. Stone, G.J. Conduit., Materials & Design, 131 (2017) 358-365.
[5] J.W. Lee, C. Park, B.D. Lee, J. Park, N.H. Goo, K.S. Sohn., Sci. Rep., 11 (2021) 11012.
[6] J. Huang, D. Ando, Y. Sutou., Materials & Design, 243 (2024) 113057.
[7] A. Monzamodeth Román-Sedano, V. Aranda, E. Hernández-Mecinas, S. Espinosa-Rangel, J. Villalobos, I.A. Figueroa, G. González., Materials Today Communications, 47 (2025) 113102.
[8] A. Ghafarollahi, M. J. Buehler., PNAS, 122 (4) (2025) e2414074122.

The 56th International October Conference on Mining and Metallurgy
22-25 October 2025, Bor Lake, Bor, Serbia
www.ioc.tfbor.bg.ac.rs

DOI: 10.5937/IOC25308C Original scientific paper

OVERVIEW OF METHODS FOR BOR SEPARATION

Vesna Conić, Milos Janošević, Dragan Milanović, Ivana Jovanović, Daniela Urošević, Mile Bugarin

Mining and Metallurgy Institute Bor, Alberta Ajnštajna 1, 19210 Bor, Serbia
vesna.conic@irmbor.co.rs, 0000-0002-4268-3626
milos.janosevic@irmbor.co.rs, 0000-0002-0818-1235
dragan.milanovic@irmbor.co.rs, 0000-0002-5589-9127
ivana.jovanovic@irmbor.co.rs, 0000-0002-7450-6632
daniela.urosevic@irmbor.co.rs, 0000-0003-3490-7834
mile.bugarin@irmbor.co.rs, 0000-0002-6992-5154

Abstract

The paper presents the research on the selective extraction of boron and lithium from clay lithium resources-ore. Two options for separating B from Li showed good results. The first option was the application of a two-stage leaching of Li ore using H_2SO_4, where 95 % B and 8.31 % Li were recovered in the first phase, while 85 % Li and 4 % B were recovered in the second phase. The second option was the leaching of Li ore using 30 g/L Na_2CO_3, where the leaching was 85.20 % B and 1.33 % Li. The applied procedures achieved satisfactory selectivity of B from Li.

This work may provide guidelines for the selective extraction of lithium and boron from clayey lithium resources-ore in the future.

Keywords: *Clay-type Li resources-ore, Selective extraction, Sodium carbonate, Sulfuric acid*

1. INTRODUCTION

Lithium is the lightest known metal and is widely used in ceramics, glass, aluminum and pharmaceuticals [1,2]. Global consumption of lithium battery products has been reported to have increased by more than 20% per year over the past few years, indicating a strong demand for lithium [3]. As a result of the increased demand for lithium, the price of lithium salts has increased significantly. Nearly 50% of the lithium produced worldwide comes from lithium solutions, which are found almost exclusively in South America, which could lead to a monopoly. Chloride metallurgy is emerging as an alternative process, which has been shown to be more efficient and cheaper to extract. However, such a process is complicated and requires corrosion-resistant equipment [4−6]. The huge growth in demand for lithium batteries used in hybrid and fully electric cars over the next century has raised great concerns about the future availability of lithium. For this reason, to meet the growing demand for lithium, lithium mineral raw materials could be a valuable resource. To meet the growing demand, in recent years, more and more researchers have been working on the treatment of lithium-bearing minerals, including spodumene, lepidolite, zinnwaldite, and petalite. Various methods have been developed to obtain lithium from lithium ores [7−9]. The precipitation of boron from leaching solutions has been presented in many papers[10−12]. If, in addition to boron, lithium also leach, losses of lithium would be inevitable during boron precipitation.

For selective separation of boron from lithium ore, obtained from lithium Europe ore through participation in the EU project Li4Life (GA 101137932), in this paper the possibility of selective boron leaching using H_2SO_4 in one case and Na_2CO_3 in the other case is shown. From this direct separation boron from lithium, almost no leaching of lithium occurred.

2. EXPERIMENTAL

Many experiments on the separation of B from Li have been performed, and only representative ones are shown in the paper. Boron leaching experiments from lithium ore were performed at the laboratory level using 100 g of lithium ore in each experiment. The goal was to leach boron with avoiding lithium leaching in order to achieve selectivity of boron over lithium and minimize Li losses.

2.1 Two stage leaching using H_2SO_4

The leaching was carried out in two stages, in which the first stage used H_2SO_4 with a concentration of 8.8 %, and the solid residue after the first stage was subjected to a second stage of leaching using sulphuric acid with a concentration of 6.6 %. The temperature in the first stage of leaching was 25 °C, while in the second stage it was increased to 80 °C. The leaching time for each stage was 3 h, and the phase ratio S:L=1:4 (w/v).The conditions and results are presented in the Table 1.

Table 1. Conditions and results of leaching Li ore using H_2SO_4

	H_2SO_4, %	Temp., °C	Leach. Time, h	Phase ratio, (w/v)	Recovery, %	
					Li	B
I stage	8.8	25	3	S:L=1:4	8.31	95.00
II stage	6.6	80	3	S:L=1:4	85.00	4.00
Solid residue					6.69	0.65

From the Table 1, it can be concluded that two-stage leaching in H_2SO_4 of different concentrations at different temperatures can provide a certain selectivity Li from B. The higher leaching of Li in the second stage reflects:

- failure to rinse the solid residue after the first leaching stage, whereby the acid from the first leaching stage remain and an additional amount of acid is added to it in the second stage

- the leaching time is extended 3 h + 3 h

- the leaching temperature is increased from 25 °C to 80 °C in comparison with leaching in I stage leaching.

Based on the results obtained, it can be concluded that using 8.8 % sulfuric acid in the first stage of leaching of Li ore achieves 95 % B leaching, while using 6.6 % sulfuric acid in the second stage of leaching of the solid residue obtained from the first stage of leaching achieves 85 % Li leaching. From the above data, the selectivity of B from Li can be achieved.

2.2 Leaching using Na_2CO_3

Leaching was carried out using Na_2CO_3 concentrations of 25 g/L and 30 g/L on a temperature of 85 – 95 °C, at a leaching time of 3.5 h and a phase ratio of S:L=1:4 (w/v). The conditions and results are presented in the Table 2.

Table 2. Conditions and results of leaching Li ore using Na_2CO_3

	Na_2CO_3, g/L	Temp., °C	Leach. Time, h	Phase ratio	Recovery	
					Li, %	B, %
1.	25	80 – 95	3.5	S:L=1:4	0.44	61.68
2.	30	80 – 95	3.5	S:L=1:4	1.33	85.20

From Table 2, it can be concluded that in the first experiment, good selectivity of B from Li was achieved but the B leaching was low, while in the second experiment, significant B leaching was achieved with ensuring very high selectivity B from Li.

3. CONCLUSION

Selective leaching with H_2SO_4 was carried out under the following conditions: (8.8 % H_2SO_4, 25 °C, 3 h, S:L=1:4 (w/v)) and wit Na_2CO_3 under the conditions (30 g/L Na_2CO_3, 80 – 95 °C, 3.5h, S:L=1:4 (w/v)). It is possible to achieve B selectivity from Li in favor of a high B leaching recovery, 95 % and 85.20 % respectively, and a low Li leaching recovery, 8.31 % and 1.33 % respectively.

Based on the results obtained, it can be concluded that B from Li selectivity can be achieved using the above H_2SO_4 and Na_2CO_3 as leaching agents.

From the results of selective leaching, it can be seen that by applying leaching with Na_2CO_3 the losses are unknown and amount to 1.33% and that the leaching of B is satisfactory and is 85%. The advantages of leaching with Na_2CO_3 are reflected in the following:

1. Borax is obtained directly

Sodium carbonate selectively reacts with borates, forming the sodium borate salt, borax ($Na_2B_4O_7 \cdot 10H_2O$), which is readily soluble and a commercially valuable product.

2. There is less dissolution of unwanted components (eg iron, aluminum), which facilitates subsequent separation.

3. Less corrosivity

In comparison with strong acids (eg H_2SO_4, HCl), Na_2CO_3 solution is less corrosive to equipment, which reduces maintenance costs and extends the life of the plant.

4. More environmentally friendly

Alkaline solutions are less hazardous to handle and have a lower risk of contamination in case of leakage. Neutralization of waste water is simpler and cheaper than with acidic waste water.

5. Easier reagent regeneration

Na_2CO_3 can be partially regenerated from waste solutions, which reduces operating costs.

After the success of the process of selective leaching and separation of B from Li, the solid residue will be further treat with a more ecologically and economically acceptable bioleaching process in order to leach Li. In this sense, the idea of mixing sulphide ore raw material to the primary sample of Li clay ore will be implemented, considering that the characterization of the clay ore showed the presence of traces of sulphide ore mass, which provides the basis for the possibility of a bioleaching process, i.e. the first in string adaptation proces of the *At.Ferrooxidans* and *At. Thiooxidans* microbes to this mixed ores raw materials.

ACKNOWLEDGEMENT

This paper has been developed under the framework of Li4Life project (Grant Agreement n° 101137932), and all results can be found on its official website [13] and social channels [14].

Views and opinions expressed are however those of the author(s) only and do not necessarily reflect those of the European Union or the European Climate, Infrastructure and Environment Executive Agency (CINEA). Neither the European Union nor CINEA can be held responsible for them

REFERENCES

[1] A. Ebensperger, P. Maxwell, C. Moscoso, Resour. Policy, 30 (3) (2005) 218−231.
[2] R. Ferro, R. Pipoli The future of lithium. Mining intelligence series [EB/OL]. http://www.salareslithium.com/i/pdf/Media/Lithium_ 2010_BNA.pdf.
[3] H. Wang, K. Huang, S. Liu, J. Power Sources., 196 (2) (2011) 788−792.
[4] P.K. Jena, F. Barbosa, I.C. Vasconcelos, Hydrometallurgy, 52 (2) (1999) 111−122.
[5] E.A Brocchi, F.J. Moura, Miner. Eng., 21 (2) (2008) 150−156.
[6] H.U. Tian-xi, Y.U. Jian-guo, The Chinese Journal of Process Engineering, 10 (4) (2010) 701−705. (in Chinese)
[7] A. Büyükburç, D. Maslioglu, M.S. Ugur Bilici, G. Köksal, Miner. Eng., 19 (5) (2006) 515−517.
[8] B.F.R. Haus, Miner. Eng., 23 (8) (2010) 659−661.
[9] S. You-run., Rare Metals and Cemented Carbides of China, 143 (2000) 22−26. (in Chinese)
[10] A. Erdem Yilmaz, R. Boncukcuo, S. Bayar, B. Ali Fil, M. Muhtar Kocakerim, Korean J. Chem. Eng., 29 (10) (2012) 1382-1387.
[11] J. Wang, J. Wang, J. Zhu, J. Zhou, H. Gu, Journal of Guangdong Non-ferrous Metals of China, 4 (2) (1994) 107−112. (in Chinese)
[12] A. Büyükburç, D. Maslioglu, M.S. Ugur Bilici, G. Köksal, Miner. Eng., 19 (5) (2006) 515−517.
[13] https://li4life.eu/
[14] https://www.linkedin.com/company/li4life-eu-project https://x.com/li4LIFEProject

The 56th International October Conference on Mining and Metallurgy
22-25 October 2025, Bor Lake, Bor, Serbia
www.ioc.tfbor.bg.ac.rs

DOI: 10.5937/IOC25312G Original scientific paper

THE POSSIBILITY OF USING COPPER SLAG AGGREGATE IN CONCRETE

Sandra Guševac[1a], Nevena Marković[1b], Jelena Đorđević[1c], Jelena Stefanović[1d]

[1] Mining and Metallurgy Institute Bor, Alberta Ajnštajna 1, 19210 Bor, Serbia
[1a] sandra.filipovic@irmbor.co.rs; 0000-0002-6776-9899
[1b] nevena.markovic@irmbor.co.rs; 0009-0005-1278-8805
[1c] jelena.djordjevic@irmbor.co.rs; 0000-0001-5406-0074
[1d] jelena.stankovic@irmbor.co.rs; 0000-0001-6418-1814

Abstract

Copper slag, produced as a by-product of the pyrometallurgical process of obtaining copper from copper ore in Bor, is disposed as waste in landfills. Despite the favorable physical and mechanical properties of concrete made with copper slag aggregate, such as higher compressive strength (40.8 MPa), higher tensile splitting strength (10.3 MPa), higher pull-off strength (3.1 MPa) and lower water permeability, its use in the construction industry has not been sufficiently investigated. The paper shows the possibility of using copper slag aggregate (CSA) in concrete as a potential replacement for natural river aggregate (RA).

Keywords: *Copper slag; natural aggregate; concrete; compressive strength; tensile strength.*

1. INTRODUCTION

Copper slag, being derived from non-hazardous chemical constituents, offers potential as a mineral raw material across a variety of manufacturing industries [1]. Bipra Gorai et al. [2] reviewed prior research on its potential applications and concluded that, due to its favorable physical and mechanical properties, copper slag can be widely employed in the production of cement, abrasives, cutting tools, aggregates, roofing materials, glass, tiles, and other products. Among the most promising reuse pathways is its incorporation in cement and concrete production. Utilizing copper slag aggregate as a partial cement replacement can yield substantial energy savings in binder manufacturing, since the process requires only grinding of the slag. Furthermore, significant quantities of copper slag can serve as fine and coarse aggregates in concrete (CSA), given that aggregates account for more than 70% of the concrete volume. A critical review of the literature reveals a notable scarcity of studies investigating the effects of coarse CSA fractions as substitutes for equivalent fractions of river aggregate (RA), as well as the performance characteristics and potential applications of such concretes.

Fine-grained copper slag can be used as a substitute for sand in concrete production, serving either as an aggregate or as a binding agent that helps bond larger gravel particles within the concrete matrix. When applied in this manner, copper slag generally enhances the performance characteristics of concrete [3]. Moreover, such concrete exhibits improved fire resistance, as copper slag slows down the transfer of heat and the spread of flames. This material is also a popular alternative to sand as a medium for industrial abrasive blasting. Through blasting or high-pressure spraying techniques, copper slag is employed to clean large smelting furnaces and other equipment. Slag blasting is also used to remove rust, paint, and other materials from metal, concrete, or stone surfaces, thereby facilitating surface preparation for painting or simply removing unwanted coatings or deposits. Certain properties of copper slag also indicate its potential application in pavement construction. The most effective use of CSA is in ways that take advantage of its favorable physico-mechanical characteristics. Such applications not only utilize its beneficial properties but also address the issue of slag disposal. Consequently, the use of copper slag aggregate holds significance in the waste management industry [2].

Ravindra et al. [4] investigated the geotechnical properties of copper slag and found that it is a non-plastic material with greater compressibility compared to sand. The internal friction angle of copper slag is similar to that of sand, and its use as backfill behind retaining structures reduces active lateral earth pressure. Furthermore, copper slag is suitable for use in construction as a fill material. Since it has no harmful environmental impact, it can be incorporated into soil as a load-bearing layer in pavement structures, railway tracks, as a subbase layer in building foundations, or in other types of civil engineering works.

C. Shi, C. Meyer, and A. Behnood [5] examined the potential of copper slag as a raw material in clinker production and concluded that its use improves clinker grindability, acting as a grinding intensifier. When used as a substitute for cement or aggregate, concrete (or mortar) containing various forms of copper slag generally exhibits equal or greater strength compared to concrete made with ordinary Portland cement. Such studies are increasingly important given that Portland cement production is an energy-intensive process that releases substantial amounts of CO_2. In recent years, copper slag has been used as a replacement for cement [5,6]. It has also been evaluated as a pozzolanic substitute for cement, as 70% of the world's copper slag contains a favorable combination of $SiO_2 + Al_2O_3 + Fe_2O_3$ [7,8]. However, due to its large specific surface area in raw form (approximately 400 m^2/kg) and high hardness, the grinding and comminution of copper slag require a significant energy input [9].

2. MATERIALS AND METHODS

The copper slag used in this study originated from a landfill, formed by the rapid cooling of molten copper matte. In addition to loose fine material, this process also produces large chunks unsuitable for direct use in concrete; however, their potential application can be realized through further crushing and grinding. The copper slag aggregate samples used in the present research were sieved through a series of standard sieves and separated into two size fractions: 8/16 mm and 16/31.5 mm, as shown in Figures 1a and 1b.

(a) (b)

Figure 1. Macroscopic appearance of copper slag aggregate: fraction III (a) and fraction IV (b).

The natural aggregate used in this study was sourced from the "Nova separacija" plant and originates from the Velika Morava River, near Paraćin (Figure 2). Four standard fractions of this river aggregate were used in the investigation: I (0/4 mm), II (4/8 mm), III (8/16 mm), and IV (16/31.5 mm).

Figure 2. Natural aggregate from the "Nova separacija" plant near Paraćin.

Table 1. Mix designs of concrete mixtures.

Mixture	RA (kg/m^3)		CSA (kg/m^3)	Water (kg/m^3)	Portland cement (PC) (kg/m3)	v/c
	0/4 mm	4/31.5 mm	8/31.5 mm			
ETALON	732	1045	/	212	398	0.533
20% III+20% IV	732	753	394			
20% III+50% IV	732	659	529			

The cement used in this study was a composite Portland cement (PC) designated as CEM II/A-L 42.5R, with a specific gravity of 3.15 Mg/m³. Cement classification was carried out in accordance with the European standard SRPS EN 197-1.

The baseline for designing the concrete mixtures used in these experiments was an existing mix design from a local concrete plant in Bor, corresponding to concrete grade MB40. The quantities of materials required for producing 1 m³ of the tested concrete mixtures are presented in Table 1. The purpose of using an existing mix design in this investigation was to modify a formulation already applied in practice by incorporating copper slag [10].

3. RESULTS OF TESTING CONCRETE MIXTURES

The results of compressive strength testing indicated that, compared to the control mixture, mixtures containing copper slag aggregate (CSA) exhibited higher compressive strengths at all concrete ages. For example, at 28 days, the mixtures with 20% III + 20% IV and 20% III + 50% IV substitutions achieved strength increases of 10.2% and 12.6%, respectively, compared to the control mix. A similar trend was observed in the hardened concrete bulk density, which increased by 2.3% and 2.5%, respectively [11].

The splitting tensile strength test results showed that, compared to the control mixture, concretes with CSA also achieved higher splitting tensile strengths. At 28 days, the mixtures with 20% III + 20% IV and 20% III + 50% IV substitutions recorded strength increases of 6.2% and 22.1%, respectively, relative to the control mix.

The pull-off tensile strength test results demonstrated that, at 28 days, the mixtures with 20% III + 20% IV and 20% III + 50% IV substitutions exhibited increases in tensile strength of 13.8% and 11.2%, respectively, compared to the control mixture [12].

Table 2. Physical and mechanical properties of concrete mixtures.

Property	Standard	Concrete mixture		
		Etalon	20% III + 20% IV	20% III + 50% IV
Compressive strength	SRPS EN 933-4	36.3	40.0	40.8
Splitting tensile strength	SRPS EN 1097-6	7.25	8.49	10.26
Pull-off tensile strength	SRPS EN 1097-6	2.69	3.06	2.99

An increase in water penetration depth was also observed in concretes with a percentage replacement of aggregate by CSA compared to the control mixture. The recorded maximum water penetration for the 20% III + 20% IV and 20% III + 50% IV mixtures was 12% and 55% higher, respectively, than that of the control mix.

Table 3. Results of water permeability testing of concrete mixtures.

Concrete mixture	Water penetration depth (mm)
Etalon	83
20% III+20% IV	93
20% III+50% IV	129

4. CONCLUSION

This study examined the potential use of copper slag aggregate as a replacement for natural river aggregate in concrete production, as well as the possibilities for applying such concretes. The conclusions drawn from these tests, aimed at evaluating and expanding the potential applications of the aforementioned concretes in construction, are as follows:

- Replacing RA fractions of 8/16 mm and 16/31.5 mm with CSA aggregate in amounts of 20% III + 20% IV and 20% III + 50% IV resulted in an increase in compressive strength of 10.2% and 12.6%, respectively.
- Increasing the CSA content in concrete, as a partial replacement for coarse fractions of natural aggregate, led to an increase in splitting tensile strength of 6% and 22%, respectively.
- A partial replacement of coarse aggregate with copper slag in 28-day-old concretes resulted in a pull-off tensile strength increase of 13.8% for the second group mixture (20% III + 20% IV) and 11.2% for the third group mixture (20% III + 50% IV).
- The use of CSA aggregate as a replacement for RA reduces the water impermeability of concrete due to increased porosity of the cement paste.

ACKNOWLEDGEMENTS

This work was supported by the Ministry for Education, Science and Technological Development of the Republic of Serbia, research project Grant No. 451-03-9/2021-14/200052.

REFERENCES

[1] R. Sharma, R.A. Khan, J. Clean. Prod. (2017) 179–192.
[2] B. Gorai, R.K. Jana, Resour Conserv Recycl (2003) 299–313.
[3] D. Brindha, S. Nagan, Asian Journal Of Civil Engine (2010) 563–578.
[4] R.K. Dhir, J. de Brito, R. Mangabhai, C.Q. Lye. Use of Copper Slag in Geotechnical Applications, In Sustainable Construction Materials: Copper Slag, Elsevier, 2017; 211–245.
[5] C. Shi, C. Meyer, A. Behnood, Resour Conserv Recycl (2008) 1115–1120.
[6] R. Neves, F. Branco, J. de Brito., Cem Concr Compos (2013) 9–15.
[7] R. Sharma, R.A. Khan, Constr Build Mater (2017) 617–629.
[8] C. Shi, J. Qian., Resour Conserv Recycl (2000) 195–207.
[9] D. Wang, Q. Wang, Z. Huang, Resour Conserv Recycl (2020).
[10] S. Filipović, S. Marinković, D. Zakić, Building Materials and Structures (2022).
[11] S. Filipović, D. Zakić, J. Đorđević, F. Gramić, Copper slag from the Mining and Smelting Basin "Bor" as a partial replacement of natural concrete aggregate, Građevinski kalendar 2022.
[12] S. Filipović, O. Đokić, A. Radević, D. Zakić, Minerals 2021.

The 56th International October Conference on Mining and Metallurgy
22-25 October 2025, Bor Lake, Bor, Serbia
www.ioc.tfbor.bg.ac.rs

DOI: 10.5937/IOC25316S Original scientific paper

LEACHING BEHAVIOUR OF PHOSPHOGYPSUM WITH DIFFERENT ACIDS

Emine Sayılgan[1,2a], Patrick Zhang[2b]

[1] Engineering and Natural Sciences Faculty, Suleyman Demirel University, 32260, Isparta, Turkiye
[2] FIPR, Florida Polytechnic University, Bartow, Florida, USA
[1,2a] eminesayilgan@sdu.edu.tr, 0000-0002-6756-1545
[2b] jzhang@floridapoly.edu, 0000-0003-2762-3235

Abstract
This study was conducted with different experimental conditions such as acids, temperatures, and reaction times for investigating leaching behavior for rare earth element (REE) leaching. In this study, phosphogypsum (PG) sample was obtained from a real PG plant in Florida and sample characteraziton was evaluated for REE, P_2O_5, ^{238}U, and ^{232}Th contents. Then preliminary leaching experiments were conducted as kinetic experiments with 9 different experimental conditions. These leaching tests showed that leaching yield was not so high. PG sample's leaching was so difficult, complex to get into solution also the REE concentration was small.

Keywords:*Leaching, phosphogypsum, acids*

1. INTRODUCTION

Many research has recently been conducted on the end-of-life products containing high concentrations of REEs, such as lamps or magnets, there is less attention has been paid to industrial landfilled stocks [1] such as PG. However, PG seems contain lower REE concentrations but have huge volume and considered a promising source of REEs also environmental concern due to the high content of metals, metalloids and radionuclides [1] and also various impurities such as residual acid (P_2O_5), fluorine compound [2-4]. In this regard, PG considered as a significantly value added component for both environmentally and techno-economic side due to REEs and radioactive elements content.

It is quite difficult to selectively separate REEs and radionuclides from PG. Because REE and radionuclides in PG are in low concentration and both pass into solution with applied acidic leaching methods. As a second step, a selective recovery method or its ability to be selectively leaching in a more economically effective way should be considered. Inorganic acids could leach REE and some radionuclides like U. In this study preliminary test results were evaluated for leaching of REEs from PG.

2. EXPERIMENTAL

In this study, PG sample was obtained from a real PG plant in Florida and sample characteraziton was evaluated for REE, P_2O_5, ^{238}U, and ^{232}Th contents. Then preliminary leaching experiments were conducted as kinetic experiments with 9 different experimental conditions. Preliminary experiments were conducted to determine optimum leaching acids for subsequent experiments. In this purpose, 9 experimental set up was conducted with H_2SO_4, citric acid, ascorbic acid, boric acid, and combination of inorganic and organic acids.

For leaching experiments, leaching experiments at room temperatures conducted in orbital shaker in 0.7 L solution while the experiment at 60 °C was conducted in three necked temperature controlled reactor as 1.3 L. Leaching experiments were conducted with 15% S/L ratio of PG

sample. For this purpose, for experiment 7, firstly 1 M H_2SO_4 was prepared and put in the reactor and the temperature of solution acid was controlled. After obtaining 60°C in the solution, calculated citric acid and PG sample was added to solution and solution was mixed at 350 rpm. After 30 min, 1-2-3-4-6-8 h later approximately 15 mL sample were taken and centrifuged at 5000 rpm for 5 min. After liquid phase separated and REE, P_2O_5, ^{238}U, and ^{232}Th concentration was analyzed with ICP-OES. After 8 h experimental time, the solution was filtered and washed approximately 500 mL distilled water, then filtrate was dried at oven at 105 °C and then after grinding, REE, P_2O_5, ^{238}U, and ^{232}Th concentration of residues were also measured with ICP-OES. After 8 h experimental time pH of solution was also measured. Table 1 shows preliminary experimental leaching conditions.

Table 1. Preliminary experimental leaching conditions

Experiments	PG samples	Acids	Concentrations	Temperature
1	15% S/L raw	H_2SO_4	1 M	Room T.
2	15% S/L raw	H_2SO_4 Citric acid	1 M 20 g/L	Room T
3	15% S/L raw	Citric acid	20 g/L	Room T
4	15% S/L raw	H_2SO_4 Ascorbic acid	1 M 20 g/L	Room T
5	15% S/L raw	H_2SO_4 Citric acid	1 M 40 g/L	Room T
6	15% S/L raw	Ascorbic acid	20 g/L	Room T
7	15% S/L raw	H_2SO_4 Citric acid	1 M 20 g/L	60 °C
8	15% S/L raw	Oxalic acid	20 g/L	Room T
9	15% S/L raw	Boric acid	20 g/L	Room T

3. RESULTS AND DISCUSSION

Characterization results shows that raw PG sample contains 230.64 ppm REEs with 13.23 ppm U and 0.63 ppm Th. Leaching results of impurities, REEs and radionuclides with 1 M H_2SO_4 was shown in Table 2.

Table 2. Leaching results of impurities, REEs and radionuclides with 1 M H_2SO_4 (15% S/L, room temp.)

Reaction Time	P_2O_5	Insol	MgO	Al_2O_3	Fe_2O_3	CaO	Total REE	U	Th
h	%						ppm		
0.5	0,00		0,00	0,00	0,00	0,00	9,01	0,50	0,00
1	0,00		0,00	0,00	0,00	0,00	10,02	0,56	0,00
2	0,00		0,00	0,00	0,00	0,00	10,23	0,62	0,00
3	0,08		0,00	0,01	0,01	0,00	11,48	0,77	0,00
4	0,07		0,00	0,01	0,01	0,00	15,10	1,27	0,00
6	0,08		0,00	0,01	0,01	0,00	11,76	0,83	0,00
8	0,08		0,00	0,01	0,01	0,00	12,39	0,88	0,00
Residue	0,02	10,80	0,01	0,09	0,09	25,81	184,44	4,17	0,43

Leaching results with 1 M H_2SO_4 at room temperature showed that REE recovery was increased with reaction time till 4 h (Table 2). After 4 h leaching recovery was decreased. Lower REEs recovery was obtained with 1 M H_2SO_4 at room temperature. It may be due to the using lower acid concentration and working at room temperature. Leaching results with other conditions was given as only results without any tables. Leaching with 1 M H_2SO_4 and 20 g/L citric acid for REEs and U leaching were increased with increasing leaching time. However, adding 20 g/L citric acid

concentration to 1 M H_2SO_4 could not reach the recovery yields comparing to experimental results conducted with 1 M H_2SO_4. While the experiments were conducted with only 20 g/L citric acid, REEs concentrations were about 3-6 ppm for all reaction time and did not change with increasing reaction time. The recovery yield of both REEs and U were lower than leaching results obtained with 1 M H_2SO_4 and 1 M H_2SO_4 with 20 g/L citric acid. Also, the leaching results with only 20 gl/L ascorbic acid could not leach REEs from PG at studied conditions. These results show that, inorganic acids showed better removal efficiency rather than organic acid.

When the leaching temperature increased to 60°C, increasing temperature could not achieve the REE extraction however slightly increase U leaching. Also, leaching experiments were conducted with 20 g/L oxalic acid and 20 g/L boric acid. There was no REE leaching with 20 g/L oxalic acid and 20 g/L boric acid. The solution pH was 1.22 in oxalic acid solution and 2.64 in boric acid solution. In our previous experience, these organic acids could consider while the selective leaching of metals.

4. CONCLUSION

This study was conducted with different experimental conditions such as acids, temperatures, and reaction times for investigating leaching behavior for REE leaching. These leaching tests showed that leaching yield was not so high. PG sample's leaching was so difficult, complex to get into solution also the REE concentration was small.

ACKNOWLEDGEMENTS

This study was a grant by The Scientific and Technological Research Council of Turkey (TUBITAK) as 2219 International Post Doctoral Research Fellowship Programme. Authors thank to Tubitak for supporting Emine Sayilgan for conducting this study.

REFERENCES

[1] CR. Canovas, S. Chapron, G. Arrachart, S.Pellet-Rostaing, J. of Cleaner Prod., 219 (2019) 225-235.
[2] O.A. Karagoz, H., Oguz, Cem. Concr. Res. 34 (2005) 2079–2082.
[3] H. Taybi, C., Gasco, N., Navarro, A., Lopez-Delgado, M., Choura, F.J., Alguacil, F.A., Lopez, J. Environ. Prot. 2 (2011) 168–174
[4] I., Hammas-Nasri, K., Horchani-Naifer, , M., Férid D., Barca, Int. J. of Mineral Processing 149 (2016) 78–83.

The 56th International October Conference on Mining and Metallurgy
22-25 October 2025, Bor Lake, Bor, Serbia
www.ioc.tfbor.bg.ac.rs

DOI: 10.5937/IOC25319M *Original scientific paper*

ELECTRICAL RESISTIVITY OF THE AL-BI-GE TERNARY ALLOYS

Duško Minić[1a], Milena Zecevic[1b], Aleksandar Djordjevic[1c], Veljko Minic[2a],

[1] University in Pristina, Faculty of Technical Science, Kos. Mitrovica, Serbia
[2]University of Belgrade, Faculty of Technology and Metallurgy, Belgrade, Serbia
[1a] dusko.minic@pr.ac.rs, 0000-0002-3251-9777
[1b] milena.premovic@pr.ac.rs, 0000-0003-0532-7048
[1c] aleksandar.djordjevic@pr.ac.rs, 0000-0002-2020-6976
[2a] veljkominic3@gmail.com, 0009-0002-0812-6460

Abstract
In this work, the ternary system Al-Bi-Ge has been studied. Twelve ternary samples were prepared and used for experimental testing of electrical conductivity. Based on those experimental results electrical resistivity was calculated. This information, were used for graphical presentation of the electrical resistivity of the ternary Al-Bi-Ge alloys depending on the mole fraction of different components.

***Keywords**: Bi-Ge-Pb ternary system, experimental characterization, electrical resistivity*

1. INTRODUCTION

Ternary Al-Bi-Ge alloys belong to the group of ternary monotectic Al alloys [1-3]. These alloys are promising for different applications because of very specific microstructure development during solidification [4]. They have a great potential to be used as plain bearing alloys [4-6]. A typical plain bearing alloy consists of three main materials, the hard matrix material aluminum, soft components and small amounts of various additives. Additives are important to modify the structure and properties of the matrix metal [7]. The practical use of these materials strongly depends on their properties (physical, structural and thermal characteristics). Therefore, a fundamental knowledge of the phase relationships of the respective alloy system is of great importance.

The ternary Al-Bi-Ge system was studied by Minic et al. extensively [8]. In this study results of the electrical resistivity were presented. The results of the electrical resistivity were calculated using the appropriate formula. For this calculation experimental results of electrical conductivity were used.

2. EXPERIMENTAL

Experimentally investigated samples with a wide range of compositions were prepared from high purity metals Al, Bi and Ge (99.99 %). In total 12 ternary samples were weighed, mixed and melted in an electric arc furnace under high-purity argon atmosphere. The samples were melted and re-melted five times until homogeneity was maintained. The average weight loss during melting and re-melting was abouth 0.5 mass %. After it samples were metallographically prepared for electrical conductivity measurements. The electrical conductivity measurements were carried out at frequency of f=120 kHz using the SIGMATEST 2.069 eddy current meter from Foerster.

3. RESULTS AND DISCUSSION

The ternary Al-Bi-Ge system consists of three binary systems. The constitutive binary phase diagrams are Al-Bi, Al-Ge and Bi-Ge. According to the literature, the solid phases that could be expected in the ternary system are summarized in Table 1 [9-11].

Table 1. Considered phase, their crystallographic data and database names for the solid phases of the ternary Al-Bi-Ge system [9-11]

Thermodynamic database name	Phase	Pearson symbol	Space group	Refs.
FCC_A1	(Al)	*cF4*	$Fm\bar{3}m$	[9]
DIAMOND_A4	(Ge)	*cF8*	$Fd\bar{3}m$	[10]
RHOMBO_A7	(Bi)	*hR2*	$R\bar{3}m$	[11]

Beside three solid phases (Al), (Bi) and (Ge) solid solution in ternary system liquid phase L should appear and no ternary compound.

Electrical conductivity measurements were performed on the samples (No. 1 to 12) and the results are summarized in Table 2.

Table 2. Electrical conductivity (EC) of the alloys of the ternary Al-Bi-Ge system

No.	Mole fraction			Electrical conductivity (EC), MS/m					Mean value of EC, MS/m
	x(Al)	x(Bi)	x(Ge)	1	2	3	4	5	
1.	0.2	0.4	0.4	0.661	0.663	0.684	0.653	0.680	0.668±0.013
2.	0.4	0.3	0.3	0.513	0.507	0.504	0.519	0.528	0.514±0.009
3.	0.6	0.2	0.2	10.303	10.228	10.274	10.320	10.140	10.253±0.072
4.	0.8	0.1	0.1	14.834	14.764	14.631	14.909	14.851	14.798±0.107
	1	0	0						38 [20]
5.	0.4	0.2	0.4	6.428	6.184	6.724	6.126	6.254	6.343±0.241
6.	0.3	0.4	0.3	0.575	0.588	0.584	0.581	0.579	0.582±0.005
7.	0.2	0.6	0.2	0.538	0.517	0.525	0.543	0.519	0.528±0.012
8.	0.1	0.8	0.1	0.534	0.559	0.533	0.538	0.513	0.536±0.016
	0	1	0						0.77[20]
9.	0.4	0.4	0.2	0.635	0.651	0.644	0.650	0.641	0.644±0.007
10.	0.3	0.3	0.4	0.490	0.472	0.492	0.501	0.505	0.492±0.013
11.	0.2	0.2	0.6	1.083	0.879	0.994	1.113	1.087	1.031±0.096
12.	0.1	0.1	0.8	0.715	0.718	0.653	0.695	0.732	0.702±0.031
	0	0	1						0.002 [20]

According to the experiments and predictions, the electrical conductivity in the ternary Al-Bi-Ge alloys increases towards the aluminum corner. Since it has been shown [8], that all ternary alloys have the same three phases in all composition ranges at 25 °C, the proportions of these three phases significantly influence the electrical conductivity. Thus, if the proportion of the (Al) phase is dominant, the electrical conductivity is high. The ternary alloy 4, $Al_{80}Bi_{10}Ge_{10}$, have an electrical conductivity of 14.798±0.107 MS/m, which is due to the 80 % proportion of the (Al) phase in the alloy.

The experimentally determined value of electrical conductivity, which is given in Table 2, is used to calculate the electrical resistivity. The electrical conductivity is the reciprocal of the electrical resistivity and the calculated values are given in Table 3.

Table 3. Calculated value of electrical resistivity based on experimental value of electrical conductivity given in table 6 for ternary Al-Bi-Ge alloys

No.	Mole fraction			Electrical resistivity, μΩ·m					Mean value, μΩ·m
	x(Al)	x(Bi)	x(Ge)	1	2	3	4	5	
1.	**0.2**	0.4	0.4	1.513	1.508	1.462	1.532	1.470	1.497±0.030
2.	**0.4**	0.3	0.3	1.949	1.973	1.983	1.928	1.895	1.946±0.035
3.	**0.6**	0.2	0.2	0.097	0.098	0.097	0.097	0.099	0.098±0.001
4.	**0.8**	0.1	0.1	0.067	0.068	0.068	0.067	0.067	0.068±0.001
	1	0	0						0.0263 [21]
5.	0.4	**0.2**	0.4	0.156	0.162	0.149	0.163	0.160	0.158±0.006
6.	0.3	**0.4**	0.3	1.738	1.700	1.712	1.720	1.728	1.719±0.014
7.	0.2	**0.6**	0.2	1.859	1.935	1.905	1.843	1.928	1.894±0.41
8.	0.1	**0.8**	0.1	1.872	1.789	1.874	1.859	1.950	1.869±0.057
	0	**1**	0						1.2987 [21]
9.	0.4	0.4	**0.2**	1.576	1.535	1.553	1.539	1.560	1.553±0.016
10.	0.3	0.3	**0.4**	2.039	2.117	2.031	1.996	1.978	2.032±0.054
11.	0.2	0.2	**0.6**	0.923	1.138	1.006	0.898	0.920	0.977±0.099
12.	0.1	0.1	**0.8**	1.399	1.394	1.532	1.439	1.366	1.426±0.065

Mean values of electrical resistivity are graphically presented in Figure 1.

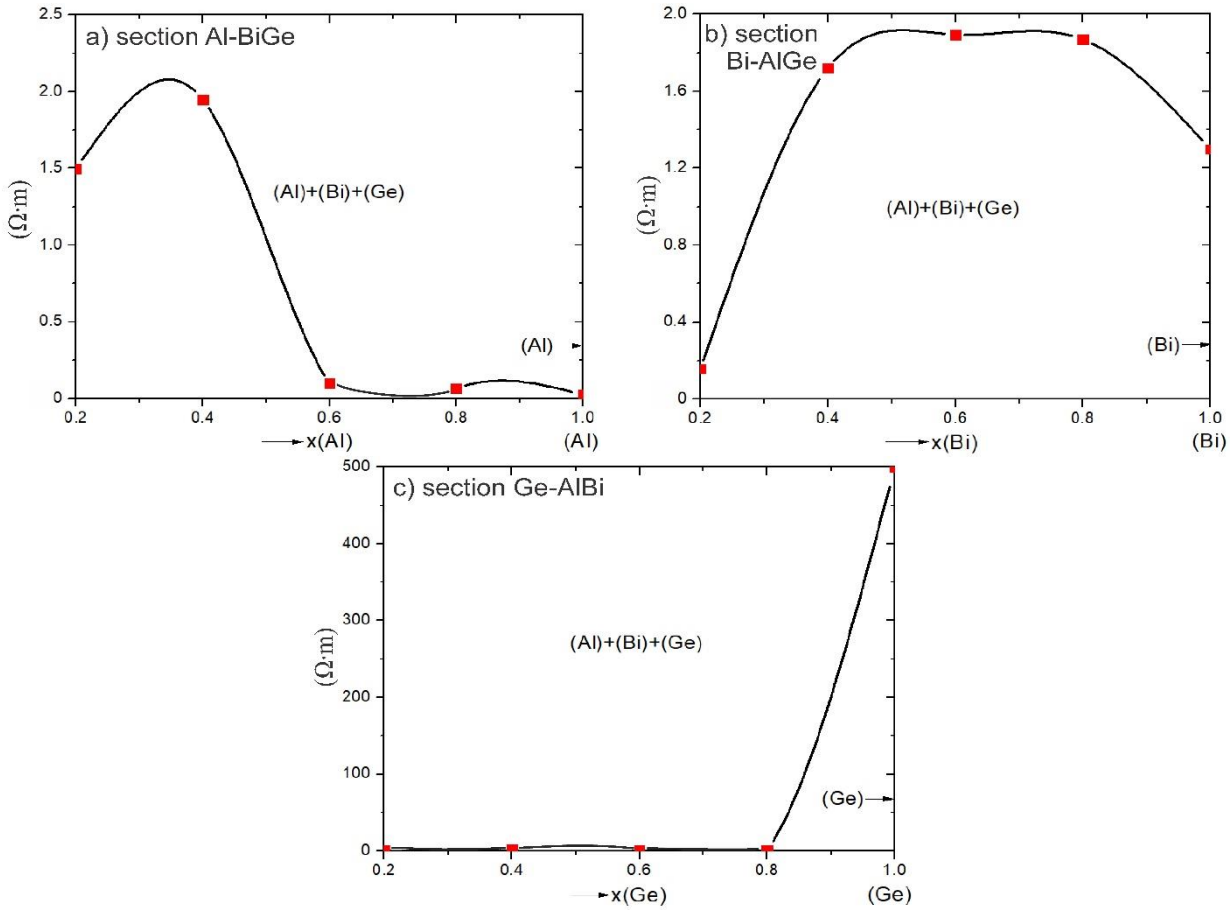

Figure 1. Graphical presentation of the electrical resistivity of the ternary Al-Bi-Ge alloys depending on the mole fraction of different components

For alloy 4, $Al_{80}Bi_{10}Ge_{10}$ resistivity was 0.068±0.001 μΩ·m, while the highest resistivity of 2.032±0.054 μΩ·m was obtained for alloy 10, $Al_{30}Bi_{30}Ge_{40}$.

4. CONCLUSION

Electrical conductivity of the ternary alloys was measured. For this test 12 ternary samples were prepared. Experimental tests shows that sample 4, Al80Bi10Ge10, had the best electrical conductivity of 14.798±0.107 MS/m. The electrical resistivity was calculated as reciprocal of electrical conductivity and the highest resistivity value of 2.032±0.054 μΩ·m refers to alloy 10, with nominal composition Al30Bi30Ge40.

REFERENCES

[1] Dj. Mirković, J. Gröbner, R. Schmid-Fetzer, Acta Mater., 56 (18) (2008) 5214-5222.
[2] D. Manasijevic, D. Minic, Lj. Balanovic, M. Premovic, M. Gorgievski, D. Zivkovic, D. Milisavljevic, J. Alloys Compd., 687 (2016) 969-975.
[3] D.M. Herlach, Phase Transformations in Multicomponent Melts, WILEY-VCH Verlag GmbH & Co. KGaA, Weinheim, 2008.
[4] J. Grobner, D. Mirkovic, R. Schmid-Fetzer, Acta Mater., 53 (2005) 3271-3280.
[5] L. Ratke, S. Diefenbach, Mater Sci. Eng. Reports, 15 (7-8) (1995) 263-347.
[6] J.Z. Zhao, J. He, Z.Q. Hu, L. Ratke, Zeitschrift für Metallkunde, 95 (2004) 362-368.
[7] D. Kopeliovich, A. Shapiro, V. Shagal, US Patent No. US6273970 B1, Aug. 14 2001.
[8] V. Minic, M. Popovic, M. Zecevic, J. Miladinovic, A. Djordjevic, CALPHAD: Computer Coupling of Phase Diagrams and Thermochemistry, 89 (2025) 102834.
[9] B. Predel, D.W. Stein, J. Less-Comm. Met., 17 (4) (1969) 377-390.
[10] A.S. Cooper, Acta Crystallogr., 15 (1962) 578-582.
[11] P. Cucka, C.S. Barrett, Acta Crystallogr., 15 (1962) 865-872.

The 56th International October Conference on Mining and Metallurgy
22-25 October 2025, Bor Lake, Bor, Serbia
www.ioc.tfbor.bg.ac.rs

DOI: 10.5937/IOC25323S *Original scientific paper*

ON THE LEACHABILITY OF COPPER FROM COPPER-IRON MINERALS MIXTURE

Velizar Stanković[1a], Miljan Marković[1b], Milan Gorgievski[1c], Stefan Đorđievski[2a]

[1] Technical Faculty Bor, University of Belgrade, V.J. 12 19210 Bor, Serbia
[2] Mining & Metallurgy Institute (MMI Bor) Alberta Ajnštajna 1, 19210 Bor, Serbia
[1a] stankovic.velizar@gmail.com, 0000-0002-1399-3481
[1b] mmarkovic@tfbor.bg.ac.rs, 0000-0002-4734-1481
[1c] mgorgievski@tfbor.bg.ac.rs, 0000-0002-9899-719X
[2a] stefan.djordjievski@irmbor.co.rs, 0000-0003-1737-8766

Abstract

Sulphuric acid leaching of the ore sample from the MCM (Mauritanian Copper Mine) was carried out. The achieved leaching degree was ≤ 38%. To improve copper leachability from the ore, TG (thermogravimetric), DSC (differential scanning calorimetry, and DTA (analyses differential thermal analysis) were conducted on the ore, and XRD (X-ray diffraction) analysis was performed on the leach residue. Thermal analysis has shown that goethite quickly transforms to hematite at ≈ 300 °C. The XRD pattern reveals the presence of four main minerals in the leach residue of the ore sample. Among them, the goethite peaks are the most intense. It seems as if the decomposition of goethite (thermally or chemically) could be a cornerstone in increasing the copper leaching degree. Both pathways were checked, and in both cases, a significant increase in the leaching degree was achieved.

Keywords: *Copper leaching; Thermal analysis; XRD pattern; Sulphation*

1. INTRODUCTION

There are cases in hydrometallurgical literature where some targeted metals cannot be leached from ore to a satisfactory extent, because they are strongly bound to other minerals [1-4]. To increase the leachability, such an ore must be pretreated by introducing either mechanical (additional milling), thermal (calcination), or chemical energy (sulphation) into the ore before leaching.

So happened with the ore, which is the subject of this study. Chemical analysis of the ore, considered in this study, revealed 1.3% Cu, 10% SiO_2, smaller amounts of Mg and Ca (<2%) and a very high concentration of iron minerals (Fe >50%) [1]. The most common among them is goethite. The other heavy metals are present in ppm concentration. Besides, the ore contains 1.3 g/t of Au, as well. Mineralogical analysis of the ore [2] revealed copper oxides and carbonates (sulphides in traces), and those were mostly bound to goethite. In the preliminary experiments, the ore sample was conventionally leached with sulfuric acid solutions. By them, a very modest copper leaching degree of 38 % was achieved. Almost two-thirds of the total copper content remains untouched in the leach residue.

Decomposition of goethite could be a cornerstone in increasing the copper leaching degree. Two pathways can be applied to the leach residue, produced in the classical acid leaching, to recover the remaining copper captured in it:

- thermal degradation of the present goethite, or

- chemical decomposition of the leach residue with H_2SO_4 to convert the locked copper minerals into corresponding sulphates, followed by washing them out with water [3, 4]. Aiming to get a better copper leachability from the ore, TG, DSC and DTA analyses are carried out on the ore sample, as well as XRD analysis of the leach residue.

2. EXPERIMENTAL

The sample of ore was leached with 0.5M H_2SO_4 solution for half an hour, filtered; the solid residue rinsed with distilled water, dried and stored in a desiccator (the residue in the further text), to serve for further investigations, which consisted of thermal degradation of degradable minerals (goethite) and chemical decomposition – sulphation of some minerals from the residue. For that purpose, the dried residue was divided into two parts. The one for thermal degradation and the other for XRD analysis.

A small amount of the leached residue (6 mg) was taken for thermal analysis. The analysis was performed using a DSC-TGA SDT Q600 device (Oxford Instruments). Nitrogen was used as the purging gas, and the flow rate was controlled at 100 mL min^{-1}. The weight of the leached residue (≈ 6 mg) was heated at a heating rate of 10 °C/min in the temperature range of 20 to 500 °C.

XRD analysis was performed on both the residue and the sulphated sample after rinsing and drying, using the Rigaku Mini Flex 600. Other used equipment is common laboratory equipment.

The sulphated sample was prepared by mixing the residue (20 g) with H_2SO_4 (25mL). The obtained paste was heated at 90 °C for 30 minutes and rinsed with warm water for 1 h. In this way, the achieved total copper leaching degree is 98 - 99%.

3. RESULTS

3.1 Thermal analysis

It was assumed that a significant increase in the leaching degree can be obtained by extracting the copper intercalated in the goethite. To confirm this hypothesis, a TG-DTA analysis was performed to get an insight into how goethite will behave under heating. The DTA curve recorded under the above conditions is presented in Figure 1.

According to the TG-DTA analysis, heating the sample, a total weight loss of 5.94 % is detected. One endothermic peak at 299.26 °C appeared during the heating process. This peak corresponds to the goethite dehydration, followed by the formation of hematite according to the equation [5]:

$$2FeOOH \rightarrow Fe_2O_3 + H_2O$$

The process occurs quickly and is completed within 4.5 to 5 minutes. Based on the DSC analysis, it was found that the heat energy of 11.27 J/g, spent at 299.67 °C. According on the literature data [5], the authors assumed that the obtained heat energy could be attributed to the phase transition from goethite to hematite [5].

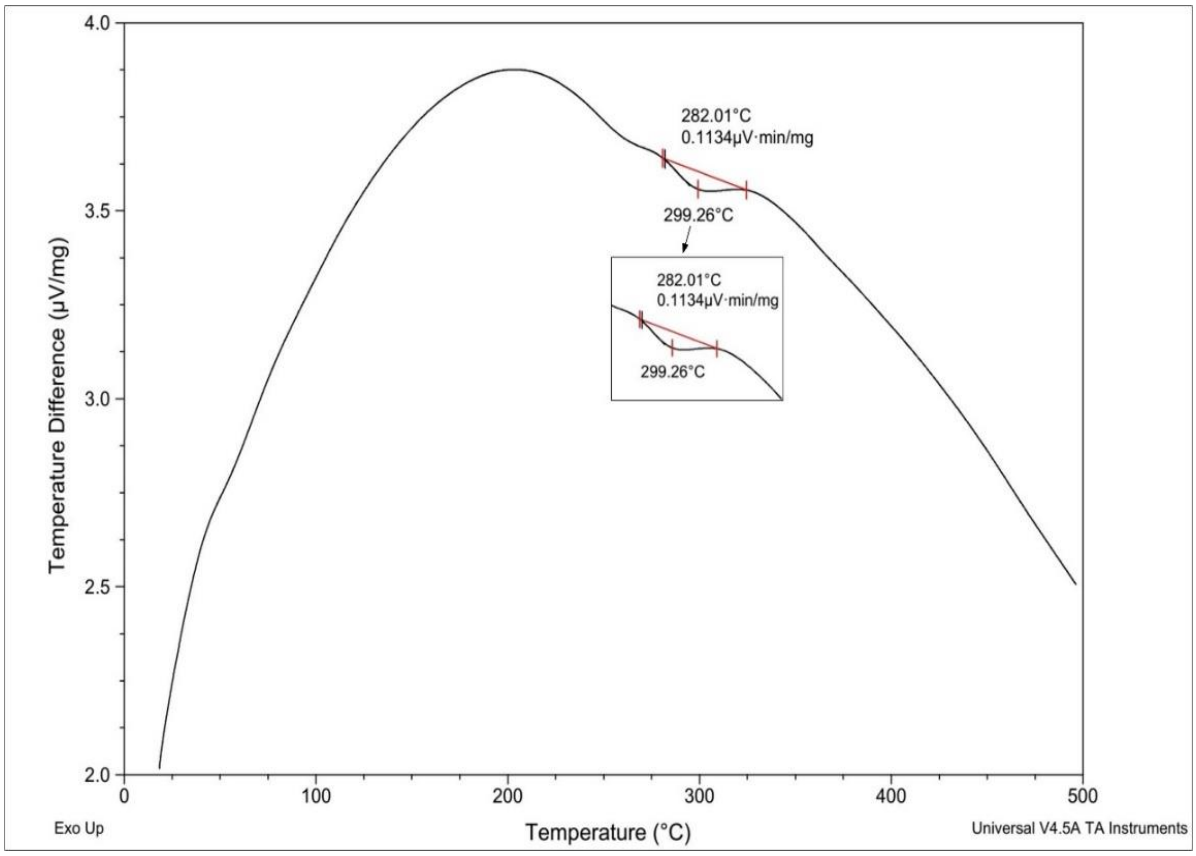

Figure 1. DTA curve of the residue

Thermal analysis defined the conditions for the phase transformation of goethite to hematite (>300 °C). Calcination of the residue at temperatures >300 °C converts goethite to hematite, allowing the leaching agent to reach copper minerals trapped within the iron ones, to leach them out. That would result in an overall increase in the degree of copper leaching. To confirm this, a portion of the residue was calcined at 400 °C for 30 minutes. After cooling the calcined residue, it was leached under the same conditions as before. The overall achieved leaching degree was 67%.

3.2 XRD analysis

XRD analysis (Figure 2) of the leach residue revealed strong peaks for goethite and hematite, as well as quartz and clinochlore, and less abundant amphibole and spinel on the diffractogram. A notable change in the diffractogram was observed after treating the leach residue with sulphuric acid at an elevated temperature of 90°C, followed by washing it with water. Due to the sulphation reactions, the intensity of the goethite peaks became slightly smaller, while those of clinochlore decreased significantly. Peaks of hematite became more intense.

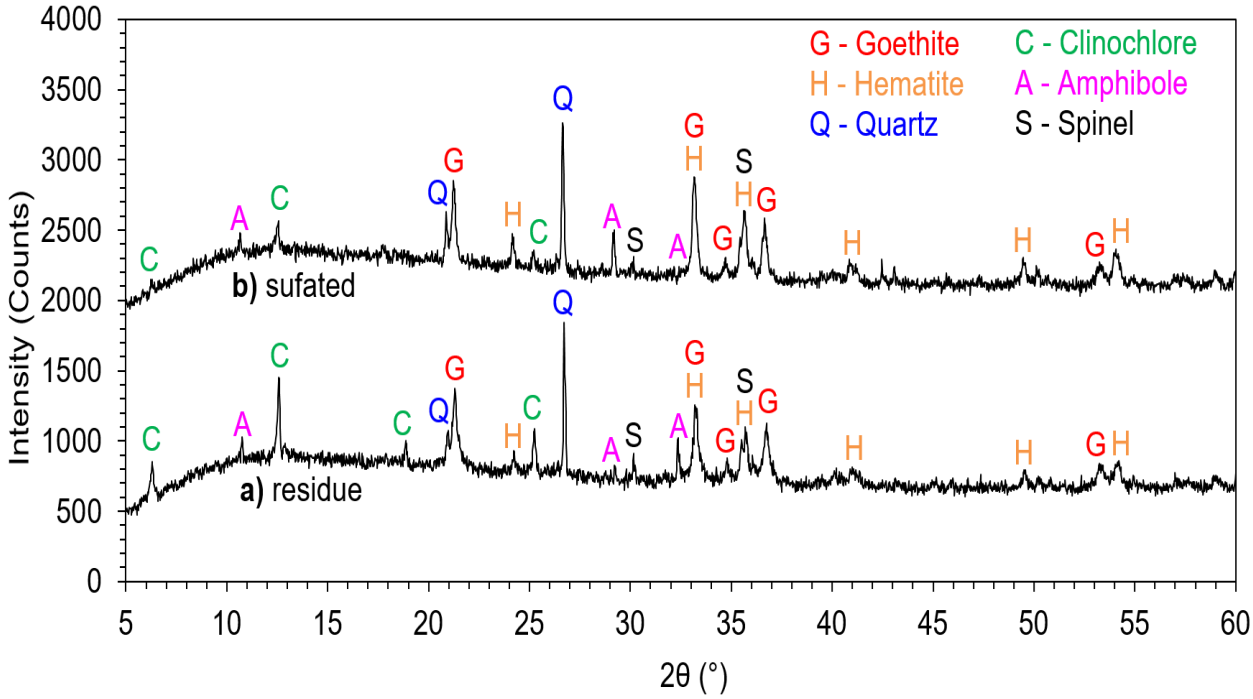

Figure 2. XRD pattern of the residue (a) and after sulphation, rinsing and drying (b)

4. CONCLUSION

It is possible to achieve a high percentage of copper leaching by pretreating the residue from the first stage of leaching, either through thermal or chemical destruction of goethite, which is a major carrier of the locked-in copper.

Chemical decomposition of the leach residue by sulphation seems to be more efficient in terms of the achieved leaching degree than the thermal destruction of goethite.

REFERENCES

[1] Group of authors, TF Bor University of Belgrade, Serbia: A report on the study Hydrometallurgical testing of the copper oxide ore parties from the Mauritanian Copper Mines (MCM), Archive of the TF, 2023.
[2] Experts Process Solution; Study on “Oxide Ore Au Deportment Study, MCM”, April 2021
[3] V. L. Gontijo, L. A. V. Teixeira, V. S.T. Ciminelli; Hydrometallurgy 197(2020) 1-10
[4] K. Liu, Q. Chen, and H. Hu; Hydrometallurgy 98 (2009) 281–286
[5] Y.H. Chen., J. Alloys Compd., 553 (2013) 194-198.

The 56th International October Conference on Mining and Metallurgy
22-25 October 2025, Bor Lake, Bor, Serbia
www.ioc.tfbor.bg.ac.rs

DOI: 10.5937/IOC25327K *Original scientific paper*

RECOVERABLE Pd AND Pt ACCUMULATION IN A $Ca(OH)_2$ BASED CO_2 FILTER OF A HYDROGENATION ORGANIC BYPRODUCT INCINERATION PLANT

Ferenc Kristály[1,2a], László Farkas[1,2b], Andrea Mihalkó[1c], Bence Tamás[1d], Balázs Szeleczki[2a]

[1] Wanhua-BorsodChem Zrt, Bólyai sq. No 1. 3700 Kazincbarcika, Hungary
[2] University of Miskolc, 3515 Miskolc-Egyetemváros, Hungary
[1a] ferenc.kristaly@borsodchem.eu, ferenc.kristaly@uni-miskolc.hu 0000-0002-0075-5994
[1b] laszlo.farkas@borsodchem.eu 0000-0003-4328-486X
[1c] andrea.mihalko@borsodchem.eu 0000-0002-9061-5599
[1d] bence.tamas@borsodchem.eu 0009-0007-5416-5037
[2a] balazs.szeleczki@uni-miskolc.hu 0009-0005-8822-2322

Abstract
Hydrogenation processes are strongly relying on Pd and Pt based catalysts, which are degraded, consumed and discharged during the industrial processes. The mining and beneficiation of these noble metals has increased environmental footprint and increasing costs. Thus, any possibility for recovery, recycling and reuse is an option which must be accurately investigated. In our study we present a case where easily recoverable Pd and Pt bearing waste is generated as a product of incineration gases capture. The hydrated lime based CO_2 capture system produces a $CaCO_3$ matrix containing Fe-oxides aggregated, cemented Pd-Pt accumulations.

***Keywords**: catalysts, recycle, carbon capture*

1. INTRODUCTION

The tar byproduct of an aniline plant reactor must be decomposed by incineration, as the chemically and environmentally most secure method. Variable amount of the applied Pd-Pt-Fe based catalyst will be removed from the reactor together with the tar, as part of the routine operation. The incineration gases – mostly CO_2, with minor residual SO_x and NO_x contribution – and the fly ash product are captured in $Ca(OH)_2$ treated filter bags. As a result Ca-carbonate will be generated, as a matrix of captured product, with variable amounts of Ca-sulphate and the aggregates of the Pd-Pt-Fe system with specific transformations developed during incineration. Thus, the resulting capture waste is a potentially high values secondary raw material [1], requiring a processing route in compliance with the reuse and recycle developments. The first step of such a development is the detailed compositional characterization of the material, presented in this study.

2. EXPERIMENTAL

Samples were prepared by water based separation, magnetic separation and hydrochloric acid dissolution. Crystallographic analysis was carried out by X-ray powder diffraction (XRD, Bruker D8 with Cu-alpha radiation, 40 kV and 40 mA) on air dried specimen. After phase identification, Rietveld refinement was carried out to validate the presence of phases and refine crystallographic data. The chemical structure of components was studies by Fourier-transformed infrared spectroscopy in attenuated total reflection mode (ATR-FTIR). Textural and microchemical characteristics of the material was observed by scanning electron microscopy investigations (scanning electron microscopy with energy dispersive X-ray spectrometry, SEM+EDX) provide a basis for the recycling technology.

3. RESULTS AND DISCUSSION

Crystallographic (Figure 1) and chemical structure (Figure 3) characterization revealed calcite (trigonal $CaCO_3$) as the matrix material, with high amount of residual $Ca(OH)_2$, and sulphates like anhydrite ($CaSO_4$), bassanite ($CaSO_4*0.5H_2O$) gypsum ($CaSO_4*2H_2O$) and cesanite ($Na_7Ca_3(SO_4)_6(OH)*0.8H_2O$).

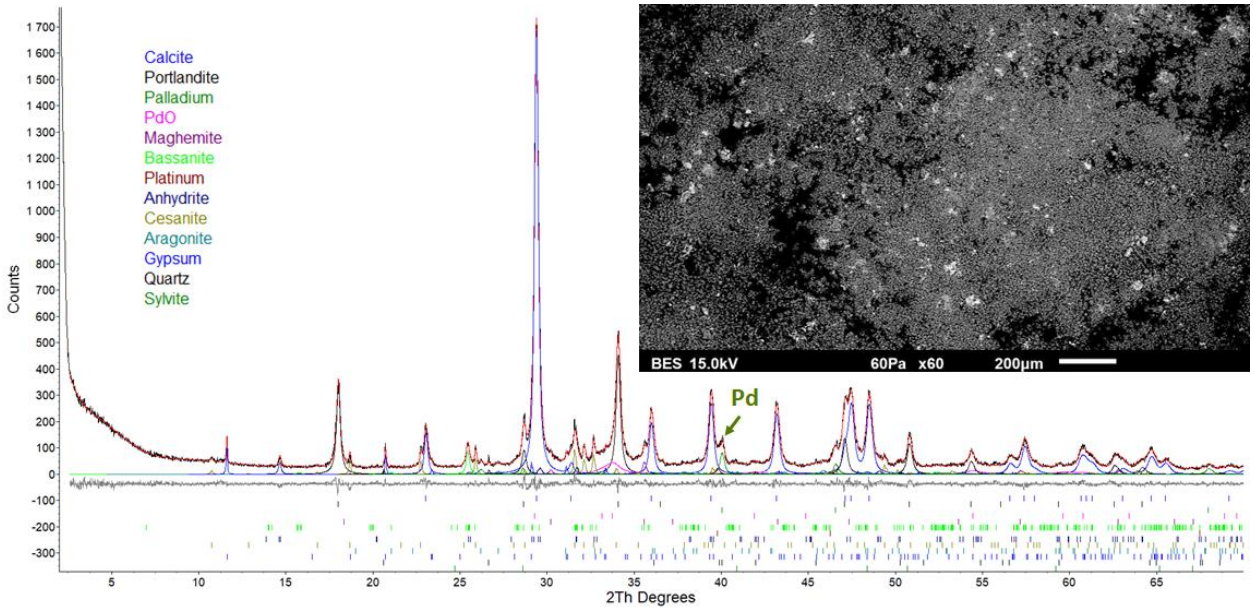

Figure 1. XRD pattern with Rietveld refinement and distribution of Pd-Pt rich fragments (inset, back-scattered electron image)

Minor associated phases are aragonite (orthorhombic $CaCO_3$), quartz (trigonal SiO_2), sylvite (KCl) and maghemite (cubic, gamma-Fe_2O_3).

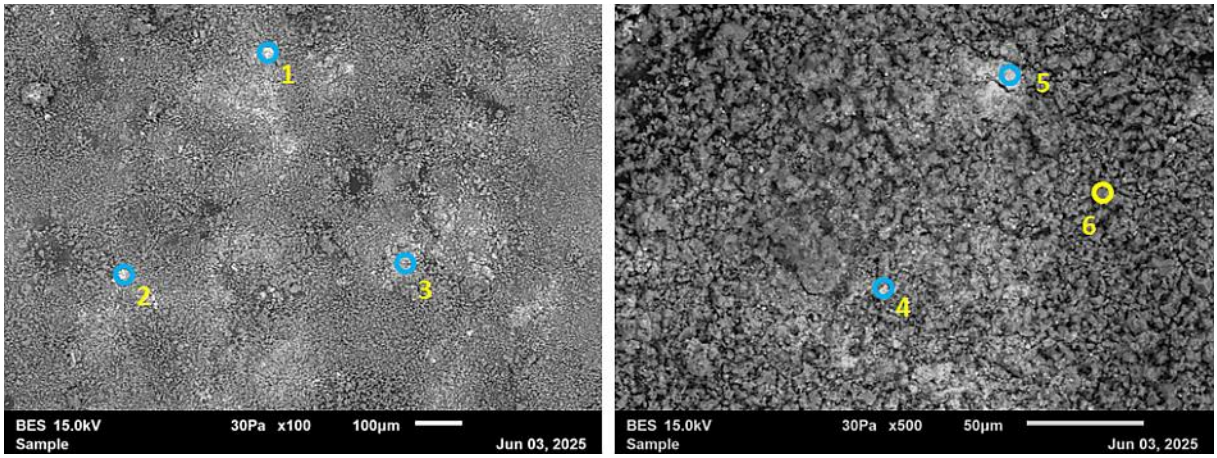

Figure 2. Distribution of high atomic number components in the carbonate matrix, back-scattered electron images, circles mark EDX analysis spots.

These phases provide an insight into the incineration and gas capture reactions and completed with SEM+EDX investigations (Figure 2) provide a basis of metallurgy for recycling technology planning [2]. The high average atomic number spots (numbered spots in Figure 2) in the carbonate matrix show elevated Fe content, with associated rise in Pd and Pt content. Trace amounts Si and Al are related to glass like silicate components revealed by acid leaching of the carbonates. Carbon quantitative data is considered only as indicative, since the powder was mounted on adhesive-

conductive carbon tape. However, its directly proportional variation with Ca content is supporting the observation, that only Ca produces carbonate phases, the calcite and aragonite.

Table 1. EDX measurements marked on the BES images in Fig 2 (non-standardized weight percents)

	P	Fe	K	O	C	Na	Mg	Al	Si	S	Cl	Ca	Pd	Pt
1	0,29	19,25	0,14	36,79	10,54	2,77	0,47	0,12	0,77	2,62	0,37	8,85	14,27	2,76
2	0,11	15,07	0,16	38,65	13,85	1,2	0,37	0,06	0,81	2,65	0,45	17,93	7,46	1,21
3	0	1,66	0,11	48,18	14,73	0,67	0,35	0,05	0,16	1,39	0,44	30,97	1,23	0,06
4	0,28	20,7	0,2	34,96	10,62	2,65	0,4	0,14	0,76	2,54	0,36	8,27	14,99	3,12
5	0,37	19,53	0,23	29,6	8,92	1,84	0,91	0,07	0,96	3,22	0,52	9,94	21,2	2,69
6	0,12	25,63	0,33	24,77	12,13	1,19	0,46	0,09	0,75	4,41	0,42	17,3	11,25	1,15

Chemical structure investigations (Figure 3) support the presence of S in the sulphate minerals found by XRD, the Mg incorporation in calcite crystal lattice and presence of reactive portlandite. Upon water immersion and subsequent drying, the portlandite OH-band is eliminated, transformed into carbonate phase. However, it was observed during this rehydration process, that pH rises to 10-11 and if ultrasonic stirring is applied, the dispersion of the metal-rich particles will increase.

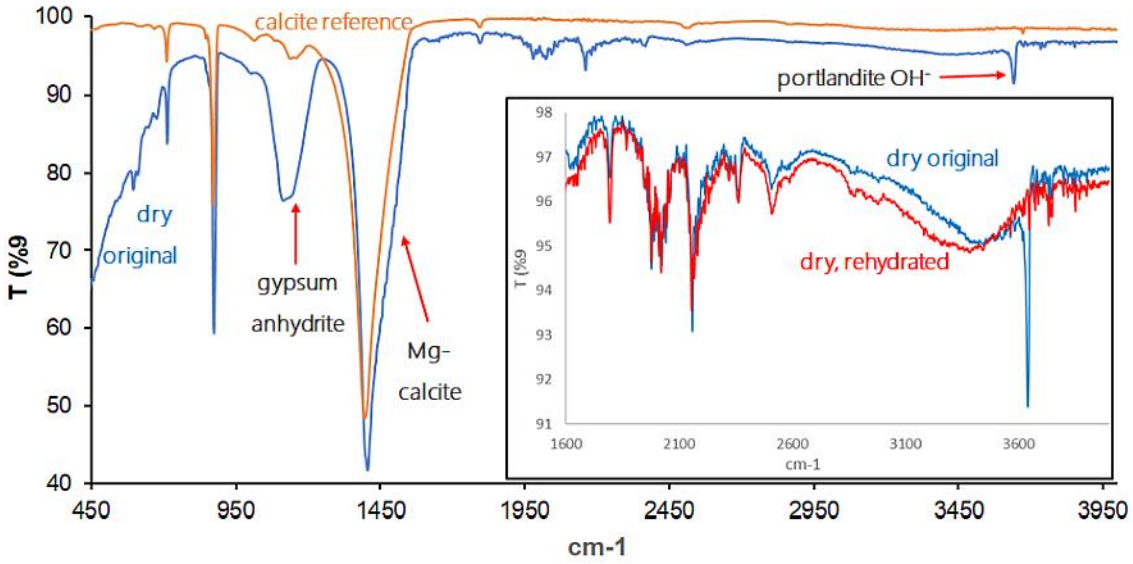

Figure 3. ATR-FTIR spectra of original filter product sample, calcite reference and rehydrated product (red spectra, inset).

The residual but reactive $Ca(OH)_2$ indicates that carbonatation reactions create a semi-continuous shell which hinders CO_2 capture, while aragonite is the product of fast carbonate crystallization – these two processes might be interrelated, and their relevance in the subject is not determined. The sulfate phases are mostly present as individual grains or aggregates of several micrometers. The most important relation is found between maghemite and the Pd and/or Pt phases. Due to the size of these phases their metallic, oxide or mixed nature cannot be determined, thus an assumption is made that PdO observed by XRD coexists with Pd and is a host for Pt.

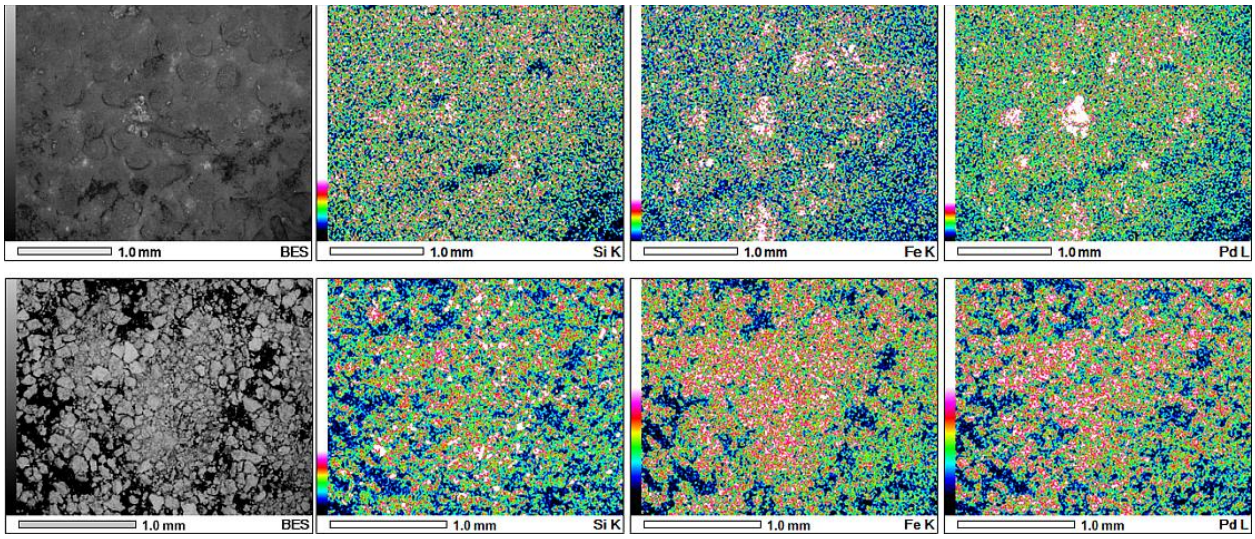

Figure 4. Effect of HCl treatment on elements enrichment, upper row the original sample, lower raw the acid insoluble residue (colors mark concentration increase towards white)

These phases occur in a wide size range, the larger are aggregates of tens of millimeters, built up by smaller irregular units, strongly associated to the Fe-oxide (Figure 4). Since only maghemite was identified by XRD, it is assumed but not assured, that other Fe-oxide phases, nor amorphous oxides are present.

4. CONCLUSIONS

Preliminary test results show, that Fe-oxide cements the Pd-Pt phases, since their concentration is possible by magnetic separation. Also, the residual $Ca(OH)_2$ can be utilized as a useful component, in water immersed dispersing tests it was evidenced, that Fe-oxide cemented aggregates are liberated from the carbonate matrix as a result of pH swing and carbonate dissolution-reprecipitation.

The cubic Fe_2O_3 is a useful component for enrichment/separation of metal bearing aggregates with several physical methods, however the catalysts metals are only partially contained in the oxidic aggregates.

The nature of the gas filtration products opens the possibility of chemical, physical or metallurgical processing for noble metal recovery, the most probable solution being the combination of the above, based on the preliminary experiments.

ACKNOWLEDGEMENTS

This research has been financially supported by the ARIZO project 2020-1.1.2-PIACI-KFI-2020-00121 financed by the Ministry of Innovation and Technology of Hungary.

REFERENCES

[1] M. Economidou, N. Mistry, K.M. Wheelhouse, D.M. Lindsay, Org. Process Res. Dev., 27 (9) (2023) 1585-1615.
[2] I. Chidunchi, M. Kulikov, R. Safarov, E. Kopishev, Heliyon, 10 (3) (2024) e25283.

The 56th International October Conference on Mining and Metallurgy
22-25 October 2025, Bor Lake, Bor, Serbia
www.ioc.tfbor.bg.ac.rs

DOI: 10.5937/IOC25331D Original scientific paper

EXAMPLE OF DENSE MEDIA CYCLONE SELECTION

Oliver Dimitrijević, Ivana Jovanović, Vesna Conić, Dragan Milanović, Tanja Stanković

Mining and Metallurgy Institute Bor, Alberta Ajnštajna 1, 19210 Bor, Serbia
oliver.dimitrijević@irmbor.co.rs, 0000-0002-9573-1943
ivana.jovanovic@irmbor.co.rs, 0000-0002-7450-6632
vesna.conic@irmbor.co.rs, 0000-0002-4268-3626
dragan.milanovic@irmbor.co.rs, 0000-0002-5589-9127
tanja.stankovic@irmbor.co.rs, 0000-0002-2714-7016

Abstract
Dense medium cyclones separate particles based on their density due to centrifugal force induced by the swirling flow. They are usually used in the coal industry to separate lighter coal from denser ash, but can be used for other raw materials, such as lead-zinc ore. There are several methodologies used to select and calculate DM cyclones. This paper deals with two methods related to the selection and calculation of DM cyclone capacity on the example of lead-zinc ore preconcentration.

***Keywords**: DM cyclone, device selection, capacity*

1. INTRODUCTION

The main idea behind dense medium separation (DMS), a beneficiation technique that separates valuable minerals from waste material, is to separate low-density material from high-density material. This separation is accomplished by using a dense medium. After being employed in a separation vessel, the medium is subsequently recovered [1]. DMS is utilized extensively in coal preparation, and are also used as the first concentration step in diamond recovery, iron ore concentration, base metal pre-concentration, and some industrial minerals. The application will determine the operating medium density [2]. Ferrosilicon is utilized as the medium in the ore processing of heavy metals like iron and lead [1].

A circuit for dense medium separation is shown in Fig. 1.

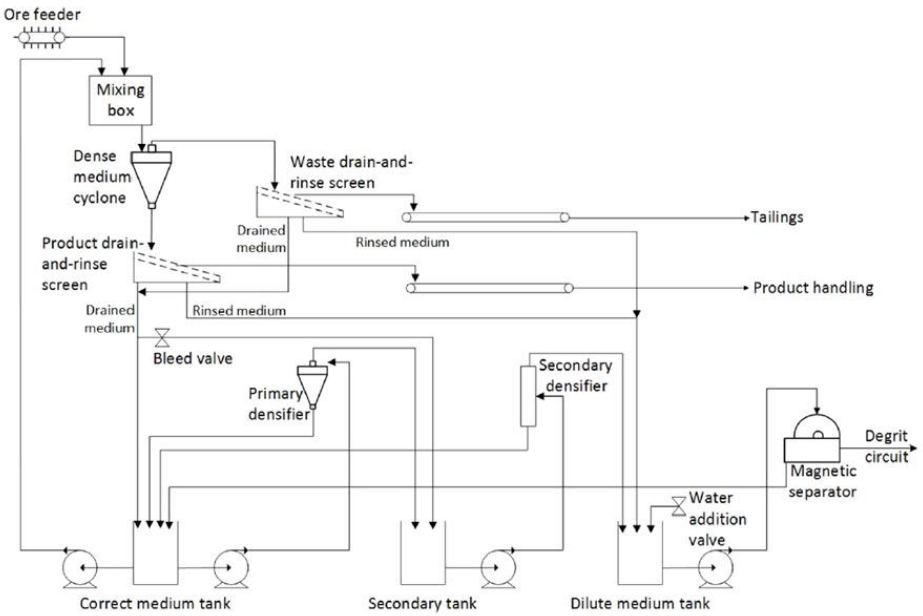

Figure 1. Diagram of a dense medium separation circuit [1].

When properly sized ore is fed into a dense medium cyclone (DMC), lower density waste form the overflow and higher density valuable material constitute the cyclone's underflow. The cyclone's overflow is sent to a drain-and-rinse screen. After being drained from the waste, the medium slurry is transferred to the appropriate medium tank. After that, the leftover waste in the screen is rinsed, and the rinsed medium is sent to the tank of diluted medium. Conveyor belts carry the waste from the screen's overflow to the tailings dump. Additionally, the cyclone's underflow (concentrate) is directed to a drain-and-rinse screen. After being drained from the concentrate, the medium slurry is transferred to the appropriate medium tank. Wash water is used to rinse the leftover concentrate particles from the screen. The diluted medium tank receives the washed medium slurry. Conveyor belts are used to move the concentrate in the screen overflow to product stockpiles. The medium is regenerated through a separate system of devices and returned to the beginning of the process [1].

Operating principle of dense media cyclone (DMC) can be briefly explained as follows (Figure 2). DMC separates the heavy and light particles on basis of density difference under the influence of centrifugal forces. Medium with ore particles fed tangentially through the cyclone inlet where the centrifugal forces are produced due to which the heavier density particles moves towards the wall and passes through underflow as reject. Lower density particles moves along the forced vortex and passes through overflow due to drag dominance [3].

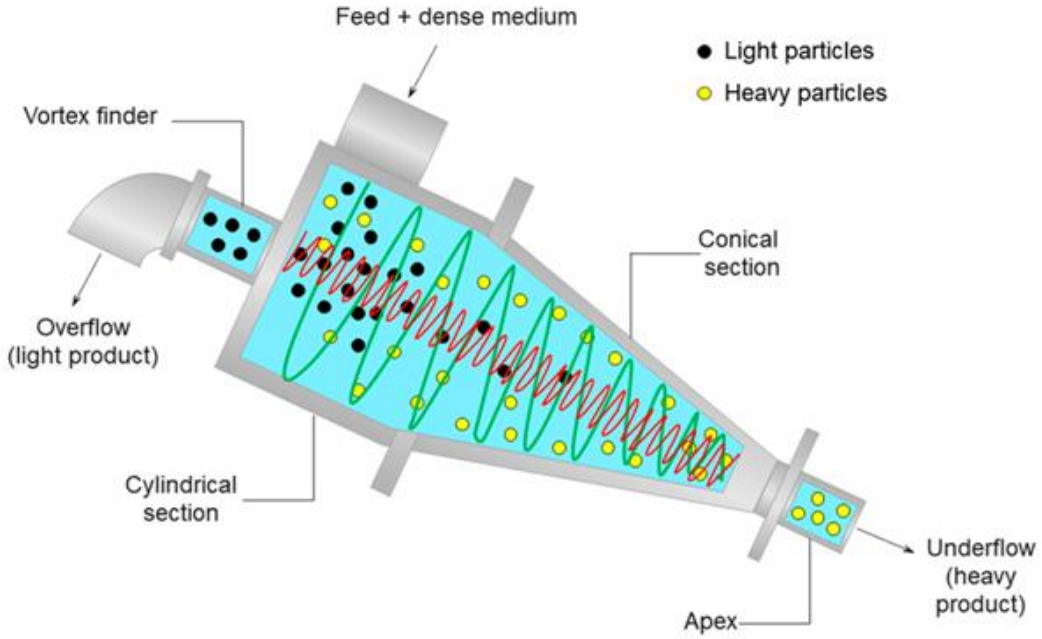

Figure 2. Scheme of a conventional dense-medium cyclone [4].

2. SELECTION OF DMC

Selection and calculation of DMC depends on its operating conditions. Different methodologies are used for the selection and calculation of DM cyclones, and in this paper an example of selecting a DMC based on two methodologies is given: (1) JKMRC method [5] and (2) DSM method [6]. The calculation was made based on the assumed process capacity of 500.00 m^3/h, for the separation of lead-zinc preconcentrate from tailings. The assumed medium is ferrosilicon.

The basic data required for the calculation of the DM cyclone are:

- Pulp volume flow at the dense media cyclone inlet . . . . . V_p = 500.0 m^3/h
- Fluctuation coefficient . . . . . k = 1.2
- Increased pulp volume flow at DMC inlet due to fluctuations . . . . . V_{pmax} = 600.0 m^3/h
- DMC diameter . . . . . Dc = 900 mm

- Length of the rectangular section of the inlet pipe . . . . . *a* = 160 mm
- Width of the rectangular section of the inlet pipe. . . . . *b* = 180 mm
- Equivalent inlet pipe diameter* . . . . . *Di* = 191.5 mm
- Overflow pipe diameter . . . . . *Do* = 440 mm
- Underflow pipe diameter . . . . . *Du* = 370 mm
- Pressure at the DMC inlet expressed in diameters . . . . . *P* = 11 D
- Pressure at the DMC inlet . . . . . *P* = 9.5 m
- Etalon head (etalon pressure at the DMC inlet) . . . . . *He* = 10 m
- A factor that depends on the DMC diameter . . . . . *f* = 0.76

* It is counted as $Di = \sqrt{4ab/\pi}$

According to ***JKMRC methodology***, DMC capacity (Q_c) is calculated based on the following equation:

$$Q_C = 2.87 \cdot 10^{-5} \cdot D_c^{2.30} \cdot P^{0.46} \cdot \left(\frac{D_u}{D_o}\right)^{0.17}$$

Where:

D_c – DMC diameter [mm]
D_o – overflow pipe diameter [mm]
D_u – underflow pipe diameter [mm]
P – operating pressure of the pulp at the DMC inlet, expressed in diameters of the DMC

Accordingly,

$$Q_C = 2.87 \cdot 10^{-5} \cdot 900^{2.30} \cdot 11^{0.46} \cdot \left(\frac{370}{440}\right)^{0.17} = 523.5\ m^3/h$$

By the ***DSM methodology***, the first should calculate the capacity of the reference DM cyclone (Q_{CE}), i.e. capacity of DM cyclone operating at the inlet pressure of *He* = 10 m:

$$Q_{CE} = f \cdot \frac{D_o \cdot D_u}{100} = 0.76 \cdot \frac{370 \cdot 440}{100} = 640.35\ m^3/h$$

Where:

f – a factor that depends on the diameter of the DMC [6]. For the given case, D_c = 900 mm, is adopted f = 0.76

Actual capacity of DM cyclone (Q_C) is calculated based on the equation:

$$Q_C = Q_{CE} \cdot \sqrt{\frac{P}{H_e}} = 640.35 \cdot \sqrt{\frac{9.5}{10}} = 624.14\ m^3/h$$

Where:

P – operating pressure of the pulp at DMC inlet expressed in meters
He – etalon operating head [m], *He* = 10 m

Based on the obtained results, it is concluded that by application of the first methodology (JKMRC) selected DMC does not provide a satisfactory outcome for the maximum capacity that can occur in the plant (2 DMCs are needed). On the other hand, according to the DSM method this DM cyclone has satisfactory performances (1 DMC is enough). Given the conflicting results, the equipment manufacturer's recommendation should be taken into account when choosing a device.

3. CONCLUSION

The selection and calculation of the dense media cyclone was carried out on the example of pre-concentration of lead-zinc ore, by means of two methodologies based on the assumed capacity and type of medium. According to one methodology, the performance of the selected cyclone is satisfactory and one DMC is sufficient for operation in the plant, while according to another methodology it is necessary to adopt two DMCs for smooth operation of the plant. For the final decision on the choice of device, it is necessary to consult the equipment manufacturer.

ACKNOWLEDGEMENTS

Authors thank the Ministry of Science, Technological Development and Innovation of the RS under contract no. 451-03-136/2025-03/200052 for funding support.

REFERENCES

[1] C.S. Lowry, J.D. le Roux, I.K. Craig., Miner. Eng. 210 (2024) 108652
[2] T. Napier-Munn, Miner. Eng., 116 (2018) 107-113.
[3] T.R. Vakamalla, N. Mangadoddy., Powder Technol., 277 (2015) 275-286.
[4] W.M. Ambrós., Recycling, 8 (6) (2023) 85.
[5] https://millops.community.uaf.edu/amit-145/amit-145-lesson-3/
[6] H. Crowden, B. Atkinson, C. Clarkson, B. Firth, M. O'Brien, D. Wiseman, C. Wood, (2013). ACARP Dense Medium Cyclone Handbook, Australian Coal Preparation Society, ISBN 978-0-9589344-2-8

The 56th International October Conference on Mining and Metallurgy
22-25 October 2025, Bor Lake, Bor, Serbia
www.ioc.tfbor.bg.ac.rs

DOI: 10.5937/IOC25335R *Original scientific paper*

SELECTIVE RECOVERY OF COPPER FROM HYDROMETALLURGICAL PROCESSING OF E-WASTE

Petra Růžičková[1a], Klaudia Kundráková[1b], Kristína Talianová[1c], Jakub Klimko[1d], Dušan Oráč[1e]

[1] Technical University of Košice, Faculty of Materials, Metallurgy and Recycling, Institute of Recycling and Environmental Technologies, Letná 1/9, Košice 042 00, Slovakia
[1a] petra.ruzickova@tuke.sk, 0009-0008-9542-6042
[1b] klaudia.kundrakova@tuke.sk, 0009-0009-5393-744X
[1c] kristina.talianova@tuke.sk, 0009-0006-2167-994X
[1d] jakub.klimko@tuke.sk, 0000-0002-5369-4283
[1e] dusan.orac@tuke.sk, 0000-0003-0392-8544

Abstract
One of the environmental aspects of processing electronic waste using hydrometallurgical methods is the generation of waste solutions. Solutions after leaching and recovery of target metals are destined for disposal and contain valuable non-ferrous metals such as Cu, Sn, Ni, and others. Their disposal leads to wasting their material potential. The aim of this work is to propose a method by which selected non-ferrous metals can be selectively recovered from these solutions prior to disposal. The results of the experimental work show that the combination of pH adjustment with sodium hydroxide followed by cementation with iron is a suitable procedure for copper displacement from the solution. The cemented copper contains impurities. Removal of these impurities is possible by washing in sulfuric acid. pH adjustment can also be achieved using waste material containing copper. The results confirm that copper can be selectively recovered from waste solutions.

Keywords: *Hydrometallurgy, Waste from electrical and electronic equipment, Precipitation, Copper, Recycling*

1. INTRODUCTION

Waste from electrical and electronic equipment (WEEE), also known as e-waste, belongs to the fastest-growing waste streams worldwide. The expansive growth of the electronic sector, driven by increasing demands for efficient information and telecommunication systems, causes accelerated device obsolescence and thus a significant rise in the volume of waste produced. WEEE includes a wide range of discarded electronic devices, their components, and consumables [1], [2].

In 2019, 53.6 million tons of this waste were generated globally, of which only 9.32 million tons were officially collected and subsequently recycled. This type of waste contains significant amounts of hazardous substances, such as halogen compounds and toxic metals, the presence of which poses serious ecological and health risks [1].

Despite these environmental risks, e-waste is a valuable source of secondary raw materials. It contains important metals such as copper, iron, aluminum, nickel, gold, silver, and platinum group metals, whose recovery through recycling contributes to reducing the need for primary raw material extraction. Efficient management of WEEE supports the principles of the circular economy. Due to the presence of toxic substances and valuable secondary raw materials in e-waste, proper management is essential. They are processed by various methods using pyrometallurgy, hydrometallurgy, or a combination of both. In the case of hydrometallurgical processing, the by-product is wastewater, i.e., waste solutions, which may contain low concentrations of valuable metals. For this reason, before neutralization or disposal, it is advisable to first recover the metals.

Various methods exist for metal recovery from solutions, such as cementation, precipitation, or electrolysis [3].

The subject of this work is the recovery of metals from waste solutions after hydrometallurgical processing of e-waste using precipitation.

2. EXPERIMENTAL

2.1 Hydrometallurgical processing of WEEE

Hydrometallurgical processing of WEEE consists of mechanical pretreatment of the material transfer of metals into solutions, and subsequent selective recovery of metals from solutions. The advantages of hydrometallurgical processing compared to pyrometallurgy include lower energy consumption and operating costs, higher selective yield of metals, and a smaller environmental footprint. However, compared to pyrometallurgical methods, hydrometallurgical procedures are often more time-consuming [4].

2.2 Mechanical pretreatment

Before hydrometallurgical processing, WEEE must first undergo mechanical pretreatment to release metals from the composite structure of e-waste. This may include manual dismantling prior to mechanical-physical processing. Mechanical-physical treatment involves crushing and grinding the material, which is subsequently subjected to separation of individual fractions based on different physical and chemical properties. Examples include density separation, particle size classification, magnetic separation, or eddy current separation [5], [6].

2.3 Leaching

After mechanical pretreatment, the material undergoes leaching processes to transfer target substances into solution. Leaching agents may include organic or inorganic substances such as sodium hydroxide (NaOH), sulfuric acid (H2SO4), hydrochloric acid (HCl), nitric acid (HNO3), aqua regia (3HCl + HNO3), acetic acid, oxalic acid, citric acid, and others. Thermodynamic studies of leaching are an integral part of research, as they indicate which metals will or will not dissolve in different reagents. The leaching process is also influenced by temperature, mixing speed, and the pH of the leaching medium [4].

2.4 Metal recovery methods

Various methods are used to recover metals from solutions. The choice of method depends mainly on metal concentration. They are classified as physical, chemical, and physico-chemical, including crystallization, ion exchange, precipitation, cementation, electrolysis, solvent extraction, and others. The selection depends on multiple physical and chemical factors; therefore, it is important to choose methods that enable selective recovery of present components [7].

Cementation

Cementation is an electrochemical process for recovering metals from solutions, based on displacing a more noble metal with a less noble one according to the electrochemical series. An example is copper displacement using iron [7]. The principle is illustrated in Equation 1:

$$2Fe + Cu(NO_3)_2 = 2Fe(NO_3)_3 + Cu \qquad (1)$$

Precipitation

Precipitation is a process of recovering metals based on reactions between chemical agents and metals in solution, forming poorly soluble compounds. The reaction rate and efficiency of precipitation can be enhanced by increasing the initial metal concentration, adjusting pH, or raising

the temperature. In practice, heavy metals are most commonly removed as hydroxides, sulfides, or carbonates [8], [9].

2.5 Characterization of waste water solutions

The waste solutions used for experiments were from hydrometallurgical processing of WEEE. While the target metals are mainly platinum group metals, gold, and silver, e-waste also contains other valuable metals such as copper, nickel, zinc, and lead. Different reagents are used to transfer metals into solutions, followed by various methods for selective recovery.

First solution, named IH, contains a solution of spent nitric acid, second one, named LK, contains spent aqua regia, and OV contains spent sulfuric acid. These were analyzed by atomic absorption spectrometry (AAS) using a Varian SpectrAA20+ device with a detection limit of 0.3–6 ppb, wavelengths of 213.9–422 nm, and lamp current of 4–12 mA, manufactured in Belrose, Australia. The results are shown in Table 1.

Table 9. Chemical analysis results

		Cu	Sn	Ni	Pb	Fe	Zn	Al	Ca	Ag	Pt	Pd	Au
LK	[μg/ml]	74100	3980	3293	1807	1247.2	515	241	188	32.79	4.3	2.5	0
IH		124373	41.3	2215.6	476	4154	2009	141	50.8	1.42	2.7	0.73	0
OV		6135	312	57.7	1.67	18.12	101	0	13.7	0	8.3	1.01	0

The analyses revealed the presence of copper, tin, nickel, lead, iron, zinc, aluminum, calcium, and trace amounts of silver, platinum, and palladium. Copper was the most abundant element, with 124.373 g/l in the waste solution IH, 74.1 g/l in waste solution LK, and 6.135 g/l in waste solution OV.

Based on the chemical analysis of the waste solutions, a material balance was calculated to determine which solution has the highest material potential. Considering the differences in metal prices, it is possible that metals with lower concentrations but higher market values may represent economically valuable products. Table 2 presents the material potential of individual metals in the solutions, calculated as the concentration of a metal per unit volume of solution (l or m^3) multiplied by the current market price of the metal (expressed in USD per ton).

Table 10. Material potencial of solutions

		Cu	Sn	Ni	Pb	Fe	Zn	Al	Ag	Pt	Pd
LK	[$/m3]	683.35	117.37	99.92	3.93	-	1.75	0.64	25.58	140.91	135.78
IH	[$/m3]	1 146.97	1.22	67.23	1.03	-	6.81	0.37	1.11	88.48	39.65
OV	[$/m3]	56.58	9.20	1.75	0.00	-	0.34	-	-	271.99	54.85

From the material balance calculations, it follows that the most valuable element in solution IH is copper, with a potential value of 1,146.97 $/m³. Solutions LK and OV are also of interest due to their platinum and palladium contents. In LK, platinum reaches a value of 140.91 $/m³ and palladium 135.78 $/m³, while in OV, platinum reaches 271.99 $/m³.

For the experimental study of metal precipitation, the waste solution IH was chosen, as it showed the highest material potential.

2.6 Thermodynamic study

Based on thermodynamic studies, sodium hydroxide (NaOH) was chosen as the precipitating agent for selective copper recovery from solution IH. Precipitation reactions are shown in equations (2)–(7).

$Cu(NO_3)_2 + 2NaOH = 2NaNO_3 + Cu(OH)_2$ $\Delta G°_{293,15}$= -125,031 (2)
$Fe(NO_3)_3 + 3NaOH = 3NaNO_3 + Fe(OH)_3$ $\Delta G°_{293,15}$= -327,833 (3)
$Ni(NO_3)_2 + 2NaOH = 2NaNO_3 + Ni(OH)_2$ $\Delta G°_{293,15}$= -164,884 (4)
$Fe(NO_3)_2 + 2NaOH = NaNO_3 + Fe(OH)_2$ $\Delta G°_{293,15}$= -176,031 (5)
$Sn(NO_3)_2 + 2NaOH = 2NaNO_3 + Sn(OH)_2$ $\Delta G°_{293,15}$= -227,737 (6)
$Zn(NO_3)_2 + 2NaOH = 2NaNO_3 + Zn(OH)_2$ $\Delta G°_{293,15}$= -170,167 (7)

Fractional precipitation diagrams constructed with Medusa/Hydra indicate precipitation pH values as follows:

- Cu^{2+}: begins at pH 3.5, complete at pH 5
- Sn^{2+}: begins at pH 3, complete at pH 4
- Ni^{2+}: begins at pH 6, complete at pH 7
- Zn^{2+}: begins at pH 7, complete at pH 8.5
- Fe^{2+}: begins at pH 7, complete at pH 8.5
- Fe^{3+}: begins at pH 1.5, complete at pH 2
- Sn^{4+}: begins at pH 0, complete at pH 1

2.7 Precipiation of metals from waste water solution IH

In the experimental part, NaOH solution was added in volumes of 0.5–4.5 ml to 20 ml of IH solution. After precipitation, 5 ml samples were taken, and pH was measured. Recorded pH values ranged from 0 to 7.4.

AAS results combined with pH measurements (Figure 1) revealed that iron started precipitating after the first NaOH addition and was completely removed at pH 2.63. Compared to theoretical predictions, copper precipitation occurred earlier—already after the first NaOH addition. Lead, aluminum, and tin also precipitated immediately. Nickel and zinc followed a similar trend.

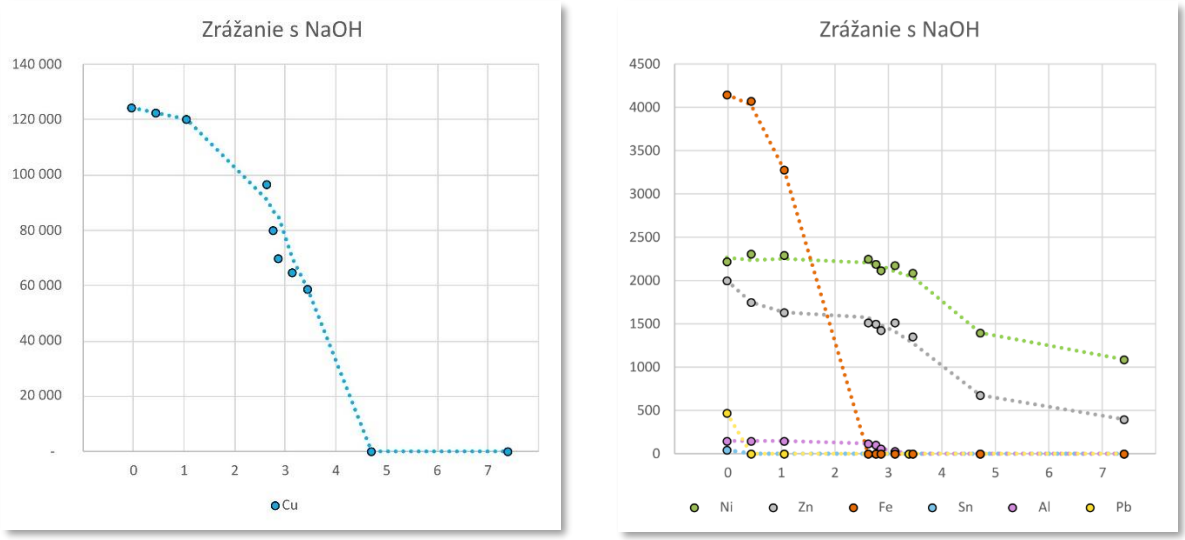

Figure 10. Results of the precipitation of Cu, Fe, Zn, Ni

The results confirm that selective recovery of copper from the solution is not possible by this method due to the presence of impurities in the form of iron, zinc, nickel, tin, lead, and aluminum.

The aim of the second precipitation experiment was first to remove iron from the solution, which is completely precipitated at pH 2.63 using sodium hydroxide, and then to selectively precipitate copper. The results confirmed that during iron precipitation, 22% of copper is lost, as it begins to precipitate together with iron. The remaining 78% of copper present in the solution can be removed by further precipitation; however, it contains impurities in the form of nickel and zinc. Figure 2 shows the filtered copper hydroxide obtained after precipitation with NaOH.

Figure 11. Precipitated copper hydroxide

The resulting blue-green copper powder contains not only copper but also nickel and zinc. Such a product is unsuitable for commercial use. Precipitation is therefore evaluated as an inappropriate selective method. Cementation is proposed as an alternative approach for copper recovery from the solution and will be the subject of further study.

3. CONCLUSION

E-waste is a type of waste whose annual production is continuously increasing. Due to the content of valuable metals in this waste, their recycling is essential. Recycling prevents the depletion of primary raw materials. The most widely used methods for recycling e-waste are pyrometallurgical or hydrometallurgical approaches, each with their own advantages and disadvantages. A drawback of hydrometallurgical recycling is the generation of waste solutions. These waste solutions may contain low concentrations of valuable metals, which should be recovered before disposal. Metals are most often recovered from solutions using precipitation, cementation, or electrolysis.

The experimental part of this work focused on the processing of waste solutions with the aim of recovering selected target metals using precipitation. Analysis of the solutions and calculation of the material balance showed that copper is the most valuable element present in the waste solutions. For this reason, copper was chosen as the target metal for recovery by precipitation.

The experimental results showed that copper can be recovered from solution, but up to pH 2.63 it co-precipitates with iron. During iron removal, 22% of copper is lost, which means material losses. The remaining 78% of copper can be precipitated later, but this product also contains nickel and zinc. Copper contaminated with these metals is not a suitable marketable product.

Thus, precipitation proved to be a non-selective method for copper recovery from waste solutions. The subject of further research will be the use of cementation as a method for recovering copper from waste solutions after hydrometallurgical processing of e-waste.

ACKNOWLEDGEMENTS

This work was created within the framework of the VEGA project of the Ministry of Education, Science and Technology of the Slovak Republic 1/0678/23.

This work was created within the framework of the APVV project of the Ministry of Education, Research, Development and Youth of the Slovak Republic APVV-23-0051.

REFERENCES

[1] “Electronic waste (e-waste)”. Cit: 26. marec 2024. [Online]. Available at: https://www.who.int/news-room/fact-sheets/detail/electronic-waste-(e-waste)

[2] Slov-lex, “79/2015 Z.z. - Zákon o odpadoch a o zmene a doplne...”, Slov-lex. Cit: 28. apríl 2024. [Online]. Available at: https://www.slov-lex.sk/pravne-predpisy/SK/ZZ/2015/79/

[3] "Hazardous Substances in e-Waste | ECS Environment". Cit: 28. apríl 2024. [Online]. Available at: https://www.ecsenvironment.com/what-is-e-waste/hazardous-substances-in-e-waste/
[4] V. Gunarathne, A. Upamali Rajapaksha, M. Vithanage, D.S. Alessi, R. Selvasembian, M. Naushad, S. You, P. Oleszczuk, Y. Sik Ok, Crit. Rev. Environ. Sci. Technol., 52 (6) (2022) 1022–1062.
[5] L.M. Martelo, M.M.S.M. Bastos, H.M.V.M. Soares, Miner. Eng., 206 (2024) 108529.
[6] Z. Wang, Y. Zhang, P. Feng, L. Meng, J. Wang, Z. Guo, Z. Gong, J. Environ. Chem. Eng., 12 (1) (2024) 111801.
[7] T.T.H. Nguyen, M.S. Lee, Hydrometallurgy, 215 (2023) 105969.
[8] R. Sarup, K. Behl, M. Joshi, a S. Nigam, "Chapter 18 - Heavy metal removal by cyanobacteria", v New Trends in Removal of Heavy Metals from Industrial Wastewater, M. P. Shah, S. Rodriguez Couto, a V. Kumar, Ed., Elsevier, 2021, s. 441–466. doi: 10.1016/B978-0-12-822965-1.00018-0.
[9] A. Santaolalla, P.N.L. Lens, A. Barona, N. Rojo, A. Ocio, G. Gallastegui, Minerals, 11 (9) (2021).

Alloys, Composites, and Advanced Materials

The 56th International October Conference on Mining and Metallurgy
22-25 October 2025, Bor Lake, Bor, Serbia
www.ioc.tfbor.bg.ac.rs

DOI: 10.5937/IOC25343C *Review paper*

STRONTIUM PHOSPHATE CONVERSION COATINGS: A SHORT REVIEW

Anca Cazac[1a], Diana-Petronela Burduhos-Nergis[1b], Andrei Victor Sandu[1c], Mihai Popa[1d] Costica Bejinariu[1,2e]

[1] Gheorghe Asachi Technical University of Iasi, D. Mangeron 67, 700050, Iasi, Romania
[2]Academy of Romanian Scientists, Ilfov 3, 050044, Bucharest, Romania
[1a] anca.cazac@student.tuiasi.ro, 0009-0009-0815-8770
[1b] diana-petronela.burduhos-nergis@academic.tuiasi.ro, 0000-0002-0680-9885
[1c] andrei-victor.sandu@academic.tuiasi.ro, 0000-0002-9292-749X
[1d] mihai.popa@academic.tuiasi.ro, 0000-0002-8509-7395
[1.2e] costica.bejinariu@academic.tuiasi.ro, 0000-0003-1973-7240

Abstract
Phosphating is the process of deposition through conversion, of a layer of soluble phosphate compounds, on the surface called support. Although phosphate chemical conversion coatings have been studied since the early 19th century, they are not only still under study, but are an area of interest due to their numerous applications. In particular, chemical conversion coatings represent a cost-effective approach to achieving satisfactory corrosion resistance, while being easily obtainable at reasonable costs. Strontium phosphate-based coatings can be used in the medical field and help improve the biological character of implants. The properties of biocompatible alloys include low density, biocompatibility, and good osseointegration properties. Titanium is the most widely used metal material for implants in both orthopedic and dental fields. Due to the environment in which implants are placed, their corrosion resistance is seriously impaired once the surface passivation layer is damaged, leading to bone resorption and soft tissue infection. This can be improved by using various types of phosphate coatings that help biological response, osseointegration, etc. Strontium (Sr), a trace element in the human body, has been reported to be beneficial in enhancing bioactivity and biocompatibility. Sr ions suppress bone resorption, develop the mechanical properties of bone, enhance the replication of preosteoblast cells, and stimulate bone formation, thus ultimately preventing bone loss. Strontium ions have the same physiological and chemical behavior as Ca^{2+}, the major component of bone, and can be incorporated into the mineral structure of bone by ionic substitution for Ca. Although the beneficial effects of Sr on bone regeneration are clear, studies exploring the effect of Sr-coated Mg-based biomaterials on either biodegradation inhibition or osseointegration are rare to date. However, chemical conversion coatings of strontium phosphate on various substrates have rarely been investigated, and this requires further research. This paper aims to analyze the research conducted to date on strontium phosphate used in the field of biomaterials and beyond.

Keywords: *phosphating, biomaterials, conversion coatings, strontium phosphate, osseointegration.*

1. INTRODUCTION

Phosphating is the process of depositing, by conversion, a layer of soluble phosphate compounds on the surface of the metal. Although phosphate coatings have been studied since the beginning of the 19th century, they are not only still under study, but are an area of interest due to their numerous applications [1].

The advantages of these types of coatings are well known, such as the low cost of the deposition process, improved corrosion resistance properties and improved wear resistance and eventual adhesion of subsequent deposited layers, such as paint. All this leads to studies on the constant improvement of the properties of the phosphate coating, by modifying the parameters of the phosphating process, as well as by modifying/replacing the substances used in the phosphating solutions with "environmentally friendly" solutions. Also due to these advantages, several

researchers are studying the possibility of using phosphate coatings in fields such as civil engineering or medicine - coatings with biomaterials [1,2].

In particular, chemical conversion coatings represent a cost-effective approach to achieving satisfactory corrosion resistance, while being easily obtainable at reasonable costs. Also due to these advantages, several researchers are studying the possibility of using phosphate coatings in fields such as civil engineering or medicine - coatings with biomaterials [1,2].

2. STRONTIUM PHOSPHATE COATINGS

Strontium (Sr) discovered in the 19th century and is part of second group of the periodic table. In nature, Sr occurs as a mixture of four stable isotopic forms: $_{88}$Sr (82.6%), $_{86}$Sr (9.9%), $_{87}$Sr (7.0%), and $_{84}$Sr (0.6%). This metal is easily oxidized to form strontium oxide; therefore, Sr does not naturally exist in free form. Celes-tine ($SrSO_4$) and strontianite ($SrCO_3$) are the main minerals, which are present in nature [3,4]

In the human body, strontium is a trace element. The daily strontium intake by an adult is approximately 4 mg. The main sources of this element are leafy vegetables, grains and dairy products (amounting to about 1.2–2.3 mg/day). Drinking water provides approximately 0.7–2 mg/day [4,5]. Strontium is poorly absorbed by the body, with an absorption level of approximately 25–30% [4].

Most of the absorbed element is found in the skeleton, but its content is only 0.035% of the calcium content [5,6]. In the organism, strontium is probably built into the crystals of biological apatite. It can form carbonate, citrate, and lactate salts, and it can also bind with calcium-transporting proteins.

Early studies provided pharmacological evidence that strontium reduces osteoclast differentiation, activity and bone resorption in vitro [7,8]. More recent studies provided some mechanistic input into this effect. SrRan reduces the adherence of osteoclasts to bone by disrupting the actin containing sealing zone [9].

Pagani et. all in their 2025 test in vitro, the osteoinductivity induced by the addition of bone morphogenetic protein-2 (BMP-2) or amorphous calcium phosphate granules with strontium ions (Sr-ACP), in order to improve the clinical regeneration of subchondral bone, still incomplete. Results show that the modified scaffolds, particularly the one containing Sr-ACP, increased the expression of the osteoclasts' typical markers and decreased the OPG/RANKL ratio. Both types of scaffold modification were able to increase the osteoinductivity with respect to the original scaffold used in clinical practice. BMP-2 modification seemed to be more slightly oriented to sustain NHOst activity, and Sr-ACP seemed to be more slightly oriented to sustain the osteoclast activity. These could provide a concerted action toward better regeneration of the entire osteochondral unit [10].

To improve implant osseointegration while preventing infection, Lai Y. and Mo A. developed a strontium (Sr)-doped $Ti_3C_2T_x$ MXene coating on titanium, aiming to synergistically enhance bone integration and antibacterial performance. MXene is a family of two-dimensional transition-metal carbides/nitrides whose abundant surface terminations endow high hydrophilicity and bioactivity. The coating was fabricated via anodic electrophoretic deposition (40 V, 2 min) of $Ti_3C_2T_x$ nanosheets, followed by $SrCl_2$ immersion to incorporate Sr^{2+}. Characterization confirmed that the MXene/Sr composite retained the layered architecture and primary chemistry of pristine MXene without structural compromise. Collectively, the Sr-doped Ti3C2Tx MXene coating provides dual functionality—promoting bone regeneration and imparting antibacterial activity—and thus offers a promising strategy for the surface modification of dental and orthopedic implants [11].

Ielewi, N.H. and Abdul-Ameer, F.M. did a study about the effect of adding bioactive glass infused with strontium on the surface hardness and surface roughness properties of a heat-cured acrylic-

based soft liner. This study looks at how strontium-infused phosphate bioactive glass affects a heat-cured acrylic-based soft liner, focusing on the surface hardness and the surface roughness of the material. The 7 wt.% PBG*Sr specimens exhibited the lowest surface hardness, suitable for soft lining material, and improved the surface morphology of acrylic soft liners compared with the control and other concentrations [12].

The increasing replacement of calcium with strontium ions was observed to cause a significant increase in the solubility of the substituted synthetic hydroxyapatite: $Ca_{10}(PO_4)_6(OH)_2$ (HA), which was ascribed to a destabilization of the structure due to the presence of the bigger substituent ion [13]. The results of infrared and Raman absorption studies confirmed the expansion of the unit cell and the structural distortion induced by strontium [14,15]. In particular, the shift of the phosphate absorption band to lower energies was suggested to be due to a decrease in the repulsion between anions, which are more separated when the structure hosts the large strontium ion [14].

The substitution of calcium with strontium in β-TCP has been obtained through synthesis in solution, followed by heat treatment at high temperatures, as well as through solid-state reactions at high temperatures and by using a mechano-chemical activation method. The results of the different studies generally agree on the possibility of strontium ions entering this structure in relatively large amounts, up to about 80 at%, provoking a linear expansion of the cell parameters [14,17,18,19,20,21,22]. Strontium compounds have been widely used to improve the radiopacity of various materials. Ideally, dental materials should have sufficient radiopacity to be detected by X-ray during dental inspection and distinguished from adjacent carious tooth structure [23,24]. According to ISO standards and American Dental Association (ADA)recommendations, the minimal radiopacity of a 1 mm material should be equivalent to 1 mm of aluminum [22,25]. Strontium, a heavy metal with an atomic mass of 87.62 [26], has a higher density and consequently higher radiopacity when detected by X-ray [27].

Kavitha et. al conducted a study about deposition of strontium phosphate coatings on magnesium by hydrothermal treatment (HT): characteristics, corrosion resistance and bioactivity. The study reveals that Sr-P coatings can be deposited on Mg by HT at 80, 120, 150 and 200 °C for 30 min and the coating formation is highly influenced by the treatment temperature. The study concludes that Sr-P coatings deposited on Mg by HT exhibit good structural integrity, higher corrosion resistance and bioactivity [28].

Based on the morphological variability of phosphate crystals, the microstructure of the coating can be regulated by designing the composition of the phosphate solution. In this study, a strontium-zinc-phosphate ($SrZn_2(PO_4)_2$, SZP) coating was prepared on titanium (Ti) surface by phosphate chemical conversion method. It was identified that the Zn^{2+} concentration in phosphate solution played a pivotal role in regulating the structure and crystal morphology of the SZP coating. With the increase of Zn^{2+} concentration in the solution, the crystal morphology of the SZP coating gradually evolved from irregular granular to cubicblock, and the corresponding hydrophilicity and corrosion resistance were improved [29].

3. CONCLUSIONS

Strontium phosphate-based coatings can be used in the medical field and help improve the biological character of implants. The properties of biocompatible alloys include low density, biocompatibility, and good osseointegration properties. Titanium is the most widely used metal material for implants in both orthopedic and dental fields. Due to the environment in which implants are placed, their corrosion resistance is seriously impaired once the surface passivation layer is damaged, leading to bone resorption and soft tissue infection. This can be improved by using various types of phosphate coatings that help biological response, osseointegration, etc. In particular, chemical conversion coatings represent a cost-effective approach to achieving satisfactory corrosion resistance, while being easily obtainable at reasonable costs. Analyzing

current research related to strontium phosphate, we observe its intensive use in the field of biomaterials and beyond. However, chemical conversion coatings of strontium phosphate on various substrates have rarely been investigated, and this requires further research.

ACKNOWLEDGEMENTS

This work was supported by a National Research Grants of the TUIASI, project number GNaC 2023_272/2024, Straturi inovative obținute prin conversie chimică pentru îmbunătățirea răspunsului biologic al implanturilor din titan (BioTiC) - Innovative layers obtained through chemical conversion to improve the biological response of titanium implants (BioTiC).

REFERENCES

[1] D.P. Burduhos-Nergis, A.V. Sandu, D.D. Burduhos-Nergis, P. Vizureanu, C. Bejinariu, Arch. Metall. Mater. 68 (3) (2023) 1029-1034.
[2] P. Lazar, N. Cimpoesu, B. Istrate, A.M. Cazac, D.P. Burduhos-Nergis, M. Benchea, A.C. Berbecaru, G. Badarau, G.D. Vasilescu, M. Popa, C. Bejinariu, Coatings, 14 (2) (2024) 182.
[3] P. Watts, P. Howe, Strontium and Strontium Compounds, World Health Organization, Geneva, Switzerland, 2010.
[4] P.J. Marie, P. Ammann, G. Boivin, C. Rey, Calcif. Tissue Int., 69 (2001) 121.
[5] B. Kołodziejska, N. Stępień, J. Kolmas, Int. J. Mol. Sci., 22 (2021) 6564.
[6] J.B. Cannata-Andía, M. Rodríguez-García, C. Gómez-Alonso, Rev. Osteoporos. Metab. Miner., 2 (2010) 5–9.
[7] Z. Saidak, P.J. Marie, Pharmacol. Ther., 136 (2012) 216-226.
[8] R. Baron, Y. Tsouderos, Eur. J. Pharmacol., 450 (1) (2002) 11-17.
[9] E. Bonnelye, A. Chabadel, F. Saltel, P. Jurdic, Bone, 42 (1) (2008) 129-138.
[10] S. Pagani, M. Salerno, J. Locs, J. Vecstaudza, L. Dolcini, M. Fini, G. Giavaresi, G. Filardo, M. Columbaro, J. Funct. Biomater., 16 (2025) 302.
[11] Y. Lai, A. Mo, Coatings, 15 (2025) 847.
[12] N.H. Ielewi, F.M. Abdul-Ameer, Prosthesis, 7 (2025) 69.
[13] H.B. Pan, Z.Y. Li, W.M. Lam, J.C. Wong, B.W. Darvell,; K.D. Luk, W.W. Lu, Acta Biomater., 5 (2009) 1678–1685.
[14] A. Bigi, E. Boanini, C. Capuccini, M. Gazzano, Inorg. Chim. Acta, 360 (2007) 1009–1016.
[15] G. Cheng, Y. Zhang, H. Yin, Y. Ruan, Y. Sun, K. Lin, Ceram. Int., 45 (2019) 11073–11078.
[16] S. Kannan, S. Pina, J.M.F. Ferreira, J. Am. Ceram. Soc., 89 (2006) 3277–3280.
[17] G. Renaudin, P. Laquerriere, Y. Filinchuk, E. Jallot, J.M. Nedelec, J. Mater. Chem., 18 (2008) 3593–3600.
[18] A.A. Belik, F. Izumi, S.Y. Stefanovich, A.P. Malakho, B.I. Lazoryak, I.A. Leonidov, O.N. Leonidova, S.A. Davydov, Chem. Mater., 14 (2002) 3197–3205.
[19] Y. Naciri, A. Hsini, Z. Ajmal, A. Bouddouch, B. Bakiz, J.A. Navío, A. Albourine, J.C. Valmalette, M. Ezahri, A. Benlhachemi, J. Colloid Interf. Sci., 572 (2020) 269–280.
[20] A. Bigi, E. Foresti, M. Gandolfi, M. Gazzano, N. Roveri, J. Inorg. Biochem., 66 (1997) 259–265.
[21] E. Boanini, M. Gazzano, C. Nervi, M.R. Chierotti, K. Rubini, R. Gobetto, A. Bigi, J. Funct. Biomater., 10 (2019) 20.
[22] I.V. Fadeeva, D.V. Deyneko, A.A. Forysenkova, V.A. Morozov, S.A. Akhmedova, V.A. Kirsanova, I.K. Sviridova, N.S. Sergeeva, S.A. Rodionov, I.L. Udyanskaya, I.V. Antoniac, J.V. Rau, Molecules, 27 (2022) 6085.
[23] M.M. Abdalla, O. Sayed, C.Y.K. Lung, V. Rajasekar, C.K.Y. Yiu, J. Funct. Biomater., 15 (2024) 216.
[24] S. Shahid, U. Hassan, R. Billington, R. Hill, P. Anderson, Dent. Mater., 30 (2014) 308–313.
[25] ISO 9917-1; Dentistry-Water-Based Cements-Part 1: Powder/Liquid Acid–Base Cements. International Organization for Standardization: Geneva, Switzerland, 2007.
[26] R. Rana, M. Höcker, E.G. Myers, Phys. Rev. A, 86 (2012) 050502.
[27] J. You, J.S. Yoo, K.Y. Kum, S.H. Hong, J. Korean Ceram. Soc., 58 (2021) 330–336.
[28] R.J. Kavitha, K. Ravichandran, T.S.N. Sankara Narayanan, J. Alloys Compd., 745 (2018) 725-743.
[29] K. Zuo, Z. Gong, G. Xiao, S. Huang, C. Du, B. Liu, D. Zhang, Y. Lu, Surf. Coat. Technol., 433 (2022) 128143.

The 56th International October Conference on Mining and Metallurgy
22-25 October 2025, Bor Lake, Bor, Serbia
www.ioc.tfbor.bg.ac.rs

DOI: 10.5937/IOC25347V *Original scientific paper*

INFLUENCE OF HEAT TREATMENT ON MECHANICAL PROPERTIES OF ALUMINIUM ALLOY EN AW-2011

Maja Vončina[1a], Jožef Medved[1b], Tinkara Smolar[2a], Matej Steinacher[2b]

[1] Department of Materials and Metallurgy, Faculty of Natural Sciences and Engineering, University of Ljubljana, Aškerčeva 12, 1000 Ljubljana, Slovenia
[2] IMPOL 2000 d.d., Partizanska 38, 2310 Slovenska Bistrica, Slovenia
[1a] maja.voncina@ntf.uni-lj.si; 0000-0002-2563-1103
[1b] jozef.medved@ntf.uni-lj.si; 0009-0007-6931-5595
[2a] tinkara.smolar@impol.si; 0000-0002-2563-1103
[2b] matej.steinacher@impol.si; 0009-0004-2870-4082

Abstract
The EN AW-2011 alloy is semi-continuously cast into billets, which are extruded into semi-finished products such as bars, tubes, and wires, and are further processed into final products for the following applications: screw machine products, application parts and equipment, weaponry, the automotive industry, electronics, hardware, and machine parts. For precipitation hardening alloys, heat treatment is just as important as forming. Homogenization, which is carried out before extrusion, and aging, which takes place after extrusion, represent the important parts of the research questions in the field of industrial energy and economy. The optimization of time- and temperature-efficient heat treatments represents a challenge for research and scientific institutions that contributes to the further development of the metallurgical profession and industrial plants. Despite possible changes, the end products must have an appropriate microstructure and mechanical properties.
The heat treatment (homogenization) was carried out on samples from vertically semi-continuously cast billets made from EN AW-2011 alloy at a temperature of 520 °C and over 8 different time periods. Differential scanning calorimetry was carried out to define and confirm the success and suitability of the experimental heat treatment. Based on these results, optimal homogenization parameters were selected for further investigations. This was followed by artificial aging that included two different aging temperatures and correspondingly adapted time intervals.
The most optimal homogenization was selected at 520 °C for 4 hours and artificial aging at 170 °C for 14 hours.

Keywords: *Alloy EN AW-2011, heat treatment, homogenization, artificial ageing, mechanical properties*

1. INTRODUCTION

The aluminium alloys of the 2xxx series, based on the Al-Cu system, have high strength and low specific weight, which ensures the wide use of extruded products made of such alloys for structural components, especially for military applications. It is important to emphasize that these alloys have a low degree of deformation during extrusion, which requires high pressures during processing, resulting in a low extrusion factor [1, 2]. Alloy EN AW-2011 is cast semi-continuously into billets, which are extruded into semi-finished products such as bars, tubes and wires and further processed into finished products [3]. An important step in the manufacture of products from the alloy EN AW-2011 is homogenization, which achieves a rounded and more compact form of the eutectic phases [4-6], and aging, which causes the precipitation of copper-based precipitates [5, 7]. Copper contributes significantly to the strength properties of the alloy during aging [8-10].

2. EXPERIMENTAL

The experimental section was designed based on initial calculations with the Thermo-Calc software (TC) and the TCAL6 database using the actual chemical composition of the EN AW-2011 alloy samples and the results of the differential scanning calorimetry analysis (STA 449C

Jupiter, Netzsch). Based on these results, the homogenization of as-cast samples taken at D/4 of the billet at a constant temperature of 520 °C in a laboratory furnace (Bosio) for eight different times was performed. The results of the billets homogenized for different times were compared with the results of the analyzes using light microscopy (Zeiss Axio Observer 7), scanning electron microscopy (SEM, JEOL JSM 6610) and measured Brinell hardness (WICK ZHU 250CL). The samples for the investigation of the influence of homogenization and aging on the mechanical properties were taken from rods extruded on an indirect extruder and previously homogenized at 520 °C for 4, 5 and 6 hours. Aging was carried out at two different temperatures (170 °C and 190 °C) and ten different times (8, 9, 10, 11, 12, 13, 14, 15, 16 and 17 h). After determining the optimum temperature and time based on the hardness of the samples, the tensile tests (Zwick Roell, the samples were prepared according to the DIN 50125 – B 14 × 70 standard, and the tensile test was carried out according to the ISO 6892-1 standard) were performed only on selected samples.

3. RESULTS AND DISCUSION

Table 1 shows the chemical composition of the experimental alloy. Figure 1a illustrates the non-equilibrium solidification of the EN AW-2011 alloy according to the Scheil diagram. Solidification of the primary α-Al solid solution begins at 642.7 °C, followed by eutectics: α-Al + $Al_{13}Fe_4$ at 627.3 °C, α-Al + $Al_{13}Fe_4$ + Bi at 618.3 °C, α-Al + Al_7Cu_2Fe + Bi at 594.5 °C, and finally α-Al + Al_2Cu + Bi at 542.5 °C, which continues until the end of solidification at 519.0 °C. At this temperature, α-Al + β-Si + Al_2Cu + Bi also appears. DSC heating (Fig.1b) showed precipitation at 267.8 °C (due to non-equilibrium solidification). Eutectic melting started at 542 °C (θ-Al_2Cu, solidus), followed by eutectic melting at 566 °C (Al_7Cu_2Fe), 619.8 °C ($Al_{13}Fe_4$) and finally at 633.5 °C (α-Al). Upon cooling, the liquidus appeared at 635 °C (according to TC at 642 °C), then the eutectic with Al_7Cu_2Fe at 580 °C and the eutectic with θ-Al_2Cu at 528 °C (according to TC).

Table 1. Average chemical composition of alloy EN AW-2011

Element	Si	Fe	Cu	Mn	Mg	Ni	Ti	Pb	Sn	Bi	Al
wt/%	0.15	0.45	5.44	0.01	0.007	0.006	0.006	0.31	0.002	0.52	Ost.

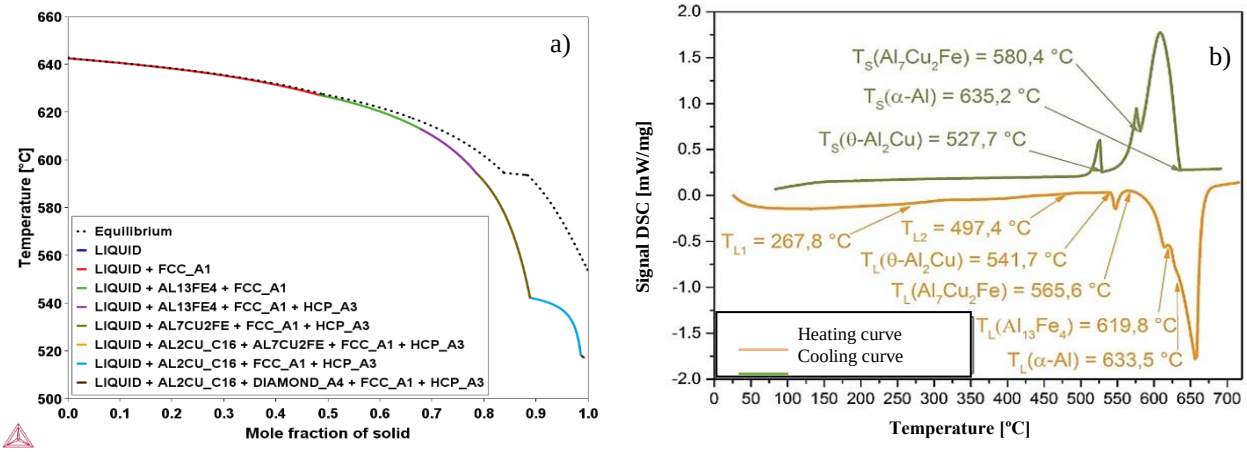

Figure 1. Scheil diagram of non-equilibrium solidification of EN AW-2011 alloy according to TC calculations (a) and DSC heating and cooling curve for EN AW-2011 alloy (b)

The hardness criterion 58 HB after homogenization at 520 °C was used to select the optimum homogenization method. All samples achieved a hardness of 60 HB, with a range between 60 HB and 90 HB (Fig.2a). The hardness increases with the homogenization time, reaches a maximum after four hours and starts to decrease with increasing time. Based on these results, homogenization at 520 °C for 4 hours, cooled in water, can be considered for the most optimal homogenization method. The decrease in hardness after a certain time is a consequence of the formation of the equilibrium phase θ [11, 12] whereby the hardness in the microstructure with a combination of the phases θ and θ' is the highest.

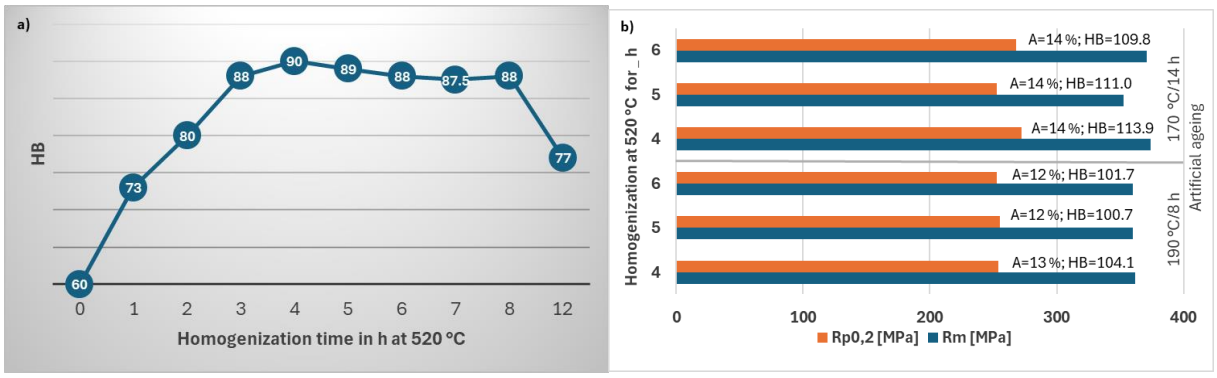

Figure 2. Graphical representation of measured hardnesses for samples homogenized at 520 °C at different times, cooled in water (a) and results of mechanical properties for homogenized billets at 520 °C for 4, 5 or 6 h, extruded and artificial aged at 190 °C for 8 h or 170 °C for 14 h (b).

The microstructure analysis (Fig.3) was intended to confirm the optimum homogenization regime that had already been predicted based on the measured hardness criteria. At a homogenization time of 4 h, the microstructure differs significantly from the as-cast microstructure, as the eutectic networks change from continuous to discontinuous during homogenization. Already after 4 h a more uniform distribution of eutectics between the grains was observed, but at the same time no larger, coarser Cu eutectics was detected. No major changes were observed for longer periods of time. In addition to the hardness of the material, the optimum homogenization regime at 520 °C for 4 h was also determined by analysing the microstructures.

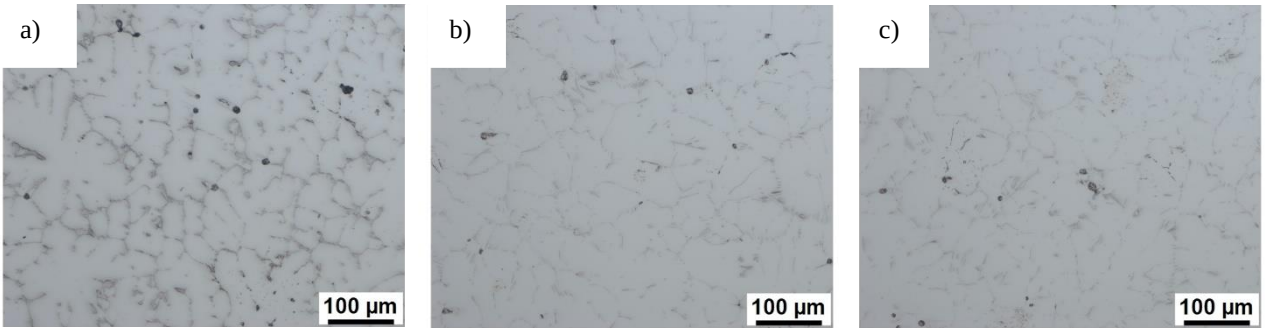

Figure 3. Microstructural images of as-cast state (a) and after homogenization at 520 °C for 4 h (b) and 8 h (c), cooled in water

The results of the EDS analysis of the average value of several measurements are shown in Fig.4. In the cast sample, the copper content in the matrix is significantly lower than in the homogenized samples. Only one type of intermetallic eutectic phase was observed in the as-cast sample. A similar type of eutectic phase was observed in all other homogenized samples. In the homogenized samples, an additional acicular phase occurs in addition to the honeycomb eutectic phase. During the homogenization process, Cu increases in α-Al up to the maximum solubility of Cu. The process of dissolution of AlCuFe into AlCu takes place. Particles based on Bi and Pb remain unchanged during the homogenization process.

The billets were homogenized (4–6 hours at 520 °C), extruded and aged at 170 °C and 190 °C for different times. Tensile tests were only carried out on the samples that showed the most favorable properties, i.e. after 4, 5 and 6 hours of homogenization at 520 °C and 14 hours of aging at 170 °C and 8 hours of aging at 190 °C (Fig. 2b). A 4-hour homogenization followed by ageing at 170 °C/14 h resulted in the highest tensile properties achieving suitable hardness of 113.9 HB. The R_m values analyzed were between 353 MPa and 374 MPa. Based on the measured $R_{p0.2}$ values of 268 MPa, the more favorable ageing behavior at a lower temperature (170 °C) and a longer time (14 h) can be determined.

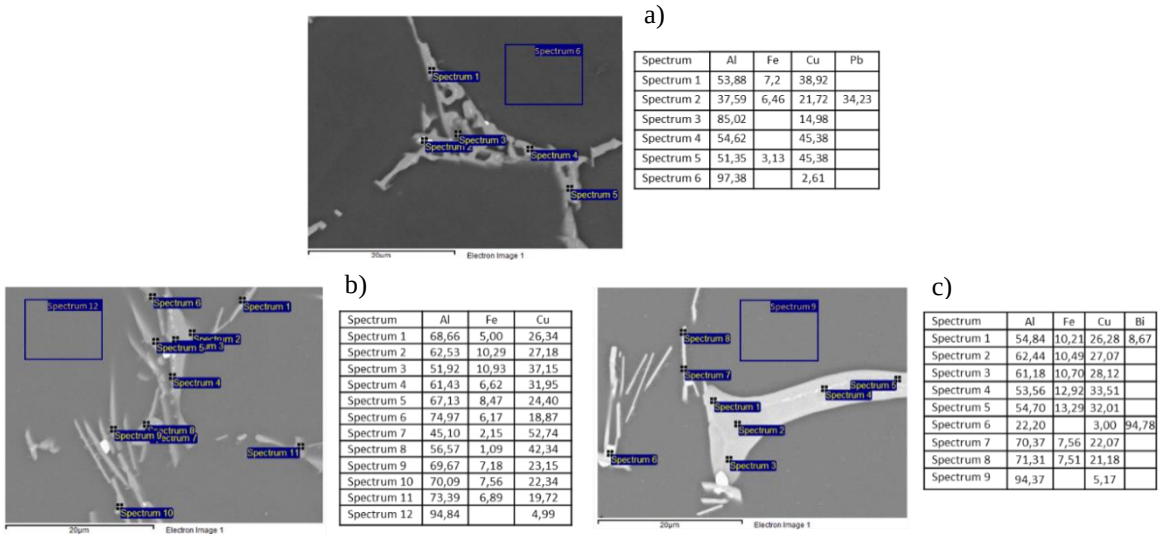

a)

Spectrum	Al	Fe	Cu	Pb
Spectrum 1	53,88	7,2	38,92	
Spectrum 2	37,59	6,46	21,72	34,23
Spectrum 3	85,02		14,98	
Spectrum 4	54,62		45,38	
Spectrum 5	51,35	3,13	45,38	
Spectrum 6	97,38		2,61	

b)

Spectrum	Al	Fe	Cu
Spectrum 1	68,66	5,00	26,34
Spectrum 2	62,53	10,29	27,18
Spectrum 3	51,92	10,93	37,15
Spectrum 4	61,43	6,62	31,95
Spectrum 5	67,13	8,47	24,40
Spectrum 6	74,97	6,17	18,87
Spectrum 7	45,10	2,15	52,74
Spectrum 8	56,57	1,09	42,34
Spectrum 9	69,67	7,18	23,15
Spectrum 10	70,09	7,56	22,34
Spectrum 11	73,39	6,89	19,72
Spectrum 12	94,84		4,99

c)

Spectrum	Al	Fe	Cu	Bi
Spectrum 1	54,84	10,21	26,28	8,67
Spectrum 2	62,44	10,49	27,07	
Spectrum 3	61,18	10,70	28,12	
Spectrum 4	53,56	12,92	33,51	
Spectrum 5	54,70	13,29	32,01	
Spectrum 6	22,20		3,00	94,78
Spectrum 7	70,37	7,56	22,07	
Spectrum 8	71,31	7,51	21,18	
Spectrum 9	94,37		5,17	

Figure 4. SEM SEI images with marked points and areas of EDS analysis of as-cast sample (a) and samples homogenized at 520 °C 4 h (b) and 8 h (c), cooled in water

4. CONCLUSIONS

Thermodynamic calculations and DSC analysis confirmed the appropriateness of the choice of homogenization temperature of 520 °C. According to the results of the measured hardness, LM and SEM-EDS microstructural properties, the homogenization process at 520 °C is completed after 4 hours for the investigated alloy. The existing homogenization regime, 6 hours at 520 °C, can be optimized to only 4 hours at the same temperature.

The optimization of the reduction of the homogenization time consequently led to a change in the aging heat treatment regime. The best results in terms of mechanical properties were obtained when aging at 170 °C for 14 hours.

ACKNOWLEDGEMENTS

We gratefully acknowledge the financial support of the Slovenian Research and Innovation Agency (ARIS) for funding under program grant P2-0344(B).

REFERENCES

[1] Y. Birol, Mater. Chem. Phys., 131 (2012) 694-697.
[2] C.K.S. Moy, M.Weiss, J. Xia, G. Sha, S.P. Ringer, G. Ranzi, Mater. Sci. Eng. A., 552 (2012) 48-60.
[3] J.R. Davis, Aluminum and Aluminum Alloys, Ohio: ASM International, 2001, p.65
[4] S-M. Liang, R. Schmid-Fetzer, CALPHAD: Comput. Coupling Phase Diagrams Thermochem., 51 (2015) 252-260.
[5] O. Zobac, A. Kroupa, A. Zemanova, K.W. Richter, Metall. Mater. Trans. A., 50A (2019) 3805-3815.
[6] M. Vončina, I. Paulin, A. Debevec, A. Nagode, Mater. Tech., 55 (2021) 327-333.
[7] J-H. Jang, D-G. Nam, Y-H. Park, I-M. Park, Trans. Nonferrous Met. Soc. China, 23 (2013) 631-635.
[8] C. Vargel, Corrosion of Aluminium: Second Edition. Oxford: Elsevier, 2019, p.858.
[9] S. SAMARAS, G.N. Hademenopoulos, Conference: 1st International Conference on Manufacturing Engineering, Halkidiki, Grece, 2002.
[10] D. Mirković, J. Gröbner, I. Kaban, W. Hoyer, R. Schmid-Fetzer, Int. J. Mater. Res., 100 (2009) 176-188.
[11] D.J. Chakrabarti, D.E. Laughlin, Prog. Mater. Sci., 49 (2004) 389-410.
[12] M. Vončina, A. Nagode, J. Medved, I. Paulin, B. Žužek, T. Balaško, Metals, 11 (2021) 1211.

The 56th International October Conference on Mining and Metallurgy
22-25 October 2025, Bor Lake, Bor, Serbia
www.ioc.tfbor.bg.ac.rs

DOI: 10.5937/IOC25351T *Original scientific paper*

AN ASSESSMENT OF CORROSIVE PERFORMANCE OF BIODEGRADABLE ZnMgTi ALLOYS

Alexandra-Tamara Șutic[1a], Gheorghe Bădărău[1b], Romeu Chelariu[1c], Ramona Cimpoeșu[1d], Ana-Maria Roman[1e], Mihai-Adrian Bernevig[1f], Nicanor Cimpoeșu[1g,*]

[1] Faculty of Materials Science and Engineering, "Gheorghe Asachi" Technical University of Iasi, 41 Dimitrie Mangeron Blvd., 700050 Iasi, Romania
[1a] alexandra-tamara.sutic@student.tuiasi.ro, 0009-0000-4525-1661
[1b] gheorghe.badarau@academic.tuiasi.ro, 0000-0003-4233-5231
[1c] romeu.chelariu@academic.tuiasi.ro, 0000-0002-5211-358X
[1d] ramona.cimpoesu@academic.tuiasi.ro, 0000-0002-5128-4491
[1e] ana-maria.roman@academic.tuiasi.ro, 0000-0001-8798-1849
[1f] mihai-adrian.bernevig@academic.tuiasi.ro, 0000-0003-2364-3589
[1g,*] nicanor.cimpoesu@academic.tuiasi.ro, 0000-0003-4373-017X

Abstract
This study explores the viability of a novel experimental alloy, composed of zinc, magnesium, and titanium, as a prospective biodegradable metallic material for medical applications. In order to determine the samples' corrosion rates, they were subjected to electro-chemical corrosion analysis by linear and cyclic potentiometric methods. The chemical analysis of the samples was performed through the use of EDX, scanning electron microscopy (SEM), with the samples being examined in Dulbecco's Phosphate-Buffered Saline (DPBS). The obtained results revealed the impact of alloying elements on the degradation behavior, accompanied by the formation of numerous corrosion compounds. Furthermore, the study yielded findings that elucidate the interplay between microstructure, chemistry, and degradation level during the alloy's interaction with physiological fluids.

***Keywords**: ZnMgTi alloys; biodegradable metallic material; corrosion; degradation.*

1. INTRODUCTION

Research on the biodegradation properties of zinc-based alloys used for temporary medical implants remains a popular topic in the scientific community.

The experimental research on ZnTi, ZnMg, and ZnMgTi alloys generally involves the use of electrochemical methods, such as potentiostat and galvanostat, to determine corrosion potential and corrosion current density [1,2]. Additionally, gravimetric methods are employed to assess mass loss and degradation rate in artificial liquid media with a composition comparable to that of human blood plasma [3,4].

The available international literature on ZnTi and ZnMgTi alloys indicates that the addition of Ti to Zn or ZnMg systems results in the formation of intermetallic phases. These phases have been observed to act as local barriers against corrosion propagation, thereby reducing the degradation rate and favoring the formation of passive layers on the material surface [5,6]. These layers can temporarily protect the material from corrosive attack, ensuring a more controlled and predictable degradation [7].

A study by Jin et al. [5] showed that adding small amounts of Mg (<0.1 wt.%) to Zn leads to the formation of the intermetallic Mg_2Zn_{11} phase. This phase acts as a microanode in the alloy structure, accelerating the galvanic corrosion mechanism and consequently increasing the degradation rate.

Zhang et al. [6] reported that adding Mg and Ti to pure Zn creates intermetallic Mg_2Zn_{11} and $TiZn_{16}$ compounds that modify the anodic and cathodic processes on the surface of the material. This influences the corrosion mechanism through the formation of galvanic microcells and increases the degradation rate.

2. EXPERIMENTAL

An experimental ZnMgTi alloy was developed in a laboratory electric furnace with an Argon controlled atmosphere. The initial chemical composition of the ZnMgTi alloy (Table 1) was as follows: Zn: 94.91 wt% (88.04 at%), Mg: 4.49 wt% (11.20 at%) and Ti: 0.60 wt% (0.76 at%), a typical composition for modified zinc alloys for biomedical applications, where the mechanical properties and corrosion resistance of zinc are desired to be improved by the addition of elements such as Mg and Ti.

Table 1. The initial chemical composition of the experimental ZnMgTi alloy.

Element	Zn		Mg		Ti	
	wt%	at%	wt%	at%	wt%	at%
comp	94.91	88.04	4.49	11.20	0.60	0.76
St. Dev. %	0.7		0.6		0.04	

The material's electrochemical corrosion resistance was evaluated in a 3-electrode cell configuration using a potentiostat [3]. The sample surface was examined post-electrochemical corrosion resistance test using scanning electron microscopy (SEM; VegaTescan LMH II, SE detector, 30 kV) and chemical EDS analysis (Bruker 6I/10 detector, automatic and mapping analysis modes).

3. RESULTS AND DISCUSSION

Following the implementation of linear polarization and cyclic voltammetry tests in Dulbecco's Phosphate-Buffered Saline (DPBS), the results presented in Figure 1 indicate a substantial decrease in zinc (71.05 wt%, from 94.91 wt%), a decrease in Mg (2.56 wt%, from 4.49 wt%), an increase in Ti (2.67 wt%, from 0.60 wt%), and the emergence of new elements. The percentage values for O (18.52 wt%), Cl (2.52 wt%), and P (2.68 wt%) represent the mean values obtained from the analysis of three distinct regions on the surface, as detailed in Table 2.

Table 2. The chemical composition of ZnMgTi alloy after linear polarization and cyclic voltammetry in Dulbecco's Phosphate-Buffered Saline (DPBS).

Element / Solution	Zn		Mg		Ti		O		Cl		P	
	wt%	at%	wt%	at%	wt%	at%	wt%	at%	wt%	at%	wt%	at%
DPBS	71.05	42.4	2.56	4.12	2.67	2.17	18.52	45.16	2.52	2.78	2.68	3.38
EDS error %	1.86		0.31		0.17		3.98		0.18		0.23	

This decline in Zn and Mg content signifies a substantial corrosion of the reactive components (Zn and Mg), which dissolve in the salt solution. Zn is the primary component and the most vulnerable to anodic corrosion, particularly in media containing chloride ions (Cl-), as found in DPBS. The observed increase in Ti content is presumably attributable to the development of a passivating layer on the surface. This assertion is supported by the established stability of Ti in corrosive environments, where it has been observed to form a protective TiO_2 layer. Furthermore, elements

that dissolve reduce the proportion of other more stable components. Therefore, the relative increase in Ti may also be a concentration effect. The presence of oxygen, phosphorus, and chlorine suggests the formation of oxides or hydroxides, such as ZnO, $Mg(OH)_2$, and TiO_2. P originates from phosphates in DPBS, indicating the potential for the formation of metal phosphates (e.g., Zn(PO)) and similar compounds. Cl is corrosive and promotes galvanic corrosion, leading to the formation of corrosion products in the form of metal chlorides.

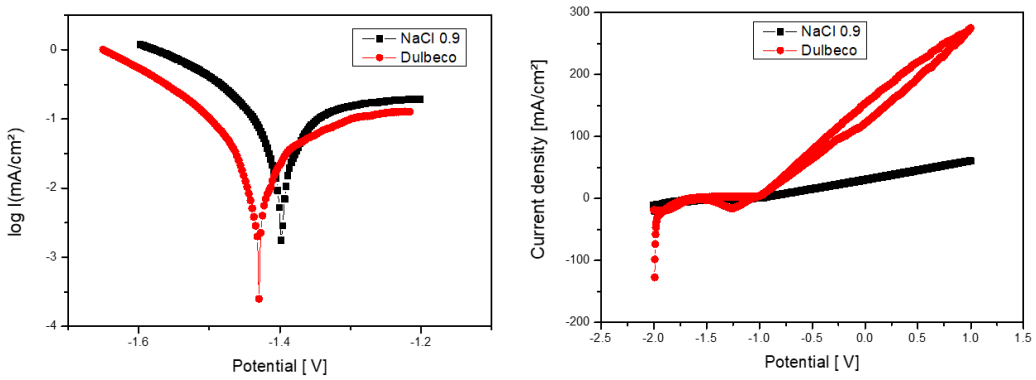

(a) *(b)*

Figure 1. Electro-corrosion results of the experimental alloys (in DPBS): (a) Tafel diagrams; (b) voltammograms with cyclic curves.

The ZnMgTi alloy exhibited substantial levels of corrosion in DPBS, as evidenced by notable losses of Zn and Mg. However, the presence of Ti contributes to the formation of a protective layer that can inhibit further corrosion evolution. The presence of oxide and phosphate compounds on the surface indicates a partial self-passivation mechanism, yet it is insufficient to fully impede the dissolution of reactive metals. The electrochemical corrosion process parameters for the ZnMgTi alloy in DPBS were as follows: corrosion potential (Ecorr): -1430 mV, corrosion current density (Icorr): 0.0647 mA/cm², polarization resistance (Rp): 1.47 kO-cm² and a corrosion rate (CR) of 1.492 mm/yr. A comparison of ZnMgTi with a ZnMg alloy [8] reveals that the former exhibits a more negative corrosion potential (-1430 mV), suggesting a more anodic character. However, the low Icorr and high Rp indicate a lower corrosion rate compared to ZnMg, suggesting enhanced stability in physiological environments. The corrosion rate (1.492 mm/year) was lower than those reported for ZnMg (2-4 mm/year), which indicates that the addition of Ti contributes to the formation of a passivating layer [9, 10]. From the SEM images presented in Figure 2, it can be observed that the surface shows an uneven morphology, with preferential attack zones, but also smooth regions. Superficially deposited corrosion products can be observed as dispersed aggregates or layers.

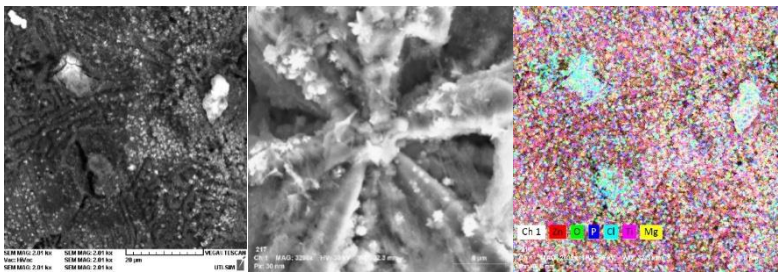

(a) *(b)* *(c)*

Figure 2. SEM images (a), (b) and EDS mapping after the electro-corrosion test in DPBS in (c).

As illustrated in Figure 2(c), the element distribution demonstrates that O is distributed extensively, thereby confirming the formation of oxides (ZnO, TiO_2). Ti is present in certain regions, potentially as either clusters or dispersed particles, suggesting a selective formation of the TiO_2 passive layer. The presence of chlorine, although not predominant, suggests the occurrence

of chloride ion adsorption without significant soluble chloride formation [11,12]. As phosphorus was detected, the potential for the formation of metal phosphates (e.g., $Zn_3(PO_4)_2$) is suggested, which may serve a protective function.

4. CONCLUSION

The ZnMgTi alloy exhibited susceptibility to corrosion in physiological environments (DPBS). However, the presence of Ti offered some degree of protection. The observed behavior is promising for biomedical applications, such as biodegradable implants, in a number of ways:

- The material's degradation is characterized by a controlled process, a property that is advantageous in specific applications.
- It has been demonstrated to be an effective method of regulating the corrosion rate.
- Corrosion products may have the potential to exhibit biocompatibility.

Incorporating Ti into the ZnMg alloy has been observed to enhance corrosion resistance by reducing Icorr and CR, and increasing Rp. This addition promotes the formation of a more stable surface, characterized by the presence of protective oxides, particularly TiO_2. This results in a more controlled distribution of corrosion products and a less aggressive morphology compared to ZnMg. These observations indicate that the ZnMgTi alloy is particularly well-suited for biomedical applications, where the controlled and uniform degradation of the material is a critical factor.

ACKNOWLEDGEMENTS

This work was supported by a National Research Grant of TUIASI, project number GNaC2023_285/2024.

REFERENCES

[1] X. Liu, J. Sun, Y. Yang, F. Zhou, Z. Pu, L. Li, Y. Zheng, Mater. Lett., 162 (2016) 242-5.
[2] Z. Yin, Microstructural evolution and mechanical properties of Zn-Ti alloys for biodegradable stent applications. M.S. Thesis, Michigan Technological University, 2017.
[3] A.T. Șutic, R. Chelariu, R. Cimpoeșu, A.M. Roman, B. Istrate, V. Goanță, M. Benchea, M. Moscu, A. Alexandru, N. Cimpoeşu, G. Zegan, Metals, 14 (7) (2024) 764.
[4] C. Panaghie, G. Zegan, A. Sodor, N. Cimpoeșu, N.M. Lohan, B. Istrate, A.M. Roman, N. Ioanid, Materials, 16 (2023) 3092.
[5] H. Jin, S. Zhao, R. Guillory, P.K. Bowen, Z. Yin, A. Griebel, J. Schaffer, E.J. Earley, J. Goldman, J.W. Drelich, Mater. Sci. Eng C., 84 (2018) 67-79.
[6] S. Zhang, P. Yuan, X. Wang, T. Wang, L. Zhao, C. Cui, Materials, 15 (3) (2022) 940.
[7] C. Ji, A. Ma, J. Jiang, D. Song, H. Liu, S. Guo, J. Alloys Compd., (2024) 174669.
[8] C. Panaghie, R. Cimpoeșu, G. Zegan, A.M. Roman, M.C. Ivanescu, A.A. Aelenei, M. Benchea, N. Cimpoeșu, N. Ioanid, Appl. Sci., 12 (2022) 2727.
[9] P.K. Bowen, J. Drelich, J. Goldman, Adv. Mater. Commun., 25 (18) (2013) 2577-2582.
[10] C. Ji, A. Ma, J. Jiang, D. Song, H. Liu, S. Guo, J. Alloys Compd., 993 (2024) 174669.
[11] A.T. Șutic, R. Chelariu, R. Cimpoeșu, M. Axinte, A.-M. Roman, G. Bădărău, N. Cimpoeșu, Biodegradable materials based on Zn-Mg-Ti in medicine: a promising solution for sustainable medical applications, Bulletin of the Polytechnic Institute of Iași, published by "Gheorghe Asachi" Technical University of Iaşi, Section Materials Science and Engineering, 70 (74) (2024) p. 31.
[12] C. Panaghie, R. Cimpoeșu, B. Istrate, N. Cimpoeșu, M.A. Bernevig, G. Zegan, A.M. Roman, R. Chelariu, A. Sodor, Materials, 14(10) (2021) 2505.

The 56th International October Conference on Mining and Metallurgy
22-25 October 2025, Bor Lake, Bor, Serbia
www.ioc.tfbor.bg.ac.rs

DOI: 10.5937/IOC25355M *Original scientific paper*

IN-SITU SYNTHESIS OF Mg_2Si-REINFORCED AMC

Jožef Medved[1a], Tilen Balaško[1b], Stanislav Kores[2a], Maja Vončina[1c,*]

[1] Department of Materials and Metallurgy, Faculty of Natural Sciences and Engineering, University of [1]Ljubljana, Aškerčeva 12, 1000 Ljubljana, Slovenia
[2] TALUM d.d., Tovarniška cesta10, 2325 Kidričevo, Slovenia
[1a] jozef.medved@ntf.uni-lj.si, 0009-0007-6931-5595
[1b] tilen.balasko@ntf.uni-lj.si, 0000-0002-4735-9390
[2a] stanislav.kores@talum.si, 0009-0009-3836-8744
[1c,*] maja.voncina@ntf.uni-lj.si, 0000-0002-2563-1103

Abstract

Aluminium Matrix Composites (AMC) are advanced materials composed of an aluminium alloy reinforced with ceramic or metallic particles, fibres, or whiskers to enhance properties such as strength, stiffness, wear resistance, and thermal stability. These composites offer a high strength-to-weight ratio, improved mechanical performance, and corrosion resistance, making them ideal for aerospace, automotive, and defence applications.

The purpose of the research was to synthesise, homogenise and characterise Al-Mg_2Si composite samples. We plotted the equilibrium phase diagram and Scheil curves using the Thermo-Calc software. Based on the results of the thermodynamic simulations of equilibrium and non-equilibrium solidification, we prepared the appropriate raw materials and melted them in a BN-coated steel crucible in an induction furnace. The most appropriate ratio was calculated to be Mg/Si = 1.74. Due to the high casting temperature, shrinkage and gas porosity occur in the samples. The cooling rate during solidification should be as high as possible to achieve the appropriate microstructure. We also performed simple thermal analysis (ETA) and plotted cooling curves in the Origin software and differential scanning calorimetry (DSC). Microstructural characterisation was also carried out to define the type, proportion and morphology of phases in the as-cast and homogenised state.

According the thermodynamic calculation under all conditions the primary phase Mg_2Si solidifies first, then the $Al_{13}Fe_4$ phase and finally the eutectic (α_{Al} + Mg_2Si). It is also possible that the eutectic (α_{Al} + Mg_2Si + β_{Si}) solidifies last. The results of the DSC and metallographic analysis show the primary Mg_2Si phase, the eutectics (α_{Al} + $Al_{13}Fe_4$), (α_{Al} + Mg_2Si) and (α_{Al} + Mg_2Si + β_{Si}) in the as-cast samples. The solidification of the investigated composite takes place in the range between 750 ºC and 540 ºC. Upon the homogenisation process, the rounding of the edges of the primary solidified Mg_2Si particles, and the rounding and growth of the eutectic Mg_2Si phase was observed in the microstructure.

***Keywords**: Aluminium matrix composite (AMC), primary Mg_2Si, Thermodynamics, DSC*

1. INTRODUCTION

Composites are mixtures of two or more solid materials that are, in principle, mechanically separable and exhibit complementary properties [1]. They consist of a matrix and a reinforcement phase [2]. In recent years, aluminium matrix composites (AMCs) have gained increasing attention in advanced structural and functional applications. Due to their low density and high performance, aluminium and its alloys are widely employed in the automotive and aerospace industries [3, 4]**.** AMCs offer exceptional properties such as high specific strength, excellent wear and corrosion resistance, low density, and high specific stiffness. Aluminium composites can be reinforced with particles, whiskers or short fibres, continuous fibres, and monofilaments. Among the particle-reinforced AMCs, composites strengthened by the intermetallic Mg_2Si phase (Al-Mg_2Si) have recently emerged as particularly attractive to researchers and engineers. These composites can be produced using relatively simple casting techniques, whereby the Mg_2Si phase is formed "*in situ*" [5] through a chemical reaction between silicon and magnesium. Al-Mg_2Si composites represent

a new class of ultralightweight materials with significant potential for aerospace, automotive, and other high-performance applications [6]. The Mg_2Si compound is characterized by low density, a high melting point, a high elastic modulus, and excellent hardness [7].

Nevertheless, during solidification, Mg_2Si particles tend to crystallize as coarse, irregularly shaped particles that are often inhomogeneously distributed within the matrix. This can adversely affect the mechanical properties, particularly tensile strength. These issues can be mitigated through homogenisation treatment, which reduces the effects of microsegregation [8]. During homogenisation, the particles of both, the primary and eutectic Mg_2Si phases, become more spheroidal [6].
The objective of research was to synthesize, homogenise, and characterise Al-Mg_2Si composite samples subjected to various annealing durations, employing light and electron microscopy as well as differential scanning calorimetry (DSC).

2. EXPERIMENTAL

To produce the Al-Mg_2Si composite, designed to contain 18–20 wt.% Mg and 10–11 wt.% Si with a Mg/Si mass ratio of 1.74, 1629 g of AlSi10Mg alloy and 139 g of high-purity magnesium (99.9%) were weighed. Due to the high reactivity and rapid oxidation of magnesium, an additional 10 wt.% excess was added. The composite was melted in an induction furnace using a steel crucible coated with BN. The melt was intermittently stirred with a steel rod, ensuring the temperature did not exceed 770 °C. After melting, the alloy was cast into two moulds: a steel bar-shaped mould preheated to 450 °C, and a Croning measurement cell for simple thermal analysis (ETA). Homogenisation of the samples was carried out in an electric resistance furnace—initially at 430 °C for 4 hours, followed by further annealing at 520 °C for durations of 12, 24, 48, and 96 hours. The equilibrium phase diagram and Scheil solidification curves were calculated using the Thermo-Calc software. After the thermal analysis (ETA) was performed, and cooling curves were plotted using Origin software. Additionally, differential scanning calorimetry (DSC) was conducted. Microstructural characterization was carried out to identify the type, volume fraction, and morphology of phases in both, the as-cast and homogenised samples.

3. RESULTS AND DISCUSION

Based on thermodynamic calculations using the Thermo-Calc software, equilibrium solidification proceeds in the following sequence: primary Mg_2Si and $Al_{13}Fe_4$ phase, primary α_{Al} dendrites, eutectic (α_{Al} + Mg_2Si + $Al_{13}Fe_4$), and finally eutectic (α_{Al} + Mg_2Si + $Al_{13}Fe_4$ + β_{Si}). Non-equilibrium solidification, as predicted by the Scheil model, occurs in the following order: solidification of the primary Mg_2Si phase, followed by primary $Al_{13}Fe_4$ phase, and then the eutectic (α_{Al} + Mg_2Si) (Fig. 1). In cases where only magnesium is a fast-diffusing element—or when neither magnesium nor silicon are fast diffusing—the eutectic (α_{Al} + Mg_2Si + β_{Si}) also forms at lower temperatures. Experimental thermal analysis (ETA) revealed that solidification of the primary Mg_2Si phase begins at 705.9 °C. The eutectic (α_{Al} + Mg_2Si) solidifies at 580.0 °C, followed by the eutectic (α_{Al} + β-Al_3Mg_2) at 447.8 °C. Final solidification is completed at 433.9 °C. From the heating DSC curve of the as-cast sample, the melting temperatures of the following phases were determined: at 450.6 °C the eutectic (α_{Al} + β-Al_3Mg_2); at 525.5 °C the eutectic (α_{Al} + Mg_2Si + β_{Si}); at 589.5 °C the eutectic (α_{Al} + Mg_2Si); and at 598.7 °C the eutectic (α_{Al} + $Al_{13}Fe_4$). The primary Mg_2Si phase melts over a temperature range from 620.2 °C to 783.4 °C. From the cooling DSC curve of the same sample, the solidification sequence was determined as follows: solidification of the primary Mg_2Si phase begins at 751.5 °C, followed by the eutectic (α_{Al} + $Al_{13}Fe_4$) at 589.6 °C, and the eutectic (α_{Al} + Mg_2Si) at 582.9 °C. Significant differences were observed in the melting and solidification enthalpies of the primary Mg_2Si phase, particularly between samples K-0 and K-96 (Fig. 2), indicating that the sample homogenised for 96 hours contains the lowest amount of primary Mg_2Si. It was further observed that the eutectic (α_{Al} + β-

Al_3Mg_2) is present only in the as-cast sample and disappears after homogenisation. Light and scanning electron microscopy revealed that the polygonal morphology of the primary Mg_2Si phase begins to round after 24 hours of homogenisation and becomes significantly more rounded after 96 hours (Fig. 3). With increasing homogenisation time, the eutectic (α_{Al} + Mg_2Si) also becomes finer and more spheroidized (Fig. 3).

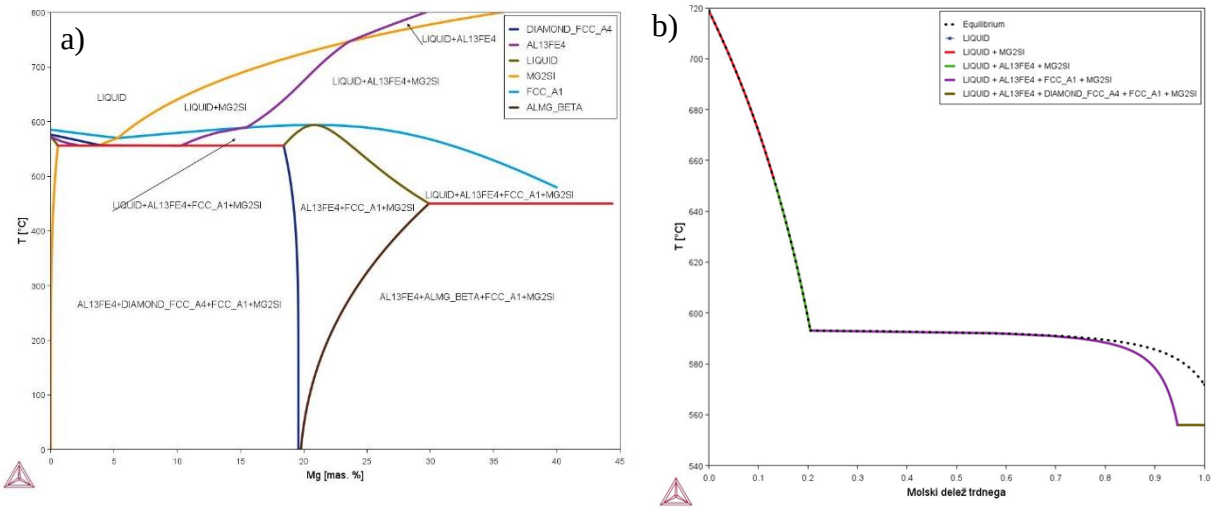

Figure 1. Thermodynamic calculation of Al-Mg-Si-Fe system, a) equilibrium isopleth phase diagram and b) Scheil model of solidification

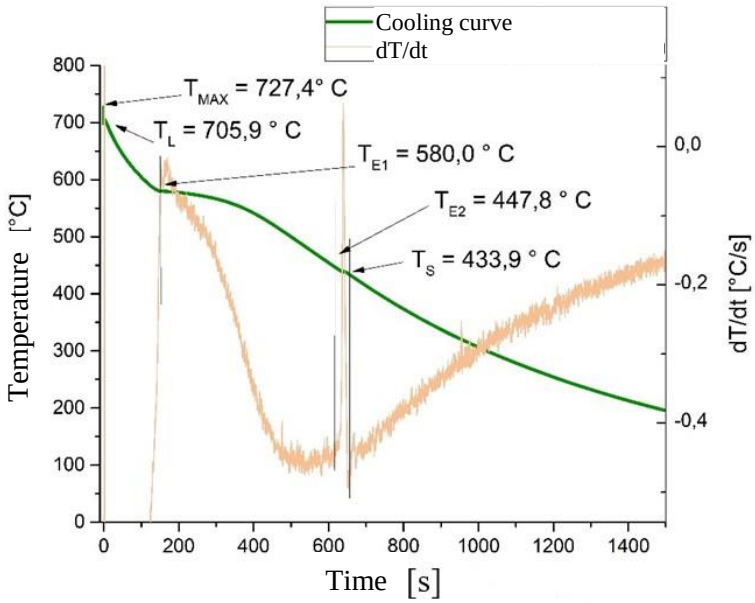

Figure 2. Cooling curve of synthetised Al-Mg_2Si composite

Point and area EDS analyses (Fig. 4) confirmed the presence of the following phases in the microstructure of both, the as-cast and homogenised samples: the primary Mg_2Si phase, the eutectic $Al_{13}Fe_4$ phase, mixed α_{Al} crystals enriched with magnesium, and the eutectic (α_{Al} + Mg_2Si).

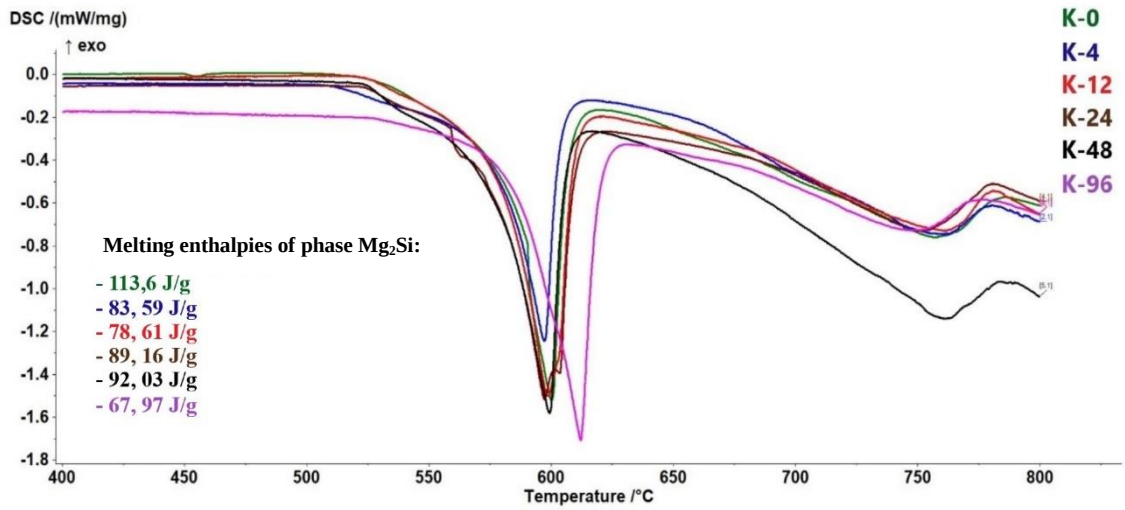

Figure 3. Comparison of heating DSC curves of samples K-0, K-4 and K-96

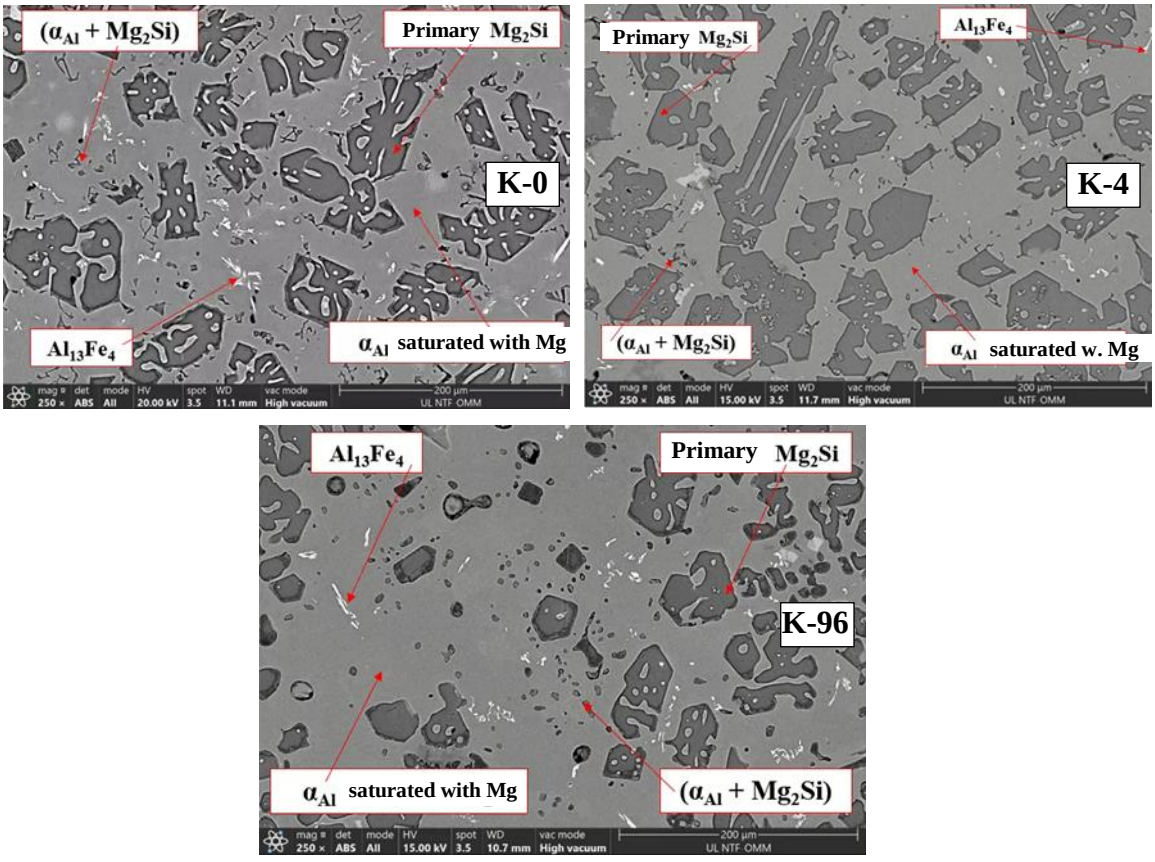

Figure 4. Microstructures of samples K-0, K-4 and K-96

4. CONCLUSIONS

The investigation of the synthesized and homogenised in-situ aluminium matrix composite (AMC) revealed that, based on the DSC heating curve, solidification occurs in the following sequence: at 751.5 °C solidification of the primary Mg_2Si phase begins; at 589.6 °C solidification of $Al_{13}Fe_4$ phase follows; and at 582.9 °C the eutectic (α_{Al} + Mg_2Si) solidifies. In the case of sample K-96, the eutectic (α_{Al} + Mg_2Si + β_{Si}) solidifies last, at 540.0 °C. The microstructure of both, the as-cast and homogenised samples, contain the following constituents: the primary Mg_2Si phase and the

eutectics (α_{Al} + $Al_{13}Fe_4$), (α_{Al} + Mg_2Si), and (α_{Al} + Mg_2Si + β_{Si}). The eutectic (α_{Al} + β-Al_3Mg_2) is present only in the as-cast sample and disappears after homogenisation. Morphological changes were observed in the primary Mg_2Si phase: polygonal particles began to round after 24 hours of homogenisation and became significantly more rounded after 96 hours. With increasing homogenisation time, the (α_{Al} + Mg_2Si) eutectic also became finer and more spheroidized. Based on the measured melting enthalpies, it was concluded that the initial as-cast sample (K-0) contains the highest amount of primary Mg_2Si phase, while the sample homogenised for 96 hours (K-96) contains the lowest.

ACKNOWLEDGEMENTS

We gratefully acknowledge the financial support of the Slovenian Research and Innovation Agency (ARIS) for funding under program grant P2-0344(B).

REFERENCES

[1] A.B. Strong, Fundam. Compos. Manuf.: Mater. Methods Appl., 2nd ed., Society of Manufacturing Engineers, Dearborn, Michigan, 2008.
[2] C. Zweben, Composite Materials, Vol. I: Mater. Eng. Mech., Devon, Pennsylvania, 2015, Ch. 10.
[3] P. Samal, P.R. Vundavilli, A. Meher, M.M. Mahapatra, J. Manuf. Process., 59 (2020) 131–152.
[4] M.K. Surappa, Sādhanā, 28 (2003) 319–334..
[5] L. Singh, S. Kumar, S. Raj, S. Badhani, P. Badhani, IOP Conf. Ser.: Mater. Sci. Eng., 1149 (2021) 012017.
[6] E. Georgatis, A. Lekatou, A.E. Karantzalis, H. Petropoulos, S. Katsamakis, A. Poulia, J. Mater. Eng. Perform., 22 (2013) 729–741.
[7] E. Safary, R. Taghiabadi, M.H. Ghoncheh, Int. J. Miner. Metall. Mater., 29 (2022) 1249–1260.
[8] P. Biswas, M. Paliwal, M.K. Mondal, Mater. Today Commun., 35 (2023) 105557.

The 56th International October Conference on Mining and Metallurgy
22-25 October 2025, Bor Lake, Bor, Serbia
www.ioc.tfbor.bg.ac.rs

DOI: 10.5937/IOC25360R *Original scientific paper*

STATISTICAL EVOLUTION OF NON-METALLIC INCLUSIONS IN CONTINUOUS CAST Al-KILLED STEEL

Karlo Raić[1], Mile Djurdjević[2], Srećko Manasijević[3], Aleksandra Patarić[4a], Marija Mihailović[4b]

[1] Faculty of Technology and Metallurgy, University of Belgrade, Karnegijeva 4, 11000 Belgrade, Serbia
[2] University of Applied Sciences, Roseggerstraße 15, 4600 Wels, Austria
[3] Lola Institute Ltd, Kneza Viseslava 70a, Belgrade, Serbia
[4] University of Belgrade - Institute of Chemistry, Technology and Metallurgy - National Institute of the Republic of Serbia, Njegoseva 12, 11000 Belgrade, Serbia
[1] karlo@tmf.bg.ac.rs, 0000-0002-1713-0130
[2] miledjurdjevic@yahoo.ca, 0009-0007-4561-3547
[3] srecko.manasijevic@li.rs, 0000-0002-4277-9783
[4a] aleksandra.pataric@ihtm.bg.ac.rs, 0000-0002-2734-0262
[4b] marija.mihailovic@ihtm.bg.ac.rs, 0000-0003-2451-4818

Abstract
The objective of this study is to develop statistical relationships that will enable the quantification of non-metallic inclusion content in continuously cast low-carbon, aluminum-killed deep-drawing steel in situations where standard techniques make metallographic control challenging or impossible. Further considerations can be focused on predicting the model of the size distribution curve after the quantitative characterization of non-metallic inclusions in steel is completed. So, the potential of reconstructing the entire content of non-metallic inclusions in steel will be estimated, and the influence of limiting factors can be assessed.

Key words: *non-metallic inclusions; Al-killed steel; log-normal distribution*

1. INTRODUCTION

Nonmetallic inclusions are a byproduct of deoxidization from the steelmaking process. Three spontaneous processes determine their final quantity and shape in the steel structure: (i) stable nuclei form from oxygen in steel and added deoxidizer, (ii) inclusions grow through various mechanisms, with collisions being the most effective, and (iii) non-metallic inclusions float and transition to slag or adhere to the refractory lining. The initial oxygen level in steel before deoxidation, as well as the available time between the start of deoxidation and steel solidification, are process parameters that influence the final number and size of inclusions following steel hardening [1].

Chemical analysis of oxygen, which, when combined with deoxidizers, forms non-metallic oxide inclusions, is used to calculate the bulk inclusion content in steel and to assess the cleanliness of the steel. Because oxygen solubility in the metal matrix is extremely low, the bulk oxygen concentration in steel can be estimated using the oxide inclusions content. The disparity between the oxygen content acquired by chemical analysis and the calculated one demonstrates that regular steel inspection does not allow for the determination of all parameters. The shape of the inclusions distribution curve is influenced by several factors, including the concentration of oxygen in the melt at the time of outflow (ΣO), the amount of residual oxygen after inclusions float (O), and the time (τ) available for inclusions to grow through collisions before the steel solidifies [2,3].

2. ELEMENTS OF ALGORITHM

The normal distribution law (Gaussian distribution) governs the distribution of several variables that can be used to verify statistical tests. It is recommended that the measurement findings be categorized into sets based on size, with each set encompassing 30–100 neighboring view fields, because the mean value distribution of non-metallic inclusions volume fractions (X) does not follow the normal law of distribution [x]. Calculating the four mean values of momentum (U_1, U_2, U_3, U_4) based on the mean values of each set (X_1, X_2,…, X_n) is the typical procedure to assess the normality of the data distribution. Zero momentum (A_1, A_2, A_3, A_4) must be established to compute them [4,5]. The calculation flow is given in Table 1.

Table 1. Procedure of the algorithm [6]

$A_1 = \sum(X_1 + X_2 + X_3 + \cdots + X_n)$	(1)	$U_2 = V_2 - V_1^2$	(6)
$A_2 = \sum(X_1^2 + X_2^2 + X_3^2 + \cdots + X_n^2)$	(2)	$U_3 = V_3 - 3V_1V_2 + 2V_1^3$	(7)
$A_3 = \sum(X_1^3 + X_2^3 + X_3^3 + \cdots + X_n^3)$	(3)	$U_4 = V_4 - 4V_1V_3 + 6V_1^2V_2 - 3V_1^4$	(8)
$A_4 = \sum(X_1^4 + X_2^4 + X_3^4 + \cdots + X_n^4)$	(4)	$\beta_1 = \frac{U_3 \cdot \lvert U_3 \rvert}{(U_2)^3}$	(9a)
$V_i = A_i / n$	(5)	$\beta_2 = \frac{U_4}{(U_2)^2}$	(9b)
$[\%\, O] = NI(\%)\ \frac{\rho_{NI} \cdot 3M(O)}{\rho_{steel} \cdot (2M(Al) + 3M(O))}\, [ppm]$	(10)	$NI = (A_{theor} / A_{exp}) * 100\ (\%)$	(11)

The arithmetic mean value of each measurement set is determined by Eq. 5, where n is the number of measured values. These mean values of the measuring sets are used to determine the moments of the mean values (U) of the third and fourth orders, as shown in Eqs. 6 to 8. The coefficient of asymmetry β_1 and the coefficient of excess β_2 are calculated according to the Eqs. 9a and 9b.

Based on Eqs. 1 to 9, the algorithm for predicting possible distribution in the case of very clean steels can be evaluated. In the case of Al killed steel, non-metallic inclusions are of the Al_2O_3 type. The further calculation is as follows in Eq. 10. Non-metallic inclusions surface share, NI (%), can be expressed in Eq. 11, where: A_{exp} is the examined surface area, and A_{theor} is the total surface with inclusions on the examined surface. $A_{exp} = (a \cdot b) \cdot N_{fields} = (205 \times 140) \times 100 = 2{,}870{,}000$ m²; a and b are the dimensions of a view field, and N_{fields} is the number of examined fields. For the sake of comparison between different arrays, the number of fields is normalized to 100 [6].

The total surface occupied by inclusions on the examined surface may be calculated according to: $A_{theor} = (d^2 \cdot \pi/4) \cdot N$, where: N is the number of inclusions for each size class, and d is the mean diameter of the inclusions of a given size class. So, the mean diameter of the inclusions can be expressed as Eq. 12.

$$d = \sqrt{\frac{4 \cdot [\%O] \cdot A_{exp}}{\pi n \cdot const \cdot 100}} \qquad \text{(Eq. 12)}$$

For the aluminate type of non-metallic inclusions, the constant can be calculated based on atomic mass and density, as follows: const = 0.233795 [6–8].

3. EXPERIMENTAL

The chemical composition of the steel is given in Table 2, and the industrial casting conditions are shown as follows: slab thickness 1040x200 mm, cast speed was 0.55 m/min, number of oscillations 50–70 o/min, working rollers pressure 1.12 MPa, and cast temperature 1570 °C. The amount of Al after deoxidation, in addition to the steel composition, is shown in Table 2.

Table 2. Chemical composition of the steel in mass percent (%)

C	Si	Mn	P	S	Al	Cu	[O]
0.07–0.06	0.03–0.02	0.37–0.35	0.02–0.018	0.026–0.025	0.06–0.043	0.07	0.0054

A sample is taken from a slab with a cross-section of 200 x 1400 mm, encompassing its half-thickness. The non-metallic inclusions are examined on the surface oriented perpendicularly to the casting direction, sized 3x3 mm, with a center distance of 63.5 mm from the slab surface.
For final polishing, both 1 μm and 1/4 μm diamond polish pastes are used. The same sample surface was examined for each polish variation at x400 and x1024 magnification. At a magnification of x400, the entire sample surface of 9 mm² was examined, paying attention not to overlap adjacent view fields. The sum of 320 view fields was observed. At the magnification of x1024, the equidistantly distributed view fields over the sample surface were examined, and the sum of 100 view fields amounted to 0.4736 mm^2 [6–8].

4. RESULTS AND DISCUSSION

According to Table 3, it is obvious that for the same oxygen content, the coefficient of excess (β_2) increases with the increase of the time that the inclusions had at their disposal. The asymmetry coefficient (β_1) within lot 4, with O = 67 ppm, decreases with increasing time, whereas for lot 11, with *O* = 54 ppm, it remains constant. **Note:** Samples from position A are in the surface zone of the ingot, where the time for growth is shortest, while samples at position D had an additional 15–20 minutes for growth [6-8].

Table 3. Summary of the coefficients that define the distribution curve's shape [7,8]

Field position /lot	Coefficient of asymmetry (β_1)		Coefficient of excess (β_2)	
	Experimental	Theoretical	Experimental	Theoretical
A-4	2.87	0.07	8.32	2.60
B-4	0.19	0.008	2.70	2.75
C-4	0.001	0.05	3.29	3.02
D-4	0.73	0.02	4.39	3.50
A-11	0.01	0.007	2.25	2.35
B-11	0.4	0.007	2.45	2.50
C-11	0.04	0.007	6.87	2.50

The asymmetry coefficient of 0.0619. The average curve computed for Lot 11 has an excess coefficient of 2.45 and an asymmetry coefficient of 0.0417.
The typical characteristics of the oxide non-metallic inclusion distribution in the aluminum-killed, continuously cast steel should be included in the average distribution. The distribution of [O] ppm by size classes can be derived from the previously reported percentage distribution of oxygen by classes, assuming that the steel with 6 ppm [O] is examined. Eq. 12 can be used to determine the diameter of the greatest inclusion in class I, assuming that there is only one (which is typically the case). It becomes feasible to compute diameters in every other class based on the step between the size classes.
The method indicates that the newly obtained distribution for Lot 4 is also log-normal, with an asymmetry coefficient of 0.0535 and an excess coefficient of 2.36. The newly obtained distribution in Lot 11 has an asymmetry coefficient of 0.0493 and an excess coefficient of 2.16. Table 4 provides a summary of all these coefficients.
Based on the newly acquired inclusions diameter data, the amount of oxygen they would represent, expressed in parts per million (ppm), is calculated to be 5.74 ppm, fully satisfying the original assumption regarding steel with 6 ppm of oxygen.

Table 4. Asymmetry and excess coefficient: average and using algorithm calculated [7,8]

Non-metallic inclusions distribution	Coefficient of asymmetry (β_1)	Coefficient of excess (β_2)
Average distribution Lot 4	0.0619	2.65
Average distribution Lot 11	0.00417	2.45
Distribution L4 per algorithm, N_I=1	0.0535	2.36
Distribution L11 per algorithm, N_I=1	0.0493	2.16
Distribution L4 per algorithm, N_I=2	0.0527	2.31
Distribution L11 per algorithm, N_I=2	0.0493	2.16

5. CONCLUSIONS

This approach is suitable for continuously cast steel that has been deoxidized with aluminum, for which the oxygen concentration at pouring time and the hydrodynamic regime of ladle processing are not well understood [9-11]. Therefore, based on the established relations, a potential model algorithm based on mapping the distribution for higher oxygen contents determined by metallographic counting techniques and graphical reconstruction can be provided to describe the formation of the distribution of deoxidation products by size when metallographic control is difficult or not feasible by usual performance.

ACKNOWLEDGEMENTS

The authors are grateful for financial support within the framework of institutional funding by the Ministry of Science, Technological Development and Innovation of the Republic of Serbia (contract numbers: 451-03-136/2025-03/200066 and 451-03-136/2025-03/200026).

REFERENCES

[1] A. Costa e Silva, J. Mater. Res. Technol., 7 (3) (2018)283–99.
[2] P. Kaushik, J. Lehmann, M. Nadif., Metall. Mater. Trans. B, 43 (4) (2012) 710–25.
[3] D. You, SK Michelic, P. Presoly, J. Liu, C. Bernhard, Metals, 7 (11) (2017) 460.
[4] R. Kiessling, Non-metallic Inclusions in Steel, Part V, The Institute of Metals, London (1989)142-165.
[5] G.F. Vander Voort, Inclusion Measurement, Metallography as a Quality Control Tool, ed. J.L. McCall &P.M. French, Plenum Press, N.Y. (1980).
[6] M.D. Mihailović, MS Thesis, Faculty of Technology and Metallurgy, Belgrade (2000), pp. 106.
[7] M. Mihailović, K. Raić, Metall. and Mater. Eng., 27 (4) (2021) 437–447.
[8] M. Mihailović, Particle Size Distribution in Metals, Chapter 2, in Advances in Chemistry Research Vol. 78, Edited by James C. Taylor, Nova Science Publishers, (2023). 27–49.
[9] L. Zhang, Q. Ren, H. Duan, Y. Ren, W. Chen, G. Cheng: Miner. Process. Extr. Metall., 129 (2020) 184–206.
[10] Y. Wu, H. Zhang, L. Jian, Z. Lv, Adv. Eng. Inform., 62 (A) (2024) 102629.
[11] S. Gao, Y. Jiang, T. Xia, Y. Li, Y. Zhu, L. Xi, Adv. Eng. Inform., 64 (2025) 103080.

The 56th International October Conference on Mining and Metallurgy
22-25 October 2025, Bor Lake, Bor, Serbia
www.ioc.tfbor.bg.ac.rs

DOI: 10.5937/IOC25364B *Original scientific paper*

MICROSTRUCTURAL ANALYSIS AND THERMAL PROPERTIES OF Ag-Sn ALLOYS

Kristina Božinović[1a], Dragan Manasijević[1b], Ljubiša Balanović[1c], Milan Gorgievski[1d], Uroš Stamenković[1e], Miljan Marković[1f]

[1] Technical Faculty Bor, University of Belgrade, V.J. 12, 19210 Bor, Serbia
[1a] kbozinovic@tfbor.bg.ac.rs, 0000-0002-9834-448X
[1b] dmanasijevic@tfbor.bg.ac.rs, 0000-0002-7828-8994
[1c] ljbalanovic@tfbor.bg.ac.rs, 0000-0002-3551-6731
[1d] mgorgievski@tfbor.bg.ac.rs, 0000-0002-9899-719X
[1e] ustamenkovic@tfbor.bg.ac.rs, 0000-0002-7579-2159
[1f] mmarkovic@tfbor.bg.ac.rs, 0000-0002-4734-1481

Abstract
The Ag–Sn system represents one of the most significant binary alloy systems in the development of lead-free solder materials and high-performance electronic interconnections. In this study, thermal properties, microstructural evolution, and thermodynamic behavior of the Ag–Sn system were investigated. Alloys were synthesized from high-purity Ag and Sn and characterized using differential scanning calorimetry (DSC), flash method for the analysis of thermal properties (DXF) and scanning electron microscopy with energy dispersive spectroscopy (SEM-EDS), enabling precise determination of phase transitions and microstructural features across the composition range. The obtained results were compared with available thermodynamic assessments and phase diagram data, highlighting both agreements and discrepancies in reported invariant reactions. The findings contribute to a deeper understanding of the solidification paths and stability of phases in Ag–Sn alloys, which is of particular importance for optimizing solder joint reliability in microelectronic applications.

Keywords*: Ag–Sn alloys, microstructure, thermal conductivity, electrical conductivity, microhardness*

1. INTRODUCTION

For more than two decades, since the RoHS directive was introduced [1], the scientific community has been in pursue of the suitable replacement for Sn-Pb soldering alloy [2]. The last couple of years the research was aimed on the third-generation Pb-free solders, focusing on alloys with high Ag content among the other ones [2-4]. The third-generation Pb-free solders emerged when a need for high reliability solders arose with the development of vehicle electronics. Dynamic, "under the hood" conditions limited the usage of the globally used near-eutectic SAC alloys, because of their poor resistance to mechanical shock [2, 4-6].

The Ag–Sn system represents one of the most significant binary alloy systems in the development of lead-free solder materials and high-performance electronic interconnections [1, 2]. As a part of a ternary Sn-Ag-Cu system (SAC), this system has been of interest and therefore investigated numerous times [1-6]. The researches were mainly focusing on the eutectic Sn-3.5 mass%Ag alloy and there are only few investigations considering the influence of Ag content on the properties of alloys [3, 7]. Even so, the content of silver was always relatively low with most of the interest on low-Ag alloys, taking the economic variable into account. The low-Ag composition, which corresponds to near-eutectic SAC alloys, has already been investigated, and it is well established that these alloys exhibit poor thermal fatigue resistance, therefore not suitable for "under the hood" conditions of severe thermal cycling [8, 10]. Therefore, the focus of this paper will be the influence of Ag content on alloy properties but from a different point of the Ag-Sn phase diagram (Ag based).

Special attention was given to thermo-physical properties of the regarded system, most importantly thermal conductivity, thermal diffusivity and specific heat capacity as contribution to a more complete knowledge of the thermal transfer behavior of these alloys.

2. EXPERIMENTAL

The metals used for the preparation of selected samples (Table 1) were silver and tin of > 99.9% purity (Alfa Aesar). Investigated alloys were prepared by melting weighted masses of pure metals in a chamber furnace under inert argon atmosphere at maximum temperature of 1100 °C. The total masses of the prepared samples were about 2 g. After melting and stirring, the molten alloys were allowed to solidify into graphite crucibles. Prepared alloy ingots were re-melted at least 3 times to assure homogeneous compositions. The obtained samples were cut into two parts. Smaller part of the sample was used for DSC analysis, and the remaining part was pressed on a hydraulic press to obtain samples of the same dimensions, a tablet shape of 12.7 mm in diameter. The sample with the highest Ag content was pressed with the force of 10 kN. After pressing, annealing was done in order to perform recovery and recrystallization, remove internal stresses and micro segregations. The annealing was carried out at 500 °C, in a closed chamber furnace, in a protected atmosphere, for 24^{h}. For the other samples, brittleness caused by deformation hardening in combination with the formed intermetallic compounds, was noticed, increasing with the increase of Sn content. For other samples, the cycling combination of pressing and annealing was done in order to obtain the dimension of the samples required for further testing.

The annealed samples were then used for investigation of thermal conductivity and diffusivity, electrical conductivity and structural investigation. Microstructural observations were carried out using a combined application of optical microscopy and SEM accompanying with EDS energy-dispersive X-ray spectrometry (EDS) was used for composition determination and identification of coexisting phases. Light optical microscopy was performed by using a Carl Zeiss Jena Epityp 2 microscope. The samples were prepared through three steps including grinding, polishing and structure development (etching solution of $K_2Cr_2O_7$ in H_2SO_4). SEM–EDS analysis was performed on a TESCAN VEGA3 scanning electron microscope operated at 20 kV. The EDS (Oxford Instruments X-act) was employed for measurements of overall compositions and compositions of individual phases. The TGA–DSC/DTA simultaneous thermal analyzer (TA Instruments SDT Q600) was used for the investigation of melting and phase transformation temperatures. The instrument was calibrated by measuring the melting temperatures and the heat of melting of standard materials (pure metals: Ag and Sn). The measurements were performed in an argon atmosphere. The masses of the samples were about 10–20 mg, and a heating rate was $10°Cmin^{-1}$. Thermal diffusivity was measured by using Discovery Xenon Flash (DXF-500) instrument over a range of temperatures from 25 to 400 °C. Thermal conductivity of the investigated samples was determined using the following relation:

$$\lambda = \alpha \cdot \rho \cdot C_p \tag{1}$$

where λ is thermal conductivity ($Wm^{-1}K^{-1}$), α is thermal diffusivity (m^2s^{-1}), ρ is density (kgm^{-3}) and Cp is the calculated specific heat capacity ($Jkg^{-1}K^{-1}$). The densities of the investigated alloys at room temperature were determined using the indirect Archimedean method, following the procedure outlined in previous research [15]. The specific heat capacities were evaluated through the CALPHAD approach [16], employing optimized thermodynamic parameters from the COST 531 lead-free solder thermodynamic database [17]. Electrical conductivity was measured using the Foerster SIGMATEST 2.069 instrument. Based on the measured value of thermal and electrical conductivities at the room temperature and Wiedemann–Franz law (2), electronic and phonon contributions to the thermal conductivity of studied alloys were calculated.

$$\frac{\lambda}{\sigma} = \mathrm{L} \cdot \mathrm{T} \quad (2)$$

The microhardness of the samples was evaluated by the Vickers method in accordance with the ASTM E384 standard [18], using a PMT-3 Vickers microhardness tester.

3. RESULTS AND DISCUSSION

Identified individual phases based on the results of SEM/EDS analysis for all alloys are given in Table 1 along with the composition of the investigated alloys.

Figure 1a, c and e illustrate microstructures of the samples, while the 1b, d and f showcase the detailed microstructures of the same alloys on high-magnification SEM micrographs. The calculated equilibrium (Lever Rule) and non-equilibrium (Scheil model) solidification paths for the studied alloys were used as an aid in the analysis of as-solidified microstructures of the Ag - Sn alloys. The equilibrium and non-equilibrium solidification paths were calculated using thermodynamic parameters from [17].

Table 1.Molar composition of investigated alloys in Ag-Sn system, overall composition and identified individual phases based on the results of SEM/EDS analysis

Sample label	Nominal composition		Composition		Identified phases
	Ag/at%	Sn/at%	Ag/at%	Sn/at%	
A1	95	5	95.11	4.89	(Ag)
A2	89	11	89.34	10.66	(Ag) + ζ
A3	85	15	85.40	14.60	ζ

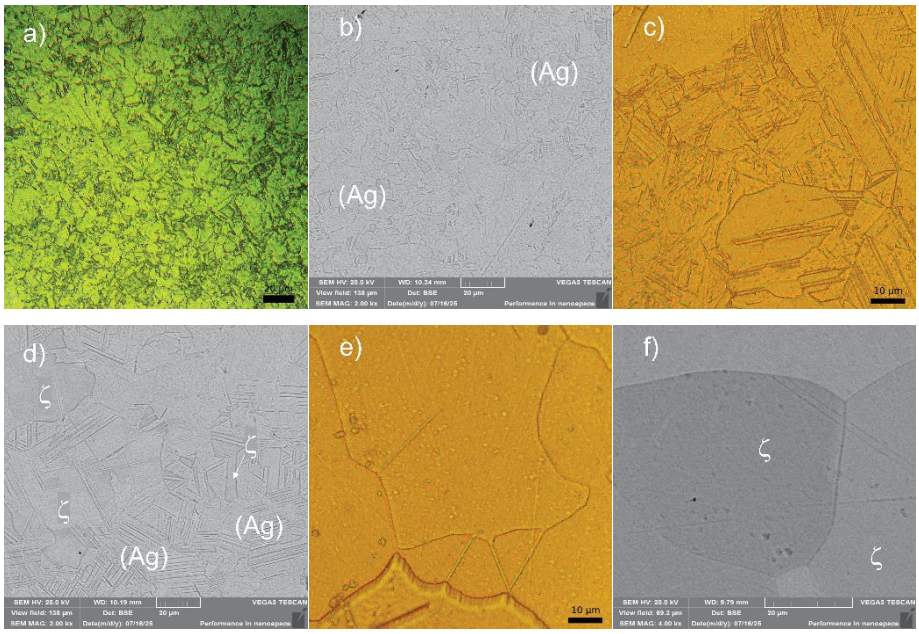

Figure 1. Optical and detailed micrographs of the samples: a), b) A1; c), d) A2 and e), f) A3

According to the results of thermodynamic calculations, equilibrium solidification (Figure 2) in all three cases begins with the precipitation of primary crystals of the (Ag) phase. For the sample A1, it is followed by solidification at around 720 °C in the same monophase area, which is confirmed by the results of the EDS (Table 1) and DSC (Table 2) analysis. The sample A2 follows the same path, however, ζ phase detected does not appear in the results of thermodynamic

calculations. Additionally, using thermodynamic parameters from [17], phase fraction diagram was calculated (Figure 2c). What must be taken into account here is the annealing at 500 °C. Therefore, the following thermodynamic calculations were observed at 500 °C and the experimental results were in a good agreement. According to the phase fraction diagram for alloy A2, bellow solidus temperature, (Ag) is stable until slightly below 650 °C. Bellow that point, due to the solid state reactions, stable phases are (Ag) and ζ, which were confirmed in the experimental process. The sample A3 also follows the path of equilibrium solidification, followed by the invariant reaction at 719.3 °C whereby the primarily formed crystals of the (Ag) phase react with the liquid: Liq + (Ag) → ζ. The remaining melt solidifies at around 683 °C, in ζ monophase area, which is also confirmed by the results of the EDS and DSC analysis.

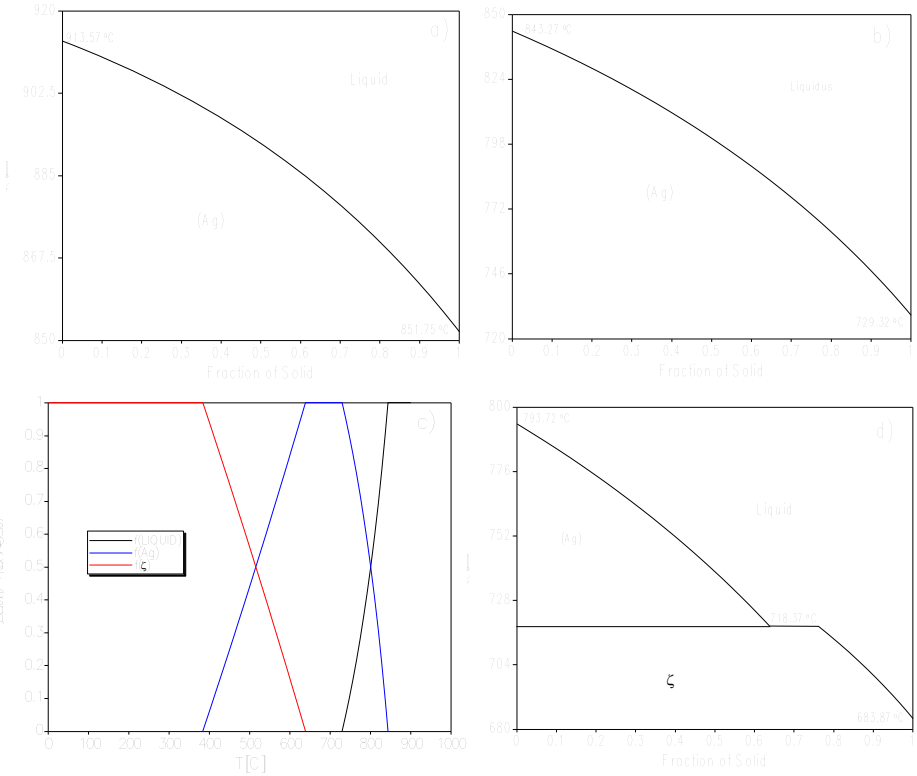

Figure 2. Equilibrium (Lever Rule) solidification paths simulation of samples: a) A1, b) A2, c) A2 – phase fraction diagram, d) A3

The solidus temperature was determined from the extrapolated onset of the first heating peak, while the liquidus temperature corresponded to the peak temperature of the final thermal event. The melting behavior of all alloys is summarized in Table 2, with representative DSC heating curve for sample A2 shown in Fig. 3. For the sample A3, due to the close proximity of the solidification and peritectic reactions, only one peak is distinguished in the thermogram at 727 °C.

Table 2. Phase transitions temperatures for examined alloy compositions obtained by the DSC analysis and comparison with thermodynamic calculation

Sample label	Experimental phase transition temperatures /°C		Calculated phase transition temperatures (equilibrium) /°C		
	solidus	liquidus	solidus	peritectic reaction [19]	liquidus
A1	872.06	921.11	851.75	/	913.57
A2	727.56	855.78	729.32	724	843.27
A3	723.54	822.72	683.87	724	793.72

Experimentally determined densities of investigated alloys, used in the further calculation of thermal properties, are presented graphically as a dependence of the composition in Figure 4.

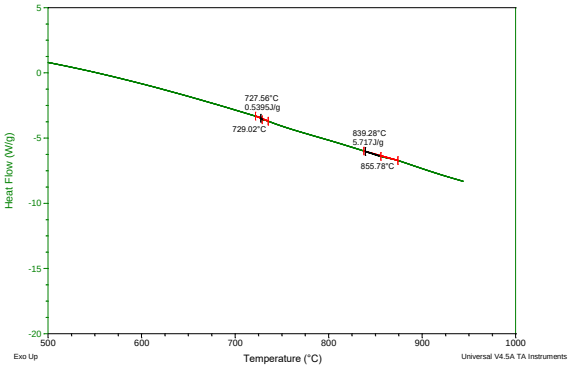

Figure 3 - DSC heating curve for alloy A2

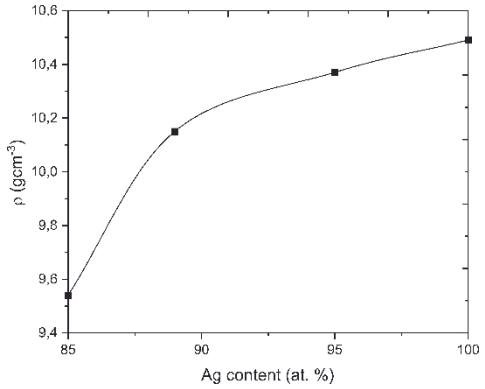

Figure 4 - Experimentally determined densities of investigated alloys

Calculated and experimentally obtained values of thermal diffusivity, specific heat capacity and thermal conductivity for the samples A1 and A2, investigated in the temperature range from 25 to 400 °C, are given in Table 3. In spite of all efforts, sample A3 did not reach the desired dimension due to brittleness, therefore couldn't be used for thermal properties investigations.

Both Ag–Sn alloys show a slight increase in specific heat capacity with temperature, with little difference between A1 and A2, indicating that Sn addition has minimal effect on this property. In contrast, thermal diffusivity and conductivity are strongly composition dependent. The sample A1 exhibits higher values compared to A2 across the 25–400 °C temperature range, however, compared to pure silver, which is considered to be the best heat conductor of all metals, both alloys show markedly reduced values. The higher Sn content diminishes the electronic contribution to heat transfer and enhances scattering effects, which together limit thermal transport. Consequently, increasing the Sn fraction leads to reduced thermal diffusivity and conductivity, while the heat capacity remains almost unaffected. This makes the Ag-rich alloys more advantageous for applications where efficient thermal management is critical.

Table 3. Specific heat capacity, thermal diffusivity, and thermal conductivity of the investigated Ag -Sn alloys in the temperature range 25–400 °C.

Sample label	Temperature /°C	Specific heat capacity /$Jg^{-1}K^{-1}$	Thermal diffusivity /mm^2s^{-1}	Thermal conductivity /$Wm^{-1}K^{-1}$
A1	25	0.235	12.8	31.18
	100	0.238	13.9	34.39
	200	0.243	15.5	39.07
	300	0.248	17.0	43.65
	400	0.253	18.7	49.12
A2	25	0.234	7.6	18.24
	100	0.239	8.7	21.09
	200	0.244	9.9	24.62
	300	0.248	10.9	27.41
	400	0.252	11.5	29.48

The results of the electrical conductivity measurements are given in Table 4 along with the results of microhardness testing. The microhardness measurements show a clear growth with increase of Sn content. This strengthening effect is attributed to the higher fraction of intermetallic phases (ζ) that form with increasing Sn concentration. These phase is inherently harder and less ductile than the Ag matrix, thereby increasing resistance to localized plastic deformation. In addition, the repeated pressing–annealing cycles applied to A2 and A3 during preparation may have further contributed to hardening through deformation-induced defects and microstructural refinement.

Table 4. Electrical conductivity measurements. calculations based on Wiedemann-Franz law and the results of microhardness testing

Alloy	σ /MSm^{-1}	λe /WmK^{-1}	λe/%	λph /WmK^{-1}	λph /%	$HV_{0.1}$
A1	4.8 ± 0.15	34.90	89	11	3.72	78.62
A2	4.7 ± 0.11	34.17	53	47	15.93	104.42
A3	4.5 ± 0.08	/	/	/	/	126.65

The electrical conductivity measurements show only a slight decrease with increasing Sn content. Calculations based on the Wiedemann–Franz law indicate that in alloy A1, thermal conductivity is predominantly governed by the electronic contribution, with a much smaller share from phonons. In contrast, alloy A2 shows a reduced electronic contribution and a significantly larger phonon contribution, highlighting the strong effect of higher Sn content on heat transport mechanisms. This shift reflects enhanced scattering and reduced electron mobility in A2, which lowers the dominance of electronic thermal conduction and increases the relative role of phonons. Thus, while overall electrical conductivity decreases only moderately, the balance between electronic and phonon contributions to thermal transport changes considerably with composition.

4. CONCLUSION

The results show that alloy composition and preparation route both play a decisive role in determining the properties of Ag–Sn alloys. While A1 (Ag–5Sn) was sufficiently ductile to be pressed and annealed once, A2 (Ag–11Sn) and A3 (Ag–15Sn) exhibited brittleness due to deformation hardening and intermetallic formation, requiring repeated pressing–annealing cycles to achieve workable samples. Microstructural analysis confirmed that solidification is dominated by (Ag) primary phase formation, with increasing Sn content leading to the appearance of ζ intermetallic phase. Thermal characterization revealed that specific heat capacity is only slightly affected by Sn, whereas thermal diffusivity and conductivity decrease sharply with the addition of tin, a consequence of reduced electronic heat transport and stronger scattering. Electrical conductivity dropped only moderately, but the Wiedemann–Franz analysis highlighted a transition from electron-dominated to more phonon-influenced heat conduction. Microhardness measurements confirmed strengthening due to the higher Sn content, correlating with intermetallic formation and processing-induced hardening. Overall, Ag-rich alloys such as Ag–5Sn retain slightly higher thermal conductivity and good mechanical stability, making them preferable for applications where reliable thermal management is essential, while higher Sn contents increase hardness at the expense of thermal efficiency and processability.

ACKNOWLEDGEMENTS

The research presented in this paper was done with the financial support of the Ministry of Science. Technological Development and Innovation of the Republic of Serbia. within the funding of the scientific research work at the University of Belgrade - Technical Faculty in Bor. according to the contract with registration number 451-03-137/2025-03/200131.

REFERENCES

[1] Restriction of Hazardous Substances in Electrical and Electronic Equipment (RoHS). https:// envir onment. ec. europa. eu/ topics/waste- and- recyc ling/ rohs- direc tive_ en. Accessed 01 Aug 2025.
[2] W.N.C. Weng. Evolution of Pb-free solders. In: Mohamad. AA editor. Recent Progress in Soldering Materials. 1st ed.. 2017. 91–108.
[3] K. Božinović. D. Manasijević. L. Balanović. I. Marković. M. Gorgievski. U. Stamenković. M. Marković. JTAC. (2025) pp.1-18.
[4] E. Dalton. G. Ren. J. Punch. M.N. Collins. Mater. Des.. 154 (2018) 184-191.
[5] R. Coyle. M. Reid. C. Ryan. R. Popowich. P. Read. D. Fleming. et al.. "The influence of the Pb-free solder alloy composition and processing parameters on thermal fatigue performance of a ceramic chip

resistor." in Electronic Components and Technology Conference. 2009. ECTC 2009. 59th. 2009. pp 423-430.
[6] D.A. Shnawah. M.F.M. Sabri. I.A. Badruddin. Microelectronics Reliab.. 52 (2012) 90-99.
[7] D. Manasijević. L. Balanović. I. Marković. M. Gorgievski. U. Stamenković. A. Đorđević. D. Minić. V. Ćosović. Solid State Sci.. 119 (2021) 106685.
[8] R. Novakovic. S. Delsante. J. Lee. G. Borzone. J. Mater. Sci.: Mater. Electron.. 29(20) (2018) 17108-17121.
[9] K. Suganuma. S.H. Huh. K. Kim. H. Nakase. Y. Nakamura. Mater. Trans.. 42 (2) (2001) 286-291.
[10] E. Çadırlı. M. Şahin. R. Kayalı. M. Arı. S. Durmuş. 2011. J. Mater. Sci.: Mater. Electron.. 22 (11) (2011) 1709-1714.
[11] S. Choi. T.R. Bieler. K.N. Subramanian. J.P. Lucas. SMT. 13 (2) (2001) 26-29.
[12] F. Meydaneri. B. Saatçi. M. Ozdemir. Kovove Mater.. 51 (2013) 173-181.
[13] P. Fima. Appl. Surf. Sci.. 257 (8) (2011) 3265-3268.
[14] M. Reid. J. Punch. M. Collins. C. Ryan. SMT. 20 (2008) 3-8.
[15] D. Manasijević. L. Balanović. I. Marković. M. Gorgievski. U. Stamenković. K. Božinović Thermochim. Acta. (2021).
[16] H.L. Lukas. S.G. Fries. B. Sundman Computational Thermodynamics: the Calphad Method. Cambridge: Cambridge University Press; 2007.
[17] A. Kroupa. A. Dinsdale. A. Watson. J. Vrestal. J. Vízdal. A. Zemanova JOM (2007).
[18] ASTM:E384-10. „Standard test method for Knoop and Vickers hardness of materials. ASTM international. West Conshohocken. USA.“ 2010.
[19] I. Karakaya. W. T. Thompson. Bull. Alloy Phase Diagrams. 8 (1987). 340-347.

The 56th International October Conference on Mining and Metallurgy
22-25 October 2025, Bor Lake, Bor, Serbia
www.ioc.tfbor.bg.ac.rs

DOI: 10.5937/IOC25371M *Original scientific paper*

THE EFFECT OF THE FREE ENERGY CHANGE ON CRYSTALLIZATION IN LITHIUM-GERMANATE GLASS

Srđan Matijašević[1a], Marko Grubišić[1b], Nataša Đorđević[1c], Ana Radosavljević-Mihajlović[1d], Slavica Mihajlović[1e]

[1]Institute for Technology of Nuclear and other Mineral Raw Materials, 86 Franchet d' Esperey St, Belgrade, Serbia,
[1a] s.matijasevic@itnms.ac.rs, 0000-0002-3897-8085
[1b] m.grubisic@itnms.ac.rs, 0009-0007-9705-2796
[1c] n.djordjevic@itnms.ac.rs, 0000-0002-2353-6751
[1d] a.radosavljevic@itnms.ac.rs, 0000-0002-9194-161X
[1e] s.mihajlovic@itnms.ac.rs, 0000-0003-0904-3878

Abstract
This paper presents the effect of free energy change on crystallization studied by the analysis of nucleation behaviour in lithium-germanophosphate glass with content of 8.6 Al_2O_3 (wt%). It was shown that approximation where the heat capacities of liquid and crystalline phases are the same for this glass, is not enough reliable. To calculate ΔG, the determination of ΔC_p is necessary.

***Keywords**: crystallization, lithium-germanophosphate glass, crystal/liquid interfacial energy*

1. INTRODUCTION

Crystallization in glass is determined by thermodynamic parameters. The crystallization process is controlled by two parameters - the nucleation rate and the rate of crystal growth. Phase transformation and the formation of a phase boundary between the newly formed and parent phase leads to a change in the free energy in the system.
In a number of studies of the volume crystal nucleation in silicate glasses, the classical nucleation theory (CNT) was used [1]. Nucleation, or the process of formation of the precursors of the crystalline phases, may occur by different mechanisms. Commonly one divides these processes into homogeneous and heterogeneous nucleation. Homogeneous nucleation is a stochastic process occurring with the same probability in any given volume (or surface) element [2]. Phase transformation and the formation of a phase boundary between the newly formed and parent phases leads to a change in the free energy in the system. According to this theory, the steady-state homogeneous nucleation rate (I) was described by an exponential dependence of two terms: the thermodynamic barrier (W^*) and the kinetic barrier (ΔG_D) for nucleation.

In the present work the influence of temperature dependence of ΔG estimated on the nucleation of lithium-germanophosphate glass with 8.6 (wt%) Al_2O_3 was investigated. Lithium germanophosphate glasses have recently emerged as multipurpose materials and have drawn great attention because of their potential applications in various solid state devices [3].

2. EXPERIMENTAL

The starting materials used are reagent grade Li_2CO_3, Al_2O_3, GeO_2, and P_2O_5. The appropriate batch composition was melted at 1400 °C for 1 h in a Pt crucible. The melts were cast on a steel plate and cooled in air.

X-ray powder diffraction analysis (XRD)(Philips PW-1710), confirmed that the quenched melts were vitreous. The chemical analysis was performed using spectrophotometer AAS PERKIN

ELMER Analyst 703. The peak temperature of crystallization T_p, and melting T_m, as well as crystallization ΔH_c, and melting enthalpy ΔH_m, of the crystalline phase were determined by DSC run of glass powder 0.5-0.65 mm (SDT Q600 V7.0 Build instrument).

For studying the structure and phase compositions, the bulk glass samples were isothermally treated at selected temperatures for different times. Identification of the phase crystallized and its morphology was performed with the XRD and SEM measurements (MIRA 3 XMU).

3. RESULTS AND DISCUSSION

The obtained glass samples were transparent, without visible residual gas bubbles. The results of the chemical analysis show that a glass composition of $6.4Li_2O \cdot 8.6Al_2O_3 \cdot 42GeO_2 \cdot 43P_2O_5$ (wt%, LAGP) was obtained.
In the case of spherical nucleus (homogeneous, volume nucleation) the thermodynamic barrier is given by:

$$W^* = 16\pi V_m^2 \sigma^3 / \Delta G^2 \quad (1)$$

where V_m, σ and ΔG are the molar volume of the crystal phase, the crystal/liquid interfacial energy and the molar free energy difference between the liquid and crystal phase, respectively [4]. Because of I on ΔG dependence, the accuracy of ΔG estimation is very important if ΔG is using in the analysis of nucleation phenomena in glasses.

The temperature dependence of ΔG in the undercooled region can be obtained if the heat capacities of the liquid and crystalline phases of the glasses are known. However, the metastable nature of the undercooled phase makes it difficult to obtain the heat capacity data experimentally. For this reason, the estimation of the temperature dependence of ΔG is very important when ΔG is using in analysis of nucleation phenomena. Many attempts have been made to derive analytical expressions for ΔG in different materials. There is no expression for ΔG which is universally applicable and the choice of the approximation depends on the type of material.

The difference in free energy between the liquid and crystalline phase for one component system (the thermodynamic driving force for crystallization) can be approximated by [5]:

$$\Delta G = -\Delta H_m (T_m - T)/T_m + \Delta C_p[(T_m - T) - T\ln(T_m/T)] \quad (2)$$

where T_m is the melting temperature, ΔH_m the enthalpy of fusion and $\Delta C_p = C^l_p - C^x_p$ is the difference between the specific heats of undercooled liquid and the crystal at constant pressure. In the case for an ideal behaviour of these phases, $\Delta C_p = 0$ can be assumed which transforms Eq.2 to :

$$\Delta G = -(\Delta H_m/T_m)(T_m - T) \quad (3)$$

For the silicate glasses as satisfactory approximation (upper bound), Eq. (3) was often used. However, there is no enough reliable data for the lithium-germanophosphate glasses. Therefore, for this analysis the data obtained from DSC run were used (Figure 1).

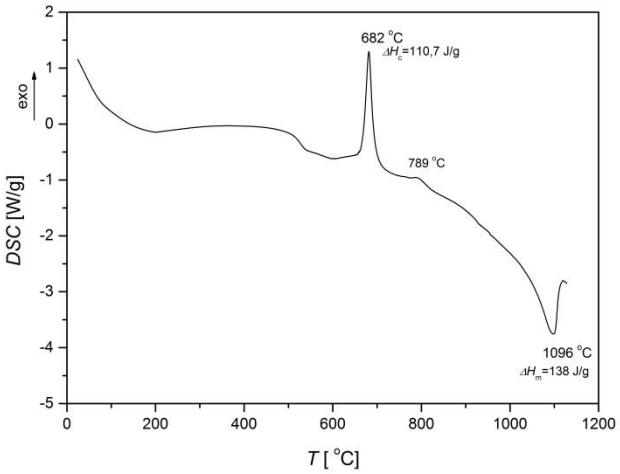

Figure 1. DSC diagram of LAGP glass composition [6]

Table 1. Parameters used to calculate free energy difference ΔG, determined by DSC measurements

Run	T_p [K]	T_m [K]	ΔH_c [kJ/mol]	ΔH_m [kJ/mol]
DSC	955.16	1368.65	48.391	60.325

From the ratio $\Delta C_p \sim (\Delta H_m - \Delta H_c)/(T_m - T_p)$, ΔC_p was calculated, and the plot of ΔG as function of temperature in the range 450-700°C is shown in Fig.2.
As may be seen from Fig.2, the values of ΔG according to Eq.(2) ($\Delta C_p \neq 0$) and Eq. (3) ($\Delta C_p = 0$) differ, so that it has the significant effects on the nucleation rate.

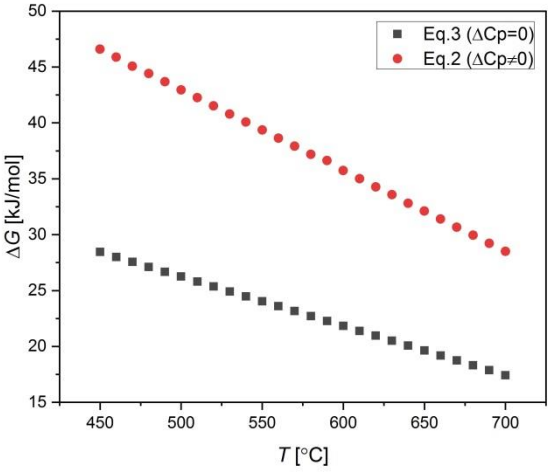

Figure 2. ΔG calculated according to Eq.(2) (■) and Eq.(3) (●)

XRD pattern of the heated glass shows that the composition of NASICON crystalline $LiGe_2[PO_4]_3$ phase formed. SEM investigation was displayed the presence of volume crystallization with the crystals growth in the form of spherulites that signifies the homogenous nucleation. The steady-state homogeneous nucleation rate is given [4,5]:

$$I=[AcT/\eta] \exp(-W^*/kT) \qquad (4)$$

where Ac is constant, T is temperature, η is the viscosity and k is the Boltzmann constant. Using η by [4] and ΔG from Eq.(2) and Eq.(3), it can be calculated, Fig.3.

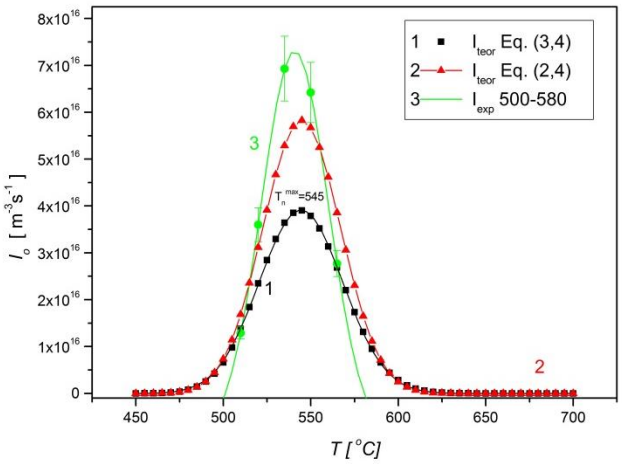

Figure 3. Theoretical plots of I according to Eq.(3,4), (curve 1, black), Eq.(2,4) (curve 2, red) and experimental data (curve 3, green) of nucleation rate [4]

Fig. 3, shows experimental results of the determination of the nucleation rate by the standard microscopic method at interval temperatures (500 - 580°C). Fig. 3, clearly shows the better agreement of the nucleation rate curve calculated by Eq. (2) with the experimental results. This analysis shows that for this lithium-germanate glass the free energy change of crystallization estimated for $\Delta C_p=0$ is not appropriate approximation for the analysis of the nucleation behaviour.

4. CONCLUSION

The results presented show that the heat capacities of the liquid and crystalline phases of the lithium-germanophosphate glass analysed significantly differ, so that the free energy change of crystallization estimated for $\Delta C_p=0$, is not enough reliable approximation in the analysis of nucleation phenomena. To calculate ΔG, $\Delta C_p \neq 0$ must be assumed.

ACKNOWLEDGEMENTS

The authors would like to thank the Ministry of Science, Technological Development and Innovations of the Republic of Serbia for support (Grant No: 451-03-136/2025-03/200023).

REFERENCES

[1] J.W.P. Schmelzer, T.V. Tropin, Int. J. Appl. Glass Sci., 13 (2022) 171–198.
[2] V.M. Fokin, E.D. Zanotto, N.S. Yuritsyn, J.W.P. Schmelzer, J. Non-Cryst. Solids, 352 (26-27) (2006) 2681-2714.
[3] S. Matijašević, S. Grujić, V.Topalović, J. Nikolić, S.Smiljanić, N. Labus, V. Savić, Sci. Sinter., 50 (2018) 193-203.
[4] S. Matijašević, S. Grujić, J. Nikolić, V.Topalović,V. Savić, S. Zildžović, N. Labus, Sci. Sinter., 54 (2022) 321-334.
[5] K.N. Lad, K.G. Raval, J. Non-Cryst. Solids, 334&335 (2004) 259-262.
[6] S. Matijašević, V.Topalović, S. Grujić, V. Savić, J. Nikolić, N. Labus, S. Zildžović, Sci. Sinter., 53 (2021) 301-310.

The 56th International October Conference on Mining and Metallurgy
22-25 October 2025, Bor Lake, Bor, Serbia
www.ioc.tfbor.bg.ac.rs

DOI: 10.5937/IOC25375R *Original scientific paper*

INFLUENCE OF THE HEAT TREATMENT ON THE STRUCTURAL PARAMETERS OF THE CuCrZr-TiB2 ALLOY

Jovana Ružić [1,2a], Jelena Stašić [1,2b], Marko Simić [1,2c], Andrijana Žekić[3d], Branislava Vučetić[3e] Dušan Božić [1,2f]

[1] Department of Materials, "Vinča" Institute of Nuclear Sciences - National Institute of the Republic of Serbia, University of Belgrade, P.O. Box 522, 11000 Belgrade, Serbia
[2] Center of Excellence "CEXTREME LAB", Vinča Institute of Nuclear Sciences – National Institute of the Republic of Serbia, University of Belgrade, 11000 Belgrade, Serbia
[3] Faculty of Physics, University of Belgrade, Studentski trg 12, 11001 Belgrade, Serbia
[1,2a] jruzic@vinca.rs 0000-0002-8076-0012
[1,2b] jelsta@vinca.rs 0000-0002-3900-3298
[1,2c] marko.simic@vinca.rs 0000-0003-4474-0257
[3d] andrijana@ff.bg.ac.rs, 0000-0001-7720-5846
[3e] b_misailovic@ff.bg.ac.rs, 0000-0001-9621-0376
[1,2f] dbozic@vinca.rs 0000-0002-0556-4708

Abstract

Powder metallurgy (PM) is used for the CuCrZr-TiB_2 alloy synthesis by employing mechanical alloying and hot pressing techniques. Powder mixture containing prealloyed CuCrZr powder, 7 wt.% Ti, and 3.2 wt.% B was firstly homogenized, and then mechanically alloyed (MA) for 27 hours. MA powders were hot pressed (HP) in protective atmosphere at temperature of 950 °C, with applied pressure of 45 MPa, and duration of 2.5 hours. Heat treatment (HT) of HP CuCrZr-TiB2 alloy was performed in two steps: (1) solution annealing (SA) at 1000 °C for 5 hours, and (2) age hardening (AH) at 470 °C for 3 hours. Changes in the structural parameters of the MA powders, and obtained compacts (HP, HT) were investigated by X-ray diffraction. Williamson-Hall equation was applied for calculation of the crystallite sizes (D, nm), lattice parameter (nm), and lattice strain (ε, %). The results show that heat treatment has significant influence on the structural parameters. After each step of HT, crystallite size and lattice strain decrease compared to HP samples owing to more homogeneous distribution of TiB_2, precipitate formation, and consequently restriction of the large grains recrystallization. Heat treatment, as well as structural parameters exhibit great influence on the mechanical properties of CuCrZr alloy. Therefore, these results indicate relation between specific heat treatment parameters, and structural parameters of the CuCrZr alloy, which may contribute to the future design of CuCrZr alloy with improved mechanical and physical properties.

***Keywords**: CuCrZr alloy; structural parameters; heat treatment; powder metallurgy*

1. INTRODUCTION

CuCrZr alloys have emerged as a prime candidate for applications in modern industry where excellent electrical and thermal conductivity, high thermal stability, and high strength and hardness are irreplaceable properties [1]. In order for CuCrZr alloys to be a good fit in above mentioned high-performance applications, the relationship between structural parameters and mechanical properties is crucial. Structural parameters such as grain size, dislocation density, and the morphology of precipitated phases play a determining role in their mechanical behavior [2]. Fine-grained structure, achieved through controlled thermo-mechanical processing, improves yield strength due to grain boundary strengthening, while also enhancing fatigue resistance [3].

The high strength of CuCrZr alloys comes from the formation of nanoscale Cr-rich and Zr-rich precipitates during aging and particle-dispersion strengthening mechanisms [4]. These particles block dislocation movement, increasing strength without significantly reducing electrical conductivity, thanks to the limited solubility of Cr and Zr in the copper matrix [5]. As the alloy ages, the solid solution breaks down into fine, evenly distributed phases that improve mechanical

properties while keeping conductivity high [6]. Although there is usually a tradeoff between strength and conductivity, CuCrZr alloys are known for maintaining a good balance between the two [7]. Therefore, optimizing the heat treatment becomes essential in order to achieve this favorable balance. Extensive research has been conducted examining mechanical and electrical properties, as well as the microstructure, of the heat treated alloy.

The aim of this study is to determine the effect that heat treatment parameters on the structural parameters of the reinforced CuCrZr alloy. By determining such relation, it can provide a potential for future design and cost-effective manufacturing of the reinforced CuCrZr alloys with improved mechanical properties.

2. EXPERIMENTAL

Prealloyed CuCrZr powder, with 7wt.% Ti, and 3.2wt.% B powders were homogenized, and then mechanically alloyed (MA) for 27 hours in the high-energy ball mill – shaker mill, in argon inert atmosphere. Hot pressing (HP) of the MA powders was done in protective argon atmosphere, at temperature of 950 ℃, with 45 MPa applied pressure, and 2.5 hours duration. Heat treatment (HT) of HP CuCrZr-TiB_2 alloy contained solution annealing (SA) at 1000 ℃ for 5 hours, and age hardening (AH) at 470 ℃ for 3 hours. Structural parameters of the MA powders, and obtained compacts (after HP, and HT) were investigated by X-ray diffraction using Rigaku Ultima IV. PDXL software was used to calculate structural parameters according to Williamson-Hall analysis: crystallite sizes (D, nm), lattice parameter (nm), and lattice strain (ε, %).

3. RESULTS AND DISCUSION

Structural and phase analysis were investigated using XRD. The obtained XRD pattern (Figure 1) of the powder after mechanical alloying identified presence of the elemental powders Cu and Ti, while powders B, Cr and Zr were not detected due to instrumental limitation. Furthermore, in Figure 1 all XRD patterns of compacts CuCrZr-TiB_2 (HP), CuCrZr-TiB_2 (SA), and CuCrZr-TiB_2 (SA-AH) indicate in situ formation of the TiB_2reinforcing particles and CuZr phase.

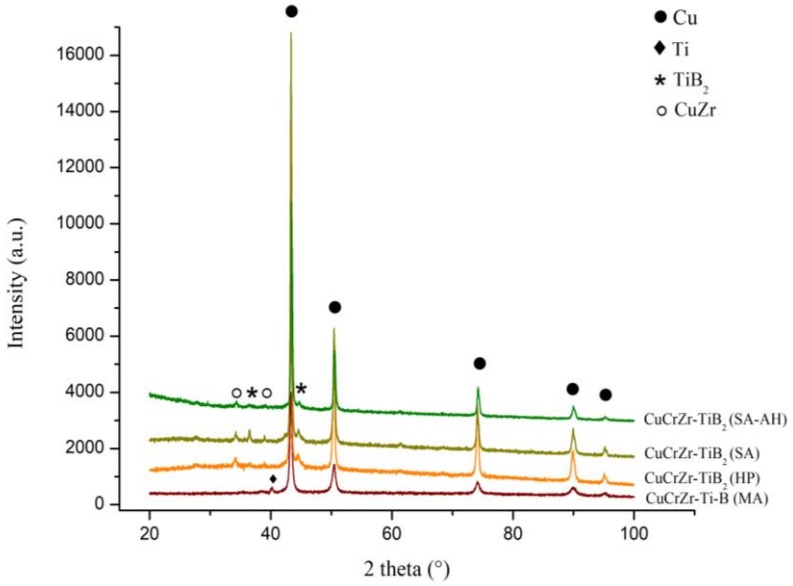

Figure 1. XRD patterns of the powders CuCrZr-Ti-B (MA), and CuCrZr-TiB_2 (HP), CuCrZr-TiB_2 (SA), and CuCrZr-TiB_2 (SA-AH) compacts.

Structural parameters, given in Table 1, were calculated using Williamson-Hall analysis. It can be observed that value of lattice parameter of non-treated CuCrZr powder is lower compared to MA CuCrZr-Ti-B powders, while crystallite size increased as a consequence of the high-energy collisions between ball-powders-ball and ball-powders-wall mill, as well as changes in particles'

shape. After hot pressing, the in situ formation of the TiB_2 particles was detected and drastic changes may be noted regarding crystallite size enlargement. Also, lattice parameter and strain slightly increased. During applied heat treatment, solid solution is formed, then solute atoms precipitate out of the solid solution (after aging) leading to a formation of new phases. These phenomena strongly affect the structural parameters of the copper matrix as can be seen in Table 1. After solution annealing significant decrease of the lattice parameter and crystallite size values was recorded, while lattice strain remains almost the same. This trend continued after age hardening, with harsh decline of lattice strain owing to grain recrystallization of the Cu matrix.

Table 1. Structural parameters of Cu and CuCrZr starting and MA powders.

	Lattice parameter, a [A]	Crystallite size, D [nm]	Lattice strain, ε [%]
CuCrZr	3.6276	66.7	0.10
CuCrZr-Ti-B (MA)	3.6201	120	0.12
CuCrZr-TiB_2 (HP)	3.6213	2275	0.31
CuCrZr-TiB_2 (SA)	3.6207	1259	0.29
CuCrZr-TiB_2 (SA-AH)	3.6139	289	0.07

Dislocation density values, calculated by using obtained values of the structural parameters [4], show that during heat treatment dislocation density increased from $0.33*10^{16}$ m^{-2} up to $1.24*10^{16}$ m^{-2}. These results confirm improvement of the CuCrZr-TiB_2 alloys' mechanical properties after heat treatment.

4. CONCLUSION

Influence of the applied heat treatment on the structural parameters of the reinforced CuCrZr alloy was investigated. XRD analysis exhibited in situ formation of the reinforcing particles (TiB_2) during hot pressing at 950 ℃. Heat treatment included solution annealing at 1000 ℃, and age hardening at 470 ℃. It was shown that heat treatment has great effect on the structural parameters of CuCrZr- TiB_2 alloy, leading to an increase in dislocation density and consequently improvement of its mechanical properties.

ACKNOWLEDGEMENTS

This work was funded by the Ministry of Science, Technological Development and Innovations of the Republic of Serbia (Contract No. 451-03-136/2025-03/200017) and by the Science Fund of the Republic of Serbia, Grant No. 7365, Development of dispersion-strengthened metal-based materials for applications in fusion reactor - DisSFusionMat.

REFERENCES

[1] N. Liang, J. Liu, S. Lin, Y. Wang, J. T. Wang, Y. Zhao, Y. Zhu., J. Alloys Compd., 735 (2018) 1389-1394
[2] J. Li, H. Ding, B. Li, L. Wang, Mater. Sci. Eng. A., 819 (2021) 141464
[3] S. Przybysz, M. Kulczyk , J. Skiba, M. Skorupska, Bull. Pol. Acad. Sci. Tech. Sci., 70 (4) (2022) 141725
[4] M. Simic, J. Stasic, D. Bozic, M. Milojevic, A. Zekic, J. Ruzic, Proceedings of International Symposium of Procesing, 29-31. May, Belgrade, Serbia, 2024
[5] J. Zhou, D. Zhu, L. Tang, X. Jiang, S. Chen, X. Peng, C. Hu, Vacuum, 131 (2016) 156-163
[6] W.X. Qi, J. Tu, F. Liu, Y.Z. Yang, Mater. Sci. Eng. A., 343 (1-2) (2003) 89-96
[7] N. Liang, J. Liu, S. Lin, Y. Wang, J. T. Wang, Y. Zhao, Y. Zhu, J. Alloys Compd., 735 (2018) 1389-1394

The 56th International October Conference on Mining and Metallurgy
22-25 October 2025, Bor Lake, Bor, Serbia
www.ioc.tfbor.bg.ac.rs

DOI: 10.5937/IOC25378A *Original scientific paper*

OBTAINING AND CHARACTERIZATION OF HIGH-YTTRIA CONTENT ZIRCONIA COATINGS

Ionuț Adomniței[1a], Daniela Lucia Chicet[1b], Bogdan Istrate[2a], Marcelin Benchea[2b], Gheorghe Bădărău[1c], Nicanor Cimpoeșu[1d*]

[1] Faculty of Materials Science and Engineering, "Gheorghe Asachi" Technical University of Iasi, 41 Dimitrie Mangeron Blvd., 700050 Iasi, Romania
[2] Faculty of Mechanical Engineering, "Gheorghe Asachi" Technical University of Iasi, 43 Dimitrie Mangeron Blvd., 700050 Iasi, Romania
[1a] ionut.adomnitei@student.tuiasi.ro, 0009-0000-7135-7494
[1b] daniela-lucia.chicet@academic.tuiasi.ro, 0000-0002-0904-4355
[1c] gheorghe.badarau@academic.tuiasi.ro, 0000-0003-4233-5231
[1d*] nicanor.cimpoesu@academic.tuiasi.ro, 0000-0003-4373-017X
[2a] bogdan.istrate@academic.tuiasi.ro, 0000-0003-0817-3523
[2b] marcelin.benchea@academic.tuiasi.ro, 0000-0001-9961-5125

Abstract
Ceramic coatings are regarded as suitable materials for high-temperature applications due to their excellent stability, both mechanical and chemical. Zirconia stabilized with yttria is a material that presents many advantages when used as a bulk or coating material in applications where exposure to high temperatures is a factor. The atmospheric plasma spraying technique was utilized in the fabrication of ceramic coatings, characterized by elevated yttria content and stabilized zirconia, on metallic substrates. The structural, chemical and mechanical properties of the coatings were investigated through a range of analytical methods, including scanning electron microscopy (SEM – SE detector), energy dispersive spectroscopy (EDS – automatic and mapping) and tribo-indenter equipment (indentation and scratch). The fabrication process was successful in producing homogenous ceramic layers with a thickness of 150 µm.

***Keywords**: ceramic coating, microstructure, TBC, SEM, EDS.*

1. INTRODUCTION

Yttria-stabilized zirconia (YSZ) ceramic coatings have found widespread application as thermal barrier coatings (TBCs) in the domain of air turbines and internal combustion engines. This can be attributed to their remarkable high-temperature resistance and chemical stability. The material's notable advantages include low thermal conductivity, tetragonal phase stability at elevated temperatures, and favorable thermal compatibility with metal substrates [1,2]. The most common deposition methods include thermal sputtering (atmospheric plasma, APS, and vacuum plasma, VPS) and electron beam vacuum deposition (EB-PVD). Each method exerts a distinct influence on the microstructure and performance of the coating. As demonstrated in the studies by Levi et al. [3] and Padture et al. [4] YSZ-based TBC systems have been shown to exhibit superior performance. In addition, Clarke and Levi [5] have proposed criteria for assessing durability based on microstructure and degradation mechanisms [1-5].

In numerous instances, the scratch test has been recognized as a versatile instrument for evaluating the mechanical integrity of a surface. Its utility has been demonstrated in a wide range of materials research and industrial R&D applications. In the early stages of research on the interpretation of scratch marks, the defect's location along the scratch trace was determined through the use of optical microscopy [6] or scanning electron microscopy (SEM) [7].

2. EXPERIMENTAL

The plasma spray method was employed to produce ceramic layers, with the samples being prepared from YSZ ceramic powders, some of which contained an anchor layer of metal powders. The ceramic layers were deposited on structural steel by successive passes, and the thickness of the ceramic layer was measured to be 125-150 μm [8].

Microscratch testing is a mechanical characterization method used to evaluate the interfacial adhesion and cohesive strength of thin films and surface treatments [9,10]. Two experimental protocols were performed: the first involved constant normal load scratching, and the second involved scratching with a linear load increase. The experimental tests were conducted under a maximum vertical load of 15 N, over a distance of 1 cm, with a translation velocity of approximately 0.15 mm/s. The tests were conducted using a blade-type indenter (Nvidia model) with a tip radius of curvature of 0.4 mm.

The surface condition subsequent to the scratch test was examined through the use of scanning electron microscopy (SEM; VegaTescan LMH II, VegaTescan LMH II, SE detector, 30kV, 15.5 mm WD) and dispersive EDS spectroscopy (Bruker detector, 6I10, Automatic and Mapping modes).

3. RESULTS AND DISCUSSION

The driving forces for the failure of the coating-substrate system in the scratch test are a combination of elastic-plastic indentation stresses, frictional stresses, and residual internal stresses present in the coating (usually as a result of the deposition process) [11,12]. When a progressive load scratch test is carried out, a series of consecutive coating failure events can be observed. As the load increases, the final event usually corresponds to total delamination. The critical load is contingent upon several parameters; some are intrinsic to the test itself, while others are extrinsic to the coating-substrate combination.

As illustrated in Figure 1(a), a substantial and unstable variation in the coefficient of friction was observed along a 10-mm displacement under a load of 15 N. This oscillation can be attributed to the inadequate adhesion of the ceramic layer to the metal substrate, resulting from the absence of an anchor layer. The sudden fluctuations in COF (friction coefficient) are indicative of micro-decohesivity processes, partial exfoliation of the layer, and potential local exposure of the substrate. Furthermore, intermittent rubbing has the potential to generate uneven wear, thereby reducing the reliability of the protective coating.

The tangential force is the most frequently recorded force signal. It can be correlated with the scratch deterioration points and used to recalculate the measured coefficient of friction (COF). The COF is defined as the ratio of the tangential force (Ft) to the normal force (Fn).

In the afferent plot of the sample lacking an anchor layer, a sudden and irregular increase in COF is observed after a specific distance. The perforation of the ceramic layer occurs in the region where the COF exhibits a substantial increase or abrupt fluctuation, indicating the exposure of the steel substrate and a modification in tribological behavior. The estimated piercing occurs within the range of 5-6 mm, with the point estimated to be around 5.5 mm, where a discernible transition in the COF curve is observed. The distribution of elements on the coated and scratched surface (Figure 2(a)) has also been shown to confirm this behavior. In this figure, the Fe substrate is observed to appear in the middle of the scratch.

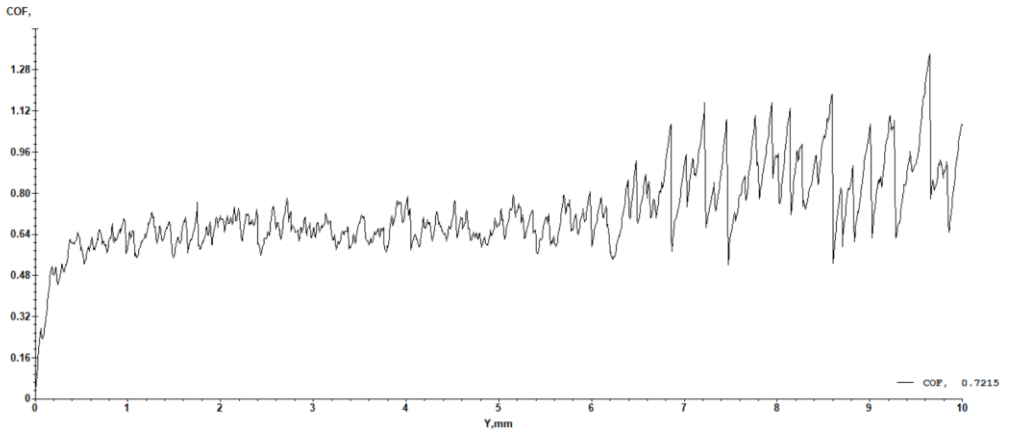

(a)

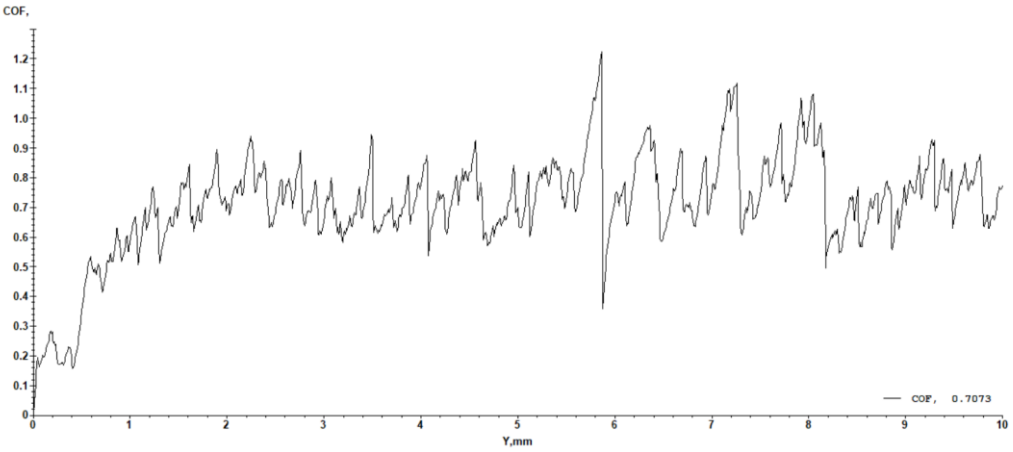

(b)

Figure 1. COF variation of steel coated sample (a) without and (b) with a bonding layer.

As illustrated in Figure 1(b), the graph demonstrates a significantly more stable and uniform evolution of the coefficient of friction, exhibiting relatively constant values throughout the entire test length. This stability is indicative of the robust adhesion between the ceramic layer and the steel substrate, thereby ensuring uniform load distribution and enhanced resistance to delamination. The metallic anchor layer functions as a mechanical and thermal transition, thereby reducing stress concentrations and enhancing overall tribological behavior. The curve is more uniform in comparison to sample (a), yet a slight change in the COF slope is observed in the ~7-8 mm region. This subtle, yet persistent, modification may signify the breakthrough of the ceramic layer and subsequent contact with the metallic anchor layer. Given the intermediate properties of the anchor layer, which exhibit a transition between those of ceramic and steel, the COF does not undergo a sudden variation but rather undergoes a smooth transition.

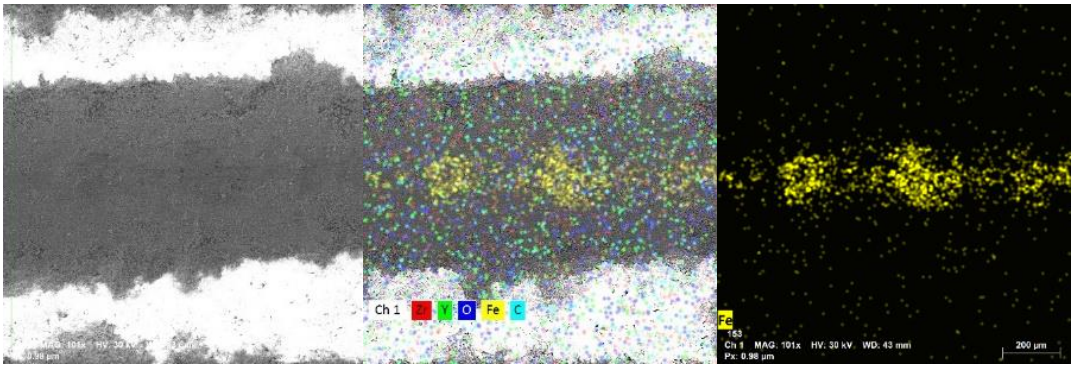

(a)

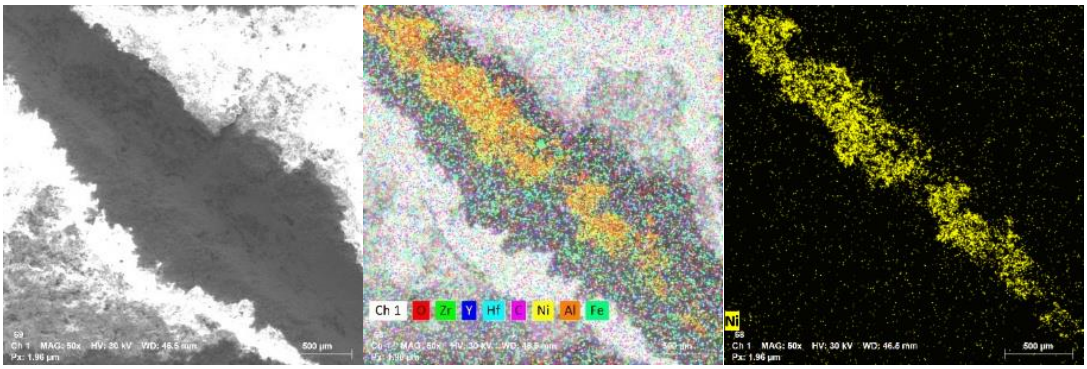

(b)

Figure 2. Scratch mark on the ceramic coating (a) SEM and elemental distribution for the sample without the bonding layer and (b) SEM and elemental distribution for the sample with the bonding layer.

The coefficient of friction signal can also function as an indicator of a critical deterioration point of the ceramic layer, even when the corresponding frictional force signal shows minimal change. However, the recalculated friction coefficient signal exhibits an observable transition corresponding to the cracking of the coating. This transition can be accurately evaluated by fitting straight lines to the two portions of the data, as illustrated in Figure 1(a) and (b). The cracking of a hard coating can originate from a surface crack or an internal (subsurface) crack. Both of these types of cracks can occur in some systems at very low loading values, as illustrated in Figure 1(b). This phenomenon elucidates the possibility of catastrophic coating failure during the second pass of a multi-pass scratch test, even when the constantly applied load is only a small fraction (< 40%) of the known critical failure load as defined by a progressive loading test.

4. CONCLUSION

A comparison of the two graphs revealed that the incorporation of an anchor layer resulted in a substantial enhancement in tribological performance. As demonstrated in sample (b), a more constant friction characteristic and stable behavior under identical load and displacement conditions are exhibited. This result indicates the effectiveness of the metallic interface layer in optimizing adhesion and mechanical strength. The presence of the anchor layer facilitated a seamless transition, thereby maintaining a more stable COF even after penetration of the ceramic layer. This discrepancy underscores the significance of the anchor layer in applications subject to recurrent or substantial mechanical stresses.

REFERENCES

[1] V. Kulyk, Z. Duriagina, B. Vasyliv, V. Vavrukh, T. Kovbasiuk, P. Lyutyy, V. Vira, Materials, 15 (8) (2022) 2707.
[2] H. Zhang, Y. Chen, L. Li, D. Yang, X. Liu, A. Huang, X. Zhang, J. Lu, X. Zhao, J. Eur. Ceram. Soc., 44 (8) (2024) 5154-65.
[3] C. G. Levi, J. W. Hutchinson, M. H. Vidal-Sétif, C. A. Johnson, Mater. Sci. Eng. A, 245 (1) A (1999) 239–248.
[4] N. P. Padture, M. Gell, E. H. Jordan, Science, 296 (5566) (2002) 280-284.
[5] D. R. Clarke, C. G. Levi, Annu. Rev. Mater. Res., 33 (1) (2003) 383-417.
[6] M. Lucanu, R. Cimpoeşu, M. Abrudeanu, C. Munteanu, S.G. Moga, M. Coteata, G. Zegan, M. Benchea, N. Cimpoeşu, A.M. Murariu, Crystals, 13 (4) (2023) 614.
[7] R. Cimpoeşu, M. Luţcanu, A.M. Cazac, I. Adomniței, C. Bejinariu, L. Andrușcă, M. Prelipceanu, L.I. Cioca, D.L. Chicet, A.M. Radu, N. Cimpoeşu, Appl. Sci., 14 (23) (2024) 10877.
[8] I. Adomniței, R. Cimpoeşu, D.L. Chicet, M. Coteață, F.C. Lupu, C. Bejinariu, L. Andrușcă, P. Paraschiv, M. Axinte, G. Bădărău, N. Cimpoeşu, Materials, 18 (2) (2025) 400.
[9] M. Luţcanu, C. Munteanu, G. Kicsi, A.M. Roman, C.G. Croitoru, B.A. Prisecariu, M.M. Cazacu, I. Ştirbu, D.L. Chicet, N. Cimpoeşu, Mater. Today, 72 (2023) 550-3.
[10] M. Luţcanu, M. Coteață, M.A. Bernevig, C.D. Nechifor, M.M. Cazacu, P. Paraschiv, B. Istrate, G. Bădărău, I.G. Sandu, N. Cimpoeşu, Arch. Metall. Mater., 67 (2) (2022) 479-485.
[11] M. Luţcanu, C. Croitoru, I. Ioniță, N. Cimpoeşu, , BIPI , 69 (73), 1-4, (2023), 9-15.
[12] N X. Randall, Surface and Coatings Technology, 380, (2019), 125092, ISSN 0257-8972

The 56th International October Conference on Mining and Metallurgy
22-25 October 2025, Bor Lake, Bor, Serbia
www.ioc.tfbor.bg.ac.rs

DOI: 10.5937/IOC25382S *Original scientific paper*

USING ENERGY DISPERSIVE SPECTROSCOPY (EDS) FOR A STAINLESS STEEL-BRASS WELDING INTERFACE CHARACTERISATION

Florin-Sorin Todirică[1a], Daniela-Lucia Chicet[1b], Dragoș-Cristian Achiței[1c], Vasile Manole[1d], Mihai-Adrian Bernevig[1e], Ioan Știrbu[1f], Nicanor Cimpoeșu[1g,*]

[1] "Gheorghe Asachi" Technical University of Iasi, 67 Dimitrie Mangeron Blvd., 700050 Iasi, Romania
[1a] florin-sorin.todirica@student.tuiasi.ro, 0009-0007-5119-6794
[1b] daniela-lucia.chicet@academic.tuiasi.ro, 0000-0002-0904-4355
[1c] dragos-cristian.achitei@academic.tuiasi.ro, 0000-0002-8562-9507
[1d] vasile.manole@academic.tuiasi.ro, 0000-0003-2221-300X
[1e] mihai-adrian.bernevig@academic.tuiasi.ro, 0000-0003-2364-3589
[1f] ioan.stirbu@academic.tuiasi.ro, 0000-0002-2715-0557
[1g,*] nicanor.cimpoesu@academic.tuiasi.ro, 0000-0003-4373-017X

Abstract
A welded sample of SS-brass was polished and the resulting mirror-like surface was analysed (without chemical etching) to determine the main element's variation. The gradual elemental transition indicated a good metallurgical bond. The elemental maps (e.g. Fe, Cr and Ni for stainless steel and Cu and Zn for brass) showed a gradient rather than an abrupt cutoff, which often indicates solid-state diffusion and a potentially coherent or semi-coherent interface. A smooth transition area usually indicates limited intermetallic formation, which is favourable for mechanical strength and interface stability. Zinc penetration into stainless steel suggests interdiffusion to some extent, but excessive zinc at high temperatures could cause porosity or weaken the steel matrix. As the elemental distribution maps showed a continuous and graded elemental transition with no visible cracking or voids, the interface was likely to exhibit coherent or semi-coherent bonding, which is consistent with controlled brazing and suggests good mechanical integrity.

Keywords*: stainless steel-brass; welding interface; EDS; TIG.*

1. INTRODUCTION

Welding stainless steel to brass is challenging due to the significant differences in their chemical, thermal and physical properties. The key issues are: different melting points (stainless steel: ~1400–1450°C; brass: ~900–940°C depending on the composition), meaning that in this case, the brass can melt or vaporize (especially zinc) before the stainless steel even begins to melt; thermal expansion, whereby brass expands more than stainless steel when heated, leading to stress and warping at the joint; electrochemical compatibility, as dissimilar metals can create galvanic corrosion, especially in humid or marine environments.

Analyzing the chemical composition of alloys is essential for determining the elemental composition of metallic materials, as well as assessing their quality, performance and compatibility. One of the most widely used methods is optical emission spectrometry (OES), which enables the rapid and accurate analysis of metallic elements by measuring the radiation emitted by electrically excited atoms [1]. Inductively coupled plasma mass spectrometry (ICP-MS) is often used for superior accuracy and sensitivity, as it is capable of detecting trace elements at ppm or even ppb levels [2,3]. X-ray fluorescence spectrometry (XRF) is also an effective, non-destructive method for the qualitative and quantitative identification of elements in a variety of alloys, and is commonly used in quality control [4]. For local, small-scale analysis, energy dispersive X-ray spectroscopy (EDS), which is integrated into scanning electron microscopes (SEM), provides information about the distribution and chemical nature of elements in cross-

sections or metal surfaces [5, 6]. Depending on the analysis requirements — such as accuracy, sensitivity, spatial localisation, or non-destructive character — each technique has its advantages and limitations. In practice, they are often used as complementary techniques to provide a full characterisation of alloys.

EDS (energy dispersive spectroscopy) is a semi-quantitative method of localised chemical analysis based on the detection of X-rays emitted by excited atoms in the electron beam of the SEM. The main advantages of the technique are rapid elemental identification and spatial mapping. It enables linear or surface analysis and is ideal for elements with $Z > 5$ (from boron upwards). However, the main accuracy limitations derive from the limited spatial resolution (~1-2 μm), which is greater than the thickness of the thermally affected zone in some cases. Additionally, the detection of light elements ($Z < 10$; e.g. C and O) is less accurate, and spectral line interference (e.g. Cr and Mn) can occur. The results are semi-quantitative; for accurate values, WDS analysis or wet chemical methods are required.

2. EXPERIMENTAL

The experimental welding was performed using a modern arc welding machine. The process involved electric welding in a shielding gas environment with a non-fusible electrode (TIG 316L) for stainless steel. For the TIG procedure, a welding machine equipped with inverter technology and high-frequency arc initiation was used. These features ensure a stable and controlled arc, which is essential for obtaining a homogeneous weld bead. TIG 316L rod was used for welding 304L stainless steel, containing a high percentage of Cr (18%) and Ni (12%), as well as additions of Mo and Cu, to ensure increased corrosion resistance and good performance at high temperatures. Surface chemical analysis was performed using two established modes of analysis: Line and Mapping.

3. RESULTS AND DISCUSSION

A clear transition area separates the two materials. The central area shows a gradual change in composition, indicating that diffusion between the materials occurred during welding. No large porosities or cracks were visible in the image, suggesting good weld quality. Figure 1(b) shows the linear distribution of elements across the interface.

Chromium (Cr) and nickel (Ni) predominantly appear on the stainless-steel side (left), gradually decreasing towards the right, while copper (Cu) and zinc (Zn), elements specific to brass, are absent on the left and increase significantly towards the right. There is a region of diffuse overlap where all these elements are present in varying amounts, indicating significant interfacial diffusion.

The presence of low levels of Fe or Cr diffusion in brass suggests that sufficient atomic mobility occurred during the brazing or solid-state welding process to lead to atomic-level bonding. A narrow interdiffusion region of less than 10–20 μm is common in well-controlled brazing operations. However, zinc-rich zones at the interface may pose a risk of void formation due to zinc evaporation. Sharp interfaces (i.e. no gradient) could imply weak mechanical bonding or a lack of metallurgical interaction, which would likely lead to delamination under stress. The formation of Cu-Zn-Fe or Cu-Cr intermetallics can embrittle the interface if cooling is too slow or if peak temperatures are too high.

The distribution map for the entire area (Fig. 1c) corroborates the findings of the linear analysis. The elemental maps suggest that there is no significant contamination between the pure zones of each material, with the transition being relatively steep but sharp. A limited mixing zone is indicated, which is most likely the result of the low thermal conductivity of the brass.

(a)

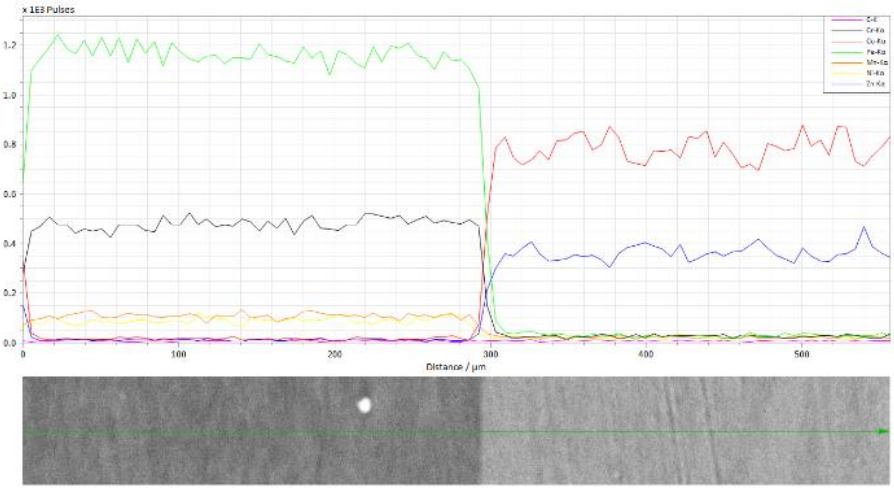

(b)

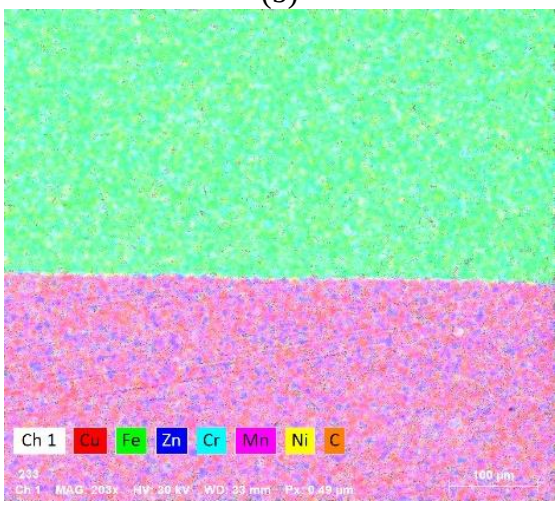

(c)

Figure 1. Surface images of the welded samples: (a) the area where the chemical composition analysis was performed; (b) the linear distribution of the elements of the welded materials (stainless steel on the left and brass on the right); (c) the distribution of the characteristic elements of the two materials.

The results of the chemical analysis revealed that the elements chromium (Cr) and nickel (Ni) were present in high concentrations on the left (304L stainless steel), decreasing towards the interface. The elements Cu (copper) and Zn (zinc), which are characteristic of brass (on the right), increased significantly beyond the interface. An interfacial diffusion zone is present where all these elements are found together, indicating thermal reactions at the atomic level in the molten zone and partial

mixing between the two materials, probably occurring in the rapid solidification zone of TIG welding.

The lack of sharp variations in the distribution curves indicates good local accuracy of the EDS. However, to accurately assess the exact composition (e.g. atomic percentage or mass percentage), calibration with a standard or ZAF corrections (Z = atomic number, A = absorption, F = fluorescence) is required. Regarding spatial resolution, it is sufficient for the fused zone (visible diffusion of 10–100 μm). For elemental sensitivity, it is effective for Cr, Ni, Cu and Zn (heavy elements with a clear signal). The quantitative accuracy is average without standardisation or mass percentage reporting, but the practical relevance is high as it clearly differentiates between welded zones and diffusion detection.

4. CONCLUSION

- TIG welding between 304L stainless steel and brass resulted in a high-quality joint without any macroscopic defects. Elemental distribution analysis revealed a clearly defined transition zone with bidirectional diffusion of the characteristic elements of each material.
- The EDS technique was suitable for this analysis, which involved observing the elementary transition between two materials in the welded zone. It provided relevant data on the chemical composition and revealed an area of metallurgical mixing, which is essential for characterising welds. The accuracy is adequate for qualitative and semi-quantitative analysis, but complementary techniques would be needed for more accurate data (e.g. WDS, ICP-OES or microanalysis with standards).

REFERENCES

[1] G.M. Hieftje, J.D. Ingle, S.R. Crouch, Spectrochemical Analysis. Prentice Hall, (2007).
[2] A. Montaser, (Ed.), Inductively Coupled Plasma Mass Spectrometry, Wiley-VCH, (1998).
[3] S.R. Khan, B. Sharma, P.A. Chawla, R. Bhatia, Food Anal. Methods, 15 (2022) 666–688.
[4] R. Jenkins, X-ray Fluorescence Spectrometry, 2nd Edition. Wiley-Interscience, (1999).
[5] J.I. Goldstein, D.E. Newbury, J.R. Michael, N.W. Ritchie, J.H. Scott, D.C. Joy, Scanning electron microscopy and X-ray microanalysis, Springer, (2017).
[6] A.M. Roman, V. Geantă, R. Cimpoeșu, C. Munteanu, N.M. Lohan, G. Zegan, E.R. Cernei, I. Ioniță, N. Cimpoeșu, N. Ioanid, Materials, 15 (2022) 568.

The 56th International October Conference on Mining and Metallurgy
22-25 October 2025, Bor Lake, Bor, Serbia
www.ioc.tfbor.bg.ac.rs

DOI: 10.5937/IOC25386T Original scientific paper

ANALYSIS OF THE VARIATIONS OF THE WING LIFT COEFFICIENT OF UNMANNED AERIAL VEHICLES WITH INCREASING REYNOLDS NUMBER OF AIRFLOW

Shehret Tilvaldyev[1a], América Yamile Amaya Diaz[1b], Adrian Alberto Castro De La Cruz[1c],

[1] Autonomous University of Ciudad Juárez, Manuel Díaz H. No. 518-B Zona Pronaf Condominio, 32315 Juárez, Chih., Mexico

[1a] shehret@uacj.mx, 0000-0003-1671-852X

[1b] al189618@alumnos.uacj.mx, 0009-0003-4030-7015

[1c] al200042@alumnos.uacj.mx, 0009-0003-2060-766X

Abstract

Unmanned aerial vehicles (UAVs) are one of the fastest growing segments of the aviation market. The concept of UAV development includes military and civilian applications. According to these objectives, the criteria for selecting parameters for micro and mini-UAVs are primarily range and flight duration. Consequently, micro and mini-UAVs should have a high level of aerodynamic quality. The usual behavior of the maximum lift coefficient (CL) of wing profiles with increasing Reynolds number is an increase. However, in some cases, the wing profiles may show the opposite - a decrease in the maximum lift coefficient (CL) with increasing Reynolds number (Re). We have analyzed this effect for a finite span wing and for a wing profile segment.

Keywords*: wing profiles, lift coefficient, UAV development, boundary layer, Reynolds number*

1. INTRODUCTION

In the design of UAVs, in general, the well-known principles set forth in [1-5] are used, but it is necessary to consider the peculiarities inherent in unmanned vehicles. The class of unmanned aerial vehicles differs from manned vehicles, first, in the absence of the need to ensure the safety of a person (pilot) on board. In addition, the absence of a pilot allows the aircraft to be miniaturized [6]. Miniaturization is possible for many tasks where the mass and dimensions of the payload are smaller than the mass of a human, such as surveillance and reconnaissance missions. The transition to smaller size and lower mass allows us to reduce the cost of the task compared to the use of traditional manned aircraft.

Many works devoted to various peculiarities of aerodynamics of small-sized drones confirm the relevance of the discussed topic. In [6], the separation of the boundary layer at a relatively small Reynolds number ($Re = 1.7x10^5$) is considered, and the essential influence of the degree of turbulence of the onrushing flow on the formation of the detachment flow and on the integral aerodynamic characteristics is emphasized. In [7], a comprehensive study of a small-size unmanned aerial vehicle including calculation, wind tunnel experiment and flight experiment was carried out. In continuation of this topic, the authors of [8] carried out a more detailed computational study of the layout of a small-sized unmanned aerial vehicle of small elongation.

In general, it is well known that the Lift force is a component of the total aerodynamic force perpendicular to the velocity vector of the airflow, resulting from the asymmetry of the flow around the airfoil. The total aerodynamic force is the integral of the pressure around the contour of the wing profile. As the angle of attack increases, the lift coefficient increases, but only up to a

value of Critical Angle of Attack. At Critical Angle of Attack vortices disrupt the airflow from the wing, preventing lift from occurring and causing a stall.

The usual response of the lift coefficient (CL) of profiles with the increasing Reynolds number (Re) is an increase. However, in some cases, wing profiles may induce the opposite, i.e., a decrease in the maximum lift coefficient (CL) with increasing Reynolds number (Re). This effect can be obtained experimentally on a finite span wing or on a wing profile segment.

We have analyzed data for variable wing profiles and for flat wings of constant symmetric cross-section and summarized a huge number of experimental materials obtained by us earlier and by other authors in aerodynamics wind tunnels with a low degree of flow turbulence, in the range of Reynolds numbers $7x10^5 – 25x10^6$.

2. ANALYSIS OF THE CHANGE IN LIFT COEFFICIENT WITH INCREASING REYNOLDS NUMBER

The type of airflow separation from the wing surface depends on the airfoils' profile, thickness-to-chord ratio, leading edge radius, and Reynolds number (Re**)**. In this paper we are investigating only the factor of Reynold's number (Re**)**. On profiles for cruising flights at low subsonic speeds and low Reynolds numbers (Re**)** (e.g., for unmanned aircraft layouts), the following main types of wing boundary layer separation [9, 10] are possible in the general case:

- separation of the laminar boundary layer at the leading edge or further downstream;

- separation of a turbulent boundary layer at the trailing edge;

- a combination of these.

2.1 Separation of the laminar boundary layer at the leading edge

The separation of laminar flow is usually combined with the subsequent attachment of a free viscous layer, where the transition to turbulent flow regime takes place. A local closed zone of detachment flow (detachment flow bubble) is formed. The laminar bubble can be "short" *(0.5 - 1.0% of the chord)* or "long" *(>2% of the chord)* depending on the value of the Reynolds number (Re**)** and the pressure gradient. It should be noted that the velocity profile in the boundary layer at the attachment point corresponds to the profile at the separation point. Therefore, the boundary layer immediately after attachment is neither typically laminar nor typically turbulent and only at further motion of the attachment point does the flow regime approaches turbulent.

Typically, increasing the angle of attack after the formation of a short bubble results in a shift of the attachment point upstream to a region of greater surface curvature. Starting at some Angle of Attacks (AOA), the turbulent free viscous displacement layer no longer attaches to the surface, and there is a sharp drop in lift and an increase in drag (Stall) (Figure 1A).

This "explosion" of a laminar breakaway bubble is commonly referred to as a leading-edge detachment (short bubble detachment). Separation with formation of a short bubble can occur on the most common profiles with moderate thickness-to-chord ratio ***(0.09<t/c<0.15)***. The formation of a short bubble has practically no effect on the aerodynamic performance until the flow is abruptly disrupted by its "collapse".

When a long bubble is formed, an increase in the angle of attack causes the point of attachment of the free viscous layer to move downstream. The length of the bubble increases and at some angle of attack the bubble stretches to the trailing edge and there is a complete separation of the laminar flow.

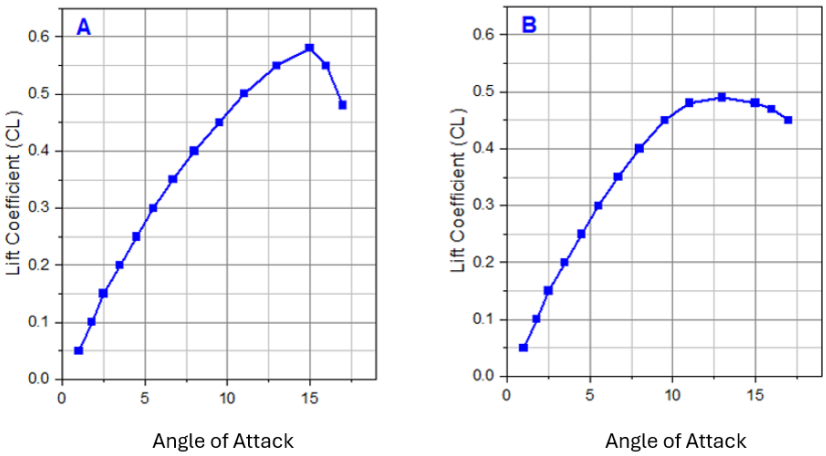

Figure 1. Airflow disruption on the profile with formation of a short bubble in the flow (A) and disruption with formation of a long bubble in the breakaway flow (B).

Further increase in the angle of attack leads to a gradual decrease in the lifting force (Stall) (Figure 1B). Such separation can occur at profiles t/c<0.9 and is commonly referred to as thin profile separation (long bubble separation). Although this bubble causes a gradual flow stall rather than a sudden one as in the case of a short bubble, it nevertheless has a significant effect on drag, lift, and longitudinal momentum over a fairly large range of angles of attack. This is because the appearance and development of a long bubble of detachment flow changes, and quite noticeably, the pressure distribution along the chord. At the trailing edge at separation of the long bubble, the pressure is positive, and the main changes in the pressure diagram occur at the front part of the profile.

2.2 Separation of a turbulent boundary layer at the trailing edge

The separation of the flow from the trailing edge (Figure 2) is typical for "thick" profiles ***t/c>0.12*** and occurs in the chord sections with a boundary layer that has already entered the turbulent state.

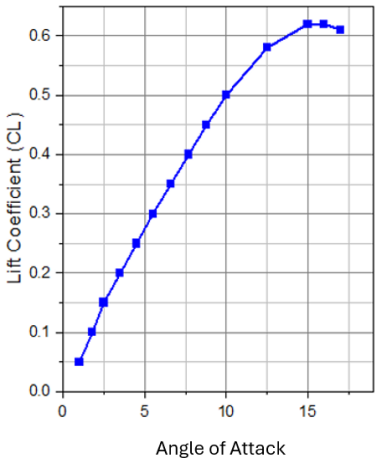

Figure 2. Airflow disruption at the trailing edge of the airfoils profile.

An increase in the angle of attack causes a constant upstream displacement of the separation point and a gradual, rather than an abrupt, decrease in lift. In this type of separation, a depression occurs at the trailing edge of the profile, and the main changes in the pressure diagram occur at the trailing edge of the profile.

2.3 Combination of Separations of boundary layer at the leading and trailing edges

On some profiles, in a certain range of Reynolds numbers (Re**)**, both breakaway flow bubbles and trailing edge separation can be observed simultaneously (Figure 3).

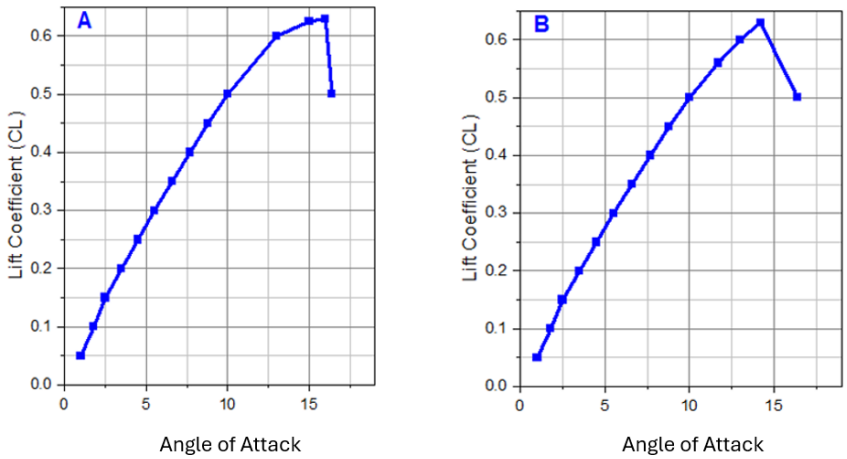

Figure 3. Combined Airflow separation: breakaway flow with bubble formation in the flow (A), and separation at the trailing edge (B).

Consequently, there can be a combination of different types of separation with features typical of both closed bubble and trailing edge separation. This intermediate type of separation is called a combined separation.

3. CONCLUSION

The effect of decreasing maximum lift force with increasing Re number is reviewed. This behavior is not typical for profiles, but there are mentions and explanations of this effect in the literature. From the point of view of the cruising flight of the vehicle, the stall speed margin is important, and hence the behavior of the maximum lift coefficient by the Reynolds number (Re**)**.

Since wing design to maximize aerodynamic quality or flight duration parameter may require a significant reduction of the chord at the wing tip, and stall at the wing tip is most dangerous in terms of stall, consideration of profiles with inverse behavior of the maximum lift coefficient with respect to Reynolds number (Re**)** may be useful.

The main conclusion is that for any profile, when changing the Reynolds number (Re**)** (flow velocity), a consistent change (and quite cardinal) in the type of flow stall and, consequently, in the values and dynamics of aerodynamic characteristics at different angles of attack is possible.

REFERENCES

[1] S.V. Serokhvostov, Ways and technologies required for MAV miniaturization. Braunschweig, Germany, 2008.
[2] T.J. Mueller, Aerodynamic measurements at low reynolds numbers for fixed wing micro-air vehicles, development and operation of UAVs for military and civil applications, VKI, Belgium, 1999.
[3] T.J. Mueller, Low reynolds number vehicles, editor Reshotko E, AGARD, 1985.
[4] G.K. Ananda, P.P Sukumar., M.S. Selig, Aerosp. Sci. Technol., 42 (2015) 392–406.
[5] A. Gopalarathnam, J. Aircr., 40 (4) (2003) 768–775.
[6] V.A. Kornushenk, Numerical, experimental and flight investigation of MAV aerodynamics, Toulouse, France, 2007.
[7] M. Drela, J. Aircr., 25 (8) (1988) 724–732.
[8] L.W. Traub, J. Aircr., 50 (2) (2013) 626–634.
[9] P.D. Chappell, Aeronaut. J. R. Aeronaut. Soc., 72 (1968) 82–90.
[10] S. Tilvaldyev, A. Paz Perez, E. Alfonso Munoz, Impact of right-angled winglets on vibration generation by wing prototype with symmetrical airfoil, Cenid AC, 2024, 111-136. https://doi.org/10.23913/9786078830343

The 56th International October Conference on Mining and Metallurgy
22-25 October 2025, Bor Lake, Bor, Serbia
www.ioc.tfbor.bg.ac.rs

DOI: 10.5937/IOC25390T *Original scientific paper*

INVESTIGATION OF THE INFLUENCE OF RESIDUAL STRESSES ON THE MECHANICAL PROPERTIES OF ALUMINUM ALLOY STRIPS

Nebojša Tadić[1a], Žarko Radović[1b]

[1] Faculty of Metallurgy and Technology, University of Montenegro, Cetinjski put bb, 81000 Podgorica, Montenegro
[1a] nebojsa@ucg.ac.me, 0009-0007-5458-8232
[1b] zarkor@ucg.ac.me, 0009-0005-3699-9869

Abstract
In the paper, the influence of residual stresses on the mechanical properties of cold-rolled strips made from 2024 and 5083 alloys was investigated. The relatively low values of residual stresses (≤ 75 MPa) and the large number of influencing parameters make it difficult to precisely determine their impact on mechanical properties. The initial material properties, deformation hardening, and relaxation parameters have a significantly greater influence than the values and distribution models of residual stresses. It is reasonable to assume that the effect of residual stresses is manifested only at the onset of plastic flow and is limited to 5–10% of the total energy accumulated during plastic deformation.

***Keywords**: 2024 and 5083 alloys, residual stresses, mechanical properties*

1. INTRODUCTION

Previous research has shown that residual stresses can significantly affect the behavior of metal parts during processing and exploitation [1, 2]. To analyze these phenomena, modeling of the residual stress distribution across the cross-section of the part and the effects of superposition with external loads is applied, based on which correlations with mechanical properties are derived [3].

In the process of cold rolling of strips, a plane state of residual stresses is induced, with stress components in the longitudinal (rolling) direction and transverse direction. The longitudinal residual stresses have a dominant influence on the appearance and properties of the strips [4].

In this paper, the influence of longitudinal residual stresses on the mechanical properties of strips made from aluminum alloys 2024 and 5083 was analyzed. Alloys 2024 and 5083 are widely used in the aerospace and automotive industries for component production. A significant number of these components are manufactured through cold rolling. The investigation was conducted on samples in cold-rolled, mechanically relaxed, and thermally relaxed states.

2. EXPERIMENTAL

For the investigation, commercial aluminum alloys 2024 and 5083 were selected. The starting materials for both alloys were 1.28 mm thick sheets in the annealed condition. Samples for rolling were cut from these annealed sheets. These samples were cold rolled with reduction rates of 20% and 50% in a single pass on a laboratory duo rolling mill.

One part of the cold-rolled samples was subjected to mechanical relaxation of residual stresses through uniaxial tension with a plastic deformation degree of 0.66÷1.1%. The other part of the cold-rolled samples underwent thermal relaxation of residual stresses under the conditions of 140°C/5 min for alloy 5083 and 130°C/5 min for alloy 2024. The relaxation temperature was chosen from the lower range of the recovery temperature interval $(0.25 \div 0.3) \cdot T_{melt}$, which enables relaxation effects up to 75% [5].

Tensile testing for all conditions was conducted on a universal testing machine type FPZ/100 and

included the determination of yield strength ($R_{p0.2}$), tensile strength (R_m), and total elongation (A), as well as the construction of strain-hardening curves.

Residual stresses were measured using the deflection method. This method is based on disturbing the stress balance by removing metal layers from one side of the sample and subsequently measuring the resulting elastic line. The equation for the calculation of the residual stresses is derived from the equality of the moment load from the residual stresses and the equivalent external moment load corresponding to the given elastic line model. A detailed description of the procedure is given in a previous study [6].

3. RESULTS AND DISCUSSION

Longitudinal residual stresses in flat-rolled strips have an approximately linear distribution across the cross-section, with tensile stresses in the surface layers, compressive stresses in the central layers, and maximum value at the surface of the strip (Figure 1) [6]. Under external loading, for mechanical behavior, the resultant load of the effective external and effective residual stress is relevant. According to this model, residual stresses represent a pre-load that affects the resultant stress, and consequently, the onset of plastic flow as well as other mechanical properties.

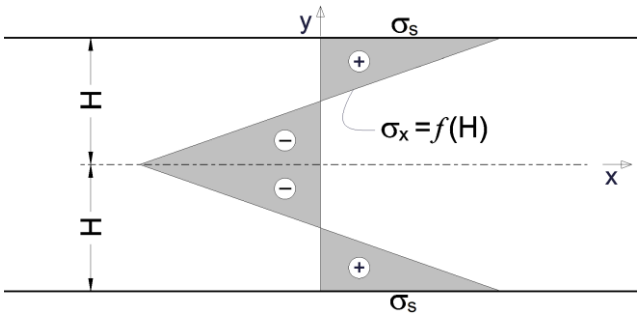

Figure 1. Model of longitudinal residual stress distribution across the strip thickness

Figures 2a and 2b show the experimental strain hardening curves for all tested conditions in both alloys. The recognizable influence of deformation processes (cold rolling, mechanical relaxation) and thermal treatments on the yield stress and the course of strain hardening curves is clearly visible. Table 1 presents the results of mechanical properties testing, average values of residual stresses (σ_s), and approximations of strain hardening curves using the Ludwik equation:

$$\sigma = \sigma_0 + K \cdot \varphi^n \quad (1)$$

where: σ - yield stress, σ_0 - experimentally measured initial value of yield stress, K - strength coefficient, and φ - true logarithmic strain in tension, n - strain hardening exponent.

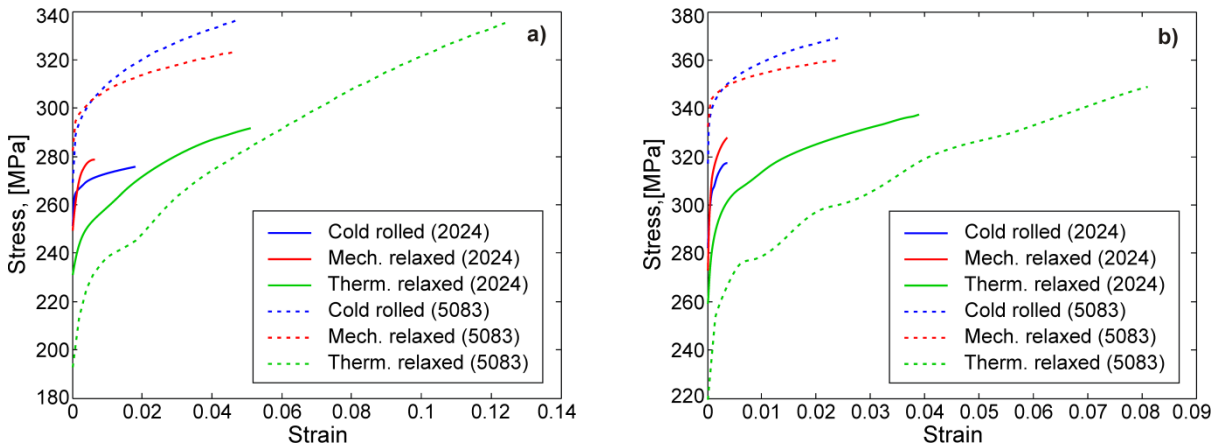

Figure 2. Stress-strain curves for conditions with reduction ratios of 20% (a) and 50% (b)

In processes involving strain hardening, a large number of influential parameters complicates the precise analysis of the impact of residual stresses on mechanical characteristics. The initial properties of the material, strain hardening, type of loading, and relaxation conditions have a significantly greater influence than the value and distribution model of residual stresses [7]. This is particularly evident in cold-rolled strips of the tested alloys where residual stresses reach relatively low values of up to 75 MPa [6].

Table 1. Mechanical properties, strain hardening curve equations, and average values of residual stresses

States	ε [%]	Mechanical properties			$\sigma = \sigma_0 + K \cdot \varphi^n$, [MPa]	σ_s [MPa] [6]
		$R_{p0.2}$ [MPa]	R_m [MPa]	A [%]		
Alloy 2024						
Cold rolled	20	267.05	273.34	2.62	$\sigma = 251.14 + 55.41 \cdot \varphi^{0.203}$ (± 0.3)	36.2
MR (φ_t = 0.66 %)		270.43	273.76	2.34	$\sigma = 250.97 + 468.34 \cdot \varphi^{0.528}$ (± 1.2)	0
TR (130°C/5 min)		243.11	277.94	5.22	$\sigma = 231.80 + 265.42 \cdot \varphi^{0.492}$ (± 1.0)	28.3
Cold rolled	50	312.97	317.37	1.10	$\sigma = 286.65 + 445.37 \cdot \varphi^{0.469}$ (± 1.1)	31.8
MR (φ_t = 0.47 %)		321.76	324.16	1.25	$\sigma = 279.97 + 872.97 \cdot \varphi^{0.489}$ (± 2.0)	0
TR (130°C/5 min)		294.43	324.85	3.87	$\sigma = 262.61 + 251.74 \cdot \varphi^{0.352}$ (± 3.0)	25.2
Alloy 5083						
Cold rolled	20	290.64	318.54	5.44	$\sigma = 269.34 + 179.36 \cdot \varphi^{0.323}$ (± 2.3)	68.5
MR (φ_t = 1.10 %)		298.16	312.32	5.47	$\sigma = 282.69 + 107.98 \cdot \varphi^{0.318}$ (± 0.9)	0
TR (140°C/5 min)		212.70	297.73	12.68	$\sigma = 194.01 + 357.09 \cdot \varphi^{0.459}$ (± 2.3)	25.3
Cold rolled	50	345.35	355.42	1.81	$\sigma = 317.23 + 131.03 \cdot \varphi^{0.248}$ (± 0.8)	40.8
MR (φ_t = 0.72 %)		345.63	354.43	2.75	$\sigma = 331.45 + 72.51 \cdot \varphi^{0.260}$ (± 0.9)	0
TR (140°C/5 min)		258.39	323.81	8.13	$\sigma = 222.75 + 303.26 \cdot \varphi^{0.357}$ (± 2.1)	15.5

ε - reduction ratio; MR - mechanically relaxed; φ_t - deformation degree during mechanical relaxation; TR - thermally relaxed; σ_s - average values of residual stresses.

By comparing the values of mechanical properties for rolled and mechanically relaxed states, data on the impact of relaxation by uniaxial tension and residual stresses on the mechanical characteristics of cold-rolled strips can be obtained. Previous research has shown that residual stresses are fully relaxed at very low degrees of tensile deformation (0.5÷1.1%) [5]. Experimental results show small differences in mechanical properties between cold-rolled and mechanically relaxed states (Table 1). Therefore, it is reasonable to assume that the influence of residual stresses is manifested only at the onset of plastic flow, while other changes in the stress-strain curves are a consequence of initial differences and deformation changes during previous tensioning.

If the degree of tensile deformation (φ_t) of rolled strips is inserted into the Ludwik equation for the rolled state and the stress value σ is calculated, then this value should be comparable to the experimentally determined value of the yield stress ($\sigma_{0(MR)}$) in the mechanically relaxed state. The obtained results with differences expressed in absolute and relative terms are shown in Table 2. The calculated values of yield stress (σ) in all cases are higher than the experimentally measured ones ($\sigma_{0(MR)}$), and the differences (Δσ) are within the range of residual stress variations. These results suggest that the influence of residual stresses can be associated with residual elastic energy, which amounts to 5÷10% of the total energy required for deformation.

During thermal relaxation, when the minimum temperature required for thermally activated processes is achieved, the release of energy accumulated during deformation occurs. This is accompanied by the relaxation of residual stresses as well as the softening of the metal. The degree of recovery that can be achieved decreases with increasing previous deformation, and increases with increasing temperature and annealing time. As a result of low-temperature recovery, changes in the yield strength are limited to 10% for the 2024 alloy and 27% for the 5083 alloy, compared to the rolled state.

Table 2. Relationship between calculated and measured yield stress values for mechanically relaxed states

Alloy / state	φ_t	$\sigma = \sigma_0 + K \cdot \varphi_t^n$ [MPa]	$\sigma_{0(MR)}$ [MPa]	$\Delta\sigma = \sigma - \sigma_{0(MR)}$ [MPa]	$\Delta\sigma/\sigma$ [%]
2024 / rolled 20%	0.0066	271.1	250.97	20.13	7.4
2024 / rolled 50%	0.0047	322.7	279.97	42.73	13.2
5083 / rolled 20%	0.0110	311.2	282.69	28.51	9.2
5083 / rolled 50%	0.0072	355.7	331.45	24.25	6.8

Relaxation of residual stresses under the same conditions amounts to an average of 21% for the 2024 alloy and 63% for the 5083 alloy (Table 1). It is evident that the ~3 times greater softening and relaxation of residual stresses in the 5083 alloy compared to the 2024 alloy are the consequences of the selected annealing temperature and the more intense occurrence of thermally activated processes in the 5083 alloy. Namely, in these time-temperature conditions, the effects of the recovery of the deformed structure are limited. In alloy 2024, changes occur in the content and size of precipitates (artificial aging), the presence of which has a strengthening effect. On the other hand, in alloy 5083, there is a redistribution of the phases of the alloying elements so that a more homogeneous microstructure is created, which results in an increase in ductility. Since the relaxation of residual stresses under the selected conditions is not complete, especially for the 2024 alloy, the analysis of its impact on mechanical properties is also more challenging. However, it can be confidently stated here that the reduced yield strength primarily arises from softening caused by the thermal activation of structural mechanisms, and to a lesser extent, from the relaxation of residual stresses. Such changes are also reflected in the entire course of the strain-hardening curves (Figures 2a and 2b).

4. CONCLUSION

The research has demonstrated that the influence of residual stresses on the mechanical properties of cold-rolled strips must be considered in the context of the material type, strain hardening, and relaxation conditions. The derived model shows minor differences in mechanical properties between the cold-rolled and mechanically relaxed states, indicating that the effect of residual stresses manifests only at the onset of plastic flow and is limited to 5÷10% of the total energy accumulated during plastic deformation. During low-temperature recovery, the effects of residual stress relaxation on mechanical properties are negligible compared to structural effects. These findings may contribute to the optimization of post-deformation treatments in industrial rolling processes.

REFERENCES

[1] F.G. Rammerstorfer, F.D. Fischer, N. Friedl, J. Appl. Mech., 68 (2001) 399-404.
[2] Y.S. Lim, S.H. Kim, K.J. Lee, Adv. Mater. Sci. Eng., 2018 (2018) 9890234.
[3] V. Hauk, Eigenspannungen und Lastspannungen, Carl Hanser Verlag, Wien, 1982.
[4] D.C. Tran, N. Tardif, A. Limam, Int. J. Solids Struct., 69-70 (2015) 343–349.
[5] N. Tadić, M. Jelić, D. Lučić, M. Mišović, Mat. in Tehn., 45 (5) (2011) 467-475.
[6] N. Tadić, PhD Dissertation, University of Montenegro, Podgorica, 2011.
[7] O. Voehringer, In Handbook: A (E. A.Niku-Lari) Pergamon Press, Oxford, 1987, p. 367.

The 56th International October Conference on Mining and Metallurgy
22-25 October 2025, Bor Lake, Bor, Serbia
www.ioc.tfbor.bg.ac.rs

DOI: 10.5937/IOC25394I Original scientific paper

INFLUENCE OF DIMENSIONAL SIZE OF ROLLED PRODUCT MADE OF S690QL STEEL ON IMPACT TOUGHNESS AND GRAIN SIZE

Aida Imamović[1a], Mirsada Oruč[1b], Milenko Rimac[1c], Gorazd Kosec[2], Safet Hamedović[1d]

[1]Fakultet inženjerstva i prirodnih nauka, Univerzitet u Zenici, B&H
[2]SIJ Acroni d.o.o. Jesenice, Slovenia
[1a] aida.imamovic@unze.ba, 0009-0000-5902-9906
[1b] mirsada.oruc@unze.ba, 0000-0002-9980-7650
[1c] milenko.rimac@gmail.com, 0009-0007-1045-0346
[2] gorazd.kosec@acroni.si, 0009-0002-6930-964X
[1d] safet.hamedovic@unze.ba, 0009-0000-3443-9546

Abstract

Fine-grained structural steel of the S690QL designation is widely used due to its very good mechanical properties and good weldability and bending, resistance to abrasion and corrosion. It is most often made in the form of plates of different thicknesses. S690QL steel plate has excellent performance characteristics and is used when low temperature resistance and important strength components are required. It is used in addition to applications for construction machines and structures, mining machines and in the energy sector, highways, railway bridges, etc.

Since this steel is used in very demanding conditions such as low temperature, it is very important to test the mechanical properties of the impact toughness at these temperatures. Toughness is an important property that can indicate a material's tendency towards brittle fracture. In this work, a large number of samples were tested for this property, i.e. impact toughness at a temperature of -40°C taken from plates of different thicknesses made of S690QL steel. In addition to this property, the grain size of this steel after heat treatment is also taken into account. These characteristics and their mutual dependence provide directions for correcting the production of semi-finished products or finished products

Key words: *steel S690QL, dimensions of rolled plates, impact toughness, grain size*

1. INTRODUCTION

S690 QL steel is a high-strength, fine-grained structural steel that, in quenched and tempered condition, has a minimum yield strength R_{eH} of 690 MPa with guaranteed toughness (Charpy impact toughness) of 30 J at a temperature of -40°C, for rolled plates with thicknesses ranging from 3 to 50 mm.

Since S690 QL is a high-strength structural steel produced in accordance with the EN 10025-6 standard, it is thermally treated by quenching and tempering and possesses good bending and welding properties. According to EN 10025-6:2004+A1:2009 and the DIN EN 10025-1 standard, which is harmonized with the former, impact toughness tests are conducted on both longitudinal and transverse sections of the samples at a temperature of -40°C.

Testing and evaluation of results were carried out in accordance with the EN 10025-6 and DIN EN 10025-1 standards, using standard procedures applied in the accredited Mechanical and Metallographic Testing Laboratory of the "Kemal Kapetanović" Institute at the University of Zenica. It is important to note that the delivery standard EN 10025-6 prescribes testing of tensile properties and impact toughness only on the longitudinal section at a temperature of -40°C [1].

In this study, in addition to impact toughness testing on the longitudinal direction of the rolled plate samples, tests were also conducted on samples taken in the transverse direction, as well as

grain size analysis. The aim was to determine the correlation between these parameters and to identify potential directions for further improvement of mechanical properties.

2. CHARACTERISTICS OF S690QL STEEL PLATES

Structural steel S690QL belongs to the group of high-quality high-strength steels, which are fully killed during production. The chemical composition of this steel is shown in Table 1, and its mechanical properties are shown in Table 2.

Table 1. Chemical composition of S690QL steel products in quenched and tempered condition according to EN 10025-6:2004+A1:2009 (max. %)

Steel	**C**	**Si**	**Mn**	**P**	**S**	**N**	**B**	**Cr**	**Cu**	**Mo**	**Nb**	**Ni**	**Ti**	**V**	**Zr**
S690QL	0.22	0.86	1.80	0.025	0.012	0.016	0.006	1.6	0.55	0.74	0.07	2.1	0.07	0.14	0.17

Depending on the product thickness and production conditions, the manufacturer may add one or more alloying elements to the steel up to the maximum values in order to achieve the desired properties. At least 0.010% of grain-refining elements must be present. Aluminum is also one of these elements. The minimum content of 0.010% refers to soluble aluminum, and this value is considered achieved if the total aluminum content is at least 0.013% [2].

Table 2. Mechanical properties of S690QL steel products according to EN 10025-6 for plate thicknesses less than 50 mm and greater than 3 mm

Steel	R_{eH}, MPa	Rm, MPa	A, %	KV at -40°C, J, longitudinal	KV at -40°C, J, transverse
S690QL (1.8928)	Min.690	770-940	Min.14	30	27

The standard EN 10025-6:2004+A1:2009 has also been adopted as a Bosnian-Herzegovinian standard, with the latest edition published as BAS EN 10025-6+A1:2024 (Hot-rolled products of structural steels – Part 6: Technical delivery conditions for flat products of high yield strength structural steels in the quenched and tempered condition).

This steel is designed to provide an excellent combination of high strength, toughness, abrasion resistance, and weldability. The main reasons for the widespread use of high-strength steels of this class are their exceptionally high mechanical properties, such as tensile strength and yield strength, as well as favorable impact toughness and fracture energy [3].

3. IMPACT TOUGHNESS

Impact toughness testing is performed according to the customer's requirements, and in this study, the results are presented for unfavorable service conditions, i.e., tests conducted at a temperature of -40°C. The tests were carried out on a large number of samples taken from test plates in both the longitudinal and transverse directions, using the Charpy V-notch method, in the accredited Mechanical Laboratory of the "Kemal Kapetanović" Institute at the University of Zenica, in accordance with the BAS EN ISO 148-1:2017 standard.

After quenching and tempering, the plates exhibit an improved structure typical of hot-rolled plates that have undergone subsequent heat treatment.

It should be noted that toughness is influenced by the average grain size, not by isolated clusters of larger grains, as long as the majority of grains are small on average. It can be assumed that such larger grains are mainly associated with non-uniform distribution of certain elements, i.e., their

uneven concentration (especially those that, through precipitation of their compounds, influence grain size).

A variety of factors affect the toughness of a material during testing, such as:

- testing temperature,
- microstructure (especially grain size),
- shape and dimensions of the notch,
- specimen dimensions,
- impact velocity, etc.

Testing temperature has the greatest influence on toughness, i.e., on the material's impact toughness. In general, material toughness decreases as the testing temperature decreases. This is because a lower temperature reduces the plasticity or deformability of the material [4].

Microstructure also has a significant impact on the toughness of the material. The smaller the crystalline grain size, the higher the toughness. In steels, reducing the grain size by one unit on the ASTM E112 scale lowers the transition temperature by approximately 15°C. Deformed materials also exhibit greater toughness, i.e., a lower transition temperature, due to their anisotropic structure, especially in the longitudinal direction [4].

In plate materials (e.g., sheet metal), the highest impact energy is observed in the rolling direction (1), slightly lower in the transverse direction (2), and the lowest in the through-thickness direction (3) (see Fig. 1).

Alloying elements (C, Ni, Al, Mo...) and elements generally classified as impurities (P, S, O, N...) in steels can be divided into two groups based on their effect on impact toughness:
– elements that reduce impact toughness, and
– elements that increase impact toughness.
The first group, which reduces impact energy, includes carbon (C) and phosphorus (P). Carbon increases the content of cementite and pearlite, thereby raising the ductile-to-brittle transition temperature. Phosphorus reduces the plasticity and toughness of steel. During cold working, phosphorus causes brittle fracture due to the formation of a brittle solid solution (iron phosphide) that segregates along grain boundaries and in interdendritic regions.

The second group, which increases impact energy, includes nickel (Ni), molybdenum (Mo), and aluminum (Al). Nickel expands the γ-phase region and significantly improves the toughness of the material. Molybdenum promotes carbide formation, which contributes to improved toughness by producing a fine-grained, evenly distributed structure. Aluminum, as a deoxidizing element, helps develop a fine-grained microstructure, thereby increasing the steel's toughness. Additionally, through the formation of aluminum nitride (AlN), it reduces the nitrogen (N) content in the solid solution, which further enhances material toughness [5].

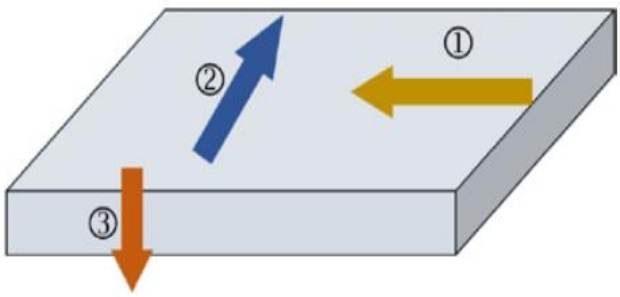

Figure 1. Impact fracture work of the material depends on the sampling direction [5]

3. EXPERIMENTAL PART

In the experimental part of this study, 60 samples of rolled test plates of different thicknesses were examined, ranging from 7.96 mm to 40.72 mm. Test specimens for impact fracture work were made from these plates, with smaller specimens being prepared from plates thinner than 10 mm. The dimensions of the specimens affect the material's toughness in different ways. The specimen length has the least effect, while width and thickness similarly contribute to the reduction of toughness. The most important factor is the ratio between notch depth and specimen thickness. Therefore, the standards for the acceptance and delivery of general structural steels (DIN 17100) prescribe lower values of impact toughness (KV) for narrower specimens [4].

It should be noted that there is no clear correlation between toughness or impact fracture work and other mechanical properties of the material. However, it is generally true that materials with high toughness or impact toughness usually have lower strength values and higher values for elongation and reduction of area.

3.1. Impact Fracture Work Testing

Standard EN 10025-6 for hot-rolled plates in quenched and tempered condition, made of S690 QL steel, prescribes for impact toughness testing at a temperature of -40°C a minimum average value of 30 J from three tests on longitudinal specimens, and 27 J on transverse specimens of the plate.

The appearance of the test plates from which the samples were taken for testing is shown in Figure 2.

Figure 2. Test plates from which specimens for impact toughness and grain size testing were taken

The obtained values from the impact toughness tests at a temperature of -40°C, as well as the grain sizes for the samples taken from plates of different thicknesses (ranging from 7.96 mm to 40.72 mm), were thoroughly analyzed and presented in the form of a diagram.

4. ANALYSIS OF TEST RESULTS

This study analyzed the influence of product dimensions on impact toughness and grain size, as well as their mutual relationship. The results obtained from 60 tested plate samples with thicknesses ranging from 7.96 mm to 40.72 mm are presented in a diagram, Figure 3.

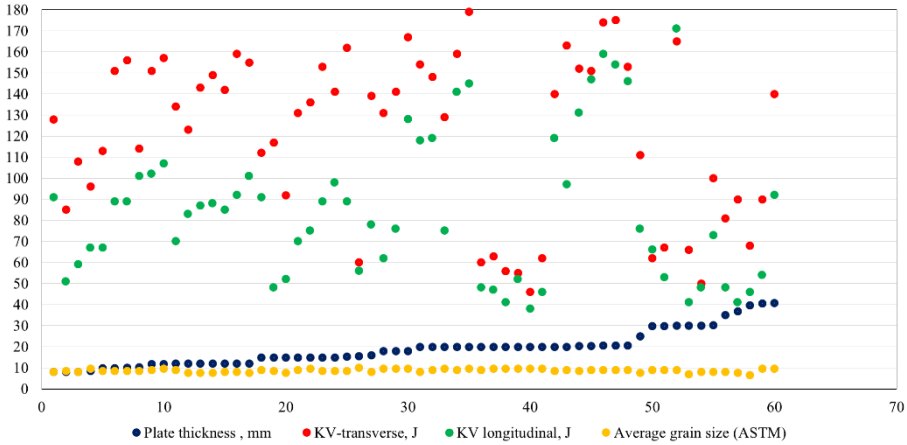

Figure 3. Presentation of test parameter results for 60 tested plate samples with thicknesses ranging from 7.96 mm to 40.72 mm

From Figure 3, it can be seen that the impact toughness results are inconsistent, but fall within the acceptable values required by the standard. As the plate thickness increases, the impact toughness decreases in both the longitudinal and transverse directions, while the grain size remains fairly uniform in both directions. It can also be observed that, for some samples (mostly those of smaller dimensions), the impact toughness values in the transverse direction are somewhat higher than in the longitudinal direction. This should be the subject of future analysis, as it is possibly influenced by the sampling location, the marking of the rolling direction, or internal irregularities (such as segregation, inclusions, etc.).

For a more detailed analysis, correlations of the mentioned values were performed. Thus, Figure 4 shows the relationship between the impact toughness in the longitudinal and transverse directions, and a strong correlation between these parameters is evident, as indicated by the high correlation coefficient.

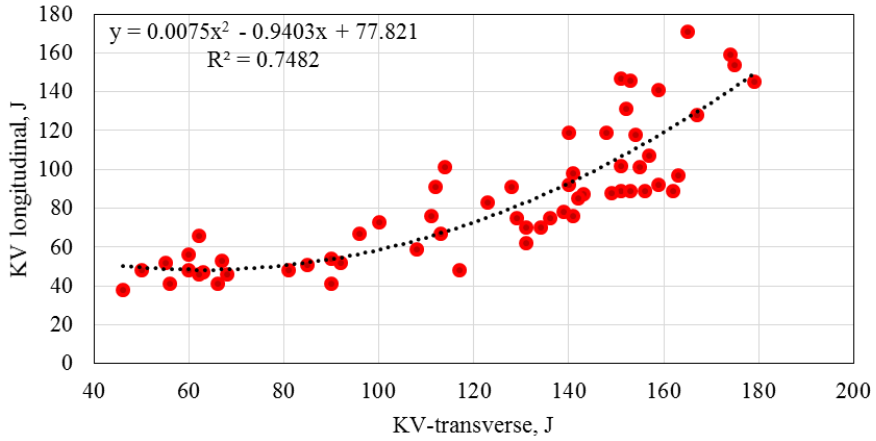

Figure 4. Dependence of impact toughness in the transverse direction on the impact fracture work in the longitudinal direction

In Figures 5, 6, 7, and 8, attempts were made to establish correlations between product dimensions and the impact toughness of samples in both the transverse and longitudinal directions, as well as between impact toughness and the average grain size. Since the results are quite scattered, the presented correlations have low correlation coefficients. However, they may indicate certain trends for further analysis and possible adjustments in the production technology.

As shown in Figures 5 and 6, the values of impact toughness in both transverse and longitudinal directions decrease with increasing dimensions (which was expected) and are mostly grouped around the lower dimension range (from 7.96 mm to approximately 20 mm).

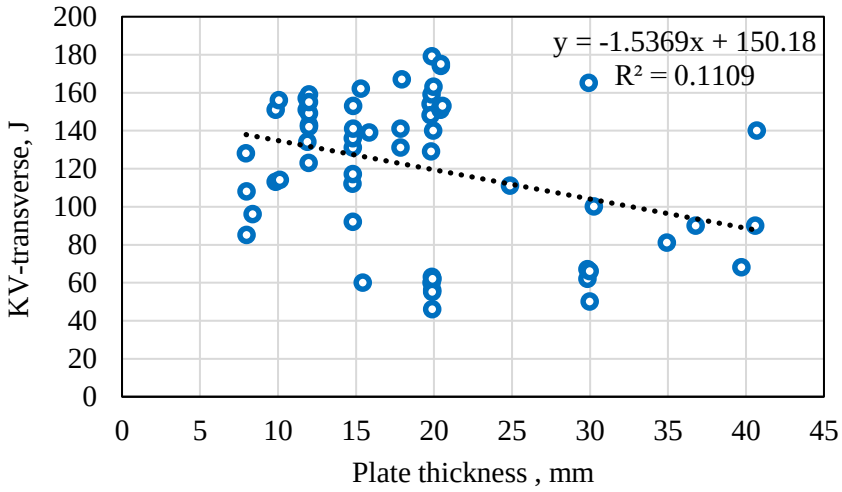

Figure 5. Dependence of plate thickness and impact i toughness n the transverse direction

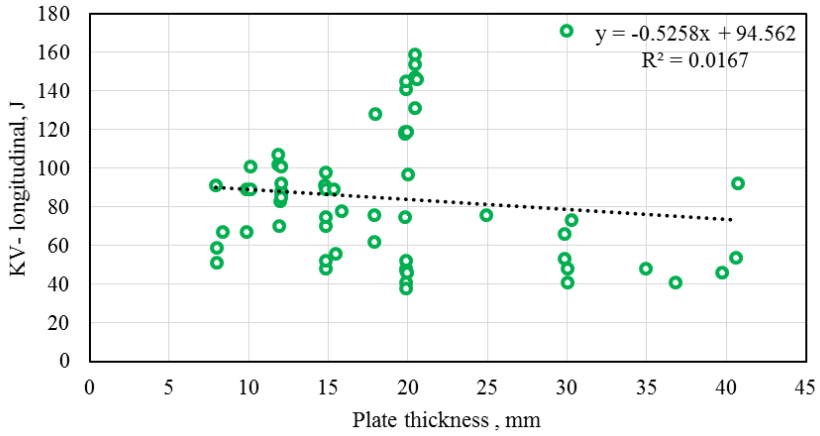

Figure 6. Dependence of plate thickness and impact toughness in the longitudinal direction

Figures 7 and 8 show the dependence of impact toughness on the average grain size. The correlation of impact toughness for samples taken in the transverse and longitudinal directions relative to grain size is not reliable due to the scatter of values (the correlation coefficient is low). However, it is still noticeable that the impact toughness is lower for larger grain sizes, which is expected, and vice versa-especially in the testing of samples in the longitudinal direction.

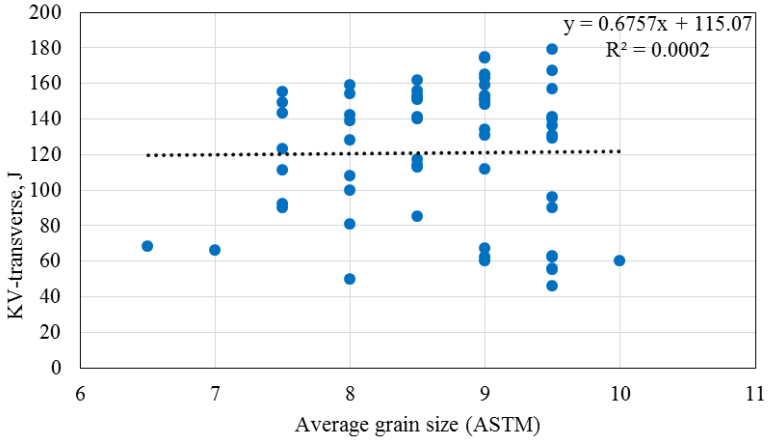

Figure 7. Dependence of impact toughness (transverse) on average grain size

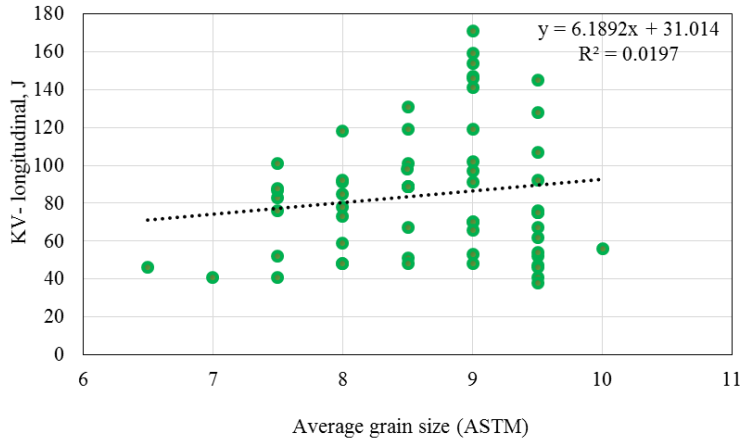

Figure 8. Dependence of impact toughness (longitudinal) on average grain size

5. CONCLUSION

Steel S690QL is designed to provide an excellent combination of high strength, toughness, abrasion resistance, and good weldability. The main reasons for the widespread use of high-strength steels of this grade are their exceptionally high mechanical properties, such as tensile strength and yield stress, as well as favourable impact toughness, i.e., impact fracture work.

Impact toughness tests were conducted at low temperatures on samples taken from different lengths of rolled plates to determine their mutual dependence and provide guidelines for further production technology. Additionally, the average grain size was determined for all samples except for the microstructure. The grain size obtained for all samples is quite uniform, with no significant deviations, apart from occasional clusters of somewhat larger grains, which did not show any significant impact on the required properties.

The anisotropy of microstructure and grain size is not pronounced to a great extent in the longitudinal and transverse test samples, which also influenced the impact toughness results.

Testing of toughness, i.e., impact fracture work at a temperature of -40°C, showed that all average and individual values are significantly above the required standards.

It was also observed that some samples (mostly those with smaller dimensions) had somewhat higher impact toughness values in the transverse direction than in the longitudinal direction. This should be the subject of future analysis, as the influence of sampling location, rolling direction marking, or internal irregularities (segregation, inclusions, etc.) on these values is possible.

All conducted tests provide directions for improving production technology and the stability of the production process.

REFERENCES

[1] M. Oruč, G. Kosec, A. Imamović, R. Sunulahpašić., EFFECT GRAIN SIZE OF S690QL STEEL ON IMPACT FRACTURE AT LOW TEMPERATURE, 14th Scientific-Research Symposium with International Participation, Metallic and Nonmetallic Materials , Zenica, 27th-28th April 2023, B&H, ISSN 2566-4352.
[2] EN 10025-6.2004+A1:2009
[3] ZAVARIVANJE ČELIKA S690QL,Društvo za Tehniku Zavarivanja https://dtzsb.unisb.hr › SBZ_2023_paper_363-373 (Access December 2024.)
[4] I. Vitez, M. Oruč, R. Sunulahpašić: Ispitivanje metalnih materijala,mehanička i tehnološka ispitivanja, FMM, Univerzitet u Zenici, Zenica, 2006.
[5] Univerzitet Crne Gore https://www.ucg.ac.me › objava_187444 › fajlovi (Access December 2024.)

The 56th International October Conference on Mining and Metallurgy
22-25 October 2025, Bor Lake, Bor, Serbia
www.ioc.tfbor.bg.ac.rs

DOI: 10.5937/IOC25401P *Review paper*

PHASE TRANSFORMATIONS IN A WELDED JOINT OF UNALLOYED STEEL AFTER LONG-TERM SUBCRITICAL ANNEALING

Krzysztof Pańcikiewicz[1a], Mariusz Maślak[2a], Paulina Zajdel[2b], Marcin Klimek[2c]

[1] AGH University of Cracow, Mickiewicza 30, 30-059 Cracow, Poland
[2] Cracow University of Technology, Warszawska 24, 31-155 Cracow, Poland
[1a] kpanciki@agh.edu.pl, 0000-0003-3486-3819
[2a] mmaslak@pk.edu.pl, 0000-0003-3592-429X
[2b] paulina.zajdel@pk.edu.pl, 0000-0002-1940-0106
[2c] marcin.klimek@doktorant.pk.edu.pl, 0009-0009-3278-7374

Abstract
In the article the effect of long-term exposure of a structural weld made of unalloyed steel on permanent changes in its microstructure and mechanical properties is discussed in detail. First, the welding process itself is considered in the context of the properties of the weld obtained in it, as well as those revealed in the heat-affected zone adjacent to this weld. On this basis, a detailed analysis is carried out of possible structural changes of a permanent nature resulting from the impact of a long-term fire incident on the weld which was previously made.

***Keywords**: welded joint, phase transformation, long-term subcritical annealing*

1. INTRODUCTION

It is common knowledge that in the welding process, as a result of the impact of high temperature on the joined steel, a local permanent change in the material structure occurs, both in the weld itself and in the area of the heat-affected zone adjacent to this weld. The impact of a more or less developed fire episode on a previously made weld should be treated as another process of its exposure to high temperature, resulting in subsequent changes to the structure of this weld, and consequently potentially permanently changed its properties. The process of changes in the material temperature in fire conditions is undoubtedly random in nature. However, it can be argued that the values of this temperature are definitely lower in a fire than those generated in the weld during the welding process. In these considerations, the potential impact of a fire, both on the weld itself and on its immediate vicinity, is simulated by keeping the tested material for a long time at a fixed temperature with an intentionally selected value of 600°C. As one can see, this temperature may be interpreted as subcritical in relation to the A_1 temperature, associated for typical mild structural steel with the austenitic transformation. This method of a thermal impact formally corresponds to classical annealing of such the material. In the presented article the authors would like to show that the structure and the mechanical properties of a given weld, identified for it after a fire episode, may be significantly different from those that described the same weld before the fire [1, 2].

2. CHARACTERISTIC OF A WELDED JOINT OF UNALLOYED STEEL

A typical welded joint of unalloyed steel consists of three parts: the base material, the heat-affected zone and the weld metal. The thermal cycle of the welding process, in addition to enabling local melting of the steel, heats it to a high temperature in the vicinity of the fusion line. Moving away from this fusion line, the effect of heat impact becomes smaller. The maximum temperature obtained in a given place determines its microstructure and mechanical properties. The amount of heat input has a significant effect on the range of its impact, and consequently the width of the individual heat-affected zones, their microstructure and mechanical properties [3]. It is usually

assumed that for unalloyed steels the influence on the welded material is not noted up to the A_1 temperature of 727°C. This is caused by relatively fast heating, short holding at the maximum temperature and fairly fast cooling (fig. 1a).

Above the A_1 temperature, in the area called the intercrititacal HAZ, a complete transformation of pearlite and a partial transformation of ferrite into austenite occur. Nucleation of new austenite grains causes the structure to be refined in this area. Re-cooling leads to obtaining a microstructure consisting of untransformed ferrite grains of a size similar to that of the base material and a fine-grained ferrite-pearlite microstructure formed from supercooled austenite (Fig. 1b). Reaching a temperature higher than A_3 causes the structure to be completely recrystallized – the transformation of pearlite and ferrite into austenite. As long as the temperature in the area is higher than A_3, the only existing phase is austenite. During cooling, below A_3 level, a pearlite transformation begins, leading to the formation of a ferrite-pearlite structure. If the maximum temperature is not higher than approximately 1000°C, a fine-grained structure is obtained and the area is called the fine grain HAZ (Fig. 1c), whereas if it is higher, a coarse-grained structure is obtained (coarse grain HAZ, Fig. 1d).

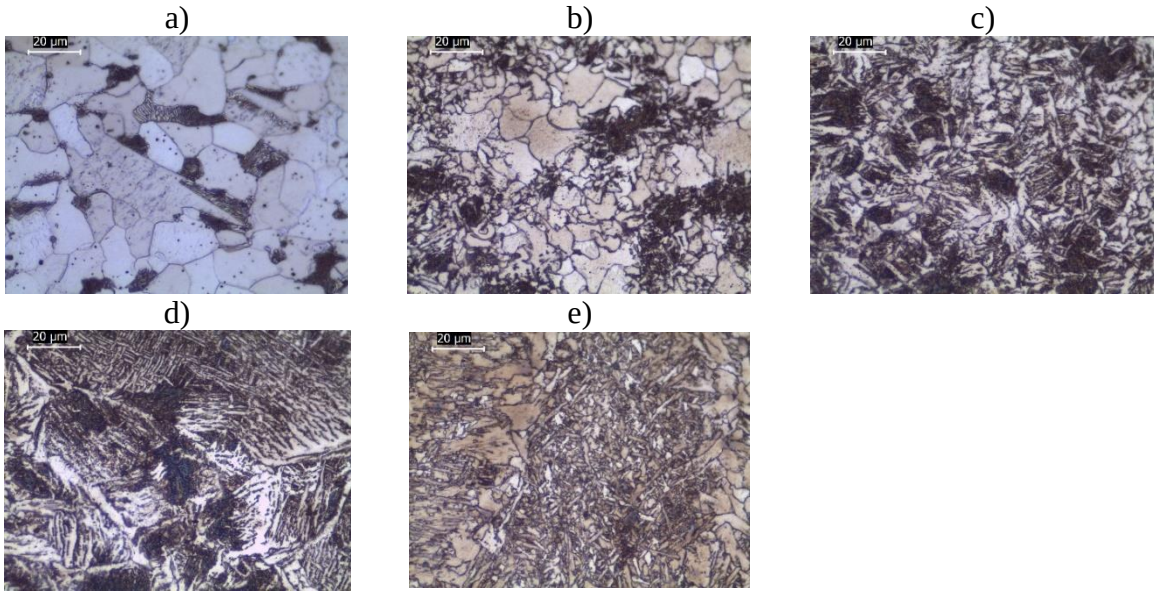

Figure 1. Microstructure of the welded joint of unalloyed steel S235JR in the as-welded condition: a) base material, b) intercritical HAZ, c) fine-grain HAZ, d) coarse-grain HAZ, e) weld metal.

A dendritic structure, characteristic of castings, is observed in the weld metal. The microstructure corresponds to the base material in terms of the obtained phases, but they differ significantly in terms of their morphology. During cooling from the liquid phase, the first nuclei of high-temperature δ-ferrite are formed, which undergo a transformation into austenite during further cooling, and then the austenite transforms into ferrite with pearlite. In this way, a microstructure is obtained with polygonal ferrite on the crystallite boundaries, from which plate ferrite (Widmanstatten) and fine-plate ferrite depart. Fine cementite occurs on the plate boundaries. Nucleation of polygonal ferrite occurs on the austenite grain boundaries when the cooling rate is relatively slow. With slightly faster cooling, the speed of movement of the ferrite grain boundary surfaces decreases, which is why side plates grow from them, growing into the austenite grains. At a higher cooling rate, the share of fine-plate ferrite increases, nucleating inside the austenite grains on small non-metallic inclusions (e.g. oxides). The cooling rate affects the weld microstructure, but consequently also its mechanical properties. An increase in the share of fine-plate ferrite has a positive effect on the impact strength of the weld. The introduction of a higher amount of heat causes a higher share of polygonal and plate ferrite, and the impact strength of the

weld decreases. An example of the microstructure of a welded joint of unalloyed steel S235JR welded by the MAG method with G 42 2 M G2Si wire is shown in Figure 1e.

3. LONG-TERM SUBCRITICAL ANNEALING OF A WELDED JOINT

Fire episodes can have a significant impact on the microstructure and mechanical properties of both steel products and welded joints. Many aspects of the fire should be considered during the analysis, but the greatest impact is the effect of heat (e.g. from the flame). The behaviour during and after the fire should also be taken into account.

If this impact is not large, i.e. it causes heating of elements and welded joints made of unalloyed steel to a temperature below A_1 level and the time of such impact is relatively short, then no significant changes in the microstructure and mechanical properties are observed after the fire. Paradoxically, such an episode may even be beneficial, because after the heat impact the structure becomes relaxed, i.e. the stresses related to welding are removed.

Extending the fire time can lead to serious microstructural changes during the fire, which will also result in changes in the microstructure and mechanical properties in the post-fire state. The main phenomenon responsible for the changes will be the spheroidization of cementite (iron carbide) in pearlite. The microstructure obtained in this process is spheroidite, defined as a characteristic soft microstructure consisting of spherical cementite particles in a ferrite matrix. The spheroidization process diagram is shown in Figure 2. The microstructure of the welded joint of unalloyed S235JR steel welded by the MAG method with G 42 2 M G2Si wire after long-term holding at 600°C (> 4000 h) is shown in Figure 3.

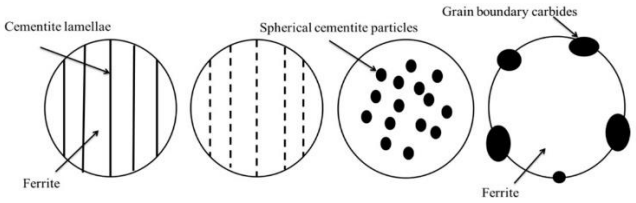

Figure 2. Scheme of spheroidization of cementite in pearlite [4].

The change in the form of cementite leads to a decrease in hardness, which has a direct impact on the change in other mechanical properties. In [5] it has been shown that for unalloyed steel after its 24 hours holding at a temperature of 700°C a decrease in hardness and tensile strength by 10% and an increase in plasticity (elongation) by 12% were observed.

In order to proceed the fastest for the spheroidization process without phase change, it is necessary to approach the temperature A_1 and next hold this temperature for a long time. Heating the considered material to a lower temperature may give the same effect but it will require more time. To calculate the equivalent time, related to an action at a lower temperature, which will give an identical effect to the analogous effect of the same action carried out for a shorter time and at a higher temperature, the Hollomon-Jaffe relationship (1) can be used, extended to include the heating and cooling time t_p (2). This leads to the final equation given in a form (3):

$$H_P = T\big(C + log(t)\big)10^{-3} \tag{1}$$

$$t_P = T\left(2{,}3 \cdot v \cdot \big(20 - log(v)\big)\right)^{-1} \tag{2}$$

$$H_P = T\left(C + log\big(t + t_p\big)\right)10^{-3} \tag{3}$$

in which: H_p – Hollomon-Jaffe parameter, T – temperature (given in Kelvins), t – time (given in seconds), t_p – equivalent heating and cooling time (given in seconds), v – heating or cooling rate

(given in K/h), C – constant value in the range 15-21 (for mild structural steel it is usually assumed to set 19.5) [6]. For example, keeping the material at 700°C for 24 hours will be an equivalent to analogous keeping the same material at 650°C for 345 hours and also its keeping at 600°C for 6750 hours.

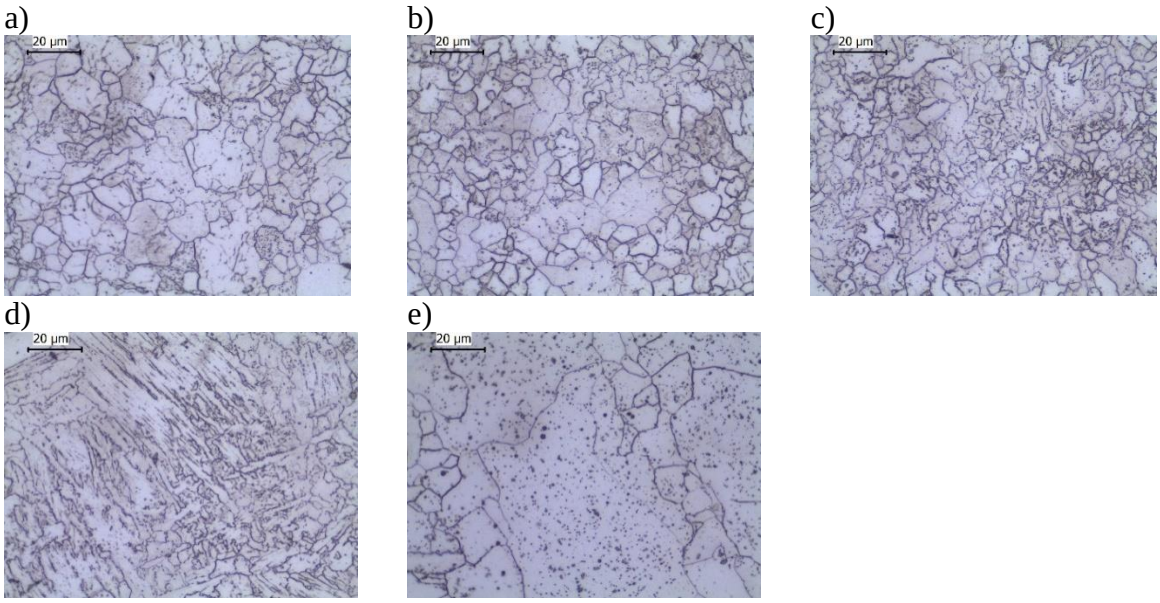

Figure 3. Microstructure of the welded joint made for S235JR unalloyed steel in the as-welded condition after its long-term keeping at constant temperature 600°C: a) base material, b) intercritical HAZ, c) fine-grain HAZ, d) coarse-grain HAZ, e) weld metal.

4. CONCLUSIONS

Knowledge of the original structure of a welded joint made in the welding process is the basis for understanding the subsequent changes occurring in the area of this joint during a fire episode. The features of such joint observed after a fire depend not only on the analogous features identified for it before this fire but also on the scenario of the fire itself. The most important parameters of such scenario seem to be the maximum steel temperature reached during a fire and also the time it was maintained in such conditions. However, the way in which the heated steel was cooled in practice is no less important in this matter. The question is whether the considered joint was cooling slowly during self-extinguishing of a fire or rather it was cooling rapidly in water mist, which usually takes place during the fire-fighting operation.

ACKNOWLEDGEMENTS

This research was funded by National Science Centre, Poland, grant number 2024/53/B/ST11/01331.

REFERENCES

[1] A.H. El Ghor, E.G. Hantouche, Fire Technol., 58 (4) (2022) 1995-2015.
[2] D. Radu, T. Galatanu, S. Sedmak, Eng. Fail. Anal., 106 (2019).
[3] K. Pańcikiewicz, B. Filar, B. Smoleń, Manuf. Lett., 31 (2022) 6-9.
[4] S. Wang, L. Cao, Z. Zhang, Metals, 9 (2019) 1221.
[5] Z. Nasiri, H. Mirzadeh, J. Min. Metall., Sect. B Metall., 55 (2019) 405–411.
[6] E. Tasak, Welding Metallurgy, JAK Editions, Cracow, Poland, 2008.

The 56th International October Conference on Mining and Metallurgy
22-25 October 2025, Bor Lake, Bor, Serbia
www.ioc.tfbor.bg.ac.rs

DOI: 10.5937/IOC25405K Original scientific paper

ANALYSIS OF CRACK FORMATION IN AlSi11 ALLOY AUTOMOTIVE RIM

Franjo Kozina[1a], Zdenka Zovko Brodarac[1b], Ivica Buljeta[2a], Natalija Dolić[1c]

[1]Faculty of Metallurgy, University of Zagreb, Aleja narodnih heroja 3, 44000 Sisak, Croatia
[2]Jajce Alloy Wheels d.o.o., Divičani b.b, 70 101 Jajce, Bosnia and Herzegovina
[1a] fkozin@simet.hr, 0000-0002-3219-7771
[1b] zovko@simet.hr, 0000-0002-7892-2633
[1c] ndolic@simet.hr, 0000-0001-5686-6426
[2a] buljeta_ivicay@hoo.com, 0000-0003-0429-5291

Abstract
When manufacturing components with high safety-critical requirements, integrity and reliability must be guaranteed despite the possibility of systemic or random failures. This is complicated by the fact that any of these failures may be caused by random defects inherent in the manufacturing process or operating conditions. The investigation was performed to determine the cause of a permanent random failure in the form of a crack observed during the manufacture and testing of an AlSi11 automotive rim. By correlating the results of chemical composition analysis, thermodynamic calculations, and metallographic analysis, it was found that the crack nucleated on the previously formed shrinkage porosity and propagated across the non-metallic inclusions, the over-modified eutectic ($\alpha_{Al} + \beta_{Si}$), Al_5FeSi (β) and $Al_8FeMg_3Si_6$ (π) phases with characteristic morphologies.

***Keywords**: safety-critical requirements, automotive rim, AlSi11 alloy, microstructure, failure*

1. INTRODUCTION

Components with high safety-critical requirements must be designed and developed to guarantee integrity, and reliability throughout the entire life cycle of the product [1]. In the automotive industry, safety is defined as freedom from intolerable risk [2] and includes component malfunction, hazardous situations, the risk of damage or harm and the required risk reduction based on an acceptable level of risk. The severity of the safety requirements assigned to a component or system is defined by the Automotive Safety Integrity Levels (ASIL) and aims to prevent system failures [3]. The identification of hazardous components and the allocation of appropriate ASILs ensures both the intrinsic and functional safety of critical systems without imposing unnecessarily stringent safety-critical requirements on all components [4]. While intrinsic safety ensures that components or systems are designed to minimize the risk of accidents [5], functional safety guarantees that critical systems continue to function even in the event of systemic or random failures. Process-related problems that require changes in design, development, manufacture, operating procedures or documentation are classified as systemic failures. They are usually foreseeable and typically affect multiple units or models of vehicles [4]. Random failures, also known as permanent or transient faults, are caused by random defects innate to the manufacturing process or operating conditions. The main difference between these two types of random failures is that a transient fault is likely to be resolved after a system reset or a change in operating conditions, while a permanent fault is associated with long-term damage that requires physical repair or component replacement [6]. In this study, the permanent random failure in the form of a crack observed during the manufacturing and testing of AlSi11 automotive rim is analyzed. Although the mechanical properties that comply with the standard [7] were achieved, additional tests were performed on the casting to determine the mechanism of crack formation.

2. EXPERIMENTAL

The crack was detected during a radial fatigue test simulating the dynamic load on the wheel when cornering. The crack formed in the hotspot area nucleating on the internal surface of the central

cap and propagated towards the inner part of the spoke (Figure 1). As two parts of the rim with different geometries were affected, the investigated area was cut into two parts (Figure 1; positions 1 and 2), with three different positions for testing (Figure 1; positions A, B, C).

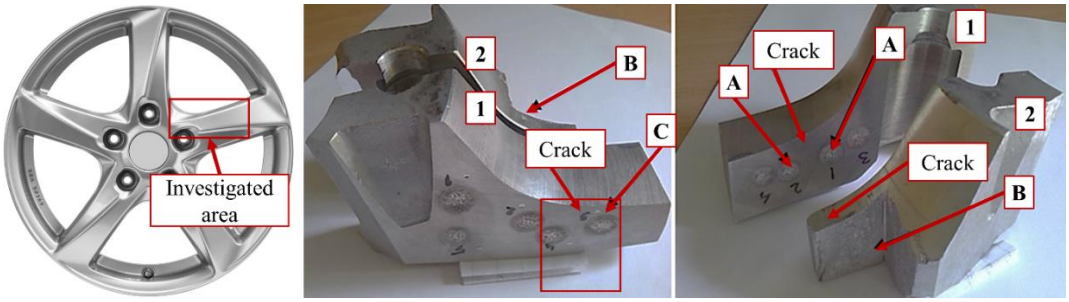

Figure 1. Sampling in the investigated area with the indicated positions for testing (A, B, C)

Since the hotspot is characterized by a lower cooling rate and is the last to solidify, the chemical composition at all three positions (Figure 1; positions A, B, C) was measured spectroscopically using the Thermo Scientific ARL 3460 Metals Analyzer. The analysis of the chemical composition was not only important to verify compliance within the range for EN AC AlSi11 alloy indicated in standard [7] but also served as an input parameter for the calculation of the non-equilibrium solidification sequence. The thermodynamic calculations performed by CALPHAD method using Themo-Calc 2022a TCAL9 technical sheet for aluminum, were based on the classical Scheil-Gulliver model and were calculated in the temperature range from 20.0 °C to 750.0 °C at a default pressure of 100 00.0 Pa for 1.0 g of the melt. The sample for metallographic analysis was cut from the central part of the hotspot (Figure 1, position B), perpendicular to the crack, and prepared using standard metallographic preparation techniques. The sample was then etched for approximately 5 s in a 0.5% aqueous solution of hydrofluoric acid. Light microscopy was performed using an Olympus GX51 inverted metallographic microscope equipped with a DP70 digital camera and AnalySIS Materials ResearchLab software. Electron microscopy was performed using a Tescan, Vega TS 5136 MM scanning electron microscope in combination with a Bruker energy dispersive spectrometer (EDS). The distribution of the elements within the individual microstructural components was determined by point analysis. Based on the research results, the influence of the microstructure on the mechanism of crack formation and propagation will be determined.

3. RESULTS AND DISCUSSION

The chemical composition of the investigated area is shown in Table 1.

Table 1. The mean value and standard deviation of chemical composition measurements at the positions A, B and C (Figure 1)

Chemical composition, wt.%	Si	Fe	Mn	Mg	Sr	Al
Mean value	10.89	0.107	0.002	0.194	0.037	balance
EN AC AlSi11 [7]	10.5-11.8	≤0.15	≤0.05	/	0.025-0.05	balance

The chemical composition corresponds to the values for the EN AC AlSi11 alloy (Table 1) prescribed by standard [7]. The hypoeutectic Si content indicates that the microstructure development will begin with the solidification of the primary α_{Al} dendrites, followed by the eutectic reaction and the solidification of the (α_{Al} + β_{Si}) eutectic phase. The amount of Sr (Table 1) is nominally sufficient to fully modify the (α_{Al} + β_{Si}) eutectic phase and achieve fiber morphology. An unfavorable Mn/Fe of 0.02 along with low cooling rate due to the section thickness can lead to the preferred precipitation of an Al_5FeSi (β) phase with a needle-like morphology.

The invariant reactions of the non-equilibrium solidification sequence are given in Table 2. The solidification sequence begins with the development of the primary α_{Al} dendrites (Table 2, reaction

1) followed by the solidification of the eutectic (α_{Al} + β_{Si}) (Table 2, reaction 2). Solidification of the Al_2Si_2Sr phase (Table 2, reaction 3) points to the addition of the excess amount of modifier during melt processing causing the over-modification of the eutectic (α_{Al} + β_{Si}) and negatively affecting the mechanical properties. Due to their coarse, brittle and angular morphology, the Al_5FeSi (β) phase particles (Table 2, reaction 4) enable local stress concentration and formation of microcracks. The negative effect of Al_5FeSi (β) phase is partially reduced by the solidification of $Al_8FeMg_3Si_6$ (π) phase (Table 2, reaction 5) which has a compact morphology and solidifies at the grain boundaries [8]. The non-equilibrium solidification ends with the formation of Mg_2Si phase (Table 2, reaction 6).

Table 2. The invariant reactions of the non-equilibrium solidification sequence

Reaction No.	Reaction	Temperature, °C
1.	LIQUID (L) + FCC_A1 (α_{Al})	588.4
2.	L + DIAMOND_A4 + FCC_A1 (α_{Al} + β_{Si})	576.3
3.	L+ AL2SI2SR (Al_2Si_2Sr) + (α_{Al} + β_{Si})	573.4
4.	L + Al_2Si_2Sr + (α_{Al} + β_{Si}) + AL9FE2SI2 (Al_5FeSi (β))	570.7
5.	L+ Al_2Si_2Sr + (α_{Al} + β_{Si}) + AL18FE2MG7SI10 ($Al_8FeMg_3Si_6$ (π))	558.7
6.	L + Al_2Si_2Sr + (α_{Al} + β_{Si}) + π-$Al_8FeMg_3Si_6$ + MG2SI_C1 (Mg_2Si)	557.6

The microstructure at the crack root is given in Figures 2 a – 2 c, while the scanning electron images (SEI) of microstructural constituents affecting the crack propagation are shown in Figures 2 d – 2 e. The results of EDS analysis performed on the indicated positions (Figure 2 d to e) are shown in Table 2.

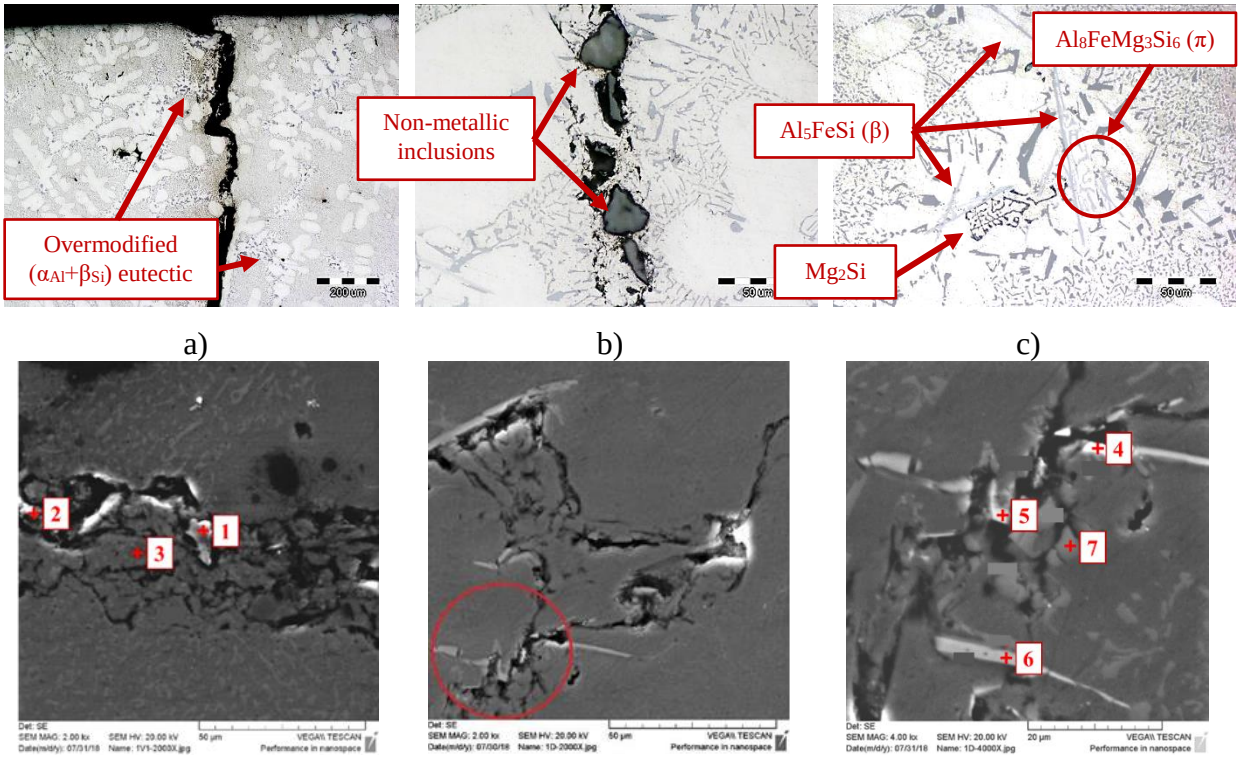

Figure 2. The microstructure at the crack root (a, b, c) and SEI of microstructural constituents affecting the crack propagation (d, e, f)

The microstructure of the sample in the investigated area consists of the primary α_{Al} dendrites and the eutectic (α_{Al} + β_{Si}) (Figure 2). In addition to the fibrous morphology, an over-modified eutectic (α_{Al} + β_{Si}) in acicular morphology can be observed at the grain boundaries (Figure 2 a), followed

by solidification of $Al_8FeMg_3Si_6$ (π) and Mg_2Si phases. The Al_5FeSi (β) phase is found between the branches of primary α_{Al} dendrites (Figure 2 c). The local stress concentration during the radial fatigue test allowed crack propagation via non-metallic inclusions (Figure 2 b) and intermetallic phases at the grain boundaries (Figure 2 c). The results of SEM and EDS analysis confirmed the involvement of non-metallic inclusions of the alumino-silicate type (Figure 2 d, Table 3, positions 1 and 2), over-modified eutectic (α_{Al} + β_{Si}) (Figure 2 f, Table 3, positions 6), Al_5FeSi (β) and $Al_8FeMg_3Si_6$ (π) phase (Figure 2 f, Table 3, positions 4, 5 and 7).

Table 3. Results of energy dispersive spectroscopy performed at the locations marked on Figure 3

Location	Chemical composition, mass. %				
	Al	Si	Mg	Fe	Mn
1	1.71	96.14	0.74	0.37	0.31
2	4.38	93.60	0.92	0.40	0.31
3	74.11	24.22	1.01	0.30	0.18
4	61.58	13.71	2.21	24.00	2.16
5	60.67	12.95	3.34	22.57	3.43
6	11.92	86.64	0.21	0.36	0.70
7	65.11	12.12	2.36	23.23	0.32

4. CONCLUSION

This research was performed to determine the cause of permanent random failure in the form of a crack that was observed during production and testing of the AlSi11 automotive rim. The chemical composition is in accordance with HRN EN 1706:2021 for investigated alloy. The results of the non-equilibrium solidification sequence indicated development of primary α_{Al} dendrites followed by the solidification of the eutectic (α_{Al} + β_{Si}), Al_2Si_2Sr, Al_5FeSi (β), $Al_8FeMg_3Si_6$ (π) and Mg_2Si phases. The solidification of Al_2Si_2Sr phase pointed to the excess amount of modifier and over-modification of the eutectic (α_{Al} + β_{Si}). The crack nucleation occurred on the grain boundaries and propagated across the non-metallic inclusions, over-modified eutectic (α_{Al} + β_{Si}), Al_5FeSi (β) and Al_8FeMg_3Si6 (π) phase.

ACKNOWLEDGEMENTS

The investigation was performed within the research topic "Design and Characterization of Innovative Engineering Alloys", Code: FPI-124- ZZB funded by University of Zagreb within the Framework of Financial Support of Research and Infrastructural scientific projects: Center for Foundry Technology, Code: KK.01.1.1.02.0020 and VIRTULAB - Integrated Laboratory for Primary and Secondary Raw Materials, Code: KK.01.1.1.02.0022 funded by European Regional Development Fund, Operational Programme Competitiveness and Cohesion 2014 - 2020

REFERENCES

[1] D.J. Thomas, J. Fail. Anal. Prev., 17 (1) (2017) 1–3
[2] ISO 26262-1:2018 Road vehicles — Functional safety (2020).
[3] Y. Gheraibia, S. Kabir, K. Djafri, H. Krimou, J. Fail. Anal. Prev., 18 (3) (2018) 707–720.
[4] P. Okoh, T. Myklebust, Saf. Reliab., 43 (2) (2024) 114–130.
[5] M. V. Kapitonov, Transp. Res. Procedia, 61 (2022) 556–560.
[6] A.C. Bagbaba, F.A. da Silva, M.S. Reorda, S. Hamdioui, M. Jenihhin, C. Sauer, Electron., 11 (3) (2022) 1–26.
[7] HRN EN 1706:2021 Aluminum and aluminum alloys – Castings – Chemical composition and mechanical properties (EN 1706:2020+A1:2021)
[8] H.H. Xi, J.J. Xu, X. Yuan, W.Q. Ming, Z. Zhang, J.H. Chen, Mater. Charact., 199 (2023) 112839

The 56th International October Conference on Mining and Metallurgy
22-25 October 2025, Bor Lake, Bor, Serbia
www.ioc.tfbor.bg.ac.rs

DOI: 10.5937/IOC25409T *Review paper*

CARBON-BASED ELECTROCHEMICAL SENSORS MODIFIED WITH METAL OXIDE NANOPARTICLES

Žaklina Tasić[1a], Marija Petrović Mihajlović[1b], Ana Simonović[1c], Milan Radovanović[1d], Milan Antonijević[1e]

[1] Technical Faculty Bor, University of Belgrade, V.J. 12, 19210 Bor, Serbia
[1a] ztasic@tfbor.bg.ac.rs, 0000-0001-6544-1980
[1b] mpetrovic@tfbor.bg.ac.rs, 0000-0001-5486-3870
[1c] asimonovic@tfbor.bg.ac.rs, 0000-0003-2392-0048
[1d] mradovanovic@tfbor.bg.ac.rs, 0000-0002-5175-6022
[1e] mantonijevic@tfbor.bg.ac.rs, 0000-0002-2201-066X

Abstract
Carbon-based electrochemical sensors are of great importance in analytical chemistry due to their high conductivity, chemical stability and cost-effectiveness. They are widely used for the detection of various analytes, including heavy metals, biomolecules and pharmaceutical compounds. Since the electrochemical sensors can be easily modified with different materials to improve their sensitivity and selectivity, they offer advantages over other traditional analytical techniques. Among these modifiers, metal oxide nanoparticles are of particular importance due to their large surface area, catalytic activity and good electrochemical properties. Their incorporation into carbon electrodes improves detection limits, reproducibility and stability, making them very effective for advanced sensing applications.

Keywords*: carbon paste electrode, electrochemical sensors, metal oxide nanoparticles, electrochemical methods*

1. INTRODUCTION

Various analytical methods can be used to determine and quantify different target analytes, including high-performance liquid chromatography or spectrophotometric methods. However, electrochemical methods are attracting increasing attention from researchers as they provide rapid results, are easy to handle and are cost-effective compared to analytical methods. In addition, electrochemical methods have good sensitivity to the target analyte and the ability to modify the electrode surface can also offer some notable advantages in electrochemical reactions [1,2]. Electrochemical sensors enable the highly sensitive detection of various analytes, including biomolecules, pharmaceutical substances and environmental pollutants [3]. Due to the low background current and the good electrical conductivity, electrochemical activity and porous structure, carbon paste electrodes (CPEs) can be used for the determination of these compounds [4]. In addition, the carbon paste electrodes are inexpensive and easy to manufacture, they work in wide potential window and offer flexibility in optimizing the composition of the paste, which can improve the sensitivity and selectivity of the sensor [5,6,7]. This article provides a brief overview of the literature in which modified CPEs have proven successful for the detection and determination of various target analytes.

2. MODIFIED CARBON-BASED SENSORS

CPEs can be modified with various materials to improve their sensitivity, selectivity and stability. The most commonly used modifiers include polymers, enzymes, complex metal ligands and metal oxide nanoparticles. Metal oxide nanoparticles such as ZnO, TiO_2, Fe_3O_4 and CeO_2 are particularly important as they have a large surface area, good conductivity and catalytic activity, making them ideal for improving the electrochemical performance of sensors [2,8,9]. According

to Parvin et al. [4], metal nanoparticles improve the detection limit of the target analyte and facilitate electron transfer. Compared to organic modifiers, nanoparticles of metal oxides are more resistant to chemical changes under aggressive conditions, enable higher adsorption of analytes and better electrochemical activity [8]. Various techniques such as electropolymerization, physical adsorption, covalent bonding and electrodeposition can be used to modify the sensor surface with metal oxide nanoparticles [10].

Farhan et al. [11] and Zoubir et al. [12] developed a CPE sensors modified with ZnO nanoparticles (ZnO NPs) and tested them for the determination of difloxacin HCl and hydroxychloroquine, respectively. Both research groups came to the conclusion that the ZnO nanoparticles improve the active surface of the electrode and provide more catalytically active sites as well as contribute to a better electron transfer compared to the unmodified CPE. The results obtained are shown in Table 1. In addition to ZnO NPs, Fe_2O_3 and CuO NPs were also used as modifiers for CPE and the resulting sensor was tested for the determination of paracetamol (PA) and dopamine (DA) [13] as well as for guanine, adenine and thymine [14]. By comparing the cyclic voltammetry curves of PA and DA (Figure 1) in phosphate buffer solution at the bare carbon paste electrode (BCPE) and at the iron oxide modified carbon paste electrode (IOCPE), enhanced anodic and cathodic peaks were observed for both PA and DA at the IOCPE. This behavior indicates the catalytic effect of Fe_2O_3 NPs. After 120 days, the experiments were repeated and the developed IOCPE showed good stability and sensitivity to PA and DA [13].

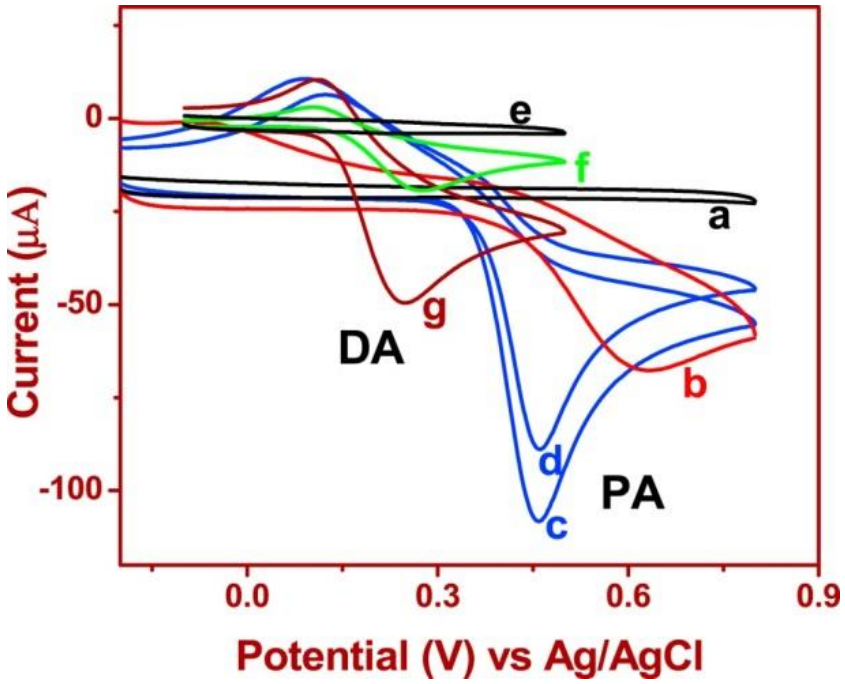

Figure 1. CV's of: (a) and (e) buffer at IOCPE; 1 mM PA at (b) BCPE; (c) and (d) IOCPE; and 1 mM DA at (f) BCPE; (g) IOCPE at scan rate of 100 mV s^{-1} ((d), (e), (f) and (g) obtained at IOCPE after 120 days). Reprinted from [13]

Nano-cobalt (II,III) oxide was also used as a modifier for CPE and the sensor thus developed was tested for the determination of caffeine in 0.01M H_2SO_4 in the presence of sodium dodecyl sulfate (NCOMCPE/SDS) [1]. The detection limit obtained for caffeine is shown in Table 1. The authors indicated that SDS was adsorbed on the NCOMCPE surface due to hydrophobic interactions between the SDS molecules and the hydrophobic binder in the carbon paste, resulting in a threefold higher sensitivity for caffeine. It was also found that the best electrocatalytic activity for caffeine oxidation was observed in highly acidic solutions (pH 0.75) and electron transfer was faster than in media with higher pH values. Apart from metal oxide nanoparticles, Mahanthappa et al. [16]

synthesised CuS nanoparticles by co-precipitation and used them as a modifier for CPE. The resulting CuS NPs MCPE was used for the determination of caffeine in acetate buffer solution. The authors concluded that the applied modifier contributed to the shift of the caffeine oxidation potential towards a negative value compared to the bare CPE and that the oxidation peak was improved. The detection limit obtained is shown in Table 1.

Table 1 - Modified carbon paste electrode as electrochemical sensor for determination of different target analytes

Modifier	Target analyte	Medium	Electrochemical method	Concentration range	LOD	Real sample	Ref
Nano-cobalt (II,III) oxide	Caffeine	0.01M H_2SO_4 in the presence of SDS	DPV	5.0– 600 μM	0.016 μM	Commercial samples	[1]
ZnO NPs	Difloxacin HCl	/	Potentiometric titration	6.3×10^{-6}–10^{-2} M	6.3×10^{-6} M	Pharmaceuticals formulation	[11]
ZnO NPs	Hydroxychloroquine	PBS pH 7.0	SWV	1×10^{-3} – 0.8×10^{-6} M	1.33×10^{-7} M	Human urine and pharmaceutical samples	[12]
Fe_2O_3 NPs	Paracetamol	0.1M PBS pH 7.0	DPV	2–150 μM	1.16 μM	Pharmaceutical samples	[13]
	Dopamine		SWV	2–170 μM	0.79 μM		
CuO NPs	Guanine	PBS	DPV	1–80 μM	0.687 μM	/	[14]
	Adenine			1–80 μM	0.472 μM		
	Thymine			1–210 μM	0.111 μM		
TiO_2/Fe_3O_4/MWCNTs nanocomposite	Morphine	PBS pH 7.0	SWV	2.5×10^{-8} – 6.0×10^{-4} M	1.5×10^{-8} M	Urine and pharmaceutical samples	[15]
CuS NPs	Caffeine	0.1 M ABS pH 7.0	DPV	2–120 μM	0.0186 μM	Commercial tea and coffee samples	[16]

LOD – limit of detection; SWV – square wave voltammetry; DPV – differential pulse voltammetry, PBS – phosphate buffer solution, ABS – acetate buffer solution, / – no data.

According to the results in Table 1, the prepared modified CPEs were successfully used for the determination of compounds of interest in various real samples with acceptable recoveries. In addition, the effect of interference on modified sensors has been studied by adding different ions such as Na^+, K^+, Li^+, Ca^{2+}, Ba^{2+}, Mg^{2+}, Cl^-, Br^-, SCN^-, NO_3^-, ClO_4^-, SO_4^{2-} and sugars such as glucose, fructose and sucrose [13,15,16]. The results obtained in these studies show that interferences have no influence on the current peak and the potential peak of the target analytes.

3. CONCLUSIONS

Carbon-based electrochemical sensors are important tools for testing various compounds such as nucleic acids and pharamceutical compounds in different media. The importance of metal oxide nanoparticles for the development of electrochemical sensors is also presented in this article. Various research groups have shown that ZnO, Fe_2O_3 and Co(II, III) oxide nanoparticles can be successfully used as modifiers for CPE. The developed sensors have proven their applicability in various media including acidic aqueous solutions (pH 0.75) and buffered media (phosphate and acetate buffer solutions). It has been shown that the use of these nanoparticles as modifiers enables fast electron transfer and more sensitive determination of the target analytes due to their catalytic effect and the larger surface area of the modified electrodes.

ACKNOWLEDGEMENTS

The research presented in this paper was done with the financial support of the Ministry of Science, Technological Development and Innovation of the Republic of Serbia, within the funding of the scientific research work at the University of Belgrade, Technical Faculty in Bor, according to the contract with registration number 451-03-137/2025-03/200131.

REFERENCES

[1] A.M. Fekry, M. Shehata, S.M. Azab, A. Walcarius., Sensor. Actuat. B- Chem., 302 (2020) 127172.
[2] E. Molaakbari, A. Mostafavi, H. Beitollahi., Sensor. Actuat. B- Chem., 208 (2015) 195-203.
[3] Q. He, B. Wang, J. Liang, J. Liu, B. Liang, G. Li, Y. Long, G. Zhang, H. Liu., Mater. Today Adv., 17 (2023) 100340.
[4] M.H. Parvin, M.B. Golivand, M. Najafi, S.M. Shariaty, J. Electroanal. Chem., 683 (2012) 31-36.
[5] I. Svancara, K. Vytras, K. Kalcher, A. Walcarius, J. Wang, Electroanalysis, 21 (2009) 7-28.
[6] X. Zuo, B. He, D. Li, Sensor. Actuat. B- Chem., 284 (2019) 216-229.
[7] Ľ. Švorc, M. Rievaj, D. Bustin, Microchem. J., 108 (2013) 112-119.
[8] M. Arvanda, R.M. Mazhabi, A. Niazi, Electrochim. Acta, 89 (2013) 669-679.
[9] A. Yildirim, M. Maral, B.T. Zaman, A. Bozoglu, C. Demir, S. Bakırdere, A. Erdem, J. Electroanal. Chem., 965 (2024) 118345.
[10] A.S. Agnihotri, A. Varghese, N. M, Applied Surface Science Advances, 4 (2021) 100072.
[11] M.K. Farhan, N.S. Ismail, M.H. Tamam, M.S. Abdel-Mottaleb, M. Saif, J. Solid State Electrochem., 28 (2024) 33-48.
[12] J. Zoubir, I. Bakas, S. Qourzal, M. Tamimi, A. Assabbane, J. Appl. Electrochem., 53 (2023) 1279-1294.
[13] M.M. Vinay, Y. Arthoba Nayaka, JS: AMD, 4 (3) (2019) 442-450.
[14] K.S. Siddegowda, B. Mahesh, N. Kumara Swamy, Sensor Actuat. A-Phys., 280 (2018) 277-286.
[15] E.D. Razmi, H. Beitollahi, M.T. Mahani, M. Anjomshoa, Russ. J. Electrochem., 54 (12) (2018) 1132-1140.
[16] M. Mahanthappa, S. Yellappa, N. Kottam, C.S. Rao Vusa, Sensor Actuat. A-Phys., 248 (2016) 104-113.

The 56th International October Conference on Mining and Metallurgy
22-25 October 2025, Bor Lake, Bor, Serbia
www.ioc.tfbor.bg.ac.rs

DOI: 10.5937/IOC25413G *Original scientific paper*

TESTING THE IMPACT TOUGHNESS OF THE WELDED JOINT OF STEEL S21800

Almaida Gigović-Gekić[1a], Elvis Agović[1b], Hasan Avdušinović[1c], Branka Muminović[2a]

[1] Faculty of Engineering and Natural Science, University of Zenica, Travnička cesta 1, 72000 Zenica, Bosnia and Herzegovina
[2] Institute "Kemal Kapetanović", University of Zenica, Travnička cesta 7, 72000 Zenica, Bosnia and Herzegovina
[1a] almaida.gigovic-gekic@unze.ba, 0009-0005-7938-520X
[1b] agovic.elvis20@gmail.com , 0009-0005-4823-197X
[1c] hasan.avdusinovic@unze.ba, 0009-0004-0923-4732
[2a] branka.muminovic66@gmail.com, 0009-0002-7432-7156

Abstract
Steel S21800 is an austenitic stainless steel with higher mechanical strength than 316 stainless steel, as well as excellent resistance to corrosion, galling, and wear. Thanks to its specific chemical composition — including elevated levels of manganese, silicon, and nitrogen — this material is increasingly used in industrial applications that demand high reliability and resistance to both mechanical and chemical aggression. Welding such a material requires special attention, as the alloying elements can influence the microstructure and, consequently, the mechanical properties, particularly impact toughness. In this study, the weldability of S21800 steel was evaluated using the TIG welding method, with a focus on assessing the impact toughness of the welded joint. Testing was performed on two types of samples with different chemical compositions. The research included metallographic analysis and impact toughness testing using the Charpy method, targeting the heat-affected zone (HAZ) and the weld metal (WM). The results showed that the chemical composition of both base and filler materials, along with the welding method, plays a crucial role in determining joint quality. The observed differences in toughness between the WM and the HAZ were attributed to variations in delta ferrite content.

***Keywords**: austenitic steel, weldability, delta ferrite, impact toughness*

1. INTRODUCTION

UNS S21800 is an austenitic stainless steel specifically designed to offer enhanced wear and galling resistance. It is a nitrogen-strengthened alloy, with increased levels of silicon and manganese. These additions improve its wear resistance and mechanical strength without compromising corrosion resistance at ambient and elevated temperatures. This steel offers better corrosion resistance than type 304 and is nearly comparable to type 316 in many environments, including marine and chloride-exposed conditions. Because of its unique combination of strength, galling resistance and corrosion behavior steel S21800 is used in: automotive valves, fastener galling, pins and marine shafts [1]. In this work, the weldability of S21800 steel was tested with an emphasis on the evaluation of the impact toughness of the welded joint. In order for the weldability of a material to be satisfactory, it is necessary to find the most adequate type of welding and the conditions in which welding will be performed. Weldability of a steel depends on the type of the material (chemical composition, microstructure...), filler material and welding process. Austenitic stainless steels are weldable and can be joined using all fusion and resistance welding processes. The TIG method is the most commonly used welding technique for stainless steels and is therefore considered suitable for this study [2,3].

2. EXPERIMENTAL

The welding process was performed on steel samples with a diameter of 15 mm which have different delta ferrite contents in their initial microstructure. The chemical composition of S21800

steel, according to the ASTM A276 standard [4], along with the delta ferrite content of the tested samples, is given in Table 1. The Ferritoscope MP30E, manufactured by Helmut Fischer GmbH, was used to determine the delta ferrite content. According to the literature [5], for steels used at elevated temperatures and under high stress, such as S21800, it is recommended that the delta ferrite content does not exceed 3%.

Table 1. Chemical composition and the content of delta ferrite for the steel S21800

Standard/ Melts	Chemical composition (wt. %)								Average content of delta ferrite for base metal (%)	Average content of delta ferrite for weld metal (%)
	C	Si	Mn	Cr	Ni	P	S	N		
ASTM A276	≤0.10	3.4-4.5	7-9	16-18	8-9	≤0.006	≤0.03	0.08-0.18		
No.1	0.05	4.5	8.6	16	8	0.007	0.016	0.147	1.95	5.5
No.2	0.05	3.8	8.9	17	9	0.007	0.005	0.161	0.12	2.4

The standard electric arc welding process – TIG in a protective argon atmosphere – was used for welding. The welding conditions were the same for all samples (current strength: 70–80 A, wire feed rate: 0.5 m/min, gas flow rate: 10 l/min), and 316L AISI stainless steel [6] was used as a filler metal. The metal pieces were welded using butt welding, a process in which two pieces of metal are placed end-to-end without overlap and then welded. The impact toughness test was conducted according to the ISO 148 – 1 standard using the Charpy method, targeting the heat-affected zone (HAZ) and the weld metal (WM) [7]. It is important to determine the fracture location and analyze the fracture surface to see if any irregularities are present. Microstructure of the samples are austenitic with the particles of chromium carbides and delta ferrite. The presence of the sigma phase on delta ferrite islands is visible in the base material as well as in the heat affected zone and weld metal. The microstructure of the weld metal is a cast microstructure, Figure 1 [8].

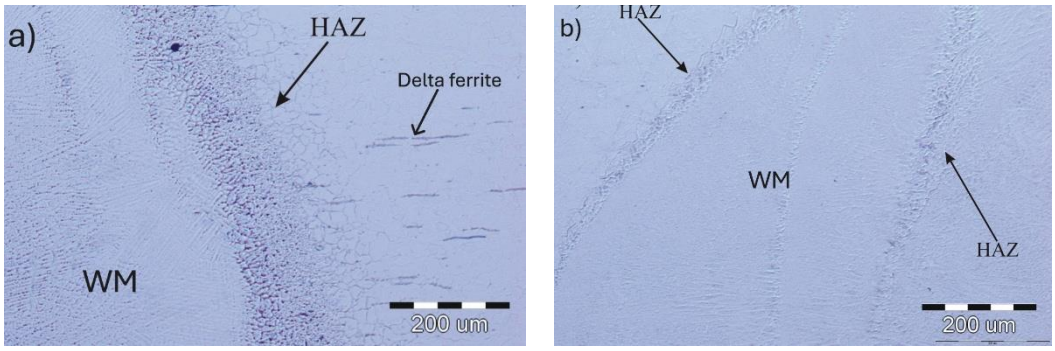

Figure 1. Microstructure of the welded joints: a) sample No1 and b) sample No2 [8]

3. RESULTS AND DISCUSSION

The results of the Charpy pendulum impact test are given in Figure 2. The tests were conducted on three samples for each test and the average absorbed energy value is shown in the figure. can be seen, the highest absorbed energy has sample No2 with a notch in the HAZ. Sample No1 with the same notch location has a much lower absorbed energy, which is influenced by the microstructure. The microstructure in this zone is austenitic but with much more precipitated delta ferrite, carbide and sigma phase [8].

Delta ferrite represents the place where carbide and sigma phase precipitation occurs, Figure3. The absorbed energy value in WM is similar, which was influenced by the welding method. Complete penetration did not occur at the welded joint location for both samples, Figures 4 and 5. According to EN ISO 5817, an imperfection in the form of lack of penetration (402) in a butt joint (partial penetration) is classified as a short imperfection [9].

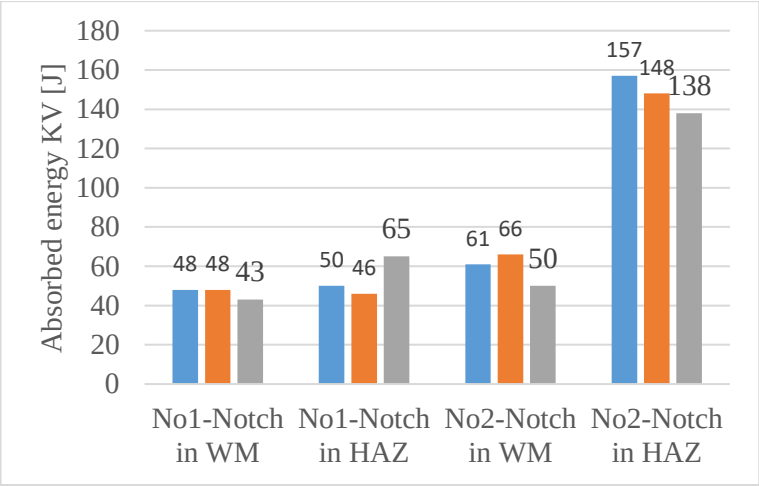

Figure 2. The results of the Charpy pendulum impact test

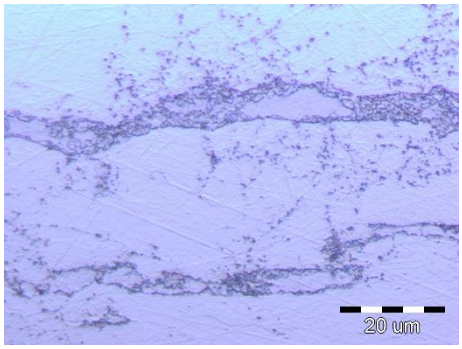

Figure 3. Delta ferrite with precipitated carbides and sigma phase

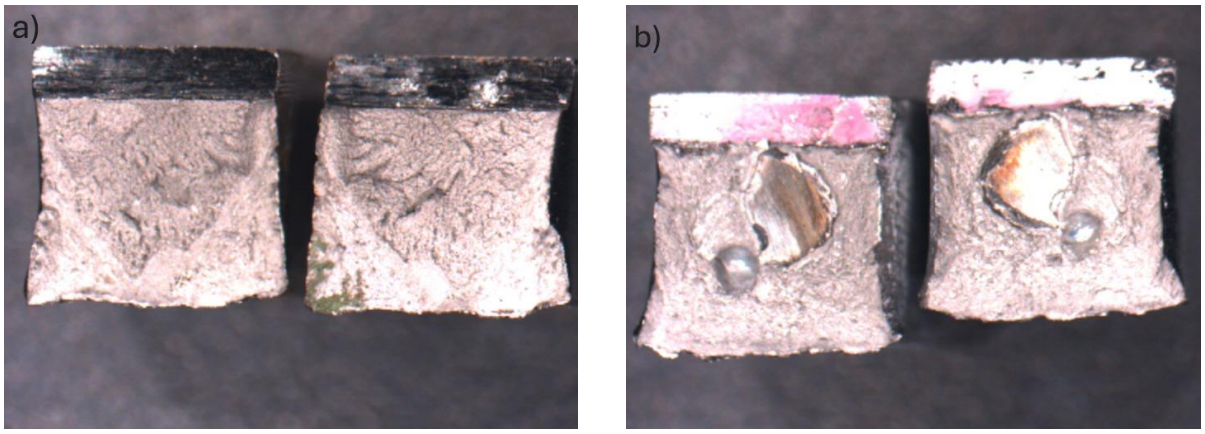

Figure 4. The surface fracture of the No1 sample: a) with a notch in the HAZ and b) with a notch in the WM, 6.3x

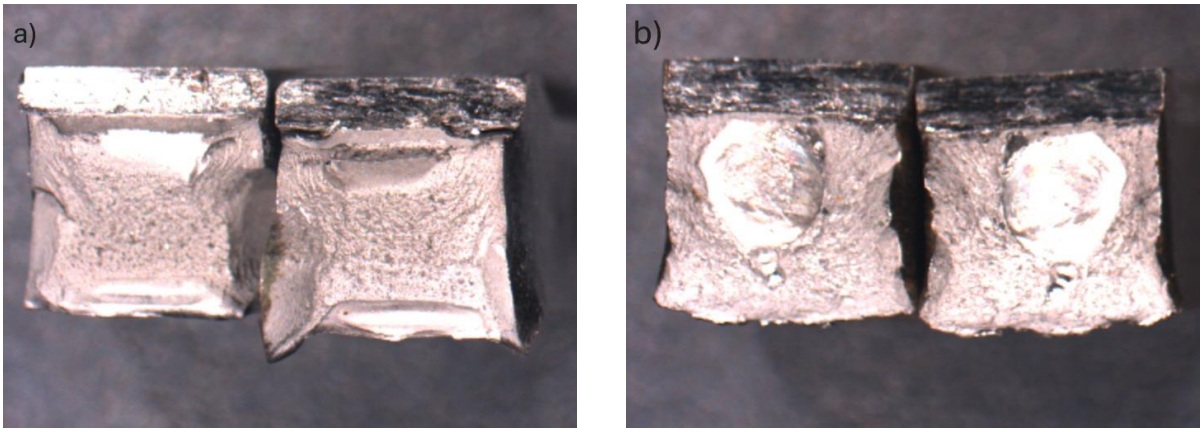

Figure 5. The surface fracture of the No2 sample: a) with a notch in the HAZ and b) with a notch in the WM, 6.3x

4. CONCLUSION

The results of the Charpy pendulum impact test for the sample No1 are generally worse than the results for the No2. It can be concluded that with an increase in the delta ferrite content and the presence of the sigma phase and carbides, the toughness of steel S21800 decreases. Carbides and sigma phase usually participate on the delta ferrite. Fracture analysis showed that brittle fracture dominates in the No1 sample, while in the case of the No2 samples, it is a ductile fracture, especially in the heat-affected zone. When analyzing the fracture surface, it was found that during welding, complete fusion of the metal in the weld metal did not occur, which had a negative impact on the mechanical properties of the welded joints.

REFERENCES

[1] https://www.hpalloy.com/Alloys/descriptions/NITRONIC60.aspx?utm_source (20.06.2025.)
[2] Dž. Hadžihafizović, Welding of Stainless Steel, Sarajevo 2024. Available online: https://www.researchgate.net/publication/375343015_Welding_of_Stainless_Steel (05.04.2024)
[3] E. Agović, Ispitivanje zavarljivosti čelika Nitronic 60, Master thesis, University of Zenica, Faculty of Metallurgy and Technology, Zenica, 2022.
[4] Standard ASTM A276
[5] P. Pavlović, Materijal čelik, SKTH/Kemija u industriji, Zagreb, 1990
[6] Elektroda-Zagreb-Katalog. Available online: https://ezg.hr/https-ezg-hr-wp-content-uploads-2024-03-elektroda-zagreb-katalog-2022-hrv-compressed-1-pdf/ (10.04.2024)
[7] Standard ISO 148 – 1: 2016
[8] A. Gigović-Gekić, E. Agović, B. Fakić, H. Avdušinović, Proceedings of the 54th International October Conference on Mining and Metallurgy, October 18th – 21th, Bor Lake, Serbia, 2023
[9] Standard EN ISO 5817:2023

The 56th International October Conference on Mining and Metallurgy
22-25 October 2025, Bor Lake, Bor, Serbia
www.ioc.tfbor.bg.ac.rs

DOI: 10.5937/IOC25417L *Review paper*

TEM INVESTIGATION OF Cu-10Al-7Ag SHAPE MEMORY ALLOY IN AS-CAST STATE

Lovro Liverić[1a], Tamara Holjevac Grgurić[2a], Marko Kršulja[1c], Matej Fonović[3a],

[1] Faculty of Engineering, Jurja Dobrile University of Pula, Nergrijeva ulica 6, 52100 Pula, Croatia
[2] Faculty of Engineering, Catholic University of Croatia, Ilica 242, 10 000 Zagreb, Croatia
[3] Faculty of Engineering, University of Rijeka, Vukovarska ulica 58, 51000 Rijeka, Croatia
[1a] lovro.liveric@unipu.hr, 0000-0001-8714-6771
[2a] tamara.grguric@unicath.hr, 0000-0002-2973-2200
[1b] marko.krsulja@unipu.hr, 0000-0003-0823-8083
[3a] matej.fonovic@uniri.hr, 0000-0001-7334-7089

Abstract

Shape memory alloys (SMAs) are smart materials that exhibit thermoelastic martensitic transformations so that they can return to their original shape when heated or relieved. While NiTi is still the most commonly used SMA, copper-based SMAs have gained attention due to their cost-effectiveness and good functional properties. In this study, the as-cast microstructure of a Cu-10Al-7Ag SMA alloy is investigated by transmission electron microscopy (TEM). The addition of silver as a microalloying element is of particular interest due to its limited solubility in the β-phase and its potential influence on phase stability and transformation behavior. TEM analysis revealed the presence of fine martensitic structures and potential nanoscale precipitates that could play a role in transformation temperatures and mechanical behavior. The analyzes confirmed the presence of martensitic structures; mainly the 18R (β_1') martensite phase. The results are discussed in the context of phase evolution from the high-temperature β phase and the influence of Ag on the suppression of eutectoid decomposition and the improvement of microstructural refinement. These findings provide valuable contributions to optimize the composition of Cu-based SMAs for improved functional performance.

***Keywords**: Shape memory alloy, Cu-Al-Ag alloy, TEM analysis, martensitic transformation, microstructure*

1. INTRODUCTION

Shape memory alloys (SMAs) are a class of functional materials that can recover large, apparently plastic strains through a reversible, diffusionless martensitic transformation [1-3]. NiTi continues to dominate among commercially relevant systems; however, copper–based SMAs have gained renewed attention as they combine low raw material cost with high electrical/thermal conductivity, ease of casting and welding, and broad tunability of transformation temperatures [1-5]. In Cu-Al alloys, thermoelastic β → martensite transformation is responsible for both the one-way and two-way shape memory effects as well as superelasticity. The crystal structure of martensite can adopt several long-period stacking variants (2H, 18R, 6R, etc.), the selection of which is sensitively controlled by the Al content, the alloying additions and the cooling rate [1,4,5]. Recent calorimetric and in-situ diffraction studies suggest that Ag can retard long-range ordering ($A2 \rightarrow B2 \rightarrow L2_1$) during cooling, broadening the β-phase field and facilitating the formation of modulated 18R martensite instead of eutectoid equilibrium products [1-5].

Despite these advantages, systematic electron microscopic investigations of Cu-Al-Ag alloys are still not so well studied. Most reports focus on the bulk thermomechanical behaviour or on Ag-free Cu-Al-Mn and Cu-Al-Ni counterpart alloy systems [1-5]. This TEM investigation is based on the as-cast nano-surface of the Cu-10Al-7Ag alloy. Using bright field/dark field imaging, electron diffraction (SAED) and nanometre-scale energy dispersive X-ray spectroscopy (EDS), we (i) identify the predominant martensitic variant (18R/β_1'), (ii) reveal a sub-100 nm precipitate

population with increased Ag content and (iii) correlate these features with the solidification pathway, which can be deduced from phase diagrams.

2. EXPERIMENTAL

The Cu-10Al-7Ag shape memory alloy was prepared by melting high-purity raw materials: copper (99.9%), aluminum (99.5%), and silver (99.99%) supplied by Mateck Material-Technologie & Kristalle (Jülich, Germany). Melting was carried out in an electric-arc furnace that was vacuumed and purged multiple times with argon to reduce oxidation. The alloy was remelted more than four times to ensure chemical homogeneity and then cast into cylindrical molds measuring 8 × 12 mm. For metallographic preparation, samples were sectioned and mechanically ground using silicon carbide abrasive papers with grit sizes of 320#, 600#, 800#, 1200#, and 2400#. Final polishing was performed using 1 μm and ≤0.2 μm diamond paste on automated polishing systems (Citopress-20 and Tegramin-30, Struers, Willich, Germany).

Transmission electron microscopy (TEM) investigations were conducted using lamellae prepared by focused ion beam (FIB) milling with a Helios 650HP SEM/FIB dual beam system (Thermo Fisher, USA), equipped with an Octane Pro EDS detector (EDAX Inc.). TEM imaging utilized two advanced microscopes: a Tecnai G2 F20 operating at 200 kV with energy dispersive X-ray microanalysis (EDX), HAADF detector for STEM imaging, and high-resolution Gatan UltraScan and SIS Megaview cameras; and a Titan 80–300 S/TEM microscope operated at 300 kV with spherical aberration correctors for both probe and imaging optics. TEM modes included bright field, dark field, selected area electron diffraction (SAED), and high-angle annular dark field (HAADF), applied to lamellae approximately 10 × 8 μm in size.

3. RESULTS AND DISCUSSION

Figure 1. shows the bright field (BF) and dark field (DF) images as well as the diffraction pattern of the selected area (SADP) of the as-cast sample. The images clearly show martensite plates with a width of 150 to 800 nm, which were identified as the 18R phase. The SADP corresponds exactly to the [010] zone axis of the R18 martensite and exhibits a very slight monoclinic distortion with $\beta = 89.7°$. This diffraction pattern exhibits a contrast with a periodicity of 0.619 nm, which is characteristic of the 18R stacking sequence visible in the DF image of the (0012) spot. The streaks observed between the stacking patches likely result from numerous structural defects within the martensite variants, probably caused by internal stresses.

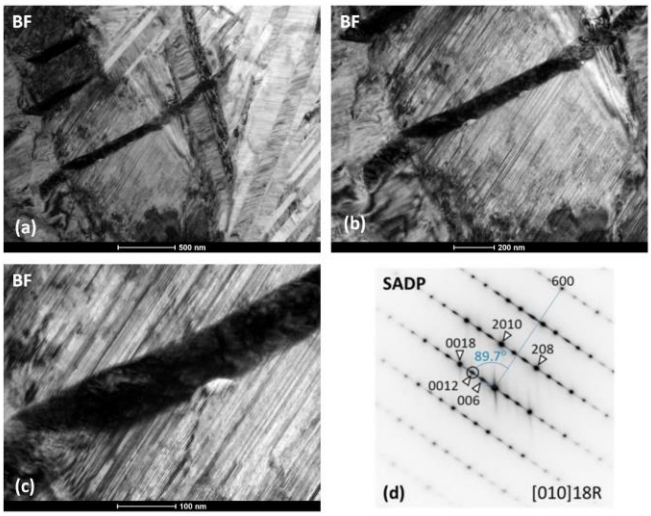

Figure 1. TEM images of the Cu-10Al-7Ag SMA alloy in cast condition: (a) bright-field TEM image taken at higher magnification and (b) dark field TEM image revealing 18R stacking sequence, (c) bright field TEM image taken at low magnification and corresponding (d) dark-selected area diffraction pattern (SADP).

A STEM analysis was carried out to determine the distribution of the most important alloying elements. Figure 2 shows the STEM-HAADF image together with the corresponding element distribution maps. It can be seen that the elemental maps show a random, highlighted area, an Ag precipitate within the as-cast Cu-Al matrix, with the image highlighting that the alloy matrix contains high concentrations of Cu and Al. The length of these precipitates ranges from approximately 0.5 microns to several microns.

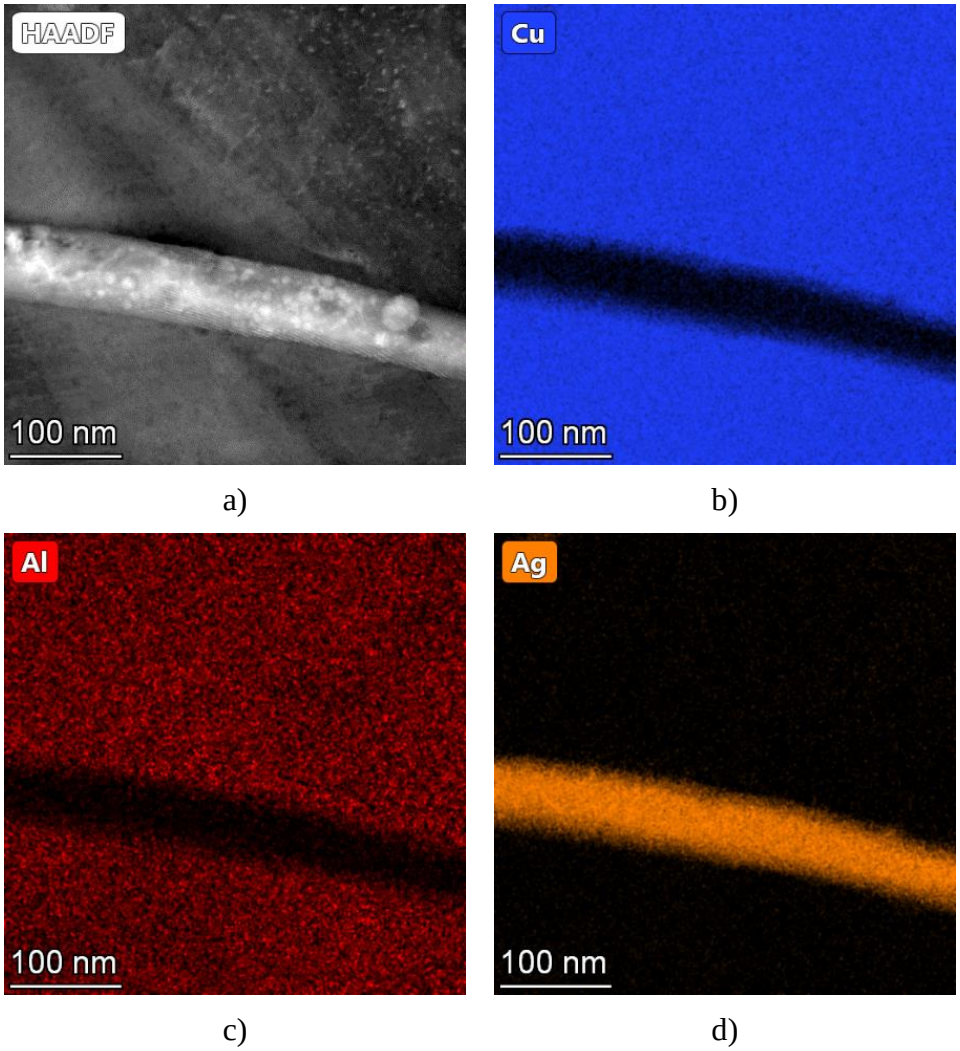

Figure 2. STEM HAADF and EDS elemental maps of the Cu-10Al-7Ag SMA alloy in as-cast condition (a) STEM-HAADF image, (b) Cu element distribution map, (c) Al element distribution map, (d) Ag element distribution map.

Figure 3. shows the results of the quantitative chemical analysis carried out for the indicated areas and indicates the composition of the three microstructural constituents observed in the as-cast sample. It can be seen that the general composition of the as-cast sample (matrix plus Ag precipitates) differs slightly from the nominal composition. The measured composition is depleted in both Al and Ag, which is most likely due to the high heterogeneity of the as-cast sample. This heterogeneity may be mainly related to the different density of Ag precipitates in the microstructure, as they also contain a considerable amount of Cu and a small amount of Al, as can be seen in Figure 3.

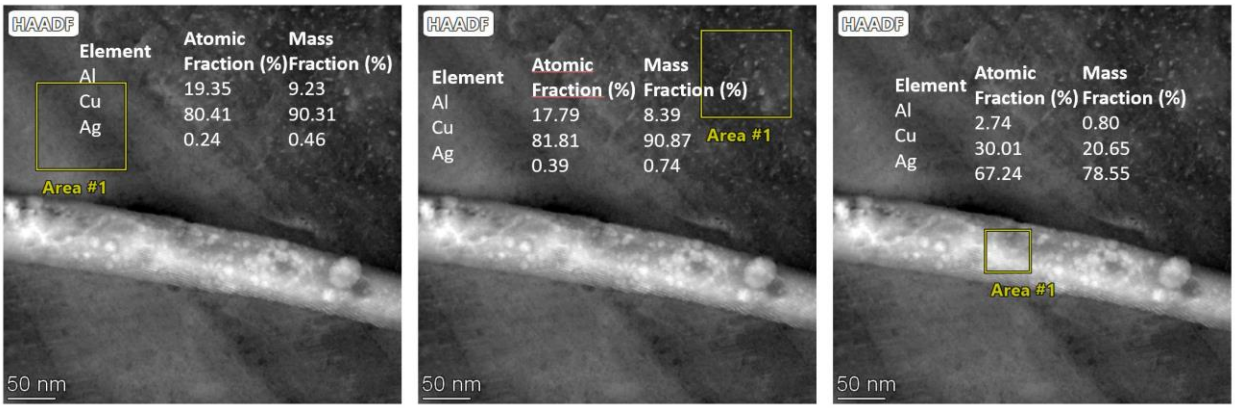

Figure 3. STEM HAADF and results of chemical analyses performed in the indicated areas of the Cu-10Al-7Ag SMA alloy in as-cast condition.

4. CONCLUSION

The Cu-10Al-7Ag shape memory alloy was successfully melted by vacuum electric-arc furnace by several remelting cycles to ensure chemical homogeneity. TEM analysis revealed the presence of martensitic plates with a width of 150 to 800 nm, which were identified as the 18R phase. This was confirmed by diffraction patterns in selected areas showing a characteristic 18R stacking periodicity and a slight monoclinic distortion. STEM-HAADF imaging and elemental mapping showed a largely random distribution of Ag precipitates in the as-cast Cu-Al matrix, with precipitate lengths ranging from about 0.5 to several microns. Quantitative chemical analysis indicated slight deviations from the nominal composition, in particular a depletion of Al and Ag, which was attributed to microstructural heterogeneity caused primarily by the different density of Ag precipitates with Cu and low Al contents. Overall, these results provide valuable insights into the microstructural properties and chemical distribution within the as-cast Cu-10Al-7Ag alloy, which are essential for understanding its shape memory behaviour and guiding future alloy design and processing.

ACKNOWLEDGEMENTS

TEM operators:

dr. sc. Anna Wójcik - Institute of Metallurgy and Materials Science, Polish Academy of Sciences, 25 Reymonta Street, 30-059 Kraków, Poland and Faculty of Metals Engineering and Industrial Computer Science, AGH University of Science and Technology, Al. A. Mickiewicza 30, 30-059 Kraków, Poland

Krzysztof Matus - Materials Research Laboratory, Faculty of Mechanical Engineering, Silesian University of Technology, Konarskiego 18a St., 44-100 Gliwice, Poland

REFERENCES

[1] L. Liverić, W. Sitek, P. Snopiński, W. Maziarz, T.H. Grgurić, Symmetry, 16 (2024) 545.
[2] L. Liverić, T.H. Grgurić, V. Mandić, R. Chulist, Materials, 16 (2023) 5782.
[3] L. Liverić, T.H. Grgurić, E.G. Bajsić, M. Kršulja, Chem. Biochem. Eng. Q., 37 (2023) 153–161.
[4] T.H. Grgurić, D. Manasijević, S. Kožuh, I. Ivanić, I. Anžel, B. Kosec, M. Bizjak, E.G. Bajsić, L. Balanović, M. Gojić, J. Alloys Compd., 765 (2018) 664–676.
[5] D. Manasijević, T. H. Grgurić, L. Balanović, U. Stamenković, M. Gorgievski, M. Gojić, Chem. Biochem. Eng. Q., 58 (2020) 293–299.

The 56th International October Conference on Mining and Metallurgy
22-25 October 2025, Bor Lake, Bor, Serbia
www.ioc.tfbor.bg.ac.rs

DOI: 10.5937/IOC25421K *Original scientific paper*

COMPARISON OF NON-DESTRUCTIVE AND DESTRUCTIVE WELDING ASSESSMENT TESTS ON MAG-WELDED AISI316L AND DH36 STEELS USING K-309LT FILLER

Marko Kršulja[1a], Damir Karabaić[1b], Lovro Liverić[1c], Samir Grudić[1d]

[1] Faculty of Engineering, Juraj Dobrila University of Pula, Nergrijeva ulica 6, 52100 Pula, Croatia
[1a] marko.krsulja@unipu.hr, 0000-0003-0823-8083
[1b] damir.karabaic@unipu.hr, 0000-0001-6151-2235
[1c] lovro.liveric@unipu.hr, 0000-0001-8714-6771
[1d] samir.grudic@unipu.hr, 0009-0004-6257-6280

Abstract
This study provides a comparative analysis of non-destructive testing (NDT) and destructive testing (DT) applied to MAG welding of dissimilar AISI316L and DH36 steels using K-309LT filler wire. The welding process, performed in vertical and horizontal positions on a ceramic support, was optimized for mechanical integrity. NDT techniques such as ultrasonic, visual and penetrant testing, enabled the detection of internal and superficial defects such as porosity, lack of fusion and cracks without affecting the test samples. However, they did not provide information on mechanical performance under load. DT methods, including tensile, impact, bending and hardness tests, provided critical data on weld structural integrity, toughness, ductility and the effects of heat input on the microstructure, particularly in the fusion and heat-affected zones. These destructive tests confirmed the nature of the defects, detected, and assessed their impact on the performance of the weld. The study concludes that, while non-destructive testing is essential for preliminary quality control, it should be complemented by DT for a complete understanding of weld behavior under service load. The synergy of both approaches is crucial to ensure safety, durability and optimal performance of welded structures made of different steels.

Keywords: *MAG welding, AISI316L, DH36, K-309LT filler, non-destructive testing (NDT), destructive testing (DT), welding quality control*

1. INTRODUCTION

The field of welding and fabrication plays a crucial role in various industrial sectors, including manufacturing, construction, and shipbuilding. Welding parameters in industry significantly influence production quality [1], with proper selection of parameters, suitable material choice [2], and stable arc conditions and methods used in welding [3] being key factors for achieving optimal results. Among diverse welding processes, Metal Active Gas (MAG) welding has gained popularity due to its versatility and efficacy, particularly for thick section welding. This study focuses on the specific case of MAG welding involving two different grades of steel, AISI316L and DH36, using K-309LT filler [4]. Despite its wide usage, the integral question of weld quality assurance in this process remains a subject of considerable debate and investigation. Weld quality can be evaluated through various testing methods, broadly categorized as non-destructive testing (NDT) and destructive testing (DT). While NDT allows for the detection of defects without causing damage to the test piece, its inability to measure mechanical properties is a limitation. On the other hand, DT provides a comprehensive understanding of the mechanical and metallurgical properties of the weld but compromises the integrity of the test samples [5]. This paper aims to compare and contrast NDT and DT methods applied to the MAG welding process of AISI316L and DH36 steels using K-309LT filler. The objective is to highlight the strengths and limitations of each testing method and ascertain their optimum utilization for quality assurance in welding different grades of steel on this particular case. Through this comprehensive comparison, the study seeks to provide valuable insights that can enhance the efficiency, reliability, and service life of

welded structures. The findings of this research will be highly beneficial for industries relying heavily on welding dissimilar steels, promoting safer and more efficient operations.

2. EXPERIMENTAL

Materials used in this research include two types of steel and one welding wire, with their chemical compositions presented in Table 1.

Table 1. Chemical composition comparison

Element (Fe Bal.)	AISI 316L (%)	DH 36 (%)	Kiswel K-309LT (%)
C	≤ 0.03	0.18	0.03
Si	≤ 1.0	0.50	0.4
Mn	≤ 2.0	1.6	1.2
P	≤ 0.045	0.035	0.03
S	≤ 0.03	0.035	0.03
Cr	16-18	0.20	23.7
Ni	10-14	0.40	13.2
Mo	2-2.5	0.08	-
N	≤ 0.1	-	-
Cu	-	0.35	-
Cb	-	0.05	-
V	-	0.10	-
FN	-	-	12

AISI 316L stainless steel (EN: X2CrNiMo18-14-3, material number 1.4435) belongs to the austenitic stainless steel group, commonly known as inox, prochrom, or marine steel. This steel typically contains 0.02–0.15% carbon, 16–24% chromium, 8–12% nickel, and can be alloyed with molybdenum, niobium, nitrogen, tantalum, and titanium. Its primary advantage is resistance to intergranular corrosion, while its drawback is reduced yield strength due to the low carbon content. DH 36 steel (EN 10025) belongs to high-strength shipbuilding steels, characterized by maintaining yield strength of at least 355 N/mm² even at -20 °C. It is distinguished by good weldability and machinability, owing to its low carbon content (0.18%). Due to these favorable mechanical characteristics, DH 36 steel is primarily used for constructing ship hulls. Unlike AISI 316L, DH 36 steel is not corrosion resistant and thus requires proper protective coatings to prevent corrosion. The welding filler material Kiswel K-309 LT is a flux-cored wire designed for MAG welding of similar and dissimilar stainless steels. It exhibits excellent weldability and allows welding in various positions using either 100% CO_2 or a gas mixture containing 82% Ar and 18% CO_2. This filler material provides deep penetration and excellent mechanical properties of the weld joints, especially when using a spray arc transfer mode. It is also employed for cladding purposes. The welded joint was prepared between two different steel types, AISI 316L and DH36, using the Kiswel K-309LT welding wire. Both steel plates, 25 mm thick, were beveled at a 45-degree angle, forming a "V" joint configuration suitable for welding in a vertical position. A ceramic backing strip was positioned on the backside of the joint to facilitate root pass welding and prevent melt-through. The welding parameters were meticulously selected according to the welding procedure specification (WPS), ensuring consistent quality across all passes. A total of 30 welding passes were applied, with inter-pass slag removal and surface grinding after each pass to maintain weld integrity. The inter-pass temperature was controlled not to exceed 150 °C. The weld quality was evaluated using non-destructive testing (NDT) techniques, including visual inspection, penetrant testing, and ultrasonic testing. Visual inspection identified surface defects, penetrant testing was applied to detect any surface-breaking discontinuities, and ultrasonic testing assessed internal defects within the welded joint. Destructive tests (DT) conducted included tensile testing, impact testing, bending tests, and hardness measurements. Tensile tests determined the ultimate tensile strength and ductility of the weld. Impact tests, performed using the Charpy impact method at 0

°C, assessed weld toughness. Bending tests were conducted from both root and face sides to evaluate the ductility and potential for cracking under bending stress. Hardness was measured using the Vickers method across the weld metal, heat-affected zone (HAZ), and base materials.

3. RESULTS AND DISCUSSION

Non-Destructive Testing (NDT)

Penetrant Testing

Penetrant testing was performed using TIEDE-PEN PWL-1 penetrant, DL-20 developer, and RL-40 surface cleaner. The surface was brushed and cleaned with water, at an ambient temperature of 20 °C. The penetrant dwell time was 20 minutes, with a developing time of 20 minutes. The examination was concluded with acceptable results.

Ultrasonic Testing

Ultrasonic testing was carried out using KRAUTKRAMER USN-52 equipment with probes MWB 60-4 MHz and MWB 70-4 MHz. The calibration block used was 1.2 mm, with a gauging range from 100 to 200 mm. Couplant ZG was used, and the sensitivity was rated as E1. The gain was set between 46-52 dB. The examination results were acceptable.

Visual Control

Visual control was conducted following standards HRN EN ISO 5817 and HRN EN 970, with a sandblasted surface condition. The examination indicated an acceptable result.

Visual inspection revealed uniform bead formation without significant surface defects. Penetrant testing did not show any surface discontinuities. Ultrasonic testing confirmed the absence of significant internal defects, indicating good weld integrity.

Destructive Testing (DT)

The hardness of the samples was measured using the ZHU 187.5 universal hardness tester with Vickers (HV 10) hardness pyramid indenter. In addition, all tensile and bending tests in this study were performed at room temperature using a universal tensile testing machine ZWICK Z/100.

Tension Testing

Results of tension test are seen in table 2. All samples failed outside the weld area, indicating satisfactory weld performance.

Table 2. Tension test of welded example

Sample No.	Cross-section (mm^2)	Force (F/N)	Tensile Strength (N/mm^2)	Yield Point (F/N)	Yield Limit (N/mm^2)	Elongation (mm)	Reduction of Area (%)
1	14.0 x 25.0	198800	568	140000	400	429	–
2	14.0 x 25.0	200500	573	141000	404	413	–
3	14.0 x 25.0	198000	566	140500	402	424	–
4	14.0 x 25.0	200000	571	141500	404	419	–

Impact Testing

Impact testing was performed at 25 °C on standard test size 10 mm x 10 mm x 55mm. Results showed on Table 3. have satisfactory toughness values, especially in the fusion zone.

Table 3. Impact dynamic testing results of welded example

Sample No.	Impact Toughness (J)	Position	Average Impact Toughness (J)
6	63	center weld	60.0
7	58	center weld	60.0
8	59	center weld	60.0
9	133	fusion zone	137.67
10	132	fusion zone	137.67
11	148	fusion zone	137.67
12	137	2 mm from fusion zone DH36	144.0
13	140	2 mm from fusion zone DH36	144.0
14	155	2 mm from fusion zone DH36	144.0

Banding Test

Results for three-point banding test are seen in Table 4. All bending tests passed, demonstrating good ductility and soundness of the weld.

Table 4. Bending test results of made samples from welding example

Sample No.	Dimensions (mm)	Diameter (mm)	Angle (°)	Test Type	Result
1	10 x 25	40	180	side bending	O.K.
2	10 x 25	40	180	side bending	O.K.
3	10 x 25	40	180	side bending	O.K.
4	10 x 25	40	180	side bending	O.K.

Hardness Test

Hardness testing was performed by Vickers hardness test, three locations were tested and micro locations on each sample are shown on Figure 1. The hardness values seen in Table 5. represent the average of five measurements with the standard deviation. The carburized layer was removed before the test. The hardness values obtained after welding are consistent with the data reported in the experimental literature of chosen steels [1-5].

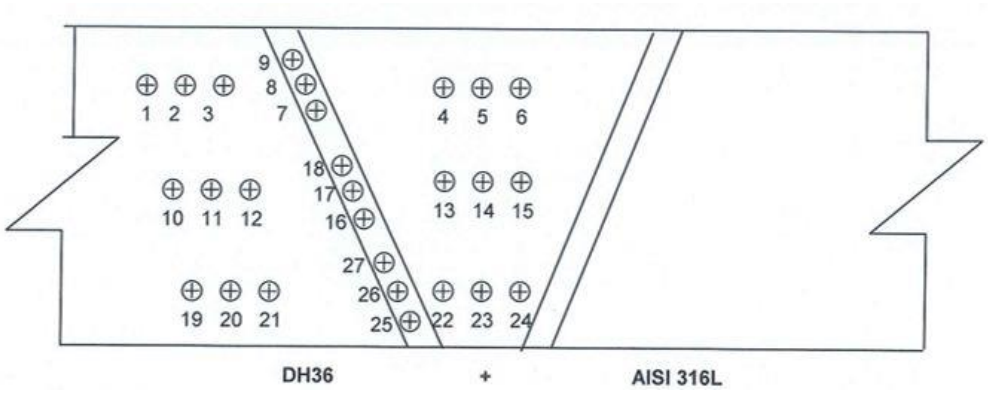

Figure 1. Positions of measure micro point locations for Vickers hardness test

The results of the destructive tests provided detailed data on the mechanical properties. Tensile tests confirmed satisfactory strength and ductility, with failures predominantly in the base metal, emphasizing the weld's excellent integrity. Impact tests demonstrated robust toughness, highlighting the weld's suitability for dynamic or low-temperature applications. Bending tests

confirmed excellent ductility, with no cracking observed, indicating strong resistance to deformation.

Table 5. Hardness Vickers measurements of samples

Sample No. 1. (Upper side)		Sample No. 1. (Middle side)		Sample No. 1. (Lower side)	
Measure point	Results	Measure point	Results	Measure point	Results
1	202	10	176	19	171
2	185	11	170	20	178
3	206	12	187	21	197
4	253	13	272	22	285
5	250	14	272	23	264
6	243	15	274	24	274
7	250	16	245	25	272
8	289	17	319	26	242
9	300	18	270	27	274
HV 10 max.	350	HV 10 max.	350	HV 10 max.	350

The presented results demonstrate the effectiveness and complementarity of non-destructive testing (NDT) and destructive testing (DT) methods in assessing the quality of MAG welded joints between AISI 316L and DH36 steels using Kiswel K-309LT welding wire. NDT methods, including visual, penetrant, and ultrasonic testing, confirmed the absence of significant defects, indicating good preliminary weld quality. The DT provided comprehensive insight into mechanical properties, complementing NDT by validating weld integrity through mechanical performance data. Hardness profiles indicated appropriate heat management, reflected by gradual changes in hardness from the weld metal to the base metal. The synergy between NDT and DT emphasizes that integrating both test methods is essential for thorough quality control in practical welding applications. This study offers valuable insights into material behavior during MAG welding of AISI 316L and DH36 steels with K-309LT filler, underscoring the importance of scientific methodology and adherence to standards for achieving high-quality welded joints and maintaining professional standards in production practices.

4. CONCLUSION

This study has confirmed that MAG welding of dissimilar steels (AISI 316L and DH36) using Kiswel K-309LT filler wire can produce welds of excellent mechanical and structural integrity. Non-destructive testing methods effectively detected initial defects, while destructive testing enabled a comprehensive assessment of mechanical properties. The combination of both testing approaches is crucial to accurately determine weld quality, ensuring the reliability and durability of welded structures in real-world applications. Further study will be focused on the quality of the operator or welding machine, as well as the welding positions used in joining material plates, in order to ensure the final weld quality and meet the requirements set by the classification society Bureau Veritas.

REFERENCES

[1] M. Kršulja, B. Barišić, J. Kudlaček, *Comprehensive Study of Strip Selection and Weld Errors in a Steel Tube Erw Welding Process,* DAAAM International Vienna, Beč, 2009, pp. 683-684.
[2] M. Kršulja, Z. Car, H. Radelja, Metalurgija, 51 (2) (2012) 203–206.
[3] M. Kršulja, S. Mijić, B. Barišić, Z. Car, Manuf. Ind. Eng., 11 (2) (2012) 38–43.
[4] S. Khrais, H. Al Hmoud, A. Abdel Al, T. Darabseh, Impact of Gas Metal Arc Welding Parameters on Bead Geometry and Material Distortion of AISI 316L. J. Manuf. Mater. Process. 7 (2023) 123.
[5] C. MacLeod, Y. Javadi, Chapter 12 - Advanced nondestructive evaluation for welded joints, Editor(s): Fuad Khoshnaw, Welding of Metallic Materials, Elsevier, 2023, 431-461.

The 56th International October Conference on Mining and Metallurgy
22-25 October 2025, Bor Lake, Bor, Serbia
www.ioc.tfbor.bg.ac.rs

DOI: 10.5937/IOC25426B *Original scientific paper*

EFFECT OF BERYLLIUM ADDITION ON THE MICROSTRUCTURE AND PHYSICAL PROPERTIES OF Al-Si ALLOYS WITH LOW SILICON CONTENT

Dana Bolibruchová[1a], Martina Sýkorová[1b], Marek Matejka[1c]

[1]University of Žilina in Žilina, Faculty of Mechanical Engineering, Department of Technological Engineering, Univerzitná 1, 01026 Žilina, Slovakia
[1a] danka.bolibruchova@fstroj.uniza.sk, 0000-0002-7374-9763
[1b] martina.sykorova@fstroj.uniza.sk, 0000-0001-6418-8450
[1c] marek.matejka@fstroj.uniza.sk, 0000-0002-4156-5521

Abstract
This article analyzes the influence of beryllium (Be) as an alloying element on the structural properties of the AlSi5Cu2Mg alloy. Specifically, it examines the ability of Be to affect crystallization and the electrical and thermal conductivity. The goal is to implement a non-standard alloy into a low-silicon aluminum alloy that would show improved physical properties, refined structure, and stabilization of intermetallic phases. Such a modified alloy could be used for large aluminum castings in the automotive industry, especially for lightweight electric vehicles. It's also suitable for castings requiring balanced mechanical properties and high ductility, as well as for special high-pressure die casting (HPDC) parts that demand higher physical properties than standard aluminum alloys. The analysis shows that adding Be in the range of 0.05, 0.08, and 0.12 wt.% to the AlSi5Cu2Mg alloy refines the grain and changes the morphology of the eutectic silicon. Using a separated remelting method with AlBe5, no Be burnout occurred in the alloy. An addition of 0.12 wt.% Be to the tested alloy resulted in an increase in both electrical and thermal conductivity.

***Keywords**: AlSi5Cu2Mg, alloying, beryllium, electrical conductivity, thermal conductivity, microstructure*

1. INTRODUCTION

Currently, the field of aluminum castings production and metallurgy is facing significant challenges in developing new materials. Standard aluminum alloys are often unable to meet many of the required properties, such as high ductility (10-20%) while maintaining high strength, hardness, or specific electrical and thermal demands for castings. Challenges also arise when casting exceptionally large aluminum components (~1-2 m x 1.5-2 m x 0.5 m) and ensuring they have the necessary properties, with a strong emphasis on quality. When developing new aluminum alloys for the automotive industry, it is crucial to focus not only on mechanical and chemical properties but also on physical properties like thermal and electrical conductivity. In aluminum-silicon (Al-Si) alloys, silicon (Si) is a key element that influences both fluidity and shrinkage. However, alloys with a eutectic composition have low ductility, and the eutectic Si cannot be effectively modified to achieve non-standard values. A common compromise is to use aluminum alloys with a lower silicon content, around 7 wt.% Si or less, which is not typical for high-pressure die casting (HPDC) in our region. These alloys are expected to have balanced flowability and suitable mechanical characteristics, including ductility. In addition to low Si content and a small amount of Mg, researchers are searching for elements and alloys that would be active in these processes, despite being significantly more expensive than standard alloys [1-4]. Therefore, the objective of this paper is to determine the effect of adding beryllium on the microstructure and

physical properties of low-silicon Al-Si alloys. Due to the limited scope of this paper, only partial results will be presented.

2. METHODOLOGY OF EXPERIMENTAL WORK

For the experimental work, the aluminum alloy AlSi5Cu2Mg was selected. This is a hypoeutectic alloy with a low silicon content. The chemical composition of the base AlSi5Cu2Mg alloy is shown in Table 1.

Table 1. Chemical composition of the AlSi5Cu2Mg alloy [wt.%].

Alloy as-cast state	Si	Cu	Mg	Mn	Fe	***Be***	***Ti***	***Sr***	Al
AlSi5Cu2Mg + **0 wt. % Be**	6.77	2.54	0.153	0.015	0.23	*0.0002*	*0.016*	*0.01*	Bal.

The primary AlSi5Cu2Mg alloy was melted in an electric resistance furnace using a graphite crucible. Experimental alloys were prepared by alloying the primary AlSi5Cu2Mg with 0.05, 0.08, and 0.12 wt. % Be, which was added in the form of an AlBe5 master alloy. The amounts of added Be were chosen based on a literature review. To improve the utilization of the alloying element, reduce oxidation, and prevent excessive burnout, the master alloy was melted separately for a short time (2 to 3 minutes) in an electric induction furnace in a graphite crucible. It was then poured into the molten aluminum alloy. The alloying temperature was in the range of 730 to 740 °C. The melted alloy was consequently gravity casted into a metal mold at a temperature of 740 to 750 °C. The mold temperature was maintained between 140 and 150 °C. The chemical composition of the experimental alloys is shown in Table 2.

Table 2. Chemical composition of the experimental alloys [wt.%].

alloy as-cast state	Si	Cu	Mg	Mn	Fe	Ti	Sr	Be
AlSi5Cu2Mg + **0.05 wt.% Be**	6.84	2.66	0.157	0.0146	0.247	0.016	0.043	*0.0487*
AlSi5Cu2Mg + **0.08 wt.% Be**	6.78	2.54	0.166	0.0155	0.236	0.0153	0.0049	*0.0787*
AlSi5Cu2Mg + **0.12 wt.% Be**	6.82	2.49	0.168	0.012	0.233	0.0015	0.072	*0.115*

Five samples were cast from each experimental variant to test and evaluate the physical properties and microstructure. The microstructure was evaluated in the as-cast state using a Keyence VHX-7000 digital optical microscope. The eutectic silicon morphology was assessed on deeply etched samples using and scanning electron microscope SEM LMU II scanning electron microscope with a BRUKER EDX analyzer). According to Nemak Slovakia s.r.o.'s measurement methodology, the electrical conductivity values of the alloys were determined using cylindrical test samples with a diameter of 40 mm and a height of 60 mm. Three measurements were performed on each sample at different locations. The values presented in Table 3 are the averages of these measurements in the as-cast state. The measurements were carried out at a laboratory temperature ranging from 23 to 25 °C. To determine electrical conductivity, a Sigma Check 2 conductometer with a contact measuring probe was used. The device recorded electrical conductivity values in International Annealed Copper Standard (IACS) units as a percentage. These values were then used in empirical relationship (1) to calculate thermal conductivity. The relationship is based on the recommended calculation method for determining the thermal conductivity of the AlSi5Cu2Mg alloy from Nemak Slovakia s.r.o.

$$\lambda = 4.29 \cdot \sigma - 13.321 \quad (1)$$

where: λ = thermal conductivity [$W \cdot m^{-1} \cdot K^{-1}$]; σ = electric conductivity [% IACS]

2. RESULTS AND DISCUSSION

2.1 Microstructure evaluation

The microstructure of the as-cast AlSi5Cu2Mg alloys consists of the α-phase, eutectic silicon, and intermetallic phases based on copper and iron. Because the base alloy composition was inoculated and pre-modified, the structures of all the developed alloy variants (Figs. 1–3) were refined. An increasing addition of wt.% Be led to the refinement of the α-phase and fragmentation of dendrites in all the tested alloys. In the metallographic cross-section plane, eutectic silicon is visible as imperfect and perfect rounded grains. No angular, plate-like forms occurred. Therefore, it can be concluded that the alloy has optimal phase shapes to achieve the expected balanced mechanical characteristics. The morphology of the intermetallic phases was not evaluated in this case.

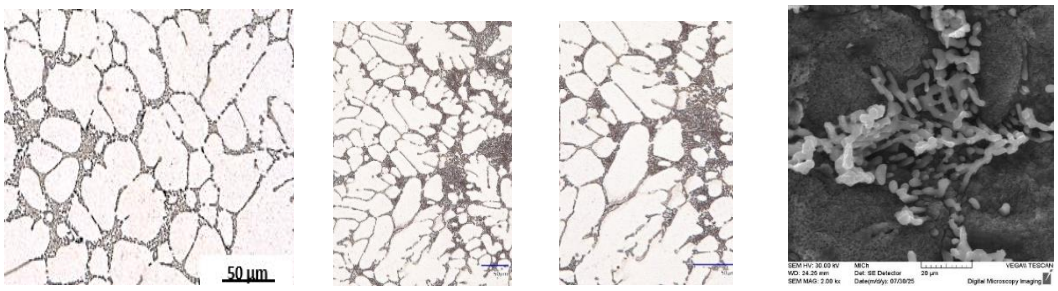

a) b) c) d)

Figure 1. Microstructure of the AlSi5Cu2Mg alloy in the as-cast state: a) 0 wt.% Be, b) 0.05 wt.% Be, c) detail, d) deep etching,0.05 wt.% SEM

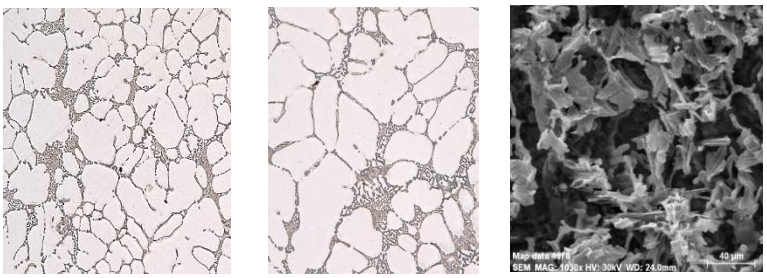

a) b) c)

Figure 2. Microstructure of the AlSi5Cu2Mg alloy in the as-cast state: a) 0,08 wt.% Be b) detail, c) deep etching, SEM

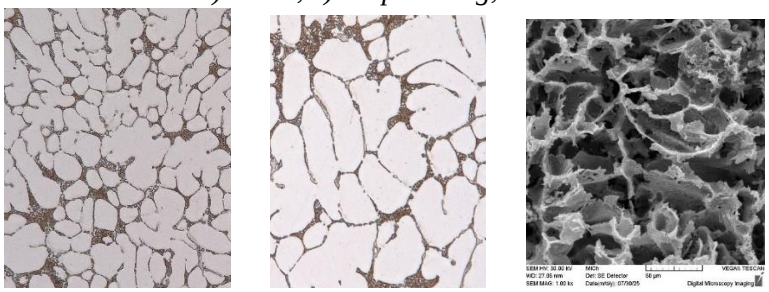

a) b) c)

Figure 3 Microstructure of the AlSi5Cu2Mg alloy in the as-cast state: a) 0,12 wt.% Be b) detail, c) deep etching, SEM

The addition of Be led to the refinement of the α-phase (Figs. 1 b,c; 2 a,b; 3 a,b), which indicates that Be has a grain-refining effect in the tested alloy. The most significant structural refinement was achieved with the highest Be addition (Figs. 3a, b). Conversely, the addition of Be caused the eutectic Si in the tested alloy to change its morphology from rod-like shapes (Fig. 1d) to plate-like ones (Figs. 2c, Fig. 3c). This suggests that Be caused a "demodification" of the alloy, even though several authors have confirmed the modifying effect of Be in various aluminum alloys [5-7].

2.2 Evaluation of physical properties

Based on the results of the electrical conductivity measurements and calculation of thermal conductivity values, the highest electrical and thermal conductivity (Table 3) was achieved by the alloy with an addition of 0.12 wt.% Be. Additions of 0.05 wt.% and 0.08 wt.% had a negative impact on the physical properties, performing worse than the alloy without any alloying additions.

Table 3. Electrical and thermal conductivity results

Alloy as-cast state	Electrical conductivity σ [% IACS]	Thermal conductivity λ [W · m^{-1} · K^{-1}]
AlSi5Cu2Mg + **0 wt.% Be**	36.4	143.0
AlSi5Cu2Mg + **0.05 wt.% Be**	34.9	136.4
AlSi5Cu2Mg + **0.08 wt.% Be**	35.5	138.9
AlSi5Cu2Mg + **0.12 wt.% Be**	37.5	147.8

3. CONCLUSION

Based on the obtained results, though they are partial, it can be concluded that:

- The structural analysis confirmed the positive effect of adding Be to the AlSi5Cu2Mg alloy.
- The Be has a grain-refining effect on the tested alloy, specifically on the α-(Al) phase.
- The refining effect increased with a higher proportion of the alloying element.
- The Be influences the physical properties of the tested alloy in the as-cast state.
- The most significant effect was observed with an addition of 0.12 wt.% Be.
- The shape, size, and morphology of the phases fundamentally influence electrical and thermal conductivity, which depends on the mobility of free electrons and the vibrational waves of the crystal lattice. Lattice defects (e.g., intermetallic phases, inclusions, and porosity) act as sites where electrons are scattered, leading to decreased conductivity.

The study on the effect of Be on the low-silicon alloy confirmed its positive influence on grain refinement in the as-cast state. Further research will focus on analyzing mechanical characteristics, porosity, the effect of non-standard heat treatment regimes, and the influence of Be on the morphology of iron-rich phases.

ACKNOWLEDGEMENTS

The article was created as part of the KEGA 003 ŽU- 4/2024 and VEGA grant agency project: VEGA 1/0160/22. The authors thank for its support.

REFERENCES

[1] Q. Wang, A. Wang, J. Coryell, China Foundry, (N.5) (2024) 397-408.
[2] Ducker Frontier: North America light vehicle aluminum content and outlook. Final Report Summary: July (2020).
[3] H. Fuse, T. Haga, Metals 15(8) (2025) 91.
[4] F. Hesami: https://www.linkedin.com/pulse/giga-casting-presses-automotive-industry-farshid-hesami-jmumf/.
[5] H.R. Ammar, E. Samuel, F.H. Samuel, E. Elsharkawi, H.W. Doty. V. Songmene, International Journal of Metalcasting. American Foundry Society, (2025)
[6] A. Hartlieb, M. Hartlieb, The impact of giga-castings on car manufacturing and aluminum content. https://www.lightmetalage. com/news/industry-news/automotive/the-impact-of-giga-castingson-car-manufacturing-and-aluminum-content, (2023) July 10.
[7] B. Callegari, T. Nunes Lima, R. Santiago Coelho, Metals, (13) (2023) 1174.

The 56th International October Conference on Mining and Metallurgy
22-25 October 2025, Bor Lake, Bor, Serbia
www.ioc.tfbor.bg.ac.rs

DOI: 10.5937/IOC25430N *Original scientific paper*

MICROSTRUCTURES AND WETTABILITY BEHAVIOR OF Sn-0.7Cu SOLDER DOPED WITH GRAPHENE NANOSHEETS

Milan Nedeljković[1a], Srba Mladenović[1b], Vladan Ćosović[2c], Ivana Marković[1d], Jasmina Petrović[1e], Uroš Stamenković[1g], Milijana Mitrović[1g], Avram Kovačević[1h]

[1]Technical Faculty Bor, University of Belgrade, V. J. 12, 19210 Bor, Serbia
[2]University of Belgrade, Institute of Chemistry, Technology and Metallurgy-National Institute of the Republic of Serbia, Njegoševa 12, 11000 Belgrade, Serbia
[1a]mnedeljkovic@tfbor.bg.ac.r, 0000-0002-7927-1334
[1b]smladenovic@tfbor.bg.ac.rs, 0000-0002-3844-7399
[2c]vlada@tmf.bg.ac.rs, 0000-0001-7644-4036
[1d]imarkovic@tfbor.bg.ac.rs, 0000-0003-4431-9921
[1e]jpetrovic@tfbor.bg.ac.rs, 0000-0002-9131-339X
[1f]ustamenkovic@tfbor.bg.ac.rs, 0000-0002-7579-2159
[1g]mmitrovic@tfbor.bg.ac.rs, 0000-0001-7478-2453
[1h]akovacevic@tfbor.bg.ac.rs, 0000-0003-4009-4876

Abstract

The effect of graphene nanosheets (GNS) on the wettability and microstructure of Sn-0.7Cu-xGNS (x = 0, 0.02, 0.04, 0.06, 0.08, and 0.1 wt.%) nanocomposite solders was investigated. The composites were produced using the powder metallurgy (PM) technique. The microstructures of the solder joints between the solders and copper substrates were examined using a scanning electron microscope (SEM), and the presence of intermetallic compounds (IMCs) was confirmed by energy-dispersive spectroscopy (EDS). The thickness of the intermetallic layer formed at the solder/Cu interface was reduced by 64.6% with the addition of up to 0.1 wt.% GNS, compared to the Sn-0.7Cu base solder. The wettability of the samples was evaluated by measuring the spreading area of the solders on the copper substrates. The results showed that the addition of up to 0.1 wt.% GNS significantly improved wettability, as evidenced by a 95.2% increase in spreading area compared to the unreinforced solder.

***Keywords**: (powder metallurgy, nanocomposite, graphene nanosheets, intermetallic compounds)*

1. INTRODUCTION

Tin–lead (Sn–Pb) solders have been widely used in the electronics industry due to several advantages, including a low melting point, good wettability, and cost-effectiveness [1]. However, growing environmental and health concerns related to lead toxicity, along with international regulations, have led to a global shift toward the development of lead-free solder materials. As a result, significant research efforts have been focused on identifying suitable alternatives that can match or exceed the performance of traditional Sn–Pb solders [2, 3].

Among lead-free solder systems, Sn–Cu, Sn–Bi, Sn–In, Sn–Sb and Sn–Ag–Cu alloys, particularly Sn-0.7Cu, are considered promising due to their low cost, environmental compatibility, and acceptable mechanical properties [4]. However, they often exhibit poor wettability and the formation of coarse IMCs, which can reduce joint reliability. To improve these properties, recent studies have explored the addition of various types of carbon nanoparticles, such as fullerenes (FNS), graphene nanosheets (GNS), carbon nanotubes (CNT), single-walled carbon nanotubes (SWCNT) and multi-walled carbon nanotubes (MWCNT). Among these, GNS has garnered significant attention due to its exceptional properties, including high thermal and electrical conductivity, mechanical strength and large surface area [5, 6]. GNS exhibits poor dispersibility in metal matrices due to strong Van der Waals forces, which lead to low wettability and particle agglomeration [7]. To overcome these limitations, the mechanical alloying (MA) process is commonly employed to enhance the interaction between graphene and the metal matrix. This

method involves cold welding, fracturing, and rewelding of powder particles in a high-energy ball mill. However, the effect of GNS addition on the Sn-0.7Cu solder system has not been thoroughly investigated. According to the available literature, only Yang and his associates have studied the effect of varying GNS contents (0.02, 0.05, 0.075, and 0.10 wt.%) on the properties of the Sn–0.7Cu base alloy. Their findings indicated improvements in wettability, microhardness and microstructural refinement of the solders [8, 9].

In this study, the wettability and microstructure of the solder joints formed between Sn-0.7Cu-xGNS solders and the copper substrates were investigated. The graphene-reinforced composite solders were synthesized using the PM technique, which included MA, cold pressing and sintering.

2. EXPERIMENTAL

Materials used in this work were powders of tin (Sn), copper (Cu) and GNS. First, Sn and Cu powders (particle size up to 75 μm) were mixed in a specific ratio using a "Turbula T2F" three-axis mixer at 50 rpm for 30 hours to form the Sn-0.7Cu base alloy. The mixture was then MA with GNS (with an average diameter of 5-10 μm and a thickness of 3-5 nm) in a high-energy planetary ball mill "FRITSCH Planetary Ball Mill P-7" at 100 rpm for 3 hours. After MA, the obtained powders were compacted under 300 MPa using a hydraulic press to form green compacts with a diameter of 12.7 mm. Finally, the green compacts were sintered in an argon atmosphere at 185 °C for 3 hours. As a result, the Sn-0.7Cu-xGNS nanocomposite materials (x = 0, 0.02, 0.04, 0.06, 0.08, and 0.1 wt.% GNS) were obtained.

The wettability of the composite solders was determined by measuring the spreading area of the solders on copper substrates. Cylindrical sintered samples (3 mm in diameter and height) were placed at the center of the copper substrates (20×20×1 mm). To prevent oxidation during soldering, RMA223 flux was applied. The soldering process was performed on a hot plate at 250 °C for 1 minute in air. After soldering, the spreading areas were measured using ImageJ software. Subsequently, the microstructures of the solder joints at the solder/Cu interface were examined using a scanning electron microscope (SEM), and the presence of IMC was identified through energy-dispersive spectroscopy (EDS). The microstructural analysis was performed on standard metallographically prepared samples using a "Tescan Vega 3 LMU" SEM equipped with an "Oxford Instruments X-act" EDS detector.

3. RESULTS AND DISCUSSION

Figure 1 shows the spreading behavior of Sn-0.7Cu-xGNS solders on Cu substrates after soldering, while Figure 2 presents the changes in the spreading area as a function of GNS content in the composite solders.

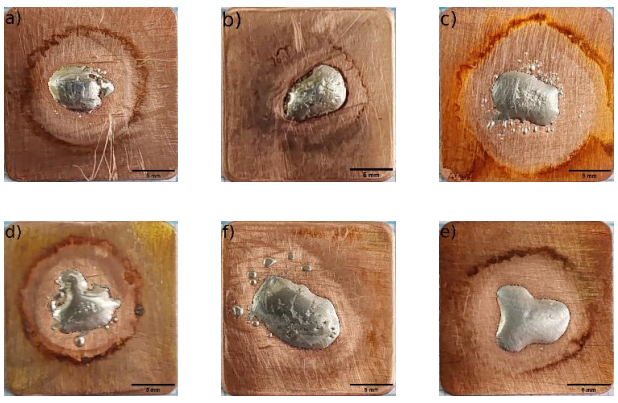

Figure 1. Spreading of solders on the Cu substrates: (a) Sn-0.7Cu; (b) Sn-0.7Cu-0.02GNS; (c) Sn-0.7Cu-0.04GNS; (d) Sn-0.7Cu-0.06GNS; (e) Sn-0.7Cu-0.08GNS; (f) Sn-0.7Cu-0.10GNS

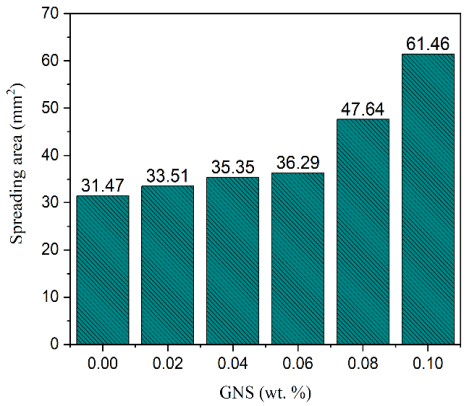

Figure 2. Changes in the spreading area as a function of GNS content in Sn-0.7Cu-xGNS solders

The results presented in Figures 1 and 2 demonstrate that the addition of GNS increases the spreading area of the composite solders, indicating improved wettability. The base Sn-0.7Cu solder exhibited a spreading area of 31.47 mm^2, while the composite solder with a GNS content of 0.10 wt.% has a spreading area of 61.46 mm^2, which is approximately 95.3% higher than the base solder. This improvement can be attributed to the reduction in surface tension between the solder and Cu substrate due to the presence of GNS, as well as enhanced oxide layer removal due to the action of the flux. These results suggest that the addition of GNS leads to the formation of a wider and more stable bond between the solder and the substrate, enhancing the mechanical reliability of the solder joint.

Following the wettability test, the microstructure of the intermetallic layer at the solder/Cu interface was examined. Figure 3 presents the corresponding SEM images obtained after the soldering process.

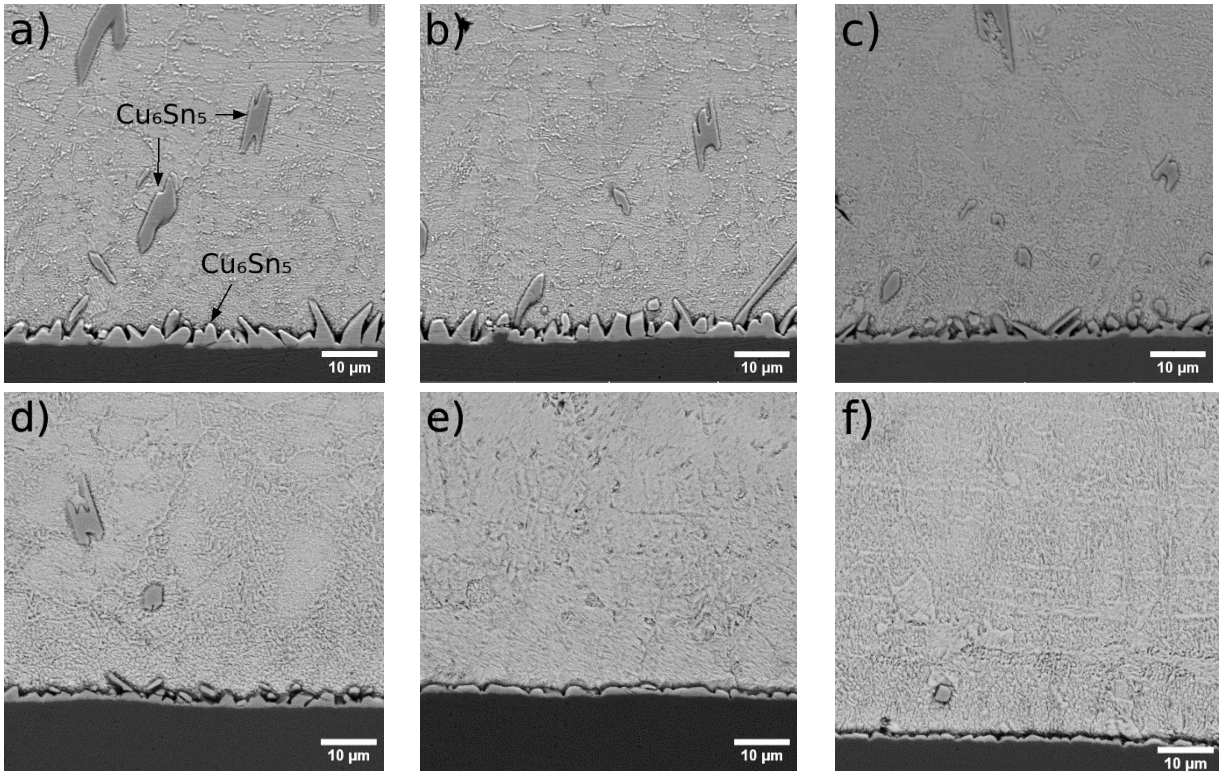

Figure 3. SEM micrographs of the intermetallic layer between Sn-0.7Cu-xGNS solders and Cu substrates (a) Sn-0.7Cu; (b) Sn-0.7Cu-0.02GNS; (c) Sn-0.7Cu-0.04GNS; (d) Sn-0.7Cu-0.06GNS; (e) Sn-0.7Cu-0.08GNS; (f) Sn-0.7Cu-0.10GNS

As observed, a typical wave - serrated Cu_6Sn_5 intermetallic layer was formed at the solder/Cu interface. ImageJ software was used to measure the thickness of the intermetallic layer. The analysis showed that the thickness decreased by 64.62% with an increase in GNS content up to 0.1 wt.%. The presence of GNS in the solder leads to a reduction in the thickness of the IMC layer due to several factors. The high specific surface area of GNS inhibits the diffusion of metal atoms by acting as a barrier to the diffusion of Sn and Cu atoms. Additionally, due to their low density and tendency to agglomerate, GNS accumulate at the solder/substrate interface, further limiting the diffusion of Cu atoms from the substrate. As a result, the reduced diffusion of Cu slows down the formation and growth of the IMC layer at the solder/substrate interface. This is consistent with the results that have been reported in the literature [10, 11]. The presence of the Cu_6Sn_5 intermetallic phase (spectrum 1-3) was confirmed by EDS analysis, as shown in Figure 4. Furthermore, the detection of carbon at the solder/substrate interface (spectrum 4 and 5) suggests that GNS serves as a diffusion barrier for Cu and Sn atoms, leading to the formation of a thinner intermetallic layer.

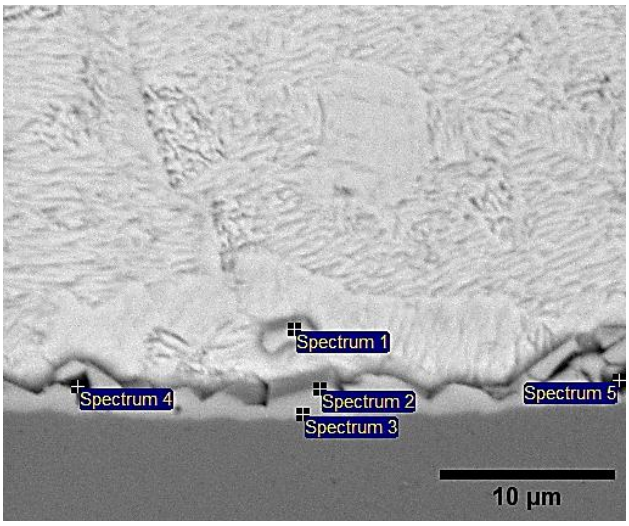

Spectrum	C (wt.%)	Cu (wt.%)	Sn (wt.%)
Spectrum 1	/	35.28	64.72
Spectrum 2	/	40.57	59.43
Spectrum 3	/	43.48	56.52
Spectrum 4	82.32	12.17	5.51
Spectrum 5	87.15	7.14	5.71

Figure 4. EDS analysis of the intermetallic layer between Sn-0.7Cu-0.1GNS solder and Cu substrate

4. CONCLUSION

In this study, Sn-0.7Cu-xGNS (x = 0, 0.02, 0.04, 0.06, 0.08, and 0.1 wt.%) nanocomposite solders were successfully synthesized using the powder metallurgy technique. The experimental results show that increasing the GNS content up to 0.1 wt.% improves wettability and significantly reduces the thickness of the Cu_6Sn_5 intermetallic layer formed at the solder/substrate interface. These improvements promote the formation of a wider and more stable solder joint, leading to enhanced mechanical reliability of the connection.

ACKNOWLEDGEMENTS

The research presented in this paper was done with the financial support of the Ministry of Science, Technological Development and Innovation of the Republic of Serbia, with the funding of the scientific research work at the University of Belgrade, Technical Faculty in Bor, according to the contract with registration number 451-03-137/2025-03/200131.

REFERENCES

[1] A. Sharma, H. R. Sohn, J. P. Jung, Metall. Mater. Trans. A, 47 (2016) 494-503.
[2] D. A. Cory-Slechta, B. Weiss, C. Cox, Toxicol. Appl. Pharmacol., 71 (3) (1983) 342-352.
[3] K. Suganuma, Curr. Opin. Solid. State. Mater. Sci., 5 (1) (2001) 55-64.
[4] K. N. Subramanian, I. E. Anderson, Lead-Free Electronic Solders, Springer, Boston, 2007, p. 55-76.
[5] A. K. Geim, K. S. Novoselov, Nat. Mater., 6 (3) (2007) 183-191.
[6] X. D. Liu, Y. D. Han, H. Y. Jing, J. Wei, L. Y. Xu, Mater. Sci. Eng. A, 562 (2013) 25-32.
[7] F. Lin, M. Ren, L. Zhu, F. Jia, Z. Jiang, Adv. Nanocompos., 2 (2024) 59-85.
[8] W. Yang, Y. Lv, X. Zhang, X. Wei, Y. Li, Y. Zhan, J. Mater. Sci. Mater. Electron., 31 (2020) 14035-14046.
[9] Y. Lv, W. Yang, J. Mao, Y. Li, X. Zhang, Y. Zhan, J. Mater. Sci. Mater. Electron., 31 (2019) 202-211.
[10] M. S. Kang, D. S. Kim, Y. E. Shin, Materials, 12 (6) (2019) 936.
[11] M. L. Li, L. L. Gao, L. Zhang, N. Jiang, S. J. Zhon, L. Zhang, J. Mater. Sci. Mater. Electron., 32 (2021) 26666-26675.

The 56th International October Conference on Mining and Metallurgy
22-25 October 2025, Bor Lake, Bor, Serbia
www.ioc.tfbor.bg.ac.rs

DOI: 10.5937/IOC25434M *Original scientific paper*

STRUCTURAL CHARACTERIZATION OF WELDED JOINTS OF AlSiMg ALLOYS

Srba Mladenović[1a,2a], Nikola Marinković[2b], Dragica Milojković[2c], Jasmina Petrović[1b], Milan Nedeljković[1c]

[1]Technical Faculty Bor, University of Belgrade, V. J. 12, 19210 Bor, Serbia
[2]IMW institute, Lužnice
[1a,2a] smladenovic@tfbor.bg.ac.rs, 0000-0002-3844-7399
[2b] nikola.marinković@imw.rs, 0009-0007-3844-997X
[2c] dragica.milojkovic@imw.rs, 0009-0002-7660-4225
[1b] jpetrovic@tfbor.bg.ac.rs, 0000-0002-9131-339X
[1c] mnedeljkovic@tfbor.bg.ac.rs, 0000-0002-7927-1334

Abstract

The structural characterization of welded joints is described in the standard SRPS EN ISO 17639. The purpose of these tests is to evaluate the crystal structure, morphology, and orientation, as well as the presence of precipitates and inclusions, independently and/or in correlation with various cracks, voids, and other phenomena in metallic materials. The paper presents the results of metallographic examinations of welded joints of 6082 T6 and 6005A alloys. Al 5087 alloy was used as the filler metal. The characteristics of macro and microstructural examinations are presented in terms of detecting irregularities (defects) in the welded component, along with an assessment of the sensitivity of the optical microscopy method in microstructural analysis.

***Keywords**: Macrostructure, microstructure, welded joint, aluminum*

1. INTRODUCTION

Aluminum alloys from the 6000 series, due to their low specific weight, high strength, and good corrosion resistance, are used in almost all industries. Compared to the EN AW 6005 alloy, the EN AW 6082 alloy contains significantly more Mn, which improves the crystal structure and provides greater strength and corrosion resistance. However, the 6005 alloy has better formability in the extrusion process.

Both alloys can be successfully joined by arc welding. The quality of the welded joint depends on several factors. The choice of appropriate filler material, welding technique and procedure, as well as the knowledge of the base material's sensitivity to the occurrence of critical defects during welding (cracks, voids, pores, etc.), represent some of the factors that must be considered to achieve a good welded joint [1].

Hot cracks and voids are two negative phenomena that may occur during the welding process. The mechanisms of their formation different. Hot cracks (solidification/liquation cracks) can occur during the solidification of the welded metal or of the partially melted base metal. The occurrence of these cracks may be caused by a wide solidification range of the welded metal and/or the presence of low-melting eutectics (Al-Mg_2Si, Al-Si, Al-Fe-Si). Voids (shrinkage cavities) form due to the difference in shrinkage between the liquid and solid metal. This phenomenon can also induce crack formation under stresses (if present) that are lower than the material's strength limit [2].

The described defects in the welded material may be localized on the surface and/or in the interior and may affect the quality of the joint. Standard EN ISO 10042 defines the limits of these phenomena for quality levels D, C, and B.

This paper presents the micro- and macrostructural characterization of a welded joint of two aluminum alloys, with special emphasis on the microstructure of the heat-affected zone.

2. EXPERIMENTAL

The MIG welding process (equipment – Kemppi X5) was used to join the aluminum alloys EN AW 6082 and EN AW 6005. A V-groove butt joint of two profiles, each 14 mm thick, was made, with welding performed from one side and with the use of a metallic backing. The material was preheated to a temperature of 100–120 °C, and a forward welding technique without weaving was applied. A schematic of the joint preparation is presented in Figure 1.

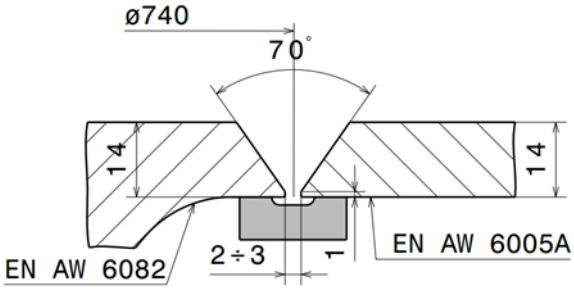

Figure 1. Joint preparation layout

Metallographic examinations of the welded joint were carried out using a Leica DM4 microscope, while macrostructural examinations were performed on a Struers device with magnification up to 50x.

3. RESULTS AND DISCUSSION

The macrostructure of the cross-section of the welded joint of aluminum profiles is shown in Figure 2.

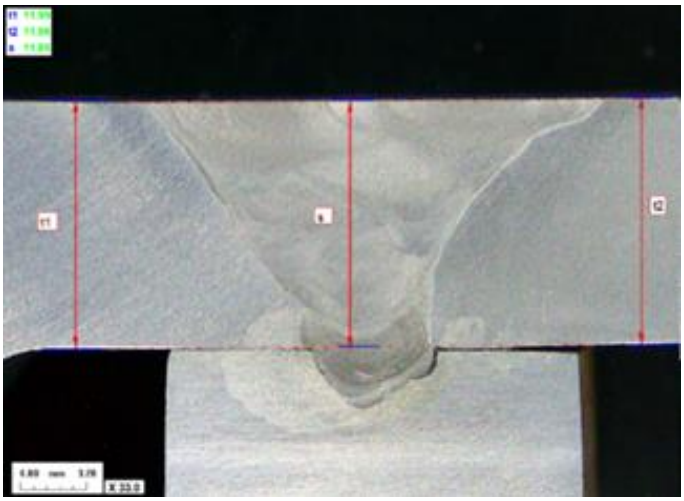

Figure 2. Macrostructure of the welded joint

Table 1 presents the measured characteristics of the welded joint.

Table 1. Thickness of the Al profiles and the welded joint

Marking	Description	Value (mm)
t1	Thickness of base material 1	11.99
t2	Thickness of base material 2	11.96
s	Thickness of butt welded joint	11.89

The quality of the achieved joint can be assessed based on macroscopic and/or microscopic examinations. To a large extent, almost all metallographic characteristics of welded metallic materials can also be evaluated through macroscopic inspection. From the macrograph of the welded Al alloy joint obtained at 30x magnification, it is possible to assess the absence of defects

such as lack of fusion, incomplete root penetration, excess weld metal, excessive penetration, or overlap of the base metal, etc. However, the morphology of the metal structure (appearance, shape and size of grains, structural orientation, precipitates, presence of inclusions) necessarily requires microscopic examination.

Furthermore, surface and internal defects such as cracks, microcracks, pores (individual or localized in lines or clusters, evenly distributed), and cavities can be properly assessed only through metallographic investigations.

In the examined welded joint of aluminum profiles, the microstructure image (Fig. 3) reveals the presence of a defect which, according to the categorization given in ISO 6520-1, can be classified as a type 100 defect [3].

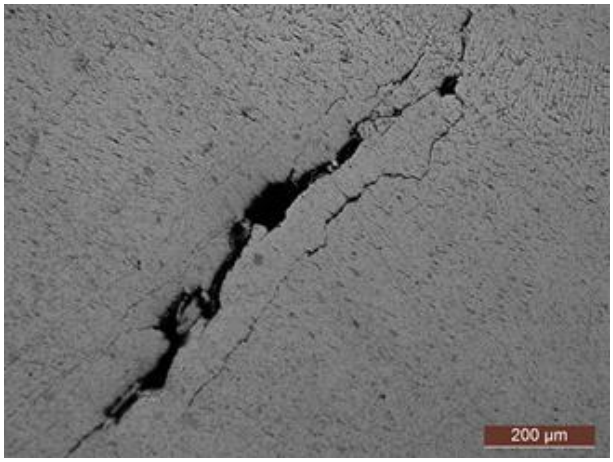

Figure 3. Root crack in the weld

The microstructure of the welded joint (for the 6082 alloy) in the heat-affected zone (HAZ) is shown in Figure 4. In the lower right corner of the image, the base metal structure can be recognized.

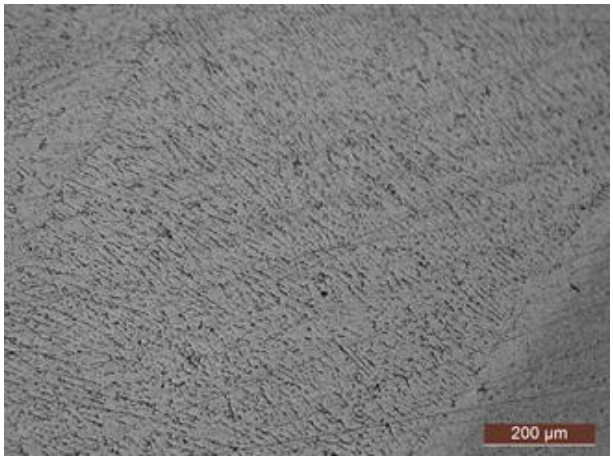

Figure 4. Microstructure of the HAZ, base material 6082 alloy

The transition zone is clearly evident, featuring columnar crystals with oriented alignment in the direction of intense heat dissipation, and the area where the weld structure changes into a cellular structure. On the other side of the welded joint, the microstructure of the HAZ (for the 6005A alloy) is shown in Figure 5.

Significant differences in the morphology of the welded joint between the 6082 and 6005A alloys cannot be observed. The structural morphology is quite similar. Here, the columnar crystal zone is also present, although it appears less pronounced and less developed compared to the HAZ microstructure shown in the previous figure [4].

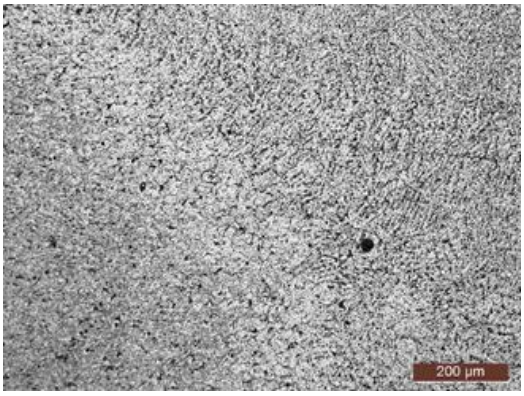

Figure 5. Microstructure of the HAZ, base material 6005A alloy

4. CONCLUSION

In this study, the micro and macrostructure of the welded joint of two aluminum alloys with different compositions was investigated. Structural characterization of the joint was carried out with particular emphasis on the presence of defects identified and categorized according to standard ISO 6520-1. Additionally, the sensitivity of the optical microscopy method was examined regarding its ability to detect fine differences in the microstructure of the HAZ. The following conclusions can be drawn:

1. Macrostructural examinations can fully determine welding flaws (defects) resulting from the welding technique itself, such as lack of fusion, incomplete root penetration, excess weld metal, excessive penetration, etc.
2. Microstructural examinations are indispensable when it is necessary to determine the morphology of the microstructure (grain shape and size, structural orientation, cellular or dendritic type, etc.). More detailed and accurate assessment of the presence of defects (surface and internal), such as cracks of various origins, pores, shrinkage cavities, inclusions, etc., can be performed using optical microscopy for microstructural analysis of metals and alloys.
3. The sensitivity of the optical microscopy method is defined by its ability to resolve fine elements within the microstructure. More detailed investigation of microstructural features (precipitates, specific inclusions, eutectics, etc.) can be achieved using other complementary techniques, such as SEM-EDS and XRD, which supplement the capabilities of optical microscopy.

ACKNOWLEDGEMENTS

The research presented in this paper was done with the financial support of the Ministry of Science, Technological Development and Innovation of the Republic of Serbia, with the funding of the scientific research work at the University of Belgrade, Technical Faculty in Bor, according to the contract with registration number 451-03-137/2025-03/200131.

REFERENCES

[1] P. Kah, E. Hiltunen, J. Martikainen, Proceedings of the 63rd Annual Assembly & International Conference of the International Institute of Welding, 11-17 July, Istanbul, Turkey, 2010.
[2] C.E. Cross, T. Böllinghaus. Weld. world, 50 (2006) 51-54.
[3] SRPS EN ISO 6520-1:2013, Weldin and allied processes- Clasification of geometric imperfections in metallic materials – Part 1, Institut za standardizaciju Srbija, (2013).
[4] F. Mazzolani, Aluminium alloy structures, CRC Press, (1994).

The 56th International October Conference on Mining and Metallurgy
22-25 October 2025, Bor Lake, Bor, Serbia
www.ioc.tfbor.bg.ac.rs

DOI: 10.5937/IOC25438S *Original scientific paper*

DEVELOPMENT OF THE AL-SI ALLOY WITH NIOBIUM ADDITION FOR GIGACASTINGS

Martina Sýkorová[1a], Dana Bolibruchová[1b], Marek Matejka[1c]

[1] Faculty of Mechanical Engineering, University of Žilina, Univerzitná 8215/1, 010 08, Žilina, Slovakia
[1a] martina.sykorova@fstroj.uniza.sk, 0000-0001-6418-8450
[1b] danka.bolibruchova@fstroj.uniza.sk, 0000-0002-7374-9763
[1c] marek.matejka@fstroj.uniza.sk, 0000-0002-4156-5521

Abstract

The article focuses on developing a new aluminum alloy based on Al-Si that is alloyed with the non-standard element niobium (Nb). The research aims to evaluate the effect of Nb addition on the microstructure and porosity area fraction of the AlSi5Cu2Mg alloy. The study will determine the optimal amount of Nb to add. Microstructural analysis revealed that adding Nb refines the primary phase, α-(Al), and the eutectic Si and reduces the size of the iron-rich phases. Nb's effectiveness as a modifier and inoculant increases with greater additions. Adding Nb resulted in a favorable decrease in the area fraction of porosity in the aluminum alloy, with the area fraction of porosity decreasing with increasing Nb additions.

***Keywords**: aluminum alloys, niobium, gigacastings.*

1. INTRODUCTION

The automotive industry is under increasing pressure to reduce emissions, improve energy efficiency, and optimize manufacturing processes. Amid these challenges, large-scale aluminum castings, or "gigacasts," are gaining prominence by combining multiple vehicle parts into one component [1]. The advantages of using large-scale castings include reduced weight, fewer welded joints, and enhanced structural integrity. In electromobility, large-scale castings contribute to an extended driving range, higher energy efficiency, and reduced overall energy consumption. However, the practical application of large-scale castings presents several design and technological challenges. These include difficulty ensuring a uniform microstructure, risk of porosity and cracking, and limited repairability. Nevertheless, large-scale castings have the potential to become a key element in the future of automotive manufacturing. [2,3]

Aluminum-silicon (Al-Si) alloys with approximately 10 wt.% Si are standard structural materials for large-scale castings. While these alloys have excellent casting properties, their mechanical properties often fail to meet requirements for large-scale structural castings, limiting their application. An effective way to optimize the mechanical properties of Al-Si alloys is to lower the silicon content. Decreasing the silicon content reduces the amount of brittle eutectic phases, thereby improving the mechanical properties. Another promising approach to improving the properties of aluminum alloys for large-scale applications is using transition elements (e.g., Nb, Zr, and Ni) as alloying elements. These elements are notable for their tendency to form thermodynamically stable Al_3X dispersoids. Thermally stable niobium-based phases play a significant role in maintaining mechanical properties under elevated operating conditions. Current research focuses on developing a novel, low-silicon, Al-Si-based aluminum alloy with niobium as an unconventional alloying element for large-scale structural castings [4,5].

2. EXPERIMENTAL METHODOLOGY

For experimental purposes, a hypoeutectic aluminum alloy, AlSi5Cu2Mg, was selected. This alloy is characterized by a low silicon content (5.0 – 6.5 wt.% Si). The chemical composition of the AlSi5Cu2Mg alloy is provided in Table 1.

Table 1. Chemical composition of the AlSi5Cu2Mg alloy [wt.%].

Alloy	Si	Cu	Mg	Mn	Fe	Cr	Sr	Al
AlSi5Cu2Mg	6.48	1.92	0.29	0.013	0.19	0.004	0.03	Bal.

The hypoeutectic aluminum alloy AlSi5Cu2Mg was melted in an electric resistance furnace using a graphite crucible. Experimental alloys were prepared by alloying the AlSi5Cu2Mg base alloy with 0.1, 0.15, and 0.20 wt.% Nb. Niobium was added to the melt in the form of an AlNb10 master alloy. This master alloy was melted separately in an electric induction furnace within a graphite crucible and then added to the main melt. Experimental samples were cast using a gravity casting technique in an open atmosphere with a permanent mold. The permanent mold, treated with a graphite coating, was maintained at a temperature of 150 ± 5 °C. The casting temperature was set at 750 ± 5 °C. The chemical composition of the experimental alloys is provided in Table 2. Chemical analysis revealed a discrepancy between the nominal and actual measured Nb additions. This difference could be attributed to the limited solubility of Nb, Nb segregation during solidification, or losses during melt handling.

Table 2. Chemical composition of the experimental alloys [wt.%].

Alloy	Si	Cu	Mg	Mn	Fe	Sr	Nb	Al
AlSi5Cu2Mg + 0.10 wt.%	6.52	2.40	0.25	0.012	0.23	0.004	**0.049**	Bal.
AlSi5Cu2Mg + 0.15 wt.%	6.58	2.46	0.19	0.014	0.23	0.005	**0.063**	Bal.
AlSi5Cu2Mg + 0.20 wt.%	6.82	2.34	0.19	0.012	0.22	0.006	**0.076**	Bal.

For each experimental variant, a set of 10 test samples was prepared for the analysis of mechanical and physical properties. Half of these samples were subjected to a T7 heat treatment regime, which consisted of solution heat treatment (500 ± 5 ºC for 6.5 h), rapid cooling (85 ± 5 ºC), and aging (250 ± 5 ºC for 4 h). Microstructural analysis and evaluation of area fraction porosity were performed on samples that demonstrated an optimal combination of mechanical and physical properties. The microstructure of the experimental alloys was examined in both the as-cast condition and after T7 heat treatment using a Keyence VHX – 7000 digital microscope. Porosity was determined based on the assessment of the area fraction of pores, which was evaluated using the graphical software Quick Photo Industrial 3.1.

3. RESULTS AND DISCUSSION

3.1 Microstructure analysis

The microstructure of the AlSi5Cu2Mg alloy without Nb addition consists of the primary α-(Al) phase, eutectic Si, and Cu- and Fe-based phases (Figure 1a). In the plane of the metallographic cross-section, the eutectic Si appears as imperfectly rounded grains. The morphology of the as-cast eutectic Si does not exhibit the typical plate-like shape because the AlSi5Cu2Mg alloy was supplied in a pre-modified state. The Fe-based intermetallic phases were observed in two morphologies: plate-like β-Al_5FeSi and segmented chinese script-like $Al_{15}(FeMn)_3Si_2$. Cu-rich intermetallic phases were precipitated as a compact ternary eutectic of Al-Al_2Cu-Si or as isolated Al_2Cu particles. Microstructures of the alloys with graded Nb additions are shown in Figure 1b-d. The addition of Nb led to a significant grain refinement of the primary α-(Al) phase and refinement of the eutectic Si. A reduction in size and fragmentation of the Fe-based intermetallic phases were also observed in the metallographic cross-sections of the Nb-containing alloys. Microstructural

analysis demonstrated a clear correlation between the Nb addition and the refinement of the AlSi5Cu2Mg alloy's microstructure, with the most significant refinement achieved at the highest Nb content. In the alloy with a 0.10 wt.% Nb addition, large compact particles were locally observed. These particles were identified as Nb-rich phases. These phases were not observable in the alloys with 0.15 and 0.20 wt.% Nb additions.

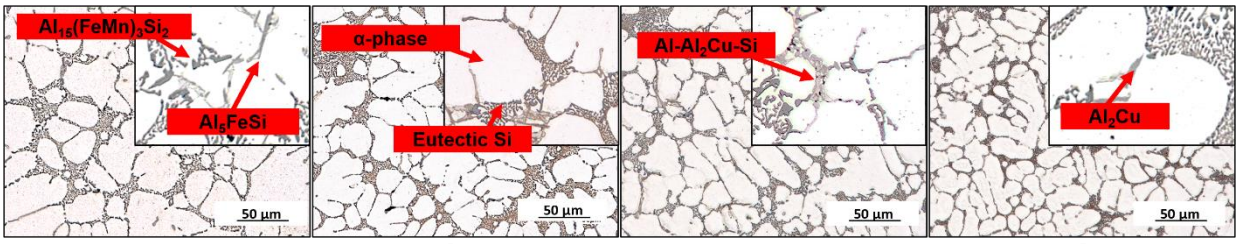

Figure 1. Microstructure of the AlSi5Cu2Mg alloy in the as-cast state: a) 0 wt.% Nb, b) 0.10 wt.% Nb, c) 0.15 wt.% Nb, d) 0.20 wt.% Nb.

The microstructure of the AlSi5Cu2Mg alloy without Nb after T7 heat treatment is shown in Figure 2a. The T7 treatment leads to the spheroidization of eutectic Si, which precipitates in the form of perfectly rounded grains. The Mg- and Cu-rich intermetallic phases were dissolved during the T7 heat treatment and subsequently reprecipitated as strengthening precipitates. Fe-based phases were observed in the metallographic cross-section of the AlSi5Cu2Mg alloy in the form of plate-like β-Al_5FeSi. Similar to the as-cast state, grain refinement of the primary α-(Al) phase and refinement of the eutectic Si were also observed after the T7 treatment due to the Nb addition. Locally, fragmentation of the eutectic Si was observed, appearing as very small, perfectly rounded particles. The T7 heat treatment did not cause a change in the morphology or size of the segregated Nb-based phases, which were observed as large compact particles. This observation indicates the high thermal stability of the Nb-based phases.

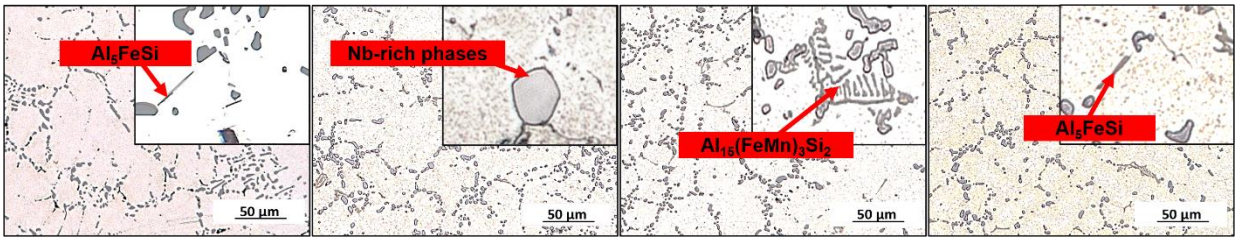

Figure 2. Microstructure of the AlSi5Cu2Mg alloy after T7: a) 0 wt.% Nb, b) 0.10 wt.% Nb, c) 0.15 wt.% Nb, d) 0.20 wt.% Nb.

3.2 Evaluation of the area fraction of porosity

The area fraction of porosity was determined based on the average of five measurements taken at randomly selected locations on the metallographic cross-sections of the experimental alloys. The values for the area fraction of porosity are listed in Table 3. The area fraction of porosity of the alloy without Nb addition was 0.6%. Alloys with an Nb addition showed a decrease in the area fraction of porosity compared to the alloy without Nb, with the area fraction of porosity decreasing as the Nb wt.% increased. An addition of 0.1 wt.% Nb led to a minimal decrease in the area fraction of porosity by 3% compared to the alloy without an Nb addition. The addition of 0.15 and 0.20 wt.% Nb resulted in a more significant decrease in the area fraction of porosity by 27% and 37%, respectively, compared to the alloy without Nb. In this case, Nb acts as an effective inoculant and

also favorably modifies the eutectic Si. Due to the inoculating and modifying effects, a finer microstructure is formed, which minimizes porosity formation [6].

Table 3. Area fraction of porosity of experimental alloys.

Alloy	AlSi5Cu2Mg	+ 0.10 wt.% Nb	+ 0.15 wt.% Nb	+ 0.20 wt.% Nb
Area fraction of porosity	0.60 %	0.58 %	0.44 %	0.38 %

4. CONCLUSION

The article focused on evaluating the effect of graded Nb addition on the microstructure and surface porosity of the AlSi5Cu2Mg aluminum alloy. Based on the summarized results, the following conclusions can be drawn:

- Microstructural analysis showed that the Nb addition led to grain refinement of the primary α-(Al) phase, refinement of the eutectic Si, and a reduction in the size and fragmentation of the Fe-based phases.
- The effectiveness of Nb in refining the microstructure of the AlSi5Cu2Mg alloy increased with a higher Nb content (wt.%).
- Due to the inoculating and modifying effect of Nb, a favorable decrease in the area fraction of porosity was observed. The area fraction of porosity of the aluminum alloys decreased with an increasing wt. % of Nb.

This article demonstrated that, due to its effective grain refinement and modifying effect, niobium has a beneficial influence on the microstructure and area fraction of porosity of the investigated AlSi5Cu2Mg aluminum alloy. Nb appears to be a promising alloying element for aluminum alloys intended for large-scale castings. Therefore, in the next step, the research will focus on investigating the influence of Nb on the foundry, mechanical, and physical properties of the AlSi5Cu2Mg aluminum alloy.

ACKNOWLEDGEMENTS

The article was created as part of the VEGA grant agency project: VEGA 1/0160/22. The authors thank for its support.

REFERENCES

[1] A. Hartlieb, M. Hartlieb., The Impact of Giga-Castings on Car Manufacturing and Aluminum, Light Metal Age, (2023) [Accessed on: 2025-08-10]. Available at:
https://www.lightmetalage.com/news/industry-news/automotive/the-impact-of-giga-castings-on-car-manufacturing-and-aluminum-content/
[2] Qg. Wang, A. Wang, J. Coryell., China Foundry., 21 (2024) 397-408.
[3] Fraunhofer IFAM., Castings for Electromobility., Fraunhofer Institute for Manufacturing Technology and Advanced Materials IFAM, n.d., [Accessed on: 25-08-10] Available at:
https://www.ifam.fraunhofer.de/en/technologies/castings-for-electromobility.html
[4] M. Cijo, K. Pratheesh, C. K. Varghase., Int. J. Eng., 29 (6) (2015) 299-303.
[5] Ch. Gao, I. Zhang, B. Zhang., Metals., 11 (2) (2021) 357.
[6] M. Çolak, Ö. Yalçin., Int. J. Met., (2025).

The 56th International October Conference on Mining and Metallurgy
22-25 October 2025, Bor Lake, Bor, Serbia
www.ioc.tfbor.bg.ac.rs

DOI: 10.5937/IOC25442S Original scientific paper

INSIGHTS INTO THE GLASS NETWORK STRUCTURE OF COAL FLY ASH-BASED GLASS

Veljko Savić[1a], Vladimir Topalović[1b], Jelena Nikolić[1c], Marija Djošić[1d], Milena Obradović[1e], Danijela Smiljanić[1f], Snežana Grujić[2a]

[1]Institute for Technology of Nuclear and Other Mineral Raw Materials, Bulevar Franše d'Eperea 86, 11000, Belgrade, Serbia
[2]University of Belgrade, Faculty of Technology and Metallurgy, Karnegijeva 4, 11000, Belgrade, Serbia
[1a] v.savic@itnms.ac.rs, 0000-0002-8602-8260
[1b] v.topalovic@itnms.ac.rs, 0000-0002-4177-4649
[1c] j.nikolic@itnms.ac.rs, 0000-0002-9624-8865
[1d]m.djosic@itnms.ac.rs, 0000-0002-0869-2182
[1e]m.obradovic@itnms.ac.rs, 0000-0002-1349-1924
[1f]d.smiljanic@itnms.ac.rs, 0000-0003-3560-1415
[2a] grujic@tmf.bg.ac.rs, 0000-0002-9123-6830

Abstract
Coal fly ash is the by-product of coal combustion in thermal power plants. The chemical composition of coal fly ash allows it to be utilized as a secondary raw material for glass production. Na_2CO_3 and $CaCO_3$ were introduced in the batch as raw materials for glass network modification. Dark homogenous glass was obtained by melting the batch and quenching it on the stainless steel in the air. This research investigates the relative share of structural units of the glass network by deconvolution of the part of the FTIR spectra. Results show that most dominant structural units contain one and two bridging oxygen per [SiO_4] tetrahedral indicating low glass network connectivity.

Keywords: *Coal fly ash, Glass, FTIR, Deconvolution*

1. INTRODUCTION

The global reliance on coal for electricity generation has resulted in the large-scale production of coal fly ash, raising significant environmental concerns. Coal fly ash, a fine particulate residue generated during the combustion of pulverized coal in thermal power plants, represents one of the most abundant industrial by-products worldwide. Traditionally viewed as waste, coal fly ash is typically disposed of in landfills or ash ponds, posing long-term environmental and economic challenges [1]. However, due to its rich chemical composition- primarily consisting of silicon dioxide (SiO_2), aluminum oxide (Al_2O_3), calcium oxide (CaO), and other oxides- fly ash is increasingly being recognized as a valuable secondary raw material for various industrial applications. It can be utilized as a secondary raw material in applications such as cement additives, road construction, filter and adsorbent synthesis, geopolymer production, etc [2-4]. Among these applications, the utilization of fly ash in the production of glassy materials has gained considerable attention. The high content of glass network-forming oxides makes fly ash an attractive alternative to conventional raw materials. Through appropriate thermal processing, fly ash can be melted and vitrified to form homogeneous glass. Recycling fly ash into glass products not only reduces the environmental burden associated with its disposal but also supports the principles of the circular economy by converting industrial waste into high-value materials. This approach offers a sustainable pathway for the development of new construction materials, coatings, insulating components, and other functional products [5]. The present study investigates the potential of coal fly ash as a primary component in glass synthesis. Modifying cations were introduced in the batch to reduce the amount of bridging oxygen in [SiO_4] tetrahedra. The lower amount of bridging oxygen per tetrahedra implies the lower viscosity of the melt which benefits glass formation. Using

Fourier Transform Infrared Spectroscopy (FTIR) analysis and deconvoluting the part of the spectra gives information on the types of structural units of the glass network and the amount of bridging oxygen in the produced glass.

2. EXPERIMENTAL

The glass was prepared using coal fly ash, Na_2CO_3, and $CaCO_3$ as raw materials as described in the previous research [1]. The chemical composition of the glass was determined using an Atomic Absorption Spectrometer (AAS) Perkin Elmer 703. The structural characteristics of the produced glasses and glass-ceramics were analyzed using Fourier Transform Infrared Spectroscopy (FTIR). The measurements were conducted with a Nicolet iS50 spectrophotometer (Thermo Fisher Scientific, Waltham, MA, USA) over the wavenumber range of 4000 to 400 cm^{-1}.

3. RESULTS AND DISCUSSION

The chemical composition of the obtained glass is presented in Table 1.

Table 1. Chemical composition of the glass

Oxide	SiO_2	Al_2O_3	CaO	MgO	Na_2O	K_2O	TiO_2	Fe_2O_3
mol %	49.95	11.99	21.92	2.18	10.69	0.57	0.70	2.00

Dark homogenous glass was produced with a high amount of modifying oxides which enabled good pourability of glass melt. The structure analysis of the glass by FTIR method is presented in Figure 1.

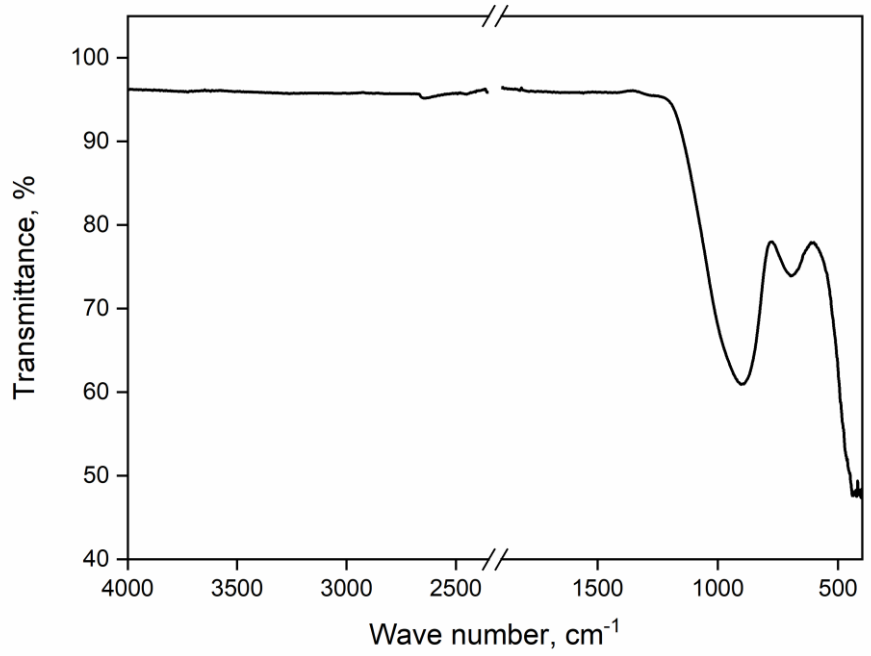

Figure 1. FTIR analysis of the glass sample

Figure 1 shows three absorption zones typical of aluminosilicate glasses. The first zone, at about 470 cm^{-1}, corresponds to bending vibrations of bridging oxygen in Si-O-Si or Si-O-Al bonds

within tetrahedral structures. The second one, at approximately 710 cm^{-1}, corresponds to symmetric stretching vibrations in X-O-X structures (X=Si, Al or Fe). The third and broadest zone, between 1200 and 800 cm^{-1}, represents strong absorption bands related to asymmetric stretching of bridging oxygen in Si-O-Si or Si-O-Al bonds, and stretching vibrations of non-bridging oxygen in O-Si-O linkages [6, 7]. Deconvolution of the third zone of the spectra can give insights into a glass network structure. The band at 1200-800 cm^{-1} can be divided into five individual bands, Q^n (n=0-4), where n represents the number of bridging oxygen in the tetrahedral [SiO_4] structure. Figure 2 presents the deconvoluted part of the spectra.

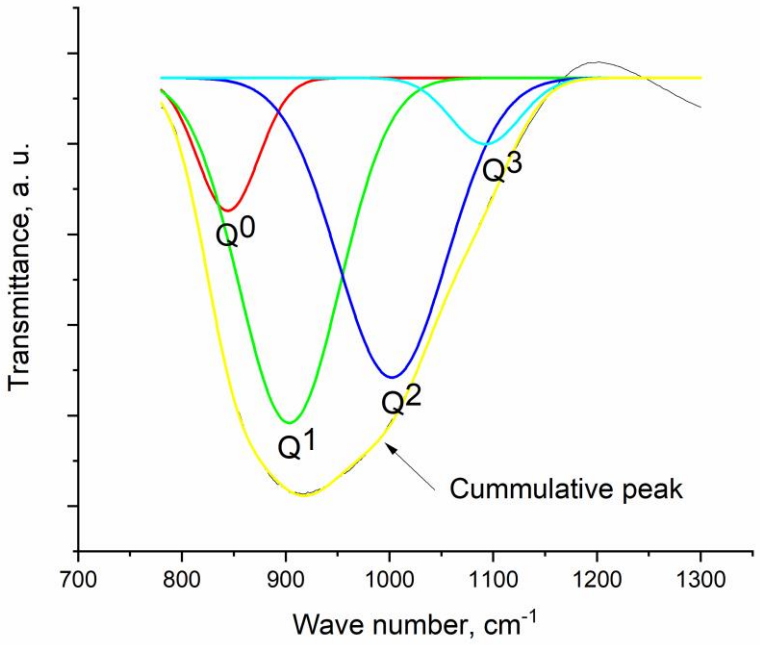

Figure 2. Deconvolution of the part of FTIR spectra

It can be observed that the glass sample does not contain structural units with all four bridging oxygens (Q^4 units), indicating that the introduction of modifying cations in the glass batch has disrupted the silicate network. These modifiers break Si–O–Si bonds and generate structural units containing non-bridging oxygens, most dominantly Q^2 and Q^1 species, which are characterized by silicon tetrahedra containing two and one bridging oxygen atoms, respectively. Table 2 presents Q-units and their corresponding Infrared (IR) band wave numbers [8].

Table 2. IR bands of Q^n structural units

Name of the structural unit	Number of non-bridging oxygen	IR band according to literature [8], cm^{-1}	IR band (this research), cm^{-1}
Q^0	4	840-890	844
Q^1	3	900-950	903
Q^2	2	960-1030	1002
Q^3	1	1050-1100	1092
Q^4	0	1160-1190	/

The relative distribution of tetrahedral structural units within the glass network is as follows: Q^0 units comprise 10.12%, Q^1 units 43.33%, Q^2 units 40.84%, and Q^3 units 5.7%. This distribution indicates a predominantly disrupted silicate network, with a high proportion of Q^1 and Q^2 units. Number of bridging oxygen per tetrahedra (BO/T) was calculated according to equation 1 [7]:

$$BO/T = 0 \cdot Q^0 + 1 \cdot Q^1 + 2 \cdot Q^2 + 3 \cdot Q^3 + 4 \cdot Q^4 \quad (1)$$

The number of bridging oxygen per tetrahedral is 1.42 indicating low glass network connectivity. The introduction of CaO and Na_2O into the glass batch composition acts as a network modifier, disrupting the continuous silica network by breaking Si–O–Si bonds. This disruption results in the formation of non-bridging oxygen. The presence of these non-bridging oxygens reduces the overall connectivity of the silicate network, thereby lowering the glass's viscosity. This reduction in viscosity is crucial during the melting process, as it enables optimal conditions for the glass melting process. The low amount of bridging oxygen per tetrahedra is expected knowing that a high amount of modifying cations were introduced in the batch.

4. CONCLUSION

The dark homogenous glass was produced by melting and quenching on the stainless steel batch that contains coal fly ash, Na_2CO_3, and $CaCO_3$. FTIR analysis showed spectra typical of aluminosilicate glasses. Deconvolution of the part of the spectra between 1200 and 800 cm^{-1} gave insights into glass network structure. There was no detected Q^4 structural unit and 1.42 bridging oxygen per [SiO_4] tetrahedral indicating low glass network connectivity.

ACKNOWLEDGEMENTS

This work was supported by the Ministry of Science, Technological Development and Innovation of the Republic of Serbia (Contract No. 451-03-136/2025-03/200023 and 451-03-136/2025-03/200135).

REFERENCES

[1] V. Savić, M. Dojčinović, V. Topalović, I. Cvijović-Alagić, J. Stojanović, S. Matijašević, S. Grujić, Int. J. Environ. Sci. Technol., 21 (2024) 6065–6074.
[2] E. Ercenk, T. Yasar, S. Demirkiran, S. Yilmaz, J. Therm. Anal. Calorim., 148 (10) (2023) 4015–4031.
[3] X. Zhao, H. Zhao, X. Huang, L. Wang, F. Liu, X. Hu, et al., Ecotoxicol. Environ. Saf., 223 (2021) 112550.
[4] Z. Hussain, N. Chang, J. Sun, S. Xiang, T. Ayaz, H. Zhang, et al., J. Hazard. Mater., 422 (2022) 126778.
[5] E. Worrell, M.A. Reuter., Handbook of Recycling: State-of-the-art for Practitioners, Analysts, and Scientists, Elsevier, Waltham, MA, 2014.
[6] E. Montoya-Quesada, M.A. Villaquirán-Caicedo, R.M. De Gutiérrez, Bol. Soc. Esp. Ceram. Vidr., 61 (4) (2022) 284–299.
[7] C. Zou, J. Cao, M. Zhao, Z. Wang, J. Lu, J. Eur. Ceram. Soc., 39 (15) (2019) 4979–4987.
[8] W. Xu, K. Shen, Z. Cao, F. Liu, Y. Zhang, T. Zhang, N. Wu, S. Ouyang, Mater. Chem. Phys., 263 (2021) 124334.

The 56th International October Conference on Mining and Metallurgy
22-25 October 2025, Bor Lake, Bor, Serbia
www.ioc.tfbor.bg.ac.rs

DOI: 10.5937/IOC25446S Original scientific paper

THERMOMECHANICAL TREATMENT OF S275JR STEEL: IMPACT ON MICROSTRUCTURE, HARDNESS, AND IMPACT TOUGHNESS

Uroš Stamenković[1a], Ivana Marković[1b], Dragan Manasijević[1c], Milan Nedeljković[1d]

University of Belgrade - Technical Faculty Bor, V.J. 12, 19210 Bor, Serbia
[1a] ustamenkovic@tfbor.bg.ac.rs, 0000-0002-7579-2159
[1b] imarkovic@tfbor.bg.ac.rs, 0000-0003-4431-9921
[1c] dmanasijevic@tfbor.bg.ac.rs, 0000-0002-7828-8994
[1d] mnedeljkovic@tfbor.bg.ac.rs, 0000-0002-7927-1334

Abstract
This study investigates how different thermomechanical treatment procedures affect the hardness, microhardness, impact toughness, and microstructure of S275JR structural steel. For the experiment, an as-received rectangular bar of structural steel was normalized at 900 °C for 60 minutes. Following normalization, the samples were pre-strained (cold deformed) by 8% at room temperature using a rolling mill. After deformation, the samples were aged for 30 minutes at temperatures of 100 °C, 150 °C, 200 °C, and 250 °C. The hardness, microhardness, impact toughness, and microstructure were analyzed for both the as-received sample and treated samples. The results indicated that normalization improved both hardness and impact toughness due to grain refinement. The straining conducted after normalization led to an increase in hardness but a decrease in impact toughness as a result of work hardening. The subsequent aging further strengthened the material, likely due to the interaction between dislocations and secondary phase particles, such as Fe_3C and other alloying elements.

***Keywords**: S275JR steel, normalization, strain aging, impact toughness, hardness*

1. INTRODUCTION

Steel ranks as the most widely utilized material in the 21st century. Its affordability and ease of processing make it a desirable option for various industries [1]. General structural mild steels, classified within a broader category of steels, are valued in various industries for their strength, ductility, and good weldability [2, 3]. Structural steels are classified as carbon-manganese steels, and their microstructure can be altered through heat treatment. This ability enables a straightforward enhancement of their mechanical properties. As a result, the automotive industry considers these steels highly desirable for applications in body panels, chassis parts, and other structural components [4-6]. S275JR structural steel, classified as low- to medium-carbon steel with approximately 0.2% carbon content, has limited options for heat treatment. These steels are rarely used in a quenched state because the martensitic transformation can lead to brittleness. The heat treatment process for this type of steel generally involves heating it above the eutectoid temperature and then cooling it in a controlled manner. This approach aims to achieve a balanced microstructure consisting of a mixture of ferrite, pearlite, and/or bainite, which helps promote optimal hardness and toughness [7-9]. Strain aging is a specific heat treatment technique commonly used for low-carbon and low-alloy steels. Strain aging in steels involves plastic deformation at room temperature, typically following a normalizing or annealing treatment. The material is then aged at room or slightly elevated temperature (~200 °C). This heat treatment allows dislocations created during the plastic deformation to become pinned by diffusing atoms, such as nitrogen, carbon, or manganese. As a result, the steel's strength is increased; however, this comes at the cost of reduced ductility and toughness [2]. The aim of this paper was to investigate the influence of strain aging on hardness, microhardness, impact toughness, and microstructure. Various properties were examined after normalizing heat treatment at 900 °C for 60 minutes,

followed by air cooling. Once normalized, the samples were subjected to an 8% strain (cold deformation) and then aged for 30 minutes at 100 °C, 150 °C, 200 °C, and 250 °C.

2. EXPERIMENTAL

The hot rolled 12×12×1000 mm rectangular S275JR steel bar was used in this study. Before the thermomechanical treatment, the as-received (*AR*) samples were cut and prepared for hardness, microhardness and impact toughness measurements. One of them was left for further testing and all other samples were normalized at 900 °C for 60 minutes, followed by air cooling. This was done in order to remove the as-received structure and further refine the microstructure. After cooling, two normalized (N) samples were separated for analysis: one was used for impact toughness testing, and the other for all remaining tests. Other normalized samples were then subjected to 8% strain (cold deformation) on Joliot Paris rolling mill. These samples were labeled as *N+D* (normalized and deformed). After deformation, four samples were strain aged for 30 minutes at 100 °C (*NDA100*), 150 °C (*NDA150*), 200 °C (*NDA200*), and 250 °C (*NDA250*). After aging the samples were separated for individual analyses.

During the thermomechanical treatment hardness was measured on VEB Leipzig hardness tester with a 15 kg load and a 15 s dwelling time following the ASTM E92-17 [10]. Also, microhardness values were measured using a PMT-3 Vickers microhardness tester using 150 gf loads with load duration of 15 s, according to ASTM E384-22 [11]. The impact toughness was determined using the VEB Leipzig Charpy pendulum, following the EN ISO 148-1:2016 [12]. The samples were machined to dimensions of 10×10×55 mm with a V-notch that is 2 mm deep. The mass of the pendulum hammer was 18.65 kg.

For microstructural analysis, the specimens were sanded using emery paper ranging from Grit 3 to Grit 0000, and then polished with an alumina slurry with particle size of 0.3 and 0.05 microns. To reveal the microstructure, the specimens were etched with a 2% Nital solution (2 ml of HNO_3 mixed with 98 ml of C_2H_5OH) for 15 seconds. The microstructures were examined using Carl Zeiss Jena Epytip 2 optical microscope.

3. RESULTS AND DISCUSSION

Figure 1 illustrates the results of hardness and microhardness measurements taken after each step of the thermomechanical treatment. From the figure, it can be concluded that both hardness and microhardness increased following the normalization treatment (sample N). The structure of the as-received (AR) sample was refined after heat treatment, which contributed to the increase in hardness and microhardness values. Further analysis revealed that the introduction of cold deformation resulted in a significant increase in both hardness and microhardness due to work hardening. When an 8% strain was applied gradually through rolling, the dislocation density increased, which hindered further dislocation movement and resulted in the hardening of the material. Following strain aging, the hardness and microhardness of the deformed samples exhibited notable variations. Aging at 100 °C for 30 minutes resulted in a slight increase in both properties compared to the N+D sample. In contrast, subsequent aging at more elevated temperatures (150 °C and 200 °C) led to a modest reduction in hardness and microhardness values. The highest measurements were observed after strain aging at 250 °C for 30 minutes. The increase in both hardness and microhardness can be attributed to diffusion of interstitial atoms such as C and N. At elevated temperatures, interstitial atoms become mobile and diffuse through the lattice, where they interact with dislocations to form Cottrell atmospheres, effectively impeding further dislocation motion [2, 13-16]. An addition to this mechanism, strengthening can also arise from interactions between dislocations and secondary particles, such as Fe_3C (cementite) or other precipitates formed from alloying elements [17]. Moreover, cold deformation lowers the activation energy required for diffusion, thereby facilitating these strengthening mechanisms [2].

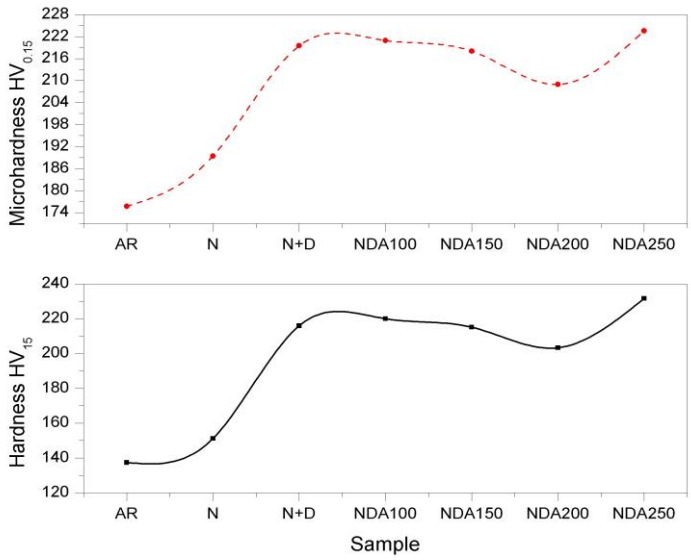

Figure 1 – The change in hardness and microhardness values as a function of thermomechanical treatment

Table 2 – The results of the Charpy V-notch impact test of the selected samples

Sample	Impact toughness (J)
AR	175.31
N	196.42
N+D	88.3
NDA100	120.2
NDA250	83.38

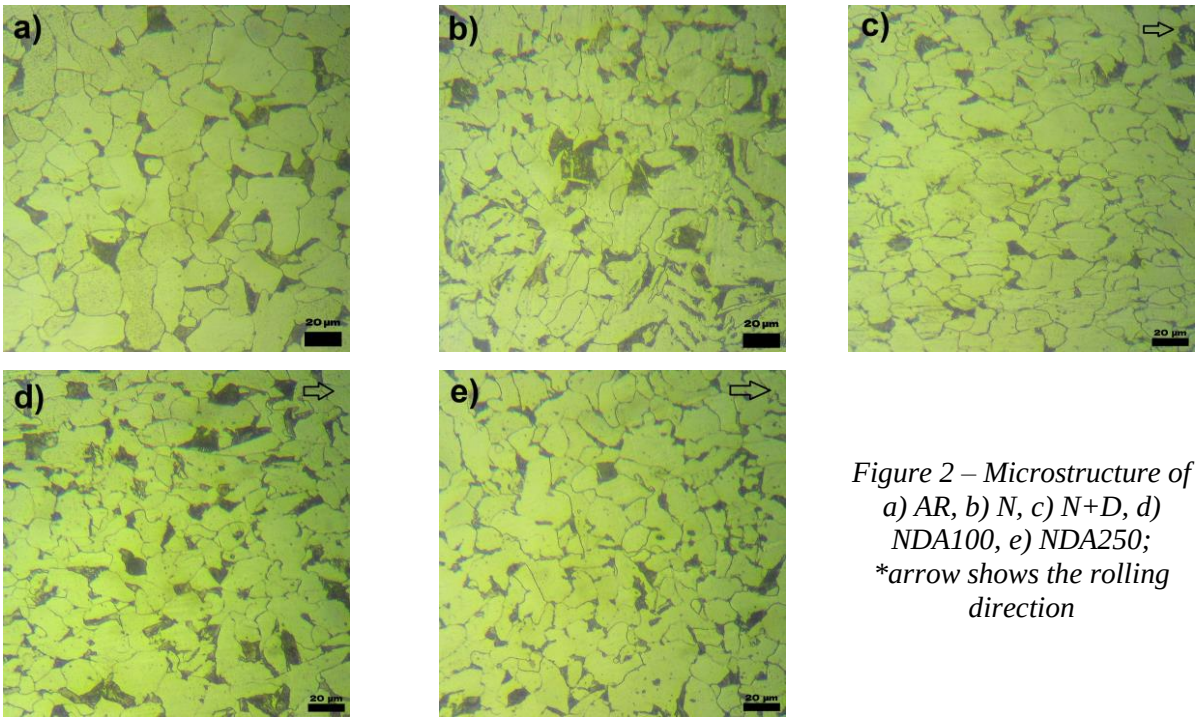

*Figure 2 – Microstructure of a) AR, b) N, c) N+D, d) NDA100, e) NDA250; *arrow shows the rolling direction*

Table 2 presents the results of the Charpy V-notch impact toughness test. The data indicate that normalization led to a slight increase in impact toughness, as evidenced by the comparison between the as-received (AR) and normalized (N) samples. J. Brnic et al. obtained somewhat similar results [18]. This improvement is attributed to grain refinement, which enhanced the material's ability to absorb energy during impact. In contrast, the introduction of plastic deformation resulted in a significant reduction in impact toughness, with values decreasing by more than 50%, from 196.42 J to 88.3 J. For the strain-aged samples (NDA), aging at 100 °C resulted in a considerable increase in impact toughness, whereas aging at 250 °C led to a decline in toughness values. Typically, strain aging promotes the formation of Cottrell atmospheres, which generally reduce impact toughness while increasing strength and hardness, as observed in the NDA250 sample. However, in some cases, mild strain aging (characterized by low deformation and short aging duration) can enhance toughness, as demonstrated by the NDA100 sample. In summary, the strengthening mechanisms

responsible for the increased hardness and microhardness values generally correspond to a decrease in impact toughness, with the notable exception of the NDA100 sample, where strain aging improved both hardness and toughness.

Figure 2 presents the microstructure after each stage of the thermomechanical process. The microstructural analysis supports the previously discussed explanations for the changes in mechanical properties. A comparison of Figures 2a and 2b indicates that normalization resulted in grain refinement. Following rolling, the grains became elongated in the rolling direction, as observed in Figures 2c through 2e. The microstructure of all samples consists of a ferrite and pearlite. Similar microstructures were also observed by other authors [1, 2, 7].

4. CONCLUSIONS

This study investigates the effects of various thermomechanical treatment procedures on the hardness, microhardness, impact toughness, and microstructure of S275JR structural steel. Normalization resulted in microstructural refinement, leading to increased values across all tested properties. Cold plastic deformation introduced work hardening, which significantly increased hardness while reducing impact toughness. Subsequent strain aging at 100 °C and 250 °C further increased both hardness and microhardness. Notably, strain aging at 100 °C also led to an increase in impact toughness, which is atypical for steels. Microstructural analysis confirmed that normalization refined the microstructure of the as-received sample through grain size reduction.

ACKNOWLEDGEMENTS

The research presented in this paper was done with the financial support of the Ministry of Science, Technological Development and Innovation of the Republic of Serbia, with the funding of the scientific research work at the University of Belgrade, Technical Faculty in Bor, according to the contract with registration number 451-03-137/2025-03/200131.

REFERENCES

[1] S. Parapurath, L. Jacob, E. Gunister, N, Vahdati, Metals, 12 (2022) 1386.
[2] A. Bulbul, R. Kacar, Mater. Res., 20 (1) (2017) 210-217.
[3] N. Torić, I. Boko, V. Divić, I.W. Burgess, Metals, 8 (2018) 874.
[4] B. Sun, A.K. da Silva, Y. Wu, Y. Ma, H. Chen, C. Scott, D. Ponge, D. Raabe, Int. Mater. Rev., 68 (7) (2023) 786–824.
[5] CEN. Eurocode 3 – Design of steel structures – Part 1–2: General rules – Structural fire design, CEN, Brussels, 2005.
[6] X. Qiang, X. Jiang, F.S.K. Bijlaard, H. Kolstein, Eng. Struc., 112 (2016) 60-70.
[7] S.M. Aktarer, NOHU J. Eng. Sci., 14 (1) (2025) 360-369.
[8] L.A. Dobrzański, R. Honysz, J. Achiev. Mater. Manuf. Eng., 55 (2012) 461–468.
[9] P. Chakraborty, S. Neogy, N.K. Sarkar, H. Donthula, S.K. Ghosh, H.K. Nandi, B. Gopalakrishna, I.Balasundar, R. Tewari, Steel Res. Int., 96 (2) (2025) 2400593.
[10] ASTM International. ASTM E92-17: Standard Test Method for Vickers Hardness of Metallic Materials. West Conshohocken, PA: ASTM International, 2017. https://www.astm.org/e0092.
[11] ASTM International. ASTM E384-22: Standard Test Method for Microindentation Hardness of Materials. West Conshohocken, PA: ASTM International, 2022. https://www.astm.org/e0384.
[12] International Organization for Standardization. EN ISO 148-1:2016: Metallic Materials — Charpy Pendulum Impact Test — Part 1: Test Method. Geneva: ISO, 2016. https://www.iso.org/standard/65668.html.
[13] A.H. Cottrell, B.A. Bilby, Proceedings of the Physical Society. Section A, 62 (1) (1949) 49. [14] D.B. Park, J.W. Lee, Y.S. Lee, K.T. Park, W.J. Nam, Met. Mater. Int., 14 (2008) 59-64.
[15] B. Soenen, A.K. De, S. Vandeputte, B.C. De Cooman, Acta Mater., 52 (12) (2004) 3483-3492.
[16] N. Tsuchida, E. Baba, K. Nagai, Y. Tomota, Acta Mater., 53 (2) (2005) 265-270.
[17] W.A. Herman, M.A. Erazo, L.R. Patto, M. Sekizawa, A.W. Pense, Weld. Res. Counc. Bull., 322 (1987) 1-13.
[18] J. Brnic, G. Turkalj, J. Niu, M. Canadija, D. Lanc, Mater. Des., 47 (2013) 497-504.

The 56th International October Conference on Mining and Metallurgy
22-25 October 2025, Bor Lake, Bor, Serbia
www.ioc.tfbor.bg.ac.rs

DOI: 10.5937/IOC25450P *Original scientific paper*

FLAMMABILITY ASSESSMENT OF ACOUSTIC INSULATION MATERIALS USING MASS LOSS CALORIMETRY

Milan Protić[1a], Momir Praščević[1b], Nikola Mišić[1c], Miomir Raos[1d], Viša Tasić[2a]

[1] University of Nis, Faculty of Occupational Safety in Nis, Carnojevica 10A, 18000 Nis, Serbia
[2] Mining and Metallurgy Institute Bor, Alberta Ajnštajna 1, 19210 Bor, Serbia
[1a] milanprotic@gmail.com, 0000-0003-4957-7882
[1b] momir.prascevic@znrfak.ni.ac.rs, 0000-0002-7017-1038
[1c] nikola.misic@znrfak.ni.ac.rs, 0000-0003-2314-4851
[1d] miomir.raos@znrfak.ni.ac.rs, 0000-0001-5586-0276
[2a] visa.tasic@irmbor.co.rs, 0000-0001-6710-6529

Abstract
Acoustic insulation materials are widely used across construction and industrial applications, primarily valued for their noise attenuation capabilities. However, their flammability characteristics are rarely evaluated despite their potential impact on fire safety. This study investigates the fire behavior of three representative sound-insulating materials through cone calorimetry, using a mass loss calorimeter under a constant radiant heat flux of 50 kW/m² in accordance with ISO 13927:2023. The tested samples, differing in thickness and structural rigidity (labeled as 10 mm soft, 4 mm hard, and 6 mm soft), exhibited notably high flammability metrics. Time to ignition ranged from 10 to 12 seconds, with peak heat release rates (HRR) exceeding 200 kW/m² in all cases and reaching a maximum of 275.6 kW/m² for the slimmest sample. Mass loss rates and total heat release values further confirmed the materials' low resistance to sustained combustion. The findings emphasize the need to incorporate flammability testing into routine evaluation protocols for acoustic materials, especially in contexts where fire exposure is a relevant hazard.

Keywords*: acoustic insulation materials, flammability testing, heat release rate, mass loss calorimeter*

1. INTRODUCTION

Acoustic insulation products are widely deployed in buildings, vehicles, and industrial enclosures for noise control, yet their fire performance is often treated as secondary to acoustic and mechanical criteria. Historical incidents have shown that acoustic foams, especially those based on non-retarded polyurethane, can significantly accelerate early fire growth when exposed to ignition sources, emphasizing the need for systematic screening of such materials [1]. This oversight is particularly concerning given the proliferation of novel polymer and composite materials whose fire behavior is not well-documented.

The fire risk associated with these materials is multifaceted. Properties that can enhance acoustic performance, such as a low-density, can significantly contribute to fire hazard by increasing the surface-area-to-volume ratio and entrapping oxygen. This can potentially lead to rapid flame spread and high heat release rates. While fire standards and building codes exist, they often apply to well-defined material classes. A significant gap remains in the literature regarding the comprehensive flammability characterization of commercially available acoustic products, particularly when their exact chemical composition is not disclosed by manufacturers [2,3]. This lack of data makes it difficult for engineers and safety professionals to conduct accurate risk assessments.

This paper summarizes the results of flammability testing conducted on three acoustic insulation materials with good sound insulation performance but unknown composition, differing primarily in thickness and rigidity (10 mm soft, 6 mm soft, and 4 mm hard).

2. MATERIALS AND METHODS

Three black, rectangular acoustic materials of unknown chemical structure were supplied and cut to 100 mm × 100 mm specimens per ISO 13927 [4] requirements. The samples were labeled 10 mm soft, 6 mm soft, and 4 mm hard based on rigidity and measured thickness. Flammability testing was performed on a Mass Loss Calorimeter - MLC (Fire Testing Technology, UK) in accordance with ISO 13927:2023 at a nominal external heat flux of 50 kW m^{-2} with spark ignition. The apparatus uses a conical radiant heater with thermopile detector and integrated load cell. Exhaust ventilation and data acquisition followed the standard's prescriptions and whole installation is shown and explained in our previous work [5].

Time to ignition (t_{ign}), heat release rate HRR, mass loss rate MLR, and total heat released THR were recorded. Because ISO 13927 determines HRR via thermopile/mass-loss methods (rather than oxygen consumption), absolute HRR values can differ from ISO 5660 cone calorimeter results. However, the MLC provides decision-useful ranking and production control data, particularly for ignitability and mass loss driven HRR behavior.

3. RESULTS AND DISCUSSION

All three acoustic insulation specimens ignited rapidly under a radiant heat flux of 50 kW m^{-2}, with times to ignition in the narrow range of 10–12 s (Table 1).

Table 1. Summary of flammability metrics

Sample	DTT (s)	TTI (s)	pHRR (kW·m^{-2})	tHRR (s)	THR (MJ·m^{-2})	pMLR (g·s^{-1})	Mass loss (%)
10 mm soft	921	10	211.9	474	119.6	0.199	65.9
6 mm soft	489	10	228.1	257	66.3	0.187	66.9
4 mm hard	399	12	275.6	119	58.3	0.214	70.9

Legend: DT - duration of test; TTI - time to ignition; pHRR-peak heat release rate; tHRR-time to attain the PHRR; THR - total released heat; pMLR -peak mass loss rate

Even though their ignitability was similar, their burning patterns differed significantly (Figure 1).

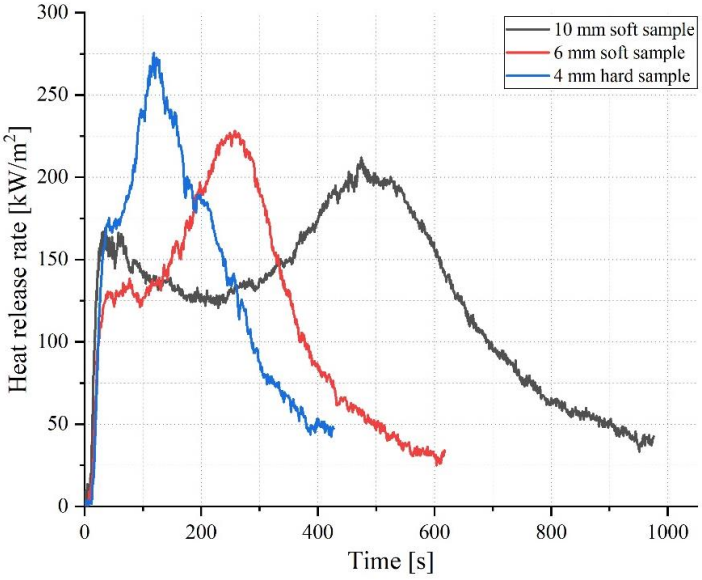

Figure 1. Comparison of heat release rate curves for different material types and thicknesses

The 4 mm hard specimen had the highest peak heat release rate (pHRR) of 275.6 kW m^{-2} and reached this maximum early (119 s). The 6 mm soft specimen produced an intermediate pHRR (228.1 kW m^{-2}) at a later time (257 s). The 10 mm soft specimen displayed the lowest pHRR (211.9 kW m^{-2}) with the most delayed and broadened maximum (474 s). These trends are consistent with the HRR time histories, where the thinnest sample exhibits a sharp release of energy, and the thicker samples burn more progressively.

The materials were further distinguished by their total energy output. The 10 mm soft specimen maintained flaming for the longest duration (app. 15 min) and yielded the largest total heat released (THR) (119.6 MJ m^{-2}), indicating a substantial overall fire load despite its comparatively modest peak intensity. In contrast, the 4 mm hard specimen burned out more quickly and produced a lower THR (58.3 MJ m^{-2}). The 6 mm soft specimen exhibited intermediate behavior in both duration and THR (66.3 MJ m^{-2}). The 4 mm hard specimen showed the highest peak mass-loss rate (0.214 g s^{-1}) and the largest percentage mass loss (70.9%). This behavior suggests an intense devolatilization phase and pronounced flaming during the initial stage of the test. The thicker 10 mm specimen lost mass more gradually over an extended period.

The highest peak heat release rate (pHRR), observed for the slimmest specimen (4 mm thick), can be attributed to the combined influence of two interrelated mechanisms. First, the low thermal inertia of the thinner material significantly reduces the amount of energy required to elevate the entire cross-section to pyrolysis temperatures. This promotes rapid thermal penetration, minimizing internal heat-sink effects and reducing the pre-heating and devolatilization stages. As a result, the mass-loss rate becomes highly concentrated in a shorter time frame, leading to a sharper and more intense HRR peak. Additionally, the surface-level dynamics of thin, rigid materials further reinforce this behavior. When volatile release occurs rapidly and uniformly across the surface, the proximity of the flame zone enhances radiative and convective heat feedback. This heat is efficiently returned to the material surface, accelerating further pyrolysis and establishing a positive thermal feedback loop. The synergy of these effects ultimately drives the HRR to its maximum value in a short span of time. By contrast, thicker specimens typically exhibit slower in-depth heat penetration, greater opportunity for transient char layer formation or structural swelling, and distributed volatile release over a longer time, all of which dampen peak HRR even if the total energy (THR) is larger, because more fuel is present.

The obtained results, in which the slimmest sample exhibited a high peak heat release rate (pHRR) over a short duration and the thicker samples produced a lower pHRR along with a greater total heat release (THR) over an extended period, are consistent with fundamental heat transfer principles and the pyrolysis behavior of materials with differing thermal thicknesses. From a practical perspective, these results indicate distinct fire-hazard profiles. The 4 mm hard material exhibits greater early-stage fire growth potential, which is particularly relevant to flashover propensity and sprinkler activation times. In contrast, the 10 mm soft material contributes a higher overall fire load, with implications for suppression demand and total energy release. The 6 mm soft material demonstrates an intermediate behavior, balancing between early fire growth potential and total fire load contribution. Selection and placement of such products should therefore consider both pHRR and THR, not just ignitability, particularly in enclosures or assemblies with known ignition sources.

4. CONCLUSION

Under a 50 kW m^{-2} radiant exposure, all three acoustic insulation materials ignited rapidly (10–12 s) and exhibited appreciable heat release. The 4 mm hard sample produced the highest peak HRR (275.6 kW m^{-2}) and the highest peak MLR (0.214 g s^{-1}), indicating the most severe early-stage fire growth potential. The 10 mm soft sample yielded the largest THR (119.6 MJ m^{-2}) and the longest burning duration (cca.15 min), implying a larger overall fire load. The 6 mm soft sample fell between these extremes. These findings support the view that flammability screening of acoustic insulation should complement acoustic/mechanical qualification, particularly in enclosures or wall/ceiling assemblies where ignition sources are credible. For design-level decision-making, supplemental ISO 5660 cone calorimetry is advisable to obtain oxygen-consumption HRR data.

ACKNOWLEDGEMENTS

This work is supported by the Ministry of Science, Technological Development and Innovation of the Republic of Serbia pursuant to agreement № 451-03-137/2025- 03/200148 with the University of Niš, Faculty of Occupational Safety, NATO Science for Peace and Security Programme under grant SPS MYP G6006 "Acoustic Multi-Functional Composites for Environmental Risks and Health Hazards Reduction" and ERASMUS+ Jean Monnet Module "Workplace and Process Safety in Next Generation Europe - Teaching for Learning".

REFERENCES

[1] https://www.nist.gov/el/key-findings-and-recommendations-improvement-nist-investigation-station-nightclub-fire
[2] N.H. Bhingare, S. Prakash, V.S. Jatti, Polym. Test., 80 (2019) 106142.
[3] A. Danihelová, P. Sčensný, T. Gergeľ, V. Ondrejka, M. Němec, R. Igaz, J. Štefko, I. Mitterová, Polymers, 13 (16) (2021) 2598.
[4] ISO 13927:2023. Plastics — Simple heat release test using a conical radiant heater and a thermopile detector. International Organization for Standardization.
[5] M. Protić, N. Mišić, M. Raos, M. Mančić, M. Popović, (2024). Overview of common methods for fire testing. Facta Universitatis, Series: Working and Living Environmental Protection, 019-035.

The 56th International October Conference on Mining and Metallurgy
22-25 October 2025, Bor Lake, Bor, Serbia
www.ioc.tfbor.bg.ac.rs

DOI: 10.5937/IOC25454M *Original scientific paper*

ANALYSIS OF SELECTED PROPERTIES OF Al-Si-Cu BASED ALLOY WITH TUNGSTEN ADDITION

Marek Matejka[1a], Dana Bolibruchová[1b], Martina Sýkorová[1c]

[1] Faculty of Mechanical Engineering, University of Žilina, Univerzitná 8215/1, 010 26 Žilina, Slovakia
[1a] marek.matejka@fstroj.uniza.sk, 0000-0002-4156-5521
[1b] danka.bolibruchova@fstroj.uniza.sk, 0000-0002-7374-9763
[1c] martina.sykorova@fstroj.uniza.sk, 0000-0001-6418-8450

Abstract
Al-Si-Cu based alloys are key structural materials in industry due to their favorable combination of low weight, casting, and mechanical properties. In recent years, the influence of refractory metal additions has been investigated, with tungsten being a subject of interest for its potential to influence the crystallization process. This work deals with the effect of tungsten addition on the microstructure and porosity of the AlSi5Cu2Mg alloy. The experimental alloy was alloyed with tungsten in concentrations of 0.05, 0.10, and 0.15 wt.%. The addition of tungsten showed a significant effect on the size of the primary α(Al) phase dendrites as well as on the morphology of the eutectic silicon. The most significant refinement of the dendritic network was observed at the highest concentration of 0.15 wt. % W. Analysis of microporosity revealed that while the 0.05 wt.% W addition suppressed pore formation, higher concentrations led to its significant increase in the as-cast state.

***Keywords**: Al-Si-Cu alloy, tungsten, microstructure, microporosity*

1. INTRODUCTION

Al-Si-Cu based alloys are widely used materials in the automotive, aerospace, and mechanical engineering industries, mainly due to their excellent casting properties, favorable strength-to-weight ratio, and good thermal properties. The quality of these alloys can be significantly influenced by the addition of microalloying elements, which serve to refine the microstructure and improve mechanical properties [1]. Tungsten is a refractory metal with an extremely high melting point and thermal stability, the presence of which in Al-Si based alloys can fundamentally affect their behavior during solidification [2].

Previous studies indicate that the addition of tungsten can significantly influence the crystallization process and the resulting properties of Al-Si based aluminum alloys. It has been shown that an optimal amount of tungsten leads to a significant refinement of the structure, specifically to the transformation of coarse plates of eutectic silicon into a fine fibrous morphology and to a uniform distribution of the eutectic. This subsequently results in an increase in tensile strength, yield strength, and elongation. The mechanism of this influence is complex. On one hand, tungsten can act as a refractory element creating nuclei for crystallization, thereby shifting the onset of eutectic crystallization to higher temperatures and refining the structure. On the other hand, at high cooling rates, supersaturation of the α(Al) solid solution with tungsten atoms can occur, leading to its strengthening [3,4]. Tungsten can also lead to the formation of thermally stable tungsten-containing intermetallic phases. At higher concentrations, it can promote the formation of primary intermetallic phases, such as $Al_{15}(Fe,Mn,W)_3Si_2$. These phases can act as effective barriers against the movement of grain boundaries during thermal stress, thereby increasing high-temperature strength, but they can also have a negative effect if their size and quantity are excessive. The mechanisms by which tungsten interacts with the main alloying elements and its influence on the development of the microstructure and the resulting mechanical properties have not yet been fully explored [5].

2. EXPERIMENTAL METHODOLOGY

A non-standardized hypoeutectic AlSi5Cu2Mg alloy, which is used for casting high-duty components due to its specific properties, was chosen as the experimental material. The AlSi5Cu2Mg alloy in its original state served as the reference material for comparing the results.

Within the experiment, three variants of the AlSi5Cu2Mg alloy were prepared with defined additions of tungsten in concentrations of 0.05, 0.1, and 0.15 wt.%. The melting of the base charge took place in an electric resistance furnace at a stable temperature of 750 ± 5 °C. To ensure homogeneous distribution, the tungsten addition was prepared in advance in the form of an AlW5 master alloy, which was melted separately in an induction furnace with a graphite crucible. After its complete melting, the liquid metal was added in a precisely calculated dosage to the main melt in the resistance furnace. From the thus modified alloy, a series of ten identical experimental castings for each variant was subsequently cast by gravity die casting into preheated permanent molds with a temperature of 150 ± 5 °C. The results of the chemical composition of the alloys are listed in Table 1. Half of the samples were heat-treated using the T7 regime, which included solution treatment (500 ± 5 °C / 6.5 h), quenching in water (85 ± 5 °C), and artificial aging (250 ± 5 °C / 4 h) with final air cooling.

Table 1. Chemical composition of the experimental AlSi5Cu2Mg alloys [wt.%].

Alloy	Si	Cu	Mg	Mn	Fe	Cr	W	Al
AlSi5Cu2Mg - Reference	6.77	2.54	0.15	0.015	0.23	0.004	-	90.16
AlSi5Cu2Mg + 0.05 hm. % W	6.58	2.38	0.16	0.014	0.22	0.007	0.020	90.55
AlSi5Cu2Mg + 0.10 hm. % W	6.31	2.36	0.22	0.013	0.22	0.006	0.044	90.74
AlSi5Cu2Mg + 0.15 hm. % W	6.41	2.37	0.18	0.012	0.23	0.006	0.075	90.65

The preparation of samples for structural analysis was carried out according to standard metallographic procedures. After the preparation of the metallographic sections, the samples were etched with a 0.5 % solution HF. The thus-prepared microstructure was subsequently observed using light and scanning electron microscopy. The quantification of the areal microporosity of the samples was performed on five random fields of each section using a Keyence microscope.

3. RESULTS AND DISCUSSION

3.1 Microstructure evaluation

The observed structure of the reference alloy consisted of the primary α-Al phase, Al-Si eutectic components, and intermetallic phases containing elements such as Cu, Mg, and Fe (Figure 1a). The addition of tungsten to the AlSi5Cu2Mg alloy showed a clear influence on the refinement of its microstructure, which was mainly manifested in the morphology of the primary α(Al) phase dendrites. Compared to the reference alloy without additions, which exhibited a coarser and branched dendritic structure, the addition of tungsten in the amount of 0.05 wt.% led to a visible reduction in dendrites (Figure 1b). Observations showed that the presence of tungsten caused a reduction in the distance between the dendrite arms. A subsequent increase in the amount of tungsten to 0.10 and 0.15 wt.% resulted in only a slight further reduction of the dendrites (Figure. 1c,d). This refinement can be attributed to the action of tungsten as a heterogeneous nucleating agent. Insoluble tungsten particles, or intermetallic phases containing it, serve as nuclei for the crystallization of α-Al, leading to a higher grain density.

The refining effect of tungsten was also evident on the eutectic silicon. While in the reference alloy it occurred in the form of imperfectly rounded grains (Fig. 1a), after the addition of tungsten, a gradual reduction in their size was observed (Figure 1b). At higher tungsten contents, large clusters

of small and fine rounded grains of eutectic Si were more frequently observed (Figure 1c,d). This refinement is closely related to the refinement of the dendritic network, which creates smaller interdendritic spaces and thus limits the growth of silicon particles.

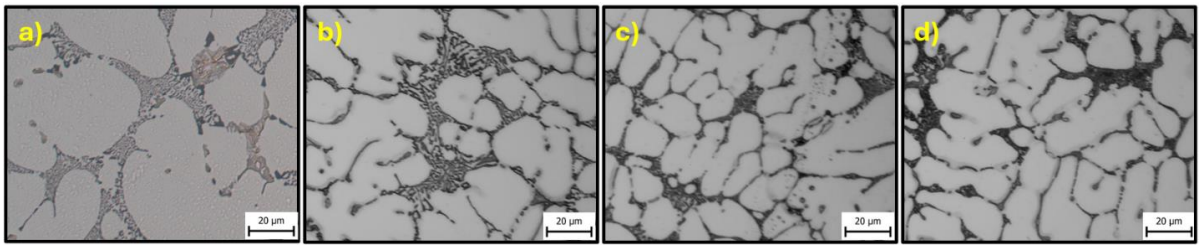

Figure 1. Microstructure of the AlSi5Cu2Mg alloy in the as-cast state: a) 0 wt.% W, b) 0.05 wt.% W, c) 0.10 wt.% W, d) 0.15 wt.% W.

After the application of T7 heat treatment, the morphology of the eutectic silicon further changed towards compact, rounded to spheroidized grains (Figure 2a). This process was most pronounced in the alloys with tungsten (Figure 2b, c), with the microstructure being significantly fine, with spheroidized silicon, at the highest addition of 0.15 wt.% W (Figure 2d). The pronounced spheroidization is an expected consequence of solution annealing at high temperature, where the system minimizes its surface energy. The finer initial structure in the tungsten-containing alloys probably accelerates this process. These morphological changes have a direct impact on potential mechanical properties, as the transformation of irregular particles into fine, rounded grains significantly reduces internal stress concentrations.

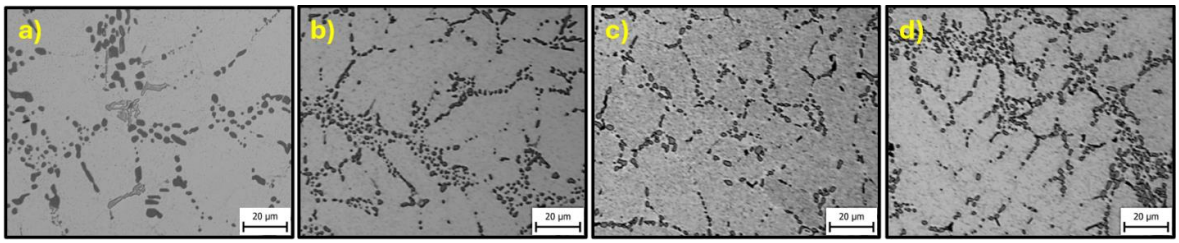

Figure 2. Microstructure of the AlSi5Cu2Mg alloy after heat treatment: a) 0 wt.% W, b) 0.05 wt.% W, c) 0.10 wt.% W, d) 0.15 wt.% W.

Detailed observation of the eutectic Si morphology (Figure 3) confirmed these trends. In the as-cast state with 0.05 wt.% W, eutectic Si had a predominantly rod-like morphology with rounded edges (Figure 3a), while at 0.15 wt.% W, it was already in the form of clusters of fine, rounded grains (Figure 3b). After heat treatment, the eutectic silicon was more uniformly distributed in rounded particles (0.05 wt.% W, Figure 3c) up to almost perfectly round grains in the alloy with the highest tungsten content (0.15 wt.% W, Figure 3d).

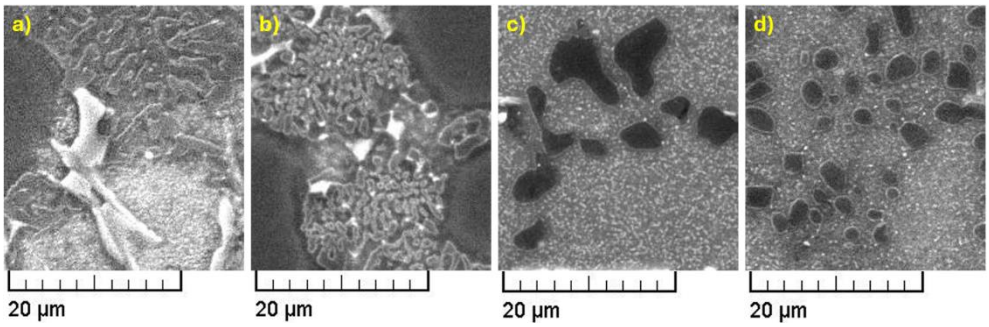

Figure 3. Detail of eutectic Si morphology: a) 0.05 wt.% W in as-cast state, b) 0.15 wt.% W in as-cast state, c) 0.05 wt.% W after heat treatment, d) 0.15 wt.% W after heat treatment.

3.2 Microporosity evaluation

Analysis in the as-cast state revealed that the sample with the lowest addition of 0.05 wt. % tungsten exhibited minimal pore occurrence with an average areal microporosity 0.15 %, which suggests that a low concentration of tungsten effectively suppresses their formation. However, with an increasing content of tungsten to 0.10 and 0.15 wt. %, a significant increase in the areal microporosity to 0.29 % and 0.45 %, respectively, occurred. This trend indicates a correlation between tungsten concentration and the tendency for pore formation, which may be related to changes in the solidification mechanism. The application of heat treatment resulted in an expected increase in microporosity in all tested samples, with the highest value of 0.73 % being measured at the highest concentration of 0.15 wt. % W. This increase can be explained by the coalescence of existing pores or the formation of new ones due to volume changes associated with phase transformations. Observation of the microstructure revealed an irregular shape of the pores, suggesting that the micorporosity originated primarily due to shrinkage in the interdendritic regions during solidification. The resulting values of areal microporosity are shown in Table 2.

Table 2. Areal microporosity in samples of AlSi5Cu2Mg alloy with different tungsten content in the as-cast state and after heat treatment.

State	**As-cast state**			**After heat treatment**		
Alloy	0,05 W	0,10 W	0,15 W	0,05 W	0,10 W	0,15 W
Microporosity	0.15 %	0,27 %	0.45 %	0.34 %	0.37 %	0.74 %

4. CONCLUSION

This study investigated the influence of tungsten additions in amounts of 0.05, 0.10, and 0.15 wt.% on the microstructure and porosity of a cast AlSi5Cu2Mg alloy. It was confirmed that the addition of tungsten acts as an effective refining agent for the primary α(Al) phase, leading to a visible reduction in dendrites. A positive influence was also observed on the morphology of eutectic silicon, which was refined and, after T7 heat treatment, acquired a more compact, spheroidized structure. However, the analysis of microporosity revealed a complex relationship, where the lowest porosity (0.15%) was measured in the as-cast alloy with 0.05 wt.% W, but further increases in tungsten content led to its significant increase. The T7 heat treatment consistently increased porosity in all samples, with the highest value (0.73%) being found in the alloy with 0.15 wt.% W. The results suggest that while tungsten promotes the refinement of phases, at higher concentrations it may negatively affect the solidification mechanism and promote the formation of shrinkage porosity in interdendritic areas.

ACKNOWLEDGEMENTS

*The article was created as part of the **VEGA** grant agency project: **VEGA 1/0160/22**. The authors thank for its support.*

REFERENCES

[1] D. Bolibruchová, M. Matejka, M. Brůna, M. Kuriš, A. Michalcová., Int. J. Met., 17 (4) (2023) 2584-2597.
[2] T. Szymczak, G. Gumienny, T. Pacyniak, K. Walas., Arch. Foundry Eng., 15 (3) (2015) 61-66.
[3] T. Szymczak, G. Gumienny, T. Pacyniak., Arch. Metall. Mater., 61 (4) (2016) 2103–2110.
[4] A. Zykova, N. Martyushev, V. Skeeba, D. Zadkov, A. Kuzkin. Materials., 12 (6) (2019) 981.
[5] T. Szymczak, G. Gumienny, L. Klimek, M. Goły, J. Szymszal T. Pacyniak., Materials., 13 (21) (2020) 4861.

The 56th International October Conference on Mining and Metallurgy
22-25 October 2025, Bor Lake, Bor, Serbia
www.ioc.tfbor.bg.ac.rs

DOI: 10.5937/IOC25458M *Original scientific paper*

OVERVIEW OF INSTALLATIONS AND METHODOLOGIES FOR CONVEYOR IDLERS TESTING – DEVELOPED AT THE FACULTY OF MECHANICAL ENGINEERING AT THE UNIVERSITY OF BELGRADE

Žarko Mišković[1a], Radivoje Mitrović[1b], Danilo Pejčić[1c], Jovana Antić[1d]

[1] Faculty of Mechanical Engineering, University of Belgrade, Kraljice Marije 16, 11120 Belgrade, Serbia
[1a] zmiskovic@mas.bg.ac.rs, 0000-0002-8320-7191
[1b] rmitrovic@mas.bg.ac.rs, 0000-0003-0513-6540
[1c] dpejcic@mas.bg.ac.rs, 0009-0007-1661-2924
[1d] jrantic@mas.bg.ac.rs, 0009-0002-6452-0294

Abstract
Many studies have demonstrated that a significant share of energy losses in thermal power plants comes from transportation systems – especially belt conveyors and their critical components: conveyor (carrying) idlers. Conveyor idlers are mechanical assemblies responsible for transferring the combined load of the conveyor belt and the transported material to the support frame. Among their components, rolling bearings are the most critical, often representing the primary cause of failure. Rolling bearings are machine elements that transfer loads from rotating to stationary parts while maintaining the necessary precision and stiffness between components in relative motion. Considering the vast number of conveyor idlers and built-in bearings used in surface coal mines – often numbering in the hundreds of thousands – even modest advancements in understanding underexplored phenomena, optimizing existing idler and bearing designs, or developing reliable laboratory testing methodologies and installations can lead to substantial energy and cost savings at both local and global levels. This paper focuses on these challenges, providing a comprehensive overview of specialized laboratory installations developed at the University of Belgrade – Faculty of Mechanical Engineering (UB FME), aimed at testing and improving the performance and reliability of conveyor idlers.

***Keywords**: Conveyor Idlers, Experimental Testing, Testing Methodologies*

1. INTRODUCTION

The efficient transport of bulk materials requires equipment capable of spanning long distances while minimizing both energy consumption and material losses. Since their widespread adoption in the late 19th century, belt conveyors have become the primary solution for handling bulk materials – especially in coal mining operations. Their cost-efficiency, straightforward design, adaptability to various terrains, and strong resistance to environmental contaminants [1] make them vastly superior to other transport methods, which are now rarely used in large-scale energy systems. Despite these advantages, belt conveyors are still being developed, especially when it comes to their key components: conveyor (carrying) idlers [2]. A conveyor idler is a mechanical assembly consisting of a bearing unit (typically a pair of rolling-element bearings, though other configurations may also be used), sealing components, a shaft, and a cylindrical shell. The primary role of the idler is to transfer the combined load of the conveyed material and the belt's own weight onto the conveyor frame. During operation, the idlers are in direct contact with the conveyor belt, which drives their rotation through friction—similar to the principle of friction-based power transmission, where the driving element is a continuously moving flat surface, and the driven component is a friction wheel. To meet the diverse functional requirements and accommodate various types of bulk materials, multiple types of conveyor idlers have been developed, but the most commonly used type in the open pit coal mines of the Republic of Serbia has dimensions of Ø194 x 750 mm.

1.1 Conveyor idlers standardized technical requirements

Within the European Union, the primary standard governing the specifications of conveyor idlers is DIN 22112 – Parts 1, 2, and 3 [3]. This standard is the basis for national regulations in both EU member states and non-member countries, including the Republic of Serbia. According to this standard, conveyor idlers are required to meet the following key technical requirements:

- Idler Body (Shell) Material - The idler body must be made exclusively from welded steel tubes. The material should be S235JR or a comparable easily weldable high-strength steel according to DIN EN 10025. The nominal wall thickness must be 4 mm, with an actual minimum wall thickness of 3,7 mm. When refurbishing used idlers, a minimum wall thickness of 3,0 mm is permitted.
- Bearings - The idlers must be equipped with deep groove ball bearings, classification R0, with radial clearance grade C4. The angular misalignment between the inner and outer rings under maximum load must not exceed 10 arc minutes.
- Lubrication - Lubrication must be provided by lithium-based greases filling 2/3 to 3/4 of the free volume within the built-in bearing. The grease must be resistant to aging and capable of preventing corrosion.
- Service Life - With appropriate bearing selection, lubrication, and sealing, the idler must achieve a minimum service life of 20,000 hours at an operating speed of 650 rpm.
- Rotational Resistance - Rotational resistance is defined by the peripheral force acting on the idler shell (contact area with the conveyor belt). Maximum allowable values depend on the idler diameter.

2. UB FME CAPACITIES FOR CONVEYOR IDLERS TESTING

The conveyor idler testing equipment developed at the University of Belgrade – Faculty of Mechanical Engineering (UB FME) enables the examination of all conveyor idler technical requirements defined by the DIN 22112 standard and outlined in the previous chapter. Original experimental testing methodologies have been defined for the custom-developed test rigs, while standardized testing of rolling bearings' characteristics is conducted using certified equipment within the Laboratory for Testing of Machine Elements and Systems – LIMES.

2.1 Standardized rolling bearings testing methodologies

The standardized testing of rolling bearings installed in conveyor idlers is carried out in the LIMES Laboratory (within UB FME), using specialized equipment that is routinely maintained and calibrated to ensure accuracy. Established in 2002, since the year of 2008, LIMES has been accredited for the testing of bearings dimensions, radial clearance, vibration levels, and material hardness (accreditation number: 01-304), in accordance with the standards listed in Table 1. The laboratory team comprises five Ph.D. and two M.Sc. mechanical engineers, as well as one technician, all actively involved in the testing and research processes.

Table 1. Standardized rolling bearings testing methodologies – Laboratory LIMES 2025

Characteristic	Standard
Bearing inner diameter tolerances – d Bearing outer diameter tolerances – D Bearing radial clearance – C	SRPS ISO 1132-2:2017
Bearing vibration in the frequency ranges: 100–300 Hz, 301–1800 Hz, 1801–10000 Hz	SRPS ISO 15242-1,2,3:2018
Bearing ring hardness measured by Rockwell C method	SRPS EN ISO 6508-1:2024

2.2 Original conveyor idlers testing installations and methodologies

The experimental determination of the service life of conveyor idlers involves subjecting the idlers to various levels of maximum loads until failure occurs - i.e., until the allowable vibration or bearing temperature limit is exceeded - under unidirectional bending fatigue. The testing is conducted on a custom-built test frame developed at the UB FME, with its components and overall look shown in Figure 1. A specially developed testing methodology is employed for this purpose, which also enables measurement of rotational resistance at different rotational speeds. Also, an additional test frame was developed for evaluating the quality of the conveyor idlers sealing groups.

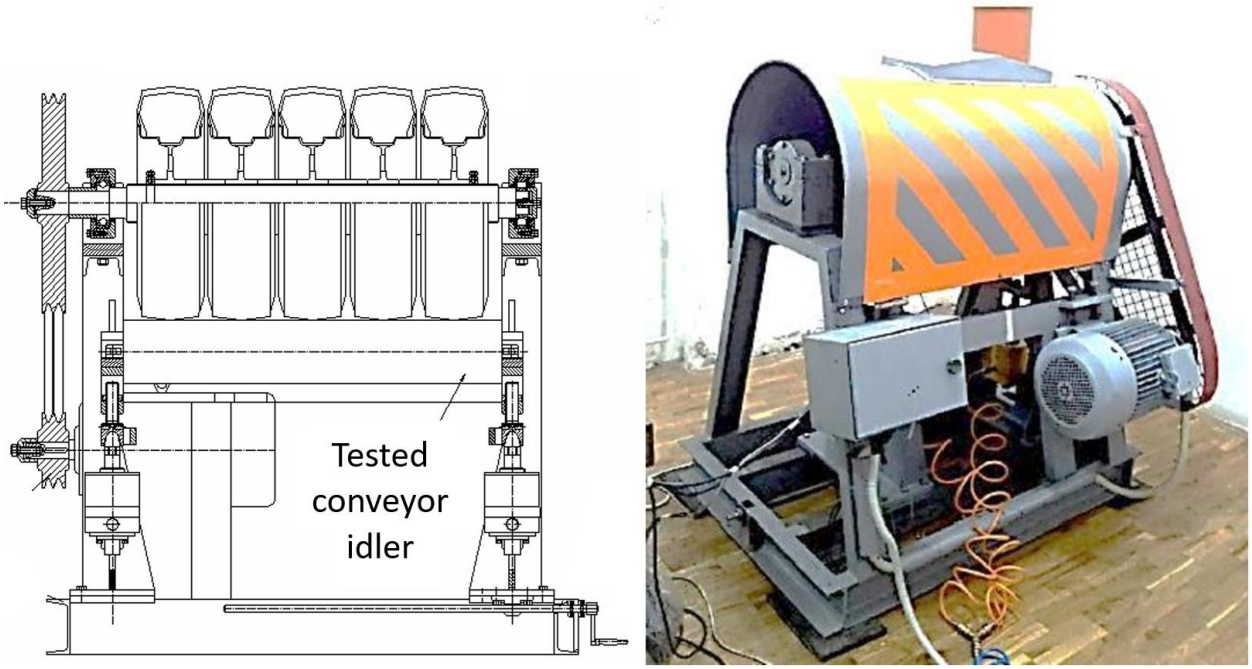

Figure 1. Original conveyor idler test frame developed at the University of Belgrade – Faculty of Mechanical Engineering

3. EXAMPLE PERFORMANCE TESTING RESULTS OF CONVEYOR IDLERS - WITH DISCUSSION

Figures 2 and 3 shows the performance testing results of conveyor idlers Ø194 x 750 mm produced by three well-known manufacturers from Serbia, during the 10hrs long testing.

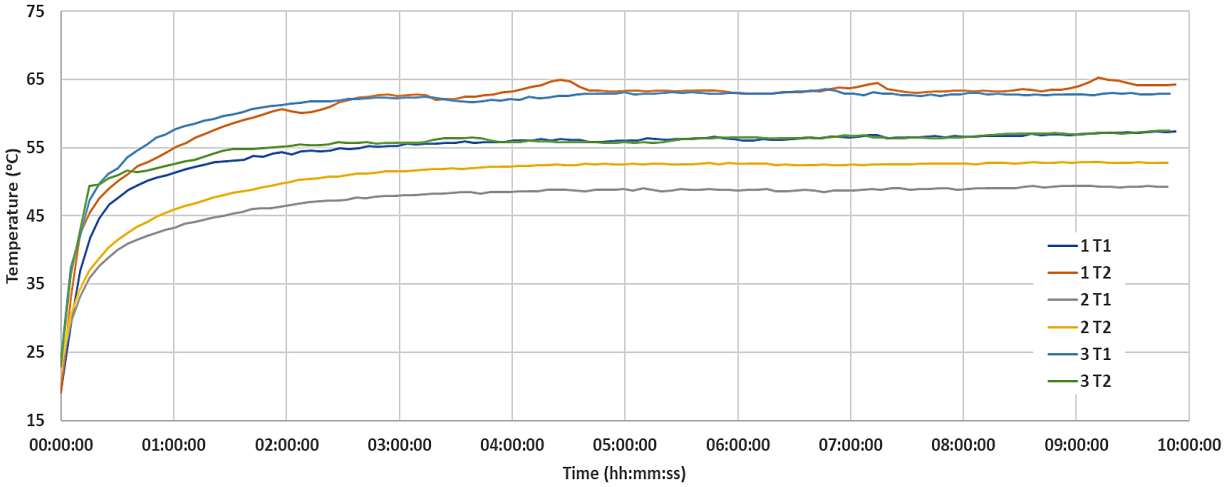

Figure 2. Measured bearing temperatures of Ø194 x 750 mm conveyor idlers – during 10hrs of testing

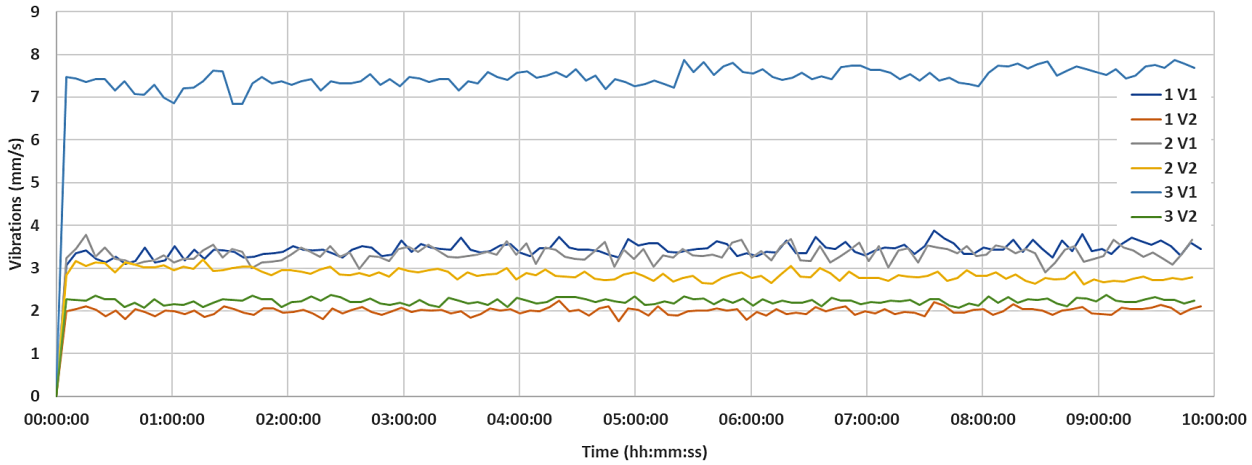

Figure 3. Measured bearing vibrations of Ø194 x 750 mm conveyor idlers – during 10hrs of testing

Based on the results presented in Figures 2 and 3, it can be concluded that the bearing temperatures of conveyor idlers from Manufacturers 1 and 3 are higher than those of the idler from Manufacturer 2. In terms of vibration levels, one bearing of the idler from Manufacturer 1 exhibits the lowest vibration among all measured values, while the vibration at the second bearing position is lower than that measured on the idler from Manufacturer 3. The vibration levels of the bearings in the idler from Manufacturer 2 fall between the values recorded for Manufacturers 1 and 3. This aligns with the temperature measurement findings, confirming that the conveyor idler from Manufacturer 2 exhibit the best characteristics.

4. CONCLUSIONS

Testing the performance of conveyor idlers is essential because these assemblies play a vital role in the performance, reliability, and energy efficiency of belt conveyor systems [4]. High-quality idlers reduce friction, prevent excessive wear on the conveyor belt, and contribute to smooth, uninterrupted operation. Through comprehensive testing, manufacturers can evaluate design integrity, verify material properties, and optimize key elements such as bearings and sealing systems. This process ensures compliance with international standards, improves operational safety, and significantly extends the service life of both idlers and conveyor belts. In large-scale applications – such as mining and energy production – regular testing helps reduce maintenance costs, minimize downtime, and achieve substantial energy and financial savings. The importance of laboratory testing of conveyor idlers performance – using original equipment and methodologies developed at the UB FME – has been recognized by the leading conveyor idlers manufacturers in the Republic of Serbia: Kolubara Metal, Ansal Steel, and PRIM Kostolac. As a result, these companies periodically send their conveyor idlers to the UB FME for testing, in order to verify the quality of their products and ensure the reliability of their manufacturing processes.

REFERENCES

[1] Ž. Mišković, R. Mitrović at all, Technical Gazzete, Josip Juraj Strossmayer University of Osijek, ISSN 1330-3651, 24 (6) (2017) 1941–1950.
[2] Z. Folta, P. Čamlik, Mechanical Series, 15 (1) (2009) 81 – 86.
[3] DIN 22112-1, 2, 3: Gurtförderer für den Kohlenbergbau unter Tage – Tragrollen
[4] X. Liu, Prediction of Belt Conveyor Idler Performance, Delft University of Technology, Faculty of Mechanical engineering, Ph.D. Thesis, ISBN 978-90 5584-207-0, 2016.

The 56th International October Conference on Mining and Metallurgy
22-25 October 2025, Bor Lake, Bor, Serbia
www.ioc.tfbor.bg.ac.rs

DOI: 10.5937/IOC25462D *Original scientific paper*

ROLE OF MAGNESIUM IN SOLIDIFICATION FEEDING OF HYPOEUTECTIC Al-Si5-Mg ALLOYS

Mile B. Djurdjević[1a], Srećko Manasijević[2b], Aleksandra Patarić[3c], Marija Mihailović[3d], Karlo Raić[4e]

[1] University of Applied Sciences, Roseggerstraße 15, 4600 Wels, Austria
[2] Lola Institute Ltd, Kneza Viseslava 70a, Belgrade, Serbia
[3] University of Belgrade - Institute of Chemistry, Technology and Metallurgy - National Institute of the Republic of Serbia, Njegoseva 12, 11000 Belgrade, Serbia
[4] Faculty Technology and Metallurgy University of Belgrade, Karnegijeva 4, 11000 Belgrade, Serbia
[1a] miledjurdjevic@yahoo.ca, 0009-0007-4561-3547
[2b] srecko.manasijevic@li.rs, 0000-0002-4277-9783
[3c] aleksandra.pataric@ihtm.bg.ac.rs, 0000-0002-2734-0262
[3d] marija.mihailovic@ihtm.bg.ac.rs, 0000-0003-2451-4818
[4e] karlo@tmf.bg.ac.rs, 0000-0002-1713-0130

Abstract
The growing demand for high-performance Al-Si casting alloys stems from their excellent mechanical properties in engineering applications. Hypoeutectic Al-Si-Mg alloys offer superior fluidity, low thermal expansion, and corrosion resistance; however, they face solidification challenges such as shrinkage porosity. This study investigates magnesium's influence on feeding regions in AlSi5Mg alloys. Results show that increasing magnesium content from 0% to 0.6% significantly affects interdendritic and burst feeding regions, potentially impacting shrinkage porosity formation.

***Keywords**: AlSi5Mg alloys, Magnesium, Thermal analysis, Feeding effectiveness*

1. INTRODUCTION

The growing demand for AI-Si casting alloys with superior mechanical properties has increased interest in hypoeutectic AI-Si-Mg alloys. These alloys are widely used in many engineering fields due to their excellent fluidity, low thermal expansion, high strength-to-weight ratio, and corrosion resistance [1,2]. Silicon and magnesium are the primary alloying elements defining microstructure and mechanical properties [3]. Silicon enhances fluidity and castability while reducing shrinkage porosity, whereas magnesium improves strength, hardness, and fatigue properties [4–6]. However, these alloys face challenges during solidification, particularly shrinkage porosity caused by volume contraction. Aluminum-silicon hypoeutectic alloys shrink 4–8 % depending on composition [1]. Campbell [2] identified five feeding regions during solidification: liquid feeding (LF), mass feeding (MF), interdendritic feeding (IDF), burst feeding (BF), and solid feeding (SF). Understanding these regions is essential for optimizing casting quality. Multiple factors influence feeding ability, including chemical composition, solidification characteristics, casting design, process parameters, and environmental conditions [2,3,5]. While silicon's effects have been extensively studied [1, 3, 6], limited data exist on the impact of magnesium on feeding regions. This study examines the impact of magnesium content (0–0.6 wt.%) on characteristic solidification temperatures and feeding regions in AlSi5Mg alloys, aiming to determine whether increased magnesium levels contribute to the formation of shrinkage porosity. Thermal analysis was used to achieve these objectives.

2. EXPERIMENTAL

Experiments were maintained under constant conditions, except for alloy composition, by controlling gas/oxide content and ensuring uniform mold filling. All melts were free of trace elements (Sr, Na, Sb, Ti, P, B, Pb, Sn…) affecting solidification temperatures. Pure aluminum (99.7 %), silicon (99.9 %), and magnesium (99.9 %) were melted in a 10 kg electric furnace without additives. Alloy compositions (Table 1) were determined by OES analysis to investigate magnesium's influence on feeding behavior.

Table 1. Chemical compositions of synthetic AlSi5Mg alloys

Alloy	wt.%						
	Si	Mg	Cu	Mn	Cr	Ni	Zn
AlSi5	4.96	0	0.007	0.02	0.001	0.001	0.006
AlSi5Mg0.2	4.86	0.209	0.008	0.003	0.002	0.002	0.007
AlSi5Mg0.4	5.11	0.405	0.007	0.004	0.001	0.002	0.008
AlSi5Mg0.6	4.84	0.590	0.021	0.004	0.002	0.001	0.008

Thermal analysis used 200±10 g samples in conical steel crucibles (60×50 mm) with two calibrated K-type thermocouples positioned at the wall and center, 20 mm from the bottom. Temperature was recorded between 700–400 °C (±0.10 °C accuracy) using a National Instruments system (NI cDAQ-9171) at five data points per second. A constant cooling rate of 10 °C/min was maintained. Experiments were replicated for each alloy composition from Table 1.

3. RESULTS AND DISCUSSION

Porosity is the key defect in aluminum castings, caused by insufficient feeding and hydrogen precipitation. This study quantifies the impact of magnesium on solidification temperatures and feeding regions in AlSi5Mg alloys with varying magnesium concentrations (0–0.6 wt.% Mg). Figure 1 shows cooling curves, ΔT curves, and derivatives for all alloys. Liquidus and solidus temperatures were determined from first derivatives, while dendrite coherency and rigidity temperatures were determined from ΔT minima. Following Huber et al. [7], these define five feeding regions: liquid, mass, interdendritic, burst, and solid feeding.

Figure 1 shows cooling curves (blue-full line), first derivative curves (red-dotted line), and ΔT curves (gray-interrupted line) of Al-Si-Mg alloys. The green points indicate how characteristic solidification temperatures (Liquidus, Dendrite coherency, Rigidity, and Solidus) have been determined using the cooling curve or ΔT curve.

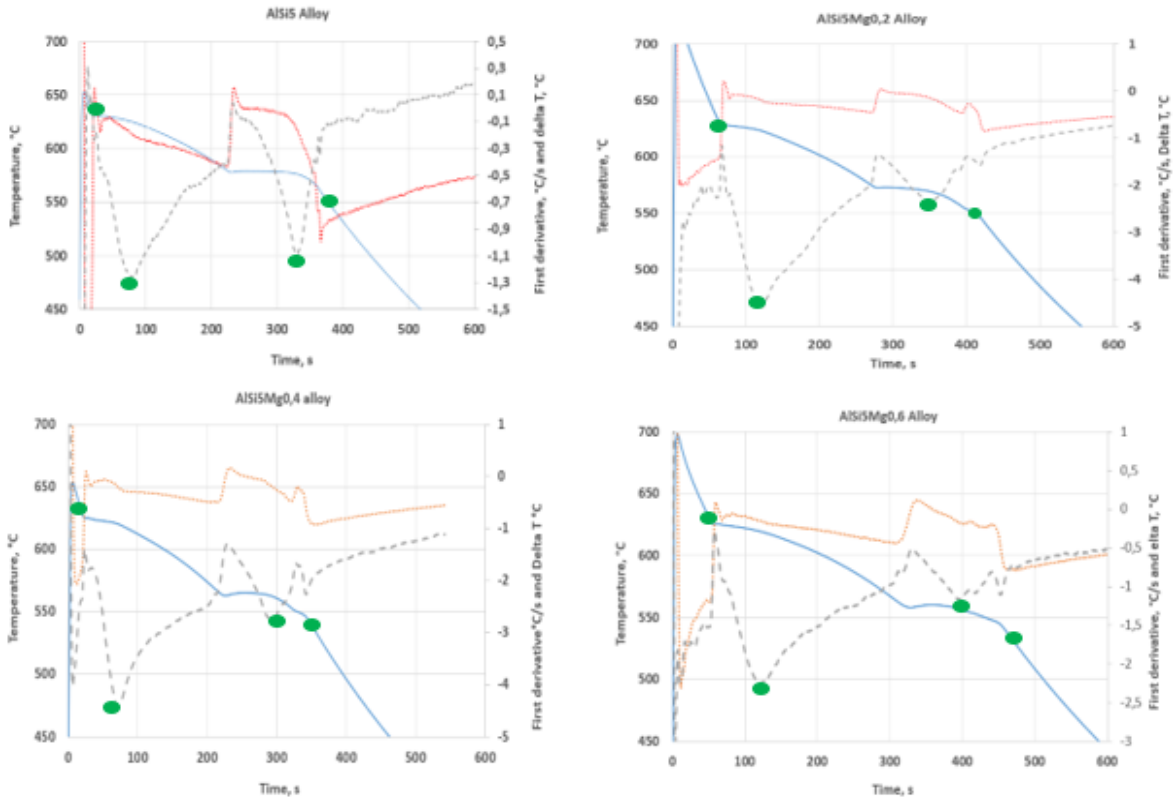

Figure 1. Cooling curves, ΔT curves and derivatives for all alloys

Figure 2 demonstrates that increasing magnesium content significantly lowered rigidity (green-dotted line) and solidus temperatures (light blue-dotted line) while slightly decreasing liquidus (dark blue-dotted line) and dendrite coherency (orange-dotted line) temperatures. Magnesium addition up to 0.6 wt.% reduced liquidus temperature by 5.9 °C, dendrite coherency by 4.9 °C, and rigidity temperature by 20.3 °C. This occurs because higher magnesium concentrations induce finer dendrites and form Mg_xSi_y based precipitates (primarily Mg_2Si), altering solidification behavior [1, 8].

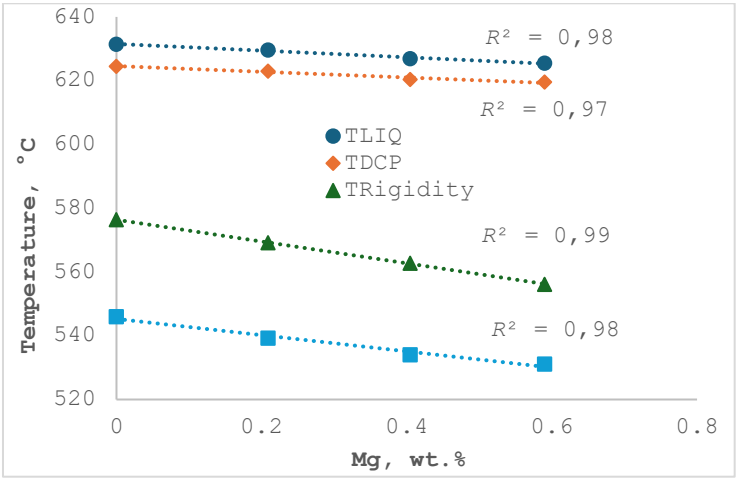

Figure 2. Impact of various contents of magnesium on the characteristic solidification temperatures of AlSi5Mg alloys

As illustrated in Figure 3, the presence of magnesium yields notable effects on both interdendritic and burst feeding regions. With an incremental rise in magnesium content from 0 to 0.6 wt.%, the temperature ratio within the interdendritic constrained feeding areas increases by 10.8 %.

Conversely, the temperature ratios within the burst feeding regions decrease by approximately 9 %. This alteration is visually depicted in Figure 3, where the interdendritic feeding expands while the burst feeding diminishes in duration. These fluctuations in temperature ratios across interdendritic and burst feeding domains could potentially influence the formation of shrinkage porosity in the resultant cast structures.

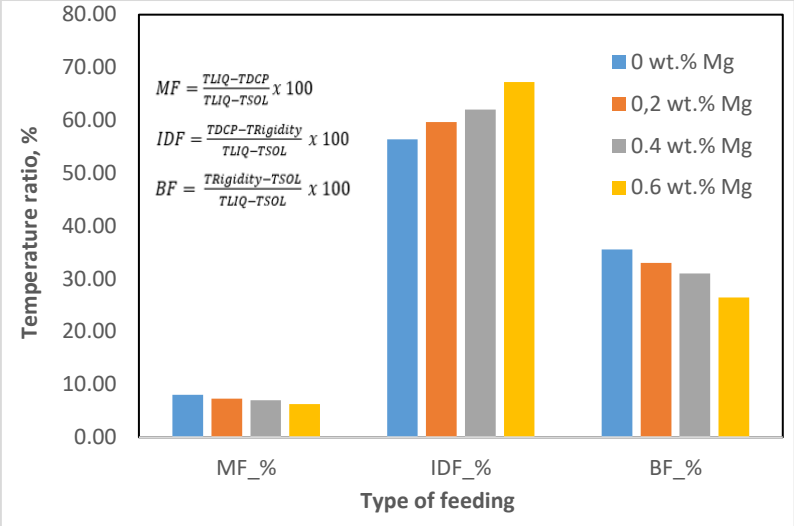

Figure 3. The impact of magnesium on the temperature ratio of different feeding regions

4. CONCLUSION

In this work, the impact of Mg on the different feeding regions of AlSi5Mg alloys is studied using thermal analysis techniques. It was found that magnesium has an effect on mass, interdendritic, and burst feeding regions. It can be assumed that the interdendritic constraint feeding region is more responsible for defect formation in gravity castings. In contrast, the burst feeding controls the formation of defects in high-pressure die castings.

ACKNOWLEDGEMENTS

The paper was the result of a successful collaboration between researchers from Lola Institute Ltd, Belgrade, Serbia; University of Belgrade - Institute for Chemistry, Technology and Metallurgy - National Institute of the Republic of Serbia; Institute for Process Metallurgy and Metal Recycling, RWTH Aachen University, and University of Applied Sciences Upper Austria. The authors acknowledge financial support from the Ministry of Science, Technological Development and Innovation of the Republic of Serbia (Contracts No: 451-03-136/2025-03/ 200066 and 451-03-136/2025-03/200026).

The work is aligned with the United Nations Sustainable Development Goals #7 - Ensure access to affordable, reliable, sustainable and modern energy for all.

REFERENCES

[1] B. Callegari, T.N. Lima, R.S. Coelho, Metals, 13 (1744) (1023) 1–36.
[2] J. Campbell., Int. J. Cast Met. Res., 5 (1969) 1–8.
[3] P.L. Schaffer, Y.C. Lee, A.K. Dahle., (J. Hryn), TMS, The Minerals, Metals and Materials Society, Warrendale, PA, USA, 2001, pp. 87–94.
[4] M.Di Sabatino, S. Shankar, D. Apelian, L. Arnberg., Shape Casting: The John Campbell Symposium, TMS Annual Meeting: San Francisco, California, USA, February 13–17, 2005, pp. 193–202.
[5] M. Jolly, L. Katgerman., Prog. Mater. Sci., 123 (2022) 1–38.
[6] M.Di Sabatino, L. Arnberg., Trans. Indian Inst. Met., 62 (4) (2010) 321–325.
[7] G. Huber, M. Djurdjevic, M. Rafetzeder., Mater. Sci. Forum., 879 (2016) 784–789.
[8] M. Dash, M. Makhlouf., J. Light Met., 1 (4) (2001) 251–265.

The 56th International October Conference on Mining and Metallurgy
22-25 October 2025, Bor Lake, Bor, Serbia
www.ioc.tfbor.bg.ac.rs

DOI: 10.5937/IOC25466G
Original scientific paper

CASTING OF BRONZE CASTINGS WITH THIN WALLS USING WAX-PARAFFIN MODELS AND CO_2 HARDENED SAND MOLDS

Jelena Gligorijević Sokolović[1a], Jasmina Petrović[1b], Emina Požega[1c]

[1a] Mining and Metallurgy Institute Bor, Alberta Ajnštajna 1, 19210 Bor, Serbia
[1b] Technical Faculty Bor, University of Belgrade, V.J. 12, 19210 Bor, Serbia
[1c] Mining and Metallurgy Institute Bor, Alberta Ajnštajna 1, 19210 Bor, Serbia
[1a] jelena.gligorijevic.sokolovic@irmbor.co.rs, 0009-0003-6713-760X
[1b] jpetrovic@tfbor.bg.ac.rs, 0000-0002-9131-339X
[1c] emina.pozega@irmbor.co.rs, 0000-0001-6797-2435

Abstract
This paper presents an alternative method for precision casting of thin-walled bronze castings (3-5 mm) from RG5 bronze alloy, using expendable models made from a wax and paraffin mixture (60:40%), along with CO_2 hardened sand molds based on sodium silicate. The process is designed as a low-budget alternative to the conventional ceramic shell method, while maintaining high surface quality and dimensional accuracy. The expendable model is made in a multi-part plaster mold, which allows the production of complex and curvilinear geometries. After the model is removed from the plaster mold, it is drained from the hardened sand mold previously formed around it, with the sand mold being heated in a drying oven to 105°C. By avoiding the creation of cores and finishing machining, additional savings are achieved. Results of dimensional measurements, metallography, hardness, and surface characteristics are presented, along with graphical representations. Surface treatment with sodium thiosulfate contributes to the artistic expression of the castings. The paper demonstrates the full justification for applying this method in artistic and special production.

Keywords: *casting, wax-paraffin models, CO_2, RG5 bronze.*

1. INTRODUCTION

The casting of metal components using expendable models—most notably through the lost wax process—has long been recognized as a superior method for achieving high dimensional accuracy, surface quality, and design complexity [1]. Historically used in art and jewelry, and later adapted for industrial applications, this approach allows the faithful reproduction of intricate geometries that would be difficult or impossible to machine.

Traditional lost wax casting typically involves the use of ceramic shell molds formed by repeated dipping and stuccoing, which, although effective, require extensive equipment, prolonged drying and firing cycles, and significant cost investment [2]. In contrast, the variant explored in this study replaces the ceramic shell with a CO_2-hardened sand mold, using sodium silicate as a binder.

This substitution dramatically simplifies the process and reduces production costs, while still enabling the creation of thin-walled (3–5 mm), complex bronze castings.

The expendable model, formed from a wax-paraffin mixture (60:40), is produced using a multi-part plaster mold, enabling the replication of artistic or freeform designs with great fidelity [1]. Once embedded in the sand mold and hardened with CO_2, the model is thermally removed at moderate temperature (105°C), leaving behind a precise cavity. This cavity is then filled with molten RG5 bronze alloy, yielding high-quality castings without the need for internal cores or additional machining [3].

The method offers several key advantages:

• Rapid mold production and hardening (20–30 seconds) using CO_2
• Avoidance of firing kilns or complex shell building
• Minimal material loss, making it suitable for artistic series or one-of-a-kind pieces
• Environmental and practical feasibility for educational, prototyping, or low-budget settings

This paper presents the entire process workflow, including experimental procedures, dimensional analysis, hardness testing, and metallographic characterization. The goal is to assess the technical soundness and versatility of this modified lost wax process and to highlight its potential in both technical and creative domains.

2. EXPERIMENTAL

2.1. Alloy

The RG5 bronze alloy used has the following chemical composition:
DIN1705 CuSn5ZnPb (alloy number 2.1096)/EN 1982 CuSn5Zn5Pb5-C (alloy numberCC491K)

2.2. Model Production

“Lost Wax" bronze castings The original sculpture is now used exclusively as a reference point. From the "negative" mold, a wax "positive" must be created. The models were made in multi-part plaster molds, coated with shellac solution. A wax and paraffin mixture in a 60:40 ratio was used. The model is carefully removed from the plaster mold and used to form the sand mold.

Figure 1. „Positive models”

2.3. Molds

Sodium silicate (~4%) was used as the binder for the sand. The mold hardens after CO_2 gas is passed through it for 20-30 seconds at a pressure of 1.5 bar. The chemical reaction for hardening is:

$Na_2SiO_3 + CO_2 \rightarrow Na_2CO_3 + SiO_2\downarrow$

2.4. Casting

This process is customizable for different types of metal casting, along with shapes, sizes, and more. Non-ferrous alloys most commonly used in casting are bronze, brass, copper and aluminum. If you are working with precious metals in a jewelry studio, you may work with silver, copper, gold, and platinum. In this paper, RG5 bronze was used — a tin bronze also known as red bronze, leaded bronze, or Gunmetal Bearing Bronze — selected for its excellent castability, making it particularly suitable for thin-walled castings (3–5 mm). This alloy offers good machinability, is weldable with brass, and maintains dimensional stability during solidification.

The RG5 (Cu Sn5 Pb5 Zn5) metal is melted at 1150°C and poured into the pre-heated mold, from which the model was drained in the drying oven (105°C). The process is carried out gravimetrically with controlled filling. After cooling, the mold is broken and the casting is removed.

Figure 2. a) Thin-walled artistic bronze castings b) Silumin casting by volatile model technology

2.5. Surface Treatment

For artistic effect, sodium thiosulfate solution is used. The reaction with the surface of the bronze forms a dark layer of Cu_2S, which gives a characteristic patina:

$$Cu^{2+} + S_2O_3^{2-} \rightarrow Cu_2S\downarrow + SO_3^{2-}$$

2.6. Characterization

Dimensional measurements, roughness Ra, hardness HB, and optical microscopy (40x) of the wall cross-section were performed. Results were compared to conventional methods and standards ISO 8062-3:2007.-3:2007.

3. RESULTS AND DISCUSSION

The results are given in Table 1.

Table 1 - Dimensional deviations (n = 5)

Location	Drawing (mm)	Measured (mm)	SD (mm)
Height	220	219.8	0.3
Wall thickness	4.0	4.1	0.2
Base width	80	79.9	0.1

Hardness along the height of the figure
(Values are fictional – use for artistic or technical processing)
• Lower zone: 95 HB
• Middle: 102 HB
• Upper zone: 100 HB

Metallographic analysis (optical microscope, 40x)
• α-Cu matrix with fine Pb inclusions evenly distributed,
• No microporosity, good homogeneity,
• Elliptical grains, oriented in the melting direction,
• Clearly separated phases without segregation at grain boundaries.

Advantages of the Method

- Thin-walled and hollow castings → reduced consumption of RG5 alloy
- Finished dimensions without machining → no further processing required
- No cores → no insertion or positioning errors
- Multi-part plaster molds → allow complex shapes and multiple parting lines
- Wax/paraffin model (60:40) is eliminated at 105°C from the sand mold
- CO_2 process enables quick hardening (20-30 sec)
- Low-budget approach — no special equipment, applicable in schools and small workshops

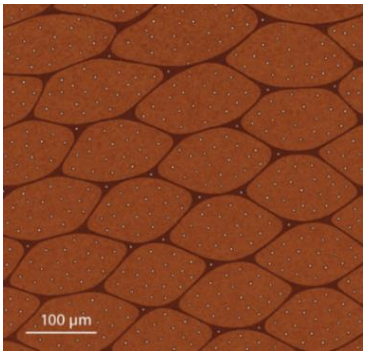

Figure 3. Simulated metallography of RG5 bronze (α-Cu matrix with Pb inclusions)

3. CONCLUSION

The method with wax-paraffin models and CO_2 hardened sand molds has proven to be an economical, safe, and practical technique for casting artistic and technical castings. By combining easily accessible materials and a simple process, it enables the production of accurate, hollow, and complex shapes without additional processing, with significant aesthetic and functional value.
In modern lost wax casting practices, there is also a clear trend towards replacing traditional wax-paraffin mixture models with 3D printed models. This innovation offers significant advantages, including increased precision, the ability to create more complex geometries, and reduced model production time. Like conventional wax-paraffin models, 3D printed models serve as expendable patterns for mold formation, enabling the direct casting of detailed and accurate castings. In addition to bronze casting, this approach using expendable 3D printed models can also be successfully applied to silumin casting. Silumin alloys can be poured into molds formed by evaporating 3D printed patterns, resulting in high-quality castings with well-defined details and fewer defects. This technology opens new possibilities for precision casting and expands the range of alloys used in industry. Thus, the art of lost wax casting transcends mere technique - it becomes a timeless medium for preserving memory, replicating form, and giving shape to ideas that no other process can capture. The casting of art itself.

ACKNOWLEDGEMENTS

This work was financially supported by the Ministry of Science, Technological Development and Innovation of the Republic of Serbia, Contract on realization and financing of the scientific research work of the Mining and Metallurgy Institute Bor in 2025, contract number: 451-03-136/2025-03/ 200052.

REFERENCES

[1] D.R. Askeland, P.P. Phulé, *The Science and Engineering of Materials*, 6th Ed., Cengage Learning, 2010.
[2] J. Campbell, *Castings*, 2nd Ed., Butterworth-Heinemann, 2003.
[3] R.W. Heine, C.R. Loper, P.C. Rosenthal, *Principles of Metal Casting*, McGraw-Hill Education, 1967.
[4] ISO 8062-3:2007, *Geometrical product specifications (GPS) – Dimensional and geometrical tolerances for moulded parts*.

The 56th International October Conference on Mining and Metallurgy
22-25 October 2025, Bor Lake, Bor, Serbia
www.ioc.tfbor.bg.ac.rs

DOI: 10.5937/IOC25470W *Original scientific paper*

METALLURGICAL AND PROCESS CHALLENGES IN FLASH BUTT WELDING OF DIFFERENT DIMENSIONS OF MICRO-ALLOYED STEEL ON CONTINUOUS PICKLE LINE

Shi Wenli[1a], Tanja Marinković Stojanović[1b], Aleksandar Đuga[1c], Marko Radosavljević[1d], Stefan Nešić[1e]

[1]HBIS Serbia, Smederevo, Carigradska 55, 11300 Smederevo, Serbia
[1a] ShiWenli@hbisserbia.rs , 0009-0002-3874-7807
[1b] TSMarinkovic@hbisserbia.rs, 0009-0002-7055-0473
[1c] ADjuga@hbisserbia.rs, 0009-0006-0603-9338
[1d] MRadosavljevic@hbisserbia.rs, 0009-0009-5092-5742
[1e] SNesic@hbisserbia.rs, 0009-0002-1143-5416

Abstract

Flash Butt Welding (FBW) is a critical process in continuous steel production, particularly within the pickling line. While highly efficient with modernized software-driven machines, the FBW of microalloyed steels such as S355J2+N and S355MC presents significant metallurgical and process challenges. This study describes critical welding points and the complexities arising from the steel's microstructure under the influence of the Heat Affected Zone (HAZ). The study is focused on presentation of FBW tests on different thicknesses of microalloyed steels, the selection and adjustment of essential process parameters, as well as the testing and analysis of welds using various methods and metallographic analyses. Tests were conducted after the modernization of the welding machine on Pickling Line 2 at the cold rolling mill, carried out by Taylor-Winfield (TW) in 2022. The aim of the study is a holistic approach and understanding of the complex interdependencies between process parameters (defining and selecting an adequate "welding curve"), material properties, welding equipment mechanics, and the resulting weld quality, as well as the monitoring and quality control system. A poor weld poses a significant risk of strip breakage in the line and is a cause of line stoppage, which can lead to mill downtime and financial losses.

Keywords: *Flash Butt Welding, microalloyed steels, welding defects, weld testing methods*.

1. INTRODUCTION

(FBW) is a resistance welding technique widely used across various industrial sectors. This method uses a combination of heating and forging to achieve high-quality welded joints between two metal components. At HBIS Serbia's Cold Rolling Mill (CRM), the automated FBW process was enhanced through the modernization of the welding machine on the pickling line. The main goal of this upgrade was to improve weld quality, ensuring that high percentage of unbroken joints could pass through both the pickling and rolling lines. Another objective was to enable the welding of high-strength steels, including micro-alloyed steels (HSLA). Although all parameters were initially set in the software by the manufacturer, Taylor-Winfield, we concluded that a series of tests and trials were essential to determine the optimal settings. This was necessary to achieve a 100% sound weld across the full range of steel sheet dimensions and grades.

2. EXPERIMENTAL SECTION

Characteristics and Weldability of Micro-Alloyed Steels: (HSLA) are generally considered "well-weldable" due to their low carbon content. However, the presence of micro-alloying elements introduces new complexities to the (FBW) process. Consequently, the good weldability of these steels is highly dependent on the choice of welding process. This study focuses on weldability of two micro-alloyed steel grades, S355J2+N and S355MC of the same and different thicknesses. While S355J2+N exhibits good weldability with conventional welding processes (111, 135, 141...), FBW is performed without a shielding gas. Thus, the amount of inclusions

becomes a critical factor affecting weld quality [1]. Micro-alloying elements, together with other alloying constituents, form highly stable oxides, nitrides, and carbides (e.g., TiN, NbC, TiC, MnO, and SiO_2). This necessitates precise optimization of welding parameters to ensure effective removal of these oxides from the weld zone. Inadequate expulsion results in brittle, glassy non-metallic films within the weld, which inhibit metallurgical bonding between the sheets. Moreover, excessive heat input during welding of these steel grades promotes grain coarsening and deterioration of mechanical properties in the (HAZ).

Weld Quality Assessment: Weld quality is primarily assessed through two testing phases. In the initial phase, samples are taken from different locations along the welded joint and prepared for bend testing. These samples are clamped in a vise and subjected to bending or punching forces to evaluate their plasticity and resistance to defects. A representative section of the welded joint is then sent to the mechanical testing laboratory. There, standardized samples are subjected to a tensile test to determine tensile strength, elongation, and the location of the fracture. The parameter optimization and testing is repeated until consistent weld quality is achieved.

Weld Integrity Testing on S355MC Micro-Alloyed Steel (3 mm to 4.5 mm)

Initial trials using the parameters established by Taylor-Winfield specialists produced inconsistent results (Figure 1, Figure 2). After performing a series of welding tests on S355MC of various thicknesses, the welding curve was modified to achieve a sound weld [2].

Figure 1: initial testing of 3mm

Figure 2: Joining 3.5mm to 3,5mm

Figure 3: confirmed good quality on 3.5mm

When initially testing the welding of 3.5 mm steel coils to other 3.5 mm coils, and 4 mm coils to other 4 mm coils, the success rate was about 85%. Failures primarily occurred next to the weld, not in the weld itself. After optimizing and fine-tuning the parameters (such as upset time and flash time), weld samples passed tensile strength testing in the mechanical laboratory with a 100% success rate. Welding thicker sheets and sheets of different thicknesses of this same steel grade will require additional tests to confirm a 100% quality weld. The successful parameters have been archived and now serve as the standard setup for welding the **S355MC** grade (see Table 1).

Table 1: Welding paameters for S355MC

	PARAMETERS - S355MC							
Thickness [mm]	Flash time [s]	Upset distance [in]	Upset current [%]	Upset time [cycles]	Gaugebar step	Ramp time [s]	Ramp distance [in]	Tap setting
3.0-3.0	14	0.13	90	19	2	0	0	5
3.5-3.5	14	0.13	90	19	2	0	0	5
3.5-4	18	0.2	90	24	2	0	0	6
4.0-4.0	20	0.2	90	24	3	0	0	6
4.5-4.5	22	0.22	90	24	2	2	0.02	7
4.5-5	24	0.25	90	28	2	2	0.02	8
5.0-5.0	26	0.25	90	28	1	2	0.02	8
5.0-6.0	26	0.25	90	28	1	2	0.02	8

FBW Parameter Testing for S355J2+N Steel

Weld tests were conducted on steel sheets of two types: joints between two sheets of 4 mm × 1240 mm, and joints between 5 mm × 1240 mm and 4.5 mm × 1240 mm sheets (Figure 4).

Figue 4: Tensile testing of welded joints.

For the 4.5mm thick sheets, setting the upset time to 14 cycles resulted in weld failure in 33% of the tested samples. For the 4mm strips, the failure rate during mechanical testing was 18.5%.

Of the 12 samples welded with an upset time of 10 cycles, only one sample failed the bend test, while the tensile test results indicated a sound weld. Based on these findings, we concluded that an upset time of 10 cycles is optimal for welding 4 mm thick material. For the 5mm thickness, out of 12 welded samples, six (50%) failed completely during testing, and two exhibited cracking. Tensile test results remained consistent despite varying the upset time. Specifically, three samples failed with an upset time of 16 cycles, and three failed with an upset time of 12 cycles.

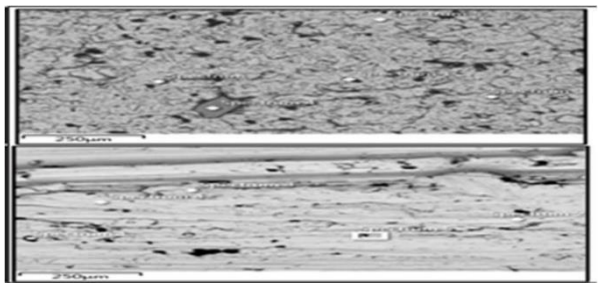

Figure 5: SEM analysis

All failed samples were subsequently analysed using SEM and EDS to identify the cause of fracture and to compare them with a sound weld sample. Detailed examination confirmed a significantly higher concentration of non-metallic inclusions along the fracture line in the failed welds.

3. RESULTS AND DISSCUSION

Some samples welded with identical parameters exhibited good performance in tensile and bend tests, with fractures occurring outside the weld joint. EDS analysis showed these samples still contained inclusions, though smaller and less dense (Figure 6), confirming that slight reductions in oxide formation and inclusion size significantly improve mechanical properties. Our tests demonstrated a strong interdependence between transformer tap setting, upset distance and flash time. Adjusting the transformer tap alone, without corresponding upset distance adjustment, was ineffective at fully expelling oxides from the weld center, resulting in trapped inclusions [3]. Increasing flash time promotes greater heat dissipation into the base material, reducing the temperature gradient at contact surfaces, combined with a large upset distance, this can cause excessive deformation. Conversely, very short flash times produce high temperature gradients that, when paired with a large upset distance lead to grain elongation perpendicular to deformation direction as well as formation of cold spots.

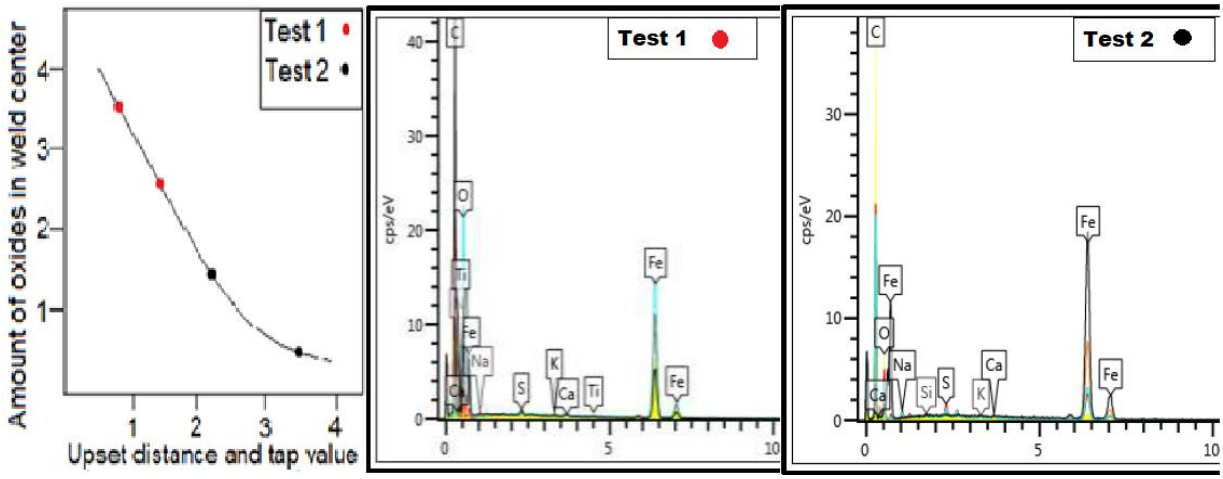

Figure 6: Interdependance of tap settings and upset distance on the amount of nonmetallic inclusions.

Uneven Heat Distribution and Plasticization in Dissimilar Joints. Further welding and testing were performed on dissimilar joints joining 5 mm and 4.5 mm thick sheets. Initially, most samples failed due to brittle fracture along the weld. Increasing upset distance and adjusting tap settings improved results, but consistent quality remained challenging. Optimizing parameters for the thicker sheet risks overheating or local melting of the thinner side, while optimization for the thinner sheet can cause insufficient plasticity on the thicker side, leading to cold welds or fusion defects [4].

4. CONCLUSION

Modernization of the welding machine on the D2 line at HBIS cold rolling mill, combined with thorough testing and parameter optimization, has significantly improved welding of micro-alloyed steels. For S355MC, success reaches 100% across nearly all dimensions. For S355J2+N, sound welds occur in 83% of 4 mm strips but are rare and inconsistent for 5 mm strips. Further testing is required to optimize parameters for these challenging welds. Further testing may consider the use of shielding gas to effectively mitigate oxidation-related defects.

REFERENCES

[1] C.W. Ziemian, M.M. Sharma, D.E. Whaley, Mater. Des., 33 (2012) 175-184.
[2] T. Jovanovic, Testiranje niskougljenicnih i mikrolegiranih celika na postrojenju D2, CRM - HBIS , Tehnicki izvestaji 1-10,
[3] Y. Ichiyama, T. Saito, Weld. Int., 18 (6) (2004) 436-443
[4] N.F.H. Kerstens, I.M. Richardson, J. Mater. Process. Technol., 209 (5) (2009) 2715-2722.

The 56th International October Conference on Mining and Metallurgy
22-25 October 2025, Bor Lake, Bor, Serbia
www.ioc.tfbor.bg.ac.rs

DOI: 10.5937/IOC25474M Original scientific paper

STRUCTURAL CHANGES IN PYROPHYLLITE INDUCED BY MECHANOCHEMICAL MODIFICATION AND ZINC OXIDE DOPING

Emina Međedović[1a], Vanja Asanović[1b], Milena Tadić[1c], Jasmina Grbović Novaković[2a], Irena Nikolić[1d], Anđela Mitrović Rajić[3a]

[1] Faculty of Metallurgy and Technology, University of Montenegro, Džordža Vašingtona bb, Podgorica, Montenegro
[2] Centre of Excellence for Hydrogen and Renewable Energy, Laboratory of Physics, Vinča Institute of Nuclear Sciences - National Institute of Republic of Serbia, University of Belgrade, Belgrade, Serbia
[3] Institute of Technical Sciences of SASA, Kneza Mihaila 35/IV, 11000 Belgrade, Serbia
[1a] emedjedovic8@gmail.com, 0009-0001-9573-3252
[1b] vanjaa@ucg.ac.me, 0000-0001-8592-3266
[1c] milenak@ucg.ac.me, 0000-0001-7321-8842
[2a] jasnagn@gmail.com, 0000-0002-8481-6407
[1d] irena@ucg.ac.me, 0000-0001-6781-3485
[3a] andjelamitrovicfh@gmail.com, 0000-0003-3004-8139

Abstract

This study investigates the structural modifications of natural pyrophyllite that occur following mechanochemical treatment and subsequent doping with zinc oxide. Pyrophyllite ore with an initial particle size of approximately 180 µm was mechanically milled using a SPEX Mixer mill at 30 Hz for 15 minutes. Mechanochemically activated samples were then doped with 2 wt% ZnO and subjected to the same milling conditions. The structural and morphological transformations of the samples were examined using X-ray diffraction (XRD), scanning electron microscopy equipped with energy-dispersive spectroscopy (SEM-EDS), and particle size analysis by laser diffraction. XRD analysis revealed a decrease in reflection intensity, accompanied by broadening of the reflections, indicating a disorder in the crystal structure of the modified pyrophyllite sample. The introduction of zinc oxide led to a further decrease in peak intensities. SEM analysis revealed the formation of aggregates in the mechanically milled sample. The decrease in particle size was observed for doped samples. Particle size analysis confirmed a reduction in median particle size from 172 µm to 3.997 µm after milling, with a slight increase to 4.980 µm following ZnO doping. Specific surface area increased significantly with mechanochemical activation, from 0.04 m²/g to 2.25 m²/g, and slightly decreased to 2.06 m²/g after doping. These results confirm the effectiveness of mechanochemical treatment and ZnO doping in modifying the structural and surface characteristics of pyrophyllite, implying potential for enhanced sorption capacity, which is necessary for removing pollutants from wastewater.

***Keywords**: Pyrophyllite, mechanochemical modification, doping, sorption*

1. INTRODUCTION

Pyrophyllite, with a chemical formula $Al_2Si_4O_{10}(OH)_2$, has a continuous layered structure and is typically found in combination with other minerals such as quartz, mica minerals, kaolinite, epidote, and rutile [1]. Pure pyrophyllite consists of 28.3% Al_2O_3, 66.7% SiO_2, and 5% H_2O [1]. The water, which is distributed between two silica tetrahedral layers, is linked with aluminium to form an “aluminium hydroxide” layer - [$Al(OH)_3$]. The structural lamellae mainly depend on van der Waals forces, and they are easily slipped under shear action, making them an ideal pressure-transmission medium [2]. The physicochemical and mechanical properties of pyrophyllite enable its application in various fields, including metallurgy, ceramic material production, and the chemical industry [2], as well as in the pharmaceutical industry, pesticide production, paints, plastics, cement, and rubber manufacturing [1]. Pyrophyllite can be used as a substitute for

kaolinite in ceramic and pottery production, and it can also replace talc in many fields, particularly in the pharmaceutical industry and medicine [1].

Pyrophyllite's layered structure provides a large surface area for adsorption. It is resistant to most chemical attacks, making it suitable for harsh industrial wastewater environments. The mechanochemical process is an effective method for producing fine-structured products from raw materials, including clay minerals [3], which not only causes a decrease in particle size but also induces structural changes that lead to an increase in chemical reactivity [4]. Mechanical milling of solid substances causes various phase transformations, cracks, and the formation of new surfaces [5]. It was found that the mechanochemical activation of pyrophyllite may affect its structural order and reactivity [3,4]. In the present study, we will investigate how doping mechanochemically activated pyrophyllite with zinc oxide induces the development of a new structure and enhances the characteristics of the resulting material.

2. EXPERIMENTAL

The powder of pyrophyllite with a particle size of about 180 μm originating from the ore deposited in Parsovići (Bosnia and Herzegovina) was mechanically milled using a SPEX Mixer mill 5100 for 15 minutes at 30 Hz, while the ratio of the weight of the balls to powder was 10:1. Mechanochemicaly activated pyrophyllite was then doped with 2% of zinc oxide - two powders where subjected to the mechanical milling for 15 minutes at 30 Hz.

The crystal structure of the samples was examined using a Philips PW 1050 diffractometer with nickel-filtered CuK$\alpha_{1,2}$ radiation (λ =0.1540 nm). The X-ray spectra have been recorded in the (2θ) range from 5° to 80° in steps of 0.02° for 10 s. The microstructure of natural pyrophyllite, activated pyrophyllite and doped samples was examined by scanning electron microscopy (SEM) using FEI SCIOS 2 Dualbeam. A Malvern 2000 Mastersizer laser scattering particle size analyser has been employed to determine the particle size distribution of samples. The designated resolution range of the system was sub-micrometre to 2 mm. As the suspension medium, 2-propanol was used. All samples underwent ultrasonication for 10 minutes before measurement. All measurements were conducted at a uniform stirring speed and obscuration level.

3. RESULTS AND DISCUSSION

X-ray diffraction (XRD) analysis has revealed that natural pyrophyllite ore consists of pyrophyllite, kaolinite, muscovite, quartz, and calcite. Mechanochemical modification of pyrophyllite ore results in changes to its crystal structure. Compared to the initial sample, the XRD profile of the mechanically modified pyrophyllite sample showed a significant decrease in the typical XRD reflection intensities (Figure 1). In addition, the broadening of the reflections was also observed. In the case of pyrophyllite doped with 2% zinc oxide, the diffraction results show a decrease in the intensity of the diffraction peaks.

Compared to the initial sample of pyrophyllite ore, which contains particles with rough surfaces and non-uniform sizes, and single particles showing a laminar structure [6], morphological characterisation of mechanochemically modified pyrophyllite using scanning electron microscopy with energy-dispersive spectroscopy (SEM-EDS) has shown significant disruption of laminar structure, and smaller particles formed by fragmentation form aggregates (Figure 2). SEM analysis of material obtained by doping modified pyrophyllite with 2% zinc oxide reveals changes in surface morphology, including the distribution of oxide particles over the surface of pyrophyllite, which maintains a laminar structure with a slight increase in roughness (Figure 2). Chemical composition of the particles is shown in Table 1.

The effect of mechanochemical activation and doping on the pyrophyllite with zinc oxide on particle size distribution is shown in Figure 3. The values of specific surface area and d (0.1), d (0.5) and d (0.9) particle size of examined samples are presented in Table 2. The median particle

size of natural pyrophyllite decreased from 172 μm to 3.997 μm during mechanical milling, while doping caused an increase to 4.980 μm. Mechanical milling resulted in a change in the structure of the pyrophyllite, leading to an increase in the specific surface area from 0.04 m²/g to 2.25 m²/g. In contrast, additional doping induced a slight decrease to 2.06 m²/g. Repeated fracture during treatment leads to a significant reduction in particle size, thereby increasing the specific surface area of the material particles. Increasing the specific surface area of pyrophyllite through mechanochemical modification implies that its sorption properties will be improved, which are necessary for removing pollutants from wastewater.

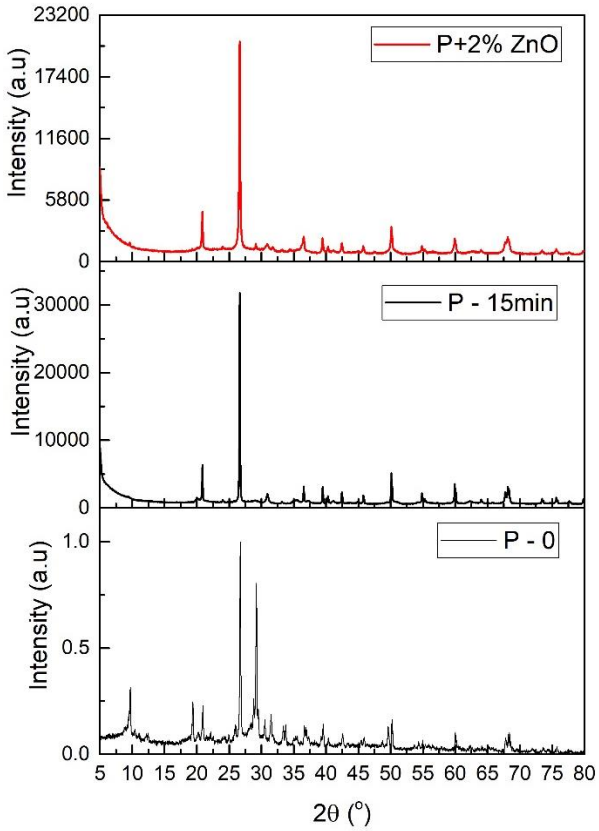

Figure 1. XRD patterns of natural pyrophyllite ore (P – 0), modified pyrophyllite (P – 15 min) and doped pyrophyllite (P+2%ZnO)

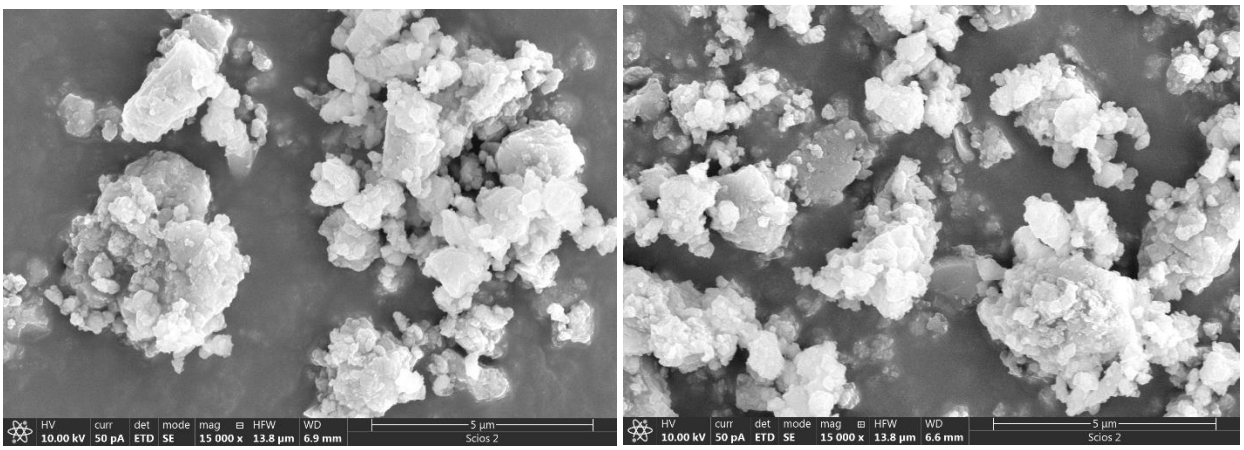

a) b)

Figure 2.SEM micrographs of mechanically modified pyrophyllite and doped pyrophyllite

Table 1. Chemical composition of the particles

Specimen	Chemical composition [weight %]									
	Si	Al	O	Mg	Ca	K	C	Zn	Na	F
modified pyrophyllite	30.284	11.220	46.957	1.786	4.153	0.832	4.000		0.202	0.566
doped pyrophyllite	32.409	8.704	44.902	0.995	2.279	0.759	6.896	3.056		

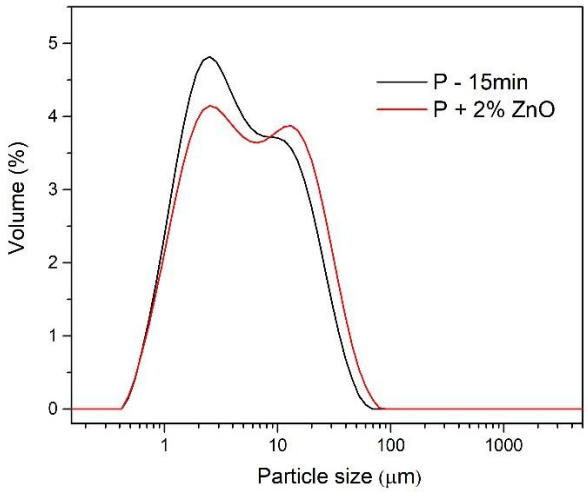

Figure 3. Particle size distribution of pyrophyllite sample (P – 15 min) and doped pyrophyllite (P+2%ZnO)

Table 2.Specific surface area and particle size of examined samples

Specimen	Specific surface area [m^2/g]	d (0.1) [μm]	d (0.5) [μm]	d (0.9) [μm]
modified pyrophyllite	2.25	1.135	3.997	18.105
doped pyrophyllite	2.06	1.180	4.980	22.542

4. CONCLUSION

Mechanochemical activation significantly alters the structural and morphological properties of natural pyrophyllite, reducing particle size and increasing specific surface area due to repeated fracture and increased disorder. Doping with 2 wt% zinc oxide further modifies these characteristics, slightly increasing particle size and influencing surface morphology. The combined treatment demonstrates an effective approach for tailoring the microstructure and enhancing the reactivity of pyrophyllite, potentially expanding its applicability in areas such as pollutant adsorption.

ACKNOWLEDGEMENTS

This work is funded by the Innovation Fund of Montenegro, Grant Contract No**.** POC-018-24.

REFERENCES

[1] M.A. Ali, H.A.M. Ahmed, H.M. Ahmed, M Hefni. Appl. Sci. 11 (23) (2021) 11357.
[2] X. Qin, J. Zhao, J. Wang, M. He, Minerals, 10 (9) (2020) 778.
[3] J. Zhang, Y. Zhou, M. Jiang, J. Li, J. Sheng. J. Mol. Liq. 209 (2015) 267–271.
[4] I. Tole, K. Habermehl-Cwirzen, A. Cwirzen. Miner. Petr. 133 (2019) 449-462.
[5] J.F. Fernández-Bertran, Pure. Appl. Chem. 71 (4) (1999) 581-586.
[6] A. Mitrović Rajić et al. Sci. Sinter. 55 (2023) 453-467.

The 56th International October Conference on Mining and Metallurgy
22-25 October 2025, Bor Lake, Bor, Serbia
www.ioc.tfbor.bg.ac.rs

DOI: 10.5937/IOC25478Z *Original scientific paper*

EFFECT OF COPPER CONTENT ON PHASE FORMATION AND MECHANICAL RESPONSE OF Al–Cu ALLOYS

Biljana Zlatičanin[1a], Branislav Radonjić[1b]

[1] Faculty of Metallurgy and Technology, Cetinjski put bb, 81000 Podgorica, Montenegro
[1a] biljana@ucg.ac.me, 0000-0002-9659-3191
[1b] bradonjic@t-com.me, 0009-0005-8158-1023

Abstract
This study investigates the effect of Cu content (5–36 wt.%) on the microstructural evolution and mechanical behavior of Al–Cu alloys. Experimental results demonstrate that increasing Cu content promotes eutectic phase formation θ-Al_2Cu in as-cast microstructures, accompanied by a transition from dendritic to cellular dendritic grain morphology. Hypereutectic Al-Cu alloy is an ideal candidate for producing in situ composites because the multiphase structure that reinforced phases (θ-Al_2Cu phase) embedded in a flexible matrix eutectic phase can be directly achieved by casting. Al_2Cu is an intermetallic formed at the last stages of solidification.

***Keywords**: Al-Cu alloys, Brinell hardness, compression strength*

1. INTRODUCTION

Aluminium is the most abundant metal in the earth's crust. It makes up about 8% by weight of the earth's solid surface. Aluminium alloys with a wide range of properties are used in engineering structures. These properties can be largely modified by changing the alloy composition. Silicon, copper, zinc and magnesium are the most commonly used elements in aluminium alloying, which have sufficient solid solubility. In general, aluminium - copper alloys are used for many of the applications where higher strength is needed [1]. Currently, many types of Al-Cu alloys with different mechanical and technological properties are being produced. The most important factors shaping these properties include the content of alloying elements (mainly the addition of copper), as well as parameters of plastic forming and heat treatment [2].

In this paper, the effects of copper contents in the interval of 5 – 36wt.% on the mechanical properties of aluminium-copper alloy were examined. Namely, copper content in the standard alloys ranges up to around 5wt.% since the maximum solubility of copper in hard state, at eutectic temperature (548^{o}C) is 5,65wt.%. Alloys containing copper up to 36wt.% have been also tested, that is why a considerable eutectic phase appears in the microstructure. With standard alloys the primary α - super saturated solid solution crystalizes in a dendritic form. With higher copper contents, eutectic appears in the interdendritic space and between grains. Microstructure can be influenced by controlling technological parameters and by addition of titanium and boron in form of AlTi5B1 containing fine insoluble crystals of TiB_2 phase acting as nucleants, first for $TiAl_3$ phase, and further for the aluminium phase and/or of the α- super saturated solid solution [3].

2. EXPERIMENTAL

Al-Cu alloys with the compositions given in Table 1. were prepared in an electrical resistance furnace from 99.5% pure aluminium and 99.9 % pure copper. To study the variations in the mechanical properties with respect to copper content, special attention was given to an assessment of the different properties of the materials: hardness and determination of compression strength. Hardness of the samples has been measured by use of the Brinell method. Compression strength of the cast samples has been tested on a universal electronic tensile testing machine of $1x10^4$ kg.

Average size of samples was as follows: diameter D_o=10mm and height H_o=20mm. All of the tested samples have been fractured. Compression strength is measured in the moment of fracture.

Table 1. Chemical composition of the investigated alloys (in wt.%)

Type of sample		%Fe	%Si	%Ti	%Cu	%Zn	%Al
Al-Cu5	0%Ti	0.11	0.07	0.000	5.90	0.054	93.86
	0.02%Ti	0.11	0.07	0.023	4.44	0.050	95.31
	0.08%Ti	0.12	0.07	0.094	4.34	0.050	95.33
	0.15%Ti	0.12	0.07	0.195	6.38	0.053	93.19
	0.25%Ti	0.11	0.07	0.276	4.28	0.049	95.22
Al-Cu36	0%Ti	0.15	0.07	0.000	36.46	0.091	63.22
	0.02%Ti	0.14	0.08	0.027	36.22	0.094	63.44
	0.08%Ti	0.15	0.08	0.111	35.54	0.089	64.03
	0.15%Ti	0.14	0.07	0.202	35.35	0.090	64.14
	0.25%Ti	0.14	0.08	0.345	35.57	0.091	63.78

3. RESULTS AND DISCUSSION

Copper has been the most common alloying element almost since the beginning of the aluminium industry, and a variety of alloys in which copper is the major addition, were developed. In the binary aluminium-copper system, the aluminium-rich terminal solid solution is in equilibrium with the intermetallic phase θ, which has approximately the formula Al_2Cu, although some solid solubility exists. The Brinell hardness and the compression strength are shown in Table 2 and 3.

Table 2. Hardness of the investigated alloys with different amounts of titanium

Type of sample		HB_1	HB_2	HB_3	HB_4	$HB_{average}$
Al-Cu5	0%Ti	52.5	56.1	57.5	56.1	55.55
	0.02%Ti	60.5	62.1	59.0	57.5	59.77
	0.08%Ti	62.1	63.7	64.3	67.3	63.92
	0.15%Ti	62.4	63.7	64.7	64.9	64.35
	0.25%Ti	63.6	64.9	64.9	67.5	65.22
Al-Cu36	0%Ti	180.0	178.0	185.0	179.0	180.50
	0.02%Ti	193.0	195.0	189.0	195.0	192.50
	0.08%Ti	194.0	197.0	202.0	197.0	197.50
	0.15%Ti	202.0	207.0	202.0	207.0	205.50
	0.25%Ti	204.0	211.0	204.0	211.0	207.50

The changes in chemical composition of the alloy cause changes in the structure that are reflected in the Brinell hardness and the compression strength. The hardness of the modified alloy is higher than the hardness of the alloy without any modification treatment. By increasing the content of titanium, compression strength also increases.

Table 3. Compression strength of the investigated alloys with different amounts of titanium

Type of sample		$F_{P0.2}$ (N)	$R_{P0.2}$ (N/mm^2)	F_{PM} (N)	R_m (N/mm^2)	d_P (%)	Y_P (%)
Al-Cu5	0%Ti	6600	84.08	24800	315.92	39.70	50.59
	0.02%Ti	7000	89.17	26000	331.21	36.99	46.18
	0.08%Ti	8000	101.92	37600	478.98	35.12	43.27
	0.15%Ti	8080	102.93	37640	479.49	22.73	25.79
	0.25%Ti	8200	104.46	37720	480.51	21.72	24.48
Al-Cu36	0%Ti	31000	394.90	42800	545.22	2.04	2.06
	0.02%Ti	38000	484.07	45800	583.44	1.02	1.02
	0.08%Ti	39400	501.91	52800	672.61	0.85	0.85
	0.15%Ti	40800	519.74	52840	673.12	0.68	0.68
	0.25%Ti	40800	519.74	52920	674.14	0.68	0.68

In Al-Cu alloys, strengthening takes place with the precipitation of the intermetallic Al_2Cu phase. The present intermetallic phases can be determined by determination of the chemical composition using EDS analysis. Typical EDS spectra of θ-phase and α-phase are shown in Figure 1 and 2. The chemical compositions matched the stoichiometric composition of Al_2Cu, and was confirmed by EDS analysis. In Al–Cu alloys, higher Cu content increases the volume fraction of θ (Al_2Cu) precipitates; their size is mainly controlled by cooling rate and aging conditions, not just copper content. In the Al–Cu system, the intermetallic compound Al_2Cu forms during the binary eutectic reaction: L → α-Al + Al_2Cu (at ~548°C, ~33wt.% Cu in the eutectic). When the local liquid composition reaches the eutectic composition at the solid–liquid interface, the eutectic reaction occurs, producing a mixture of α-Al and Al_2Cu. The Al_2Cu may appear in blocky or lamellar forms depending on solidification conditions.

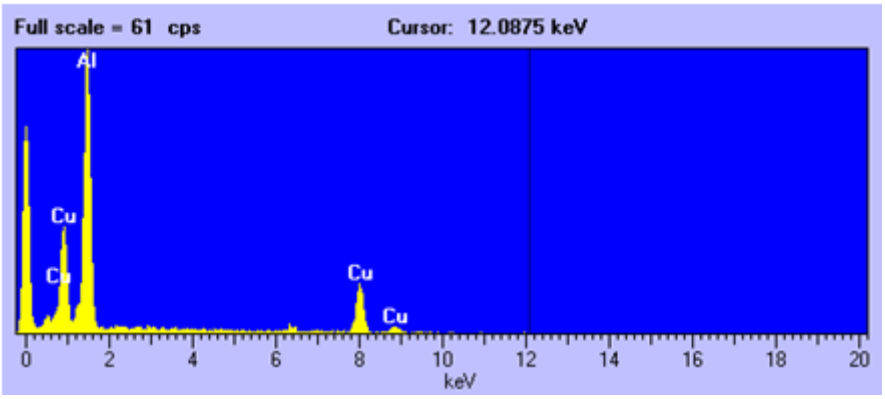

Figure 1.EDS microanalysis of Al_2Cu phase

In as-cast Al–Cu alloys, the microstructure typically consists of primary α-Al and the intermetallic Al_2Cu (θ) phase, arranged as a eutectic mixture in an Al-rich matrix. The Al_2Cu phase often forms along α-Al grain boundaries, with morphologies ranging from continuous networks to isolated sectored plates, depending on composition and cooling rate.

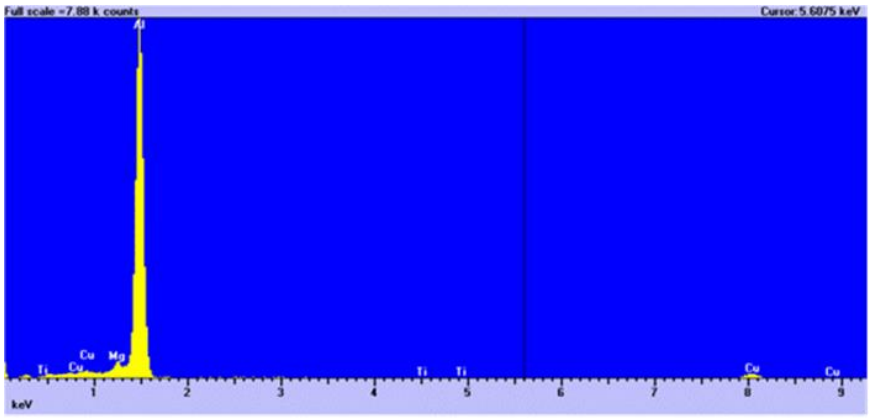

Figure 2. EDS microanalysis of α-phase

4. CONCLUSION

From the obtained data the following conclusions can be drawn: The compression strength and hardness of Al-Cu alloy increases with the increase in Cu content. When the Cu content increases from 5wt.% to 36wt.% the strength increases by 40%, and hardness increases over 220%. In Al-Cu alloys, copper content is critical because the temperature-dependent solubility of Cu in aluminum enables heat treatment; through precipitation hardening, this allows control and enhancement of mechanical properties. In Al–Cu alloys, higher Cu content increases the potential hardening effect, with the θ (Al_2Cu) phase playing a central role in precipitation strengthening.

REFERENCES

[1] H. Rashed, E. Ashrafi, A. Hasan, Mater. Trans., 64 (1) (2023) 177-183.
[2] B. Płonka, K. Żyłka, K. Remsak, M. Rajda, J. Zdunek, D. Moszczyńska, ACME, 24 (8) (2024) 8-17.
[3] B. Zlatičanin, B. Radonjić, S. Đurić, B. Jordović, B. Stojanović, Mater. Technol., 36 (1-2) (2002) 49-51.

The 56th International October Conference on Mining and Metallurgy
22-25 October 2025, Bor Lake, Bor, Serbia
www.ioc.tfbor.bg.ac.rs

DOI: 10.5937/IOC25482Z Original scientific paper

COMBINED EFFECT OF COOLING CONDITIONS AND Mg CONTENT ON THE MICROSTRUCTURE AND PROPERTIES OF Al-Cu15 Alloys

Biljana Zlatičanin[1a], Branislav Radonjić[1b]

[1] Faculty of Metallurgy and Technology, Cetinjski put bb, 81000 Podgorica, Montenegro
[1a] biljana@ucg.ac.me, 0000-0002-9659-3191
[1b] bradonjic@t-com.me, 0009-0005-8158-1023

Abstract
Results presented in this paper contribute to investigation of the cooling conditions and addition of magnesium on the microstructure of Al-Cu alloys. In this paper 4 samples were solidified by different cooling rates. The examined Al-Cu-Mg alloys contain intermediate phases $CuAl_2$ and $CuMgAl_2$ that appear in different quantities depending on the chemical composition and parameters of the technological process. With the addition of magnesium, the compressive strength and hardness of the aluminum-copper alloy increases.

***Keywords**: Al-Cu alloys, Al-Cu-Mg alloys, cooling rate*

1. INTRODUCTION

Al-Cu alloy is widely used in aerospace and other fields due to its high tensile strength, elastic modulus, good fatigue performance, and corrosion resistance [1,2]. Interest in the Al-Cu15 alloys during last decades was due to the wide use of these alloys in diffrent industries. Depending on the casting conditions and alloy composition, microstructure, properties, and characteristics of the Al-Cu alloys will be different. The cooling rate affects the structure of as-cast alloys in a well-established manner, i.e. the grain size and the size of structure constituents (both primary and eutectic) decrease with the increase in cooling rate. A series of casting experiments were performed with binary Al-Cu alloys with varying cooling rates and cooling conditions [3]. This paper analyzes the influence of cooling rate and addition of Mg on the microstructure and properties of Al-Cu15 alloys.

2. EXPERIMENTAL

Experimental work can be divided in two phases. The first phase comprises of melting and casting of Al-Cu and Al-Cu-Mg alloys. Four samples were prepared by melting raw materials. The chemical composition (in wt. %) of the Al-Cu and Al-Cu-Mg alloys was specified by quantometery analysis and the results are reported in Table 1. The second phase includes characterization of cast samples by quantitative microstructure analysis. To study the variations in the mechanical properties with respect to cooling rate, the alloys were cast by conventional methods that include air or water-cooling. After applying different cooling methods, the hardness and compression strength were investigated. Hardness has been measured using the Brinell method. Compression strength of the samples has been determined on an electronic tensile testing machine of 10t.

Table 1. Chemical composition of the investigated alloy (in wt.%).

Type of sample	%Fe	%Si	%Ti	%B	%Cu	%Zn	%Mg	%Al
Al-Cu15	0.13	0.07	0.000	0.000	14.25	0.062	0.00	85.48
Al-Cu15-Mg1	0.15	0.07	0.002	0.000	14.30	0.080	1.139	84.23

3. RESULTS AND DISCUSSION

The effects of different process parameters during the solidification of the AlCu and AlCuMg alloys were examined. The changes in the microstructure were caused mainly by the different cooling rates of the sample. It is well known that the cooling rate plays an important role in the refinement of metal structures. Increasing the cooling rate is an effective way to change the morphology of an intermetallic. Number of primary grains is one of the most important factors for determining the quality of castings. The final grain density in the casting depends on the nucleation process at the beginning of solidification. Figure 1 shows the microstructures of Al-Cu15 alloy obtained after different cooling rates. The microstructures consists of dendrites and the interdendritic eutectic. For Al-Cu15 alloys, in both cooling rates, equilibrium eutectic is formed during solidification. Figure 2 shows the microstructure of Al-Cu15-Mg1 alloy obtained after a higher cooling rate (water cooled). From the presented figure, it can be concluded that the higher cooling rate along with the Mg addition, produced finer grains. The two present phases in the microstructure are the primary phase (alpha solid solution) and the secondary phases.

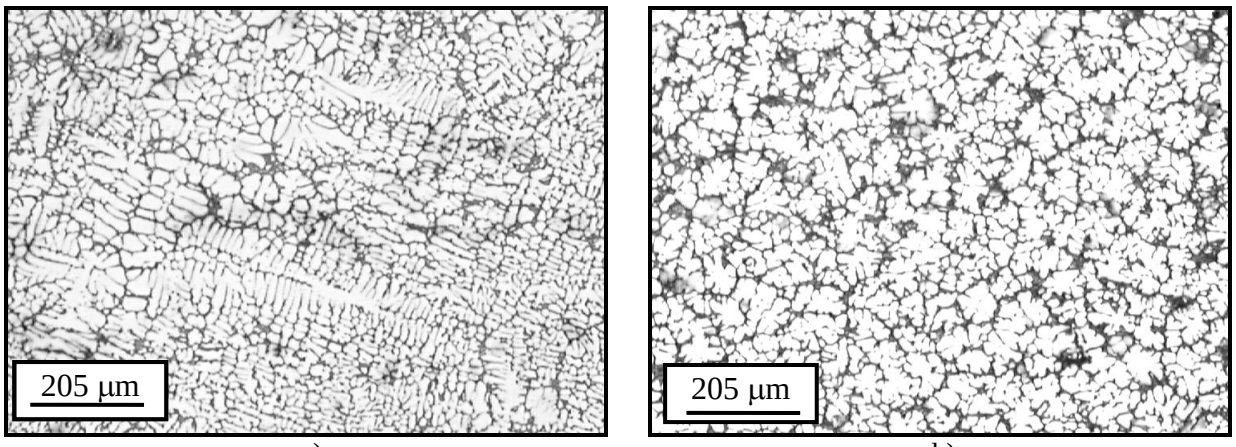

Figure 1. Microstructure of Al-Cu15 samples with different cooling rates: a) air-cooled, b) water-cooled

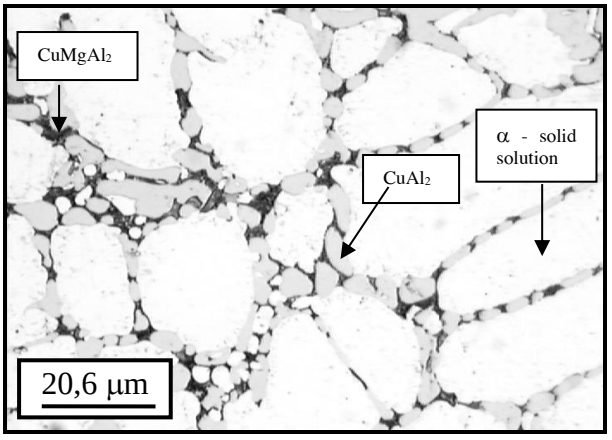

Figure 2. Microstructure of Al-Cu15-Mg1 sample (water-cooled)

Fast cooling rate facilitated the grain refinement. The sizes of the grains for the Al-Cu15 alloy decreased from 810.48 μm (air-cooled) to 560.08 μm (water cooled). For the Al-Cu15-Mg1 alloy grain size decreased from 233.37 μm (air-cooled) to 160.08 μm (water-cooled) after which, a fine uniform grain structure was obtained, as shown in figure 2. Also, addition of magnesium to the

aluminum-copper alloy, decreased the mean value of the grain size, from 810.48 μm (air-cooled) to 233.37 μm (air - cooled) and produced a finer, more uniform microstructure.

Under industrial conditions, in standard aluminium-copper alloys a dendritic grain structure is typical. In the binary aluminium-copper system, the aluminium-rich solid solution phase is in equilibrium with the intermetallic compound θ, which has approximately the formula $CuAl_2$, although some solid solubility exists. The addition of magnesium allows the formation of more intermetallic compounds, such as $CuMgAl_2$, $CuMg_4Al_6$, CuMgAl and $Cu_6Mg_2Al_5$. Magnesium is added to strengthen the solid solution. The addition of 1 wt.% magnesium to aluminum alloys sharply increases the strength of the alloy. In Al-Cu15-Mg1 alloys, $CuAl_2$ phase and $CuMgAl_2$ phase are dominant [3]. This is in agreement with the fact that the addition of Mg tends to increase the formation of the $CuMgAl_2$ phase (Figure 2). The dominant strengthening phase in the tested AlCu15Mg1 alloys is the $CuMgAl_2$ phase. The addition of Mg to the alloy causes the deposition of a fine $CuMgAl_2$ phase when compared to the case of the alloy without Mg.

In this study the mechanical properties like compressive strength and hardness of both air-cooled and water-cooled cast specimens were tested and the results were compared (Tables 2 - 4). Increases in hardness and compressive strengths of the water - cooled cast specimen have been encountered from the present work. This result reveals that increase in cooling rate leads to enhancement of the mechanical properties. The maximum hardness increases for air-cooled samples from 89.7 BHN for the alloy with Al-15wt.%Cu to 146.0 BHN for the alloy Al-15wt.%Cu-1wt.% Mg. At room temperature, the strength increases for water-cooled samples from 491.72 MPa for the alloy with Al-15wt.%Cu to 673.7 MPa for the alloy Al-15wt.%Cu-1wt.% Mg.

Table 2. Hardness of the investigated alloys

Type of sample	$HB_{average}$, water-cooled	$HB_{average}$, air-cooled
AlCu15	90.0	89.7
AlCu15Mg1	148.0	146.0

Table 3. Compression strength of the investigated alloys (air-cooled samples)

Type of sample	$F_{P0.2}$ (N)	$R_{P0.2}$ (N/mm^2)	F_{PM} (N)	R_m (N/mm^2)	δ_P (%)	Ψ_P (%)
Al-Cu15	14800	188.54	38600	491.72	31.05	37.18
Al-Cu15-Mg1	17520	223.18	43800	557.96	24.43	28.02

Table 4. Compression strength of the investigated alloys (water-cooled samples)

Type of sample	$F_{P0.2}$ (N)	$R_{P0.2}$ (N/mm^2)	F_{PM} (N)	R_m (N/mm^2)	δ_P (%)	Ψ_P (%)
Al-Cu15	16800	214.01	40000	509.55	27.15	31.67
Al-Cu15-Mg1	19200	264.9	52800	673.7	19.94	22.24

The addition of magnesium to the Al-Cu15 alloy significantly increases the hardness (HB). The most important contribution of magnesium is in increasing strength. We found that 1wt.% of magnesium increases the strength by about 50 MPa for air-cooled samples and by about 180 MPa for water-cooled samples. As the magnesium content increases, the compressive strength and hardness of the aluminum-copper alloy also increases. In FCC metals such as aluminum, grain refinement contributes to strengthening, though generally less strongly than in BCC metals. In Al–

Mg alloys, Mg primarily strengthens through solid solution hardening, while in Al–Mg–Si and related systems, precipitation (e.g., Mg_2Si) plays a key role in enhancing strength.

4. CONCLUSION

The aim of this research was to investigate how addition of 1wt.%Mg to the Al-Cu alloy affect the solidification process, development of microstructure and mechanical characteristics of Al-Cu-Mg alloys. With the Mg addition the strength of Al-Cu alloy increases by 10% for air-cooled samples and by about 35% for water-cooled samples, and hardness increases by 60%.

The microstructure and mechanical properties of cast products are greatly influenced by the cooling rate during their solidification. It is evident that the increase in cooling rate improves the compression strength for 20% for the cast Al-Cu15-Mg1 alloy. The grain size decreases with increasing cooling rate, and the hardness and strength increase correspondingly. In addition, higher cooling rates produced a finer primary α-phase.

REFERENCES

[1] H. He, Y. Yi, S. Huang., J. Mater. Sci. Technol. 35 (1) (2019) 55–63.
[2] Y. Zhou, X. Lin, N. Kang., J. Mater. Sci. Technol. 37 (2020) 143–153.
[3] B. Zlatičanin, B. Radonjić, S. Đurić, B. Jordović, B. Stojanović., Mater. Technol., 36 (1-2) (2002) 49-51.

The 56th International October Conference on Mining and Metallurgy
22-25 October 2025, Bor Lake, Bor, Serbia
www.ioc.tfbor.bg.ac.rs

DOI: 10.5937/IOC25486G *Original scientific paper*

IMPROVEMENT IN THE TECHNOLOGY OF POURING COPPER PLATES FOR THEIR FURTHER USE IN ELECTROLYSIS PRODUCTION

Vladimir Glushchenkov[1a]

[1] Samara State Aerospace University (National Research University)
[1a] imp@ssau.ru, 0000-0001-8368-2905

Abstract

The existing technology of pouring of copper into ingot molds to produce anode plates for further use in the electrolysis production is considered. An assessment of the quality of the plates obtained by the existing technology of pouring is given. A new technical solution is proposed in which the copper melt after pouring it into an ingot mold is subjected to the pulsed magnetic field (PMF). Thermal-force action of the PMF on the melt improves the quality of the free surface of the plates, structure, and properties of the metal throughout the volume after crystallization. An evaluation of the factors of the pulsed-magnetic action is given. The mechanism of such action is described. The advanced considerations are confirmed by experiments. Proposals for cooperation to realize the new technical solution are stated.

Keywords: *copper anode plates, pulsed magnetic field, electrolysis, crystallization, eddy currents*

1. INTRODUCTION

High-quality copper is obtained using copper anodes by the electrolysis method [1]. The copper anodes are produced by pouring crude copper into ingot molds. The quality of the anodes is largely determined by the experience and qualification of the operator performing the pouring. Casting defects – nonuniformity of properties of the metal after crystallization, presence of micro and macro irregularities on the surface – depended on the skill of the operator. During further electrolysis, inadequate quality of the anodes leads to nonuniformity of thermal and current load, to the increased consumption of electrical energy. The process of pouring is performed on rotary machines with a large number of ingot molds (Figure. 1) and lasts a few hours. In this case, fatigue of the operator leads to a departure of the plates from given geometry, weight, and properties of the metal. That is why the task of improving the quality of anode copper plates is very urgent.

Figure. 1. Rotary machine furnace for pouring crude copper into ingot molds.

2. EXPERIMENTAL

The essence of the proposed technical solution, leading to an improvement in the quality of cast anode plates, is the action upon the free surface of the melt in the ingot mold by the pulsed magnetic field (PMF) (Figure. 2).

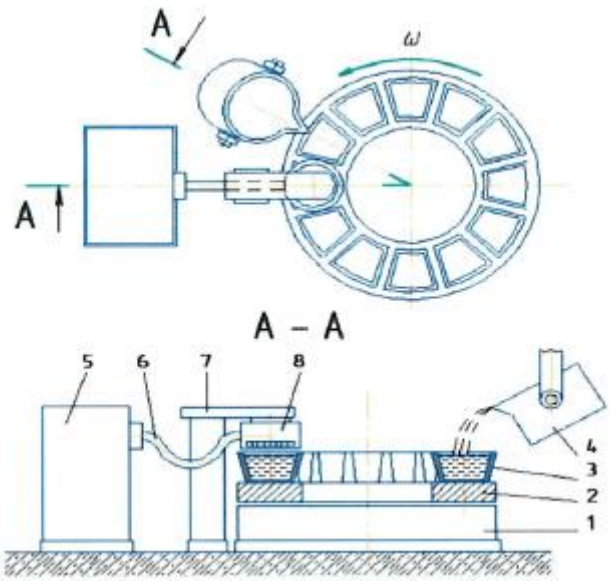

Figure. 2. Scheme of PMF action on copper melt: 1 – Base with actuator for table rotation:2 – Rotary table, 3 – Ingot mold, 4 – Ladle, 5 – PMI, 6 – Cable adapter, 7 – Inductor holder, 8 – Inductor.

The inductor (a multi-turn flat coil) is fitted on the rack above the ingot mold. The inductor is connected with the pulse-magnetic installation (PMI) [2]. At the time of discharge of the PMI's capacitor bank into the inductor, the pulsed magnetic field (PMF) is formed around turns of the inductor. Under action of the PMF, eddy currents of tens to hundreds of kilo-amperes are induced in the melt. Between the current in the inductor and that in the melt, electrodynamic repulsive forces arise. In this case, the time of action on the melt is $10^{-3} \div 10^{-4}$s. During the passage of the ingot mold with the melt under the inductor, the repeated force action of the PMF is performed in the whole time interval of the crystallization curve (Figure. 3).

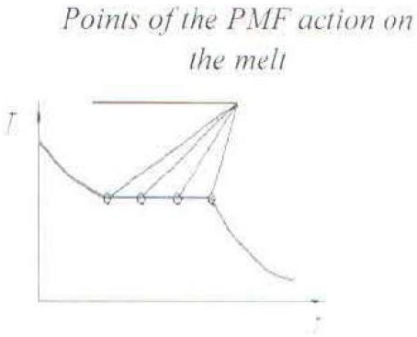

Figure. 3. Scheme of the repeated action of the PMF on the melt in the process of its crystallization.

As the carousel rotates, new ingot molds with the just-poured melt are brought under the inductor consecutively. The rack with the inductor is placed above the ingot mold immediately behind the pouring ladle. Movement of the inductor with the ingot mold for one step of carousel advance (rotation) is possible.

3. RESULTS AND DISCUSSION

Factors and the mechanism of the pulse-magnetic action on the copper melt [3].

The intensity of the pulse-magnetic action on the melt is determined by the value of electrical energy stored in the PMI's capacitor bank (W=CU2/2), whereas the shape of the originated force action is defined by the shape of the current curve of the discharge circuit (installation – inductor – melt)

The eddy currents, induced in the melt, are distributed with depth unevenly: they are maximum at the surface and decrease with the melt depth according to the exponential law (skin effect). The depth of the skin layer is $= \sqrt{\frac{2}{\omega\gamma\mu}}$. Consequently, the force action on the melt is three-dimensional.

Heat action. The eddy currents are additional internal heat sources changing temperature conditions of crystallization. The amount of heat released in the skin layer leads to the temperature increase $\Delta T = \int_0^T \frac{R*I_{max}^2}{2*Y*C_y}$

Force action. Three-dimensional electrodynamic forces, arising in the melt, lead to initiation of stress waves, metal-flows, and propagation of them over the mold volume, resulting in changing the structure and properties of the metal, their homogeneity, as well as assisting in degassing and eliminating of micro and macro defects on the surface. Control over the thermo-force action is possible by choosing the energy W, by varying the parameters of the discharge circuits of the installation and inductor [4], their orientation relative to the melt surface, the number of loading pulses, and time intervals between them.

Evaluation experiment [5].

The conducted experiments on the action of the PMF on the aluminum melt (Silumin) have shown the feasibility and effectiveness of such action from the viewpoint of improvement in both the structure and properties of the metal (Figure. 4).

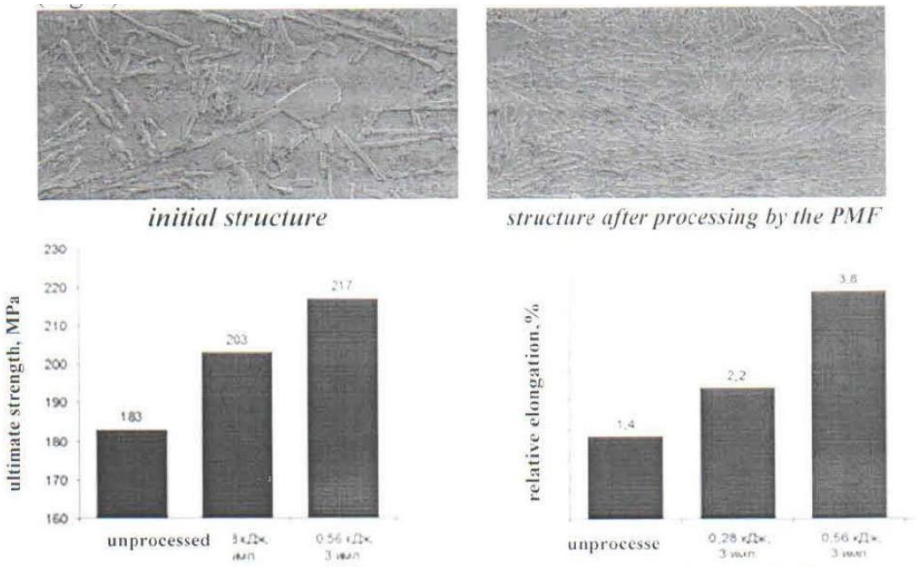

Figure. 4. Changes in structure and properties of the metal after the PMF action

As the PMF acts on a weld seam during arc-argon welding [6], effects of smoothing off the surface of strengthening of the weld seam as a whole were observed.

4. CONCLUSION

1. A new technical solution aimed at upgrading the quality of anode copper plates under the action of the pulsed magnetic field was proposed. A scheme of modernization of the rotary machine, needed for realization of the proposed technical solution, was developed.
2. Factors of the pulse-magnetic action on the copper melt – energy, frequency, the number of pulses, etc. – were determined, and the mechanism of such thermo-force action was stated: additional internal heat sources, stress waves, metal-flows.
3. The feasibility of the proposed technical solution was confirmed by experimental investigations performed with the aluminum melt.

To put the proposed technology into practice, the following needs to be done: 1) Creation of a procedure for calculation of parameters of the action and a procedure for simulation of processes occurring in the melt; 2) Performance of experimental investigations and assessment of quality of the plates; 3) Execution of design works and pilot-industrial mastering of the process. This amount of work can be performed with the joint efforts of universities and industrial enterprises interested in the results of the work.

REFERENCES

[1] Electronic resource. Encyclopedia of Mechanical Engineering XXL (http://mash-xxl.info/info/590841/) p. 170
[2] R. Yu. Yusupov, V.A. Glushchenkov, Energy Installations for Magnetic Processing of Materials: Monograph. – Samara: Fedorov Publishing House, 2013. – 128 p.
[3] V.A. Glushchenkov, V.F. Karpukhin – Technology of Magnetic-Pulse Processing of Materials: Monograph – Samara: Fedorov Publishing House, 2014. – 208 p.
[4] V.A. Glushchenkov, Inductors for Magnetic-Pulse Processing of Materials: Textbook. – Samara: Educational Literature Publishing House, 2013. – 148 p.
[5] V.A. Glushchenkov, F.V. Grechnikov, V.I. Nikitin, D.G. Chernikov, A.Yu. Igolkin, K.V. Nikitin, A.A. Pozdnyakov, Influence of High-Intensity Pulsed Magnetic Field on Properties of Liquid Aluminum Alloys, Russian Foundryman, 2010, No. 7. P. 34-39.
[6] V.F. Karpukhin, V.A. Glushchenkov, O. Al-Erhayem, V. Karpukhin, V. Glushchinkov, O. Al-Erhayem, Features, Possibilities, and Applications of Magnetic-Pulse Welding. Peculiarities, Possibilities, and Fields of Application of Pulse-Magnetic Welding. In Proceedings of the International Conference JOV-15, Helsingør, Denmark, May 3-6, 2009.

The 56th International October Conference on Mining and Metallurgy
22-25 October 2025, Bor Lake, Bor, Serbia
www.ioc.tfbor.bg.ac.rs

DOI: 10.5937/IOC25490P *Original scientific paper*

CAVITATION RESISTANCE OF TALC-REINFORCED PYROPHYLLITE CERAMICS

Marko Pavlović[1a], Marina Dojčinović[2a], Mirjana Stojanović [3a]

[1] Faculty of Mechanical Engineering, University of Belgrade-Innovation Center,Kraljice Marije 16, 11000, Serbia
[2] Faculty of Technology and Metallurgy, University of Belgrade, Karnegijeva 4, 11000 Belgrade, Serbia
[3] Engineering Academy of Serbia, Belgrade, SERBIA
[1a] pavlovic.marko38@gmail.com, 0000-0002-7098-6421
[2a] rina@tmf.bg.ac.rs, 0000-0002-8158-3468
[3a] mira1412@gmail.com, 0000-0003-4509-391X

Abstract
The paper describes the effects of changing the properties of pyrophyllite ceramics reinforced with different proportions of talc (%): 10; 20; 30. Pyrophyllite powders with a grain size of 20 μm and talc powders with a grain size of 15 μm were homogenized, pressed and sintered at a temperature of 1200ºC. The cavitation resistance of the sintered samples was determined by the ultrasonic vibration method with a stationary sample according to the ASTM G32 standard. The evolution of surface morphology and damage was examined by scanning electron microscopy (SEM). The aim of the research was to obtain a compact ceramic with improved properties of resistance to wear and cavitation. The quality of the sintered samples was evaluated according to the values of cavitation rates and the analysis of the surface damage.

Keywords: *pyrophyllite, talc, sintering, cavitation resistance*

1. INTRODUCTION

In the conditions of cavitation, damage occurs and develops on the surface of the material under the influence of shock waves, micro-jets, cavitation vortices, or some other cavitation structures. Cavitation is a type of wear and represents the appearance, growth, and implosion (collapse) of vapor or vapor-gas bubbles in a flowing liquid. During this, shock waves are created, high temperatures and pressures develop, and the released energy is absorbed by a solid surface that is in contact with the flowing liquid. Absorbed energy in the material causes elastic-plastic deformations or destruction of the material, which represents damage under the effect of cavitation (erosion) [1]. The extent of material degradation during cavitation depends on its type, microstructure, and mechanical properties-particularly its strength and hardness. According to the literature, cavitation in refractory materials results in surface damage and mass loss, typically without plastic deformation [2,3].

In our earlier research, the possibility of using pyrophyllite in cavitation conditions was investigated [4]. Small resistance properties were obtained, which gave the idea to investigate the possibility of using other materials as a reinforcement, and above all, talc, which is similar in properties to pyrophyllite. Pyrophyllite is a phyllosilicate mineral with the chemical formula $Al_2Si_4O_{10}(OH)_2$. The most important physical and chemical characteristics of pyrophyllite are: high melting point, high thermal conductivity, density (2,65 to 2,90 g/cm^3), softness (hardness according to Mohs scale 1 to 2), inertness, purity, and whiteness. Pyrophyllite has a layered structure, and the bonds between the layers are weak van der Waals bonds that can be easily broken, so the layers slide over each other. This property is important for the modification of pyrophyllite and the improvement of its physical and chemical characteristics (chemical modification, modification in the mill, as well as the application of physical methods, such as ultra sound, plasma and similar methods). Pyrophyllite is used in the paper industry, pharmacy, ceramics, environmental protection, cosmetics, agriculture, as well as for processing materials [5].

Talc is magnesium hydrosilicate with the general formula $3MgO{\cdot}4SiO_2{\cdot}H_2O$, containing impurities such as Al_2O_3, FeO, NiO, and CaO. Minerals commonly associated with talc include chlorite, tremplite, anthophyllite, and quartz. Talc has a leafy structure and low hardness. The most important physico-chemical and mineralogical properties of talc include a high melting point, chemical inertness (resistance to acids, alkalis and heat), low hardness and density, good grindability, low thermal conductivity, low coefficient of linear thermal expansion, and excellent adhesion and coating ability. It is used in the paint, pharmaceutical, chemical, and construction industries, as well as in medicine, cosmetics, rubber, and paper manufacturing, among other applications [6]. The goal of this research was to develop pyrophyllite ceramics with enhanced properties, particularly improved cavitation resistance, by incorporating talc as a reinforcing agent. To achieve the desired microstructure and properties, raw materials were prepared through crushing, grinding, and mechanical activation, followed by sample synthesis via sintering. These preparation and synthesis procedures were optimized and characterized to ensure quality samples.

2. EXPERIMENTAL

Three series of samples were used in the experiment: pyrophyllite 90% + talc 10% (label PT10); pyrophyllite 80% + talc 20% (PT20); pyrophyllite 70% + talc 30% (PT30). For the experiment, pyrophyllite (label: P) was obtained from the Parsovići – Konjic deposit, Bosnia and Herzegovina. The sample was prepared by crushing and grinding to a maximum grain size of 20 μm. The talc sample (label: T) was obtained by a combined procedure for the preparation of mineral raw materials (shredding, leaching) of raw talc. The sample was ground to a grain size of 15 μm for better compatibility with larger pyrophyllite particles. Table 1 shows the chemical composition of the initial pyrophyllite and talc fillers. The mixture of components of three series of samples was homogenized and pressed into tablets with a diameter of 30 mm and a thickness of 5 mm under a pressure of 10 MPa with the addition of carboxy methyl cellulose as a binding agent. For each series of samples, 10 tablets were made.

Table 1. Chemical composition of pyrophyllite and talc refractory fillers

Fillers	Oxide content, %							
	SiO_2	Al_2O_3	Fe_2O_3	MgO	CaO	Na_2O	K_2O	LoI*
P	63.55	14.85	1.24	1.46	7.53	0.29	0.3	5.90
T	60.88	4.14	0.85	32.50	1.07	-	-	6.90

*Loss on ignition at 1000 °C

After pressing, the tablets were sintered in a laboratory furnace at 1200 °C, according to the sintering regime: raising the temperature to 1000 ºC at a rate of 5 ºC/min for 250 min; 1000-1200 ºC with a heating rate of 2 ºC/min for 150 min; at 1200 ºC, the sintering of the samples lasted 60 min.

To determine the properties of the cavitation resistance of the tested samples, the ultrasonic vibration method was applied with a stationary ASTM G32 sample. The device and testing methodology were described in earlier works [3,7]. The samples were tested with different intervals of exposure to the effect of cavitation (min): 30; 60; 90 and 120. During the determination of the resistance to the effect of cavitation, the change in the mass of the samples as a function of the time of cavitation was monitored and the cavitation rate of the samples was determined. Measurements of the samples were made using an analytical balance with a precision of ± 0.1 mg. The formation and development of damage to the surface of the samples under the effect of cavitation were monitored by recording on an electron microscope brand MIRA3 FEG-SEM, Tescan (Brno, Czech Republic). The samples that were examined on the SEM were coated with gold before recording, the thickness of the layer was 5 nm.

3. RESULTS AND DISCUSSION

During the sintering process, a compact structure was achieved, which had a positive effect on the increased resistance of the samples during tests on the effect of cavitation. The sintering process contributed to a series of thermal transformations of phyrophyllite: removal of water present in the structure, dihydroxylation of pyrophyllite, decomposition of pyrophyllite into amorphous quartz and mullite, crystallization of cristobalite from amorphous quartz, and the resulting crystalline phases in the structure contributed to an increase in the hardness of sintered pyrophyllite [5]. The application of a mixture of pyrophyllite powder and talc of different grain sizes contributed to a better arrangement of the particles with each other, which contributed to the achievement of a higher density of the pressed samples. By inspecting the surfaces of the sintered P+T samples before and during the cavitation effect test, it is noted that there was no visible damage to the surface of the samples, nor breakage and degradation of the samples, as shown in Figure 1. The formation and development of damage to the surface of the samples took place at a low rate, and the loss of mass of the samples during exposure was small, Figure 2.

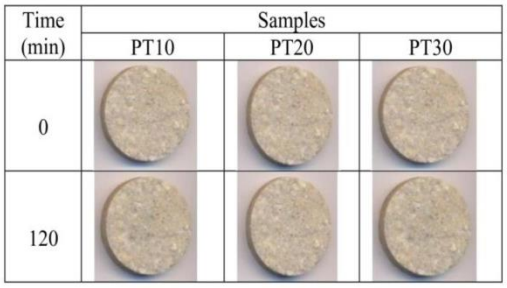

Figure 1. Photographs of the surfaces of sintered samples P+T before and after exposure.

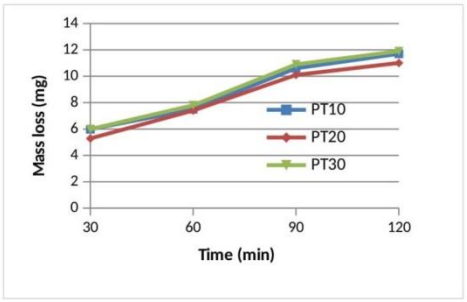

Figure 2. Cavitation rate of sintered samples P+T.

The process of surface damage takes place very slowly, without the appearance of cracks or a major loss of mass of the samples. The eroded surfaces are smooth, which indicates that the damage and loss of mass took place by removing particles from the surface without deformation, Figure 3.

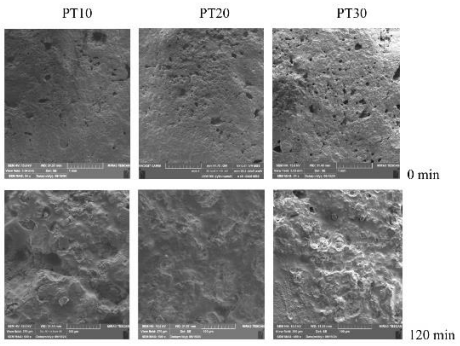

Figure 3. SEM microphotographs of the surface of P+T samples before cavitation and 120 min of exposure.

Figure 2 shows that all samples have low mass losses during exposure, and PT20 samples show the lowest mass loss and the lowest cavitation rate. The total mass loss at the end of the test lasting 120 min was: 11,70 mg (sample PT10); 11.01mg (sample PT20); 11.9 mg (sample PT30). The calculated cavitation rates of P+T samples were: V= 0.098 mg/min (PT10); V=0.092mg/min (PT20); V=0.099 mg/min (PT30), which indicates good cavitation resistance of all sintered samples.

4. CONCLUSION

Research on the effects of applying talc to improve the resistance properties of pyrophyllite-based ceramics has shown positive results. Pyrophyllite and talc are known to have low hardness, 2 and 1 on the Mohs scale, respectively. This affects the low cavitation resistance of sintered samples of pyrophyllite and talc, as shown by earlier research. With the addition of talc, which is similar to pyrophyllite and has high adhesion and surface coating properties, the cavitation resistance of the samples is significantly increased. The different sizes of pyrophyllite and talc grains, 20μm and 15μm, respectively, contributed to obtaining a compact structure of the samples, which improved mixing and stacking of particles with each other. By pressing and sintering the mixtures prepared in this way, compact structures of samples with improved properties of resistance to cavitation shocks were obtained. A series of crystalline phases created by sintering, primarily quartz, mullite, and cristobalite, contributed to the increase in the hardness of the samples, and thus to the increase in cavitation resistance. The cavitation resistance of the samples was determined based on the cavitation rate and analysis of the morphology of the damaged surface: the cavitation rates were low, from 0.092-0.099 mg/min, the erosion loss of the sample mass in 120 min was 1.9 mg, and the eroded surfaces of the samples were without visible damage. The obtained results showed that sintered samples based on pyrophyllite reinforced with talc have good resistance to cavitation impact and can be used in conditions where the presence of cavitation processes is expected.

ACKNOWLEDGEMENTS I

This work was supported by the Ministry of Science, Technological Development and Innovation of the Republic of Serbia (Contract No. 451-03-136/2025-03/ 200213 and 451-03-136/2025-03/200135).

ACKNOWLEDGEMENTS II

The authors would like to thank AD Harbi-Sarajevo BiH for providing samples of pyrophyllite for experimental research.

REFERENCES

[1] D.E. Zakrzewska, A.K. Krella, Adv. Mater. Sci., 19(4) (2019).
[2] G. Garcia- Atance Fatjao, M. Hadfield, C. Vieillard, J. Sekulic, CERAM 35 (8) (2009) 3301-3312.
[3] M. Pavlović, M. Dojčinović, Cavitation damage of refractory materials, Monograph, Akademska misao, Belgrade, 165 (in Serbian), (2020).
[4] Lj. Andrić, M. Pavlović, M. Dojčinović, D. Radulović, Zaš. Mater. 62 (2) (2021).
[5] M. Ali, H. Ahmed, H. Ahmed, M. Hefni, Appl. Sci., 11, 11357 (2021).
[6] Z. Aćimović, A. Terzić, Lj. Andrić, M. Pavlović, Mater. Technol., 49 (2015) 157-164.
[7] M.Pavlović, M. Dojčinović, J. Nikolić, S. Aleksić, N. Tucović, Z. Čeganjac, S. Drmanić, Materials, 18 (5) (2025) 1034.

The 56th International October Conference on Mining and Metallurgy
22-25 October 2025, Bor Lake, Bor, Serbia
www.ioc.tfbor.bg.ac.rs

DOI: 10.5937/IOC25494C *Original scientific paper*

PROBABILISTIC ANALYSIS OF PRESS FIT JOINT LOAD CARRYING CAPACITY

Salko Ćosić[1a], Almir Osmanović[1b], Jasmin Halilović[1c]

[1] Faculty of Mechanical Engineering, University of Tuzla, U. Vejzagića br.4, 75000 Tuzla, BiH
[1a] salko.cosic@untz.ba, 0009-0009-1416-0797
[1b] almir.osmanovic@untz, 0000-0002-6839-1234
[1c] jasmin.halilovic@untz.ba, 0009-0005-5265-4561

Abstract
This paper presents a procedure for probabilistic analysis of joint load carrying capacity as a randomly variable quantity on the example of a cylindrical press fit joint of a bronze ring with teeth and a worm gear hub. By fitting the set of results obtained by a series of FEM simulations for characteristic values of input parameters (interference and material characteristics), the coefficients of a second-order multidimensional polynomial as a "response surface" for the output quantity - joint load carrying capacity were determined. By MC simulation, generating random parameters according to the known laws of statistical distributions and evaluating the previously obtained higher-order polynomial, a statistical set was obtained, the processing of which determines the distribution parameters of the randomly variable output quantity. The described procedure is applicable to a wide class of probabilistic design problems that are analyzed using FEM analysis.

***Keywords**: Probabilistic design, FEM simulation, Monte-Carlo simulation, statistical distribution*

1. INTRODUCTION

Design parameters such as load, mechanical or physical characteristics of materials, geometric characteristics (tolerances of length, shape or position) change in some range with previously unknown (small) deviations from nominal values and can be considered as randomly changing (stochastic) quantities. The deterministic concept implies that the design parameters have known nominal values with which calculations are performed. The ever-present uncertainty in the actual values of the parameters is taken into account by adopting an factor of safety. Compared to the previous one, the probabilistic concept is more advanced and more recent. It originated in the field of electronic equipment in aviation and gradually spread to other areas of technology. In this design approach, the desired reliability of the component (failure-free life) is adopted in advance and then, knowing the statistical laws of distribution of randomly variable construction parameters (factors) on which it depends, the necessary parameter values, e.g. dimensions that ensure the given, pre-adopted reliability for the adopted construction criterion, are determined in a complex calculation or numerical Monte-Carlo (MC) simulation. In our case, the strength or load carrying capacity of the press fit joint is an output quantity that depends on several design parameters that are randomly variable. Finite Element Method (FEM) has established itself as a reliable analysis method, but for more complex (non-linear) problems, the modeling procedure and its execution on a computer require a lot of time and computing resources. Even with the application of model symmetry and parametric programming of the FEM application (Parametric Design Languages or Python scripts), the computational scope of nonlinear simulations is still demanding and valid only for one set of input parameter values. Instead of such a computationally demanding approach (a series of dozens of FEM simulations), here, using a designed experiment for characteristic values of the input parameters, the minimum required number of FEM analyses is performed according to the plan of experiment, and for the obtained set of results (load capacity of the joint, F), the corresponding multidimensional polynomial of higher order (response surface) is determined by regression analysis. The general form of the second-order regression polynomial is given by (1):

$$F\left(X_1, X_2, \ldots X_k\right) = b_0 + \sum_{1 \le i \le k} b_i X_i + \sum_{1 \le i \le j \le k} b_{ij} X_i X_j + \ldots + \sum_{i_1, i_2, \ldots i_k} b_{i1,i2,\ldots ik} \times X_1^{i_1} X_2^{i_2} \ldots X_k^{i_k} \qquad (1)$$

where Xi - input variables (factors) and b_0, b_i, b_{ij} are regression coefficients obtained as a solution to the corresponding system of linear equations. After that, by generating randomly variable input variables (X_i) according to the known laws of statistical distribution, in an external program, using the same polynomial (1), a larger number of output variable values are calculated (MC simulation) and the set of results is statistically processed in order to determine the parameters of the output variable distribution (F). The process is schematically, for the general case shown in Figure 1.

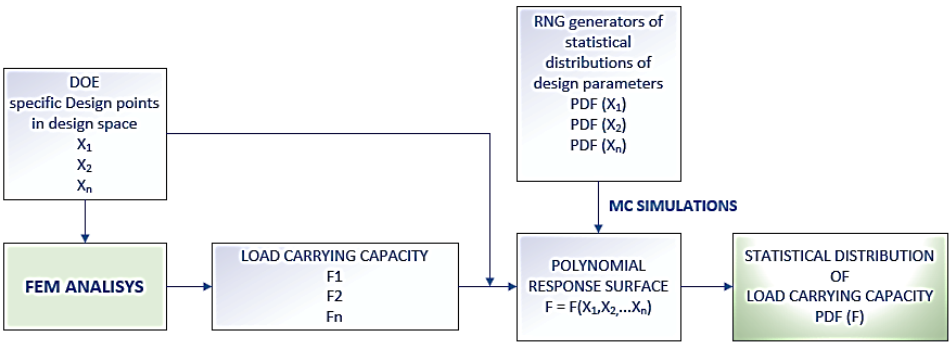

Figure 1. Process of probabilistic analysis of presss fit joints

The adequacy of this meta-model (the degree of agreement between the value of the load-bearing capacity (F) predicted by expression (1) and the value of the same for the case of performing FEM analysis with the same parameters) was confirmed after FEM simulations with randomly generated parameter values using Fisher's test (F distribution). Here, instead of a physical experiment, a computer (FEM) simulation is performed that is completely deterministic so the conditions for statistical tests also differ from the usual ones. Alternatively, instead of the regression polynomial (1) for the set of experimental points in the design space, a multi-dimensional polynomial obtained by expanding the output quantity 'F' in Taylor series in the vicinity of the central point in design space can be used using numerically calculated values of the higher-order derivatives of the output with respect to all input quantities. Although this 'variational technology' approach has some advantages, there are also significant difficulties associated with the numerical calculation of higher-order derivatives in FEM analysis.

2. FEM ANALYSIS OF PRESS FIT JOINT

A typical design of a press fit joint often used in mechanical engineering is shown in Figure 2. Saving on material leads to the use of joints with a bronze gear ring (CuSn12-C) and a cast iron hub (GG25, EN-GJL-250). In addition to the size of the interference, the dispersion of the achieved load capacity in pairs with different materials is also influenced by the elastic moduli E_1 and E_2, Poisson's constants μ_1 and μ_2, the operating temperature (thermal expansion), the dispersion of the of surface roughness, R_{z1} and R_{z2}, the coefficient of adhesion(friction), as well as deviations in the shape and position of both contact surfaces. The actual load-bearing capacity of joint is a random variable that depends on the previously mentioned input quantities (parameters, factors) Due to the complexity and the required minimum number of FEM analyses, the most influential input factors here are the interference (dimensions) and the mechanical properties of the material (E) of both parts in contact with three factors with three levels of values, so the experiment plan requires

$N = 3^3 = 27$ FEM analyses.

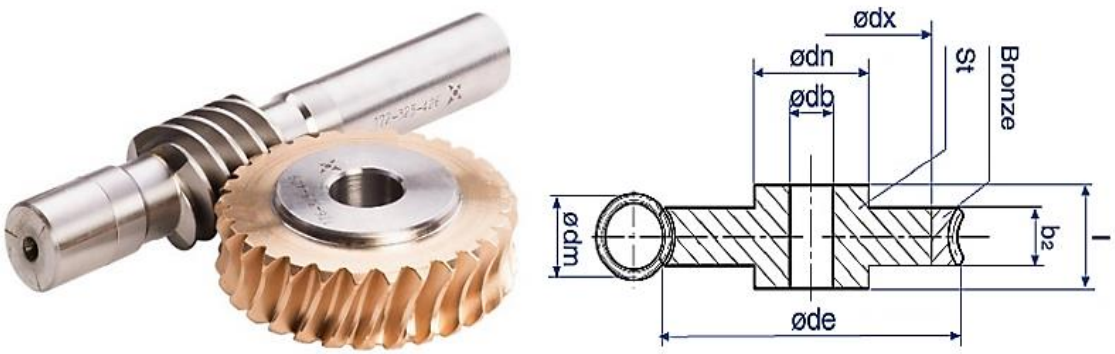

Figure 2. A typical design of a press fit joint, DIN 3975/3976 [1]

In Figure 3, for the nominal values of the parameters (central point of experiment) the distribution of the pressure over the cylindrical contact surface (a) and along the joint (b) is shown,. The axial symmetry and the even number of teeth (z=38) allow the analysis to be performed on 1/4 of the model. Due to the presence of the gear ring, the oscillation of the contact pressure along the contact surface was determined, as well as its significant increase at the exit edges, which is a consequence of the sudden change in stiffness, (b).

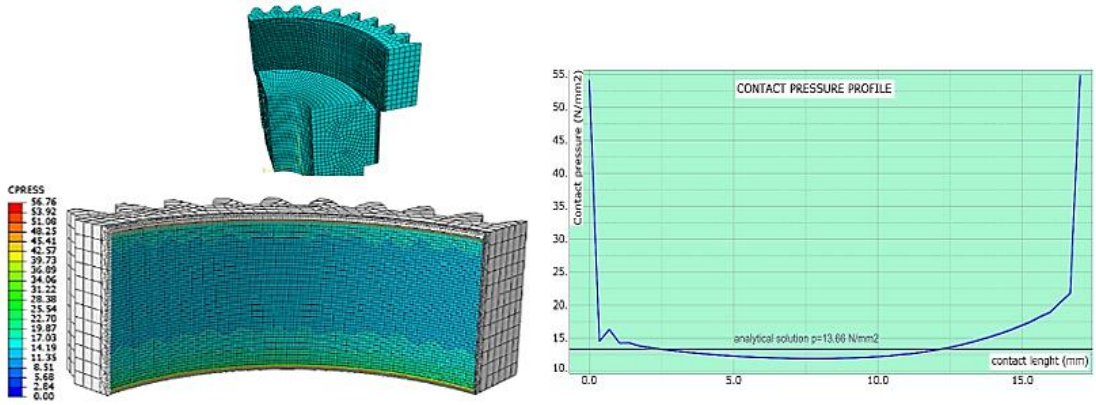

(a) (b)

Figure 3. Contact pressure (a) for the nominal values of input parameters, φ59 H7/s6, L=18 mm,

contact pressure along the joint (b)

The approximate value of the load carrying capacity of a press-fit joint for cylindrical, axisymmetric geometry and for the elastic stress range can be determined from the theory of elasticity using the well-known Lame formulas (2) which form the basis of the standardized DIN 7190 procedure for the calculation of cylindrical press-fit joints [2]:

$$F_T = p \cdot A \cdot \mu = \frac{\left[\Delta - 0.8(R_{z1} + R_{z1}) - f(T, c_1, c_2)\right] \cdot \pi \cdot L \cdot \mu}{\frac{1}{E_I}(1 - \nu_I) + \frac{1}{E_o}\left(\frac{D_O^2 + D^2}{D_O^2 - D^2} + \nu_O\right)}; \quad (2)$$

Formula (2), valid for coupled thick-walled cylinders of infinite length in the elastic region, gives approximate values for finite-length joints because they do not take into account a significant increase in pressure at the ends of the joint. In this case, it was found that Lame's analytical formula for contact pressure matches well with the results of the FEM analysis (Figure 3). Therefore, it is acceptable to use Lame's formula with 6 random parameters as the ‘response surface’ for the case of an axisymmetric press fit joint instead of the quadratic 3D polynomial (1) obtained by fitting a series of FEM simulations. It gives a nonlinear 6D 'response surface' and allows variations of six input (random) parameters to be taken into account in the MC simulation of the load carrying capacity distribution as an output quantity.

3. MONTE-CARLO SIMULATIONS

The following distributions were adopted for the selected parameters (factors):
• interference - normal distribution, with the geometric interference reduced by the shear size of the peaks of the asperities for which DIN 7190 recommends a value of $0.8*(R_{za}+R_{zi})$ where R_z is the height of the surface asperities on the contact surfaces.
• elastic moduli of joint materials (E_1 and E_2) - normal distribution with a coefficient of variation $\beta = 0.05$ for both materials.
In our own code, the mentioned distributions were implemented using a Pseudo-Random-Number-Generators and then, using a series of generated random values, expression (1) was evaluated as a 'response surface' for the axial force F as the output quantity. In this way, a set of results is obtained, the statistical processing of which determines the parameters of the distribution of the output quantity - the axial load carrying capacity of the press fit joint (μ_{Fax}=2.57 kN, σ_{Fax}=589.13 N, β_{Fax} = 23%). The histogram of the distribution of force F is shown in Figure 4 (a).

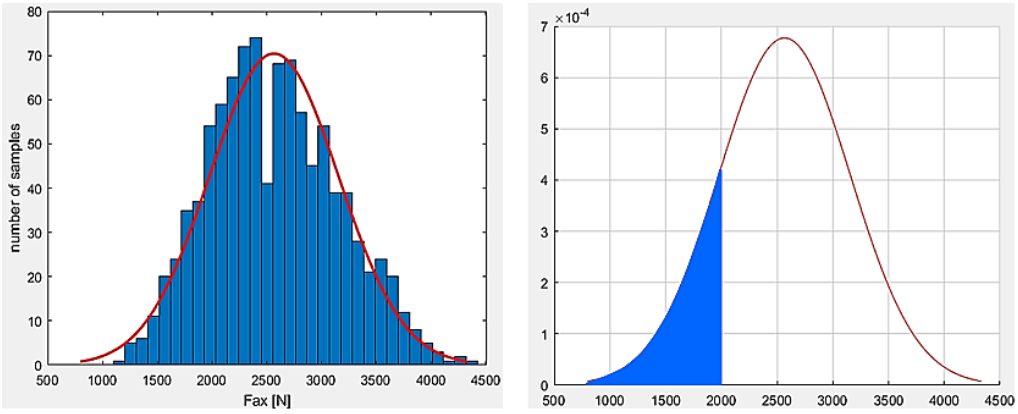

(a) (b)

Figure 4. Histogram of load carrying capacity F_{ax}, (a), probability of F_{ax} to be less then 2000 N (b)

4. CONCLUSION

Statistical processing of the data obtained according to the procedure in Figure 1. has determined an approximately normal distribution of the load carrying capacity F of the pair with parameters $F(F_m,\sigma_m)$. It allows us to determine the values of dispersion, the probability of the load capacity in an arbitrary part of the interval F_{min}-F_{max}, the probability that the load capacity is outside the predicted interval (failure) and also the sensitivity of the output quantity to variations of each of the input quantities. This provides the possibility of a probabilistic estimate of the load carrying capacity value, which is certainly more useful than the unknown load capacity increased by an empirical factor of safety as is done in the deterministic concept. Procedure described in Figure 1. is general and often the only possible in the general case, when we do not have valid analytical solutions. It is applicable to a wide class of problems that are analyzed by FEM analysis.

REFERENCES

[1] WMH Transmision Limited, www.wmh-trans.co.uk
[2] German Institute for Standardisation, 2017, Interference fits – Part 1: Calculation and design rules for cylindrical self-locking pressfits, doi: http://doi.org/10.31030/2414563
[3] X. Wang, Z. Lou, X. Wang, X. Hao, Y. Wang, Proc IMechE Part C: J Mechanical Engineering Science, 233 (8) (2019) 2834–2846,
[4] H.L. Nguyen, V.P. Lam, Study of interference fit between steel and brass parts, EUREKA Physics and Engineering, 5 (2022).

The 56th International October Conference on Mining and Metallurgy
22-25 October 2025, Bor Lake, Bor, Serbia
www.ioc.tfbor.bg.ac.rs

DOI: 10.5937/IOC25498M Original scientific paper

INFLUENCE OF COLD ROLLING AND ANNEALING ON THE HARDNESS OF Cu-Al BIMETALLIC STRIP

Saša Marjanović[1], Milijana Mitrović[1], Emina Požega[2], Dragana Božić[2]

[1] Technical Faculty Bor, University of Belgrade, V.J. 12, 19210 Bor, Serbia
[2] Mining and Metallurgy Institute Bor, Alberta Ajnštajna 1, 19210 Bor, Serbia
[1] smarjanovic@tfbor.bg.ac.rs, 0000-0001-6930-2232
[1] mmitrovic@tfbor.bg.ac.rs, 0000-0001-7478-2453
[2] emina.pozega@irmbor.co.rs, 0000-0001-6797-2435
[2] dragana.bozic@irmbor.co.rs, 0000-0003-1055-8449

Abstract
Cu–Al bimetallic strips were subjected to cold rolling with varying degrees of thickness reduction, followed by annealing of the most severely deformed samples at different temperatures for one hour. The hardness of the constituent layers was determined as a function of both deformation degree and annealing temperature. The results revealed a systematic increase in hardness with progressive deformation: the aluminum layer exhibited an almost linear dependence, while the copper layer displayed a three-stage response. In contrast, annealing at elevated temperatures induced a pronounced reduction in hardness in both aluminum and copper layers.

***Keywords**: bimetallic strip, hardness, deformation degree, annealing*

1. INTRODUCTION

Bimetallic materials are increasingly used because they combine the advantageous properties of different metals within a single structure. Copper-aluminum (Cu-Al) bimetallic strips are of particular interest due to their favorable electrical, thermal, and mechanical characteristics. Cold rolling is a common processing method that ensures bonding between the layers and significantly affects hardness through work hardening. On the other hand, annealing reduces internal stresses and enables recovery and recrystallization, leading to changes in mechanical properties. This study investigates the combined effect of cold rolling and annealing on the hardness of Cu-Al bimetallic strips, with the aim of better understanding the relationship between processing conditions and material performance.

2. EXPERIMENTAL

Specimens were prepared from a Cu–Al–Cu plate, 10.4 mm thick, produced by explosive cladding. After removing one copper layer, bimetallic strips of 8.4 mm were obtained, consisting of 6.4 mm Al and 2 mm Cu. Rolling was carried out in multiple passes with a reduction of 2.5% per pass until total reductions of 10%, 20%, 30%, 40%, 50%, 60%, 70%, and 80% were achieved. After each deformation level, the strip thickness and individual layer thicknesses were measured.

The samples deformed with maximum deformation degree, ε_{max}=80%, were subjected to annealing. Annealing was carried out in a protective nitrogen atmosphere for one hour at temperatures of 200, 250, 300, and 400 °C.

Hardness measurements were performed after all degrees of deformation and after the annealing.

The experimental flow is shown schematically in figure 1.

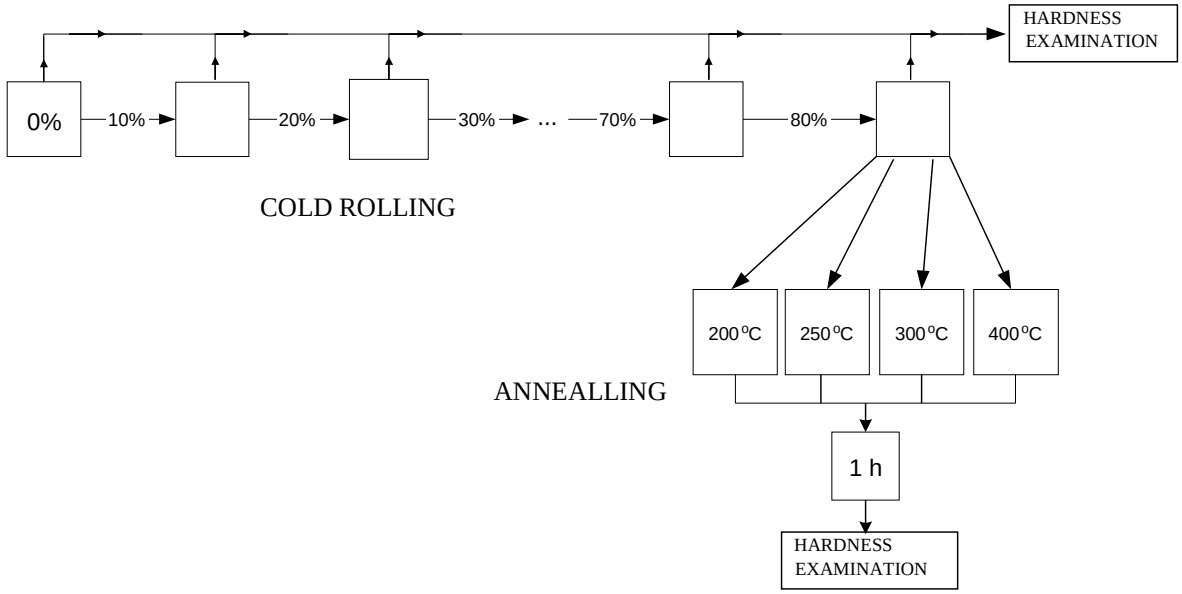

Figure 1. Schematic diagram of the experimental flow

3. RESULTS AND DISCUSSION

The obtained data for the hardness measurements, depending on the total deformation degree are given in Table 1. and Figure 2.

Table 1. Dependence of the hardness of bimetallic strip layers on the degree of deformation

ε (%)	HV (daN/mm^2)	
	Al	Cu
0	43.83	106.00
10	44.20	115.75
20	46.33	117.00
30	47.27	120.40
40	48.04	121.67
50	48.44	125.50
60	49.20	131.80
70	49.80	136.00
80	51.05	146.75

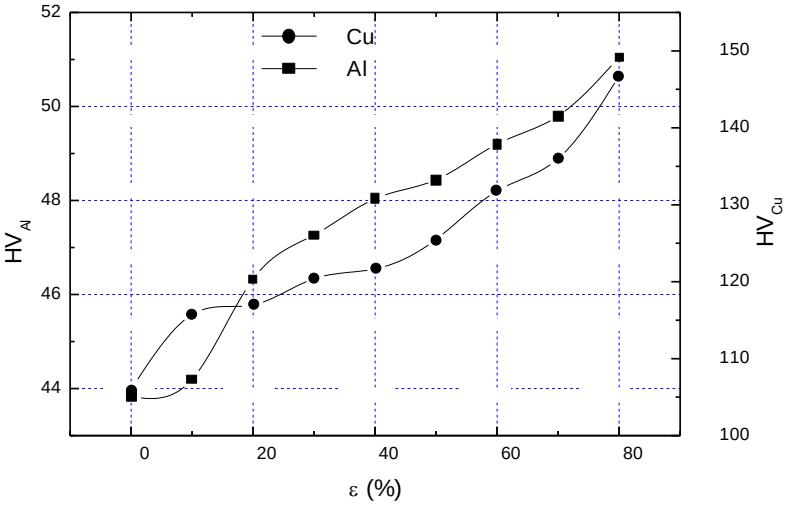

Figure 2. Diagram of the dependence of the hardness of the bimetallic strip layers on the degree of deformation

From the diagram, it can be seen that the overall trend of the hardness–total deformation curves is increasing, with the hardness of aluminum rising approximately linearly with the increase in the degree of deformation.

The hardness–deformation dependence curve of the copper layer can be divided into three parts.

In the first part of the curve, up to 10% deformation, the hardness of the copper layer increases sharply; in the second part, up to 50% deformation, it rises slowly, and then it increases again more rapidly until reaching the maximum value of 146.75 daN/mm² at a total deformation of the bimetallic strip of 80%.

In addition to the observed hardness changes, it should be emphasized that the linear increase in the hardness of the aluminum layer reflects its limited work-hardening capacity due to its high stacking fault energy. In contrast, copper exhibits a more complex three-stage hardening response, characteristic of materials with lower stacking fault energy where dynamic recovery processes occur more gradually.

Samples with a total deformation degree of ε = 80% were annealed for one hour in a protective nitrogen atmosphere at different temperatures (200°C, 250°C, 300°C, 400°C).

The obtained hardness (HV) test results as a function of annealing temperature are presented in Table 2 and in the diagram shown in Figure 3.

Table 2. Dependence of the hardness of bimetallic strip layers on the annealing temperature

t(°C)	HV (daN/mm^2)	
	Al	Cu
200	42.30	137.00
250	40.12	130.50
300	28.86	63.52
400	25.57	55.72

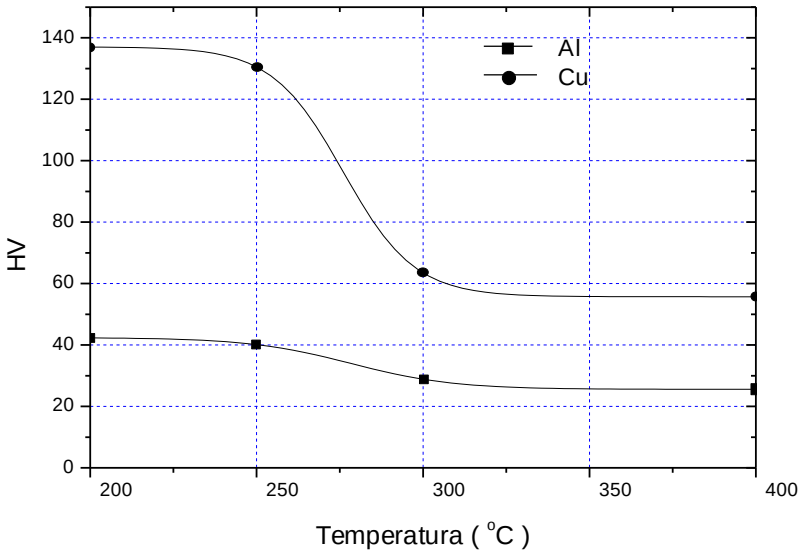

Figure 3. Diagram of the dependence of the hardness of the bimetallic strip layers on the annealing temperature

From the figure, a decrease in hardness with increasing annealing temperature can be observed, both in the aluminum layer and in the copper layer.

It can be seen that the hardness decreases slightly up to T = 250°C, after which it drops sharply in both layers in the temperature range of 250–300°C, when recrystallization of both layers occurs [6,7].

With further increases in annealing temperature up to 400°C, no significant additional reduction in the hardness of the layers is observed.

The sharp drop in hardness in the range of 250–300 °C is a clear indication of recrystallization in both layers, consistent with recent findings in Cu–Al laminated composites [1,3,6,7]. These results highlight the importance of controlling rolling reduction and annealing schedules in order to balance hardness and ductility. Similar behavior has been reported in other laminated systems where recrystallization strongly influences mechanical performance [2,4,9]. The industrial relevance of these findings lies in the optimization of Cu–Al laminates for applications such as electrical connectors and thermal conductors, where a trade-off between hardness and conductivity must be carefully managed [5,8,10].

4. CONCLUSION

The overall trend of the hardness–total deformation curves is increasing, with the hardness curve for aluminum being approximately linear and always lower than the hardness curve for copper, whose progression can be divided into three parts. These findings contribute to a clearer understanding of the deformation and annealing behavior of Cu–Al laminates, with practical implications for tailoring processing routes to achieve desired mechanical performance [2,4,9]. Future research should focus on microstructural characterization (SEM/TEM) to confirm recrystallization mechanisms, as well as on the relationship between hardness and other functional properties such as electrical conductivity.

With increasing annealing temperature of the cold-deformed bimetallic strip (ε = 80%), the hardness decreases in both the aluminum and copper layers—slightly up to 250°C, and then sharply in the range of 250°C to 300°C, when recrystallization of both layers occurs [6,7].

ACKNOWLEDGEMENTS

The research presented in this paper was done with the financial support of the Ministry of Education, Science and Technological Development of the Republic of Serbia, within the funding of the scientific research work at the University of Belgrade, Technical Faculty in Bor, according to the contract with registration number 451-03-137/2025-03/ 200131.

REFERENCES

[1] J. Chen, Y. Li, P. Liu, X. Zhang, H. Zhou., M. Sci. Eng. A., 835 (2022) 142642.
[2] L. Wang, Y. Zhao, Z. Sun, Q. Liu., J. Alloys Compd., 872 (2021) 159685.
[3] S. Zhang, W. Li, K. Chen, J. Yang., Materials Characterization, 169 (2020) 110606.
[4] C. Lee, J. Park, S. Kim., Metals, 12 (4) (2022) 673.
[5] F. Gao, Y. Yuan, Z. Chen., Materials, 12 (23) (2019) 3871.
[6] J. Xu, G. Huang, Y. Liu., J. Mater. Res. Technol., 12 (2021) 1284–1293.
[7] H. Li, J. Zhou, X. Wang, MSF, 1085 (2023) 233–240.
[8] H. Park, M. Choi, S. Yoon, Mater. Sci. Technol., 36 (15) (2020) 1645–1653.
[9] T. Zhao, J. Sun, Y. Wu., J. Mater. Process. Technol., 302 (2022) 117497.
[10] Y. Lin, Y. Zhang, Q. Chen., Mater. Today Commun., 28 (2021) 102595.

The 56th International October Conference on Mining and Metallurgy
22-25 October 2025, Bor Lake, Bor, Serbia
www.ioc.tfbor.bg.ac.rs

DOI: 10.5937/IOC25502P

Original scientific paper

PROPERTIES OF Se DOPED Bi_2Te_3 BASED MATERIAL: PART I

Emina Požega[1a], Slavko Bernik[2b], Dragana Božić[1c], Srđana Magdalinović[1d], Miloš Đukić[1e], Jelena Gligorijević Sokolović[1f], Radmilo Rajković[1g]

[1] Mining and Metallurgy Institute Bor, Alberta Ajnštajna 1, 19210 Bor, Serbia
[2] Jozef Stefan Institute, Jamova 39, 1101 Ljubljana, Slovenia
[1a] emina.pozega@irmbor.co.rs 0000-0001-6797-2435
[2b]slavko.bernik@ijs.si 0000-0001-7330-3094
[1c] dragana.bozic@irmbor.co.rs 0000-0003-1055-8449
[d] srdjana.magdalinovic@irmbor.co.rs 0000-0002-2916-2850
[1e] milos.djukic@irmbor.co.rs 0000-0002-3307-4669
[1f] jelena.gligorijevic.sokolovic@irmbor.co.rs, 0000-0002-2003-1141
[1g] radmilo.rajkovic@irmbor.co.rs 0000-0001-5905-6613

Abstract

Thermoelectric materials are attracting attention because of their ability to directly convert heat into electricity. Bismuth tellurides (Bi_2Te_3) are important thermoelectric materials used to convert heat into electricity and vice versa. The application of thermoelectric devices requires materials that exhibit superior thermoelectric performance. This work investigates the thermoelectric properties of $Bi_2Te_{2.7}Se_{0.3}$ single crystal synthesized via Bridgman method by spontaneous nucleation. The Seebeck coefficient (S) is negative, which means that this crystal has electrons as the main charge carriers. The Seebeck coefficient values range from -163 $\mu V \cdot K^{-1}$ at 300°C to -188 $\mu V \cdot K^{-1}$ at 40°C. As part of research on the influence of selenium as dopant on bismuth telluride, a successful synthesis of n type single crystal was carried out. The $Bi_2Te_{2.7}Se_{0.3}$ single crystal in 11 mm × 80 mm size was grown. The obtained empirical formula does not deviate from the given compound formula. The single crystal was characterized by measurements of Seebeck coefficient (S), conductivity (κ) and resistivity (ρ) measurements as a function of temperature in the range of 40-320°C by a home-made impedance meter. The prepared single crystal exhibited a figure of merit (Z) of 1.77 x 10^{-3} K^{-1} at 300°C. Figure of merit was calculated using measured values for resistivity, Seebeck coefficient and conductivity.

***Keywords**: single crystal, semiconductor, Bridgeman method, doping, thermoelectric properties*

1. INTRODUCTION

Thermoelectric (TE) technology enables direct heat to electricity conversion by the thermoelectric effect. The TE performance of materials is evaluated by the dimensionless figure of merit $zT = S^2\sigma T/k$, where S, σ, T, and k represent the Seebeck coefficient, electrical conductivity, absolute temperature and thermal conductivity, respectively.

A key challenge in thermoelectric materials development is achieving low thermal conductivity without compromising the Seebeck coefficient and electrical conductivity. To improve thermoelectric properties of a material, the carrier concentration needs to be optimized first. The increase of carrier concentration usually results in degraded carrier mobility, which restricts the enhancement in thermoelectric performance [1].

Bi_2Te_3-based alloys have excellent thermoelectric performance at room temperature. They are mainly used in refrigerators and generators, and also find applications in optoelectronic and electrochemical devices such as heat pumps, infrared sensors, and high efficiency photovoltaic cells [2].

Thermoelectric transport properties of doped Bi_2Te_3 have been examined for a long time [2-6].

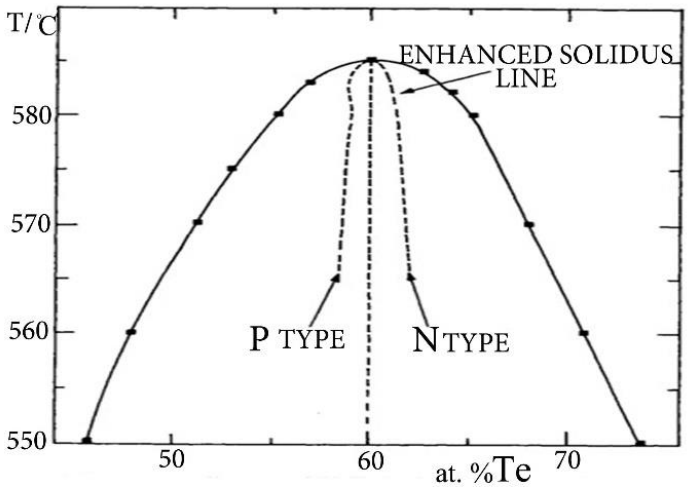

Figure 1. Phase diagram of Bi-Te in the region around Bi_2Te_3 [7]

From Figure 1, it can be seen that a material rich in bismuth is of p-type and that rich in tellurium is of n-type.

The best TE materials near room temperature are p-type $Bi_{2-x}Sb_xTe_3$ and n-type $Bi_2Te_{3-y}Se_y$. The compositions of commercialized p-type and n-type ingots are near $Bi_{0.5}Sb_{1.5}Te_3$ and $Bi_2Te_{2.7}Se_{0.3}$ respectively, and their ZT values are about 1.0 at 27°C [8-10].

In practice, massive semiconductor materials from bismuth telluride, Bi_2Te_3 (doped with Sb, Se, etc.) with a value of $ZT \approx 1$, are now most widely used. An important subject in the field of materials science and technology is to find out the mechanism of improving the properties of thermoelectric materials [11].

As fabrication techniques of Bi–Te semiconductor bulk materials, there are the melting techniques based on the Bridgman [7], Czochralski [7] and zone-melting methods and also the powder metallurgy techniques such as hot-pressing and hot extrusion methods [12]. The products fabricated by these methods were often subjected to annealing in various atmospheres to raise the ZT value as high as possible. One of the most commonly used methods for obtaining a high-quality single crystal is the Bridgman method. It enables the growth of single crystals from the melt under controlled conditions. Bridgman technique utilizes various parameters like rotation speed, pulling rate, and temperature to control the growth of the crystals. Obtaining high-quality single crystals remains challenging.

2. EXPERIMENTAL

Single crystal ingot of Bi_2Te_3 doped with selenium was synthesized using the Bridgman method at the maximum temperature of about 700ºC. High purity elements (5 N) were used as the source material. Tellurium (Sigma – Aldrich, 99.999%), bismuth (Sigma – Aldrich, 99.999%) and selenium (Alfa Aesar, 99.999%) were taken in a certain proportion.

The temperature gradient was 2ºC/mm in the zone of heating and 5ºC/mm in the zone of cooling. The ingot was grown at the speed of 2.2 mm/h.

Measurements of the thermoelectric properties of the single crystal were carried out by home-made impedance meter based on the ″Lagre ΔT method″ [13] with temperature range from 40 to 320°C. Home-made impedance meter simultaneously measured all three thermoelectric parameters, Seebeck coefficient, conductivity and resistivity. The measurement process was performed in vacuum of 10^{-2} to 10^{-3} Pa on a sample with a height of about 11 mm and a diameter of 80 mm and took at least 15 hours.

The measurement principle is such that the sample in a vacuum is heated on the hot side to a temperature determined by the measurement program. Once this temperature is reached, the heater is turned off, and the measurements begin. These measurements are taken during the cooling process of the sample at one-minute intervals until the sample cools down below 40°C. The entire process is automated, and the measurement results are recorded on a computer. It is essential that the upper and lower surfaces of the sample are plane-parallel to ensure optimal contact between the sample and the hot and cold sides of the system.

3. RESULTS AND DISCUSSION

Bismuth, tellurium and selenium are merged in a stoichiometric ratio of 2:3, namely with given compound formula of $Bi_2Te_{2.7}Se_{0.3}$.

The results of resistivity measurements in the temperature ranges from 40 to 320°C for a bulk n-type single crystal are shown in Figure 2.

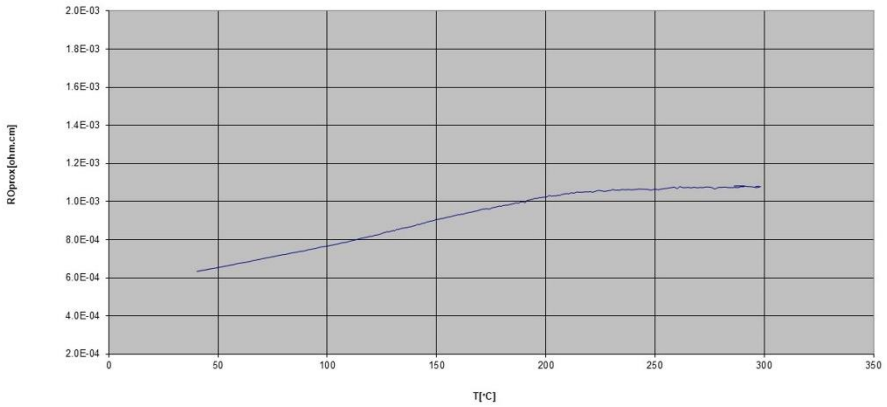

Figure 2. Temperature dependence of resistivity for sample $Bi_2Te_{2.7}Se_{0.3}$

Resistivity (ρ) as a function of temperature (T) is displayed in Figure 2. The R–T curve shows that resistivity increases with rising temperature. This trend has been kept to about 200°C. Values of resistivity are from 6.35 x 10^{-4} Ωcm at 40°C to 1.02 x 10^{-3} Ωcm at 200°C In the temperature interval from 200 to 300°C, resistivity remains fairly constant (1.02-1.08 x 10^{-3} Ωcm).

Our material exhibits a ZT of 1 at 300°C, which is significantly higher than that of Bi_2Te_3-based alloys and commercialized n-type ingots $Bi_2Te_{2.7}Se_{0.3}$ (ZT values are about 1.0 at 27°C). The ZT value of the Bi_2Te_3 based alloys starts to drop above 75°C and is below 0.25 at 250°C [1,9]. The peak of dimensionless figure of merit (ZT) of Bi_2Te_3based n-type single crystals is about 0.85 in the ab plane at room temperature [14]. Thermal conductivity is 1.14 $Wm^{-1}K^{-1}$ at 40°C and 1.36 $Wm^{-1}K^{-1}$ at 300°C.

4. CONCLUSION

The possibility of producing high quality Bi_2Te_{3-x} single crystal doped with Se using the Bridgman method was examined. A single crystal was successfully prepared. Measurements of the thermoelectric properties indicate that the bulk sample exhibited n-type conductivity, suggesting that major conductivity carriers were electrons. The resistivity (ρ), conductivity (k) and Seebeck coefficient (S) were measured simultaneously in temperature range from 40°C to 320°C. The obtained Seebeck coefficient (S) results were presented in our earlier investigation.

The obtained empirical formula does not deviate from the given compound formula.

ACKNOWLEDGEMENTS

The authors wish to thank Academician Professor Pantelija Nikolić† for his great and selfless efforts and assistance in all stages of investigations. The authors also wish to thank Stevan Vujatović†, a specialized technician, for manufacturing high-quality monocrystalline ingot and Professor Phd Slavko Bernik from Jozef Stefan Institute, Department of Nanostructured Materials, for measurements of thermoelectric properties.

This work was financially supported by the Ministry of Science, Technological Developmentand Innovation of the Republic of Serbia, Contract on realization and financing of the scientific research work of the Mining and Metallurgy Institute Bor in 2025, contract number: 451-03-136/2025-03/ 200052.

REFERENCES

[1] E. Požega, N. Vuković, L. Gomidželović, M. Janošević, M. Jovanović, S. Marjanović, M. Mitrović, Sci. Sintering, 55 (2023) 55-70.
[2] J. Bhakti, S. Dimple, N. M. Ravindra, J. Electron. Mater., 44 (6) (2015), 1509-1516.
[3] L. P. Bulat, I. A. Drabkin, V. V. Karatayev, V. B. Osvenskii, Y. N. Parkhomenko, M. G. Lavrentev, A. I. Sorokin, D. A. Pshenai-Severin, V. D. Blank, G. I. Pivovarov, J. Electron. Mater., 42 (2013), 2110-2113.
[4] J. Chen, X. Zhou, C. Uher, X. Shi, J. Jun, H. Dong, Y. Li, Y. Zhou, Z. Wen, L. Chen, Acta Mater., 61 (2013) 1508-1517.
[5] M. Chitroub, S. Scherrer, H. Scherrer, J. Phys. Chem.Solids, 61 (2000) 1693-1701.
[6] R. G. Cope, A.W. Penn, J. Mater. Sci., 3 (1968) 103–109.
[7] E. Požega, Synthesis and characterization of bismuth and tellurium single crystals doped with selenium, zirconium and arsenic, PhD thesis, University of Belgrade, Technical Faculty Bor, Serbia, 2018. (in Serbian)
[8] H. Mun, K. Hyoung Lee, S. Jun Kim, J. Young Kim, J. Hoon Lee, J. Hong Lim, H. Jung Park, J. Wook Roh, S. Wng Kim, Materials, (2015) 959-965.
[9] B. Poudel, Q. Hao, Y. Ma, Y. Lan, A. Minnich, B. Yu, X. Yan, D. Wang, A. Muto, D. Vashaee, X. Chen, J. Liu, M. Dresselhaus, G. Chen, Z. Ren, Mater. Sci. Eng., (2008) 634-638.
[10] J. Snyder, E. Toberer, Nat. Mater., (2008) 105-114.
[11] E. Požega, S. Bernik, S. Marjanović, A. Petrović, I. Svrkota, A. Stojić, D. Simonović, Sci. Sintering, 56 (2024) 395-403.
[12] E. Požega, S. Marjanović, N. Vuković, L. Gomidželović, M. Mitrović, M. Janošević, D. Adamović, Sci. Sintering, (2023) 55 (3), 331-338.
[13] S. Bernik, M. Pribošek, Proceedings of the 49th International conference on Microelectronics, Devices and Materials, Kranjska Gora, Slovenia, 2013.
[14] P. Jianlu, L. Yefan, L. Chong, W. Zumin, L. Yongchang, L. Huijun, J. Mater. Sci. Technol., 52 (2020) 162-171.

The 56th International October Conference on Mining and Metallurgy
22-25 October 2025, Bor Lake, Bor, Serbia
www.ioc.tfbor.bg.ac.rs

DOI: 10.5937/IOC25506G *Original scientific paper*

A STUDY OF SINGLE PIECE CERAMIC SHELL CORE FOR GEOMETRICALLY COMPLEX INVESTMENT CASTING

Nandita Gupta[1a], Kamlesh Kumar Singh[1b], Manoj Kumar[1c], Himanshu Khandelwal[1d]

[1]National Institute of Advanced Manufacturing Technology, Ranchi, Jharkhand, India

[1a] nanditagupta@niamt.ac.in, 0000-0001-8276-807X
[1b] kksingh@niamt.ac.in, 0000-0001-8311-2056
[1c] manojkumar@niamt.ac.in, 0000-0001-7525-6842
[1d] himanshukhandelwal@niamt.ac.in, 0000-0001-5603-9252

Abstract

Investment Casting is a manufacturing processes that uses a ceramic mould to create complex high details near net shape components with excellent dimensional accuracy and surface finish. These castings have tighter tolerances and the capability to produce thin walled sections. In Investment Casting for the production of Complex Castings still waxes are the suitable materials for making pattern by injecting the liquid wax in metal dies. Hence it is also called lost wax process. If the design have complex inner cavity configuration the soluble core can be incorporated into investment casting. The use of soluble salt cores allow for more intricate cavity patterns to be included in the casting reducing or eliminating the need for additional machining. The aim of this study is to describe the possibilities of using salt cores. The primary secondary and final residual strength test were carried on three different composition for salt core is tested in order to evaluate the possibility of salt core utilization. Further it is focused on the development of better mechanical properties of the casting. The positive impact of these cores on the environment were also studied.

Keywords: *Salt core, expendable core, strength, solub*ility

1. INTRODUCTION

Traditionally undercuts, channels or passages are formed by the cores in the casting. After production of the casting the core is removed with the help of solvent, heating in a steam autoclave or flash firing at very high temperature. These procedures make the casting parts become more expensive but of low efficiency [1-3].

For many castings with complicated openings undercuts, channels or passages the salt or ceramic cores do not need, while the wax pattern can be used directly. The problem of making difficult wax pattern is eliminated with the water soluble cores. These salt cores appear in foundry in the year 1970s and its extensive expansion took place in 1990s in the mass production of diesel engine pistons. The cores of simple forms like rings, holes channels are made from cooking salt (NaCl) by high pressure compacting and they serve for blank casting with an advantage that complex design can be produced where castings are hardly accessible to mechanical cleaning[4-6]. The salt meet the requirements regarding the primary strength (cold strength) and hot strength (650-700ºC) of cores.

The salt melt is cast in core boxes and to prevent the moistening, the crystallized cores are stored in an oven (a minimum of 200ºC) cores are made by a mildly moistened salt compacted under high pressure. Grains are conglomerated and recrystallization along the grain boundaries takes place either under low pressures 30-50 MPa and at the heating temperature of 500-750ºC or under high compacting pressure (136-362.8MPa) and low sintering temperature (180-300ºC) allowing a stress release another possibility is manufacturing cores by shooting the mixture with inorganic binders

like Na_2CO_3 and hardened either with the aid of CO_2 or with thermal dehydration normally at (180-210ºC) All these cores show a relatively low strength and they do not suit for high pressure castings[7-9]. Polyvinyl Glycol is a waxy material that can be sufficiently dissolved in water and can be leached away from the pattern waxes, polyvinyl glycol has low hygroscopic coefficient, as a result soluble cores remains for longer time. It is nontoxic and currently available in market. PVG cores have a deficiency that it is supposed to be used under pasty conditions. When the core solidifies, it is easy to form cracks on the surface [10-12]. The research aimed at applying three variations of binders and checking the strength (bending) improvement, the influence of salt crystal shapes, granulometry and above all the composite salts with additives as well as the hydration and kinetics during dissolution of the cores in water [13-15] .

2. EXPERIMENTAL

The material used here is Mica Powder, sodium chloride, the plasticizer was made from paraffin and polyethylene Paraffin was used as a solvent to dissolve polyethylene. The amount of polyethylene glycol should be strictly controlled. Paraffin is mixed in 0%, 5%, 10% to make three different composition. The salt mixture were melted in an alumina crucible with an electric resistance heater, then granular polyethylene(100ºC+-2ºC) was dissolved completely by stirring. Then polyethylene Glycol was added into the liquid and they were stirred untill the slurry became homogeneous. The samples of 8mmx8mmx12mm is composed for various test. Then Bending strenght test, compression strength test hygroscopic property and solubility test are done on all the three samples. The composition of the respective ingredients are given in the table 1

Table 1. Component of soluble core material (wt %)

Sample No.	Polyehtylene Glycol	Mica Powder	Sodium Chloride	Plastisizer
1	45	30	25	0
2	43	28	24	5
3	40	27	23	10

The compressive strength of different samples was measured by using universal strength testing machine . The bend strength was measured by three point bending fixture. For the solubility rate the sample was put into water and the solubility rate is calculated. Part of the sample is exposed in air at room temperature (Relative humidity was 50%-70%) for one month and the change of the sample mass were measured to calculate the hygroscopic coefficient.

The hygroscopicity can be calculated by the equation

$H=[(wt-w0)/w0]x100\%$ wt=mass of the sample exposed in air per month

w0=initial mass of the sample

Solubility rate can be claculated by,

$R=M/SxT$,

R=solubility of the sample,

M=Mass

S=Surface area

T=Time of solubility

3. RESULT AND DISCUSSION

1) A novel soluble core is successfully developed. The yield strength of the soluble core material can reach 1MPa and the highest compressive strength can reach 4MPa (figure1) the bending strength of the soluble core materials is 4.08 to 6.65 MPa Table4. The hygroscopic coefficient is 0.06% to 0.22% per month (Table 2) under ambient conditions. The solubility rate of core materials with zero plasticizer is 55.75g/min-m^2 with 5wt% plasticizer 35.7g/min-m^2 it has a reducing trend with more plasticizer. Exposing the core for one hour the surface of soluble core is loose without plasticizer (Table 3) Mica is found to be a good substitute to provide strength, smoothness etc. It is economic and ecofriendly. Polyethylene is ductile it is also nontoxic, It is found abundant in nature. The bend strength (figure 2, 3) is due to fibrous nature of plasticizer so increasing plasticizer the bend strength increases. Though mica and polyethylene do not absorb moisture from atmosphere, they are contributing to the stability of the water soluble cores. The compressive strength is shown in figure 1 for four different composition of core with 0% plasticizer, 5% plasticizer and 10% plasticizer while making it with wax it is found that wax pattern cannot sustain the stresses at 0% plasticizer and with 10% plasticizer. Whereas 5% plasticizer give modified compressive strength, this shows its suitability for the production of cores. Mica and polyethylene reduce the contact surface area between the core material and the contact surface area between core material and the moisture. Upto 5% weight of polyethylene glycol prevent formation of cracks provide smooth surface and make the core stable. Beyond 5% polyethlene glycol reduces the solubility rate of the core. A recommended mixture composed of 43% weight of mica powder, 30% weight of sodium chloride powder, 25% weight of plasticizer, 5 weight percent polyethylene glycol give optimum strength. This kind of soluble core cannot be broken during the injection of composite pattern and it can be leached out at suitable time. Hardness plays an important role in preventing cracks. It is also found that increasing strength reduce the collapsibility of cores and thus need more core removal time.

Table 2. Mass and hygroscopic coefficient of the core material

Core material Plasticizer wt%	W0/g	Wt/g	Wt-w0/g	H/%
0	0.5313	0.5325	0.0012	0.22
5	0.5192	0.5199	0.0007	0.13
10	0.4975	0.4978	0.0003	0.06

Table 3. Different sample mass, surface area and soluble time

Plasticizer wt%	Initial wt/g	Surface area/m2	Time/min	Final wt/g	Solubility rate /g/min-m2
0	0.5352	0.000320	30	0	55.75
5	0.5120	0.000310	30	0.1080	35.7
10	0.4970	0.000311	30	0.4800	1.82

Table 4. Bending Strength

Plasticizer wt%	Bending Strength (MPa)
0	4.08
5	4.80
10	6.65

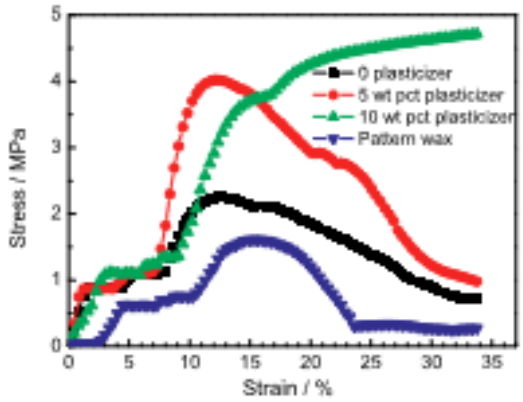

Figure 1. Compressive stress and strain curves of wax and core material

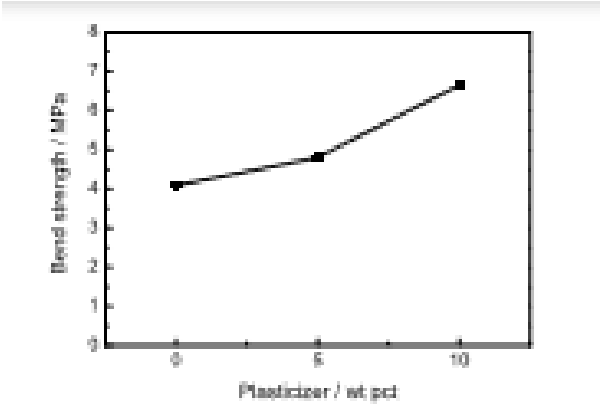

Figure 2. The relationship between bend strength and the amount of plasticizer

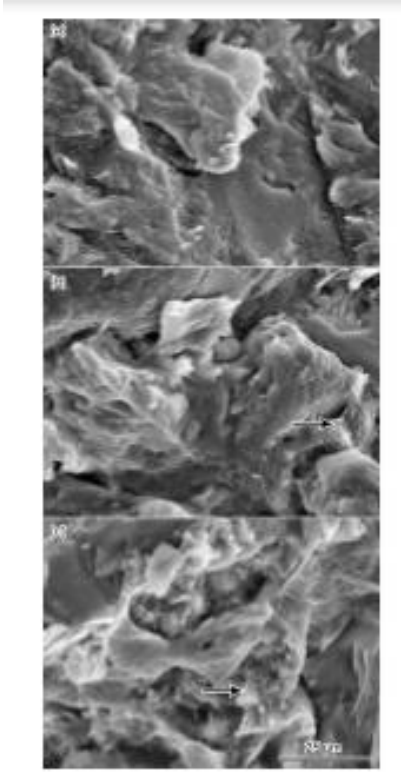

Figure 3. Fracture surface micrograph of the soluble core material with plasticizer 0 (a), 5 wt pct (b) and 10 wt pct (c) 15 wt pct

CONCLUSION

1. Production of dimensionally accurate and smooth castings without the use of protective coats
2. The cores though are soluble in water the possibility of recyclability of the salts and water is there
3. The produced cores are environmentally friendly
4. The core do have sufficient storage ability under common climatic condition
5. Mechanical properties are find to be improved

6. The drawback of salt cores is that a contraction and volume shrinkage occur during solidification
7. Sometimes high density of these cores prevents the dissolution in the water and therefore the cast cores are difficult to remove
8. To eliminate shrinkage a mixture of salt and sand is recommended having melting point 820ºC and production of core under pressure is recommended

REFERENCES

[1] Y. Pati, M. Karate, K.P. Karunakaran, A. K.Patel, Y.G. Mittal, G.D. Gote., Rapid Prototyp. J. 31 (2025) 32-61.
[2] Aslam, A. Can., IJMC, (2025) 1-12.
[3] Y.G. Mittal, Y. Patil, P. Kamble, G. Gole, A.K. Mehta, K.P. Karunakaran., Int. J. Adv. Manuf. Technol. 134 (2024) 3905-3923.
[4] R.W. Joliat, D. Penner., Mater. Trans. 9 (6) (2023) 1631-1642.
[5] Z. Chen, S. Fan, L. Peng, X. Gong, X. Liu., IJMC, 17 (2023) 988-977.
[6] R. Hoagin, Y.G. Mittal, P. Kamble, G. Gote, Y. Patil, A.K. Patel., Int. J. Precis. Technol. 24 (5) (2023) 853-866.
[7] X. Gong, X. Liu, Z. Chen, Z. Yang, W. Jiang, Z. Fan., Int. J. Adv. Manuf. Technol., 118 (2022) 2993-3003.
[8] Y.E. Asan, M. Colak., JST, 15 (2022) 14-27.
[9] T. Hancerlioglu., J. Sci. 18 (2021) 141-147.
[10] C. Cantas, B. Baksan., Int. J. Metalcast. 15 (2021) 839-851.
[11] P. Lynch, C.R. Hasbrouck, J. Wilck, M. Kay, G. Managhran., Rapid Prototyp. J. 26 (2020) 1145-1154.
[12] F. Liu, X. Gong, G. Li, W. Jiang, X. Liu., Mater. Cham. Phys. 252 (2020) 123157.
[13] A. Haleem, M. Javaid., Journal.Ind.Integr. Manag. 4 (2019) 1930001.
[14] S.G. Sarvankar, S.N. Yewale., Int. J. Re. Aeronaut. Mech. Engg. 7 (2019) 1-10.
[15] M. Jimenez, L. Romero, L.A. Dominguez, M.D.M. Espinoso, M. Dominguez., Complexity. (2019) 1-30.

The 56th International October Conference on Mining and Metallurgy
22-25 October 2025, Bor Lake, Bor, Serbia
www.ioc.tfbor.bg.ac.rs

DOI: 10.5937/IOC25511M *Original scientific paper*

EXPERIMENTAL CHARACTERIZATION OF THE Bi-Ge-Pb TERNARY ALLOYS

Veljko Minic[1a], Jelena Miladinovic[1b], Miljana Popovic[1c], Milena Zecevic[2a], Aleksandar Djordjevic[2b]

[1] University of Belgrade, Faculty of Technology and Metallurgy, Belgrade, Serbia
[2] University in Pristina, Faculty of Technical Science, Kos. Mitrovica, Serbia
[1a] veljkominic3@gmail.com, 0009-0002-0812-6460
[1b]duma@tmf.bg.ac.rs, 0000-0001-6259-8245
[1c]miljana@tmf.bg.ac.rs, 0000-0002-4691-0603
[2a] milena.premovic@pr.ac.rs, 0000-0003-0532-7048
[2b] aleksandar.djordjevic@pr.ac.rs, 0000-0002-2020-6976

Abstract
In this work, the ternary system Bi-Ge-Pb has been studied. Sixteen ternary samples were prepared for experimental tests. Selected samples were subjected to phase transition temperatures and phase equilibria tests. Used experimental techniques were differential thermal analysis (DTA), X-ray diffraction (XRD) and scanning electron microscopy (SEM) with energy dispersive spectrometry (EDS). Results of DTA detected temperatures of two invariant reactions, monovariant phase transition and liquidus curves.

***Keywords**: Bi-Ge-Pb ternary system, phase transition temperatures, experimental characterization.*

1. INTRODUCTION

Reason for choosing Bi-Ge-Pb ternary system is due to the possible application as a low-melting point alloys, (LMPA). These alloys are required for a wide variety of applications, including thermal fuse application, rapid prototyping, die casting, mercury replacement, thermal cooling, heating designs, and soft solder formulation [1]. They also represent promising candidates for metallic phase-change materials (PCMs) for thermal storage (TS) [2-3].

Ternary Bi-Ge-Pb alloys were prepared and tested experimentally for the first time. The knowledge of the ternary alloys is very important for future possible application of these alloys. The aim of this study was to investigate Bi-Ge-Pb ternary system using a combination of different experimental techniques (DTA, XRD, SEM/EDS). In total 16 ternary samples were prepared. Prepared alloys were are located along three vertical sections Bi-GePb, Ge-BiPb and Pb-BiGe and one isothermal section at 100 °C.

2. EXPERIMENTAL

Experimentally investigated samples with a wide range of compositions were prepared from high purity metals Bi, Ge and Pb (99.99 %) produced by Alfa Aesar, Germany. In total, 16 ternary samples were weighed, mixed and melted in an electric arc furnace under high-purity argon atmosphere. The samples were melted and re-melted five times until homogeneity was maintained. The average weight loss during melting and remelting was approximately 0.5 mass %.

The samples were divided into two groups (one group with 12 samples and the other group with 4 samples). The samples of the first group after melting, were left in furnace to slowly cool down to the room temperature. Those samples were used for DTA measurements. Second group of 4 alloy samples were placed in a quartz tube and annealed at 100 °C for four weeks (28 days). After annealing, the samples were quenched in ice-cold water. These samples were divided into two

parts. One part was pulverized and used for the XRD measurement. The second part was metallographically prepared and used for SEM-EDS analysis.

The DTA measurements were performed with an SDT Q600 (TA Instruments). Alumina crucibles were used and measurements were performed under a flowing argon atmosphere with an empty alumina crucible as reference material. Samples weighing between 20 and 30 mg were analyzed at a heating rate of 5 °C/min with three heating and cooling cycles. The overall uncertainty of the determined phase transformation temperatures was estimated to be ±1 °C. Before realizing the DTA experiments temperature calibration of DTA were performed by measuring the melting temperature, of pure elements (In, Sn, Pb, Bi, Zn, Sb, Al, Ag and Ge) using the same working conditions.

TESCAN VEGA3 scanning electron microscope (SEM) with energy dispersive spectrometer (EDS) (Oxford Instruments X-act) was used for microstructural investigation. SEM-EDS analysis of the prepared ternary alloy was carried out at an accelerating voltage of 20 kV. Overall composition and compositions of coexisting phases were determined using EDS area and point analysis. All SEM images of the microstructures were taken on the polished surfaces of the studied alloy samples in backscattered electron mode.

Powder X-ray diffractometer D2 PHASER (Bruker, Karlsruhe, Germany), equipped with a dynamic scintillation detector and a ceramic X-ray Cu tube (KFL-Cu-2K) in a 2θ range from 10° to 75° with a step size of 0.02°. The samples were analyzed using Topas 4.2 software, ICDD databases.

3. RESULTS AND DISCUSSION

According to literature information, ternary Bi-Ge-Pb systems have not been studied previously. The available literature information are related to constitutive binary systems. The ternary Bi-Ge-Pb system consists of three binary systems. The constitutive binary phase diagrams (Bi-Ge [4], Ge-Pb [5] and Bi-Pb [6]) have been studied in the past [4-6]. According to the literature, the solid phases that could be expected in the ternary system are summarized in Table 1 [7-10].

Table 1. Considered phase, their crystallographic data and database names for the solid phases of the ternary Bi-Ge-Pb system [6-9].

Thermodynamic database name	Phase	Reference
RHOMBO_A7	(Bi)	[7]
DIAMOND_A4	(Ge)	[8]
FCC_A1	(Pb)	[9]
HCP_A3	ε	[10]

In total four solid phases and one liquid phase should be expected in ternary Bi-Ge-Pb system. Solid phases are (Pb), (Bi) and (Ge) solid solution and ε phase. Liquid phase is L and no information about ternary compound.

Experimental results of the DTA test are summarized in Table 2.

Table 2. Phase transition temperatures of the studied alloys from the ternary

Bi-Ge-Pb system determined by DTA.

Sample no. and nominal composition at. %	Temperatures of phase transformation in °C	
	Invariant reaction and Monovariant phase transition	Liquidus
Vertical section Bi-GePb		
Sample 1, $Bi_{20}Ge_{40}Pb_{40}$	55.20; 191.13	827.93

Sample 2, $Bi_{40}Ge_{30}Pb_{30}$	134.21; -	846.27
Sample 3, $Bi_{60}Ge_{20}Pb_{20}$	133.67; 209.66	810.41
Sample 4, $Bi_{80}Ge_{10}Pb_{10}$	134.58; 254.93	735.11
Vertical section Ge-BiPb		
Sample 5, $Bi_{40}Ge_{20}Pb_{40}$	127.32; 149.21	814.86
Sample 6, $Bi_{30}Ge_{40}Pb_{30}$	131.09; 148.11	865.13
Sample 7, $Bi_{20}Ge_{60}Pb_{20}$	130.19; 145.43	877.80
Sample 8, $Bi_{10}Ge_{80}Pb_{10}$	123.11; 144.51	881.75
Vertical section Pb-BiGe		
Sample 9, $Bi_{40}Ge_{40}Pb_{20}$	127.13; 173.87	867.81
Sample 10, $Bi_{30}Ge_{30}Pb_{40}$	126.62; 180.69	852.39
Sample 11, $Bi_{20}Ge_{20}Pb_{60}$	190.02; 246.62	789.69
Sample 12, $Bi_{10}Ge_{10}Pb_{80}$	298.95	753.38

According to the appearance of DTA peaks it is discovered existence of reactions, monovariant phase transition and liquidus transformation. So, determined temperatures of phase transitions are divided into two groups. The first group are the temperatures of the invariant reaction and the peak of the mono-variant phase transition. The last peak detected is described as a liquidus temperature. First detected temperature in samples 2 to 10 correspond to the ternary eutectic reaction L→(Ge)+ε+(Bi) while the temperature of 191.13 °C in sample 1 and 190.02 °C in sample 11 corresponds to the reaction L+(Pb)→(Ge)+ε. These conclusions are supported by construction of related vertical sections by using literature information of reference [4-6].

Samples annealed at 100 °C were experimentally tested and results of the experimental analyses are summarized in Table 3.

Table 3. Results of EDS and XRD tests of samples 13 to 16 annealed at 100 °C.

No.	Composition, at. %	Determined phases		Composition of phase, at. %			Lattice parameter, Å	
		EDS	XRD	Bi	Ge	Pb	a=b	c
13	4.75 Bi 51.70 Ge 43.55 Pb	(Ge) (Pb)	(Ge) (Pb)	0.52±0.3 9.67±0.1	99.35±0.5 0.31±0.8	0.13±0.8 90.02±0.1	5.6552±0.0002 4.9521±0.0003	5.6552±0.0002 4.9521±0.0003
14	10.59 Bi 69.17 Ge 20.24 Pb	(Ge) ε	(Ge) ε	0.52±0.8 35.51±0.5	99.05±0.2 0.29±0.7	0.43±0.8 64.20±0.2	5.6560±0.0004 3.2648±0.0002	5.6560±0.0004 5.3866±0.0001
15	38.16 Bi 39.67 Ge 22.17 Pb	(Ge) (Bi) ε	(Ge) (Bi) ε	0.52±0.8 99.01±0.4 39.50±0.2	98.77±0.2 0.86±0.9 0.89±0.7	0.71±0.8 0.13±0.7 59.61±0.1	5.6549±0.0002 4.5467±0.0001 3.2641±0.0001	5.6549±0.0002 11.8628±0.0003 5.3869±0.0004
16	63.24 Bi 12.21 Ge 24.55 Pb	(Ge) (Bi) ε	(Ge) (Bi) ε	0.16±0.9 98.71±0.1 39.81±0.7	99.08±0.1 1.14±0.5 0.46±0.3	0.76±0.7 0.15±0.7 59.73±0.1	5.6553±0.0003 4.5460±0.0003 3.2645±0.0004	5.6553±0.0003 11.8631±0.0001 5.3862±0.0005

Three different phase regions were experimentally investigated. In sample 13, the two phases that are defined are (Ge) and (Pb). In sample 14, two other phases are defined, (Ge) and ε. While in samples 15 and 16, three phases are present, (Ge), (Bi) and ε. The SEM microstructure of sample 14 is shown in Figure 1 as an illustration.

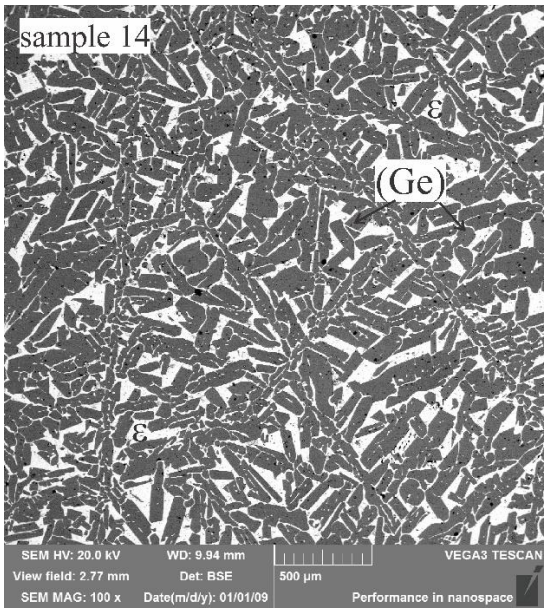

Figure 1. SEM micrograph of the sample 14 annealed at 100 °C.

4. CONCLUSION

In this paper ternary Bi-Ge-Pb system have been studied experimentally and theoretically, as the data about investigation of this system are not available in already published literature. The DTA analysis showed the existence of two reactions, one at a temperature in the range of 123.11 to 134.58 °C and the second at a temperature in the range of 190.02 °C to 191.13 °C. The first temperature is related to the ternary eutectic reaction $L \rightarrow (Ge) + \varepsilon + (Bi)$ and according to the calculation, this reaction is predicted at 124.985 °C. The second reaction is $+(Pb) \rightarrow (Ge) + \varepsilon$, which is predicted at 183.623 °C.

The phase regions of isothermal section at 100 °C were experimentally confirmed by 4 samples annealed at 100 °C for 28 days. Confirmed regions are (Ge)+(Pb), (Ge)+ε and (Ge)+ε+(Bi).

REFERENCES

[1] M. Kamal, A.-B. El-Bediwi, R.M. Shalaby, M. Younus, J. Adv. Phys., 7 (2) (2015) 1404-1414.
[2] X.H. Yang, S.C. Tan, J. Liu, Int. J. Heat Mass Transf., 100 (2016) 899–907.
[3] D. Manasijević, Lj. Balanović, V. Ćosović, D. Minić, M. Premović, M. Gorgievski, U. Stamenković, N. Talijan, Metall. Mater. Eng., 25 (4) (2019) 325-334.
[4] P.Y. Chevalier, Thermochim. Acta, 132 (1988) 111–116.
[5] P.Y. Chevalier, A thermodynamic evaluation of the Germanium-Indium, Germanium-Lead, Germanium-Antimony, Germanium-Thallium and Germanium Zinc systems, 155 (1989) 227-240.
[6] D. Boa, I. Ansara, Thermochim. Acta., 314(1) (1998) 79-86.
[7] P. Cucka, C.S. Barrett, Acta Crystallogr., 15 (1962) 865-872.
[8] A.S. Cooper, Acta Crystallogr., 15 (1962) 578-582.
[9] H.E. Swanson, E. Tatge, Natl. Bur. Stand. Circular, 539 (1953) 539A.
[10] T. Takahashi, H. K. Mao, W. A. Bassett, Science, 165 (1969) 1352-1353.

The 56th International October Conference on Mining and Metallurgy
22-25 October 2025, Bor Lake, Bor, Serbia
www.ioc.tfbor.bg.ac.rs

DOI: 10.5937/IOC25515K *Original scientific paper*

INVESTIGATION OF GAS AND SHRINKAGE POROSITY IN ALSI10MG ALLOY GEARBOX CASTINGS MANUFACTURED BY HPDC

Ondrej Kožej[1a], Iveta Vasková[1b], Ladislav Jankovčin[1,2c]

[1] Faculty of Materials, Metallurgy and Recycling , Technical University of Košice, Letná 9, 04200 Košice, Slovakia
[2] Handtmann Kechnec s.r.o, 04458 Kechnec, Slovakia
[1a] ondrej.kožej@gmail.com, 0009-0009-5245-5166
[1b] iveta.vaskova@tuke.sk, 0000-0001-6820-4876
[1,2c] Ladislav.Jankovcin@handtmann.sk, 0009-0008-1021-6346

Abstract
This paper analyses internal defects in aluminium gearbox castings manufactured using the high-pressure casting method. Two defective parts were examined using X-ray imaging, optical and electron microscopy. The results revealed that these defects were a combination of gas and shrinkage porosity. The aim was to identify the causes of these defects and suggest ways to improve the technological process. Analysis of the defects revealed that they were caused by the molten metal's inability to flow freely in the mould cavity.

***Keywords**: high pressure die casting, porosity, casting defects*

1. INTRODUCTION

High-pressure die casting (HPDC) of aluminium alloys represents one of the most advanced and efficient manufacturing technologies for the production of precision metallic castings. This process is characterized by excellent repeatability, short cycle times, and the ability to manufacture geometrically complex components with superior surface quality. HPDC has become particularly important in the automotive and electrical engineering industries, where the demand for lightweight, high-strength, and multifunctional components continues to increase.

In Slovakia, more than ten foundry enterprises are currently engaged in HPDC of aluminium alloys. Among the most prominent are international companies such as Handtmann Slovakia and the newly established Volvo Cars plant in Košice, as well as long-standing domestic firms including MOPS PRESS, ALCAST, and BCB. These foundries supply a broad spectrum of industrial sectors and are strategically located in regions with a well-developed engineering infrastructure and in close proximity to automotive assembly plants, which provides significant advantages in logistics and supply-chain integration [1].

The process predominantly employs aluminium-silicon (Al–Si) based alloys, such as $AlSi_9Cu_3(Fe)$, $AlSi_{12}$, and $AlSi_{10}Mg$, along with their modified variants. These alloys combine favourable castability, mechanical strength, and corrosion resistance. The selection of a specific alloy is dictated by the required mechanical properties, machinability, and thermal resistance of the component [2].

Annual production volumes differ substantially depending on the size of the foundry and its degree of automation. Smaller enterprises typically produce between 500 and 1,500 tonnes of castings per year, whereas larger operations, such as Handtmann Slovakia, exceed 5,000 tonnes annually or more than one million individual castings. The newly constructed Volvo Cars facility in Košice is expected to implement megacasting technology using two Giga Press machines (Idra Group) with a clamping force of 9,000 tonnes. This positions Slovakia among the technological leaders in the field of large-scale aluminium die casting [3].

Given the stringent quality requirements for structural components such as chassis, engine, and body parts, strict control of process parameters throughout the entire production chain is essential. This includes alloy selection, optimization of technological settings, subsequent heat treatment, and microstructural evaluation. Typical defects such as porosity, shrinkage cavities, cold shuts, and inclusions can significantly impair the functional performance of cast products. Consequently, their prevention and reduction are subjects of ongoing intensive research and process optimization.

2. EXPERIMENTAL

The High-pressure die casting (HPDC) is a modern manufacturing technology designed for the efficient production of large-series aluminium castings with high dimensional accuracy and superior surface quality. The process takes place in a closed steel die, into which the molten metal is injected under pressure exceeding 100 MPa. The flow behaviour of the melt within the shot chamber significantly influences the final quality of the casting.

Different piston motion profiles, combined with parameters such as piston diameter, melt height, and chamber length, can result in various flow regimes. If the piston moves too slowly (Figure 1a), the rebound of the molten metal from the chamber wall may cause disturbed flow and impaired venting. Conversely, excessively high piston velocity (Figure 1c) results in turbulent metal flow and increased air entrapment, which promotes porosity formation. The optimal condition is achieved through a smooth acceleration phase (Figure 1b), where the metal surface maintains a slight inclination away from the piston without abrupt deformations [4].

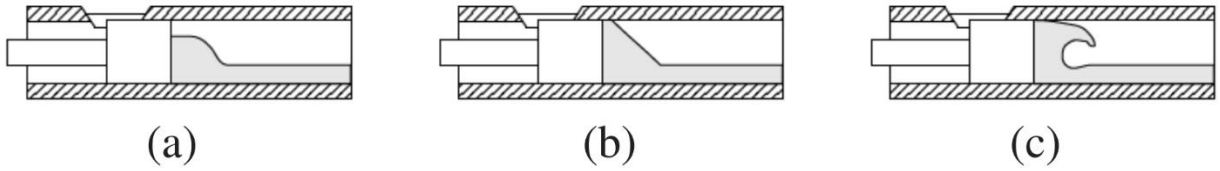

Figure 1. Metal flow in the shot chamber depending on piston velocity in the HPDC process

To minimize air inclusions, the injection process is divided into a slow and a fast phase. During the slow phase, the piston accelerates until the molten metal reaches the end of the shot chamber, after which it moves at a constant velocity until entering the die cavity.

Despite these advantages, one of the major technological challenges of the HPDC process remains the formation of internal defects, with porosity being the most common, either gas porosity or shrinkage porosity. These defects arise as a result of turbulent die filling, insufficient venting, high hydrogen content in the melt, as well as inadequate feeding of solidifying regions in the casting. Their occurrence negatively affects the mechanical properties of the final product [5].

2.1 The formation of gas porosity

Gas porosity arises primarily due to:

- High hydrogen content in the melt (hydrogen is the only gas highly soluble in liquid aluminium),
- Air entrapment during turbulent die filling,
- Degradation of lubricants or wear of piston and cylinder surfaces.

The key mechanism of gas pore formation is associated with the decrease in hydrogen solubility during solidification. As the temperature decreases, hydrogen is released from the liquid phase. When the solubility limit is exceeded, bubbles form, which subsequently expand but may become trapped in the interdendritic regions, where they remain as permanent pores after solidification [6].

The equilibrium condition for pore growth can be expressed as [6]:

$$P_{gas} \geq P_{atm} + P_{met} + P_{retrait} + P_{surface}$$

Where:

P_{gas} – gas pressure inside the pore

P_{atm} – atmospheric pressure

P_{met} – metallostatic pressure

$P_{retrait}$ – pressure induced by metal shrinkage

$P_{surface}$ – pressure of surface tension

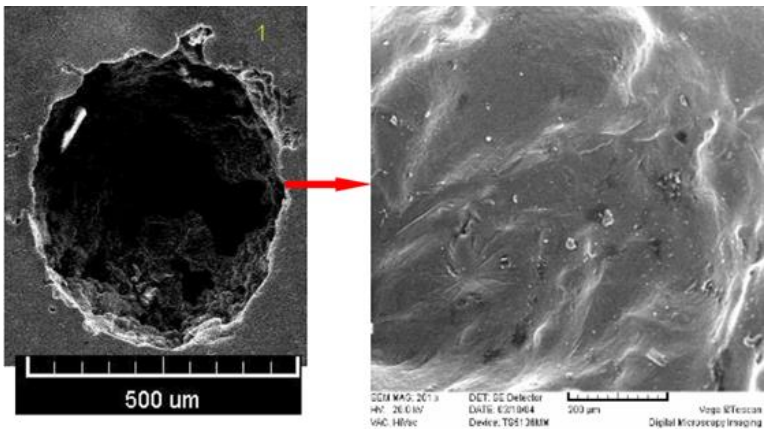

Figure 2. Example of gas porosity [5]

As shown in Figure 2, gas pores are usually round with a smooth or shiny surface and are often found in the upper part of the casting where the gas phase is lighter than the metal. They typically occur in areas of turbulent flow, such as where the metal first makes contact with the mould or in the venting channels [7].

2.2 The formation of shrinkage porosity

Shrinkage pores occur as a result of volume contraction during metal solidification. Microscopic or macroscopic cavities are formed due to the speed of solidification, geometric compression and the limited ability to supply additional liquid to the solidifying area. These cavities most often form in densely cooled or massive parts of the casting, where solidification is slowest [5, 8].

Typical characteristics of shrinkage porosity include [5]:

- Irregular, rough, or jagged morphology (Figure 3),
- Occurrence in internal regions with limited metal feeding,
- Dendritic structures surrounding the pores (observable through SEM analysis).

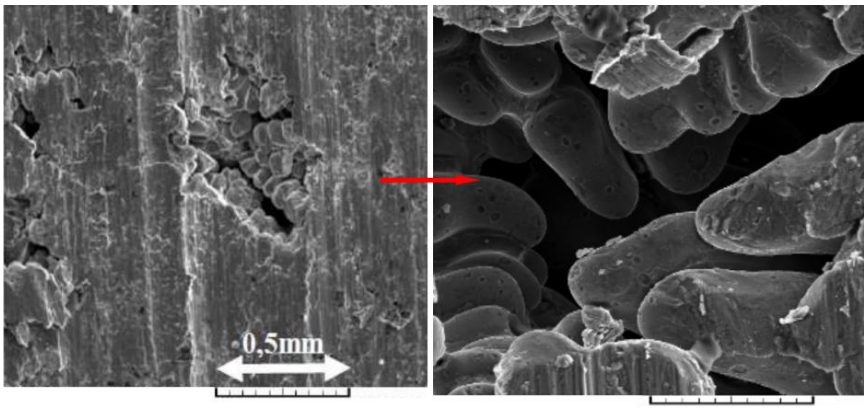

Figure 3. Example of shrinkage porosity [5]

The frequency and size of such pores are influenced by the width of the solidification interval. A wide interval increases the tendency for microporosity formation, whereas a narrow interval (e.g., in eutectic alloys) promotes the development of macroporosity [9].

2.3 Interaction of shrinkage and gas porosity

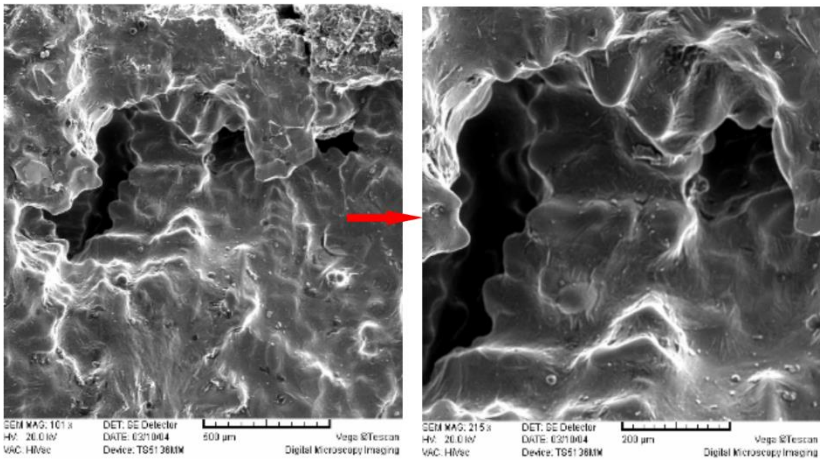

Figure 4. Interaction between shrinkage and gas porosity

High-pressure castings often exhibit combined porosity, where gas trapped in the metal forms bubbles that "branch out" into shrinkage cavities as the metal volume decreases.

Electron microscope images document the connection between gas and shrinkage porosity and indicate their joint evolution during solidification [5,6].

3. RESULTS AND DISCUSSION

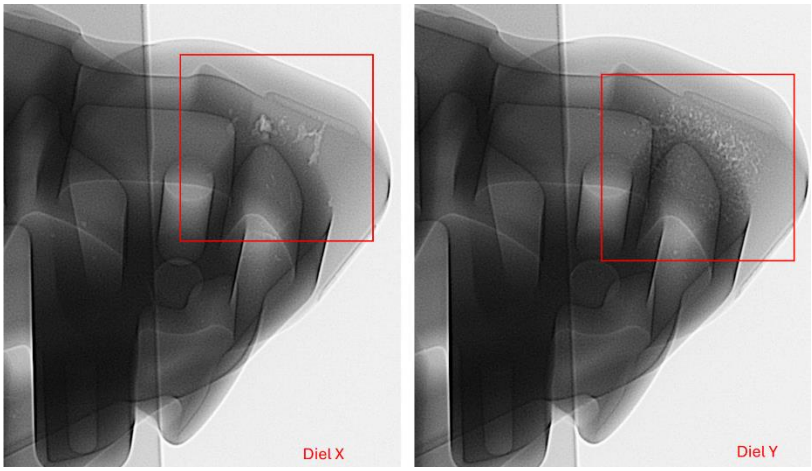

Figure 5. X-ray image of parts X and Y

As part of the analysis of AlSi10Mg aluminum alloy gearbox castings produced by high-pressure die casting (HPDC), two parts were selected in which internal defects occurred during production. These parts were designated as part X and part Y.

Based on visual inspection and quality monitoring, areas with suspected internal porosity were identified on the selected parts. These areas were then subjected to X-ray (RTG) analysis, which confirmed the presence of defects (Figure 5). The X-ray images clearly showed a concentration of porosity in the thicker cross-sections of the parts. Samples of material were then cut from both parts at the examined locations. The samples were cleaned and prepared for metallographic analysis. Special emphasis was placed on maintaining the integrity of the pores and minimizing deformation during cutting to avoid artifacts in further analysis, as shown in Figure 6.

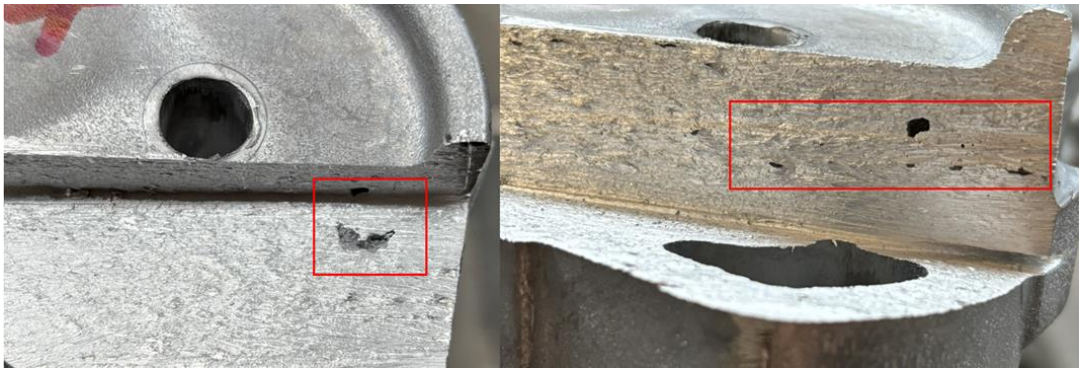

Figure 6. Porosity shown on Sample X after cutting in the examined area

Figure 7. Metallographic samples prepared for analysis

The samples were labeled Sample X and Sample Y, each originating from an identified defect location on the respective casting (Figure 7).

The initial analysis was performed using optical microscopy (Figure 8), which identified the basic characteristics of porosity, their distribution, morphology, and orientation relative to the casting structure. Both samples showed significant deviations in pore distribution. Sample X showed clusters of irregularly shaped pores that corresponded to areas of thicker cross-section. Sample Y contained smaller, evenly distributed pores, but with the occurrence of a larger cavity located centrally, which again supports the hypothesis of combined porosity.

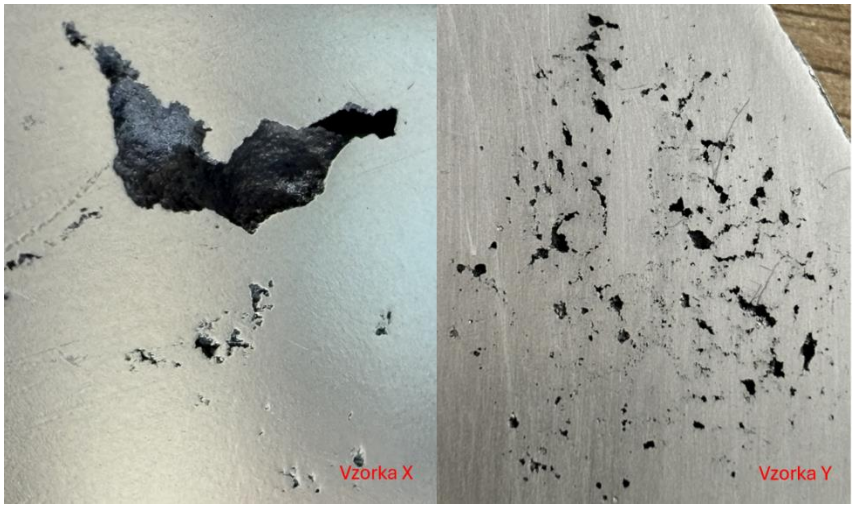

Figure 8. Visible differences in porosity on the examined samples

To determine the type of porosity in more detail, scanning electron microscopy (SEM) with additional energy-dispersive X-ray spectroscopy (EDX) was applied. These methods made it possible to more accurately determine the shape, size, and chemical composition of the areas around the pores.

• **Sample X** – at magnification, distinct spherical pores could be observed, which is a typical sign of gas porosity. EDX analysis also confirmed the presence of oxide inclusions (primarily aluminum oxide – Al_2O_3), which may indicate the introduction of gases into the melt during injection (Figure 10).

• **Sample Y** - larger cavities with irregular shapes and signs of alloy separation were recorded, indicating shrinkage porosity. However, the chemical composition of the cavity surfaces did not contain a significant proportion of oxides, suggesting that gas filling was not a dominant factor in this case.

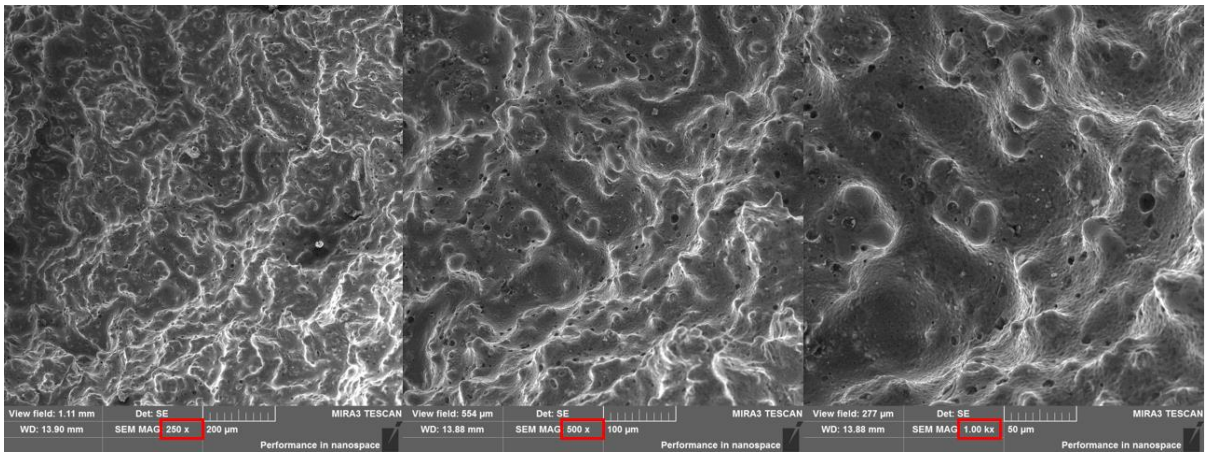

Figure 9. EDX analysis of samples X at magnification 250x, 500x, 1000x

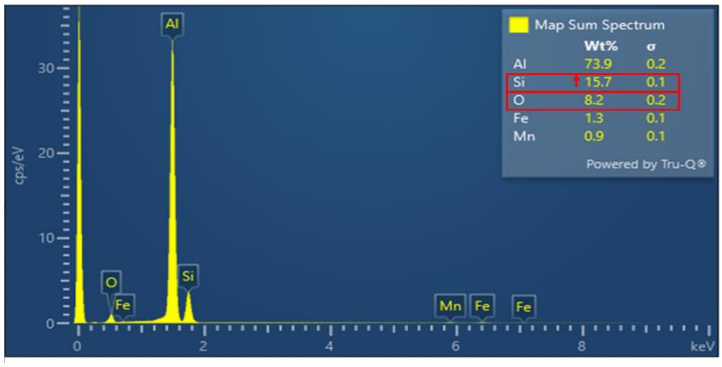

Figure 10. Chemical composition of sample X in the monitored pore

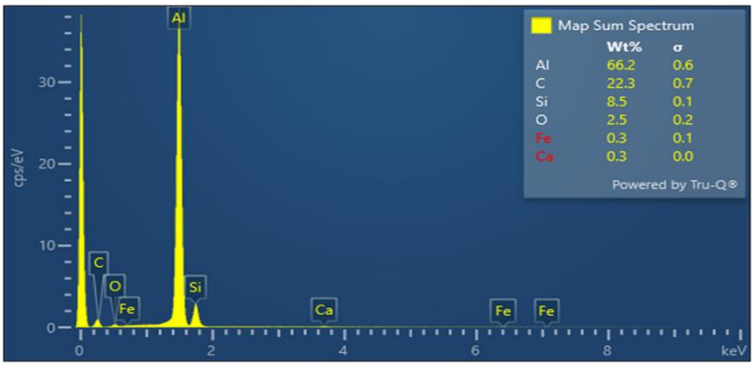

Figure 11. Chemical composition of sample Y in the monitored pore

4. CONCLUSION

Based on the analysis of two problematic parts made of AlSi10Mg aluminum alloy using high-pressure casting, it can be concluded that the cause of internal defects was a combination of gas and shrinkage porosity. X-ray images confirmed the concentration of pores in areas with a thicker cross-section, which correlates with shrinkage defects. SEM analysis together with EDX identified the presence of oxide inclusions and spherical pores, which are typical for gas filling. The results indicate the need for more thorough control of the technological parameters of the casting process, in particular the control of metal temperature, mold temperature, filling phase parameters, and mold venting in order to eliminate combined defects and improve the quality of the resulting castings.

In addition to the adjustment of technological parameters, the elimination of the observed defects was achieved by modifying the size and geometry of the squeeze pin. This optimization improved the feeding of solidifying regions, reduced the risk of interdendritic porosity, and enhanced the

overall structural integrity of the castings. The results underline the importance of continuous research focused on the design and efficiency of squeeze pins and related HPDC components, as this field represents a critical factor in defect prevention and in further improvement of casting quality and reliability in industrial practice.

REFERENCES

[1] O. Kožej, I. Vasková, Eng. Proc., 64 (1) (2024) 14.
[2] J. Campbell, High pressure die casting. In Die Casting Engineering, Woodhead Publishing, 2012, p. 99-123.
[3] R. Turza, Volvo má plán pre Slovensko. V Košiciach sa vydá cestou Tesly, získa veľkú výhodu. Hospodárske noviny. (2023). – In Slovakian Available online: https://hnonline.sk/finweb/ekonomika/96115638-volvo-ma-plan-pre-slovensko-v-kosiciach-sa-vyda-cestou-tesly-ziska-velku-vyhodu
[4] M. Bertoglio, M. Fabbri, Fluids, 6 (11) (2021) 386.
[5] Z. Ignaszak, J. Hajkowski, Defect and Diffusion Forum, 364 (2015) 80–92.
[6] A.M. Samuel, E. Samuel, V. Songmene, F.H. Samuel, Materials, 16 (5) (2023) 2047.
[7] A. Wilczek, P. Długosz, M. Hebda, J. Nondestruct. Eval., 34 (2015) 24.
[8] M. Di Sabatino, L. Arnberg, Trans. Indian. Inst. Met., 62 (4–5) (2009) 321–325.
[9] L. Kucharčík, M. Brůna, A. Sládek, Arch. Foundry Eng., 14 (2) (2014) 5–8.

The 56th International October Conference on Mining and Metallurgy
22-25 October 2025, Bor Lake, Bor, Serbia
www.ioc.tfbor.bg.ac.rs

DOI: 10.5937/IOC25522P *Original scientific paper*

EFFECT OF OXY-FUEL CUTTING ON THE MICROSTRUCTURE AND HARDNESS OF HIGH-CARBON STEEL

Jasmina Petrović [1a], Srba Mladenović[1b], Uroš Stamenković [1c], Milan Nedeljković [1d], Milijana Mitrović [1e]

[1]Technical Faculty Bor, University of Belgrade, V. J. 12, 19210 Bor, Serbia
[1a]jpetrovic@tfbor.bg.ac.rs, 0000-0002-9131-339X
[1b]smladenovic@tfbor.bg.ac.rs, 0000-0002-3844-7399
[1c]ustamenkovic@tfbor.bg.ac.rs, 0000-0002-7579-2159
[1d] mnedeljkovic@tfbor.bg.ac.rs, 0000-0002-7927-1334
[1e]mmitrovic@tfbor.bg.ac.rs, 0000-0001-7478-2453

Abstract

This study investigates the influence of heat input during oxy-fuel cutting on the microstructure and hardness of high-carbon steel. The material analyzed was a steel bar designed for use in mining mills, processed through this thermal cutting technique. After cutting, a detailed metallographic analysis of the heat-affected zone (HAZ) was carried out using optical microscopy, while Vickers hardness (HV20) was measured at various distances from the cut edge. The results showed that, due to the high temperatures generated during cutting, significant structural changes occurred within the HAZ. At the surface edge, hardness measurements revealed a slight increase, indicating localized hardening associated with rapid cooling and the resulting microstructural changes. The obtained results were compared with relevant literature data, providing a deeper understanding of the thermal effects on the microstructure in this type of steel.

***Keywords**: Oxy-fuel cutting, heat-affected zone, microstructures, mechanical property.*

1. INTRODUCTION

High-carbon steels (with carbon content greater than 0.6%) are known for their exceptional hardness and wear resistance, making them suitable for the production of cutting tools, milling equipment, and various machine components subjected to high mechanical stresses [1]. Consequently, the processing of these steels, including cutting operations, represents a significant technological challenge in modern industrial practic [2].

One of the most commonly used methods for cutting high-carbon steels is autogenous (oxy-fuel) cutting, typically performed using a combination of acetylene and oxygen as the heat source and reactive gas. This process belongs to a broader group of thermal cutting techniques known as oxy-fuel gas cutting (OFC), which are based on controlled oxidation reactions. The cutting procedure begins with heating the surface of the workpiece to the ignition temperature using a fuel gas flame. Once the material reaches this temperature, a jet of pure oxygen is directed at the heated zone, initiating rapid oxidation and enabling material removal [2, 3].

Due to its simplicity, cost-effectiveness, and high efficiency, this method is widely applied for cutting carbon and low-alloy steels of various thicknesses. However, during the cutting process, the localized application of intense heat leads to melting and significant thermal gradients in the material near the cut edge. The temperature in the cutting zone can exceed 1200 °C, resulting in pronounced microstructural changes in the immediate vicinity of the cut. This thermally altered region is known as the heat-affected zone (HAZ). The transformations occurring within the HAZ directly affect the mechanical properties of the material, particularly hardness and fracture toughness. These changes are of critical importance for applications where the reliability and longevity of components are essential [4].

Previous research on OFC of high-carbon steels has extensively analyzed the relationship between thermal cycles and microstructural transformations. Tuz et al. [3] emphasized that the heat-affected zone in steels with high carbon content can exhibit significant hardening due to martensite formation during rapid cooling after austenitization. Similarly, Górka et al. [5] highlighted that variations in torch speed and oxygen pressure have a direct impact on the thickness and microstructure of the HAZ, as well as on the material's mechanical properties. Brykov et al. [6] conducted metallographic analyses of thermally cut high-carbon steels and pointed out that inadequate process control can cause excessive residual stresses and brittle zones, stressing the necessity of post-cutting heat treatment for stress relief. Furthermore, Górka [7] explained the thermodynamic aspects of thermal cutting, noting that local overheating followed by rapid quenching leads to the formation of highly non-uniform microstructures that differ significantly from the base material.

Most previous studies have focused on the properties of flame-cut steel, while the characterization of the HAZ has often been neglected. However, investigating the HAZ formed due to thermal cutting is essential for understanding changes in material properties near the cut edge caused by thermal exposure.

2. EXPERIMENTAL

For the purpose of this study, a steel bar was used, with its chemical composition presented in Table 1. Based on its composition, the steel is classified as a low-alloy high-carbon steel, and its carbon content closely corresponds to that of eutectoid steel. The bar was cut using the autogenous (oxy-fuel) cutting process, with acetylene used as the fuel gas.

Table 1. Chemical composition of the investigated steel

Element	C	Si	Mn	P	S	Cr	Ni	Al	Cu	Ti	V	Mg	As	Fe
wt.%	0.7	0.36	0.84	0.003	0.002	0.45	0.118	0.024	0.33	0.024	0.007	0.004	0.005	97.128

After cutting, the specimens were prepared for metallographic analysis through grinding, polishing, and etching using a suitable etchant. The microstructural analysis was performed using an optical microscope. Micrographs were captured starting from the flame-cut edge, continuing through the HAZ, and extending into the base (unaffected) material.

In addition, Vickers hardness measurements were performed using a 20 kg load (HV20) at five distinct locations, positioned at increasing distances from the cut edge: 0 mm, 1 mm, 2 mm, 3 mm, and 5 mm. Measurements were taken along a line normal to the cut surface, moving away from the cutting edge.

3. RESULTS AND DISCUSSION

In OFC, the microstructure within the HAZ is often highly complex, due to non-uniform temperature distribution and cooling rates. Metallographic analysis confirmed that a distinct HAZ developed beneath the cutting interface. Figure 1(a–e) presents microstructures captured at various distances from the cutting edge.

Figure 1a shows the microstructure immediately adjacent to the cut edge, where the high temperature (above the A_3 point) during cutting caused complete austenitization. The structure is dominated by martensite, which formed due to rapid cooling after intense heating during OFC [3]. The presence of martensite indicates increased hardness, accompanied by higher brittleness. It can also be assumed that the light regions correspond to retained austenite, while the darker, finer areas between grains may represent bainite, particularly if the cooling rate was not extremely high in all areas [6]. Figures 1(b–d) represent microstructures within the HAZ. In Figure 1b, partial transformation of pearlite and ferrite into austenite occurred during cutting, which then

transformed – depending on the local cooling rate – into fine bainite and small amounts of martensite.

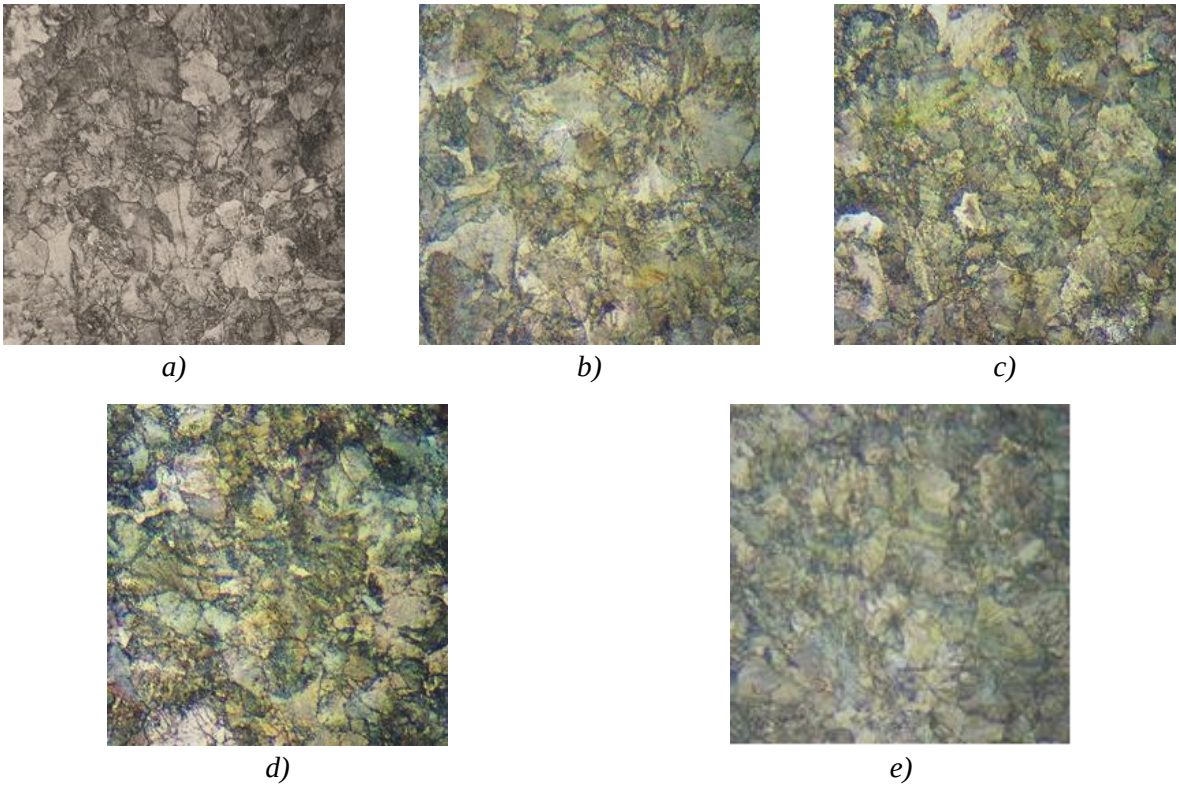

Figure 1. Microstructures in the heat-affected zone after oxy-fuel cutting of high-carbon steel: (a) martensitic structure adjacent to the cut edge; (b) partially transformed zone with bainite and minor martensite; (c) pearlite with a small fraction of martensite; (d) fine pearlite and ferrite; (e) base metal with typical pearlite–ferrite structure.

The grains appear partially elongated, and the structure becomes more heterogeneous, confirming that this zone was exposed to elevated temperatures without melting. In Figure 1c, pearlite and a very small fraction of martensite are visible, while Figure 1d shows fine pearlite and ferrite. This indicates that the influence of heat decreases with increasing distance from the cut edge. Figure 1e presents the microstructure of the base material, consisting of a typical pearlite-ferrite structure characteristic of eutectoid steels. The microstructure is uniform and unaffected by thermal influence. This region serves as a reference for assessing the changes that occurred during cutting.

The hardness measurement results are presented in Figure 2.The measured hardness at the region closest to the cut edge was 371 HV20. Although the microstructural analysis confirmed the presence of martensite, the measured hardness was lower than the expected values for fully developed martensite in steel containing ~0.70% carbon. According to the literature, fully formed martensite in such steels typically exhibits hardness in the range of 650–700 HV. It can be assumed that martensite transformation was incomplete, since during OFC the heating and cooling cycles are extremely rapid, but in some areas the thermal cycle may not have been sufficient to achieve full austenitization. Consequently, a mixed structure (martensite and bainite) developed, lowering the overall hardness.

Additionally, due to the amount of heat input and the short holding time at elevated temperatures, part of the martensite may have undergone self-tempering, producing tempered martensite, which slightly reduces hardness but improves toughness. This is consistent with other studies showing that OFC of high-carbon steels does not always lead to complete martensite transformation [3], but instead results in the formation of a complex, partially hardened structure. Another factor to consider is the hardness testing method itself.

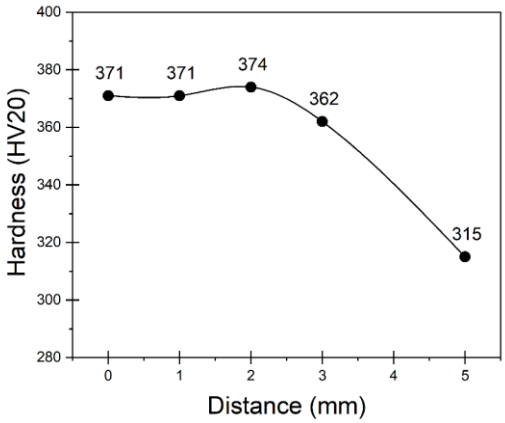

Figure 2. Hardness distribution from the cutting surface

Using HV20 load, the indentation depth includes different microphases. If martensite is concentrated only near the surface, while softer structures are present beneath, the measured hardness represents an average value. Within the HAZ, hardness gradually decreases. The highest values were observed at distances of 1 mm and 2 mm from the edge (371 HV20 and 374 HV20), corresponding to regions where martensite and bainite are present. A slight decrease at 3 mm (362 HV20) indicates a transitional microstructure. The lowest hardness (315 HV20) in the base material confirms the presence of a pearlite-ferrite structure unaffected by the heat from cutting.

4. CONCLUSION

The results indicate that OFC significantly influences the microstructure and mechanical properties of high-carbon steel. The microstructure transforms from ferrite–pearlite in the base material to martensite near the cut edge. Hardness values increase from 315 HV20 in the base material to 374 HV20 closer to the HAZ, after which they stabilize. Although martensite was observed near the cut edge, the measured hardness values suggest a limited depth or degree of transformation. It is concluded that during OFC, martensite can indeed form in the HAZ even under air cooling, due to very rapid localized heat extraction. This leads to the formation of a hard and brittle zone, which explains why the HAZ is often considered unfavorable. This region is susceptible to cracking and therefore requires mechanical or thermal treatment after cutting.

ACKNOWLEDGEMENTS

The research presented in this paper was done with the financial support of the Ministry of Science, Technological Development and Innovation of the Republic of Serbia, with the funding of the scientific research work at the University of Belgrade, Technical Faculty in Bor, according to the contract with registration number 451-03-137/2025-03/200131.

REFERENCES

[1] R. Singh, Applied Welding Engineering (Second Edition), Chapter 6 - Classification of Steels, Butterworth-Heinemann, 2016, 57-64.
[2] T. Pasko, Heat-Affected Zone Studies of Thermally Cut Structural Steels, Virginia, 1994.
[3] L.Tuz, A. Ziewiec, K. Pańcikiewicz, Materials,(1284) (14) (2021), 2-10.
[4] Y. Kalinin, M. Brykov, I. Petryshynets, V. Efremenko, O. Hesse, M. Kunert, M. Andrushchenko, M. Osipov, S. Berezhny, O.Bykovskiy, Acta Metallurgica Slovaca, (2) (25) (2019), 114-122.
[5] J Górka, T Poloczek, Sci. Eng. (400) (2018), 022032.
[6] M.N. Brykov, I. Petryshynets, M. Džupon, Y.A. Kalinin, V.G. Efremenko, N.A. Makarenko, D.Y. Pimenov, F. Kováč, Materials, (5059) (13) (22) (2020).
[7] J. Górka, D. Janicki, M. Fidali, Int. J. Thermophys., (38) (2017), 183.

The 56th International October Conference on Mining and Metallurgy
22-25 October 2025, Bor Lake, Bor, Serbia
www.ioc.tfbor.bg.ac.rs

DOI: 10.5937/IOC25526M *Original scientific paper*

CHANGES IN HARDESS AND MICROSTRUCTURE DURING ISOTHERMAL AGING OF NICKEL-ALUMINUM BRONZE

Ivana Markovic[1a], Uroš Stamenković[1b], Dragan Manasijević[1c], Ljubiša Balanović[1d]

[1] University of Belgrade - Technical Faculty Bor, V.J. 12, 19210 Bor, Serbia
[1a] imarkovic@tfbor.bg.ac.rs, 0000-0003-4431-9921
[1b] ustamenkovic@tfbor.bg.ac.rs, 0000-0002-7579-2159
[1c] dmanasijevic@tfbor.bg.ac.rs, 0000-0002-7828-8994
[1a] ljbalanovic@tfbor.bg.ac.rs, 0000-0002-3551-6731

Abstract
In this paper, the properties and microstructural changes in Cu-Al-Ni-Fe bronze were studied during isothermal aging. The alloy was annealed at 900 °C for 2 hours following the casting process and quenched rapidly in cold water. Isothermal aging was then carried out up to 10 h at 350 °C, 400 °C, and 450 °C. During isothermal aging, hardness was tested and microstructure was examined using the scanning electron microscope. Isothermal aging at all selected temperatures contributed to a significant increase in hardness values. The alloy aged at 400 °C for 1 h achieved the highest relative hardness increase of 35 %, compared to the quenched state.

***Keywords**: nickel-aluminum bronze, isothermal aging, microstructure, hardness*

1. INTRODUCTION

Nickel-aluminum bronzes (NABs) are copper-based alloys containing 8–13% aluminum and 3–6% nickel, often with small amounts of iron, manganese, and other elements added to increase strength and corrosion resistance. NABs are highly valued in marine and industrial applications for their excellent combination of strength, toughness, and corrosion- and wear-resistance [1-4].

Microstructure of NABs is complex and has a significant influence on their mechanical and corrosion-resistant properties. Copper-rich α-phase is the dominant phase, which has a face-centered cubic crystal structure. The α-phase forms the alloy matrix and is relatively soft and ductile. During solidification and subsequent heat treatments, several intermetallic phases known as κ phases precipitate. These κ phases have a high concentration of aluminum, nickel, and iron and occur as small particles that harden the alloy by preventing dislocation movement, thereby improving strength and hardness. Examples of common κ phases include κ_I, κ_{II}, κ_{III}, and κ_{IV}, which differ in composition and morphology. The particle size, morphology, and distribution of these κ phases are highly susceptible to cooling rates and heat treatment conditions. Controlled precipitation of κ phases under proper conditions increases mechanical properties [1, 4-9].

Heat treatment constitutes a critical phase in achieving the maximum properties of the NABs. The alloys are typically solid solution-annealed and quenched rapidly to preserve a supersaturated solid solution. Intermediate-temperature aging treatments subsequently cause precipitation of κ phases. Aging enables precipitates of fine κ phase to develop in a homogeneous distribution within the α matrix. The precipitates increase hardness and strength through a resistance to dislocation flow. Changing the microstructure is possible through control over the heat treatment parameters. The combination of α-phase matrix and highly dispersed κ phases provides optimal wear resistance, toughness, and endurance to mechanical stresses [1, 5, 9].

A low nickel/iron CuAl9Ni2.6Fe3.3 is between the binary and multicomponent alloys in microstructure and mechanical properties. It shows a good combination of ductility with strength

and hardness [10, 11]. But their mechanical properties are lower compared to standard NABs with higher Fe and Ni content. These properties can be improved by heat treatment, which was studied in this paper.

2. EXPERIMENTAL

After weighing the required quantities of copper and alloying elements (aluminum, nickel, and iron), the materials were melted in a flame-fired furnace. The molten alloy was then cast into a mold made up of a mixture of sand and clay. The obtained ingot, with a composition of CuAl9Ni2.6Fe3.3 (in wt.%), was cut using the "Mesotom - Struers" machine on samples for subsequent heat treatment processes. For solution treatment, samples were annealed at 900 °C for 2 h in the hydrogen-reducing atmosphere using a "T 40/600" tube furnace. The specimens were quenched instantly in cold water so that they would have a supersaturated solid solution. Quenched samples were aged in a furnace "Heraeus K 1150/2". Isothermal aging was conducted at 350 °C, 400 °C, and 450 °C, for a period of up to 10 h. In all the stages of heat treatment processes, hardness was tested and microstructure was studied. Hardness was determined using "VEB Leipzig" Vickers hardness tester with an applied load of 15 kg. Microstructural observation was performed by scanning electron microscopy (SEM) on a "Tescan Vega 3LMU" system.

3. RESULTS AND DISCUSSION

In the as-cast condition, the CuAl9Ni2.6Fe3.3 alloy demonstrated a hardness of approximately 150 HV_{15}. After solution treatment at 900 °C followed by rapid quenching, the hardness increased to 176 HV_{15}, indicating the formation of a supersaturated solid solution. The evolution of hardness during isothermal aging at 350 °C, 400 °C, and 450 °C is shown in Fig. 1.

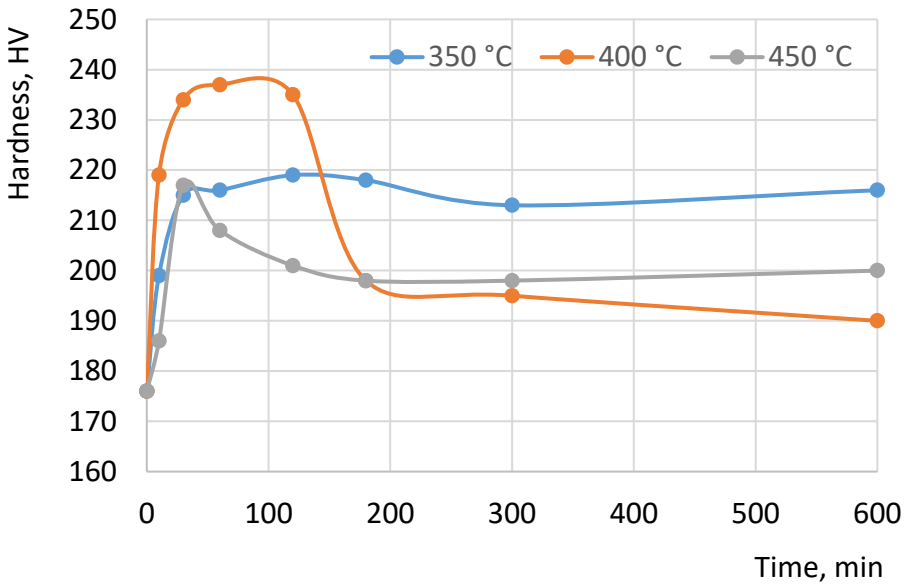

Figure 1. Hardness evolution during isothermal aging at 350 °C, 400 °C, and 450 °C after quenching from 900 °C

Aging at 350 °C led to a gradual increase in hardness with increasing aging duration. The maximum hardness of 219 HV_{15} was recorded after 2 h of aging, representing a significant enhancement compared to the quenched state. Further prolongation of aging up to 10 h did not result in a notable decrease, suggesting the alloy remained within the effective precipitation strengthening range.

The most substantial increase in hardness was observed at 400 °C, where a peak value of 237 HV_{15} was achieved after 1 h of aging. This corresponds to an absolute increase of 61 HV_{15}, or a relative

improvement of approximately 35 % compared to the quenched condition. However, aging durations beyond 2 h resulted in a significant drop in hardness.

At the highest aging temperature of 450 °C, the alloy also exhibited an increase in hardness, reaching a maximum of 217 HV_{15} after only 30 min. However, the overall hardening response at this temperature was less pronounced. Prolonged aging beyond this point led to a decrease in hardness, indicating that the kinetics of overaging were accelerated at this temperature.

It is evident that with increasing aging temperature, the time required to reach peak hardness decreases. The highest overall hardness values were observed at the intermediate temperature of 400 °C, particularly in the aging range of 30 min to 2 h.

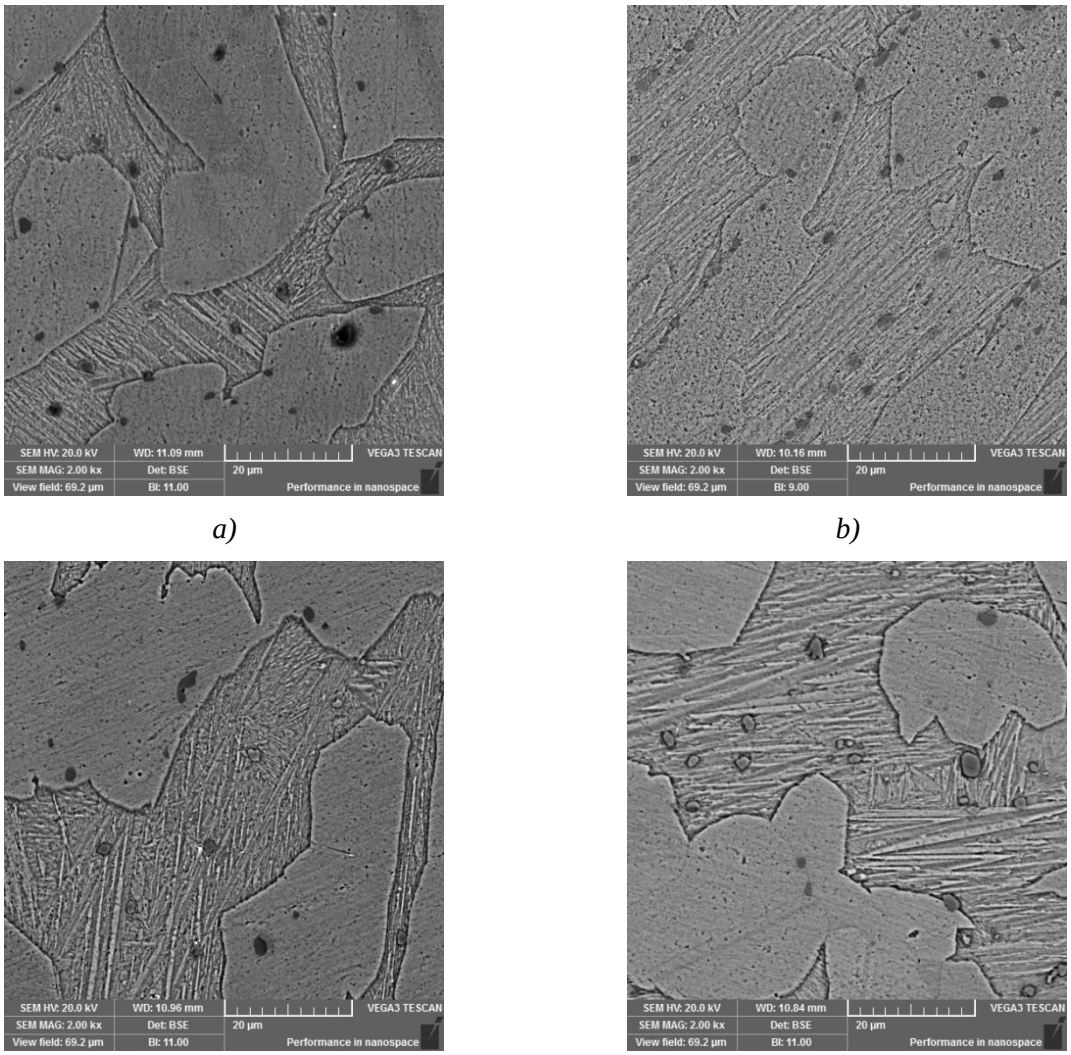

Figure 2. Microstructure of CuAl9Ni2.6Fe3.3 alloy after (a) quenching from 900 °C and (b) aging at 350 °C; (c) aging at 400 °C; (d) aging at 450 °C

Fig. 2a shows the microstructure of the CuAl9Ni2.6Fe3.3 alloy after quenching at 900 °C. A α phase, a needle-like β' phase, as well as precipitates of the ƙ phases are observed. By quenching, the high-temperature β phase transformed into β' martensite. Eutectoid with the κ_{III} phase is not observed, because the κ_{III} phase dissolved at 800 °C, and at 850 °C the fine precipitates of the κ_{IV} phase also dissolved in the α solid solution [6]. Thus, α and β' phases and large spherical precipitates of κ_I and κ_{II} phases are presented in the microstructure.

Similarly, the microstructures of aged alloy (Fig. 2b-d) show the α phase and needles of β' martensite with spherical κ phases. Based on data from the literature, β' martensite does not

transform into the α phase until above 550 °C [8,9]. Aging up to 450 °C of previously quenched samples from 900 °C did not cause significant microscopically visible changes in the size and shape of the main phases under the magnification of 2000x. The κ phases that precipitated during aging are finer (nano size) [12,13] than the precipitates formed during casting, so they are not distinguishable in the microstructure at this magnification.

4. CONCLUSION

After quenching, there was a slight increase in the hardness of the CuAl9Ni2.6Fe3.3 alloy compared to the as-cast state. Aging at all selected temperatures contributed to a significant increase in hardness values. The alloy aged at 400 °C for 1 h achieved the highest hardness values of 237 HV_{15}. With an increase in the aging temperature, there is a decrease in the aging time at which the maximum increase in hardness occurs. After aging at selected temperatures, α solid solution, β' martensite and ƙ phases are still observed in the microstructure, as in the microstructure of the quenched alloy.

ACKNOWLEDGEMENT

The research presented in this paper was done with the financial support of the Ministry of Science, Technological Development and Innovations of the Republic of Serbia, with the funding of the scientific research work at the University of Belgrade, Technical Faculty in Bor, according to the contract with number 451-03-137/2025-03/ 200131.

REFERENCES

[1] G. Lin, H. Wang, Y. Wei, Z. Zhang, K. Zhou, J. Mater. Res., 31 (2016) 3832–3840.
[2] F.A. Anene, V.U. Nwoke, S.M.O. Obiorah, Int. J. Multidiscip. Res. Dev., 2 (6) (2015) 338-341.
[3] K.K. Alanemea, U. J. Anaelea, A. E.Okotetea, Sci. Afr., 12 (2021) e00760.
[4] R. Chen, Z. Liang, W. Zhang, D. Zhang, Z. Luo, Y. Li, Trans. Nonferrous Met. Soc. China, 17 (6) (2007) 1254-1258.
[5] Y. Lv, L. Wang, Y. Han, X. Xu, W. Lu, Mater. Sci. Eng. A., 643 (2015) 17–24.
[6] P. Sláma, J. Dlouhý, M. Kövér, Materials and Technology, 48 (2014) 599–604.
[7] B.P. Pisarek, Arch. Foundry Eng., 11 (3) (2011) 187-194.
[8] M. Moradlou, N. Arab, R. Emadi, M. Meratian, J. Am. Sci., 7 (7) (2011) 717-722.
[9] Y. Lv, M. Hu, L. Wang, X. Xu, Y. Han, W. Lu, J. Mater. Res. 30 (20) (2015) 3041–3048.
[10] C.H. Meigh, Cast and wrought aluminium bronzes properties, processes and structure. McLean: Copper Development Association, 2008.
[11] H. Jiang, X. Zhang, R. Yang, Mater. Today Commun., 38 (2024)108152.
[12] Marković, M. Banković, D. Manasijević, Lj. Balanović, J. Petrović, Mater. Sci. Technol., 2025, doi: 10.1177/02670836241310747
[13] J.M. Da Silva, B.C.E.S. Kurelo, W.R. De Oliveira, A.G.M. Pukasiewicz, G.B. de Souza, S.F. Brunatto, Surf. Topogr.: Metrol. Prop., 10 (2022) 024007.

The 56th International October Conference on Mining and Metallurgy
22-25 October 2025, Bor Lake, Bor, Serbia
www.ioc.tfbor.bg.ac.rs

DOI: 10.5937/IOC25530K

Original scientific paper

MICROSCALE FEATURES OF Pd-Pt AGGREGATES RESULTED FROM ANILINE HYDROGENATION TAR INCINERATING PROCESS

Ferenc Kristály[1,2a], László Farkas[1,2b], Andrea Mihalkó[1c], Bence Tamás[1a], Balázs Szeleczki[2a]

[1] Wanhua-BorsodChem Zrt, Bólyai sq. No 1. 3700 Kazincbarcika, Hungary
[2] University of Miskolc, 3515 Miskolc-Egyetemváros, Hungary
[1a] ferenc.kristaly@borsodchem.eu, ferenc.kristaly@uni-miskolc.hu 0000-0002-0075-5994
[1b] laszlo.farkas@borsodchem.eu 0000-0003-4328-486X
[1c] andrea.mihalko@borsodchem.eu 0000-0002-9061-5599
[1d] bence.tamas@borsodchem.eu 0009-0007-5416-5037
[2a] balazs.szeleczki@uni-miskolc.hu 0009-0005-8822-2322

Abstract
The Ca-carbonate carbon capture filter product of a tar incineration plant captures the degraded and discharged catalyst metals also, which are Pd and Pt. The electron microscopy investigations have revealed a wide range of sizes and morphologies existent for the metal rich particles. Detailed investigations after different disaggregation procedures show the size scale dependent differentiation of metals and oxidic components. The smaller, submicrometric particles tend to be Pt-rich, while with increasing particle sizes aggregates are developed, with increasing Pd and possibly PdO content. The role Fe-oxide is the cementing phase of the Pd-rich larges aggregates.

***Keywords**: recovery, PGE, nanoscale*

1. INTRODUCTION

As a most suitable elimination process of the tar (non-utilizable byproduct) generated in an aniline plant is incineration, with flue gas neutralization system. In the generated ash fraction, removed by the flue gas filter system, the escaping catalyst residue is also captured, mostly as Fe-oxide cemented aggregates but also individual Pd +/- Pt grains. From the viewpoint of metal recovery and recycling, the morphological and aggregation state of catalyst metal components is of primary importance [1]. In order to draw a detailed picture about this issue, scanning electron microscopy and energy dispersive X-ray spectrometry (SEM+EDX) investigations have been carried out beyond bulk compositional analysis. The target of present study is on the microscale characterization of Pd and Pt distribution in the Ca-carbonate and hydroxide matrix, developed by the flue gas treatment process.

2. EXPERIMENTAL

Analytical sample preparation methods were adjusted to the scope of the investigations, the main focus being put on scanning electron microscopy with energy dispersive X-ray spectrometry (SEM+EDX) on samples prepared by water-based separation, magnetic separation and hydrochloric acid dissolution. Each treatment procedure revealed new and useful insights into the micro- and nanostructure of the oxide matrix – metallic particles relations and additional low amount components.

3. RESULTS AND DISCUSSION

XRD analysis (Figure 1) showed calcite (trigonal $CaCO_3$) as the matrix material, with significant amount of residual $Ca(OH)_2$, Ca-sulfates (as anhydrite, bassanite and gypsum) and Ca-Na sulfate as cesanite. Minor components are more numerous, including the Pd, Pt, PtO, maghemite,

aragonite, quartz and sylvine. The residual portlandite was also confirmed by the pH swift to 11 upon distilled water immersion, while the high Ca-carbonate content was supported by the weight loss upon HCl treatment.

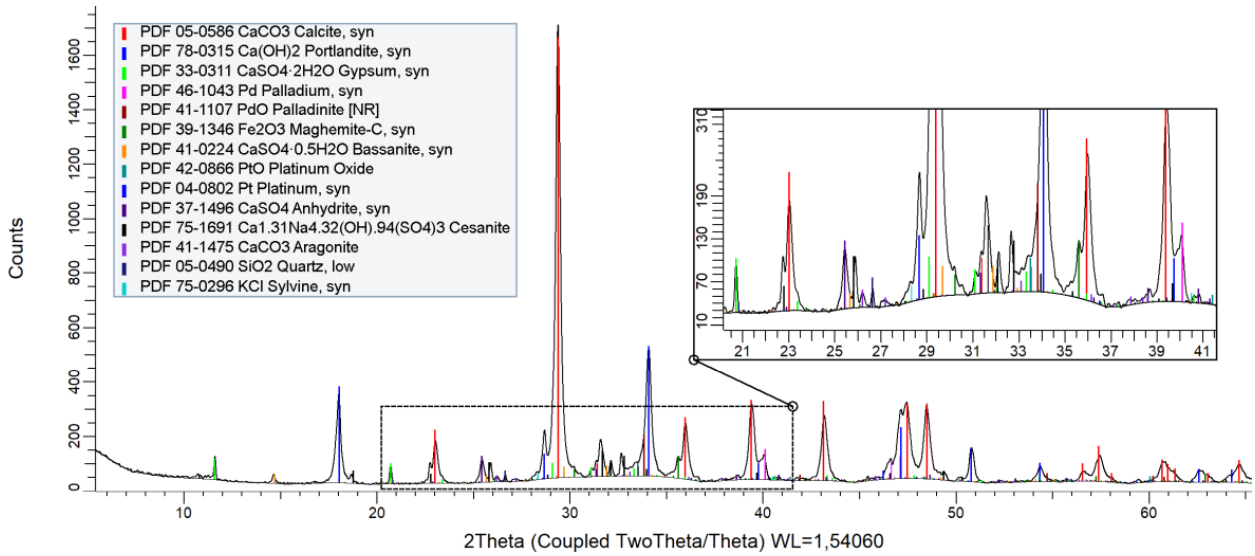

Figure 1. XRD pattern with database entries for the identified crystalline phases.

The relation between maghemite and Pd was clearly defined by X-ray mapping (Figure 2), with the intensity distributions suggesting that higher Pd and Pt concentrations are strongly related to the increase of Fe presence. While only maghemite (γ-Fe_2O_3) was identified as Fe-oxide by XRD, due to the large number of crystalline minor phases we cannot exclude the existence of wuestite (FeO), magnetite (Fe_3O_4) or even hematite (α-Fe_2O_3) – at an insignificant level due to their trace amounts, if present.

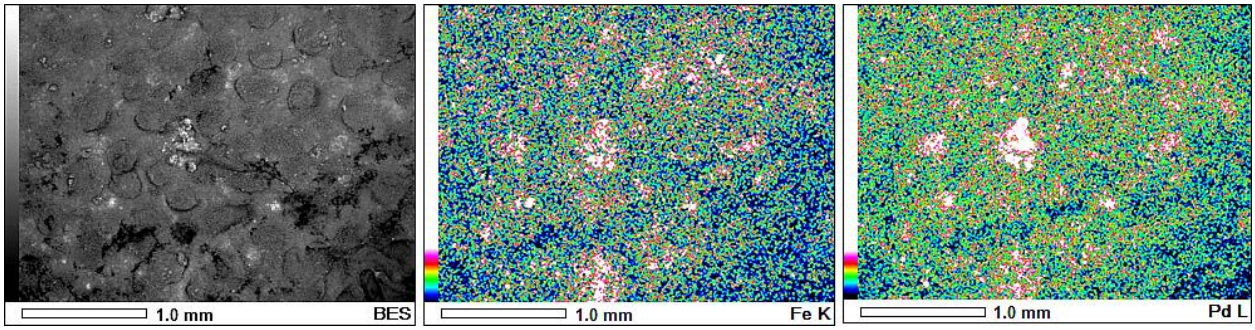

Figure 2. Relation of Fe and Pd agglomerations in the carbonate matrix (colors mark concentration increase towards white)

Microchemical measurements confirm the presence of Pd and Pt enrichment and its relation to Fe-oxide(s), also showing the chemical elements (Table 1) expected upon the XRD results. Distribution of S is mostly homogeneous in the Ca-carbonate matrix, returning weight percentages in the 0.2-0.8 range, thus a finely dispersed submicrometric presence of sulphate phases can be expected. A similar situation is observed for Mg, as a substituting cation for Ca in the crystal lattice of calcite, while Na, Al and Si is in the composition of ceramic or glass trace material, insignificant at these percentages.

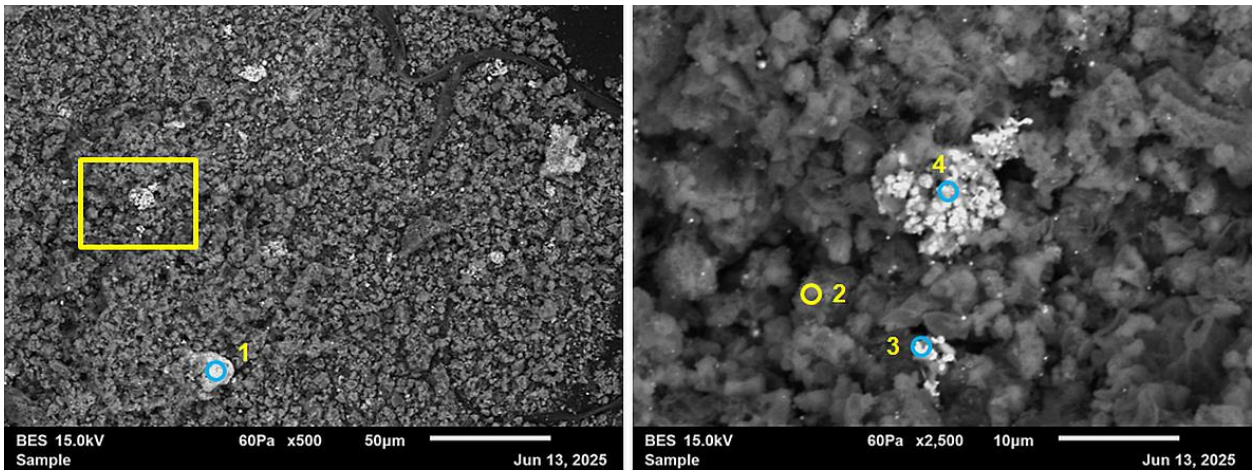

Figure 3. Distribution of Fe-rich grains and spherules in the carbonate matrix, back-scattered electron images, circles mark EDX analysis spots.

The size distribution of Pd and Pt bearing particles has a large range, from submicrometric single particles to different levels of aggregation and agglomeration. The smallest particles are spherical formations, with lower associated Fe-content, although due to the small sizes their precise chemical composition cannot be measured by SEM+EDX. With the increase of aggregate sizes, the Fe and Pd percentage is also increasing (Table 1), indicating the role of Fe-oxide(s) as cementing/binding phase(s).

Table 1. EDX measurements marked on the BES images in Fig 1 (non-standardized weight percents)

	Fe	O	C	Na	Mg	Al	Si	S	Ca	Mn	Zn	Pd	Pt
1	13.47	34.70	22.38	0.20	0.50	0.20	1.04	0.45	13.33			12.13	1.59
2	2.65	48.88	19.08	0.21	0.45	0.10	0.33	0.48	25.70			1.96	0.15
3	19.45	38.79	15.87	0.17	0.34	0.15	0.28	0.28	10.14	0.20		13.16	1.17
4	23.08	32.09	15.19	0.14	0.34	0.16	0.46		9.7	0.37	0.88	15.28	2.30

Examined at higher magnification, two types of Pd-Pt formations can be distinguished: nanoscale spherical particles dispersed individually of aggregated to a scale of several micrometers, and Fe-oxide cemented aggregates (Figure 4). Also in the Fe-oxide matrix nanoscale spherules can be observed, while some part of at least Pd is chemically dispersed, possibly as oxide phase

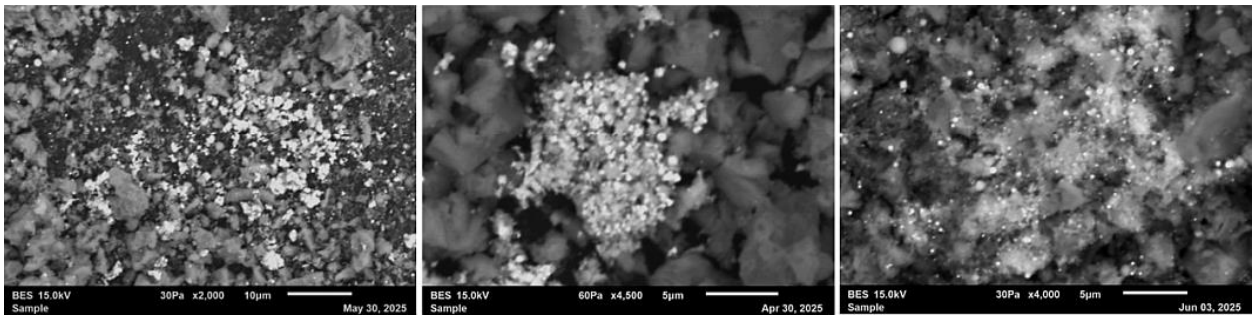

Figure 4. Distribution of Fe-rich grains and spherules in the carbonate matrix, back-scattered electron images

Due to the size of these phases their metallic, oxide or mixed nature cannot be determined, thus an assumption is made that PdO observed by XRD coexists with Pd and is a host for Pt.

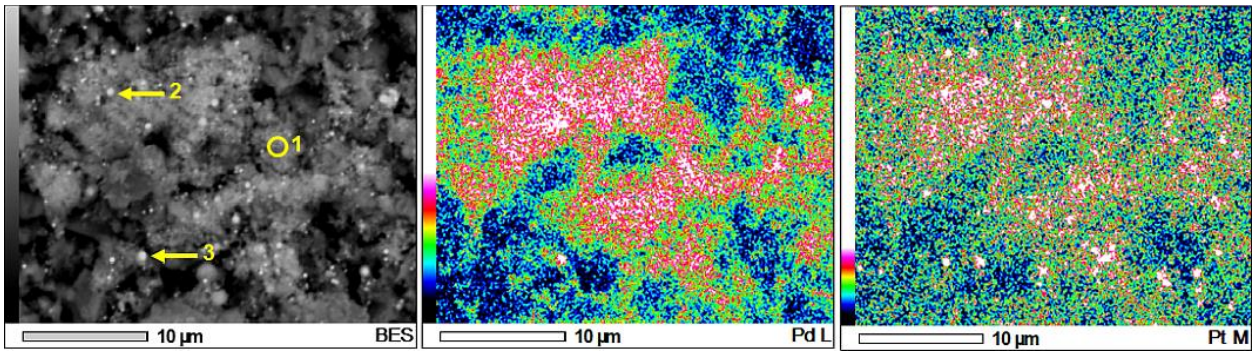

Figure 5. Submicrometric Pt-rich spherules in the Pd-rich Fe-oxide cement (colors mark concentration increase towards white)

High magnification X-ray mapping (Figure 5) brings evidence for the existence of Pt-enriched spherical single particles, supported by EDX analysis also (Table 2), although with limited accuracy since the particles are smaller than the excitation volume of the focused electron beam (cca. 2 µm for the given matrix).

Table 2. EDX measurements marked on the BES images in Fig 5 (non-standardized weight percents)

	P	Fe	K	O	C	Na	Mg	Al	Si	S	Cl	Ca	Pd	Pt
1	0,15	10,52	0,16	42,97	13,39	1,68	0,38	0,07	0,42	3,01	0,43	16,66	8,62	1,55
2	0,14	21,74	0,08	33,38	9,69	2,05	0,3	0,1	0,63	1,67	0,25	6,08	16,05	7,82
3	0,19	26,23	0,07	24,89	6,56	0,55	0,13	0,08	0,24	1,42	0,23	10,51	20,51	8,4

4. CONCLUSIONS

The capture of CO_2 generates a mineralized system in which colloidal and ash-type fragments from the decomposed catalyst are concentrated and captured. The deposition of Fe happens as oxide instead of carbonate, strongly linked to Pd and Pt, suggesting a pre-incineration history of these phases. Nanoscale spherical particles tend to be Pt-rich, while the larger Fe-oxide cemented aggregates accumulate Pd.

Recovery is expected to be complicated in the case of submicrometric particles, probably requiring a precisely adjusted multi-step chemical process [2], since physical concentration and extraction methods are not performing well in the observed particle size range.

ACKNOWLEDGEMENTS

This research has been financially supported by the ARIZO project 2020-1.1.2-PIACI-KFI-2020-00121 financed by the Ministry of Innovation and Technology of Hungary.

REFERENCES

[1] Ş. Sarioğlan, 2013. Platin. Met. Rev., 57 (4) (2013) 289-296.
[2] A. Ding, C. Liu, C. Xiao,. Green Chem., 26 (16) (2024) 9220-9229.

The 56th International October Conference on Mining and Metallurgy
22-25 October 2025, Bor Lake, Bor, Serbia
www.ioc.tfbor.bg.ac.rs

DOI: 10.5937/IOC25534M
Original scientific paper

REINFORCEMENTS IN COMPOSITE MATERIALS

Sandra Milutinović[1a], Ljubiša Obradović[1b], Sanja Petrović[1c], Srđana Magdalinović[1d], Ivana Mikić[1e]

[1] Mining and Metallurgy Institute Bor, Alberta Ajnštajna 1, 19210 Bor, Serbia
[1a] sandra.milutinovic@irmbor.co.rs, 0000-0003-0146-8636
[1b] ljubisa.obradovic@irmbor.co.rs, 0000-0002-6715-4173
[1c] sanja.bugarinovic@irmbor.co.rs, 0000-0001-5197-1614
[1d] srdjana.magdalinovic@irmbor.co.rs, 0000-0002-2916-2850
[1e] ivana.mostarac@irmbor.co.rs, 0009-0006-2592-1916

Abstract
Composite materials are created by combining two or more components with different properties, resulting in a material with improved characteristics. They consist of a matrix, which connects and transfers the load, and a reinforcement, which provides strength, stiffness, and specific functional properties. Unlike alloys, in composites each component retains its identity. Reinforcements play a key role in defining the ultimate performance of composites, so their application is the basis for the development of modern materials in industry, transport, and modern technologies. Therefore, reinforced composites are widely used in the aviation, automotive, and construction industries, energy, medicine and sports.

***Keywords**: composites, materials, reinforcements*

1. COMPOSITE MATERIALS

Composite materials are defined as the combination of two or more materials for the purpose of obtaining unique properties. In composite materials, unlike metal alloys, each material retains its own chemical, physical, and mechanical properties. Composite materials consist of two basic constituents: matrix and reinforcement.

The properties of composite materials depend on both the continuous and discontinuous phases, as well as on the formed border area between them. The discontinuous phase, in addition to the mechanical properties, can modify other properties of the composite (for example, thermal, acoustic, electrical, magnetic, or optical) and is then called an active filler [1].

To have a good understanding of the behavior of composite materials, it is necessary to first have a good understanding of the role of reinforcement, i.e., fibers and matrices in them.

The task of the matrix is to:

- holds the reinforcement together
- protects against external influences
- has an important function in transferring the load to the reinforcement
- gives the external form to the composite
- determines its properties in view of the action of the atmosphere.

The basic functions of reinforcement in composite materials are:

- To bear the mechanical load.
- To ensure rigidity, strength, thermal stability and other structural properties.
- To provide electrical conductivity or electrical insulation depending on the type of fiber, etc.

1.1. Reinforcements in composite materials

Reinforcements in composite materials represent an additional phase in the structure that is incorporated into the matrix to improve its properties. Their basic role is to increase strength, stiffness, and resistance to various external influences, which makes composites more suitable for demanding technical applications. Composites are divided according to the form of reinforcement into three basic groups, and each group can be further divided into smaller groups. The basic division of composites according to the form of reinforcement is [4]:

- composites reinforced with particles
- fiber reinforced composites
- structural composites.

Such reinforcements have their own characteristic applications, although fibers as reinforcements have the most advantages and have the greatest importance.

1.1.1 Reinforcements in composite materials in the form of particles

Particle-reinforced composites consist of a matrix in which particles of different shapes, but approximately the same dimensions in all directions, are placed. The size and volume fraction of the particles significantly influence the properties of these composites. To achieve the necessary reinforcement, the particles should be less than 1μm in diameter and evenly distributed in the matrix. The volume fraction of particles usually amounts to 30-40%. The most famous composites from this group are cermets.

Reinforcement with particles increases the resistance of the material (matrix) to distortion, and this resistance depends on the way the particles are dispersed within the matrix. The particles are mostly oxides, nitrides, carbides, borides. (Shown in table 1)

Table 1.Overview of types of reinforcement in the form of particles and tiles in composite materials with a metal and ceramic matrix [1]

Base element	Carbide	Nitride	Boride	Oxide
Pine	B_4C	BN	-	
Tantalum	TaC		-	
Zirconium	ZrC	ZrN	ZrB_2	ZrO_2
Hafnium	HfC	HfN	-	HfO_2
Aluminum	-	AIN	-	Al_2O_3
Silicon	SiC	Si_3N_4	-	-
Titan	TiC	TIN	TiB_2	-
Chrome	CrC	CrN	CrB	Cr_2O_3
Molybdenum	Mo_2C, MoC	Mo_2N, MoN	Mo_2B, MB	-
Tungsten	W_2C, WC	W_2N, WN	W_2B, WB	-
Thorium				ThO_2

The size of the particles and their distribution is determined by granulometric analysis, using different sedimentation methods or sieving techniques. For use in composite materials, the shape of the particles is very important and they can be in the form of spheres, cubes, prisms, tiles, rollers, cones with more or less regularity in shape, which primarily depends on the conditions of production. Spherical, cuboidal and approximately equiaxial particles are less desirable compared to plate-like, rod-like and needle-like shapes that significantly affect the properties of the composite.

1.1.2 Whiskers as reinforcements in composite materials

Whiskers are monocrystalline discontinuous fibers with extremely high mechanical strength because there are no crystal structure errors such as dislocations in their structure [1.]. Whiskers have a diameter of several micrometers and a length of several millimeters, so their length-to-diameter ratio is very large and varies, which is why they belong to fibrous reinforcements. Whiskers are usually not circular in cross-section and do not have uniform dimensions and

properties, which is perhaps their biggest drawback, and there are no grain boundaries in their structure.

The connection between the whiskers and the matrix is determined by the shape of the whiskers and the size of the boundary surface, which greatly affects the physical and mechanical properties of the composite, they can be in the form of triangles, hexagons, rhombuses, etc.

The modern application of whiskers is focused on the production of composites with metal and ceramic matrices, and due to the high costs of production, the price of whiskers is still high. The incorporation of whiskers in metals improves the stiffness, resistance to creep and wear of composites, while their incorporation in ceramics improves the fracture toughness of ceramic composites.U tabeli 3 dat je pregled koercijalno dostupnih keramičkih viskersa i njihova svojstva.

Table 3.Overview of coercively available ceramic whiskers and their properties [1]

Material	Type	Phase	Manufacturer	Diameter, μm	Density, g/cm^3	Thermal expansion coefficient.x10^{-6}°C^{-1}	Elasticity Modulus GPa	Tensile Strength, GPa	Length, mm
SiC	Silar Sc9	α.	ASM	0,6	3,2	4,7	690	6,89	10-80
SiC	SCW	95% β + 5% α	Tateho Chemical	0,05-0,2	3,21	4,4-4,7	483	20,68	10-40
SiC	Tokama	β	Tokai Chemical	0,1-0,5	3,19		400-700	3,14	50-200
SiC	VLS	β	Los Alamos	5-6			578	8,40	~5000
Si_3N_4	SNW	>97% α	Tateho Chemical	0,2-0,5					50-300
Si_3N_4	UBE SNWB	β	UBE Industries	0,1-2					1-20
NbC	W179		AIM		7,6	6,6	340		
TiC	W444		AIM		4,93	7,4	430		
TiN	W483		AIM		5,22	9,4	250		
TaC	W329		AIM		13,90	6,3	370		
C			Nik Kiso	<1,0					Do 2000
SiO_2	XPVI	Amorfan	J.M. Huber Corp.		2,25	1,9	400		10-20

1.1.3 Reinforcements in composite materials in the form of sheets and tiles

Reinforcements in the form of sheets and tiles are developed and produced primarily because of their lower health risk compared to whiskers because they have a flat surface and less anisotropy. Research and development of the production of this form of reinforcement is still current, and the cheapest reinforcement that has been used for years is clay.

1.1.4 Fibers as reinforcements in composites

Thin flexible materials whose length is many times greater than the transverse dimensions are called fibers. Many fiber-reinforced materials achieve excellent physical and mechanical properties, which is why their application is the most widespread. Fibers differ according to type, length, diameter, orientation, hybridization.

There are different forms in which fibers are used. The first level of form in which fibers occur is an individual fiber (monofilament) with a diameter of up to 10 micrometers. The second level of form is a bundle of fibers (multifilament) which can contain up to several thousand fibers and is therefore marked with 3k, 6k, 12k, etc. The final level is actually a composite material that is created by transforming the textile form of the fibers in the presence of the matrix material using various processes.

Fibers as reinforcements in composite materials are based on:

- small fiber diameter,
- the optimal ratio of fiber length and diameter if they are discontinuous-short fibers i
- high flexibility of fibers.

The small diameter of the fibers allows a greater proportion of the theoretical strength of the material to be achieved than in a larger diameter of the same material because there is less probability of defects or deficiencies in the structure of the material contributing to the reduction of strength. The optimal ratio of the length and diameter of the fibers enables the successful transfer of the external load from the matrix to the fiber of the transboundary surface [2].

The characteristic of fibers to bend easily without breaking is of great importance in the production of composite materials, especially in the production of fabrics used as reinforcement. For high ductility (the ability of the material to deform without breaking) and toughness of the composite as well as better transfer of load from the matrix to the fibers, the composites require a larger interface between the fiber and the matrix. The parameter that defines the size of the surface and volume of the fiber is called the specific area of the fiber and for fibers of circular cross-section it is equal to:$Sv=\frac{2\pi r}{\pi r^2}=\frac{2}{r}=\frac{4}{d}$

If the fibers are used for reinforcement, they must have a high modulus of elasticity, high and uniform tensile strength, satisfactory thermal stability as well as marked flexibility during processing into textile fabrics. Fibers are divided into inorganic and organic. Inorganic fibers can be non-metallic and metallic, and organic carbon and polymer. As for non-metallic fibers, they can be ceramic, glass and mineral and whiskers. And ceramic fibers can be oxide and non-oxide. Organic fibers can be carbon and polymer.

2. CONCLUSION

Composite materials have been around and used for thousands of years. They are created by combining two or more materials with different physical and mechanical properties. The starting materials have mutually different properties, and their combination gives a completely new material that has unique, completely new, different properties compared to the constituent components.

In the search for new composite materials, new combinations between the basic classes of materials are constantly appearing: metals, ceramics and polymers. This approach enables the development of structurally very complex multifunctional materials in which the design of the structure extends from the nano level (nanocomposite materials) to the macro level.

On average, about 10 million tons of composite materials are produced annually, with production increasing by 5-10% every year.

ACKNOWLEDGEMENTS

This work was financially supported by the Ministry of Education, Science and Technological Development of the Republic of Serbia, contract no. 451-03-136/2025-03/ 200052.,

REFERENCES

[1] R. Aleksić, I. Živković, P. Uskoković: "Composite materials", Belgrade, 2015.
[2] I. Živković: Damage analysis of multi-layer composite materials using general fibers, Doctoral dissertation, TMF, Belgrade, 2014.
[3] https://www.fsb.unizg.hr/zavod_za_materiale/download/8f5b1e68977077c0bc5053548b756 28c.pdf, September 1, 2015.
[4] Filetin, T., Kovačićek, F., Indof, J. Properties and application of materials, Faculty of Engineering and Shipbuilding, Zagreb, 2011.

The 56th International October Conference on Mining and Metallurgy
22-25 October 2025, Bor Lake, Bor, Serbia
www.ioc.tfbor.bg.ac.rs

DOI: 10.5937/IOC25538M *Original scientific paper*

INFLUENCE OF TEMPERATURE AND ANNEALING TIME ON CHANGES OF THE MECHANICAL PROPERTIES OF THE CuFe1 ALLOY

Milijana Mitrović[1a], Saša Marjanović[1b], Biserka Trumić[2a], Milan Nedeljković[1c], Jasmina Petrović[1d], Uroš Stamenković[1e]

[1]Technical Faculty Bor, University of Belgrade, V. J. 12, 19210 Bor, Serbia
[2]Mining and Metallurgy Institute Bor, Alberta Ajnštajna 1, 19210 Bor, Serbia
[1a] mmitrovic@tfbor.bg.ac.rs, 0000-0001-7478-2453
[1b] smarjanovic@tfbor.bg.ac.rs, 0000-0001-6930-2232
[1c] mnedeljkovic@tfbor.bg.ac.rs, 0000-0002-7927-1334
[1d] jpetrovic@tfbor.bg.ac.rs, 0000-0002-9131-339X
[1c] ustamenkovic@tfbor.bg.ac.rs, 0000-0002-7579-2159
[2a] biserka.trumic@irmbor.co.rs: 0000-0001-8328-7315

Abstract
This work includes experimental studies of the influence of thermomechanical processing regime on the mechanical properties of CuFe1 alloy, in the form of a wire Ø1,0 mm. The CuFe1 alloy was melted and homogenized in a medium-frequency induction crucible furnace, and casting was performed by the crystallization method above the melt using a casting machine. The resulting cast wire Ø8,0 mm was drawn on a multi-stage drawing machine according to a drawing plan identical to the Cu wire. Interphase annealing was performed at a temperature of 650 °C in a bell furnace with a protective nitrogen atmosphere for 1 hour. Final annealing of the samples was carried out at temperatures of 320, 400, 450, 500, 550, 650 and 800 °C for 1h and 0,5h. By combining temperatures and annealing times, the aim was to achieve a primarily appropriate elongation value (A ≥ 25 %) dictated by the exploitation conditions in which this wire is used. The results showed that the optimal conditions for the required mechanical characteristics of the material, primarily elongation, were achieved at an annealing temperature of 650 °C for a time duration of 0,5h.

***Keywords**: CuFe alloy, plastic processing, mechanical characteristics.*

1. INTRODUCTION

The wider application of Cu in industry is usually explained by its excellent physicochemical properties, electrical and thermal conductivity, corrosion resistance and ability to be processed in a plastic state. Depending on the area of application, pure Cu cannot meet all requirements in terms of mechanical properties, which is a problem for parts that work for a long time at elevated temperatures [1,2]. Therefore, its standard properties are corrected by alloying with appropriate metals, which in two-component or multi-component systems improve the existing properties of Cu [3].

Cu alloys with Fe are usually two- or multi-component alloys, so in addition to Fe they may also contain some common amounts of P and Zn, which are introduced primarily as agents for Cu deoxidation. Wang et al., indicate that the presence of Fe up to 5 wt% positively affects the mechanical properties of Cu alloys [4]. Due to the low solubility of Fe in Cu, an uneven distribution of the Fe phase occurs during the solidification of CuFe alloys, which leads to serious macrosegregation that deteriorates the performance of these alloys [5,6]. Therefore, CuFe alloy with relatively uniform composition and uniform structure, especially alloy with Fe content higher than 5 wt%, is difficult to prepare by traditional casting methods [4].

A higher Fe content has a negative effect on processing by deformation, both in cold and hot conditions, because after processing by deformation, the hardness and brittleness of Cu alloys

increases. For the above reasons, Cu should be alloyed with strictly dosed amounts of Fe, in order to be viewed as a positive admixture that leads to the creation of materials with a very fine-grained structure, which, with properly selected thermomechanical processing regimes, improves the mechanical properties of these alloys.

The aim of this work is to determine the optimal thermomechanical regime for the production of wire from CuFe1 alloy, as well as to determine the optimal interphase annealing temperature. By understanding the dependence of the properties of the CuFe1 alloy on the degree of cold deformation and the time of interphase annealing, i.e. on the temperature of the interphase and final annealing, the manufacturer is enabled to select the optimal regime in order to obtain the predetermined properties of the final product.

2. EXPERIMENTAL

To obtain the CuFe1 alloy, electrolytic Cu and technically pure Fe (ARMCO Fe) were used. The charge calculation was made on a quantity of 100 kg.

Fe was in strip form, while Cu was cut from the cathode of controlled chemical composition in plate form. The melting was carried out in a medium-frequency induction crucible furnace under a layer of charcoal which has role to protect the melt from the influence of oxygen. The addition of Cu was carried out in smaller portions, and after complete melting at a temperature of about 1150 °C, intensive mixing was carried out with a graphite rod. To eliminate the gas present in the melt, a small amount of "logos" degasser was added. The next stage of melting included the addition of Fe, which had been previously heated to a temperature of 250 °C. Fe was added in small portions with intensive stirring until completely dissolved in the melt. Casting was performed by the crystallization method above the melt using a casting machine. The obtained cast wire with a diameter of Ø8,0 mm was drawn on a multi-stage drawing machine with an output of Ø1,0 mm. The draw was carried out according to passages plan identical to the Cu wire. Interphase annealing was performed at a temperature of 650 °C in a bell furnace with a protective nitrogen atmosphere for 1h. After cooling, the wire with a diameter of Ø1,8 mm was drawn to a final dimension of Ø1,0 mm.

The final annealing was performed with the aim of achieving the appropriate condition of the alloy through a combination of temperature and annealing time. The main goal of this research is to achieve primarily the appropriate elongation ($A \geq 25$ %) dictated by the exploitation conditions in which the wire is used.

Since it is known that soft-annealed materials possess good mechanical and physical properties with a fine-grained structure, the aim was to achieve complete recrystallization by combining annealing time and temperature, while avoiding the appearance of coarsening of the structure. The samples were annealed at temperatures of 320, 400, 450, 500, 550, 650 and 800 °C with annealing times of 1h and 0,5h. To fix the structures obtained at these temperatures, the samples were cooled in water, after which mechanical tests were performed.

3. RESULTS AND DISCUSSION

The results of testing the mechanical properties of CuFe1 alloy are given in Tables 1 and 2, and the diagrams of the dependence of mechanical properties on annealing temperature are shown in Figures 1 and 2.

The presence of Fe in the alloy (1 wt%) refines the structure and delays the recrystallization of Cu, which leads to an increase in mechanical properties [7,8]. It is known that grain size, which is a significant factor in defining mechanical properties, depends not only on the degree of deformation, but also on the height of the annealing temperature, annealing time, and the cooling rate after annealing.

Table 1. Values of mechanical properties of CuFe1 alloy after one-hour annealing

No.	Sample state	Annealing time, (h)	T, (°C)	R_m, (MPa)	$R_{p\,0,2}$, (MPa)	A, (%)
1	Hard deformed	/	/	481,0	463,0	2,0
2	annealed	1	320	435,0	427,0	5,0
3	annealed	1	400	402,0	383,0	7,5
4	annealed	1	450	330,0	213,0	21,0
5	annealed	1	500	323,0	206,0	23,5
6	annealed	1	550	317,0	192,0	25,0
7	annealed	1	650	308,0	157,0	28,5
8	annealed	1	800	273,0	150,0	30,0

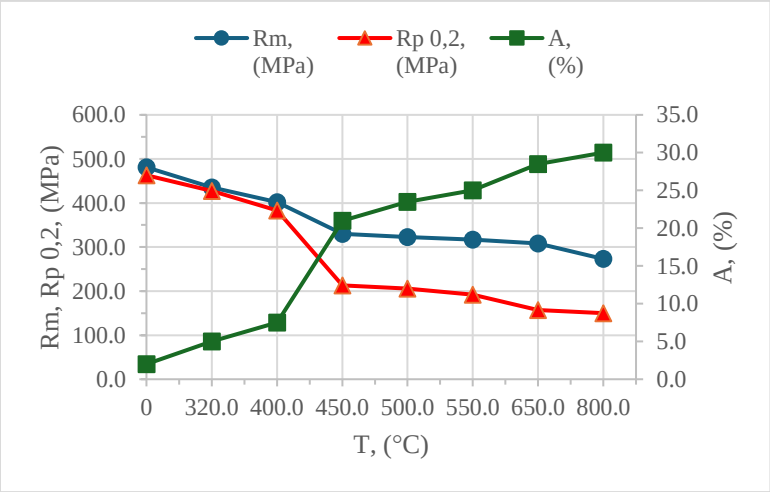

Figure 1. Dependence of the mechanical properties of CuFe1 alloy on temperature, for 1h of annealing

Since the recrystallization temperature of pure copper is 200 °C [2] it is logical that the presence of Fe will increase the recrystallization temperature, therefore the experiment plan included the lowest annealing temperature being 320 °C and the highest 800 °C.

By analyzing the diagram of the dependence of mechanical properties on temperature, at a constant annealing time of 1h (Figure 1), it can be concluded that with increasing annealing temperature, the values for R_m and $R_{p0.2}$ decrease, while the values for A increase. In the initially annealed samples at temperatures of 320 and 400 °C, the values for R_m, $R_{p0.2}$ and A did not change drastically compared to the hard state (cold deformed), which indicates incomplete recrystallization. Complete recrystallization occurred at higher temperatures, which caused a more intense drop in strength and an increase in elongation.

To see how much the annealing time affects the change in mechanical properties, annealing was performed at temperatures of 550, 650 and 800 °C for 0,5h (Table 2). The temperature selection was made based on the previous experiment, and the criterion was that $A \geq 25$ %.

Table 2. Values of mechanical properties of CuFe1 alloy after half an hour annealing

No.	Sample state	Annealing time, (h)	T, (°C)	Rm, (MPa)	$R_{p\,0,2}$, (MPa)	A, (%)
1	hard deformed	/	/	481,0	463,0	2,0
2	annealed	0,5	550	320,0	168,0	25,5
3	annealed	0,5	650	308,0	160,0	28,5
4	annealed	0,5	800	279,0	150,0	30,0

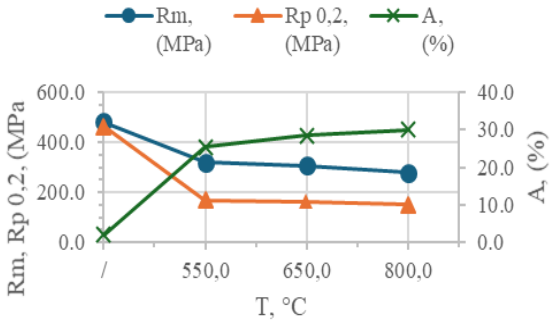

Figure 2. Dependence of mechanical properties of CuFe1 alloy on temperature, for 0,5h of annealing

With both variants of annealing, there is no significant difference in the obtained values for R_m, $R_{p0,2}$ and A, but there is in relation to the relevant data given in the literature for pure copper [9]. This difference is a consequence of the Fe presence, which significantly affects changes in mechanical and structural properties. Since Fe dissolves very little in Cu, it is present in the alloy in the form of dispersed α-Fe particles, and on their size and distribution depend the mechanical properties of the alloy. By increasing the temperature and extending the annealing time, it leads to significant coarsening of this particles, which is why shorter time and optimal annealing temperature are recommended. The results showed that the required elongation was obtained at a temperature of 550 °C and a time of 0,5h, which represents the lower limit. Due to the safety factor in the industrial conditions of exploitation of this alloy, an annealing temperature of 650 °C and an annealing time of 0,5h were adopted as the optimal thermal regime.

4. CONCLUSION

Based on the performed tests and the obtained results, the following can be concluded: At lower annealing temperatures (320 °C and 400 °C), the values of mechanical properties did not change drastically compared to the cold deformed state, which indicates incomplete recrystallization; Complete recrystallization occurred at higher annealing temperatures, which caused a more intense drop in tensile strength (R_m) and yield strength ($R_{p0,2}$), and an increase in elongation (A); Optimal conditions for the required mechanical characteristics of the CuFe1 alloy were achieved at an annealing temperature of 650 °C, in a duration of 0,5 h.

ACKNOWLEDGEMENTS

The research presented in this paper was done with the financial support of the Ministry of Science, Technological Development and Innovation of the Republic of Serbia, with the funding of the scientific research work at the University of Belgrade, Technical Faculty in Bor, according to the contract with registration number 451-03-137/2025-03/200131.

REFERENCES

[1] M. Mitkov, D. Boţić, Z. Vujović, Powder metallurgy, Institute of Nuclear Sciences "Vinca", Belgrade, 1998.
[2] H. Šuman, Metallography, Faculty of Technology and Metallurgy, University of Belgrade, Belgrade, 1989.
[3] K.X. Song, J. Xing, B.H. Tian, P. Liu, Q. Dong, Trans. Nonferrous Met. Soc. China, 15(1) (2005) 139-143.
[4] M. Wang, Y. Jiang, Z. Li, Z. Xiao, S. Gong, W. Qiu, Q. Lei, Mater. Sci. Eng. A, 801 (2021) 140379.
[5] M. Wang, R. Zhang, Z. Xiao, S. Gong, Y.B. Jiang, Z. Li, J. Alloys Compd., 820 (2020) 153323.
[6] C.P. Wang, X.J. Liu, Y. Takaku, I. Ohnuma, R. Kainuma, K. Ishida, Metall. Mater. Trans. A, 35 (2004) 1243−1253.
[7] B. Rouxel, C. Cayron, J. Bornand, P. Sanders, E.R. Logé, Mater. Des., 213 (2022) 110340.
[8] H. Yu, Y. Zeng, R. Hong, Mater. Sci., 3(1) (2021) 10.
[9] D. Guskovic, B. Stankovic, S. Stevic, Modern methods of obtaining copper wires, Technical Faculty in Bor, University of Belgrade, Bor, 1997.

The 56th International October Conference on Mining and Metallurgy
22-25 October 2025, Bor Lake, Bor, Serbia
www.ioc.tfbor.bg.ac.rs

DOI: 10.5937/IOC25542K *Original scientific paper*

LIMITATIONS FOR WIDER USAGE OF GOLD-ALUMINUM ALLOYS BASED ON INTERMETALLIC COMPOUND $Au-Al_2$

Zoran Karastojković[1a], Radiša Perić[2b], Srba Mladenović[3c]

[1] Society for ethics and evaluation in culture and science, 11000 Belgrade, Strahinjića bana 27, Serbia
[2] "Perić&Perić" d.o.o, 12000 Požarevac, Dunavska 114-116, Serbia
[3]Technical faculty Bor, Unuversity of Belgrade, 19210 Bor, VJ 12. Serbia
[1a] zoran.karastojkovic@gmail.com, 0009-0007-0852-1897
[2b] pericradisa@gmail.com, 0009-0002-1067-217X
[3c] smladenovic@tfbor.bg, 0000-0002-3844-7399

Abstract

Gold and golden alloys have had remarkable applications in many fields, through the entire human history. Many alloys were chosen according to their mechanical properties, and good anticorrosive properties, while color was rarely of importance in most industrial materials, except for bronze, stainless steels or nickel alloys. A common limitation for a wide use of golden alloys lies in their high price, while the alloys from Au-Al system should not be an expensive alloy, anyway. One specific advantage comes from one golden alloy which shows an intriguing violet color, as a result of the presence of an intermetallic $AuAl_2$ compound. This alloy, composed of 79%Au and 21%Al, shows good anticorrosive properties, but also critical mechanical properties, namely pronounced brittleness, which is a serious drawback in its use. From this point of view the casting is preferred over shaping by any metal working/deformation method.

Keywords: *$Au-Al_2$ compound, decorative properties, brittleness, casting*

1. INTRODUCTION

Gold and copper are well known metals from the antique times, while aluminum is discovered much later. Gold always was and still is an expensive metal, but copper and aluminum are not, as well as zinc. It is well known that alloying (of gold) is provided not only for lowering the price, but for improving the strength of such alloy, with changing the other desired properties (thermal, electrical, color, density, etc.) [1]. One of the ways to strengthen an alloy is based on the possibility of forming an intermetallic compound, if it is possible in such an alloying system [2,3].
By changing the properties of a metal through the introduction of one or more elements to form an alloy, new fields of application may be expected. Here, some important properties and limitations of an alloy from the Au–Cu–Al system, known for its violet color, will be analyzed.

2. COLORS OF Au-Al ALLOYS

Pure gold is a shining yellow metal, while aluminum is bright white. The yellow or white golden alloys are pretty well known, while other colored golden alloys as blue, green, or black, are less known. One of the less known golden alloy is violet in color, which belongs to the Au-Al system. The phase diagram Au-Cu is well investigated, but this could not be said for Au-Al system. n this system, more than one intermetallic compound can be found (Fig. 1a). Among these compounds, $AuAl_2$ possesses the highest melting temperature, similar to that of gold, and also the highest thermal stability [2]. Not all intermetallic compounds have the same color; for example, the intermetallic compound Au_5Al_2 is white, while $AuAl_2$ is purple. Both compounds are pretty brittle, and they create so called *plague*. The $AuAl_2$ compound forms within a narrow concentration interval (Fig. 1a); see also the diagram in Fig. 1b for the Au–Cu–Al alloying system.

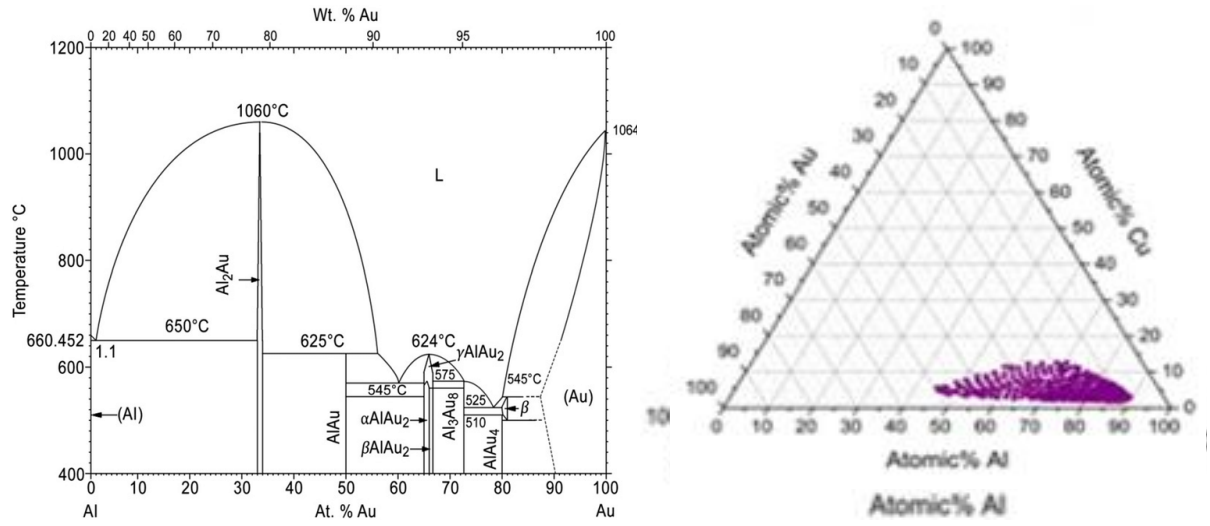

a) b)

Figure 1. (a) Au–Al phase diagram, and (b) concentration region for violet-colored alloys in the Au–Cu–Al system

The mentioned intermetallic compounds are poor electrical conductors, but during solidification they cause the reduction in volume. Such behavior usually creates the gap between gold and aluminum, causing the mechanical failure at the joint [2-7].

3. TWO EXAMPLES OF APPLICATION

Gold–aluminum alloys still do not have significant applications, so they may be used for specific purposes. Two typical examples from electronics and jewelry are presented in Fig. 2.

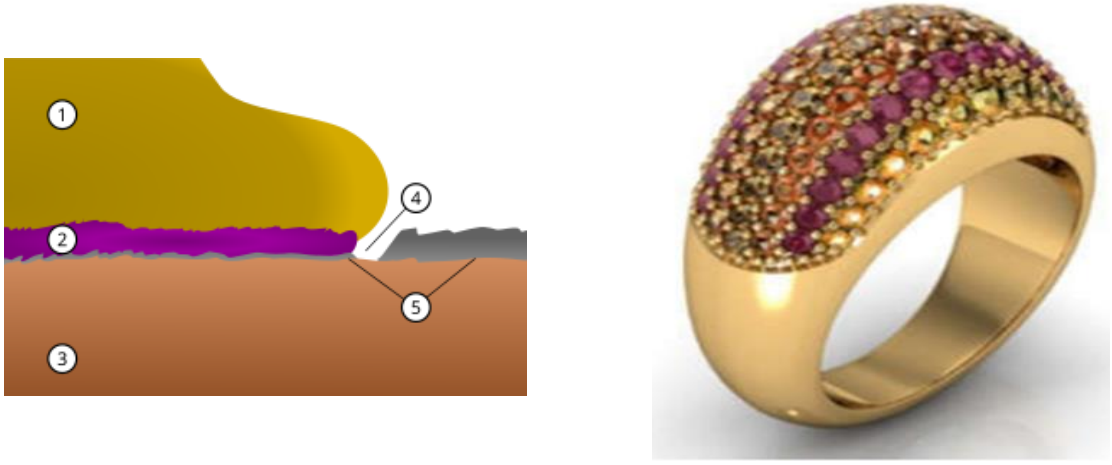

a) b)

Figure 2. Two applications of violet gold alloys: a) in microelectronics for brazing (violet color between gold and aluminum) and b) for decoration purposes in jewelry

**In Fig. 2a): 1- gold wire, 2- purple plague, 3 - copper substrate, 4- gap eroded by wire-bond and 5- aluminum contact*

In the gap (4) between gold (1) and copper (3), a violet alloy (2) is formed by the addition of aluminum (5). This behavior has attracted further investigations into diffusion and atomic-level migration. Mechanisms for alloy strengthening in the Au–Cu system have been studied much more thoroughly [9] than those in the Au–Al system.

From the another point of view, it is practically established that making a jewelry product using only the violet Au-Al alloy is impossible, because this alloy does not possess satisfactory

mechanical properties, so it should be used only as inlay or similar decoration techniques in jewelry.
Decoration at one gold ring, as shown in Fig. 2b), is provided by 3D printing when various gold alloys were applied in different colors. The phenomenon of producing a gap, with reduced strength but increased brittleness at a joint, is known as the *purple/violet plague*. Atomic diffusivity in this case primarily occurs when gold and aluminum thin sheets are in contact. A more detailed study is needed at an academic level, particularly through the Kirkendall effect [3,6], for numerical modeling.

4. VOIDING IN GOLD-ALUMINIUM ALLOY AND DISCUSION

Voids, or voiding, are essential for ensuring the homogeneity of any material, meaning they enable the full properties of a product or structure. Voiding has been well studied in sintered materials but less so during welding or brazing, as is the case with the $AuAl_2$ violet alloy.
For alloys in the Au–Al system, some efforts have been made to investigate atomic migration caused by the Kirkendall effect, which can lead to the formation of voids (or porosity). This effect in the Au–Al system was first observed in microelectronics (during wire bonding), as suggested in Fig. 2a, where the intermetallic compound $AuAl_2$ forms at the contact between the two metals through a diffusion mechanism [5–6]. Such reactions are the subject of study in physical metallurgy [3], where mathematical approaches to diffusivity and related phenomena are Many experiments have shown that the element with the lower melting point—in this case, aluminum—diffuses faster [2,3] than gold. This behavior is not observed only in alloys where solid solutions are formed, such as in brass. If atomic diffusion in an alloy leads to the formation of voids, the strength will be reduced, while brittleness is increased, making mechanical failure of the joint more likely.
Voiding during the formation of the intermetallic compound causes a reduction in volume, possibly creating a gap at the Au–Al interface (see Fig. 2a). It is worth mentioning that the formation of this gap obviously reduces other properties, such as electrical conductivity, specifically at the interface.
Such behavior is observed in alloys composed of the metals Au, Cu, and Al (see Fig. 1a), which crystallize in a face-centered lattice and are all known as ductile metals, meaning metals with high toughness. This example shows that every alloying process, such as the formation of $AuAl_2$, must be carefully monitored, even when soft metals are used. It is worth underlining that these soft metals are not brittle in their pure state.
Similar disintegration in metals was first observed in tin (also known as “tin disease,” tin pest, or tin leprosy), when an allotropic conversion from white to grey tin occurred at lower temperatures [3], accompanied by significant changes in properties. However, the $AuAl_2$ compound is not formed through a solid-state phase transformation mechanism (see Fig. 1a).
Such behavior may influence the production schedule of the violet Au-Al alloy. To avoid undesirable effects, longer heating for atomic diffusion can be minimized by using 3D printing, with the final product shown in Fig. 2b. The 3D welding technique is quite fast, meaning it does not require much time, and the nicely colored golden balls can be successfully joined to the parent metal—of course, only as decorative elements. For the 3D welding method, the desired metal is used in wire form, and there is no need to apply any kind of flux, which is a very common practice in many brazing or soldering technologies. Such fluxing materials (in any form) may be a source of gas bubbles, which can lead to defects in the solidified metal.
The 3D machine in this case utilizes arc welding, possibly with a laser beam [9], based on CAD drawings, enabling the production of versatile, complex, and high-quality metal products—one of which is shown in Fig. 2b. This technique allows easy changes of cladding materials, as seen in the rows of very small balls in various colors in the same figure; however, all of these colored balls were made from the same gold content. The production of the ring shown in Fig. 2b using any casting or classical foundry method [10] would be practically impossible.

5. CONCLUSION

Golden alloys are often produced in various colors, especially for jewelry making. In industry, however, this demand is never of primary interest; price and other useful properties are more important. Alloys from the Au–Al system might be significant due to the low price of aluminum compared to gold. Furthermore, the Au–Cu–Al ternary alloys have not been studied as extensively as the Au–Cu–Zn system.

Intermetallic compounds, in general, may have an important influence on metal properties and, consequently, on their applications. With respect to the properties of the $AuAl_2$ compound, it serves as a good example for studying its attractive violet color but poor brittleness. In this case, the "violet plague" of the Au–Al_2 alloy becomes very important for understanding its limited uses, such as in electronics and jewelry.

The formation of an intermetallic compound from gold and aluminum at the interface, as the violet plague, is shown in Fig. 1a at position (4). This violet plague is, however, the main limitation for the wider use of such an intermetallic compound between gold and aluminum. The violet $AuAl_2$ alloy may be used in jewelry only as an inlay or in similar decorative methods, but not for components or products exposed to tensile or impact loads/stresses.

Given these limitations, the use of this attractive but brittle violet alloy from the Au–Cu–Al system cannot be recommended, especially for structural applications in industry.

REFERENCES

[1] Z. Karastojković, R. Perić, Materijali i postupci obrade u juvelirstvu, in Serbian, CIK Beograd, Beograd, 2017, 28-40.
[2] Gold–aluminium intermetallic - Wikipedia
[3] R.E. Reed-Hill, Modern Physical Metallurgy, D. van Nostrand Co, New York, 1973, p. 386-397.
[4] T. Egami, M. Ojha, D.M. Nicholson, D. Louzgine, N. Chen, A. Inoue, Philos. Mag., 92 (6) 2012 655-665.
[5] R. Becker, J. Mech. Phys. Solids, 35 (5) 1987 577-599.
[6] V.K. Bhatia, F.C. Levey, C.S. Kealley, A. Dowd, M.B. Cortie, Gold Bull., 42 (3) 2009 201-208.
[7] S.Z. Bokštejn, Struktura i svojstva metalličeskih splavov, in Russian, Metallurgija, Moskva 1971, p. 159-182.
[8] N.M. Matveeva, E.V. Kozlov, Uporjadečennie fazi v metalličeskih sistemah, in Rusian, Akademia nauk SSSR, Moskva, 1989, p. 108-139.
[9] N. Rykalin, A. Uglov, I. Zuev, A. Kokora, Laser and electron beam material processing, MIR, Moscow, 1988, p. 358-418.
[10] B. Kočovski, Metalurgija legura obojenih metala II, in Serbian, Tehnički fakultet u Boru, Bor 1999, p. 277-293.

The 56th International October Conference on Mining and Metallurgy
22-25 October 2025, Bor Lake, Bor, Serbia
www.ioc.tfbor.bg.ac.rs

DOI: 10.5937/IOC25546J
Original scientific paper

DEVELOPMENT OF 12,0mm THICK HOT ROLLED STRIP OF S460MC GRADE STEEL IN HBIS SERBIA

Dragan Jeremić[1a], Željko Šutović[1b], Milić Ječmenica[1c], Dragomir Glišić[2a], Stefan Dikić[2b], Nenad Radović[2c]

[1] Quality Assurance, HBIS GROUP Serbia Iron & Steel d.o.o., Bulevar Mihajla Pupina 6, Belgrade, Serbia
[2] Faculty of Technology and Metallurgy, University of Belgrade, Karnegijeva 4, 11000 Belgrade, Serbia
[1a] draganjeremic@hbisserbia.rs, 0009-0009-0187-6577
[1b] ZSutovic@hbisserbia.rs, 0009-0002-3351-8212
[1c] MJecmenica@hbisserbia.rs, 0009-0002-9689-600X
[2a] gile@tmf.bg.ac.rs, 0000-0001-7132-0245
[2b] sdikic@tmf.bg.ac.rs, 0000-0003-2700-0628
[2c] nenrad@tmf.bg.ac.rs, 0000-0002-9521-6159

Abstract
The aim of this paper is to present development of hot rolled coils of microalloyed S460MC grade steel in 12.00x1500 mm dimension in HBIS Serbia hot strip mill, according to European Standard EN 10149-2:2013. The basis for this development was present experience in production of grade S460MC in dimension 6.00-8.00x1500 mm. In the first step, modification of chemical composition required the increase in the content of microalloying elements. Second step included modification of parameters of rolling technology (transfer bar thickness, reheating temperature/time etc.). Finally, after cooling and coiling, hot-rolled strips were tested by means of tensile testing and Charpy impact toughness. The results show that, in all cases, yield strength, ultimate tensile strength, elongation and Charpy impact toughness meet the requirements of EN 10149-2:2013.

Keywords: *microalloyed steel, control rolling, grade S460MC*

1. INTRODUCTION

Microalloyed steels are most commonly used group of structural steels, due to their good combination of strength and toughness, together with good weldability. Their microstructure is characterized by very small ferritic grains with or without a small presence of pearlite, with precipitates within grains. Due to low carbon content and low content of alloying elements, microalloyed steels are characterized by very good weldability. Since microalloyed steels are produced at hot strip mill, obtaining final microstructure does not require quenching and tempering, making them much cheaper in comparison to quenched and tempered steels. Main alloying elements in microalloyed steels are Ti, Nb and V. All these elements share the same feature, that they are prone to intensive precipitation below solubility product. The main task of conventional controlled rolling of microalloyed steels is to obtain the structure consisting of uniform small ferrite grains with fine second phase particles in order to provide good mechanical and technological properties [1-10].

The aim of this work was to produce hot rolled strip of grade S460MC (with guaranteed minimal yield strength of 460 MPa) on the existing equipment and process conditions of HBIS-Serbia, with a target thickness of 12.00 mm and a target width of 1500 mm.

2. EXPERIMENTAL

Chemical composition and mechanical properties must comply with European standard EN10149-2:2013 [11] – selected data are extracted and given in Tables 1 and 2. The basis for this development was present experience in production of grade S460MC 6.00-8.00 mm thick hot strip.

Table 1. Chemical composition of the ladle analysis for thermomechanically rolled S460MC steel

Grade	C max	Si max*	Mn max	P max	S max	Al min	Nb max	V max	Ti max	(Nb+V+T)max
S460MC	0.12	0.50	1.60	0.025	0.015	0.015	0.09	0.20	0.15	0.22

* Suitability for hot-deep zinc-coating: Category A: Si≤0.03% and Si+2,5P≤0.090; Category B: 0.14%≤ Si ≤0.25% and; Category D: 0.25%< Si ≤0.35%.

Table 2. Mechanical properties for thermomechanically rolled S460MC steel

Grade	ReH min, [MPa]	Rm min, [MPa]	Rm max, [MPa]	A min (H≥3,0 mm), %	Bending at 180° min	KV_2 at -20°C min
S460MC	460	520	670	14	1 x t	40

Tensile Test - Longitudinal test specimen; Bending Test - Transversal test specimen; Impact Test - Longitudinal test specimen

In order to provide strength of 460MPa, it is necessary to increase the content of alloying elements, i.e Nb, V and Mn, due to slower cooling of thick cross-sections. Also, in order to obtain homogenous solid solution before roughing rolling, increased content of alloying elements requires higher slab soaking temperature and longer total slab reheating time. Therefore, starting Manufacturing Procedure Specification (MPS) for 6.00-8.00 mm thick S460MC hot-rolled strips (KW39), was modified, for 12.00 mm (KW54) thicknesses, and given in Table 3.

Table 3. MPS for S460MC hot-rolled strips with different thickness

PARAMETER	UNIT	KW39		KW54	
		min.	max.	min.	max.
H_{ST}	[wt.%]	6.00	8.00	10.01	12.00
C	[wt.%]	0.066	0.094	0.075	0.095
Mn	[wt.%]	1.195	1.405	1.346	1.505
Si	[wt.%]	-	0.030	0.146	0.254
Al	[wt.%]	0.020	0.050	0.020	0.045
N	[wt.%]	0.0066	0.0094	0.0070	0.0095
Nb	[wt.%]	0.040	0.050	0.045	0.055
Ti	[wt.%]	0.010	0.015	0.010	0.015
V	[wt.%]	0.045	0.055	0.060	0.070
T_{SS}	[°C]	1230	1240	1230	1250
t_{RH}	[min]	210		230	
T_{TB}	[°C]	1040	1060	1040	1060
H_{TB}	[mm]	32	37	37	39
T_{FRT}	[°C]	830	850	830	850
T_{CT}	[°C]	580	620	580	620

Where:
H_S, B_S are : specified thickness and width of hot-rolled strip, respectively
T_{SS} : slab soaking temperature
t_{RH}: total slab reheating time
T_{TB}: transfer bar temperature, measured at the end of roughing mill
H_{TB} : transfer bar thickness, measured at the end of roughing mill
T_{FRT} : finish rolling temperature, measured at 12.5 m from the last finishing mill stand
T_{CT} :coiling temperature, measured at a distance of 28 m in front the downcoiler
Mechanical properties of Hot strip were tested by means of uniaxial testing and Charpy impact testing.

3. RESULTS AND DISCUSSION

Actual chemical composition of steel and actual parameters of hot rolling are given in Tables 4 and 5, respectively.

Table 4. Actual chemical composition of casted KW54 slabs

	C	Si	Mn	P	S	Al	Nb	Ti	V	N	Ca
avg.	0,086	0,191	1,465	0,012	0,0044	0,038	0,047	0,013	0,066	0,0076	0,0028

Table 5. Actual parameters of hot rolling of KW54 slabs

	T_{SL}	t_{RH}	T_{TB}	H_{TB}	T_{FRT}	STD $_{FRT}$	T_{CT}	STD T_{CT}
avg.	1219	261	1039	37	846	14	602	30

The chemical composition is in general agreement with designed values. Contents of Nb and V were targeted to middle of the interval between minimum and maximum values. Hot rolling parameters were also within designed range.

Tensile properties. Values of Yield Strength (YS), Ultimate tensile strength (UTS) are shown in Figure 1a while elongation values are presented in Figure 1b.

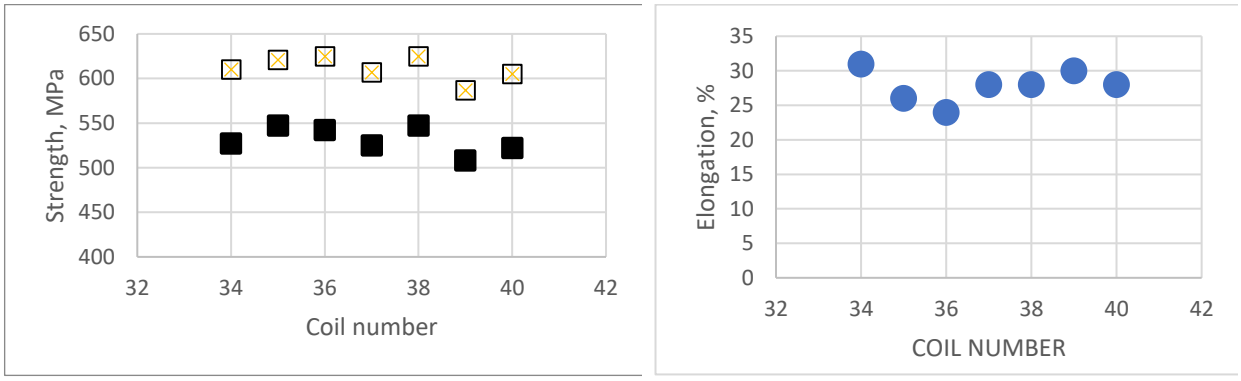

(a) (b)

Figure 1.Mechanical properties of hot strip: (a) Strength - YS-closed symbols: UTS – open symbols; (b) Elongation

In all hot strips, obtained values for Yield Strength, Ultimate tensile strength and elongation for 12.0 mm are in agreement with values required by EN10149-2:2013 [11].

Impact toughness. Measured values are presented in Figure 2. Results of impact toughness are much higher than required 40 J at -20 °C, showing small scatter.

It should be pointed out that a different thickness of hot strip requires mandatory modification of chemical composition. The cooling from F_{RT} to T_{CT} of 6 mm strip is much faster than cooling of 12 mm strip, leading to a higher driving force for ferrite nucleation and smaller ferritic grain. On the other hand, slower cooling in 12.00 mm strip can't produce grain size as small as in 6.00 mm thick strip. One of the limitations is the capacity of the cooling section in Hot strip mill, i.e. present cooling rate is considered to be ultimate cooling rate [13]. Therefore, it is necessary to compensate driving force by additional increase in content of alloying elements to more efficiently suppress recrystallization [1-3,9,10]. Consequently, increased presence of alloying elements, requires increase both of soaking temperature in reheating furnace and time for soaking, in order to provide dissolution of all particles that contains V and Nb [1-3,9]. Detailed results with all measured and monitored values are available in [12]. The parameters that are to be optimized are related to rolling forces in all stands (temperature and thickness of transfer bar etc).

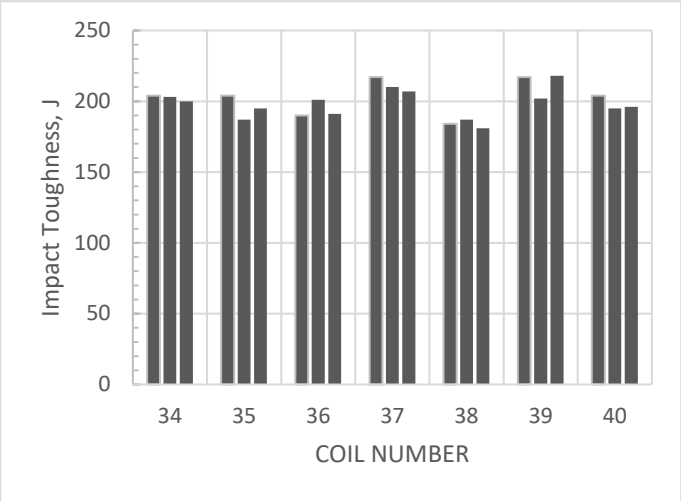

Figure 2. Impact toughness of hot strips

4. CONCLUSIONS

- S460MC grade microalloyed steel was developed successfully in HBIS Serbia Hot Strip Mill, in 12.00 mm thickness.
- All mechanical properties are above required level.
- In future work, rolling forces are to be optimized.

ACKNOWLEDGEMENT

This work was funded by HBIS Co, Shijiazhuang, China through Contract No 449-2025. Authors greatly acknowledge the cooperation with colleagues from HBIS Serbia Hot Strip Mill.

REFERENCES

[1] T. Gladman, Physical Metallurgy of Microalloyed Steels, IOM London (1997).
[2] Microalloying 75, Proceedings of the Int.Conf, Union Carbide, New York (1975).
[3] M.Sellars, The Physical Metallurgy of Hot Working, The Metals Society, London (1980) 3-14.
[4] N.Yurioka, Science and Technology of Welding and Joining in the 21th Century and Prospectives toward the 21th Century, Document IIW IX-1963-2000 (2000) 1-10.
[5] B. De Meester, ISIJ International, 37 (1997) 537-551.
[6] W.Roberts, Deformation, Processing and Structure, ed.by G.Krauss, ASM, Metals Park, (1984) 111.
[7] D.Q.Bai et al., Processing, Microstructure and Properties of Microalloyed and Other Low Alloy Steels, ed by A.J.DeArdo, TMS, Warrendale, (1991) 165
[8] N.Radovic, Dj.Drobnjak, ISIJ International, 39 (1999) 575.
[9] N.Radović, G.Vukićević, D.Jeremić, Dj.Drobnjak, J. Mater. Process. Technol., 172 (2001) B.9.1-10.
[10] G.Vukicevic, N.Radovic, D.Jeremic, Dj. Drobnjak, Mathematical modelling of mechanical properties of microalloyed hot strip, Proceedings of the Int.Conf on Thermomechanical Processing: Mechanics, Microstructure & Control, Eds. E.J.Palmiere, M.Mahfouf and J.Beynon, 23-26 June 2002 Sheffield , University of Sheffield, (2002) 413-417
[11] EUROPEAN STANDARD EN 10149-2:2013, ICS 77.140.50, CEN-CENELEC Management Centre: Avenue Marnix 17, B-1000 Brussels (2013).
[12] D. Jeremić et al, Production of Hot-Rolled Coils in S460MC-En 10149-2:2013 Grade Internal Report, HBIS Group Serbia Iron & Steel Beograd d.o.o., Quality Assurance Department, (2025).
[13] G.Vukićević et al., Capability of hbis serbia global grades production, Internal document of HBIS GROUP Serbia Iron & Steel d.o.o. Beograd (2023).

Technology and Energy

The 56th International October Conference on Mining and Metallurgy
22-25 October 2025, Bor Lake, Bor, Serbia
www.ioc.tfbor.bg.ac.rs

DOI: 10.5937/IOC25552G Original scientific paper

DECAY TIME DETERMINATION FROM LUMINESCENCE EMISSIONS OF Eu^{3+} DOPED Y_2O_3 POWDER

Margarita García-Hernández[1,2a], Alejandro Cruz-Ramírez[2b], Ángel de Jesús Morales-Ramírez[3a], José Enrique Sanchez-Vite[3b], Teresita del Refugio Jiménez-Romero[3c]

[1] CECyT 16, Instituto Politécnico Nacional, DESCTI, San Agustín Tlaxiaca, 42162, Hidalgo, México
[2] UPIIH, Instituto Politécnico Nacional, DESCTI, San Agustín Tlaxiaca, 42162, Hidalgo, México
[3] ESIQIE, Instituto Politécnico Nacional, UPALM, 07738, Ciudad de México, México
[1,2a] margarciah@ipn.mx, 0000-0002-3850-3901
[2b] alcruzr@ipn.mx, 0000-0002-0972-596X
[3a] amoralesra@ipn.mx, 0000-0002-5143-2626
[3b] jsanchezv2105@alumno.ipn.mx, 0009-0006-5001-0495
[3c] tjimenezr@ipn.mx, 0009-0003-8012-6817

Abstract

Yttrium oxide (Y_2O_3) is a phosphor material, since as an inorganic solid compound that can absorb energy and transfer it to a luminescent center and subsequently emit it as light when the excitation source is removed. The emitted color intensity and decay time of the emission of the phosphor depend strongly on the structure of the host material and the choice of the emission center. The aim of this research is to determine the decay times at different molar concentrations of europium doping ion into yttrium oxide matrix. The experimental methodology involved synthesizing yttrium oxide via the sol-gel method doping at concentrations ranging from 0 to 5 mol % of Eu^{3+}. Upon exposing the experimental matrix to an excitation source of λ = 254 nm, different intensities of red emissions were obtained. These emissions were characterized by emission spectroscopy and luminescent decay times were determined. Based on the results, europium-doped yttrium oxide powder with a cubic structure and decay times ranging from 1632 to 1857 µs is a promising phosphor for applications in fields such as optics and/or biomedicine.

Keywords: *sol-gel, Y2O3, europium, luminescence, decay time*

1. INTRODUCTION

Yttrium oxide (Y_2O_3) is a widely used phosphor in materials science due to its effectiveness as a host matrix for rare earth ions, which introduce new emission bands across various regions of the electromagnetic spectrum [1]. Luminescent materials, or phosphors, are predominantly solid inorganic compounds composed of a host matrix deliberately doped with activator ions capable of absorbing energy and subsequently emitting light once the excitation source is removed [2], [3]. Light emission in phosphor materials is generated from electronic transitions within the solid-state structure. When energy is absorbed, electrons are promoted to higher energy states, and visible light is subsequently emitted as they return to lower energy levels [4]. The emission color and intensity are predominantly influenced by the characteristics of the luminescent center and the crystallographic environment of the host matrix. Europium-doped yttrium oxide (Y_2O_3:Eu^{3+}) is widely recognized as an efficient red-emitting phosphor under ultraviolet excitation [5], [6]. However, the practical application of a phosphor depends not only on its emission intensity but also on its emission duration after the excitation source is removed. For example, in emissive displays, such as mobile phone screens, the decay time must be as short as possible to prevent image retention. Conversely, for illumination devices like LEDs, longer decay times are preferable to ensure consistent light output.

2. EXPERIMENTAL PROCEDURE

2.1 Materials and methods

Yttrium oxide powders were synthetized by sol-gel method following the route proposed by Mellado et. al.[7] 0.001044 mol of yttrium nitrate hexahydrate ($Y(NO_3)_3{\cdot}6H2O$, 99.8 %, Sigma Aldrich), europium nitrate pentahydrate ($EuNO_3)_3{\cdot}5H2O$, 99.9 %, Sigma Aldrich) were dissolved in methyl alcohol (CH_3OH, 99.8 %, Sigma Aldrich) in a molar ratio of $CH_3OH/Y=123$ under vigorous stirring during 15 minutes. Acetylacetone, AcAc; ($C_5H_8O_2$, 99.9 %, Sigma Aldrich) was added into solution in a molar ratio of AcAc/Y= 1:1 to obtain a stable solution of Y_2O_3. Sol was obtained after 15 minutes. Sol was dried in an oven at 100 °C for 24 h. Finally, the xerogel obtained was calcined at 300, 500 and 700 °C for 1 h. Yttrium oxide pure and yttrium oxide doped at 0.5, 1.5, 2.5, 3.5, 4.5 y 5 % mol of europium ions were obtained. The europium ions concentrations were proposed in according of Kumar at al. [8], in their research determine that the maxima luminescent intensity is in 5 % mol of europium.

2.2. Characterizations

Structural characterization for the undoped powder of Y_2O_3 synthetized was carried out in a D8 ADVANCE Bruker diffractometer equipment with CuKα (λ=1.5406 Å) radiation, from 20° to 80° with steps of 0.2°. Luminescent analyses were made in a Fluorescence Spectrophotometer F-700 HITACHI equipped with a 150 W xenon lamp, R955 Hamamatsu photomultiplier tube for visible emissions, and a stigmatic concave diffraction grating (900 lines/mm). All luminescent measurements were performed at room temperature.

3. RESULTS AND DISCUSSION

3.1 Structural studies

Figure 1(a) shows the X-ray diffraction pattern of doped-yttrium oxide powders obtained by sol-gel process after an annealing treatment at 700 °C for 1 h. The diffraction peaks correspond to BCC yttrium oxide with representative planes (211), (222), (400), (440) and (622) in according to crystallographic cubic structure of Y_2O_3 cart ICDD# 41-1105.

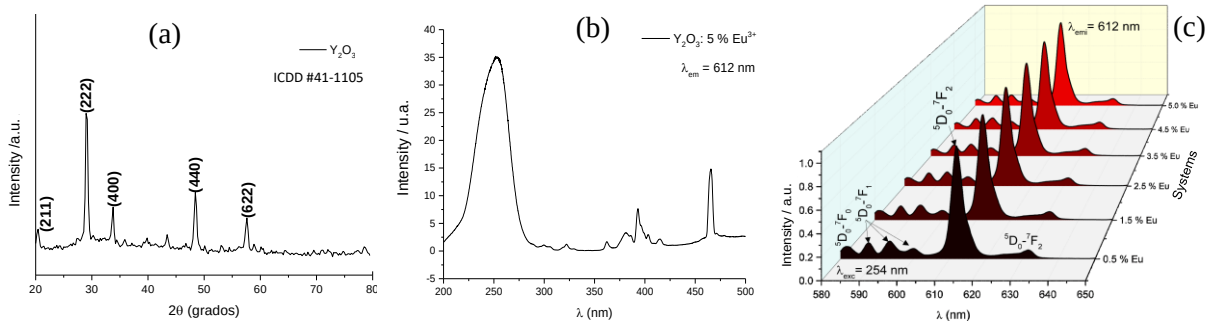

Figure 1. DRX pattern of Y_2O_3 powder heat-treated at 700 °C (a), absorption spectrum of Y_2O_3: 5 mol% Eu^{3+} (b), and emission results of Eu^{3+} doped Y_2O_3 (c).

3.2 Luminescence analyses

Luminescence emissions were studied trough emission spectroscopy excited under UV radiation. The wavelength of excitation was determined by absorption analysis to produce the typical 612 nm line reddish emission of europium ions. The absorption spectra of Y_2O_3: 5 mol % of Eu^{3+} is presented in Figure 1(b). The wide absorption band is observed in 254 nm, corresponding to the so-called Charge transition Band (CTB) which implies that the energy is absorbed by the Y_2O_3 structure and is transferred to the emission centers by the Eu-O bond.

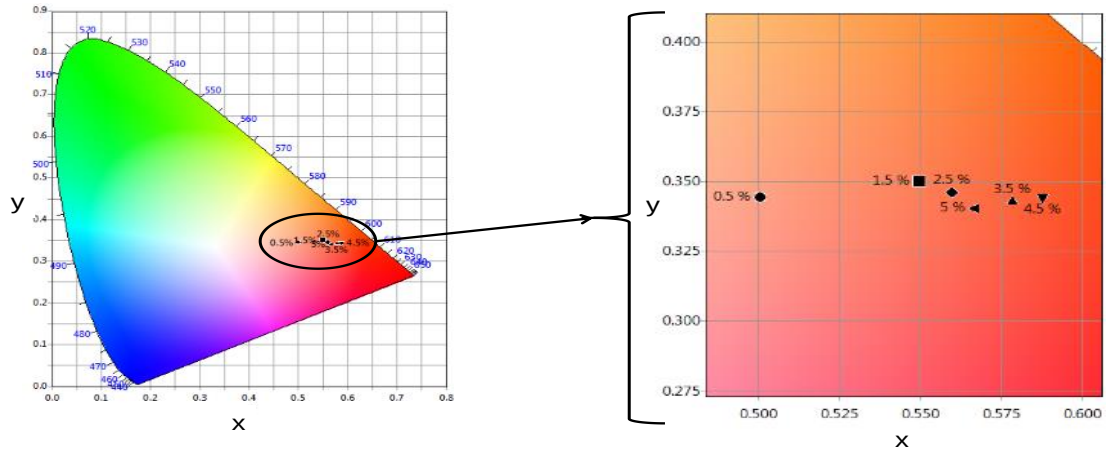

Figure 2. CIE diagram of luminescence red systems excited at λ= 254nm.

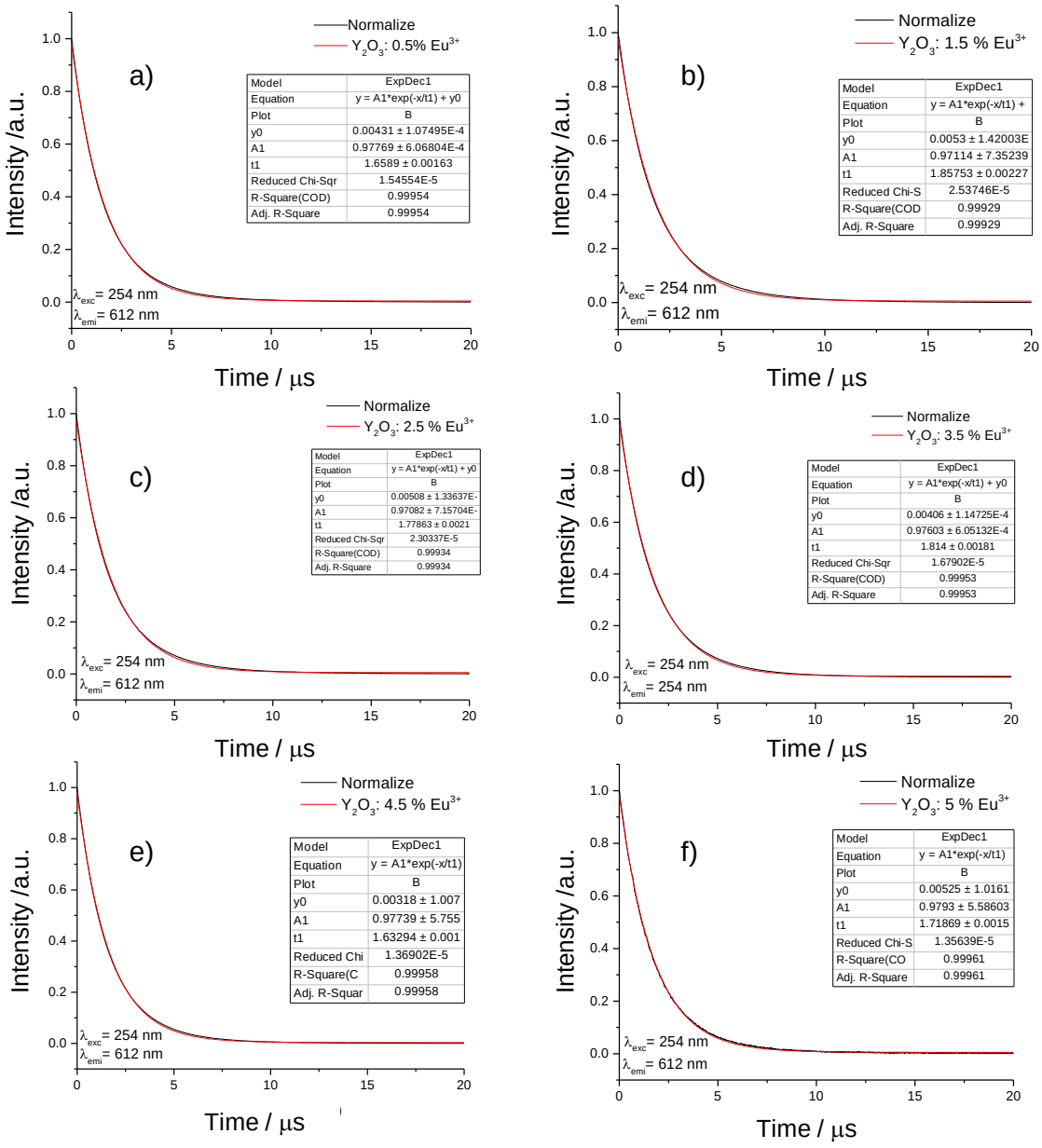

Figure 3. Decay time of the a) 0.5 %; b) 1.5 %; c) 2.5 %; d) 3.5 %; e) 4.5 % and f) 5.0 %mol of europium doped Y_2O_3 systems measurement at room temperature.

Since this the most prominent band, the luminescent measurements were carried out under this wavelength. For this reason, the system of europium doped yttrium oxide powder was excited at 254 nm. In Figure 1(c) emission spectra of europium doped yttrium oxide excited at 254 nm are presented. The doped system at 0.5, 1.5, 2.5, 3.5, 4.5, 5.0 % mol of Eu^{3+} ion presented the characteristic emission lines of Eu^{3+} ion. The emission at 612 is attributed to $^5D_0 \rightarrow {}^7F_2$ transition associated to red region of electromagnetic spectrum [9][10]. In Figure 2 are presented the coordinated of europium doped yttrium oxide system in the CIE diagram. The coordinates were: 0.5006 & 0.3442, 0.5498 & 0.35, 0.5597 & 0.3462, 0.5783 & 0.3429, 0.5876 & 0.3447, 0.5669 & 0.3405 for 0.5, 1.5, 2.5, 3.5. 4.5 and 5.0 %mol of europium in Y_2O_3 powder. Decay time of luminescent system were measurement at λ=612 nm. The obtained values were normalized and adjusted to ExpDec1 model with R>0.99. In Figure 3 are shown the luminescence lifetime for europium doped yttrium oxide systems at different concentration of doping ion excited at λ=254 nm. It´s observed that, as the Eu^{3+} content increases, the life-time also increases, as result of a boost of emission centers, however after 3.5 mol %, the values decrease, due to quenching effects.

4. CONCLUSION

Europium-doped yttrium oxide powders exhibited a body-centered cubic structure and luminescent lifetimes ranging from 1632 to 1857 μs. This is due to their capability to absorb ultraviolet radiation and emit visible light, particularly in the red region of the spectrum. The study of their luminescent behavior under UV excitation at 254 nm demonstrated efficient energy transfer from the Y_2O_3 host lattice to the Eu^{3+} emission centers. The CIE chromatic coordinates confirm the red luminescence, and decay time measurements revealed a strong dependence on europium concentration. The luminescence lifetime increases with Eu^{3+} content up to 3.5 mol %, after which it decreases due to concentration quenching effects. These findings highlight the potential of Y_2O_3:Eu^{3+} as an efficient red-emitting phosphor for advanced technological applications.

ACKNOWLEDGEMENTS

The authors acknowledge IPN and SIP-IPN for 20253472 and 2389 projects for supporting this work. The experimental support of CNMN-IPN in the execution of the presented work is also acknowledged.

REFERENCES

[1] K. Binnemans, Chem. Rev., 109-9 (2009) 4283–4374.
[2] A. Yousif, B.H. Abas, S. Som, N.J. Shivaramu, H.C. Swart, Mater. Res. Bull., 124 (2020) 1-9.
[3] I. Ayoub, U. Mushtaq, G.B. Nair, G. Sundaram, H.C. Swart, V. Kumar, Small., 21-13, (2025) 1-18.
[4] G.S. He, L.S. Tan, Q. Zheng, P.N. Prasad, Chem. Rev. 108 (2008) 1254-1330.
[5] X. Wu, Y. Liang, R. Liu, and Y. Li, Mater. Res. Bull., 45-5 (2010) 594–597.
[6] S. Singh, D. Singh, P. Siwach, I. Gupta, P. Kumar, Appl. Res. 4-1 (2025) 1-18.
[7] R. Mellado-Vázquez, M. García-Hernández, A. López-Marure, P.Y. López-Camacho, A.J. Morales-Ramírez, H.I. Beltrán-Conde, Materials, 7 (2014) 6768-6778.
[8] Y. Kumar, M. Pal, M. Herrera, X. Mathew, Opt. Mater., 60 (2016) 159–168.
[9] J. Petry, R. Komban, C. Gimmler, H. Weller, Nanoscale Adv., 4-3 (2022) 858–864.
[10] C.F. Hernández-Fuentes, M.L. Carrera-Jota, M.G. Hernández, F. Juárez-López, J. Roque-de la Puente, Á. de J. Morales-Ramírez, J. Mol. Struct. , 1322 (2025) 1-9.

The 56th International October Conference on Mining and Metallurgy
22-25 October 2025, Bor Lake, Bor, Serbia
www.ioc.tfbor.bg.ac.rs

DOI: 10.5937/IOC25556P

Original scientific paper

CLARIFICATION OF THE DESCRIPTION OF THE HIGH-TEMPERATURE HEAT CAPACITY OF PHASES WITH WURTZITE AND SPHALERITE STRUCTURES

Valery Pierre Vassiliev [1a,*], Cristopher Stanley [2b]

[1] Lomonosov Moscow State University, Chemistry Department, Moscow 119992, Russia
[2] R.B. Annis School of Engineering, University of Indianapolis, 1400 E Hanna Ave Indianapolis, IN 46227, USA
[1a] valeryvassiliev@yahoo.fr; 0000-0002-7178-512x
[2b] stanleyc@uindy.edu; 0000-0002-0595-3877

Abstract

The description of the experimental data $C_p(T)$ of substances in the solid state was carried out separately for phases with wurtzite (hexagonal) and sphalerite (cubic) structures. The fitting parameters of the multiparameter function (X), where X = {T_o, a, b, A_1, A_2, Θ_1, Θ_2} are different for different structures. The X parameters, in turn, are a function of the atomic number of the fourth group element or half the sum of the atomic numbers of the $A^{III}B^{V}$ or $A^{II}B^{VI}$ binary phases, while the element germanium has a specific point for the X parameters vs. atomic number. In this case, either a breakpoint or an inflection point attributable to germanium is observed for parameter dependencies on Ln(N). The high-temperature coefficient b occupies a special position which, which, within the limits of experimental errors, has the same values for both structural types. The coefficient b has no effect on the low-temperature region of $C_p(T)$.

***Keywords**: optimization, heat capacity, wurtzite, sphalerite*

1. INTRODUCTION, MODEL and RESULTS

Analysis of the coefficients of the multiparameter function [1, 2] carried out for the Debye-Maier-Kelley model $\sigma^2(T_0, X) = \sum_{i=1}^{n}\left(C_p(X) - C_p^{(exp)}(T_i)\right)^2 / n$ (1)

where the independent adjustable parameters (*X*) of the function (1) is

$$X=\{T_0,a,b,A_1, A_2,\Theta_1,\Theta_2\} \text{ with } A_1,A_2\geq 0 \text{ and } A_2 = 1 - A_1$$

Equation 1 is suitable for describing both the heat capacity of phases with the sphalerite and wurtzite structures. At the same time, the coefficient (b), responsible for describing the heat capacity $C_p(T)$ of the high-temperature region for both types of structures, showed that these coefficients do not differ from each other within the limits of experimental errors.

Tables 1 and 2 show the coefficients of the multiparameter function (1). These coefficients' dependence on the natural logarithm of N (Ln(N)) is shown for each coefficient in both types of structures. In this paper, Fig. 1 shows the new values of the coefficients (b). For each value of Ln(N), the coefficient (b) for both types of phases lies within the experimental errors. The other coefficients mentioned remained unchanged. As an illustration, Fig. 2-4 shows the heat capacity graphs $C_p(T)$ for AlN, Si (AlP) and TlN.

Table 1. Coefficients of the multiparameter function (1) sphalerite structure

Phase	Ln(N)	a ±0.003	$b \cdot 10^{-3}$ ±0.1	T_0 ±1	Θ_1 ±1	Θ_2 ±1	A_1 ±0.001	C_{p298} J/mol-at K (±0.02)
Diamond	1.79176	24.943	0.222	1350	1850	1944	0.479	5.89
AlN	2.30259	24.455	1.702	1031	500	1075	0.389	17.38
Si,AlP	2.63906	24.211	2.346	825	341	847	0.361	19.96
GaN	2.94444	24.042	2.792	629	253	695	0.351	21.53
GaP, AlAs	3.13549	23.959	3.021	513	216	617	0.348	22.22
InN	3.33220	23.894	3.226	395	190	537	0.347	22.93
Ge, GaAs	3.46574	23.860	3.34	320	185	483	0.347	23.28
InAs, GaSb	3.71357	24.398	3.261	251	145	384	0.351	24.19
TlN	3.78419	24.570	3.206	232	134	356	0.355	24.45
HgS	3.87120	24.808	3.126	210	121	323	0.360	24.79
Sn	3.91202	24.938	3.084	200	115	307	0.363	24.95
HgSe	4.04305	25.393	2.930	167	96	257	0.374	25.52
NhN	4.09434	25.604	2.860	154	88	237	0.379	25.77
HgTe	4.18965	26.049	2.709	131	75	201	0.390	26.27
Pb	4.40672	27.353	2.201	80	45	121	0.418	27.70
Fl	4.74620	30.37	0.508	3	0.4	0.5	0.475	30.52

Table 2. Coefficients of the multiparameter function (1) wurtzite structure

Phase	Ln(N)	a ±0.003	$b \cdot 10^{-3}$ ±0.1	T_0 ±1	Θ_1 ±1	Θ_2 ±1	A_1 ±0.001	C_{p298} J/mol-at K (±0.02)
BN	1.79176	24.33	0.222	1137	1400	1730	0.400	8.31
AlN	2.30259	22.75	1.702	920	650	1235	0.364	15.07
Si	2.63906	22.54	2.346	777	550	1181	0.373	16.10
GaN	2.94444	22.37	2.792	648	458	1105	0.403	17.38
InN	3.33220	22.18	3.226	480	340	987	0.461	19.15
Ge,	3.46574	22.14	3.34	426	300	940	0.490	19.79
TlN	3.78419	22.45	3.206	324	219	759	0.549	21.47
Sn	3.91202	22.78	3.084	284	188	675	0.577	22.19
NhN	4.09434	23.55	2.860	226	149	551	0.616	23.27
Pb	4.40672	25.95	2.201	127	89	316	0.683	25.92
Fl	4.74620	30.37	0.508	20	43	44	0.75	30.47

The smoothed values of the coefficients b are the same for each of the values of Ln(N) in Tables 1 and 2, regardless of the type of crystal lattice, and are presented in Fig. 1. The values of other coefficients of the multiparameter function (1) vs. Ln(N) can be easily plotted graphically using the data in Tables 1 and 2.

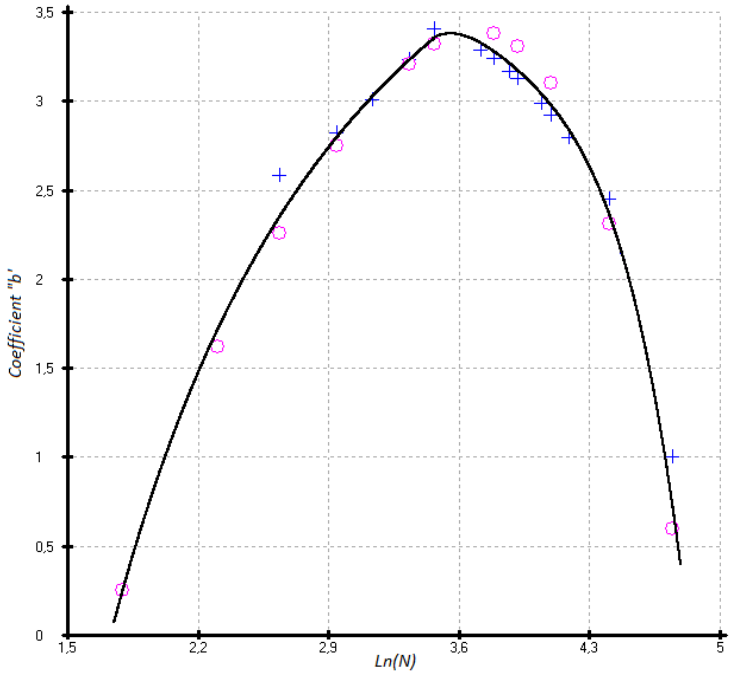

Figure 1. Joint description of coefficients 'b' vs. Ln(N) of the Maier-Kelley equation with wurtzite (o) and sphalerite (+) structures. The maximum of the curve occurs at of Ln(N) of Ge

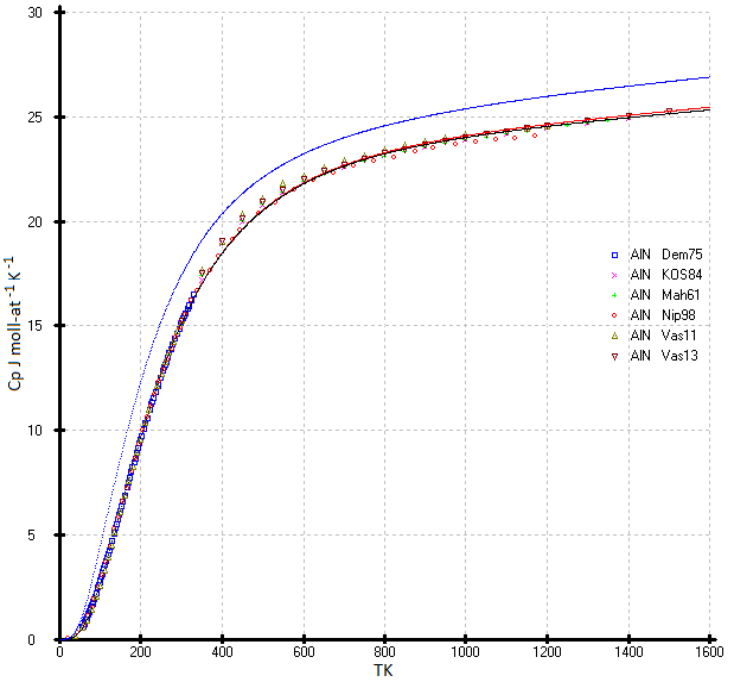

Figure 2. C_p(T)AlN_w [2] black curve, AlN_w [this work] red curve, AlN_{sph} [1] blue curve

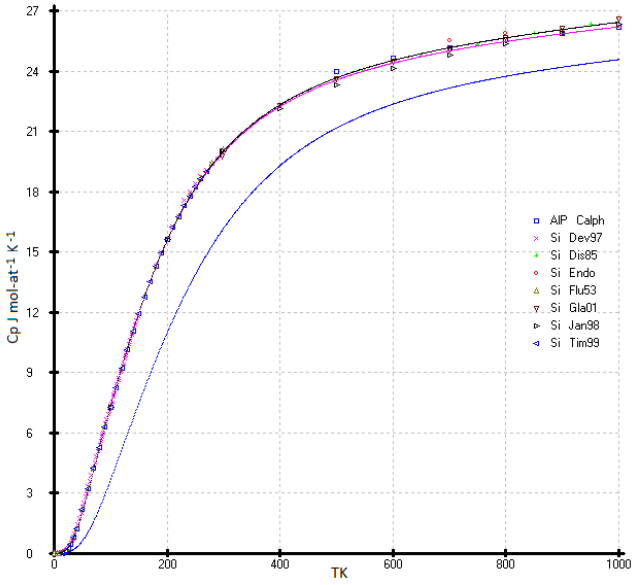

Figure 3. $C_p(T)Si_w$ [2] blue curve, Si_{sph} [this work] red curve, Si_{sph} [1] black curve

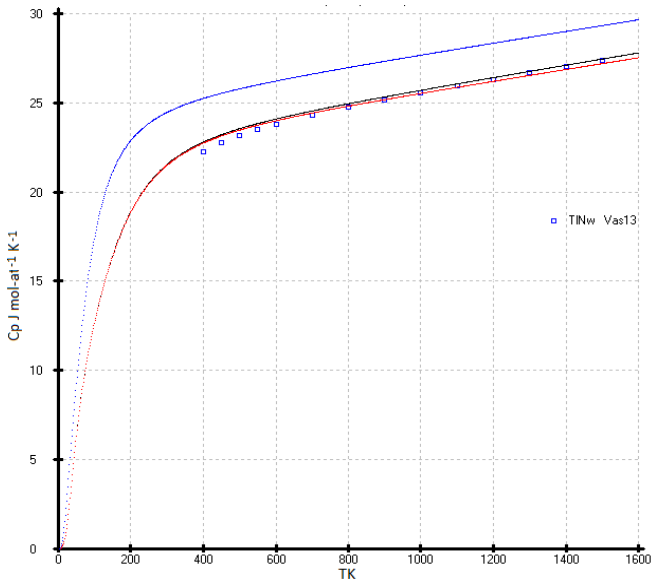

Figure 4. $C_p(T)TlN_w$ [2] black curve, TlN_w [this work] red curve, TlN_{sph} [1] blue curve

The values of heat capacity $C_p(T)$ can be reconstructed based on Tables 1 and 2 and the MATLAB program.

The necessary literature references on the heat capacity of phases with sphalerite and wurtzite structure can be taken from [1-3].

2. CONCLUSION

The data obtained on the heat capacity of phases with the wurtzite and sphalerite structures can be used as reliable reference data.

REFERENCES

[1] V.P. Vassiliev, A.S. Leonov, S.A. Kulinich. CALPHAD, 85 (2024) 102687.
[2] V.P. Vassiliev, C. M. Stanley, Calphad, 89 (2025) 102824.
[3] V. P. Vasilliev, W. Gong, A F Taldrik,S.A. Kulinich. J. Alloys Comp. 552 (2013) 248-254.

The 56th International October Conference on Mining and Metallurgy
22-25 October 2025, Bor Lake, Bor, Serbia
www.ioc.tfbor.bg.ac.rs

DOI: 10.5937/IOC25560J Original scientific paper

PREDICTING CO EMISSIONS USING NOVEL NUMERICAL MODEL FOR PARTICLE IGNITION/COMBUSTION

Rastko Jovanović[1a], Ivan Lazović[1b], Milić Erić[1c], Zoran Marković[1d], Marija Živković[1e]

[1] „VINČA" Institute of Nuclear Sciences - National Institute of the Republic of Serbia, University of Belgrade, M.A. 12-14 11000 Belgrade, Serbia
[1a] virrast@vinca.rs, 0000-0003-0265-2304
[1b] ivan.lazovic@vinca.rs, 0000-0002-3877-5157
[1c] milic@vinca.rs, 0000-0001-6850-3112
[1d] zoda_mark@vinca.rs, 0000-0003-0553-3263
[1e] marijaz@vinca.rs, 0000-0002-3415-5145

Abstract
This work presents development and implementation of sophisticated user defined numerical model for particle ignition/combustion. The proposed model was built in the framework of comprehensive CFD code ANSYS FLUENT. The model is based on structural sub-model for particle devolatilization and realistic mechanism for particle ignition/combustion, which allows for both homogeneous and heterogeneous particle ignition. The user model performance was compared with ANSYS FLUENT standard ignition/combustion models. Models' calculated values of CO mass fraction from semi-industrial furnace were compared against experimentally determined values. The obtained results showed that the advanced user model is superior, in predicting CO mass fractions in furnace near burner zone, compared with ANSYS FLUENT default models. It is expected that the suggested model will be utilized in calculating ignition/combustion behavior of realistic furnaces and boilers.

Keywords: *CFD, devolatilization, ignition, combustion, emissions.*

1. INTRODUCTION

The main aim of this paper is development and implementation of advanced models for pulverized coal combustion and gasification. CFD code ANSYS FLUENT [1] has capability to model solid fuels combustion and gasification. However, significant challenges appear when standard ANSYS FLUENT models are used. Thus, sophisticated combustion/gasification user defined model was suggested. The novel model incorporates all combustion/gasification phases: ignition, devolatilization, gas phase combustion, and char combustion/gasification.

The main subject of this paper is three-dimensional CFD modeling of high-bituminous pulverized coal combustion inside 2.4 MW_t IFRF furnace [2]. Performances of totally three different combustion/gasification models were compared with experimental data. The two models are incorporated inside ANSYS FLUENT by default, and the third is user defined implemented using UDFs written in C programming language [3].

2. MATHEMATICAL MODELING

The main features of the three utilized mathematical models for combustion/gasification are presented in the paragraphs bellow. The main goal of this work was comparison between standard ANSYS FLUENT combustion/gasification models and suggested sophisticated user implemented combustion/gasification model in predicting CO and NO pollutants emissions.

2.1 Eddy dissipation combustion model (EDM)

Model is composed of the following sub-models for different combustion/gasification phases: Single kinetic rate devolatilization model [4]; Gas phase reactions: default ANSYS FLUENT global reaction mechanism composed of totally two reactions was modeled using "Eddy Dissipation" model for reaction rates modeling [5]; Char combustion reactions: single global reaction was modeled using "kinetic-diffusion limited" approach [6, 7].

2.2 Finite rate/Eddy dissipation combustion model (FR/EDM)

Model is composed of the sub-models listed below: Single kinetic rate devolatilization model [4]; Gas phase reactions: ANSYS FLUENT global reaction mechanism was used as in the previous case (EDM model) [5]; Single reaction for char combustion was modeled using "kinetic/diffusion-limited" approach [6,7].

2.3 User Defined Finite rate/Eddy dissipation combustion model (UDF FR/EDM)

Sub-models, implemented using UDFs written in C language [3], for different combustion phases are as follows: Functional group devolatilization model with distributed activation energy model – DAEM [8,9,10]. Gas phase reactions: Semi-global reaction mechanism composed of totally six global reactions was implemented based on "Finite Rate/Eddy Dissipation" model. The reactions were built in ANSYS FLUENT code using UDFs [3]. Char reactions: Totally three global reactions were implemented utilizing UDFs based on "kinetic/diffusion-limited" approach [3]. Particle ignition/combustion mechanism: Default ANSYS FLUENT mechanism, which assumes that char combustion occurs only after particle is completely devolatilized was substituted with novel, user-defined combustion/ignition mechanism. The suggested mechanism allows for all possible means for particle ignition/combustion. That is, it allows that particle combustion can take place before devolatilization is completed. Necessary condition for this to occur is that oxidation of the particle is faster than its devolatilization.

3. EXPERIMENTAL DATA

Experimental data for model validation were taken from work [2]. Measuring axes are located near burner front at distances $z = 0.25\ m$ and $z = 0.85\ m$.

Initial computational grid consisted of 52000 computational cells. This grid was gradually refined in near-burner region until the obtained solution stopped changing with the number of computational cells. Final computational mesh, adopted for all simulations in this work has totally 428000 cells.

4. RESULTS AND DISCUSSION

Logarithmic distribution of CO mass fraction along radial axis at distance $z = 0.25\ m$ is shown in Figure 1. CO distribution obtained using EDM model does not agree well with experimental data. EDM model predicts sharp decrease in CO mass fraction. Based on this, it can be concluded that EDM model is not suited even for qualitative comparison with experimental data.

Similar conclusion can be made in case of FR/EDM model predicted results in comparison with measurements. Namely, FR/EDM model severely underpredicts CO mass fraction values at radial distances up to 0.15 *m* from the burner front.

UDF FR/EDM model calculated results follow experimentally measured data. It is imported to note that the closest agreement between numerical and experimental data obtained at the close distances from the burner front, up to 0.18 *m*. Both curves, model calculated and experimentally measured, predict small increase of CO mass fraction in this zone, although experimental dependence has somewhat lower values.

CO mass fraction logarithmic distribution along radial axis at distance $z = 0.85$ *m* from the burner front is shown in Figure 2.

EDM calculated curve follows experimental trend qualitatively at small distances from the burner front, up to 0.15 *m*. However, model calculated values are significantly higher than experimentally determined. Further down from the burner front EDM calculated values drop sharply to about 10 *ppm* at the radial distance 0.28 *m*. This is in keen contrast with the experimental results.

FR/EDM model, similarly to EDM model, does not show satisfying performance in determining CO mass fraction. Although FR/EDM calculated curve has similar behavior to experimental, FR/EDM values are much higher than experimentally measured. UDF FR/EDM model exhibits significantly better performance in predicting CO mass fraction values compared with two previously described models, EDM and FR/EDM. UDF FR/EDM calculated curve follows trend of experimentally measured data.

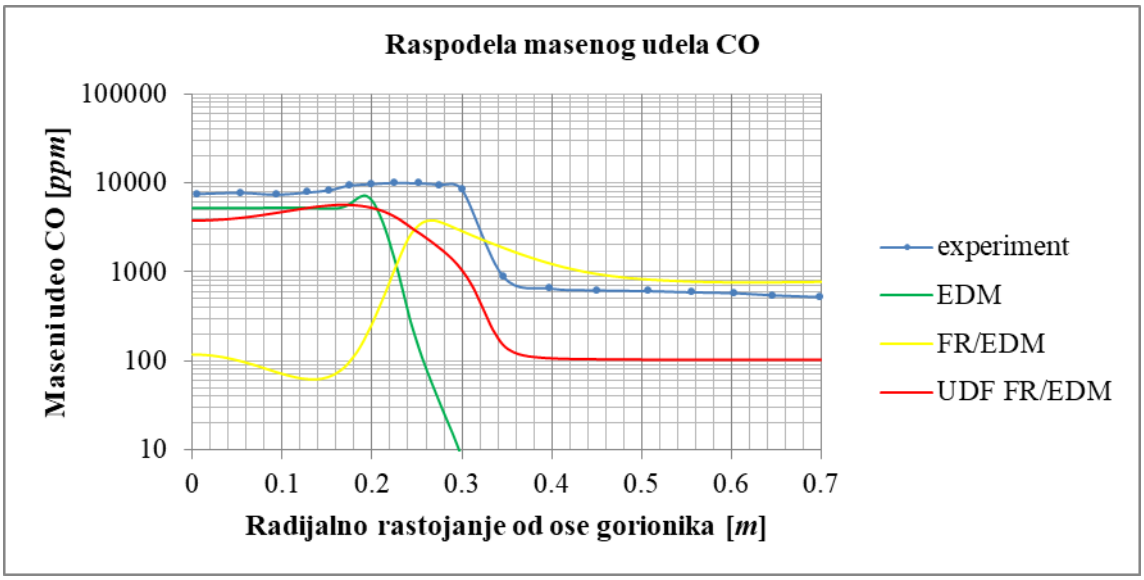

Figure 1. CO mass fraction logarithmic distribution along radial axis at distance z = 0.25 m from the burner front

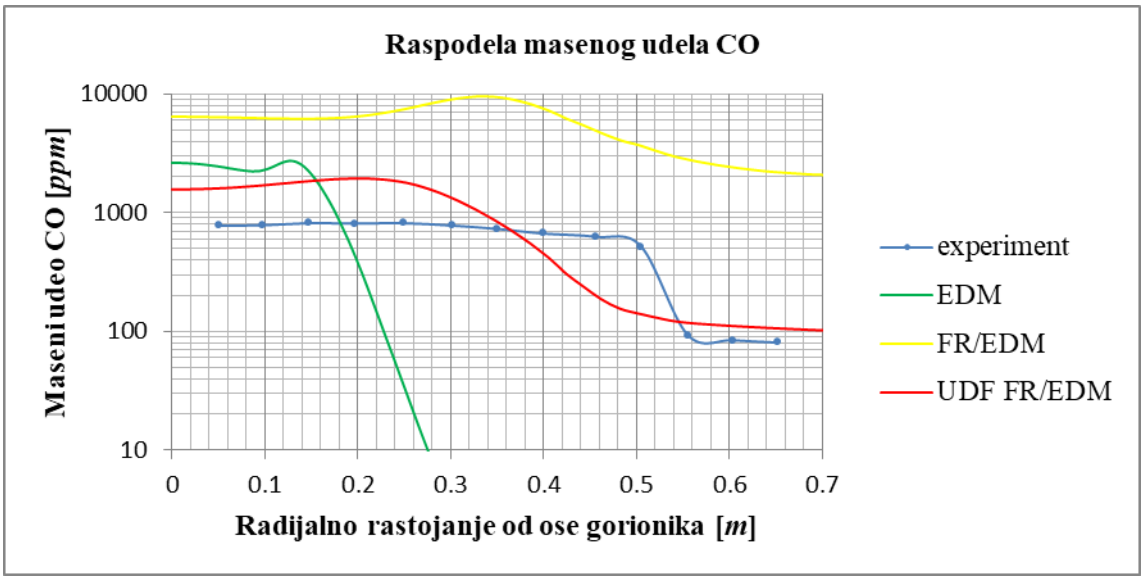

Figure 2. CO mass fraction logarithmic distribution along radial axis at distance z = 0.85 m from the burner front

5. CONCLUSIONS

The following conclusions were drawn based on the performed work: Novel combustion model for particle ignition/combustion was suggested; The proposed model was developed and built in ANSYS FLUENT framework using UDFs; Model performance was tested against experimental data available in scientific literature; It was shown that the user model outperforms standard ANSYS FLUENT ignition/combustion models in predicting CO emissions from experimental furnace; The novel model showed high accuracy in predicting CO emissions in near burner zone; Model accuracy is largely based on built in structural devolatilization and ignition/combustion sub-models; The next step is model utilization is in numerical calculations of combustion in real scale furnaces and boilers.

ACKNOWLEDGEMENTS

The research was funded by the Ministry of Education, Science and Technological Development of the Republic of Serbia.

REFERENCES

[1] Ansys Fluent Theory Guide, ANSYS, Inc., Canonsburg, PA 15317, 2021, p. 222.
[2] F. Peters, R. Weber., Combust. Sci. Technol., 122 (1997) 131-182.
[3] Ansys Fluent Customization Manual, ANSYS, Inc., Canonsburg, PA 15317, 2024.
[4] S. Badzioch, P. G. W. Hawksley., Ind. Eng. Chem. Process Des. Dev., 9 (1970) 521-530.
[5] F. Magnussen, B. H. Hjertager., Proc. Combust. Inst., 16 (1976) 719-729.
[6] M.M. Baum, P. J. Street., Combust. Sci. Technol., 3 (1971), 231-243.
[7] M.A. Field., Combust. Flame, 13 (1969), 237-252.
[8] M.A. Serio, D.G. Hamblen, J. R. Markham, P. R. Solomon., Energy Fuels, 1 (1987) 138-152.
[9] D.B. Anthony, J.B. Howard, H. C. Hottel, H. P. Meissner., Proc. Combust. Inst., 15 (1974), 1303-1317.
[10] S. C. Saxena., Prog. Energy Combust. Sci., 16 (1990), 55-94.

ABBREVIATIONS

CFD	Computational Fluid Dynamics
DAEM	Distributed Activation Energy Model
EDM	Eddy Dissipation Model
FG	Functional Group
FR	Finite Rate
IFRF	International Flame Research Foundation
UDF	User Defined Function

The 56th International October Conference on Mining and Metallurgy
22-25 October 2025, Bor Lake, Bor, Serbia
www.ioc.tfbor.bg.ac.rs

DOI: 10.5937/IOC25564J
Original scientific paper

BIOMASS TO BIOSNG – METHANATION OF SYNGAS FROM BIOMASS GASIFICATION

Marija Jeremić[1a], Andreas Krammer[1b], Markus Lehner[1c]

[1] Chair of Process Technology and Environmental Protection, Montanuniversität Leoben, Franz-Josef Straße 18, 8700 Leoben, Austria
[1a] marija.jeremic@unileoben.ac.at, 0009-0006-9274-9650
[1b] andreas.krammer@unileoben.ac.at, 0000-0002-4987-7044
[1c] markus.lehner@unileoben.ac.at, 0000-0002-9189-0154

Abstract

The conversion of biomass into synthetic natural gas from biogenic sources (bioSNG) via thermochemical routes is a promising approach for integrating renewable energy into existing gas infrastructure. A key step in this pathway is the catalytic methanation of synthesis gas (syngas), typically consisting of H_2, CO and CO_2. This study focuses on the experimental investigation of syngas methanation using a fixed-bed reactor cooled by thermal oil, with the aim of assessing the influence of various process conditions on reactor performance and methane concentration. The experimental setup comprises a tubular reactor operating with a commercial Ni-based catalyst under steady-state conditions. External temperature regulation is achieved via a thermal oil cooling, enabling effective control of the exothermic reaction. A series of experiments were conducted to examine the effects of gas hourly space velocity (GHSV), reactor pressure, and thermal oil temperature on the methanation process. Higher pressures and lower GHSV values resulted in enhanced methane concentrations and more pronounced exothermic behavior, while the thermal oil temperature played a crucial role in heat removal and reactor stability. In addition, the study explored the effects of higher hydrocarbons, specifically ethene (C_2H_4) and the water content in the feed gas, as well as the impact of increased hydrogen/water content on the methanation reaction. To assess the latter, a feed gas mixture containing 15% H_2O, 55% H_2 and the rest of the original gasification product gas was used. These feed gases were again evaluated under varying pressures, GHSV values, and oil temperatures. The presence of ethene was found to positively influence methane formation, leading to higher methane concentration. Furthermore, the H_2/H_2O mixture was shown to improve methane concentration likely due to enhanced hydrogenation reactions, while an increase in water content alone led to reduction in methane formation. These findings provide valuable insights into the complex heat and mass transfer phenomena occurring during catalytic methanation and highlight the importance of feed composition, as well as thermal management, in reactor design and operation. This work contributes to a better understanding of methanation processes in thermally regulated systems and offers data for the further development and optimization of bioSNG production technologies based on biomass gasification.

***Keywords**: biomass gasification, methanation, bioSNG, thermal oil-cooled reactor, catalyst performance*

1. INTRODUCTION

The production of synthetic natural gas (SNG) from biomass is a promising pathway for renewable storage and decarbonization of the gas grid. [1] This process involves several key steps: biomass gasification, gas cleaning, methanation, and final conditioning of the gas for the injection into the natural gas network. [2]

In the first step, biomass is converted to a raw synthesis gas (syngas) through thermal gasification, typically in a dual fluidized bed (DFB) gasification reactor. [3] This raw gas contains a mixture of hydrogen (H_2), carbon monoxide (CO), carbon dioxide (CO_2), methane (CH_4), steam, nitrogen (N_2), as well as impurities such as tars, sulfur compounds, and particulates. [2] The typical composition of the dry product gas following gasification is presented in Table 1.

Table 1. Typical composition of dry product gas after biomass gasification [4]

Component	Volume fraction [vol. %]
H_2	30-45
CO	20-25
CO_2	20-25
CH_4	6-12
N_2	0-1

After extensive gas cleaning to remove contaminants, the syngas is subjected to methanation, where CO and CO_2 react with H_2 to form CH_4 and water. The main reactions involved are [2]:

$$CO + 3H_2 \rightleftarrows CH_4 + H_2O, \Delta Hr^\circ = -206\ \frac{kJ}{mol} \quad (1)$$

$$CO_2 + 4H_2 \rightleftarrows CH_4 + 2H_2O,\ \Delta Hr^\circ = -165\ \frac{kJ}{mol} \quad (2)$$

These reactions are strongly exothermic, making temperature control within the reactor essential to avoid catalyst deactivation and ensure selectivity towards methane [2].

The resulting product gas – often called bioSNG – must meet strict specifications regarding Wobbe index, calorific value, and methane content before injection into the natural gas grid. [5]

A simplified process flow diagram of the related bioSNG production process investigated within the research project BioHeat is shown in Figure 1.

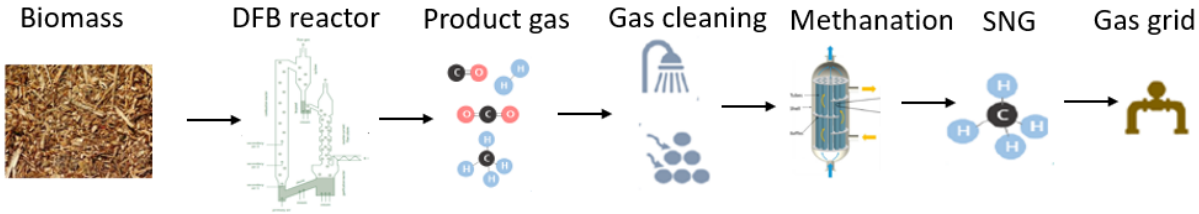

Figure 1. Schematic overview of the bioSNG production process from biomass including dual-fluidized bed gasification and methanation

2. EXPERIMENTAL

This work focuses on the methanation step of the bioSNG process, using a laboratory-scale oil-cooled fixed-bed reactor operated with synthetic gas mixtures that mimic cleaned gasification products. To illustrate the overall setup used for the methanation experiments, a simplified process flow diagram of the test rig is shown in Figure 2. The setup includes the gas supply system, heating and cooling loops, fixed-bed reactors, and analytical equipment for gas composition monitoring. The gas mixture is precisely adjusted using mass flow controllers, allowing for flexible operation under different feed compositions. The thermal oil loop ensures almost isothermal conditions along the reactor wall, which is critical for understanding reaction kinetics and thermal behavior under various operating scenarios. Data acquisition and control are managed through an automated system, enabling reliable and reproducible experimental conditions. This setup provides a robust platform for studying key influences on methane formation and for evaluating potential process optimizations for SNG production.

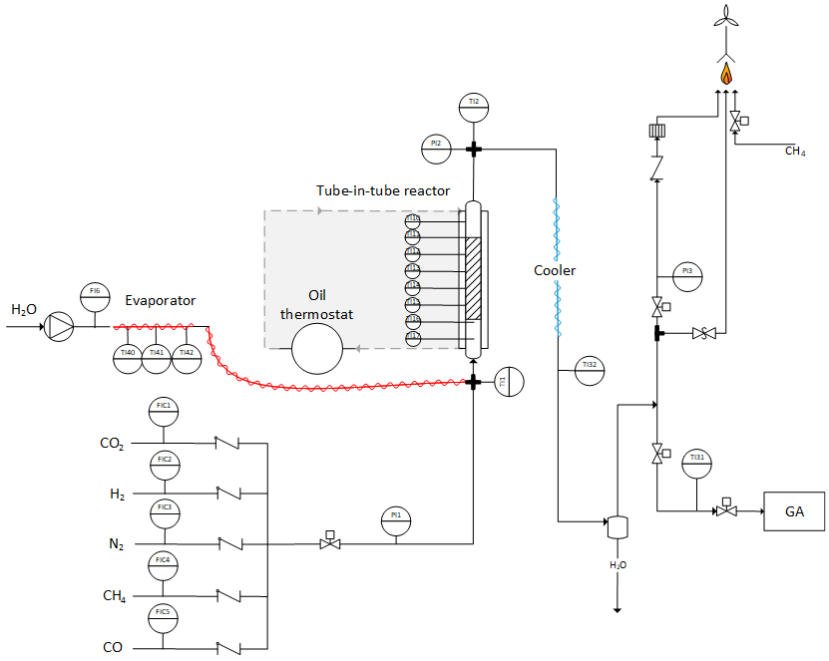

Figure 2. P&I diagram of methanation laboratory-scale pilot plant

The reactor is a single tube stainless steel reactor, filled with a commercial nickel-based catalyst. Eight thermocouple elements are inserted along the reactor axis to monitor the axial temperature profile. The reactor is thermally regulated using a surrounding oil jacket to ensure reactor cooling.

The influence of varying gas hourly space velocity (GHSV), oil temperature, and pressure was investigated at a constant inlet gas composition, as well as under different feed gas types containing water vapor, ethene, or hydrogen/steam mixtures to simulate various operating scenarios.

Gas compositions were selected to match typical outputs of DFB gasifiers after tar and sulfur removal including different amounts of steam or hydrogen addition to counter carbon formation in the reactor. Table 2 summarizes the tested gas compositions in 4 different feed gases.

Table 2. Compositions of tested feed gases (in vol.%)

	50 vol.% H_2O	40 vol.% H_2O	50 vol.% H_2O + ethene	H_2/H_2O mixture
H_2O	50.0	40.0	50.0	15.0
H_2	20.5	24.0	20.5	55.0
CO	12.0	14.5	12.0	12.2
CO_2	11.5	14.0	11.5	11.7
CH_4	6.0	7.5	5.0	6.1
C_2H_4	0.0	0.0	1.0	0.0

3. RESULTS AND DISCUSSION

The experimental investigation focused on how specific components in the feed gas influence methane formation in an oil-cooled fixed-bed methanation reactor. In particular, the addition of higher hydrocarbons – specifically ethene (C_2H_4) – was found to significantly enhance methane production. As illustrated in Figure 3, introducing C_2H_4 into the feed led to a pronounced increase in CH_4 concentration, especially at lower gas hourly space velocities (GHSV). This behavior can be attributed to the rapid and highly exothermic hydrogenation of ethene, which not only boosts local reaction rates but also raises the reactor temperature. The elevated temperatures in turn promote CO and CO_2 methanation, contributing further to the overall methane production.

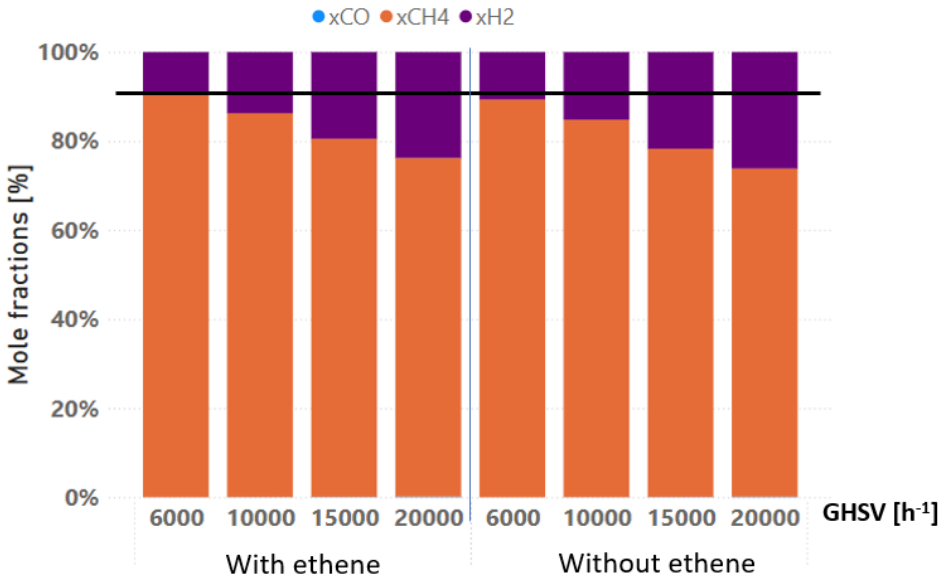

Figure 3. Influence of ethene on methane production under varying process conditions

In addition to this case, the influence of steam concentration (40 vol.% vs. 50 vol.% H_2O) and hydrogen-rich H_2/H_2O mixture on the methanation performance was also investigated. While the detailed diagrams will be presented in a separate publication, it can already be stated that steam content has a strong effect on thermodynamic limits, and that the use of hydrogen-rich mixture enables the production of injection-grade bioSNG under appropriate process conditions.

4. CONCLUSION

The experimental results emphasize the crucial impact of feed gas composition on the efficiency of the methanation process. While high water content alone can limit methane formation due to equilibrium constraints, hydrogen-rich mixtures with added steam (H_2/H_2O) demonstrate a favorable effect when applied under suitable conditions. Additionally, the introduction of higher hydrocarbons, particularly ethene (C_2H_4), significantly enhanced methane production through rapid hydrogenation. These findings highlight the potential of optimizing feed gas composition not only to avoid negative effects but also to actively enhance methane production. As such, careful management of the feed gas composition is essential for maximizing the performance of industrial methanation systems.

REFERENCES

[1] A. van der Drift, R.W.R.Zwart, B.J.Vreugdenhil, L.P.J.Bleijendaal., Comparing the options to produce SNG from biomass, Presented at the 18th European Biomass Conference and Exhibition, Lyon, France, 2010.
[2] J. Ren, Y. Liu, X. Zhao, J. Cao., Int. J. Hydrogen Energy 45 (2019) 4223-4243.
[3] H. Wan, F. Feng, B. Yan, J. Liu, G. Chen, J. Yao., Energy Convers. Manage., 318 (2024).
[4] R. Rauch, J. Hrbek, H. Hofbauer., Wiley Interdiscip. Rev. Energy Environ., 3 (2014) 343-362.
[5] Österreichische Vereinigung für das Gas und Wasserfach (ÖVGW), Richtlinie G B210 Gasbeschaffenheit, Regel der ÖVGW, 2021.

The 56th International October Conference on Mining and Metallurgy
22-25 October 2025, Bor Lake, Bor, Serbia
www.ioc.tfbor.bg.ac.rs

DOI: 10.5937/IOC25568K Original scientific paper

HIGH-PRESSURE OXYGEN LEACHING OF TIONITE RESIDUE FOR TITANIUM RECOVERY

Duško Kostić[1a], Mitar Perušić[1b], Srećko Stopić[2a], Dragana Kostić[1c], Jelena Vuković[1d], Nebojša Vasiljević[1e], Radislav Filipović[1,3a], Vladimir Damjanović[3b]

[1] Faculty of Technology Zvornik, University of East Sarajevo, Karakaj 34a, 75400 Zvornik, Republic of Srpska, Bosnia and Herzegovina
[2] IME Process Metallurgy and Metal Recycling, RWTH Aachen University, 52056 Aachen, Germany
[3]Alumina Ltd., Karakaj 105e, 75400 Zvornik, Republic of Srpska, Bosnia and Herzegovina
[1a] dusko.kostic@tfzv.ues.rs.ba, 0000-0002-4115-8571
[1b] mitar.perusic@tfzv.ues.rs.ba, 0000-0001-9335-1405
[2a] sstopic@ime-aachen.de, 0000-0002-1752-5378
[1c] dkostic585@gmail.com, 0009-0008-1775-9079
[1d] jelena.vukovic@tfzv.ues.rs.ba, 0000-0001-8850-1640
[1e] nebojsa.vasiljevic@tfzv.ues.rs.ba, 0000-0002-3789-9975
[3a] radislav.filipovic@birac.ba, 0009-0000-9938-2499
[3b] vladimir.damjanovic@birac.ba, 0000-0002-5375-440X

Abstract
Tionite is a solid residue formed during the production of titanium dioxide through the chloride process. This material is acidic and contains a high concentration of titanium, which makes it a potential secondary resource for titanium recovery. Instead of being disposed of as hazardous waste, tionite can be processed to extract valuable metals, particularly titanium. In this study, the recovery of titanium from tionite was carried out using an autoclave leaching method under high-pressure oxygen conditions. The presence of oxygen under pressure promotes the formation of titanium oxysulfate, which enhances the dissolution of titanium into solution. This approach enables selective leaching of titanium while limiting the dissolution of other unwanted elements. The leaching experiments were designed to explore optimal conditions for efficient titanium recovery, including temperature, pressure, and leaching time. The main objective of this research is to present a viable route for the valorisation of tionite by turning a hazardous acidic waste into a valuable source of titanium. This process contributes to waste reduction in the titanium dioxide industry and supports more sustainable resource management.

***Keywords**: titanium, high pressure leaching, hydrometallurgy, tionite, waste management*

1. INTRODUCTION

The chloride process (Figure 1), first commercialised by DuPont in the 1950s, has become the dominant method for producing high-purity titanium dioxide (TiO_2) pigments. Compared to the traditional sulfate process, it offers advantages in terms of energy efficiency, product quality, and waste management. This method typically utilises high-grade titanium-bearing raw materials such as rutile, synthetic rutile, and ilmenite, which are chlorinated in a fluidised bed reactor at elevated temperatures to produce titanium tetrachloride ($TiCl_4$). After purification, $TiCl_4$ is oxidised to form TiO_2, while chlorine is recovered and recycled. Despite its industrial advantages, the chloride process generates solid acidic residues and waste streams that require careful handling [1, 2].

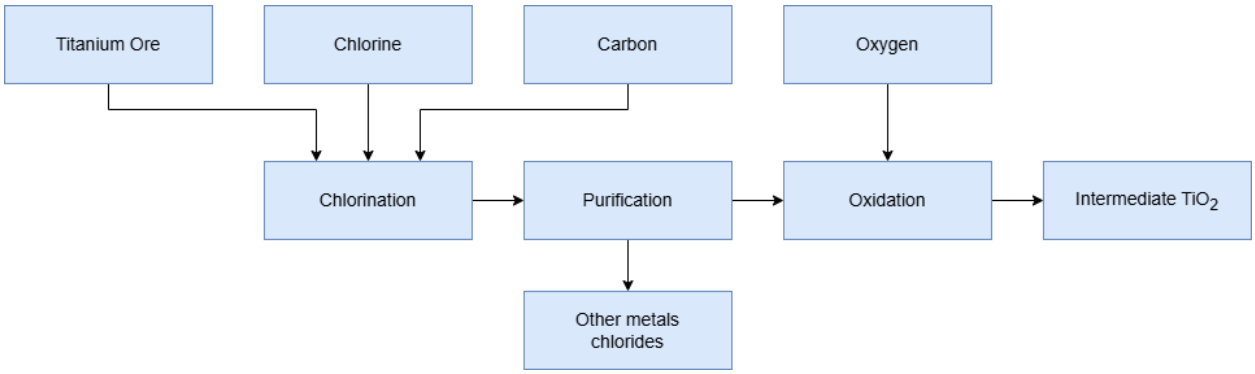

Figure 1. Flowsheet of chlorine process [3]

One such residue is tionite, a residue rich in titanium compounds, formed from unreacted ore, coke, and metal chlorides that are not volatilized during chlorination. Tionite is typically neutralised and landfilled, but its high titanium content makes it an attractive candidate for recovery and reuse. Utilising tionite for titanium extraction not only reduces environmental burdens associated with its disposal but also supports circular economy strategies within the titanium industry [4–6].

Several approaches have been explored for the valorisation of tionite, including pyrometallurgical and hydrometallurgical routes. Among them, hydrometallurgical methods such as acid leaching offer a selective and potentially scalable pathway for dissolving titanium into a recoverable form. Titanium can be leached as titanium oxysulfate in acidic media under oxidative conditions, and subsequently recovered through precipitation or solvent extraction. However, research on oxidative autoclave leaching of tionite under high-pressure oxygen remains limited [7–11].

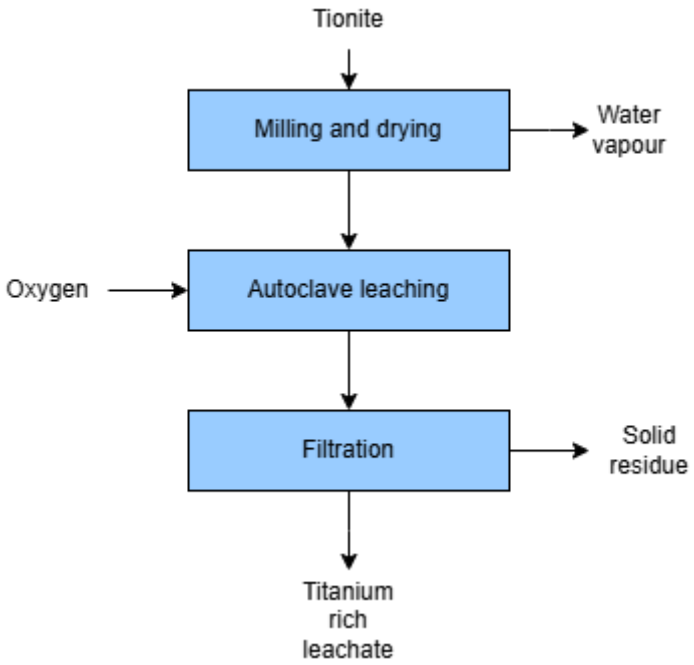

Figure 2. "State of the art" tionite processing

This study investigates the use of high-pressure oxygen in autoclave leaching to promote selective titanium dissolution from tionite, aiming to produce a titanium-rich solution suitable for further processing (Figure 1). The goal is to demonstrate a feasible and sustainable method for transforming hazardous industrial waste into a valuable resource, contributing to both environmental protection and material efficiency in titanium production.

2. EXPERIMENTAL

2.1 Methods

The mineralogical composition of the tionite was investigated using X-ray diffraction (XRD). Analyses were carried out at ambient conditions using a Rigaku Ultima IV diffractometer equipped with CuKα radiation. Operational parameters included a generator voltage of 40 kV, current of 40 mA, and a scan range of 10° to 100° 2θ, at a step size of 0.02° and scan speed of 1°/min. A D/TeX Ultra detector was employed in continuous scan mode. Samples were prepared on glass holders, and phase identification was performed using PDXL2 software (v2.8.4.0) in conjunction with the ICDD powder diffraction database.

The morphological and microstructural features of tionite, both before and after leaching, were examined using scanning electron microscopy (SEM). A Quattro S microscope (Thermo Fisher Scientific, USA) was operated in high vacuum mode at accelerating voltages between 5 and 20 kV. Energy-dispersive X-ray spectroscopy (EDS) was used alongside SEM to determine the elemental distribution across the sample surfaces, with a focus on titanium and associated elements.

The elemental concentrations in both solid samples and leachates were quantified using inductively coupled plasma optical emission spectroscopy (ICP-OES), performed on a Spectro Genesis system. This technique enabled precise multi-element detection across a wide atomic mass range.

Leaching experiments

Titanium extraction experiments were conducted using a Büchi high-pressure autoclave (1.53 L capacity), engineered specifically for acidic leaching operations. The unit supports a maximum operating pressure of 200 bar and temperature up to 270 °C. The autoclave was operated with sulfuric acid as the leaching medium and oxygen overpressure (6–9 bar) to facilitate oxidative dissolution of titanium. Total system pressure ranged from 12 to 15 bar, accounting for both oxygen and steam.

The system features include a thermostatically controlled heat exchanger, mechanical stirring, real-time pressure and temperature monitoring (via manometer and digital probes), and sampling capability during operation. Heating was applied at a controlled rate of 10 °C per minute, and cooling was performed using an integrated chiller unit. Each experiment began with a manual sealing procedure and pressure integrity check.

2.2 Materials

In this study, tionite, a solid residue generated from the chloride-route titanium dioxide production process, was sourced from Venator GmbH. The raw material was initially dried and milled to achieve a uniform powder suitable for subsequent characterisation and processing.

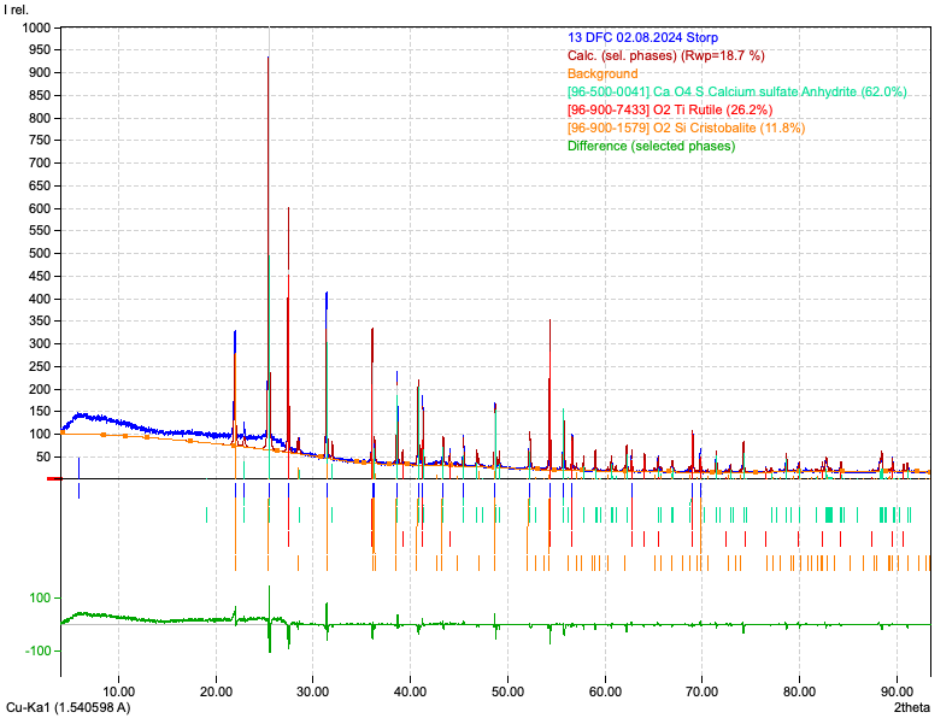

Figure 3. XRD analysis of tionite

The X-ray diffraction (XRD) analysis of the tionite sample revealed a complex multiphase composition, as shown in the diffractogram. The dominant crystalline phase identified in the sample is anhydrite ($CaSO_4$), comprising approximately 62.0 wt%. This phase is characteristic of residues resulting from sulfate-rich neutralisation processes in titanium dioxide production. Rutile (TiO_2), accounting for 26.2 wt%, is the principal titanium-bearing phase, confirming the potential of tionite as a source for titanium recovery through selective leaching. A minor phase, cristobalite (SiO_2), was also detected at 11.8 wt%, likely originating from inert siliceous components that remain unreacted during chlorination. The combination of these phases reflects the mineralogical complexity of tionite and supports its evaluation as a candidate for further hydrometallurgical processing.

Table 1. Tionite elemental composition

Material	Ti	Si	Al	Fe	Ca
Tionite	13.86 %	1.76 %	2.57 %	10.64 %	32 %

Based on the provided elemental composition from ICP analysis, it is evident that the results support the findings from the XRD analysis.

The high calcium content (32%) aligns well with the dominant presence of anhydrite ($CaSO_4$) identified by XRD, confirming that calcium is primarily present in the form of calcium sulfate. The significant titanium concentration (13.86%) corresponds to the rutile (TiO_2) phase detected in the diffraction pattern, validating that titanium is present in a crystalline, leachable form. Additionally, the presence of silicon (1.76%) is consistent with the identification of cristobalite (SiO_2), although it appears in a lesser amount both chemically and mineralogically. Aluminium and iron, though not directly observed as major crystalline phases in the XRD pattern, are present in considerable quantities (2.57% and 10.64% respectively), likely occurring in amorphous or minor crystalline phases not resolved in the diffractogram.

Table 2. Design of leaching experiments

Exp No.	Temperature (°C)	Pressure (bar)	Concentration of acid (mol/dm^3)	Time (min)
1	150	6	2,5	60
2	150	6	5	120
3	180	6	5	120
4	150	9	5	120
5	150	9	5	60

The leaching experiments were conducted at the Institute of Metallurgy and Metal Recycling (IME), RWTH Aachen University, to investigate the effect of various parameters on titanium recovery from tionite. A total of five experiments were performed in a controlled autoclave environment. In all experiments, a solid-to-liquid ratio of 1:10 was maintained, and continuous mixing was ensured at a speed of 500 RPM to promote homogeneous reaction conditions. This experimental design allowed for the evaluation of the influence of individual and combined parameters on the leaching efficiency and titanium dissolution behaviour.

3. RESULTS AND DISCUSSION

Leaching has been done using sulfuric acid. After the experiments, ICP analysis has been done, and the leaching efficiency calculated (Figure 4).

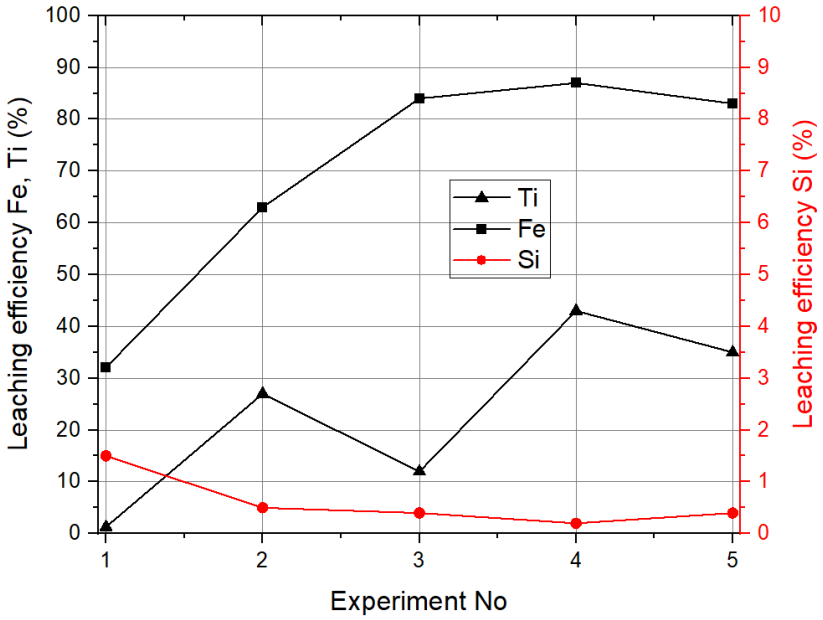

Figure 4. Leaching efficiency for different elements

The leaching efficiency results demonstrate varying behaviours of titanium (Ti), iron (Fe), and silicon (Si) under different experimental conditions. Titanium shows a gradual increase in leaching efficiency across the experiments, with the highest value around 43% achieved in Experiment 4, conducted at 150 °C, 9 bar oxygen pressure, 5 mol/dm³ sulfuric acid concentration, and 120 minutes of leaching time. This suggests that higher oxygen pressure and acid concentration significantly enhance titanium dissolution.

However, the maximum titanium recovery remains relatively low. This limited leachability, despite aggressive conditions, indicates that the primary titanium-bearing phase (rutile) is highly resistant to dissolution. Rutile's compact and stable crystalline structure makes it difficult to break down under typical hydrometallurgical conditions, even in an oxidising and acidic environment.

Iron shows fluctuating leaching behaviour, with its highest efficiency (~88%) in Experiment 4. The lower and less predictable dissolution of iron may be influenced by secondary phase stability or partial passivation during leaching. Silicon consistently exhibits very low leaching efficiency (below 2%), reflecting its low solubility under the experimental conditions and suggesting prevention of silica gel formation.

Overall, the results confirm that while titanium can be partially recovered through high-pressure oxygen leaching, the process is hindered by the refractory nature of rutile. Future improvements may require additional pretreatment steps to disrupt the rutile structure or alternative leaching strategies to enhance titanium recovery.

SEM analysis coupled with EDS of solid residue from experiment 4 has confirmed leaching results (Figure 5).

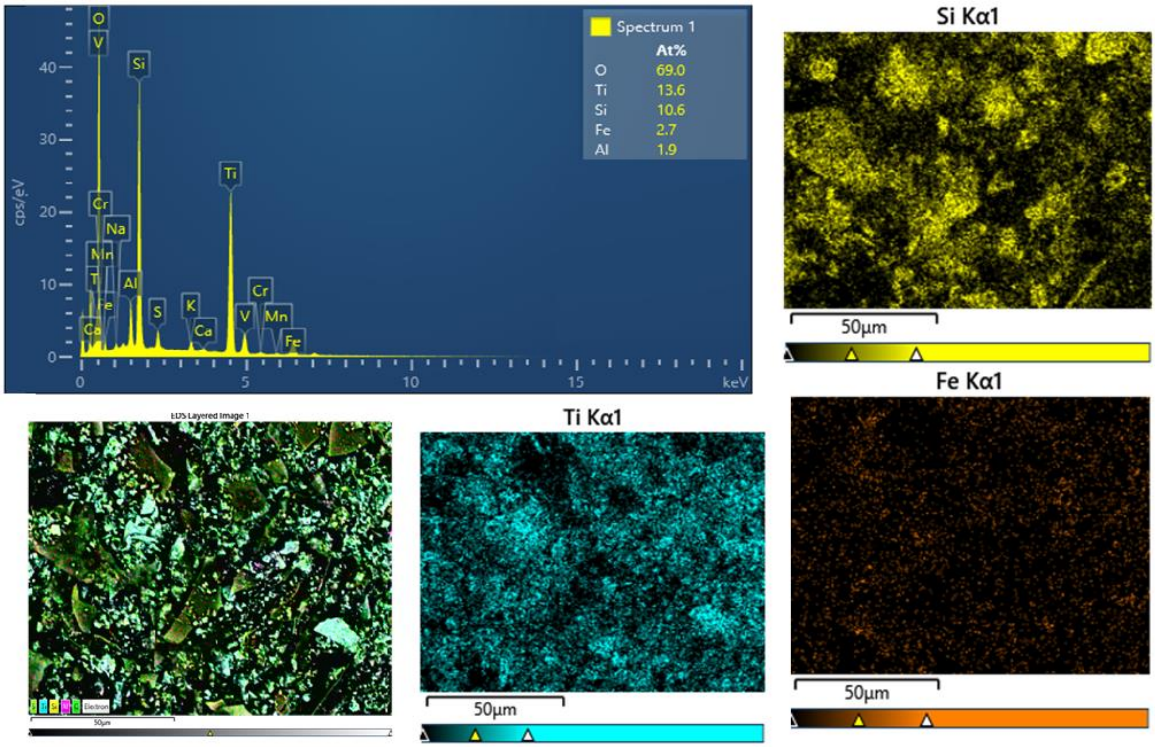

Figure 5. SEM-EDS analysis of solid residue from experiment 4

The SEM-EDS analysis of the solid residue from Experiment 4 provides additional insights into the elemental distribution and confirms the observed leaching efficiencies. The EDS spectrum (top left) shows dominant peaks for oxygen and titanium, with a measured atomic percentage of 13.6% Ti and 10.6% Si, while iron is present at only 2.7%. This aligns well with the quantitative leaching results, where iron exhibited the highest leaching efficiency, confirming its effective removal from the solid matrix.

The element mapping images support these findings:

- The Fe Kα1 map shows a very faint and sparse distribution of iron, indicating that most of the iron was successfully leached from the solid during high-pressure oxygen leaching.
- The Ti Kα1 and Si Kα1 maps reveal a dense and uniform presence of titanium and silicon, respectively, across the entire residue surface. This suggests that a significant portion of both elements remains in the solid phase, reflecting only modest titanium leaching (~40% at best conditions) and poor silicon leaching (under 2%).

These results confirm that titanium, present largely in the rutile phase (as shown in the XRD analysis), exhibits structural resistance to dissolution under the tested leaching conditions. Silicon,

likely present as cristobalite, also shows limited reactivity, remaining in the residue in high amounts. In contrast, iron appears to be present in more soluble phases, explaining its near-complete extraction under optimised conditions.

4. CONCLUSIONS

The conducted leaching experiments using sulfuric acid under varying temperature, pressure, and acid concentration conditions demonstrated distinct behaviours for iron, titanium, and silicon recovery from tionite. The process proved highly effective for iron extraction, achieving a maximum leaching efficiency of approximately 88% under optimized conditions (150°C, 9 bar oxygen, 5 mol/dm³ H2SO4, 120 min). This high iron recovery indicates that iron-bearing phases in the material are readily soluble under the applied oxidative acidic environment.

Titanium exhibited moderate leaching performance, with a maximum recovery of approximately 43% under the same experimental conditions. The limited leachability of titanium is attributed to its presence primarily in the rutile phase, a highly stable and refractory mineral. The strong crystalline structure of rutile resists leaching, even under elevated temperature and pressure, highlighting the need for alternative or additional treatment methods to improve Ti recovery.

Silicon leaching remained consistently low across all tests, with efficiencies below 2%. This minimal dissolution suggests that silica remains largely in the solid phase, likely in the form of cristobalite, and does not form problematic silica gel during leaching. The absence of gel formation is a favourable outcome, simplifying solid-liquid separation and downstream processing.

Overall, the study confirms that high-pressure oxygen leaching is a promising method for efficient iron removal from tionite. However, due to the refractory nature of rutile, future research will focus on enhancing titanium recovery, potentially through pretreatment strategies or alternative leaching systems to improve titanium extraction.

ACKNOWLEDGEMENTS

This research was funded by the European Commission, grant number 101135077 (EUROTITAN).

REFERENCES

[1] M. Contreras, J. Gázquez, J.P. Bolívar, Journal of Waste Recycling, 2 (2017).
[2] D. Filippou, G. Hudon, JOM, 61 (10) (2009) 36–42.
[3] How to manufacture titanium dioxide by chloride process. https://www.fangyuan-tio2.com/how-to-manufacture-titanium-dioxide-by-chloride-process.html (accessed 29 July 2024).
[4] M.J. Gázquez, J.P. Bolívar, R. Garcia-Tenorio, F. Vaca, MSA, 5 (2014) 441–458.
[5] W. Zhang, Z. Zhu, C.Y. Cheng, Hydrometallurgy, 108 (2011) 177–188.
[6] J. Vuković, M. Perušić, S. Stopić, D. Kostić, S. Smiljanić, R. Filipović, V. Damjanović, "Ovidius" Univ. Ann. Chem., 35 (2024) 165–173.
[7] F. Meng, T. Xue, Y. Liu, W. Wang, T. Qi, Hydrometallurgy, 161 (2016) 112–116.
[8] Chen: Practical Questions and Answers in the Production... - Google Академик. https://scholar.google.com/scholar_lookup?title=Practical%20Questions%20and%20Answers%20in%20the%20Production%20of%20Titanium%20Doxide%20from%20Sulfate%20Process&publication_year=2009&author=D.B.%20Chen (accessed 18 August 2024).
[9] W. Hajjaji, G. Costa, C. Zanelli, M.J. Ribeiro, M.P. Seabra, M. Dondi, J.A. Labrincha,. J. Eur. Ceram. Soc., 32 (2012) 753–764.
[10] J.A. Labrincha, J.I. Marques, W. Hajjaji, L. Senff, C. Zanelli, M. Dondi, F. Rocha, Waste Biomass Valorization, 5 (2014) 385–392.
[11] S. Stopic, D. Kostić, E. Emil-Kaya, E. Uysal, S. Gürmen, A. Mitrašinović, M. Perušić, B. Friedrich, Surfaces, 7 (2024) 1096-1108.

The 56th International October Conference on Mining and Metallurgy
22-25 October 2025, Bor Lake, Bor, Serbia
www.ioc.tfbor.bg.ac.rs

DOI: 10.5937/IOC25575A *Review paper*

CATHODIC PROTECTION OF METALS

Zoran Avramović[1a], Dragana Božić[1b], Vanja Trifunović[1c], Jelena Stefanović[1d]

[1] Institute for Mining and Metallurgy, Albert Einstein 1, 19210 Bor, Serbia
[1a] zoran.avramovic@irmbor.co.rs, 0009-0006-7585-976X
[1b] dragana.bozic@irmbor.co.rs, 0000-0003-1055-8449
[1c] vanja.trifunovic@irmbor.co.rs, 0000-0003-4839-8751
[1d] jelena.stankovic@irmbor.co.rs, 0000-0001-6418-1814

Abstract
Electrochemical corrosion and electrochemical corrosion protection share the same fundamental principles. Cathodic protection processes can be scientifically explained much more concisely than many other protective systems. The corrosion of metals in aqueous solutions or in soil is primarily an electrolytic process controlled by electrical voltage, i.e., by the potential of the metal in the electrolytic solution. According to the laws of electrochemistry, the tendency and rate of the reaction decrease as the potential decreases. Although these relationships have been known for more than two centuries and although cathodic protection has been applied in isolated cases for a long time, its widespread technical application required a longer period. This may have been because cathodic protection once seemed unusual and strange, and the demands of electrical engineering hindered its practical implementation. In practice, cathodic protection is indeed more complex than its theoretical basis.

Keywords: *corrosion, cathodic protection, anodes*

1. INTRODUCTION

When in contact with an electrolyte, metal undergoes corrosion, and one of the most effective methods for preventing metal corrosion is cathodic protection [1]. Cathodic protection of metals is based on cathodic polarization, which is achieved by connecting the metal to the negative terminal of a direct current source or to a metal whose electrode potential is sufficiently more negative than the equilibrium potential of the protected metal, in order to provide an adequate voltage for current flow [2]. Unlike impressed current anodes, the use of galvanic anodes (so-called "sacrificial" anodes) is limited by their electrochemical properties. Galvanic anodes should have the lowest possible polarizability. The degree of their polarization is important for the strength of the current they can provide [3].

Cathodic protection of unalloyed carbon steels and low-alloy steels can be achieved using galvanic anodes made of zinc, aluminium, or magnesium [4]. Today, iron anodes are used for structures with relatively positive protection potentials, especially when only a slight potential decrease is desired. Anodes are generally not made of pure metals, but of alloys. Certain alloying elements are used to achieve a fine-grained structure, which leads to relatively uniform metal loss from the surface. Other elements serve to reduce self-corrosion and increase current efficiency. Finally, alloying additions can prevent or reduce the tendency toward surface film formation or passivation. Such activating additives are necessary in the case of aluminum [5]. When the sacrificial anode and the protected system are placed in an electrically conductive medium (electrolyte), a galvanic cell (couple) is formed. In this process, two main reactions occur: one at the anode and the other at the cathode (the protected system). Anodic reactions are always oxidative, during which the metal dissolves into the electrolyte in the form of ions, oxides, or hydroxides [6]. It is said that the anode corrodes or oxidizes, which manifests as metal loss, while at the cathode, reduction reactions

occur that have little effect on the cathodic metal, as it is already in a reduced state in most cases [7].

2. THEORETICAL AND PRACTICAL CONSIDERATION

High-purity zinc resists surface passivation and is commonly used [8]. Ultra-high-purity zinc (99.995% Zn, <0.0014% Fe) is approved by the German Navy. When alloyed with small amounts of cadmium and aluminum, it wears evenly as an anode. However, zinc anodes are rarely used in freshwater or soil due to passivation. Advantages include high efficiency, low cost, and no sparking on steel contact—important for oil tanker protection. The main drawback is the small potential difference from steel (~0.25 V) [9].

A new Al-Zn-In-Sn-La alloy was developed and compared to commercial Al-Zn-In under simulated marine conditions using mass loss, potential, and polarization tests [10]. The new alloy showed slightly higher discharge capacity and 90.01% current efficiency (vs. 75.87%) in shallow-sea and 82.99% (vs. 75.48%) in deep-sea conditions. This improvement is due to the destabilization of the passive film and increased ion migration from the synergistic effects of In, Zn, and Sn.

Al-Zn-0.03In-1.30Mg alloys with varying Zn content were tested. Zn between 0.60% and 2.00% yielded optimal results, with uniform dissolution, potentials below –1.05 V (vs. SCE), and capacity over 2570 $A \cdot h \cdot kg^{-1}$. Above 5.00% Zn caused dendritic structures and localized corrosion. The 0.60% Zn alloy showed low environmental impact and promise as an eco-friendly anode [11,12].

Pure aluminum is prone to passivation, but Al alloys with Zn (up to 8%) and/or Mg (up to 5%), and activators like Cd, Ga, In, Hg, or Tl, remain active. These alloys cover potentials from –0.75 V to –1.3 V. Al-Zn-In alloys are especially valued for low polarizability and are widely used in marine and offshore protection [13].

Gallium's effect in Al-Zn-In-Mg alloys was tested in 3.5 wt% NaCl. The Al-Zn-In-Mg-0.03Ga alloy showed the best discharge performance and 98.25% current efficiency. The benefit followed a parabolic trend, peaking at 0.03 wt% Ga [14].

Magnesium has the highest driving force (potential difference) among common anode materials and is less prone to passivation than zinc and aluminum, making it suitable for use as a galvanic anode [15]. However, its pronounced tendency toward self-corrosion—especially in environments with higher salt content—significantly reduces its effective current efficiency. Therefore, magnesium anodes are typically made from alloys with additions of Al, Zn, and Mn. Low pH values accelerate self-corrosion, while a pH above 10.5 has the opposite effect. For surface protection, an anode mass of 200–250 g/m^2 is recommended, and the appropriate shape ensures uniform consumption—ranging from cylindrical and plate-shaped to disc-shaped and custom-designed for the structures they protect, such as heat exchangers and condensers [16].

In this studies a new anticorrosion method combining impressed current cathodic protection (ICCP) with coatings that can be applied to marine atmospheric environments is proposed [17,18]. As the corrosion medium fills the cracks and pores of the coating, an electrolyte film layer is inevitably formed on the metal surface. By studying the surface corrosion morphologies and electrochemical signals of the coating samples at different protection potentials and coating thicknesses, the optimal potential is determined to be 0.6V, and the optimal coating thickness is determined to be 20μm.

In cathodic protection, a Direct Current DC power source (usually an Alternating Current (AC) rectifier) turns the metal into a cathode. The auxiliary anode is connected to the positive terminal, with electrons flowing externally and ions through the electrolyte. Impressed current systems supply uniform electrons, ideal for large structures in high-resistivity soils like pipelines and tanks [3,19].

Table 1.The electrochemical properties of these materials [19].

Parameters	Base metal of the protector		
	Zn	Mg	Al
Standard potential of the base metal, V	-0,76	-2,38	-1,66
Standard potential of the protector relative to the $Cu/CuSO_4$ electrode, V in soil	-0,9 do -1,1	-1,4 do -1,6	-0,9 do -1,2
In seawater	-1,1	-1,55 do -1,75	-1,0 do -1,2
Couple potential (steel/protector), V	0,35-0,55	0,85-1,2	0,35-0,65
Theoretical capacity, A·s/kg	$295{,}2 \cdot 10^4$	$792 \cdot 10^4$	$1072{,}8 \cdot 10^4$
Actual capacity, A·s/kg	$(280\text{-}290) \cdot 10^4$	$(395\text{-}430) \cdot 10^4$	$(540\text{-}870) \cdot 10^4$
Protective efficiency of the protector, %	do 95%	50-55	50-80
Theoretical material consumption, mg/A·s	0,339	0,126	0,093
Actual material consumption, mg/A·s	0,38	0,25	0,11-0,18

Efficiency is judged by protection potential and current density. Steel's steady-state potential is –0.50 V to –0.65 V (vs. $Cu/CuSO_4$). Polarizing to –0.85 V provides full protection. Current density is harder to define and seldom used [8,19,20]. Cathodic protection works well for subsea pipelines [21,22]. Drawbacks: materials dissolve irreversibly and need replacement; corrosion products may pollute; unsuitable for high-resistivity environments; lower protective currents [23,24].

Ship cathodic protection includes hulls, tanks, and piping. Reinforcement in concrete is passivated by alkaline conditions. Applying cathodic protection to reinforced concrete requires technical and economic analysis. It's not used for prestressed concrete with insulated ducts unless directly connected, e.g., buried pipelines with zinc anodes.

3. CONCLUSION

One of the most effective methods of corrosion protection is certainly cathodic protection, both by protectors and by an external current source. There are many standards regulating cathodic protection, and the application of these standards ensures high-quality and efficient protection. The most effective protection is achieved with new structures, which is also the most cost-effective case. Cathodic protection of older structures requires additional resources and time to prepare their surfaces, so the protective effect on such structures is uncertain. The application of cathodic protection to slow down or stop corrosion is present in reinforced concrete structures, ships, heat exchangers, tanks—in short, wherever structures are in contact with a conductive environment. To achieve a high effect of cathodic protection, the anode material must be carefully selected, as well as the appropriate current capacity when protection is applied using an external current source. Today, there is a wide range of protectors and anode systems with different protective capacities and shapes, and their proper selection can provide maximum—but not absolute—protection of the structures being protected.

REFERENCES

[1] R. W. Revie, H. H. Uhlig., Corrosion and Corrosion Control, Wiley, New York, 2008.
[2] D. A. Jones, Principles and Prevention of Corrosion, Pearson Education, Reno, 2013.
[3] A. J. Sedriks, Corrosion of Metals: Physical and Chemical Principles, Wiley-Interscience, 1996.
[4] J. Zhang, J. Liu, J. Peng, X. Zhang, K. Wu, J. Chin. Soc. Corros. Prot., 44 (5) (2024) 1223-1233.
[5] Y. Deng et al, Coatings, 14 (5) (2024) 524.
[6] W. D. Callister, D. G. Rethwisch, Materials Science and Engineering: An Introduction, Wiley, 2020.
[7] M. G. Fontana, Corrosion Engineering, McGraw-Hill, 1986.
[8] W. von Baeckmann, W. Schvenk, Handbook of Cathodic Corrosion Protection, Elsevier Science, USA, 1997.
[9] C. Pei, D. Sun, J. Wang, L. Wang, Corros. Sci., 226 (2024) 111123.
[10] Z. Juhuan, L. Jing, P. Jingjing, Z. Xian, W.U. Kaiming., J. Chin. Soc. Corros. Prot. 44 (5) (2024) 1223.
[11] Y. Liu et al. J. Mater. Sci. Technol., 144 (2024) 98–107.

[12] L. Weihua, W. Haitao, Y. Lin, X. Shi, L. Zhaoxin, G. Yu, W. Tingyong, J. Chin. Soc. Corros. Prot., 43 (5) (2023) 1071-1078.
[13] Y. Liu, et al., J. Alloys Compd., 945 (2024) 169065.
[14] Y. Xi, M. Jia, J. Zhang, W. Zhang, D. Yang, L. Sun, Coatings, 12 (1) (2022) 53.
[15] H. Wang, D. Zhang, Y. Liu, J. Mater. Sci. Technol., 143 (2023) 187–196.
[16] G. Song, A. Atrens., Corros. Sci., 195 (2021) 109997.
[17] P. Deng, J. Shangguan, J. Hu, H. Huang, L. Zhou., Coatings, 14 (5) (2024) 524.
[18] X. Li, D. Zhang, Z. Liu, Z. Li, C. Du, C. Dong., Nature, 527 (2015) 441–442.
[19] S. Mladenović, G. Rikovski, *in Serbian:* Korozija i zaštita materijala, IRO RAD, Beograd, 1985, p.280-306.
[20] J. Pjescic, D. Radonjic, D. Vuksanovic, Lj. Samardzic., Mat. Prot., 50 (2) (2010) 94.
[21] S. M. A. Bukhari, S. A. R. Gardezi, N. Husnain, R. Ahmad, M. F. Zaman, R. Qurashi, N. Baloch., Asia Pac. J. Sci. Technol., 30 (01) (2025).
[22] D. Kuang., Y. F. Cheng, Corros Sci., 99 (2015) 249-257.
[23] E. Ghali., Mater. Sci. Forum, 350-351 (2000) 261-272.
[24] S. Stankov., Mat. Prot., 53 (1) (2012) 73.

The 56th International October Conference on Mining and Metallurgy
22-25 October 2025, Bor Lake, Bor, Serbia
www.ioc.tfbor.bg.ac.rs

DOI: 10.5937/IOC25579Z *Original scientific paper*

ATR-FTIR CHARACTERIZATION OF THE WHITE WILLOW BARK EXTRACT USED AS A COPPER CORROSION INHIBITOR

Milica Zdravković[1a], Slađana Savić[2b], Vesna Grekulović[1c], Dalibor Stanković[2d], Iva Dimitrievska[3e]

[1] Technical Faculty Bor, University of Belgrade, V.J. 12, 19210 Bor, Serbia
[2] Faculty of Chemistry, University of Belgrade, Studentski trg 16, Belgrade, Serbia
[3] Faculty of Technology and Metallurgy, University Ss Cyril and Methodius, R. B. 16, 1000 Skopje, North Macedonia
[1a] mboskovic@tfbor.bg.ac.rs, 0000-0001-9488-9151
[2b] sladjana@chem.bg.ac.rs, 0000-0002-1483-110X
[1c] vgrekulovic@tfbor.bg.ac.rs, 0000-0001-6871-4016
[2d] dalibors@chem.bg.ac.rs, 0000-0001-7465-1373
[3e] iva@tmf.ukim.edu.mk, 0000-0002-7196-1875

Abstract
As proved inhibitor of copper corrosion in saline environment, the white willow bark (WWB) extract was characterized using the Attenuated Total Reflectance-Fourier Transform Infrared spectroscopy (ATR-FTIR) method. By identifying the bands typical for phenolic profile of WWB extract, the anti-corrodic properties of WWB were explained. The hydrogen-bonded O-H stretching vibrations present in WWB extract is attributed to the phenolic hydroxyl groups and alcoholic hydroxyl groups within glycosides. The C-H stretching vibrations typical for salicin and for glucoside part of salicin aromatic were also identified, as well as the C=C ring stretching vibrations and C-O stretching vibrations that can be attributed to phenolic and alcoholic groups. The presence of these functional groups confirms the presence of a protective film of the WWB extract on the copper surface, protecting the metal from the corrosive effect of chloride ions.

***Keywords**: white willow bark, ATR-FTIR, copper, corrosion inhibitor*

1. INTRODUCTION

Attenuated Total Reflectance-Fourier Transform Infrared (ATR-FTIR) spectroscopy is a frequently applied method for the analysis of environmentally friendly corrosion inhibitors for metals [1,2]. Corrosion inhibitors are useful for avoiding the dissolution of metal in different corrosive environments [1,3]. The effectiveness of organic inhibitors, including those derived from plants, is related to the chemical structure and physicochemical properties. These include functional groups, electron density at the donor atom, p-orbital character, and the electronic structure of the molecule [4,5]. The performance of organic inhibitors depends on several factors, such as the adsorption of the molecules or their ions on anodic and/or cathodic sites, an increase in cathodic and/or anodic over voltage, and the formation of a protective barrier film [4]. The ATR-FTIR method is significant for examining the film formation and functional groups of molecules that participate in the adsorption process, providing a detailed analysis of corrosion inhibitors [6]. For example, functional groups such as azole, thiol functional groups, and carboxylate tail group can influence the adsorption of corrosion inhibitors on the copper surfaces in a chloride environment. The thiol group improves the adsorptive interaction with the surface, while the carboxylate groups provide additional intermolecular attraction [7].

Recent research indicates the possibility of using white willow bark (WWB) extract can inhibit copper corrosion in a 0.5 M NaCl solution [8]. Also, WWB extracts have anti-inflammatory, antipyretic, and analgesic effects, making them popular in sports performance and weight loss products. Although these extracts are generally standardized to salicin, they also contain other

beneficial ingredients, including other salicylates, polyphenols, and flavonoids, which may play prominent roles in the therapeutic actions [9]. In addition to the use of white willow bark for pharmaceutical purposes, research shows that it can be used for phytoremediation [10,11].

In this paper, the ATR-FTIR results for WWB extract obtained by extraction with distilled water are shown. The goal is to determine the functional groups present in the extract and to explain in more detail their role in inhibiting copper corrosion in a 0.5 M NaCl solution.

2. EXPERIMENTAL

2.1 Preparation of white willow bark extract

WWB extract was obtained by extracting the white willow bark sample with distilled water and then evaporating it. Distilled water was chosen as a cheap, universal, and environmentally friendly solvent. The dry and ground WWB was manufactured by "Adonis" company, located in Sokobanja, Serbia. The dry bark mass was poured with hot distilled water (95 °C) in a solid:liquid ratio of 1:3. After 12 h at room temperature, the mixture was filtered using a Buchner funnel with filter paper No. 1. The filtered solution was evaporated on a rotary evaporator Buchi R-210 (72 mbar, 40 °C). WWB extract and hydrolate were obtained as products, as shown in Figure 1.

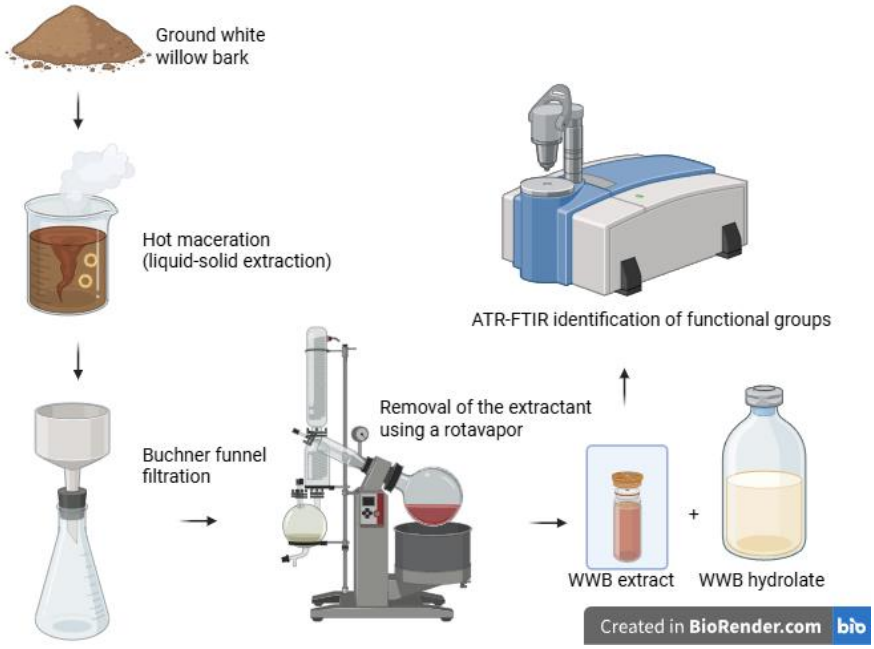

Figure 1. Scheme of obtaining WWB extract and its hydrolate

2.2 ATR-FTIR analysis

The ATR-FTIR characterization of the WWB extract was conducted using a Smart iTR Nicolet iS50 FTIR spectrophotometer (Thermo Fisher Scientific, USA), as reported elsewhere [12].

3. RESULTS AND DISCUSSION

The ATR-FTIR spectra (Figure 2) of the WWB extract reveals characteristic bands consistent with its expected main constituents, such as salicin and its derivatives, other phenolic glycosides, along with tannins and flavonoids [13]. The prominent and broad band at ~3246 cm^{-1} (with percentage transmittance of 64%) indicates the presence of hydrogen-bonded O-H stretching vibrations, attributed to the phenolic hydroxyl groups and alcoholic hydroxyl groups in glycosides. The signal at 2933 cm^{-1} (79%), appearing as a shoulder to O-H band, indicates C-H stretching vibrations, typical for salicin [14]. The bands at ~1604 cm^{-1} (60%) and ~1521 cm^{-1} (73%) correspond to

aromatic C=C ring stretching vibrations. Furthermore, C-H bending, indicated by a band at 1374 cm^{-1} (62%), is characteristic of the glucoside part of salicin. Finally, C-O stretching vibrations are indicated by the band at ~1246 cm^{-1} (61%), whereas a strong peak at ~1032 cm^{-1} (36%) can be attributed to phenolic and alcoholic groups.

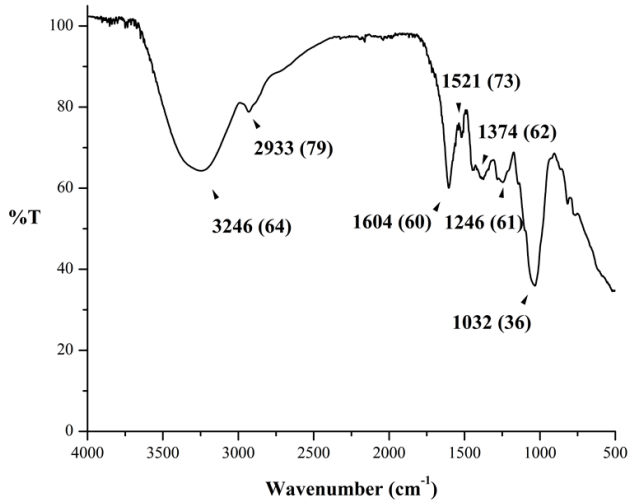

Figure 2. ATR-FTIR spectrum of WWB extract with the most prominent bands marked

The presence of certain functional groups affects the molecular interface adsorption. Some studies have shown that some coordination compounds exhibit good adsorption on the metal surfaces [15]. Heterocyclic compounds containing functional groups such as –OH, $–NH_2$, $–OCH_3$, –NHMe, $–NMe_2$, –CN, $–CONH_2$, $–COOC_2H_5$, –O–, $–NO_2$ have proven to be effective inhibitors of metal corrosion. Extensive conjugation in the form of non-bonding and π electrons of hetero and homo electrons, such as >C=O, >C=N–, >C=S, –C≡N, –N=O, –N=S, >C=C<, –N=N–, and –C≡C,– interact with metal surfaces as electron-rich adsorption centers [16]. On the other hand, organic compounds with electron-donor functional groups (–OH, $–NH_2$ and $–CH_3$) have a positive effect on the inhibition of metal corrosion, while those with electrons-acceptors groups (–CN, $–COOC_2H_5$, and $–NO_2$) have a negative effect, *i.e.* reduce the effectiveness of corrosion inhibition [17].

The presence of functional groups determined by the ATR-FTIR method confirms the capacity of WWB extract to act as an inhibitor of copper corrosion in saline environment. The hydrogen-bonded O-H stretching vibrations, attributed to the phenolic and alcoholic hydroxyl groups within glycosides, were determined. Previous research confirms the effect of herbal extracts containing glycosides and polysaccharides moieties are effective green and cost-efficient corrosion inhibitors [18]. The C-H stretching vibrations, aromatic C=C ring stretching vibrations, and C-O stretching vibrations are typical indicators of copper corrosion inhibitors [19,20,21,22].

4. CONCLUSION

The identification of functional groups in the WWB extract using the ATR-FTIR method indicates the presence of numerous functional groups that act as metal corrosion inhibitors. The presence of hydrogen-bonded O-H stretching vibrations, attributed to the phenolic hydroxyl groups and alcoholic hydroxyl groups within glycosides, C-H stretching vibrations, typical for salicin, aromatic C=C ring stretching vibrations, C-H bending characteristic for glucoside part of salicin, and C-O stretching vibrations attributed to phenolic and alcoholic groups was confirmed. This confirms the potential of WWB extract as an inhibitor of copper corrosion in chloride conditions.

ACKNOWLEDGEMENTS

The research presented in this paper was done with the financial support of the Ministry of Education, Science and Technological Development of the Republic of Serbia, within the funding of the scientific research work at the University of Belgrade, Technical Faculty in Bor, according to the contract with registration no. 451-03-137/2025-03/200131.

REFERENCES

[1] H. Hassannejad, A. Nouri., J. Mol. Liq., 254 (2018) 377-382.
[2] K. Haruna, I.B. Obot, N.K. Ankah, A.A. Sorour, T.A. Saleh., J. Mol. Liq., 264 (2018) 515-525.
[3] R. Aslam, M. Mobin, S. Zehra, J. Aslam., J. Mol. Liq., 364 (2022) 119992.
[4] B.A. Rani, B.B. Basu., Int. J. Corros., 2012 (1) (2012) 380217.
[5] D.K. Verma, R. Aslam, J. Aslam, M.A. Quraishi, E.E. Ebenso, C. Verma., J. Mol. Struct., 1236 (2021) 130294.
[6] M.Z. Khan, M.A. Aziz, M.R. Hasan, M.R. Al-Mamun., Anti-Corros. Methods Mater., 63 (4) (2016) 308-15.
[7] G.Ö. Tansuğ, T.U. Tüken, E.S. Giray, G. Fındıkkıran, G. Sığırcık, O.N. Demirkol, M.E. Erbil., Corros. Sci., 84 (2014) 21-9.
[8] M. Zdravković, V. Grekulović, E. Huseinović, R. Vianello, N. Štrbac, M. Huremović, M. Gorgievski, Proceedings of XVI International Mineral Processing and Recycling Conference, 28-30.05.2025., Belgrade, Serbia, 2025.
[9] J. G. Al-shattrawi, H. Cent. Asian J. Med. Sci., 6(2) (2025) 659-678.
[10] J.A. Malik, A.A. Wani, K.A. Wani, M.A. Bhat., Bioremediation and Biotechnol.: Sustain. Approaches to Pollut. Degrad., (2020) 257-68.
[11] M. Zdravković, V. Grekulović, J. Suljagić, D. Stanković, S. Savić, M. Radovanović, U. Stamenković., Bioelectrochem., 151 (2023) 108401.
[12] J. Dou, P. Ilina, C.D. Cruz, D. Nurmi, P.Z. Vidarte, M. Rissanen; P. Tammela, T. Vuorinen., J. Agric. Food Chem., 71 (44) (2023) 16554–16567.
[13] A. Căta, I.M.C. Ienaşcu, A. Frum, D. Ursu, P. Svera, C. Orha, G. Rusu, A.A. Chiș, C. M. Dobrea, C. Morgovan, O.-R. Pop., Pharm., 16 (3) (2024) 369.
[14] I. Mishra, J. Aslam, C. Verma, M.A. Quraishi, E.E. Ebenso, J. Taiwan Inst. Chem. Eng., 114 (2020) 341-358.
[15] W. Guo, M. Talha, Y. Lin, Y. Ma, X. Kong, J. Colloid Interface Sci., 597 (2021) 242-259.
[16] A. Mishra, J. Aslam, C. Verma, M.A. Quraishi, E.E. Ebenso, J. Taiwan Inst. Chem. Eng., 114 (2020) 341-358.
[17] H. Assad, A. Kumar, J. Mol. Liq., 344 (2021) 117755.
[18] K. Zakaria, M. A. Abbas, M. A. Bedair, J. Mol. Liq., 352 (2022) 118689.
[19] S.U. Ofoegbu, T.L. Galvão, J.R. Gomes, J. Tedim, H.I. Nogueira, M.G. Ferreira, M.L. Zheludkevich, Phys. Chem. Chem. Phys., 19(8) (2017) 6113-29.
[20] F.P. Eng, H. Ishida, J. Mater. Sci., 21 (1986) 1561-8.
[21] G. Vengatesh, M. Sundaravadivelu, J. Adhes. Sci. Technol., 34(19) (2020) 2075-106.
[22] Y. Sun, Y. Zhang, C. Xu, B. Tan, W. Li, X. Zheng, A. Brahmia, Ind. Crops Prod. 197 (2023) 116551.

The 56th International October Conference on Mining and Metallurgy
22-25 October 2025, Bor Lake, Bor, Serbia
www.ioc.tfbor.bg.ac.rs

DOI: 10.5937/IOC25583Z *Original scientific paper*

EXTRACTION OF BIOACTIVE COMPOUNDS FROM NETTLE SEEDS AS A POTENTIAL INHIBITOR OF METAL CORROSION

Milica Zdravković[1a], Edina Huseinović[2b], Jasmina Dedić[2c], Emir Horozić[3d], Vesna Grekulović[1e]

[1] Technical Faculty Bor, University of Belgrade, V.J. 12, 19210 Bor, Serbia
[2] Department of Chemistry, Faculty of Natural Sciences and Mathematics, University of Tuzla, Bosnia and Herzegovina
[3] Faculty of Technology, University of Tuzla, Bosnia and Herzegovina
[1a] mboskovic@tfbor.bg.ac.rs, 0000-0001-9488-9151
[2b] edina.huseinovic@untz.ba, 0009-0007-0222-383X
[2c] jasmina.dedic@untz.ba, 0009-0009-4768-2225
[3d] emir.horozic@untz.ba, 0000-0003-0242-3093
[1e] vgrekulovic@tfbor.bg.ac.rs, 0000-0001-6871-4016

Abstract
The aim of the research is to determine the effectiveness of ultrasonic extraction of nettle seeds (Urtica dioica) whose products can be used as potential metal corrosion inhibitors. Different solvents were used (water, methanol, ethanol, acetone) in terms of total phenol content (TPC), flavonoids (TFC) and antioxidant activity (DPPH and FRAP). The results show that the aqueous extracts have the highest TPC and antioxidant capacity in both tests. The high correlation between TPC and antioxidant activity (R ≈ 0.98) confirms that phenolic compounds are key contributors to antioxidant capacity. These findings suggest that nettle seeds can be examined as a potential metal corrosion inhibitor.

***Keywords**: Urtica dioica L., ultrasonic extraction, bioactive compounds, antioxidant activity*

1. INTRODUCTION

Plants are a rich source of bioactive compounds that possess numerous biological activities, including antioxidant, antimicrobial, anti-inflammatory, cytotoxic and antiviral effects [1]. Nettle (*Urtica dioica L.*), also known as common nettle, is a perennial weed plant native to Eurasia, today widespread almost all over the world [2]. Nettle is a multi-purpose plant known for being used as both food and medicine since ancient times [3]. Recently, the plant has attracted a lot of attention due to numerous important biological activities and applications in the food industry [4]. Nettle is rich in proteins, minerals, vitamins (A, C, E), carotenoids and fibers [5]. Antioxidant effect of nettle is considered key for its pharmacological potential [6]. Also, nettle proved to be a good inhibitor of steel in an acidic environment [7,8].

Nettle seeds (*Urtica dioica L.*) are a rich source of bioactive compounds that possess significant biological activity, including antioxidant, anti-inflammatory, antimicrobial and anticancer activity. Nettle seeds are rich in various bioactive components, including phenolic acids, flavonoids, fatty acids and sterols. Phenolic acids, such as ferulic and caffeic acid, are present in significant concentrations and contribute to the antioxidant activity of the seeds. These components contribute to the antioxidant activity of the seeds, neutralizing free radicals and reducing oxidative stress. For example, the presence of 5-O-caffeoylquinic acid, an ester of caffeic and quinic acids, was identified as a major peak in nettle seed extracts, indicating a significant concentration of these compounds [9]. Although nettle seed has not yet been investigated as a metal corrosion inhibitor, it is a potential corrosion inhibitor due to the presence of caffeic acid. Caffeic acid has been shown to be an effective corrosion inhibitor of steel and copper [10,11].

Flavonoids, such as quercetin, kaempferol and isorhamnetin, are present in nettle seeds, often in the form of glucosides or rutinosides. These compounds have pronounced antioxidant, anti-

inflammatory and antimicrobial activity [12]. Extracts rich in quercetin-3-O-glucoside, kaempferol-3-Oglucoside and isorhamnetin have proven to be effective inhibitors of metal corrosion [13,14]. Nettle seeds contain sterols, such as β-sitosterol, which have antioxidant properties and can contribute to the reduction of LDL cholesterol levels in the blood. Research shows that β-sitosterol isolated from rice husks and extracted from *Croton Persimilis* acts as an green inhibitor of mild steel corrosion in an acidic environment [15,16]. Nettle seeds are rich in fatty acids, including linoleic, oleic and α-linolenic acids. These essential fatty acids play an important role in maintaining the health of the heart and blood vessels, reducing the risk of cardiovascular diseases [17]. The fatty acid have an impact on adsorption and corrosion inhibition of iron by amine-fatty acid salts in acidic solution [18]. Also, fatty acids and its derivatives act as corrosion inhibitors for mild steel in various medium [19].

Considering these characteristics, the aim of this study is to investigate the chemical profile of nettle seeds, with a special focus on phenolic and flavonoid compounds, and to evaluate their contribution to antioxidant activity as an important factor of metal corrosion inhibitors. By applying ultrasonic extraction with the use of solvents of different polarities and chemical properties, the potential of nettle seeds is investigated in detail, with the aim of improving its applications in functional food and natural therapeutic products.

2. EXPERIMENTAL

2.1. Preparation of plant samples and chemicals

Nettle seeds (*Urtica dioica L.*) were harvested in a field near Tuzla, Bosnia and Herzegovina, were crushed into a homogeneous powder. The extraction was carried out in an ultrasonic bath at room temperature, using 0.5 g of powder in 50 mL of demineralized water for 2 hours. After filtering the samples, spectrophotometric analysis was performed on a UV-VIS device (Perkin Elmer Lambda25) at wavelengths of 510-765 nm in order to determine phenolic and antioxidant compounds.

2.2. Determination of total phenolic content (TPC)

Total phenolic content (TPC) was determined according to the method of Singleton et al. (1999), with minor adjustments [20]. In the analysis, 200 μL of extract was mixed with 10% Folin–Ciocalteu reagent and 10% Na_2CO_3, and incubated for 1 hour at room temperature. After dilution with distilled water, the absorbance was measured at 765 nm. The results are expressed as mg of gallic acid per gram of dry weight (mg GAE/g DM), with a standard curve ($y = 0.0042x + 0.0076$; $R^2 = 0.9998$) [21].

2.3. Determination of total flavonoid content (TFC)

Total flavonoids content (TFC) was determined spectrophotometrically according to the modified protocol of Olajira and Azeez [22]. The extract sample was treated with $NaNO_2$, $AlCl_3$ and NaOH, and then diluted to 10 mL. Absorbance was measured at 510 nm, and the results were expressed as mg quercetin per gram dry mass (mgQE/g DM), using a standard curve ($y = 3.024x – 0.0034$; $R^2 = 0.9984$) [23].

2.4. Ferri-reducing antioxidant capacity (FRAP)

The antioxidant potential of the samples was assessed using the FRAP method according to Benzie and Strain[24]. The extract (100 μL) was incubated with 3 mL of FRAP reagent at 37°C for 30 minutes, and the absorbance was measured at 593 nm. Results are expressed as μmol Fe^{2+}/g dry weight, using a standard curve ($y = 0.001x + 0.0698$; $R^2 = 0.9997$).

2.5. DPPH test

The antiradical activity was determined by the DPPH method according to the adapted protocol of Horozić et al. [25]. The extract (2 mL, 0.5 mg/mL) was mixed with 0.5bmL of DPPH solution (0.5bmM in methanol) and incubated for 30 minutes in the dark at room temperature. The absorbance was measured at 517 nm, and the activity was expressed as a percentage of radical inhibition:

$$I\ (\%) = [(Ac - As) / Ac] \times 100$$

where Ac and As are the absorbances of the control and tested samples [26,27].

3. RESULTS AND DISCUSSION

Ultrasonic extraction significantly improves the extraction of bioactive compounds from nettle seeds, thanks to the cavitation effect that breaks the cell structures and increases the availability of phenols and flavonoids. The following table shows a comparison of antioxidant activity and quantitative analysis of phenols and flavonoids in extracts prepared with different solvents.

Table 1. Antioxidant activity and content of bioactive compounds in ultrasound extracts of nettle seeds

Sample	Solvent	FRAP [μmol/g]	DPPH inhibition [%]	TPC [mg GAE/g]	TFC [mg QE/g]
A-1	ethanol	699.6	8.15	1.73	0.0227
A-2	methanol	943.1	24.8	6.83	0.165
A-3	acetone	476	6.85	0.54	0.2286
A-4	water	967.3	44.69	23.47	0.091

Aqueous extracts showed the highest FRAP result (967.3 μmol Fe^{2+}/g), which indicates a strong reducing power, while methanol was second with 943.1 μmol/g. Ethanol and acetone provided significantly lower values, indicating a weaker reduction potential. This trend confirms general observations in plant extraction, where polar solvents such as water and methanol more efficiently extract polar bioactive compounds, including phenols and flavonoids. In the DPPH test, the aqueous extract was again the leader with 44.69% inhibition, followed by methanol with 24.8%, while ethanol and acetone showed minimal activity (8.15% and 6.85%, respectively). This confirms that water extracts more effectively neutralize free radicals, which is in accordance with the findings from the literature where water as a solvent gives superior antioxidant results in ultrasonic nettle extraction [28]. Based on these results, it can be assumed that the extract obtained by extraction with water has the highest potential to act as a corrosion inhibitor [29].

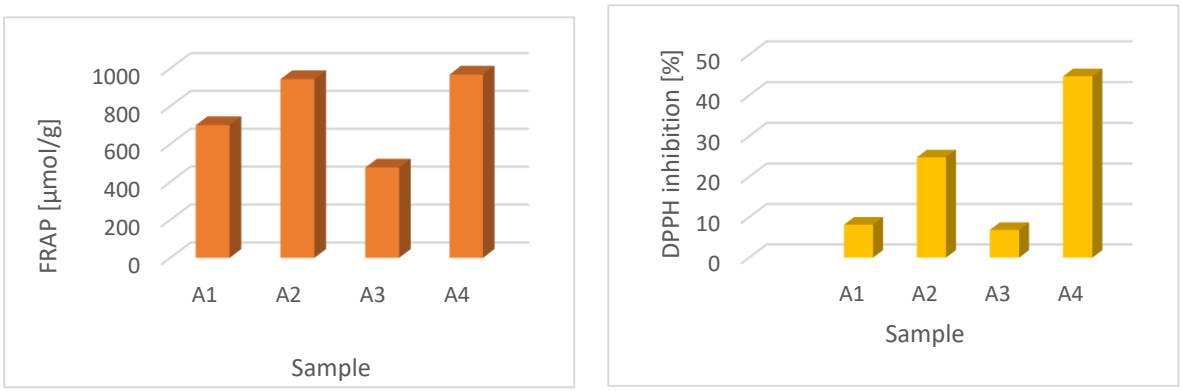

Figure 1. Comparative analysis of reduction potential (FRAP) and inhibition of DPPH radicals in ultrasound extracts of nettle seeds

The total phenolic content (TPC) was significantly highest in the water extract (23.47 mg GAE/g), followed by the methanol extract (6.83 mg GAE/g), while ethanol and acetone had low values (1.73 and 0.54 mg GAE/g). This points to the superior ability of water to extract phenolic compounds from nettle seeds. The high correlation between TPC and antioxidant activity (FRAP and DPPH) is in accordance with the results of other works [30] where $R \approx 0.98$ confirms that phenols are the primary carriers of antioxidant activity in plant extracts.
The highest content of flavonoids (TFC) was recorded in acetone extract (0.2286 mg QE/g), followed by methanol (0.165 mg QE/g), while ethanol (0.0227 mg QE/g) and water (0.0910 mg QE/g) showed significantly lower content. This result suggests that the polyphenolic profiles of nettle seeds may contain specific flavonoids more soluble in medium-polar solvents such as acetone and methanol. The results of earlier research show that extraction solvents have significant effects on TPC, TFC, CTC and inhibition properties of extracts, on the basis of which the effect of aqueous and acetone extracts of nettle seeds can be expected as potential corrosion inhibitors [31].

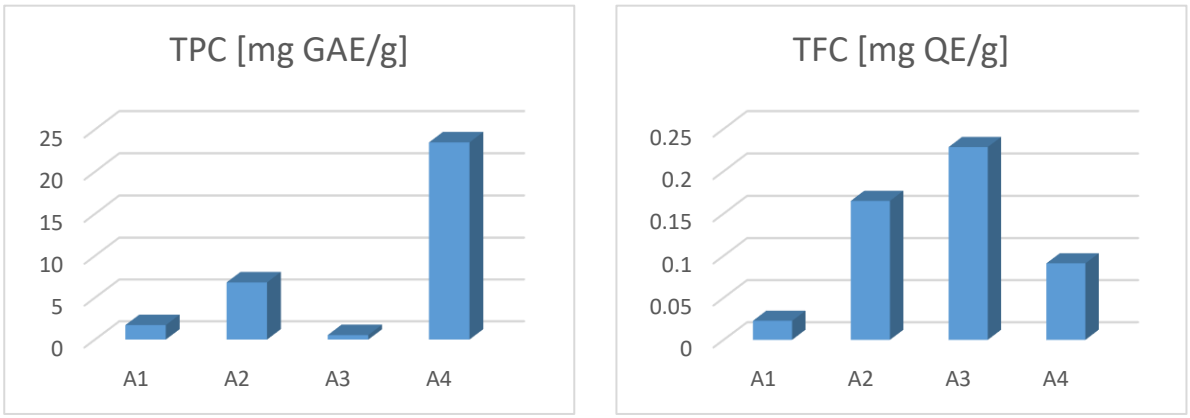

Figure 2. Comparison of the content of polyphenols and flavonoids in ultrasound extracts of plants

4. CONCLUSION

The results of this research confirm the high efficiency of ultrasonic extraction in the isolation of bioactive compounds from nettle seeds (*Urtica dioica L.*), for potential application as metal corrosion inhibitors. The results show that water as a solvent shows superior results compared to methanol, ethanol and acetone. The highest total phenolic content and antioxidant activity in DPPH and FRAP tests were recorded in aqueous extracts, which is consistent with the findings of other studies that highlight the advantages of using water as a solvent in the ultrasonic extraction of nettle. Further research will be focused on the optimization of extraction conditions, the identification of specific bioactive compounds and the evaluation of their biological activities in order to maximize the potential of nettle seeds in various industrial applications.

ACKNOWLEDGEMENTS

The research presented in this paper was done with the financial support of the Ministry of Education, Science and Technological Development of the Republic of Serbia, within the funding of the scientific research work at the University of Belgrade, Technical Faculty in Bor, according to the contract with registration no. 451-03-137/2025-03/200131.

REFERENCES

[1] A. Uysal, G. Zengin, A. Mollica, E. Gunes, M. Locatelli, T. Yilmaz, A. Aktumsek, Phytomedicine, 23 (2016) 979–988.
[2] R. Upton, J. Herb. Med., 3 (1) (2013) 9–38.
[3] D. Brown, Encyclopedia of Herbs and Their Uses, Dorling Kindersley, London, 1995.

[4] V. Jaiswal, H.J. Lee, Antioxidants (Basel), 11 (12) (2022) 2494.
[5] H.P. Devkota, K.R. Paudel, S. Khanal, A. Baral, N. Panth, A. Adhikari-Devkota, N.K. Jha, N. Das, S.K. Singh, D.K. Chellappan, Molecules, 27 (16) (2022) 5219.
[6] M. Oplanić, S. Jokić, M. Molnar, J. Food Process. Preserv., (2017).
[7] A. Zaabar, R. Aitout, L. Makhloufi, K. Belhamel, B. Saidani, Pigm. resin technol., 43 (3) (2014) 127-38.
[8] R. Maizia, A. Zaabar, A. Djermoune, D. Amoura, S.A. Martemianov, A. Thomas, A. Alrashdi, L. Makhloufi, H. Lgaz, A. Dib, M. Chafiq, Arab. J. Chem., 16 (8) (2023) 104988.
[9] S. Đurović, I. Kojić, D. Radić, Y.A. Smyatskaya, J.G. Bazarnova, S. Filip, T. Tosti, Int. J. Mol. Sci., 25 (6) (2024) 3430.
[10] F.S. de Souza, A. Spinelli, Corros. Sci., 51 (3) (2009) 642-9.
[11] L. Vrsalović, S. Gudić, M. Kliškić, E.E. Oguzie, L. Carev, Int. J. Electrochem. Sci. 11 (1) (2016) 459-74.
[12] K. Wójcik-Borowska, W. Wójciak, M. Żuk, P. Luchowski, A. Skalska-Kamińska, W. Pacuła, I. Sowa, M. Wójciak, Molecules, 30 (12) (2025) 2515.
[13] C. Coy, L.D. Becerra, S. Torres, V. Gonzalez, Results Chem., (2025) 102498.
[14] M. Zdravković, V. Grekulović, J. Suljagić, D. Stanković, S. Savić, M. Radovanović, U. Stamenković, Bioelectrochemistry, 151 (2023) 108401.
[15] M. Prabakaran, S.H. Kim, A. Sasireka, V. Hemapriya, I. M. Chung, New J. Chem., 41 (10) (2017) 3900-7.
[16] V.K. Thomas, J.K. Thomas, V.P. Raphael, K. Ragi, R. Johnson, R. Babu, J. Bio- Tribo-Corros., 7 (3) (2021) 121.
[17] Z. Petkova, G. Antova, M. Angelova-Romova, Grasas Aceites, 71 (1) (2020).
[18] T. Szauer, A. Brandt, Electrochim. Acta., 26 (9) (1981) 1257-60.
[19] P.N. Swathi, K. Rasheeda, S. Samshuddin, V. D.Alva, J. Asian Sci. Res., 7 (8) (2017) 301.
[20] V.L. Singleton, R. Orthofer, S. Lamuela-Raventós, R.M. Lamuela-Raventos, Methods Enzymol., 299 (1999) 152-178.
[21] R.E.K. Dibacto, B.R.T. Tchuente, M.W. Nguedjo, Y.M.T. Tientcheu, E.C. Nyobe, F.L.E. Edoun, M.F.G. Kamini, R.F. Dibanda, G. B. Medoua, Sci. World J., (1) (2021) 8882594.
[22] A.A. Olajire, L.A. Azeez, Afr. J. Food Sci., 2 (2) (2011) 022-029.
[23] C-C. Chang, M-H. Yang, H-M. Wen, J-C. Chern, J. Food Drug Anal., 10 (3) (2002) 178-182.
[24] I.F.F. Benzie, J.J. Strain, Methods Enzymol., 299 (1999) 15-27.
[25] E. Horozić, A. Zukić, L. Kolarević, D. Bjelošević, Z. Ademović, B. Šarić-Kundalić, D. Husejnagić, A. Kudumović, S. Hamzić, Technics Technologies Education Management. (2019) 14-19.
[26] A. Wojdylo, J. Oszmianski, R. Czemerys, Food Chem., 29 (11) (2007) 940–949.
[27] E. Horozić, J. Dedić, E. Huseinović, Rad. Šumar. fak. Univ. Sarajevu., 2024.
[28] M. Flórez, P. Cazón, M. Vázquez, Molecules, 27 (18) (2022) 6015.
[29] I.M. Ienașcu, A. Căta, A.A. Chis, M.N. Ştefănuț, P. Sfîrloagă, G. Rusu, A. Frum, A.M. Arseniu, C. Morgovan, L.L. Rus, C.M. Dobrea, Materials. 16 (8) (2023) 2967.
[30] I. Spiridon, R. Bodirlau, C-A. Teaca, Cent. Eur. J. Biol., 6 (3) (2011) 388-396.
[31] K.W. Tan, M.J. Kassim, A Corros. Sci. 53(2) (2011) 569-74.

The 56th International October Conference on Mining and Metallurgy
22-25 October 2025, Bor Lake, Bor, Serbia
www.ioc.tfbor.bg.ac.rs

DOI: 10.5937/IOC25588Z *Original scientific paper*

HPLC-DAD IDENTIFICATION OF COMPOUNDS IN CORROSION INHIBITOR *SALIX ALBA* BARK EXTRACT AND THE HYDROLATE

Milica Zdravković[1a], Slađana Savić[2b], Vesna Grekulović[1c], Dalibor Stanković[2d]

[1] Technical Faculty Bor, University of Belgrade, V.J. 12, 19210 Bor, Serbia
[2] Faculty of Chemistry, University of Belgrade, Studentski trg 16, Belgrade, Serbia
[1a] mboskovic@tfbor.bg.ac.rs, 0000-0001-9488-9151
[2b] sladjana@chem.bg.ac.rs, 0000-0002-1483-110X
[1c] vgrekulovic@tfbor.bg.ac.rs, 0000-0001-6871-4016
[2d] dalibors@chem.bg.ac.rs, 0000-0001-7465-1373

Abstract
The compounds present in Salix alba bark (SAB) extract and its hydrolate were identified using high-performance liquid chromatography with diode array detection (HPLC-DAD). SAB extract and its hydrolate were obtained by evaporating a macerate of dried, ground white willow bark and hot distilled water. A total of 19 standard polyphenolic compounds were used for the HPLC analysis. Results indicate that only 4-hydroxybenzoic acid (4-HBA) was detected in the SAB hydrolate. In contrast, both gallic acid and caffeic acid were present in the SAB extract. The presence of 4-HBA indicates the potential possibility of using SAB hydrolate as a starting component for the synthesis of parabens and other 4-HBA derivatives. Additionally, the identification of gallic and caffeic acids in the SAB extract further confirms the effect as a cathodic inhibitor of copper corrosion in chloride environments, because both acids are proven cathodic inhibitors of copper in different corrosion environments.

Keywords*: white willow bark, HPLC, caffeic acid, gallic acid, 4-hydroxybenzoic acid*

1. INTRODUCTION

Identification of compounds in herbal corrosion inhibitors is often performed using the HPLC method [1,2]. In this way, it is possible to determine which of the compounds have the greatest effect on corrosion inhibition, enabling a better understanding of the electrochemical properties and reaction mechanisms of corrosion inhibition processes [3]. Also, based on the compounds present, it is possible to additionally understand the complexity of inhibiting metal corrosion, especially when organometallic complexes occur between plant corrosion inhibitor molecules and metal ions due to corrosion processes [4]. The chemical structure and physicochemical properties of these compounds, like functional groups, electron density at the donor atom, p-orbital character, and the electronic structure of the molecules, should be considered [5,6]. The compounds present in the herbal corrosion inhibitor adsorb onto the metal surfaces, and thus protect them from the corrosive effect of the electrolyte [7].

Salix alba bark (SAB) extract, better known as white willow bark extract, has been identified as a cathodic type of corrosion inhibitor that exhibited protective properties against copper corrosion in chloride conditions (specifically, in a 0.5 M NaCl solution) [8]. However, the specific compounds in this extract remain unclear. It is well-known that white willow bark contains salicin, which acts as an effective corrosion inhibitor of some metals [9]. Furthermore, white willow is the main source of salicin and other salicylic derivatives - salicortin, 2'-O-acetylsalicortin, and tremulacin, that share structural similarities with aspirin (acetylsalicylic acid) [10].

The aim of this work is to identify the compounds in SAB extract and hydrolate using the HPLC method. This will help determine whether salicin or its derivatives function as corrosion inhibitors or if other compounds affecting copper corrosion are present. Hydrolate analysis was performed to determine the possible application of SAB hydrolate, which is a by-product of obtaining SAB

extract. By determining the potential application of SAB hydrolate, it is possible to achieve a circular process, considering that the residual plant material from willow bark can be used in biosorption and applications in the pulp industry [11].

2. EXPERIMENTAL

2.1 Preparation of white willow bark extract

SAB extract and hydrolate were obtained from a white willow bark macerate. This macerate was prepared by pouring hot distilled water over ground white willow bark. After filtration of the mixture on a Buchner funnel under vacuum, the filtrate was transferred to a rotary evaporator Buchi R-210. The solvent removal process was carried out at 72 mbar and 40 °C, resulting in a brown extract, which resembles resin, and the hydrolate.

2.2 Chemicals

A mixture of methanol (HPLC grade, Sigma Aldrich) and water (HPLC grade, Sigma Aldrich) in a 70/30 (v/v) ratio was used to dilute the extract prior to high-performance liquid chromatography with diode array detector (HPLC-DAD) analysis. Acetonitrile (eluent A, HPLC grade, Sigma Aldrich) and water (eluent B, HPLC grade, Sigma Aldrich) were used as mobile phases, both with 0.1 % of formic acid (HPLC grade, Fluka) in HPLC-DAD analysis. 4-Hydroxybenzoic acid, 4-hydroxyphenylacetic acid, aesculetin, apigenin, arbutin, caffeic acid, chlorogenic acid, ellagic acid, gallic acid, isorhamnetin, isorhamnetin-3-o-glycoside, kaempferol, kaempferol-3-o-glycoside, luteolin, neochlorogenic acid, p-coumaric acid, quercetin, quercetin-3-O-glycoside, and syringic acid were used as standard polyphenolic compounds.

2.3 HPLC analysis

The SAB hydrolate and extract were analyzed by the HPLC-DAD system (Thermo Ultimate 3000 RS, Germany), alongside thestandards. Hydrolate and standards were filtered (0.22 μm syringe filters, PTFE membrane, 15 mm, Agilent Technologies) before HPLC-DAD analysis. The extract sample was weighed (0.0864 g) and diluted with methanol/water mixture up to 25 cm^3, assisted by an ultrasound bath. This solution was then syringe-filtered, like the rest of the samples. The HPLC-DAD analysis was conducted as reported elsewhere [12], using the Chromeleon software, v6.8 (ThermoFisher Scientific, Germany) for instrument manipulation and data processing.

3. RESULTS AND DISCUSSION

3.1 HPLC profile of willow bark hydrolate and extract

The chromatographic profile of SAB hydrolate and extract are shown in Figure 1. The number and intensity of peaks clearly indicate that the extract has a more complex composition than the hydrolate [13]. Out of 19 screened polyphenolic compounds, only 4-hydroxybenzoic acid (4-HBA, retention time 12.4 min) was identified in the hydrolate sample (Figure 1A). This compound was not identified in the extract (Figure 1B), which had gallic acid (at 7.7 min) and caffeic acid (at 9.8 min).

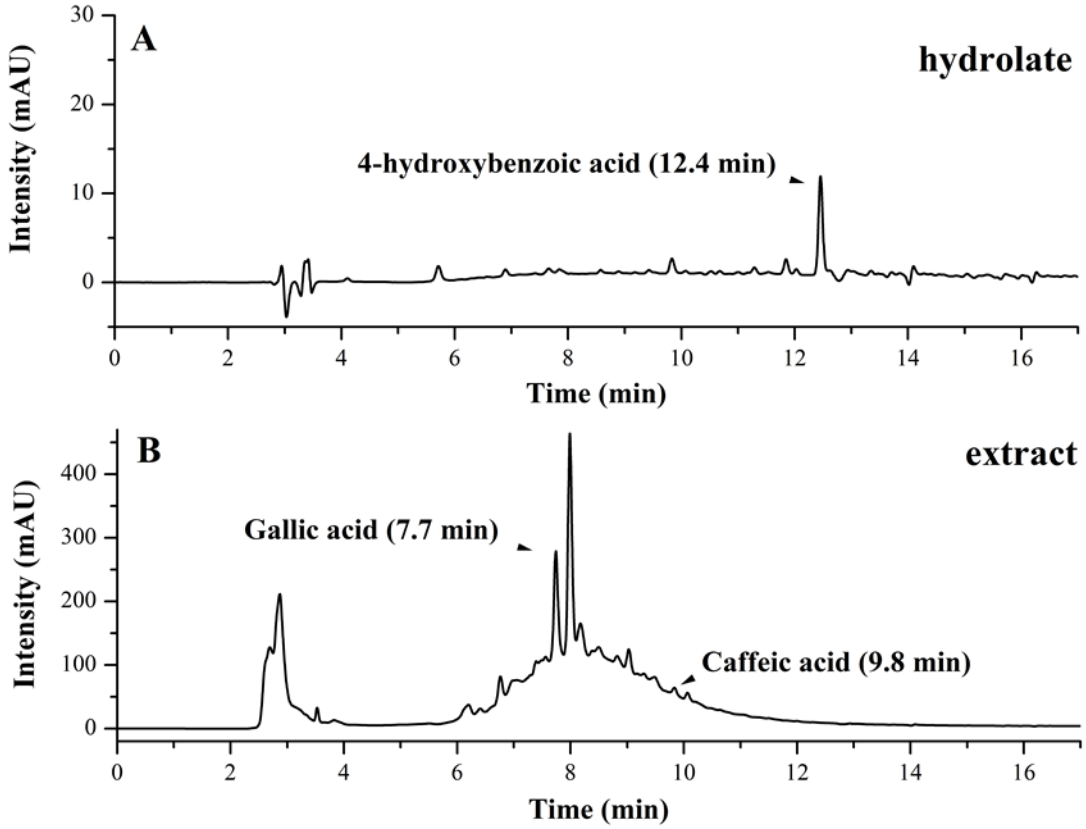

Figure 1. Chromatograms of willow bark hydrolate (A) and extract (B) at 254 nm

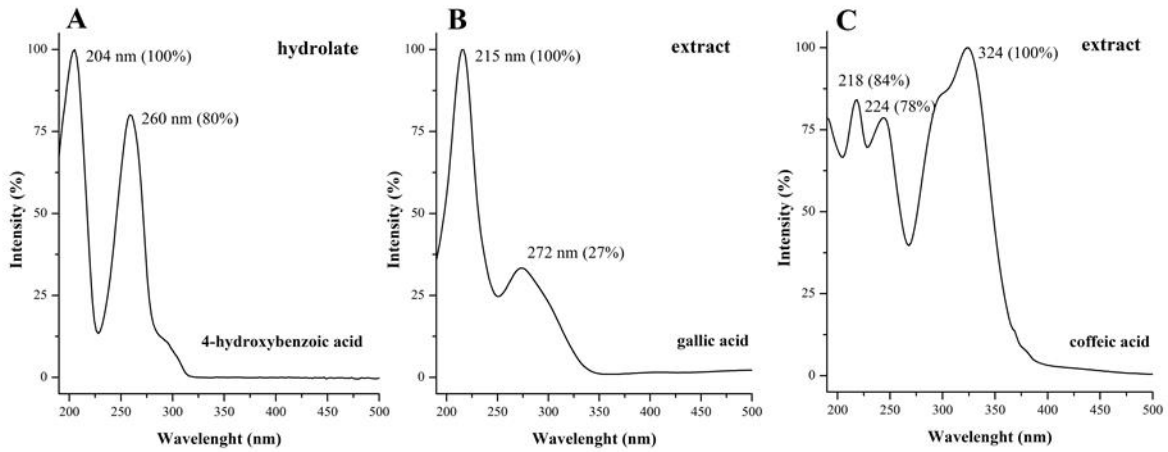

Figure 2. UV-Vis spectra of 4-hydroxybenzoic acid (A), gallic acid (B), and caffeic acid (C) from the corresponding chromatographic peaks at 254 nm

The typical UV-Vis spectra for the identified compounds are provided in Figure 2. Surprisingly, neither the extract nor the hydrolate showed evidence of quercetin and p-coumaric acid content [14,15,16], which was found in willow wood samples from Quebec by Brereton *et al.* using LC-MS analysis [14]. Other compounds, such as salicin and its derivatives, tannins, flavonoids, and various phenolic glycosides, were also anticipated, but were not detected due to lack of appropriate standards [14,17,18,19]. The content of polyphenolic compounds in SAB hydrolate and extract detected, based on their peak areas at 254 nm, is shown in Table 1.

Table 1. Content of polyphenolic compounds in SAB hydrolate and extract detected based on their peak areas at 254 nm

Sample name	Compound Name	Retention time (min)	Amount	Compound structure
SAB hydrolate	4-hydroxybenzoic acid (4-HBA)	12.4	1.22 mg/L	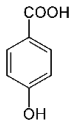
SAB extract	gallic acid	7.7	18.88 g/kg	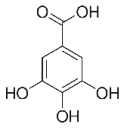
SAB extract	caffeic acid	9.8	0.25 g/kg	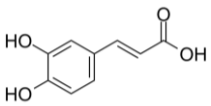

SAB hydrolate has not been chemically analyzed so far, However, the presence of 4-HBA enabled assessing its further use as a by-product in the extraction of SAB. Recent research has shown that various biosynthetic techniques have been developed for producing the 4-HBA and 4-HBA-based products. The 4-HBA is a promising intermediate for several value-added bioproducts with potential biotechnological applications (food, cosmetics, pharmacy, fungicides, etc.) [20]. Apart from its well-known application in the synthesis of parabens, it can also serve as a monomer for the synthesis of liquid crystalline polymers. This compound has various biological properties including hypoglycemic, anti-inflammatory, antiviral, and antioxidative activities [21,22].

Furthermore, SAB extract has demonstrated its effectiveness as an inhibitor of copper corrosion in chloride environments [8]. Its inhibitory effect is supported by the anti-corrosive properties of gallic and caffeic acid towards copper [23,24]. Wherein gallic acid may be considered to be a cathodic inhibitor that does not interfere directly with the cathodic process, but modifies the corrosive environment [23]. In addition to copper, gallic acid also acts as an aluminum and carbon steel corrosion inhibitor [25, 26]. Caffeic acid has also been shown to be an effective corrosion inhibitor of copper in 0.5 M NaCl solution and sulfuric acid, acting as a cathodic corrosion inhibitor [24, 27].

4. CONCLUSION

Using 19 standards polyphenolic compounds, the presence of compounds in the SAB extract and hydrolate was evaluated by the HPLC analysis. The chromatographic profile of the analyzed samples revealed that the SAB extract consisted of significantly more compounds compared to its hydrolate. In the hydrolate, only 4-hydroxybenzoic acid was confidently identified, whereas the presence of gallic and caffeic acid was confirmed in the extract. The presence of these components indicates the possibility of using SAB hydrolate as a starting component for synthesis, while SAB extract may be used as an effective metal corrosion inhibitor.

ACKNOWLEDGEMENTS

The research presented in this paper was done with the financial support of the Ministry of Education, Science and Technological Development of the Republic of Serbia, within the funding

of the scientific research work at the University of Belgrade, Technical Faculty in Bor, according to the contract with registration no. 451-03-137/2025-03/200131.

REFERENCES

[1] H.L.Y. Sin, A. Al-Shishani, A.A. Rahim, B. Saad, B.R. Pandian, Prog. Org. Coat., 135 (2019) 536-544.
[2] X. Wang, L. Chen, F. Yang, Q. Xiang, J. Liu, J. Adhesion Sci. Technol., 37(21) (2023) 2919–2943.
[3] Y. Fang, B. Suganthan, R.P. Ramasamy, J. Electroanal. Chem., 840 (2019) 74-83.
[4] M. Zdravković, V. Grekulović, J. Suljagić, N. Štrbac, I. Marković, M. Gorgievski, M. Marković, Prot. Met. Phys. Chem. Surf., 60 (2024) 544-453.
[5] B.A. Rani, B.B. Basu., Int. J. Corros., 2012 (1) (2012) 380217.
[6] D.K. Verma, R. Aslam, J. Aslam, M.A. Quraishi, E.E. Ebenso, C. Verma., J. Mol. Struct., 1236 (2021) 130294.
[7] I. Miralrio, A. Espinoza Vázquez, Processes, 8(8) (2020) 942.
[8] M. Zdravković, V. Grekulović, E. Huseinović, R. Vianello, N. Štrbac, M. Huremović, M. Gorgievski, Proceedings of XVI International Mineral Processing and Recycling Conference, 28-30.05.2025., Belgrade, Serbia, 2025.
[9] N. Bhardwaj, P. Sharma, V. Kumar, Prot. Met. Phys. Chem. Surf., 57 (2021) 1076–1084.
[10] M. Neagu, C. Luntraru, A. Bira, J. Tomescu, N. Ionescu, R. Stan, U.P.B. Sci. Bull., Series B, 83 (3) (2021).
[11] M. Zdravković, V. Grekulović, N. Štrbac, B. Zdravković, M. Gorgievski, M. Marković, M. Marković, Ecologica, 31 (114) (2024) 137-143.
[12] M. Zdravković, V. Grekulović, J. Suljagić, D. Stanković, S. Savić, M. Radovanović, U. Stamenković., Bioelectrochem., 151 (2023) 108401.
[13] S. Levin, E. Grushka, Anal. Chem., 58(8) (1986) 1602-7.
[14] K. Warmiński, M.J. Stolarski, Ł. Gil, M. Krzyżaniak, Ind. Crop. Prod., 171 (2021) 113976.
[15] N.J.B. Brereton, N. Berthod, B. Lafleur, K. Pedneault, F.E. Pitre, M. Labrecque, Ind. Crop. Prod., 97 (2017) 525–535.
[16] A. Freischmidt, G. Jürgenliemk, B. Kraus, S.N. Okpanyi, J. Müller, O. Kelber, D. Weiser, J. Heilmann, Phytomed., 19 (3) (2012) 245–252.
[17] N. Huynh, J.J. Valle-Delgado, W. Fang, S. Arola, M. Österberg, Carbohydr. Polym., 317 (2023) 121095.
[18] I. Kammerer, R. Kahlich, C. Biegert, C.H. Gleiter, L. Heide, Phytochem. Anal., 16 (6) (2005) 470–478.
[19] J. Dou, P. Ilina, C.D. Cruz, D. Nurmi, P.Z. Vidarte, M. Rissanen, P. Tammela, T. Vuorinen, J. Agric. Food Chem., 71 (44) (2023) 16554–16567.
[20] S. Wang, M. Bilal, H. Hu, W. Wang, X. Zhang, Appl. Microbiol. Biotechnol., 102 (2018) 3561-71.
[21] J.O. Krömer, D. Nunez-Bernal, N.J. Averesch, J. Hampe, J. Varela, C. Varela, J. Biotechnol., 163(2) (2013) 184-93.
[22] O.K. Sytar, M. Brestic, M. Rai, H.B. Shao, J. Med. Plants. Res., 6(13) (2012) 2526-39.
[23] A.M. Beccaria, E.D. Mor, Br. Corros., J. 11(3) (1976) 156-60.
[24] L. Vrsalović, S. Gudić, M. Kliškić, E.E. Oguzie, L. Carev, Int. J. Electrochem. Sci., 11(1) (2016) 459-74.
[25] P. Kwolek, K. Dychtoń, B. Kościelniak, A. Obłój, A. Podborska, M. Wojnicki, Metals., 12(2) (2022) 250.
[26] S.J. Keny, A.G. Kumbhar, C. Thinaharan, G. Venkateswaran, Corros. sci., 50(2) (2008) 411-9.
[27] F.S. de Souza, C. Giacomelli, R.S. Gonçalves, A. Spinelli, Mater. Sci. Eng. C., 32(8) (2012) 2436-44.

The 56th International October Conference on Mining and Metallurgy
22-25 October 2025, Bor Lake, Bor, Serbia
www.ioc.tfbor.bg.ac.rs

DOI: 10.5937/IOC25593D *Original scientific paper*

INTERNAL QUALITY CONTROL OF ICP-MS METHOD FOR WATER ANALYSIS

Miloš Đukić[1a], Stefan Đorđievski[1b], Sanela Vasiljević[1c], Dragana Adamović-Marković[1d], Emina Požega[1e], Jelena Nikolić[2a], Vesna Stankov-Jovanović[2b]

[1]Mining and Metallurgy Institute Bor, Alberta Ajnštajna 1, 19210 Bor, Serbia,
[2] Faculty of Sciences and Mathematics – University of Niš, Višegradska 33, 18000 Niš, Serbia,
[1a] milos.djukic@irmbor.co.rs, 0000-0002-3307-4669
[1b] stefan.djordjievski@irmbor.co.rs, 0000-0003-1737-8766
[1c] sanela.vasiljevic@irmbor.co.rs, 0000-0001-6478-5335
[1d] dragana.adamovic@irmbor.co.rs, 0000-0003-3683-4122
[1e] emina.pozega@irmbor.co.rs, 0000-0001-6797-2435
[2a] jelena.cvetkovic@pmf.edu.rs, 0000-0002-9351-331X
[2b] vesna.stankov-jovanovic@pmf.edu.rs, 0000-0001-7885-0476

Abstract
Reliability of analytical results in determining the content of metals in water samples depends not only on the instrument performance, but also on the implementation of the internal quality control measures. The confirmation of results validity is one of the fundamental principles of the ISO/IEC 17025 standard and represents a key requirement for the accredited laboratories. The aim of this study is to demonstrate the application of certified reference material (CRM) in combination with X- control charts to assess the stability and accuracy of the ICP-MS method. The obtained results showed that the values for As, Cd, and Mn were within the specified limits, thereby confirming the stability of the ICP-MS method. It was concluded that integrating CRMs with graphical tools for monitoring results represents an efficient and practical approach to ensure the reliability of ICP-MS analyses, and that internal quality control is of essential importance when analyzing environmental samples.

***Keywords**: Control Charts, CRM, ICP-MS*

1. INTRODUCTION

The Chemical Testing Laboratory of Mining and Metallurgy Institute in Bor has a tradition of more than half a century and holds a significant position in the field of analytical chemistry. In addition to the analysis of geological samples and finished metallurgical products, an important segment of its work today also involves the testing of environmental samples.

The reliability of these analytical results is particularly important for environmental monitoring. As an accredited laboratory, the Institute is obliged to meet the requirements of ISO/IEC 17025, among which is ensuring the validity of results. This is carried out through internal quality control, which includes the use of certified reference materials (CRMs), blanks, and standard solutions [1].

One of the most powerful tools for statistical process control is the control chart. Its application enables simple and efficient monitoring of result stability, provides a clear visual overview of process status, and facilitates the timely detection of deviations. The basic elements of a control chart are the center line and the lower and upper warning and action limits, whose application indicates when a process correction is required or when the effects of implemented measures should be confirmed. In this way, the continuous validity of ICP-MS analyses in routine work is ensured [2,3].

The aim of this paper is to present the application of certified reference materials (CRMs), in conjunction with X-control charts, to assess the stability and accuracy of the ICP-MS method for

the analysis of water samples, specifically for the determination of arsenic (As), cadmium (Cd), and manganese (Mn).

2. EXPERIMENTAL

In addition to routine water samples, the certified reference material *WP Trace Metals VHG-QWPTM-15* (VHG Labs, USA) was analyzed. The CRM was prepared according to the manufacturer's instructions, with a 10-fold dilution using ultrapure water. The certified values for As, Cd, and Mn were 637, 497, and 1680 µg/L, respectively.

The contents of arsenic (As), cadmium (Cd), and manganese (Mn) were determined by Inductively Coupled Plasma Mass Spectrometry (ICP-MS) using a NexION 1000 instrument (PerkinElmer, USA). Instrument parameter control and data processing were carried out with Syngistix software. Before each analytical run, instrument performance was optimized using a *Tuning solution* (Be, Ce, Fe, In, Li, Mg, Pb i U, 1 µg/L, PerkinElmer, USA).

Calibration was performed using a multielement standard solution containing As, Cd, and Mn (AccuStandard, USA), while single element solutions of rhenium (Re) and rhodium (Rh) (AccuStandard, USA) were used as internal standards. The calibration range comprised seven points: 0, 1, 5, 10, 50, 100, and 200 µg/L.

The control charts were constructed based on the certified values of the CRM. The central line represents the certified value, while the warning limits were defined according to the QC acceptance limits and the action limits according to the Performance Acceptance Limits issued by the manufacturer.

3. RESULTS AND DISCUSSION

During CRM analysis, the measured value is entered into the control chart and interpreted. The method is considered out of control if: (1) one value lies beyond the action limit (red line); (2) two consecutive values lie beyond the warning limits (orange line); or (3) 10–11 consecutive values fall on the same side of the center line (green line) [2].

Figure 1 shows the X-control chart for As; since all values fell within the warning limits, we conclude that the method was in control and that the obtained analytical results are valid.

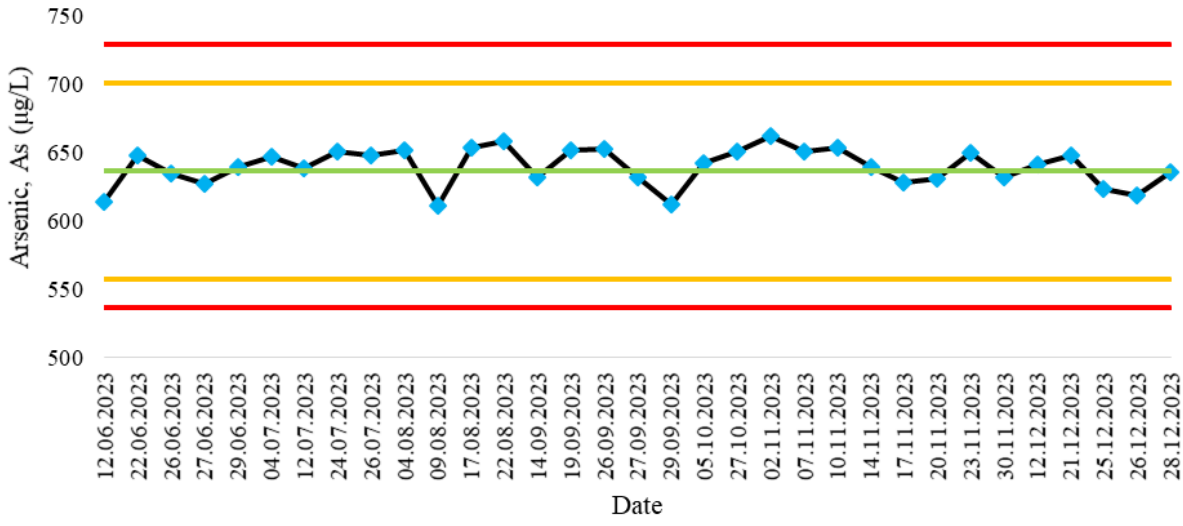

Figure 1. X-control chart for As

Figure 2 shows the X-control chart for Cd. Two values on 27 June and 7 November 2023 exceeded the warning limits; however, since the preceding and subsequent values were within the warning limits, the method remained in control.

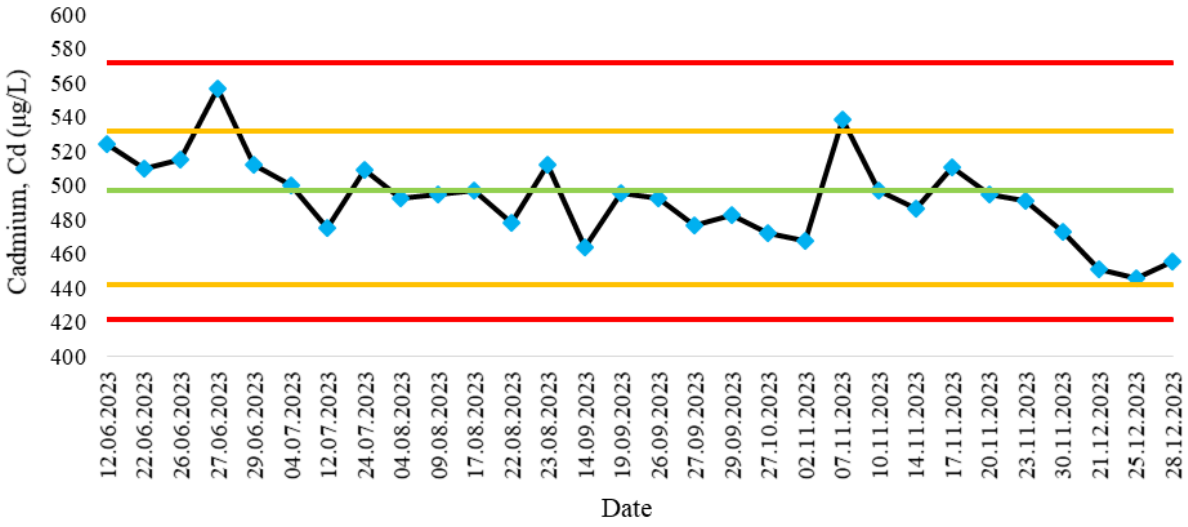

Figure 2. X-control chart for Cd

Figure 3 presents the X-control chart for Mn; since all values were within the warning limits, we concluded that the method was in control and that the obtained analytical results are valid.

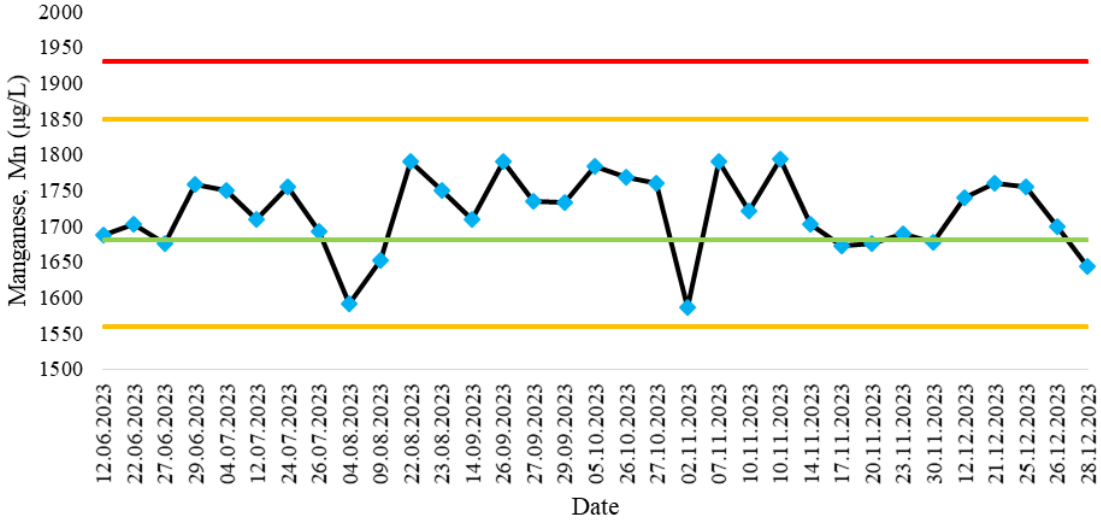

Figure 3. X-control chart for Mn

4. CONCLUSION

The results of six months of monitoring showed that all CRM values for As, Cd, and Mn were within the permissible limits defined by the manufacturer. This confirmed the reliability of the ICP-MS method and ensured the conditions for issuing valid analytical results, enabling the laboratory to report results with confidence in accordance with ISO/IEC 17025 requirements.

ACKNOWLEDGEMENTS

This paper was financially supported by the Ministry of Science, Technological Development and Innovation of the Republic of Serbia, contract numbers: 451-03-136/2025-03/ 20052 and 451-03-65/2025-03/200124.

REFERENCES

[1] ISO/IEC 17025, General requirements for the competence of testing and calibration laboratories. International Organization for Standardization/International Electrotechnical Committee, Geneva, 2017, p.13-14.
[2] M.B. Rajkovic, M. Mitrovic, S. Antic-Mladenvic, Zast. Mater., 60 (4), (2019) 342-359.
[3] H. Hovind, B. Magnusson, M. Krysell, U. Lund, I. Mäkinen, Internal Quality Controll, Oslo, 2008, p.11-13.

Environmental Protection, Remediation and Risk Assessment

The 56th International October Conference on Mining and Metallurgy
22-25 October 2025, Bor Lake, Bor, Serbia
www.ioc.tfbor.bg.ac.rs

DOI: 10.5937/IOC25599G *Original scientific paper*

APLLICATION OF NANOMATERIALS IN WATER TREATMENT FROM MANGANESE

Aleksandar Grigorov[1a], Silviya Lavrova[1b], Daniela Grigorova[1c]

[1] University of Chemical Technology and Metallurgy, 8 Kl. Ohridski, 1756 Sofia, Bulgaria
[1a] a.l.grigorov@abv.bg, 0009-0005-3429-9199
[1b] engeco2001@uctm.edu, 0000-0001-5507-3467
[1c] d.dimitrova@uctm.edu, 0000-0001-8440-4368

Abstract
Wastewater treatment is of crucial importance for the growing global water scarcity. Mining and processing industries generate wastewater containing toxic elements discharged into rivers and lakes. One of these highly toxic elements polluting water is manganese. The possibility for manganese removal from synthetic wastewater by using carbon nanotubes as an adsorbent has been examined. Carbon nanotubes have promising potential for water purification due to their tunable and distinctive physical and chemical characteristics. It was found that up to 99% purification effect is achieved at low concentrations of manganese ions in water.

***Keywords**: carbon nanotubes, water treatment, manganese, electrical conductivity*

1. INTRODUCTION

Water scarcity and water quality regulation is a major challenge for sustainable development [1]. Contaminated water has a major impact on public health, and it is expected that nearly 800 million people worldwide will soon lack access to good quality water for domestic use [2, 3]. The European Water Framework Directive 2000/60/EC [4] aims at a more sustainable use of water resources, encouraging technological development towards systems for treatment of all water, especially industrial wastewater. Goal 6, which is a key target in the United Nations 2030 Agenda [5], concerns sustainable management of water resources, which is consistent with circular economy strategies. Most of the industrially polluted water are characterized by a low pH and a high content of dissolved metals, such as copper, iron, manganese, etc.

Manganese is a naturally occurring element found in rocks, soil, water, and food [6]. In humans and animals, this trace element plays a role in bone mineralization, energy balance, metabolic regulation, and cellular defense [7]. On the other hand, in high concentrations, manganese is very toxic and can lead to a permanent neurological disorder known as manganism with symptoms that include tremors, difficulty walking and facial muscle spasms, irritability, aggressiveness and hallucinations, among others. Traditional water purification techniques, including filtration, distillation, coagulation-flocculation, biofiltration, and reverse osmosis, fail to remove all heavy metal ions from contaminated water. These methods are not sufficient to provide good quality water, which enforces the search for new energy-saving technologies for this purpose [9].

The application of nanomaterials (NM) in water purification is of utmost importance for the rapid removal of contaminants through adsorption or decomposition processes. Nanotechnology seems to offer promising applications in the field of water purification and remediation [10].

The interest in using carbon nanotubes in wastewater treatment is due to their exceptional properties such as larger surface area, higher binding capacity, higher chemical and thermal stability, and hollow structure, which also determines the possibility of their interaction with pollutants. The aim of this work is to investigate the possibility of effective treatment of manganese-contaminated wastewater.

2. EXPERIMENTAL

The laboratory studies were conducted with model aqueous solutions containing manganese, imitating the concentrations of this metal in wastewater from various industries. Multi-walled carbon nanotubes, representing carbon atoms arranged in the form of a hexagonal lattice in cylindrical macromolecules with the trade name - "A.R.T. NANO P", were used. The carbon nanotubes used in this study were supplied by ARTMONBAT AD. The nanotubes were produced by the so-called chemical vapor deposition method, at the company's production facility in the Republic of Bulgaria. The equipment for the synthesis of the nanotubes was entirely designed and patented by the company. In the experimental work, model aqueous solutions were used, obtained after dissolving appropriate amounts of $MnSO_4$ in distilled water. The metal concentrations were determined using ICP spectrometer with inductively coupled plasma model-VARIAN VISTA-MPX. The electrical conductivity of the aqueous solutions was measured using a μS-tester. The removal efficiency (%) was calcualted as follows:

$$RE = \frac{(C_o - C_e)}{C_o} * 100 \quad (1)$$

Where C_o and C_e are the initial and equilibrium ions concentrations (mg/L).

The equilibrium capacity (q_e, mg/g) of the CNTs was calcualted as follows:

$$q_e = \frac{(C_o - C_e)V}{m} \quad (2)$$

Where V is the volume of solution (L), and m is the mass of the adsorbent (g).

The adsorption equilibrium for the Mn^{2+} removal was studied using 50 mL model solutions, containing manganese in concentrations between 10 and 300 mg/L, pH 4.6, contacting with 2.5 g of CNTs. Shaking was carried out for 24 hours at 200 rpm using DIAB SK-0180-Pro shaker. Then samples were taken, filtered through blue ribbon filter paper to remove adsorbent particles and analyzed. The obtained results were described by Langmuir, BET and Toth equilibrium models (Table 1).

Table 1. Isotherm models used for experimental results interpretation.

Isotherm	Non-linear expression	Plot
Langmuir	$q_e = \frac{q_m K_L C_e}{1 + K_L C_e}$	q_e *vs.* C_e
BET	$q_e = \frac{q_{mBET} K_{BET1} C_e}{(1 - K_{BET2} C_e)(1 - K_{BET2} C_e + K_{BET1} C_e)}$	
Toth	$q_e = \frac{K_T C_e}{(a_T + C_e^z)^{1/z}}$	

3. RESULTS AND DISCUSSION

The structure of the CNTs used in the experimental work (Figure 1) was determined using an X-ray diffractometer (PANalytical Empyrean) and a computed X-ray microtomograph (Bruker SkyScan 1272). The specification of the nanotubes is presented in Table 2, and the SEM image is shown in Figure 2. The SEM image in Figure 2 shows a network of thin nanotubes, with a distinct fibrous structure. They appear to be highly intertwined, which is typical for CNTs, especially when they are short and multi-walled. The magnification in the upper right corner shows the diameter of one of the tubes, which is approximately 20 nm. The tubes are randomly oriented with non-directional growth. The structure of the material is complemented by the XRD result (Figure 1). The main peak is around $2\theta \approx 26°$, which is a characteristic peak for the (002) plane of a graphite-like structure, which is associated with well-ordered carbon layers (π-π stacking). In nanotubes (especially multi-walled) this peak is a strong indicator of crystallinity along the c-axis. Weaker

peaks are observed in the range of ~42°–44° and 54°–55°, which corresponds to (100) and (004) of graphite, further confirming the presence of crystalline carbon. Table 2 summarizes the results of the CNTs studies presented by the manufacturer.

Table 2. Nanotubes charachteristics.

Condition	Powdered
Type	Polyhedral
Length	≥ 2 μm
Diameter	10-40 nm
Number of walls	10-20
Specific surface area	55 m^2/g
Carbon content	≥ 90 wt.%
Bulk density	0.2 g/cm^3
True (pycnometric) density	2.2 g/cm^3
Ash content	7 wt.%

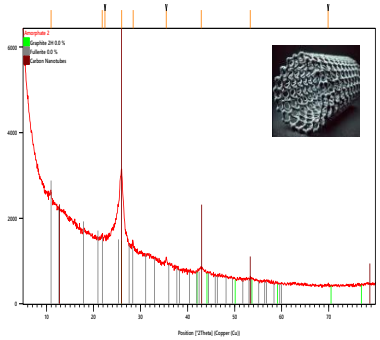

Figure 1. XRD pattern of CNTs.

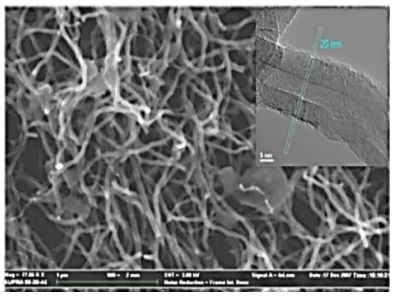

Figure 2. SEM of CNTs.

Figure 3 and Figure 4 present the relationships between the initial concentration of manganese ion, the removal efficiency, and the adsorption capacity, respectively. The results show that as manganese ion concentration increases, the removal efficiency drops significantly (Figure 3). This is likely due to the limited number of active sites on the nanotube surface, as indicated by its specific surface area (55 m^2/g).

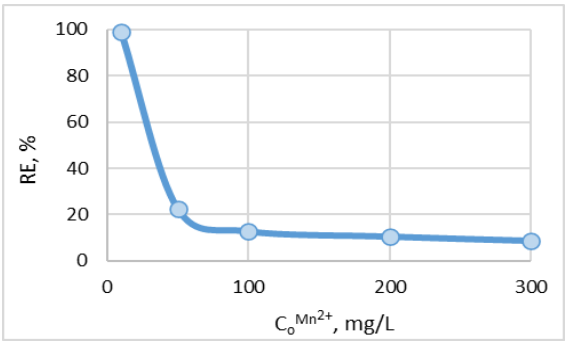

Figure 3. Dependence between the initial concentration of the element and the removal efficiency.

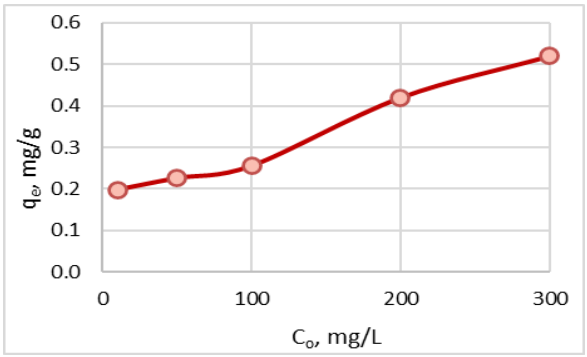

Figure 4. Adsorption capacity of the carbon nanotubes.

However, the adsorption capacity increases with higher initial concentrations (Figure 4). Figure 5 present the experimental equilibrium data of the manganese ions sorption on carbon nanotubes, and the applied three isotherm models: Langmuir, BET, and Toth. The calculated isotherm model parameters for the investigated system, as well as the values of the error functions are presented in Table 3. The non-linear regression is the most effective method for selecting the best-fitting isotherm. As shown in Figure 5 and supported by the high R^2 value (close to 1) and the low error function values in Table 3, the Toth model provides the best fit for the adsorption data.

Table 3. Values of the equilibrium model parameters and error functions.

System	Manganese ions – Carbon nanotubes			
Equilibrium model	Model parameters		Error function	
Langmuir	q_m	0.356	R^2	0.650
	K_L	12.327	SSE	0.058
			MSE	0.014
			RMSE	0.120
BET	q_{mBET}	-0.189	R^2	0.858
	K_{BET1}	-0.321	SSE	0.038
	K_{BET2}	-0.327	MSE	0.013
			RMSE	0.113
Toth	K_T	0.059	R^2	0.987
	a_T	-0.308	SSE	0.002
	z	0.491	MSE	0.001
			RMSE	0.027

The Toth isotherm is a modified form of the Langmuir model that improves prediction accuracy by accounting for sub-monolayer coverage, which means that less than a full single layer of adsorbate molecules has formed on the surface of the adsorbent - not all sites are filled and the surface is only partially covered.

This often occurs at low adsorbate concentrations or when adsorbate molecules are unevenly distributed due to surface heterogeneity or weak interactions. It means that the nanotubes surface needs to be modified to better metal ions removal.

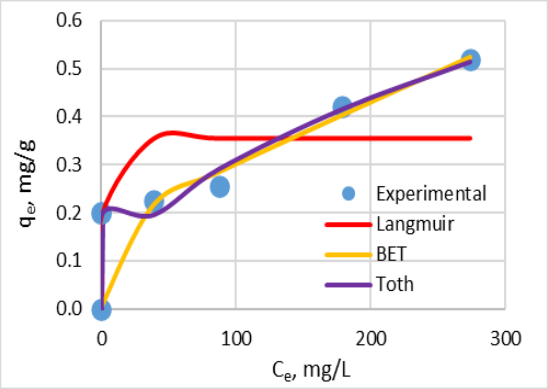

Figure 5. Experimental and model isotherms of the manganese ions sorption on carbon nanotubes.

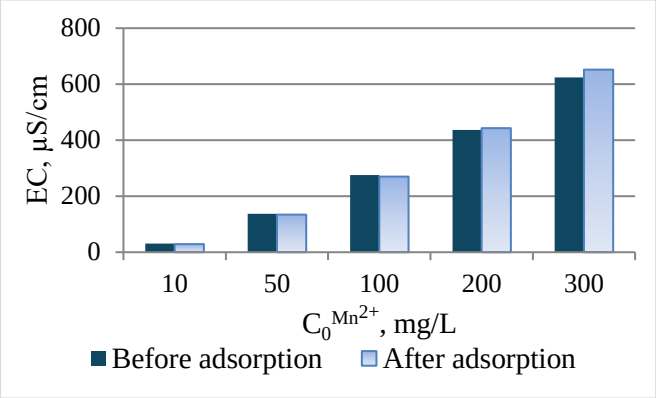

Figure 6. Comparison of electroconductivity of samples before and after adsorption

The Langmuir model describes chemical adsorption, and the BET model-physical adsorption. The R^2 in Langmuir model is low, which probably means that there is no chemical interaction between adsorbate molecules and the surface of the adsorbent.

Figure 6 presents the results of the electrical conductivity measurements of the five solutions with concentration variations from 10 to 300 mg/L. At low concentrations (10-100 mg/L), the electrical conductivity decreases after adsorption, suggesting that the Mn^{2+} ions are retained by the nanotubes and removed from the solution.

At higher concentrations (200-300 mg/L) the electrical conductivity increases after adsorption, meaning that the nanotubes are unable to adsorb Mn^{2+} and the metal ions remain in solution.

If the tubes are functionalized (e.g. by oxidation), they can acquire a negative charge, which increases the electrostatic attraction of the positively charged Mn^{2+} ions. Surface modification of nanotubes is the subject of further research.

4. CONCLUSION

It can be summarized that at low manganese concentrations, carbon nanotubes effectively adsorb metal ions, leading to a decrease in the solution's electrical conductivity. At higher concentrations, adsorption decreases - likely due to surface heterogeneity or weak interactions, and conductivity rises. Enhancing the adsorption capacity requires surface modification of the nanotubes.

REFERENCES

[1] A. Biswas, S. Sarkar, S. Das, *et al.*, Cambridge Prisms: Water, 3 (4) (2025).
[2] H. Shemer, S. Wald, and R. Semiat, Membranes, 13. (6) (2023) 612.
[3] E. Vallino, L. Ridolfi, and F. Laio, Environ. Sci. Policy, 114 (2020) 73–85.
[4] European Commission (Ed.), Report from the Commission to the European Parliament and the Council on the Implementation of the Water Framework Directive (2000/60/EC) 2019.
[5] United Nations Environment Programme (UNEP), "Why do sustainable development …– Goal 6.
[6] F.C. Wedler, Biochemical and nutritional role of Mn: An overview, LA: CRC Press, 1994, p 1–36.
[7] C.L. Keen and S. Zidenberg-Cher, Manganese in Present Knowledge in Nutrition, DC: ILSI Nutrition Foundation, 1990, p. 279–286.
[8] M. Williams, G.D. Todd, N. Roney, et al., Toxicological Profile for Manganese, Atlanta, GA: Agency for Toxic Substances and Disease Registry (US), 2012.
[9] U. Wajid, M.Z. Rehman, M. Umair, et al., Use of nanotechnology for wastewater treatment, 2022.
[10] L.P. Lingamdinne, Y.Y. Chang, J.K. Yang, et al., Chem. Eng. J., 307 (2017) 74–84.

The 56th International October Conference on Mining and Metallurgy
22-25 October 2025, Bor Lake, Bor, Serbia
www.ioc.tfbor.bg.ac.rs

DOI: 10.5937/IOC25603M *Original scientific paper*

ASSESSMENT OF MERCURY CONTENT IN DIFFERENT FUEL TYPES

Ana Marinković[1a], Jovana Buha Marković[1b], Jasmina Savić[1c], Milica Mladenović[1d], Milić Erić[1e], Zoran Marković[1f], Biljana Vučićević[1g]

[1] Vinča Institute of Nuclear Sciences – National Institute of the Republic of Serbia, University of Belgrade, Serbia
[1a] aradojevic@vinca.rs, 0000-0002-3206-1102
[1b] jbuha@vinca.rs, 0000-0002-5820-6541
[1c] jasnas@vinca.rs, 0000-0003-1094-7292
[1d] mica@vinca.rs, 0000-0003-1924-0437
[1e] milic@vinca.rs, 0000-0001-6850-3112
[1f] zoda_mark@vinca.rs, 0000-0003-0553-3263
[1g] bee@vinca.rs, 0000-0002-5817-0171

Abstract

Mercury is a highly toxic trace element that poses a serious global environmental threat due to its mutagenic properties, persistence in ecosystems, and its capacity for bioaccumulation. Combustion of fossil fuels, particularly coal, is one of the primary sources of atmospheric mercury emissions, prompting many countries to implement stringent regulatory limits. In response, this study aims to investigate and compare the mercury content in various types of coal and biomass fuels (wood chips and pellets) to evaluate their environmental suitability for energy production. The results demonstrate a clear and substantial difference in mercury concentrations between the two fuel groups. All analyzed coal samples contain significantly higher levels of mercury compared to biomass fuels. This variation is strongly influenced by sulfur content and other key fuel quality parameters, including calorific value, ash content, and elemental composition. These findings are essential for understanding how intrinsic fuel properties affect mercury emissions during combustion. Ultimately, the study aims to inform cleaner energy production practices by guiding fuel selection and optimizing combustion technologies to minimize environmental mercury release.

Keywords: *coal, wood biomass, mercury, direct mercury analyzer, environmental protection*

1. INTRODUCTION

Mercury, a globally recognized toxic pollutant, exists in several chemical forms, including elemental (Hg^0), oxidized (Hg^{2+}), particulate-bound (Hg^p), and organic (MeHg), which differ in mobility, reactivity, and toxicity, resulting in complex environmental behavior [1]. Among the specified mercury forms, methylmercury (MeHg) is the most hazardous due to its neurotoxic effects and ability to bioaccumulate. Mercury has been identified as a harmful air pollutant, and its regulation in the United States was formalized by the Clean Air Act Amendments in 1990. A significant milestone came in 2012 when the US EPA implemented the Mercury and Air Toxics Standards (MATS) to limit power plant emissions [2]. These regulations have been highly effective, significantly reducing mercury emissions and preventing thousands of premature lives annually.

Mercury appears in the atmosphere both from natural and anthropogenic sources. Coal-fired power plants and combustion facilities that burn different biomass fuels represent a significant anthropogenic contributor. Mercury emissions are not solely a function of the utilized combustion technology or operating conditions; they also depend on fuel type and characteristics such as ash and volatile yield, carbon and sulfur content [3, 4]. Generally, higher mercury content in coals is associated with elevated carbon content (organic matrix), particularly in higher-rank fuels such as

bituminous and anthracite coals. Furthermore, sulfur (particularly pyritic sulfur) contained in coals usually results in elevated mercury levels, owing to mercury's affinity for sulfide minerals and its relationship with pyrite. This underscores the need to consider mercury content as a fundamental fuel characteristic when assessing environmental impact.

The prior literature analyzes the mercury concentration of coal and biomass [5, 6]. Given the variety of factors that impact the composition and characteristics of these fuels, it is critical to quantify and compare the mercury content of various fuel samples available in this climate. This study aims to assess, compare, and correlate the mercury content among different fuel types with their properties.

2. EXPERIMENTAL

Brown coal, anthracite, lignite, wood pellet and wood chips were analysed in this study. The proximate and ultimate analyses were done by LECO TGA 70 and LECO CHN 628 Series with a Sulfur add-on module, respectively. The heating value was determined using an IKA C200 calorimeter. Mercury content in samples was determined on Direct Mercury Analyzer- DMA1 evo. Standard methods were applied for all analyses [7, 8]. All samples are anlaysed in triplicate. The data obtained from tests at the same conditions were averaged to get the final results.

3. RESULTS AND DISCUSSION

The quality of feed fuels used for energy production (coal and biomass samples) is evaluated by proximate and ultimate analysis. The results of these analyses are presented in Table 1. As can be seen, there are significant differences among the investigated coals. Anthracite has much lower ash and volatile content, much higher heating value, and carbon content than lignite and brown coal, which is expected. Furthermore, samples of wood pellets and chips compared with all investigated coal samples have much higher volatile and oxygen content (Table 1). This is in accordance with the literature [5, 6], where the volatile yield in biomass samples includes light hydrocarbons, CO, CO_2, H_2, moisture and tars, and its content is usually much higher than in coal samples [9]. Additionally, wood pellets and chips have considerably lower ash content than lignite, while their carbon content and calorific value are slightly higher.

Table 1. Proximate and ultimate analysis of different coal and biomass types

		Anthracite	Brown Coal	Lignite	Wood pellet	Wood chips
Proximate analysis (%)	Inherent Moisture*	3.48	2.96	3.39	4.38	5.47
	Ash	4.64	6.16	33.73	0.51	1.28
	Total Sulfur	0.75	0.78	1.52	0.04	0.02
	C-fix	88.05	44.96	25.97	15.50	17.49
	Volatile	7.30	45.92	40.31	83.99	81.23
Heating value (MJ/kg)	High	32.86	27.63	17.80	22.40	19.68
	Low	32.46	26.58	16.90	21.10	18.45
Ultimate analysis (%)	Carbon	87.08	67.63	44.33	50.96	49.56
	Hydrogen	1.93	5.11	3.90	6.31	5.97
	Com. Sulfur	0.64	0.30	0.80	/	/
	Nitrogen	1.09	1.39	0.75	0.08	0.29
	Oxygen	4.62	19.22	16.50	42.14	42.90

*as determined; all other data are given on a dry basis

Figure 1 shows the mercury and sulfur content of analyzed coal and biomass samples. Wood chips and wood pellets have significantly lower sulfur content compared to the coal samples. It is in accordance with literature data, which indicates that the sulfur content in biomass typically ranges from 0.01% to 2.30%, except in bark and straw, which usually have higher sulfur content than wood samples [10]. Among all investigated samples, lignite has the highest sulfur content.

As can be seen, mercury content varies in coals from 0.053 ppm (brown coal) to 0.874 ppm (lignite), while in biomass samples, concentrations are much lower, ranging from 0.003 ppm (wood chips) to 0.007 ppm (wood pellets).

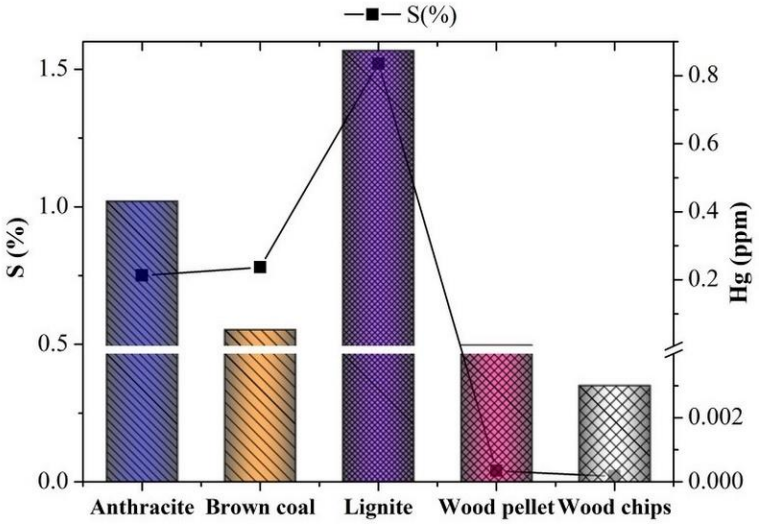

Figure 1. Mercury and sulfur content in different types of coal (anthracite, brown coal and lignite) and biomass (wood pellet and wood chips)

Although biomass samples generally contain very low Hg concentrations, this trace element exhibits high volatility during combustion. Studies have shown that mercury released during biomass combustion can be deposited through both dry and wet pathways, thereby contributing to the formation of toxic methylmercury species that bioaccumulate in living tissues [11]. Within biomass matrices, mercury may be bound to both organic components, such as thiol groups, and inorganic components, such as pyrite [5]. Global studies on coal indicate that mercury is primarily associated with pyrite in higher-rank coals, whereas lower-rank coals tend to have a higher proportion of organically bound mercury [12].

In this study, a notable correlation was observed between sulfur and mercury content. Fuels characterized by low sulfur content, such as wood pellets and chips, exhibited significantly reduced mercury concentrations, aligning with observations reported in the literature [5]. Additionally, biomass samples displayed substantially higher volatile matter yields compared to coal samples (Table 1) despite their markedly lower mercury concentrations. This finding is consistent with existing studies that report a negative correlation between volatile matter and mercury contents [6].

4. CONCLUSION

In this study, proximate, ultimate and mercury analyses were conducted on coal and biomass samples to explore their interrelationships. Among investigated samples, wood pellets and wood chips were characterized by significantly lower ash and sulfur contents. Still, they exhibited higher volatile matter yields, whereas anthracite showed the highest heating value, as anticipated. Investigated low-sulfur and high volatile biomass fuels show significantly lower mercury content. These correlations are consistent with previous literature and highlight the crucial role of fuel composition in mitigating mercury emissions during biomass combustion.

ACKNOWLEDGEMENTS

This work was supported by the Ministry of Science, Technological Development and Innovation of the Republic of Serbia; grant number 451-03-136/2025-03/200017.

REFERENCES

[1] S. Zhao, D. Pudasainee, Y. Duan, R. Gupta, M. Liu, J. Lu, Prog. Energy Combust. Sci. 73 (2019) 26-64.
[2] National Emission Standards for Hazardous Air Pollutants: Coal- and Oil-Fired Electric Utility Steam Generating Units—Subcategory of Certain Existing Electric Utility Steam Generating Units Firing Eastern Bituminous Coal Refuse for Emissions of Acid Gas Hazardous Air Pollutants, US EPA, Durham, N.C., 2020.
[3] X. Bai, W. Li, Y. Wang, H. Ding, Int. J. Coal Sci. Technol. 4 (2017) 172-182.
[4] I. Kursun Unver, M. Terzi, J. Min. Environ. 9 (2018) 641-655.
[5] A. Marinković, J. Buha Marković, J. Savić, M. Mladenović, N. Petrov, Therm. Sci. 26 (2022) 138.
[6] J. Buha Marković, A. Marinković, J. Savić, M. Erić, Z. Marković, A. Milićević, M. Gigov, Lignite combustion in Thermal power plant Kolubara A as a source of mercury pollution, SimTerm Proceedings, Niš, Serbia, 2024.
[7] S.V. Vassilev, D. Baxter, L.K. Andersen, C.G. Vassileva, Fuel, 89 (2010) 913-933.
[8] I. Obernberger, G. Thek, BMSBEO 27 (2004) 653-669.
[9] H.R. Friedli, L.F. Radke, J.Y. Lu, C.M. Banic, W.R. Leaitch, J.I. MacPherson, Atmos. Environ. 37 (2003) 253-267.
[10] T. Dziok, A. Strugała, A. Rozwadowski, Fuel 159 (2015) 206-213.
[11] A. Kolker, C.L. Senior, J.C. Quick, Appl. Geochem. 21 (2006) 1821-1836.
[12] S. Vassilev, C. Vassileva, M. Georgieva, B. Barbov, G. Velyanova, S. Georgiev, Content, Geol. Balk. 53 (2024) 69-87.

The 56th International October Conference on Mining and Metallurgy
22-25 October 2025, Bor Lake, Bor, Serbia
www.ioc.tfbor.bg.ac.rs

DOI: 10.5937/IOC25607K *Original scientific paper*

TREE LEAF BIOCHAR AS POTENTIAL ADSORBENT FOR LEAD ION REMOVAL FROM AQUEOUS SOLUTION

Marija Koprivica[1a], Marija Simić[1b], Jelena Petrović[1c], Jelena Dimitrijević[1d], Marija Ercegović[1e], Marija Marković[1f]

[1]Institute for Technology of Nuclear and Other Mineral Raw Materials, Franchet d'Esperey 86, 11000 Belgrade, Serbia

[1a] m.koprivica@itnms.ac.rs, 0000-0002-1451-5959
[1b] m.petrovic@itnms.ac.rs, 0000-0003-1717-7796
[1c] j.petrovic@itnms.ac.rs, 0000-0003-4841-1899
[1d] j.dimitrijevic@itnms.ac.rs, 0000-0002-3830-2392
[1e] m.ercegovic@itnms.ac.rs, 0000-0002-7145-8671
[1f] m.markovic@itnms.ac.rs, 0000-0001-6787-1933

Abstract

Industrial wastewater is a type of environmental pollution and, in the 21st century, is one of the major problems for humanity and nature. Lead is a metal that negatively impacts the environment and human health. Therefore, great attention has been paid to removing this metal from waste effluents generated during mining activities and various industrial processes. Adsorption technology is a powerful tool for the removal of pollutants from wastewater. During past years, there has been an increase in the use of plant waste and its products for this application. In this study, Paulownia tree leaves (PL) were structurally changed by the pyrolysis process and converted to biochar (PLB), which was used as a Pb ion adsorbent. The obtained material was characterized via FTIR and SEM-EDX analysis before and after Pb ion removal. The results of the FTIR analysis showed differences in the intensity of the surface functional groups, especially the aromatic and oxygen functional groups. These changes confirm that behind ion exchange, the complexation, and/or cation-π electron interaction done too. The SEM-EDX also showed changes in the surface structure and elemental content. The surface exhibited newly formed cracks and pores during Pb ion adsorption. Also, the EDX confirmed that the percentages of O, N, K, Mg, and Ca decreased while the lead content increased significantly. The summarized results from this work revealed that leaves from trees are valuable biomass for sustainable biochar production, supporting waste valorization, and contributing to pollution control efforts, making them suitable for adsorption of metal ions.

***Keywords**: pyrolysis, biochar as adsorbent, Pb(II) ion removal, FTIR analysis, SEM-EDX analysis*

1. INTRODUCTION

Mining and industrial activities are responsible for why lead (Pb) is one of the most abundant and toxic heavy metals that occurs in nature. Since it can result in a range of health problems not only for humans but also for plant and animal life, it is imperative to remove it from the environment as effectively as possible [1,2]. One of the best solutions for removing heavy metals from wastewater is adsorption using various effective materials. Potential materials for adsorption can be obtained from waste biomass [1,2,3,4]. In this regard, this work aims to evaluate the possibility of obtaining an efficient lead ion (Pb^{2+}) adsorbent from aqueous solutions by pyrolysis of Paulownia tree leaves (PL), which represent a cheap and economical source of raw materials. The FTIR and SEM-EDX analyses of the obtained biochar (PLB) before and after lead ion adsorption were performed for characterization.

2. EXPERIMENTAL

2.1 Materials preparation

The initial feedstock of obtained biochar was leaves from the Paulownia tree (PL). It was collected in a Belgrade park, washed with distilled water, air-dried for three weeks, and crushed with a grinder to obtain a finer sample. The biochar was obtained from 10g of the tree leaf powder via the slow pyrolysis process at 400 °C, 2 hours under argon gas flow in a laboratory furnace (Nabertherm, Germany). After pyrolysis, the biochar (PLB) was stored in a desiccator until adsorption tests were performed.

2.2 Preliminar adsorption test

Adsorption isotherms studies were conducted by stirring 0.02 g of the PL or the PLB powder with 20 mL of Pb solutions at a concentration of 100 mg/L for 24 hours at room temperature. The solution was separated from the adsorbent by filtration, and Pb^{2+} concentrations before and after adsorption were determined using an atomic adsorption spectrophotometer (AAS, PerkinElmer, PinAAcle 900T).

The amount of Pb^{2+} ions adsorbed on the PL and PLB surface was calculated using equation:

$$q = (C_0\text{-}C_{eq})/m \times V \quad (1)$$

Where q [mg/g] was the adsorbent capacity, C_0, and C_{eq} [mg/L] were initial and after adsorption concentration of Pb ions, m [g] was the amount of adsorbent and V [L] was volume of the Pb^{2+} solutions.

2.3 Characterization of material before and after lead ions adsorption

FTIR analysis was used to determine the presence of functional groups on the surface of the PLB before and after the lead sorption process. The samples' FTIR analysis was recorded on a Thermo Fisher Scientific Nicolet IS-50 spectrophotometer in the spectral range of 400–4000 cm^{-1} in transmission mode. All samples were converted into pellet form using KBr.

The surface morphology of the PLB before and after lead ions adsorption was observed using SEM-EDX analysis (JEOL JSM-6610LV SEM, JEOL Inc., USA). All samples were cathodic-coated with gold, placed on an adhesive carbon disc, and recorded in a vacuum under a voltage of 20 kV.

3. RESULTS AND DISCUSSION

3.1 Preliminar adsorption test

The preliminary adsorption test revealed that the PL and PLB exhibited different adsorption affinity toward Pb^{2+} (Figure 1a). As can be observed in Figure 1a, the pyrolysis process improved the adsorption properties of PL (from q= 45.18 mg/g to q=71.67 mg/g). Similar findings were showed with the results for Ginkgo tree leaf and it biochar obtained at 400°C, where pyrolysis improved adsorption efficiency for Pb ions removal from q=24.81 mg/g to q=51.13 mg/g [4].

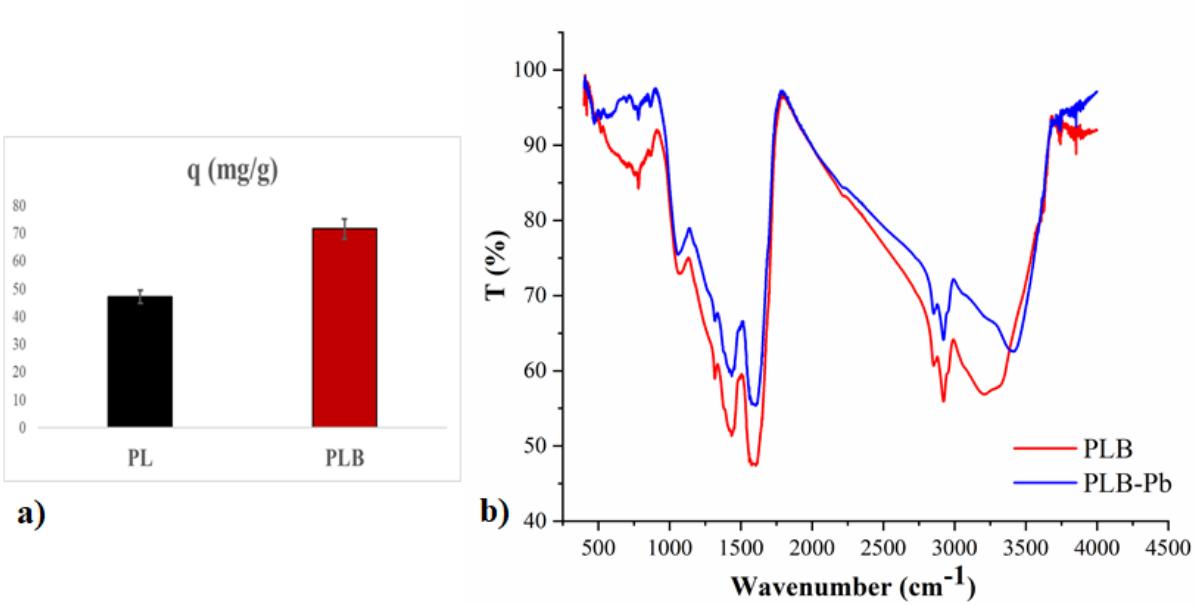

Figure 1. a) Comparison at Pb^{2+} ions adsorption effectiveness between PL and PLB, b) FTIR spectrum before and after Pb ion adsorption at PLB surface.

3.2 Characterization of material before and after lead ions adsorption

A decrease and shift in the frequencies of characteristic vibrations, such as -OH groups around 3300-3500 cm^{-1}, suggests interactions between functional groups on the adsorbent surface and Pb^{2+} ions (Figure1b) [1,2,4]. These appearances indicated bond weakening due to Pb^{2+} ion binding, implying hydrogen exchange, complexation, or covalent interactions [2,5]. Besides, spectral changes in the form of a decrease of intensity at about 1000-2000 cm^{-1} may indicate metal ion binding through interactions with aromatic and oxygen functional units on the adsorbent surface [1,2,4]. Also, the peak at about 800 cm^{-1}, which originated from aromatic C-H vibration, was reduced after adsorption [1,4,6]. Changes in the FTIR spectrum after Pb^{2+} ion adsorption suggest that the primary binding mechanisms involve ion exchange and complexation with functional groups on the adsorbent (Figure 1b) [5,6]. These findings align with the results of Zhao et al., where ion exchange mechanisms and interactions with surface groups were identified as key for Pb^{2+} removal from wastewater [6].

After the adsorption of Pb^{2+} ions onto the PLB surface, significant structural changes were observed in the SEM images (Figure 2). In addition to the bound Pb ions visible at specific locations, the surface exhibited more pronounced cracks and deeper pores, indicating modifications due to adsorption. The EDX analysis revealed that the PLB surface predominantly contained carbon (approximately 70%) and oxygen (around 20%), highlighting its carbon-rich structure and the presence of oxygen-containing functional groups, which are key contributors to metal ion adsorption, as supported by previous studies [1,3,5].

The EDX analysis further confirmed the adsorption mechanism involving ion exchange (Figure 2). The adsorption of Pb^{2+} ions led to a slight increase in the carbon content on the PLB surface, while the percentages of K, Mg, Ca, O, and N decreased. These changes in elemental composition provide valuable insights into the mechanisms of ion binding on the biochar surface [5,6]. The lead content increased significantly, from 0% to an average of 1.50%, demonstrating the PLB's adequate capacity for Pb^{2+} ion adsorption.

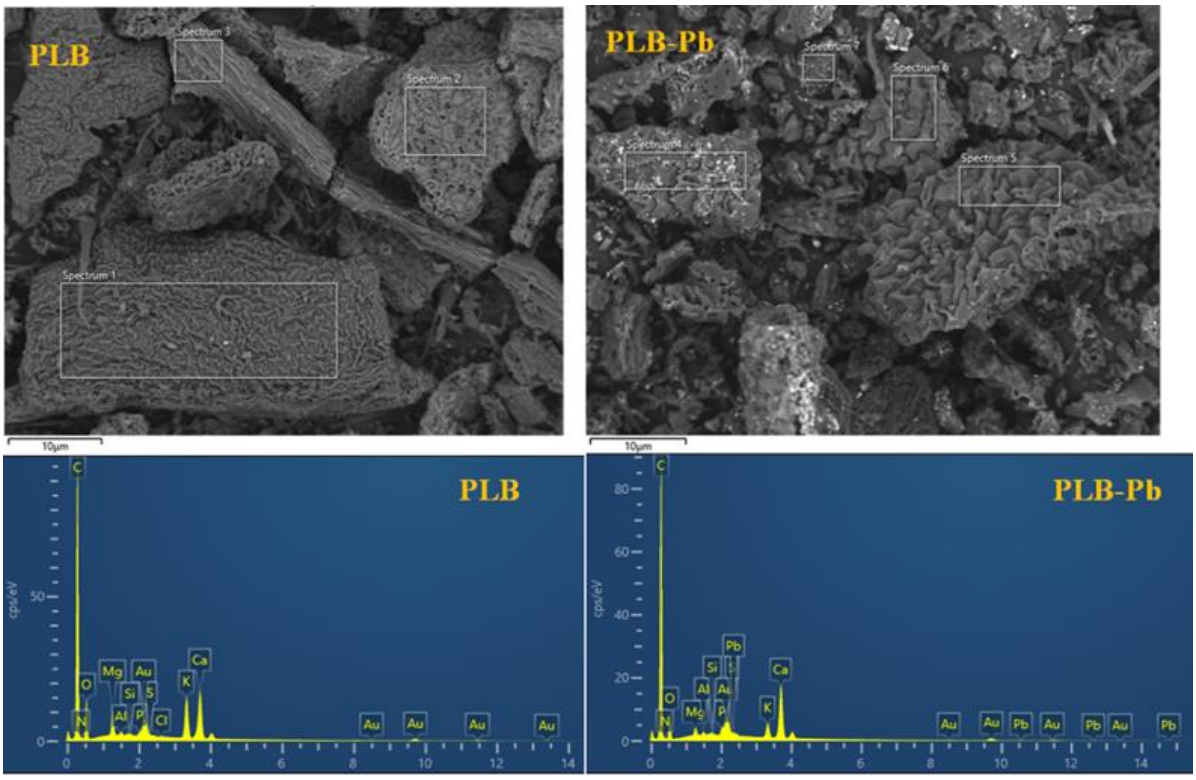

Figure 2. SEM-EDX analysis of the PLB surface before and after Pb^{2+} ions adsorption.

4. CONCLUSION

The results of the FTIR analysis showed differences in the intensity of the surface functional groups, especially the aromatic and oxygen functional groups. These changes confirm that the complexation and/or cation-π electron interaction are also done behind ion exchange. The SEM-EDX showed changes in the surface structure and elemental content. The surface exhibited newly formed cracks and pores during Pb^{2+} ion adsorption. Also, the EDX confirmed reduction of the O, N, K, Mg, and Ca amounts, while the Pb content increased significantly. The summarized results from this work revealed that leaves from trees could be valuable biomass for sustainable biochar production, and making them suitable for the adsorption of metal ions.

ACKNOWLEDGEMENTS

The authors are grateful to the Ministry of Education, Science and Technological development of the Republic of Serbia for financial support according to the contract with the registration number (e.g. 451-03-136/2025-03/200023).

REFERENCES

[1] M. Koprivica, M. Simić, J. Petrović, M. Ercegović, J. Dimitrijević, Processes, 11 (5) (2023) 1327.
[2] J. Petrović, M. Stojanović, J. Milojković, M. Petrović, T. Šoštarić, M. Laušević, M. Mihajlović, J. Environ. Manag., 182 (2016) 292-300.
[3] M. Ercegović, J. Petrović, M. Koprivica, M. Simić, M. Grubišić, N. Vuković, J. Krstić, Water, 16 (15) (2024) 2177.
[4] M-E. Lee, J.H. Park, J.W. Chung, Int. J. Environ. Res. Public Health, 14 (2017) 1528.
[5] C. Wang, X. Wang, N. Li, J. Tao, B. Yan, X. Ciu, G. Chen. Clean Technol., 4 (3) (2022) 629-652.
[6] M. Zhao, Y. Dai, M. Zhang, C. Feng, B. Qin, W. Zhang, N. Zhao, Y. Li, Z. Ni, Z. Xu, D. Tsang, R. Qiu, Sci. Total Environ., 717 (2020) 136894.

The 56th International October Conference on Mining and Metallurgy
22-25 October 2025, Bor Lake, Bor, Serbia
www.ioc.tfbor.bg.ac.rs

DOI: 10.5937/IOC25611K *Original scientific paper*

MULTIVARIATE STATISTICAL EVALUATION OF AGRICULTURAL SOIL CONTAMINATION NEAR THE CITY OF BOR

Vesna Krstić[1a,2], Danijela Simonović[1b], Renata Kovačević[1c], Daniel Kržanović[1d], Mirjana Šteharnik[1e], Daniela Urošević[1f], Sunčica Stanković[3a]

[1] Mining and Metallurgy Institute Bor, Alberta Ajnštajna 1, 19210 Bor, Serbia
[2] Technical Faculty Bor, University of Belgrade, V.J. 12, 19210 Bor, Serbia
[3] Faculty of Management, Metropolitan University, 11158 Belgrade, Serbia
[1a,2] vesna.krstic@irmbor.co.rs, 0000-0002-1110-0547
[1b] danijela.simonovic@irmbor.co.rs, 0000-0001-7945-693X
[1c] renata.kovacevic@irmbor.co.rs, 0000-0003-4108-0855
[1d] danijel.krzanovic@irmbor.co.rs, 0000-0003-3841-8667
[1e] mirjana.steharnik@irmbor.co.rs, 0000-0002-2733-3599
[1d] daniela.urosevic@irmbor.co.rs, 0000-0003-3490-7834
[3a] suncica.stankovic@metropolitan.ac.rs, 0000-0001-8824-1973

Abstract
This study investigates the concentrations of heavy metals in agricultural soils surrounding the Zijin Copper Bor mining complex in Eastern Serbia, focusing on four locations: Veliki Krivelj, Oštrelj, Brezonik, and Zlot. The presence of the following elements was analyzed using inductively coupled plasma mass spectrometry (ICP-MS): Cr, Mn, Fe, Co, Ni, Cu, Zn, As, Cd, and Pb. To provide a comprehensive assessment of contamination levels and inter-element relationships, the following statistical methods were applied: descriptive analysis, principal component analysis (PCA), correlation analysis with heatmap visualization, and hierarchical cluster analysis (HCA). PCA results revealed latent factor groupings that reflect the influence of mining activities, metallurgical processes, and contaminant migration within the soil matrix.
Keywords: *soil contamination, heavy metals, ICP-MS, multivariate statistical analysis, PCA, HCA*

1. INTRODUCTION

Soil contamination by heavy metals represents one of the most pressing environmental challenges in urban and industrial areas worldwide. Mining operations and metallurgical activities—particularly in regions with intensive smelting—lead to the accumulation of potentially toxic elements in arable soils, directly threatening agroecological functions, biodiversity, and human health [1–3]. The city of Bor in Eastern Serbia, with over a century of mining tradition, is considered one of the most polluted areas in the region due to emissions of arsenic, cadmium, lead, copper, and other metals from ore processing facilities [4,5]. Numerous studies have reported concentrations of these metals far exceeding permissible threshold values, especially in zones adjacent to the smelter [6,7].

Principal Component Analysis (PCA) has proven to be an effective statistical tool for identifying and characterizing metal distributions, enabling differentiation of pollution sources and reduction of data complexity [8,9]. When integrated with Geographic Information Systems (GIS), PCA further facilitates spatial visualization of contamination risk and the delineation of critical zones for remediation [10].

The aim of this study is to apply PCA to a dataset of heavy metal concentrations in soils surrounding the Bor mining complex, with a focus on identifying dominant contamination factors and their spatial distribution. The results may serve as a foundation for defining remediation strategies and sustainable land management practices in mining-affected regions.

2. EXPERIMENTAL

Soil sampling was conducted at four representative locations: Veliki Krivelj (L1), Oštrelj (L2), Brezonik (L3), and Zlot (L4), all situated in close proximity to the mining and smelting complex. The sites were selected based on prior contamination reports, their geographic position relative to sources of mining waste, and the spatial distribution of mining infrastructure. The sampling plan was developed in accordance with ISO 18400-101:2017. All procedures were carried out by accredited personnel from the Institute for Mining and Metallurgy Bor (IRM Bor), in compliance with ISO standards 18400-102:2017, 18400-104:2018, and 18400-105:2017.

3. RESULTS AND DISCUSION

Descriptive statistical analysis of heavy metal concentrations in agricultural soils surrounding the Zijin Copper mine in Bor, Serbia—covering the locations Veliki Krivelj, Oštrelj, Brezonik, and Zlot (Table 1)—reveals pronounced variability in Fe, Mn, and Cu levels. The distributions of most metals are mildly asymmetric and platykurtic (kurtosis < 0), indicating a flattened shape relative to the normal distribution.

Table 1 – Descriptive statistics of heavy metal concentrations in agricultural soils at Veliki Krivelj, Oštrelj, Brezonik, and Zlot

	mean	std	min	25%	50%	75%	max	skewness	kurtosis
Cr	32.9	17.3	15.9	19.3	33.4	47.1	49.2	-0.021	-1.938
Mn	973.1	447.9	482.7	650.3	1007.5	1330.2	1394.5	-0.104	-1.817
Fe	39235.0	10805.8	29982.4	30520.3	37364.2	46078.9	52229.4	0.272	-1.641
Co	16.6	7.8	11.0	11.7	13.7	18.6	28	0.957	-0.845
Ni	14.9	5.6	9.9	10.7	14.1	18.3	21.7	0.294	-1.583
Cu	385.5	169.9	192.7	312.8	371.9	444.7	605.5	0.27	-1.016
Zn	79.5	9.9	72.9	73.7	75.5	81.3	94.1	1.052	-0.755
As	28.8	6.3	20.4	25.7	30.5	33.7	33.8	-0.544	-1.311
Cd	-0.132	0.034	-0.149	-0.149	-0.149	-0.132	-0.081	1.155	-0.667
Pb	36.8	10.8	28.8	30.2	32.9	39.5	52.6	0.962	-0.832

The strength of association between heavy metals in soils surrounding the Zijin Copper mine (Bor, Serbia) was assessed using correlation analysis. This method evaluates both the direction and magnitude of the relationship between two variables. The correlation coefficient (r) quantifies the degree of statistical interdependence between two random variables (x and y), ranging from –1 to +1. A value of zero indicates no significant association.

According to Evans [11], the absolute value of the correlation coefficient can be interpreted as follows: from 0.00 to 0.19 - very weak, from 0.20 to 0.39 – weak, from 0.40 to 0.59- moderate, from 0.60 0.79 – strong and from 0.80 to 1.00 - very strong. The results revealed very strong positive correlations between Cd–Pb (r = 0.97), Mn–Fe (r = 0.96), and Cu–Pb (r = 0.94), suggesting that these metals may originate from a common pollution source or exhibit similar accumulation behavior in soil. A moderate positive correlation was observed between As–Zn (r = 0.54), indicating partial overlap in their sources. Conversely, very strong negative correlations were found between Cr–Mn (r = –0.97), Cr–Fe (r = –0.91), and Cu–Co (r = –0.85). Strong negative associations were also noted for Co–As (r = –0.78) and Ni–Zn (r = –0.60). Very weak correlations were observed between Ni–As (r = 0.023, positive) and Fe–Ni (r = –0.006, negative), implying negligible association. These findings suggest that certain metals tend to co-occur, while others exhibit opposing behavior, likely due to differing contamination sources or specific geochemical mechanisms in the soil. Additional correlation results, including determination coefficients, are presented in Figure 1.

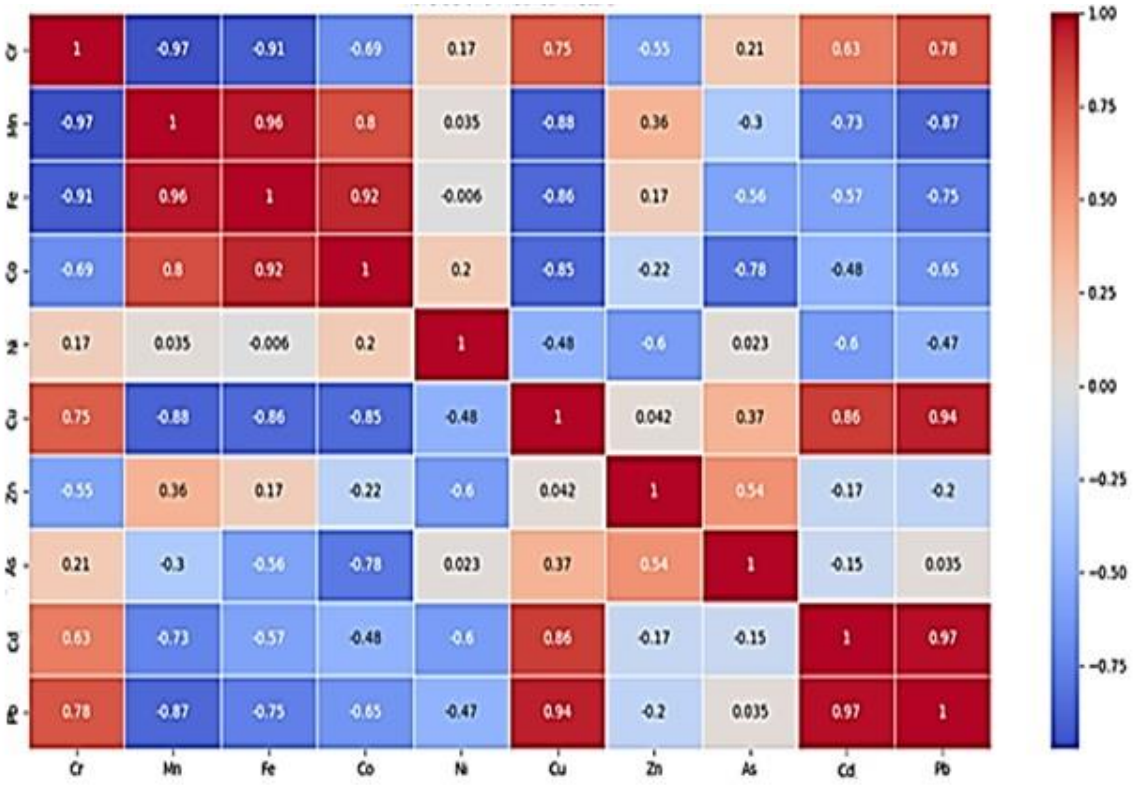

Figure 1 – Correlation Matrix

To identify relatively homogeneous clusters of elements, exploratory factor analysis (EFA) was applied. Factor extraction was based on Kaiser's criterion, which retains only components with eigenvalues greater than 1 [12]. The EFA revealed three components with eigenvalues exceeding 1: the first component accounted for 60.47% of the total sample variance, the second for 21.50%, and the third for 18.03%, as shown in Table 2.

Table 2 – Results of Exploratory Factor Analysis

Component	Initial Eigenvalues			Extraction Sums of Squared Loadings		
	Total	% of Variance	Cumulative %	Total	% of Variance	Cumulative %
1	6.047	60.470	60.470	6.047	60.470	60.470
2	2.150	21.497	81.968	2.150	21.497	81.968
3	1.803	18.032	100.000	1.803	18.032	100.000

The selection of a three-component solution as optimal was further supported by the scree plot criterion (Figure 2), based on Cattell's scree test. The plot displays a sharp decline in eigenvalues between the first and third components, while the remaining components exhibit negligible values (≈ 0), indicating minimal explanatory power. The curve shows a clearly defined "elbow point" after the third component, which reinforces the decision to retain only the first three components.

The results of the confirmatory factor analysis (Principal Component Analysis, PCA) confirmed that the heavy metals are grouped into three distinct components. Each component explains a specific portion of the total variance in the dataset. Component 1: factor loadings range from –0.965 to 0.919. Component 2: loadings range from –0.710 to 0.994. Component 3: loadings range from –0.974 to 0.733. These results are presented in Table 3 – Rotated Component Matrix.

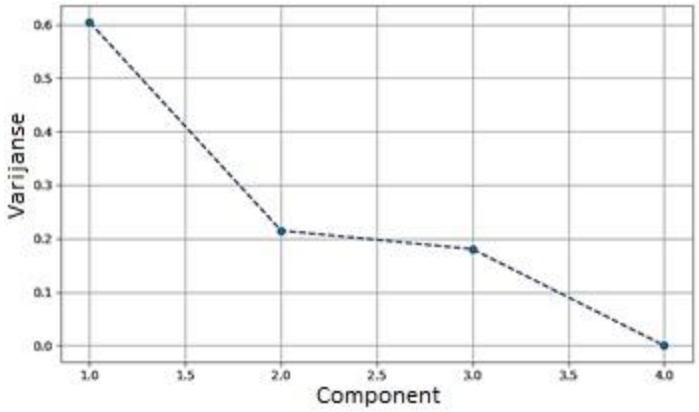

Figure 2 – Scree Plot (Cattell's Criterion)

Table 3 Rotated component matrix

	Component		
	1	2	3
Mn	-.965		
Pb	.963		
Cr	.919		
Cu	.914		
Cd	.879		
Fe	-.863		
As		.994	
Co		-.710	
Ni			-.974
Zn			.733

It can be concluded that all metals within the first component exhibit high factor loadings, suggesting a common origin or source of contamination. This component likely reflects a shared process or pollution source—such as mining-related activities. As shown in Table 3, the first component includes metals directly associated with copper mining operations (Pb, Cu, Cd, Cr). Mn and Fe display negative loadings, indicating an inverse relationship with the other metals in this component, which may suggest their affiliation with the natural geochemical background. The second component is dominated by As (0.994) and Co (–0.710), both showing strong loadings. This component likely represents a distinct source or process linked to arsenic and cobalt contamination. The negative loading of Co implies an opposing behavior relative to As, possibly due to differing geochemical pathways or mobility in soil. The third component comprises Ni (–0.974) and Zn (0.733). Led by Ni, this component may reflect diffuse migration processes of metals into deeper soil layers. The PCA results indicate that Cu, Pb, Cd, and Cr are strongly associated with the first component, Zn and As with the second, and Ni with the third. This separation suggests the presence of multiple contamination factors: mining origin, industrial emissions, and geochemical behavior of metals in soil.

Thus, the PCA identifies three components that explain the presence and behavior of heavy metals in the soil: mining influence, secondary industrial processes, and subsurface migration of contaminants. These findings enable differentiation of impact zones, which is essential for targeted ecological monitoring and land management in the vicinity of the mining complex.

The dendrogram (Figure 3) reveals two distinct clusters: locations L1 and L2 form one group, while L3 and L4 form another. These clusters are clearly separated. L1 and L2 likely share a similar contamination profile, possibly due to a common pollution source such as similar geological substrate or agricultural practices. In contrast, L3 and L4 are internally similar but differ from the first group—potentially influenced by other environmental factors such as wind dispersion or topography.

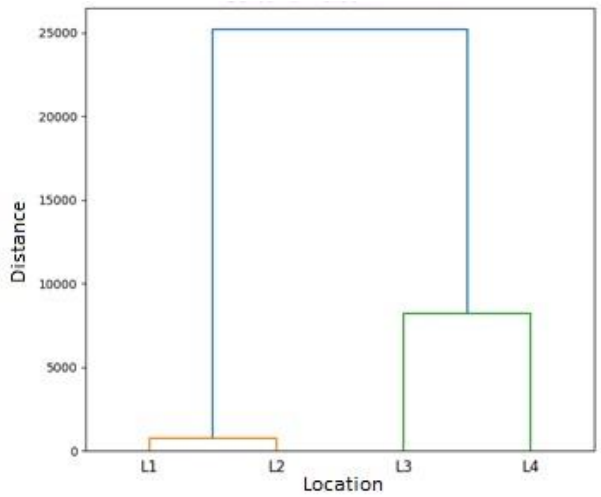

Figure 3 – Dendrogram of Sampling Locations

4. CONCLUSION

The application of multivariate statistical methods enabled the identification of heavy metal contamination in agricultural soils surrounding the Zijin Copper mining complex in Bor, Serbia. Principal Component Analysis (PCA) revealed distinct factor groupings indicative of dominant mining and metallurgical influences, while correlation and cluster analyses confirmed inter-element relationships and spatial differentiation of contamination patterns. The findings underscore the necessity for continuous environmental monitoring and integrated risk assessment in agroecological zones exposed to industrial pressure.

ACKNOWLEDGEMENTS

The research presented in this paper was done with the financial support of the Ministry of Science, Technological Development and Innovation of the Republic of Serbia, within the Contract No. 451-03-136/2025-03/200052.

REFERENCES

[1] B. Tang, C. Christia, B.-X. Mai, Environ. Pollut., 306 (2022) 119469.
[2] O. Adedeji, A. Olusola, G. James, H.A. Shaba, I.R. Orimoloye, S.K. Singh, S. Adelabu, Environ. Monit. Assess., 192 (12) (2020) 798.
[3] Y.B. Sun, Q.X. Zhou, X.K. Xie, R. Liu, J. Hazard. Mater., 174 (1-3) (2010) 455-462.
[4] Đ. Nikolić, N. Milošević, Ž. Živković, I. Mihajlović, R. Kovačević, J. Serb. Chem. Soc., 75 (4) (2010) 625-641.
[5] V. Tasić, R. Kovačević, B. Maluckov, T. Apostolovski-Trujić, B. Matić, M. Cocić, M. Šteharnik, Water Air Soil Poll., 228 (6) (2017) 230
[6] R. Kovačević, V. Tasić, T. Apostolovski-Trujić, A. Ivanović, Atmosphere, 15(12) (2024) 1549.
[7] S. Šerbula, T. Kalinović, J. Kalinović, A. Ilić, ESPR, 20 (12) (2013) 8919-8929.
[8] Gergen, M. Harmanescu, hem. Cent. J.6 (1) (2012) 156.
[9] C. Kahangwa, J. Munganga, B. Mbuyu, GEP, 10 (4) (2022) 1-14.
[10] Y. Gonzales-Castanedo, T. Moreno, R. Fernández-Camacho, et al., Atmos. Environ., 92 (2014) 130-137
[11] J.D. Evans, Straightforward statistics for the behavioral sciences. Thomson Brooks/Cole Publishing Co. (1996).
[12] B.G. Tabachnick, L.S. Fidell, Using Multivariate Statistics (6th Edition). NY: Pearson Education, Inc. (2013).

The 56th International October Conference on Mining and Metallurgy
22-25 October 2025, Bor Lake, Bor, Serbia
www.ioc.tfbor.bg.ac.rs

DOI: 10.5937/IOC25616P *Review paper*

APPLICATION OF COPPER FOAMS FOR THE WATER PURIFICATION PROCESS

Ana Petrović[1a], Stefan Đorđievski[1b], Miloš Đukić[1c], Emina Požega[1d], Jelena Gligorijević Sokolović[1e], Dragana Adamović[1g]

[1] Mining and Metallurgy Institute Bor, Alberta Ajnštajna 1, 19210 Bor, Serbia
[1a] ana.petrovic@irmbor.co.rs, 0000-0002-9815-6884
[1b] stefan.djordjievski@irmbor.co.rs, 0000-0003-1737-8766
[1c] milos.djukic@irmbor.co.rs, 0000-0002-3307-4669
[1d] emina.pozega@irmbor.co.rs, 0000-0001-6797-2435
[1e] jelena.gligorijevic.sokolovic@irmbor.co.rs, 0009-0003-6713-760X
[1f] dragana.adamovic@irmbor.co.rs, 0000-0003-3683-4122

Abstract
Water contamination represents a critical global challenge, demanding safe and efficient purification technologies. Conventional disinfection methods such as chlorination, ozonation, and UV irradiation are limited by high energy demand and toxic by-products. In this study, a novel nanocomposite material, three-dimensional copper foam modified with Ag nanoparticles and CuO nanowires, was investigated for antibacterial activity. The material demonstrated strong efficiency in removing Escherichia coli and Staphylococcus aureus, achieving up to 99.9% removal under optimized conditions. Results indicate that bacterial elimination improves with voltage intensity and decreases with flow rate, confirming the nanocomposite's potential for practical water purification applications.

Keywords*: metal foams, wastewater, copper foams*

1. INTRODUCTION

Water contamination from industrial effluents, agricultural runoff, and microbial pathogens presents a growing global challenge, necessitating innovative, sustainable treatment strategies. Conventional methods such as chlorination and UV disinfection often entail high operational costs and generate toxic by-products, prompting research into novel materials with multifunctional capabilities [1]. Among these, copper foams have emerged as promising candidates due to their open-cell, high-porosity structure and superior conductivity, which enhance pollutant contact efficiency and support electrochemical treatment processes [2].

With porosity often exceeding 85–95% and specific surface areas reaching 5,000–10,000 m^2/m^3, copper foams facilitate effective adsorption, filtration, and electrochemical degradation of contaminants, while their natural antibacterial properties, stemming from the controlled release of Cu^{2+} ions, significantly reduce microbial load including E. coli and S. aureus. Moreover, copper's robustness under diverse environmental conditions translates to prolonged material life spans—often several times longer than activated carbon—resulting in reduced maintenance and operational costs [1,2].

Morphological studies using scanning electron microscopy (SEM) reveal copper foam's intricate networks of interconnected struts, high pore interconnectivity, and variable pore sizes, optimizing flow dynamics and surface interactions [2]. Beyond microbial inactivation, modified copper foams (e.g., superhydrophobic variants) demonstrate high efficiency for oil–water separation, achieving over 95% separation and maintaining stability under thermal and chemical stress [3].

Building upon these advantageous properties, this paper examines the application of copper foams in water purification, focusing on mechanisms of pollutant removal, and material durability. The

aim is to highlight copper foam's potential as an effective, cost-efficient solution for future water treatment systems.

2. APPLICATION OF METAL FOAM FOR WATER PURIFICATION PROCESS

Water pollution and therefore the lack of clean water, occurs as a consequence of economic development. It is an important global issue that must be seriously considered, because the life and health of people and animals are seriously endangered. Contaminated water can transmit diseases such as diarrhea, cholera, dysentery, typhoid and polio. Over the years, many water purification technologies have been developed in order to overcome this problem. Some of the methods currently used for water disinfection are chemical or physical treatments: chlorination, ozonation, ultraviolet (UV) radiation, reverse osmosis and advanced oxidation processes. One of the major disadvantages of traditional water disinfection methods is the carcinogenic by-products, which are formed primarily during the chlorination and ozonation of water. On the other hand, the UV water disinfection method consumes a large amount of energy [4].

Electroporation sterilization technology is a new method for water disinfection. This method has been shown to be very effective against bacteria and viruses. One of the important advantages is that it does not produce harmful by-products because chemical impurities are not involved in the process. However, the energy consumption during electroporation disinfection can be enormous, therefore it cannot be applied to disinfect large volumes of contaminated water. Another limiting factor for their practical application is the low speed of the water treatment process [5].

A group of researchers [1] developed a new composite material, a 3D copper foam co-modified with Ag nanoparticles-CuO nanowires. The copper foams were purchased from the Chinese company Shanghai Macklin Biotechnology Co. The main components of the nanocomposite are Cu, Ag and O. The preparation of the nanocomposite based on copper foams was carried out in two steps. The first step consists of preparing CuO nanowires in a mixture of NaOH and $(NH_4)_2S_2O_8$ for 10 minutes at 40°C, followed by heating them in air at 180°C for 3 hours. The thus prepared CuO nanowires were grown on Cu foam by a wet chemical process. In order to remove oxides on the surface, the Cu foam was immersed in 1.0 M HCl solution for 2 minutes, then rinsed with deionized water and dried using high-purity N_2. The second step involves immersing the thus prepared copper foam in a plating solution (pH 7.5) at room temperature to deposit Ag nanoparticles. The solution contains $AgNO_3$ (3.5 g L^{-1}), $[(NH_4)_2S_2O_3]$ (25 g L^{-1}) and ($K_2S_2O_5$) (3.5 g L^{-1}). The coating of copper foam with Ag nanoparticles lasted for 30 s, at a cathodic current density of 0.1 A dm^{-2}. Heating in air at 180°C for 1 h completes the preparation of the nanocomposite. The aim of this study was to investigate the efficient removal of gram-negative Escherichia coli (E. coli) and gram-positive Staphylococcus aureus (S. aureus) from water. The bacteria were cultured for 12 h, and by diluting with NaCl 9.0 g L−1, different concentrations of the solution were obtained in the range of 102 to 108 colony units per mL. The nanocomposite was placed in a filter device with two parallel electrodes under a voltage of 10 V. The colony count (CFU) method was used to calculate the bacterial removal.

Figure 1 shows a graph of the dependence of the removal rate of E. coli and S. aureus, using the prepared nanocomposite, on the applied voltage, liquid flow rate and bacterial concentration. As can be seen in Figures 2a and d, with increasing voltage, the removal rate of E. coli and S. aureus also increases. Based on this, it can be concluded that the stronger the electric field, the more effective the disinfection will be. Also, a comparison is given in the efficiency of bacterial removal using the nanocomposite and CuO nanowires without the addition of Ag. While the nanocomposites show disinfection performance even in the absence of an applied voltage, CuO does not have the ability to disinfect without an applied voltage, which indicates that Ag is responsible for killing bacteria. After applying voltage, disinfection was significantly improved. The maximum removal of E. coli and S. aureus was achieved at a voltage of 10 V and was 97.77% and 99.87%, respectively. The effect of fluid flow rate on the bacterial removal rate is shown in Figure 1b and e. In real water treatment processes, the water flow rate is usually 1–5 L min^{-1}, to

ensure effective water sterilization and reasonable energy consumption. In contrast to the previously discussed parameter, with the increase of flow rate, the removal rate of E. coli and S. aureus decreases. When the flow rate was 0.5 L min−1, both the nanocomposite and CuO nanowires had 99.9% removal of E. coli and S. aureus. By increasing the flow rate to 2 L min^{-1}, the nanocomposite maintains a bacterial removal rate of 75%, while on the other hand, CuO nanowires show poor disinfection performance. Figure 1c and f show a graph of the bacterial removal rate as a function of bacterial concentration. The highest removal rate of E. coli and S. aureus for both materials is 99.9%, at a bacterial concentration of 102 CFU mL^{-1}.
The disinfection efficiency of the nanocomposite is not significantly affected by the change in the concentration of bacteria in the solution, while in the case of CuO nanowires it is clearly observed that the rate of removal of bacteria decreases with increasing concentration of bacteria [1].

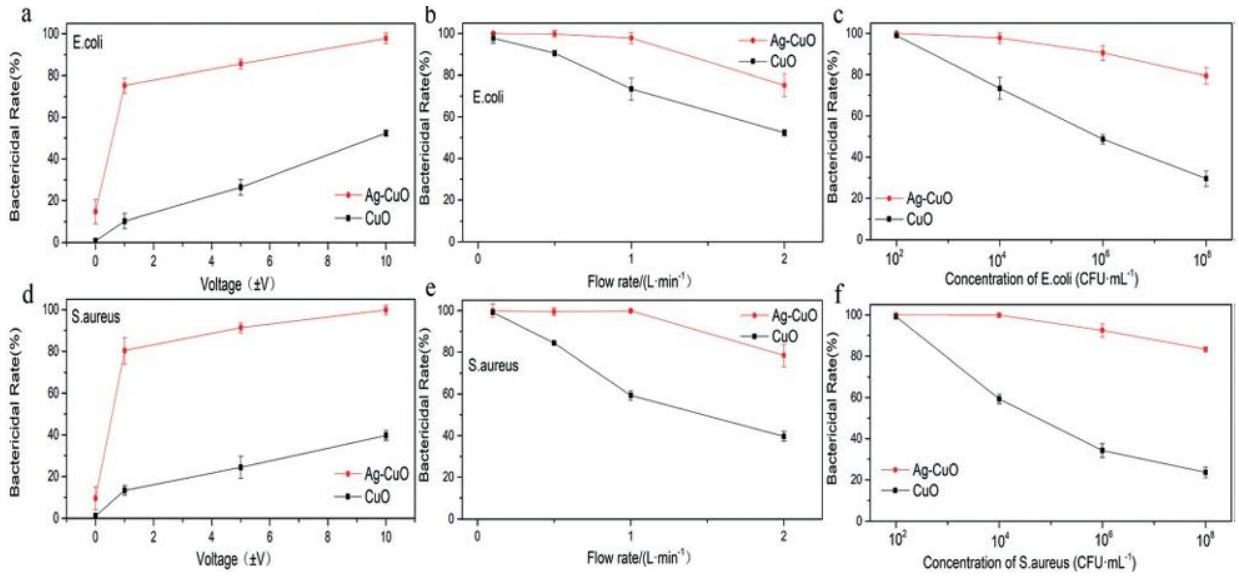

Figure 1.E. coli and S. aureus removal efficiency in the flow test: (a) and (d) effect of voltage; (b) and (e) effect of flow rate; (c) and (f) effect of E. coli (S. aureus) concentration [1]

The results show that the nanocomposite has a high sterilization effect, with a rate higher than 99.9% at a liquid flow rate of 1 L min^{-1} and has significant potential for practical application. However, in water heavily contaminated with bacteria, the nanocomposite would not maintain high bacterial removal efficiency unless a high voltage was applied [1].

4. CONCLUSION

The earth is continuously contaminated with numerous toxic substances from both natural and anthropogenic sources. Rapid population growth and increasing industrial development have caused the release of various toxic elements, compounds or materials into the environment. Many new chemicals are used without proper assessment of their environmental risks and effects on human health. The discharge of untreated industrial wastewater into water and soil, the use of pesticides and fertilizers in agriculture, the inadequate use of harmful chemicals in consumer products and the burning of fossil fuels are some of the main causes of water pollution. Due to the increasing consequences caused by polluted waters, the scientific community has a responsibility to develop effective technologies to prevent further contamination of the environment [4].
So far, great progress has been made in the study of metal foams as adsorbents of heavy metals and polluting components from the aquatic environment. In this paper, emphasis is placed on metal foams based on copper, because they are adsorbents that are easy to face the growing challenges of environmental protection, especially bacteriological remediation of water. Copper foams offer numerous advantages over other adsorbents and possess unique properties, including stiffness,

light weight, and the most important feature of metal foams is their low density. The development of cheap and efficient adsorbents is an imperative in current research, because it is necessary to take into account the cost factor in order to enable the mass application of adsorbents [2].
Based on previous experiments, copper foams have proven to be excellent adsorbents for bacteria (fungi, algae and molds), especially E. coli and S. aureus. Their effectiveness depends on a number of parameters such as the initial concentration of the polluting component, the flow rate, the density of the applied Cu foam, the voltage at which the adsorption process takes place and the time of contact between the adsorbent and the treated solution. In lakes, rivers and oceans, the application of Cu foam is not a widely applied technology for water pollution control, because despite the good results of experiments at the laboratory level, the technology has not yet been fully explored. An environmental and human health risk assessment should be carried out before mass application, as metallic foams often have toxic effects on aquatic organisms when applied in high concentrations [1].

ACKNOWLEDGEMENTS

This work was financially supported by the Ministry of Science, Technological Development and Innovation of the Republic of Serbia, Contract on realization and financing of the scientific research work of the Mining and Metallurgy Institute Bor in 2025, contract number: 451-03-136/2025-03/ 200052.

REFERENCES

[1] L. Yue, S. Chen, S. Wang, C. Wang, X. Hao, Y.F. Cheng, Environ. Sci., Nano 6 (9) (2019) 2801–2809.
[2] M. Oruc, R. Sunulahpašić, Savremeni metalni materijali, Fakultet za metalurgiju i materijale, Univerzitet u Zenici, Zenica, 2005, p.151-163.
[3] A. Baxevani, F. Stergioudi, N. Patsatzis, L. Malletzidou, G. Vourlias, S. Skolianos, Coatings 13 (2) (2023) 355.
[4] T. Manasfi, in Comprehensive Analytical Chemistry (T. Manasfi, J. L. Boudenne), Elsevier, Amsterdam, 2021, p. 85–116.
[5] J. Zhou, Y.C. Hung, X. Xie, Wat. Res., 207 (2021) 117817.

The 56th International October Conference on Mining and Metallurgy
22-25 October 2025, Bor Lake, Bor, Serbia
www.ioc.tfbor.bg.ac.rs

DOI: 10.5937/IOC25620T *Original scientific paper*

STATE OF AIR QUALITY IN THE CITY OF BOR IN 2024

Viša Tasić[1a], Tatjana Apostolovski-Trujić[1b], Renata Kovačević[1c], Bojan Radović[1d], Nevena Ristić[1e]

[1] Mining and Metallurgy Institute Bor, Alberta Ajnštajna 1, 19210 Bor, Serbia
[1a] visa.tasic@irmbor.co.rs, 0000-0001-6710-6529
[1b] tanja.trujic@irmbor.co.rs, 0000-0002-9369-160X
[1c] renata.kovacevic@irmbor.co.rs, 0000-0003-4108-0855
[1d] bojan.radovic@irmbor.co.rs, 0000-0003-4884-1418
[1e] nevena.ristic@irmbor.co.rs, 0000-0003-1408-237X

Abstract

In 2024, the air quality in the city of Bor was classified as Category III, indicating polluted air, according to the Mining and Metallurgy Institute (MMI) Bor annual report. While the Krivelj and Metovnica measuring points recorded Category I air quality, signifying clean or slightly polluted air, the Oštrelj and Brezonik sites experienced excessive levels of PM_{10}, exceeding the daily limit value for more than 35 days. Despite meeting other air quality parameters, these sites were classified as Category III. The Institute site reported arsenic (As) concentrations in PM_{10} samples that exceeded the annual target value (6.8 ng/m^3 compared to 6 ng/m^3). Similarly, the Town Park site showed elevated levels of arsenic and cadmium (Cd) in PM_{10}, with concentrations of 16.8 ng/m^3 and 9.5 ng/m^3, respectively, surpassing the target annual values. The Jugopetrol site was notably affected, with 77 days of PM_{10} concentrations exceeding the daily limit, arsenic concentrations of 42.0 ng/m^3, and cadmium concentrations of 19.8 ng/m^3, both significantly above their respective target values. The overall air quality assessment for the Bor agglomeration in 2024 was determined based on the most polluted measuring site, resulting in a Category III classification, indicating polluted air. This highlights the need for continued monitoring and mitigation efforts to improve air quality in the region. The air quality in the city of Bor in 2024 is worse compared to 2023 due to higher concentrations of Cd in PM_{10} samples measured at the Jugopetrol and Town Park monitoring sites, as well as a greater number of days exceeding the daily limit value for PM_{10} concentrations. If domestic copper concentrates do not contain Cd in significant percentages the question arises: What kind of imported concentrates are being smelted in the Bor copper smelter in 2023 and 2024 to cause such high Cd concentrations in PM_{10} samples?

***Keywords**: air quality, monitoring, suspended particles, arsenic, cadmium*

1. INTRODUCTION

Air pollution refers to the presence of chemicals, particles, or biological materials that cause harm or discomfort to humans and other living organisms, or that threaten the natural environment in the atmosphere [1]. Air pollution occurs when gases and microscopic dust particles (PM_{10} and $PM_{2.5}$) and soot are released into the atmosphere, altering the natural balance and concentration of the fundamental components of air. In some cases, these particles enter the atmosphere through natural processes, such as emissions from wildfires. However, more frequently, they are introduced as a result of human activities. Until 2016, outdated copper concentrate smelting technology was used at the copper smelter in Bor, leading to environmental pollution. Elevated concentrations of sulfur dioxide, exceeding the legally prescribed hourly and daily limits, were frequently detected at all air quality monitoring stations in Bor. Since 2016, the flash smelting technology has been employed at the Bor copper smelter [2, 3, 4], with all waste gases from the flash furnace being processed at a sulfuric acid plant. This study analyzes air quality in Bor during 2024 by comparing the air quality data with that obtained in 2023.

2. EXPERIMENTAL

Ambient air quality monitoring in Bor and its suburban settlements was conducted to obtain data necessary to properly select measures to protect and improve human health and preserve the environment. The Mining and Metallurgy Institute Bor holds an accreditation certificate that confirms that, during 2023 and 2024, the organization met the requirements of the ISO/IEC 17025:2017 standard for performing air quality monitoring according to the ambient air monitoring program for the city of Bor and its suburban settlements. This paper presents the results from the annual air quality monitoring reports for Bor in 2023 and 2024 [5].

3. RESULTS AND DISCUSSION

Table 1 presents the average annual concentrations of SO_2 in Bor in 2023 and 2024 [5]. Based on the data from Table 1, at most monitoring stations, the annual mean SO_2 concentrations in 2024 are approximately the same or slightly higher than those recorded in 2023. During 2024, three exceedances of the average daily limit value for SO_2 concentration (125 μg/m3) were recorded at the Jugopetrol monitoring station, while in 2023, no exceedances of the daily limit value for SO_2 concentration were observed at any monitoring station [5].

Table 1 - Mean annual concentrations of sulfur dioxide (μg/m^3) in Bor in 2023 and 2024 (Technical Faculty - TF, Town Park - TP, Institute - IN, Jugopetrol - JP, Brezonik - BR, Slatina - SL, Krivelj - KR, Annual Limit Value - LV)

Year	TF SO_2	TP SO_2	IN SO_2	JP SO_2	BR SO_2	SL SO_2	KR SO_2
2023	8.8	11.6	8.1	17.9	12.1	11.1	12.4
2024	11.6	11.0	16.0	26.3	11.2	11.5	12.7
LV	50						

The average annual concentrations of PM_{10} at monitoring sites in Bor for the years 2023 and 2024 are presented in Table 2. Throughout 2023, no exceedances of the annual limit value for PM_{10} concentrations were recorded at any monitoring site. However, exceedances in the number of days (more than 35 days) during which the average daily PM_{10} concentration exceeded the daily limit value (50 μg/m^3) were observed at the following monitoring sites: JP (52 days) and BR (48 days) [5]. In 2024, exceedances in the number of days (more than 35 days) with average daily PM_{10} concentrations above the daily limit value were recorded at the following monitoring sites: BR (86 days), JP (77 days), and OS (75 days) [5]. Across all monitoring sites, an increase in the number of days exceeding the daily PM_{10} limit in 2024 compared to 2023 is evident [5].

Table 2 - Mean annual concentrations of PM_{10} (μg/m^3) in Bor in 2023 and 2024 (Town Park - TP, Institute - IN, Jugopetrol - JP, Krivelj - KR, Brezonik - BR, Oštrelj - OS, Industrial zone - IZ, Metovnica - ME, Annual Limit Value - LV)

Year	PM_{10}_TP	PM_{10}_IN	PM_{10}_JP	PM_{10}_KR	PM_{10}_BR	PM_{10}_OS	PM_{10}_IZ	PM_{10}_ME
2023	23.4	33.8	35.1	28.5	34.2	28.8		
2024	32.5	30.7	37.0	26.8	39.6	36.7	32.8	22.6
LV	40							

Table 3 shows the annual concentrations of arsenic in PM_{10} samples in Bor, by measuring points, in 2023 and 2024. During 2024, the annual target value for arsenic concentration in PM_{10} (6 ng/m^3) was exceeded at TP, IN, JP, and IZ measuring sites. Extremely high concentrations of arsenic in PM_{10} samples were detected at the measuring points JP and IZ because they are located in the dominant wind direction, which carries pollution from the copper smelter to these sites.

Table 3 - Mean annual concentrations of arsenic in PM_{10} ($\mu g/m^3$) in Bor in 2023 and 2024 (Town Park - TP, Institute - IN, Jugopetrol - JP, Krivelj - KR, Brezonik - BR, Oštrelj - OS, Industrial zone - IZ, Metovnica - ME, Annual Target Value - ATV)

Year	As_TP	As_IN	As_JP	As_KR	As_BR	As_OS	As_IZ	As_ME
2023	15.4	12.2	39.8	1.7	6.6	3.1		
2024	16.8	6.8	42.0	1.4	5.6	3.3	15.1	2.3
ATV	6							

Table 4 shows the annual concentrations of cadmium in PM_{10} samples in Bor by measuring point in 2023 and 2024. From the results given in Table 4, an increase in the annual values of cadmium concentrations in PM_{10} samples can be observed at all measuring points in 2024 compared to 2023. During 2024, the annual target value for the concentration of cadmium in PM_{10} samples was exceeded at the measuring points TP, JP and IZ.

Table 4 - Mean annual concentrations of cadmium in PM_{10} ($\mu g/m^3$) in Bor in 2023 and 2024 (Town Park - TP, Institute - IN, Jugopetrol - JP, Krivelj - KR, Brezonik - BR, Oštrelj - OS, Industrial zone - IZ, Metovnica - ME, Annual Target Value - ATV)

Year	Cd_TP	Cd_IN	Cd_JP	Cd_KR	Cd_ BR	Cd_ OS	Cd_IZ	Cd_ME
2023	3.1	2.0	5.6	0.5	1.8	1.1		
2024	9.5	3.9	19.8	0.7	2.7	1.4	8.0	0.7
ATV	5							

During the reconstruction of the copper smelter (2021-2022), when the copper smelter was out of operation, high concentrations of As and Cd in PM_{10} were not detected at any measuring point in Bor [5]. Therefore, it is concluded that high concentrations of As and Cd in PM_{10} samples were detected during 2024 at the measuring site of JP, originating from the copper smelter; that is, they are the result of the processing of copper concentrate with an increased content of As and Cd. This means that the percentage values of these carcinogenic elements in the copper concentrate in some periods were higher to the values predicted in the environmental impact assessment study of the project: Increasing the capacity of the copper smelter within the "Serbia Zijin Copper" DOO Complex [3]. For this reason, it is necessary to implement additional measures to regularly control the composition of the concentrates processed in the copper smelter in Bor and harmonize them with the prescribed values in the study [3] to bring the content of carcinogenic elements in the suspended particles of the PM_{10} fraction to the values provided by law, at all measuring points in Bor.

In 2024, 14 days were recorded with exceeding the daily limit value for the concentration of Pb in PM_{10} samples at the measuring site JP, while in 2023, an exceedance was recorded for 2 days. The above results indicate an increase in the processing of imported copper concentrates in the copper smelter in Bor because there is no Pb in domestic copper concentrates. In 2024, there was no exceedance of the target value for Ni concentration in PM_{10} at any measuring point.

4. CONCLUSION

This paper analyzes the air quality in the city of Bor in 2024. Despite the reconstruction of the copper smelter, the problem of the emission of high concentrations of carcinogenic elements in PM_{10} samples persists. The air quality in Bor in 2024 is worse compared to 2023 due to higher concentrations of Cd in PM_{10} samples measured at the Jugopetrol and Town Park monitoring sites, followed by a higher number of days exceeding the daily limit value for PM_{10} concentrations.

So that, it is necessary to apply additional measures to reduce these emissions to the values provided by law, which relate to the regular control of the composition of the copper concentrate processed in the copper smelter in Bor and harmonization with the prescribed values for the percentage composition of carcinogenic elements in the copper concentrate provided for in the Study on the Impact Assessment on project environment: Increasing the capacity of the copper smelter within the "Serbia Zijin Copper" DOO Complex [3].

ACKNOWLEDGEMENTS

This work was financially supported by the Ministry of Science, Technological Development and Innovation of the Republic of Serbia, Contract on realization and financing of the scientific research work of the Mining and Metallurgy Institute Bor in 2025, contract number: 451-03-136/2025-03/200052. Funding for this work has also been provided by the European Union's Horizon Europe Research and Innovation program under grant agreement no.101060170 - WeBaSOOP, "Research Reinforcing in the Western Balkans' in Offline and Online Monitoring and Source Identification of Atmospheric Particles."

REFERENCES

[1] D. Knežević, D. Nešić, A. Cvjetić, D. Ranđelović, Z. Ssekulić, Environmental Monitoring – Selected Chapters, (Editor: A. Ganić), University of Belgrade - Faculty of Mining and Geology, Belgrade, 2015, p.139-168. ISBN: 978-86-7352-288-3.

[2] I.V. Kojo, H. Storch, International Symposium on Sulfide Smelting, San Diego, California, 2006. https://www.researchgate.net/publication/278030036_COPPER_PRODUCTION_WITH_OUTOKUMPU_FLASH_SMELTING_AN_UPDATE [accessed 24 March 2025]

[3] Environmental Impact Assessment Study of the Project: Increasing the Capacity of the Copper Smelter within the "Serbia Zijin Copper" Complex, Faculty of Technology and Metallurgy, University of Belgrade, July 2021, with an addendum from April 2022. (MMI Bor Archive).

[4] V. Tasić, T. Apostolovski-Trujić, B. Radović, R. Kovačević, N. Ristić, T. Urošević, V. Kamenović, Bakar, 48(1) (2023) 53-62. (E. Editor), Publisher, City, 2000, p.123.

[5] Mining and Metallurgy Institute Bor (MMI Bor), Laboratory for Chemical Testing, Department for Environmental Protection and Climate Change, Bor, Serbia: Annual and Monthly Reports on Ambient Air Quality in Bor for the Period 2021-2024 (MMI Bor Archive).

The 56th International October Conference on Mining and Metallurgy
22-25 October 2025, Bor Lake, Bor, Serbia
www.ioc.tfbor.bg.ac.rs

DOI: 10.5937/IOC25624P *Original scientific paper*

DISTRIBUTION OF PAHs IN SOILS FROM THE BOR REGION, TAKEN FROM THE ROOTING ZONE OF POISON IVY

Aleksandra Papludis[1a], Slađana Alagić[1b], Snežana Milić[1c], Dragana Medić[1d], Jelena Nikolić[2a], Snežana Jevtović[2b], Ivana Zlatanović Đaić[2c]

[1]Technical Faculty in Bor, University of Belgrade, V.J. 12, 19210 Bor, Serbia
[2]Faculty of Sciences and Mathematics, Department of Chemistry, University of Niš, Višegradska 33, 18000 Niš, Serbia
[1a] apapludis@tfbor.bg.ac.rs, 0000-0002-5388-2428
[1b]salagic@tfbor.bg.ac.rs, 0000-0002-2893-9285
[1c]smilic@tfbor.bg.ac.rs, 0000-0002-5000-9156
[1d]dmedic@tfbor.bg.ac.rs, 0000-0001-9980-5949
[2a]jelena.cvetkovic@pmf.edu.rs, 0000-0002-9351-331X
[2b]snezana.jovanovic@pmf.edu.rs, 0000-0002-3486-0047
[2c]ivana.zlatanovic@pmf.edu.rs, 0000-0002-6473-4236

Abstract
In this work, the distribution of polycyclic aromatic hydrocarbons (PAHs) was examined in the soil from the Bor region, sampled from the rooting zones of poison ivy. The samples were taken from different locations in the Bor town and its surroundings and analyzed using gas chromatographic-mass spectrometric method, and hierarchical cluster analysis with the average linkage between groups as an appropriate statistical method. The obtained results soundly illustrated the distribution of individual PAHs in soil and simultaneously, they indicated probable PAH sources, i.e., anthropogenic or natural. In accordance with the obtained hierarchical dendrogram, it can be supposed that only benzo(a)pyrene had a natural origin (from different processes in the soil), whereas all other PAHs had anthropogenic, i.e. atmospheric origin. The grouping of the latest compounds showed that they were kept in soil for different - longer or a shorter time.

***Keywords**: HCA, distribution, soil PAHs*

1. INTRODUCTION

Polycyclic aromatic hydrocarbons (PAHs) are ubiquitous pollutants with complicated aromatic structures in their molecules. Their lipophilic features (Table 1), coming from the present benzene molecules, allow an easy connection to soil particles, i.e., soil organic matter, where they can stay for a very long time [1, 2, 3]. In addition, they can be generated in soils from different diagenetic, and biogenic sources [2, 4]. The most important PAH compounds, together with their main characteristics are given in Table 1.

The main problem with these dangerous pollutants is their persistence in soil (the so called "ageing" with time), and generally – persistence in the complete environment; their toxicity, and in some cases, even carcinogenicity is also of concern (Table 1). For example, PAHs that contain 3 to 5 benzene rings, can survive in the atmosphere for a few hours or days, while in soil, they can be present for decades [6]. Decades ago, at the beginning of industrial period, most kinds of soils (without a direct exposition to PAH sources), had low concentrations of individual PAHs: 1–10 μg/kg; however, at the beginning of 21st century, this range extended to 100 μg/kg [3]. Recently, as informed by Gąsecka et al. [7], some studies found that the concentrations of individual PAHs in soils can vary from "not detected" (nd) to several hundred of μg/kg. For instance, Awere et al. [8] reported that in Ghana, near an e-waste recycling site, it was detected 390–710 ng of PAHs in a 1 g of soil.

Table 1 - Polycyclic aromatic hydrocarbons with their physical and chemical properties[a]

Compound / Abbreviation	Molecular Weight	Solubility (µg/L)	Vapor Pressure[c] (mm Hg)	Henry's Law Constant[c] (atm·m³/mol)	Log K_{ow}[d]	Log K_{oc}[e]
LMW (Low Molecular Weight: 2–3 rings)						
Naphtalene / Nap	128.19	31.69	0.087	$4.83\cdot10^{-04}$	3.36	2.97
Acenaphthylene / Acy	152.20	3.930	$2.9\cdot10^{-02}$	$1.45\cdot10^{-03}$	4.07	1.40
Acenaphthene / Ace	154.21	1.930	$4.5\cdot10^{-03}$	$1.91\cdot10^{-05}$	3.98	3.66
Fluorene / Flr	166.20	1.680–1.980	$3.2\cdot10^{-04}$	$1.00\cdot10^{-04}$	4.18	3.86
Anthracene / Ant	178.20	76	$1.7\cdot10^{-05}$	$1.77\cdot10^{-05}$	4.45	4.15
Phenanthrene / Ant	178.20	1.200	$6.8\cdot10^{-04}$	$2.56\cdot10^{-05}$	4.45	4.15
MMW (Medium Molecular Weight: 4 rings)						
Fluoranthene / Flt	202.26	200–260	$5.0\cdot10^{-06}$	$6.50\cdot10^{-06}$	4.90	4.58
Pyrene /Pyr	202.30	77	$2.5\cdot10^{-06}$	$1.14\cdot10^{-05}$	4.88	4.58
Benzo(a)anthracene[b] / BaA	228.29	10	$2.2\cdot10^{-08}$	$1.00\cdot10^{-06}$	5.61	5.30
Chrysene[b] / CHR	228.30	2.8	$6.3\cdot10^{-07}$	$1.05\cdot10^{-06}$	5.16	5.30
HMW (High Molecular Weight: ≥ 5 rings***)***						
Benzo(a)pyrene[b] / BaP	252.30	2.3	$5.6\cdot10^{-09}$	$4.90\cdot10^{-07}$	6.06	6.74
Benzo(b)fluoranthene[b] / BbF	252.30	1.2	$5.0\cdot1^{-07}$	$1.22\cdot10^{-05}$	6.04	5.74
Benzo(e)pyrene / BeP	252.30	6.3	$5.7\cdot10^{-09}$	NA	NA	NA
Benzo(k)fluoranthene[b] /BkF	252.30	0.76	$9.6\cdot10^{-11}$	$3.87\cdot10^{-05}$	6.06	5.74
Benzo(j)fluoranthene / BjF	252.32	6.76	$1.5\cdot10^{-08}$	$1.00\cdot10^{-06}$	6.12	4.7–4.8
Indeno(1,2,3-c,d)pyrene[b] / IcP	276.30	62	$1.0\cdot10^{-11}$–$1.0\cdot10^{-06}$	$6.95\cdot10^{-08}$	6.58	6.20
Benzo(g,h,i)perylene / BgP	276.34	0.26	$1.0\cdot10^{-10}$	$1.44\cdot10^{-07}$	6.50	6.20
Dibenz(a,h)anthracene[b] / DhA	278.35	0.5	$1.0\cdot10^{-10}$	$7.30\cdot10^{-08}$	6.84	6.52

[a] Table adapted from [5]
[b] Classified by US EPA as a probable human carcinogen [9]
[c] Indicates the chemical's potential to volatilize
[d] Provides an indication of the potential for the organic compound to partition from water into lipids
[e] Indicates a compound's potential to bind to organic carbon in soils
NA = no data available

In Bor′s region, the concentrations of soil PAHs were investigated mostly through examinations of plants′ bioremediation and phytoremediation potentials [10, 11] and in this work, the spatial soil samples taken from the roots of poison ivy (PI), collected from different locations, were also used for the detection of present PAHs and a processing by the related statistical method that may help in illustration of PAH distribution in soil of the studied region.

2. EXPERIMENTAL

The concentrations of soil PAHs were determined in the related spatial soil samples of PI as described in Papludis et al. [12]. Shortly, the representative soil samples of PI were taken from the rooting zone, from 9 sites in Bor′s municipality, in September 2020. Dried samples were homogenized, and then PAHs were isolated using a QuEChERS (Quick, Effective, Cheap, Easy, Rugged, Safe) method and analyzed by gas chromatographic-mass spectrometric (GC/MS) method. All samples were analyzed in triplicate and results are showed in µg/kg (dry weight, DW), in Papludis et al. [12].

Soils were collected from different sites in rural (R), and urban/industrial (UI) zone. The R zone encompasses 5 sites: Oštrelj (O), Slatina (S), Borsko jezero (BJ), Krivelj (K), and Gornjane (G), whereas UI zone had 4 sites: Flotacijsko jalovište (FJ), Bolničko naselje (BN), Slatinsko naselje (SN) and Naselje Sunce (NS).

Hierarchical cluster analysis (HCA) with the average linkage between groups as an appropriate method (for the identification of homogenous groups of the examined PAHs) was conducted in terms of getting a picture of PAH distribution in the analyzed [13]. IBM SPSS Statistics 20 software (USA) was applied.

3. RESULTS AND DISCUSSION

The detected soil PAH concentrations ranged from nd (not detected) for Ant, CHR, BkF+BbF, and DhA at many sites to over 500 µg/kg for Flt at the sites FJ, and O [12]. On the basis of these

concentrations, which were treated as variables, the average linkage between groups was applied in HCA method and the following hierarchical dendrogram was computed (Fig. 1):

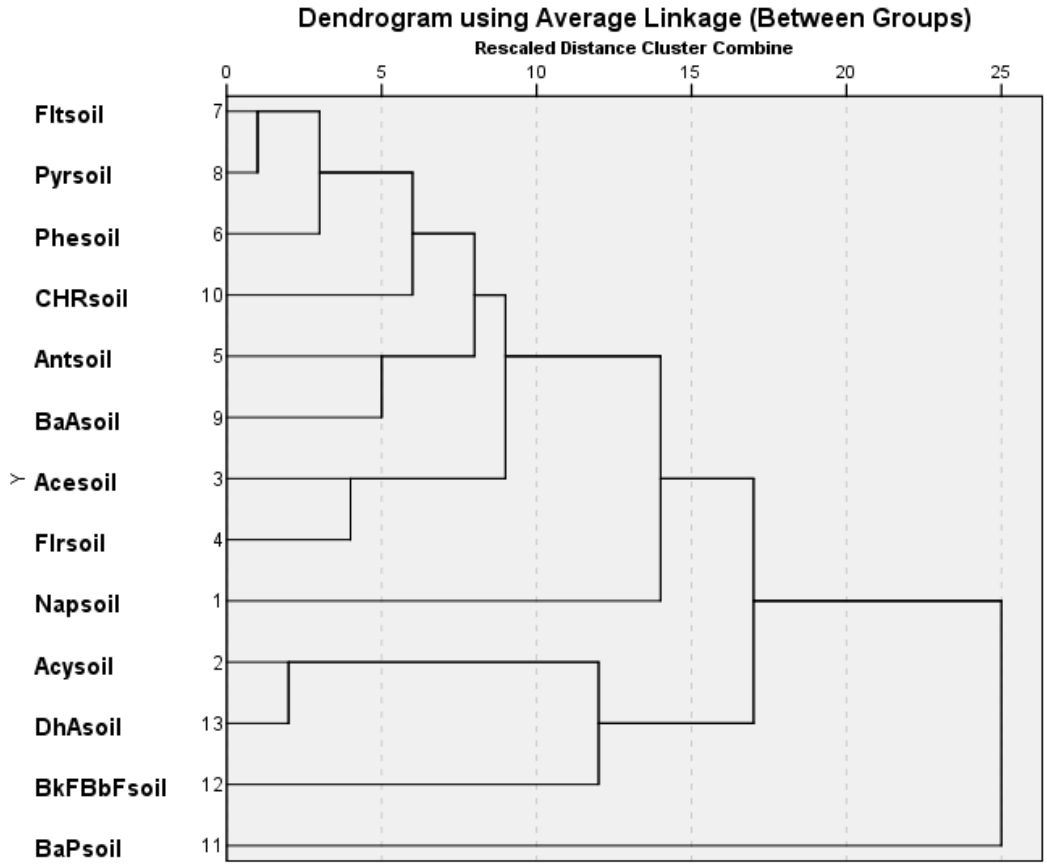

Figure 1. Homogenous groups of PAH compounds for the investigated soil in the region of Bor

The hierarchical dendrogram for the investigated soil PAHs of PI showed the two main clusters: an isolated cluster for BaP, and the other main cluster composed of all other compounds, represented in the form of numerous subclusters, in the arrangement as follows: the first main subcluster contained several subclusters such as: BbF+BkF/DhA-Acy, and the second main subcluster containing an isolated subcluster for Nap, and the other subcluster with the following groupings of compounds: Flr-Ace, BaA-Ant, and CHR/Phe/Pyr-Flt (Figure 1). This dendrogram clearly showed that the greatest distance occurred between the latest group of compounds (CHR/Phe/Pyr-Flt), and BaP (which formed an isolated cluster from all other compounds), which further pointed on its dissimilar origin; namely, it was probably mainly formed in the soil, during some natural processes [2, 4]; finally, the lowest concentrations of individual soil PAHs were found in this particular case, i.e., in the case of BaP. At the same time, it can be supposed that the latest mentioned group of compounds, i.e., CHR, Phe, Pyr, and Flt, had the most similar origin (which is the most dissimilar in comparison with the origin of BaP). This may signify that their origin can be connected with the influence of anthropogenic, practically, atmospheric pollution. More precisely, it can be say that this group of compounds "came" to soil the most recently, representing the "freshest" anthropogenic PAHs in the investigated soils. For all other compounds, it can be also assumed that they originated from the atmosphere but probably, they were not so "fresh", i.e. it is very possible that, in some extent, they were subjected to different "ageing" processes.

4. CONCLUSION

The results obtained from the applied chemical, and statistical methods soundly reflected the distribution of individual PAHs in soil of the region of interest and at the same time, pointed on

probable PAH sources, i.e., anthropogenic or natural. According to the obtained hierarchical dendrogram, it can be said that only BaP originated from natural processes in soil, whereas all other PAHs originated from anthropogenic, i.e. atmospheric sources; these latest compounds were retained in soil for a longer or a shorter time.

ACKNOWLEDGEMENTS

The research presented in this paper was done with the financial support of the Ministry of Science, Technological Development and Innovation of the Republic of Serbia, within the funding of the scientific research work at the University of Belgrade, Technical Faculty in Bor (contract number 451-03-137/2025-03/200131), and at the University of Niš, Faculty of Science and Mathematics in Niš (contracts' numbers 451-03-137/2025-03/200124, and 451-03-136/2025-03/200124).

REFERENCES

[1] S.S. Núnez, J.A. Conesa, J. Molto, A. Fullana, Resour. Conserv. Recy., 195 (2024) 107017.
[2] A. Ukalska-Jaruga A, B. Smreczak, Molecules, 25 (11) (2020) 2470.
[3] W. Wilcke, J Plant Nutr. Soil Sci., 163 (2000) 229-248.
[4] R.A. Lourenço, G.V. Lube, R. De L. Jarcovis, M.J. da Silva, A.C. de Souza, Mar Pollut Bull., 197 (2023) 115764.
[5] S.Č. Alagić, B.S. Maluckov, V.B. Radojičić, Clean Technol. Envir., 17 (3) (2015) 597-614.
[6] J.E Balmer, H. Hung, Y. Yu, R.J. Letcher, D.C.G. Muir, Emerg. Contam., 5 (2019) 128-142.
[7] M. Gąsecka, M. Włodarczyk-Makuła, A. Popenda, K. Drzewiecka, Phytoremediation of PAH-Contaminated Areas (Editors: A.A. Ansari, S.S. Gill, R. Gill, G.R. Lanza, L. Newman), Phytoremediation: Management of Environmental Contaminants, Volume 1, Springer International Publishing, Switzerland (2015) 295-309.
[8] E. Awere, P.A. Obeng, A. Bonoli, P.A. Obeng, Environ Technol. Rev., 9 (1) (2020) 1-19.
[9] USEPA, United States Environmental Protection Agency (2024), Available at: https://www.epa.gov/risk/regional-screening-levels-rsls-generic-tables (accessed 23 October 2024).
[10] S.Č. Alagić, V.P. Stankov Jovanović, V.D. Mitić, J.S. Cvetković, G.M. Petrović, G.S. Stojanović, Sci Total Environ., 562 (2016) 561-570.
[11] S.Č. Alagić V.P. Stankov Jovanović, V.D. Mitić, J.S. Nikolić, G.M. Petrović, S.B. Tošić, G.S. Stojanović, Environ. Sci. Pollut. Res., 24 (18) (2017) 15609-15621.
[12] A. Papludis, S. Alagić, S. Milić, D. Medić, I. Zlatanović, J. Nikolić, V. Stankov-Jovanović, Zaštita Materijala, 64 (1) (2023) 13-21.
[13] J.N. Miller, J.C. Miller, Statistics and Chemometrics for Analytical Chemistry, Pearson Education Limited, London, 2005.

The 56th International October Conference on Mining and Metallurgy
22-25 October 2025, Bor Lake, Bor, Serbia
www.ioc.tfbor.bg.ac.rs

DOI: 10.5937/IOC25628R

Original scientific paper

EFFECT OF AIR OXYGEN ENRICHMENT ON GASEOUS FUELS COMBUSTION AND GHG EMISSION

Žarko Radović, Nebojša Tadić

University of Montenegro, Faculty of Metallurgy and Technology,
Cetinjski put, bb, 81000 Podgorica, Montenegro
zarkor@ucg.ac.me, 0009-0005-3699-9869
nebojsa@ucg.ac.me, 0009-0007-5458-8232

Abstract

The subject of this article is an analysis of the influence of air oxygen enrichment on the gaseous fuel combustion and the GHG emision. Combustion conditions for three different chemical compositions and heating values of gaseous fuels are defined by changes in values of $\%O_2$ (21-30). GHG emission is defined as the sum of CO_2 and NO_x. For all analyzed gaseous fuels, the correlation of $\%O_2$, flame temperature, volume of combustion products and GHG emissions was calculated. The results were obtained using analytical method.The flame temperature increase with increasing values of $\%O_2$ and as a results of this, emission of NO_x increases. This can be explained by statement that at higher combustion temperature, volume of thermal NO_x increase.

***Keywords**: air enrichment, flame temperature, NOx*

1. INTRODUCTION

Improvements in the overall energy efficiency of an industrial plant are primarily achieved by reducing the energy input values and also the energy losses on the output side of a process step [1]. The amount of waste flue gases can be minimized and the heating rate of the unit can be increased by the oxygen enrichment of combustion air. With the same fuel input, enriched air for combustion raises the flame temperature of a given fuel, thereby improving the heat-transfer rate and increasing the production. Oxygen influences the burning process primarily by reducing nitrogen concentration in the gaseous combustion products, which results in fewer combustion products, higher flame temperature, etc.[2]. Oxygen-enriched combustion technology is accomplished by raising the oxygen content in the intake air, enabling combustion to be mainly governed by the mass ratio of oxygen to fuel instead of the conventional air–fuel ratio [3]. Yilmaz et al. have been analysed the effect of oxygen enrichment on the flame stability and emissions during biogas combustion [4]. A novel combustion technology which combines colorless distributed combustion (CDC) and oxygen enriched combustion (OEC) air is examined to achieve optimum benefits of both technologies and to foster novel technologies for cleaner environment [5]. One of the key objectives of thermal engineering calculations for fossil fuel combustion is to define the conditions and determine the quantities that influence heat exchange intensification, reduce specific fuel consumption, and minimize the harmful impact of exhaust gases on the environment.

2. EXPERIMENTAL

The central hypothesis of this paper is that an analytical correlation exists between the chemical composition of the fuel mixture, the air enrichment , and the emission of primary combustion byproducts (CO_2, NO_x), which have a dominant impact on air pollution.

For these calculation the varying composition of gaseous fuels (G1,G2,G3) are used as shown in the Table 1.

Table 1. The chemical composition of gaseous fuels (%)

Fuel	CH_4	H_2	CO	C_2H_4	C_2H_6	CO_2	O_2	H_2O	N_2
G1	84	-	-	0,5	0,7	-	-	8,2	8,6
G2	10,2	27,4	15,4	1,5	-	4	2,4	1,6	33,5
G3	24,4	4,2	3,8	12,5	4,1	1,2	1,1	0,8	47,9

The values of the oxygen content in combustion air for each analyzed fuel were selected from a range 21÷30%, (Table 2). The heating values (Qd) are calculated on the base of fuel chemical composition.

Table 2. The content of the oxygen in combustion air and Qd for analyzed fuels

	G1	G2	G3
% O_2	21÷30	21÷30	21÷30
Qd (MJ/m^3)	30,99	9,47	19,85

3. RESULTS AND DISCUSSION

As a consequence of the intensification of the combustion process, there is a change in the flame temperature and the volume of the combustion products formed. As typical, representative examples of the interdependence of the mentioned parameters, graphs related to the average value of the coefficient λ=1,12, from the analyzed range for all types of fuel, are presented (Figures 1 and 2).

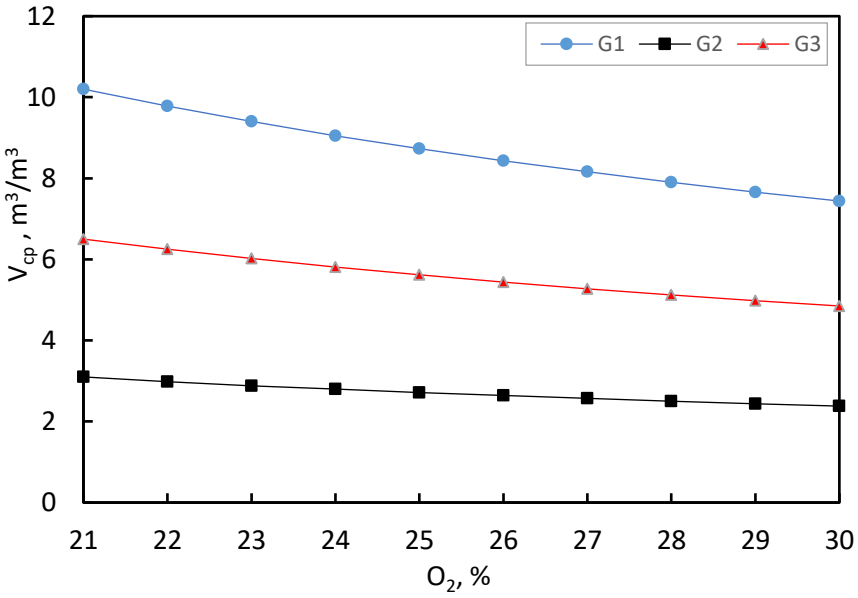

Figure 1. The influence of oxygen enrichment on the combustion products volume

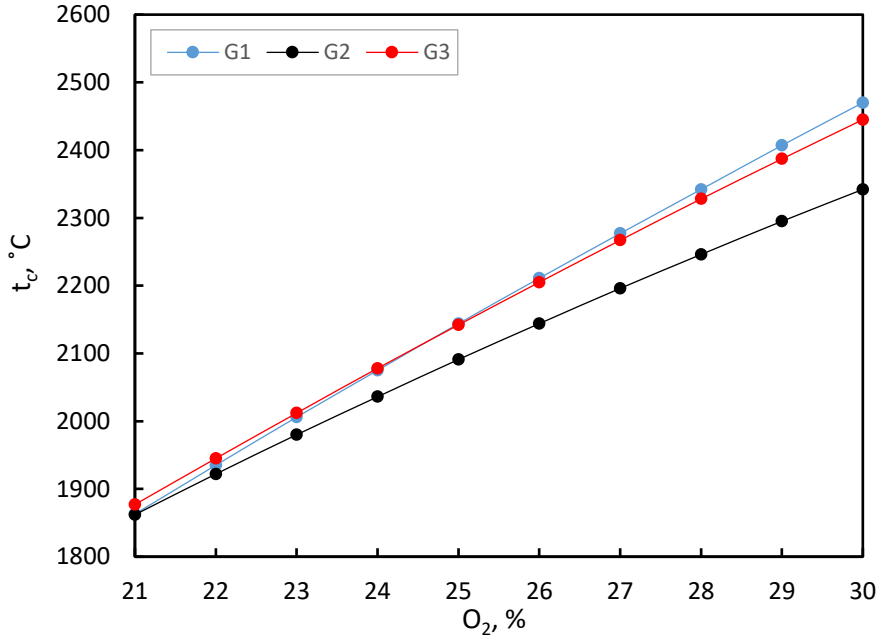

Figure 2. The influence of oxygen enrichment on the combustion temperature

Graphical presentations of the derived calculations show that, for all types of fuel, with the enrichment of air for combustion, i.e., with the increase in the percentage of oxygen in it, the volume of combustion products decreases, and the flame temperature increases.

In addition, the lines of change in combustion temperatures tG1 and tG3 intersect at 25% O_2, indicating a different intensity of their increase. This occurs as a result of significant differences in the chemical composition and lower heating value of the analyzed gaseous fuels.

The results of the calculations clearly show that CO_2 emissions depend solely on the initial carbon content and stoichiometric correlations, and not on the degree of air enrichment. The values of the calculated volumetric emissions and the CO_2 emission coefficient per unit of combusted fuel are shown in Table 3.

Table 3. The volume and K(CO_2) for analyzed fuels

*	**G1**	**G2**	**G3**
V(CO_2), m^3/m^3	0,86	0,33	0,63
K(CO_2), [kg/GJ]	54,8	59,3	60,8

The lower volumetric CO_2 emissions for gaseous fuels can be explained by the lower carbon content in the total mass of the fuel, which results in lower Qd values. Although a lower Qd is not favorable from a heat technology standpoint, considering K(CO_2) as an important reference parameter for environmental impact, it is observed that its values are relatively low for gaseous fuels.

The influence of the O_2 content in enriched air on the volumetric emission of NO_x and the emission coefficient K(NO_x) is shown in the Figure 3. Analytical calculations were performed for all types of fuel and all values of the excess air coefficient, but only the graphical dependencies for the average value of λ=1,12 are shown. For all analyzed fuels, it is observed that NO_x emissions increase with air enrichment, i.e., with the increase in % O_2, more or less according to an approximately exponential law.

It is characteristic that the presented correlations for gaseous fuels do not follow the principle that a higher initial N_2 content leads to a higher K(NO_x), because the highest value of the emission

coefficient is for G2 and the lowest for G1. Since K(NO_x) is directly proportional to the initial % N_2 and inversely proportional to the heating values of the fuel (Qd), it is evident that complete synergy of these two factors exists for G1 (low %N_2 and high Qd). In the case of G2, despite the relatively high nitrogen content, the heating value of the fuel is extremely low, so the influence of Qd dominates, causing high values of K(NO_x).

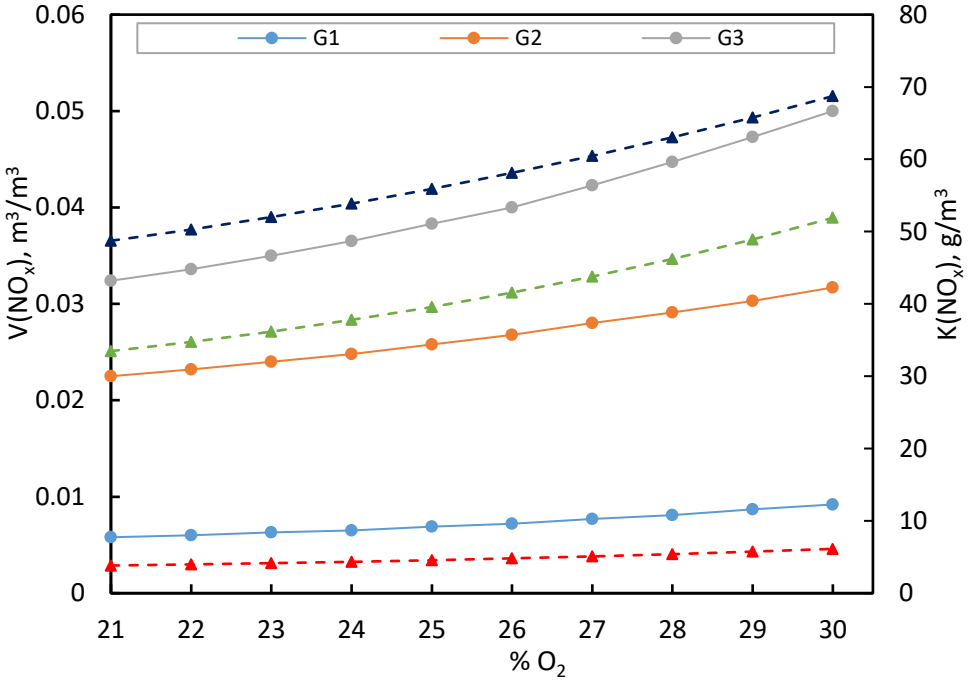

Figure 3. The influence of oxygen enrichment on the volume and the emission coefficient K(NOx)

4. CONCLUSION

For all analyzed fuels, with the increase in % O_2, the volume of combustion products decreases, and the flame temperature increases. Considering this, the most favorable heat technology indicators are achieved at an enrichment of 30% O_2, but the environmental effects must also be taken into account.

The influence of %O_2 in the air is twofold. On one hand, with the increase in %O_2, the %N_2 in the air decreases, thereby reducing one of the available "sources" of NO_x formation. However, on the other hand, with the increase in O_2 content, the combustion temperature significantly increases, which is the basic precondition for the formation of "thermal" NO_x.

It is obvious that the second influence is dominant, so, ultimately, enriching the air with oxygen leads to an increase in NO_x emissions.

REFERENCES

[1] M. Lalović, Ž. Radović, N. Jauković, Mater. Tehnol., 40 (3) (2006) 89-92.
[2] A.K Gupta, S. Ibrahim, A. Al Shoaibi, PECS, 54 (2016) 65–92.
[3] H.Y. Wang, X. Yang, Z.Y. Li, C. Zhang, X. Zhu, R. Zhang, J. Du, S. Zhang, Processes, 12 (2024) 2282.
[4] İ. Yilmaz, B. Alabaş, M. Taştan, G. Tunç, Fuel, 280 (15) (2020) 703.
[5] O. Ahmed, R. Said, A.K. Gupta, J. Energy Resour. Technol., 137 (4) (2015) 203.
[6] H.A. Alabaş, B.A. Çeper, J. Energy Inst., 111 (2023) 420.

The 56th International October Conference on Mining and Metallurgy
22-25 October 2025, Bor Lake, Bor, Serbia
www.ioc.tfbor.bg.ac.rs

DOI: 10.5937/IOC25632N

Original scientific paper

OPTIMIZING CADMIUM ION ADSORPTION: PREDICTIVE MODELING BASED ON LITERATURE DATA

Maja Nujkić[1a], Žaklina Tasić[1b], Sonja Stanković[1c], Dragana Medić[1d]

[1] Technical Faculty Bor, University of Belgrade, V.J. 12, 19210 Bor, Serbia
[1a] mnujkic@tfbor.bg.ac.rs, 0000-0002-6110-5135
[1b] ztasic@tfbor.bg.ac.rs, 0000-0001-6544-1980
[1c] sstankovic@tfbor.bg.ac.rs, 0000-0003-0745-5422
[1d] dmedic@tfbor.bg.ac.rs, 0000-0001-9980-5949

Abstract

The contamination of water with various heavy metal ions is a global problem and a challenge for research. Heavy metals in concentrations that exceed the permissible limits lead to considerable health problems. Accordingly, researchers are constantly working to find the most suitable technique for their removal. Among the conventional methods, adsorption stands out, in which various natural materials can be used to remove heavy metal ions, including cadmium ions. In this paper, a literature review is given on various natural materials that can be successfully used as biosorbents and optimization has been carried out to obtain optimal conditions for the removal of cadmium ions.

Keywords: *natural materials, wastewaters, Cd^{2+} ions, biosorption, response surface method*

1. INTRODUCTION

Water pollution with heavy metals is a serious environmental problem that threatens human health and aquatic ecosystems. Heavy metals such as lead, mercury, cadmium and arsenic are toxic and carcinogenic, and their presence in water can lead to serious health problems. They also tend to accumulate in organisms over time. Long-term exposure can cause a range of health problems, including damage to the kidneys, nervous system and reproductive organs, as well as an increased risk of cancer [1]. The main sources of water pollution from heavy metals include industrial processes, mining activity, agricultural runoff and inadequate waste disposal [2,3]. Numerous researchers are concentrating on finding a suitable method for removing cadmium ions from wastewater, as they are persistent and toxic. They end up in the water because compounds containing cadmium are inadequately disposed of in mines, paint factories, electroplating, plastics and cadmium-nickel batteries. There are several conventional methods for removing heavy metals from water, such as precipitation, ion exchange, reverse osmosis, adsorption, coagulation and flocculation [4,5]. However, adsorption stands out from the other methods as it has significant advantages, such as low cost, efficiency, ease of implementation and the possibility of using various agricultural materials (biomass) as adsorbents [5]. Agricultural materials are readily available, inexpensive and can be regenerated. The aim of this work is to summarize potential natural adsorbents for the removal of cadmium ions based on a literature review. The adsorption activities were also investigated using a Box-Behnken design to find the optimal parameters for successful removal of cadmium ions.

2. EXPERIMENTAL

In order to determine the optimal conditions for the removal of Cd^{2+} ions, experimental data from previously published studies were collected and analyzed. Numerous research groups have employed natural biosorbents to remove Cd^{2+} from wastewater, including black cumin seeds [5], banana, kiwi, and tangerine peels [6], watermelon rinds [7], chicken eggshells [8], *Rosa damascena* waste [9], and *Ziziphus lotus* fruit powder [10]. These biosorbents were tested under varying experimental conditions.

To optimize the biosorption process, the response surface methodology (RSM) was applied. A Box-Behnken experimental design was used to investigate the influence of three independent variables on cadmium removal efficiency: A - solution pH, B - initial concentration of cadmium ions (C_0), and C - biosorbent dosage. The ranges of investigated parameters were as follows: pH from 4 to 12, Cd^{2+} concentration from 10 to 200 mg/L, and biosorbent dosage from 0.03 to 20 g/L. The collected data were subjected to statistical analysis, including analysis of variance (ANOVA), to evaluate the adequacy and significance of the model used [11].

3. RESULTS AND DISCUSSION

The adsorption efficiency reported across different studies ranged from 33% to 91%, depending on the type of biosorbent and experimental conditions. It was found that the isotherms of Cd^{2+} removals on different adsorbents are best described by the Langmuir model [5,9,10], followed by the Freundlich [8] and Dubinin-Radushkevich models [7]. The kinetics of the process generally corresponds to a pseudo-second order model.

The results of the Analysis of variance are presented in Table 1 and show that the model is significant.

Table 1 - Analysis of variance for the removal of Cd^{2+}

Source	Sum of Squares	Degree of freedom	Mean Square	F-value	p-value	
Model	4211.95	9	467.99	2.553E+05	< 0.0001	significant
A-pH	1013.73	1	1013.73	5.529E+05	< 0.0001	
B-Co	101.94	1	101.94	55604.89	< 0.0001	
C-m	1482.28	1	1482.28	8.085E+05	< 0.0001	
AB	477.03	1	477.03	2.602E+05	< 0.0001	
AC	1105.92	1	1105.92	6.032E+05	< 0.0001	
BC	278.12	1	278.12	1.517E+05	< 0.0001	
A^2	793.05	1	793.05	4.326E+05	< 0.0001	
B^2	0.3229	1	0.3229	176.14	0.0009	
C^2	84.40	1	84.40	46037.63	< 0.0001	
Pure Error	0.0055	3	0.0018			
Cor Total	4211.95	12				

The model Fischer value (F-value) of 255269.55 implies the model is significant. There is only a 0.01% chance that an F-value this large could occur due to noise. Probability values (p-value) are lower than 0.05 indicating the significance of investigated parameters on the efficiency of uptaking Cd^{2+} [12]. In accordance with the F-value in Table 1, the dosage of the biosorbent can be considered the most important factor for the removal of Cd^{2+}, followed by the interaction between the dosage of the biosorbent and the pH and the initial pH of the solution. Equation (1) represents a quadratic response model in which all linear, quadratic and elementary linear interactions are taken into account [12,13].

$$E = -740.00930 + 205.97983\,pH - 0.942410\,C_0 + 95.47519\,m + 0.292469\,pH \cdot C_0 - 13.65316\,pH \cdot m - 0.690388\,C_0 \cdot m - 13.18421\,pH^2 - 0.000148\,{C_0}^2 + 1.30600\,m^2 \quad (1)$$

The robustness of the model can be assessed using the experimentally determined (R^2) and the predicted ($R^2_{adjusted}$) coefficient of determination, both of which are 1.0000 [13]. The plot of actual versus predicted responses is shown in Figure 1a.

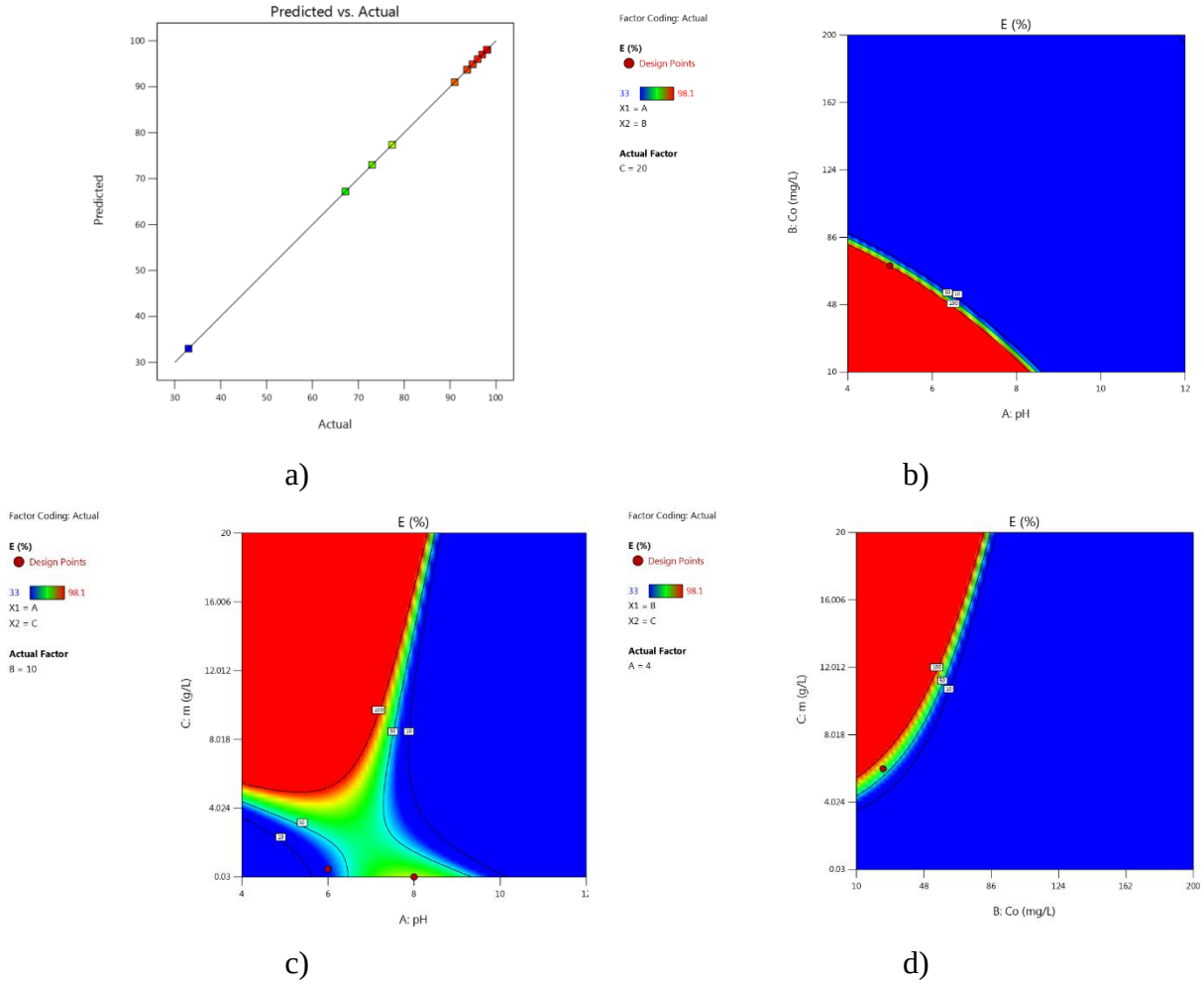

Figure 1. 2D surface response plots for the removal of Cd^{2+} (a) Actual vs predicted responsesand, the interaction between (b) pH and initial concentaration of Cd^{2+}, (c) pH and dosage of biosorbent, (d) initial concentaration of Cd^{2+} and dosage of biosorbent

Figure 1 (b, c and d) shows the 2D response surface plots of the interaction effects between the independent variables and the response. As shown in Figure 1b, the efficiency of Cd^{2+} removal is higher in an acidic environment than in a neutral or alkaline environment. Figure 1c illustrates the interaction between the pH value and the dosage of the biosorbent. Increasing the dose of biosorbent in an acidic environment also increases efficiency. A higher dose of biosorbent at a lower initial concentration of Cd^{2+} enables better removal of these heavy metal ions, as shown in Figure 1d. Based on the optimization carried out, it was found that the optimum values of the process parameters are as follows: pH 4, biosorbent dose 7.4 g/L and initial concentration of Cd^{2+} 30 mg/L. This is in good agreement with Assimeddine et al. [12], who stated that the adsorption process is more favourable at lower pH values than at higher pH values. In addition, a higher dose of biosorbent provides more binding sites that remove more Cd^{2+} ions.

4. CONCLUSIONS

Pollution of water bodies by heavy metals is a major environmental problem that endangers both human health and aquatic ecosystems. Heavy metals such as lead, mercury, cadmium and arsenic are toxic and carcinogenic, and their presence in water can lead to serious health problems. The removal of heavy metal ions from water is of great importance and the use of natural materials as biosorbents is increasingly being explored by researchers. The aim of this study is to determine the optimal conditions for the removal of Cd^{2+} from wastewater by analyzing available literature data and predictive models. The predictions suggest that optimal removal of Cd^{2+} occurs under more acidic conditions (pH 4), lower initial metal concentrations (30 mg/L) and higher biosorbent doses (7.4 g/L). However, these results need to be experimentally validated to ensure their reliability. Nevertheless, such predictions play a crucial role in the planning and optimization of experimental studies.

ACKNOWLEDGEMENTS

The research presented in this paper was done with the financial support of the Ministry of Science, Technological Development and Innovation of the Republic of Serbia, within the funding of the scientific research work at the University of Belgrade, Technical Faculty in Bor, according to the contract with registration number 451-03-137/2025-03/200131.

REFERENCES

[1] P. Salehi, F.M. Tajabadi, H. Younesi, Y. Dashti., Clean: Soil, Air, Water 42 (2014) 243-250.
[2] N. Sultana, S.M. Zakir Hossain, M. Ezzudin Mohammed, M.F. Irfan, B. Haq, M.O. Faruque, S.A. Razzak, M.M. Hossain., Sci. Rep., 10 (2020) 15068.
[3] L. Shen, R. Chen, J. Wang, L. Fan, L. Cui, Y. Zhang, J. Cheng, X. Wu, J. Li, W. Zeng., RSC Adv., 11 (2021) 18637.
[4] K.S. Rao, M. Mohapatra, S. Anand, P. Venkateswarlu., Int. Eng. Sci. Technol., 2 (2010) 81-103.
[5] P.M. Thabede, N.D. Shooto, T. Xaba, E.B. Naidoo., J. Environ. Chem. Eng., 8 (2020) 104045.
[6] K.M. Al-Qahtani., J. Taibah Univ. Sci., 10 (2016) 700-708.
[7] Q. Wang, Y. Wang, L. Yuan, T. Zou, W. Zhang, X. Zhang, L. Zhang, X. Huang., J. Adv, Chem. Eng., 12 (2022) 100393.
[8] M.S. Tizo, L.A.V. Blanco, A.C.Q. Cagas, B.R.B. Dela Cruz, J.C. Encoy, J.V. Gunting, R.O. Arazo, V.I.F. Mabayo., Sustain. Environ. Res., 28 (2018) 326-332.
[9] F. Batool, A. Mohyuddin, A. Amjad, A. Hassan, S. Nadeem, M. Javed, M.H.D. Othman, K.W. Chew, A. Rauf, T.A. Kurniawan., Chem. Eng. Sci., 280 (2023) 119072.
[10] N. El Yakoubi, M. Ennami, Z.N. El Ansari, F.A. Lhaj, L. Bounab, M.L'. El Kbiach, B. El Bouzdoudi., Ecol. Eng. & Environ. Technol., 24(3) (2023) 135-146.
[11] C. Ai, D. Zhou, Q. Wang, X. Shao, Y. Lei., Solar Energy 113 (2015) 34-42.
[12] M. Assimeddine, Z. Farid, M. Abdennouri, N. Barka, E.M. Lemdek, M. Sadiq., ESPR 30 (2023) 62494-62507.
[13] S.B. Moussa., J. Photochem. Photobiol. A: Chem., 447 (2024) 115284.

The 56th International October Conference on Mining and Metallurgy
22-25 October 2025, Bor Lake, Bor, Serbia
www.ioc.tfbor.bg.ac.rs

DOI: 10.5937/IOC25636M

Original scientific paper

STATISTICAL MODELING OF COPPER IONS BIOSORPTION ONTO SUNFLOWER HULLS

Miljan Marković[1a], Milan Gorgievski[1b], Marina Marković[1c], Vesna Grekulović[1d], Nada Štrbac[1e], Kristina Božinović[1f], Milica Zdravković[1g]

[1] Technical Faculty Bor, University of Belgrade, V.J. 12, 19210 Bor, Serbia
[1a] mmarkovic@tfbor.bg.ac.rs, 0000-0002-4734-1481
[1b] mgorgievski@tfbor.bg.ac.rs, 0000-0002-9899-719X
[1c] marina.markovic@tfbor.bg.ac.rs, 0009-0007-7553-6423
[1d] vgrekulovic@tfbor.bg.ac.rs, 0000-0001-6871-4016
[1e] nstrbac@tfbor.bg.ac.rs, 0000-0003-4836-1350
[1f] kbozinovic@tfbor.bg.ac.rs, 0000-0002-9834-448X
[1g] mzdravkovic@tfbor.bg.ac.rs, 0000-0001-9488-9151

Abstract
The statistical modeling of the copper ions biosorption onto sunflower hulls is presented in this work. The analysis was conducted using the Response Surface Methodology coupled with the Box-Behnken Design. The software experimental design, consisting of 17 experiments, was applied to optimize the biosorption process. The obtained results indicated that the used model is statistically significant, and that the optimal conditions for copper ions biosorption onto sunflower hulls are: 0.7 g sunflower hull sample mass, 0.1 g dm^{-3} initial copper ions concentration, and pH of the solution 5. The analysis indicated that all three analyzed parameters are significant model terms.

***Keywords**: Response surface methodology; Box-Behnken design, biosorption, sunflower hull*

1. INTRODUCTION

In recent years, rapid industry growth accelerated the discharge of large amounts of pollutants into the surface and groundwater. Wastewater polluted with heavy metals is a serious worldwide environmental issue. Heavy metals are non-degradable pollutants, that tend to accumulate in living organisms, and cause a wide array of diseases and disorders. These pollutants are present in discharges from various industries, including metal processing, mining, surface treatment of metals, energy sector, etc. [1,2].

As a trace element, it is essential in living organisms as it participates in the synthesis of different types of enzymes. However, in bigger concentrations it is toxic to living organisms, as it affects the metabolism, cell growth, and other processes [3].

On the industrial scale, many technologies have been used to treat wastewater and remove toxic pollutants, including electrodialysis, chemical precipitation, adsorption, chemical precipitation, membrane separation, and others. These technologies come with several limitations and difficulties, that include high operating costs, high reagent usage, sludge production, high energy requirements, and inefficiency when it comes to low heavy metal concentrations [1,2].

Biosorption, i.e. the adsorpton of toxic pollutants using biological materials as adsorbents (biosorbents) has become a popular alternative method to conventional technologies. Biosorbents are economically and environmentally friendly, and have shown, to some extent, selectivity towards heavy metals, and can be used in a wide range of physico-chemical conditions [2].

2. EXPERIMENTAL

The sunflower hulls were ground and then sieved through a set of laboratory sieves, and the fraction (-1+0.4) mm was used for the Cu^{2+} biosorption experiments. The experiments were performed using synthetic copper solutions prepared using $CuSO_4 \cdot 5H_2O$ (p.a. purity). The pH value of the solutions was adjusted with 0.1 M KOH, and 0.1 M HNO_3. The chemicals used were manufactured by LACHEMA (Czech Republic).

The RSM-BBD experimental design, which was used to optimize the biosorption process, consisted of 17 experiments. The design was applied comparing three selected factors: biosorbent mass (A), initial copper ion concentration (B), and pH value of the solution (C). The test series and their values are listed in Table 1.

Table 1. Experimental ranges and their levels

Factors	Range level		
	-1	0	1
A – biosorbent mass, g	0.3	0.5	0.7
B – initial copper ion concentration, g dm^{-3}	0.1	0.2	0.3
C – pH of the solution	3	4	5

3. RESULTS AND DISCUSSION

The biosorption process was optimized using Response Surface Methodology (RSM) coupled with the Box-Behnken Design (BBD). The process optimization experimental design, given in Table 1, was applied to optimize the copper biosorption process onto sunflower hulls. The matrix of the experimental design, and the obtained results (response R – biosorption degree) are shown in Table 2.

Table 2. Experimental ranges and their levels

Run	A – biosorbent mass, g	B – initial copper ion concentration, g dm^{-3}	C – pH of the solution	R – biosorption degree, %
1	0	1	1	24.036
2	0	-1	-1	52.564
3	0	1	-1	15.433
4	-1	0	-1	11.726
5	1	0	-1	18.613
6	0	-1	1	75.396
7	0	0	0	40.007
8	-1	-1	0	64.556
9	0	0	0	30.026
10	0	0	0	32.221
11	-1	0	1	27.351
12	-1	1	0	15.537
13	1	-1	0	74.086
14	1	1	0	35.557
15	1	0	1	45.475
16	0	0	0	32.377
17	0	0	0	35.348

A polynomial equation (1) was fitted in order to describe the correlation between the independent variables: linear (β_1, β_2, β_3), quadratic (β_{11}, β_{22}, β_{33}), interaction terms (β_{12}, β_{13}, β_{23}) and the response (R) [4]:

$$R = \beta_0 + \beta_1 A + \beta_2 B + \beta_3 C + \beta_{11} AA + \beta_{22} BB + \beta_{33} CC + \beta_{12} AB + \beta_{13} AC + \beta_{23} BC \quad (1)$$

The results obtained are shown in Table 2. The copper ions biosorption onto sunflower hulls can be expressed as:

$$R = 33.99 + 6.82A - 22.01B + 9.24C + 2.62A \cdot B + 2.81A \cdot C - 3.56B \cdot C - 1.31A^2 + 14.75B^2 - 6.89C^2 \quad (2)$$

The ANOVA statistical analysis was performed to determine the statistical significance of the applied model. The obtained results are given in Table 3. The significance of the individual coefficients is analyzed by the F-values and p-values. The coefficient is more significant as the F-value is higher and p-value lower. p-values below 0.0500 indicate a highly significant regression at a confidence level of 95 % [5,6].

Table 3. ANOVA analysis for the Response Surface model for copper ions biosorption onto sunflower hulls

Source	Sum of squares	df	Mean square	F-value	p-value	
Model	6116.00	9	679.56	61.42	< 0.0001	significant
A-A	372.11	1	372.11	33.63	0.0007	
B-B	3873.72	1	3873.72	350.12	< 0.0001	
C-C	683.06	1	683.06	61.74	0.0001	
AB	27.51	1	27.51	2.49	0.1588	
AC	31.57	1	31.57	2.85	0.1350	
BC	50.62	1	50.62	4.57	0.0697	
A^2	7.27	1	7.27	0.6570	0.4443	
B^2	916.31	1	916.31	82.82	< 0.0001	
C^2	199.92	1	199.92	18.07	0.0038	
Residual	77.45	7	11.06			
Lack of Fit	17.95	3	5.98	0.4024	0.7598	not significant
Pure Error	59.49	4	14.87			
Cor Total	6193.44	16				

The obtained F- and p-values (61.42 and < 0.0001) indicate that the model is significant, with further indication that there is only a 0.01% chance that this F-value appeared due to noise. The model fit was also confirmed by the regression coefficients of the predicted and experimental values (R^2 = 0.940 and adj-R^2 = 0.971).

P-values above 0.1000 indicate that the analyzed model terms aren't significant. In this case, A-A, B-B, C-C, BC, B^2 and C^2 are significant model terms.

The plot of actual vs predicted responses (shown on Figure 1) can also give insight into the significance of the applied model [6]. The obtained results show a good agreement between the experimental and the model predicted responses.

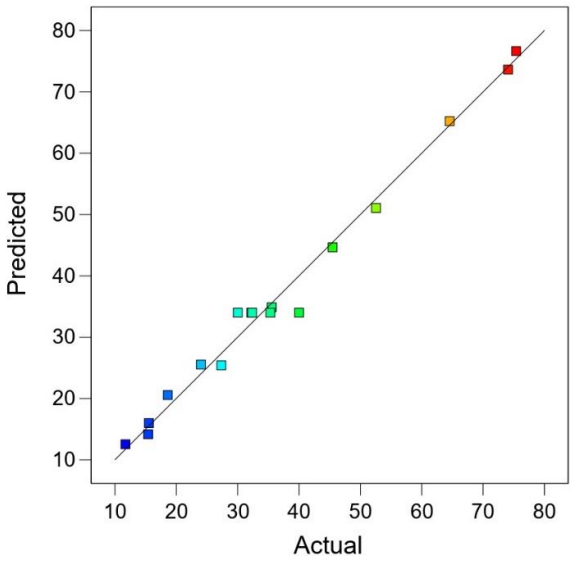

Figure 1. Actual vs model predicted responses

3D surface plots, illustrating the influence of the analyzed parameters on the system response (R) are shown on Figure 2.

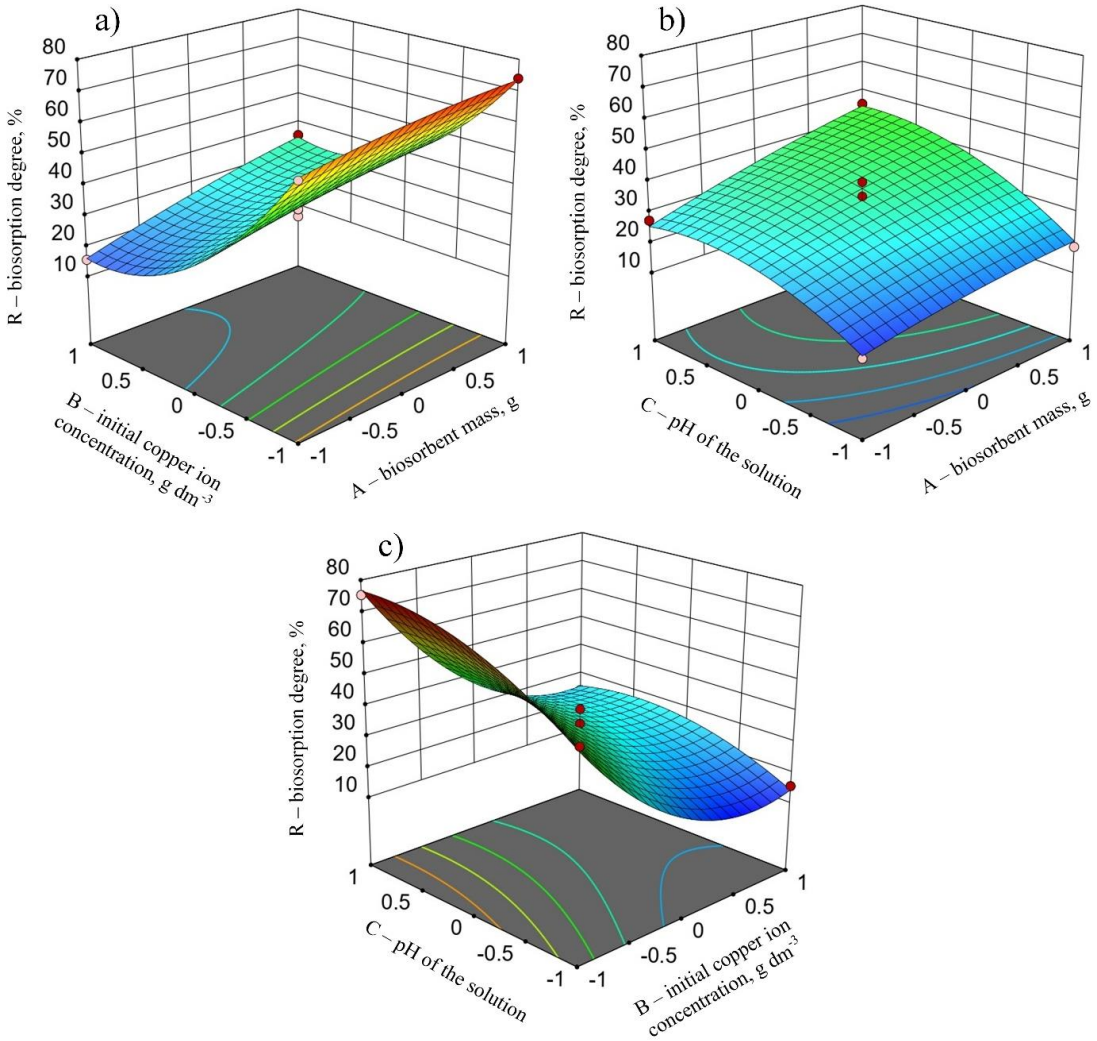

Figure 2. Response surface plots showing the interaction and influence on the biosorption rate (R) of (a) biosorbent mass (A) and initial copper ions concentration (B); (b) biosorbent mass (A) and pH of the solution (C); (c) initial copper ions concentration (B) and pH of the solution (C)

Figure 2a indicates that low initial copper concentrations in combination with high biosorbent mass led to a high response (biosorption degree). The interaction between the biosorbent mass and pH of the solution is shown on Figure 2b. It can be seen that higher biosorbent mass along with higher pH value of the solution led to a higher response, i.e. biosorption degree. Figure 2c (interaction between initial copper concentration and pH of the solution) indicated that lower initial copper concentrations in combination with higher pH values of the solution gave higher system responses, i.e. higher biosorption degree.

4. CONCLUSIONS

The optimization of the copper ions biosorption onto sunflower hulls was performed using the RSM-BBD method. The influence of three process parameters, i.e. the mass of the biosorbent, the initial copper ion concentration, and the pH of the solution was evaluated. The used model was determined to be statistically significant. The performed analysis suggested that the optimal conditions for copper ions biosorption onto sunflower hulls are: 0.7 g biosorbent mass, 0.1 g dm^{-3} initial copper concentration, and pH of the solution 5.

ACKNOWLEDGEMENTS

The research presented in this paper was done with the financial support of the Ministry of Science, Technological Development and Innovation of the Republic of Serbia, within the funding of the scientific research work at the University of Belgrade - Technical Faculty in Bor, according to the contract with registration number 451-03-137/2025-03/200131.

REFERENCES

[1] C.I. Orozco, M.S. Freire, D. Gomez-Diaz, J. Gonzalez-Alvarez, Sustain. Chem. Pharm., 32 (2023) 101016.
[2] N.E. Davila-Guzman, F.J. Cerino-Cordova, E. Soto-Regaldo, J.R. Rangel-Mendez, P.E. Diaz-Flores, M.T. Garza-Gonzalez, J.A. Lorendo-Medrano, CLEAN-Soil Air Water., 41 (6) (2013) 557-564.
[3] C. Tu, Y. Liu, J. Wei, L. Li, K.G. Scheckel, Y. Luo, ESPR, 25 (2018) 24965-24974.
[4] A. Choinska-Pulit, J. Sobolczyk-Bednarek, W. Laba, Ecotoxicol. Environ. Saf., 149 (2018) 275.
[5] W. Yuan, J. Cheng, H. Huang, S. Xiong, J. Gao, J. Zhang, S. Feng, Ecotoxicol. Environ. Saf., 175 (2019) 138-147.
[6] M. Marković, M. Gorgievski, N. Štrbac, V. Grekulović, M. Zdravković, M. Marković, D. Stanković, J. Serb. Chem. Soc., 90 (2025) 1-21.

The 56th International October Conference on Mining and Metallurgy
22-25 October 2025, Bor Lake, Bor, Serbia
www.ioc.tfbor.bg.ac.rs

DOI: 10.5937/IOC25641S

Original scientific paper

ENVIRONMENTAL SAMPLING STRATEGY FOR THE ROMANIA–SERBIA BORDER MINING REGION

Miloš Stojanović[1a], Nicoleta Sorina Nemes[2a], Adina Negrea[3a], Mihaela Ciopec[3b], Ivan Svrkota[1b], Daniel Kržanović[1c], Igor Svrkota[1d]

[1] Mining and Metallurgy Institute Bor, Alberta Ajnštajna 1, 19210 Bor, Serbia
[2] Research Institute for Renewable Energies - ICER, Gavril Musicescu, 138, 300501 TM, Romania
[3] Politehnica University Timişoara, Chemical Engineering Faculty, Vasile Pârvan 6, Timisoara, Romania
[1a] milos.stojanovic@irmbor.co.rs, 0000-0003-0044-5491
[2a] nicoleta.nemes@upt.ro, 0000-0003-2532-2893
[3a] adina.negrea@upt.ro, 0000-0001-7572-3703
[3b] mihaela.ciopec@upt.ro, 0000-0001-6760-1511
[1b]ivan.svrkota@irmbor.co.rs, 0000-0002-1105-1554
[1c]daniel.krzanovic@irmbor.co.rs, 0000-0003-3841-8667
[1d]igor.svrkota@irmbor.co.rs, 0000-0002-3779-6327

Abstract
This paper presents an environmental sampling strategy for the Romania–Serbia border region, developed within the ERA-MIN_RO-SRB framework. The approach includes identification of mining-related pollution sources and spatially optimized selection of sampling points for air, water, and soil monitoring. Sites were determined using wind rose data, hydrographic analysis, and proximity to tailings and waste deposits at five active mining locations. Control points were included to establish natural baselines. The strategy enables consistent, cross-border data collection and supports scientifically robust environmental risk assessments in mining-affected transboundary areas.

***Keywords**: enviromental, sampling, cross-border*

1. INTRODUCTION

Mining activities in border regions can have transboundary environmental impacts, necessitating cooperative monitoring strategies. The Romania–Serbia border mining region (spanning the Moldova Nouă area in Romania and the Bor-Majdanpek area in Serbia) has a long history of copper mining and smelting, leaving a legacy of soil, water, and air pollution [1]. Large volumes of mining waste (tailings) containing high concentrations of metals and sulfide minerals have been disposed of in this region. When exposed to air and water, sulfide-rich tailings oxidize to produce acid mine drainage (AMD) – acidic, metal-laden leachate that contaminates nearby rivers and soils. These processes release toxic heavy metals (e.g. Cu, Zn, Pb, As, Cd, Ni) into the environment, posing risks to ecosystems and human health. A recent cross-border study confirmed that surface waters near the Bor mining complex in Eastern Serbia are highly polluted with heavy metals (Fe, Mn, Cu, Zn, As, Ni, Pb, Cd), with concentrations diminishing at greater distances from the sources. On the Romanian side, the abandoned tailings ponds near Moldova Nouă similarly contribute to pollution; wind-blown dust from these ponds disperses across the Danube into Serbia, depositing heavy metals on soils and degrading air quality over large areas.

2. IDENTIFICATION OF POLLUTION SOURCES AND SITE SELECTION STRATEGY

A comprehensive assessment of pollution sources was conducted to accurately guide the selection of sampling sites within the Romania–Serbia border mining region. The study area includes

significant active and historical mining operations, specifically around the Bor and Majdanpek mining districts in Serbia, and the Moldova Nouă area in Romania.

In the Serbian section, key mining locations encompass both underground and open-pit mines, including Jama Bor (underground), Čukaru Peki (underground), Veliki Krivelj (open-pit), Cerovo (open-pit), and Majdanpek (open-pit). Ore extraction and processing operations generate large volumes of waste materials, such as flotation tailings, waste rock dumps, and process waters, which are significant potential sources of heavy metal contamination, acid mine drainage (AMD), and particulate emissions. A major concern in this area is related to flotation tailing facilities, often located near watercourses or in exposed locations subject to wind erosion. These tailings ponds, especially around Veliki Krivelj and Jama Bor, are sources of heavy metals and other toxic compounds through wind dispersal of fine particles and leaching into surface water bodies. Smelting operations, particularly the Bor smelter, add further complexity, emitting sulfur dioxide (SO_2) and heavy metals into the atmosphere [1]. In the Moldova Nouă region of Romania, abandoned tailings impoundments near the Danube River represent historical but persistent pollution sources. Wind erosion of fine-grained tailings deposits has repeatedly resulted in dust storms, dispersing toxic heavy metals across the border into Serbia and negatively impacting soil and air quality on both sides of the river. Ultimately, combining these analytical approaches allowed for a thorough characterization of the primary and secondary pollution sources, thereby laying a robust foundation for the spatially optimized environmental sampling strategy described in subsequent sections. The selection of environmental sampling sites was designed as a structured, spatially optimized process aimed at ensuring representative monitoring across the transboundary mining region. The primary objective was to capture the variability of environmental conditions influenced by mining operations while enabling data comparability between Romania and Serbia. The methodology combined remote sensing, field reconnaissance, geospatial analysis, and environmental criteria to define locations for sampling of surface water, soil, and air (Figure 1).

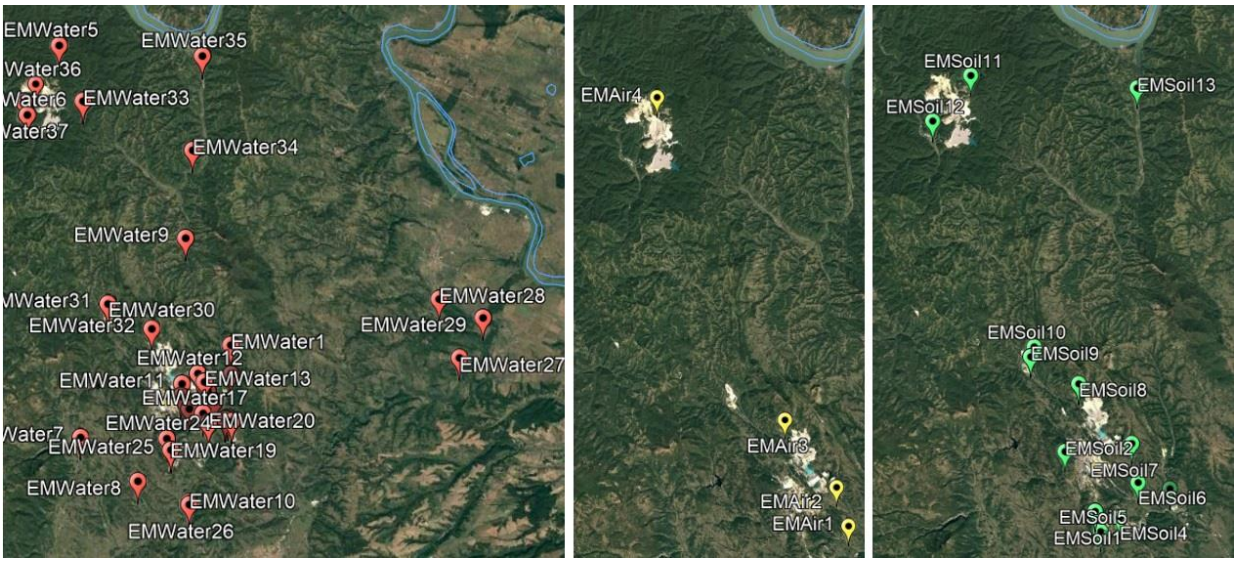

Figure 1. Sampling location maps (surface water, air, soil)

The process began with the mapping of pollution hotspots, including operational mines, ore processing facilities, flotation tailings ponds, waste rock dumps, and historical contamination sites. This information was gathered from satellite imagery, environmental impact assessments, and official mining concession maps. For surface water, a hydrographic analysis was conducted to delineate the network of rivers and streams intersecting or bordering mining areas. Main attention was given to the Bor and Krivelj rivers, the Brestovačka and Suva rivers, and the drainage basins near Cerovo and Majdanpek. Sampling points were planned both upstream and downstream of mining discharge locations to assess pollutant loading and enable calculation of mass balances for

contaminants. In addition to proximity to pollution sources, site accessibility and safety were evaluated during field inspections.

Terrain slope, vegetation density, road access, and visibility were considered to ensure repeatability of sampling and personnel safety, especially during unfavorable weather conditions.

Where necessary, sampling points were adjusted to ensure safe operation while maintaining representativeness. Each proposed site was documented through a standardized Sample Point Determination Report, which included GPS coordinates and elevation, photographic documentation, type of sampling (water, soil, air), expected exposure to mining-related contaminants, sampling frequency and on-site environmental observations (e.g., vegetation, dust accumulation, water turbidity).

Surface water sampling represents a fundamental component of the environmental monitoring framework, as watercourses are the primary media for the transport of dissolved and suspended pollutants originating from mining activities. Surface waters such as the Bor, Krivelj, and Pek rivers in Serbia, and the Danube and its tributaries near Moldova Nouă in Romania, are especially vulnerable to contamination from active and legacy mining sources [1].

Sampling frequency is quarterly (four times per year), covering spring, summer, autumn, and winter conditions. This temporal distribution allows the capture of seasonal dynamics such as snowmelt, reduced flow in drought periods, and increased runoff during heavy rainfall events—all of which influence contaminant mobility. At each location, field measurements are conducted in situ using multiparameter probes and portable devices. These include water temperature, pH, electrical conductivity (EC), dissolved oxygen (DO) and oxidation-reduction potential (ORP).

Water samples are collected following ISO 5667-6 and ISO 5667-10 protocols, ensuring standardization of sampling depth, container type, preservation, and transport. Grab samples are taken at mid-depth and mid-stream whenever possible, avoiding stagnant zones or surface films unless otherwise justified by site conditions.

Overall, the surface water sampling plan ensures that the strategy captures spatial gradients, temporal trends, and critical contamination hotspots. It provides a reliable dataset for evaluating the impact of mining on aquatic ecosystems, human health risks from water use, and compliance with national and EU water quality standards. The soil sampling plan is designed to evaluate the extent and intensity of heavy metal accumulation in surface soils resulting from long-term mining activities, dust deposition, and contaminated runoff [2].

Given the legacy and intensity of ore extraction, flotation, and smelting operations in the Bor–Moldova Nouă region, soil pollution is a significant concern, particularly in agricultural zones and residential areas situated near tailings and waste rock facilities. Soil sampling points were selected based on key factors: dominant wind direction (downwind from major pollution sources), land use sensitivity (e.g., agricultural and urban green areas), surface runoff patterns (downhill from discharge sites), and proximity to populated areas to assess potential human exposure. Sampling is conducted quarterly, with the goal of tracking seasonal changes in surface soil properties and deposition dynamics [2]. At each location, a composite sample is collected from the topsoil layer (0–10 cm) by combining five sub-samples from within a 10 × 10-meter grid. This method reduces small-scale heterogeneity and ensures that results are representative of actual environmental conditions.

Each sampling location is georeferenced, photographed, and documented using a Soil Sample Record Sheet, which includes notes on land use, vegetation condition, color, texture, and presence of visible pollutants (e.g., slag fragments, discoloration, ash). Several control locations positioned in forested or agricultural areas distant from known emission sources are included to provide background values against which impacted zones can be assessed.

3. RESULTS

The implementation of the environmental sampling strategy across the Romania–Serbia border mining region provided key baseline data for assessing mining-related pollution. A total of 55 sampling sites were established: 37 for surface water, 14 for soil, and 4 for air quality monitoring.

Preliminary Preliminary findings indicate clear spatial patterns in pollutant distribution, with the highest concentrations of heavy metals expected in areas located directly downstream or downwind of active or legacy mining facilities. Windborne dust from tailings sites near Moldova Nouă and Bor has been identified as a major vector of transboundary pollution, while river systems such as the Krivelj and Bor are projected to retain elevated metal concentrations for several kilometers downstream from discharge points.

Despite existing regulatory differences between the two countries, the harmonized sampling protocol is expected to enable consistent and comparable data collection, facilitating a reliable assessment of environmental conditions on both sides of the border. This coordination is anticipated to play a key role in identifying pollution pathways and delineating zones of cumulative impact.

4. CONCLUSION

The cross-border environmental sampling strategy developed within the ERA-MIN_RO-SRB project provides a robust and scalable framework for monitoring mining-related pollution. Through the integration of surface water, soil, and air sampling—guided by geospatial and field analysis, the strategy ensures representative, reproducible, and policy-relevant data collection.

The results confirm the persistent influence of mining on environmental quality in the region, with measurable transboundary impacts via air and water pathways. Reference sites played a critical role in contextualizing contamination levels and distinguishing local pollution from background variability. This approach supports alignment with EU environmental directives and demonstrates the value of standardized, bilateral monitoring systems. It also offers a replicable model for other mining-impacted border regions.

Further work should focus on expanding air quality coverage, integrating biomonitoring, and establishing a shared digital platform for cross-border environmental data exchange.

Its successful implementation demonstrates how coordinated science-based frameworks can directly support environmental policy and cross-border resource management in Europe’s mining intensive regions.

ACKNOWLEDGEMENTS

This work was financially supported by the Ministry of Science, Technological Development and Innovation of the Republic of Serbia, Contract No. 451-03-136/2025-03/ 200052.

REFERENCES

[1] S. Raischi, E. Pană, E. Holban, Ș. Zamfir, M. Raischi, G. Deák, IJESD, 10 (6) (2019) 162-170.
[2] M.N. Filimon, R. Popescu, F.G. Horhat, O.S. Voia, Knowl. Manag. Aquat. Ecosyst. 417 (2016).

The 56th International October Conference on Mining and Metallurgy
22-25 October 2025, Bor Lake, Bor, Serbia
www.ioc.tfbor.bg.ac.rs

DOI: 10.5937/IOC25645K

Review paper

APPLICATION OF WASTE MATERIALS IN GREEN ROOFS

Danka Kostadinović[1a], Milić Erić[1b], Ivan Lazović[1c]

[1] Vinča Institute of Nuclear Sciences-National Institute of the Republic of Serbia, University of Belgrade, Mike Petrovića Alasa 12-14, 11000 Belgrade, Serbia
[1a] dankak@vin.bg.ac.rs, 0000-0003-2890-4979
[1b] milic@vin.bg.ac.rs, 0000-0001-6850-3112
[1c] lazovic@vin.bg.ac.rs, 0000-0002-3877-5157

Abstract

Green roofs are becoming increasingly popular as a sustainable architectural solution that provides numerous economic, environmental, and social benefits. Selecting a suitable substrate and drainage layers is important for having a sustainable green roof with good water retention and energy-saving potential, runoff water quality, and plant growth. There is a need to replace materials currently used in green roofs with more environmentally friendly products. Within such context, this paper discusses the application of different recycled and waste materials in green roofs and identifies what waste materials can be used in green roofs in Serbia. The use of locally available recycled materials can reduce the carbon footprint of green roofs, improve their life cycle, and reduce the cost of construction. This paper sheds light on the design of green roofs with better performance and reduced environmental impact.

***Keywords**: green roof, waste, recycling*

1. INTRODUCTION

In recent years, green roofs have gained more attention due to the numerous economic, environmental, and social benefits they can provide. They reduce energy consumption, air pollution, the urban heat island effect, stormwater runoff, etc. [1]. Green roofs are a part of green infrastructure especially important in densely built urban environments. Installing green roofs on existing buildings can significantly increase the percentage of green spaces in cities. Green roofs consist of the following common components from bottom to top (Figure 1): waterproof layer, root barrier, drainage layer, filter layer, growing substrate, and vegetation. The first layer of green roofs, which is installed directly on the roof structure, is the waterproofing layer, which protects the roof from water penetration. For existing roofs, bitumen, gravel, polyurethane coatings, or foils are mainly used. For new roof constructions, single-layer membranes, such as ethylene propylene diene monomer rubber or thermoplastic polyolefin, are used. Root barrier protects the waterproofing layer and roof structure from possible penetration of plant roots and fertilizers, as well as from mechanical damage that can occur during the installation of the green roof. For this layer polyethylene foil, rubber, or some other artificial material is used. The function of the drainage layer is to enable the drainage of excess water from the green roof.

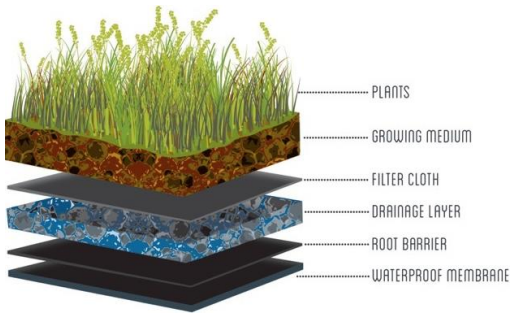

Figure 1. Green roof layers [2]

The drainage layer can be made of artificial material or in the form of a granular layer of expanded clay or gravel. The filter layer prevents the passage of the substrate components to the drainage layer. It is usually made from geotextile. The growing, substrate as the most important component of a green roof, should provide nutrients and water for plants. This layer consists of 80% natural or artificial mineral ingredients (stone, brick, perlite, clay) and 20% organic matter (pine bark and compost). The vegetation type depends on the climatic conditions, the roof slope and orientation, and the thickness and composition of the substrate. Construction waste encompasses all waste generated as a result of demolition, construction, and renovation activities in Europe, accounting for 25-30% of total generated waste [3]. The efforts of the European Union are focused on recycling 70% of construction waste. There is potential to achieve additional benefits by using recycled and waste materials in green roofs.

2. WASTE MATERIALS IN GREEN ROOFS

The use of recycled waste materials for drainage and substrate layers of green roofs can be the solution to reduce the overuse of natural materials. Porous stone materials such as expanded clay, pumice, or natural pozzolana are used for drainage layers in green roofs, whereas rubber crumbs from waste tires have recently been employed as a substitute [4]. Experimental results showed that rubber crumbs can be a good substitute for stone materials contributing to the reduction of waste and energy required for the transformation of stone materials. Green roof led to a 5% lower consumption of electrical energy when rubber crumbs were used, while a 14% reduction when pozzolana was used [5]. The polyethylene granules, from recycled agricultural plastic waste used for greenhouse covering, have physical properties comparable to those of perlite and, therefore, are suitable for the drainage layer in green roofs [6]. Compared to the perlite, granules have a lower specific weight while higher permeability thanks to larger particle size and to the cavities on the granule surface that allow water storage and evaporation, providing support to vegetation development. Foam glass and crushed porcelain are the most common recycled waste materials used in the substrate layer to improve green roof hydrological performance [7]. Crushed bricks in green roof substrates was found to have lower bulk density and higher porosity than crushed concrete, making them suitable for green roof substrates [8]. Medium-sized crushed brick particles (3-5 mm) exhibit the most significant potential for enhancing the functionality of green roof substrates and facilitating plant growth, while construction waste particles that are either too small or too large are unsuitable for use in green roof substrates.

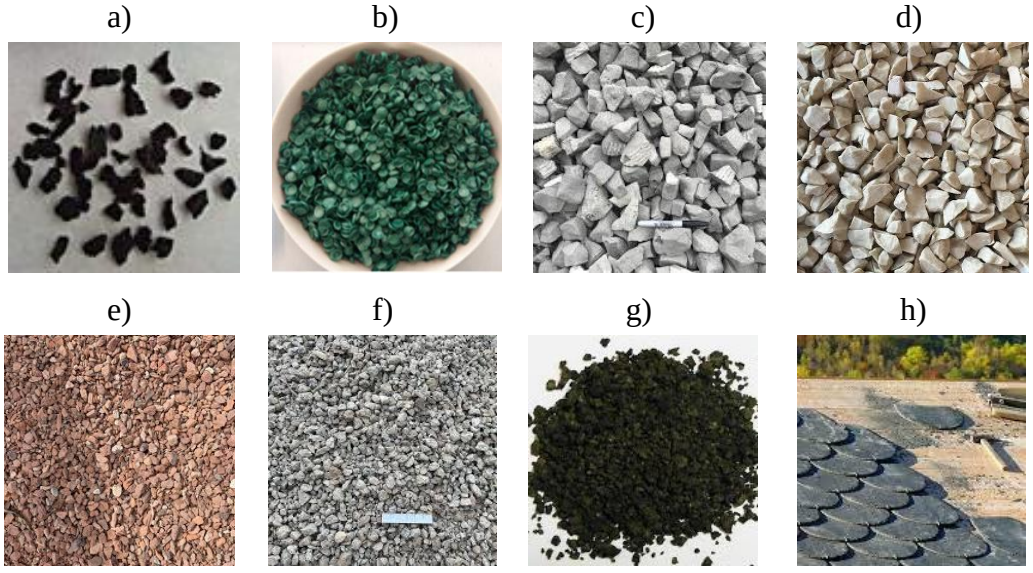

Figure 2. Waste materials used in green roofs: a) rubber crumbs, b) recycled polyethylene, c) foam glass, d) crushed porcelain, e) crushed brick, f) crushed concrete, g) cork granules, h) roof shingles

The study [9] presents a "Geogreen" modular system design with plants and substrate made from the mixture of two industrial wastes used as precursors, mine waste mud, milled glass, and expanded black cork granules. Roof shingles processed into aggregate form have a high conductivity value, which may result in good plant growth and reduce roof loads [10]. Experimental testing of green roof substrates made from waste clay from excavations, fly ash and sewage sludge, paper ash from recycled newspapers, and carbonated limestone from quarry fines had legal leachate limits for drinking water [11]. Moreover, the addition of organics reduced the pH of the recycled aggregates, making growing conditions for plants more favorable in these substrates. When it comes to LCA, recycled lightweight local materials used in green roofs instead of natural ones reduce environmental impacts, however, high energy is consumed for the tile, brick, or concrete crushing [12]. Coal bottom ash and fly-ash-based lightweight aggregates had good performance with minor environmental damage [13]. Non-recyclable sewage waste, such as used tampons, sanitary pads, and wet wipes compressed into panels can be used as a base for plant growth in green roofs. These lightweight products often contain absorbing polymers, which are bad for the environment, but can absorb a lot of water in green roofs [14].

3. WASTE IN SERBIA

Construction waste accounts for more than 75% of all waste in Serbia, while around 100 million tons of construction waste is generated in Serbia annually, according to the Serbian Association for Demolition, Decontamination, and Recycling [15]. 75% of construction waste is soil excavations while 12-25% is rubble, concrete, tiles and the rest are wood and metals. About 50% of the housing stock in the country is ready for a serious restructuring or removal, while more than 3 million of them are in the final phase of their life cycle [16]. Currently, less than 5% of construction waste is recycled in Serbia. The country aims to recycle 40% of this construction waste by 2030. Only 60% of the total amount of waste in Serbia is disposed of in a controlled way on the municipal sanitary landfill [17]. From April 2025, contractors are obliged to prepare a waste management plan and obtain approval for that plan from the competent authority as a prerequisite to the issuance of a construction permit, according to the new Rulebook on Arranging, Managing, Disposing and Landfilling Construction Waste [18]. This should reduce the number of illegal construction waste dumps. There is currently no practice of separate collection and scheme for recycling waste from construction and demolition in Serbia. Only high-value recyclable waste, such as metal, is recycled, while other recyclable materials are disposed of in landfills or at unsecured local dumpsites [3]. By the end of 2027, Serbia will build five construction waste processing plants in the Srem-Mačva regions, the city of Pirot, Subotica, Užice, and Valjevo. The gravel, worn-out wooden materials, or concrete will be turned into a new construction material in the processing facility. About 40 million tons of mining waste are produced each year which is regulated by the Law on Mining and Geological Explorations [18]. Power utility "Elektroprivreda Srbije" generates around 7 million tons of ash per year, where only 3% is used in the cement industry, while most is disposed of in ash and slag dumps [19].

4. CONCLUSION

This research investigates the innovative use of different waste and recycled materials in green roofs. The previous studies were mainly focused on the reuse of crushed brick, crushed concrete, porcelain, and foam glass in the substrate and drainage layers to improve the stormwater hydrological performance of green roofs. The reuse of waste material can provide potential benefits such as savings of resources and raw materials, reduction of material costs, transport, and machinery. This paper demonstrates how implementing circular principles in green roofs can contribute to resource conservation and environmental protection. The reduction of waste disposal to landfills and costs can be achieved by making it mandatory for green roofs to contain a certain percentage of waste materials. The use of recycled waste for more efficient green roofs can ensure more sustainable communities.

ACKNOWLEDGEMENTS

The research was funded by the Ministry of Science, Technological Development and Innovation of the Republic of Serbia (Grant No. 451-03-136/2025-03/200017).

REFERENCES

[1] C.N. Nguyen, N. Muttil, Muhammad A.U.R. Tariq, A.W.M. Ng, Water, 14 (1) (2022) 68.
[2] https://www.bernardowills.com/news/greenroof
[3] J. Radosavljević, A.Vukadinović, Facta Univ., Work. Living Environ. Prot., 21 (2) (2024) 133-141.
[4] A. Vila, G. Pérez, C. Solé, A. I. Fernández, L. F, Cabeza, Build. Environ., 48 (2012) 101-106.
[5] R. Lídia, C. Julià, P. Gabriel, C. Albert, B. Dieter, F. C. Luisa, Build. Environ., 74 (2014) 22-30.
[6] S. Cascone, Laboratory study on the use of recycled plastic granule from agricultural waste as drainage layer in green roofs, Colloqui.AT.e 2022. Memory and Innovation, September 2022, Genova, Italy
[7] E. Mert, D. Rowe, Urban For. Urban Green., 20 (4) (2016) 81-88.
[8] N. Jiang, W. Zou, Y. Lu, Z. Liao, L. Wu, Sustainability, 16 (1) (2024) 414.
[9] M. Manso, J. Castro-Gomes, B. Paulo, I. Bentes, C. A. Teixeira, Sci. Total Environ., 327 (2018) 1146-1153.
[10] T.B. Carson, R. Hakimdavar, K.J. Sjoblom, P.J. Culligan, GSP, 226 (225) (2012) 3644-3653.
[11] C. Molineux, C.H. Fentiman, A. C Gange, Ecol. Eng., 35 (10) 1507-1513
[12] D. Morau, N. R.Tsiorimalala, H.T. Rakotondramiarana, BJECC, 7 (1) (2017) 43-55.
[13] S. Pushkar, J. Clean. Prod. 227 (2019) 652-661.
[14] https://materialdistrict.com/article/green-roof-sewage-waste/
[15] https://www.mei.gov.rs/eng/news/2179/more/w/0/serbia-to-gain-five-construction-waste-processing-plants
[16] A. Radivojević, M. Nedić, S. Spasojević, Treatment of construction waste in Serbia and the life cycle of building, 2nd International Scientific Regional Conference-Development, Spatial Planning and Strategic Governance-RESPAG, May 22 - 25, 2013, Belgrade, Serbia.
[17] Pravilnik o uređivanju, upravljanju, odlaganju i deponovanju građevinskog otpada u toku izvođenja radova, Official Gazette of RS, no. 81/2024 ("C&D Waste Rulebook").
[18] Waste Management Program of the Republic of Serbia for the period 2022-2031, "Official Gazette of the RS", no 30/18.
[19] M. Vukićević, Z. Popović, J. Despotović, L. Lazarević, Transport, 33 (2) (2018) 389-398.

The 56th International October Conference on Mining and Metallurgy
22-25 October 2025, Bor Lake, Bor, Serbia
www.ioc.tfbor.bg.ac.rs

DOI: 10.5937/IOC25649M

Original scientific paper

USE OF AIRQ+ SOFTWARE IN ASSESSING THE IMPACT ON HEALTH FROM EXPOSURE TO AIRBORNE PARTICLES IN BOR, SERBIA

Branislava Matić Savićević[1a], Snežana Živković Perišić[1b], Srđan Mančević[1c]

[1]Institute of Public Health of Serbia „Dr Milan Jovanović Batut“, Belgrade, Serbia
[1a] damjanko98@yahoo.com; 0000-0001-8989-7499
[1b] snezana_zivkovic@batut.org.rs; 0000-0001-6435-1190
[1c] mancevicsrdjan@gmail.com; 0009-0005-8122-7593

Abstract

The World Health Organization (WHO) has developed and made available the AIR Q+ software tool to assess the health risks associated with exposure to pollutants. The average value of $PM_{2.5}$ (particulate matter) in Bor was calculated over a ten-year period (2014-2023), by year and as an average. Deaths from defined causes, which can be attributed, were calculated with the available data of the Statistical Office of the Republic of Serbia. The long-term effects of $PM_{2.5}$ were calculated to provide a good picture of the health consequences of air pollution. In analysis we used Estimated Attributable Proportion, Estimated Number of Attributable Cases and Estimated Number of Attributable Cases per 100,000 Population at Risk. In order to estimate the impact of air pollution on mortality from certain types of disease, the analysis also used trends in showing the estimated death rates per 100,000 people at risk of all causes of death, cardiovascular disease and respiratory diseases, lung cancer and chronic obstructive pulmonary disease (COPD) in adults, by years of follow-up and $PM_{2.5}$ values. Trend of increasing mortality rates is registered in the case of all causes of death and deaths due to cardiovascular diseases, and a decreasing trend is registered in the case of death from lung cancer and COPD.

The use of AIR Q+ has shown the huge impact of air pollution, i.e. $PM_{2.5}$, on the health of the population of Bor over a ten-year period.

***Key words**: AIR Q+, mortality, $PM_{2.5}$, Bor*

1. INTRODUCTION

Air pollution presents a significant environmental challenge that must be addressed at local, regional, and global levels. Despite substantial progress, it continues to pose threats to human health and the environment [1, 2]

Industrial facilities, motor vehicles, and household combustion devices are common sources of air pollution, emitting pollutants such as particulate matter, carbon monoxide, ozone, nitrogen dioxide, and sulphur dioxide. Particulate matter (PM) is a combination of solid and liquid particles present in the air, including “inhalable coarse particles” (PM_{10}) and “fine inhalable particles” ($PM_{2.5}$). $PM_{2.5}$ with a diameter of 2.5 micrometers or less is a significant component of ambient air pollution and poses the greatest risk to health as it can penetrate deep into the lungs and even enter the bloodstream, leading to serious health problems. Long-term exposure to fine particulate matter, or $PM_{2.5}$, is associated with a significant burden of disease including ischemic heart disease (IHD), lung cancer (LC), chronic obstructive pulmonary disease (COPD), acute lower respiratory infection (ALRI), stroke and adverse birth outcomes. This long-term exposure has been linked to increased morbidity and mortality, particularly in people with chronic heart or lung diseases, and reduced lung function growth in children [3,4,5].

In 2013, the International Agency for Research on Cancer(IARC) categorized particulate matter in Group 1 (carcinogen group), both of ambient and indoor air [6]. Adverse health effects of $PM_{2.5}$

may be different, as the main sources, area characteristics, and PMs' chemical specificity are not the same [7]. Some toxicological and epidemiological studies have concluded that PM can cause oxidative stress and inflammation on the human respiratory system [8, 9].

One of the largest copper mines, as well as the copper smelter in Europe, is located in the Town of Bor. Mining production started in 1903 with exploitation of the only underground mine, followed by exploitation of three other open pits in the Bor area (Bor, V.Krivelj and Cerovo). Fugitive emissions from the open pits, ore waste heaps, flotation waste heaps, and copper smelter, together with the emissions from point sources in the copper smelter are the main sources of PM in the Town of Bor (see Fig. 1)[10].

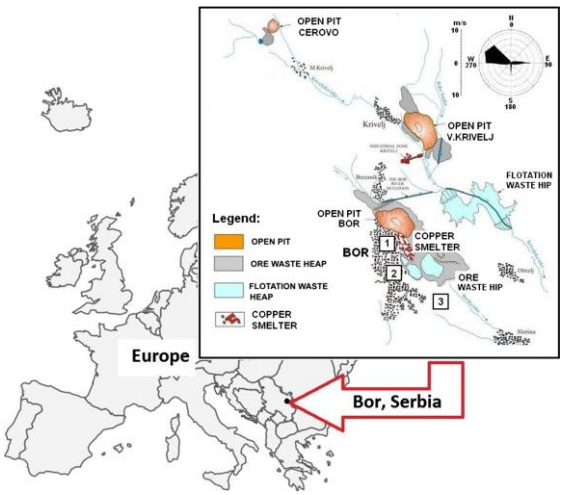

Figure 1 Location of Mining and Smelter Complex Bor with sampling points marked (1 – Park, 2 – Institute, 3 – Jugopetrol)[10]

Concerning the longevity of the established industrial site and the intensity of mining and smelting activity, the town of Bor, over time has acquired the attributes of an *industrially contaminated site*, baring all the public health risks for its population chronically exposed to pollution of all environmental media. The term „contaminated site" can have different meanings. A general definition, following the public health perspective, is "areas hosting or having hosted human activities which have produced or might produce environmental contamination of soil, surface or groundwater, air, and food chain, resulting or being able to result in human health impacts" [11,12].

2. EXPERIMENTAL

Assessments of the impact of air pollution on health were calculated using AirQ+ version 2.2 software tool of the WHO European Region, freely downloadable on-line [13]. This tool allows researchers to assess the burden of both ambient and household (indoor) air pollution. Ambient air pollution assessments are based on the WHO recommendations [14].

Data for the ambient air PM_{10} concentrations in Bor for the period 2014–2023 derived from the data base of Serbian Environment Protection Agency (SEPA), collated from the State Network of Automatic Measuring Stations (AMS) [15]. For the locations where $PM_{2.5}$ is not measured, with existing PM_{10} AMS, WHO developed Country specific conversion factors which were estimated as the mean ratio of $PM_{2.5}$ to PM_{10} of stations for the same year [16]. The conversion factor for Serbia, as given by the AirQ+ is 0.67. The average value of $PM_{2.5}$ in Bor was calculated over a ten-year period (2014–2023), by year and as an average. The average annual $PM_{2.5}$ value was used as a summary indicator for assessing the impact of air pollution on health [17]. Deaths from defined causes, which can be attributed, were calculated with the available data of the Statistical Office of the Republic of Serbia for the period under observation [18].

The long-term effects of $PM_{2.5}$ were calculated to provide a good picture of the health consequences of air pollution. Estimates are based on the assumption that there is a 6% change in deaths from all causes for every 10 $\mu g/m^3$ change in average $PM_{2.5}$ concentrations. Estimates of mortality from all causes of death, cardiovascular disease, and respiratory illness attributable to exposure to particulate matter air pollution are based on the number of deaths in adults aged 30 years or older. Also, in the analysis, estimates of mortality from lung cancer in adults and from COPD in adults over 25 years of age were made; the number of inhabitants used in the analysis is people of a certain age, the so-called population at risk, in the period from 2014 to 2023. Estimated Attributable Proportion (Proportion or Percentage of All Cases Attributable to a Particular Exposure), Estimated Number of Attributable Cases (Estimated Number of Cases Attributable to a Particular Exposure), and Estimated Number of Attributable Cases per 100,000 Population at Risk (Estimated rate of illness or death per 100,000 people at risk, attributable to specific exposure). The analysis also used a linear trend expressed through the estimated death rates per 100,000 people at risk of all-cause death, cardiovascular disease and respiratory disease, lung cancer, and COPD in adults [16, 19].

3. RESULTS AND DISCUSSION

During the analysis, common but specific parameters were used for evaluation, such as: type of analysis, type of pollutant, location, total population, years of observation, size of the area, latitude and longitude. In estimating deaths from defined causes, the percentage of all cases attributable to a particular exposure, the estimated number of cases attributable to a particular exposure, and the estimated death rate per 100,000 people at risk attributable to a particular exposure were used.

The percentage of deaths from all causes of death attributable to exposure to air pollution is based on the number of deaths in adults aged 30 years and older. The average percentage of mortality from all causes of death attributable to exposure to air pollution registered in Bor was 13.4% with an average $PM_{2.5}$ value of 23.66 $\mu g/m^3$, while the average estimated number of deaths from all causes of death in Bor, attributable to exposure to air pollution in the observed period (2014-2023) was 32 persons of both sexes aged 30+ years. and the average mortality rate was 103.3 per 100,000 for both sexes aged 30+ years.

In the case of the percentage of mortality from cardiovascular diseases attributable to exposure to air pollution in adults aged 30 years, the average registered percentage was 17.7%, and the average estimated number of deaths from cardiovascular disease attributable to exposure to air pollution in the observed period was 20 people of both sexes aged 30+ years, and the average mortality rate was 63.9 per 100,000 for both sexes aged 30+ years.

Analyzing the percentage of mortality from respiratory diseases attributable to exposure to air pollution in adults aged 30 years or older, an average value of 16.3% was registered. The average estimated number of deaths from respiratory diseases in Bor attributable to exposure to air pollution was 2 people of both sexes aged 30+ years, and the average mortality rate was 7.7 per 100,000 for both sexes aged 30+ years.

As in the case of, all-cause mortality, cardiovascular disease, and respiratory disease, the average mortality rate from lung cancer attributable to exposure to air pollution in adults was 16.8%. The average estimated number of lung cancer deaths attributable to exposure to air pollution was 2 people of both sexes, and the average mortality rate was 5.04 per 100,000 for both sexes.

In analyzing the percentage of mortality from chronic obstructive pulmonary disease attributable to exposure to air pollution, which is based on the number of deaths in adults aged 25 years and older, for calculation it was used GBD 2020 (integrated function 2019).

The percentage of mortality from COPD attributable to exposure to air pollution was 16.4% at an average $PM_{2.5}$ value of 23.66 $\mu g/m^3$. The average estimated number of deaths from COPD

attributable to exposure to air pollution in this period (2014-2023) was 1 person of both sexes of all ages, and the average mortality rate was 2.95 per 100,000 for both sexes.

Also, in order to estimate the impact of air pollution on mortality from certain types of disease, the analysis also used linear trends in showing the estimated death rates per 100,000 people at risk of all causes of death, cardiovascular disease and respiratory diseases, lung cancer and COPD in adults, by years of follow-up and $PM_{2.5}$ values (Figure 2). A trend of increasing mortality rates was registered in the case of all causes of death and death due to cardiovascular disease, and a decreasing trend is registered in the case of death from lung cancer, respiratory diseases and COPD (Figure 3).

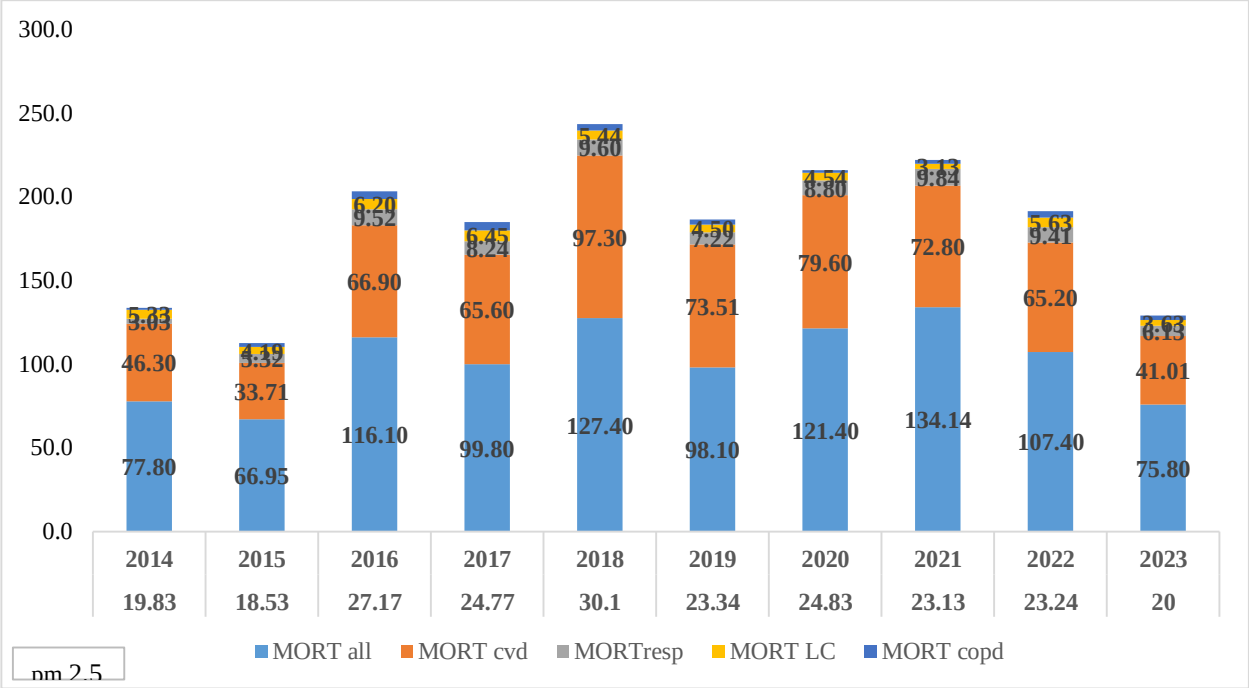

Figure 2 Estimated death rates per 100,000 people at risk of all causes of death, cardiovascular disease and respiratory diseases, lung cancer and COPD in adults, by years of follow-up and $PM_{2.5}$ values

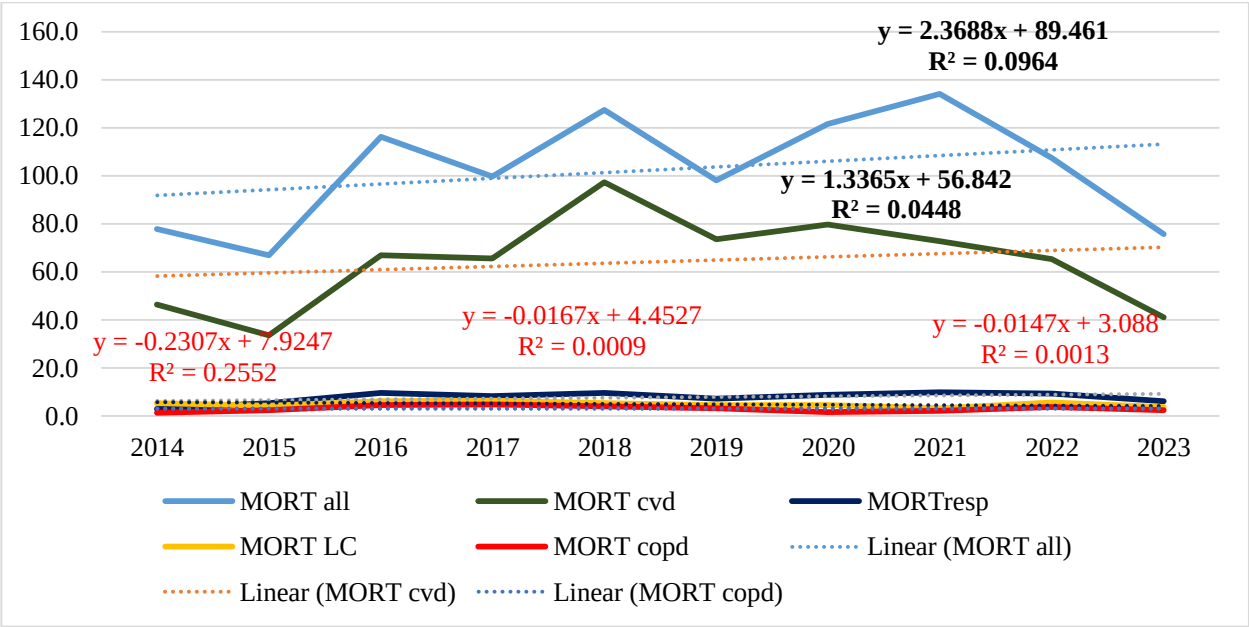

Figure 3 Trend in estimated death rates per 100,000 of all causes of death, cardiovascular disease and respiratory diseases, lung cancer and COPD by years of follow-up

The impact of air pollution on the health of the inhabitants of Bor was observed in the ten-year period from 2014 to 2023. This period is long enough to conclude on the increase or decrease in mortality from certain defined diseases and/or conditions, but certainly the COVID-19 pandemic had a great impact, especially in the period from March 2020 to the end of 2021. This is also shown in our analysis, especially when it comes to estimated mortality rates from all causes of death.

The average value of $PM_{2.5}$ particles in Bor for the observed period was 23.66 $\mu g/m^3$. Compared to the average values over 6 years out of 10, the registered values were lower than average (the lowest value was registered in 2015 and amounted to 18.53 $\mu g/m^3$). In contrast to the average, the highest values, almost 20% more, were registered in 2016 and 2018 (27.17 and 30.1 $\mu g/m^3$). In 2018, the estimated mortality rates from all causes of death, cardiovascular disease, respiratory disease, lung cancer and COPD were higher by 18.9, 34.3, 20.2, 7.4 and 24.4% compared to the average estimated rates for these defined diseases.

There are some limitations in this analysis, primarily related to the numbers obtained in the analysis which must be considered as estimates and should be used carefully. There is no threshold observed in mortality studies below which adverse health effects would not be detected, and estimates using only PM should be considered conservative, that is, they underestimate the impacts. It is important to note once again that estimates of mortality attributable to exposure to air pollution are based on the number of deaths in adults aged 30 years or older. This means underestimating the real burden and cost of air pollution, even if few deaths are expected among those under 30. Estimates of the attributed deaths were obtained by summarizing data over a ten-year period in Bor and at one measuring point. On the other hand, estimates of the impact of air pollution on health have been calculated using AirQ+ software produced by WHO European Region and available online free for download. AirQ+ allows to assess the burden of ambient air pollution as well as household air pollution and estimates for ambient air pollution are based on WHO recommendations [14].

CONCLUSION

The findings suggest that in Bor, long-term exposure to $PM_{2.5}$ had a noteworthy impact on public health, leading to a significant number of mortality cases. It is, thus, of utmost importance to reduce ambient air $PM_{2.5}$ levels in order to ultimately reduce the adverse effects on public health in the broader area of this industrially contaminated site. AirQ+ can be utilized in understanding the specific outcomes associated to ambient air pollution exposure and the extent of its impact. Together with the policy-makers and public health authorities targeted interventions could be planned and developed in order to reduce air pollution levels downsizing it to the level that could no longer present a public health threat to the potentially exposed population.

REFERENCES

[1] US EPA. Air Pollution: Current and Future Challenges (2016). https://www.epa.gov/clean-air-act-overview/air-pollution-current-and-future-challenges
[2] J. Rovira, J. L. Domingo, M. Schuhmacher, Sci. Total Environ. 703 (2020) 135538.
[3] I. Manisalidis, E. Stavropoulou, A. Stavropoulos, E. Bezirtzoglou, Front. Public. Health 8 (2020) 14.
[4] F. Wang, X. Qiu, J. Cao, L. Peng, N. Zhang, Y. Yan, R. Li, Sci. Total Environ. 757 (2021) 143775.
[5] A. Ghorani-Azam, B. Riahi-Zanjani, M. Balali-Mood, J. Res. Med. Sci. 21 (2016)
[6] D. Loomis, Y. Grosse, B. Lauby-Secretan, F. El Ghissassi,Bouvard, L. Benbrahim-Tallaa, N. Guha, R. Baan, H. Mattock, K. Straif, Lancet Oncol. 14(13) (2013) 1262-3.
[7] F. Cavalli, A. Alastuey, H. Areskoug, D. Ceburnis, J. Čech, J. Genberg, R.M. Harrison, J.L. Jaffrezo, G. Kiss, P. Laj, N. Mihalopoulos, N. Perez, P. Quincey, J. Schwarz, K. Sellegri, G. Spindler, E. Swietlicki, C. Theodosi, K.E. Yttri, W. Aas, P. Putaud, Atmos Environ. 144 (2016) 133-45.
[8] I. Kloog, B. Ridgway, P. Koutrakis, B.A. Coull, J.D. Schwartz, Epidemiology, 24(4) (2013) 555-61.
[9] Y.F. Xing, Y.H. Xu, M.H. Shi, Y.X. Lian. J. Thorac. Dis. 8(1) (2016) E69-74.

[10] V. Tasić, R. Kovačević, B. Maluckov, T. Apostolovski-Trujić, B. Matić, M. Cocić, M. Šteharnik, Water Air Soil Pollut. 228(230) (2017).
[11] World Health Organization (WHO), Contaminated Sites and Health. Report of Two WHO Workshops: Syracuse, Italy, 18 November 2011; Catania, Italy, WHO Regional Office for Europe, Copenhagen, Denmark, 21-22 June 2012. Available at: http://www.euro.who.int/__data/assets/pdf_file/0003/186240/e96843e.pdf?ua=1
[12] B. Matić, U. Rakić, S. Dejanović, V. Jovanović, M. Jevtić, N. Đonović, Tehnika – Kvalitet IMS, Standardizacija i Metrologija, 17 (2017) 441-447.
[13] World Health Organization Regional Office for Europe: AirQ+: software tool for health risk assessment of air pollution, Copenhagen, 2020. WHO/EURO 2020-1557-41308-56210. https://www.who.int/europe/tools-and-toolkits/airq---software-tool-for-health-risk-assessment-of-air-pollution
[14] World Health Organization Regional Office for Europe: WHO global air quality guidelines. Particulate matter (PM2.5 and PM10), ozone, nitrogen dioxide, sulphur dioxide and carbon monoxide. Copenhagen, 2021 ISBN 978-92-4-003422-8 (electronic version), https://iris.who.int/bitstream/handle/10665/345329/9789240034228-eng.pdf?sequence=1
[15] Republic of Serbia. Ministry of Environmental Protection.Serbian Environmental Protection Agency. Belgrade: 2025 (https://sepa.gov.rs/)
[16] Health risk assessment of air pollution – general principles. Copenhagen: WHO Regional Office for Europe; 2016. ISBN 978 92 890 51316 https://www.who.int/europe/publications/i/item/9789289051316
[17] World Health Organization: Ambient (outdoor) air pollution, (website), 2024. https://www.who.int/news-room/fact-sheets/detail/ambient-(outdoor)-air-quality-and-health
[18] Statistical Office of the Republic of Serbia; Belgrade: 2025 [website]. unpublished data (http://www.stat.gov.rs/en-us).
[19] Health impact assessment of air pollution: introductory manual to AirQ+. Copenhagen: WHO Regional Office for Europe; 2020. Licence: CC BY-NC-SA 3.0 IGO. https://iris.who.int/bitstream/handle/10665/337681/WHO-EURO-2020-1557-41308-56210-eng.pdf?sequence=1
[20] D.G. Altman, Practical Statistics for Medical Research. London: Chapman and Hall. pp. 212–220. 1991. ISBN 041227630-5. https://lib.zu.edu.pk/ebookdata/Public%20Health/Practical%20statistics%20for%20medical%20research-by%20Altman%20D.G.pdf

The 56th International October Conference on Mining and Metallurgy
22-25 October 2025, Bor Lake, Bor, Serbia
www.ioc.tfbor.bg.ac.rs

DOI: 10.5937/IOC25655K *Original scientific paper*

ASSESSMENT OF ELEMENT ACCUMULATION EFFICIENCY IN PLANT PARTS USING BIOLOGICAL FACTOR ANALYSIS

Jelena Kalinović[1a], Tanja Kalinović[1b], Ana Radojević[1c], Snežana Šerbula[1d], Jelena Jordanović[1e]

[1] Technical Faculty in Bor, University of Belgrade, V.J. 12, 19210 Bor, Serbia
[1a] jkalinovic@tfbor.bg.ac.rs, 0000-0003-0088-2683
[1b] tkalinovic@tfbor.bg.ac.rs, 0000-0003-0161-0065
[1c] aradojevic@tfbor.bg.ac.rs, 0000-0003-3138-154X
[1d] ssherbula@tfbor.bg.ac.rs, 0000-0001-7560-4130
[1e] jjordanovic@tfbor.bg.ac.rs, 0000-0002-8145-640X

Abstract
Understanding the processes of accumulation and translocation of potentially toxic elements through the soil-plant system is crucial for environmental protection and pollution risk assessment. The aim of this study is to investigate the possibility of accumulation and translocation of potentially toxic elements in Crataegus spp. and to assess the applicability of this plant species in phytoremediation.

***Keywords**: Crataegus spp., Biological factor analysis, potentially toxic elements*

1. INTRODUCTION

Potentially toxic elements in the environment can originate from natural sources, such as volcanic activities, weathering of metal-rich rocks, erosion and other geological processes, as well as from human activities, such as industrial processes, urban wastewaters, agriculture, etc. [1]. Mining represents a significant source of environmental pollution. Once toxic elements enter the soil, they can be accumulated by crops, including vegetables and other plants. The uptake of potentially toxic elements by plants from the soil is an important pathway by which toxic elements can enter the food chain. Understanding the translocation and accumulation of elements in soils and plants is of great importance for environmental protection [2]. Phytoremediation is an environmentally friendly strategy to improve contaminated areas [3].

This study aims to evaluate the possibility of accumulation and translocation of potentially toxic elements in different parts of *Crataegus* spp. and its potential for use in phytoremediation.

2. EXPERIMENTAL

Crataegus spp., a widespread perennial deciduous shrub, was selected for investigation. The plant material (roots and leaves) and the soil from the root zone were sampled during the plant's harvest period, before natural leaf fall (September to mid-October). The sampled plants were healthy with no visible signs of disease or pests. The total of 14 sampling sites were distributed into eight sampling zones (urban-industrial (UI), urban (U), suburban (SU), industrial (I1, I2, I3, I4 and I5), rural (R1 and R2), tourist (T), traffic (TR) and background (B)). The locations of the sampling sites were selected in relation to the copper smelter, open pits, ore waste heaps, and the flotation tailing ponds. The B zone was located in the rural settlement of Gornjane, 17 km from the copper smelter, which was not affected by anthropogenic pollution [4,5]. A detailed description of the sampling procedure and the sampling sites can be found in Kalinović *et al*. [5].

Biological factor analysis is used to assess the ability of plants to accumulate potentially toxic elements from the soil and translocate them through the plant. Biological factor analysis is crucial in revealing the remarkable capabilities of plants, such as their potential for environmental

remediation. The bioconcentration factor (BCF) provides information about a plant's ability to accumulate elements from the soil in the roots. The factor is calculated using equation (1) [1,6,7]:

$$BCF=C_r/C_s \quad (1)$$

where C_r is the element concentration in the plant root (mg/kg); C_s is the element concentration in the soil (mg/kg). If the BCF value is greater than 1, the accumulation of elements in the plant roots is effective [1,6,7].

The translocation factor (TF) indicates the ability of plants to transport elements from the roots to the leaves (i.e. to allow them to enter the food chain). The factor is calculated according to the following equation (2) [1,6,7]:

$$TF = C_{wl}/C_r \quad (2)$$

where C_{wl} is the element concentration in the washed leaves (mg/kg); C_r is the element concentration in the plant root (mg/kg). If the TF value is greater than 1, the elements are effectively translocated within the plant [1,6,7].

The biological absorption coefficient (BAC) is calculated by the equation (3) [8,9]:

$$BAC = C_{wl}/C_s \quad (3)$$

where C_{wl} is the element concentration in the washed leaves (mg/kg); C_s is the element concentration in the soil (mg/kg).

Depending on the BAC values, the absorption of elements in leaves from the soil can be intensive (BAC in the range of 10–100), strong (1.0–10.0), intermediate (0.1–1.0), weak (0.01–0.10), and very weak absorption (0.001– 0.010) [10]. According to Nouri *et al*. [11], plants suitable for phytoextraction generally have the values of BCF>1 and TF>1, whereas, plants suitable for phytostabilisation have BCF>1 and TF<1.

3. RESULTS AND DISCUSSION

The BCFs for As, Cd, Cu and Pb are shown in Table 1.

Table 1. Bioconcentration factor (BCF) for As, Cd, Cu and Pb

Site	As	Cd	Cu	Pb
UI	<0.006	<0.054	0.004	<0.008
U	<0.010	<0.085	0.006	<0.011
SU	<0.014	<0.103	0.007	<0.010
I1	<0.050	<0.435	0.032	<0.030
I2	<0.024	<0,299	0.099	0.039
I3	<0.057	<0.108	0.012	<0.015
I4	<0.025	<0.255	0.007	<0.025
I5	<0.029	<0.192	0.010	<0.027
R1	<0.012	0.730	0.043	<0.026
R2	0.011	0.413	0.040	0.026
T1	<0.008	<0.048	0.005	<0.012
T2	<0.007	0.267	0.049	0.055
TR	<0.086	<0.209	0.012	<0.016
B	<0.103	/	0.079	<0.053

The BCF values with the sign "<" are obtained by replacing the missing element concentration by the limit of determination of the element in the root (the LD for As and Pb is 1 mg/kg; for Cd 0.2 mg/kg); "/" Both values are missing in the calculation of the BCF.

The BCF values for all the analysed elements were below 1 at each sampling site (except at site B for Cd), indicating that *Crateaegus* spp. have a low ability to accumulate these elements in the roots from the soil.

Regardless of this, a significant correlation between the Cu concentrations in the soil and root samples (Table 2) indicates a possible accumulation of a certain amount of Cu from the soil. It was not possible to calculate the correlation for the other elements, as their concentrations were below the limit of determination for most samples.

Table 2. Spearman correlation coefficient

Element	Soil–Root	Root–Washed leaves	Soil–Washed leaves
As	/	/	0.727*
Cd	/	/	/
Cu	0.582*	0.820**	0.749**
Pb	/	/	0.429

** Correlation is significant at the 0.01 level (2-tailed); * Correlation is significant at the 0.05 level (2-tailed);
"/" The correlation coefficient was not calculated for the elements for which the number of samples is ≤5.

The TFs for As, Cd, Cu and Pb are shown in Table 3. According to the obtained values, the TFs for the analysed elements were higher than 1 in most cases (except at the sites R1, R2 and T2 for Cd and at the site T2 for Cu). These high TF values indicate that *Crataegus* spp. effectively translocated the elements from the roots to the leaves. The significant and positive correlation between the Cu concentrations in the roots and the washed leaves is in favour of an effective translocation. However, it was not possible to calculate the correlations for the other elements as their concentrations were below the limit of determination for most samples.

Table 3. Translocation factor (TF) for As, Cd, Cu and Pb

Site	As	Cd	Cu	Pb
UI	**>29.977**	**>2.596**	**9.225**	**>28.383**
U	**>2.463**	/	**3.588**	**>5.443**
SU	**>1.524**	/	**4.272**	**>3.902**
I1	**>1.474**	/	**5.279**	**>2.222**
I2	**>1.427**	/	**1.223**	**2.325**
I3	/	/	**3.286**	**>2.224**
I4	**>1.829**	/	**5.885**	**>4.712**
I5	**>2.027**	/	**4.813**	**>4.618**
R1	**>4.868**	0.761	**2.282**	**>10.325**
R2	**6.195**	0.694	**3.128**	**18.255**
T1	**>1.705**	/	**6.583**	**>8.549**
T2	**>2.628**	<0.713	0.768	**1.522**
TR	/	/	**1.152**	**>1.775**
B	/	/	**2.143**	**>1.198**

The values given in bold represent TF>1; The TF values with the sign ">" are obtained by replacing the missing element concentration by the limit of determination of the element in the root (the LD for As and Pb is 1 mg/kg; for Cd 0.2 mg/kg); "/" Both values are missing in the calculation of TF.

The BAC values for As, Cd, Cu and Pb are shown in Table 4. The determined values show a weak to intermediate absorption of the analysed elements from the soil into the leaves. A certain amount of the elements can also be absorbed from the air via the leaves. However, the significant and positive correlations between the elements in the soil and the washed leaves (except for Cd) shown in Table 2 confirm that *Crataegus* spp. absorb elements from the soil into the leaves via the roots to a certain extent. According to Baker's classification [12], *Crataegus* spp. could be categorised as an excluder due to the BAC values for As, Cd, Cu and Pb, which were below 1. Based on the values obtained for BAC and TF, it could be said that *Crataegus* spp. is unsuitable for phytoextraction or phytostabilisation of the studied elements. However, it is the plant that has adapted to the environment with different levels of pollution.

Table 4. Bioaccumulation factor (BAC) for As, Cd, Cu and Pb

Site	As	Cd	Cu	Pb
UI	0.182	0.140	0.041	0.237
U	0.025	<0.085	0.022	0.063
SU	0.023	<0.103	0.030	0.041
I1	0.075	<0.435	0.170	0.068
I2	0.036	<0.299	0.121	0.090
I3	<0.057	<0.108	0.041	0.035
I4	0.046	<0.255	0.042	0.121
I5	0.059	<0.192	0.049	0.125
R1	0.062	0.555	0.098	0.273
R2	0.067	0.286	0.125	0.472
T1	0.015	<0.048	0.033	0.107
T2	0.021	<0.191	0.038	0.084
TR	<0.086	<0.209	0.014	0.029
B	<0.103	/	0.170	0.064

The BAC values with the sign "<" are obtained by replacing the missing element concentration with the limit of determination of the element in the washed leaves (the LD for As is 1 mg/kg; for Cd 0.2 mg/kg); "/" Both values are missing in the calculation of BAC.

4. CONCLUSIONS

In this study, the accumulation and translocation of potentially toxic elements in *Crataegus* spp. were analysed. The results showed that this plant species has a low ability to accumulate As, Cd, Cu and Pb from the soil into the roots. In addition, *Crataegus* spp. has a limited potential for the translocation of these elements to the aboveground parts of the plant. Therefore, *Crataegus* spp. is not considered suitable for phytoextraction or phytostabilisation purposes.

ACKNOWLEDGEMENTS

The authors are grateful to the Ministry of Education, Technological development, and Innovations of the Republic of Serbia for financial support, within the funding of the scientific research at the University of Belgrade, Technical Faculty in Bor (No. 451-03-137/2025-03/ 200131).

REFERENCES

[1] A. Cakaj, K. Drzewiecka, A. Hanć, M. Lisiak-Zielińska, L. Ciszewska, M. Drapikowska, Environ. Res., 256 (2024) 119222.
[2] Z.J. Shen, D.C. Xu, Y.S. Chen, Z. Zhang, Ecotoxicol. Environ. Saf., 143 (2017) 19-27.
[3] X. Yan, J. An, Y. Yin, C. Gao, B. Wang, S. Wei, Sci. Total Environ., 803 (2022) 149871.
[4] J.V. Kalinovic, S.M. Serbula, A.A. Radojevic, J.S. Milosavljevic, T.S. Kalinovic, M.M. Steharnik, Environ. Monit. Assess., (2019) 191:15.
[5] J.V. Kalinović, S.M. Šerbula, T.S. Kalinović, A.A. Radojević, J.S. Jordanović, Hem. Ind., 78 (3) (2024) 265-279.
[6] Y. Du, Z. Tian, Y. Zhao, X.Wang, Z. Ma, C. Yu, J. Environ. Manage., 351 (2024) 119838.
[7] M. Haseeb, S. Iqbal, M. B. Hafeez, H. Baloch, N. Zahra, M. Mumtaz, G. Ahmad, E. M. Fatima, Jahanzaib, S. Raza, A. Raza, M. S. Saddiq, J. Agr. Food Res. 14 (2023) 100741.
[8] S. Bravo, J. A. Amorós, C. Pérez-de-los-Reyes, F. J. García, M. M. Moreno, M. Sánchez-Ormeño, P. Higueras, J. Geochem. Explor., 174 (2017) 79-83.
[9] Kabata-Pendias, A. Trace Elements in Soils and Plants, CRC Press, Boca Raton, (2011).
[10] P.J.C. Favas, J. Pratas, M.N.V. Prasad, Int. J. Environ. Sci. Technol., 10 (2013) 809-826.
[11] J. Nouri, B. Lorestani, N. Yousefi, N. Khorasani, A. H. Hasani, F. Seif, M. Cheraghi, Environ. Earth Sci., 62 (2011) 639-644.
[12] A.J.M. Baker, J. Plant Nutr., 3 (1-4) (1981) 643-654.

The 56th International October Conference on Mining and Metallurgy
22-25 October 2025, Bor Lake, Bor, Serbia
www.ioc.tfbor.bg.ac.rs

DOI: 10.5937/IOC25659G

Original scientific paper

EQUILIBRIUM AND THERMODYNAMIC ANALYSIS OF THE ADSORPTION OF COPPER IONS ON SUNFLOWER HULLS

Milan Gorgievski[1a], Marina Marković[1b], Miljan Marković[1c], Vesna Grekulović[1d], Nada Štrbac[1e], Kristina Božinović[1f], Milica Zdravković[1g]

[1] Technical Faculty Bor, University of Belgrade, V.J. 12, 19210 Bor, Serbia
[1a] mgorgievski@tfbor.bg.ac.rs, 0000-0002-9899-719X
[1b] marina.markovic@tfbor.bg.ac.rs, 0009-0007-7553-6423
[1c] mmarkovic@tfbor.bg.ac.rs, 0000-0002-4734-1481
[1d] vgrekulovic@tfbor.bg.ac.rs, 0000-0001-6871-4016
[1e] nstrbac@tfbor.bg.ac.rs, 0000-0003-4836-1350
[1f] kbozinovic@tfbor.bg.ac.rs, 0000-0002-9834-448X
[1g] mzdravkovic@tfbor.bg.ac.rs, 0000-0001-9488-9151

Abstract
This paper presents the equilibrium and thermodynamic study of the adsorption of copper ions on sunflower hulls. The results of the equilibrium analyses showed that Temkin's isothermal model was the best fit the analysed data. The calculated thermodynamic data showed that the sorption reaction is not spontaneous at the given temperatures, that the process is endothermic and that there is a reduced randomness at the solid-solution interface.

***Keywords**: copper ions, sunflower hulls, isotherms, thermodynamic*

1. INTRODUCTION

The contamination of water bodies with heavy metals, mainly from the metallurgical and mining industries and battery production, has become a serious problem. Due to their toxicity, heavy metals in wastewater threaten global ecosystems and global health. However, they are also valuable resources that should be recycled. For this reason, but above all for environmental reasons, the development of highly efficient methods for the treatment of industrial wastewater contaminated with heavy metals is very important [1, 2].

One of the most promising methods for treating industrial wastewater with low concentrations of metal ions is adsorption using natural adsorbents, known as “biosorption”. This process has several advantages over conventional technologies, such as the use of inexpensive and sustainable materials, the metabolic independence of the process, the effective utilization of waste materials and the high removal efficiency even at low heavy metal concentrations [3].

2. EXPERIMENTAL

The sunflower hulls were first ground and sieved on a set of laboratory sieves, and the fraction -1+0.4 mm was used for the adsorption experiments. Before the adsorption experiments, the sunflower hulls were rinsed with distilled water. Stock solutions of Cu^{2+} ions were prepared with $CuSO_4 \cdot 5H_2O$ from LACHEMA (Czech Republic).

3. RESULTS AND DISCUSSION

3.1 Adsorption isotherms

Adsorption isotherms represent the amount of adsorbed material as a function of the equilibrium concentration after adsorption at a constant temperature [4].

Langmuir isotherm model

Langmuir isotherm model assumes monolayer adsorption on a homogeneous surface. It also assumes that there are no interactions between the adsorbed molecules [5]. In non-linear form, the Langmuir adsorption isotherm model can be expressed as follows [6]:

$$q_e = q_m K_L \frac{C_e}{1 + K_L C_e} \tag{1}$$

where: C_e is the equilibrium concentration of metal ions in the solution (mg dm^{-3}); q_e is the equilibrium adsorption capacity, defined as the mass of metal ions per unit mass of adsorbent when the system is at equilibrium (mg g^{-1}); q_m (mg g^{-1}) and K_L (dm^3 mg^{-1}) are constants related to the adsorption capacity and the energy or net enthalpy of adsorption.

Freundlich isotherm model

Freundlich isotherm model is based on the assumption that the surface energy of the adsorbent is heterogeneous and that the stronger binding sites are occupied first. It is also assumed that the binding strength decreases as the degree of site occupation increases [7]. This model can be expressed by the following equation [8]:

$$q_e = K_F C_e^{1/n} \tag{2}$$

where: C_e is the equilibrium concentration of metal ions (mg dm^{-3}); q_e is the equilibrium adsorption capacity (mg g^{-1}); K_F is the Freundlich equilibrium constant (dm^3 g^{-1}). 1/n is the heterogeneity factor and n is a measure of the deviation from linearity of adsorption.

Temkin isotherm model

Temkin isotherm model takes into account the interaction of adsorbent and adsorbate and is based on the assumption that the free adsorption energy is a function of the surface coverage, i.e. that the adsorption energy of the molecules decreases linearly with the degree of surface coverage [9].

The Temkin isotherm is represented by the following equation [10]:

$$q_e = \frac{RT}{b} \ln\left(K_T C_e\right) = B \ln\left(K_T C_e\right) \tag{3}$$

where: T is the absolute temperature (K); R is the universal gas constant (8.314 J mol^{-1} K^{-1}); K_T is the equilibrium binding constant (dm^3 mg^{-1}); b is the change in adsorption energy (kJ mol^{-1}); C_e is the equilibrium concentration of the metal ion (mg dm^{-3}); $RT/b = B$ is the Temkin constant related to the heat of adsorption (kJ mol^{-1}).

Adsorption isotherms of copper ions on sunflower hulls

In order to obtain the adsorption isotherm data, experiments were carried out in which 0.5 g of sunflower hulls were brought into contact with 50 mL of copper ion solution, with initial concentrations ranging from 0.05 to 0.3 mg dm^{-3}. The stirring time was 60 minutes. The suspension was then filtered and the copper concentration in the filtrate was determined.

In this work, three of the most common models of the adsorption isotherm in the literature, the Langmuir model, the Freundlich model, and the Temkin model, were used to fit the experimental data of the adsorption of copper ions on sunflower hulls. The obtained results are shown in Figure 1.

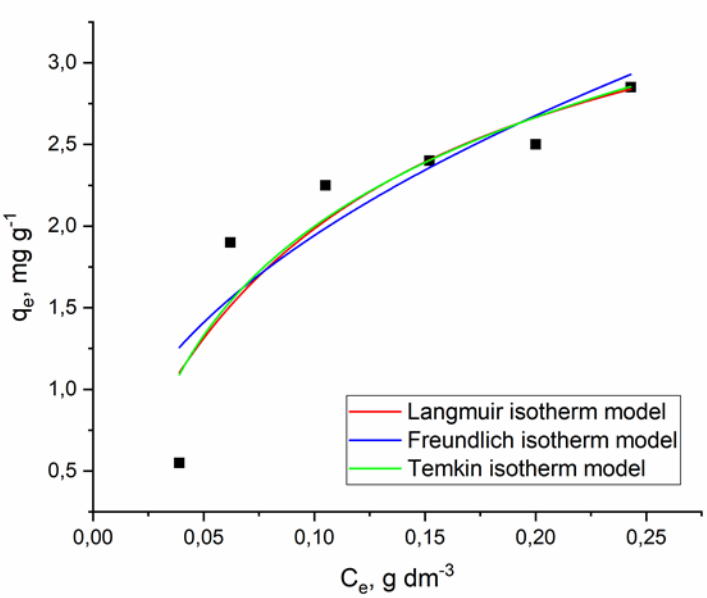

Figure 1. Isotherm data for the adsorption of copper ions on sunflower hulls

Table 1. Isotherm parameters for the adsorption of copper ions on sunflower hulls

Model	Parameters	Values
Langmuir isotherm model	K_L, $dm^3\ mg^{-1}$	9.537
	$q_{e,exp}$, $mg\ g^{-1}$	2.850
	q_m, $mg\ g^{-1}$	4.064
	R^2	0.838
Freundlich isotherm model	K_F	5.637
	1/n	0.463
	R^2	0.987
Temkin isotherm model	B, $J\ mol^{-1}$	0.964
	K_T, $dm^3\ mg^{-1}$	79.397
	R^2	0.988

Based on the values of the correlation coefficients given in Table 1, it can be concluded that Temkin isotherm model shows the best agreement with the experimental data (R^2 = 0.988) and is the best model to describe the equilibrium of adsorption of Cu^{2+} ions on sunflower hulls in the observed concentration range.

3.2 Adsorption thermodynamic

The thermodynamic parameters required to determine the spontaneity and feasibility of adsorption, such as the change in Gibbs free energy, the change in enthalpy and the change in entropy, are easy to determine because adsorption is a temperature-dependent process [11].

To determine the thermodynamic parameters, 0.5 g of adsorbent was brought into contact with 50 mL of a solution of copper ions with a concentration of 0.2 g dm^{-3}, at temperatures of 25 °C, 30 °C and 35 °C, for 60 minutes. The suspension was then filtered and the concentration of copper ions in the resulting filtrate was determined.

The thermodynamic parameters of the adsorption were calculated using the following equation [12, 13]:

$$K_c = \frac{C_A}{C_S} \tag{4}$$

$$\ln K_c = \frac{\Delta S^0}{R} - \frac{\Delta H^0}{RT} \tag{5}$$

$$\Delta G^0 = -RT \ln K_c \tag{6}$$

$$\Delta G^0 = \Delta H^0 - T\Delta S^0 \tag{7}$$

where: K_c is the equilibrium constant; C_A is the concentration of the adsorbed substance at equilibrium (mol dm^{-3}); C_S is the equilibrium concentration of the metal ions in solution (mol dm^{-3}); ΔG^0 is the Gibbs free energy (kJ mol^{-1}); R is the universal gas constant (J mol^{-1} K^{-1}); T is the temperature (K); ΔH^0 is the enthalpy change (kJ mol^{-1}); ΔS^0 is the entropy change (J mol^{-1} K^{-1}).

Figure 2 shows the dependence of $\ln K_c = f(1/T)$. Based on the given dependence and the experimental data, the thermodynamic parameters of the adsorption process of copper ions on sunflower hulls were calculated and given in Table 2.

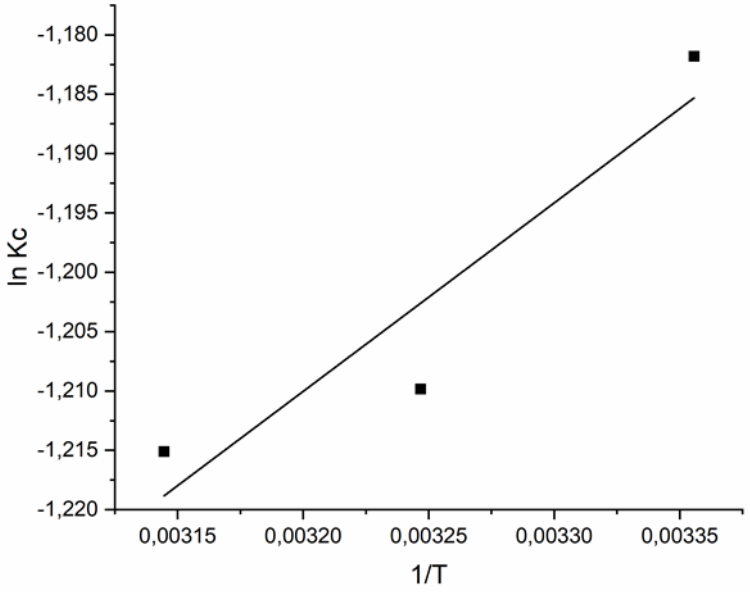

Figure 2. Thermodynamic dependence (ln Kc = f(1/T)) for the adsorption of copper ions on sunflower hulls

Table 2. Thermodynamic parameters of the adsorption process of copper ions on sunflower hulls

T (K)	ΔG^0 (kJ mol^{-1})	ΔH^0 (kJ mol^{-1})	ΔS^0 (J mol^{-1} K^{-1})
298	2.928	0.158	-1.718
303	3.098		
308	3.212		

The values obtained for the change in Gibbs free energy show that the Gibbs free energy increases with increasing temperature. Positive values of the change in Gibbs free energy indicate that there is an energy barrier for the adsorption of copper ions and that the sorption reaction does not occur spontaneously at the given temperatures. A positive ΔH^0 value indicates that the process is endothermic and a negative ΔS^0 value indicates that there is reduced randomness at the interface between the solid and solution [14].

4. CONCLUSIONS

The adsorption of copper ions on sunflower hulls was investigated and presented in this paper. The equilibrium analysis was performed using Langmuir's isothermal model, Freundlich's isothermal model and Temkin's isothermal model. Temkin's isothermal model fits the analysed data best. This model assumes that the adsorption energy of the molecules decreases linearly with the degree of surface coverage. The calculated thermodynamic data (ΔG^0, ΔH^0 and ΔS^0) show that the sorption reaction does not occur spontaneously at the specified temperatures, but is favoured at lower temperatures, that the process is endothermic and that decreased randomness is present at the solid-solution interface.

ACKNOWLEDGEMENTS

The research presented in this paper was done with the financial support of the Ministry of Science, Technological Development and Innovation of the Republic of Serbia, within the funding of the scientific research work at the University of Belgrade - Technical Faculty in Bor, according to the contract with registration number 451-03-137/2025-03/200131.

REFERENCES

[1] L. Fang, L. Li, Z. Qu, H. Xu, J. Xu, N. Yan, J. Hazard. Mater., 342 (2018) 617–624.
[2] Z. Xu, Q. Zhang, X. Li, X. Huang, Chem. Eng. J., 429 (2022) 131688.
[3] H.I. Syeda, I. Sultan, K.S. Razavi, P.S. Yap, J Water Process. Eng., 46 (2022) 102446.
[4] P. Ehiomogue, I.I. Ahuchaogu, I.E. Ahaneku, Acta Tech. Corviniensis – Bull. Eng., XIV (2021) 87-96.
[5] R. Farouq, N.S. Yousef, Int. J. Chem. Eng. Appl., 6 (5) (2015) 319-324.
[6] X. Chen, Information, 6 (1) (2015) 14-22.
[7] R.I. Yousef, B. El-Eswed, A.H. Al-Muhtaseb, Chem. Eng. J., 171 (3) (2011) 1143-1149.
[8] P.S. Kumar, S. Ramalingam, C. Senthamarai, M. Niranjanaa, P. Vijayalakshmi, S. Sivanesan, Desalination, 261 (1-2) (2010) 52–60.
[9] R.I.A. Ahad, S. Goswami, M.B. Syiem, 3 Biotech, 7 (2) (2017).
[10] Sh. Shahmohammadi-Kalalagh, H. Babazadeh, A.H. Nazemi, M. Manshouri, Caspian J. Environ. Sci., 9 (2) (2011) 243-255.
[11] A. Ebelegi, N. Ayawei, D. Wankasi, Open J. Phys. Chem., 10 (2020) 166-182.
[12] P. Rahnama Haratbar, M. Nasiri, A. Ghaemi, Iran. Polym. J., 32 (2023) 929–946.
[13] A. Ozcan, E.M. Oncu, A.S. Ozcan, Colloids Surf. A: Physicochem. Eng. Asp., 277 (2006) 90-97.
[14] L.Y. Lee, X.J. Lee, P.C. Chia, K.W. Tan, S. Gan, J. Taiwan Inst. Chem. Eng., 45 (4) (2014) 1764-1772.

The 56th International October Conference on Mining and Metallurgy
22-25 October 2025, Bor Lake, Bor, Serbia
www.ioc.tfbor.bg.ac.rs

DOI: 10.5937/IOC25664M *Original scientific paper*

KINETIC ANALYSIS OF COPPER IONS ADSORPTION ON SUNFLOWER HULLS

Marina Marković[1a], Milan Gorgievski[1b], Miljan Marković[1c], Vesna Grekulović[1d], Nada Štrbac[1e], Kristina Božinović[1f], Milica Zdravković[1g]

[1] Technical Faculty Bor, University of Belgrade, V.J. 12, 19210 Bor, Serbia
[1a] marina.markovic@tfbor.bg.ac.rs, 0009-0007-7553-6423
[1b] mgorgievski@tfbor.bg.ac.rs, 0000-0002-9899-719X
[1c] mmarkovic@tfbor.bg.ac.rs, 0000-0002-4734-1481
[1d] vgrekulovic@tfbor.bg.ac.rs, 0000-0001-6871-4016
[1e] nstrbac@tfbor.bg.ac.rs, 0000-0003-4836-1350
[1f] kbozinovic@tfbor.bg.ac.rs, 0000-0002-9834-448X
[1g] mzdravkovic@tfbor.bg.ac.rs, 0000-0001-9488-9151

Abstract
This paper presents the kinetic analysis of the adsorption process of copper ions on sunflower hulls. Three theoretical kinetic models were used to analyze the experimental results: the pseudo-first order kinetic model, the pseudo-second order kinetic model and the Elovich kinetic model. The results showed that the pseudo-second order kinetic model is the best fit for the analyzed data.

***Keywords**: sunflower hulls, copper ions, kinetic*

1. INTRODUCTION

Heavy metals such as cadmium (Cd), chromium (Cr), arsenic (As), lead (Pb) and mercury (Hg) are persistent environmental pollutants that do not degrade naturally and accumulate in the environment. If they are found in the human body, even in traces, their toxicity has a negative effect on the function of the organs and damages them [1].

Many conventional methods are used to remove heavy metals from wastewater, including chemical precipitation, ion exchange, ultrafiltration, reverse osmosis and membrane filtration [2]. However, these methods do not always provide satisfactory results, which is why it is necessary to develop a new, alternative process.

An emerging and promising alternative is biosorption, a physico-chemical process in which biological materials such as plant biomass and microorganisms are used as adsorbents to bind heavy metal ions from aqueous solutions [3]. In contrast to conventional methods, biosorption offers several advantages, including high removal efficiency even at low metal concentrations, cost efficiency and minimised secondary waste production [4].

2. EXPERIMENTAL

The sunflower hulls were first ground and sieved on a set of laboratory sieves. The fraction -1+0.4 mm was used for the experiments. Each sample was rinsed with distilled water before experiments. Adsorption experiments were carried out using a synthetic solution of Cu^{2+} ions, prepared from $CuSO_4 \cdot 5H_2O$ (LACHEMA, Czech Republic).

3. RESULTS AND DISCUSSION

3.1 Kinetic study

The study of adsorption kinetics provides information about the rate of uptake of solutes at the solid-liquid interface and the possible mechanism of the adsorption process [5]. To obtain the

experimental kinetic data, 0.5 g of sunflower hulls were brought into contact with the copper ion solutions with an initial concentration of 0.2 g dm^{-3} for different contact times between 1 and 90 minutes.

The change in adsorption capacity over time is shown in Figure 1. Figure 1 shows that at the beginning of the process, i.e. in the first 5 minutes, the capacity increases rapidly with the phase contact time. It then continues to increase, but at a slower rate. The sudden increase in adsorption capacity right at the beginning of the process is due to the availability of a large number of active sites in the structure of the adsorbent [6].

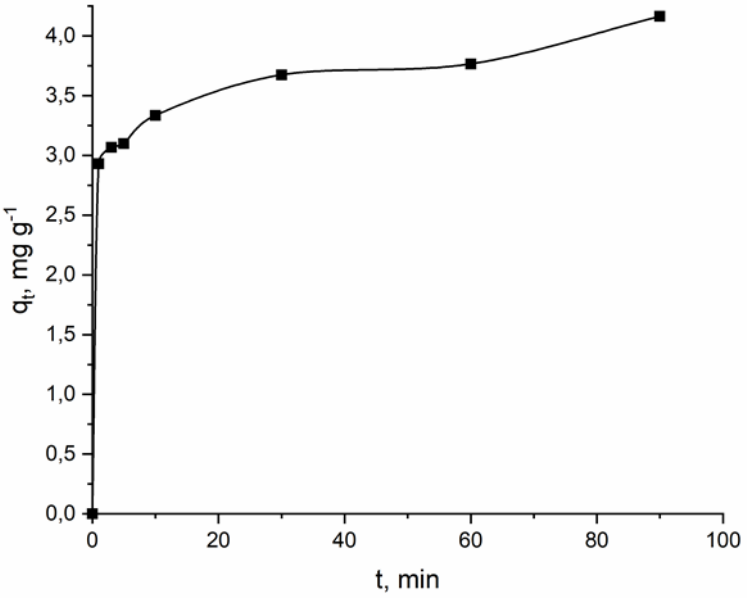

Figure 1. Change in the adsorption capacity for copper ions with time

In this paper, the pseudo-first order kinetic model, the pseudo-second order kinetic model and the Elovich kinetic model were used to analyze the obtained kinetic adsorption data.

Pseudo-first order kinetic model

The pseudo-first order kinetic model assumes that the adsorption rate is directly proportional to the number of unoccupied adsorption sites [7]. This kinetic model was proposed by Lagergren and it can be expressed in integral form as follows [8]:

$$\log(q_e - q_t) = \log(q_e) - \frac{k_1}{2.303} \cdot t \qquad (1)$$

where: q_t and q_e are the adsorption capacity defined as the mass of adsorbed metal per unit mass of adsorbent (mg g^{-1}) at time t and at equilibrium, respectively; k_1 (min^{-1}) is the rate constant for the pseudo-first order model.

A plot of $log(q_e-q_t)$ against t gives a linear dependence, from which the constant k_1 and the equilibrium adsorption capacity q_e can be determined from the slope and intercept, respectively.

The experimental data were fitted using this model (Figure 2), and the kinetic parameters were determined and shown in Table 1.

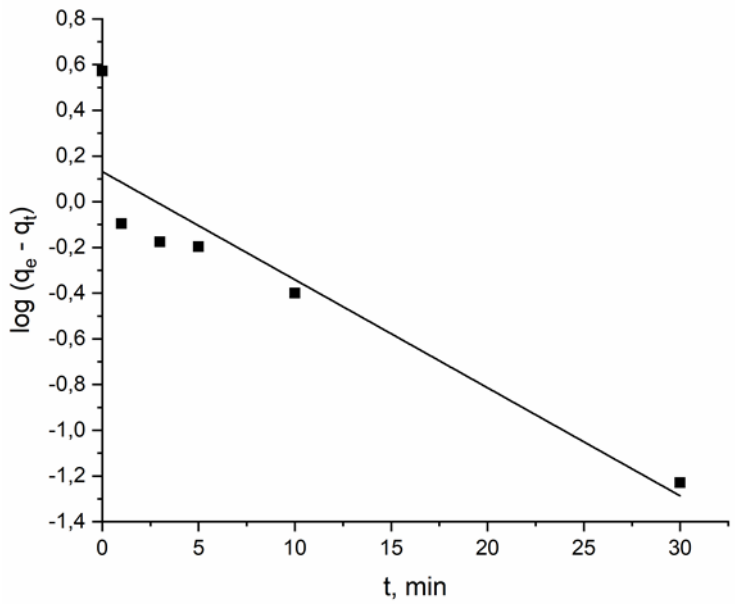

Figure 2. Pseudo-first order kinetic model for the adsorption of copper ions on sunflower hulls

Pseudo-second order kinetic model

The pseudo-second order kinetic model is based on the assumption that the rate-determining step of the adsorption process is chemisorption, i.e. the chemical interaction between the functional groups of the adsorbent and the heavy metal ions [9, 10]. This model can be expressed by the following equation [11]:

$$\frac{t}{q_t} = \frac{1}{k_2 q_e^{\,2}} + \left(\frac{1}{q_e}\right) \cdot t \tag{2}$$

where: q_t and q_e are the adsorbent capacity defined as mass of the adsorbed metal per unit mass of the adsorbent (mg g^{-1}) at time t and at equilibrium, respectively; k_2 is the rate constant for pseudo-second order kinetic model.

The values of k_2 and q_e can be calculated from the slope and intercept of the plot of t/q_t vs. t (Figure 3).

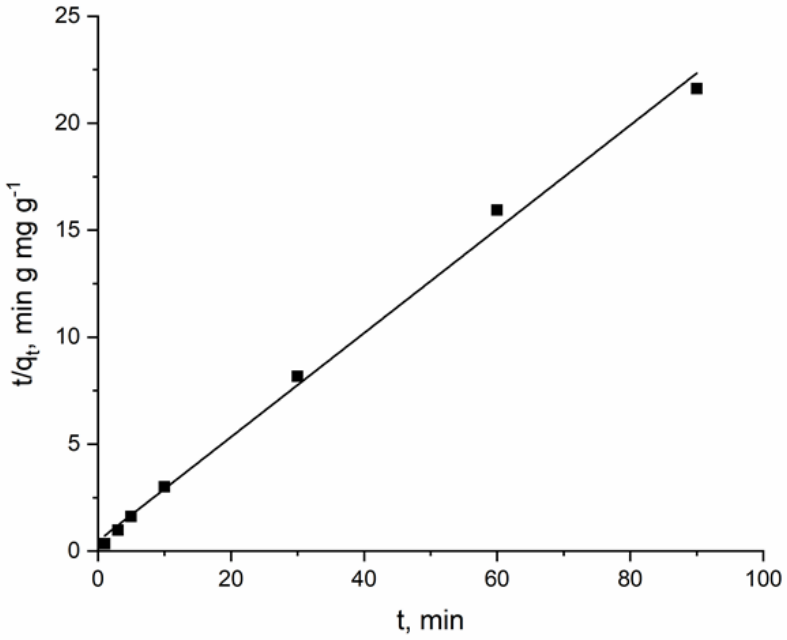

Figure 3. Pseudo-second order kinetic model for the adsorption of copper ions on sunflower hulls

Elovich kinetic model

Elovich kinetic model assumes that the surface of solids on which the adsorption process takes place is energetically heterogeneous and that with low surface coverage, neither desorption nor the interactions between the adsorbed species can significantly affect the kinetics of adsorption [12]. This kinetic model can be expressed by the following equation [13]:

$$q_t = \frac{1}{\beta}\ln(\alpha\beta) + \frac{1}{\beta}\ln t \quad (3)$$

where: α is the initial adsorption rate (mg g^{-1} min^{-1}); β is a parameter expressing the degree of surface coverage and the activation energy of chemisorption (g mg^{-1}); q_t is the adsorption capacity (mg g^{-1}), defined as the mass of adsorbed metal per unit mass of adsorbent for time *t*.
The values for the parameters α and β were calculated from the intercept and the slope of the line $q_t = f(lnt)$ (Figure 4) and are shown in Table 1 together with the correlation coefficient for copper ions.

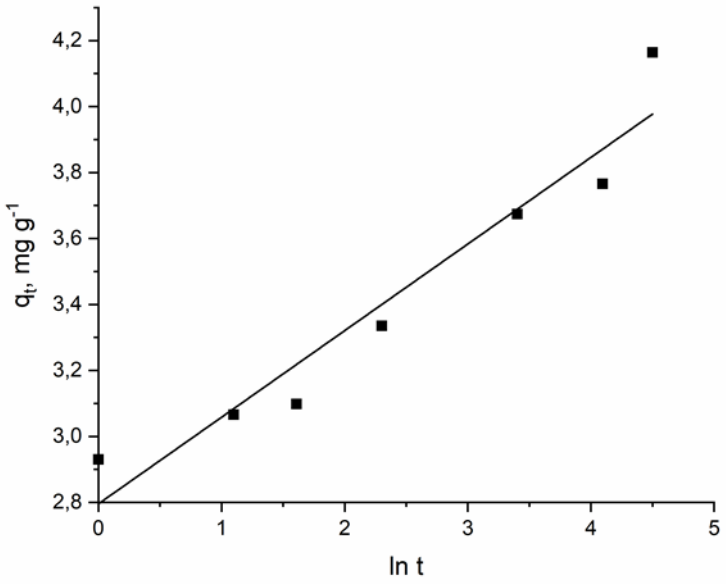

Figure 4. Elovich kinetic model for the adsorption of copper ions on sunflower hulls

Table 1. Parameters of the kinetic models for the adsorption of copper ions on sunflower hulls

Model	Parameters	Values
Pseudo-first order kinetic model	k_1, min^{-1}	0.109
	$q_{e,exp}$, mg g^{-1}	4.169
	$q_{e,cal}$, mg g^{-1}	1.355
	R^2	0.841
Pseudo-second order kinetic model	k_2, g mg^{-1} min^{-1}	0.125
	$q_{e,exp}$, mg g^{-1}	4.169
	$q_{e,cal}$, mg g^{-1}	4.116
	R^2	0.996
Elovich kinetic model	α, mg g^{-1} min^{-1}	2.795
	β, g mg^{-1}	0.263
	R^2	0.931

From the values of the correlation coefficients in Table 1, it can be concluded that the best agreement with the experimental data is achieved by the pseudo-second order kinetic model (R^2 = 0.996), indicating that the chemical reaction significantly controls the rate of copper ions adsorption on sunflower hulls.

4. CONCLUSIONS

Kinetic analysis of the copper ions adsorption on sunflower hulls was investigated and presented in this paper. Three kinetic models were used to analyze the experimental results: the pseudo-first order kinetic model, the pseudo-second order kinetic model and the Elovich kinetic model. Based on the obtained values of the correlation coefficients for each model, it can be concluded that the best agreement with the experimental data was achieved by the pseudo-second order kinetic model, which indicates that the chemical reaction significantly controls the rate of adsorption of copper ions on sunflower hulls.

ACKNOWLEDGEMENTS

The research presented in this paper was done with the financial support of the Ministry of Science, Technological Development and Innovation of the Republic of Serbia, within the funding of the scientific research work at the University of Belgrade - Technical Faculty in Bor, according to the contract with registration number 451-03-137/2025-03/200131.

REFERENCES

[1] R. Vidu, E. Matei, A.M. Predescu, B. Alhalaili, C. Pantilimon, C. Tarcea, C. Predescu, Toxics, 8 (4) (2020) 101.
[2] A.M. Renu, K. Singh, Interdiscip. Environ. Rev., 18 (2) (2017) 124–142.
[3] A. Ali Redha, Arab J. Basic Appl. Sci., 27 (1) (2020) 183–193.
[4] J. He, J.P. Chen, Bioresour. Technol., 160 (2014) 67–78.
[5] R.M. Ali, H.A. Hamad, M.M. Hussein, G.F. Malash, Ecol. Eng., 91 (2016) 317–332.
[6] S. Liang, X. Guo, N. Feng, Q. Tian, J. Hazard. Mater., 174 (1-3) (2010) 756–762.
[7] O.K. Amadi, C.J. Odidiozor, I.A. Okoro, Int. J. Eng. Inf. Syst., 1 (8) (2017) 72-85.
[8] D.H.K. Reddy, D.K.V. Ramana, K. Seshaiah, A.V.R. Reddy, Desalination, 268 (1-3) (2011) 150-157.
[9] R. Slimani, I. El Ouahabi, F. Abidi, M. El Haddad, A. Regti, M.R. Laamari, S. El Antri, S. Lazar, J. Taiwan Inst. Chem. Eng., 45 (4) (2014) 1578–1587.
[10] D. Bulgariu, L. Bulgariu, Bioresour. Technol., 103 (1) (2012) 489–493.
[11] K.D. Kowanga, E. Gatebe, G.O. Mauti, E.M. Mauti, J Phytopharmacol, 5 (2) (2016) 71-78.
[12] S.S. Gupta, K.G. Bhattacharyya, Adv. Colloid Interface Sci., 162 (2011) 39–58.
[13] C. Tejada-Tovar, Á. González-Delgado, Á. Villabona-Ortíz, Contemp. Eng. Sci., 11 (24) (2018) 1185–1193.

The 56th International October Conference on Mining and Metallurgy
22-25 October 2025, Bor Lake, Bor, Serbia
www.ioc.tfbor.bg.ac.rs

DOI: 10.5937/IOC25669S *Original scientific paper*

ASSESSMENT OF HEAVY METAL CONTAMINATION OF SOIL AND THE ECOLOGICAL RISK BASED ON NATIONAL LIMIT VALUES AND QUANTITATIVE INDICES

Danijela Simonović[1a], Daniel Kržanović[1b], Renata Kovačević[1c], Danijela Urošević[1d], Mirjana Šteharnik[1e], Sunčica Stanković[2a], Vesna Krstić[1f,3a]

[1]Mining and Metallurgy Institute Bor, Alberta Ajnštajna 1, 19210 Bor, Serbia
[2]Faculty of Management, Metropolitan University, 11158 Belgrade, Serbia
[3]Technical Faculty Bor, University of Belgrade, V.J. 12, 19210 Bor, Serbia
[1a] danijela.simonovic@irmbor.co.rs, 0000-0001-7945-693X
[1b]danijel.krzanovic@irmbor.co.rs, 0000-0003-3841-8667
[1c]renata.kovacevic@irmbor.co.rs, 0000-0003-4108-0855
[1d]daniela.urosevic@irmbor.co.rs, 0000-0003-3490-7834
[1e]mirjana.steharnik@irmbor.co.rs, 0000-0002-2733-3599
[2a]suncica.stankovic@metropolitan.ac.rs, 0000-0001-8824-1973
[1f,3a] vesna.krstic@irmbor.co.rs, 0000-0002-1110-0547

Abstract
Heavy metals were examined in arable land in the vicinity of the Zijin Copper mine, Serbia in Veliki Krivelj, Oštrelj, Brezonik and Zlot. Soil samples were analyzed by ICP-MS. In order to identify the degree of soil contamination with heavy metals and assess the potential ecological risk, a combination of quantitative indices was applied: descriptive statistics (including coefficient of variation - CV), geoaccumulation index (Igeo), enrichment factor (EF), contamination factor (CF) and site pollution index (PLI). These indices enable a multi-layered analysis — from the identification of variability and anthropogenic impact to an integrated risk classification by location. Limit values defined by the national regulations of the Republic of Serbia were used for the reference values, which ensures the regulatory relevance and practical applicability of the results in the agroecological context.

Keywords: *soil contamination, heavy metals, descriptive statistics, ecological indices*

1. INTRODUCTION

The intensification of the mining activities of the Zijin Copper company in eastern Serbia has caused increased attention of the population, but also of the professional public due to the potential impact on the quality of arable land [1]. In light of environmental challenges and increasingly frequent demands for sustainable resource management, the assessment of soil contamination with heavy metals becomes crucial for the preservation of agroecological functionality and the health of the local community. Many researchers have used pollution factors and indices in the study of soil pollution [2,3,4]. In this research, a combination of quantitative indices — including coefficient of variation (CV), geoaccumulation index (Igeo), enrichment factor (EF), contamination factor (CF) and site pollution index (PLI) — was applied to enable multi-level analysis of contamination levels and identification of anthropogenic impact. These indices have proven to be reliable tools in modern studies of land degradation in the mining zones of Serbia [5,6].

2. EXPERIMENTAL PART AND METHODOLOGY

In order to assess the ecological risk of soil contamination with heavy metals, a combination of quantitative indices and statistical methods was applied, which enable a multi-level analysis of the degree of pollution and the identification of potential anthropogenic sources. Soil samples were collected from Veliki Krivelj, Oštrelj, Brezonik and Zlot locations in the immediate vicinity of

mining activities, in accordance with the standards for environmental monitoring. Analyzes of metal concentrations (Cr, Cu, Zn, Cd, Co, Mn, Ni, Pb) were performed using the ICP-MS method (Inductively Coupled Plasma Mass Spectrometry). Instead of the metal reference value (C_b), limit values from the "Official Gazette of the RS" [7] were used, which ensured the regulatory relevance of the results.

The following indices were used to assess the degree of pollution:

- Coefficient of variation (CV), is the standard deviation (SD) divided by the mean, multiplied by 100%, equation (1):

$$CV=(SD/Mean)\times 100 \quad (1)$$

CV was used as an indicator of spatial heterogeneity of metal concentrations. For CV < 20% variability is low. CV in the range of 20–50% shows moderate variability, while CV > 50% confirms high variability.

- Geoaccumulation index (Igeo), was used to determine the degree of soil contamination with a certain element, is calculated according to equation (2):

$$Igeo = log_2(C_i/1.5\times C_{ib}) \quad (2)$$

Where C_i is the measured concentration of the i-th metal, and C_{ib} is the geochemical background concentration of the i-th metal. The formula incorporates a constant factor 1.5 to account for variations in background data as a result of natural processes [8,9]. Geoaacumulation index (I_{geo}) values were interpreted as $I_{geo} \leq 0$ – practically uncontaminated; $0 < I_{geo} \leq 1$ – uncontaminated to moderately contaminated; $1 < I_{geo} \leq 2$ – moderately contaminated; $2 < I_{geo} \leq 3$ moderately to heavily contaminated; $3 < I_{geo} \leq 4$ – heavily contaminated; $4 < I_{geo} \leq 5$ – heavily to extremely contaminated; and $5 < I_{geo}$ – extremely contaminated [10].

- Enrichment factor (EF), is a measure of the possible impact of antropogenic activity on the concentration of heavy metals in soil. EF is calculated by the following equation:

$$EF = \frac{(C_i/C_{ref})_{sample}}{(C_i/C_{ref})_{background}} \quad (3)$$

where: C_{ref} is the concentration of the selected reference element. Reference elements are characterized by the low variability of occurrence in the earth's crust, usually selected from the following group of metals: Fe, Al, Ca, Ti, Sc or Mn [10]. When EF > 2, soil enrichment is considered to be of anthropogenic origin. The EF has five classes: EF < 2, deficiency to minimal enrichment; $2 \leq EF < 5$, moderate enrichment; $5 \leq EF < 20$, significant enrichment; $20 \leq EF \leq 40$, very high enrichment; EF > 40, extremely enrichment [9].

- Contamination factor (CF), is the ratio of the concentration of each heavy metal in the soil and the concentration of the respective heavy metal in the background (pre-industrial reference value for the same element). CF is calculated according to equation ():

$$CF = C_i/C_{ib} \quad (4)$$

The CF values indicate the following levels of contamination [9]: CF < 1, low contamination; $1 \leq CF < 3$, moderate contamination; $3 \leq CF < 6$, considerable contamination; $CF \geq 6$, very high contamination.

- Pollution load index (PLI) was used for the total assessment of the degree of contamination in soil. It is defined as the n-th root of the multiplication of the CF of heavy metals involved. PLI for each location was calculated according to the following equation:

$$PLI = (CF_1 \times CF_2 \times CF_3 \times \ldots \times CF_n)^{1/n} \quad (5)$$

Where CF_i is the contamination factor for the individual element, and n is the total number of

pollution elements included in the study. PLI is usually classified as: PLI < 1 denotes no pollution, PLI =1 indicates only baseline levels of pollution and PLI >1 indicates deterioration of site quality [8,10].

3. RESULTS AND DISCUSSION

Descriptive statistics, shown in Table 1, indicate marked differences in the concentrations of heavy metals among the samples, both in terms of mean values and in terms of variability and the shape of the distribution. The coefficient of variation (CV) shows high heterogeneity for most metals. The highest variability has Cr (52.33%), Co (47.26%), and Mn (46.04%), which indicates uneven distribution and possible local sources of contamination. Zn (12.46%) shows the lowest variability, which may indicate a more uniform geogenic source or more stable mobility in the soil. The negative CV for Cd (-25.76%) is an artifact of the log-transformation and requires additional interpretation. Values were corrected due to detection limit.

Most metals exhibit negative kurtosis, indicating a flatter distribution with fewer extreme values than a normal distribution. Cd (skewness = 1.155) and Zn (1.052) show positive skewness, which may indicate the presence of samples with elevated concentrations — potentially relevant for identifying "hot spot" locations. Mn, Fe, Ni and Cu have skewness close to zero, suggesting an approximately symmetric distribution.

Fe has the highest mean concentration (39235 mg/kg), which is expected considering its natural abundance. Mn and Cu also show high values, while Ni, Co, and Cd are present in much lower concentrations. The ranges (min-max) indicate significant differences between locations, especially for Mn (482.7–1394.5 mg/kg) and Cu (192.7–605.5 mg/kg), which may indicate anthropogenic influence.

Table 1.Descriptive statistics applied to the presence of heavy metals in arable land at the locations: Veliki Krivelj, Oštrelj, Brezonik and Zlot

	mean	std	min	max	skewness	kurtosis	CV
Cr	32.9	17.3	15.9	49.2	-0.021	-1.938	52.33
Mn	973.1	447.9	482.7	1394.5	-0.104	-1.817	46.04
Fe	39235.0	10805.8	29982.4	52229.4	0.272	-1.641	27.54
Co	16.6	7.8	11.0	28	0.957	-0.845	47.26
Ni	14.9	5.6	9.9	21.7	0.294	-1.583	37.21
Cu	385.5	169.9	192.7	605.5	0.27	-1.016	44.09
Zn	79.5	9.9	72.9	94.1	1.052	-0.755	12.46
As	28.8	6.3	20.4	33.8	-0.544	-1.311	22.01
Cd	-0.132	0.034	-0.149	-0.081	1.155	-0.667	-25.76
Pb	36.8	10.8	28.8	52.6	0.962	-0.832	29.51

The highest variability, using formula (1), was shown by Cr (CV = 52.33%) and Co (CV = 47.26%), while Zn showed the lowest variability (CV = 12.46%), which indicates a more stable geogenic character. Cd was log-transformed, so the negative CV does not represent a physical value but a statistical one.

Table 2. Geoaccumulation index (Igeo) of heavy metals in agricultural soil at the locations L1 (Veliki Krivelj), L2 (Oštrelj), L3 (Brezonik) and L4 (Zlot)

	Igeo_Cr	Igeo_Mn	Igeo_Fe	Igeo_Co	Igeo_Ni	Igeo_Cu	Igeo_Zn	Igeo_As	Igeo_Pb	Igeo_Cd
L1	-1.608	-2.221	-0.398	-0.089	-2.407	3.487	-1.447	-0.201	-1.277	-0.585
L2	-1.693	-1.672	-0.388	-0.055	-1.275	2.857	-1.507	-0.110	-1.861	-0.585
L3	-3.238	-0.782	-0.231	0.060	-2.268	2.708	-1.158	-0.112	-2.054	-0.481
L4	-2.878	-0.690	-0.157	0.317	-1.610	1.835	-1.526	-0.329	-2.146	-0.532

Positive Igeo values, Table 2, for Cu (up to 3.487 at L1) indicate heavy contamination and Co (at L3 and L4), indicate while all other elements showed negative Igeo values, suggesting an uncontaminated state in relation to the limit values.

The highest value of enrichment factor (EF), Table 3, for Cu (61.635 at L3) indicates a dominant anthropogenic contribution, probably related to mining exploitation. Cd and Mn also show significant enrichment, especially at sites L3 and L4. In this study Cr was selected as reference element.

Table 3. Enrichment Factor (EF) of heavy metals in agricultural soil at the locations: L1, L2, L3, L4

	EF_Cr	EF_Mn	EF_Ni	EF_Cu	EF_Zn	EF_Cd	EF_Pb
L1	1	0.654	0.575	34.186	1.118	2.033	1.258
L2	1	1.015	1.336	23.414	1.138	2.155	0.890
L3	1	5.488	1.959	61.635	4.227	6.761	2.272
L4	1	4.557	2.409	26.239	2.553	5.086	1.661

The highest value of pollution load index (PLI), Table 4, was recorded at L2 (0.850), indicating a slightly elevated level of total contamination. All sites have PLI<1, suggesting that the soil is not in the high risk zone, but local values of Cu and Cd require further attention.

Table 4. Contamination factor (CF) and Pollution load index (PLI) of heavy metals in agricultural soil at the locations: L1, L2, L3, L4

	CF_Cr	CF_Mn	CF_Ni	CF_Cu	EF_Ni	CF_Zn	CF_Cd	CF_Pb	PLI
L1	0.492	0.322	0.283	16.819	0.575	0.550	1.000	0.619	0.823
L2	0.464	0.471	0.620	10.864	1.336	0.528	1.000	0.413	0.850
L3	0.159	0.873	0.311	9.800	1.959	0.672	1.075	0.361	0.730
L4	0.204	0.930	0.491	5.353	2.409	0.521	1.038	0.339	0.710

The combined application of these indices enables a multi-level assessment of the ecological state of the soil and the identification of heavy metals that require further attention in the context of agro-ecological security.

4. CONCLUSION

The results of descriptive statistics indicate a pronounced variability of metal concentrations, especially Cr, Co, Cu and MnThe results of the geoaccumulation index indicate that the soil in the analyzed locations is mostly uncontaminated when it comes to heavy metals Cr, Mn, Fe, Ni, Zn, As, Cd and Pb. However, the presence of positive Igeo values for Cu at all locations and Co on L3 and L4, suggests the existence of anthropogenic influence, probably related to mining exploitation and metallurgical activities in the area. The Enrichment Factor (EF) further confirms this tendency,

with extreme values for Cu and significant enrichment for Cd at sites L3 and L4. Contamination Factor (CF) and Pollution Load Index (PLI) indicate moderate overall contamination, with no site exceeding the high risk threshold (PLI > 1).
These findings confirm the need for further analysis of ecological indices and spatial characterization of contamination.

ACKNOWLEDGEMENTS

The research presented in this paper was done with financial support of the Ministry of Science, Technological Development and Innovation of the Republic of Serbia, within the Conctract No. 451-03-136/2025-03/200052.

REFERENCES

[1] V. Nikolić, N. Staletović, V. Presburger Ulniković, I. Jovanović, Bakar, 50 (1) (2025) 33-34
[2] G. Qingjiea, D. Juna, X. Yunchuanb, W. Qingfeib, Y. Liqiangb, J. China Univ. Geosci., 19 (3) (2008) 230-241.
[3] Y. Hu, X. Liu, J. Bai, K. Shih, E. Y. Zeng, H. Cheng, Environ. Sci. Pollut. Res., 20 (9) (2013) 6150-6159
[4] C.O. Ogunkunle, P.O. Fatoba, Pol. J. Environ. Stud. 22 (2) (2013) 487-493
[5] M. Antonijević Nikolić, J. Đuričić Milanković, Đ. Nikolić, D. Stanojević, Zaštita Materijala, 62 (2) (2021), 83-94.
[6] S. Šerbula, T. Kalinović, J. Kalinović, A. Ilić, ESPR, 20 (12) (2013) 8919-8929.
[7] Official Gazette of Republic of Serbia, Regulation on Limit Values for Polluting, Harmful and Hazardous Substances in the Soil, No. 30/2018 and 64/2019.
[8] J.B. Kowalska, R. Mazurek, M. Gasiorek, T. Zelenski, Environ. Geochem. Health, 40 (2018) 2395-2420.
[9] J. Kalinović, S. Šerbula, T. Kalinović, A. Radojević, J. Jordanović, Hem. Ind. 78 (3) (2024) 265-279.
[10] S.L.C. Ferreira, J.B. da Silva Junior, I.F. Dos Santos, O.M.C. De Oliveira, V. Cerda, A.F. S. Queiroz, TrEAC, 35 (2022) e00169

The 56th International October Conference on Mining and Metallurgy
22-25 October 2025, Bor Lake, Bor, Serbia
www.ioc.tfbor.bg.ac.rs

DOI: 10.5937/IOC25674P
Original scientific paper

ASSESMENT OF PAH AND PCB CONCENTRATIONS IN BOR RIVER BED SEDIMENTS AFFECTED BY MINING AND METALLURGY

Aleksandra Petrović[1a], Stefan Đorđievski[1b], Bojan Radović[1c], Renata Kovačević[1d]

[1] Mining and Metallurgy Institute Bor, Alberta Ajnštajna 1, 19210 Bor, Serbia
[1a] aleksandra.petrovic@irmbor.co.rs, 0009-0007-3518-6596
[1b] stefan.djorodjievski@irmbor.co.rs, 0000-0003-1737-8766
[1c] bojan.radovic@irmbor.co.rs, 0000-0003-4884-1418
[1d] renata.kovacevic@irmbor.co.rs, 0000-0003-4108-0855

Abstract
The aim of this study was to investigate the presence of polycyclic aromatic hydrocarbons (PAHs) and polychlorinated biphenyls (PCBs) in river bed sediment samples collected from the Bor River, an area strongly influenced by mining and metallurgical activities. The concentrations of PAHs and PCBs were determined using gas chromatography - mass spectrometry (GC-MS), which provides high sensitivity and reliability for the detection of such compounds. The results showed that the levels of PAHs and PCBs in the analyzed samples were below the limits of quantification. The results showed that, despite intensive mining and metallurgical activities in this area, there is no increase in the levels of these organic compounds in river sediments. The importance of this research lies in assessing the influence of mining and metallurgy on the environment and in evaluating the current ecological status of the Bor River.

***Keywords**: PAHs, PCBs, River sediments, Bor River, GC-MS*

1. INTRODUCTION

In this study, the concentrations of polycyclic aromatic hydrocarbons (PAHs) and polychlorinated biphenyls (PCBs) in river bed sediment samples from the Bor River were determined using Gas Chromatography – Mass Spectrometry (GC-MS). To date, a large number of studies have addressed how mining and metalurgy in the Bor region affect the contamination of water, air and soil with heavy metals and arsenic [1-3]. In the reviewed literature, no studies were found that address the pollution of river water and sediments with organic contaminants such as PAHs and PCBs. The Bor River, located in an area vulnerable to contamination, highlights the necessity of monitoring these organic compounds.

Polycyclic aromatic hydrocarbons (PAHs) are organic compounds that are colorless, white or pale yellow in solid state. They can enter in environment by dispersing through air and water as a result of many human activities [4]. Sources of PAHs in environment are: natural sources – volcanic eruptions and biomass combustion, or anthropogenic sources – combustion of fossil fuels (oil, gas), traffic emissions, industrial processes (metallurgy, petroleum refining), and waste incineration [5]. When organic substances such as fossil fuels or biomass are exposed to high temperatures under oxygen-free or low-oxygen conditions, pyrogenic PAHs are formed [5].

Polychlorinated biphenyls (PCBs) are synthetic organic compounds that contain 1–10 atoms of chlorine covalently bound to a biphenyl molecule. PCBs are synthesized through the direct chlorination of biphenyl, using $FeCl_3$, as a catalyst. The reaction proceeds via a free radical mechanism, resulting in a mixture of biphenyls with different numbers of chlorine atoms [6]. PCBs can enter environment through industrial discharges, improper waste disposal and atmospheric deposition. PCBs can be absorbed via inhalation and, to a lesser extent, through dermal contact. PCBs are considered potent toxicants that have a negative impact on endocrine, reproductive and immune system [7,8].

Gas chromatography – mass spectrometry (GC–MS) is a powerful analytic technigue that combines the separation capabilities of gas chromatography (GC) with the detection and identification abilities of mass spectromety (MS). GC is used to separate complex mixture based on the volatility and interaction of analytes with the stationary phase of the column, while MS provides qualitative and quantitative data by ionizing the separated compounds and analyzing their mass – to – charge ratios [9]. Today, this technique is widely used for detection of trace organic pollutants such as PAHs and PCBs in environmental samples due to its high sensitivity, selectivity and accuracy [9].

The objective of this study is to evaluate the levels of PAHs and PCBs in sediment samples from the Bor River, as the scientific literature lacks data on such analyses, despite the existence of numerous studies reporting concentrations of metals and arsenic.

2. EXPERIMENTAL

The sampling sites are located downstream of the village of Slatina, before the confluence of the Bor River with Krivelj River. Sampling was carried out on April 16, 2024, with the folowing labels and coordinates: BS1 (44°01'43.5"N, 22°11'10.3"E); BS2 (44°01'43.9"N, 22°11'11.6"E); BS3 (44°01'43.2"N, 22°11'13.8"E). Untampered river sediment samples were air dried at room temperature for 24 hours. After drying, the samples were homogenized and 5 g of each sample was weighed out. In each sample 1 g of Na_2SO_4 was added to additionally dry the samples and improve extraction.

Samples were prepared for extraction using the following protocol. Speed extractor (E – 916) tube bottom was covered with a paper filter, followed by a metal filter, and then 2 g of diatomaceous earth. The tube was then filled halfway with quartz sand, then 5 g of previously prepared sample was added, followed by 100 µL of internal standard (mix of deuterated PAHs in concentration of 2 mg/mL), and topped off with more quartz sand and sealed with a paper filter. Blank sample was prepared in the same way, containing everything but the sample. Extraction was performed on the Speed extractor for 52 minutes, at 100 °C, 1 bar pressure. Extraction was performed twice, each with 30 mL acetone:hexane 1:1 mixture. The acetone from the extract was then evaporated to 2–3 mL volume using a Buchi rotavapour (R – 215) at 945 mbar, 60 °C, 80 rpm. To each acetone extract, 10 mL of hexane was added, and then evaporated again at 556 mbar, 60 °C water bath, 80 rpm, also to 2–3 mL volumes. These samples were purified using chromatographic columns, packed with glass wool at the bottom, 2 g of silica gel, and 2 g of Na_2SO_4. Columns were pre-eluted with 20 mL of hexane, and then the sample was added. Elution was performed using 2x10 mL hexane, followed by 2x20 mL dichloromethane. Dichloromethane from purified samples was evaporated at 945 mbar, 60 °C water bath temperature, 80 rpm, also to 2–3 mL final volume. Hexane was added to each sample in volume of 10 mL and again evaporated under the same conditions (556 mbar, 60 °C water bath, 80 rpm) to final volume of 1 mL. The prepared samples were transferred to 2 mL vials (1 mL of sample in each) and were analyzed on Agilent 7890 B (GC) and Agilent 5977A (MSD).

3. RESULTS AND DISCUSSION

Table 1 presents the concentrations of polycyclic aromatic hydrocarbons (PAHs) and polychlorinated biphenyls (PCBs) in three sediment samples collected from the Bor River (BS-1, BS-2, BS-3). The concentrations of all assessed PAHs (naphthalene, acenaphthylene, acenaphthene, fluorene, phenanthrene, anthracene, fluoranthene, pyrene, benzo(a)anthracene, chrysene, benzo(b)fluoranthene, benzo(k)fluoranthene, benzo(a)pyrene, indeno(1,2,3-c,d)pyrene, dibenzo(a,h)anthracene, and benzo(g,h,i)perylene) and PCBs (PCB 28, PCB 52, PCB 101, PCB 118, PCB 138, PCB 153, and PCB 180) were below the limit of detection (LOD) of 0.0050 mg/kg for each individual compound. Since all measured values were below the detection limit, it can be concluded that these organic pollutants were either absent or present in concentrations below

0.0050 mg/kg. Given the environmental setting of the Bor River, this result is expected. The dominant pollution sources in the area are related to copper mining, flotation tailings, metallurgical processing, and smelting activities, which primarily release metals and arsenic, not organic compounds such as PAHs and PCBs.

Table 1. Concentration of PAHs and PCBs in river bed sediment samples from the Bor River

Parameter	Unit of measure	Sample label		
		BS-1	BS-2	BS-3
Polycyclic aromatic hydrocarbons (PAHs)				
Naphthalene	mg/kg	<0.0050	<0.0050	<0.0050
Acenaphthylene		<0.0050	<0.0050	<0.0050
Acenaphthene		<0.0050	<0.0050	<0.0050
Fluorene		<0.0050	<0.0050	<0.0050
Phenanthrene		<0.0050	<0.0050	<0.0050
Anthracene		<0.0050	<0.0050	<0.0050
Fluoranthene		<0.0050	<0.0050	<0.0050
Pyrene		<0.0050	<0.0050	<0.0050
Benzo(a)anthracene		<0.0050	<0.0050	<0.0050
Chrysene		<0.0050	<0.0050	<0.0050
Benzo(b,k)fluoranthene		<0.0050	<0.0050	<0.0050
Benzo(a)pyrene		<0.0050	<0.0050	<0.0050
Indeno (1,2,3,c,d)pyrene		<0.0050	<0.0050	<0.0050
Dibenzo(a,h)antrachene		<0.0050	<0.0050	<0.0050
Benzo(g,h,i)perylene		<0.0050	<0.0050	<0.0050
Total PAHs		<0.0750	<0.0750	<0.0750
Polychlorinated biphenyls (PCBs)				
PCB 28	mg/kg	<0.0050	<0.0050	<0.0050
PCB 52		<0.0050	<0.0050	<0.0050
PCB 101		<0.0050	<0.0050	<0.0050
PCB 118		<0.0050	<0.0050	<0.0050
PCB 138		<0.0050	<0.0050	<0.0050
PCB 153		<0.0050	<0.0050	<0.0050
PCB 180		<0.0050	<0.0050	<0.0050
Total PCBs		<0.0350	<0.0350	<0.0350

As discussed in the Introduction, PAHs are typically formed during combustion of organic matter from natural or anthropogenic sources [5], whereas PCBs are synthetic industrial chemicals produced through chlorination of biphenyl [6-8]. Since the Bor River catchment area lacks significant combustion-related or industrial PCB sources, their concentrations remain below the detection limits.

This is consistent with previous studies on environmental pollution in the Bor region. For instance, Petrović et al. [1] analyzed riparian soils affected by mining activities in Bor region and found extremely elevated copper concentrations, ranging from 188.71 mg/kg to 2,888.8 mg/kg. According to Đorđievski et al. [2], the copper concentration in riverbed sediments of the Bor River reached 14,100 mg/kg at a site situated close to the sampling location of the present study. For comparison, according to Serbian regulations, the maximum allowable concentration (MAC) for copper is 36 mg/kg, and the remediation value (RV) is 190 mg/kg [1]. These findings indicate severe soil contamination with copper, directly linked to mining and metallurgical emissions, while also explaining the absence of significant contamination from PAHs and PCBs in the studied sediments.

4. CONCLUSION

This study assessed the levels of PAHs and PCBs in sediment samples from the Bor River using GC-MS analysis. All individual compounds and total concentrations were below the detection limit of 0.0050 mg/kg, indicating that these organic pollutants are either absent or present at negligible levels. The results highlight that, despite intensive mining and metallurgical activities in the Bor region, the dominant environmental burden arises from metals and arsenic, not organic contaminants. Consequently, monitoring efforts in this area should primarily focus on metal(loid) pollution, while periodic screening for organic pollutants remains relevant to confirm potential changes in contamination sources over time.

ACKNOWLEDGEMENTS

This work was funded by the Ministry of Science, Technological Development, and Innovation of the Republic of Serbia under contract no. 451-03-136/2025-03/200052 (Mining and Metallurgy Institute Bor).

REFERENCES

[1] J.V. Petrović, S.Č. Alagić, S.M. Milić, S.B. Tošić, M.M. Bugarin, Chemosphere 262 (2020) 127808.
[2] S. Šerbula, V. Stanković, D. Živković, Ž. Kamberović, M. Gorgievski, T. Kalinović, Mine Water Environ. 35 (2016) 363-376.
[3] S. Đorđievski, D. Ishiyama, Y. Ogawa, Z. Stevanović, Environ. Sci. Poll. Res. 25 (2018) 25005-25019.
[4] F.S. Ehrenhauser, Polycycl. Aromat. Compd. 35 (2015) 161-176.
[5] T. Wenzl, R. Simon, E. Anklam, J. Kleiner, TrAC Trends Anal. Chem. 25 (2006) 716-725.
[6] I. Grabowska, Pol. J. Environ. Stud. 19 (2010) 7-13.
[7] O.M. Alharbi, A.A. Basheer, R.A. Khattab, I. Ali, J. Mol. Liq. 263 (2018) 442-453.
[8] M.M. Ododo, B.K. Wabalo, J. Environ. Pollut. Hum. Health 7 (2019) 73-77.
[9] D.D. Sparkman, Z.E. Penton, F.G. Kitson, Gas Chromatography and Mass Spectrometry: A Practical Guide, Academic Press, Oxford, 2012, p. 6299.

The 56th International October Conference on Mining and Metallurgy
22-25 October 2025, Bor Lake, Bor, Serbia
www.ioc.tfbor.bg.ac.rs

DOI: 10.5937/IOC25678D

Original scientific paper

ASSESSMENT OF THE COPPER AVAILABILITY BY EXTRACTION OF RIVERBED SEDIMENTS FROM EASTERN SERBIA WITH 0.5 M HCl

Stefan Đorđievski[1a], Ana Radojević[2a], Tanja Kalinović[2b], Maja Nujkić[2c], Jelena Kalinović[2d], Jelena Jordanović[2e], Renata Kovačević[1b], Yasumasa Ogawa[3a]

[1] Mining and Metallurgy Institute Bor, Alberta Ajnštajna 1, 19210 Bor, Serbia
[2] Technical Faculty in Bor, University of Belgrade, V.J. 12, 19210 Bor, Serbia
[3] Graduate School of International Resource Sciences, Akita University, Akita City, Japan
[1a] stefan.djordjievski@irmbor.co.rs, 0000-0003-1737-8766
[2a] aradojevic@tfbor.bg.ac.rs, 0000-0003-3138-154X
[2b] tkalinovic@tfbor.bg.ac.rs, 0000-0003-0161-0065
[2c] mnujkic@tfbor.bg.ac.rs, 0000-0002-6110-5135
[2d] jkalinovic@tfbor.bg.ac.rs, 0000-0003-0088-2683
[2e] jjordanovic@tfbor.bg.ac.rs, 0000-0002-8145-640X
[1b] renata.kovacevic@irmbor.co.rs, 0000-0003-4108-0855
[3a] y_ogawa@gipc.akita-u.ac.jp, 0000-0002-4044-3880

Abstract
This study assessed copper contamination and availability in riverbed sediments from 181 locations in Eastern Serbia. The highest total Cu concentrations (up to 26,400 mg/kg) with HCl-extractable fractions up to 80% were recorded downstream of the confluence of Bela and Timok Rivers, where secondary, highly labile copper phases dominated. In contrast, 145 of 181 samples contained <50% 0.5 M HCl-extracted Cu, indicating limited mobility. The findings highlight the need to assess both metal concentrations and speciation to evaluate ecological risk and guide site-specific management.

***Keywords**: Copper, Riverbed sediments, Bioavailability, Extraction*

1. INTRODUCTION

Mining and metallurgical activities in the Bor region have significantly polluted river water and sediments in Eastern Serbia with potentially toxic elements (PTEs). Repeated discharges of flotation tailings into local rivers have led to their accumulation on riverbeds and floodplains along the Bor, Krivelj, Bela, and Timok Rivers. These tailings are still visibly present even at the confluence of the Timok and Danube Rivers. Approximately 2,000 hectares of fertile floodplain land along the Timok River have been contaminated by these deposits. In addition to the direct deposition of tailings, metal precipitation from polluted river water has further contributed to sediment contamination throughout the river system [1,2].

Although total PTE concentrations in sediments are elevated, the bioavailability of these elements to plants remains uncertain. Sequential extraction methods, such as the BCR procedure, are commonly employed to evaluate the partitioning of PTEs among different geochemical fractions [3]. However, these procedures involve multiple steps, making them labor-intensive and less practical for routine assessments. As an alternative, single extraction using diluted HCl has been proposed as a simplified and effective approach for estimating the concentrations of labile PTE forms in sediments [4-7].

In this study, the total digestion and 0.5 M HCl extraction was performed on riverbed sediment samples from Eastern Serbia, collected from areas impacted by copper mining and processing. The main objective was to assess the availability of copper and to evaluate the spatial distribution of both total and 0.5 M HCl-extracted copper concentrations.

2. EXPERIMENTAL

Riverbed sediment samples were collected at 181 locations in Eastern Serbia during the 2015 and 2016 sampling campaigns using a scoop sampling method. An average sampling density of approximately one sample per 46 km² was achieved. The samples were transported to the laboratory in labeled plastic bags, air-dried at room temperature, and subsequently sieved. The fraction smaller than 180 μm was retained for chemical analysis and extraction.

The total concentration of copper in the sediment samples was determined by Actlabs (Canada) following total digestion and analysis by Inductively Coupled Plasma Mass Spectrometry (ICP-MS). To estimate the available fraction of copper, 0.5 g of each sediment sample was subjected to extraction with 10 mL of 0.5 M hydrochloric acid [4]. The suspensions were agitated on a mechanical shaker for 1 hour, then centrifuged at 3,000 rpm for 20 minutes to separate the extract from the solid residue. The supernatants were filtered through 0.45 μm cellulose acetate syringe filters to remove any particulate matter. The filtered extracts were analyzed for copper concentrations using Inductively Coupled Plasma Optical Emission Spectrometer (ICP-OES), model SPECTRO CIROS VISION, at the Mining and Metallurgy Institute Bor. The percentages (%) of extracted Cu, were calculated based on the total and HCl-extracted Cu concentrations.

3. RESULTS AND DISCUSSION

Table 1 summarizes the statistical parameters for total copper concentrations, 0.5 M HCl-extractable copper, and the percentage of extractable copper in riverbed sediments from Eastern Serbia. The total copper concentrations ranged from 3.1 mg/kg to 26,400 mg/kg, with a median of 49.8 mg/kg and an average of 990 mg/kg, indicating a strong spatial variability influenced by mining and metallurgy-related inputs.

Table 1. Descriptive statistics data based on the total and 0.5 M HCl-extracted Cu concentrations

Parameter	Unit	Minimum	Median	Average	Maximum
Total conc. of Cu	mg/kg	3.1	49.8	990	26,400
HCL extracted Cu	mg/kg	1.2	16.8	404	20,660
HCL extracted Cu	% of total Cu	4.7	35.4	37	99.4

Figure 1 shows the geochemical maps of total copper concentration (mg/kg) and the percentage of 0.5 M HCl-extracted copper concentrations relative to the total copper content in river bed sediments. The highest total copper concentrations were recorded in sediments from the Bor and Bela Rivers, as well as in the Timok River downstream from its confluence with the Bela River. Elevated concentrations were also observed in the middle and lower reaches of the Timok River, as well as in the Krivelj and Pek Rivers.

Among the locations with the highest total copper concentrations, the sites along the Timok River after its confluence with the Bela River exhibited the highest percentage of 0.5 M HCl-extracted copper. The source of labile copper is likely the precipitated material in the sediment that was formed by the neutralization of acidic waters from the Bela River by the alkaline waters of the Timok River [2]. Precipitated copper(II) species – such as copper(II) hydroxide ($Cu(OH)_2$), copper(II) carbonate ($CuCO_3$), and copper ions adsorbed onto iron(III) oxyhydroxides – are known to be readily soluble in acidic conditions, such as those provided by the 0.5 M HCl extraction. As a result, copper in these sediments is considered labile and may be readily mobilized under changing environmental conditions, increasing its potential bioavailability to aquatic organisms and plants.

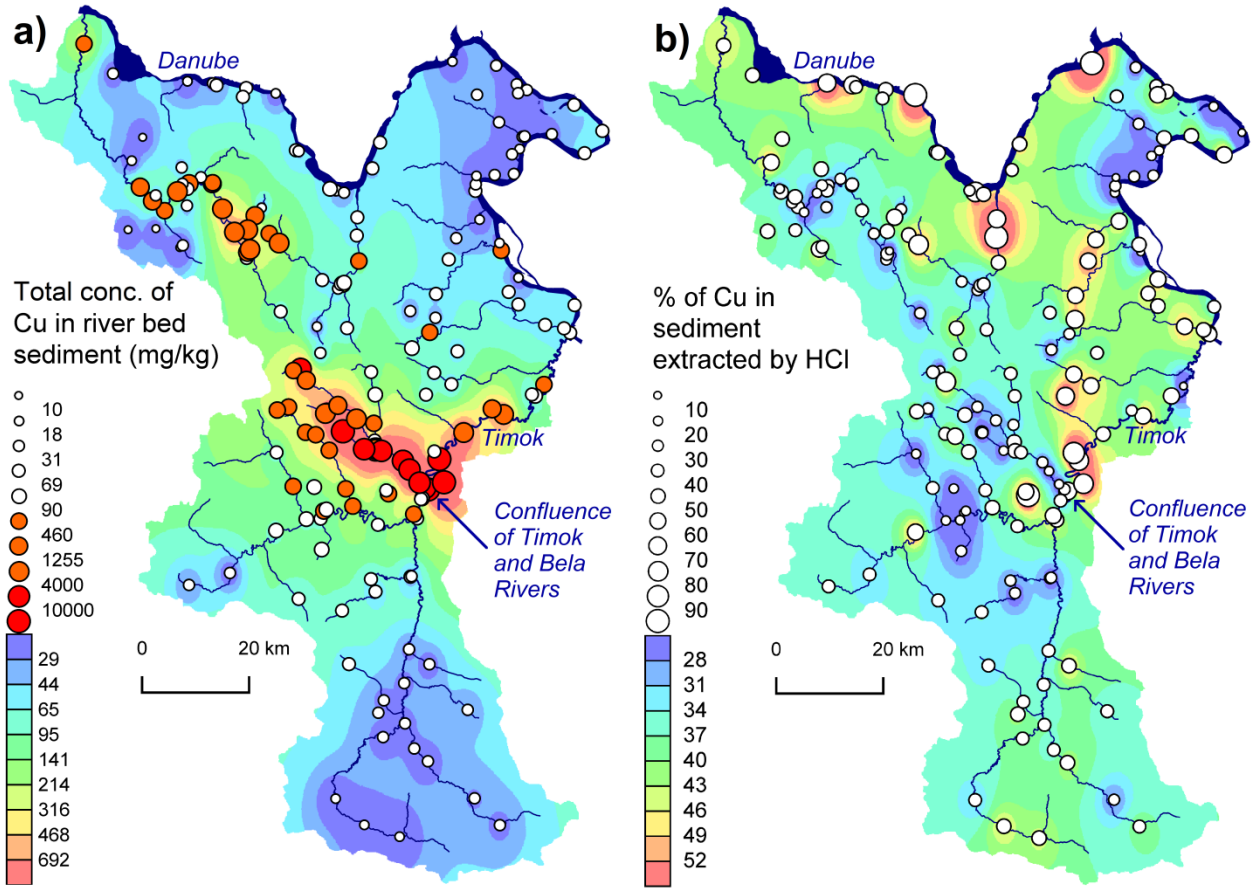

Figure 1. Geochemical maps of (a) total copper concentrations (mg/kg) and (b) the percentages of HCl-extracted copper relative to the total copper contents in river bed sediments

Figure 2 illustrates the relationship between total copper concentrations in riverbed sediments (blue bars, right y-axis) and the percentage of copper extracted using 0.5 M HCl (red line, left y-axis) for 181 sediment samples collected across Eastern Serbia. The samples are arranged in ascending order based on the percentage of 0.5 M HCl-extracted copper, enabling a direct comparison between the total copper content and its potentially available fraction.

A clear distinction is observed between samples in which copper is predominantly bound within stable mineral phases and those where it occurs in more labile, readily soluble forms. In 145 of 181 samples (~80% of samples), the percentage of 0.5 M HCl-extractable copper was below 50%, indicating that copper in the majority of samples was predominantly retained within relatively immobile mineral matrices. In contrast, two samples with the highest total copper concentrations (26,400 mg/kg and 16,300 mg/kg) also exhibited some of the highest percentages of 0.5 M HCl-extractable copper (78.3% and 79.3%, respectively). As discussed earlier, these locations are situated within 15 km downstream of the confluence of the Timok and Bela Rivers.

Some samples with relatively high total copper concentrations (5,000–15,000 mg/kg) but low extractable fractions (10–20%) still contain considerable amounts of labile copper (500–3,000 mg/kg), which may represent a potential ecological concern. The majority of these sediments were exposed to the acidic waters of the Bor and Bela Rivers, where the most mobile copper was likely already leached out. Conversely, 126 samples contained low total copper concentrations (<100 mg/kg), and although some of them exhibited relatively high percentages of mobile copper (up to 99.4%), the overall low copper content suggests that these locations are less likely to pose significant environmental risk despite the elevated copper availability.

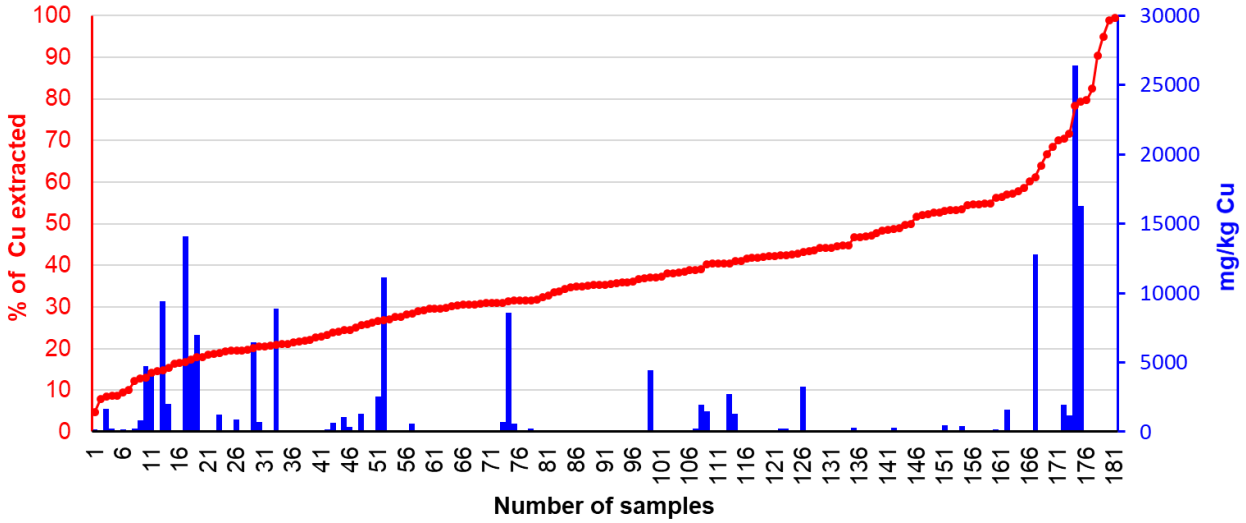

Figure 2. Total copper concentrations (blue bars) and percentages of HCl-extractable copper (red line)

4. CONCLUSION

This study demonstrates significant spatial variability in copper contamination and mobility within riverbed sediments of Eastern Serbia. While about 80% of samples contained less than 50% of 0.5 M HCl-extracted copper, indicating limited mobility, several pollution hotspots along the Timok River downstream of its confluence with the Bela River, exhibited extremely high total Cu concentrations (up to 26,400 mg/kg) combined with high extractable fractions (~80%). These locations were dominated by secondary, highly labile copper phases that can be readily mobilized under changing environmental conditions. The findings emphasize the need to assess both total metal concentrations and their chemical speciation when evaluating ecological risk and highlight the importance of site-specific management strategies.

ACKNOWLEDGEMENTS

This work was funded by the Ministry of Science, Technological Development, and Innovation of the Republic of Serbia under contracts no. 451-03-136/2025-03/200052 (Mining and Metallurgy Institute Bor) and 451-03-137/2025-03/200131 (Technical Faculty in Bor). The data was obtained in scope of the E-cube project from the SATREPS program.

REFERENCES

[1] S. Šerbula, V. Stanković, D. Živković, Ž. Kamberović, M. Gorgievski, T. Kalinović, Mine Water Environ. 35 (2016) 363-376.
[2] S. Đorđievski, D. Ishiyama, Y. Ogawa, Z. Stevanović, Environ. Sci. Poll. Res. 25 (2018) 25005-25019.
[3] R. Kubota, A. Ohta, T. Okai, Geochem. J. 48 (2014) 165-188.
[4] R. A. Sutherland, Appl. Geochem. 17 (2002) 353-365.
[5] A. Cuvier, L. Leleyter, A. Probst, J.-L. Probst, J. Prunier, L. Pourcelot, G. Le Roux, M. Lemoine, M. Reinert, F. Baraud, J. Geochem. Explor. 225 (2021) 106762.
[6] R. Devesa-Rey, F. Díaz-Fierros, M.T. Barral, J. Environ. Manag. 91 (2010) 2471-2477.
[7] S.R. Giancoli Barreto, J. Nozaki, E. De Oliveira, V.F. Do Nascimento Filho, P.H.A. Aragão, I.S. Scarminio, W.J. Barreto, Talanta 64 (2004) 345-354.

The 56th International October Conference on Mining and Metallurgy
22-25 October 2025, Bor Lake, Bor, Serbia
www.ioc.tfbor.bg.ac.rs

DOI: 10.5937/IOC25682D

Original scientific paper

CEROVO RIVER – ANNUAL MONITORING OF IMPACT OF THE CEROVO OPEN-PIT MINE

Miloš Đukić[1a], Stefan Đorđievski[1b], Sanela Vasiljević[1c], Dragana Adamović-Marković[1d], Ana Petrović[1e], Jelena Nikolić[2a], Vesna Stankov-Jovanović[2b]

[1]Mining and Metallurgy Institute Bor, Alberta Ajnštajna 1, 19210 Bor, Serbia,
[2] Faculty of Sciences and Mathematics – University of Niš, Višegradska 33, 18000 Niš, Serbia,
[1a] milos.djukic@irmbor.co.rs, 0000-0002-3307-4669
[1b] stefan.djordjievski@irmbor.co.rs, 0000-0003-1737-8766
[1c] sanela.vasiljevic@irmbor.co.rs, 0000-0001-6478-5335
[1d] dragana.adamovic@irmbor.co.rs, 0000-0003-3683-4122
[1e]ana.petrovic@irmbor.co.rs, 0000-0002-9815-6884
[2a] jelena.cvetkovic@pmf.edu.rs, 0000-0002-9351-331X
[2b] vesna.stankov-jovanovic@pmf.edu.rs, 0000-0001-7885-0476

Abstract

Cerovo River has been exposed to pollution associated with the operation of the Cerovo open-pit mine for decades and the long-term effects of mining have not been systematically quantified. In this study, annual monitoring was carried out from October 2023 to September 2024 at two strategic points: upstream (reference location, CR-1) and downstream in the zone of direct influence of the mine (CR-2). Key indicators of surface water quality, which have the greatest impact on the ecological classification of surface water, were analyzed: pH, concentration of SO_4^{2-}, Cu, Mn, and Fe. At the beginning of monitoring period, location CR-2 showed significant deviations in all tested parameters and was classified in class V - poor ecological status. After the implementation of remediation measures - redirection of acid mine drainage in February 2024, a statistically significant decrease in the concentrations of most pollutants was observed, improving the ecological status of the downstream location, whereby the ecological status was equal to the reference location, CR-1.

***Keywords**: Cerovo River, annual monitoring, acid mine drainage, Cerovo open-pit, Bor city*

1. INTRODUCTION

Since the opening of the Cerovo Cementacija 1 open-pit mine in 1991, more than 25 million tons of tailings have been accumulated until the mine was temporary closed in 2002 [1]. This amount of tailings represents a significant reservoir of sulfide minerals, which have the potential to generate long-term acid mine drainage (AMD). The AMD process is initiated by the oxidation of sulfides, resulting in the formation of sulfuric acid, which accelerates the leaching of heavy metals and the release of soluble sulfates. Consequently, this chemical contamination poses a long-term risk to the water quality of the Cerovo River. Cerovo River is a small watercourse in Eastern Serbia, flowing into the Valja Mare and continuing as the Krivelj River, thereby posing a high risk of spreading contamination throughout the entire watershed of the region.

A significant number of studies have investigated the chemical composition and the impact of acid mine drainage originating from the Cerovo open-pit mine [1–6]. However, comprehensive research analyzing the broader ecological consequences of this mine on the surrounding ecosystem has thus far been limited. Filimon et al (2021) reported on the effects of the mine on soils and plant species, while Đorđievski et al (2024) examined the impacts on the Cerovo River [1–6]. In their subsequent study Đorđievski indicated that the Cerovo River, based on 28-day monitoring downstream of the mine, was classified as Class V of water quality. This classification was attributed to persistently elevated concentrations of sulfates, copper and cadmium, with additional observations of increased pH values (over a 24-day period) and iron concentrations (throughout

28 days). These findings unequivocally confirmed the presence and intensity of chemical contamination in the watercourse.

The aim of this study was to determine the ecological status of the Cerovo River under the influence of the Cerovo open-pit mine and to evaluate the effects of remediation measures implemented during 2024. For this purpose, one-year monitoring was carried out at two strategic sites: upstream of the mine (reference location) and downstream in the zone of direct mining impact. Special attention was devoted to the ecological classification of surface waters based on key parameters: pH, sulfates (SO_4^{2-}), copper (Cu), manganese (Mn) and iron (Fe). This approach enabled a comparative assessment of upstream and downstream conditions, the evaluation of seasonal and quarterly variations, as well as the quantification of changes following the diversion of acid mine drainage flows carried out in February 2024.

2. EXPERIMENTAL

Annual monitoring of the Cerovo River quality was carried out during the period October 2023-September 2024. Sampling was conducted at two points: CR-1 – a reference location upstream of the Cerovo open-pit mine (44.181790 N, 22.021121 E), and CR-2 – a downstream location within the zone of direct mining impact (44.164412 N, 22.036635 E). Sampling was performed quarterly: Q1 (October–December 2023), Q2 (January–March 2024), Q3 (April–June 2024) and Q4 (July–September 2024). At location CR-1, samples were collected weekly throughout the study period, while at location CR-2 sampling was performed daily in the interval from October 9th to November 6th, 2023, followed by weekly sampling until the end of the monitoring period.

Water samples were filtered through "white tape" filter paper (Lab Logistics Group GmbH) to remove suspended particles and subsequently acidified with concentrated nitric acid (Zorka Šabac, Serbia). Determination of Cu, Mn and Fe was conducted by inductively couples plasma mass spectrometry (ICP-MS) NexION 1000 (Perkin Elmer, USA). All metal concentrations in this study are reported as total dissolved metal concentrations, although in natural river water these metals are predominantly present as dissolved ionic species, such as Cu^{2+}, Fe^{2+}/Fe^{3+}, and Mn^{2+}/Mn^{4+}, depending on local redox conditions. Quality control and data analysis were performed with the Syngistix software package.

A multielement standard solution containing Cu, Mn and Fe (AccuStandard, USA) was used for calibration, along with individual Re and Rh standards (AccuStandard, USA) as internal standards. Quality assurance was ensured using certifies standard reference material WP Trace Metals VHG-QWPTM-15 (VHGLABS, USA). The limits of quantification for Cu, Mn and Fe, were determined during the validation process: 1.07, 0.071 and 1.69 μg/L, respectively [7]. The pH measurements were determined in the field using a Thermo Scientific PC450 multiparameter instrument and the sulfate concentration was measured with a WTW Turb 550 IR turbidimeter using barium chloride as percipitand.

3. RESULTS AND DISCUSSION

The ecological status of the Cerovo River at sites CR-1 and CR-2 was assessed by comparing the measured values with the reference threshold values for pollutants in surface waters and sediments, as defined by national regulations („Službeni glasnik RS" br. 50/2012). Classification was carried out according to five categories (I-V), were Class I corresponds to excellent status, II to good, III to moderate, IV to poor and V bad ecological status [8].

Table 1. presents the results of the annual monitoring shown quarterly for both studied sites. The table provides mean values (average) and standard deviations (sd) for the analyzed parameters, for each quartal, at upstream (CR-1) and downstream (CR-2) sites of the Cerovo River.

Table 1. Quarterly average values of analyzed parameters (mean ± standard deviation) at upstream (CR-1) and downstream (CR-2) locations on Cerovo River

Parametar	Location	Q1	Q2	Q3	Q4
pH	CR-1	7.63±0.29	7.78±0.19	7.70±0.41	7.57±0.25
	CR-2	5.60±0.85	6.95±0.87	7.92±0.18	/
SO_4^{2-}, mg/L	CR-1	463.2±81.3	367.7±44.4	432.7±81.6	675.2±70.7
	CR-2	1321.4±391.8	679.0±258.4	496.8±85.8	/
Cu, µg/L	CR-1	35.8±24.2	27.9±14.2	27.8±17.9	5.1±1.3
	CR-2	21075.2±15221.7	4489.6±5337.3	122.3±36.3	/
Mn, µg/L	CR-1	150.3±16.0	122.7±13.5	105.6±33.4	331.9±120.0
	CR-2	4609.5±644.9	2535.5±1852.8	343.2±67.7	/
Fe, µg/L	CR-1	259.7±155.7	176.0±101.9	130.3±55.2	80.2±76.1
	CR-2	1680.1±1392.4	343.8±733.0	82.7±48.6	/

The height of each bar on Figure 1 represents the measured value of the parameter, while the bar color indicates the ecological class of the surface water: blue for Class I, green for Class II, yellow for Class III, orange for Class IV and red for Class V. Threshold values between surface water quality classes are shown as horizontal lines. Vertical axes are shown in linear scale, except for copper where logarithmic scale was used due to large differences in concentrations.

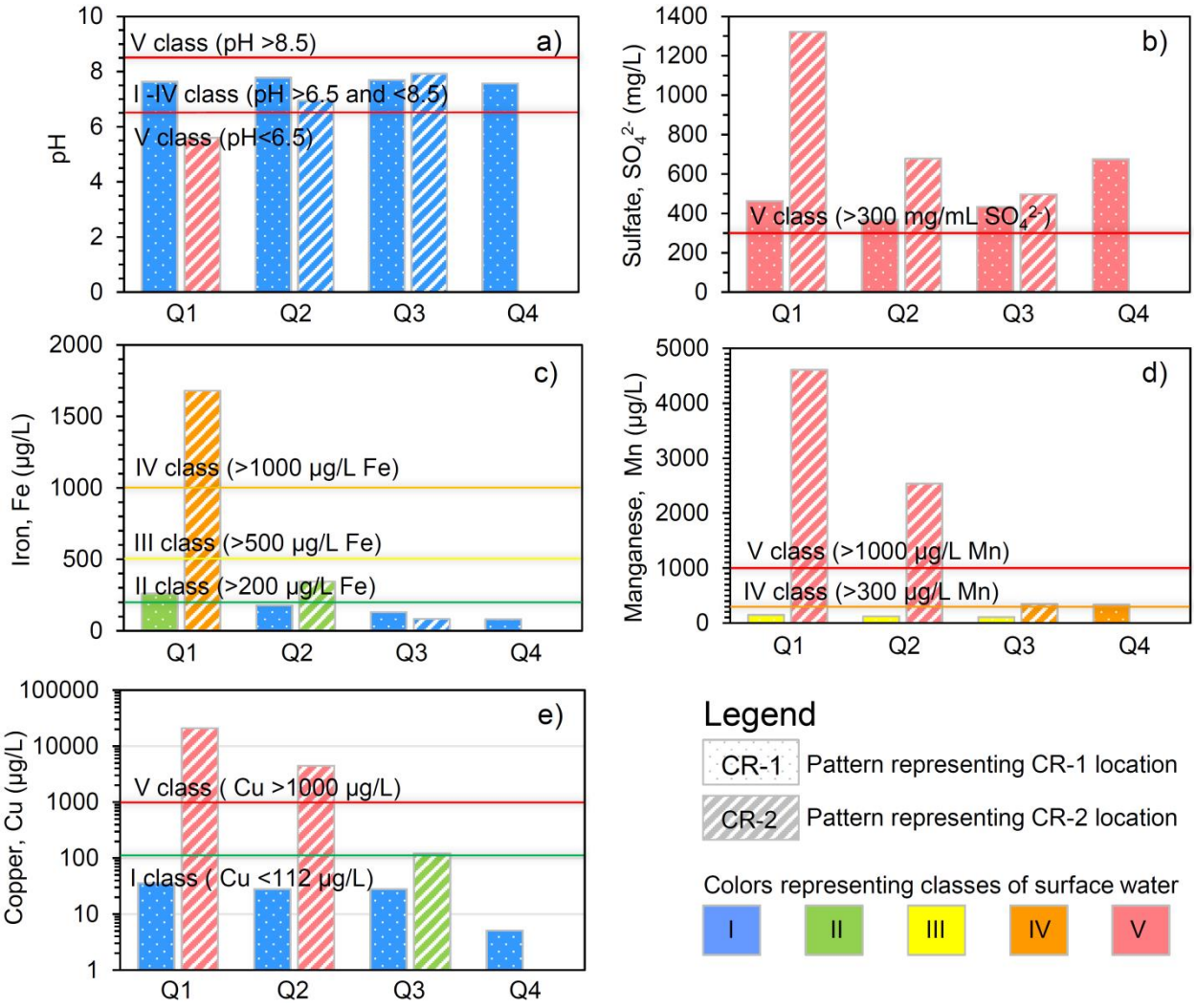

Figure 1. Variation of a) pH, b) SO_4^{2-}, c) Fe, d) Mn, and e) Cu across four quarters (Q1–Q4)

In Q1, at location CR-2, the Cerovo River was classified as Class V (poor ecological status) due to elevated concentrations of SO_4^{2-}, Cu, and Mn, as well as acidic pH values. Following the diversion of acid mine drainage flows in February 2024, a marked recovery of pH was observed during Q2 and Q3, and the water quality improved to Class I (good ecological status), indicating the cessation of active acid mine drainage inputs. Although SO_4^{2-} concentrations remained within Class V thresholds, they exhibited a substantial decrease, with Q3 levels approaching those measured at the upstream reference point (CR-1). Copper concentrations decreased by approximately fivefold in Q2 and by nearly 200-fold in Q3 compared to Q1, while Mn concentrations were reduced by about twofold in Q2 and became comparable to CR-1 values in Q3. A similar trend of Fe concentration equalization between upstream and downstream sites was also observed. During Q4, however, downstream monitoring could not be performed due to the drying of the river channel. Overall, the significant reductions in pollutant concentrations compared to Q1 indicate that the implemented wastewater management measures effectively mitigated the immediate impact of the open-pit mine on the Cerovo River ecosystem.

4. CONCLUSION

Annual monitoring of the Cerovo River clearly demonstrated the significant negative impact of the Cerovo open-pit mine on water quality, especially in terms of pH values and concentrations of sulfates and heavy metals. However, after the implementation of the remediation measure of wastewater diversion, a significant improvement in the ecological status of the downstream section was recorded, which in the final period reached the level of the reference site. This indicates the effectiveness of the applied remediation strategy.

ACKNOWLEDGEMENTS

This research was financially supported by the Ministry of Science, Technological Development and Innovation of the Republic of Serbia, contract numbers: 451-03-136/2025-03/ 20052 and 451-03-65/2025-03/200124. The data presented in this paper are obtained as part of the water monitoring project financed by the City of Bor, Serbia, contract number 404-951/2023-III/01.

REFERENCES

[1] Z. Stevanovic, M. Antonijevic, R. Jonovic, Lj. Avramovic, M. Bugarin, V. Trujic, J. Min. Metall. Sec. B Metall., 45 (1), (2009) 45-57.
[2] V. Stankovic, D. Bozovic, M. Gorgievski, G. Bogdanovic, M. Zikic, J Min Metall, JMM, 57 (A1), (2021) 33-42.
[3] M. Gorgievski, D. Božic, V. Stankovic, G. Bogdanovic, J. Hazard. Mater., 170 (2-3), (2009) 716-721.
[4] Lj. Obradovic, M. Bugarin, V. Marinkovic, Mining Engineering, 4 (2012) 191-196.
[5] M.N.Filimon, I.V. Caraba, R. Popescu, G. Dumitrescu, D. Verdes, L. Petculescu Ciochina, A. Sinitean, Int. J. Environ. Res. Public Health, 18 (4), (2021) 1516.
[6] S. Djordjievski, M. Djukic, A. Petrovic, D. Adamovic, J. Petrovic, Lj. Lekic, Proceedings of 31st International Conference Ecological Truth & Environmental Research - Ecoter'24, 18-21 June 2024, Sokobanja, Serbia
[7] M. Djukic, S. Djordjievski, S. Vasiljevic, A. Petrovic, E. Pozega, V. Stankov Jovanovic, In Proceedings-55th International October Conference on Mining and Metallurgy, 15 -17 October 2024 Kladovo, Serbia
[8] Regulation on limit values of polluting substances in surface water and groundwater and sediment and deadlines for their achievement ("Official Gazette of RS", No. 50/2012), https://pravno-informacionisistem.rs/SlGlasnikPortal/eli/rep/sgrs/vlada/uredba/2012/50/1/reg.

The 56th International October Conference on Mining and Metallurgy
22-25 October 2025, Bor Lake, Bor, Serbia
www.ioc.tfbor.bg.ac.rs

DOI: 10.5937/IOC25686S

Review paper

A REVIEW ON RECOVERY OF REEs AND RADIOACTIVE MATERIALS FROM PHOSPHOGYPSUM

Emine Sayılgan[1,2a], Patrick Zhang[2b]

[1] Engineering and Natural Sciences Faculty, Suleyman Demirel University, 32260, Isparta, Turkiye
[2] FIPR, Florida Polytechnic University, Bartow, Florida, USA
[1,2a] eminesayilgan@sdu.edu.tr, 0000-0002-6756-1545
[2b] jzhang@floridapoly.edu, 0000-0003-2762-3235

Abstract

Different types of and huge amount of wastes, residue and by-products are generated in worldwide. These wastes could be considered as flotation tails, concentrate, end-of-life products, phosphogypsum (PG), bauxite residue (red mud), mine tailings, metallurgical slags and industrial process residues from thermal treatment facilities. These kinds of different wastes may become inherently complex, heterogeneous and contain different kinds of metals, rare earth elements (REEs), radioactive elements and impurities. Recovery of these wastes, which are harmful to the environment and those with economic benefits, is very important in terms of both sustainability and protecting the environment and obtaining economic benefits. Therefore it could increase resource efficiency in the sense of a sustainable circular economy. In this paper, it was evaluated reviews studies about radionuclides contents of PGs, typical REE contents and recovery efficiencies with different experimental conditions.

***Keywords**: rare earth elements, radioactive elements, recovery, phosphogypsum*

1. INTRODUCTION

So many research has recently been conducted on the end-of-life products containing high concentrations of REEs, such as lamps or magnets, there is less attention has been paid to industrial landfilled stocks [1] such as PG. However, PG seems contain lower REE concentrations but have huge volume and considered a promising source of REES and also contains waste is of environmental concern due to the high content of metals, metalloids and radionuclides [1] and also various impurities such as residual acid (P2O5), fluorine compound [2-4]. In this regard, PG considered as a significantly value added component for both environmentally and techno-economic side due to REEs and radioactive elements content.

Natural gypsum contains small amount of impurities, but PG is accompanied by many impurities that come from the phosphate ore or formed by production process. Therefore, PG is not readily available to be unless the imprurities and radioactivities are reduced to the required accepted limits [5]. Two major disadvantages of PG were identified as its high content of both toxic elements and radioactivity and the negative effect of impurities on product quality [6].

The main environmental concern associated with PG in connection to radioactive contamination is the presence of the naturally occurring radionuclides, the ^{238}U decay series daughter products ^{226}Ra, ^{210}Pb and ^{210}Po. ^{226}Ra is considered to be the major source of radioactivity in PG and it is chemically analogous to calcium [7].

Table1 shows typical radionuclides composition of phosphogypsums.

Table 1 - Typical radionuclides composition of phosphogypsums

Source	^{235}U	^{238}U	^{226}Ra	^{228}Ra	^{232}Th	^{40}K	^{210}Pb	^{210}Po	Unit	References
Barreiro, Portugal	18.5	142	735				776			8
Egypt		164	482			72	418		Bq/kg	9
Bangladesh (fresh)			337				45	50	Bq/kg	7
Bangladesh (old)			295				39	45	Bq/kg	7
Bandırma, Turkey		9	22		1	11			Bq/kg	10
Poland			72.8-80.5			<20			Bq/kg	11
Spain		100	785				827		Bq/kg	12

The growth in global demand for the rare earth elements from 2020 to 2025 will lead to the opening of new mines or the search for an alternative source [13]. In this sense, PG emerges as an important resource. REEs normally contained in the phosphate rocks about 0.03 to 1.0 wt% [14] and PG has also relatively low REE content (~0.45%), however it seen as an anthropogenic source of REE and it has no costs for mining and disintegration of a natural raw material and recovery of valuable REEs and also radionuclides. Unlike metalloids and radionuclides, REEs show low mobility under environmental conditions [1]. Table 2 shows typical REEs composition of PGs.

Table 2 - Typical REEs composition of phosphogypsums

Source	Ca	P_2O_5	REE	Sr	Ce	La	Y	Nd	Unit	References
Russia	25	1.5	0.45	1.95	0.26	0.14	0.01	0.06	%	15
Tunisia			224.93		49.99	35.86	44.48	52.63	ppm	4
Poland					0.28-0.35	0.16-0.17	0.011-0.012	0.09	%	11

Recovery of REEs is challenging, because the elements are not found in pure form, they are in a complex form. Also, PG is usually obtained from phosphate rocks and solubility of REE-phosphates is low. Concentrated RRE minerals cannot be dissolved directly with water or mineral acids at ambient temperature. Only bastnasite mineral is partially dissolved in high concentration

hydrochloric acid solution. In order to dissolve the elements in RRE minerals, it may be necessary to convert them into soluble and easily obtained forms [15]. Nitric acid and HCl could show more effective for leaching than H_2SO_4 for the recovery of REES, but H_2SO_4 leaching was still industrially preferred due to economical reasons [14, 16] such as availiability in the system already [4] and cheaper than nitric acid. Generally, leaching of REEs with sulfuric acid provides about 30-40% [17] efficiency. However, these leaching yield could be differing for different types of wastes and methods.

2. CONCLUSIONS

Phosphogypsum contains different kinds of metals, rare earth elements (REEs), radioactive elements and impurities. Recovery of these wastes, which are harmful to the environment and those with economic benefits is very important in terms of both sustainability and protecting the environment and obtaining economic benefits. For this reason, it is necessary to conduct a detailed literature research on the subject. In this paper, it was evaluated reviews studies about radionuclides contents of PGs, typical REE contents and recovery efficiencies with different experimental conditions.

ACKNOWLEDGEMENTS

This study was a grant by The Scientific and Technological Research Council of Turkey (TUBITAK) as 2219 International Post Doctoral Research Fellowship Programme. Authors thank to Tubitak for supporting Emine Sayilgan for conducting this study.

REFERENCES

[1] C.R. Canovas, S. Chapron, G. Arrachart, S. Pellet-Rostaing., J. Clean. Prod., 219 (2019) 225-235.
[2] O.A. Karagoz, H. Oguz., Cem. Concr. Res., 34 (2005) 2079-2082.
[3] H. Taybi, C. Gasco, N. Navarro, A. Lopez-Delgado, M. Choura, F.J. Alguacil, F.A. Lopez., J. Environ. Prot., 2 (2011) 168-174.
[4] I. Hammas-Nasri, K. Horchani-Naifer, M. Férid, D. Barca., Int. J. Miner. Process., 149 (2016) 78-83.
[5] M.A. Aliedeh, N.A. Jarrah., Proceedings of the Sixth Jordanian Int. Chem. Eng. Conf., Amman, Jordan, 2012, 1-10.
[6] K. Layr, P. Hartlieb., Berg. Huettenmaenn. Monatsh., 164 (2019) 245-249.
[7] S. Ghose, B. Heaton., J. Environ. Sci. Public Health, 4 (2020) 184-196.
[8] M.J. Madruga, M.I. Prudencio, J.A. Gil Corisco, J. Mihalik, R. Marques, et al., Int. J. Waste Resour., 9 (2019) 363.
[9] H. El-Didamony, S. Abd-El-Aleem, M. Abd-El-Aziz., Ind. Ceram., 23 (2003) 19.
[10] N. Degirmenci., Constr. Build. Mater., 22 (2008) 1220-1224.
[11] K. Grabas, A. Pawelczyk, W. Stręk, E. Szeleg, S. Stręk., Waste Biomass Valorization, (2018) 1-13.
[12] M. Renteria-Villalobos, I. Vioque, J. Mantero, G. Manjon., J. Hazard. Mater., 181 (2010) 193-203.
[13] A. Masmoudi-Soussi, I. Hammas-Nasri, K. Horchani-Naifer, M. Ferid., Chem. Afr., 2 (2019) 415-422.
[14] X.S. Yang, D. Salvador, H.T. Makkonen, L. Pakkanen., Nat. Resour., 10 (2019) 325-336.
[15] I.S. Malyshev, S.V. Kirillov, E.V. Kirillov, G.M. Bunkov, M.S. Botalov, D.V. Smyshlyaev, V.N. Rychkov., AIP Conf. Proc., 2174 (2019) 020038.
[16] C. Erust, M.K. Karacahan, T. Uysal., Miner. Process. Extr. Metall. Rev., (2022) in press.
[17] T. Rödel, S. Kiefer, G. Borg., in Industrial Waste (H. Pöllmann, Ed.), De Gruyter, Berlin, 2021, Ch. 16, 505-540.

Industrial Management, Digitalization and Quality Control

The 56th International October Conference on Mining and Metallurgy
22-25 October 2025, Bor Lake, Bor, Serbia
www.ioc.tfbor.bg.ac.rs

DOI: 10.5937/IOC25691W

Review paper

INTEGRATED COMPUTATIONAL MATERIAL ENGINEERING PRACTICE PATHS BY CHANGSHA RUIRUI TECHNOLOGY: FROM CALPHAD TO PHASE FIELD AND CRYSTAL PLASTIC FINITE ELEMENT

Yufei Wang[1a], Xiaoyu Zheng[2a], Xiangyang Ying[2b], Qi Huang[2c], Xiong Shuai[2d], Changfa Du[2e], Ya Li[2f], Yingbiao Peng[1b], Yuling Liu[2g], Yong Du[2h]

[1] Changsha Ruirui Technology Co., Ltd. Changsha, Hunan Province, 410000, PR China
[2] State Key Laboratory of Powder Metallurgy, Central South University, Changsha, Hunan, 410083, PR China

[1a] 15655451323@163.com, 0009-0003-9874-5878
[2a] xiaoyu_zheng@csu.edu.cn, 0000-0002-1323-5306
[2b] xyanging@163.com, 0009-0007-8298-6342
[2c] qihuang0908@163.com, 0000-0001-7057-1720
[2d] 274011031@qq.com, 0009-0004-2286-2004
[2e] mathcfdu@163.com, 0009-0006-7828-4682
[2f] 203301017@csu.edu.cn, 0009-0001-8608-3489
[1b] pengyingbiao1987@163.com, 0000-0002-0590-6878
[2g] liu.yuling@csu.edu.cn, 0000-0001-9372-7011
[2h] yong-du@csu.edu.cn, 0000-0002-4187-3989

Abstract

This work presents a digital workflow and a suite of integrated software tools developed by Changsha Ruirui Technology Co., Ltd. for the design of metallic materials within the Integrated Computational Materials Engineering (ICME) framework. The platform seamlessly connects CALPHAD-based thermodynamic and thermophysical property calculations with phase-field microstructure simulations and crystal plasticity finite element analysis. Key in-house developed software—including ICALPHAD, CALTPP, MID-MESO, PRECALC, and CPCP—are introduced, emphasizing their interoperability and data transfer capabilities. The application of this integrated approach to an Al-Mg-Si alloy successfully predicted mechanical properties by accounting for critical microstructural features such as precipitates, texture, and grain size, demonstrating its significant potential for accelerating the development of advanced structural materials.

***Keywords**: ICME; multiscale modeling; software integration; microstructure; mechanical properties*

1. INTRODUCTION

Integrated Computational Materials Engineering (ICME) has emerged as a transformative paradigm in materials science, aiming to unify material design, manufacturing, and performance prediction through integrated multiscale modeling and simulation [1]. A cornerstone of ICME is establishing the "process-structure-property-performance" linkage. However, a significant challenge lies in effectively integrating disparate computational tools across various scales to ensure robust data transfer and theoretical consistency.

To address this challenge, a digital workflow was developed based on the "microstructure-performance correlation". It starts from scientific databases and integrates phase diagram thermodynamic calculation, thermophysical property calculation, phase field simulation, and crystal plasticity finite element calculation in sequence. For each computational stage, dedicated software tools were designed and developed. These developments focused not only on solving specific computational problems but also on ensuring theoretical connections and seamless data transfer between them, aiming to create a universal intelligent design platform for metallic structural materials, as depicted in Figure 1.

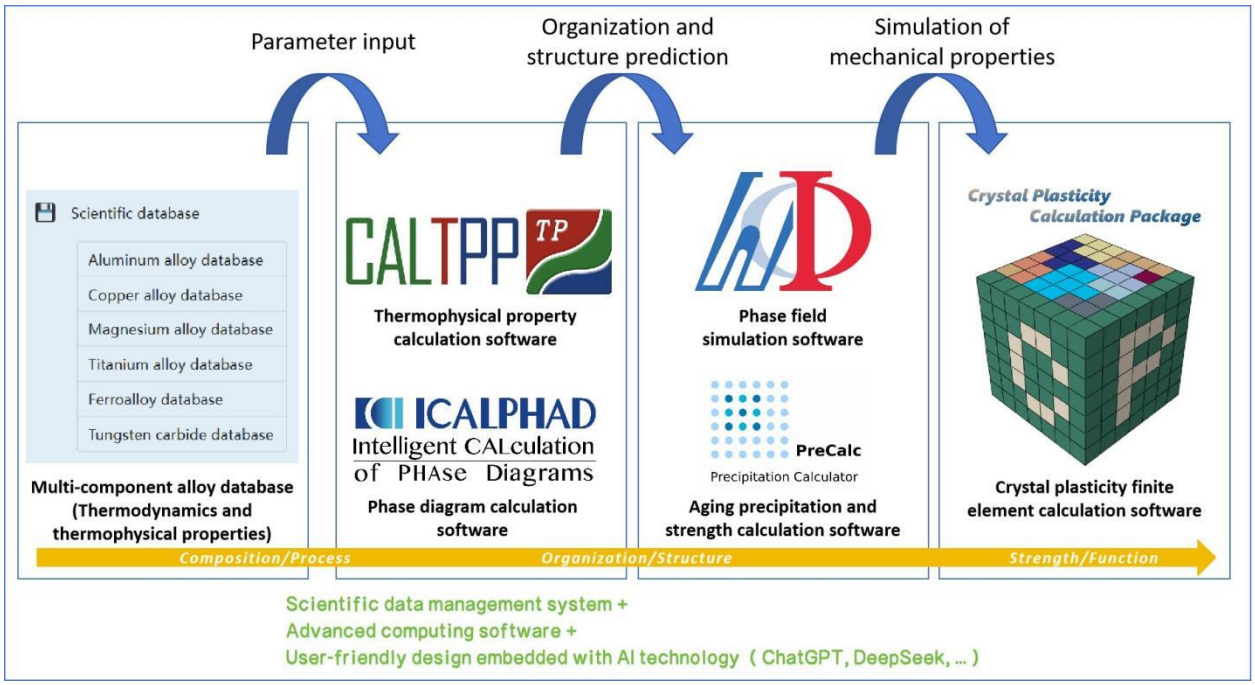

Figure. 1 ICME flowchart based on database and software

2. METHOD

The digital workflow consists of several sequentially linked computational modules, each implemented through dedicated software tools. The software in the Fig. 1 is briefly introduced as follows:

ICALPHAD (Intelligent CALculation of PHAse Diagrams) [2]:

A software tool based on the CALPHAD method for calculating phase diagrams and optimizing thermodynamic parameters of materials systems. It is used for predicting material properties and phase behavior in materials science and engineering. For more information, https://doi.org/10.1016/j.calphad.2025.102810.

CALTPP (CALculation of ThermoPhysical Properties) [3]:

Provide various thermophysical properties such as diffusion coefficient, interfacial energy, thermal conductivity, viscosity. For more information, https://doi.org/10.1016/j.jmst.2019.12.005.

MID-MESO (Microstructure Intelligent Design MESOscale) [4]:

An open-source phase-field solver package for simulating multiphase transformation and mechanical analysis of polycrystalline nanoparticles. For more information, https://github.com/Microstructure-Intelligent-Design.

PRECALC (PREcipitation CALCulator) [5]:

A computational software for age-hardening materials, integrating functions such as age precipitation and macroscopic strength and electrical conductivity prediction. For more information, https://doi.org/10.1016/j.jmrt.2024.05.145.

CPCP (Crystal Plasticity Calculation Package) [6]:

A research/teaching toolkit based on the crystal plastic finite element method. At present, it has successfully carried out calculation simulation on aluminum alloy, high-strength steel, cemented carbide, coating materials and so on. For more information, https://www.ams.org.cn/CN/10.11900/0412.1961.2024.00083.

3. RESULTS AND DISCUSSION

This series of software components involved in the workflow encompasses the transmission and circulation of various material information.

Starting from the database, phase diagram information and thermophysical data of alloy materials at specified compositions and temperatures are obtained through ICALPHAD and CALTPP software, which supports the subsequent phase field simulation (MID-MESO) and precipitation prediction (PRECALC).

After obtaining the exact state of the structure and microstructure, the mechanical property prediction under specified loads is conducted through crystal plasticity finite element software. Figure 2 shows the corresponding computational steps behind the combination of these software.

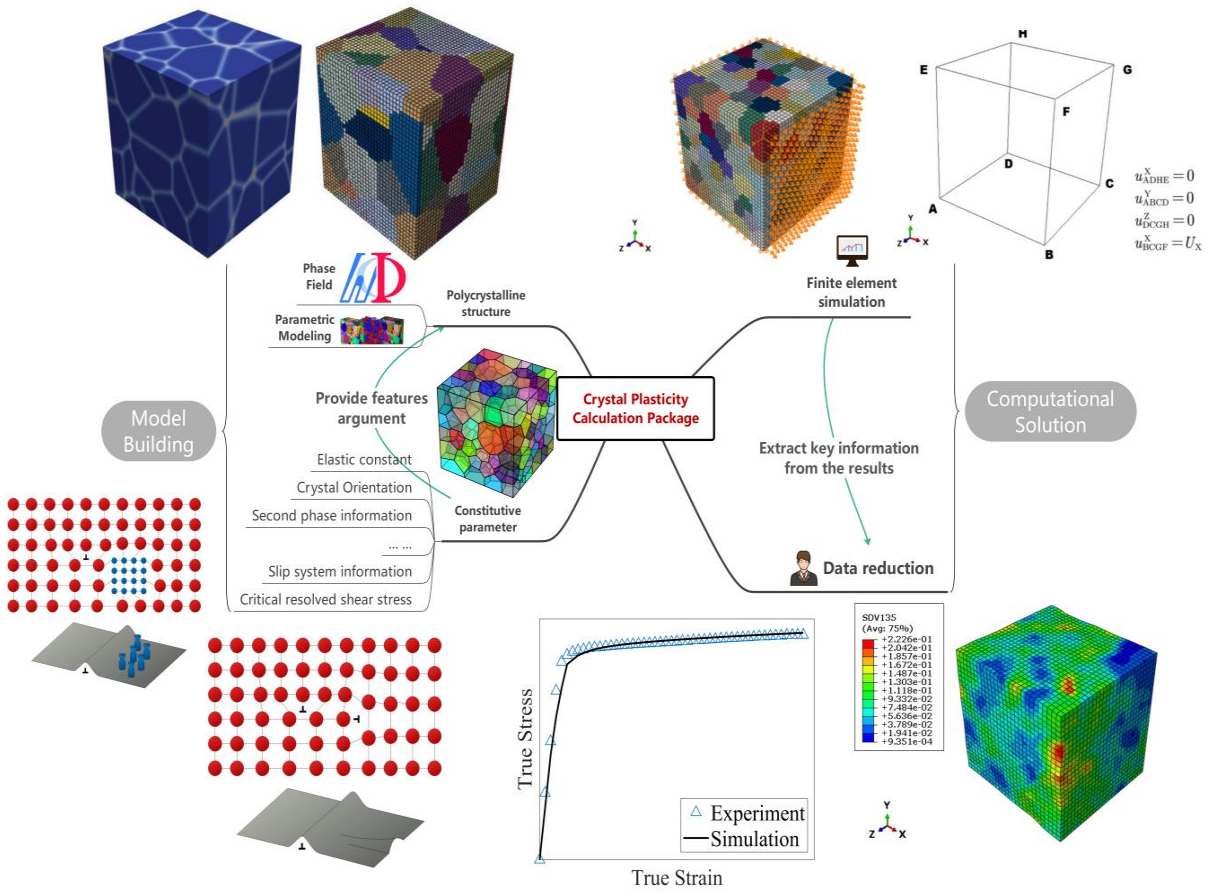

Figure. 2 Flowchart of crystal plasticity finite element calculation

Figure 3 demonstrates the application of this work in Al-Mg-Si alloys [6], where the strength and toughness are closely related to the precipitates.

Moreover, factors such as texture, grain size, and the content of solid solution phase also play significant roles in the mechanical properties of the material, which highlights the advantage of integrated computing in considering multiple microstructural features.

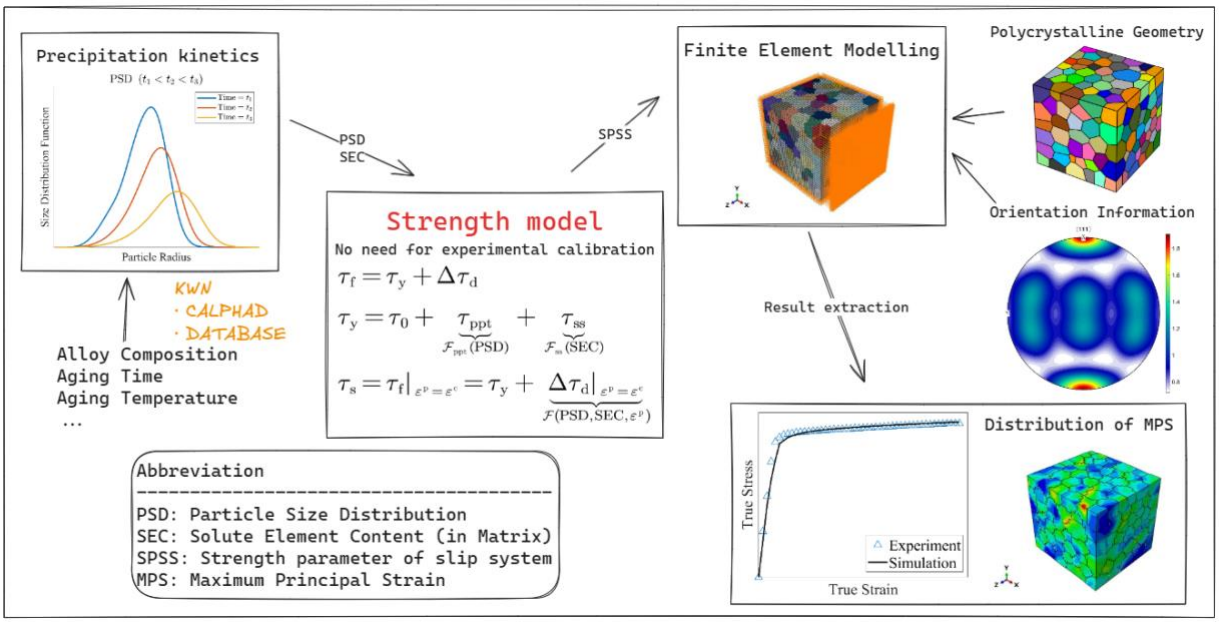

Figure. 3 Integrated calculation of aging precipitation, strengthening and crystal plasticity finite element simulation of Al-Mg-Si alloy

REFERENCES

[1] Y. Du, Schmid-Fetzer R, Wang J, et al. Computational Design of Engineering Materials[M]. Cambridge University Press, 2023.
[2] X. Zhang, L. Zhang, T. Fu, et al. Calphad, 89 (2025) 102810.
[3] L. Yuling, Z. Cong, D. Changfa, et al. JMST, 42 (2020) 229-240.
[4] Q. Huang, S. Daubner, D. Schneider, et al. Electrochim. Acta. 495 (2024) 144471.
[5] Y. Li, Q. Zeng, P. Retzl, et al. J. Mater. Res. Technol., 30 (2024) 7843-7855.
[6] X. Zheng, M. He, Q. Huang, et al. J. Mater. Sci., 59 (13) (2024) 5436-5449.

The 56th International October Conference on Mining and Metallurgy
22-25 October 2025, Bor Lake, Bor, Serbia
www.ioc.tfbor.bg.ac.rs

DOI: 10.5937/IOC25695F *Original scientific paper*

IS MINING AND QUARRYING MOST EFFICIENT AND PROFITABLE EXPORT SECTOR IN SERBIA? INSIGHTS FROM A MULTI-CRITERIA PERFORMANCE ANALYSIS

Aleksandra Fedajev[1a], Sanela Arsić[1b]

[1] Technical Faculty Bor, University of Belgrade, V.J. 12, 19210 Bor, Serbia
[1a] afedajev@tfbor.bg.ac.rs, 0000-0002-6974-6631
[1b] sarsic@tfbor.bg.ac.rs, 0000-0002-1957-566X

Abstract
The aim of this study is to compare the efficiency and profitability of companies in the mining and quarrying sector (Sector B) with those in other leading export sectors in Serbia, using a multi-criteria decision-making (MCDM) framework. The analysis is conducted using the Additive Ratio Assessment (ARAS) method, implemented under two distinct weighting scenarios: one assuming equal importance of all criteria, and other utilizing objective weights derived through the entropy method. The accounts receivable turnover ratio emerged as the most influential criterion, reflecting its critical role in indicating operational efficiency management, which is essential for sustaining competitiveness and profitability across export-oriented sectors. The findings reveal that the mining and quarrying sector demonstrates the most profitable and efficient export-oriented sector in Serbia, whereas the sector of professional, scientific, and technical activities is placed at the very bottom of the rankings. Additionally, a sensitivity analysis was conducted, which confirmed the robustness and consistency of the sectoral rankings across both scenarios.

***Keywords**: mining and quarrying sector, profitability, efficiency, Entropy method, ARAS method*

1. INTRODUCTION

The mining and quarrying sector holds a significant position within the Serbian economy, particularly due to its substantial contribution to export and GDP. Rich in mineral resources and strategically positioned in the regional market, Serbia has increasingly relied on the mining sector as a driver of economic growth, regional development, foreign direct investment, and infrastructure development, as well as solution for various social and demographic issues [1]. In recent years, the sector has attracted considerable attention due to major investments particularly in copper and gold extraction, underscoring its potential to strengthen Serbia' export competitiveness and economic resilience. Assessing the performance of this sector is therefore essential for understanding its current role and future trajectory within the national economy [2]. In broader perspective, evaluating the relative profitability and efficiency of different export sectors is crucial for accurately positioning each sector within the broader economic landscape. Such comparisons help highlight the competitive advantages and challenges of individual sectors, providing policymakers and investors with clearer guidance on where to focus support and resources in order to mitigate risks of business operations in these sectors [3]. However, comparative assessments that integrate multiple financial performance indicators using structured analytical frameworks remain scarce in the existing literature. The profitability and efficiency are especially important, since these companies operating in this sector are characterized by high investments and operating costs and significant oscillations of metals' prices in the global market [4, 5]. This study aims to fill that gap by applying multi-criteria decision-making (MCDM) approach to compare the efficiency and profitability of the mining and quarrying sector with nine other top-performing export sectors in Serbia. The evaluation is conducted using the Additive Ratio Assessment (ARAS) method under two weighting scenarios: one assuming equal importance of all criteria and the other employing objective weights derived from the entropy method. The

dual weighting approach enhances the objectivity and reliability of the results, while the inclusion of sensitivity analysis ensures the robustness of sectorial rankings.

2. RESEARCH METHODOLOGY

Multi-criteria decision-making methods (MCDM) are becoming more and more important in the assessment of sector performance, because they enable the simultaneous analysis of several criteria of different natures. The ARAS method enables the ranking of alternatives in relation to the optimal value [6, 7]. In contrast, the entropy method provides an objective way to determine the weights of the criteria, based on the variability of the information in the input data.

2.1. Selection of Criteria

The selection of evaluation criteria in this study was based on a review of relevant financial literature and previous empirical research on industrial performance assessment. Eight indicators were chosen, grouped into two main categories: efficiency ratios (accounts receivable turnover ratio - C1, average payment period - C2, total assets turnover ratio - C3, fixed assets turnover ratio - C4) and profitability ratios (operating profit margin – C5, net profit margin – C6, return on assets – C7, and return on equity – C8). The analysis is based on data provided by the Serbian Business Registers Agency, which annually publishes aggregated balance sheets and income statements at the sectoral level, incorporating summary data from all registered enterprises operating in each sector. Similar sets of indicators have been effectively used in previous studies focused on sectoral performance evaluation using MCDM techniques [8, 9].

2.2. Determination of weights

In order to determine the relative importance of each criterion in the evaluation model, two approaches were applied. In the first scenario, all criteria are assigned equal weights (0.125), assuming their equal importance in the evaluation process. In the second scenario, the weight coefficients are determined objectively (Table 1), using the Shannon entropy method, which uses the dispersion of the data to calculate the amount of information that each criterion contributes to the decision [10].

Table 1 - Caption of table

Criteria	**C1**	**C2**	**C3**	**C4**	**C5**	**C6**	**C7**	**C8**
Objective weight	0.159	0.123	0.121	0.108	0.136	0.121	0.119	0.112
Subjective weight	0.125	0.125	0.125	0.125	0.125	0.125	0.125	0.125

2.3. ARAS method

The ARAS (Additive Ratio Assessment) method evaluates and ranks alternatives by comparing their performance against criteria. Its application involves several phases [6]. The decision-making process begins with creating a matrix of alternatives and criteria, followed by normalization, weighting (using Shannon's entropy method), and calculation of utility values that represent each alternative's closeness to the ideal solution. Finally, the alternatives are ranked based on their overall utility, with the highest value placed first. This method has numerous advantages, which make it suitable for this type of analysis [11].

3. RESULTS AND DISCUSSION

The decision table shown in Table 2 consists of ten alternatives: A1 - Mining and quarrying; A2 – Manufacturing; A3 - Electricity, gas, steam and air conditioning; A4 – Construction; A5 - Wholesale and retail trade, repair of motor vehicles and motorcycles; A6 - Transportation and storage; A7 - Accommodation and food service activities; A8 - Information and communication; A9 - Professional, scientific and technical activities; A10 - Administrative and support service activities.

Table 2 - Decision table

Criteria	*Efficiency ratios*				*Profitability ratios*			
	C1	C2	C3	C4	C5	C6	C7	C8
min/max	*max*	*min*	*max*	*max*	*max*	*max*	*max*	*max*
A1	11.13	32.33	1.0	0.70	22.81	15.74	16.06	19.10
A2	5.69	63.32	1.9	0.91	5.42	3.59	4.90	7.15
A3	5.46	65.98	0.5	0.41	7.28	2.44	3.02	1.85
A4	5.25	68.61	1.2	0.55	7.05	5.43	3.90	8.54
A5	6.97	51.63	4.6	1.49	4.47	3.35	6.65	12.19
A6	6.87	52.44	0.9	0.69	4.99	2.77	3.43	4.35
A7	13.77	26.15	0.9	0.65	6.49	4.46	4.23	6.82
A8	4.29	83.83	1.0	0.64	10.82	6.09	6.93	10.04
A9	4.38	82.15	0.9	0.55	4.28	1.86	2.37	2.79
A10	4.62	77.91	1.9	0.98	6.38	4.63	6.24	11.11
wj (Scenario S_1)	0.125	0.125	0.125	0.125	0.125	0.125	0.125	0.125
wj (Scenario S_2)	0.159	0.123	0.121	0.108	0.136	0.121	0.119	0.112

In scenario S_1, where all criteria are equally weighted, each has a weight of (w_j=0.125). Scenario S_2 uses an entropy-based method to determine criterion weights. In this case, C_1 is the most significant criterion with (w_j=0.159), whereas the C_4 has the lowest importance with (w_j=0.108). This result underscores the significant role of liquidity and short-term efficiency indicators in assessing the overall performance of industrial sectors. Specifically, the high weight assigned to accounts receivables turnover ratio suggests that the speed of receivables collection substantially impacts the financial stability and profitability of a sector. These findings align with previous research emphasizing the dominance of liquidity-related criteria in multi-criteria performance evaluations. Studies by [12] and [13] have shown that liquidity ratios, especially turnover-based indicators, often exhibit a high explanatory power when comparing firm or sectoral efficiency across various MCDM methods. Furthermore, [14] highlighted that criteria reflecting short-term operational agility, such as receivables turnover or cash conversion cycle, tend to dominate in dynamic and capital-sensitive industries. The ARAS method is utilized to calculate the results needed for ranking Serbia's industrial sectors in both scenarios Table 3.

Table 3 - Ranking results of using ARAS method for scenarios S_1 and S_2

Alternative	Scenario S_1 *(Equal wj)*			Scenario S_2 *(Objective wj)*		
	S	K	Rank	S	K	Rank
A1	0.16	0.79	1	0.16	0.79	1
A2	0.07	0.36	6	0.07	0.36	6
A3	0.05	0.23	9	0.05	0.24	9
A4	0.07	0.34	7	0.07	0.34	7
A5	0.11	0.55	2	0.11	0.53	2
A6	0.06	0.29	8	0.06	0.30	8
A7	0.09	0.44	3	0.09	0.46	3
A8	0.08	0.38	5	0.08	0.38	5
A9	0.04	0.22	10	0.04	0.22	10
A10	0.08	0.40	4	0.08	0.39	4

The alternative A1 is the best alternative in both scenarios, due to highly efficient turnover and profitability indicators. The mining of precious metals and minerals is often shown to be stable and profitable when the processes are optimally organized [15]. On the other hand, the A9 achieves the weakest performance in both scenarios. Given that this sector often has high fixed asset costs and perhaps slower monetization, it ranks lower on criteria such as ROE or operating profit margin.

In order to verify the stability and robustness of the sector ranking, a sensitivity analysis was carried out using COCOSO, CODAS, COPRAS, EDAS, MABAC, VIKOR and TOPSIS methods. The obtained results are present in Figure 1.

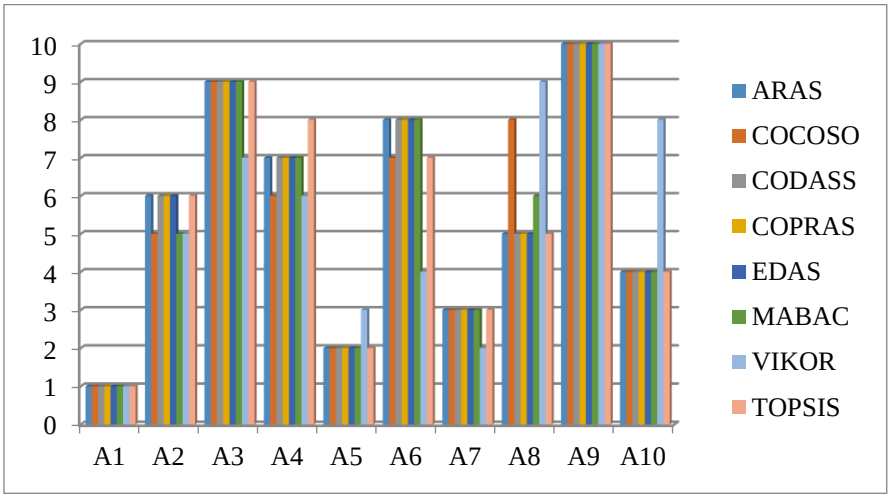

Figure 1 - Sensitive analysis

As shown in the Figure 1, the ranking positions of certain alternatives (A1–A10) remain relatively stable across different methods. Alternative A1 consistently ranks first in all methods, demonstrating a high level of robustness and consistency in the assessment.

4. CONCLUSION

The mining and quarrying sector has been gaining increasing importance in the Serbian economy, particularly over the past decade, due to its contribution to export competitiveness of national economy, regional development, and investment attractiveness. A precise assessment of the sector's efficiency and profitability is therefore essential for guiding strategic decisions made by investors and policymakers. This study employed a combined Entropy-ARAS methodology to evaluate and rank ten leading export-oriented sectors in Serbia. The results indicate that the mining and quarrying sector achieves the highest overall performance, demonstrating superior financial efficiency and profitability compared to other major export-oriented sectors. On the other end of the spectrum, the sector of professional, scientific, and technical activities are ranked at last position. Among the evaluated indicators, the accounts receivable turnover ratio was identified as the most influential, emphasizing the critical role of operational efficiency in shaping overall sector performance. Sensitivity analysis further confirmed the consistency and robustness of the rankings across both weighting scenarios. Although the findings provide useful insights, they are limited by the use of aggregated financial data, and excluding dimensions such as innovation, environmental impact, and workforce productivity. Future research should broaden the scope by including non-financial and sustainability criteria, applying additional MCDM techniques, and using multi-year data to capture sectoral dynamics more comprehensively.

ACKNOWLEDGEMENTS

The research presented in this paper was carried out with the financial support of the Ministry of Education, Science and Technological Development of the Republic of Serbia within the framework of financing scientific research work at the University of Belgrade, Technical Faculty in Bor, in accordance with the contract with registration number 451-03-137/2025-03/200131.

REFERENCES

[1] M. Ignjatović, S. Miletić, Min. Metall. Eng. Bor, (3-4) (2018) 87-96.
[2] R. Tosovic, Int. J. Res.-Granthaalayah, 4 (10) (2016) 46-52.
[3] A. Zielińska-Chmielewska, J. Kaźmierczyk, I. Jaźwiński, Agronomy, 12 (1) (2021) 92.

[4] D. Kržanović, M. Ljubojev, I. Jovanović, N. Vušović, Min. Metall. Eng. Bor, (3-4) (2017) 51-58.
[5] M. Čavlin, J. V. Tankosić, Z. Mirković, Econ. Theory Pract., 15 (3) (2022) 56-73.
[6] E. K. Zavadskas, Z. Turskis, Technol. Econ. Dev. Econ., 16 (2) (2010) 159-172.
[7] N. Liu, Z. Xu, Int. J. Intell. Syst., 36 (7) (2021) 3524-3565.
[8] A. Yazdani-Chamzini, S. H. Yakchali, E. K. Zavadskas, Econ. Res.-Ekon. Istraž., 25 (4) (2012) 869-904.
[9] S. Rezaei, N. Ahmad, M. Jamal, Financ. Innov., 9 (1) (2023) 34.
[10] E. K. Zavadskas, Z. Turskis, S. Kildienė, Technol. Econ. Dev. Econ., 22 (2) (2016) 165-200.
[11] S. S. Goswami, D. K. Behera, Mater. Today: Proc., 38 (2021) 2256-2262.
[12] M. M. Delgado, D. Hillier, D. Marques, J. Corp. Financ., 50 (2018) 287-307.
[13] A. Mardani, E. K. Zavadskas, Z. Khalifah, A. Jusoh, Econ. Res.-Ekon. Istraž., 28 (1) (2015) 516-571.
[14] G. Kou, D. Ergu, Y. Chen, C. Lin, Technol. Econ. Dev. Econ., 27 (1) (2021) 22-47.
[15] H. Yu, I. Zahidi, C. M. Fai, D. Ø. Madsen, Environ. Sci. Eur., 37 (1) (2025) 93.

The 56th International October Conference on Mining and Metallurgy
22-25 October 2025, Bor Lake, Bor, Serbia
www.ioc.tfbor.bg.ac.rs

DOI: 10.5937/IOC25700S

Original scientific paper

THE PATH TO BETTER EDUCATION OF ENGINEERS USING OPEN DATA - A PRACTICAL EXAMPLE IN THE REPUBLIC OF SERBIA

Predrag Stolić[1a], Zoran Jovanović[2a], Željko Mravik[2b], Marko Jelić[2c], Sonja Jovanović[2d], Aleksandra Milosavljević[3a]

[1] University of Belgrade - Technical Faculty Bor, V.J. 12, 19210 Bor, Serbia
[2] University of Belgrade - "Vinča Institute for Nuclear Sciences - National Institute of the Republic of Serbia", Mike Petrovića Alasa 12-14, 11351 Vinča, Belgrade, Serbia
[3] Mining and Metallurgy Institute Bor, Alberta Ajnštajna 1, 19210 Bor, Serbia
[1a] pstolic@tfbor.bg.ac.rs, 0000-0002-2574-4765
[2a] zjovanovic@vin.bg.ac.rs, 0000-0003-1727-4852
[2b] mravik@vin.bg.ac.rs, 0000-0003-2327-5165
[2c] marko.jelic@vin.bg.ac.rs, 0000-0003-3723-4313
[2d] sonja.jovanovic@vin.bg.ac.rs, 0000-0003-3577-5060
[3a] alekandra.milosavljevic@irmbor.co.rs, 0000-0003-3841-7357

Abstract
This paper presents a real-world case of using open data to improve learning outcomes in the education of future graduate engineers based on the use of open data in synergy with an open API to collect real-time data. This enables students to acquire knowledge based on real-world data rather than relying on artificially generated datasets. Such an approach allows students to encounter real-life examples during their studies and to become familiar with the entire process - from data collection at the source, through storage, filtering, and other processing steps, to obtaining meaningful and usable final results.

***Keywords**: Higher Education, Octave, Open API, Open Data, Python*

1. INTRODUCTION

Today, education entails, among other things, preparing students to work in data-driven environments [1], and more recently there are growing need for using project-based learning approaches for improving students skills and better preparation for real-world problem solving [2-4]. There is also a growing need to develop competencies through appropriate AI approaches guided by relevant principles and rules [5]. Many of these involve developing own infrastructure for generating data intended for student education, as well as leveraging advancements in the field of AI, either as a standalone solution or as a complementary approach to the aforementioned methods [6].

However, these solutions are not without existing issues, nor those expected to emerge as more significant challenges in the future, affecting users across various domains, including higher education. Emerging technologies, where AI has become an indispensable component, raise new concerns regarding the reliability of data to be used in the coming years. This is largely due to the growing prevalence of synthetic data, generated by AI itself, which introduces various risks such as data pollution, bias, lack of transparency, and related issues [7–11]. Moreover, practical implementations are already encountering certain complexity-related challenges that are likely to persist for some time, particularly during transitional periods [12].

In line with the above, in the following sections of the paper, a potential solution aimed at overcoming the aforementioned challenges will be presented. This solution is based on well-established and widely adopted techniques related to the use of open data sets. It fully relies on the application of the FAIR principles (Findability, Accessibility, Interoperability, and Reusability) in the use of digital assets [13]. The proposed solution was implemented using resources available in

the Republic of Serbia and was applied in the education of students through teaching processes within the courses Process Measurement Technique and Automation of Technological Processes at the University of Belgrade - Technical Faculty in Bor [14].

2. DATA ACQUISITION

On the official Open Data Portal of the Republic of Serbia [15], a variety of open data sets can be found, which can be used in higher education to familiarize students with different forms of processing real data, whether it involves data clustering, extracting subsets, statistical analysis, or other activities. However, students are not typically introduced to the initial stages of the process, such as data acquisition and storage. This raises the question of how to leverage open data in a way that allows students to be involved in the entire process, from data generation and acquisition from source to their processing and the presentation of results at the destination. The aforementioned is achievable if there is a certain mechanism, typically in the form of an appropriate API, that enables the proper collection of data considered to be open data.

Serbian Environmental Protection Agency (SEPA) has a system for real-time air quality monitoring based on data obtained from the National Network of Automatic Air Quality Monitoring Stations [16]. Recently, an OpenData API has been made available, allowing individuals to collect hourly air quality data. Since this is a publicly available service and accessible data, there are no barriers for using it in the teaching process. It is important to note that these are hourly data from the corresponding measurement stations. The goal is purely to train students to work with real-time, real-world data. The Air Quality OpenData API represents the aforementioned appropriate API for accessing the open data system. The entire system is documented through publicly available documentation [17], as shown in Figure 1.

The data is distributed to end users in the well-known JSON format via the API. This has enabled the development of appropriate software for students, which, thanks to this API, will collect real-time data for a specified time interval. For student purposes, the interval is defined on a daily basis and can range from a minimum of 1 to a maximum of 30 days. The data collection is limited to these time intervals in accordance with the practical requirements for conducting hands-on work with students within a single semester. Therefore, the maximum period is more than sufficient for introducing students to the entire process and obtaining an adequate data set for further work.

The software is written in Python, with data storage performed locally within an appropriate Excel file. The software allows, in addition to selecting the data collection time interval, the choice of the specific measurement station from which the data will be collected, as well as which data will be gathered. The software does not require significant resources for use and is not complex; instead, it has been maximally simplified to ensure better understanding and usability by students. It is worth noting that the software has been developed to be cross-platform for computers, with corresponding versions available for Windows, macOS, and Linux platforms. Therefore, there are no obstacles to its use in terms of platform targeting. There is also the potential for developing similar software for mobile operating systems like Android, but such functionality has not yet been implemented.

Protective functions have also been implemented in the software to prevent the occurrence of certain errors. For example, there is a safeguard mechanism that prevents the same hourly value from being read and recorded multiple times. In the event of network issues, the software also includes specific procedures that attempt to retrieve the previous hourly value at ten-minute intervals. If unsuccessful before the arrival of the new hourly value, it proceeds with the new value and records an empty field for the missing one.

3. DATA PROCESSING

Data acquisition and storage are important parts, but it is essential to complete the process with further data processing and the extraction of relevant conclusions from the data. The software allows students working with data obtained in real-time and from real, dynamic environment, rather than working with generic data sets that are typically used and often fail to adequately represent the environment. An example of a code snippet used by students is shown in Figure 2.

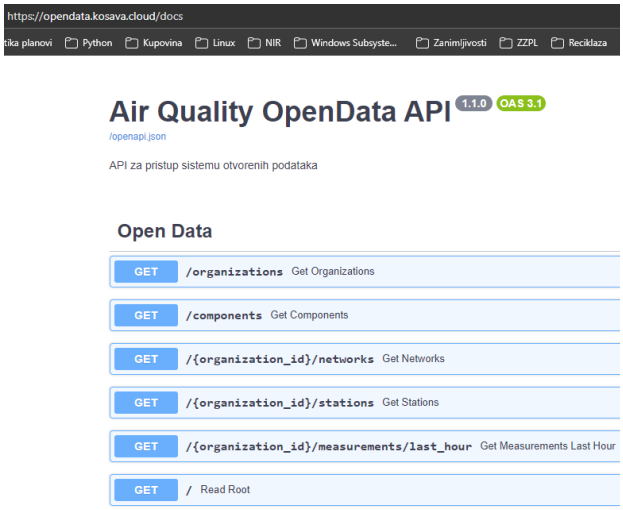

Figure 1. Official documentation for using Air Quality OpenData API

```
#PRORACUN DNEVNE ANALITIKE

i = 1;
j = 1;
while (i <= 720)
   k=1;
   while k<=24
     tmp1(k) = Beo_SG_CO(i);
     tmp2(k) = Beo_NB_CO(i);
     tmp3(k) = Beo_M_CO(i);
     i=i+1;
     k=k+1;
   endwhile
   tmp1 = tmp1(~isnan(tmp1));
   if (~isempty(tmp1))
      sr_vr_Beo_SG_CO(j)= mean(tmp1);
      std_Beo_SG_CO(j) = std(tmp1);
      std_sr_vr_Beo_SG_CO(j) = std_Beo_SG_CO(j)/sqrt(numel(tmp1));
      med_Beo_SG_CO(j) = median(tmp1);
   else
      sr_vr_Beo_SG_CO(j)= NaN;
      std_Beo_SG_CO(j) = NaN;
      std_sr_vr_Beo_SG_CO(j) = NaN;
      med_Beo_SG_CO(j) = NaN;
   endif
```

Figure 2. Part of code for data analysis written in Octave programming language.

In further work, students use the data set from the corresponding generated Excel file. In the considered case, students learn about further data processing using the Octave, which is highly suitable for use in the academic community. This is due to its math-oriented syntax and its appropriate visualization methods for both two-dimensional and multi-dimensional data representation. Additionally, in line with the aforementioned cross-platform orientation of the entire solution, Octave is also available in free versions for Windows, macOS, and Linux platforms, providing students with a certain level of platform independence.

Through this approach, students are trained to extract values from the obtained Excel file, which contains the collected data, and to format and represent these values appropriately for further manipulation and processing by the computer. Students are also taught how to appropriately handle missing values, as well as improperly represented values (e.g., in this case, the appearance of so-called Not-a-Number or NaN values), by using suitable approaches and functions (such as checks with functions like isempty, isnan, and similar). Then, students' skills are directed toward recognizing patterns in the automated data processing and making the data processing faster and more optimal in various aspects of the analysis. Regarding the calculation of specific parameters and drawing relevant conclusions from the obtained real data, students primarily perform basic statistical analysis on the data: calculating the mean, median, deviations, standard deviation, maximum and minimum values, classes, frequencies, histogram representations, and similar tasks. Finally, students are trained to record the results of the processing back into a separate Excel file locally, to maintain the consistency of the original data set with real values.

4. CONCLUSION

It is possible to train students to work in real conditions using real data without additional investments in infrastructure or implementing complex solutions. Moreover, in addition to utilizing open data access, Free and Open Source Software (FOSS) solutions were employed, meaning that the implementation of the entire system does not require significant financial

investment. Additionally, given its public availability and the software licensing, which allows for free use and redistribution, there are no legal barriers to its use. In this regard, it can be said that the proposed solution is sustainable for use in the academic domain. The results of applying such a system are yet to be seen, as the entire system is currently in the pilot phase.

ACKNOWLEDGEMENTS

This research was supported by the Science Fund of the Republic of Serbia, grant No. 6706, Low-dimensional nanomaterials for energy storage and sensing applications: Innovation through synergy of action – ASPIRE *and by the Ministry of Science, Technological Development and Innovation of the Republic of Serbia (contracts No. 451-03-137/2025-03/200131, 451-03-136/2025-03/200017 and 451-03-136/2025-03/200052)*

REFERENCES

[1] T. Mucci, What is data-driven decision-making?, IBM, 2024. https://www.ibm.com/think/topics/data-driven-decision-making
[2] R. Indiwara, J. Educ. Technol., 3 (1) (2025) 85–95.
[3] F.N. Kausar, The Critical Review of Social Sciences Studies, 3 (2) (2025) 2903-2916.
[4] S. Pandey, H. Gaikwad, S. Ghawshinde, JEET, 39 (2025) 34–43.
[5] Policy guidance on AI for children: Recommendations for building AI policies and systems that uphold child rights (Version 2.0), UNICEF, 2021.
[6] P. Stolić, Z. Jovanović, S. Jovanović, Ž. Mravik, M. Grujičić, M. Jelić, Book of proceedings of the 1st International Scientific Conference Education and Artificial Intelligence (EDAI 2024), November 29-30, Vranje, Serbia, 2024.
[7] R. Kniaz, The iNcoming Tidal Wave of Data Pollution in AI, Forbes, 2023. https://www.forbes.com/sites/robkniaz/2023/05/09/the-incoming-tidal-wave-of-data-pollution-in-ai/
[8] X. Xing, F. Shi, J. Huang, et al., Nat. Mach. Intell., 7 (2025) 172–180.
[9] E. Ntoutsi, P. Fafalios, U. Gadiraju U, et al., WIREs Data Mining Knowl Discov, 10 (3) (2020) e1356.
[10] A. Arora, M. Barrett, E. Lee, E. Oborn, K. Prince, Inf. Organ., 33 (3) (2023) 100478.
[11] T. Wiehn, S&S, 22 (4), 2024, 472-476.
[12] G. Vial, J. Jiang, T. Giannelia, A. F. Cameron, MIT SMR, 62 (2) (2021) 47-53.
[13] M.Wilkinson, M. Dumontier, I. Aalbersberg, et al., Sci Data, 3 (2016) 160018.
[14] Study Program: Mining Engineering, University of Belgrade - Technical Faculty in Bor, 2023, https://www.tfbor.bg.ac.rs/mining-engineering
[15] Open Data Portal of the Republic of Serbia, https://data.gov.rs
[16] National Network of Automatic Stations for Air Quality Monitoring, Environmental Protection Agency, Ministry of Environmental Protection, Republic of Serbia, 2015.
[17] Air Quality OpenData API, https://opendata.kosava.cloud/docs

The 56th International October Conference on Mining and Metallurgy
22-25 October 2025, Bor Lake, Bor, Serbia
www.ioc.tfbor.bg.ac.rs

DOI: 10.5937/IOC25704V

Review paper

NDT METHODS FOR MONITORING DEGRADATION OF REFRACTORY LINING FOR BLAST FURNACE AND CONVERTER

Tatjana Volkov Husović[1a], Ana Alil[2a], Sanja Martinović[2b]

[1] Faculty of Technology and Metallurgy, University of Belgrade, Karnegijeva 4,Belgrade, Serbia
[2] Institute of Chemistry, Technology and Metallurgy-National Institute of the Republic of Serbia University of Belgrade, Njegoševa 12, Belgrade, Serbia

[1a] tatjana@tmf.bg.ac.rs, 0000-0002-2667-5802
[2a] ana.alil@ihtm.bg.ac.rs, 0000-0001-7153-0621
[2b] sanja.martinovic@ihtm.bg.ac.rs, 0000-0001-8040-407X

Abstract

Refractory materials are most often used as walls of various devices in metallurgy that, as a rule, work at high temperatures. Devices in which refractory materials are installed can work continuously and discontinuously. Monitoring the behavior of refractory material in working conditions is very important, because it affects the quality of the material produced in the device, as well as the operation of the device itself. Part of the control of the refractory wall is performed during regular and extraordinary repairs of the device. The paper will present various methods for monitoring the properties of refractory walls during work in the iron and steel industry.

***Keywords**: refractory lining, monitoring, NDT methods*

1. INTRODUCTION

Refractory degradation is the primary cause of significant overhauls and relines in metallurgical and process vessels. This is why it is necessary to know the state of the refractory lining in furnaces and process vessels. Brick gaps may allow liquid metal or chemical leaks to penetrate, and a significant breach may cause a run-out, in which an unmanageable amount of molten material or undesirable chemicals spills into the environment, necessitating costly repairs and replacements as well as most importantly prolonged vessel downtime. Tons of refractory materials are dumped in landfills every year. Recently, there has been an attempt to recycle the refractory materials and repurpose them for different use [1-5]. However, a significant amount of refractories are impregnated with dangerous and aggressive compounds that have gone into the refractory pores from the process host and are unable to remove. Therefore, expensive and stringent monitoring systems are needed in landfills that contain refractory waste materials to ensure that hazardous, unstable substances won't seep into groundwater systems. Therefore, it would be ideal to reduce the amount of contaminated refractory debris at the source, through extending the campaigns for refractory lining. The NDT methods that have been applied to the inspection and monitoring of metallurgical furnaces and process vessels are briefly reviewed in the section that follows. These consist of discrete measurements like temperature analysis, infrared thermography, radioactive tracing, and refractory sounding, based on electromagnetic radar systems, magnetic-based systems, low frequency pulse ultrasonic, Acoustic Ultrasonic-Echo, and conventional thermocouple or fiber optic data. Additionally, the acoustic emission approach can be used as a continuous, long-term refractory monitoring method.

2. NON DESTRUCTIVE METHODS FOR BLAST FURNACE

Using mathematical models based on thermocouples and process-related furnace temperature measurements is the most popular method for figuring out the remaining refractory thickness in a furnace [2]. The precision and forecasting of heat transfer models and computational fluid dynamics (CFD) using finite element analysis (FEA) and other numerical techniques are predicated on the precision of the temperature data, the assumptions, the uniformity, and the accuracy of the thermal characteristics in the inner hot face, skull, and refractory. Although the thickness profiles produced by the mathematical models are essential and typical, errors are always produced when relying solely on temperatures and homogeneous parameters for heterogeneous media.

The use of ultrasonic waves to identify the remaining refractory lining is another developed method. Since the frequency of ultrasonic waves is higher than 20 kHz, their wavelengths are modest and their frequencies are typically set at the frequency of transmission. Because of their high frequencies, ultrasonic waves have a shallow penetrating depth. Furthermore, the ultrasonic waves attenuate quickly due to temperature, the multi-layered vessel cross section, and the heterogeneous refractory material properties. At most, a high energy pulser with a voltage between 2,000 and 10,000 volts or an extremely powerful energy source are needed.

Another very important issue with the ultrasonic wave is that the wave path “bends” due to high temperatures. This means that the reflections from the refractory hot faces will not echo directly back to the source. This deviation angle depends on the signal frequency, medium material properties, and temperature of the hot face [3-12].

The differences between ultrasonic and acousto ultrasonic-echo (AU-E) techniques are the followings:

- Impact produced Compared to ultrasonic pulses produced by piezoelectrics,

- AU-E pulses have a higher energy.
- Ultrasonic transmissions are narrowband, whereas AU-E signals are broadband.
- Several reflections from the surfaces aid in determining the refractory in the AU-E approach parameters, while numerous echoes and ultrasonic ringing are regarded as noise.

-The low frequency displacement Heat does not cause AU-E signals to bend, but ultrasonic waves do.

The most thorough method of keeping an eye on the status of the refractory liner in an operational blast furnace would be to combine thermal modeling based on the furnace temperature readings with a stress wave propagation methodology.

2.1. Ultrasonic

The mid-1980s saw the introduction of low frequency "Ultrasonic Pulse Velocity" (UPV) technologies like PUNDIT and V-Meter for assessing refractory quality. A refractory with a predetermined thickness is positioned between a transmitting and receiving transducer at opposite ends of the refractory sample using UPV systems. In general, low porosity, high density, and a high modulus of elasticity are indicated by high ultrasonic wave speed. In order to detect the thickness of refractory in a running furnace, "Ultrasonic Pulse-Echo" (UPE) systems are necessary. The transducers used for transmission and reception are positioned on the same surface in UPE systems. There should be very little space between the transducers used for sending and receiving. Parker et al. [13] showed that while the acoustic impedance in liquid is usually 13–15% lower than for a solid refractory or molten metal, the interface between the two produces a distinct reflecting surface accumulation, indicating that the wall is reflecting at least 10% of the waves. They showed

in their research that temperature and porosity cause a significant amount of ultrasonic energy to attenuate within the solid refractory. As the sample was heated to higher temperatures, a decrease in the amplitude of reflected ultrasonic signals was observed. The travel route of an ultrasonic waveform in a solid is likewise influenced by temperature [14]. The longitudinal or P-wave path widens with increasing temperature, leading to increased attenuation and a shift in the reflection angle.

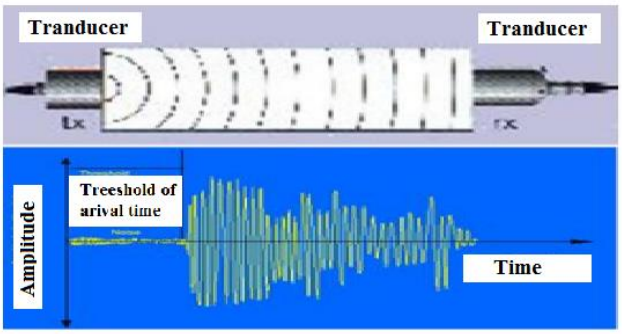

Figure 1. Ultrasonic through transmission method to determine wave speed in refractories and evaluate their QA based on longitudinal (P-wave) speed, dynamic modulus of elasticity and Poisson's ratio [7]

2.2 Acousto Ultrasonic-Echo (AU-E) Technique

In order to quantify the refractory thickness in operational metallurgical process vessels, like furnaces, the AU-E technique was created in the late 1990s. The theory and practical advantages of this non-destructive testing technique have been described in more than 80 papers to date, and it has received international patents.

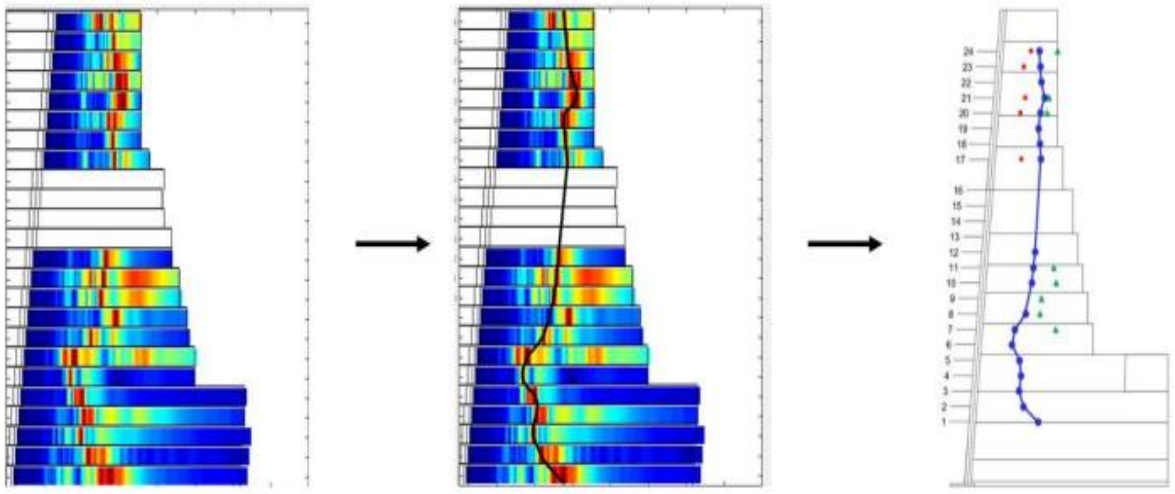

Figure 2. A typical AU-E thickness spectra accumulation for a blast furnace wall and its 2D interpretation on a furnace sidewall drawing [1,2,7]

This approach was used in developing several testing methods, such are:

- Refractory Oxidation or Brittle Zone Detection
- Sidewall Refractory Wear

2.3. Radioactive traces

In the 1960s and 1970s, refractory thickness in blast furnaces was measured using radioactive tracers. The employment of tracers in blast furnaces has been the subject of several published works of literature [15-19]. This technique makes use of short-lived radioactive isotope tracers. The radioactive tracers were first used in previous studies to the blast furnace's top. The receiver, tracer counter, or Geiger counter measured the radiation that traveled through the build-up, refractory, and shell as the tracers moved downward with the load.

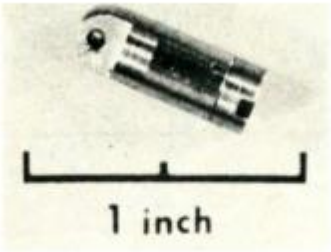

Radioactive tracer pod

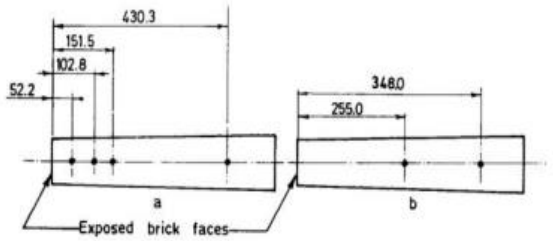

Placement of pods in carbon refractory blocks at different thicknesses

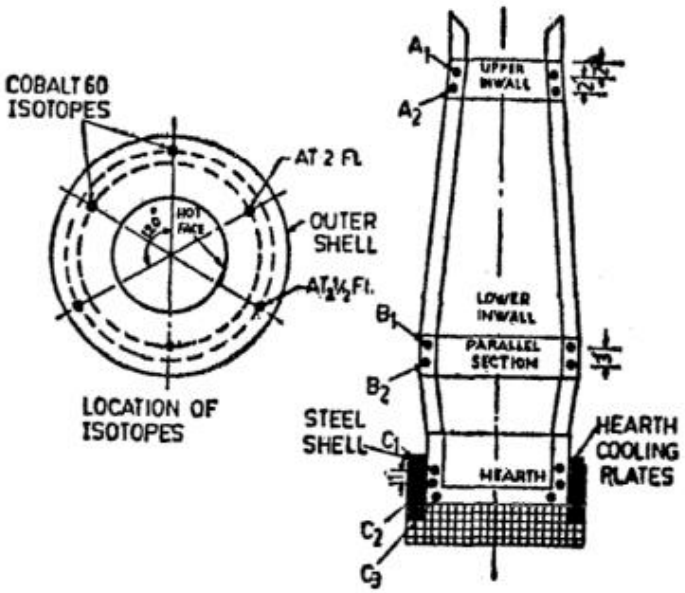

Placement of the pods in different refractories at various locations in the blast furnace

Figure 3. Radioactive tracers for refractory thickness measurements in blast furnaces [1, 15]

2.4. Thermocouple or RTD

In order to forecast the refractory and/or skull thickness in operational furnaces and process vessels, refractory thickness assessments based on thermal analysis extrapolate thermocouple or resistance temperature detector (RTD) data [1,21]. This technique uses thermocouples or RTD temperatures at predetermined points in the water and refractory.
The heat flux out of the furnace is computed using a one-dimensional steady-state heat transfer calculation using the stave temperatures. It is assumed that the refractory acts as a uniform heat conductor between the furnace shell and the hot inner face in these simplified thermal calculations. The heat flux is therefore taken to be constant throughout the refractory. The information for thermal calculations and thickness measurements is gathered using thermocouples or RTD and the water temperature in cooling blocks. Figure 4 shows an example of a standard thermocouple.

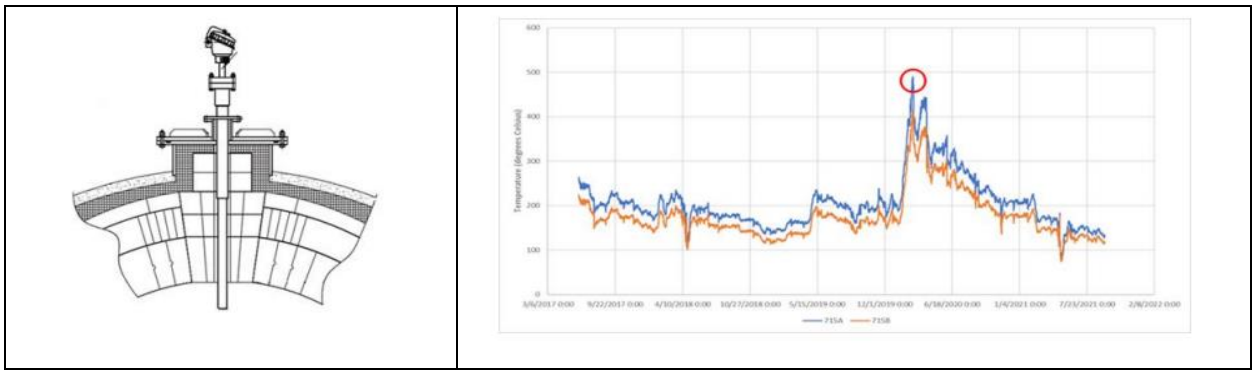

Figure 4. A typical thermocouple embedded and installed into a refractory lined vessel and Example of paired thermocouple data with analysis temperatures (degrees Celsius) highlighted in red [1]

2.5. Fibre optics

In single or multiple lined process vessels, such as kilns, reactors, and converters, magnetic systems are employed to measure the thickness of the residual refractory. The refractory strength can be ascertained using a device called a Covermeter, which is based on electromagnetics and was initially intended to detect the position of rebars in concrete elements. An electric current, also known as pulse-induction, regularly charges two coils, producing a magnetic field that produces an eddy current. A secondary, opposite field direction eddy current field is produced in the ferromagnetic body if one is close by, or more accurately, within the range. The distance between the coils and the ferromagnetic body can be ascertained by the strength of the secondary eddy current field that results. The converter probe can be positioned on the surface of the kiln or converter once the inspectors are inside. Refractory and gauge how far away the ship's shell is. Measurements are precise, especially in containers with brick linings, and many places can be measured quickly without drilling or lining removal. In Refractory anchors in castable lined vessels may pose problems if they are recognized instead of the shell; therefore, it is important to identify their position and take readings in between anchor positions (see Fig. 5) [1]

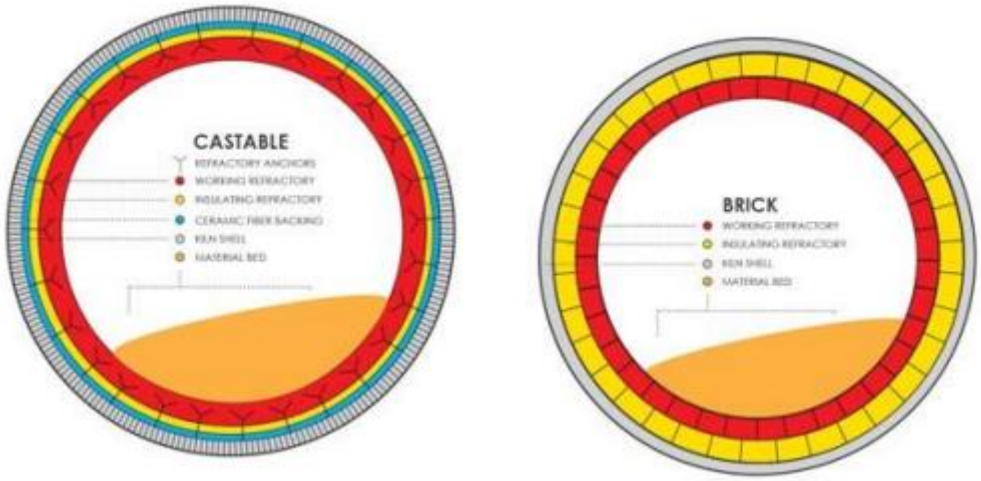

Figure 5. Castable and refractory lined kilns [1]

3. METHODS FOR CONVERTER

Many of the previously mentioned methods are available for other furnaces and devices in metallurgy, as well converter.

3.1. Laser method

A laser beam is utilized in this procedure to determine the thickness of the lining (Fig 6). The method involves bouncing a laser beam off of calibrated spots on the actual converter and comparing them to the points in the worn lining. The remaining lining thickness is then plotted using a computer analysis. Comparing the wear rates of various refractories and preventing shell damage are two other uses for this approach. This method is helpful in identifying and managing the necessary furnace maintenance through shooting. The locations that truly need gunning repair can be located and the necessary gunning maintenance can be performed by employing a laser beam.

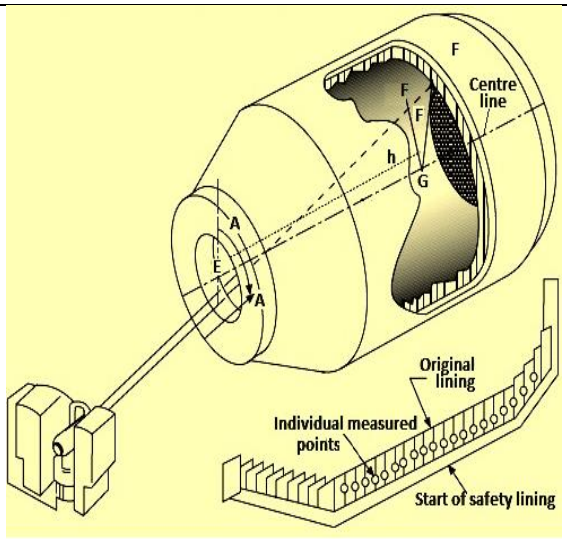

Figure 6. Measurements of refractory thickness using laser beam for converter [1,7]

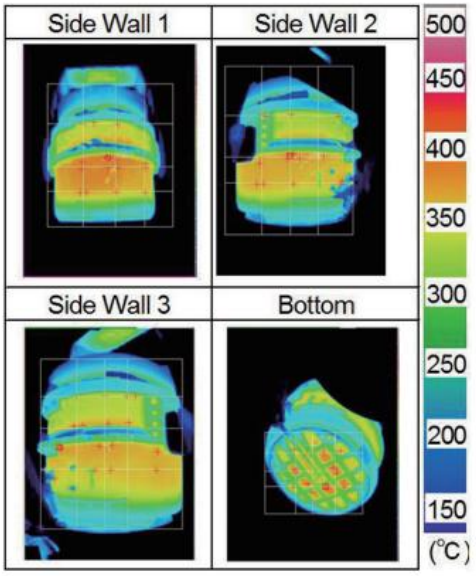

Figure 7. Picture of infrared thermography on hot metal ladle [1,20]

3.2. Infrared thermography (IR)

The most popular NDT method for identifying hotspots and possible trouble locations in a process vessel is infrared (IR) thermography, provided that the refractory and shell are securely bonded. IR cameras produce a thermal image that displays an object's temperature on a color scale, with the darker colors are hot places, whereas the lighter areas are cooler. Surface temperature variations could be the consequence of subsurface flaws or variations in refractory thickness. The primary benefits of infrared cameras are their inexpensive cost, quick inspection and interpretation speed, lack of contact, and remote use, which improves inspector safety. A wide range of methods have emerged in recent years. The primary benefits of infrared cameras are their inexpensive cost, quick inspection and interpretation speed, lack of contact, and remote use, which improves inspector safety. Many different systems have become commercially accessible in recent years, offering a wide range of various prices and image resolutions.

3.3. Ferotron

Ferrotron's LaCam systems utilize laser technology for non-contact measurement of refractory lining thickness in steelmaking vessels, including converters, ladles, and electric arc furnaces. These systems are designed to provide steel producers with accurate data for optimizing maintenance, reducing costs, and improving safety.

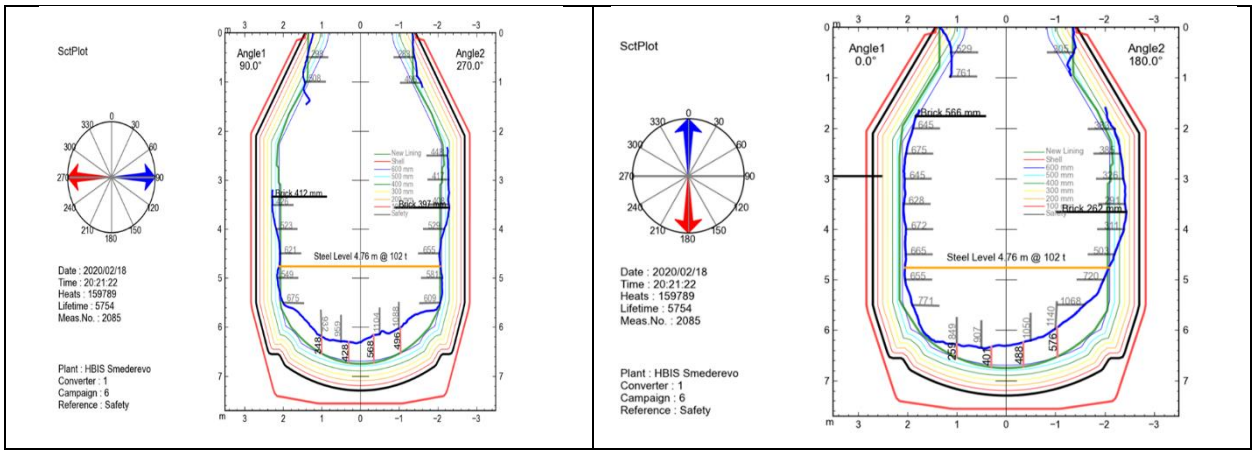

Figure 8. Ferotron measurement for converter [22]

3. CONCLUSION

The diagnosis technologies of refractories are essential in the manufacture of iron and steel production because they help to stabilize production equipment, reduce costs, and prevent issues like hot iron metal leaks and/or molten steel leaks. The use of refractory diagnostic technologies in blast furnace and converter in the steelmaking process that handles molten objects at high temperatures was the goal of this paper. Despite suggesting certain issues that need to be resolved, these diagnostic techniques are useful instruments for maintaining refractory-lined equipment. By implementing these advanced technologies on real equipment, it is crucial to improve the management accuracy of refractory-lined equipment.

ACKNOWLEDGEMENTS

This work was supported by the Ministry of Science, Technological Development and Innovation of the Republic of Serbia [grant numbers *451-03-136/2025-03/200135 and 451-03-136/2025-03/200026]*.

REFERENCES

[1] A. Sadri, W. L. Ying, NDT Techniques for Furnace Refractory Lining Assessment, e-Journal of Nondestructive Testing - ISSN 1435-4934 Issue: 2024-08 Proceedings of the NDT in Canada 2024, 11-13 June, Ottawa (Ontario) (NDT Canada 2024) Special Issue of e-Journal of Nondestructive Testing (eJNDT) ISSN 1435-4934 | Vol. 29(8)

[2] A. Sadri, Systems, methods and apparatus for non-disruptive and nondestructive inspection of metallurgical furnaces and similar vessels: patent application publication: US 2006 0186585.

[3] J. Ma, X. Wen, X. Zhao, IEEE Access, 1 (2021).

[4] A. Dmitriev, Y. Chesnokov, K. Chen, O. Ivanov, M. Zolotykh, Monitoring System of Firebrick Lining Erosion of Blast Furnace Hearth, 16th IFAC Symposium on Automation in Mining, Mineral and Metal Processing August 25-28, 2013. San Diego, California, USA

[5] A. Sadri, P. Gebski, Y. Gordon, NON-DESTRUCTIVE TESTING (NDT) AND INSPECTION OF THE BLAST FURNACE REFRACTORY LINING BY STRESS WAVE PROPAGATION TECHNIQUE, 2014. https://elar.urfu.ru/bitstream/10995/29382/1/tngg_2014_1_13.pdf, 13.06.2025.

[6] D. Roldan, Y. Zhang, R. Deshpande, D. Huang, P. Chaubal, C. Zhou, 3-D CFD Analysis for Furnace Hearth Wear // Association for Iron and Steel Technology (AISTech) Annual Conference (May 1–4). 2006. Vol. II, Cleveland, Ohio, USA, pp. 167–176.

[7] https://www.ispatguru.com/refractory-lining-of-a-basic-oxygen-furnace/

[8] R.J. O'Malley, Iron Steel Technol., (2023) 55-78.

[9] T. Gerritsen, A.H. Gunnewiek, 2011. Diagnostic system and method for metallurgical reactor cooling elements. US patent 7,976,770. Hatch Ltd.

[10] M. Wang, P.S. Salter, F.P. Payne, A. Shipley, S.M. Morris, M.J. Booth, J.A. Fells, Optics Express, 30 (9) (2022).

[11] Y. Bayram, J. Wechsel, E. Sperry, New Industry Standard in Furnace inspection, 78th Conference on Glass Problems edited by S. K. Sundaram, (2018) pp. 75-88.
[12] G. Morris, O-I Glass to deploy PaneraTech's refractory monitoring technology, Glass International, (July 26th, 2023). https://www.glass-international.com/news/o-i-glass-todeploy-paneratechs-refractory-monitoring-technology
[13] R.L. Parker, J.R. Meanning, N.C. J. Peterson, Appl. Phys., 58 (11) (1985) 4150-4164.
[14] A.Sadri, P. Gebski, H. Ghorbani, G. McGarrie, T. De Vries, JOM: A publication of the Minerals, Metals & Materials Society, 61 (10) (2009) 69-73.
[15] J. J.Borbas, R.C. Padfield, E. Moscker, J. Am. Ceram. Soc., 50 (8) (1967) 421-424.
[16] L. Staicu, R.J. Radu, Phys. D: Appl. Phys. 16(12) (1983) 2541-2546.
[17] J. Salgado, C. Oliveira, A. Moutinho, C. Silvério, Int. J. Rad. Appl. Instrum. A 39 (12) (1988) 1265–1267.
[18] A.S. Prasad, P. Sinha, M. Qamrul, A. Chatterjee, P.K. Chakravarty, Some experience with radioisotopes in the study of the wear of blast furnace linings. Tata Iron and Steel Co. Ltd., Jamshedpur, India. Research and Development Division. TISCO; 26 (3-4) (1979) 81-87 ISSN 0496-6546; Worldcat.
[19] J.F. Perko, E.J. Spirko, Blast furnace refractory lining wear status using radioactive sources. Repub Steel Corp, Cleveland, Ohio. Ind. Heat; 42 (6) (1979) 74-78.
[20] S. Sawai, K. Hashimoto, M. Shiokawa, Y. Yamada, Methods of Evaluting the Damage of Steelmaking Refractories, Nippon steel technical report No. 125, Japan, December 2020.
[21] A. Sadri, M. Henstock, W.L. Ying, B. Climenhaga, J. Allard, The Effect of Aging on Refractory Thickness Calculations for Process Vessels and Furnaces, 59TH Annual Conference of Metallurgists (COM 2020): The Canadian Institute of Mining, Metallurgy, and Petroleum. ISBN: 978-1-926872-47-6, October 14 – 15, 2020, Toronto, Ontario, Canada.
[22] L. Simić, Master thesis, Faculty of Technology and Metallurgy, 2020

The 56th International October Conference on Mining and Metallurgy
22-25 October 2025, Bor Lake, Bor, Serbia
www.ioc.tfbor.bg.ac.rs

DOI: 10.5937/IOC25712K
Original scientific paper

QUALITY CONTROL IN THE PRODUCTION OF VACUUM PUMPS FOR THE AUTOMOTIVE INDUSTRY

Maria Krasteva[1a], Petar Raykov[1b]

University of Chemical Technology and Metallurgy, Sofia, Bulgaria
[1a] mariqkrasteva@uctm.edu, 0009-0008-0375-4584
[1b] raykovche@gmail.com, 0009-0006-1383-5092

Abstract
The company "Hanon Systems Plovdiv Ltd" produces components for the automotive industry. It is a leader in the production of vacuum pumps, chassis pumps, servo pumps, transmission pumps, etc. This paper focuses on vacuum pumps and the production of their aluminum housings, manufactured for the company Daimler, a world leader in the automotive industry. The aim is to trace the quality throughout the entire process, i.e. from the production of the casing to the complete assembly of the pump and to continuously improve the processes of quality management and compliance with standards in order to meet the requirements of users (high quality, low cost and high-efficiency product capacity) in the production of vacuum pumps for engines that are not able to produce enough pressure for the brake systems of cars.

***Keywords**: quality control, vacuum pumps, automotive industry, pump housing, ISO BDS EN ISO 9001:2015*

1. INTRODUCTION

To achieve the development goals, the parts used in the automotive industry are tested according to certain quality management standards. The ISO 9000 series are international standards for quality assurance and management, established in 1987 and revised in 2015. The current standard is called BDS EN ISO 9001:2015, which combines five standards.

The ISO 9001:20015 standards consistently emphasize the need for continuous improvement of the quality management system [1].

There are six guidelines for ensuring different functions:
• Production Part Approval Process (PPAP);
• Advanced Product Quality Planning (APQP);
• Failure Mode and Effects Analysis (FMEA);
• Measurement Systems Analysis (MSA);
• Fundamental Statistical Process Control (SPC);
• Quality System Assessment (QSA).

The company producing vacuum pumps for the automotive industry, the subject of this study, uses MSA, PPAP, APQP, FMEA, SPC.

Total quality management is the effort to stimulate the production of competitive products on the market and initiates a new organizational method for continuous improvement of the quality of all processes in an organization (production, service, etc.), which is called Total Quality Management (TQM) and has been implemented in "Hanon Systems Plovdiv Ltd". ISO 9000 is a basic element in the TQM system. ISO focuses on the production process of the company (design and production of the product). TQM extends quality management to all departments and includes all employees in quality improvement teams (QIT). There is a model that makes TQM measurable with the European Quality Award (EQA). TQM is a complex system oriented towards continuous quality improvement, minimizing production losses and just-in-time delivery, based on the principle -

improvement has no limits and is called quality improvement. The four correspondences in TQM are: correspondence of the standard, of the application, of the value and of the hidden needs [2, 3].

At the company "Hanon Systems Plovdiv Ltd" for quality control of manufactured parts (vacuum pumps, chassis pumps, servo pumps, transmission pumps) for cars, process improvement is carried out using control plans, which is a procedure, repeating the main phases of collection - control and analysis. The collected data are used to calculate control limits, which are the basis for interpreting statistical control data. When a process is statistically controlled, conclusions can be drawn about its capability. In order to implement improvements in the control and capabilities of the process, common causes of variations must be identified and the process changed accordingly, after which the cycle begins again [4].

2. EXPERIMENTAL (PROCESS CONTROL TOOLS)

At the company "Hanon Systems Plovdiv Ltd", control plans (Figure 1 and Figure 2 are being developed for collecting and interpreting more data, used to perform efficiency control of manufactured vacuum pumps.

HANON SYSTEMS

Control Plan

Page 4 of 11

☐Prototype ☐Pre-launch ☒Production Plan No.: 5014449		Key Contact/Phone Thomas Nottke-Franz	Date (Orig.) Apr 30, 2024	Date (Rev.) Jun 1, 2024
Part Number/Latest Change Level 5014449 / D		Core Team Stefan Kestermann; Norbert Toepfer	Customer Engineering Approval/Date (If Reg'd)	
Part Name/Description LF19V Pump		Supplier/Plant Approval/Date	Customer Quality Approval/Date (If Reg'd)	
Supplier/Plant HCW (Serie) / 3000	Supplier Code ---------	Other Approval/Date (If Reg'd)	Other Approval/Date (If Reg'd)	

Part/Process No.	Part- / Process Name Operation Description	Machine, Device, Tools for Production	Prod. Resources		Characteristics			Methods				Response Plan
			No	Description	No.	Product/Process	spec. char. class.	Product / Process/ Specification/ Tolerance	Test Equipment	Sample	Control Method	
			6003488	Kamera	10	Stopfen per Kamera				100% inspection	Instruction	FPC-BHP-06-P-0005 Control of nok parts
5014449 N-50008752-03-20	LF19V Pump Z2/1 Flachformf. u. Ventilh. verschraub.	Montage DAG M276 Move	8720023	Elektroschrauber EM35-10J	10	Verschraubung nach SC300501		3,0 /3,5 Nm	Elektroschrauber EM35-10J	100% inspection	Instruction	FPC-BHP-06-P-0005 Control of nok parts
			6014657	Sensor misc.	20	Abfrage Ventilhalter vorhanden			Sensor misc.	100% inspection	Instruction	FPC-BHP-06-P-0005 Control of nok parts
			6014657	Sensor misc.	30	Abfrage Flachformfeder (Anzahl, Position)			Sensor misc.	100% inspection	Instruction	FPC-BHP-06-P-0005 Control of nok parts
			6005278	M270 mit NV ohne Ventilhalter N.i.O								
			6005279	M270 mit NV Bohrung FFF zu groß								
5014449 N-50008752-03-30	LF19V Pump Z2/2 Düse einpressen	Montage DAG M276 Move										

Figure 1. Control plan for vacuum pump housing

HANON SYSTEMS

Control Plan

Page 5 of 11

☐Prototype ☐Pre-launch ☒Production Plan No.: 5014449		Key Contact/Phone Thomas Nottke-Franz	Date (Orig.) Apr 30, 2024	Date (Rev.) Jun 1, 2024
Part Number/Latest Change Level 5014449 / D		Core Team Stefan Kestermann, Norbert Toepfer	Customer Engineering Approval/Date (If Req'd)	
Part Name/Description LF19V Pump		Supplier/Plant Approval/Date	Customer Quality Approval/Date (If Req'd)	
Supplier/Plant HCW (Serie) / 3000	Supplier Code ----------	Other Approval/Date (If Req'd)	Other Approval/Date (If Req'd)	

Part/Process No.	Part- / Process Name Operation Description	Machine, Device, Tools for Production	Prod. Resources		Characteristics			Methods				Response Plan
			No	Description	No.	Product/Process	spec. char. class.	Product / Process/ Specification/ Tolerance	Test Equipment	Sample	Control Method	
			6014099 6005280	NC-Fügemodul NCFT 2157A3 Fa.Kistler M270 mit NV Bohrung Sieb zu groß N.i.O	10	Einpressen Düse		600 N	NC-Fügemodul NCFT 2157A3 Fa. Kistler	100% inspection	Instruction	FPC-BHP-06-P-0005 Control of nok parts
5014449 N-50008752-03-50	LF19V Pump Z3/2 Durchflußprüfung FFF	Montage DAG M276 Move	6003130 6005281 6005282 1630294-PSP-004--	flow rate gage Flow M270 mit NV ohne FFF N.i.O M270 mit NV FFF Dicht i.O.	10	Durchflussprüfung FFF siehe PSP			flow rate gage Flow	100% inspection	Instruction	FPC-BHP-06-P-0005 Control of nok parts
5014449 N-50008752-03-60	LF19V Pump Z3/3 Durchflußprüfung Düse	Montage DAG M276 Move	6009496 6005283	Durchflussmesser PF2A510-01-2 SMC M270 mit NV Olbohrung zu N.i.O	10	Durchflussprüfung Düse siehe PSP			Durchflussmesser PF2A510-01-2 SMC	100% inspection	Instruction	FPC-BHP-06-P-0005 Control of nok parts

Figure 1.b Control plan for vacuum pump housing

After collecting extensive data from the control plans, control limits are calculated based on that data. The process is then analyzed to implement improvementsThe main indices that describe the ability and potential of the process, used in the control charts are:

- Cp or process capability index: Measures the potential capability of the process under the assumption of perfect centering.

- Cpk or process capacity index: Reflects the actual capability given the process mean.

The requirements for the control of the aluminum housing, which will subsequently be assembled into a vacuum pump, are specified in advance with the customer. The customer's design department, together with that of the company, determines the important dimensions for the functionality, the informative dimensions, the dimensions that will be monitored and which dimensions will participate in the evaluation of the indices Cp and Cpk. The dimensions that must be included for the analysis of Cp and Cpk are circled on the drawing of the part. Customer requirements are visualized precisely through a control chart and a drawing of the part.

In the company manufacturing a housing for an automotive vacuum pump, a target Cpk 1.33 corresponding to the Motorola definition of 4σ, which corresponds to the Motorola definition that the sigma level is measured in units of defects per million opportunities for defect (Defects per million opportunities – DMPO) [5].

The control chart depicts the entire process of creating the part. It starts from the arrival of the blank at the factory, through machining, washing, packaging.

The drawing of the part indicates the dimensions that are important to the customer. The control chart is the basis for process audits and audits on the customer side.

In order to implement comprehensive company quality control, the necessary control documents must be developed: Control plan (control chart); Detail drawing; Analysis of dimensions important to the customer; Self-control plan for housing production; Selection of measuring instruments for quality control [6].

3. RESULTS AND DISCUSSION

Based on the prepared control charts and a drawing of the detail of an aluminum housing for an automotive vacuum pump, it can be concluded that the benefits of using control charts for implementing quality control in the production of automotive parts are:

- used by operators for ongoing process control;
- the process is executed consistently and predictably;
- products have higher quality, lower cost and higher effective capacity; distinguishing random from common causes of variation;
- making a decision for local intervention or intervention on the system

The implementation in the company "Hanon Systems Plovdiv Ltd" of 4σ (DPMO) = 6.210 (99.98% yield; 0.02% defect rate) fully satisfies the customers and the manufacturer of aluminum housings for automotive vacuum pumps.

4. CONCLUSION

Based on a number of analyzes and protocols conducted at "Hanon Systems Plovdiv Ltd", it has been determined that the process stability indicator Cp with the lowest indicator is 1.96, which is above 1.33 or sigma 4, which are the customer requirements regarding the quality standard in the production of aluminum housing for vacuum pumps in the automotive industry.

ACKNOWLEDGEMENTS

This research is supported by the Bulgarian Ministry of Education and Science under the National Program "Young Scientists and Postdoctoral Students-2.

REFERENCES

[1] R. Ospina, P. Ocampo, A Bibliographic, 39 (2018) 45, ISSN 0798 1015.
[2] M. Talha, The Bottom Line, 17 (1) (2004) 15-19.
[3] http://diliev.com›home›KHEA›KNEA_tema_2.
[4] R. Yordanov, Quality control, Study notes, https://ptu.mf.tu-sofia.bg/lectures/RR/KK.pdf , Sofia, 2014, pp.42-59.
[5] https://www.sixsigmaonline.org/defects-per-million-opportunities-dpmo-six-sigma/ .
[6] M. Krasteva, P. Raykov, Quality control in the production of housings for vacuum pumps in the automotive industry, Proceedings of XXX International scientific and technical conference "Foundry 2025", 09-11 April, Pleven, Bulgaria, ISSN 2535-017X (Print), ISSN 2535-0188 (Online), pp. 33-36.

The 56th International October Conference on Mining and Metallurgy
22-25 October 2025, Bor Lake, Bor, Serbia
www.ioc.tfbor.bg.ac.rs

DOI: 10.5937/IOC25716S

Original scientific paper

INTRA- AND EXTRA-EU TRADE IN RECYCLABLE METALS: OPPORTUNITIES FOR INDUSTRIAL SYMBIOSIS

Anđelka Stojanović[1a], Isidora Milošević[1b], Dragan Manasijević[1c],

[1] Technical Faculty Bor, University of Belgrade, V.J. 12, 19210 Bor, Serbia
[1a] anstojanovic@tfbor.bg.ac.rs, 0000-0001-7254-4646
[1b] imilosevic@tfbor.bg.ac.rs, 0000-0001-5539-8253
[1c] dmanasijevic@tfbor.bg.ac.rs, 0000-0002-7828-8994

Abstract
Trade in recyclable metals within and outside the European Union borders is a key part of establishing patterns of circular economy and industrial symbiosis in the metalworking industry. Industrial symbiosis implies the creation of industrial synergies in areas that can utilize waste materials or by-products, and is particularly important in sectors of intensive mineral processing, as it reduces the amount of waste, the need for exploitation of primary raw materials (virgin materials), and the negative environmental impact. This paper examines the potential of European Union countries for creating industrial symbioses, based on an assessment of trade in recycled metals within the EU and with third countries. A multi-criteria analysis was employed, utilizing the MARCOS methodology to rank EU countries, thereby determining which countries have the most significant potential for recycling various types of metals and making synergies. Research on trade in recycled materials contributes to the promotion of circular and sustainable mechanisms, and the results can serve policy makers, industrial actors and researchers as a basis for investment planning, optimization of flows of secondary raw materials and development of regional centers of industrial symbiosis.

***Keywords**: industrial symbiosis, trade in recyclable metals, European Union*

1. INTRODUCTION

The economic progress we are experiencing nowadays is causing a significant increase in the required quantities of materials, especially metals. The OECD report estimates that by 2060, the need for metals will increase from 7 to 19 Gt per year. The use of such large quantities of metals in economic activities has significant environmental consequences, starting from the process of extracting materials through their use to disposal, which include greenhouse gas emissions, air pollution, land and water devastation, etc. Although there is a desire to increase efficiency and reduce the environmental impact per unit of product, due to the significant increase in global consumption, the environmental impact is actually growing. In addition to the large ecological footprint, there are also challenges related to the limited reserves of certain raw materials, especially scarce and strategic metals such as lithium, cobalt, rare earths, and indium. While some metals have relatively high recycling rates, some rare and precious metals, in addition to their low natural availability, also have extremely low recycling rates [1]. The importance of these minerals is reflected in the reliance of the energy transition on their extraction and use, as they are widely utilized in clean energy technologies, ranging from wind turbines and solar panels to electric vehicles.

Metal recycling represents one of the significant opportunities to overcome the problem and achieve sustainable resource use. Due to their physical and marketable properties, metals are among the most suitable materials for recycling. For decades, scrap metals have been used to produce new ferrous and non-ferrous metals, while retaining almost all of their functional properties. In terms of metal recycling, the potential is large. Existing data indicate that the proportion of steel waste used in steel production in the EU has been around 56% in recent years.

Of the total amount of copper waste produced in the EU, around 29% is lost due to inefficiency at the end of its life. Of the total amount of aluminum waste produced in the EU, 70% is collected and recycled annually [2]. Projections show that recycling will become increasingly competitive with the exploitation of primary raw materials, which will contribute to the recycling sector outpacing the growth of mining [3]. Metal recycling will be essential to achieve climate neutrality targets by 2050, especially in energy-intensive industries such as the metallurgical industry. Its role is clearly recognized in the European Green Deal and the Circular Economy Action Plan [2].

It is important to understand that the circular economy cannot be fully realized at the level of individual countries, but requires coordinated action at the European and global level. The trade in recyclable metals not only contributes to the development of the circular economy, but also represents a key mechanism for realizing industrial symbiosis (IS) - a concept in which waste or by-products of one industry become raw material for another [4]. Considering that IS assumes that surpluses from one production process are allocated where they are needed, through exchange of raw materials from recycling, enabling industries across different sectors to cooperate with each other. The secondary metals market enables IS regardless of geographical boundaries, thus encouraging more efficient use of resources at the regional and international level with direct benefits for the economy and the environment. For industrial symbiosis, it is necessary to harmonize the output and input of industries and to collect the necessary data on waste and recyclable materials and potential users of these resources and their needs.

The aim of this paper is to investigate the potential of industrial symbiosis and the role of recyclable metals in the transition to a circular economy, through the analysis of patterns of international trade in recycled materials. Special focus is on the identification of regional specialization in the processing of certain types of metals as well as on the assessment of the European Union's dependence on the import of secondary raw materials. This research provides a comprehensive overview of the EU market, enabling the identification of recycling metal flows, the recognition of key players, and the assessment of the potential for developing industrial symbiosis in the metal sector.

2. METHODS

The analysis is based on Eurostat data on Trade in recyclable raw materials, while a multi-criteria analysis using the MARCOS (Measurement Alternatives and Ranking according to Compromise Solution) methodology was applied as a methodological framework to identify similarities and group countries according to patterns of import and export of recyclable metals. The multi-criteria analysis approach for ranking countries has been used in numerous studies dealing with sustainability, energy efficiency and circular economy [5,6,7]. The MARCOS methodology was proposed by Stević et al. (2020) and is based on the comparison of alternatives and the determination of their positions in the ranking list based on the position in relation to the compromise solution. A compromise solution assumes the determination of the utility function in relation to the ideal and anti-ideal solution and their aggregation. The sequence of steps applied in order to obtain the final ranking of alternatives is presented in the work of [8].

3. RESULTS AND DISCUSSION

In order to carry out a comprehensive analysis, data were collected on intra- and extra-EU trade for the groups of ferrous, precious, non-ferrous (Cu, Al, Ni) and non-ferrous (other) metals. Then, through four ranking procedures, the EU countries were ranked according to criteria that represent values of trade in metals from waste or by-products, intended for further processing or recycling. The ranking results are presented graphically in Figure 1.

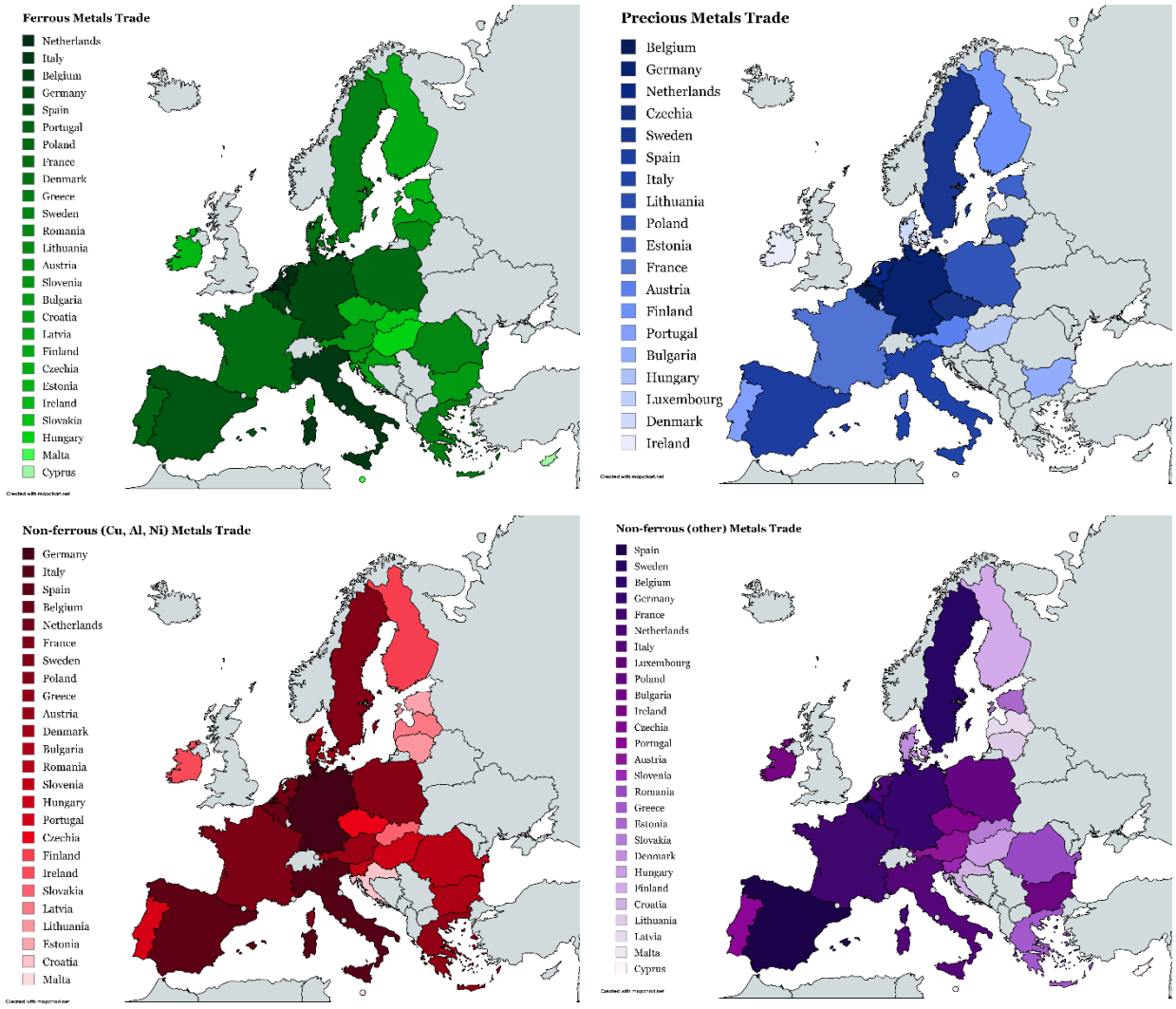

Figure 1. EU country rankings

The recycling of secondary metal raw materials represents a key step in the transition of the metal sector towards circular and sustainable practices. Among the leading countries in the trade of recyclable metals, Belgium and Germany stand out, followed by the Netherlands, Spain and Italy.

In the context of industrial symbiosis, the countries leading in the export of scrap metal usually have a developed infrastructure for collecting, sorting and transporting secondary raw materials, which makes them potential centers for the further development of these practices. Germany stands out in particular in the trade of non-ferrous metals (Cu, Al, Ni), while it also occupies a high position in the trade of precious metals. The German economy is characterized by robust industrial bases and strong environmental policies, as well as the largest number of Critical Raw Materials (CRM) recyclers in the EU [9]. The same applies to Belgium, which exhibits high levels of trade in recycled metals across all categories, and is particularly the leader in the import of precious metals. Belgium is already recognized as one of the leading centers of the metal recycling industry in Europe which is in accordance whit obtained results in this study [9].

The Netherlands is highly positioned in all rankings, although it does not have a particularly large domestic industrial base that produces metal scrap suitable for recycling. Its position is secured by high levels of trade in precious metals and significant exports of ferrous metals to countries outside the EU. Trade in secondary metal raw materials with third countries in the case of the Netherlands is largely based on its role as a transit and logistics hub, with much of the material passing through Dutch ports, even though it does not originate in the Netherlands itself.

On the other hand, the import of ferrous and non-ferrous metals (Cu, Al, Ni) is particularly important for the position of Italy, while the import of other non-ferrous metals is emphasized in Spain, which makes them suitable bases for establishing centers of industrial symbiosis. Countries such as Spain, Italy and Sweden are rapidly expanding capacity to switch to more environmentally friendly methods of steel production, thus increasing competition for high-quality scrap steel [10].

As expected, small countries with limited metal processing industries, such as Cyprus and Malta, are at the bottom of the rankings. The reason for this is the insufficient generation of metal waste, which reduces the need for large recycling facilities. In addition, since both countries are islands, the transport of scrap metal, as well as recycled material, is logistically more complex and expensive, which further limits their participation in the international trade in secondary metals.

Similarly, other EU countries that do not have a developed metal industry, nor industries that consume large amounts of metal, are lower on the rankings.

The positions of certain countries, such as Finland, Sweden and Austria, may seem surprising given their ecological tradition and developed recycling systems [11]. However, these very factors explain their relatively low volume of trade in secondary metals. These countries have developed domestic processing capacities, a high level of internal recycling and closed material flows, which means that most metal waste is processed and reused within national borders, without significant involvement in cross-border trade.

4. CONCLUSION

Research indicates that the EU's strong dependence on the rest of the world for metals is a significant issue, which is why various policies and interventions are being introduced to achieve a greater balance [12]. In recent years, the EU has established policies for trade in secondary metals, but it has also introduced restrictions on the level and prices of trade in certain types of these metals. However, the demand for metals is growing, as well as doubts about the effectiveness of some of the restrictive policies [13,14]. Therefore, recyclable metal scrap is treated as a valuable good in the EU, traded on international exchanges. Trading in recyclable metals does not hinder, but rather encourages, the establishment of a circular economy. The import of virgin raw materials into the EU has a significant negative impact on the environment and hinders the establishment of a circular economy, trade in raw materials from recycling does not have such consequences, but quite the opposite - the export of quality recycled metal from the EU can be key to achieving the goals of the European Union within the set goals of a sustainable economy.

Overall, the analysis of trade flows of recyclable metals among EU member states and towards third countries provides important insights into the availability of secondary raw materials and logistics capacities, which are key to planning and developing industrial symbiosis. Countries that combine a high level of import and export with a developed infrastructure for processing represent strategic points for strengthening the circular economy and reducing dependence on primary resources.

This research can serve as the basis for mapping the potential of industrial symbiosis in the metal sector, particularly at the international and European levels, and should be supplemented with data on quality, location, and local material flows.

ACKNOWLEDGEMENTS

This research was done within the framework of CA22110—Cooperation, development and cross-border transfer of Industrial Symbiosis among industry and stakeholders (LIAISE).

The research presented in this paper was supported by the Ministry of Science, Technological Development and Innovation of the Republic of Serbia, within the funding of scientific and

research work at the University of Belgrade, Technical Faculty in Bor, according to contract with registration number 451-03-137/2025-03/ 200131.

REFERENCES

[1] United Nations Environment Programme, Critical Transitions: Circularity, equity and responsibility in the quest for energy transition minerals, UNEP, Nairobi, 2024.
[2] European Recycling Industries' Confederation (EuRIC), EuRIC's position on free trade & metals circularity, 2021.
[3] OECD, Global Material Resources Outlook to 2060: Economic Drivers and Environmental Consequences, OECD Publishing, Paris, 2019.
[4] S. Jung, S. An, J. Park, S. Park, X. Bi, J. Ind. Ecol., (2025).
[5] J. Brodny, M. Tutak, Smart Cities, 6 (1) (2023) 339-367.
[6] V. Grybaitė, A. Burinskienė, Sustainability, 16 (21) (2023) 9582.
[7] E. Güler, Environ. Res. Commun., 7 (7) (2025) 075021.
[8] Ž. Stević, D. Pamučar, A. Puška, P. Chatterjee, Comput. Ind. Eng., 140 (2020) 106231.
[9] R. Mohan, "Critical Raw Materials Recycling: Key European Players and Capabilities," iimpcoll, 2024.
[10] Waste Transport Solutions, Metal waste vs. scrap: Exporting and recycling across Europe, Waste Transport Solutions, 2025.
[11] Alutrade, Which country recycles the most aluminium?, n.d.,
[12] T. Distefano, L. Lodi, M. Biggeri, J. Clean. Prod., 472 (2024) 143384.
[13] European Recycling Industries' Confederation (EuRIC), EuRIC Circular Metals Strategy, 2021.
[14] X. Zhou, H. Zhang, S. Zheng, W. Xing, Sustain. Prod. Consum., 33 (2022) 831-845.

The 56th International October Conference on Mining and Metallurgy
22-25 October 2025, Bor Lake, Bor, Serbia
www.ioc.tfbor.bg.ac.rs

DOI: 10.5937/IOC25721P *Review paper*

APPLICATION OF METAHEURISTIC ALGORITHMS IN METALLURGICAL INDUSTRY: A REVIEW OF METHODS AND APPLICATIONS

Marijana Pavlov-Kagadejev[1a], Aleksandra Milosavljevic[1b]

[1] Mining and Metallurgy Institute Bor, Alberta Ajnštajna 1, 19210 Bor, Serbia
[1a] marijana.pavlov@irmbor.co.rs, 0000-0003-1090-6351
[1b] aleksandra.milosavljevic@irmbor.co.rs, 0000-0003-3841-7357

Abstract
Optimization is important in metallurgy due to the complexity of processes, the large number of parameters, and the challenge of finding a balance between cost and quality. Problems associated with the traditional experimental approach are common due to nonlinearity, multi-objective goals, the high cost of experiments, as well as the time required for their execution. The application of metaheuristic algorithms has proven to be effective in solving complex problems. This paper aims to provide an overview of metaheuristic algorithms and their application in the metallurgical industry.

Keywords*: metaheuristics, metallurgical industry, optimization*

1. INTRODUCTION

The complexity of industrial processes, the large number of process parameters, and the diverse objectives that must be met have made optimization a critical component in the metallurgical industry. Furthermore, the presence of nonlinear relationships, multi-objective requirements, and the need to reduce experimental costs has highlighted the importance of optimization not only in metallurgy but across various industrial sectors. By applying optimization techniques, the duration and cost of experimental procedures can be significantly reduced, making the overall process more economical and efficient. This paper examines the use of metaheuristic algorithms in the optimization of metallurgical processes. These algorithms have shown strong potential in improving key areas such as casting and melting operations, alloy design, and production scheduling, thereby enhancing efficiency and overall performance in manufacturing systems [1, 2].

2. METAHEURISTICS

Optimization is a process used to improve performance in both decision sciences and physical system analysis. To utilize optimization correctly, it is first necessary to identify a goal - a quantitative measure of the performance of the system being studied. This objective can be profit, time, potential energy, or any quantity that can be represented by a single number. It depends on certain characteristics of the system, called variables or unknowns, and it is necessary to find the values of the variables that optimize the goal [3].

The classification of optimization algorithms can be done in several ways. One way is to divide them into deterministic and stochastic algorithms. Conventional and classical algorithms mostly belong to the group of deterministic algorithms, while heuristics and metaheuristics can be classified as stochastic algorithms. Heuristics algorithms belong to approximate algorithms and can be divided into two categories: specific heuristics and metaheuristics.

Metaheuristic algorithms represent improved heuristics. There is no agreed-upon definition of heuristics and metaheuristics in the literature. The two main components of every metaheuristic

algorithm are intensification (exploitation) and diversification (exploration). A good combination of these components can ensure reaching global optimality [4, 5].

Metaheuristic algorithms are often inspired by natural systems. Among the most well-known are swarm intelligence techniques and genetic algorithms, which mimic collective animal behavior and evolutionary processes. Others are based on physical phenomena such as gravity or electromagnetism, or abstract models including human cognition and mathematical patterns like trigonometric oscillations. These approaches provide flexible strategies for solving complex optimization problems by balancing exploration and exploitation [6].

Some of the most frequently used metaheuristic algorithms in metallurgical industry are:

- **Genetic Algorithms (GA) -** represent simulations of natural selection that can solve optimization problems. These algorithms are ideally suited for solving problems with discrete variables and, in most cases, find the global optimal solution [7].
- **Particle Swarm Optimization (PSO) -** imitates the collective behavior of birds and fish to efficiently search for food-rich areas [8].
- **Ant Colony Optimization (ACO) -** the basic idea of these optimization algorithms is to simulate the cooperative behavior of real ants in order to solve optimization problems [9].
- **Simulated Annealing (SA)** - simplest and most well-known metaheuristic methods for solving difficult global optimization problems, inspired by the annealing process used in metallurgy [10, 11].
- **Hybrid Metaheuristic Algorithms** - combination of the different methods for improved performance in complex problems.

The No Free Lunch (NFL) theorem [12] highlights that there is no algorithm that is the best for all problems, implying that an individualized approach is preferable. In recent times, the number of metaheuristics, especially those inspired by nature, is increasing daily.

Metaheuristic algorithms in the metallurgical industry are most commonly applied to optimize the following processes:

- **Casting and melting**, where parameters such as temperature, time, and alloy composition are optimized to minimize defects and improve product quality.
- **Alloy design**, in which algorithms search for an optimal alloy composition to achieve target properties like mechanical strength, material conductivity, and cost.
- **Production scheduling**, where metaheuristics optimize resource utilization-such as furnaces, materials, and personnel to improve scheduling efficiency and reduce delays.

3. PRACTICAL EXAMPLES

There are numerous examples of the metaheuristic algorithms application for process optimization in the metallurgical industry, as presented in published scientific papers. One example for each of the mentioned forms of optimization will be presented in this paper. The used algorithms will be briefly described, along with the optimized parameters.

According to [13], various metaheuristic techniques, including Genetic Algorithm (GA), Ant Colony Optimization (ACO), Simulated Annealing (SA), and Particle Swarm Optimization (PSO), were applied to optimize the feeder geometry in the casting process. The proposed methodology was applied in the design of the feeder for casting the Pelton turbine bucket, and the optimization results consist of the dimensional characteristics of the feeder. The best result from all the implemented optimization processes was selected for the final design. The validity of the proposed optimization approach was verified through numerical simulation of the casting process.

This study [14] focuses on enhancing the mechanical and electrical properties of the $CuNi_2Si_1$ alloy by combining experimental methods with metaheuristic optimization algorithms. Aging

temperature and time were varied between 450-600°C and 1-420 minutes, respectively, to optimize hardness and electrical conductivity. Among the metaheuristic approaches tested-Student Psychology-Based Optimization (SPBO), Genetic Algorithm (GA), and Particle Swarm Optimization (PSO), SPBO demonstrated the highest prediction accuracy. It predicted an optimal aging temperature of 450°C for approximately 61.75 minutes, which was confirmed experimentally. These findings emphasize the potential of metaheuristic algorithms, particularly SPBO, as effective tools for optimizing alloy design parameters and tailoring material properties for industrial applications such as aerospace and electrical engineering.

This paper [15] presents a hybrid simulation-based optimization method for production planning and scheduling in metal casting, with a focus on multi-criteria optimization, including energy efficiency. A combination of deterministic exchange-based heuristics and a customized Genetic Algorithm (GA) is applied to optimize batch assignments and furnace scheduling in the heat treatment process. The method demonstrates that smaller population sizes in the GA lead to more efficient optimization for the given problem complexity, as they maximize the limited number of iterations available for finding high-quality solutions. The approach significantly outperforms manual planning, reducing planning time and offering around a 10% global optimization potential, including a 6% improvement in energy efficiency. Figure 1 represents overview of the production layout showing five heat treatment furnaces, cooling stations, FIFO buffers, and a crane for material handling.

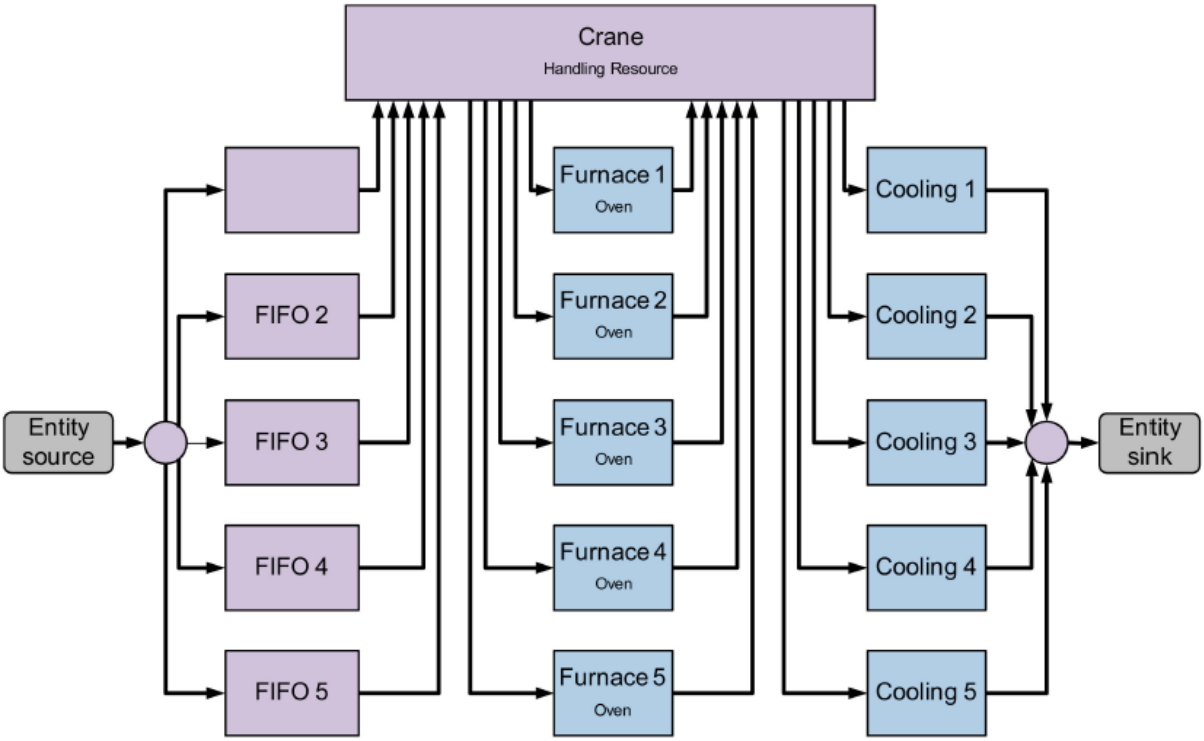

Figure 1. Schematic layout showing five heat treatment furnaces, cooling stations, FIFO buffers, and a crane for material handling [15] used under the terms of CC-BY

4. CONCLUSION

The application of metaheuristic algorithms to optimize various processes in the metallurgical industry contributes to improving product quality, reducing costs, and increasing production efficiency. Metaheuristic algorithms in the metallurgical industry are applied to optimize processes like casting and melting, alloy design, and production scheduling. Future development directions include the integration of metaheuristic algorithms with machine learning techniques and other artificial intelligence methods. Further research in this area, through the development of new

algorithms and hybrid combinations of existing ones, can significantly improve the solution of complex problems faced in the metallurgical industry.

ACKNOWLEDGEMENTS

This work was financially supported by the Ministry of Science, Technological Development and Innovations of the Republic of Serbia, Contract on Realization and Financing the Scientific and Research Work of the Mining and Metallurgy Institute Bor in 2025, Registration No. 451-03-136/2025-03/200052.

REFERENCES

[1] A. Poonia, K. Modalavalasa, K.P.R. Ayyagari, Designing of high entropy alloys with high hardness: a metaheuristic approach, *Sci. Rep.*, 14 (1) (2024) 7692.
[2] P.A. Huegler, F.J. Vasko, Metaheuristics for meltshop scheduling in the steel industry, *J. Oper. Res. Soc.*, 58 (6) (2007) 791–796.
[3] J. Nocedal, S. J. Wright, *Numerical Optimization*, Springer, New York, NY, 2006. https://doi.org/10.1007/978-0-387-40065-5
[4] E.G. Talbi, *Metaheuristics: From Design to Implementation*, John Wiley & Sons, 2009.
[5] X.S. Yang, *Nature-Inspired Metaheuristic Algorithms*, Luniver Press, 2010.
[6] I. Fister Jr., X.-S. Yang, I. Fister, J. Brest, and D. Fister, "A brief review of nature-inspired algorithms for optimization," *arXiv preprint arXiv:1307.4186*, 2013. [Online]. Available: https://arxiv.org/abs/1307.4186
[7] S. Nayak, *Fundamentals of Optimization Techniques with Algorithms*, Academic Press, 2020.
[8] J. Yang, R. Kennedy, R. Eberhart, Particle swarm optimization, in: *Proc. ICNN'95 – Int. Conf. on Neural Networks*, vol. 4, IEEE, 1995, pp. 1942–1948.
[9] M. Dorigo, *Optimization, Learning and Natural Algorithms*, Ph.D. Thesis, Politecnico di Milano, 1992.
[10] D. Delahaye, S. Chaimatanan, M. Mongeau, Simulated Annealing: From Basics to Applications, in: M. Gendreau, J.Y. Potvin (Eds.), *Handbook of Metaheuristics*, Int. Ser. Oper. Res. Manag. Sci., vol. 272, Springer, Cham, 2019.
[11] J. Derrac, S. García, D. Molina, F. Herrera, A practical tutorial on the use of nonparametric statistical tests as a methodology for comparing evolutionary and swarm intelligence algorithms, Swarm Evol. Comput., 1 (1) (2011) 3–18.
[12] D.H. Wolpert, W.G. Macready, No free lunch theorems for optimization, IEEE Trans. Evol. Comput., 1 (1) (1997) 67–82.
[13] R. Radiša, N. Dučić, S. Manasijević, N. Marković, Ž. Ćojbašić, Casting improvement based on metaheuristic optimization and numerical simulation, *Facta Universitatis, Series: Mechanical Engineering*, 15 (3) (2017) 397–411.
[14] J. Konieczny, K. Labisz, S. Ürgün, H. Yiğit, S. Fidan, M. Ö. Bora, Ş. H. Atapek, Metaheuristics algorithm-based optimization for high conductivity and hardness CuNi2Si1 alloy, Materials, 18 (2025) 1060. https://doi.org/10.3390/ma18051060
[15] T. Sobottka, F. Kamhuber, B. Heinzl, Simulation-based multi-criteria optimization of parallel heat treatment furnaces at a casting manufacturer, J. Manuf. Mater. Process., 4 (3) (2020) 94.

Abstracts

The 56th International October Conference on Mining and Metallurgy
22-25 October 2025, Bor Lake, Bor, Serbia
www.ioc.tfbor.bg.ac.rs

DOI: 10.5937/IOC25727M

Abstract

MINING AFTER MINING: REAL-TIME XRF-CPT FOR STRATEGIC RESOURCE ESTIMATION IN TAILINGS REPROCESSING

Eugeniu Martac[1a], Christine Laskov[1b], Katarzyna Staniewska[1c]

[1] Fugro Germany Land GmbH, Wolfener Str. 36U, 12681 Berlin, Germany
[1a] E.Martac@fugro.com, 0009-0006-6075-0446
[1b] c.laskov@fugro.com, 0009-0004-5826-8277
[1c] k.staniewska@fugro.com, 0009-0001-1685-9018

Abstract

"As global demand for critical raw materials intensifies, mine tailings are being re-evaluated as strategic secondary resources. Conventional resource estimation methods, reliant on sparse soil sampling and laboratory analysis, are often costly, time-consuming, and yield high uncertainty due to coarse investigation grids. This fails to capture the significant spatial heterogeneity inherent in tailings deposits, leaving their true potential unexplored.

This paper introduces an innovative, integrated site characterization technology that combines Cone Penetration Testing (CPT) with Energy-Dispersive X-Ray Fluorescence (ED-XRF) to directly address these challenges. The XRF-CPT probe enables simultaneous, real-time, in-situ logging of soil mechanics and quantitative geochemistry, providing high-resolution vertical profiles of heavy metal concentrations (e.g., Cu, Zn, Pb) alongside geotechnical parameters in tailings.

Presenting the results from various field campaigns, we demonstrate how this technology provides a rapid, cost-effective, and minimally invasive method for 3D resource delineation. It successfully identifies deep, high-grade enrichment horizons that conventional near-surface sampling consistently misses. The resulting high-density data set allows for the construction of robust 3D models critical for accurate reserve estimation, economic analysis, and the development of targeted re-mining strategies. We conclude that the XRF-CPT methodology is a transformative tool for the feasibility assessment of tailings reprocessing, turning "mining after mining" into a precise, data-driven, and economically viable operation."

Keywords: *tailings reprocessing, XRF-CPT, in-situ resource estimation*

The 56th International October Conference on Mining and Metallurgy
22-25 October 2025, Bor Lake, Bor, Serbia
www.ioc.tfbor.bg.ac.rs

DOI: 10.5937/IOC25728B

Abstract

THE ROLE OF LANTHANIUM ADDITION IN THE MICROSTRUCTURAL EVOLUTION OF AN EN AW-7175 ALLOY DURING SOLUTION ANNEALING

Tilen Balaško[1a], Aleš Nagode[1b], Jeihua Li[2a], Jožef Medved[1c], Maja Vončina[1d]

[1] University of Ljubljana, Faculty of Natural Sciences and Engineering, Aškerčeva cesta 12, Ljubljana, Slovenia
[2] Montanuniversität Leoben, Franz Josef-Straße 18, 8700 Leoben, Austria
[1a] tilen.balasko@ntf.uni-lj.si, 0000-0002-4735-9390
[1b] ales.nagode@ntf.uni-lj.si, 0000-0003-2175-0516
[1c] jozef.medved@ntf.uni-lj.si, 0009-0007-6931-5595
[1d] maja.voncina@ntf.uni-lj.si; 0000-0002-2563-1103
[2a] jiehua.li@unileoben.ac.at, 0000-0002-2079-0009

Abstract

The outstanding properties of the high-strength 7xxx aluminium alloys are achieved through critical heat treatment. This research focussed on the significant effects of lanthanum addition on the microstructural changes of EN AW-7175 alloy during solution annealing, the first stage of heat treatment. The main objective was to elucidate these microstructural changes and in particular to determine how lanthanum influences the evolution of the different phases.

To investigate the microstructural evolution, the alloys were first produced. After casting, a heat treatment, i.e. solution annealing, was carried out with holding times of 1 to 24 hours. Differential scanning calorimetry (DSC) was then carried out to analyse the characteristic temperatures and enthalpies of the samples. And finally, metallographic analysis was performed, which included scanning electron microscopy (SEM) and transmission electron microscopy (TEM) to analyse the microstructure.

The results showed that lanthanum profoundly changes the microstructure by increasing the eutectic solidus temperature, affecting the melting behaviour of Mg_2Si and promoting the formation of LaAlSi (while suppressing Mg_2Si) and increasing the melting enthalpy of the aluminium matrix. Lanthanum also accelerated the eutectic melting kinetics and effectively controlled the grain growth with an optimum annealing time of 10 hours and a minimum lanthanum concentration of 0.15 wt% to stabilise the grain size. In addition, lanthanum was involved in the development of chromium-containing phases leading to the formation of a novel $Al_{20}Cr_2La$ phase. Processing parameters such as faster cooling rates led to grain refinement due to precipitation along the grain boundaries. Longer annealing times caused a decrease in the T-phase content due to the diffusion of Mg and Zn into the matrix (Zn diffuses faster) and favoured the formation of the intermetallic phase Al_7Cu_2Fe over $Al_{13}Fe_4$.

***Keywords**: EN AW-7175, lanthanum, solution annealing, microstructure*

The 56th International October Conference on Mining and Metallurgy
22-25 October 2025, Bor Lake, Bor, Serbia
www.ioc.tfbor.bg.ac.rs

DOI: 10.5937/IOC25729S

Abstract

CONSTRUCTION AND TECHNOLOGICAL PROGRESS OF A COMPREHENSIVE CARBON REDUCTION SYSTEM FOR CCUS IN THE STEEL INDUSTRY

Wei Su[1a], Yi Xing[1b], Yang Zheng[1c], Rongrong Lei[1d]

[1] University of Science and Technology Beijing, No. 30 Xueyuan Road, Haidian District, Beijing
[1a] suwei@ustb.edu.cn, 0000-0002-9314-8068
[1b] xingyi@ustb.edu.cn, 0000-0001-7594-8398
[1c] yzheng@ustb.edu.cn, 0000-0002-9723-5687
[1d] leirongr@ustb.edu.cn, 0000-0002-6848-7084

Abstract

The development characteristics of carbon capture, utilization, and storage (CCUS) technologies in the steel industry, the establishment of a comprehensive carbon reduction system, and technological advancements have been explored. The characteristics of carbon emissions in the steel industry, the current status of carbon reduction technology development, and the distinctive features of CCUS technology have been elucidated. As a significant component of heavy industry, the combustion of fossil fuels such as coal during steel production leads to substantial carbon emissions. Although China has increasingly recognized the importance of CCUS in recent years, the overall progress remains in the early stages, and there is still a need for further improvement in technology and policy support. A "6C" system is proposed to create an integrated CCUS solution encompassing the entire process, detailing the technologies, strategies, and application cases across six aspects: carbon capture, utilization, storage, verification, monitoring, and assets. It discusses how optimization can help achieve the goal of reducing carbon emissions, while also providing valuable experiences and references for carbon emission control in other industrial sectors. The progress of CCUS technology in typical steel industry scenarios has been analyzed, and three carbon reduction pathways have been proposed. The traditional blast furnace CCUS route involves capturing and separating part of the blast furnace gas source to recycle CO and utilize CO2. Addressing the current challenges of high energy consumption and costs in carbon capture, a direct solid carbon route from end-of-pipe flue gas has been proposed to lower the purity of captured CO2. The hydrogen metallurgy coupled with CCUS route aims to produce green methanol through the integration of hydrogen production from renewable energy with CCUS. The implementation of these three carbon reduction pathways will promote traditional long-process decarbonization, reduce carbon source inputs, enhance the utilization of carbon resources, and achieve high value-added utilization of products. Future large-scale demonstration projects will facilitate the internal cycling of CO2 in the steel industry and its cross-industry utilization. Recommendations and outlook for advancing CCUS technology in the steel industry have also been presented.

***Keywords**: Steel industry, CCUS, Whole process, Carbon reduction system*

The 56th International October Conference on Mining and Metallurgy
22-25 October 2025, Bor Lake, Bor, Serbia
www.ioc.tfbor.bg.ac.rs

DOI: 10.5937/IOC25730T

Abstract

GEOLOGICAL INVESTIGATIONS OF THE 'POVLATNA ZONA' AND 'ISTOČNO POLJE' OF THE GACKO COAL BASIN (BIH) FOR COAL QUALITY ASSESSMENT AND DESIGN OF A BENEFICIATION PLANT (2023–2025)

Stefan Trujić[1a], Miroslav Popović[2a], Milenko Jovanović[1b], Katarina Milivojević[1c], Boško Vuković[3a]

[1] Mining and Metallurgy Institute Bor, Alberta Ajnštajna 1, 19210 Bor, Serbia
[2] Singidunum University Belgrade, 32 Danijelova Street, 11010 Belgrade, Serbia
[3] Univeristy of Banja Luka, Bulevar vojvode Petra Bojovića 1A, 78000 Banja Luka, Bosnia and Herzegovina
[1a] stefan.trujic@irmbor.co.rs, 0009-0003-5297-4309
[1b] milenko.jovanovic@irmbor.co.rs, 0000-0002-6757-4143
[1c] milivojevickatarina7@gmail.com, 0009-0000-1306-4044
[2a] miroslav.popovic@singidunum.ac.rs; 0000-0002-5559-3996
[3a] bosko.vukovic@ritegacko.com, 0009-0001-1088-540X

Abstract

Geological exploration conducted in the ""Gacko"" coal basin 'Povlatna zona' and 'Istočno polje' (2023–2025) aims to accurately determine coal quantity and quality as a basis for reserve categorization and the design of a coal beneficiation plant. The acquisition of this facility, represents a strategic step toward reducing harmful emissions and increasing the efficiency of the Gacko Thermal Power Plant (RiTE Gacko).

The research includes lithological mapping and laboratory analyses, focusing on reclassification of reserves to category A, considering the complex stratification of the deposit. Special attention was given to coal chemistry and the physical properties of surrounding sediments. These findings will support the optimal selection of beneficiation technology and ensure a more stable supply of higher-quality coal.

This work is crucial for addressing excessive particulate emissions and coal quality instability, particularly after flooding affected the most valuable part of the deposit in late 2023.

***Keywords**: Coal mine, geology, exploration, coal quality*

The 56th International October Conference on Mining and Metallurgy
22-25 October 2025, Bor Lake, Bor, Serbia
www.ioc.tfbor.bg.ac.rs

DOI: 10.5937/IOC25731H

Abstract

THE CONTRIBUTION AND APPLICATION OF POLYMERIC MATERIALS IN THE METALLURGICAL INDUSTRY

Roxana Hobjâlă[1a], Răzvan Mititelu Nicolae[1b], Ştefana Agop[1c], Laurenţiu Slătineanu[1d], Diana Diaconu[1e]

[1] Technical University Gheorghe Asachi Iasi, Alberta Ajnštajna 1, 19210 Bor, Serbia
[1a] roxana.hobjila@yahoo.com, 0009-0005-4800-6078
[1b] nicolae-razvan.mititelu@student.tuiasi.ro, 0009-0006-7512-2143
[1c] stefana.dochita-agop@academic.tuiasi.ro, 0009-0001-5962-5000
[1d] lslati@yahoo.com; 0000-0002-5976-9813
[1e] d.diacon27@yahoo.com, 0009-0004-4718-3681

Abstract

Since their discovery, polymeric materials have been a constant in fields such as engineering and medicine. In the field of modern metallurgy, polymeric materials have helped improve the performance of work equipment by protecting metal surfaces and contributing to optimizing the efficiency of manufacturing processes. Their use is much more pronounced in parts such as bearings, seals and coatings due to their resistance to corrosion, high temperatures and wear. At the same time, polymers also play a role in the protection of metal surfaces thanks to specialized coatings that extend the life of metal structures.

The first impact factor of polymeric materials in the metallurgical industry is in processes such as metal casting and forming, polymer-based resins and molds that have a precision with greater accuracy than before leading to the reduction of material waste. Moreover, advanced polymeric materials in thermal insulation minimize heat loss and bring a plus to energy efficiency in metallurgical processes. Polymer adhesives represent a reliable solution in bonding, substituting the classic welding method in some industrial processes.

In conclusion, the subject of polymeric materials in the metallurgical industry is present and further researched, thus, a research on polymeric materials such as Polytetrafluoroethylene (PTFE - Teflon), and Polyamide (PA - Nylon), Polyurethane (PU) can be deliberated.

***Keywords**: polymeric materials, Polytetrafluoroethylene (PTFE - Teflon), Polyamide (PA - Nylon), Polyurethane (PU)*

The 56th International October Conference on Mining and Metallurgy
22-25 October 2025, Bor Lake, Bor, Serbia
www.ioc.tfbor.bg.ac.rs

DOI: 10.5937/IOC25732A

Abstract

THE BEHAVIOR DESCRIPTION OF CUZNAL SHAPE MEMORY ALLOYS THROUGH THE DYNAMICS OF MULTIFRACTAL COMPLEX SYSTEMS

Stefana Agop[1a], Bogdan-Ionut Dochita[1b], Roxana Hobjâlă[1c], Nicanor Cimpoesu[1d], Tiberiu Sutic[1e]

[1] Technical University Gheorghe Asachi Iasi, Alberta Ajnštajna 1, 19210 Bor, Serbia
[1a] stefana.dochita-agop@academic.tuiasi.ro, 0009-0001-5962-5000
[1b] bogdandochita1995@gmail.com, 0009-0004-8564-520X
[1c] roxana.hobjila@yahoo.com, 0009-0005-4800-6078
[1d] nicanor.cimpoesu@academic.tuiasi.ro; 0000-0003-4373-017X
[1e] tiberiu.sutic@student.tuiasi.ro, 0009-0002-2651-327X

Abstract

CuZnAl alloys indicates a complex behavior due to reversible martensitic phase transitions, which provide materials which contains an unique property such as the shape memory effect. The dynamic movements of complex systems highlight some nonlinear structural transformations influenced by temperature, mechanical stresses, and the history of applied loads. Analyzing the behavior of CuZnAl alloys through the dynamics of multifractal complex systems leads to a detailed description of how the material's microstructure evolves.

By using a multifractal theory, the distribution of crystalline defects and martensitic domains can be described more precisely than with classical methods. The presence of self-similarity at the structural level of the alloy across multiple scales is characterized through a spectrum of multifractal exponents.

The dynamics of complex systems applied to CuZnAl alloys provide how external parameters, such as temperature and applied forces, influence the transitions between the austenitic and martensitic phases. These models help optimize technological processes to enhance the durability and reliability of these alloys in industrial and biomedical applications.

Integrating multifractal analysis into the study of CuZnAl alloys new possibilities for improving the performance of shape memory materials can be analized. In this regard, through the analysis of complex systems dynamics, the behavior of CuZnAl shape memory alloys can be described using modern research methods.

***Keywords**: CuZnAl alloys, shape memory effect, crystalline defects*

Publishing partners

Publishing partners

Technical Faculty in Bor

The Technical Faculty in Bor has a significant publishing activity, reflected in the publication of journals, textbooks, monographs, electronic editions, conference proceedings, and other publications.
From its founding in 1961 until today, the Faculty has published 6 journals, more than 140 textbooks and monographs, and a large number of conference proceedings from scientific meetings organized by the Faculty. At present, the Faculty publishes the following journals:

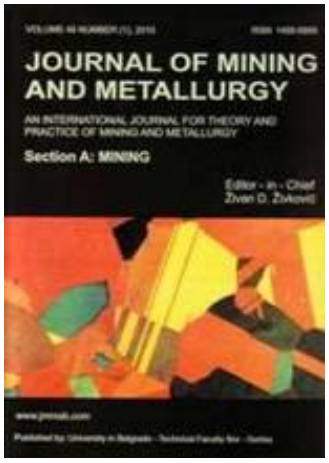

Journal of Mining and Metallurgy, Section A: Mining

Editor-in-Chief:
Prof. Grozdanka Bogdanović, PhD

Print Issue ISSN: 1450-5959
Online Issue ISSN: 2560-3159
www.jmma.tfbor.bg.ac.rs
jmma@tfbor.bg.ac.rs

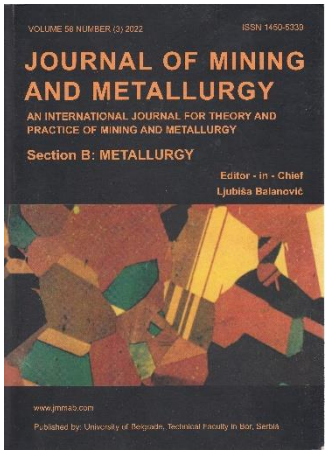

SCIE IF 2024: 1.0

Journal of Mining and Metallurgy, Section B: Metallurgy

Editor-in-Chief:
Prof. Ljubiša Balanović, PhD

Print Issue ISSN: 1450-5339
Online Issue ISSN: 2217-7175
www.jmmab.com
jmmb@tfbor.bg.ac.rs

ESCI IF 2024: 1.0

Serbian Journal of Management

Editor-in-Chief:
Prof. Ivan Mihajlović, PhD

Print Issue ISSN: 1452-4864
Online Issue ISSN: 2217-7159
www.sjm06.com
imihajlovic@mas.bg.ac.rs

Recycling and Sustainable Development Journal

Editor-in-Chief:
Prof. Milan Trumić, PhD

Print Issue ISSN: 1820-7480
Online Issue ISSN: 2560-3132
www.rsd.tfbor.bg.ac.rs
rsdjournal@tfbor.bg.ac.rs

Publishing partners

MDPI is a leader in the transition to open science by making more research free and accessible to everyone. Over 3.9 million researchers have entrusted us with publishing their scientific discoveries.

Our aim is to ensure that high-quality research is verified and made available to the research community as quickly as possible. MDPI stands at the forefront of the open access movement, having launched its first online journal Molecules in 1996. Today, MDPI is a leader in open access publishing with more than 450 journals across all research disciplines. Every article is published under a Creative Commons Attribution License.

Significant Highlights:

- **604.4 K** submissions received in 2024
- **450+** open access journals
- **17 days** from submission to first decision in 2024 (median across all journals)
- **41 days** from submission to publication in 2024 (median across all journals)
- **97%** of 2024 articles covered in Web of Science
- **90+** journals covered in SCIE (Web of Science)
- **92%** of submitting authors rate their overall experience with the peer review process as Excellent/Good
- **244.6 K** articles published in 2024

metals
an Open Access Journal by MDPI

Metals (ISSN 2075-4701) is an open access journal of related scientific research and technology development. Metals provides a forum for publishing papers which advance the in-depth understanding of the relationship between processing, structure, and properties or functions of all kinds of metals.

Minerals (ISSN 2075-163X) is an international open access journal that covers the broad fields of mineralogy, mineral geochemistry and geochronology, economic mineral resources, mineral exploration, innovative mining techniques, and advances in mineral processing.

Mining (ISSN 2673-6489) is an advanced forum for studies related to mining science and engineering in the 21st century. The research area covers all components of mining (geology; mine and extraction; ore processing and beneficiation; environmental management) and the whole mining life cycle (exploration; feasibility; construction; operation; closure).

DONORS

General sponsor

Conference is financially supported by

The Ministry of Science, Technological

Development and Innovation

of the Republic of Serbia

Platinum donor

HBIS SERBIA

Overview

HBIS Serbia was established in 2016 and is a part of HBIS Group, one of the world's largest steel producers headquartered in the People's Republic of China. The company's steelmaking facilities are located in Smederevo, where it produces iron, steel, and both hot-rolled and cold-rolled products — coils and sheets. A production facility for tinplate is located in Šabac.

With a designed capacity of 2.2 million tons of finished products annually and approximately 5,000 employees, HBIS Serbia is a driving force of industrial development in Serbia and a reliable partner to the national economy.

Since the acquisition of the Smederevo Steel Mill, the company has become a symbol of China–Serbia cooperation within the Belt and Road Initiative, as well as a bearer of the concept of "steel friendship." The visit of Chinese President Xi Jinping in 2016 provided strong momentum for development, job preservation, and the start of an investment cycle that reversed negative business results.

Successful Transformation and Results

Since 2016, HBIS Serbia has continuously invested in modernization and process automation, achieving historic production records within its first two years of operation. The company has become Serbia's largest exporter and consistently ranks among the country's top three exporters, making a significant contribution to the nation's GDP.

HBIS Serbia is a socially responsible company, firmly committed to improving working conditions, enhancing the quality of life in the local community, and protecting the environment, with a constant focus on reducing the plant's environmental impact, advancing the green transition, and improving energy efficiency. Over the past years, we have invested more than €300 million in environmental protection, primarily in large-scale projects launched in 2019 and commissioned in 2022. These investments are ongoing.

Sustainability and Green Transition

With the construction of new facilities — the New Sinter Line, Gas Holder and the Walking Beam Furnace, not only has the appearance of the plant changed, but the performance of our environmental impact has also been significantly improved. Fugitive emissions into the air have been reduced through new emitters equipped with dry dust collection systems and the installation of continuous monitoring devices on them. Since these projects were from the outset focused on energy efficiency, they have achieved significant savings by using blast furnace gas instead of the more expensive natural gas, which was previously used to a much greater extent before construction.

Following the completion of the first phase of major environmental investments, clear and measurable improvements have been recorded. A particularly significant indicator is the average annual concentration of PM10 particles in 2023, which was 36.85 $\mu g/m^3$ — marking the first time levels have fallen below the legal limit of 40 $\mu g/m^3$. This serves as concrete proof that strategic investments in environmental protection are paying off.

To reduce environmental impact, HBIS Serbia has constructed a 16-meter-high protective wall around the Ore Yard. Ongoing monitoring aims to assess the effectiveness of this barrier in containing fugitive emissions within the plant premises. The goal of this investment is to reduce emissions toward surrounding villages and within the plant itself by 75 to 90 percent. By the end of the year, comparative data from before and after the wall's construction will reveal the concrete results of this improvement.

HBIS Serbia upholds a policy of openness and transparency. The company regularly holds meetings with local community representatives to present environmental protection results and future plans. At the same time, air quality measurements from the Radinac Automatic Monitoring Station, located near the plant, are made publicly available in real time through the company's website.

The company holds an IPPC permit and numerous international certifications: ISO 9001, ISO 14001, ISO 45001, HACCP, ISO 22000, ATS laboratory certification, and is in the process of certification for ISO 50001 Energy Management.

Looking Ahead

Before HBIS's arrival, the plant's technology was outdated and environmentally unsustainable. It is already certain that the second phase of the plant's modernization will take place from 2027 to 2030, in which the plant's operation and energy efficiency will be further improved, and environmental protection will be raised to even higher level.

These improvements will strengthen production capabilities, enhance business performance, and further reinforce HBIS Serbia's commitment to social responsibility and environmental sustainability. The company is firmly on a path toward an energy-efficient and sustainable future, aiming to reduce its carbon footprint in line with the best available technologies, with a clear vision — to become one of the most competitive steel plants in Europe.

HBIS Serbia – Academic Partner and Innovation Driver

HBIS Serbia has a long-standing, productive partnership with the Technical Faculty in Bor, University of Belgrade. Students regularly participate in one-day professional practice sessions to learn about modern processes in ferrous metallurgy, while company representatives actively contribute to scientific conferences such as IOC, EcoTER, and the Conference on Minerals, through expert presentations and research papers.

HBIS Serbia's collaboration with the academic community spans decades, and in 2024 a significant milestone was achieved with the establishment of the Virtual Green Steel Manufacturing Laboratory — a joint project between the Institute for Materials in China and the Faculty of Technology and Metallurgy at the University of Belgrade. Three projects were launched to develop new steel grades with improved properties and stronger market potential. After a year of intensive work, all projects were successfully completed and validated by all partners. In the second phase, currently underway, the laboratory is taking on new development tasks aimed at further improving processes and products in line with the principles of sustainable production. The following projects are oriented towards "green" steel manufacturing.

Contact
HBIS GROUP Serbia Iron & Steel llc Belgrade
E-mail: hbisbusinessoffice@hbisserbia.rs

Platinum donor

Čukaru Peki - the first green mine in Serbia

Serbia Zijin Mining administrative building

The company Serbia Zijin Mining is the owner of the copper and gold ore deposit in Bor and the first green mine in Serbia - Čukaru Peki, which moved the boundaries in Serbian mining in terms of technologies and standards applied in the ore mining process.

The basis of green mining was established by the construction of plants that use the most modern technology and apply the highest European and world standards. The company has a unique work system and has introduced new, modern methods of ore mining. Since the ore body is deeply positioned, the method of opening with ventilation shafts and declines was adopted. The mine has a Lower Zone, where exploration works are ongoing, and an Upper Zone, where exploitation is carried out.

The ore deposit is divided into three mining areas, and the method of excavation in horizontal bands from the bottom up and the method of sub-excavation of chambers with subsequent filling was adopted. The process of thickening the tailings, which is later used for filling in underground corridors, is carried out in the unique Back filling station plant, the only one of its kind in Serbia. Apart from the excavation method, there is a unique ventilation and drainage system in the mine. The mine has an organized traffic network with light signaling, mobile signal and 4G network, as well as fixed telephony, which enables smooth communication, and for security reasons, the

system is covered by video surveillance, which monitors the mining of ore, its transport and the development of traffic.

The world's leading technology and high-efficiency equipment are integrated into the production process. In the mineral processing plant, the internationally advanced "SAB" process and the flotation system developed by the company itself are used for crushing and grinding. In the production process, only electricity is used and no harmful gases are emitted into the atmosphere. During the construction of the plant, a closed circular drainage system was constructed, which returns the technical water back to production, without releasing it into nature. The entire work procedure is carried out in accordance with the laws, national regulations and technical standards of the Republic of Serbia, and includes compliance with international regulations in the field of environmental protection.

By choosing the most innovative technological solutions, the most important foundations of green mining were laid, which, along with safety and protection at work, emphasize an ecologically sustainable production process that strives for zero pollution. From the very beginning of work, the mine has been successively carrying out reclamation and greening procedures, and the plan is to introduce renewable energy sources, which are one of the priorities of this ecologically oriented company, dedicated to environmental protection, but also to the development of the local community and the employment of young people and professional people, including numerous engineers who graduated from the Technical Faculty in Bor.

The motto of the company Serbia Zijin Mining, aimed at the welfare of local communities, citizens, society and the state, is "Mining for a better society". As a leader in innovation in terms of technology, whose function is to preserve and improve the environment, the company Serbia Zijin Mining strives wholeheartedly to contribute to the development of mining in Serbia by moving the framework in the work of the mining industry, and to place the Čukaru Peki mine in the first place among the most successful European and world copper and gold producers.

Serbia Zijin Mining d.o.o. Bor

Address: Suvaja 185a, 19210 Bor

E-mail: info@zijinmining.rs

Web: https://www.zijinmining.rs/

Gold sponsor

ABOUT THE COMPANY

DPM Metals Inc. is an international mining company engaged in the acquisition, development, extraction, and processing of metals. Founded in 2004, DPM has proven itself in the implementation of responsible mining practices. In addition to its successful mines in Krumovgrad and Chelopech in Bulgaria, DPM Metals also conducts geological exploration in Bulgaria, Ecuador, and Serbia. Recently, the high-quality Rupice project in Bosnia and Herzegovina has been added to the company's portfolio. One of the company's key principles is operating in accordance with local regulations, while adhering to the same values, ethical, and business principles wherever we operate. The company's goal is to thrive and grow together with local communities and to support their long-term sustainable development.

DPM Avala d.o.o. is a subsidiary of the international mining company DPM Metals Inc., based in Canada. DPM Avala d.o.o. is a mineral exploration company focused on the exploration and development of gold and associated metal projects in Serbia. This company is committed to the successful development of projects based on the highest standards in mining and the preservation of local communities, the environment, and long-term benefits for Serbia.

For more information, please visit our website **www.dpmmetals.com**

Gold donor

Sevojno
VALJAONICA BAKRA
COPPER MILL

The Sevojno Copper Mill was founded in 1950 by the decision of the General Directorate of the Government of the Federal People's Republic of Yugoslavia. Production at the Sevojno Copper Mill began in 1952.

From 1950 until privatization, the Sevojno Copper Mill was organized as follows: the Socially Owned Enterprise (SOUR) Copper and Aluminum Mill "Slobodan Penezić Krcun" Sevojno, the Sevojno Copper Mill with a Public Enterprise status, and the Joint Stock Company (DP) Sevojno Copper Mill. Today, the Sevojno Copper Mill is a joint-stock company under the law.

The Sevojno Copper Mill is the largest copper and copper alloy processor in the former Yugoslavia, placing it among the most well-known and giant factories in Europe and the world. The company's headquarters and production facilities are located in Sevojno.

The core activity of the Sevojno Copper Mill involves the processing of copper and copper alloy through rolling, pressing, and drawing into standard semi-finished products, including sheets, strips, foils, waist, rondels, pipes, bars, rods, profiles, and wires. Most of the products are exported to foreign markets (80%), making the Sevojno Copper Mill one of the largest exporters in Serbia, with the main exports going to Western Europe and Central and Eastern Europe.

One-third of the Sevojno Copper Mill's production consists of products used in the defense industry, which is why, in 2018, the Serbian government classified the factory as a company of strategic importance for the country.

The products of the Sevojno Copper Mill find applications in machinery manufacturing, the electrical industry, shipbuilding, petrochemicals, energy, automotive and process industries, construction, and architecture.

The designed capacity of the Sevojno Copper Mill is approximately 50,000 tons per year. The current capacity ranges from 35,000 to 45,000 tons annually, depending primarily on the product range.

In the Sevojno Copper Mill's facilities, various types of pure copper deoxidized with phosphorus and a wide range of copper alloys with zinc are cast and processed through plastic deformation in both cold and hot states, including two-components and three-components alloys (lead brass, special alloys with tin, aluminum, and nickel).

The advantages of the Sevojno Copper Mill over its competitors primarily lie in its production flexibility, characterized by the ability to produce both large quantities and small batch orders, as well as the ability to procure products related to both the Rolling Plant and the Extrusion Plant in one place.

Investing in new equipment, adopting new technologies, developing new products, further improving environmental sustainability, and investing in training and personnel development are strategic priorities and some of the aspects of the business policy for the future of the Sevojno Copper Mill.

Currently, the Sevojno Copper Mill employs approximately 1,100 people.

Address
Sevojno, industrial area of Uzice, Serbia.
Prvomajska bb, 31205 Sevojno, Serbia
Phone: +381 31 531 757;
Fax: +381 31 532 161;
office@vbs.co.rs;
www.vbs.co.rs

Gold donor

Serbia Zijin Copper DOO is a Chinese-Serbian company operating as part of the Zijin Mining Group. The company was founded on December 18, 2018, and on the same day Zijin signed the final agreements with the Government of the Republic of Serbia, acquiring a 63% ownership in RTB Bor. Zijin became the holder of 63% of the company's capital, while the Republic of Serbia retains the remaining 37%. The initial investment planned by Zijin for this project was $1.26 billion, but by the end of April 2025, the total investment reached $3.267 billion.

The company operates four copper mines ("Veliki Krivelj," "Novo Cerovo," "Jama," and "Majdanpek"), a Limestone Mine, the "Quarry" Plant, and a Smelter. As of December 2024, Serbia Zijin Copper's resources amount to 8,934,000 tonnes of copper ore with an average grade of 0.39% metal per tonne, and 345 tonnes of gold ore with an average grade of 0.151 grams per tonne. Of this total, the proven reserves within the planned mining boundaries include 6,097,000 tonnes of copper ore with an average grade of 0.421% metal per tonne, and 228 tonnes of gold ore with an average grade of 0.16 grams per tonne.

Between January and December 2024, Serbia Zijin Copper produced a total of 125,221 tonnes of copper in the concentrate, 2,674 kilograms of gold, 23,305 kilograms of silver, as well as 163,722 tonnes of cathode copper..

Since taking ownership of the former RTB Bor until the end of December 2024, Serbia Zijin Copper produced a total of 487,868 tonnes of copper in the concentrate and 12,405 kilograms of gold. The company contributed $701 million in various taxes and fees, ranking among the top corporate taxpayers in this category. In addition, Serbia Zijin Copper collaborates with more than 1,800 local suppliers, with the total value of procured goods and services exceeding $3 billion. Indirectly, this has led to the creation of over 9,000 jobs.

Serbia Zijin Copper currently employs approximately 6,000 people. The average monthly net salary of its workers exceeds 165,000 dinars, which represents a 144% increase compared to the average net income in 2018. Salaries of employees at Serbia Zijin Copper are significantly above the local per capita income and are 57.5% higher than the national average in Serbia. Since assuming management, the company has created more than 3,300 new jobs in Bor and Majdanpek, primarily for young people, making it one of the most important contributors to the economic growth of both cities. Additionally, a large number of new job opportunities for local residents has played a key role in maintaining social stability in the region.

In compliance with Serbian laws and regulations on safety and environmental protection, Serbia Zijin Copper has made significant efforts over management to investigate and resolve historical

issues in these areas. These activities have led to substantial improvements in overall safety and environmental standards. The company's safety operations are based on the concept "life comes first," and to effectively improve the enhance the immediate working environment, it has introduced modern facilities and equipment. Between January and December 2024, the incident rate per million working hours was 0.27. At the same time, $270 million was invested to enhance environmental protection and ecology. A wide range of measures were undertaken to address issues related to dust, waste, flue gases, and wastewater, resulting in significant improvements. In line with efforts to develop to develop green mines and achieving harmony between mining operations and environmental protection, more than 3.7 million square meters of land have been greened and over 1.2 million seedlings have been planted. Furthermore, 958,390 tons of non-hazardous waste and around 3,200 tons of hazardous waste were properly disposed of.

As a socially responsible company, Serbia Zijin Copper pays great attention to the sustainable development of the environment in which it operates and provides almost daily support to the local governments of Bor and Majdanpek. It continuously implements a package of plans for the joint development of local communities and conscientiously fulfills its corporate obligations. The company supports numerous cultural, educational, healthcare, tourism, and sports institutions and events, demonstrating in a direct and concrete way that it is a driving force behind the development of the Timok region and Serbia.

By the end of April 2025, Serbia Zijin Copper had carried out 312 donations and allocated around 10 million US dollars to improve healthcare, transport infrastructure, education, sports, traditional arts, entertainment for children, and other areas in Serbia.

Serbia Zijin Copper DOO

Đorđa Vajferta Street 29

19210 Bor, Serbia

zijinbor@zijinbor.com

www.zijinbor.com

Silver donor

"MC LABOR" d.o.o. Belgrade has been engaged in the sale and servicing of sophisticated analytical equipment, as well as process devices, since its establishment in 2005 up to the present day. We have been long-standing exclusive representatives of several renowned global brands, such as:

- **ANTON PAAR**
- **KPM Analytics**
- **HITACHI HighTech Analysis**
- **EQUILAB ES**

for the territories of Serbia with Kosovo, Montenegro, North Macedonia, and Bosnia & Herzegovina, depending on the specific program.

For all equipment we supply, we provide complete support carried out by our employees, including:

- Installation of devices
- User training
- Application support throughout the lifetime of the device
- In-house service
- Procurement of spare parts and consumables

All employees regularly undergo appropriate sales and service training with manufacturers on an annual basis, for which we hold numerous certificates.

We believe that this fact, along with the long-standing experience of our staff in this field and our commitment to customers, is the reason why our company has been recording growth year after year across all parameters.

For this occasion, we would particularly like to highlight that our sales program covers the complete range of devices used in mining and metallurgy:

- **Sample preparation: mills, presses, fluxers, metal processing systemy**
- **XRD device with non-ambient chambers for high-temperature measurements**
- **Particle size analyzers (granulometers)**
- **Porometers, gas adsorbers**
- **Portable and benchtop EDXRF spectrometers**
- **OES spectrometers**

If you find any of this interesting, we would be pleased to welcome you at our conference booth or at our premises in Zemun.

MC Labor d.o.o.
Dobanovačka 101, 11080 Zemun, Serbia
Mobile: +381 60 333 133 03
Tel: +381 11 40 94 436
Email: office@mclabor.co.rs
Website: www.mclabor.co.rs

Exhibition

Founded 2006, Indemak has become a well-known company in its region in a short period of time. Main reasons behind this success are the ability of combining the years of experience and know-how with new technology and keeping the customer satisfaction above all.

Indemak, operating in its modern facility over 5000 m^2 area, manufactures medium frequency induction furnaces ranging from 10 kg to 20 tons capacity. Besides induction furnaces, pipe, billet and other heating units are also being manufactured.

Indemak has offices in many countries with many satisfied clients around the world.

On the other hand, Indemak is cooperating with Pourtech-AB from Germany for heated and unheated bottom and tilted pouring furnaces for larger foundries and casting lines.

Besides, Indemak offers spare part, consultancy and technical support service for furnaces from all brands.

Our Contact Information

Address: Sarımeşe Mh. Arpalık Sk. No:19 Kartepe / Kocaeli
Telephone: +90 262 311 29 49 / +90 262 373 29 01
Fax: +90 262 311 24 49
E-Mail: info@indemak.com
Web: www.indemak.com

Vice General Manager
Anil Ataman
+90 507 576 41 94
anil@indemak.com

Representative in Serbia

Planit d.o.o.
Tomislav Gredic
+381 63 417 005
tomislav.gredic@planit.rs
www.planit.rs

Andrij Gredic
+381 63 418 774
+381 22 329 793
office@planit.rs
www.planit.rs

www.labtim.rs

One of the world's leading manufacturers of laboratory equipment, especially in the field of LC and LC/MS chromatography.

TA instrument as part of the Waters company is the world leader in Thermal Analysis, Rheology, Microcalorimetry, Biopharmaceuticals, Medical Devices, Elastomers and Rubber.

www.waters.com

Manufacturer and supplier of static tension and/or compression testing machines, designed to measure material's strength and performance.

www.tiniusolsen.com

Biotage is the world's leading supplier of high-performance systems for sample prep, synthesis of organic compaunds and synthesis of peptide and variety choice of evaporators.

www.biotage.com

Biotage is the world's leading supplier of high-performance systems for sample prep, synthesis of organic compaunds and synthesis of peptide and variety choice of evaporators.

www.biotage.com

Daliborka Crnogorac

Direktor / Managing director
Email: daliborka.crnogorac@labtim.rs
Mob:+381 66 5555 200
Tell:+381 11 770 5550
Labtim SE d.o.o.,

Tošin bunar 181a L42, 11070 Beograd, Srbija

Exhibition

KRUG INTERNATIONAL LTD.

Krug International LTD is specialized in selling and servicing laboratory equipment for the territory of Balkans mainly Serbia. We are representing several reputable companies which produce sophisticated laboratory equipment used in a wide variety of industries and academia like Malvern Panalytical, Horiba, Linseis, GBC etc of which all corporations are leaders in their segments. With 35 years of experience, 15 employees of which 4 service engineers, and presence in the Serbian industry and market we have good relations with customers and infrastructure to successfully promote, sell and service sophisticated instruments.

Miloš Hadži-Đorđević, M.Econ, B.Sc.Chem
Director
KRUG International LTD.
Deset avijatičara 2a, 11050 Beograd
Tel: +381113049730
Fax: +381113049748
Cell: +381 63 444065
e-mail: milos.hadzi-djordjevic@kruginter.com
www.kruginter.com

Exhibition

MERIS d.o.o., founded in 1992, is a Serbian company dedicated to providing economically viable process solutions with the utilization of cutting-edge technology equipment. They prioritize building enduring business relationships with their clients. The company's core activities encompass representing foreign firms, offering engineering services primarily in the field of measuring and automating processes related to the treatment of potable and wastewater, as well as the regulation and automatic control of technological processes. They also specialize in equipment supply and the maintenance and servicing of measuring instruments.

MERIS d.o.o. proudly serves as the exclusive representative for Serbia and Montenegro for renowned global companies, including ENDRESS+HAUSER, a leading manufacturer of industrial process measurement instruments, XYLEM FLYGT, known for submersible pumps and pump control equipment, and BIOCUBE, offering advanced SBR wastewater treatment systems. Additionally, they partner with AVK and TECOFI for high-quality water and industrial valves, Lutz-Jesco for chlorine dosing systems, SCHNEIDER Armaturen for measuring circuit valves, and CIMBRIA for temperature measurement equipment in silos.

The company ensures that all the equipment they introduce to the market complies with the necessary certifications for public use in the Republic of Serbia, as well as internationally recognized certifications such as PTB, LOYD, and SQS. With a team of twenty employees, including twelve engineers, **MERIS** d.o.o. is committed to delivering exceptional products and services to meet the diverse needs of its clients. For more information and references, please visit their website at **www.meris.rs.**

Our Vision – **MERIS** envisions continuous growth in its client and principal base, accompanied by an expansion of its service and product offerings, driven by a team of skilled, satisfied, and ambitious individuals who thrive both professionally and personally. **MERIS** aims to become a regional leader, always staying one step ahead, with a primary focus on customer satisfaction as a fundamental condition for its existence.

Our Mission – As a socially responsible company and a reliable partner, **MERIS** empowers its clients to develop production processes in line with the latest technological solutions. In doing so, **MERIS** promotes increased profitability, energy efficiency, environmental preservation, and enhanced business quality for its customers, thereby creating conditions for retaining talented individuals within the country.

MERIS d.o.o.
Dunavska 78a
11060 Belgrade, Serbia
t: +381 (11) 314 88 00
f: +381 (11) 314 88 11
e: meris@meris.rs

Exhibition

Altium International d.o.o. is engaged in the sales, maintenance, and servicing of equipment from renowned global manufacturers such as

- Agilent Technologies,
- Netzsch
- Skalar,

and many others. We are the only authorized provider of these services in the territories of Serbia, Montenegro, and Macedonia.

Services

- Preventive Maintenance
  Carried out according to the manufacturer's instructions, ensuring the continuous operation of your instruments and minimizing the need for service interventions.
- Instrument Qualification
  Performed in compliance with manufacturer protocols, proving that the performance of your instruments meets the manufacturer's specifications.
- Service Support
  All our service engineers have undergone training at the manufacturers' training centers and hold certificates that guarantee fast and high-quality support.
- Spare Parts
  A large stock of original spare parts enables quick troubleshooting and minimizes downtime.

Commitment to Development

As instrumental techniques are continuously evolving, Altium International d.o.o. is dedicated to the ongoing professional development of all employees, with the goal of increasing customer satisfaction, with the values TRUST, RESPECT, DEVELOP, SHARE.

Altium International d.o.o.
Jurija Gagarina 76đ, 11070 Belgrade
info.rs@altium.net
+381 60 750 04 01

Exhibition

About the Metalurg Foundry

Metalurg Foundry Ltd. in Prokuplje specializes in processing non-ferrous metals and alloys through casting. We prioritize quality, cost-efficiency, and customer satisfaction. We adhere to ISO 9001 standards for continuous improvement. With a strong presence in the domestic market, we serve over 200 clients.

Casting Methods

We employ various methods:

- Sand casting, Gravity die casting, Centrifugal casting, White metal bearing casting

Alloys We Work With

Our alloys include:

- Aluminum Bronze, Tin Bronze, Lead Tin Bronze, Manganese Bronze, White Bronze,Aluminum, Red Brass, Brass, White Metal/Babbitt

Highlights

- Sand casting suits complex designs.
- Gravity die casting offers superior quality.
- Centrifugal casting reduces inclusions and porosity.

Crafting Church Bells

We excel in crafting church bells for exceptional sound and aesthetics, guided by Russian master calculations.

Artistic Casting

We create intricate metal castings, collaborating with renowned sculptors for custom projects.

Bearing Manufacturing

With decades of experience, we produce bearings of various sizes using white metal alloys.

Contact
Metalurg Foundry Ltd.
Address: Pećka St. bb, 18400 Prokuplje
Phone: +381 27 8429-075
Website: www.livnica-metalurg.com
Email: office@livnica-metalurg.com, metalurgpk@mts.rs

Exhibition

About Fugro

Fugro is the world's leading Geo-data specialist, collecting and analyzing comprehensive information about the Earth and the built environment. With expertise in consulting, geotechnical, environmental, and geoscience services, Fugro supports clients in the market sectors

- Infrastructure,
- Energy and
- Water

to design, build, and operate assets safely and sustainably. Operating in over 60 countries, Fugro delivers innovative solutions through advanced remote sensing, AI, and digital technologies, helping clients mitigate risks, optimize performance, and enhance decision-making.

Key services for the mining industry

- Consulting – water & environment
- Geotechnical site investigation and engineering
- Groundwater modelling, dewatering, flood risk management
- Wireline logging geophysics
- Ground geophysics (seismic, geoelectric, geomagnetic, gravimetry, ground penetrating radar,
- Passive seismic (Ambient Noise Tomography, ANT)
- Hydraulic packer testing
- Inspection & monitoring
- Slope stability monitoring
- Stability investigation of tailings
- Evaluation of residual metal content in tailings (XRF-CPT)
- In-situ assessment of subsurface contaminations (VOCs, CHCs, BTEX, fuels, crude oil, tar, PAHs)
- 3D modelling of contaminated sites & remediation.

Contact
Fugro Germany Land GmbH
phone: +49 30 936 510
email: FGLG-Info@fugro.com
web: www.fugro.com
Katarzyna Staniewska | Strategic Sales & Marketing Manager | k.staniewska@fugro.com
Wolfram Felfer | Principal Project Manager Geophysics | w.felfer@fugro.com

Exhibition

ANALYSIS
LABORATORY EQUIPMENT

www.analysis.rs

Analysis d.o.o. was founded in 1996. The core business of the company is the wholesale, maintenance, and servicing of analytical, process, and general laboratory equipment, including user training, service qualification, application development, and project design.
The product portfolio of Analysis d.o.o. includes equipment used in industries such as pharmaceuticals, environmental protection, food and beverage, and other industrial sectors, as well as in science, forensics, and medicine – whether for testing, research, quality control, or process monitoring.
Since its establishment, Analysis d.o.o. has successfully cooperated with leading global manufacturers of laboratory equipment to meet customer requirements and establish long-term partnerships based on mutual satisfaction.

Analysis d.o.o. is the exclusive representative of the following renowned equipment manufacturers:

- **THERMO FISHER SCIENTIFIC (USA)**, with the following divisions and equipment:
  - Thermo Scientific – Laboratory equipment for analytics
  - Controlled Environment Equipment – Equipment for microbiology and biotechnology
- **SOTAX (Switzerland)** – Equipment for dissolution testing and physical characterization of solid dosage forms
- **WALDNER (Germany)** – Laboratory furniture and fume hoods
- **HACH (USA)** – Laboratory and process equipment for water analysis
- **RETSCH (Germany)** – Mills and sieves
- **FEDEGARI (Italy)** – Equipment for microbiology and biotechnology
- **RIEBESAM (Germany)** – Laboratory glassware washers and disinfectors
- **MICROTRAC MRB (USA)** – Particle characterization instruments
- **BERGHOF (Germany)** – Microwave digestion systems and reactors
- **MEMMERT (Germany)** – Ovens, incubators, climate chambers, and water baths
- **SCAT, SYMLINE (Germany)** – Equipment for waste chemical collection
- **BIOQUELL (UK)** – Isolators and H_2O_2 decontamination systems
- **LABINSTRUMENTS (Italy)** – Certified reference material standards (pesticides, mycotoxins, QuEChERS)
- **RECIPE (Germany)** – Kits, reagents, instruments, and consumables for clinical diagnostics
- **ATAGO (Japan)** – Refractometers and polarimeters

Through its **Service Support Department and Calibration and Validation Laboratory**, and with its own testing and measuring equipment, Analysis provides services such as installation, qualification, maintenance, and servicing of equipment, as well as user training. These services are delivered by experienced service engineers who have completed specialized courses for the respective equipment in manufacturer training centers, as confirmed by appropriate certificates.

Exhibition

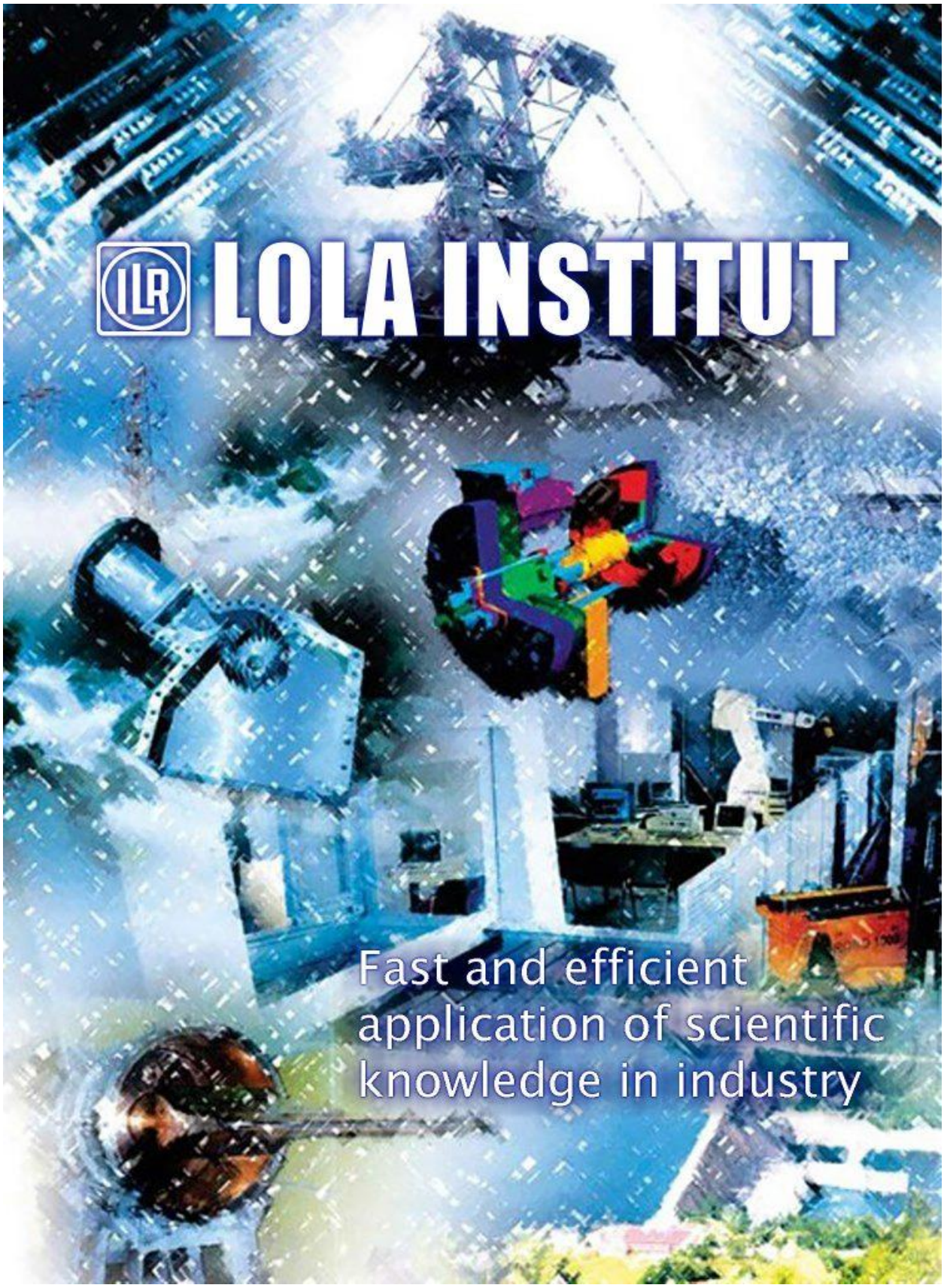
LOLA INSTITUT
Fast and efficient
application of scientific
knowledge in industry

Exhibition

Tescan

Tescan – Accelerating the Art of Discovery

Tescan is more than an instrument manufacturer. We're a global team of engineers, scientists, designers, and application experts – building advanced imaging instruments and the solutions around them.

For over 30 years, we've helped scientists see deeper with advanced SEM, micro-CT, and now 4D- STEM technologies – like our TENSOR platform, the first transmission electron microscope built from the ground up for 4D performance.

We design with real workflows in mind – from materials science and geosciences to life sciences and semiconductors – ensuring every system is intuitive, application-ready, and fully supported throughout its lifecycle.

Our Aspiration

Is to empower our customers and partners with instruments, software and service fit for the future. By transforming complex technologies into intuitive, human-centric solutions, we aim to equip the world with what it needs to move faster, think deeper, and accelerate our collective discovery.

Our Approach

Is to remove the complexity and friction between question and discovery. We're working towards a world without the barriers that have long stood in front of scientists – so they can spend less time fighting systems, and more time moving science forward.

Our Drivers

We value collaboration, forward thinking, and outcomes that truly make a difference, from the every day to the big discoveries. We believe the best solutions come from working closely – across teams, disciplines, and with our partners. We're not afraid to challenge convention or rethink what's possible, because progress demands it. And we always put experience first, designing tools that feel intuitive, human, and built for the way scientists actually work.

mikrolux
www.mikrolux.hr

Mikrolux – general representative of Tescan

Company overview: Exclusive, authorized sales and service distributor of TESCAN scanning electron microscopes and accessories.

Mission: Sale, installation, training, support, service and maintenance.

MIKROLUX d.o.o.
Ljudevita Gaja St. 35, 10290 Zaprešić, Croatia
+385 91 59 63 596
+385 1 33 98 905 (Fax)
mikrolux@mikrolux.hr

Exhibition

Trokuttest Group
Srbija

Trokut Test Serbia has been operating in the market since 2012, offering equipment from renowned global manufacturers in the fields of mechanical testing, quality control, chemical analysis, metrology, metallography, non-destructive testing (ultrasonics, radiography, magnetic testing, penetrant testing), predictive maintenance, and automation systems in production.

The Trokut Test Group consists of 6 local companies located in Croatia (headquarters), Slovenia, Bulgaria, Serbia, Bosnia and Herzegovina, and North Macedonia – our activities span across the entire Balkans and beyond.

Our expert team, along with supplier support, is at your disposal to find suitable solutions for your testing, testing, optimization, and production improvement needs.

Trokut Test Ltd.
www.trokuttest.com
Milica Antić – Business Associate
Mobile: +381 60 5557238
Email: adminsrb@trokuttest.com
Danila Bojovića 18/2
11010 Belgrade
Serbia

Novos doo Belgrade – Your Partner in the Pharmaceutical and Chemical Industry

- Founded in 1995 – exclusive distributor of Merck KGaA, Darmstadt and affiliated companies (Merck Life Science, Sigma-Aldrich, Millipore).
- 30 years of experience in the markets of Serbia and Montenegro.
- Our mission: uncompromising quality of products and services, with continuous improvement and modernization of our offering.

What We Offer:

- Chemicals and reagents for laboratories
- Solvents, raw materials for the pharmaceutical and cosmetic industries
- Microbiological media
- Laboratory water purification systems

Our Strategy:

- Top-quality products and services
- Expansion into new markets and development of innovative programs
- Social responsibility and sustainable growth

Environmental Protection:

- Integration of ecological principles into all processes
- Cooperation with associations and initiatives for sustainable development
- Using knowledge and resources for projects that improve the environment and quality of life

Novos d.o.o.

Address: Str. Cara Dusana 207, 11080 Belgrade-Zemun, Serbia

Phone: +381 (0) 11 3773 511 | Fax: +381 (0) 11 3164 339 | Mobile: +381 (0) 62 215 083

Email: jasmina.ignjatovic@novos.co.rs | Website: www.novos.co.rs

Changsha Rui Rui Technology Co., Ltd.

About Us

Changsha Rui Rui Technology Co., Ltd., established in 2021 and certified as a National High-Tech Enterprise, is a innovative provider of software and services in the field of computational materials design. Our mission is to bridge the gap between materials science theory and industrial application through robust, user-friendly digital tools.

Our Technology and Software Suite

Our flagship achievement is the development of a complete digital workflow within the Integrated Computational Materials Engineering (ICME) framework. This platform connects calculations across multiple scales to establish the crucial "process-structure-property" linkage for metallic materials.

A digital workflow was developed based on the "microstructure-performance correlation". It starts from scientific databases and integrates phase diagram thermodynamic calculation, thermophysical property calculation, phase field simulation, and crystal plasticity finite element calculation in sequence. For each computational stage, dedicated software tools were designed and developed. These developments focused not only on solving specific computational problems but also on ensuring theoretical connections and seamless data transfer between them, aiming to create a universal intelligent design platform for metallic structural materials, as depicted in Figure 1.

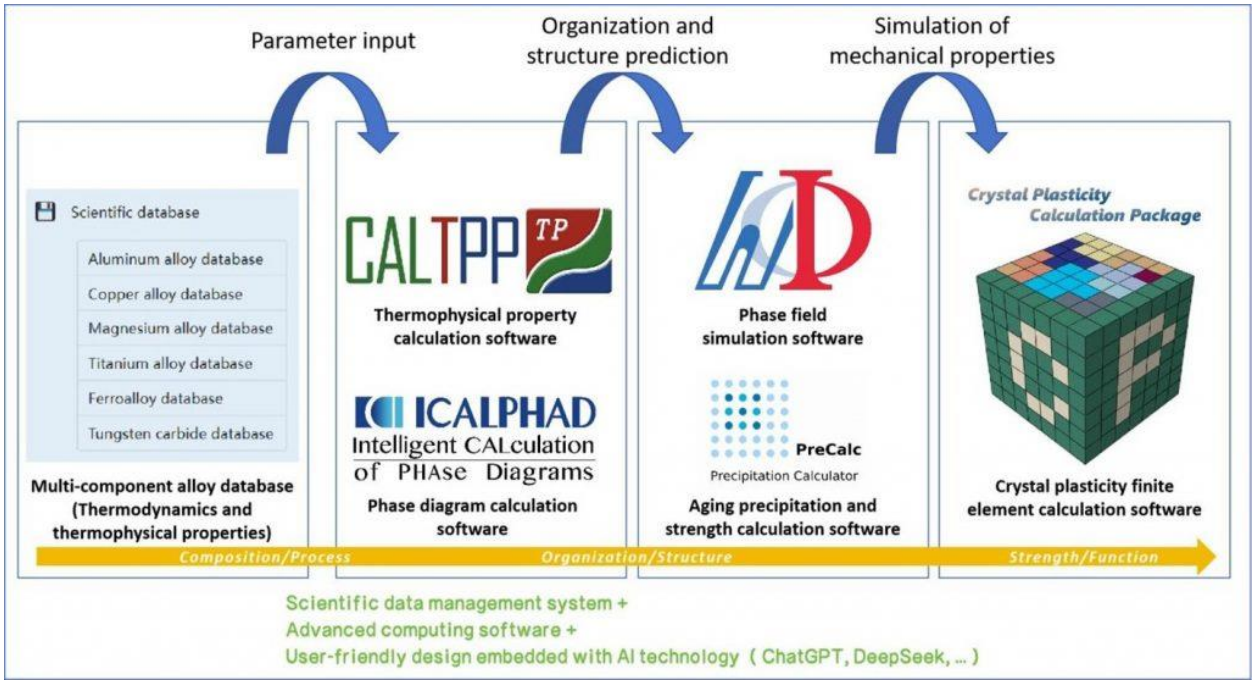

Figure. 1 ICME flowchart based on database and software

The digital workflow consists of several sequentially linked computational modules, each implemented through dedicated software tools. The software in the Fig. 1 is briefly introduced as follows:

ICALPHAD (Intelligent CALculation of PHAse Diagrams): A software tool based on the CALPHAD method for calculating phase diagrams and optimizing thermodynamic parameters of materials systems. It is used for predicting material properties and phase behavior in materials science and engineering. For more information, https://doi.org/10.1016/j.calphad.2025.102810.

CALTPP (CALculation of ThermoPhysical Properties): Provide various thermophysical properties such as diffusion coefficient, interfacial energy, thermal conductivity, viscosity. For more information, https://doi.org/10.1016/j.jmst.2019.12.005.

MID-MESO (Microstructure Intelligent Design MESOscale): An open-source phase-field solver package for simulating multiphase transformation and mechanical analysis of polycrystalline nanoparticles. For more information, https://github.com/Microstructure-Intelligent-Design.

PRECALC (PREcipitation CALCulator): A computational software for age-hardening materials, integrating functions such as age precipitation and macroscopic strength and electrical conductivity prediction. For more information, https://doi.org/10.1016/j.jmrt.2024.05.145.

CPCP (Crystal Plasticity Calculation Package): A research/teaching toolkit based on the crystal plastic finite element method. At present, it has successfully carried out calculation simulation on aluminum alloy, high-strength steel, cemented carbide, coating materials and so on. For more information, https://www.ams.org.cn/CN/10.11900/0412.1961.2024.00083.

This series of software components involved in the workflow encompasses the transmission and circulation of various material information. Starting from the database, phase diagram information and thermophysical data of alloy materials at specified compositions and temperatures are obtained through ICALPHAD and CALTPP software, which supports the subsequent phase field simulation (MID-MESO) and precipitation prediction (PRECALC). After obtaining the exact state of the structure and microstructure, the mechanical property prediction under specified loads is conducted through crystal plasticity finite element software. Figure 2 shows the corresponding computational steps behind the combination of these software.

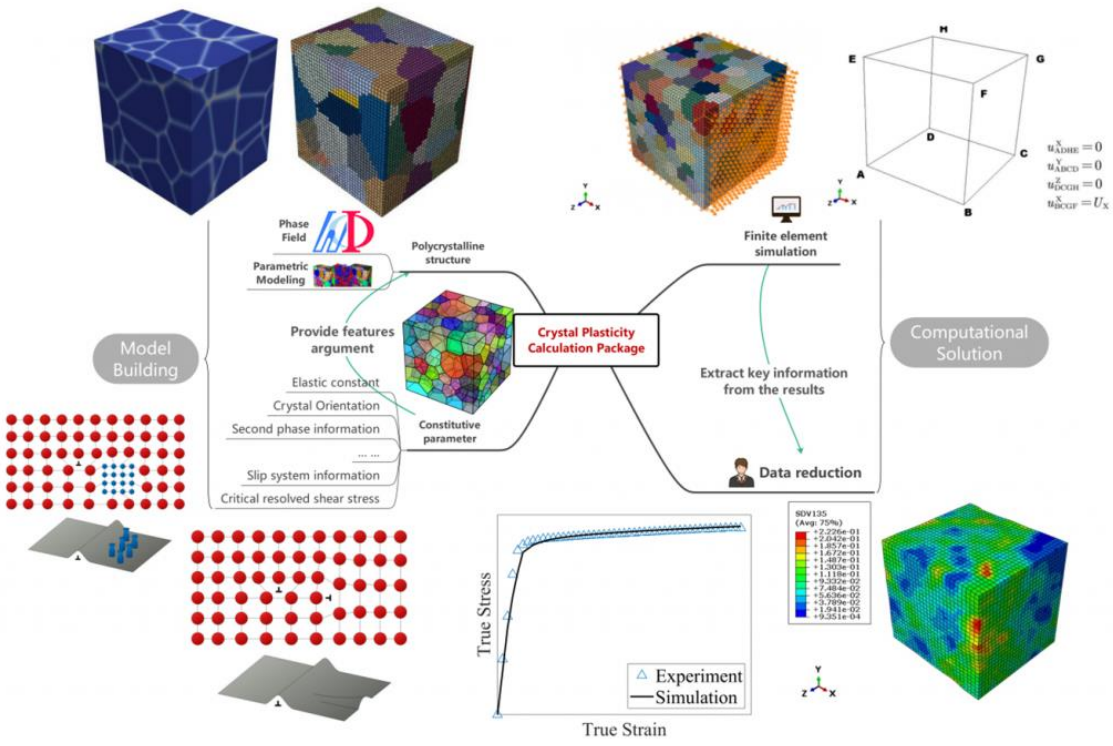

Figure. 2 Flowchart of crystal plasticity finite element calculation

Exhibition

ВИНАРИЈА МАНАСТИРА
БУКОВО

The tradition of cultivating grapevines and producing wine in the Negotin region is inextricably linked to the Bukovo Monastery. Due to its favorable geographic location, exceptional climate conditions, and unique soil type on the monastery estate, the Bukovo Monastery has been the synonymous cornerstone of viticulture and winemaking in this region for centuries.

Following the appearance of phylloxera, which seriously threatened European, including Serbian, viticulture at the end of the 19th century, the Bukovo Monastery established the first viticulture school on its estate in 1887. It became the first state agricultural school for viticulture and orcharding four years later. The monastery became the center for the revival of viticulture in the Negotin region.

Our monastery's rich history of viticulture and winemaking, serving as a unique legacy for generations, inspired Bishop Timočki Justine to continuously encourage the brotherhood under his spiritual guidance to revive and continue this tradition. These efforts have borne fruit, and the monastery's brotherhood has cultivated a unique vineyard of the Black Tamjanika grape variety on a two-hectare surface. This ancient variety has not only been preserved but has also laid the foundation for the creation of a new, authentically Serbian wine.

This specific Muscat variety is challenging to cultivate due to its periodicity in bearing fruit and yield. Black Tamjanika grapes consistently reach sugar levels between 25% and 32%, and in exceptional years, with lower yields and a "drying" phase, they can contain up to 45% sugar. This grape can produce wines with alcohol content ranging from 14% to 17.6%, with residual unfermented sugar, making it an exceptional semi-sweet Muscat wine.

The monastery expanded its grape varieties in the following years, including Cabernet, Merlot, Burgundy, Gamay, and the Chardonnay white variety.

The monks exclusively use spontaneous fermentation to produce their wine and carry out vinification by manually submerging the cap while controlling the temperature of the fermentation process.

Striving to unite tradition and modern technology in winemaking, the monks, through their hard work and dedication, seek to nurture monastery vineyards, relying on the grace of God to compensate for all our shortcomings, to reintroduce top-quality wines worthy of this climate to Serbia.

Friends of the conference

Messer Tehnogas has been part of the international Messer Group since 1997 and is the leading company in Serbia and the Balkans for the production and distribution of industrial, medical, and specialty gases, as well as cutting and welding equipment.

The company is the only producer of oxygen, nitrogen, argon, nitrous oxide, and hydrogen in Serbia. It operates facilities in Belgrade, Smederevo, Bor, Pančevo, Niš, Kraljevo, and Novi Sad, and through a network of 70 sales partners supplies more than 4,000 customers across the country and the region.

Expert teams for technical and logistical support are available 24 hours a day, all year round, supported by the company's own fleet of more than 50 trucks and tankers.

Basic contacts:
Company name: Messer Tehnogas AD Belgrade
Address: Banjički put 62, 11090 Belgrade
E-mail: postoffice@messer.rs
Website: www.messer.rs

CHINA-SERBIA JOINT LABORATORY ON GREEN STEEL MANUFACTURING

HBIS and University of Belgrade

(I) Background

HBIS Group has actively conducted collaborative innovation with the University of Belgrade. In April 2024, the "HBIS – University of Belgrade Joint Laboratory on Green Steel Manufacturing" was established. On April 15, 2024, the Secretary of Hebei Provincial Party Committee and the Serbian Minister of Science and Technology jointly unveiled the laboratory. On this basis, in October 2024, the China-Serbia Belt and Road Joint Laboratory on Green Steel Manufacturing, jointly applied for by HBIS Group and the Faculty of Technology and Metallurgy of the University of Belgrade, was successfully approved. This is HBIS's first national-level R&D platform and also the first "Belt and Road" joint laboratory in Hebei Province.

(II) Overall Objectives

Implement the spirit of the series of important instructions by the heads of state on China-Serbia cooperation, jointly build a China-Serbia community with a shared future, and develop a globally influential center for technological R&D and achievement transformation, as well as a platform for talent cultivation and cooperative exchanges. Promote industry-academia-research collaboration across the entire innovation chain in the steel sector between China and Serbia, enhance capabilities in technological innovation, industrial capacity cooperation, and coordinated development, drive multilateral cooperation and high-quality development among countries along the "Belt and Road" through radiating effects, and contribute innovative achievements and technological strength to scientific and technological exchanges and cooperation.

(III) Core Tasks

Joint project R&D: Focus on breaking through core technologies and key equipment that restrict the green and low-carbon transformation of the steel industry, providing technical support for building green and low-carbon industrial clusters in China and Serbia.

International technology transformation: Promote the transfer and transformation of joint research achievements—such as high-end product R&D, efficient low-carbon smelting, and process energy efficiency improvement—in China, Serbia, and other Central and Eastern European countries.

Driving multilateral cooperation: Leverage the demonstration role of scientific and technological achievement promotion and sci-tech cultural exchanges to drive multilateral cooperation among countries along the "Belt and Road."

Academic exchange and interaction: Establish a key academic exchange platform between China and Serbia to enhance both parties' capabilities in technological innovation and coordinated development in the field of green steel manufacturing technologies and equipment.

Youth talent cultivation: Cultivate Chinese and Serbian young scientists with international perspectives, innovative thinking, and practical abilities, providing sustained intellectual support for the development of green manufacturing in both countries.

Innovation in operational mechanisms: Explore institutional and mechanism innovations across the entire chain, establishing flexible project management mechanisms, open cooperation models, incentives for innovative talents, intellectual property transplantation, and optimized resource sharing mechanisms.

(IV) Scientific Research Projects

At present, the Joint Laboratory has incorporated the following research projects:

One national project, "Construction and Joint Research of the 'Belt and Road' Joint Laboratory on Green Steel Manufacturing between China and Serbia," is currently underway.

Two group-level projects, "Research on the Utilization of Local Mineral Hydrogen-Based Shaft Furnaces in Serbia" and "Investigation on Hydrogen Production Costs and Establishment of a Dynamic Multi-Scale Model for Hydrogen-Based Shaft Furnaces Based on CFD-DEM Coupled Simulation," are currently underway.

One provincial project, "Construction of the 'Belt and Road' Joint Laboratory for Green Steel Manufacturing between China and Serbia and R&D and Application of New Materials for High-Freshness Dual-Phase Steel Outer Plates," is currently underway.

In addition, three 2024 group-level projects carried out in cooperation with the University of Belgrade have been completed with positive results.

Zhou Yongning
HBIS MATERIALS RESEARCH INSTITUTE
No.3, Yangzi Road, Economic and Technological Development Zone, Liangcun, Gaocheng, Shijiazhuang, Hebei Province, P.R. China
Tel: +86 15032596526
Email: zhouyongning@hbisco.com

THE FOUNDATION 'B.SC. ENG. BOŠKO INJAC'

Mirjana Injac

President

Address: 12/9 Vojvoda Radomir Putnik Street,
19216 Brestovačka Banja Bor, Serbia
Phone: + 381 30 77 117, Mobile: + 381 64 265 31 14
Website: www.injac.net

In order to preserve the memory of his father Boško Injac (1946 – 1979), a graduate metallurgical engineer, who was an ambitious and creative student of the Technical Faculty in Bor, and later one of the most promising engineers in the Bor copper mine, attorney Oliver B. Injac, together with other family members, is the patron of the award to the best student of metallurgical engineering study program of the Technical Faculty in Bor, which has been traditionally awarded since 2007.

On this occasion, we should mention all the previous holders of the Charter B.Sc. Eng. Bosko Injac: Dušan Janjić (2007), Milan Georgievski (2008), Slađana Vuleta (2009), Slavko Simov (2010), Vladan Andrejić (2011), Uroš Stamenković (2012), Tatjana Momirović (2013), Ana Angner (2014), Radojica Grekulović (2015), Saša Đorđević (2016), Kristina Božinović (2017), Milko Karanfilovski (2018), Milica Jovkić (2019), Miloš Vuleta (2020), Avram Kovačević (2021), Marina Marković (2022), Aleksandar Nikolajević (2023) and Dalibor Jovanović (2024).

AUTHOR INDEX

A

Achiței Dragoș-Cristian 382
Adamović Dragana 616
Adamović-Marković Dragana 593, 682
Adomniței Ionuț 21, 378
Agop Ştefana 731, 732
Agović Elvis 413
Aksoy Cemalettin Okay 25, 81
Aksoy Güzin Gülsev Uyar 25, 81
Alagić Slađana 624
Alil Ana 704
Amdur Alexey M. 239
Andrejić Vladan 300
Antić Jovana 458
Antonijević Milan 409
Anđić Dimitrije 255, 287
Apostolovski-Trujić Tatjana 620
Arsić Sanela 695
Asanović Vanja 296, 474
Avdušinović Hasan 413
Avrachov Andrej 187
Avramović Ljiljana 260
Avramović Zoran 195, 260, 575
Axinte Mihai 21

B

Bai Chenguang 13
Balanović Katarina 229
Balanović Ljubiša 364, 526
Balaško Tilen 355, 728
Bejinariu Costica 343
Benchea Marcelin 378
Bernevig Mihai-Adrian 351, 382
Bernik Slavko 502
Bianchi Filippo 37
Bijelić Ana 110
Birich Alexander 10
Bogdanović Grozdanka 221
Bolibruchová Dana 438, 454
Božinović Kristina 247, 364, 636, 659, 664
Božić Dragana 260, 498, 502, 575
Božić Dušan 375
Brodarac Zdenka Zovko 405
Bugarin Dejan 65
Bugarin Mile 191, 308
Bugarčić Mladen 255
Buljeta Ivica 405
Bunin Igor Zh. 163
Burduhos-Nergis Diana-Petronela 343
Bădărău Gheorghe 351, 378

C

Casimiro Alberto Hernandez 183
Castellanza Riccardo 37
Cazac Anca 343
Chelariu Romeu 351
Chen Buxin 13
Chen Mao 13
Chicet Daniela Lucia 378, 382
Cimpoeșu Nicanor 21, 351, 378, 382, 732
Cimpoeșu Ramona 351
Ciopec Mihaela 641
Conić Vesna 191, 308, 331
Cruz-Ramírez Alejandro 17, 183, 552
Cárdenas Heriberto Mendoza 17

Ć

Ćosić Salko 494
Ćosović Vladan 430

D

Damjanović Vladimir 568
Dana Bolibruchová 426
Dedić Jasmina 583
De La Cruz Adrian Alberto Castro 386
Diaconu Diana 731
Diaz América Yamile Amaya 386
Dikić Stefan 546
Dimitrievska Iva 579
Dimitrijević Jelena 607
Dimitrijević Oliver 331
Dizdar Dejana 296
Dobersek Albin 187
Dochita Bogdan-Ionut 732
Dojčinović Marina 490
Dolić Natalija 405
Du Changfa 691
Du Yong 243, 691

Đ

Đaić Ivana Zlatanović 624
Đoković Jelena 136
Đorović Živko 291
Đorđević Aleksandar 319, 511
Đorđević Jelena 148, 195, 312
Đorđević Nataša 60, 371
Đorđievski Stefan 323, 593, 616, 674, 678, 682
Đošić Marija 442
Đukić Milos 593
Đukić Miloš 502, 616, 682
Đurović Dijana 277
Đurđević Mile B. 360, 462
Đuga Aleksandar 470

E

Ercegović Marija 607
Erić Milić 33, 171, 560, 603, 645
Erić Suzana 45

F

Farkas László 327, 530
Farkaš Branimir 69
Fedajev Aleksandra 695
Fedorov Sergei A. 239
Feng Peizhong 7
Filipović Radislav 568
Fonović Matej 417
Friedrich Bernd 10
Friesen Alexandra 187
Fu Taibai 243

G

Gao Minglei 167
García-Hernández Margarita 17, 183, 235, 552
Gavrilović Tamara 229
Gigovi-Gekić Almaida 413
Glišić Dragomir 546
Glushchenkov Vladimir 486
Gomilanović Miljan 90
Gorgievski Milan 247, 323, 364, 636, 659, 664
Grekulović Vesna 247, 579, 583, 588, 636, 659, 664
Grgurić Tamara Holjevac 417
Grigorov Aleksandar 599
Grigorova Daniela 269, 599
Grozdanović Milan 136
Grubišić Mirko 371
Grudić Samir 421
Grujić Snežana 442
Guo Xiaolong 281
Gupta Nandita 506
Guševac Sandra 195, 312

H

Halilović Jasmin 494
Hamedović Safet 394
Han Xing 281
Heinicke Felix 199
Hobjâlă Roxana 731, 732
Horozić Emir 583
Hoskan Samil 153
Hrastov Ana 69
Hristov Nikolay 77
Hu Meilong 13
Huang Qi 691
Hubert Artur 199
Hudáková Mária Bali 48, 52, 56
Huseinović Edina 583
Husović Tatjana Volkov 704

I

Ignjatović Snežana 144
Iliev Angel 269
Iliev Petar 225
Imamović Aida 394
Istrate Bogdan 378
Ivaničová Lucia 48, 52, 56
Ivaz Jelena 140, 304

J

Jankovčin Ladislav 515
Janosević Miloš 308
Janošević Miloš 191
Jelić Ivana 45, 60, 255
Jelić Marko 700
Jenkus Dainius 37
Jeremić Dragan 546
Jeremić Marija 564
Jevtović Snežana 624
Ječmenica Milić 546
Ji Heng 167
Jiménez-Romero Teresita del Refugio 17, 183, 235, 552
Jonović Marija 65
Jordanović Jelena 655, 678
Jovanović Aleksandar 255
Jovanović Gvozden 287
Jovanović Ivan 251
Jovanović Ivana 191, 308, 331
Jovanović Milenko 85, 90, 119, 123, 132, 730
Jovanović Nikola 148, 195
Jovanović Rastko 33, 171, 560
Jovanović Sonja 700
Jovanović Zoran 700
Jovović Nina 296
Jovčevski Milica 33, 171

K

Kahraman Bayram 153
Kalinović Jelena 655, 678
Kalinović Tanja 655, 678
Karabaić Damir 421
Karastojković Zoran 542
Kašić Vladan 60
Kazakova Nadezhda 225
Khandelwal Himanshu 506
Kiovský Alexander 48, 52, 56
Klimek Marcin 401
Klimko Jakub 215, 335
Kochanov Alexey N. 163
Koprivica Marija 607
Kores Stanislav 355
Kosec Gorazd 394
Kostadinović Danka 106, 171, 645
Kostic Dragan 568
Kostić Duško 568
Kostov Ana 251
Kovačević Avram 430
Kovačević Renata 611, 620, 669, 674, 678

Kozina Franjo 405
Kožej Ondrej 515
Krammer Andreas 564
Krasteva Maria 712
Kristaly Ferenc 327, 530
Krstić Vesna 611, 669
Kršulja Marko 417, 421
Kržanović Daniel 85, 90, 123, 132, 611, 641, 669
Krúpa Víťazoslav 48, 52, 56
Kumar Manoj 506
Kundráková Klaudia 215, 335

L

Laskov Christine 727
Lavrova Silviya 599
Lazarová Edita 48, 52, 56
Lazić Predrag 175
Lazović Ivan 33, 171, 560, 645
Lehner Markus 564
Lei Rongrong 729
Lekić Nikola 148, 195
Li Jiehua 728
Li Lanjie 167, 281
Li Pengyang 281
Li Renguo 167
Li Shiheng 7
Li Ya 691
Liu Hongqiang 281
Liu Hongqing 13
Liu Zhi 7
Liu Xiaohua 273
Liu Yuling 243, 691
Liverić Lovro 417, 421
Lucheva Biserka 225
Lukovac Sara 277
Luțcanu Marian 21
Lv Xuewei 273

M

Ma Kaihui 13
Magdalinović Srđana 502, 534
Maksimović Miroslava 85, 119
Manasijević Dragan 364, 446, 526, 716
Manasijević Srećko 360, 462
Manojlović Vaso 255
Manole Vasile 382
Mančević Srđan 649
Marilović Dragana 221
Marinković Ana 603
Marinković Nikola 434
Marinković Vladan 85, 119, 123
Maričić Anđela 119
Marjanović Saša 498, 538
Marković Branislav 287
Marković Ivana 430, 446, 526
Marković Jovana Buha 603
Marković Marija 607
Marković Marina 247, 636, 659, 664
Marković Miljan 247, 323, 364, 636, 659, 664
Marković Nevena 195, 312
Marković Zoran 33, 106, 171, 560, 603
Martac Eugeniu 727
Martina Sýkorová 426
Martinović Sanja 704
Maslak Mariusz 401
Matejka Marek 426, 438, 454
Matijašević Srđan 371
Matić Branislava 649
Medić Dragana 624, 632
Medved Jožef 347, 355, 728
Meracheva Gergana 77
Međedović Emina 474
Međedović Milica 127
Mihailović Marija 360, 462
Mihajlović Katarina M. 45
Mihajlović Marija Petrović 409

Mihajlović Slavica 45, 60, 371
Mihalkó Andrea 327, 530
Mikić Ivana 127, 132, 534
Mikić Miomir 85, 123, 127, 132
Miladinović Jelena 511
Milanović Dragan 191, 308, 331
Milivojević Katarina 730
Milić Snežana 260, 624
Milićević Aleksandar 33, 171
Milojković Dragica 434
Milosavljević Aleksandra 700, 721
Milosavljević Aleksnadra 251
Milošević Isidora 716
Milutinović Sandra 132, 534
Miljković Nikola 148
Minić Duško 319
Minić Veljko 319, 511
Mirović Dušica 211
Mishina Olga 187
Mishra Akanksha 37
Mišić Nikola 450
Mišković Žarko 458
Mitovski Aleksandra 187
Mitrović Milijana 430, 498, 522, 538
Mitrović Radivoje 458
Mladenović Milica 603
Mladenović Srba 430, 434, 522, 542
Morales-Ramírez Ángel de Jesús 235, 552
Mravik Željko 700
Muminović Branka 413
Munteanu Corneliu 21

N

Nagode Aleš 728
Nedeljković Milan 430, 434, 446, 522, 538
Negrea Adina 641
Nemes Nicoleta Sorina 641
Nešić Stefan 470
Nicolae Răzvan Mititelu 731
Nikolić Irena 277, 296, 474
Nikolić Jelena 442, 593, 624, 682
Nikolić Vladimir 179
Novaković Jasmina Grbović 474
Novaković Željana 119
Nujkić Maja 632, 678

O

Obradović Ljubiša 534
Obradović Milena 442
Ogawa Yasumasa 678
Oruč Mirsada 394
Oráč Dušan 215, 335
Osmanović Almir 494

P

Pancikiewicz Krzysztof 401
Papludis Aleksandra 624
Patarić Aleksandra 360, 462
Pavlović Marko 490
Pavlović Zlatko 148
Pavlov-Kagadejev Marijana 721
Pejčić Danilo 458
Peng Yingbiao 243, 691
Perišić Snežana Živković 649
Perić Radiša 542
Perušić Mitar 568
Pešić Živana Jovanović 136
Petrov Petar 264
Petrović Aleksandra 674
Petrović Ana 616, 682
Petrović Branislav 144
Petrović Dejan 140, 304
Petrović Jasmina 430, 434, 466, 522, 538
Petrović Jelena 607
Petrović Sanja 534
Pirošková Jana 215

Pop Mihai Alin 21
Popa Mihai 343
Popović Marjan 110
Popović Miljana 511
Popović Miroslav 730
Požega Emina 466, 498, 502, 593, 616
Praščević Momir 450
Protić Milan 110, 450

R

Radichev Petar 73
Radivojević Miljana 6
Radojević Ana 655, 678
Radonjić Branislav 478, 482
Radosavljević Marko 470
Radosavljević-Mihajlović Ana 45, 60, 371
Radovanović Milan 409
Radovanović Mladen 140, 304
Radović Bojan 620, 674
Radović Nenad 546
Radović Žarko 390, 628
Raić Karlo T. 360, 462
Rajić Anđela Mitrović 474
Rajković Radmilo 90, 123, 127, 502
Ranđelović Dragana 287
Ranđelović Dušan 106
Rao Venkateswara 203
Raos Miomir 110, 450
Raykov Petar 712
Reddy Jayapal 203
Reuter Markus A. 3
Rimac Milenko 394
Ristić Nevena 620
Ristić Tamara 300
Roman Ana-Maria 21, 351
Ružić Jovana 375
Růžičková Petra 215, 335

S

Saltykov Pavel 187
Sandu Andrei Victor 343
Sarisan Hasan Berker 25
Savaş Ozan 81
Savić Jasmina 603
Savić Slađana 579, 588
Savić Veljko 442
Sayilgan Emine 316, 686
Schulz Theresa 187
Shi Yuchao 243
Shuai Xiong 691
Simić Marija 607
Simić Marko 375
Simonović Ana 409
Simonović Danijela 611, 669
Singh Kamlesh Kumar 506
Slătineanu Laurenţiu 731
Smiljanić Danijela 287, 442
Smolar Tinkara 347
Sokić Miroslav 255
Sokolović Jelena Gligorijević 466, 502, 616
Stajić Milan 140, 304
Stamenković Uroš 364, 430, 446, 522, 526, 538
Staniewska Katarzyna 727
Stanković Dalibor 579, 588
Stanković Jelena 575
Stanković Sonja 632
Stanković Sunčica 611, 669
Stanković Tanja 65, 331
Stanković Velizar 323
Stankov-Jovanović Vesna 593, 682
Stanley Cristopher 556
Stašić Jelena 375
Stefanova Vladislava 225
Stefanović Jelena 148, 195, 312
Steinacher Matej 347

Stirbu Ioan 382
Stojanovic Jovica 45
Stojanović Anđelka 716
Stojanović Jovica 60
Stojanović Miloš 90, 94, 98, 102, 115, 641
Stojanović Mirjana 490
Stojanović Tanja Marinković 470
Stolić Predrag 700
Stopić Srećko 10, 568
Su Wei 729
Sutic Alexandra Tamara 351
Sutic Tiberiu 732
Svrkota Igor 641
Svrkota Ivan 641
Szeleczki Balázs 327, 530
Sýkorová Martina 438, 454
Sánchez-Vite José Enrique 17, 183, 235, 552

Š

Šabaz Dragan 94, 98, 102, 115
Šerbula Snežana 655
Štefičar Iva 69
Šteharnik Mirjana 611, 669
Štrbac Nada 247, 636, 659, 664
Šutović Željko 546

T

Tadić Milena 296, 474
Tadić Nebojša 277, 296, 390, 628
Talianová Kristína 335
Tamás Bence 327, 530
Tanikić Dejan 136
Tasić Viša 450, 620
Tasić Žaklina 409, 632
Telișcă Marius 21
Tian Renhao 273
Tilvaldyev Shehret 386
Todirică Florin Sorin 382
Todić Slavko 175
Topalović Vladimir 442
Trifunović Vanja 260, 575
Trpčevská Jarmila 215
Trujić Stefan 85, 730
Trumić Biserka 538
Trumić Maja 229
Trumić Milan 179

U

Urošević Daniela 191, 308, 611, 669
Utili Stefano 37

V

Vasiljević Nebojša 568
Vasiljević Sanela 593, 682
Vasková Iveta 515
Vassiliev Valery Pierre 556
Vavrek Pavol 48, 52, 56
Vlahović Milica 157
Vojinović Ivica 94, 98, 102, 115
Vončina Maja 347, 355, 728
Vuković Boško 730
Vuković Jelena 568
Vuković Nikola 255
Vuleta Miloš 300
Vušović Nenad 157
Vučetić Branislava 375
Vučićević Biljana 603

W

Wang Jiangxing 243
Wang Shiwei 167
Wang Xiaohong 7
Wang Yufei 691
Wen Shiyi 243
Wenli Shi 470

X

Xie Ziqing 243

Xing Yi 729

Y

Yang Yuankun 211

Ying Xiangyang 691

You Zhixiong 273

You Yang 273

Yu Shengli 211

Z

Zajdel Paulina 401

Zaneva-Dobranova Efrosima 77

Zdravković Milica 247, 579, 583, 588, 636, 659, 664

Zečević Milena 319, 511

Zhang Baojing 7

Zhang Liang 243

Zhang Patrick 316, 686

Zhang Xinyi 243

Zheng Xiaoyu 691

Zheng Yang 729

Zhmurova Viktoriia 187

Zlatić Milivoje 140, 304

Zlatičanin Biljana 478, 482

Zlatković Igor 291

Ž

Žekić Andrijana 375

Živanović Miloš 148

Živković Marija 560

Živković Nikola 33

Žugić Milodarka 300

IOC M&M 2025

ISBN-978-86-6305-164-5